european society for precision engineering and nanotechnology

Conference Proceedings

24th International Conference & Exhibition

Monday 10th to Friday 14th June 2024

University College Dublin, Ireland

RENISHAW
apply innovation™

euspen

Proceedings of the 24th international conference of the **eu**ropean **s**ociety for **p**recision **e**ngineering and **n**anotechnology

10th – 14th June 2024
Dublin, IE

Editors:
O. Riemer

C. Nisbet
D. Phillips

Internal Review Committee:
A. Archenti
L. Blunt
H. Mainand Durand
O. Riemer
J. A. Yagüe-Fabra

Proceedings of the 24ᵗʰ international conference of the **eu**ropean **s**ociety for **p**recision **e**ngineering and **n**anotechnology

Reviewed by:

Prof. A. Archenti, *KTH Royal Institute of Technology, Sweden*

Assoc. Prof. J.A. Albajez, *University of Zaragoza, Spain*

Dr C. Assis, *Federal Institute of Sao Paulo, Brazil*

Dr C. Bermudez, *Sensofar, Spain*

F. Blateyron, *Digital Surf, France*

Prof. L. Blunt, *University of Huddersfield, UK*

Dr H. Bosse, *Physikalisch-Technische Bundesanstalt (PTB), Germany*

Dr E. Buice, *Lawrence Berkeley National Laboratory, USA*

Dr B. Bulla, *son-x GmbH, Germany*

M. Calaon, *Technical University of Denmark (DTU), Denmark*

Dr S. Catalucci, *University of Padova, Italy*

Prof. K. Cheng, *Brunel University, UK*

Prof. B. Cheung, *The Hong Kong Polytechnic University, Hong Kong*

Dr F. Cosandier, *EPFL, Switzerland*

Dr P. de Groot, *Zygo Corporation, USA*

Prof. F. Ducobu, *UMONS, Belgium*

Dr J. Edelmann, *Fraunhofer IWU, Germany*

Asst. Prof. X. Feng, *Shanghai Jiao Tong University, China*

Prof. M. Galetto, *Politecnico di Torino, Italy*

Prof. A. Gąska, *Cracow University of Technology, Poland*

Prof. R. Goulart Jasinevicius, *University of São Paulo, Brazil*

Dr R. Grejda, *Corning Tropel, USA*

Prof. H. Haitjema, *KU Leuven, Belgium*

Prof. H. Hansen, *Technical University of Denmark (DTU), Denmark*

Dr O. Horejs, *Czech Technical University in Prague, Czech Republic*

Dr M. Janota, *Czech Technical University in Prague, Czech Republic*

Prof. K-N. Joo, *Chosun University, South Korea*

Asst. Prof. E. Kamenar, *University of Rijeka, Croatia*

Jun.-Prof. T. Kissinger, *Technical University of Ilmenau, Germany*

Dr W. Knapp, *Engineering Office, Switzerland*

Dr Y. B. P. Kwan, *Carl Zeiss SMT GmbH, Germany*

Y. J. Lee, *National University of Singapore, Singapore*

Y. Li, *Fine Optical Engineering Research Center, China*

G. Liotto, *Laser Metrology srl, Italy*

Dr S. Lou, *University of Huddersfield, UK*

Dr S. Ludwick, *Aerotech Inc., USA*

Prof. X. Luo, *University of Strathclyde, UK*

Dr H. Mainaud Durand, *CERN, Switzerland*

Dr M. Mareš, *Czech Technical University in Prague, Czech Republic*

Prof. E. Marsh, *Penn State University, USA*

Dr P. Martin, *AWE, UK*

Dr R. Meeß, *Physikalisch-Technische Bundesanstalt (PTB), Germany*

SPONSORING CORPORATE MEMBERS

eu**spen** is grateful for the generous sponsorship of a number of leading companies who set the standard for developments in precision engineering and nanotechnology:

AEROTECH

ASML

BOSCH

Cranfield Precision *fives*

HEIDENHAIN

HEXAGON

IBS Precision Engineering

KEYSIGHT TECHNOLOGIES

MI Partners — PARTNERS IN MECHATRONIC INNOVATION

MICRO-EPSILON

NPL National Physical Laboratory

Precitech

RENISHAW apply innovation™

RENISHAW™
apply innovation™

Your partner for innovative manufacturing

Integrate smart factory automation into your production processes with the help of Renishaw's industrial metrology solutions.

- Process efficiency
- Data-driven manufacturing
- Flexibility

www.renishaw.com/virtualexpo

Foreword

The 24th eu**spen** conference and exhibition will be held at University College Dublin (UCD), Ireland, from June 10th – 14th, 2024.

By way of introduction, over the last three decades Ireland's economy has grown significantly, with particular strengths in sectors such as the manufacture of medical devices, pharmaceuticals, ICT, electronics and food production. The country has the highest employment in high-technology manufacturing in the EU, with almost 30% of manufacturing jobs in high-technology sectors. This level is approximately four times the EU average. As part of the changing profile and image of a 'go green' Ireland, sustainability is at the forefront of many initiatives. This has been built on deep rooted traditions of excellence as exemplified by Arthur Guinness, an Irish brewer, entrepreneur, and philanthropist who founded the Guinness Brewery at St. James's Gate in the heart of Dublin in 1759. Those attending the conference dinner at the Guiness Storehouse, will have the opportunity to find out more about the development of this brewery. Dublin has a particularly strong cultural heritage and was home to many important writers, including Nobel Laureates William Butler Yeats, George Bernard Shaw and Samuel Beckett. Another famous writer is the UCD graduate James Joyce, author of Ulysses.

Established in 1854, UCD is Ireland's largest university with 38,000 students. It is ranked in the top 1% of higher education institutions world-wide. The campus occupies an extensive parkland estate of 133 hectares, making it one of the largest city campuses in Europe. UCD offers world-leading facilities in subject areas such as Science, Engineering, Law, Business and Medicine. This year's eu**spen** conference is being organised in conjunction with the Science Foundation Ireland funded I-Form Advanced Manufacturing Research Centre, which is headquartered at UCD.

The keynotes for eu**spen** 2024 will report on recent developments in enhancing the performance of medical devices, in the application of AI to additive manufacturing, as well as precision manufacturing issues in electric propulsion. The keynote presenters are:

- Prof. Abhay Pandit, Professor in Biomaterials and Scientific Director of a Science Foundation Ireland-funded Centre for Research in Medical Devices (CÚRAM) at the University of Galway, "Dynamic Strategies for Development of Host-Responsive Medical Devices",
- Prof. Andrew Parnell, Hamilton Professor, I-Form Centre Co-PI, Director of the Hamilton Institute at Maynooth University, "Digital Twins and Artificial Intelligence in Precision Additive Manufacturing",
- Davina Maria Di Cara, European Space Agency (ESA), NL. Deputy Manager of the ESA Propulsion Laboratory, "European Space Agency activities on Electric and Micro Propulsion: technology state of the art and needs for precision manufacturing and verification",

This conference and exhibition will provide a leading forum for industrialists and academics alike to review the best of world-wide industrial innovation, progressive research and technology development, with

relevant examples and cases from Ireland. The conference will provide ample scope for strategic networking among attendees from industry and academia and the academic contributions will be supplemented by industrial presentation and a comprehensive technical exhibition show casing leading technologies in the precision engineering sector.

We cordially invite you to UCD, Dublin, and are really looking forward to meeting you there.

Liam Blunt   Denis Dowling
eu**spen** President   Organising committee

Keynotes

Session 1: Digital Manufacturing and Automation in Precision Engineering

Session 2: Metrology

Session 3: Advances in Precision Engineering

Session 4: Mechanical Manufacturing Processes

O4.01   **Real-time motion error compensation in optical surface fabrication using a 2-DOF linear encoder**   **279**

Yan Wei[1,3], Shinya Morita[1,3], Masahiko Fukuta[2], Toru Suzuki[2], Takanobu Akiyama[2], Yutaka Yamagata[3], Takuya Hosobata[3]

[1]*Department of Advanced Machinery Engineering, Graduate School of Engineering, Tokyo Denki University, Japan*
[2]*Machine Tools Company, Shibaura Machine Corp., Japan*
[3]*RIKEN Center for Advanced Photonics, RIKEN, Japan*

O4.02   **Precision plunge grinding with coarse-grained diamond grinding wheel**   **281**

Barnabás Adam[1,2], Oltmann Riemer[1,2], Kai Rickens[1], Carsten Heinzel[1,2]

[1]*Leibniz Institut für Werkstofforientierte Technologien IWT, Laboratory for Precision Machining LFM, Badgasteiner Straße 2, 28359 Bremen, Germany*
[2]*MAPEX Center for Materials and Processes, University of Bremen, Germany)*

O4.03   **Effect of different cutting environments on surface integrity and wear resistance properties of Incoloy 925**   **285**

Shravan Kumar Yadav, Sudarsan Ghosh, Aravindan Sivanandam

Mechanical Engineering Department, Indian Institute of Technology Delhi, New Delhi, India-110016

O4.04   **Thermomechanical impact of the cutting edge microgeometry on the surface properties in turning of aluminium alloys**   **289**

Thomas Junge[1], Thomas Mehner[2], Andreas Nestler[1], Andreas Schubert[1], Thomas Lampke[2]

[1]*Micromanufacturing Technology, Chemnitz University of Technology, Reichenhainer Str. 70, 09126 Chemnitz, Germany*
[2]*Materials and Surface Engineering, Chemnitz University of Technology, Erfenschlager Str. 73, 09125 Chemnitz, Germany*

O4.05   **Benchmarking rapidly solidified aluminium alloys for ultra-precision machining of ultra-violet mirrors and diffractive optical elements**   **293**

D.A. Rolon[1,2], F. Hölzel[2], J. Kober[1], S. Kühne[1], M. Malcher[1], T.K. Naderi, [1], T. Arnold[2], D. Oberschmidt[1]

[1]*Technishce Universität Berlin, department of Micro and Precision Devices MFG, Germany*
[2]*Leibniz Institute of Surface Engineering (IOM), Germany*

P4.01   **Effect of electric fields on micro-scratching of calcium fluoride**   **297**

Yunfa Guo[1], Jiaming Zhan[1]

[1]*Department of Mechanical Engineering, College of Design and Engineering, National University of Singapore*

P4.02   **Advancing sustainable and efficient industrial cleaning: CO_2 snow jet blasting for residue-free surface cleaning**   **301**

E. Uhlmann[1,2], J. Polte[1,2], P. Burgdorf[1], W. Reder[2], J. Fasselt[1]

[1]*Fraunhofer Institute for Production Systems and Design Technology IPK, Germany*
[2]*Institute for Machine Tools and Factory Management (IWF), Technische Universität Berlin, Germany*

Session 5: Non-Mechanical Manufacturing Processes

Session 6: Mechatronics and Machine Tools

Keynotes

Dynamic strategies for development of host-responsive medical devices

Prof. Abhay Pandit

CÚRAM- SFI Research Centre for Medical Devices; University of Galway, IE

Abstract

Contemporary medical device research has shifted its focus from viewing biomaterials as static structures to utilizing functionalization and biofabrication techniques to fine-tune desired responses in both host organisms and implants. A comprehensive understanding of host responses is crucial in formulating effective strategies. To achieve this, transcriptomic- and glyco-proteomics-based methodologies are employed to explore host response insights. Host responses can be manipulated through functionalization strategies that facilitate the attachment of biomolecules to diverse structural motifs. The deliberate organization of biomolecular assembly into higher-order, self-organized systems is crucial for various biological processes and the development of advanced biomaterial systems.

Biography

Abhay Pandit is the Established Professor in Biomaterials and Scientific Director of a Science Foundation Ireland-funded Centre for Research in Medical Devices (CÚRAM) at the University of Galway. Prof. Pandit has developed the next generation of reservoir delivery vehicles with high payload capacity, programmable degradation profiles, and built-in gradients of physical, chemotropic, and protective cues, which facilitate spatiotemporal localised sustained delivery of multiple biomolecules to target injury mechanisms at the molecular and cellular levels, with thrust on glycobiology. He is the author of 28 patents and licenced four technologies to medical device companies. He has published over 348 manuscripts, including esteemed journals, such as Science Translational Medicine, PNAS, Science Advances, Nature Communications, Biomaterials, and other notable high-impact publications. He has been honoured with the esteemed *George Winter Award 2022*, *the Chandra P Sharma Award 2023*, and the *Biomaterials Advances Innovation Award 2023* for his research contributions to biomaterials. He is also a fellow of the American Institute for Medical and Biological Engineering (AIMBE), Tissue Engineering, and Regenerative Medicine International Society (TERMIS), Irish Academy of Engineering, and International Union of Societies for Biomaterials Science and Engineering (IUSBSE).

Digital Twins and Artificial Intelligence in Precision Additive Manufacturing

Prof. Andrew Parnell

Maynooth University, IE

Abstract

Precision additive manufacturing (AM) stands out as a transformative approach, offering unparalleled capabilities to produce intricate and customized products. In my talk I will discuss into the symbiotic relationship between Digital Twins — virtual replicas of physical assets — and Artificial Intelligence (AI) in enhancing AM processes. The convergence of these advanced technologies facilitates real-time monitoring, predictive maintenance, and dynamic response to changes during the production process.

Biography

Andrew Parnell is Hamilton Professor and Director of the Hamilton Institute at Maynooth University. His research is in statistics and machine learning applied to a wide variety of scientific areas. He has co-authored over 100 peer-reviewed journal and conference papers, including in Science, Nature Communications, Nature Plants, and Proceedings of the National Academy of Sciences, and has contributed foundational methodology in journals such as Statistics and Computing, Knowledge-Based Systems, and Environmetrics. He has been awarded over €3 million to date in direct funding as PI or Co-PI, and has been involved in grants totalling over €65 million as PI/collaborator. He is currently a principal investigator in the SFI I-Form Advanced Manufacturing Centre working on closed-loop control and the design of digital twins for additive manufacturing processes using artificial intelligence.

European Space Agency activities on Electric and Micro Propulsion: technology state of the art and needs for precision manufacturing and verification

Davina Maria Di Cara

European Space Agency (ESA), NL

Abstract

Europe has extensive heritage in developing Electric and Micro Propulsion technologies for Spacecraft. Recent European successes include several GEO Telecommunication satellites like ARTEMIS, AlphaSAT, Eurostar E3000, Spacebus 4000, SmallGEO, Spacebus NEO and Eurostar NEO, the ESA's SMART-1 mission to the Moon, the ESA's GOCE Earth Gravity mission and the ESA-JAXA BepiColombo mission to Mercury.

Ongoing developments target next generation GEO telecommunication satellites, large constellations of Telecommunication and Earth Observation small satellites in Low Earth Orbits, Galileo 2nd Generation Navigation constellation, Next Generation Gravity mission, Mars Sample Return and several Cubesat missions.

Electric and Micro Propulsion are considered as a strategic technology to enable mobility in space, to increase competitiveness and enhance or even unlock emerging space applications.

The European Space Agency, the European Commission, the National Space Agencies, and European Industry are working together to mature this technology via on-ground qualification and in-orbit demonstration, to improve performance and reliability, to significantly reduce prices, to increase production volume and to establish/retain leadership.

This keynote will present the state of the art of the Electric and Micro Propulsion technology in Europe, elaborate on future mission needs and technology gaps, trends and opportunities with focus on the needs for precision manufacturing and verification.

Biography

Davina Di Cara graduated in Aerospace Engineering in 2003 from Politecnico di Torino in Italy. In 2004, she started working at ESA/ESTEC as Young Graduate Trainee and, since 2006, she works at ESTEC as Electric Propulsion Engineer. Davina has contributed to several ESA projects as expert electric propulsion engineer and has managed several R&D contracts targeting development of electric propulsion technologies at different power levels, from requirements definition, though preliminary and critical design assessment, up to complete ground qualification and flight readiness. She has also tested several electric propulsion systems at the ESA Propulsion Laboratory.

At present, in addition to technically managing various R&D contracts, Davina is the ESA propulsion senior expert for the GALILEO G2A project, the coordinator of the ESA Harmonisation Roadmap on electric propulsion and cubesat propulsion technologies and the Deputy Manager of the ESA Propulsion Laboratory.

Session 1: Digital Manufacturing and Automation in Precision Engineering

Surface roughness monitoring and prediction based on audible sound signal with the comparison of statistical and automatic feature extraction methods in turning process

Yaoxuan Zhu[1], Amir Rashid[1], Tomas Österlind[1], Andreas Archenti[1]

[1]KTH Royal Institute of Technology, Department of Production Engineering, Manufacturing and Metrology Systems Division, 11428, Sweden

Yaoxuanz@kth.se

Abstract

In the turning process, the surface roughness of the machined part is considered a critical indicator of quality control. Provided the conventional offline quality measurement and control is time-consuming, with slow feedback and an intensive workforce, this paper presents an online monitoring and prediction system for the effective and precise prediction of surface roughness of the machined parts during the machining process. In this system, the audible sound signal captured through the microphone is employed to extract the features related to surface roughness prediction. However, owing to the nonlinear phenomena and complex mechanism causing surface quality in the whole process, the selection of statistical features of the sound signal in both the time and frequency domains varies from one case to another. This variation may lead to false prediction results as sufficient domain knowledge is required. Therefore, the versatile and knowledge-independent features extraction method is proposed, which exploits deep transfer learning to automatically extract sound signal features in the time-frequency domain through pre-trained convolution neural networks (pre-trained CNN). The performance of prediction models based on two feature extraction methods – statistical feature extraction and automatic feature extraction was further tested and validated in the case study. The results demonstrate that the performances of the prediction model built on the automatically extracted features outperformed that developed with the statistical feature method concerning the accuracy and generalization of the prediction model. In addition, this study also provides solid theoretical and experimental support for developing a more precise and robust online surface quality monitoring system.

Keywords: Data-driven monitoring, surface roughness prediction, transfer learning, audible sound, automated feature engineering

1. Introduction

During the machining process, the surface quality monitoring system has huge potential for online detecting and predicting surface roughness, which is regarded as a fundamental indicator of surface quality control of machined workpieces. To improve prediction performance of such system, various sensing techniques have been applied and investigated [1]. Due to easy access and low cost, the application of audible sound signals captured via a microphone has attracted more attention to the development of machining monitoring systems [2]. However, the main challenge is how to extract hidden information characteristics from the sound signal that correlates to surface roughness. An approach to tackle this is based on feature engineering – feature extraction. Although varied feature extraction methods have been independently discussed, the performance comparison of them under a unified dataset has, to the authors' knowledge, not been studied and published.

2. Methodology

To quantify the performance comparison of different feature extraction scenarios, a methodology is proposed and demonstrated as in the flowchart shown in **Figure 1**. Firstly, the raw sound signal in the time domain was recorded during the experiment (detailed description in **Section 3**) for each cutting test. Afterwards, it was divided into constant time interval length (10 s) blocks with corresponding surface roughness (R_a) measurements. The surface roughness was used as the

prediction label. To enlarge the amount of dataset for model training and testing, each collected 10 s sound signal was further subdivided into segments with three different time lengths (1 s, 5 s, and 10 s), determining the total amount of dataset. Following this, each subdivided segment was separately analysed and converted into a frequency domain by power spectrum density (PSD) and time-frequency domain in the form of a generated 2D RGB image (256x256x3) - spectrogram by short-time Fourier transformation (STFT).

To acquire hidden information characteristics of sound signal correlated to the surface roughness, two feature extraction scenarios are proposed and compared. In the statistical feature-based scenario, features of the sound signal segment in both time and frequency domains were extracted from defined statistical features shown in **Table 1**. As a mature convolution neural network (CNN) architecture, VGG16 was employed to achieve automated feature extraction in this case, which was initially developed for object recognition by Oxford's Visual Geometry Group (VGG) and then widely applied to transfer learning tasks. In transfer learning-based scenarios, each generated spectrogram was fed into pre-trained VGG16 [3], in which its architecture was modified by removing the top two layers - the fully connected and classification layer and other layers were reserved and equipped with pretrained weights acquired in the training process of ImageNet dataset. Two feature groups of each spectrogram were respectively generated from nontrainable VGG16 with fixed original pre-trained weight in each layer and from trainable VGG16, in which all weights were fine-tuned during the training process.

Features extracted based on different scenarios associated with corresponding surface roughness were used as input data. They were split into training data (70% of all data), validating data (20% of all data) and testing data (10% of all data) for the establishment of two prediction models: support vector regression (SVR) and artificial neural networks (ANN). During the training process, Bayesian optimization [4] was used for automatic hyper-parameters tuning and mean squared error (MSE) was utilized as the loss function. Iterative runs resulted in a well-trained model with optimal hyper-parameters to obtain predicted surface roughness values.

Figure 1. Flowchart of methodology.

Table 1. The type of statistical features (8 types in total) extracted from sound signal in the time domain (TDA) and frequency domain (PSD).

Statistical Feature	Formula ($\mu = \frac{\sum_{i=1}^{N=i} x_i}{N}$, $\sigma = \sqrt{\frac{\sum_{i=1}^{N=i}(x_i-\mu)}{N}}$)	Extracted Sound feature
Maximum	$f1 = max|x_i|$	$S1_{TDA}^i, S1_{PSD}^i$
Minimum	$f2 = min|x_i|$	$S2_{TDA}^i, S2_{PSD}^i$
Root means square	$f3 = \sqrt[2]{\sum_{i=1}^{N}\frac{x_i^2}{N}}$	$S3_{TDA}^i, S3_{PSD}^i$
Peak to peak	$f4 = f1 - f2$	$S4_{TDA}^i, S4_{PSD}^i$
Energy	$f5 = \sum_{i=1}^{N=i}\frac{|x_i|^2}{N}$	$S5_{TDA}^i, S5_{PSD}^i$
Skewness	$f6 = \frac{\sum_{i=1}^{N=i}(x_i-\mu)^3}{(N-1)\sigma^3}$	$S6_{TDA}^i, S6_{PSD}^i$
Kurtosis	$f7 = \frac{\sum_{i=1}^{N=i}(x_i-\mu)^4}{(N-1)\sigma^4}$	$S7_{TDA}^i, S7_{PSD}^i$
Entropy	$f8 = -\sum_{i=1}^{N=i} p(z_n)\log_2 p(z_n)$	$S8_{TDA}^i, S8_{PSD}^i$

3. Case study

The experiment was conducted to collect data containing surface roughness and sound signals in dry turning operation in a CNC lathe (SMT Swedturn 300) without significant background noise. The workpiece material is the hardened and tempered tool steel - Toolox33. The workpieces are cylindrical bars with a length of 550 mm and a diameter of Ø124 mm. The tooling system incorporates the insert (CNMG 12 04 08-PM 4425, Sandvik Coromant) with a nose radius (RE) of 0.8 mm and the tool holder (DCLNL 2525M, CoroTurn). During the machining process, two cutting parameters, cutting speed (320 and 280 m/min) and feed rate (0.4, 0.3 and 0.2 mm/rev), were set as variable factors to develop a Taguchi orthogonal experiment with six parameter combinations. The depth of cut was constant at 1 mm. Under each parameter combination, the test was replicated twice, in which the workpiece was machined from one run to another with the total cutting length 480 mm per run until flank wear of the cutting tool reached 0.3 mm as standard tool worn-out criteria, which was measured through the digital microscope (Dino-lite RK-10A). During each cutting run, the audible sound signal was captured through a microphone (Microtech GEFELL MKS 211) located at the turret, which was later processed by a data acquisition system (Siemens LMS SCADAS Mobile SCM01) with a 40 kHz sampling frequency. Subsequently, the captured signal was subdivided into each single segment with constant time interval (10 s) as each sampling area (seg.1, seg.2 …) where corresponding surface roughness – R_a (referred as arithmetic average value of surface roughness) were measured three times by profilometer (Mitutoyo SJ-210) at different angles (0°, 120°, 240°) around the cylinder bar then averaged as the input label to the prediction models, see **Figure 2**.
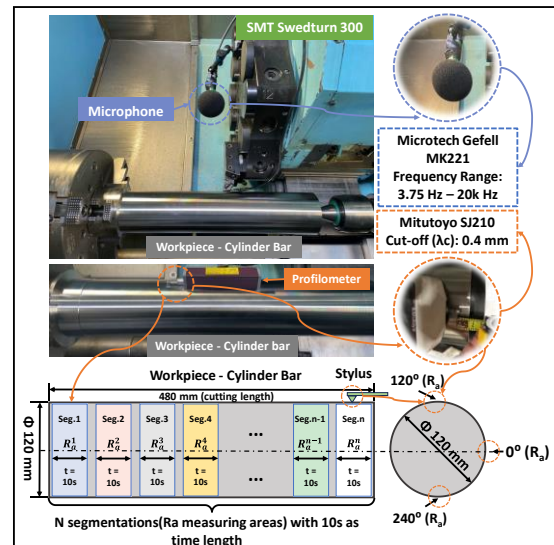
Figure 2. Experiment setup and surface roughness (R_a) measurement.

42

4. Numerical results analysis and discussion

The performance metrics were employed to estimate and compare the accuracy and reliability of two predictors: support vector regressor (SVR) and artificial neural networks (ANN) used for surface roughness prediction. The proposed metrics include means absolute error (MAE), mean square error (MSE), relative error (ER), average value and standard deviation of prediction accuracy, and coefficient of determination (R^2), which are described in Eqs. (1)-(6), respectively, where y_i denotes the actual value of measured or observed surface roughness collected in the experiment, $\hat{y}_i$ expresses the predicted surface roughness value as each single output of applied predictor, and n represents the total amount of testing data.

$$MAE = \frac{1}{n}\sum_{i=1}^{n}|y_i - \hat{y}_i| \qquad (1)$$

$$MSE = \frac{1}{n}\sum_{i=1}^{n}(y_i - \hat{y}_i)^2 \qquad (2)$$

$$Relative\ error = \left|\frac{(y_i - \hat{y}_i)}{y_i}\right| \qquad (3)$$

$$\overline{Accuracy} = \frac{1}{n}\sum_{i=1}^{n}\left(1 - \left|\frac{(y_i - \hat{y}_i)}{y_i}\right| \times 100\%\right) \qquad (4)$$

$$STD(Accuracy) = \sqrt{\frac{\sum_{i=1}^{i=n}(Accuracy_i - \overline{Accuracy})^2}{n}} \qquad (5)$$

$$R^2 = 1 - \frac{\sum_{i=1}^{n}(y_i - \hat{y}_i)}{\sum_{i=1}^{n}(y_i - \overline{y}_i)^2} \qquad (6)$$

Based on defined performance metrics, the surface roughness prediction performance of two predictors was quantitatively measured and compared on the testing dataset with different feature extraction scenarios from two aspects. Firstly, in each predictor, prediction performance was compared under three distinct feature extraction scenarios when sound signal segments were at the same time interval. Secondly, in each feature extraction scenario, the performance of each predictor was further analysed under sound signal segments with different time interval lengths.

As seen in **Figure 3**, when SVR was chosen as the prediction model, the application of input features extracted via trainable VGG16 from the sound signal segment with all three different time interval lengths (1 s; 5 s; 10 s) provided the superior prediction performance, as measured by MAE (0.10; 0.13; 0.24), MSE (0.03; 0.04; 0.12), average prediction accuracy (96.1%; 94.6%; 89.6%), and R^2 (0.97; 0.95; 0.86). These results were tightly followed by the SVR model trained with input features extracted from nontrainable VGG16, while the SVR model developed with statistical features rendered the worst prediction performance estimated and analysed with all defined performance metrics. Besides, the same conclusion is also reflected in **Figure 4**, which depicts the relative error distribution of predicted data points. With the lowest average value (3.9%; 5.4%; 10.4%) and narrowest range of relative error, the SVR model coupled with features extracted from trainable VGG16 presented the lowest prediction error regardless of time interval lengths (1 s; 5 s; 10 s) of sound signal segments applied for feature extraction. Moreover, as shown in **Figure 5** and **Figure 6**, similar behaviour occurred in the ANN model. Features extracted via trainable VGG16 achieved the best prediction performance exerting sound signal segments in all three varied time interval lengths, which can be verified with lowest MAE

(0.09; 0.15; 0.21), MSE (0.02; 0.05; 0.08), average relative error (3.4%; 5.9%; 8.7%), highest prediction accuracy (96.5%; 93.6%; 90.8%) and R^2 (0.97; 0.61; 0.90). Additionally, the exception appeared in the performance comparison between features extracted from nontrainable VGG16 and statistical features, which was different from the SVR model. When sound signal segment with 1 s and 10 s time interval lengths, it was concluded that the ANN model combined with features from nontrainable VGG16 outperformed the ANN model trained with statistical features. Nonetheless, when sound signal segments with 5 s time interval length were employed, this conclusion was the opposite: that the ANN model developed with statistical features achieved better performance than features extracted from nontrainable VGG16.

Within each feature extraction scenario, the influence of sound signals with different time interval lengths on the performance of each prediction model was further compared. In both SVR and ANN, features obtained from sound signal segments with shorter time interval lengths were prone to offer better prediction performance. One exception appeared in the ANN model trained with features extracted from nontrainable VGG16, that sound signal segments with 5 s and 1 s time intervals provided almost the same prediction performance as illustrated in **Figure 4** & **Figure 6**.
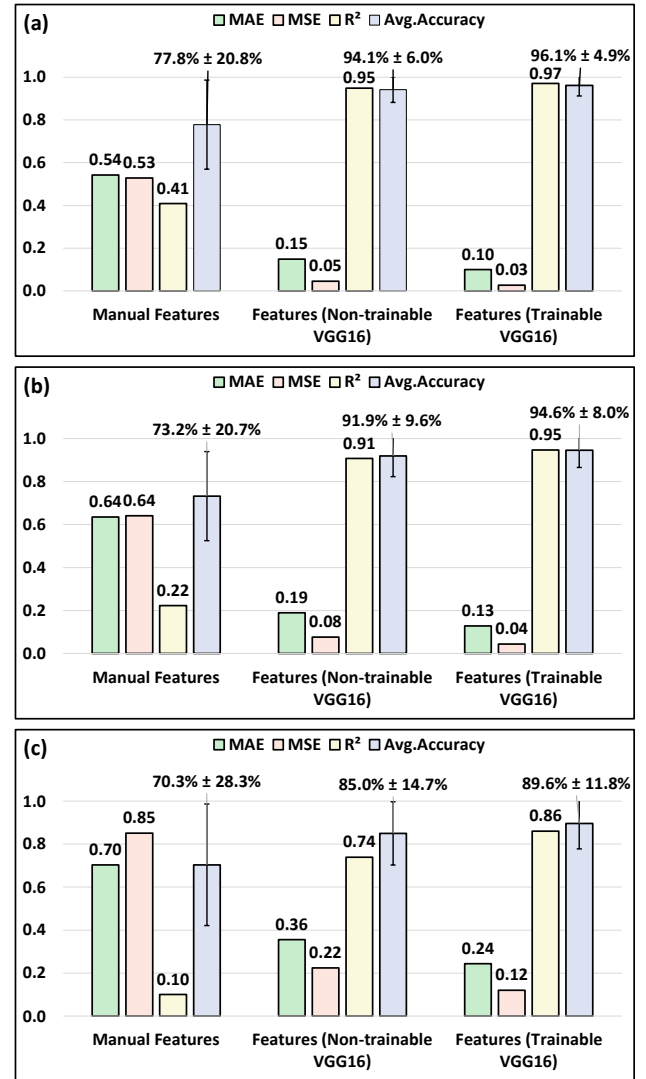
Figure 3. Performance metrics of prediction results based on multiple feature extraction methods from SVR as a predictor; (a): 1 s time length

of the sound signal as input data; (b) 5 s time length of the sound signal as input data; (c) 10 s time length of the sound signal as input data.
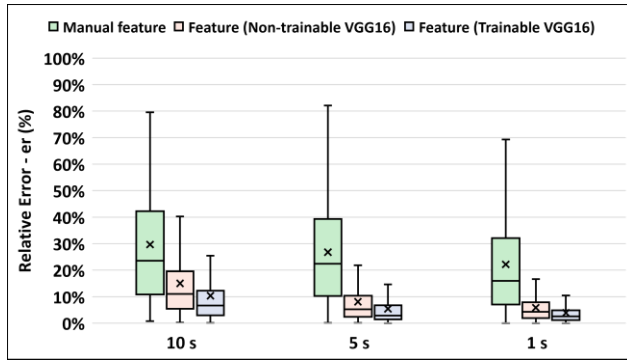
Figure 4. Relative error - er (%) of surface roughness prediction in SVR based on different feature extraction scenarios as input data with different time interval lengths of sound signal segments.

Figure 5. Performance metrics of prediction results based on multiple feature extraction methods from ANN as predictor; (a): 1 s time length

of the sound signal as input data; (b) 5 s time length of the sound signal as input data; (c) 10 s time length of sound signal input data.

Figure 6. Relative error - er (%) of surface roughness prediction in ANN based on different feature extraction scenarios as input data with different time interval lengths of sound signal segments.

5. Conclusion

This paper proposes a novel approach to verify and compare the influence of varying feature extraction scenarios applied to the sound signal segment with different time interval lengths, including (1) statistical features from both the time and frequency domain of sound signal, (2) automated features directly extracted from sound signal spectrograms via nontrainable pre-trained VGG16 and (3) automated features extracted from sound signal spectrograms via trainable or fine-tuned pre-trained VGG16 on performances of surface roughness (R_a) prediction in two predictors – support vector regression and artificial neural networks. The overall results indicate that compared with statistical features, the automated feature enables the extraction of more valuable hidden information characteristics from the sound signals, representing a stronger correlation to the final prediction target – surface roughness. Based on its superior performance, automated feature engineering is conducive to the establishment of a surface quality monitoring system in terms of improved prediction accuracy, generalization, and versatility with a low requirement for domain expertise in the condition of a large dataset. Given that only one pre-trained CNN was applied in this case, future work will be focused on the exploration of other more advanced pre-trained CNNs, including but not limited to ResNet, Inception-ResNet and vision transformer.

References

[1]   K. He, M. Gao, and Z. Zhao, "Soft Computing Techniques for Surface Roughness Prediction in Hard Turning: A Literature Review," *IEEE Access*, **vol. 7**, pp. 89556–89569, 2019, doi: 10.1109/ACCESS.2019.2926509.

[2]   P. J. Papandrea, E. P. Frigieri, P. R. Maia, L. G. Oliveira, and A. P. Paiva, "Surface roughness diagnosis in hard turning using acoustic signals and support vector machine : A PCA-based approach," *Appl. Acoust.*, **vol. 159,** p. 107102, 2020, doi: 10.1016/j.apacoust.2019.107102.

[3]   C. Chung *et al.*, "Published as a conference paper at ICLR 2015 VERY DEEP CONVOLUTIONAL NETWORKS FOR LARGE-SCALE IMAGE RECOGNITION Karen," *Am. J. Heal. Pharm.*, **vol. 75**, no. 6, pp. 398–406, 2018.

[4]   V. Nguyen, "Bayesian optimization for accelerating hyper-parameter tuning," *Proc. - IEEE 2nd Int. Conf. Artif. Intell. Knowl. Eng. AIKE 2019*, **pp. 302–305**, 2019, doi: 10.1109/AIKE.2019.00060.

Compact lever actuated direct driven 6-DoF parallel kinematic positioning system

Tillmann Volz[1], Paul Binder[1], Philipp Ritter[1], Christian Sander[1]

[1]*Physik Instrumente GmbH & Co.KG.*

T.Volz@PI.de

Abstract

In recent years, parallel kinematic machines (PKM) with sub-micrometer precision and six degrees of freedom, also known as hexapods, have seen a significant increase in demand, attesting to their growing importance in various sectors. Certainly, in the field of photonics alignment and wafer level applications, hexapods have the potential to play a significant role in future production lines. However, in industrial production, reliability, robustness and high dynamics are mandatory in order to reduce downtime and increase throughput, while the machine must maintain its high precision over an extended period of use. Therefore, Physik Instrumente GmbH Co. KG (PI) has developed, built, and qualified a functional model of a direct driven compact 6-DoF PKM that aims at enabling superior performance regarding reliability and dynamics compared to available compact spindle driven hexapods. In the developed system, the rotational motion of a motor shaft is directly translated to a circular foot point motion of six struts with constant length and five degrees of freedom using a lever arm attached to the shaft. This direct coupling of the motor rotation and top platform position enables highly dynamic motion, while the mechanical complexity of the machine and thus costs and wear and tear can be reduced. This paper focuses on a detailed description of the PKM design as well as a qualification regarding precision and dynamics to identify the potentials and challenges of direct driven hexapods based on lever actuators for industrial scale use.

Automation, Hexapod, Positioning, Precision

1. Introduction

Physik Instrumente GmbH & Co.KG. (PI) is a leading supplier of high precision positioning systems, including parallel kinematic machines, that are widely used in research facilities and a variety of industries such as automotive, photonics, semiconductors or astronomy. An ever-growing demand for high-precision 6-DoF PKM is driven especially by alignment and scanning applications that become more and more important in the photonics industry on an industrial scale. This generates a demand for compact, highly dynamic and robust systems for 6-DoF high precision positioning [1]. However, available compact spindle driven 6-DoF PKM are limited in their ability to perform motions at high frequencies and amplitudes as shown by Rudolf et al. [2]. Further, small amplitude trajectories at high frequency cause accelerated wear and tear in spindle driven machines limiting the potential in applications mentioned above. More promising candidates are direct driven PKM that provide not only higher accelerations and velocities but are also superior in terms of wear and tear thanks to a simple mechanical design. Systems using flexure hinges like the H-860 from PI [2] or the T-Flex hexapod [3] however, are rather inappropriate for an integration in industrial production lines, mainly due to their size necessary to enable usable workspaces. Motivated by the said, PI has developed a direct driven, compact 6-DoF PKM sized comparable to available compact spindle driven hexapods, aiming at high dynamic and precision applications to enable improved throughput and minimal downtime.

2. Design

The design of the newly developed lever actuated 6-DoF positioning machine (shown in fig. 1) is based on the principle of parallel kinematics. The system exists of six actuators arranged in parallel between a top and base platform. While the base platform is fixed, the top platform can be moved laterally and rotationally (X, Y, Z, pitch, roll, yaw).
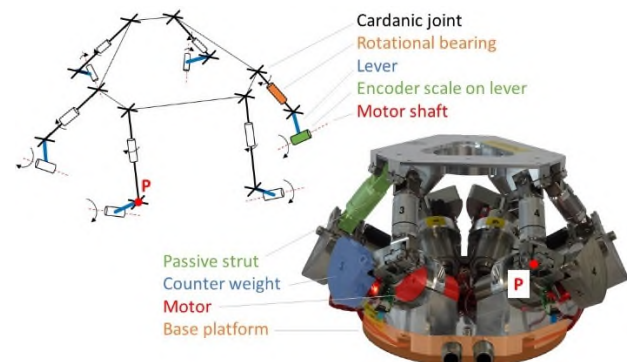
Figure 1. Lever actuated direct driven 6-Dof positioning system (line model on the left and picture on the right)

The actuators of the system are integrated in the base platform and consist of brushless BLDC motors with ceramic bearings and levers attached to the end of the motor shafts. In this setup, no sensor or power cables are moved and thus, no parasitical forces impaire the systems performance. The lever at the end of the motor shaft is connected to the top platform via passive struts with 5 degrees of freedom (two universal joints and one rotational joint). By rotating the levers, the lower strut points (marked *P* in figure 1) are moved along a circular path enabling the motion of the top platform. The position of the levers is determined using a scale opposite to the lever (figure 2). In addition, counterweights are attached to the levers that compensate the weight of the top platform and strut in the

initial position. The two universal joints in the passive struts were newly developed for the functional model. While they have to be compact and enable large joint angles for large travel ranges, they have to be light and free of backlash. While ball joints are compact and enable large joint angles, friction and hysteresis effects make them not convenient for high precision positioning. Compact flexure joints however, are hysteresis free but are limited in possible joint angles. Consequently a sub-compact cardanic joint with crossing axes and four ball bearings was developed (figure 2) that is free of backlash and enable the necessary large joint angles. Beside the universal joints, the passive struts contain another high precision rotational bearing to enable the rotation between the upper and lower joint around the struts longitudinal axis.
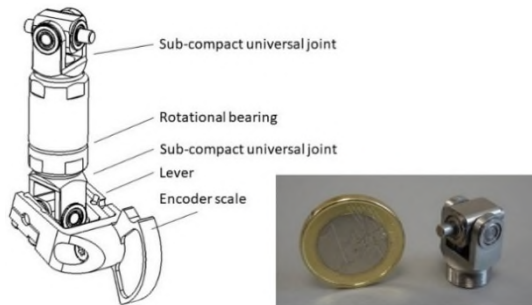
Figure 2. Passive strut with universal joints without axis offset

3. Specifications

The length of the passive struts and levers were choosen to achieve a workspace comparable to the spindle driven 6-DoF PKM H-811 from PI. The exact travel range is listed in table 1. While possible travel in X- and Y-direction is smaller for the functional model, the travel range in Z-direction is larger. Rotations around the X- and Y- axis are the same compared to the H-811 whereas the possible rotation around the Z-axis is about half. The maximum speed of the functional model was measured at about 65 mm/s with counterweights which is about six times faster than a H-811. Due to the lack of the spindle, the payload is significantly smaller compared to the H-811, however, sufficient for most alignment tasks. A summary of the systems specifications is listed in the following table 1.

Table 1. Specifications of the compact lever actuated PKM

Specification	Value
Height	104 mm
Diameter	188 mm
Translation (X, Y, Z)	±9.5 mm
Rotation (U, V, W)	± 10 mm
Payload	200 g
Maximum speed	65 mm/s
Theoretical z-resolution @ Z= -9.5 mm	27.8 nm
Theoretical z-resolution @ Z = 9.5 mm	13.6 nm
Bidirectionale Repeatability (X, Y, Z)	< 1 µm

It is to mention, that the theoretical resolution of the hexapod depends on the lever position (maximum and minimum values for pure Z motion in table 1). Along the sensor scale, it is constantly about 20 nm.

4. Technological Performance

To determine the resolution (minimal incremental motion or MIM) the system can perform consistently and reliable steps in closed loop. In this qualification the hexapod executed ten steps with different step widths around the initial position. The

resolution is at its worst around initial position. Figure 3 shows the result of 50 nm steps in Z-direction determined with an interferometer. The same measurements were performed for motions in the X- and Y-direction. While the steps are clearly visible in figure 3, noise is present when the hexapod is not moving which is expected to be caused either by the position sensors or the single axis controls. Similar results were determined for the X- and Y- axis. Summed up, in all directions, a MIM of < 100 nm is possible with the system which is comparable to the performance of the H-811.
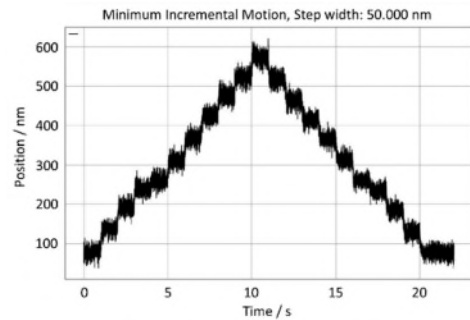
Figure 3. 50 nm steps in Z-direction around the initial position

Further, a frequency analysis was performed for a comparison to a H-811. The following figure 4 shows the amplitude error and the phase offset for different amplitudes (20 µm, 10 µm, 5 µm, 2 µm and 1 µm) and frequencies (10 Hz, 15 Hz, 20 Hz, 25 Hz and 30 Hz). The comparison (direct driven hexapod on the left and H-811 on the right) shows that the direct driven hexapod is superior in both, the phase offset and amplitude error, compared to the H-811 hexapod.
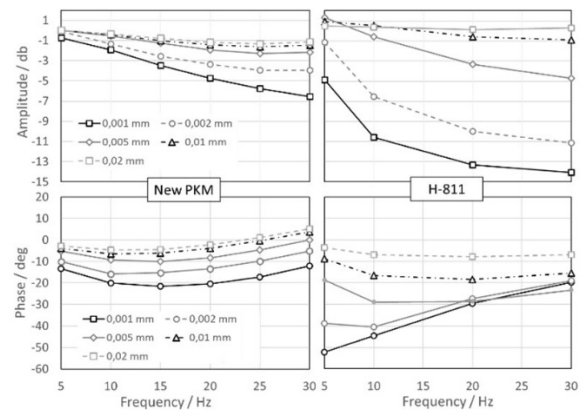
Figure 4. Comparison of frequency analysis (amplitude error and phase offset; left: direct driven hexapod; right: H-811)

5. Conclusion and Outlook

The newly developed functional model of a 6-Dof parallel kinematic lever actuated system shows very promising results regarding fast motion with small amplitudes as required in many alignment applications. However, beside first good results, lifetime tests have to prove robustness and a MIMO control is necessary to use the full potential of the system.

References

[1] Sander C et al. 2018 Development of High-Precision Parallel Kinematics for Industrial Automation and Silicon Photonics, Proc. Of the 18th Int. Conf. of the euspen
[2] Rudolf C et al. 2015 Direct Driven Hexapods for Highly Dynamic 6DoF Applications, Proc. Of the 15th Int. Conf. of the euspen
[3] Naves M et al. 2020 T-Flex: A large range of motion fully flexure-based 6-DOF hexapod, Proc. Of the 20th Int. Conf. of the euspen

An adaptive deep learning based approach to classification and labelling of image data from Additive Manufacturing

Xiao Liu1[1,2], Alessandra Mileo[1,2,3] and Alan F. Smeaton[2,3] (Fellow, IEEE)

[1]*I-FORM SFI Centre for Advanced Manufacturing, Dublin City University, Glasnevin, Dublin 9, Ireland*
[2]*School of Computing, Dublin City University, Glasnevin, Dublin 9, Ireland*
[3]*Insight SFI Centre for Data Analytics, Dublin City University, Glasnevin, Dublin 9, Ireland*

e-mail: alessandra.mileo@dcu.ie

Abstract

Advances in computer vision and in-situ monitoring, facilitated by visual sensors, enable the acquisition of extensive image datasets from the additive manufacturing (AM) process. These datasets hold significant potential for improving the quality of AM through the application of machine learning techniques. Despite the increased availability of such data, subsequent data analytics such as classification and labelling, are typically manual which does not scale and allows errors as a result of the manual process.

This paper provides a deep learning model developed for classification of image data from the AM process, along with the relevant methodology for training, labelling and associated experiments. We present an approach that employs a convolutional neural network (CNN) based classifier in combination with transfer learning and active learning strategies and we explore the minimum number of labelled images required to achieve convergence during the training process, with a focus on optimising data efficiency. Our classifier serves as a robust foundation, allowing further advances in the labelling mechanism which involves leveraging semi-supervised learning techniques with the integration of human-in-the-loop. This approach augments and refines the labelling process, capitalising on the strengths of both automated learning and human supervision to further enhance the accuracy of the labelling, the performance of the model and the applicability of our approach in the domain of additive manufacturing.

Keywords: 3D printing, artificial intelligence, classification, neural network

1. Introduction

Given rapid developments in data collocation in the domain of Additive Manufacturing (AM), the datasets developed from such collected data have potential for determining the quality of the manufactured output and the detection of defects through the use of Machine Learning (ML) during the manufacturing process. However, rather than concentrating on the method for data collection, this paper focuses on the processing and utilization of image data in ML applications which support AM.

Large and open-source datasets of annotated images containing up to millions of training examples such as ImageNet [1] which contains more than 14 million annotated images and COCO (Common Objects in Context) [2] which contains more than 200 000 labelled images, have allowed machine learning to develop hugely in recent years. This is partly due to the fact that the datasets are open, easily available and re-used by many researchers. However, to create such datasets specific to the domain of AM is still difficult because acquiring process monitoring data with annotations is cost-prohibitive in AM as shown by Manan and Shao [3]. A recent survey on the topic of image datasets [4] clearly states that sample images from the AM process, labelled with annotations of microstructure defects in the manufacture, are often difficult, expensive, and time-consuming to obtain, which creates challenges in the application of vision-related machine learning in AM.

In many practical situations, collocated image data from AM processes have a limited number of properly labelled samples and a large volume of unlabelled samples. Some researchers have named this situation the ``Small Data Challenge in Big Data

Era'' [5]. Consequently, it is desirable to have a machine learning methodology that can begin with the utilisation of the small number of labelled samples then further leverage the large number of unlabelled data to develop more labelled samples from unlabelled images. This helps to improve the performance of the ML model to achieve higher accuracy.

To overcome the challenge of providing a neural network model with limited labelled data samples, we present a method that applies transfer learning and fine-tuning on a convolutional neural network (CNN)-based neural network model to achieve improved classification on the image samples. Then, based on the outcome of the initial classification model, our methodology then involves active learning algorithms, which identifies the most informative data samples for the model to learn from as a higher priority. This reduces the number of labelled samples required in the training process. Finally, by utilising the combination of an active query strategy and a semi-supervised learning technique with Human-In-The-Loop (HITL) features, we perform automatic labelling using the model to generate larger datasets of labelled images from unlabelled samples.

2. Background knowledge

Transfer learning is a method that performs training a neural network model using data from a source domain then later applying the trained model to a target domain, different from the source. This allows rapid progress in re-training and significantly reduces the required number of training samples in the target domain. This is commonly used in computer vision tasks such as classification to support improved performance in domains which are data-poor. In recent years, transfer learning

has proved to be effective in the task of defect classification in AM, such as the work presented in [6] and [7] where transfer learning and fine-tuning were applied to training a CNN based neural network architecture.

Active learning [8] is a technique for labelling data that selects and prioritises the most informative data points for an annotator to label. Such prioritised data points have the highest potential impact on the supervised training of a machine learning model, thus improving the overall training process. The combination of transfer learning and active learning allows leveraging small amounts of labelled data to improve the performance of the training process.

Semi-Supervised Learning [9] leverages both labelled and unlabelled data to improve model performance. Among Semi-Supervised Learning techniques, Pseudo-Labelling [10], stands out as a simple but highly efficient method, which can be summarised in 3 distinct stages:

1. Using available labelled data, build an initial model.
2. Generate pseudo labels for the unlabelled data using the model.
3. Further train the model using both the original labels and pseudo labels. This additional training phase fine-tunes the model based on the augmented dataset.

However, it has 3 major drawbacks and limitations as follows:

1. If the initial model is poor or biased, pseudo-labels may also be inaccurate, leading to a propagation of errors.
2. Significant distribution mismatches between classes in the training may lead to the class imbalance issue.
3. The lack of feedback or correction mechanisms for mistakes on labels brings a risk of noise amplification.

Methods to apply these techniques in our approach and approaches to address related problems are illustrated in the next section.

3. Method

Our methodology involved the creation of a CNN-based initial model for classification followed by active learning-assisted training and semi-supervised labelling, with human supervision.
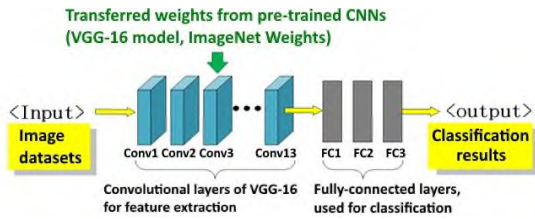
Figure 1. Architecture of our model based on VGG 16 and fully connected layers.

3.1. CNN based initial model

Our CNN based initial model relies on transfer learning in which 13 convolutional layers from a pre-trained VGG16 model [11] are used for feature extraction, the weights having been trained using ImageNet data. After the convolutional layers, 2 fully-connected layers with a ReLU activation function are added followed by 1 fully-connected layer as the output layer using Sigmoid as the activation function, since the targeted dataset is divided into 2 classes for binary classification. The architecture of this CNN based initial model is shown in Figure 1. The implementation was conducted using Python 3, Keras and scikit-learn machine learning packages within the Google Colab environment.

3.2. Fine-tuning with image datasets

To investigate the adaptability of the CNN-based model, 3 datasets with 8 different types of patterns have been tested individually by applying fine-tuning on the model. The 3 image datasets are emission images [12], DAGM patterns [13] and images from Selective Laser Sintering (SLS) [8]. Figure 2 shows examples of patterns from each dataset.
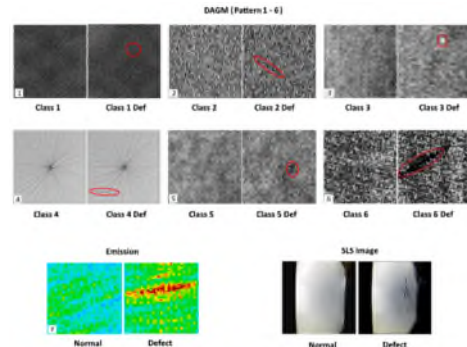
Figure 2. Examples of patterns from emission, DAGM and SLS

The emission image dataset is developed from the emission data collected by the InfiniAM monitoring suite from a Renishaw 3D printer during printing of Ti6Al4V parts. After post-processing, the dataset consists of 150 negative and 150 positive samples.

The DAGM dataset is inspired by problems from industrial image processing, where automatic visual defect detection has the potential to reduce the cost of quality assurance significantly. The DAGM datasets involves 6 different patterns while each pattern is divided into 2 classes: defect (150 samples) and normal (1000 samples). This dataset offers support to test the adaptability of our deep learning approach in the early stages when large-scale annotated image datasets are not available in the AM domain [14].

The SLS dataset contains 4,000 images, manually divided into 2 defect detection classes. The images in this dataset are separated into 3 subsets for training (2,000), testing (1,000) and validation (1,000). The dataset is used in later stages of our research on active learning assisted training and semi-supervised learning labelling.

Table 1. hyperparameters used for the training/tuning of the deep learning model

Name	Type/Value	Description
Optimizer	Adam, SGD, RMSprop	Optimizers are used to change the attributes of the neural network to reduce the losses
Loss function	binary cross entropy	Loss function computes the quantity that a model should seek to minimize during training
Learning rate	10^{-2} to 10^{-5}	The step size at each iteration while moving toward a minimum of a loss function during the training process
Batch size	4, 32, 64	The number of training samples utilized in one update of the model's parameters.
Evaluation metric	Accuracy, Loss	Function to judge the performance of the model

During the fine-tuning process of the model, combinations of hyperparameters are investigated through multiple tests using different settings. Tuning hyperparameters involves adjusting the optimiser, learning rate, batch size and training epochs. We use 3 optimisers namely Adaptive Moment Estimation (Adam), Stochastic Gradient Descent (SGD) and Root Mean Square Propagation (RMSprop) in combination with different ranges of learning rate, batch sizes and training epochs. The cost function

used in all tests is binary cross entropy. The tested values for the hyperparameters during the tuning process with relevant descriptions for each are shown in Table 1. Moreover, to combat overfitting, we introduced weight regularisers to the two dense layers employing the ReLU activation function, as previously mentioned. We applied weight decay regularisation, also referred to as L2 regularisation, which calculates the sum of squared weights. The hyperparameter tuning for weight decay regularisation spanned a range from 10^{-1} to 10^{-4} and was tested multiple times until overfitting issues no longer surfaced during training and validation. This tuning process aimed to keep a balance between model complexity and generalisation ability, ensuring the model's robustness.

Classification results on different image patterns are presented in Table 2. It is worth noting that the relationship between hyperparameters and performance is problem-dependent, and the effectiveness of a specific hyperparameter, such as batch size, can vary for different datasets and models.

Table 2. Classification results from the CNN based model with transfer learning and fine-tuning

Patterns	Avg. Val Accuracy	Avg. Val Loss	Training (epochs)
Emission	0.981	0.03	200
DAGM1	0.964	0.09	200
DAGM2	0.983	0.03	200
DAGM3	0.962	0.10	200
DAGM4	0.965	0.09	200
DAGM5	0.982	0.04	200
DAGM6	0.959	0.09	200
SLS	0.979	0.05	200

3.3. Active learning to further optimise training

With the setting up of the CNN based classifier model that effectively uses domain transfer principles across the additive manufacturing image datasets, our research makes progress to extend beyond conventional training methodologies. The active learning approach introduced a query strategy to the training of the classification model, enabling it to iteratively improve its performance by strategically selecting and labelling the most informative data samples to be used. This iterative approach allowed us to make efficient use of the labelled data and to optimise the performance of the model through active data selection. This approach was conducted through a series of steps, performing a structured and iterative approach with the following key stages: (1) active sample section, (2) query for label, (3) train with queried sample, and (4) validate for current query iteration. The cycle iterates until a human supervisor decides to complete the training phase when validation accuracy achieves a target level. Here we apply a pool-based sampling scenario and an uncertainty sampling query strategy [8]. This is the most commonly used query strategy to start generalised sampling on AM image datasets. In our previous work [15], this approach has been proven as highly sample-efficient on the SLS image dataset by Westphal *et al*. [7] during training of the model and achieves an accuracy level of over 98% in validation. This query strategy is also utilised in the development of our semi-supervised labelling method to address class imbalance and assist on the feedback mechanism with HITL.

3.4. Labelling using semi-supervised learning with HITL

The labelling mechanism involves leveraging semi-supervised learning techniques with the integration of HITL features, aims to augment and refine the labelling process by capitalising on the strengths of both automated learning and human supervision. This further enhances the accuracy of labelling, the performance of the model and the applicability of the approach

in the domain of additive manufacturing defect detection. Our proposed labelling approach can be summarised into the following 4 steps: (1) Generate pseudo-label using the trained classifier. (2) Active selection according to uncertainty and human correction on the incorrect labelled samples in the selected pseudo-labels. (3) Create a new training batch by re-sampling to address the class imbalance issues then update the classifier using the training batch. (4) Evaluate the performance of the updated classifier on the rest of the pseudo-labelled data and the original validation dataset.

3.5. Class imbalance issue

When the labels obtained for model training are a significant distribution mismatch between classes, the trained models show a bias towards the majority class. Consequently, instances belonging to the minority class tend to misclassify at a greater rate. This is particularly problematic when the class of interest corresponds to the minority class. In AM datasets, defects mostly show within the minority subset of the total data population. For this reason, when forming a new set of training data from the results of pseudo-labelling, the class imbalance problem should be considered in order to avoid over emphasis on the major class.

To address this issue, we present an approach that combines uncertainty sampling with image data augmentation. This method places a strong emphasis on selecting the most informative samples, by identifying instances where the model exhibits uncertainty in its predictions. These informative samples are then systematically re-sampled using image data augmentation techniques, including transformations such as rotation, scaling, flipping, and cropping according to the relevant data structures. The objective is to generate a diverse set of new samples while preserving spatial correlations and image quality. This approach stands out as more preferable compared to synthetic image data generation, especially in the context of additive manufacturing, where data reliability and fidelity are extremely important.

4. Experimental results

In this section, we introduce our experimental process encompassing the labelling mechanism specifically focusing on an imbalanced dataset that developed from the SLS dataset. The sequence commences with the generation of pseudo labels utilising the initial classifier. Subsequently, active sample selection and human correction steps are employed to curtail the count of incorrectly assigned pseudo labels. Following this correction phase, the rectified samples are re-sampled to create a balanced batch, which is then used to further fine-tune the classifier.

4.1. Experiments on the imbalanced dataset

Experiments are conducted to evaluate the performance of our approach on an imbalanced dataset. The imbalanced dataset is derived from the testing dataset, which initially consisted of a balanced set of 500 defect samples and 499 normal samples (out of the 500 normal samples, one image was corrupted). For the imbalanced dataset, we randomly selected 101 defect samples from the original dataset and combined them with the 499 normal samples, resulting in a new dataset with an imbalanced distribution totalling 600 samples. After initial classification on all the testing data to obtain pseudo-labels, the relevant classification results are shown in Table 3 and the ROC curve is shown in Figure 3.

Table 3. Results of pseudo labelling on the imbalanced dataset

Accuracy	Precision	Recall	F1	ROC-AUC
0.982	0.917	0.980	0.947	0.997

In the initial classification task to obtain pseudo-labels, from the confusion matrix, there are only 2 samples from the minority class and 9 samples from the majority class, which are the defect and normal class respectively, that are incorrectly labelled yielding 11 mistakes out of the total of 600

4.2. human correction and re-sampling

As further investigation, we conducted active sample selection based on the uncertainty sampling method and queried for 50 samples that are calculated as the most informative for human correction. The uncertainty sampling and human supervision results in 2 samples from the true defect class and 2 from the true normal class to be corrected. Thus, after human correction, all the defect samples are correctly labelled in this particular labelling process.
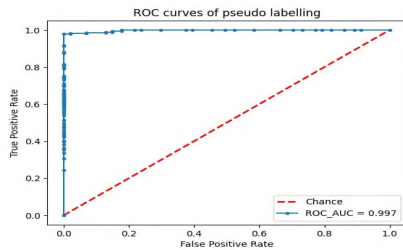
Figure 3. The ROC curves of the pseudo labelling using initial model

To address the class imbalance issue within the selected 50 samples, we conducted an examination of the class distribution of the samples which revealed that 10 samples belong to the minority class (defect), while the remaining 40 samples were from the majority class (normal). To achieve a balance between the two classes, we applied oversampling by augmenting the 10 minority class samples while retaining only the first 20 most informative samples from the majority class using an uncertainty sampling strategy. The 40 balanced samples were then added to the training data for further updating the model. To check the change in performance, the classification results on the validation dataset using the updated model are shown in Table 4.

Table 4. Results of the updated model on the validation dataset compared to the initial model

Classifier	Accuracy	Precision	Recall	F1	ROC-AUC
Initial	0.978	0.984	0.972	0.978	0.993
Updated	0.989	0.992	0.986	0.989	0.995

While our model enhances classification accuracy, it is worth noting that the absolute improvements obtained may appear relatively small due to the fact that the initial accuracies of the baseline are already quite high. Nevertheless, our primary objective was to demonstrate how HITL features can further enhance the performance of the classification model, even when starting from a high baseline level.

Using this updated classification model, we performed auto labelling again on the remaining imbalanced testing dataset, the labelling performance is shown in Table 5. Since there is no mislabelling in the minority class, the value of recall is 1 which means for this particular dataset, all the defect samples have been correctly classified. As this is a computer vision-based ML application for classification on images datasets, the results are based on ML models for classification using features extracted from the AM process, such as power bed defects in SLS. The condition of the powder significantly influences the performance of SLS sintered parts, making machine learning applications for monitoring powder bed conditions highly promising for defect detection, manufacturing efficiency, and non-destructive quality assurance.

Table 5. Evaluation of pseudo labelling on the imbalanced dataset using updated model

Accuracy	Precision	Recall	F1	ROC-AUC
0.989	0.929	1.00	0.963	0.999

5. Conclusion

This paper presents an approach that performs computer vision-based classification and labelling on image data from the additive manufacturing process. We use a CNN-based classifier in combination with transfer learning, active learning strategies and semi-supervised learning to overcome the small data challenge. We achieved accurate classification in different pattens and labelling work on an SLS image dataset. In future work we plan to further investigate the sampling strategies for active learning and to refine the labelling method.

References

[1] Jia Deng et al. "Imagenet: A large-scale hierarchical image database". In: *2009 IEEE Conference on Computer Vision and Pattern Recognition.* IEEE. 2009, pp. 248–255.

[2] Tsung-Yi Lin et al. ''Microsoft coco: Common objects in context''. In: *European Conference on Computer Vision*. Springer. 2014, pp. 740–755.

[3] Manan Mehta and Chenhui Shao. ''Federated learning-based semantic segmentation for pixel-wise defect detection in additive manufacturing''. In: *Journal of Manufacturing Systems* **64** (2022), pp. 197–210.

[4] Xiangli Yang et al. ''A survey on deep semi-supervised learning''. In: *IEEE Transactions on Knowledge and Data Engineering* (2022).

[5] Guo-Jun Qi and Jiebo Luo. ''Small data challenges in big data era: A survey of recent progress on unsupervised and semi-supervised methods''. In: *IEEE Transactions on Pattern Analysis and Machine Intelligence* **44**.4 (2020), pp. 2168–2187.

[6] X. Liu, A. Smeaton and A. Mileo, ''An adaptive human-in-the-loop approach to emission detection of Additive Manufacturing processes and active learning with computer vision. '' In: *2022 IEEE International Conference on Big Data (Big Data)*, Osaka, Japan, (2022) pp. 4021-4027.

[7] Erik Westphal and Hermann Seitz. ''A machine learning method for defect detection and visualization in selective laser sintering based on convolutional neural networks''. *Additive Manufacturing* **41** (2021), p. 101965.

[8] Burr Settles. *Active Learning Literature Survey*. Computer Sciences Technical Report 1648. University of Wisconsin–Madison, 2009.

[9] Jesper E Van Engelen and Holger H Hoos. ''A survey on semi-supervised learning''. *Machine Learning* **109**.2 (2020), pp. 373–440.

[10] Dong-Hyun Lee et al. "Pseudo-label: The simple and efficient semi-supervised learning method for deep neural networks". In: *Workshop on Challenges in Representation Learning, ICML*. Vol. **3**. 2. Atlanta. 2013, p. 896.

[11] Jia Deng et al. "Imagenet: A large-scale hierarchical image database". In: *2009 IEEE Conference on Computer Vision and Pattern Recognition.* IEEE. 2009, pp. 248–255.

[12] Xiao Liu. "Emission images defect samples". In: figshare (Oct. 2022). DOI: 10.6084/m9.figshare.21280104.v1. URL: https://figshare.com/articles/dataset/emission images defect samples/21280104.

[13] Deutsche Arbeitsgemeinschaft für Mustererkennung e.V., German Chapter of the IAPR URL: https://conferences.mpi-inf.mpg.de/dagm/2007/prizes.html

[14] Xiao Liu, Alessandra Mileo, and Alan F. Smeaton. *A Systematic Review of Available Datasets in Additive Manufacturing.* 2024. arXiv: 2401.15448 [cs.CV].

[15] Liu, X., Mileo, A. and Smeaton, A. F. (2023) "Defect Classification in Additive Manufacturing Using CNN-Based Vision Processing". *Irish Machine Vision and Image Processing Conference 2023 (IMVIP2023),* Zenodo.

Non-destructive measurement method for internal surface roughness based on a magnetic tool and machine learning model

Jiong Zhang[1,2]* and Wenwen Tian[1,3,4]

[1]Department of Mechanical Engineering, Faculty of Engineering, National University of Singapore, 9 Engineering Drive 1, Singapore 117575, Singapore
[2]Department of Mechanical Engineering, College of Engineering, City University of Hong Kong, 83 Tat Chee Avenue, Kowloon Tong, Hong Kong SAR, China
[3]School of Automation and Electrical Engineering, Lanzhou Jiaotong University, Lanzhou 730070, China
[4]School of Mechanical Engineering, Xi'an Jiaotong University, Xi'an 710049, China

*Corresponding author's Email address: jiongz@u.nus.edu

Abstract

Surface quality evaluation of internal surfaces is vital while challenging. In this paper, we proposed a novel and non-destructive method for internal surface roughness measurement based on a magnetic tool and a data-driven model named fuzzy broad learning system (FBLS). The magnetic tool is placed on the workpiece's inner surface and dragged by an external magnet. The force between the tool and the workpiece is recorded and used as input for the FBLS. FBLS combines the logical reasoning ability of a fuzzy system with the self-learning ability of a neural network. It is suitable for nonlinear and uncertainty modelling, and the computational efficiency is high. Experiments show that this method is suitable for workpieces with surface roughness (Ra) larger than 1 μm and its average measurement error is only 10.1%, which is adequate for the quality control of most engineering surfaces. This method may be further applied to surface quality evaluation of additively manufactured internal surfaces and complex channels.

Keywords: surface roughness; internal measurement; machine learning; magnetic tool; force signal

1. Introduction

Internal surfaces are widely used in daily life and industries. Representative examples include the tubes in aeroengines, sanitary pipes in the semiconductor industry, conformal cooling channels in precision moulds, manifolds in automobiles, waveguides in communication devices, etc. These internal surfaces are commonly seen as excellent carriers for gas, fluids, or electromagnetic waves [1–3]. The surface quality of these internal surfaces significantly affects their service performance [4,5]. However, there are limited methods to measure the surface finish of these internal surfaces because conventional measurement tools, e.g., a stylus probe or a microscope, cannot access the enclosed space. The most commonly used method is to cut the sample and expose the internal surface so that conventional measurement devices can be employed, which, however, is a typical destructive measurement method. In terms of the tubes with large diameters, the stylus probe can be inserted into them and conduct the profile scanning. Alternatively, an endoscope can also be put inside a tube to measure the profile via white-light interferometry [6]. Some researchers converted the internal measurement to external measurement by a silicone replica [7]. This method is only suitable for some simple tubes and still needs the assistance of a profilometer or a confocal microscope. Regarding more complex components with small openings, X-ray computed tomography (X-ray CT) can be used to obtain their volumetric information via scanning, reconstruction, and data visualization [8,9]. The reconstructed 3D model of the component contains the surface topography information of the internal features. However, the resolution of existing X-ray CT is usually larger than 5 μm and the operating expense is extremely high. Another indirect and non-destructive evaluation method for the surface quality of pipes is by analyzing the acoustic emission (AE) signal which is generated by the flowing liquid [10]. The surface state, either rough or smooth, can be distinguished by comparing the extracted features of the AE signal. Nevertheless, it is impossible to provide an accurate value of the surface roughness. Therefore, a reliable, precise, low-cost, and non-destructive measurement method needs to be developed to tackle the challenge in surface quality evaluation of internal surfaces. In this paper, an indirect measurement system based on a magnetic tool and a fuzzy broad learning model is proposed. A sphere magnet is put inside the workpiece. An external magnet is used to drive the sphere magnet to slide on the surface to be evaluated. A dynamometer is employed to record the force signal, which will be the input data into a developed fuzzy broad learning system (FBLS). This FBLS system will return the surface roughness value of the workpiece.

2. Methodology

2.1 Measurement principle

The working principle of the proposed internal measurement method (hardware and software) is illustrated in Figure 1. In the hardware setup, the workpiece tube is mounted on a dynamometer which can measure the force exerted on the workpiece. A sphere magnet is placed inside the workpiece and an external magnet is used to drive the sphere magnet. The linear motion of the sphere magnet will produce a normal force (Fn) and a friction force (Ff) which will be recorded by the dynamometer. The force measured by the dynamometer is then sent to a fuzzy broad learning system (FBLS) [11] to generate the surface roughness data.
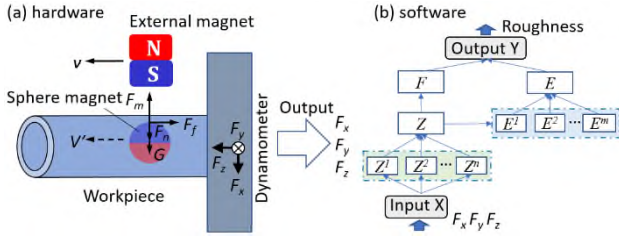
Figure 1. Working principle of the developed internal measurement technique: (a) schematic of the hardware and (b) the proposed FBLS

2.2 The developed fuzzy broad learning system (FBLS)

The basic architecture of FBLS is shown in Figure 1(b). Suppose that the FBLS consists of n fuzzy subsystems and m enhancement node groups, in which there are K_i fuzzy rules in the ith fuzzy subsystem, and there are L_j enhancement neurons in the jth enhancement node group. Given a training sample data set is represented as $S = \{X, Y\}$, $X = [x_1, x_2, \cdots, x_N]^T \in \mathbb{R}^{N \times M}$ and $Y = [y_1, y_2, \cdots, y_N]^T \in \mathbb{R}^{N \times 1}$ represent the input data and target output, respectively where $x_s = [x_{s1}, x_{s2}, \cdots, x_{sM}]$, $s = 1, 2, \cdots, N$. N represents the number of training samples and M is the dimension of features for input data.

At first, the input $x_s = [x_{s1}, x_{s2}, \cdots, x_{sM}]$ is mapped to the ith fuzzy subsystem by using the first-order Takagi-Sugeno-Kang (TSK) fuzzy system. The fuzzy if-then rule in the ith fuzzy subsystem can be represented as:

if x_{s1} is A_k^i, x_{s2} is A_{k2}^i, …, and x_{sM} is A_{kM}^i, then one can get $z_{sk}^i = f_k^i(x_{s1}, x_{s2}, \cdots, x_{sM})$, where $k = 1, 2, \cdots, K_i$.

The consequent part of the kth fuzzy rule can be defined by Eq. (1):

$$z_{sk}^i = \sum_{t=1}^M \alpha_{kt}^i x_{st} \tag{1}$$

where α_{kt}^i are randomly generated coefficients from a uniform distribution [0,1].

For the ith fuzzy subsystem, the fire strength of the kth fuzzy rule is given by Eq. (2):

$$\pi_{sk}^i = \prod_{t=1}^M \mu_{kt}^i(x_{st}) \tag{2}$$

where μ_{kt}^i is the Gaussian membership function corresponding to a fuzzy set A_{kt}^i, which is denoted by Eq. (3):

$$\mu_{kt}^i(x_{st}) = e^{-\left(\frac{x_{st} - c_{kt}^i}{\sigma_{kt}^i}\right)^2} \tag{3}$$

where c_{kt}^i and σ_{kt}^i represent the center and width of the Gaussian membership function, respectively. For the ith fuzzy subsystem, the K-means method on the training sample input data is used to obtain K_i clustering centers, which are used to initialize the centers c_{kt}^i of the Gaussian membership function. And for all fuzzy subsystems, the value of σ_{kt}^i is set to 1.

After that, the weighted fire strength of each fuzzy rule can be computed using Eq. (4):

$$\lambda_{sk}^i = \frac{\pi_{sk}^i}{\sum_{k=1}^{K_i} \pi_{sk}^i} \tag{4}$$

Before defuzzification by the TSK fuzzy subsystem, the intermediate output vector of the ith fuzzy subsystem for the sth training sample can be expressed by Eq. (5):

$$z_s^i = [\lambda_{s1}^i z_{s1}^i, \lambda_{s2}^i z_{s2}^i, \cdots, \lambda_{sK_i}^i z_{sK_i}^i] \tag{5}$$

And the intermediate output matrix of the ith fuzzy subsystem for all training samples can be denoted by Eq. (6):

$$Z^i = [z_1^i, z_2^i, \cdots, z_N^i]^T \tag{6}$$

Therefore, the intermediate output matrix for all fuzzy subsystems can be shown by Eq. (7):

$$Z = [Z^1, Z^2, \cdots, Z^n] \tag{7}$$

After that, the intermediate output matrix Z is fed into the enhancement nodes for nonlinear transformation. Then, the output matrix of the enhancement layer can be represented by Eq. (8):

$$E = [E^1, E^2, \cdots, E^m] \tag{8}$$

where $E^j = \psi(ZW_e^j + \beta_e^j)$, $j = 1, 2, \cdots, m$. W_e^j and β_e^j are the weights and bias terms respectively, which are randomly generated from [0, 1] with proper dimensions. ψ is an activation function and is usually set as a hyperbolic tangent function ($tanh$).

Since the defuzzification output of each fuzzy subsystem and the output of the enhancement layer are transmitted to the top layer together, the defuzzification output of the ith fuzzy subsystem for the sth training sample can be expressed by Eq. (9):

$$F_s^i = \sum_{k=1}^{K_i} \lambda_{sk}^i z_{sk}^i = \sum_{k=1}^{K_i} \lambda_{sk}^i \left(\sum_{t=1}^M \omega_k^i \alpha_{kt}^i x_{st}\right) =$$
$$\sum_{t=1}^M \alpha_{kt}^i x_{st} [\lambda_{s1}^i, \lambda_{s2}^i, \cdots, \lambda_{sK_i}^i] \begin{bmatrix} \omega_1^i \\ \omega_2^i \\ \vdots \\ \omega_{K_i}^i \end{bmatrix} \tag{9}$$

where the parameter ω_k^i is introduced to adjust the kth fuzzy rule, and can be defined by Eq. (10):

$$\omega^i = [\omega_1^i, \omega_2^i, \cdots, \omega_{K_i}^i]^T \tag{10}$$

The above formula can be simplified to Eq. (11):

$$F_s^i = z_s^i \omega^i \tag{11}$$

For all training samples, the defuzzification output of the ith fuzzy subsystem is Eq. (12):

$$F^i = [F_1^i, F_2^i, \cdots, F_N^i]^T = Z^i \omega^i \tag{12}$$

Then, the defuzzification output of all fuzzy subsystems can be aggregated by Eq. (13):

$$F = \sum_{i=1}^n F^i = ZW_F \tag{13}$$

where $W_F = [\omega^1, \omega^2, \cdots, \omega^n]^T$.

In the end, the defuzzification output F of all fuzzy subsystems and the output E of enhancement node groups will be concatenated into a matrix to obtain the final output of FBLS, which can be expressed by Eq. (14):

$$\hat{Y} = F + EW_E = ZW_F + EW_E = [Z \quad E] \begin{bmatrix} W_F \\ W_E \end{bmatrix} \tag{14}$$

where W_E denotes the weight matrix from the enhancement layer to the top layer.

Let $H = [Z, E]$, $W = [ZW_F, W_E]^T$, Then $\hat{Y}$ can be abbreviated by Eq. (15):

$$\hat{Y} = HW \tag{15}$$

Given the actual training target Y, the weight matrix W from the hidden layer to the final output layer can be calculated by ridge regression using Eq. (16):

$$W = (H^T H + \lambda I)^{-1} H^T Y \tag{16}$$

in which I denotes an identity matrix with proper dimensions and λ is a nonnegative constant for regularization.

3. Experiments and validation

3.1 Experimental setup

A measurement setup (Figure 2) is built based on the schematic in Figure 1(a). An external magnet is fixed on the moving axis of a three-axis automatic stage (Sherline Products Inc). The workpiece is an Al6061 plate with milled grooves to simulate the internal surface of a tube. It is mounted on a fixture connecting a dynamometer (Kistler 9256C). A sphere magnet with an 8-mm diameter is placed on the groove. Due to the magnetic force, the sphere magnet can be driven to slide on the groove surface while the dynamometer records the force interactions simultaneously. It should be noted that the dynamometer may be replaced by cheaper and portable sensors (e.g., acceleration/vibration sensors) in practical applications.
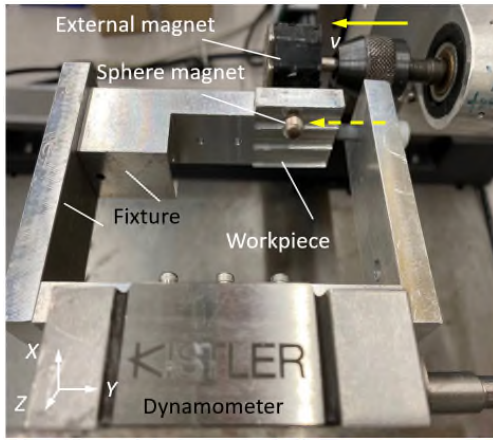
Figure 2. Experimental setup for data acquisition

3.2 Workpiece preparation and data acquisition

Totally 8 workpieces are prepared by end milling at a Makino V55 vertical milling machine. Three grooves are cut in each workpiece and a total of 23 grooves are machined (one groove failed due to tool breakage). The milling parameters i.e., spindle speed, feed rate, and tool wear condition, are varied to generate grooves with a large range of surface finish. Specifically, the varying of tool wear conditions is achieved by using milling tools with different VB values. After milling, the groove surfaces are scanned by a laser confocal microscope (Olympus LEXT OLS5000) and the surface roughness Ra is measured with a cut-off length of 0.25 mm. Three measurements are conducted for each groove. The resultant surface roughness ranges from 0.193 μm to 9.787 μm, covering the typical finish of engineering surfaces [12].

To acquire the force signal for the developed FBLS, the sphere magnet is driven to slide on the groove for 20 mm with a feed rate of 100 mm/min. And the corresponding force is recorded by the dynameter with a sampling frequency of 50 kHz. The parameters of the data acquisition process are listed in Table 1.

Table 1. Parameters of the data acquisition process for surface roughness measurement

Parameters	Values
External magnet	NdB G50 block magnet 20 mm × 10 mm × 6 mm
Sphere magnet	NdB G35 sphere magnet with 8 mm diameter
Workpiece	A6061 Aluminium plate, 8 pcs, and 23 grooves
The gap distance (mm)	5
Scratching distance (mm)	20
Feed rate (mm/min)	100
Sampling rate (kHz)	50
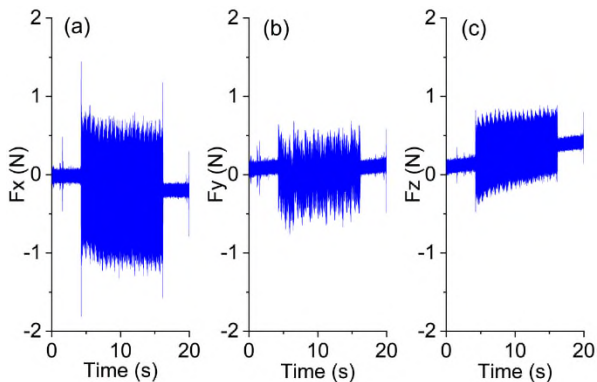
Figure 3. Segmentation of the force signal: (a) Fx, (b) Fy and (c) Fz

3.3 Pre-process of the collected force data

The X, Y, and Z force signals are effectively segmented by removing the near-zero sections at the beginning and the end, as shown in Figure 3. Besides, 8 representative time-domain features are extracted from the force signals in the three directions of X, Y, and Z, respectively, as the input of the model, with a total of 24 features, as shown in Table 2.

Table 2. Time-domain features of the force signals

No.	Feature	Equation
1	Absolute average	$X_u = \frac{1}{n}\sum_{i=1}^{n}|x_i|$
2	Variance	$X_{var} = \frac{1}{n}\sum_{i=1}^{n}(x_i - \bar{x})^2$
3	Standard deviation	$X_{std} = \sqrt{Xvar}$
4	Peak-to-Peak value	$X_{pv} = max(x_i) - min(x_i)$
5	Kurtosis	$X_{kur} = \frac{\sum_{i=1}^{n}(x_i-\bar{x})^4/n}{\left[\sum_{i=1}^{n}(x_i-\bar{x})^2/n\right]^2}$
6	Skewness	$X_{ske} = \frac{\sum_{i=1}^{n}(x_i-\bar{x})^3/n}{\left[\sum_{i=1}^{n}(x_i-\bar{x})^2/n\right]^{3/2}}$
7	Root mean square	$X_{rms} = \sqrt{\frac{1}{n}\sum_{i=1}^{n}x_i^2}$
8	Shape factor	$X_{sf} = \frac{X_{rms}}{X_u}$

4. Results

In this case study, a total of 23 groups of the force data set were collected, of which 16 data set were randomly selected for model training, and the remaining 7 samples were used for model testing.

As seen in Table 2, the time-domain features have different dimensions and unit magnitudes. Thus, it is necessary to normalize the data using a standardized transformation method. Herein the min-max standardization approach is adopted, as expressed in Eq. (17):

$$\bar{x_i} = \frac{x_i - x_{min}}{x_{max} - x_{min}} \qquad (17)$$

where x_{max} and x_{min} represent the maximum and minimum values of feature x, respectively.

To verify the feasibility of the model in predicting the surface roughness, the root-mean-square error (RMSE), mean absolute error (MAE), and mean absolute percentage error (MAPE) can be selected as the evaluation performance indicators respectively, which are expressed in Eqs. (18–20):

$$RMSE = \sqrt{\frac{1}{n}\sum_{i=1}^{n}(y_i - \hat{y_i})^2} \qquad (18)$$

$$MAE = \frac{1}{n}\sum_{i=1}^{n}|y_i - \hat{y_i}| \qquad (19)$$

$$MAPE = \frac{1}{n}\sum_{i=1}^{n}\left|\frac{y_i-\hat{y_i}}{y_i}\right| \times 100\% \qquad (20)$$

in which n is the number of observations, y_i and y_i represent the actual and predicted values for sample i, respectively.

Figure 4 presents the prediction results of the surface roughness (Ra) of the grooves by FBLS, and the values of the predictive errors are listed in Table 3. The predicted Ra shows good agreement with the experimental Ra for all evaluation criteria. Particularly, the model shows good predicting accuracy when the surface roughness Ra is larger than 1 μm if the RMSE and the MAE are employed as the evaluation criteria (Actually, there is no difference by using RMSE and MAE as the evaluation criteria), as shown in Figure 4(a) and (b). On the other hand, the model using MAPE can provide accurate predictions for the whole range of different surface finish except the Testing No. 6 (Ra 3.163 μm), as seen in Figure 4(c). Figure 5 shows the variation of RMSE against the numbers of fuzzy subsystems and fuzzy rules. With the increase in the number of fuzzy subsystems and fuzzy rules, the RMSE tends to decrease. Particularly, the influence of fuzzy rules on the RMSE is more significant. In a
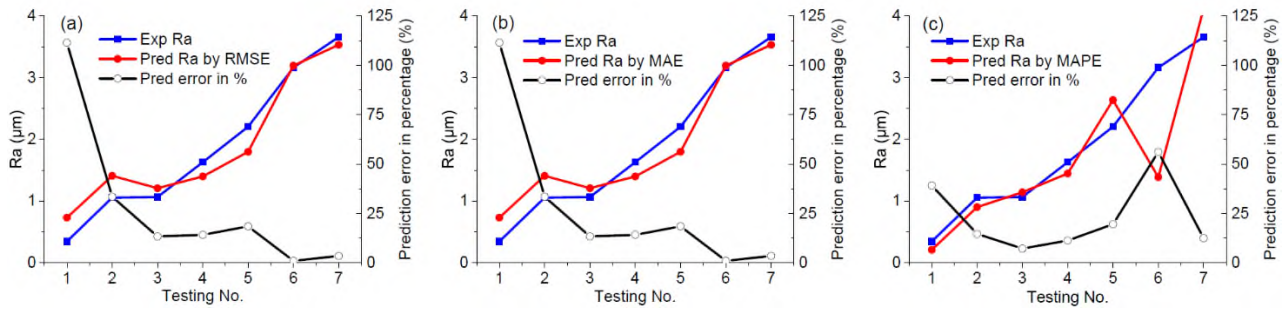
Figure 4. Measured and predicted surface roughness Ra under different evaluation criteria: (a) RMSE, (b) MAE and (c) MAPE.

word, the investigations demonstrate that the proposed method is easy to implement and can yield a promising predicting outcome compared with the X-ray CT method [9] and the AE method [10]. The proposed method also exhibits great potential to measure the surface roughness of complex internal surfaces.

Table 3. Measured surface roughness Ra and the predictive errors under different evaluation criteria i.e., RMSE, MAE and MAPE, respectively

Testing No.	Measured Ra (μm)	By RMSE (%)	By MAE (%)	By MAPE (%)
1	0.346	111.4	111.4	39.1
2	1.056	33.4	33.4	14.6
3	1.066	13.4	13.4	7.2
4	1.630	14.2	14.2	11.2
5	2.206	18.5	18.5	19.6
6	3.163	1.0	1.0	56.1
7	3.659	3.5	3.5	12.4
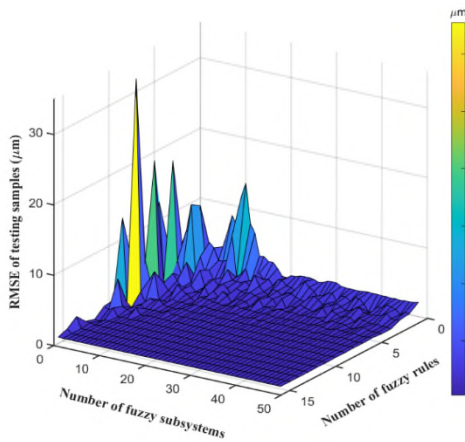
Figure 5. Dependence of RMSE values against the number of fuzzy subsystems and the number of fuzy rules

5. Conclusion Remarks

Leveraging the advantages of machine learning, this paper proposed novel internal surface measurement methods via a magnetic ball scratching on the workpiece surface. A measuring setup was built and Aluminium workpieces with milled grooves were employed as the specimens. The force interaction between the magnetic ball and the workpiece was obtained and pre-processed before being fed into a proposed fuzzy broad learning system (FBLS). By training the FBLS with limited data sets, this model demonstrates an average measurement error (using the measured Ra by a stylus profilometer as a reference) of only 10.1% for the surfaces with a roughness larger than 1 μm Ra, though the errors for finer surfaces are inadequate. The results indicate that the current measuring technique may be helpful to additively manufactured raw components that exhibt a relative rough surfaces. Future work will focus on integrating other signals (acceleration/vibration which uses much cheaper and more portable sensors rather than the dynamometer) as the input and exploring other machine learning models to improve the measuring accuracy of fine surfaces.

References

[1] J. Zhang, W. Tian, F. Zhao, X. Mei, G. Chen, H. Wang, Material Removal Rate Prediction Based on Broad Echo State Learning System for Magnetically Driven Internal Finishing, *IEEE Trans. Ind. Informatics*. (2022). https://doi.org/10.1109/TII.2022.3204003.

[2] M. Kumar, M. Das, N. Yu, Surface Roughness Simulation During Rotational–Magnetorheological Finishing of Poppet Valve Profiles, *Nanomanufacturing Metrol*. **5** (2022) 259–273.

[3] J. O'Hara, F. Fang, Magnetohydrodynamic-based Internal Cooling System for a Ceramic Cutting Tool: Concept Design, Numerical Study, and Experimental Evalidation, *Nanomanufacturing Metrol.* **6** (2023) 33. https://doi.org/10.1007/s41871-023-00210-9.

[4] J. Zhang, H. Wang, Magnetically driven internal finishing of AISI 316L stainless steel tubes generated by laser powder bed fusion, *J. Manuf. Process.* **76** (2022) 155–166. https://doi.org/10.1016/j.jmapro.2022.02.009.

[5] Z. Liu, Q. Guo, Y. Sun, W. Wang, W. Zhao, Z. Yang, Surface roughness and burr generation in micro-milling: A review, *J. Adv. Manuf. Sci. Technol.* **4** (2024) 2023017–0. https://doi.org/10.51393/j.jamst.2023017.

[6] M.W. Lindner, White-light interferometry via an endoscope, in: Interferom. *XI Tech. Anal.*, SPIE, 2002: pp. 90–101.

[7] J. Zhang, H. Wang, Generic model of time-variant tool influence function and dwell-time algorithm for deterministic polishing, *Int. J. Mech. Sci.* **211** (2021) 106795. https://doi.org/10.1016/j.ijmecsci.2021.106795.

[8] J.P. Kruth, M. Bartscher, S. Carmignato, R. Schmitt, L. De Chiffre, A. Weckenmann, Computed tomography for dimensional metrology, *CIRP Ann. - Manuf. Technol.* **60** (2011) 821–842. https://doi.org/10.1016/j.cirp.2011.05.006.

[9] A. Du Plessis, I. Yadroitsev, I. Yadroitsava, S.G. Le Roux, X-Ray Microcomputed Tomography in Additive Manufacturing: A Review of the Current Technology and Applications, *3D Print. Addit. Manuf.* **5** (2018) 227–247. https://doi.org/10.1089/3dp.2018.0060.

[10] Z.M. Hafizi, C.K.E. Nizwan, M.F.A. Reza, M.A.A. Johari, High Frequency Acoustic Signal Analysis for Internal Surface Pipe Roughness Classification, in: *Appl. Mech. Mater., Trans Tech Publ*, 2011: pp. 249–254.

[11] S. Feng, C.L.P. Chen, Fuzzy broad learning system: A novel neuro-fuzzy model for regression and classification, *IEEE Trans. Cybern.* **50** (2018) 414–424.

[12] J.T. Black, R.A. Kohser, DeGarmo's Materials and Processes in Manufacturing, Eleventh, *John Wiley & Sons, Inc.*, 2011.

Automated scheduling system for parallel gear grinding machines

Christopher Janßen[1], Melina Kamratowski[1], Mareike Davidovic[1], Thomas Bergs[1,2]

[1]Laboratory for Machine Tools and Production Engineering (WZL) of RWTH Aachen University, Campus-Boulevard 30, 52074 Aachen
[2]Fraunhofer IPT, Steinbachstraße 17, 52074 Aachen, Germany

c.janssen@wzl.rwth-aachen.de

Abstract

In gear manufacturing at the Gear Department of the WZL of RWTH Aachen University the machine scheduling approach has predominantly been manual, creating potential inefficiencies. This study presents the development of an automated scheduling system designed for the simultaneous operation of two parallel grinding machines. Starting with a detailed definition of machine scheduling requirements and an in-depth analysis of the machine environment, a mathematical formulation of the scheduling problem was established. This formulation was subsequently translated into the Python programming language for efficient implementation. To further aid planners, the system generates visual outputs in the form of Gantt charts. Based on a color-coding scheme, these charts transparently indicate which job is being processed on which machine. Upon validation, the scheduling system demonstrated that an optimized allocation plan, depending on the number of jobs, can be derived in seconds. This system significantly enhances planning processes and augments transparency and adaptability in manufacturing workflows.

Scheduling, Operations Research, Gear Manufacturing, Gear Grinding

1. Introduction

Gears are complex mechanical components that play a central role in a wide range of industrial applications. They are indispensable for the precise transmission of movements and forces in machines and technical systems. To ensure the quality and performance of gears, continuous research and further development of the load capacity and manufacturing processes of gears and gear components is necessary. The Gear Department of the Laboratory for Machine Tools and Production Engineering of RWTH Aachen University is working intensively on this scientific issue.

The organization of the manufacturing processes in the gear department of the WZL poses a major challenge due to the different types of jobs, process times and variable batch sizes. The gear manufacturing process chain includes several sequential operations, whereby gear grinding as part of hard finishing is particularly important for the quality of the final gears. Implementing a job scheduling system can increase the efficiency and reliability of planning and reduce potential bottlenecks.
The introduction of a scheduling system also leads to better traceability in planning. In addition, it is possible to react more flexibly to disruptions in the planned process, for example due to tool failures.

The primary objective of this paper is to develop and implement a job scheduling system for the gear department of the WZL of RWTH Aachen University. The specific requirements and boundary conditions of the various jobs and machines are analyzed and a suitable model is developed. The successful implementation of this system will relieve the responsible planner and at the same time increase scheduling reliability and efficiency. As a result, machine utilization could be optimized and throughput times reduced, which would lead to an overall increase in productivity in the gear department. At present, there is no adequate scheduling model that meets the requirements of gear production under the current boundary conditions and could therefore be used or adapted.

2. State of the Art

Scheduling is a decision-making process that is used in many manufacturing and service industries to optimize the distribution of resources and tasks [1]. The resources and tasks can be machines in a workshop or runways at an airport, for example [1]. Other examples include applications in the semiconductor or paper industry, optimizing catering services in a hospital or optimizing machine utilization in a factory. [2–4]

Each task can have a priority, an earliest possible start time and a due date. The goals of optimization can be, for example, to minimize the completion time or the number of delayed tasks. It is also possible to ensure optimum utilization of machines by distributing tasks. [1]

In the following, the focus is on scheduling for planning machine assignments. Job scheduling takes place directly before the jobs are released and production is carried out [5]. In machine scheduling problems, the assignment of jobs to work carriers or machines or vice versa is considered, taking into account targets and restrictions [6].

It is generally assumed in job scheduling problems that the number of jobs and machines is finite. The number of jobs is denoted by n and the number of machines by m. Usually, the index j refers to a job, while the index i refers to a machine. If a job requires a number of processing steps or operations, then the pair (i, k) refers to the processing step or operation of job j on machine k. [7]

The processing time of a job j on machine i is represented by p_{ij}. The release date of a job j is represented by r_j and can also be referred to as the provisioning time. It is the time at which job j arrives in the system, i.e. the earliest time at which job j can be processed. The actual starting time of a job is represented by t_j. [8]

The latest completion date or due date of job j is referred to as d_j and represents the binding dispatch or completion date. Completing the job after the completion date may be allowed, but will result in the imposition of a penalty. If a completion date for job j must be met, it is referred to as a deadline and is defined as $\overline{d_j}$. [1]

The makespan C_{max} is the total time required to complete a set of jobs on one or more machines. The goal in many scheduling problems is to minimize the makespan C_{max}, especially when it comes to making optimal use of the capacity of machines or workstations and minimizing idle times. An overview of these parameters is given in **Figure 1**.
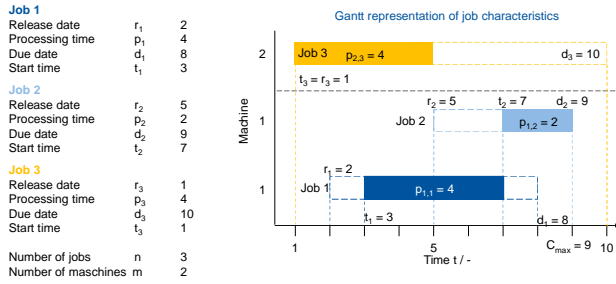
Figure 1: Representation of job characteristics

3. Objective and Approach

The aim of this report is to create a job scheduling system for optimizing production planning of gear grinding machines in a research institute's gear department. This system aims to simplify planning, improve visualization, and enhance planning reliability for both research and industrial projects. The approach involves analyzing production requirements, including existing machinery, orders, and time constraints.

Based on the requirements analysis, a mathematical formulation of the scheduling problem is derived. This involves modeling machines, orders, and time constraints while aiming for a practical yet adaptable model.

Next, the model is implemented in the programming language Python and solved using appropriate software. Validation is conducted using test data sets to assess correctness and solver performance. Both, commercial and open-source solvers are employed for this evaluation.

4. Modeling of the Scheduling Problem

This chapter elucidates the current state of machinery, clamping systems, and procedural factors impacting production order planning. It derives boundary conditions from available data and formulates assumptions for modeling the scheduling problem, culminating in its mathematical description.

4.1. Manufacturing process in the Gear Department

The gear department of the WZL of RWTH Aachen University currently possesses two machines dedicated to the hard finishing of gears. These machines are the KX 500 Flex by KAPP NILES (referred to as KX 500) and the Viper 500 by KLINGELNBERG (referred to as Viper).

Both the KX 500 and Viper machines offer versatility in gear production, and are capable of performing operations such as profile, internal profile, and generating grinding. They can handle gears with a maximum tip diameter of d_a = 500 mm. However, their technical specifications differ, particularly in terms of module range m_n and maximum gear width b.

The Viper machine primarily serves research purposes, predominantly within a university setting, where it is employed for investigating the profile grinding process. In contrast, the

Kapp KX 500 is assigned to research purposes in regard to generating grinding and the manufacturing of test gears.

In addition to these primary distinctions, various influencing factors come into play, including clamping methods, interfering contours, and tool availability, which can impact the choice between the two machines. However, the machine selection may also be swayed by factors such as the current workload and other constraints.

Current scheduling processes cover a timeframe of 3-5 months and typically involve managing approximately 10-15 jobs. Nevertheless, the ability to adapt flexibly to personnel or material shortages, whether arising from workforce constraints or tool and machinery availability, is essential. The frequency and extent of these adjustments can vary, occurring on a weekly or monthly basis depending on the specific circumstances.

4.2. Problem formalization

Considering the machine environment and the constraints or specifications of the production job, the following boundary conditions and assumptions for the model are delineated.

Boundary conditions

(1) Due dates: Each job has a fixed end time by which it must be completed at the latest.

(2) Availability: The jobs have an availability from which they can be started. They cannot be processed before this time.

(3) Sequence: There is no predefined sequence. The sequence is determined based on the availability of machine capacity and the due dates.

(4) Process times: Each job has a specific process time, which specifies how long this job takes on a machine to be fully completed.

(5) Mandrels: There is a limited number of mandrels for part clamping. If two jobs on different machines require the same mandrel, they cannot be processed at the same time. The same applies to shaft grinding.

(6) Two machines: Two gear grinding machines are available, on each of which only one job can be carried out at a time.

(7) Prioritization: The jobs are not prioritized. Prioritization is defined implicitly via the due dates of the respective job.

(8) Machine assignment: Some jobs must be executed on a specific machine, while other jobs can be processed on both machines.

(9) Machine speed: Both machines work at the same speed and have the same performance capacities.

(10) Maintenance and repair: The maintenance and repair of the machines can be specified as a job with a start and end date and an equivalent duration. This blocks other jobs at the relevant time.

Assumptions

The following assumptions are made in order to simplify the scheduling problem and map it realistically:

(1) Tools and Workpieces: It is assumed that tools and workpieces are readily available and prepared for each job as soon as the job becomes available. All requisite preparations have been executed in advance.

(2) Set-up time: The set-up time for each job is variable and cannot be standardized. It is therefore taken into account in the production time or process time of the respective job.

(3) Set-up process: The set-up process for the machines can take different lengths of time. This variance is also taken into account in the process time of the respective jobs.

(4) Quality recording: The recording of the quality of the manufactured gears during the production process is already included in the process time of the respective job.

(5) Process times: The process times are identical on both machines for all jobs. However, since a change is conceivable, the following problem is modeled with variable process times depending on the respective machine.

(6) Interruption: Jobs cannot be interrupted. Jobs with large quantities can be divided into smaller jobs.

Taking these boundary conditions and assumptions into account, the scheduling problem is modeled and a suitable strategy for optimizing production planning is developed.

4.3. Mathematical formulation

Certain indices, parameters and decision variables are required for modeling. The indices, sets and variables are shown in **Table 1**.

Table 1 Variables required for modelling

Variables	Description
C_{max}	Makespan
$i, j \in J = \{1, 2, ..., n\}$	Amount of jobs
$k \in = \{1, 2\}$	Amount of machines
r_i	Release date of job i
$\bar{d}_i$	Due date of job i
t_i	Start time of job i
p_{ik}	Process time of job i on machine k
x_{ik}	Allocation of job i on machine k
y_{ij}	Processing of job i before job j
w_{ij}	Usage of Ressources of job i and j
M	A big number e.g. 10,000

Based on the selected indices, parameters and decision variables, the scheduling problem can be defined as depicted in Figure 1 and Figure 2. The objective of the optimization is described by Eq. (1) to minimize the makespan C_{max} or the completion time, see **Table 2**. Eq. (2) defines that the start time t_i of a job i plus the respective process time p_{ik} must be less than or equal to the completion time $\bar{d}_i$. This equation prevents a production delay of the jobs. Eq. (3) specifies that the start time t_i of each job must be greater than the respective release time r_i. Provided that all release times r_i are greater than or equal to 0, it is also ensured that the start time t_i is not shifted into a negative time range.

Table 2 Equations 1-7

Description	Mathematical Formulation	
1) Objective	$\min C_{max}$	
2) Deadline	$t_i + p_{ik} \leq \bar{d}_i \quad \forall i \in J, \forall k \in K$	
3) Start time	$t_i \geq r_i \quad \forall i \in J$	
4) Sequence	$t_i + p_{ik} - M \cdot (1 - x_{ik}) \leq t_j + M \cdot (1 - y_{ij}) + M \cdot (1 - x_{jk})$	*
5) Sequence	$t_j + p_{jk} - M \cdot (1 - x_{jk}) \leq t_i + M \cdot (y_{ij}) + M \cdot (1 - x_{ik})$	*
6) Resources	$t_i + p_{ik} - M \cdot (1 - x_{ik}) \leq t_j + M \cdot (1 - y_{ij}) + M \cdot (x_{jk}) + M \cdot (1 - w_{ij})$	*
7) Resources	$t_j + p_{jk} - M \cdot (1 - x_{jk}) \leq t_i + M \cdot (y_{ij}) + M \cdot (x_{ik}) + M \cdot (1 - w_{ji})$	*
*	$\forall i, j \in J, \forall k \in K, i \neq j$	

Eq. (4) and Eq. (5) establish a direct sequential relationship between two jobs i and j. Both constraints specify that jobs processed on the same machine cannot occur in parallel. The formulation guarantees that the start time t_i and its corresponding processing time p_{ik} must be less than or equal to the start time of the succeeding job j.

Eq. (6) and Eq. (7) introduce the variable w_{ij} to consider mandrel usage and shaft grinding. Job start times t_i and t_j are determined as in Eqs. (4) and (5). However, a sequencing constraint is applied only when jobs i and j are processed on different machines, requiring limited mandrel availability.

Further mathematical formulations are depicted in **Table 3**. Eq. (8) ensures that when switching between the profile and generating grinding process for jobs i and j, an additional setup time is taken into account.

The sum of the decision variables x_{ik} across all machines k for each job i in Eq. (9) ensures that each job is assigned to a machine. If a job is already assigned to a machine by a user, the secondary condition is ignored.

Eq. (10) states that the sum of all start times and process times for all machines is less than or equal to the makespan C_{max}. The factor x_{ik} ensures that the respective process time is only taken into account if a job is actually executed on the corresponding machine.

Eq. (11) and Eq. (12) define the partial machine assignments or the mandrels used and the necessity using a shaft clamping system. If a decision variable is part of a table specified by the user for the machine assignment L_{pred} or the mandrel assignment W_{pred} (pred for predetermined), the value of the decision variable is assigned according to the specification.

Eq. (13) defines the type of decision variables for x_{ik}, y_{ij} and w_{ij}. All three decision variables are defined as binary variables. This condition means that the variables can only assume the values 0 and 1.

Eq. (14) ensures that the makespan C_{max} is greater than or equal to zero. This prevents the makespan C_{max} from being optimized into the negative range.

Table 3 Equations 8-17

Description	Mathematical Formulation
8) Process	$t_i + p_{ik} - M \cdot (1 - x_{ik}) + \text{setup} \cdot (z_i - z_j) \leq t_j + M \cdot (1 - y_{ij})$
9) Allocation	$\sum_{k \in K} x_{ik} = 1 \quad \forall i \in J$
10) Def. C_{max}	$\sum_{k \in K} t_i + p_{ik} \cdot x_{ik} \leq C_{max} \quad \forall i \in J$
11) Allocation x_{ik}	$x_{ik} = 1, \quad \forall i, k \in L_{pred}$
12) Allocation w_{ik}	$w_{ij} = 1, \quad \forall i, j \in W_{pred}$
13) Def. Variables	$x_{jk}, y_{ij}, w_{ji} \in [0, 1]$
14) Limitation C_{max}	$C_{max} \geq 0$
*	$\forall i, j \in J, \forall k \in K, i \neq j$

5. Validation of the scheduling system

To ensure the functionality of the scheduling system with regard to the boundary conditions and the target function, various scenarios are analyzed using test data sets. This is followed by a comparison of the functionality of the commercial Gurobi solver with the freely available PuLP solver.

The first test data set is used to verify whether the boundary conditions, see section 4.1, are met. These include the limitations that no jobs may be processed in parallel on a machine, the release time r_i of the jobs must be met and the due date $\bar{d}_i$ must not be exceeded. Six different jobs are scheduled for optimization in the first test data set.

All jobs have the release time $r_i = 1$, but have different process times p_{ik} and individual end times $\bar{d}_i$ at which the jobs must be completed. The results show that parallel processing on one machine can be ruled out, see **Figure 2**. Therefore, it was possible to assign a sequence relationship to all jobs.

Furthermore, all jobs were evenly distributed between the two machines in order to minimize the makespan C_{max}. Each machine was assigned a job with a process time $p_{ik} = 1$, 2 and 3 respectively. The makespan is $C_{max} = 7$, which corresponds to the

latest end time $\bar{d}_i$ of jobs 1 and 4. All specified end times were met.
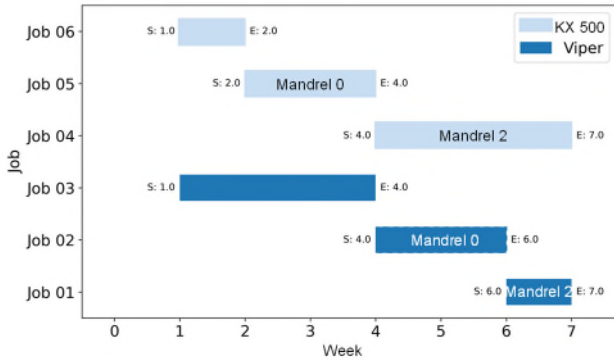
Figure 2. Results of a validation test

Due to the availability of two mandrels of the corresponding size 2, parallel machining on two machines is possible without any problems. The results of the optimization show the functionality of considering the availability of different mandrels. Jobs that require a mandrel that is only available once are not scheduled in parallel. When using mandrels that are available twice, however, jobs can be scheduled in parallel.

For the second test, the machining processes, profile grinding (P) and generating grinding (W) were specified. Based on the specified process, it is checked whether a sequence of identical processes leads to reduced setup times and the avoidance of penalty costs. The results are shown in **Figure 3**.
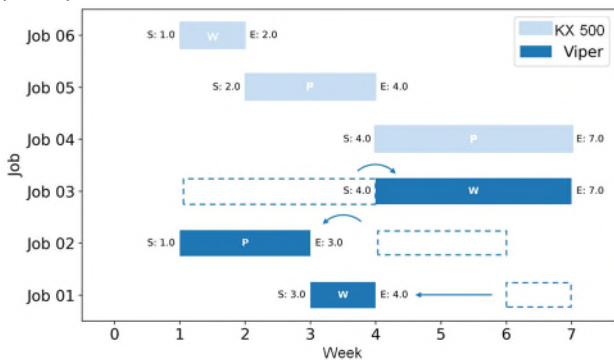
Figure 3. Results of the second validation test

There are no changes to the assignment of jobs on the KX 500 Flex, as there is already an optimum here. However, there are significant changes in the sequence on the Viper. Job 1 was scheduled to start in week 3. Job 2 starts on the same day as week 1, while the start of job 3 has been moved to week 4. This postponement ensures that the grinding process is not interrupted by another process.

6. Performance comparison

In a comparison, the solving speed of the commercial solver Gurobi and the open source solver PuLP is analyzed, see **Figure 4**. The scheduling system was implemented using the commercial solver Gurobi. To analyze the difference with an open source solution, a comparison was made. The results show that there is a critical threshold of 19 jobs, beyond which the solution time increases significantly from seconds to minutes and beyond. For example, with a job count of 20, the Gurobi solver requires 770 seconds (equivalent to approx. 13 minutes), while finding a solution with PuLP takes 5,500 seconds (approx. 1.5 hours). With a job count of 50, these times increase to 4,500 seconds (75 minutes) for Gurobi and 53,500 seconds (approx. 15 hours) for PuLP. These data illustrates the exponential influence of the number of jobs on the increasing complexity of the problem and

the associated solution time. A duration of 770 seconds can be considered acceptable in the context of optimization, as it represents a significant time saving compared to manual optimization methods. This assessment also applies to a duration of 4,500 seconds with a job count of 50. However, the comparison suggests that with increasing complexity, a commercial solver such as Gurobi is preferable.
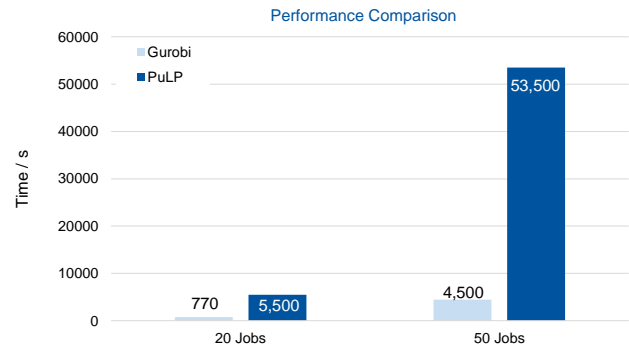
Figure 4: Results of a performance comparison

7. Summary and outlook

This report outlines the development of a tailored scheduling system for hard finishing at the gear department of WZL of RWTH Aachen University. The main goal was to create an efficient and adaptable production schedule for two specialized machines: the KX 500 Flex from Kapp Niles and the Viper 500 KW from Klingelnberg.

Through analysis, a flexible mathematical model for machine occupancy and clamping systems was formulated and implemented using Python and the Gurobi solver. Validation with two data sets confirmed functionality and adherence to specifications. A comparison with the PuLP solver showed significant time savings and efficiency gains as dataset complexity increased.

The development of a job scheduling system at WZL Gear Department not only enhances operational efficiency within this academic setting but also holds significant potential for broader industrial application. This research, while specific to the WZL's unique needs, offers a scalable and adaptable framework that can inform scheduling practices in various manufacturing sectors. This work provides a methodological blueprint for industries facing similar production challenges, emphasizing the broader applicability and potential of academic research to improve industrial production planning and efficiency.

References

[1]   Pinedo ML. Scheduling. Boston, MA: Springer US; 2012.

[2]   Dugardin F, Chehade H, Amodeo L, Yalaoui F, Prins C. Hybrid Job Shop and Parallel Machine Scheduling Problems: Minimization of Total Tardiness Criterion. In:. Multiprocessor Scheduling, Theory and Applications: I-Tech Education and Publishing; 2007. doi:10.5772/5227.

[3]   Chen JC, Wu C-C, Chen C-W, Chen K-H. Flexible job shop scheduling with parallel machines using Genetic Algorithm and Grouping Genetic Algorithm. Expert Systems with Applications. 2012;39:10016–21. doi:10.1016/j.eswa.2012.01.211.

[4]   Abderrabi F, Godichaud M, Yalaoui A, Yalaoui F, Amodeo L, Qerimi A, Thivet E. Flexible Job Shop Scheduling Problem with Sequence Dependent Setup Time and Job Splitting: Hospital Catering Case Study. Applied Sciences. 2021;11:1504. doi:10.3390/app11041504.

[5]   Kistner K-P, Steven M. Produktionsplanung. Heidelberg, sPhysica-Verlag HD; 2001.

[6]   Domschke W, Scholl A, Voß S. Produktionsplanung: Ablauforganisatorische Aspekte. Berlin: Springer; 1993.

[7]   Brucker P. Scheduling Algorithms. Berlin: Springer; 2004.

[8]   Baker KR, Trietsch D. Principles of sequencing and scheduling. Hoboken, NJ, USA: Wiley; 2019.

Artificial neural network-based tool condition monitoring of titanium alloy end mill process using time series data

Kangseok Kim[1], Miru Kim[2], Deugwoo Lee[1]

[1]Department of Nano Energy Engineering Pusan National University, Busan, Republic of Korea
[2]Dongnam Division, Korea Institute of Industrial Technology, Jinju, Republic of Korea

kimkng@pusan.ac.kr

Abstract

Titanium alloy, one of the representative difficult-to-machine materials, is light, has high high-temperature strength, and has excellent mechanical properties, so it is widely applied to major parts such as aviation and space. However, due to low thermal conductivity during cutting, a lot of heat is generated, so tool life is short and tool management is difficult. When machining titanium alloy, it is important to detect the condition of the tool and determine the appropriate replacement time when machining with one tool for a long time or when a large amount of machining is required. To monitor a tool during machining, it is necessary to measure signals generated during machining and find a way to determine the relationship between the condition of the tool and the machining signal. For this, it is useful to apply an AI-based analysis model. In this paper, a machining experiment of titanium alloy was conducted using an end mill tool with a diameter of 16mm to obtain the necessary data, and a monitoring system was created by attaching an acceleration sensor to the main axis of the machining equipment. In addition, tool wear was periodically measured using an optical microscope and used for data collection and tool condition analysis. In order to apply it to the AI-based analysis model, the signal from the acceleration sensor generated during processing was obtained as time series data. The acquired time series data was directly applied to an AI model combining CNN, LSTM, and MLP (Multi-Layer Perceptron) to train an AI model for multi-class classification that determines tool status according to signals generated during machining. Tool monitoring during the titanium alloy end mill process was performed and evaluated through an AI model learned using the acquired time series data.

End mill, Titanium alloy, Tool monitoring, AI model, Time series data

1. Introduction

Drilling and milling processes are among the oldest machining process that are still vastly practiced in the recent manufacturing industry. Modern machining sector has been establishing an effort in developing automated machines that are competent of precisely detecting tool defects to avert machining processes from continuously running with defected tools. A study disclosed that the manufacturing and production industries spend most of the whole operating costs on machine maintenance [1]. Estimating tool life is crucial, but challenging to be achieved and although tool manufacturer provides an estimated period of tool life [2], the information provided could not be fully relied on due to the fluctuation of tool lifespan [3], and implemented machining parameters.

Certain characteristics of the work materials such as low thermal conductivity, strong chemical reactivity with the cutting tool materials at high temperatures, and relatively low elastic modulus, make Titanium alloy as one of the difficult-to-cut materials [4]. The deformation or damage of the sharp edges of the cutting tool due to the interaction between the tool and the workpiece during machining is called tool wear. Deterioration of product quality due to tool wear and increase in product cost due to frequent tool replacement are major issues in machining difficult-to-cut-materials. In manufacturing, cutting tool failure increases costs and maintenance time and reduces production rates. When machining titanium alloy, it is important to detect the condition of the tool and determine the appropriate replacement time when machining with one tool for a long time or when a large amount of machining is required. To monitor a tool during machining, it is necessary to measure signals generated during machining and find a way to determine the relationship between the condition of the tool and the machining signal.

Signals obtained from sensors during processing are large amounts of complex time series data, making it difficult to find patterns. Therefore, in the case of time series data, machine learning is mainly used to process the data by characterizing it with a statistical model to find appropriate patterns and learn them. Deep learning, which even learns the process of recommending and selecting features from learning data, is suitable for real-time monitoring because it can be applied directly to time series data without characterizing it with a statistical model. Therefore, in this study, we designed deep learning models consisting of a combination of CNN MLP and CNN LSTM MLP, and examined the model's performance by directly applying time series data to the designed AI model. Vibrations generated during machine tool processing are measured using an acceleration sensor and analyzed using an AI-based analysis model to identify the relationship between the processing state of the machine tool and the tool condition. Signals that fluctuate according to the processing state of the machine tool were collected, and an AI model for multi-class classification was designed and evaluated by combining CNN, LSTM, and multi-layer perceptron (MLP).

2. Experiments

The machining experiment of titanium alloy (Ti-6Al-4V) was conducted using an end mill tool with a diameter of 16mm to obtain the necessary data, and a monitoring system was created by attaching an acceleration sensor (Kistler 8688A10) to the spindle of the machining equipment as shown in figure 1. A case for installing the accelerometer was manufactured and attached to the non-rotating part of the spindle with adhesive. NI-9234 and cDAQ-9178 were used for data acquisition, and the sampling rate was 20kHz. The cutting conditions (cutting speed: Vc, feed: fz, axial depth of cut: Ap, radial depth of cut: Ae) are showed in table 1. Side milling was applied as shown in figure 2(a), and figure 2(b) shows the state of the workpiece after processing. In addition, tool wear was periodically measured using an optical microscope and used for data collection and tool condition analysis.
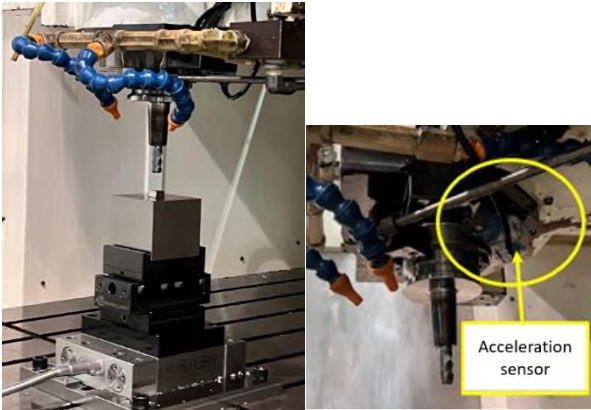
Figure 1. Experimental Set-up and installation of acceleration sensor

Table 1 Cutting conditions

Vc (m/min)	fz (mm/tooth)	Ap (mm)	Ae (mm)
80	0.1	5.0	3.0
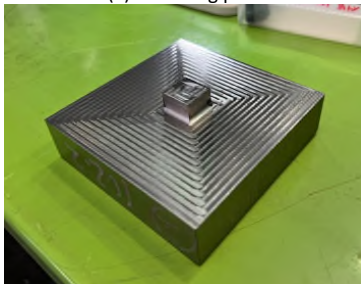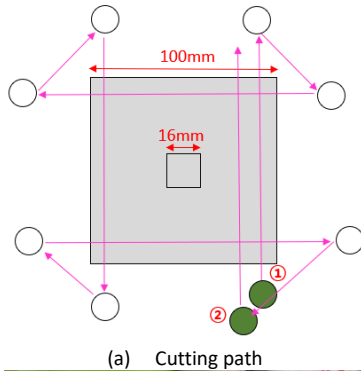
(a)   Cutting path

(b)   Workpiece after cutting

Figure 2. Cutting path and workpiece after cutting

Figure 3 shows the signal of acceleration sensor and the relation between obtained signal and tool wear. In order to obtain processing characteristic signals according to tool wear, the tool states are classified into 6 categories such as no wear

(first point), very light wear (second point), light wear (third point), moderate wear (fourth point), and severe wear(max. peak of the graph), and tool failure (fifth point).
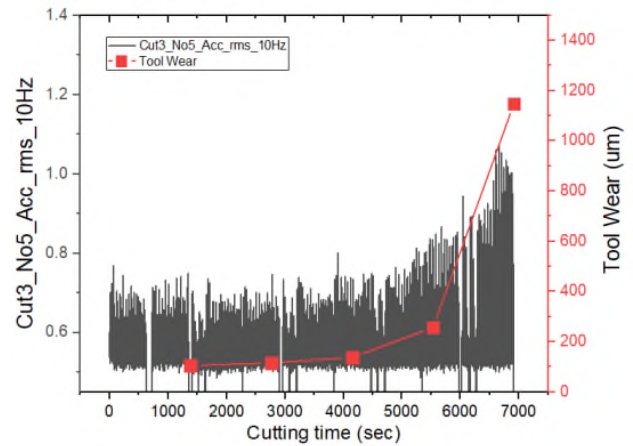
Figure 3. Data comparison between the signal of acceleration sensor and tool wear
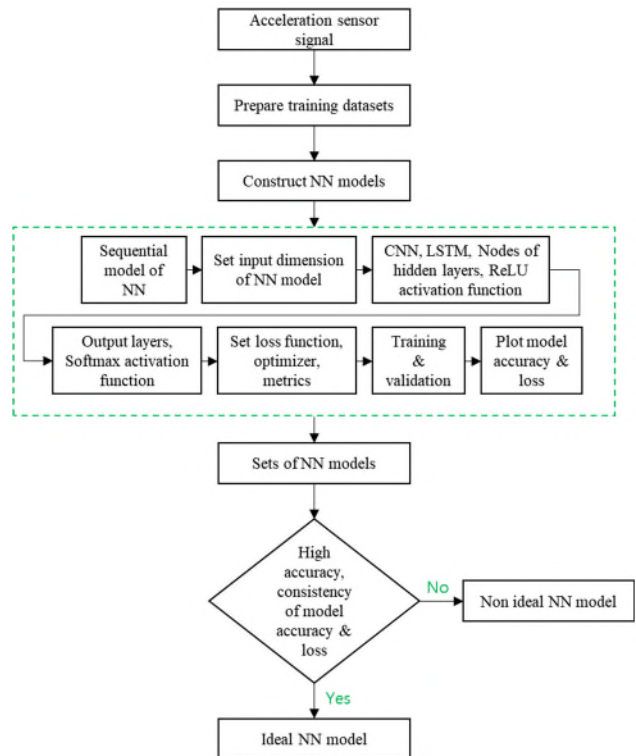
Figure 4. Flowchart of the signal analyzation through CNN LSTM MLP

3. Data analyzation methods

Recently, in the case of AI models that combine CNN (Convolution Neural Network) and LSTM (Long Short-Term Memory), there have been many reported cases of designing AI models with high accuracy and reliability by directly applying time series data to find the best features [5 - 6].

To analyze the state of the tool using the processing signal of the machine tool, we designed and trained an AI model for multi-class classification by combining CNN, LSTM, and multi-layer perceptron. The process of learning by applying acceleration sensor signals for each tool wear condition to the AI model is summarized in figure 4. A study was conducted to predict the tool wear by directly applying time series data to an AI model created using CNN and hybrid deep learning techniques, and various models combined CNN MLP and CNN LSTM MLP were reviewed.
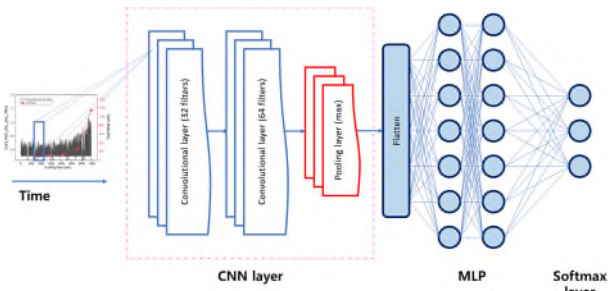
Figure 5. Architecture of CNN MLP for deep learning

Figure 5 and figure 6 show the structure of a model combining CNN MLP and CNN LSTM MLP. Figure 5 is the architecture of a model designed with an input layer, CNN layer, Dense layer, and output layer, and figure 6 is the architecture of a model designed with an input layer, CNN layer, LSTM layer, Dense layer, and output layer.
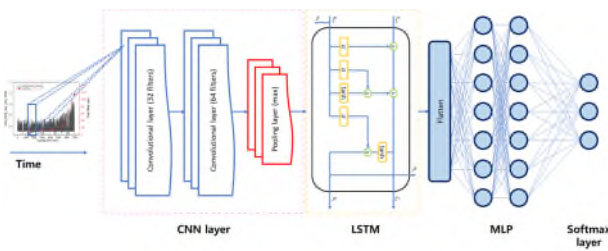
Figure 6. Architecture of CNN LSTM MLP for deep learning

4. Results and discussion

The learning curves composed of the model accuracies and losses of each CNN MLP architecture and CNN LSTM MLP architecture are presented in figure 7 and figure 9. The confusion matrix was plotted for each CNN MLP architecture and CNN LSTM MLP architecture, as shown in figure 8 and figure 10, based on the predicted and true labels for each tool condition. The evaluation metrics of the confusion matrix for each AI model is summarized in table 2. As a result of verifying the learned model with test data, the accuracy and evaluation indexes of CNN LSTM MLP architecture was higher than that of CNN MLP architecture. As a result of evaluating the AI model of CNN LSTM MLP architecture with test data, the accuracy was over 95% and the developed model was able to classify each data precisely based on the true label.
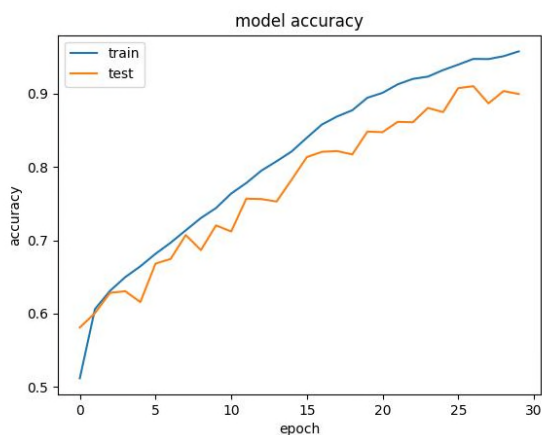
(a)   Training score
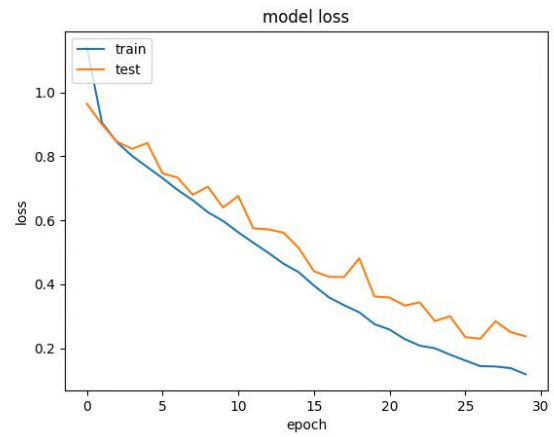
(b)   Model loss

Figure 7. Training score and model loss curve by test data (CNN MLP architecture)
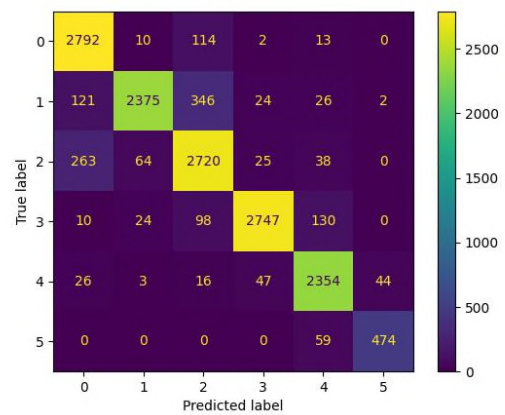
Figure 8. Confusion matrix of CNN MLP architecture plotted based on true and predicted data
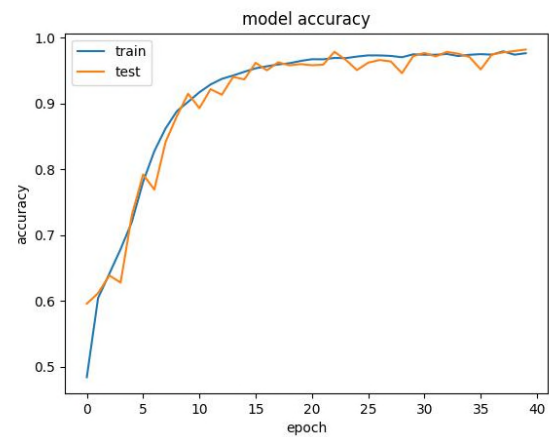
(a)   Training score
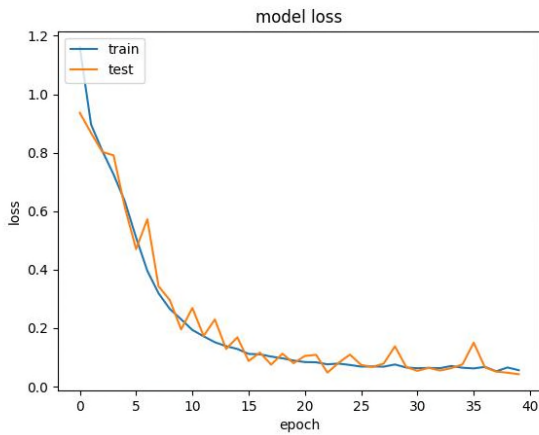
(b) Model loss

Figure 9. Training score and model loss curve by test data (CNN LSTM MLP architecture)
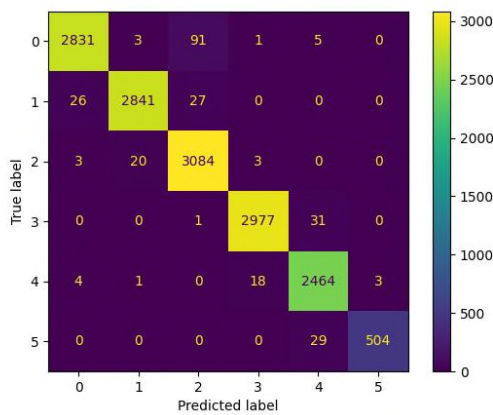
Figure 10. Confusion matrix of CNN LSTM MLP architecture plotted based on true and predicted data

Table 2 Evaluaiton metrics of the confusion matrix for each AI model

AI model	Macro precision (%)	Macro recall (%)	Macro F1-score (%)	Accuracy (%)
CNN + MLP	90	90	90	89.9
CNN + LSTM + MLP	98	98	98	98.2

5. Conclusion

In order to predict and monitor the state of the tool during processing of titanium alloys, an AI model for multi-class classification was designed and trained by combining CNN, LSTM and a multi-layer perceptron to analyze the state of a tool using processing signals of a machine tool. The performance of the AI model, which classifies the tool states into 6 categories.

To predict the tool wear by directly applying time series data obtained from acceleration sensors during machining to an AI model created using CNN and hybrid deep learning techniques, various models combined CNN MLP and CNN LSTM MLP were reviewed and evaluated. As a result of verifying the learned model with test data, the accuracy and evaluation indexes of CNN LSTM MLP architecture was higher than that of CNN MLP architecture. As a result of evaluating the AI model of CNN LSTM MLP with test data, the accuracy was over 95% and the tool state was successfully predicted. In the future, it is believed that collecting and analyzing more data can develop into predictive maintenance technology that can predict tool state abnormalities during processing.

References

[1]   R.K. Mobley, 2002, An introduction to predictive maintenance, 2nd Edition, Elsevier. https://doi.org/10.1016/B978-0-7506-7531-4.X5000-3

[2]   R. Heinemann, S. Hinduja. 2012 A new strategy for tool condition monitoring of small diameter twist drills in deep-hole drilling. International Journal of Machine Tools & Manufacture, 52, 69-76

[3]   S. Soederberg, O. Vingsbo, M. Nissle. 1982 Performance and failure of high speed steel drills related to wear. Wear, 75, 123-143

[4]   E.O. Ezugwu, Z.M. Wang, 1997 Titanium alloys and their machinability a review, Journal of Materials Processing Technology 68, 262-274

[5]   G. Ercolano, S. Rossi, 2021, Combining CNN and LSTM for activity of daily living recognition with a 3D matrix skeleton representation, Intel Serv Robotics, 14, 175–185. https://doi.org/10.1007/s11370-021-00358-7

[6]   A. Borré, L.O. Seman, E. Camponogara, S.F. Stefenon, V.C. Mariani, L.d.S. Coelho, 2023, Machine Fault Detection Using a Hybrid CNN-LSTM Attention-Based Model, Sensors, 23(9), 4512. https://doi.org/10.3390/s23094512

High-precision flexure-based XY-stage with high stiffness and load capacity

Patrick Flückiger[1], Hubert Schneegans[1], Simón Prêcheur Llarena[1], Charles Baur[1], Simon Henein[1]

[1]*Micromechanical and Horological Design Laboratory, Instant-Lab, EPFL, Switzerland*

hubert.schneegans@epfl.ch

Abstract

Typical flexure-based XY-stages have a serial design, and their layout results in the flexures being loaded in flection in face of heavy payloads or vertical loads. This paper presents a design with zero parasitic shift in which all flexures are loaded in traction/compression, resulting in a high-precision and high-load-capacity flexure-based XY-stage. A proof-of-concept demonstrator validates the concept and numerical simulations indicates sub-micron straightness error.

Flexure, XY-stage, high precision, straightness, compliant mechanism

1. Introduction

XY-stages are standard mechanical components that provide in-plane motion and are typically implemented with rolling bearings. The precision of these systems, which lies within the micron range, can be increased by turning towards flexure-based stages. These flexures, which rely on elastic deformation of flexible elements within the mechanism, are free from friction and provide a high repeatability which is desirable for high-precision applications. Moreover, flexures have the advantage of being compatible with vacuum or clean environments. In conventional designs for flexure-based XY-stages, all the blades lie within the plane of motion [1-3]. This configuration has the disadvantage of losing its straightness when high loads are applied along the z-axis, for example when moving a heavy payload (assuming the z-axis is vertical). It is indeed advantageous to avoid parts working in flection or in overhang [4]. Several XY-stage designs with parts working in traction or compression exist in the literature [5], but these suffer from parasitic motion (which forms a straightness error). This paper provides the design of a flexure-based XY-stage with zero parasitic motion and in which all key flexures are solicited in traction or compression, resulting in a high load capacity and high stiffness-to-load properties.

2. Kinematics of the mechanism and working principle

The two sources of inspiration for this design will be introduced and will then be combined to form the presented mechanism. Its mobility, internal degrees-of-freedom and overconstraints will be studied using Grubler's method. The design will then be further modified to improve its load capacity, compactness, and manufacturability.

2.1. Sources of inspiration

The compound linear stage is a well-known one-degree-of-freedom linear stage in which two parallel leaf spring stages are stacked in series to cancel out each other's parasitic motion. This design is underconstrained and requires a coupling lever that is connected to the base via a pivot, and whose role is to ensure proper synchronisation between the intermediate stage and

end-effector, as shown in Fig. 1. A connecting rod is also required between the coupling lever and both the intermediate stage and end-effector. Their role is to impose the lever's x-motion to the end-effector and intermediate stage while tolerating relative z-motion and pivoting.
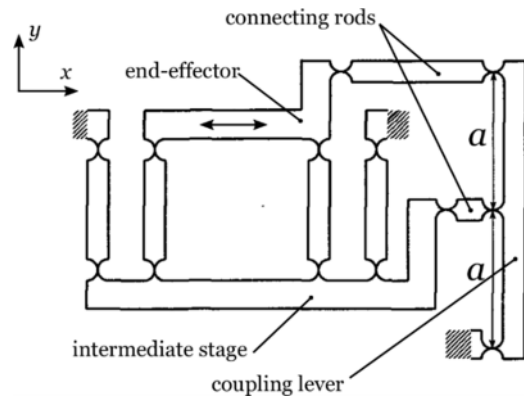
Figure 1. coupled compound flexure linear stage. This is a one-degree-of-freedom mechanism in which the end-effector moves along the x-axis.

The second source of inspiration is the three-rod-XYθ-stage presented in [6] (Fig. 2). This design allows planar XY-motion and z-rotation but suffers from a parasitic straightness error due to beam shortening.

2.2. Working principle

The presented design consists of two stacked three-rod-XYθ-stages which are synchronised with a central coupling lever, effectively creating a coupled compound XY-stage. The particularity of this slaving mechanism is that the coupling lever must now be linked to the base via a tip-tilt joint (allowing rotation around the x- and y-axes), and an equivalent to the connecting rods must be implemented which imposes both the x- and y- motion of the coupling lever to the end-effector and intermediate stage, while still tolerating relative z-motion and tilting. The tip tilt joint consists of a flexure CV-joint presented in [7] and the connecting rod equivalent is implemented with three

coplanar flexible rods. The working principle of the mechanism can be seen in Fig. 3.
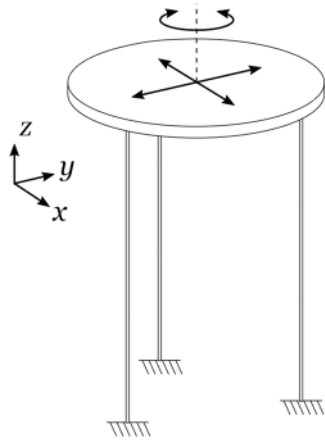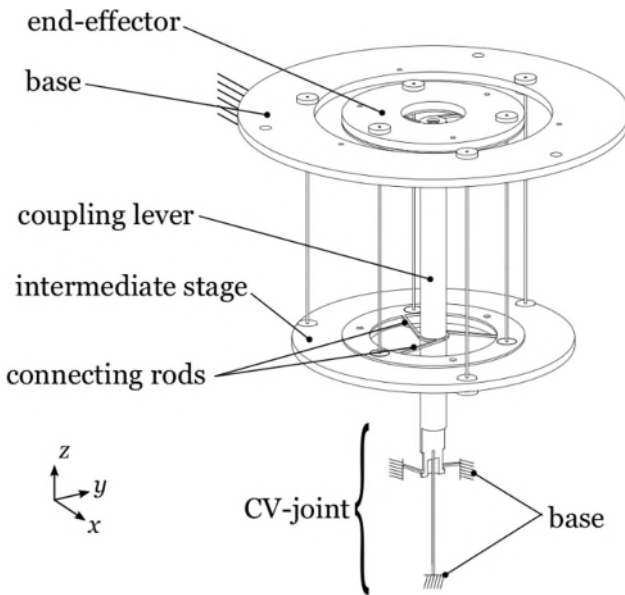
2.3. Mobility, degrees-of-freedom and overconstraints of the XY-stage

The structure's mobility is evaluated using Grubler's method. The mechanism's rods can be seen as joints with five degrees-of-freedom [5]. The resulting mobility M is given by:

$$M = 6n - \sum_{i=1}^{j}(6 - f_i) = 2,$$

with $n = 3$ being the number of moving parts, $j = 16$ being the number of joints (i.e. the number of rods) and $f_i = 5$ being the degrees-of-freedom of each rod.

The mechanism has therefore two degrees-of-freedom and is free from overconstraints and internal degrees-of-freedom.

To help the understanding of the mechanism, the rigid parts and their connectivity is shown schematically in Fig. 4:
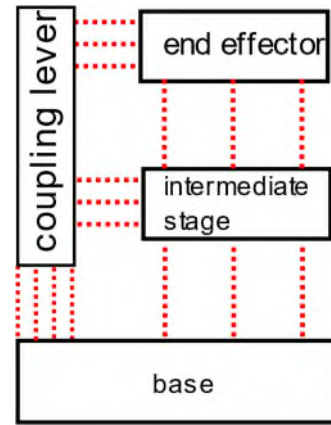
2.4. Improved flexure design

Even though the design shown in Sect. 2.3 is exactly constrained, it lacks compactness and does not have a large load capacity. Indeed, even though the six vertical rods are loaded in traction and compression, their slenderness prevents them from sustaining vertical loads efficiently.

It can also be seen in Fig. 3 that the fixed base is present in two locations: once linked to the intermediate stage, the other linked to the coupling lever. This base spanning a large distance is detrimental for precision but is best to find compact designs [4].

The improved version results in the structure shown in Fig. 5:
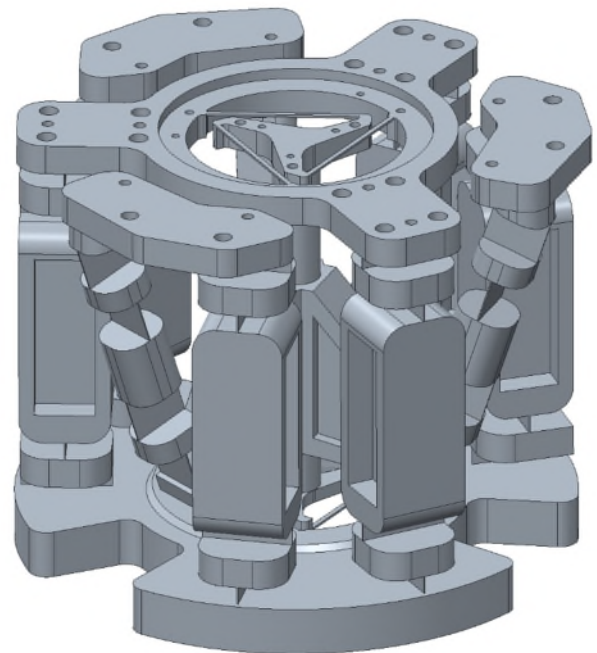
The six vertical rods are replaced by legs consisting of two pairs of stacked blades. Each pair of stacked blades acts as a two-degree-of-freedom universal joint and increases the load capacity and stiffness-to-load [5].

The coupling lever is shortened by opting for a remote centre of compliance (RCC) ball-joint, highlighted in Fig. 6. This ball-joint is based on [8], in which the flexible rods are again replaced by stacked blades. The advantages of this RCC design are its compactness and that it shares the same base as the six vertical

rods. This joint no longer blocks torsion around the z-axis and the end-effector now has three degrees-of-freedom: XY-planar motion and a z-rotation.
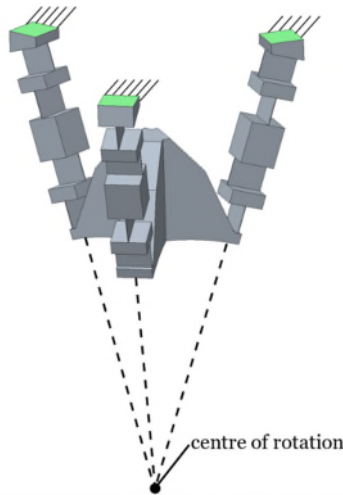
Figure 6. Highlight of the RCC coupling lever with its remote centre of rotation.

3. Demonstrator prototypes

The complexity of this design is a good opportunity to showcase the benefits of additive manufacturing. A first cheap demonstrator prototype is constructed out PA12 (Nylon) by SLS, on which the straightness of motion was experimentally measured. A second prototype made of steel and printed by SLS is currently underway, for which the numerical results for straightness and stiffness-to-load will be shown.

3.1. PA12 demonstrator prototype

The constructed demonstrator prototype out of PA12 is shown in Fig. 7:
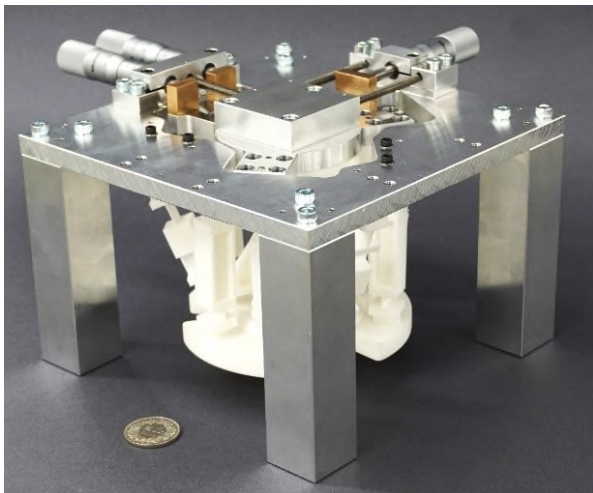
F**igure 7.** picture of the PA12 3D-printed prototype.

The XY-stage is actuated by means of three manual micrometric screws (as there are three degrees-of-freedom) with preloading springs to ensure contact between the screws and the end-effector. The straightness error was measured in a preliminary manner using a height measuring gauge, suggesting as straightness error of +-3 um. In the setup, the XY-stage was fixed to a reference Granit surface plate and the height gauge measured the z-motion of the end-effector (always on the same target fixed to the end-effector). Moreover, the linear component in the measured height was removed, as it is not a straightness error, but comes from the plane of motion not

being parallel to the Granit surface plate. After inspection however, the repeatability of the measurement was also in the range of +-3 um, meaning that a more precise measurement setup should be considered. Though the numerical values of this experiment are inconclusive, they show that the low-cost prototype is still able to provide a straightness in the order of a few microns.
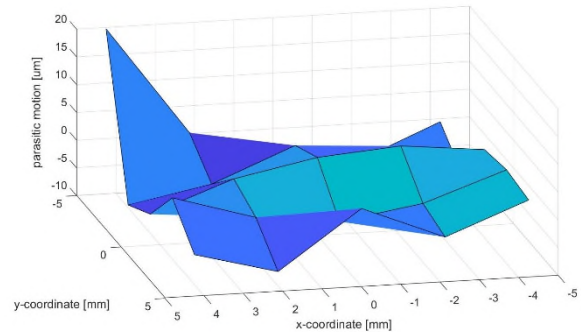
Figure 8. Measured straightness error of the PA12 demonstrator prototype. Note: the value at +20 um is most likely a measurement error, suggesting a straightness error of +-3 um.

3.2. Steel 3D-printed prototype

The second, higher quality, steel 3D-printed prototype is currently under fabrication and is shown in Fig. 9. The printing of the connecting rods is difficult for this technique as they are horizontal. For this reason, only the vertical legs and the RCC coupler are printed. The connecting rods and end effector are then added during assembly.
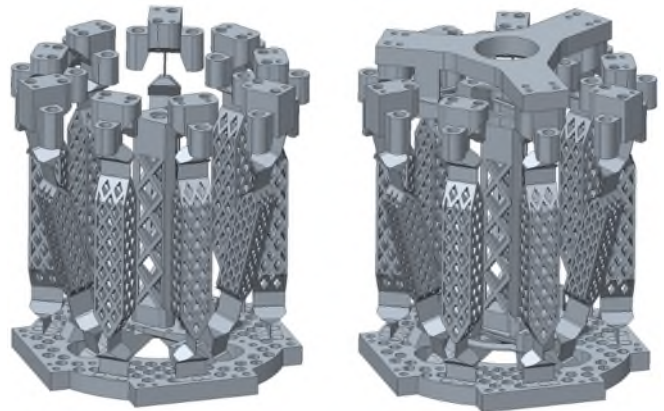
Figure 9. Left: 3D-printed part
Right: After assembly of the connecting rods and the end-effector.

The expected straightness error for the end-effector has been estimated by simulating a selection of vertical loads (in the (-z) direction). For simplicity, the stage was displaced in a single direction, therefore using only one of its two degrees-of-freedom. The results are shown in Fig. 10. It should be noted that the simulation considered geometric non-linearities.

To reduce the computation time and simulation complexity, only the flexible elements were simulated, assuming the rest of the parts as infinitely rigid, as shown in Fig. 11.
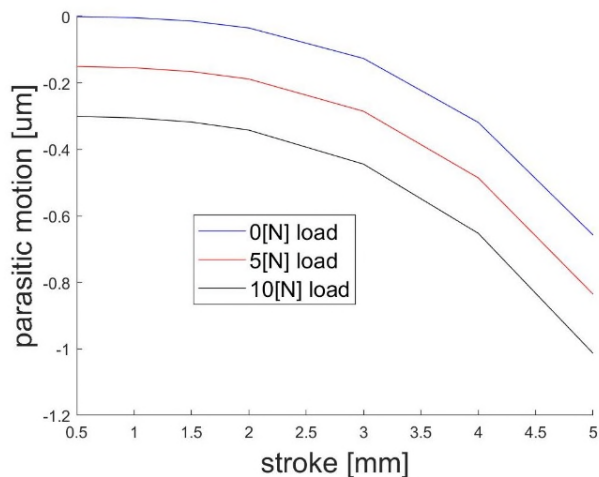
Figure 10. Simulated parasitic motion of the end effector for the steel 3D-printed stage for a selection of vertical compressive loads.

The parasitic motion lies within 0 to 1 micron for loads up to 10 N, corresponding to a straightness error of +-0.5 um. It can also be seen that the straightness errors for the 0 N and 10 N loads have an almost constant difference of 0.3 um. Last, even for zero load, the straightness error is roughly parabolic.
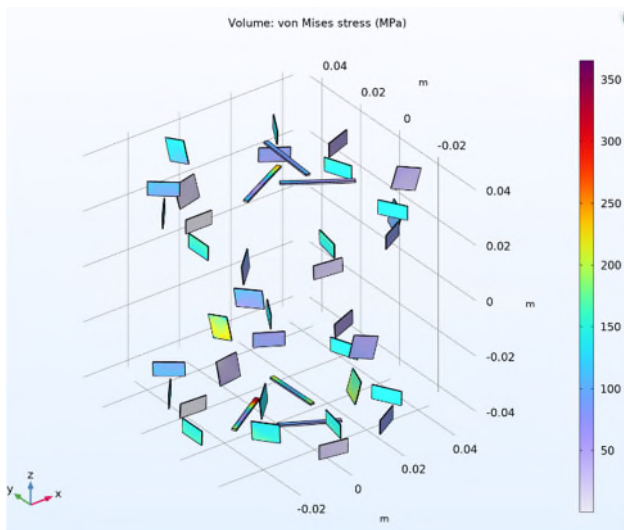
Figure 11. FEM simulation (COMSOL) of the XY-stage at 5 mm stroke. It can be seen that only the flexible elements are simulated and that the stress does not exceed 350 MPa.

4. Discussion

The PA12 demonstrator prototype validates the concept of the kinematics, as it was shown experimentally that the straightness error is within several microns. This demonstrator also highlighted the need for a more precise measurement setup, as the straightness error is within the measurement noise.

The simulated metal further consolidates the concept by reaching a straightness error of +-0.5 um for loads up to 10 N. It should be noted however that the performances will be lower for a physical prototype, as the connecting parts are not infinitely rigid and as there will misalignments between the parts.

Moreover, the small vertical shift of 0.3 um between the non-loaded and 10 N loaded stage shows how this design is well suited to move heavy objects with little loss of straightness.

Lastly, the straightness error may yet be further improved by adjusting the position of the connecting rods as these will adjust the quadratic straightness error of the stage.

5. Conclusion

This paper presented the concept, design, and kinematics of a flexure-based XY-stage. The particularity of this design is that it follows a planar motion with high-precision and that its load-bearing flexures are all solicited in traction/compression. This last property is what allows the stage to withstand higher vertical loads and to have a high stiffness to these loads.

Future work includes fabricating the steel 3D-printed prototype. It will also be necessary to implement a new measurement procedure as it was highlighted by the PA12 demonstrator. Actuation will be a key issue for the automation of this stage.

Acknowledgements

References

[1] Piyu Wang, Qingsong Xu, Design of a flexure-based constant-force XY precision positioning stage, Mechanism and Machine Theory, Volume 108, 2017, Pages 1-13, ISSN 0094-114X, https://doi.org/10.1016/j.mechmachtheory.2016.10.007.

[2] Zhang, Zhen & Yan, Peng & Hao, Guangbo. (2017). A Large Range Flexure-Based Servo System Supporting Precision Additive Manufacturing. Engineering. 3. 708-715. 10.1016/J.ENG.2017.05.020.

[3] Wang, W., Han, C., & Choi, H. (2011). 2-DOF kinematic XY stage design based on flexure element. 2011 IEEE International Conference on Mechatronics and Automation, 1412-1417.

[4] Reymond, Clavel & Bérangère, Le & Bouri, Mohamed. (2011). Ultra-High Precision Robotics: A Potentially Attractive Area of Interest for MM and IFToMM. 10.1007/978-94-007-1300-0_37.

[5] Conception des structures articulées à guidages flexibles de haute précision, Henein, Simon, 2000

[6] Fluckiger, P, Vardi, I, & Henein, S. "Design of a Flexure Based Low Frequency Foucault Pendulum." Proceedings of the ASME 2020 International Design Engineering Technical Conferences and Computers and Information in Engineering Conference. Volume 10: 44th Mechanisms and Robotics Conference (MR). Virtual, online. August 17–19, 2020. V010T10A002. ASME. https://doi.org/10.1115/DETC2020-22075

[7] I. Vardi, L. Rubbert, R. Bitterli, N. Ferrier, M. Kahrobaiyan, B. Nussbaumer, S. Henein, Theory and design of spherical oscillator mechanisms, Precision Engineering, Volume 51, 2018, Pages 499-513, ISSN 0141-6359, https://doi.org/10.1016/j.precisioneng.2017.10.005.

[8] M. Naves, R.G.K.M. Aarts, D.M. Brouwer, Large stroke high off-axis stiffness three degree of freedom spherical flexure joint, Precision Engineering, Volume 56, 2019, Pages 422-431, ISSN 0141-6359, https://doi.org/10.1016/j.precisioneng.2019.01.011.

A review and benchmark study of tool state recognition in the CNC milling process

Chen Yin[1], Jeong Hoon Ko[2*]

[1]Hong Kong Institute for Data Science, School of Data Science, City University of Hong Kong, Kowloon, Hong Kong
[2]Taizhou Institute of Zhejiang University, 618, West Section of Shifu Avenue, Taizhou City, Zhejiang Province

E-mail address: jhkolioneagle@gmail.com

Abstract

CNC milling, one of the most essential and popular machining processes in the manufacturing industry, shows highly time-varying and complicated dynamical characteristics. The importance and complexity of the milling processes have made tool condition monitoring (TCM) a hot issue over the past decades. Recently, the rapid development of machine learning has set off new waves in various fields of industry. Numerous TCM methods utilizing machine learning methods have been explored, and most of them focus on tool wear monitoring, including wear state identification and remaining useful life prediction. However, there is still a lack of capability to predict tool breakage, a more severe and unexpected cutting tool failure mode, concurrently with tool wear status using machine learning. Therefore, the article provides a state-of-the-art review of tool state recognition (TSR), indicating the identification of the holistic tool states from health, wear, and breakage. Specifically, the main sections outline traditional machine learning methods that require signal processing and feature extraction and advanced neural network models that can detect tool states across different working conditions. Three primary methodologies are selected to present a more reliable analysis and intuitive comparison, including typical traditional methods, advanced machine learning, and transfer learning. Benchmark studies are carried out for a tool vibration dataset collected by milling experiments under different working conditions to compare the recognition accuracy and computational efficiency quantitatively. The comparison results address the primary strengths and weaknesses of current methods for TSR. Finally, potential research directions are concluded to enhance TSR's accuracy, efficiency, and reliability.

Milling, Neural networks, Pattern recognition, Tool

1. Introduction

CNC milling, which utilizes rotational cutting tools to intermittently cut workpieces into desired geometric surfaces, is one of the most popular and efficient machining processes in the manufacturing industry. Due to the complex mixed physical and chemical effects caused by forces, shocks, and heat, cutting tools, which are the most active cutting element during the milling process, have high failure risks [1]. Recently, due to the fast development of sensing and information technology, various monitoring signals have been collected during the milling process, and machine learning has become the foremost tool in TCM. However, most TCM studies focus on progressive tool wear, such as wear state identification, wear volume estimation, and remaining useful life prediction. Much less attention has been paid to tool breakage, which is a more severe and unexpected tool failure mode during the milling process.

In order to illustrate the difference between tool breakage and progressive tool wear, a schematic diagram of degradation curves for both situations is given in Figure 1. The average flank wear width (VB) is a widely accepted metric to evaluate the tool life. As shown in Figure 1(a), there are three distinct stages for a progressively worn tool: initial wear, normal wear, and severe wear. The VB values of the tool increase rapidly in the initial wear stage and severe wear stage and vary slowly in the normal wear stage. However, as shown in Figure 1(b), the VB values suddenly jump to a high level close to failure once tool breakage occurs. Usually, tool breakage is prone to occur in the initial wear stage due to improper setting of cutting parameters at the beginning and in the severe wear stage due to the rapidly growing forces acting on the tool with accumulation wear. Tool breakage may also occur when the machining workpiece has a

high hardness and the tool is relatively brittle. Additionally, milling chatter is another main cause of tool breakage. Although analytical models were developed to guide parameter selections [2], the changing geometrical status of cutting tools and unexpected fluctuations in cutting depth could turn stable milling into unstable conditions, and further lead to tool breakage [3,4]. Compared to monitoring progressive tool wear, the detection of tool breakage is more difficult because the tool breakage occurs randomly and instantaneously without warning. Therefore, the quality of the monitoring signals and the detection algorithms need to be further improved to identify the tool breakage status [5].
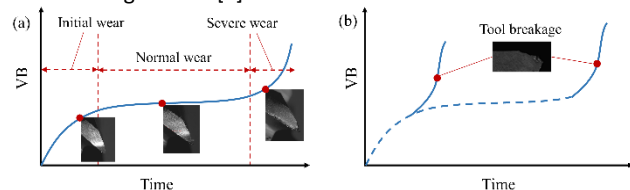
Figure 1. Schematic diagram of progressive wear and breakage degradation curves. (a) Progressive tool wear. (b) Tool breakage.

2. TSR review

2.1. Feature extraction for TSR

Generally, feature extraction methods could be categorized as time-domain methods, frequency-domain methods, and time-frequency domain methods. Time-domain analysis has the advantage of inexpensive computation. Cutting force signals can directly reflect the dynamic variation between tools and workpieces, so multiple studies extracted time-domain features from force signals for TSR [6]. Altintas et al. [7] utilized the difference of force signals to detect the tool breakage in the milling process. Since the current/power varies rapidly with the cutting force and its measurement does not require additional

sensors, various time-domain statistical features like the maximum, average, and standard deviation can be extracted from current/power signals for TSR [8]. Another efficient signal for time-domain analysis is acoustic emission, the primary advantage of which is that the significant frequency range relevant to tool status is much higher than that of the environmental noise and machine tool vibration [9].

The frequency-domain analysis utilizes the fast Fourier transform (FFT) to convert time-domain signals to the frequency domain, and tool failure features are then extracted from the frequency spectra [10]. Compared to pure frequency-domain analysis, the time-frequency analysis is more powerful and more appropriate for the nonstationary and nonlinear monitoring signals [11]. Short-time Fourier transform (STFT), empirical mode decomposition (EMD), and wavelet transform (WT) are mainstream time-frequency methods. STFT is an extension of FFT and can simultaneously analyze signals in both time and frequency domains [12]. WT and its variants, such as discrete wavelet transform (DWT), continuous wavelet transform (CWT), and wavelet packet decomposition (WPT) could be the most popular time-frequency methods. The ability to use high-frequency resolution makes them powerful in the feature extraction of TSR [13]. Compared to WT and its variants, EMD can adaptively decompose signals into a series of intrinsic mode functions (IMFs), which has the advantage of not requiring any predetermined parameters and functions [14]. Hilbert transform [15] and energy-based analysis [16] are widely combined with EMD for TSR.

2.2. Machine learning-based TSR

Machine learning is widely used in TSR to predict the tool states from extracted features, including support vector machine (SVM), hidden Markov model (HMM), random forest (RF), clustering, and artificial neural network (ANN). SVM, developed by statistical learning theory and structural risk minimization principle, is a popular machine learning algorithm [17]. HMM consists of a Markov process that describes transition sequences of hidden states and a random process that establishes observation sequences of hidden states [18]. RF is a typical ensemble learning method that combines the output of multiple decision trees to give a comprehensive prediction [19]. Dahe et al. [20] extracted statistical features from vibration signals and utilized RF to recognize tool conditions. Jogdeo et al. [21] utilized a statistical analysis method to tune hyperparameters of the random forest and achieved robust recognition of tool states.

ANN has become the most popular decision-making method in various domains, which shows excellent nonlinear learning ability to recognize tool breakage and tool wear from signal features [22]. Huang et al. [23] proposed a probabilistic neural network for the decision-making analysis of a tool breakage detection system. Different from other machine learning algorithms, clustering is an unsupervised learning method that can be used for anomaly detection purposes [24]. Torabi et al. [25] extracted wavelet features of force and vibration signals for the clustering analysis, and the results showed that clustering methods are repeatable and noise-robust in TSR. Gui et al. [26] utilized the clustering method to analyze the time-domain features for real-time tool breakage detection.

2.3. Deep learning-based TSR

Deep learning models with powerful nonlinear fitting abilities have the advantage of handling large and complex datasets [27]. Typical deep learning models for TSR include auto-encoder (AE), recurrent neural network (RNN), and convolutional neural network (CNN). AE is a powerful unsupervised learning algorithm for the extraction of tool failure features [28]. Kin et al. [29] proposed a stacked AE-based CNC machine tool

diagnosis system. Popular RNNs include long short-term memory (LSTM) [30] and gated recurrent units (GRU) [31], which are ideal options for the process of time-series tool monitoring signals [32]. Nam and Kwon [33] proposed a tool breakage monitoring system with LSTM-based autoencoders. Due to the outstanding ability of nonlinear mapping, CNN has become the actual standard in deep learning communities and is widely used in TSR [34]. Yin et al. [35] combined the one-dimensional CNN (1D-CNN) and deep generalized canonical correlation analysis for tool failure diagnosis based on multiple sensor signals.

The application of deep learning models in TSR requires a large amount of training data. However, in the practical milling process, the cutting tool is only allowed to work in health conditions. Once the tool wear/breakage occurs, the CNC machine tool will shut down immediately. Namely, limited failure samples could be collected for TSR in the practical milling process. In this case, transfer learning methods are studied to solve the data imbalanced problem [36]. Li et al. [37] proposed a Wasserstein generative adversarial network to monitor tool breakage under data-imbalanced conditions.

3. Benchmark study

3.1. Experimental setup

To perform the benchmark study of typical TSR techniques, milling experiments were carried out on a five-axis machining center. As shown in Figure 2, a three-axis accelerometer was mounted on the spindle box to collect the cutting vibration signals, and the machined workpiece is a brick with a material of #45 steel. The four-edge end milling cutter with a diameter of 12 mm was studied in the experiments, and those in health, wear, and breakage status, as shown in Figure 3, were used to machine the workpiece. The cutting depth was 1 mm, and the feed rate was set to 0.1 mm/rev. Moreover, rotation speeds of 2000 RPM, 2600 RPM, and 3200 RPM were used to collect cutting vibration signals with a sampling frequency of 12 kHz.
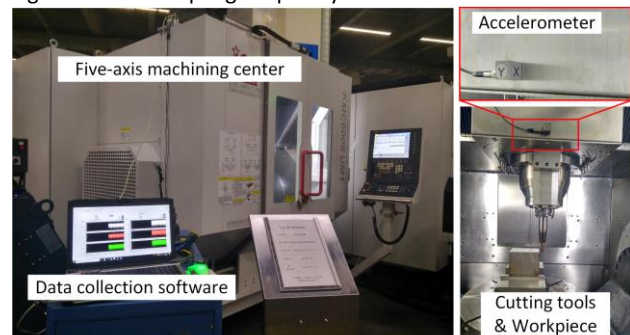
Figure 2. Milling experimental setup

(a) Health   (b) Wear   (c) Breakage
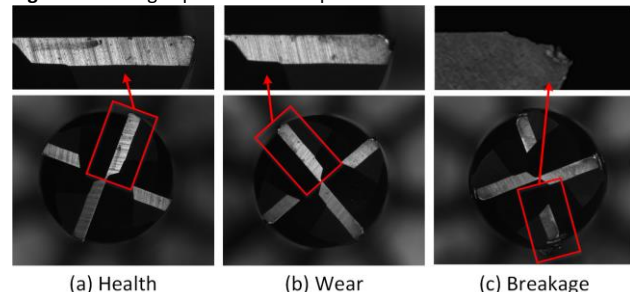
Figure 3. Three different cutting tools status

After the milling experiments, vibration signals of cutting tools under different health conditions (health, wear, and breakage) and various working conditions (2000 RPM, 2600 RPM, and 3200 RPM) were obtained. Since these vibration signals were collected under actual machining processes, signal pre-processing techniques were performed to remove the signal segments collected during air cutting. Finally, the X-directional vibration signals collected under different working conditions

are utilized to organize data samples, and a total of 1500 data samples were obtained for each condition. The constructed three datasets are shown in Table 1. The raw vibration signals as well as the frequency spectra of data samples in dataset C are visualized in Figure 4.

Table 1 Dataset definition

Dataset	Spindle speed	Tool condition	Sample Number
Dataset A	2000 RPM	Health/wear/breakage	500/500/500
Dataset B	2600 RPM	Health/wear/breakage	500/500/500
Dataset C	3200 RPM	Health/wear/breakage	500/500/500
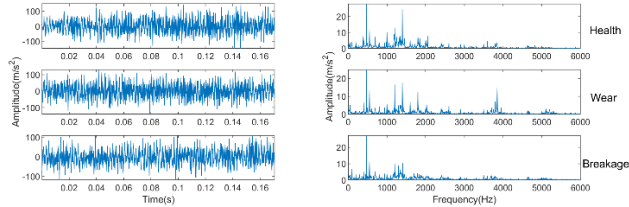
Figure 4. X-directional vibration signals collected under 3200 RPM

3.2. TSR methods selection

Three typical TSR methods are selected to present the comparative studies, which include typical machine learning methods, deep learning neural networks, and transfer learning techniques. A brief introduction to these approaches is given as follows,

1) Feature extraction with SVM (FE-SVM). As one of the most popular shallow learning approaches, SVM is widely used in TSR. Fault features extracted from the time domain, frequency domain, and time-frequency domain are utilized as the model inputs [38]. FE-SVM is introduced in comparative studies to demonstrate the performance of traditional shallow models for TSR.

2) 1-D CNN. The 1-D CNN is a standard of deep learning approaches and is also widely used in TSR. Thus, a 1-D CNN with a typical structure of two convolutional layers and three fully connected layers is studied [34], which can give a comparison of deep models to shallow ones. The frequency spectra of vibration signals are utilized as the model inputs.

3) Cross-domain adaptation networks with attention mechanism (CDATT). CDATT is an advanced transfer learning model that utilizes the attention mechanism to capture the significant fault features, and a joint distribution adaptation regularization term is constructed to solve the performance degradation under variable working conditions [39].

3.3. Results and analysis

The comparative studies are performed under nine scenarios, and the identification results are given in Table 2. It is worth noting that the ratio of training data to test data in all scenarios is 7:3, and the training and testing data are the same for all methods. For scenarios 1, 5, and 9 where the testing samples are from the same dataset as the training samples, the identification results show that the identification accuracies of FE-SVM are close to 1-D CNN and CDATT, indicating that shallow learning models can achieve competitive performance with deep learning models in the scenario of same working conditions. However, for the other scenarios where the testing samples are from different datasets, the identification results show that FE-SVM suffers from a significant performance degradation compared to 1-D CNN and CDATT in TSR. On the other hand, although the identification results of 1-D CNN are much better than FE-SVM, there is a distinct performance gap between 1-D CNN and CDATT. Namely, the results indicate that the tool failure features extracted by 1-D CNN are more robust than hand-crafted features utilized in FE-SVM, but these features cannot be well adapted to a fresh situation in TSR. In such different situations, transfer learning models like CDATT can be a good option for TSR. The ability to learn cross-domain tool failure features can solve the domain discrepancy caused by different working conditions.

Table 2 Identification accuracy (%) for different models under different scenarios.

No.	Scenario	FE-SVM	1-D CNN	CDATT
1	Dataset A to A	99.1	100	100
2	Dataset A to B	23.87	61.93	99.29
3	Dataset A to C	25.46	57.54	86.59
4	Dataset B to A	27.32	63.1	99.09
5	Dataset B to B	88.9	98.57	99.87
6	Dataset B to C	32.2	61.47	90.32
7	Dataset C to A	32.4	66.31	91.48
8	Dataset C to B	37.75	73.94	99.5
9	Dataset C to C	93.16	99.42	100

The computation burden and efficiency of the identification algorithm are other evaluation metrics in TSR. The training and testing time of different algorithms in scenario 9 are presented in Table 3. It can be seen that the training time of FE-SVM is much lower than deep learning models, and the computation burden increases with the complexity of deep learning models. Nevertheless, well-trained 1-D CNN and CDATT are more efficient in the testing stage than SVM. The results indicate that although deep learning models require more computation burden in the model training stage, they could be more efficient than shallow learning models.

Table 3 Computation time for different models in scenario 9.

Model	Training time (s)	Testing time (ms)
FF-SVM	4.31	377.65
1-D CNN	72.56	8.92
CDATT	167.05	16.14

4. Conclusion

This paper provides a comprehensive review of TSR, while feature extraction-based, machine learning-based, and deep learning-based methods are detailed and summarized. Moreover, milling experiments under different working conditions are carried out, and benchmark studies among three popular TSR approaches are presented through the collected tool data. Based on the review and benchmark studies, conclusions and suggestions for TSR, especially potential challenges for the practical application of deep learning models in TSR are summarized as follows,

1) Literature review indicates that machine learning and deep learning methods have become state-of-the-art techniques in TSR. The results of benchmark studies demonstrate that deep learning models show better identification accuracy than typical feature extraction-based shallow learning methods. Therefore, exploring more accurate and robust deep learning models in TSR can be a good research direction.

2) Regarding computation burden and efficiency, the results of benchmark studies reveal that deep learning models take more computation time but operate more efficiently in the testing stage. However, some occasions, such as online monitoring, require the TSR model iterative upgrades with increasing milling data. So, the requirements on heavy computation burden may still be a nonnegligible drawback that restricts the application of deep learning models. Therefore, research on simplifying models without degrading model performance is still a necessary and promising topic.

3) Since collecting sufficient data samples with specific milling conditions to train a deep learning model from scratch is always costly and time-consuming, the development of transfer learning TSR models can be a good solution to tackle this problem. The results of benchmark studies exhibit that the transfer learning-based model can perform well in unseen work conditions. Therefore, exploring robust and accurate TSR models on limited or even no data conditions needs more attention in future work.

4) Although advanced deep learning models show superior performance than traditional feature extraction-based models in TSR, the black-box nature and complex information mapping process make them difficult for users to understand. However, in industrial scenarios, especially high-value milling processes, the explainability and reliability of the identification algorithm are of great importance. Therefore, integrating various knowledge like physics, simulation, or theory in deep learning models and improving their interpretability is an urgent and essential topic.

5) Current TSR research concentrates on developing models with higher detection accuracy and lower prediction error but ignores the inevitable effects of uncertainties on prediction results. Typical uncertainties include milling environment fluctuation, data collection device degradation, and noise interference. Therefore, considering the uncertainty and transforming the point prediction framework into an interval prediction framework to improve model practicality are also challenging and valuable topics.

References

[1] Zhou Y. and Xue W. 2018 Review of tool condition monitoring methods in milling processes. *Int J Adv Manuf Technol.* **96** 2509–2523

[2] Ko J.H. 2015 Time domain prediction of milling stability according to cross edge radiuses and flank edge profiles. *Int J Mach Tools Manuf.* **89** 74–85

[3] Yin C., Wang Y., Ko J.H., Lee H.P. and Sun Y. 2023 Attention-driven transfer learning framework for dynamic model guided time domain chatter detection. *J Intell Manuf.* 1-19

[4] Ko J.H. 2022 Machining Stability Categorization and Prediction Using Process Model Guided Machine Learning. *Metals* **12**, 298

[5] Nath C. 2020 Integrated Tool Condition Monitoring Systems and Their Applications: A Comprehensive Review. *Procedia Manuf* **48** 852–863

[6] Zhu K., Mei T. and Ye D. 2015 Online Condition Monitoring in Micromilling: A Force Waveform Shape Analysis Approach. *IEEE Trans Ind Electron* **62** 3806–3813

[7] Altintas Y., Yellowley I. and Tlusty J. 1988 The Detection of Tool Breakage in Milling Operations. *J. Eng. Ind.* **110** 271–277

[8] Bhuiyan M.S.H. and Choudhury I.A. 2014 Review of Sensor Applications in Tool Condition Monitoring in Machining. *Comprehensive Materials Processing*. **13** 539–569.

[9] Hassan M., Sadek A., Damir A., Attia M.H. and Thomson V. 2016 Tool Pre-Failure Monitoring in Intermittent Cutting Operations. *ASME Int Mech Eng Congress Expo*. **50527** V002T02A049

[10] Hamidieh Y. A., Seth B. B. and Sridhara R. 2001. Enhancement for Frequency Domain Based Tool Breakage Detection System. In *ASME Int Mech Eng Congress Expo*. **35487** 309-316.

[11] Yin C., Wang Y., Lee H.P., He J., He Y. and Sun Y. 2021 Robust wheel wear detection for solid carbide grinding under strong noise interference: A new approach based on improved ensemble noise-reconstructed empirical mode decomposition. *Wear*. **486** 204112.

[12] Zamudio-Ramirez I., Osornio-Ríos R.A., Diaz-Saldaña G., Trejo-Hernández M. and Antonino-Daviu J.A. 2020 STFT-based induction motor stray flux analysis for the monitoring of cutting tool wearing in CNC machines. *IECON 2020 The 46th Annual Conference of the IEEE Industrial Electronics Society*. 2511–2516.

[13] Sevilla-Camacho P.Y., Herrera-Ruiz G., Robles-Ocampo J.B. and Jáuregui-Correa J.C. 2011 Tool breakage detection in CNC high-speed milling based in feed-motor current signals. *Int J Adv Manuf Technol.* **53** 1141–1148

[14] Yin C., Wang Y., Ma G., Wang Y., Sun Y. and He Y. 2022 Weak fault feature extraction of rolling bearings based on improved ensemble noise-reconstructed EMD and adaptive threshold denoising. *Mech Syst Signal Process.* **171** 108834

[15] Peng Y. 2004 Empirical Model Decomposition Based Time-Frequency Analysis for the Effective Detection of Tool Breakage. *J. Manuf. Sci. Eng.* **128** 154–166

[16] Chen Q., Xie M., Zou Z., and Yang Z. 2023 Multi-signal comparison and analysis of tool wear based on EMD energy decomposition method. *2023 4th International Conference on Mechatronics Technology and Intelligent Manufacturing* 517-521.

[17] Sun S., Hu X., Cai W. and Zhong J. 2019 Tool Breakage Detection of Milling Cutter Insert Based on SVM. *IFAC-PapersOnLine.* **52** 1549–1554

[18] Lu M.-C. and Wan B.-S. 2013 Study of high-frequency sound signals for tool wear monitoring in micromilling. *Int J Adv Manuf Technol.* **66** 1785–1792

[19] Wu D., Jennings C., Terpenny J., Gao R.X. and Kumara S. 2017 A Comparative Study on Machine Learning Algorithms for Smart Manufacturing: Tool Wear Prediction Using Random Forests. *J. Manuf. Sci. Eng.* **139**

[20] Virendra Dahe S., Sai Manikandan, G. Jegadeeshwaran, R. Sakthivel, G. and Lakshmipathi J. 2021 Tool condition monitoring using Random forest and FURIA through statistical learning. *Mater Today Proc.* **46** 1161–1166

[21] Jogdeo A.A., Patange A.D., Atnurkar A.M. and Sonar P.R. 2023 Robustification of the Random Forest: A Multitude of Decision Trees for Fault Diagnosis of Face Milling Cutter Through Measurement of Spindle Vibrations. *J. Vib. Eng. Technol.* 1-19

[22] Corne R., Nath C., El Mansori M. and Kurfess T. 2017 Study of spindle power data with neural network for predicting real-time tool wear/breakage during inconel drilling. *J Manuf Syst.* **43** 287–295

[23] Huang P.B., Ma C.-C. and Kuo C.-H. 2015 A PNN self-learning tool breakage detection system in end milling operations. *Appl Soft Comput.* **37** 114–124

[24] Fu P., Li W. and Guo L. 2011 Fuzzy Clustering and Visualization Analysis of Tool Wear Status Recognition. *Procedia Eng.* **23** 479–486

[25] Torabi A.J., Er M.J., Li X., Lim B.S. and Peen G.O. 2016 Application of Clustering Methods for Online Tool Condition Monitoring and Fault Diagnosis in High-Speed Milling Processes. *IEEE Syst J.* **10** 721–732

[26] Gui Y., Lang Z.-Q., Liu Z., Zhu Y., Laalej H. and Curtis D. 2023 Unsupervised Detection of Tool Breakage: A Novel Approach Based on Time and Sensor Domain Data Analysis. *IEEE Trans Instrum Meas.* **72** 1–13

[27] Xiao W., Huang J., Wang B. and Ji H. 2022 A systematic review of artificial intelligence in the detection of cutting tool breakage in machining operations. *Measurement.* **190** 110748

[28] Song G., Zhang J., Zhu K., Ge Y., Yu L. and Fu Z. 2023 Tool wear monitoring based on multi-kernel Gaussian process regression and Stacked Multilayer Denoising AutoEncoders. *Mech Syst Signal Process.* **186** 109851

[29] Kim J., Lee H., Jeon J.W., Kim J.M., Lee H.U. and Kim S. 2020 Stacked Auto-Encoder Based CNC Tool Diagnosis Using Discrete Wavelet Transform Feature Extraction. *Processes.* **8** 456

[30] Zhang J., Zeng Y. and Starly B. 2021 Recurrent neural networks with long term temporal dependencies in machine tool wear diagnosis and prognosis. *SN Appl. Sci.* **3** 442

[31] Wang J., Li Y., Zhao R. and Gao R.X. 2020 Physics guided neural network for machining tool wear prediction. *J Manuf Syst.* **57** 298–310

[32] Zegarra F.C., Vargas-Machuca, J. and Coronado A.M. 2023 A Comparative Study of CNN, LSTM, BiLSTM, and GRU Architectures for Tool Wear Prediction in Milling Processes. *J of Mach Eng.* **23** 122-136

[33] Nam J.S. and Kwon W.T. 2022 A Study on Tool Breakage Detection During Milling Process Using LSTM-Autoencoder and Gaussian Mixture Model. *Int. J. Precis. Eng. Manuf.* **23** 667–675

[34] Yin C., Wang Y., He Y., Liu L., Wang Y. and Yue G. 2021 Early fault diagnosis of ball screws based on 1-D convolution neural network and orthogonal design. *P I MECH ENG O-J RIS*. **235** 783-797

[35] Yin Y., Wang S. and Zhou J. 2023 Multisensor-based tool wear diagnosis using 1D-CNN and DGCCA. *Appl Intell.* **53** 4448–4461

[36] Deng C., Tang J., Miao J., Zhao Y., Chen X. and Lu S. 2023 Efficient stability prediction of milling process with arbitrary tool-holder combinations based on transfer learning. *J Intell Manuf.* **34** 2263–2279

[37] Li X., Yue C., Liu X., Zhou J. and Wang L. 2024 ACWGAN-GP for milling tool breakage monitoring with imbalanced data. *Robot Comput Integr Manuf.* **85** 102624

[38] Liao X., Zhou G., Zhang Z., Lu J. and Ma J. 2019 Tool wear state recognition based on GWO–SVM with feature selection of genetic algorithm. *Int J Adv Manuf Technol.* **104** 1051–1063

[39] He J., Sun Y., Yin C., He Y. and Wang Y. 2023 Cross-domain adaptation network based on attention mechanism for tool wear prediction. *J Intell Manuf.* **34** 3365–3387

euspen's 24th International Conference &
Exhibition, Dublin, IE, June 2024
www.euspen.eu

Energy-saving tool path generation for NC machine tools by model based simulation of feed drive system

Akio Hayashi[1], Naru Kawamura[1], Yoshitaka Morimoto[1]

[1]*Kanazawa Institute of Technology*

a-hayashi@neptune.kanazawa-it.ac.jp

Abstract

Due to the problem of depletion of energy resources and the rise in energy prices in recent years, as SDGs of section 7and 9.4, and GX (green transformation) are being advocated, energy conservation has become an essential issue in various fields. Therefore, the authors focused on the power consumption required for feeding during machine tool operation and clarified that the energy consumption differs depending on the tool path. Based on the results, we thought that it would be possible to save energy by modifying the tool path when processing the same product. In this study, we regenerated an energy-saving tool path by solving a path search problem that uses energy consumption as a weight for the tool path generated by our unique tool path generation system. This paper shows that it is possible to save energy in the tool path by considering the energy required for the feed motion of the machine tool, and its effects.

Keywords: Energy consumption, NC machine tools, Tool path, Model based simulation

1. Introduction

In recent years, reducing energy consumption at production sites is an urgent issue, and efforts are being made to make NC machine tools, which are the main production equipment for machining, more energy efficient. Measurement of power consumption, miniaturization, and improvement of efficiency have been carried out, but few have focused on the tool path. The machining tool path of NC machine tools is generated by CAM software. However, these generated programs do not consider the energy consumption of the feed drive system, and cannot be said to be an energy-saving tool path.

Therefore, the authors focused on the power consumption required for feeding during machine tool operation and clarified that the energy consumption differs depending on the tool path. In this study, we develop an energy-saving tool path generation system that takes into account the power consumption in the feed drive system of machine tools. We propose a system that performs machining simulation on 3D-CAD and obtains tool position coordinates and calculates tool paths while taking energy efficiency into consideration.

Furthermore, by using the mathematical model of the machine tool's feed drive system, we simulated the power consumption in tool paths during driving of the machine tool's moving table. Finally, we verify the energy saving effect of the proposed method by estimating the energy consumption. However, this paper only examines the energy consumption due to the tool path by the feed drive axis, and does not take into account the spindle energy required for cutting.

2. Proposed energy saving tool path generation system

In this study, we used SolidWorks as the 3D-CAD software, and created a tool position coordinate acquisition system using the VBA (Visual Basic Application) engine. CAD models of machined parts and tools are placed in the assembly as shown in Figure 1. Then, the tool is moved on the CAD so that the tool end and the part shape come into contact, and the tool center coordinates at that contact point are obtained as the tool path. Rough machining is performed using scanning line machining.

Furthermore, we developed a program that generates the shortest and energy-saving tool path from the acquired tool position coordinate points. In this study, for a method for calculating the shortest and energy-saving tool path, we adopted the greedy method that minimizes the sum of the distances of a circuit that passes through the coordinate points of all points only once.

Considering that the power consumed when moving on each axis is different, we used the power consumption of each axis as a cost index, as shown in Figure 2. The system calculate for a tool path that minimizes the total cost. Equation (1) shows the cost on the X axis as C_x, the cost on the Y axis as C_y, the cost on the Z axis as C_z, and the total cost as C_min. This results in the generation of a tool path that consumes less energy. Furthermore, by using a cost index, the proposed system can be applied even if the mechanism of the machine tool used changes.

$$C_{min} = \sum_{k=1}^{n} k\, C_x + \sum_{k=1}^{n} k\, C_y + \sum_{k=1}^{n} k\, C_z \qquad (1)$$
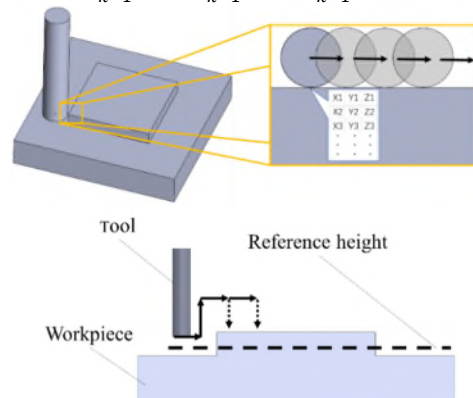
Figure 1. Schematic diagram for tool path generation on 3D-CAD
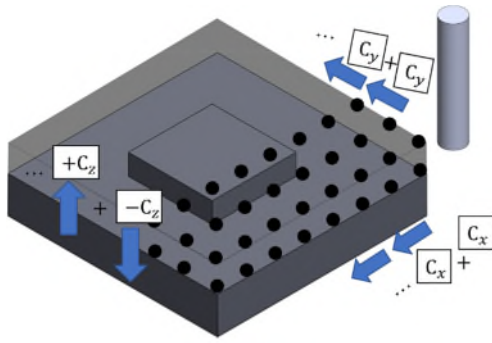
Figure 2. Schematic diagram for energy saving tool path generation

3. Evaluation of proposed method

In order to demonstrate and evaluate the energy-saving tool path generation method, tool paths were generated using a workpiece model shown in Figure 3. The tool was assumed to be a square end mill with a tool diameter of 5 mm.

Figure 4(a) shows the generated tool path when the cost values for each movement direction are set to C_x=1 and C_y=2, and Figure 4(b) shows the generated tool path when the cost values are set to C_x=2 and C_y=1.

Then, the power consumption of each axis are simurated by simulation model of the feed drive system as shown in Figure 5 [2], and calculated the energy consumption. The power consumption is simulated assuming that it is equal to the motor power, which is the multiplied of the motor torque and the angular velocity. Here, it was confirmed that the power consumption of each axis (X, Y) of the machine tool is greater for the X axis. The power consumption simulation results in tool paths are shown in Figure 6. Table 1 also shows the energy consumption.

The results for tool path (a) show that energy consumption is reduced. This is because by setting the cost values C_x=1 and C_y=2, the X-axis movement time becomes longer with low power consumption cost. From this, the effectiveness of the energy-saving route generation system was demonstrated by understanding the power consumption of the machine tool's feed axis and introducing this into the system as a cost index.

4. Conclusions

In this study, we focused on the power consumption of the feed drive system of machine tools, and developed tool path generation system that considering the energy efficiency. In addition, we performed tool path generation and simulation the energy consumption based on the model of the feed drive system, and evaluated the validity of the proposed method. The conclusions obtained in this study are shown below.

1. We proposed a tool path generation method that uses the power consumption of each axis as a cost index to generate the shortest path.

2. By the proposed tool path generation method, we achieved energy savings in the tool path based on the power consumption of each axis.

In tool path generation in this paper, only the X- and Y-axes are set as cost indicators, and the Z-axis movement is not considered. However, the power consumption of the Z-axis is extremely large, and it is known that it also varies depending on the direction of vertical movement. Taking this into account is thought to lead to further energy savings, and is the next topic of this study. In addition, the model of spindle considering cutting force will be generated. Then, the energy consumption by the cutting power can be simulated and estimated.
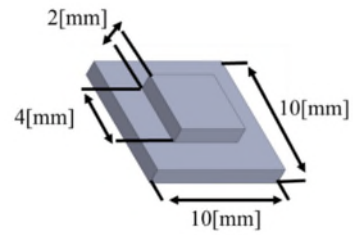
Figure 3. Workpiece model for tool path generation
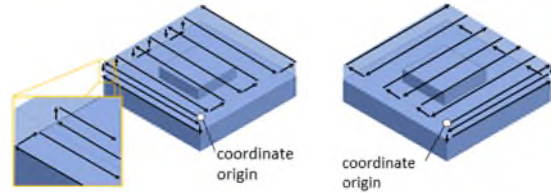
(a) C_x=1, C_y=2　　　(b) C_x=2 and C_y=1
Figure 4. Regenerated tool paths for energy-saving
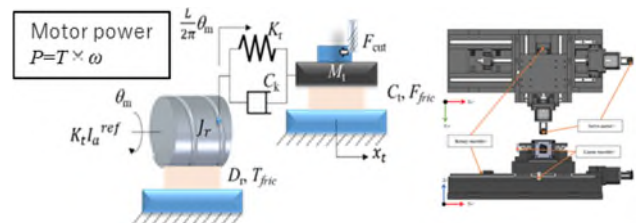
Figure 5. Two-inertia model of ball screw feed drive system [2]
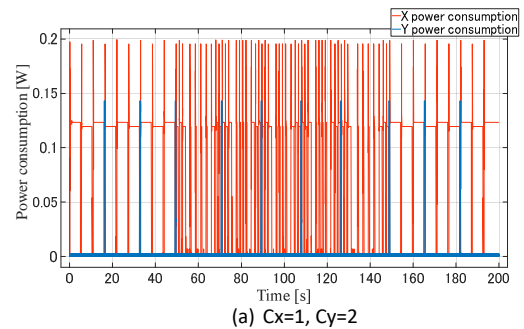
(a) Cx=1, Cy=2
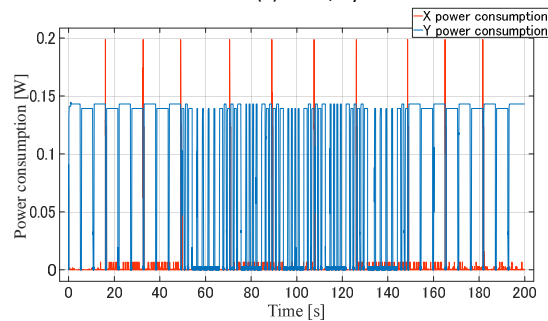
(b) Cx=2, Cy=1
Figure 6. Power consumption of regenarated tool path for energy saving

Table 1 Energy consumption in each axis

	X axis [J]	Y axis [J]	Total [J]
(a)	16.65	0.927	17.57
(b)	0.618	19.37	19.98

References

[1] Hayashi A, Arai F, and Morimoto Y, Simulation of Energy Consumption During Machine Tool Operations Based on NC Data, 2021 *Int. J. Automation Technol*. **15** 764

[2] Gobayashi K, Hayashi A, and Morimoto Y, Model based development of NC moving table by ball screw driving mechanism, 2023 *Proceedings of Annual Conference of the Society of Instrument and Control Engineers* 127

Use of digital tools to simulate the accuracy of subtractive machining processes

Simon Fletcher[2], Steve Taylor[1], Steve McVey[1], Patrick Land[1], Andrew Longstaff[2]

[1]Machine Tool Technologies Ltd
[2]University of Huddersfield

s.fletcher@hud.ac.uk

Abstract

The use of Digital tools and IIoT (Industrial Internet of Things) has been a common theme in global research and development over the past decade. This paper describes a newly developed digital environment where the simulation of the machine and machining process can be carried out, with the results indicating the process capability using inspection of a virtual part.

By developing high fidelity digital twins of systems using a process that combines pre-calibration and on-machine data captured from both the machine controller and external sensors, it is possible to use a series of mathematical models to simulate the machining process and develop an accurate prediction model of the machined parts. The digital environment combines models of known and predicted geometric and thermal errors. This process can be used to accelerate product and process development without needing to waste valuable production time or precious materials. It can also be used virtually to validate new machine concepts and de-risk high value manufacturing operations, enabling a much more cost effective and sustainable method of manufacturing machine and process design and development. This paper outlines the approach taken to enable the application of the digital tools developed and focuses on the effect of machine geometric errors in a case study. Preliminary validation is achieved by comparing virtual inspection of the virtual part with CMM data for a test part, showing good correlation of typical feature characteristics.

Keywords: Machine tool, error simulation, digital twin, virtual part production, digitalisation of manufacturing

1. Introduction

The use of Digital tools and IIoT (Industrial Internet of Things) has been a common theme in global research and development over the past decade. For machine tools, simulation of the machine is used in CAM packages to calculate nominal tool paths. Machine tools are complex mechatronic systems with build tolerances, finite stiffness and temperature variations from endogenous and exogenous sources. Models have been created to calculate these effects and, in some cases, compensate for them [1]. Some simulation tools also provide cutting force prediction for complex subtractive processes. Merdol and Altintas [1] integrated a general force model into a process simulation application to predict static cutting forces along a given toolpath. The models have been integrated into commercial software packages such as MachPro [3] to help improve quality and productivity, however the machine path in such simulations is nominal. Soori et al [4] predicted the effects of multiple machine errors sources but only a path profile was compared. Similarly, Lyu et al [5] predicted error on a complex S-shaped profile but did not have machined part comparison. Production capability for a range of parts, features and characteristics is not known unless test parts are produced and inspected. Although case- or error- specific models have been developed in the past, they have not been combined coherently and translated into a virtual part with virtual inspection to provide a general view of cumulative machining errors and feature/characteristic specific analysis for GD&T type capability analysis. This paper describes a digital environment where the simulation of the machine and machining process can be carried out efficiently, with the results indicating the process capability using CMM style inspection of a virtual part.

2. Simulation methodology

This research follows on from previous work on developing modular machine and process simulation [6] but focuses on feature generation and GD&T characteristic analysis and validation. Figure 1 shows a block diagram of the main elements of the modular program. Iso standard G-code programs are parsed and run a virtual machine that incorporates a custom interface to the highly efficient MachineWorks Limited Boolean engine. Stock, tooling, and error data (geometric in this case) are loaded as needed depending on the machine configuration.
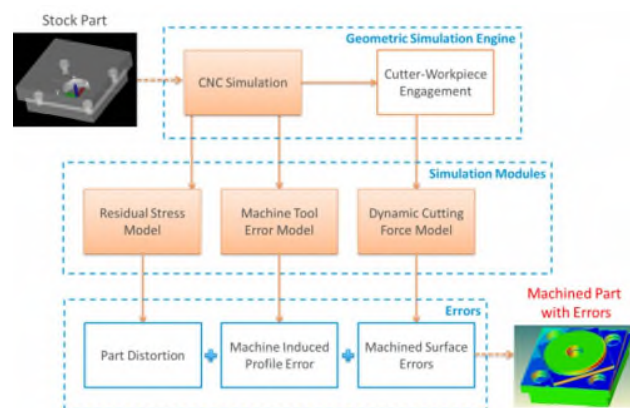
Figure 1. Modular machine and process simulation diagram

2.1 Error measurement

The simulation accuracy is dependent on the quality of the measurement data, therefore well-established measurement methods and equipment were used to capture the geometric

errors in accordance with the ISO230-2 standard. A Renishaw XM-60 multi-axis calibrator was the primary tool for efficient measurement of the axis motion errors. The squareness between the axis was obtained using a granite artefact.

2.2 Part detail and CAM setup

The test parts are based on the ISO 10791 part 7 standard with the size ranging from 150mm to 250mm stock size. The 150 mm part was machined on a small 3-axis milling machine with configuration wX'Y'bZ(C)t using ISO 10791-2 notation [7]. The 250 mm part was machined on a small to medium sized 5-axis machine with configuration wC'A'X'Y'bZ(C)t. Example configurations are shown in Figure 2. The right image from the standard has the X axis moving the column whereas the test machine had the X axis moving the tilt/rotary table.
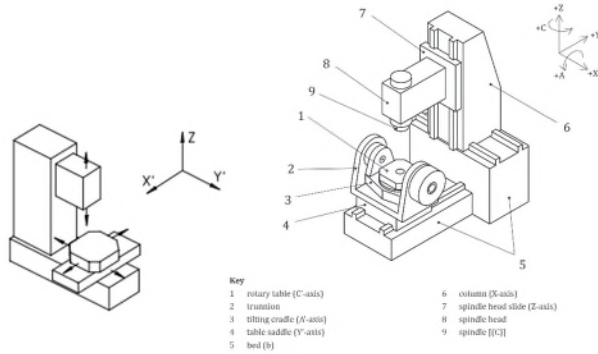
Figure 2. Machine configurations [7].

Figure 3 shows the finished 250 mm part clamped on the CNC machine. Aluminium was chosen to minimise tool wear and cutting force effects thereby reducing uncertainties associated with tool deflection which are still being worked on in the software. The machining parameters were different on each machine due to different operators and tooling availability. The brief was to minimise forces and generate good surface finish during the finishing.

A 0.1 mm axial depth of cut and 0.05mm radial depth of cut was used for the finishing cuts to further minimise cutting force effects. For the 150mm part, which was machined at MTTs facility (the company affiliate), a 16mm diameter, 2 flute cutter was used. The spindle speed was 8017 rpm and feedrate of 4810 mm/min. For the 250 mm part, a 12mm diameter, 3 flute cutter was used. The spindle speed was 5305 rpm and feedrate of 795 mm/min.
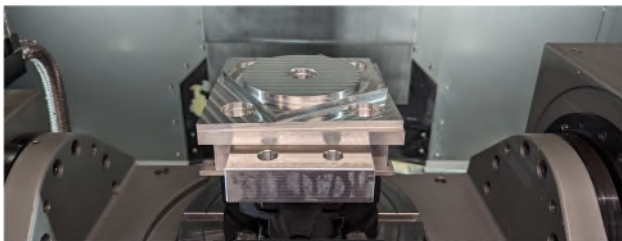
Figure 3. Aluminium test part located on the machine tool.

2.3 Virtual production

The machine geometry is usually represented by simplified structures although detailed models can be used if they are available. A Parent/child tree is built as per the machine structure with additional 6DoF added to each joint to allow the axis motion errors to be added to each axis using simple rotational and translational transformations, applied sequentially. Additional non-motion axes can be used to add additional degrees of freedom, for example for squareness

between axes or where the centre of rotation does not move with the axis. There is no algorithmic definition of the machine so developing new configurations with any configuration is very easy and accessible for many types of users. This assumes rigid body behaviour which has shown to be effective [1] and is used in most NC systems for compensating geometric errors.

During the simulation, multiple parts can be generated simultaneously in the engine, one nominal and the rest with different sets of errors active. In this case just one extra with geometric errors was used. Figure 9 (left) shoes a uniform mesh, the spatial resolution of which depends on the number of cuts and the simulation resolution. Figure 9 (right) show more variability in the face shapes due to the tool to workpiece errors. The generated meshes can also be saved as STL files for additional post processing such as virtual inspection (section 3.1).
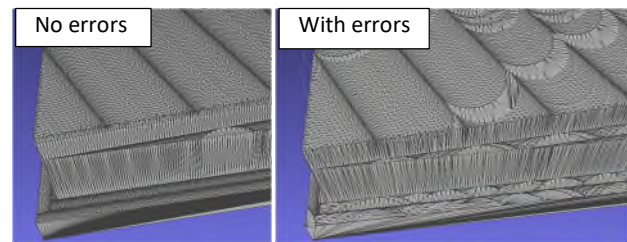
Figure 4. Generated STL surface examples with and without errors

During machining, the tool to workpiece cartesian error and orientation errors are recorded. **Figure 5** shows the errors during the full machining cycle. The number of process steps on the X axis is 1.9×10^5. The software has built in colour map analysis to show material on and off compared to set tolerances. Increasing dark red colour indicates more material off and increasingly darker blue indicates material on. The 250mm part is shown in Figure 6.
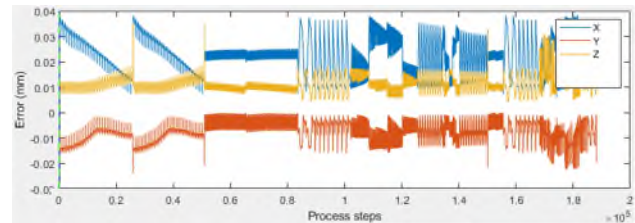
Figure 5. Full machining path tool to workpiece error record.
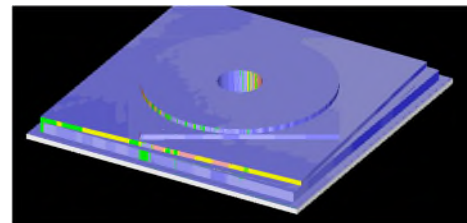
Figure 6. Colour map indicating path errors on virtual part.

3. Part inspection

Part inspection was performed on a Zeiss Prismo Access CMM in a temperature-controlled room. The volumetric accuracy of the CMM is 3 µm. Typical characteristics of size, roundness flatness and straightness were measured on the main features with a selection of these included in this short paper. Figure 7 shows the part on the CMM (inset) and some of the characteristics in the Zeiss Calypso software.

All the features were scanned so that a high number of points were available to the form characteristics. For example, the top circle scan typically includes between 500 to 1000 points depending on the size. Standard filtering and outlier elimination were used which are included in the Calypso software and which conform to the ISO standards. The typical scan speed was just 10mm/s to minimise vibration and the stylus tip was a 4 mm diameter ruby.
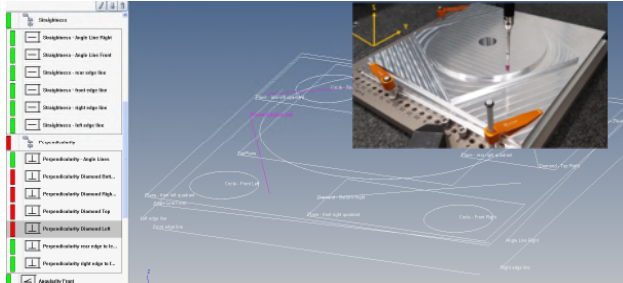
Figure 7. Modular machine and process simulation block

3.1 Inspection of virtual part

The STL file faces were selected for each of the features using a search for all contiguous faces based on how similar the normal angles are. **Figure 8** shows two example features (top cylinder and diamond edge), the faces of which are saved to be compared with the CMM probing points. In this example there are more than 2000 faces for the top cylinder but the number varies depending on the spatial resolution of the simulated cuts and the rate of change of the errors.
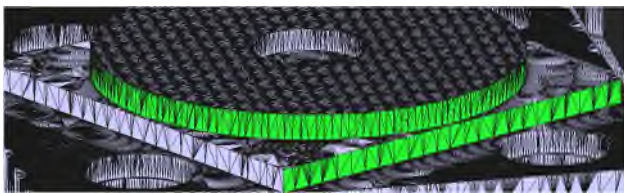
Figure 8. Selection of mesh faces for different part features.

The Zeiss CMM Calypso software stores the probe contact points and these are used to find the closest mesh faces or vertices to calculate virtual parts errors. If the virtual part datum is made the same as the CMM, then no global mesh modification is needed and the next stage is to find all the mesh faces that have a centre location nearest to all the CMM probe locations. Figure 9 shows the CMM probing points as red dots on the green mesh surface for the top circle feature. **Figure 10** shows the differences in the nearest face centre location to all the probe points for a cylinder feature and the cartesian distances are all less than 4mm. There should be negligible change in machine error over such small distances, however the option for weighted triangle centroid is being considered as future work.
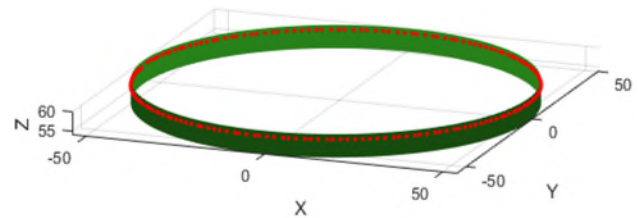
Figure 9. Imported top circle feature surface and CMM probing points.
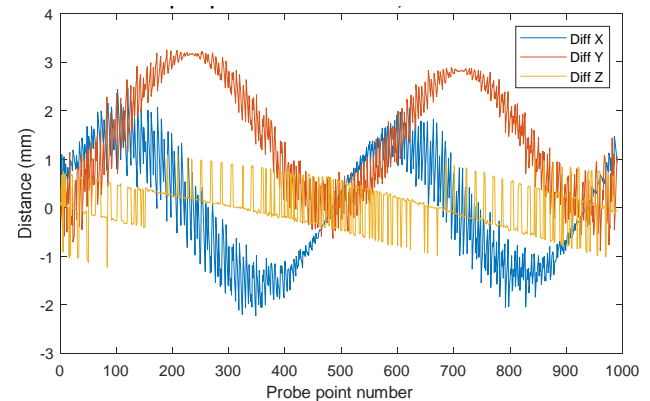
Figure 10. Variation in face centre locations to CMM probe location.

4. Virtual part inspection results

Figure 11 and Figure 12 shows the roundness plots for the same top circle feature of the real (from Zeiss Calypso software) and virtual parts respectively. The shape of the characteristic is very similar, and the roundness values are 0.024 mm for the real part and 0.028 mm for the virtual part. Similar low pass filtering was used for the Matlab calculation of roundness (A UPR of 50 is used in the Zeiss Calypso software but their implementation is not known).

So far in this work, a few characteristics have been compared and these are included in the **table 1**. The percentage correlation uses a comparison between the magnitude of the error measured by the CMM and difference between the simulated error and the CMM measured error. This did result in a relatively low correlation for the bottom roundness because the magnitude of the error is very small. In terms of dimensional differences, they are all within 6 μm.

One of the benefits of the virtual production is the potential for time and cost saving for testing new processes. Using a drawing to create a model and NC program are the same and currently the simulation does not run much faster than real machining. Most of the time saving comes from not needing fixture creation or taking a machine out of production. Another significant benefit is reduced material, tooling, and energy costs.

Table 1 Comparison of simulated inspection results to CMM results

Part	Measurement	Nominal	Sim	CMM	Sim Error	CMM Error	Difference	Correlation %
250	Diameter	160	159.966	159.969	0.034	0.031	-0.003	89
250	Roundness	0	0.028	0.024	-0.028	-0.024	0.004	82
250	Distance	150	150.032	150.027	-0.032	-0.027	0.006	79
150	Diameter	108	107.975	107.973	0.0246	0.027	0.003	90
150	Roundness	0	0.012	0.007	-0.012	-0.007	0.005	31
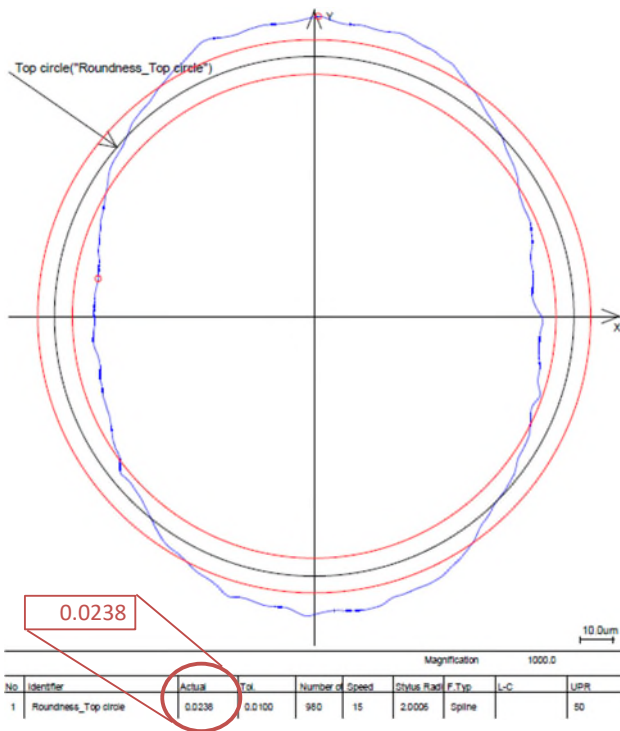
Figure 11. Roundness plot for test part top circle
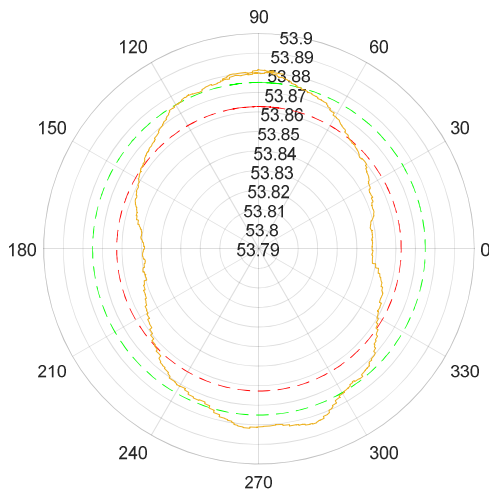
Figure 12. Roundness plot from the virtual part top circle

5. Conclusions

The correlation of the virtual part inspection characteristics with the CMM results is greater than 74% on average with deviations of less than 6 μm. With due consideration of the conformance zone, this software can be used to predict machine

Figure 13. Tool deflection during machining
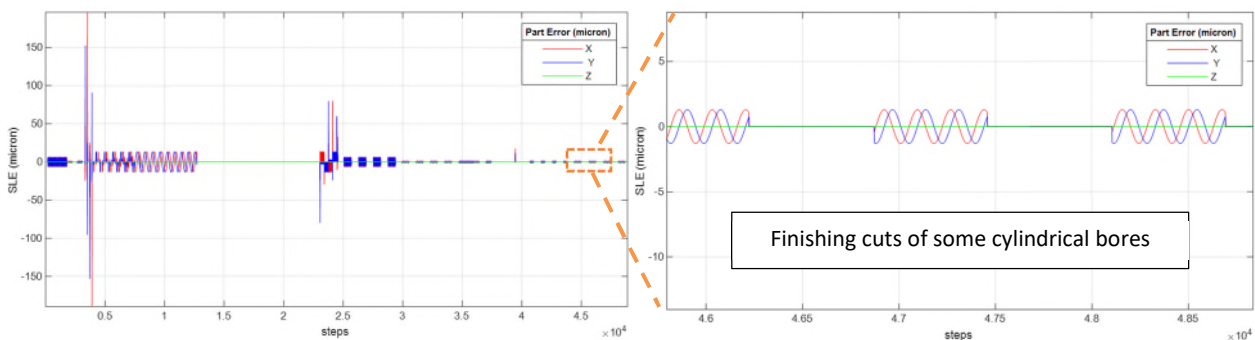
and process capability and work toward right first time or reduce the cost of prototyping and setting up new processes. It may also help schedule maintenance and calibration activity on machines. Providing the ability to derisk capital investment in machining platforms by virtually trialling operations prior to procurement and through out machine acceptance processes.

5.1 Future work

A new 5-axis test part has been designed that will be used, in combination with the ISO 230 part 12 (Test code for machine tools. Accuracy of finished test Pieces) fulcrum test, to validate 5-axis machining simulation and characteristics that involve multi axis interpolation.

Incorporating time varying and dynamic error source models is also in development using new and existing models developed in previous research.

References

[1] Ramesh R, Mannan M A, Poo A N, Error compensation in machine tools — a review: Part I: geometric, cutting-force induced and fixture-dependent errors, Int. J. of Machine Tools and Manufacture, 2000, 40(9), p1235-1256.

[2] Merdol, S D and Altintas Y, Virtual simulation and optimization of milling operations-part I: process simulation. *J of Manuf. Science & Engineering*, 2008, **130**(5), p051004.

[3] Altintas Y., Kersting P, Biermann D, Budak E, Denkena, B. and Lazoglu I, Virtual process systems for part machining operations. *CIRP Annals-Man. Tech.,* 2014 **63**(2), p585-605

[4] Mohsen S, Behrooz A, Mohsen H, Virtual machining considering dimensional, geometrical and tool deflection errors in three-axis CNC milling machines, *Journal of Manufacturing Systems* **33**,(4) 2014 p498-507

[5] Lyu D, Liu J, Luo S, Liu S, Cheng Q, Liu H. Digital Twin Modelling Method of Five-Axis Machine Tool for Predicting Continuous Trajectory Contour Error. *Processes*. 2022; **10**(12):2725.

[6] Ozkirimli O, Fletcher S, Kite J, Longstaff A P, McVey S, Ozturk E, Modelling and visualisation of machine tool and process related form errors, *6th Int. Conf. on Virtual Machining Process Technology (VMPT)*, 2017

[7] ISO 10791-2 (2023) Test conditions for machining centres. Part2: Geometric tests for machines with vertical spindle (vertical Z-axis), *International organization for standardization, Geneva, Switzerland*.

[8] ISO 230-2 (2014) Test Code for Machine Tools. Part 2: Determination of accuracy and repeatability of positioning of numerically controlled axes, *International organization for standardization, Geneva, Switzerland.*

Rehabilitation-oriented human hand model reductions

Tomislav Bazina[1,2] , Saša Zelenika[1,2] , Goran Mauša[1], and Ervin Kamenar[1,2]

[1] *University of Rijeka, Faculty of Engineering, & Centre for Artificial Intelligence and Cybersecurity, Radmile Matejčić 2, 51000 Rijeka, CROATIA*
[2] *University of Rijeka, Centre for Micro- and Nanosciences and Technologies, Radmile Matejčić 2, 51000 Rijeka, CROATIA*

ekamenar@riteh.uniri.hr

Abstract

Ischemic or hemorrhagic stroke, a common cause of loss of hand function, often results in spasticity and makes it impossible to perform activities of daily living (ADL). Recovering hand functions is therefore of vital importance. Neurorehabilitation, based on using robotic devices in the therapeutic process, is a promising way to exercise the hands, improve patient initiative, and increase neural connections with minimal intervention of the therapists. On the other hand, complex human hand anatomy complicates the development of specialised robotic rehabilitation devices. As a result, obtaining simplified but representative mathematical models of the human hand kinematics based on common grasps is crucial. The aim of this research is to identify the intra-finger dependencies for grasping types that are of utmost importance for the execution of ADL, such as opening a bottle, using a knife and holding a pen. The study is based on the largest known database of human hand movements, encompassing 77 test subjects. The first part of the research deals with data cleaning in terms of relabelling, pre-processing and filtering. The correlation analysis is performed next, enabling identification of highly correlated dependency-movement associations. The study in this work represents the foundation for further development of simplified but accurate rehabilitation-oriented human hand models.

rehabilitation robotics, rehabilitation-oriented hand modelling, dependency-movement associations, activities of daily living

1. Introduction

Stroke, increasing both in incidence and prevalence, is an ever rising society problem. Distributing timely therapy with proper intensity and frequency, critical for proper recovery, is becoming increasingly difficult. Robotic-assisted rehabilitation can be utilised as a possible solution to the problem. A fundamental problem in hand rehabilitation is selecting proper movement subsets, or grasps, which would benefit recovering ADL the most, as well as modelling them accurately and simply. Models should comprise as little as possible degrees of freedom (DOFs) while fully satisfying intended functionality. To obtain such models, it is necessary to research and understand hand kinematics using recorded hand movements. In [1, 2], kinematic models were presented, but only a few subjects were used, and grasps were divided into prismatic and circular types only. In [3], five sparse hand synergies were identified across 26 grasp types, but data from 22 subjects was used. A largest known database [4], recorded using a data acquisition glove fitted with sensors, including 77 test subjects is analysed in this paper. First, data is prepared using summary statistics and joint anatomical ranges of motion (ROMs), then correlation matrices were obtained for valid identification of highly correlated grasp-oriented intra-finger dependencies as a basis for generalisation of previously performed modelling [2] to 23 functional movements using everyday objects.

2. Data preparation and analysis

The dataset used in this paper, which contains synchronously collected values of joint angles in degrees, was prepared using Apache Spark and tidyverse [5], a collection of R packages for data science. Only the functional movements (grasps) were selected for further processing, while resting positions and different hand configurations (gestures) were omitted. All missing and duplicate values were removed from the database, as well as adduction/abduction (AA) movements since a lot of values were missing due to noise problems. Further processing was focused on identifying relationships between flexions/extensions (FE), but only reducing to intra-finger dependencies. After all subjects, movements and repetitions were concatenated, the resulting dataset contained over 50 million time recordings for 16 different finger joint angles, posing an admirable number for further analyses. Fingers were labelled using numbers (1 - thumb, 2 - index, 3 - middle, 4 - ring, 5 - little), and joints using abbreviations, list of whom can be found in [2]. The description of the database is summarised in Table 1.

Table 1. Description of the prepared database records.

Subject	Laterality	Gender	Movement	Repetition
1 - 77	right handed, left handed	male, female	1 - 23	1 - 6

2.1. Summary statistics and preprocessing

For preliminary analysis of the dataset, descriptive statistics was used since this was the most straightforward way to gain a quick insight into such a large database. The dataset was first grouped by subject, movement and joint angle, while computing boxplots (mean, min, max, median, 1st quartile Q1, 3rd quartile Q3, interquartile range IQR) considering all repetitions. It led to a conclusion that a lot of measurements fall outside joint anatomical ROM limits (adopted from [1, 6]), most likely due to sensor noise, and imperfect glove fit to different hand sizes. This necessitated the removal of errors in recorded joint angles to obtain valid data for further analysis. After data removal, some motion repetitions were left with too small sample size or diversity for proper inferences. Samples with less than 100 data points, and those with recorded

insufficient portions of the entire movement range (IQR of the sample less than 50% of mean IQR for the same movement across all subjects) were also removed from the prepared dataset. Validation boxplots for small digit MCP joint angle medians (per subject), before and after anatomical ROM filtering, are shown in Fig 1. For each of 16 investigated joints, similar validation graphs were plotted. Also, by investigating boxplots in Fig 1 (top), many outliers still remained in the data, so an additional 1.5 IQR outlier detection and removal procedure was performed. It is applied on a subject-level summary statistics, where all measurements, whose median fell outside range (Q1 - IQR, Q3 + IQR) was deemed outlier and removed from further processing. In Fig 1 (bottom) the example of summary statistics for MCP5, after preprocessing and outlier removal steps, is presented.
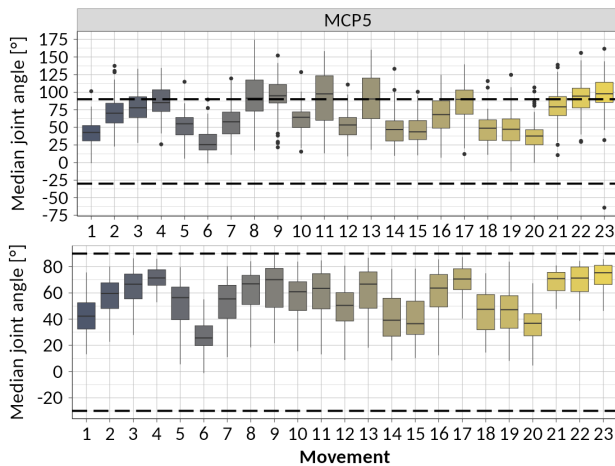
Figure 1. Validation for removing data points outside anatomical ROM.

3. Results and correlation analysis

After data preprocessing at a joint level, the subsequent steps involved forming 18 intra-finger dependencies, such that every combination of joint trajectories belonging to the same finger can be correlated using Pearson's *r*. Owing to data acquisition parameters, some repetitions comprised numerous measurements, while some only 100, resulting in disbalance in the dataset. Dependencies were observed on a repetition level as a unit for data analysis, thus balancing each subject share during further inferences since each subject performed 4 repetitions on average after data preparation. Correlation analysis was then performed, and more than 70 000 correlation coefficients obtained (matrices with combinations for each finger, movement, subject and repetition) for identifying further relationships. The same 1.5 IQR rule was then applied to correlation coefficients for each movement dependency to eliminate outliers. Only highly correlated intra-finger dependencies with absolute median correlation coefficient

larger or equal to 0.7 (breakpoint according to [7]) were isolated. Outlier removal procedure example (for Movement 10, MCP5 - PIP5 dependency) is shown in Fig 2.

The correlation analysis resulted in dependency - movement matrix in Fig 3, where only the median coefficients are visualised. From a total of 18 investigated dependencies (y-axis in Fig 3), 16 were highly correlated during at least one movement, indicating a relationship, while ring and little finger DIP and PIP joints were the only ones not correlated. On the other hand, in each of the 23 investigated movements, there is at least one correlated dependency, while in movements 2 (power grip) and 3 (fixed hook grasp) a large number of joint dependencies (10 and 11 respectively) can be identified. Also, it can be concluded that the thumb is the most independent digit, with identified only 5 dependency-movement associations, agreeing with [3].
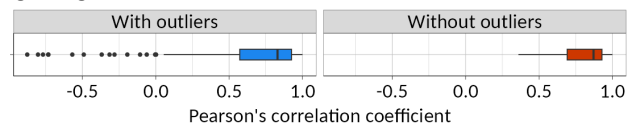
Figure 2. 1.5 IQR rule outlier removal on Movement 10, MCP5 - PIP5.

4. Conclusions and outlook

We presented a novel method for extracting useful data for grasp-oriented hand modelling using noisy sensor measurements. The validity of data was investigated, as well as 116 highly correlated dependency-movement associations identified (median absolute correlation $\geq$ 0.7). The provided identification will serve as a basis for future comprehensive modelling of hand grasps oriented at rehabilitation robotics. In future work, regression modelling is planned with the aim of estimating the corresponding coefficients for all the identified dependency-movement associations. Then, synthesis of all coefficients, using dependency matrix and clustering methods, will be necessary for presenting valid and comprehensive rehabilitation-oriented grasp models, as well as a grasp taxonomy based on similar intra-finger dependencies.

References

[1] Cobos S et al. 2010 *Comput Method Biomec* **13**(3) 305–17
[2] Bazina T et al. 2022 *Medicina Fluminensis* **58**(4) 385-98
[3] Jarque-Bou N J et al. 2020 *IEEE Trans Neural Syst Rehabil Eng* **28**(7) 1556-65
[4] Jarque-Bou N J et al. 2020 *Sci Data* **7**(12) 1–10
[5] Wickham H 2019 *JOSS* **4** 1686
[6] Holzbaur K R S et al. 2005 *Ann Biomed Eng* **33**(6) 829-40
[7] Mukaka M M 2012 *Malawi Med J* **24** 69-71
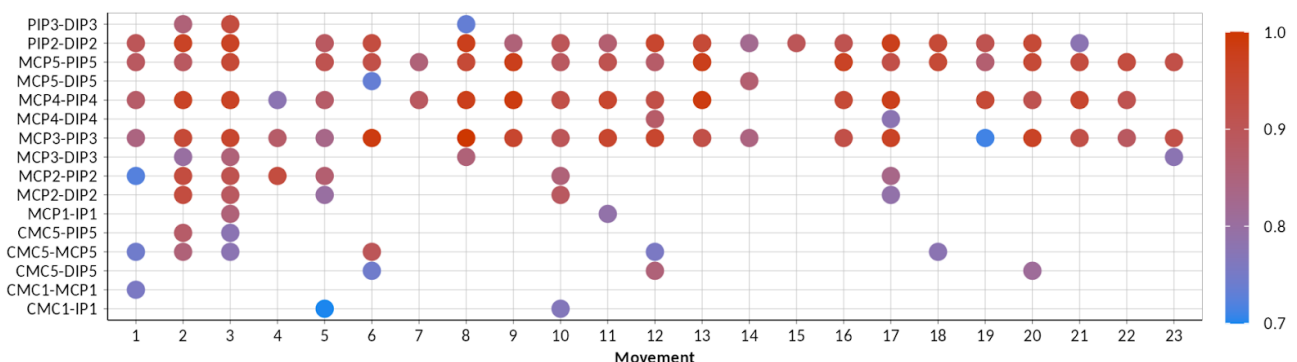
Figure 3. Correlation analysis of intra-finger joint dependency-movement association

Micro deburring of high-precision injection moulded parts using thermal energy machining

E. Uhlmann[1, 2], T. Hocke[2], C. Schmiedel[1], M. Casel[3], A. Ghani[3], C. Lahoda[2]

[1]*Fraunhofer Institute for Production Systems and Design Technology IPK, Germany*
[2]*Institute for Machine Tools and Factory Management IWF, Technische Universität Berlin, Germany*
[3]*Data Analysis and Modeling of Turbulent Flows DMF, Technische Universität Berlin, Germany*

christian.lahoda@iwf.tu-berlin.de

Abstract

Injection moulding is a widely used process in modern manufacturing, offering an economically efficient production of high-precision components in various economic sectors, e.g. for medical applications. However, an inherent challenge in injection moulding is the formation of small burrs, particularly in the regions of the mould parting line. These represent a significant risk in fluid technology applications such as cardiac support systems, where patient safety may be compromised by damage to vital blood components. Conventional deburring techniques like disc finishing or brushing prove ineffective in eliminating these microscopic burrs due to the complex and sensitive geometries. In this context, thermal energy machining represents a promising post-processing approach for deburring of high-precision injection-moulded components. Using controlled thermal energies to precisely shape and smooth the edges of these components, this technique offers a viable solution. This study includes a comparison of conventionally used edge deburring methodologies such as disc finishing, abrasive flow machining as well as thermal energy machining. These techniques were analysed to identify their efficiency in achieving edge deburring on high-precision injection moulded thermoplastic polyurethane elastomer components. Based on the results, it could be proven that only thermal energy machining enables a complete and homogeneous removal of the initial burr, whereby the edge rounding could be increased by a factor of 20 compared to the initial state. These results provide a fundamental basis for refining and optimising post-processing strategies with a particular focus on safety and performance within critical domains such as medical devices and fluid technology applications. The use of the thermal process leads to an increase in efficiency in the edge deburring process and contributes to the overall goal of improving patient safety and the overall functionality of equipment used in medical and fluid-related contexts.

Keywords: thermal energy machining, injection moulding, micro deburring

1. Introduction

The demographic change with it's increasing life expectancy of the population leads to a growing demand for medical supplies, instruments and implants [1, 2]. Technical plastics are an important factor in the manufacturing of these products as they offer significant freedom of design and fulfil the high requirements of mechanical, chemical and physical properties.

With regard to the processing of these high-performance polymers, injection moulding is one of the most economic solutions for the manufacturing of high-precision components across diverse sectors, particularly in medical applications [3]. Nevertheless, the manufacturing of high-precision polymer parts using injection moulding is limited regarding the formation of small burrs, especially along parting lines. In critical applications like fluid technologies such as cardiac support systems, these microscopic burrs result in significant risks to patient safety [4]. Conventional deburring methods like disc finishing or brushing prove inadequate due to the intricate geometries involved. As a result, the need for reliable and cost-effective post-processing technologies in this area is growing.

For this purpose, this study adresses the research regarding the capability of thermal energy machining (TEM) as a post-processing technology for deburring complex high-precision injection-moulded components. By employing controlled thermal energies E_{th} to precisely shape and smooth component

edges, this method presents a promising solution for the deburring of complex parts. Through a comparative analysis of conventional deburring methodologies including abrasive disc finishing and abrasive flow machining, the investigation aims to identify the efficiency of thermal energy machining in achieving complete and homogeneous burr removal as well as edge rounding. The results contribute to refining post-processing strategies, particularly in critical domains such as medical devices with a focus on enhancing patient safety and performance.

2. Experimental Setup

The TEM process belongs to the subgroup of chemical ablation and can effectively remove burrs and improve specific geometric parameters of the components such as edge rounding r_β, surface roughness as well as the K-factor k. It is a versatile and cost-effective method that can be used on a wide range of metallic and polymer-based materials, even in geometric hard-to-reach areas. The combustion can be as short as a few milliseconds and can reach combustion temperatures up to $\vartheta_C \leq 3{,}000\ °C$, depending on the chamber filling pressure p_C, gas type and equivalence ratio φ. Areas of the part with a large surface-to-volume-ratio ψ, such as burrs, can overheat and melt [4].

The used workpieces were high-precision injection moulded parts made of the thermoplastic polyurethane Tecobax (TPU) by the company THE LUBRIZOL CORPORATION, Wickliffe, USA.

TPU is a thermoplastic polyurethane and is characterised by high elasticity, making it suitable for applications that require excellent rebound resilience. For that reasons, the selected TPU ensures that the components maintain dimensional stability and structural integrity under varying conditions even after compression and expanding. The workpieces are characterised by a cylindrical structure with inlets providing a maximal blood flow. These consist of several small struts with a minimal geometrical width of $a_S = 0.5$ mm. The workpieces are further characterised by complex geometries, which results in challenging deburring. The use of these specific high-precision components aimed to provide a representative and practical application for evaluating the efficiency of thermal energy machining in addressing micro-burrs and sharp edges on injection moulded polymer parts.

The high-precision injection-moulded components underwent the post-processing deburring using the TEM machine type iTem Plastics by the company ATL ANLAGENTECHNIK LUHDEN GMBH, Luhden, Germany. The schematic layout of the machine is shown in Figure 1.
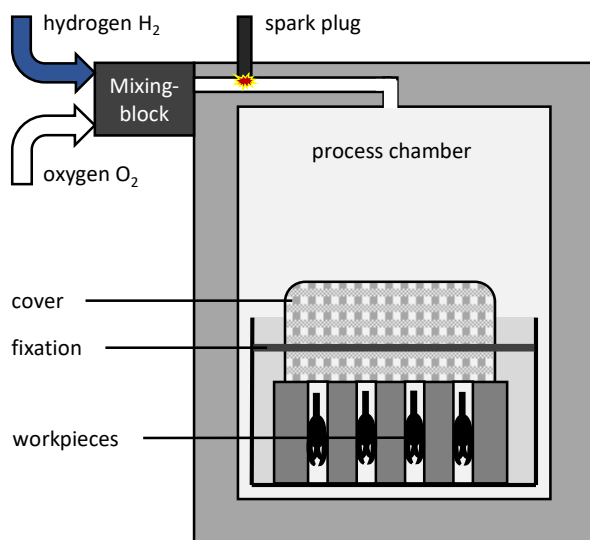
Figure 1. Schematic Layout of the TEM machine iTem Plastics

The configuration of the process chamber encompasses several critical components. The centrepiece of this system is the process chamber, which positions the parts to be deburred. This chamber is fortified with a hydraulically sealable door, which has to withstand the forming pressures p_D generated during the deburring operation. Preceding their placement within the process chamber, the components are loaded into a carrier basket. This basket supports loading and unloading processes as well as optimising efficiency in the operation of the deburring chamber. The total deburring time of $t_D = 5$ min includes the application of the vacuum and the injection of the gas. For this reason, the carrier basket is important for the economical operation, as new components can be already loaded during the deburring process.

Recognising the potential destructive force by the deflagration, precautions are taken to shield the small structures of the components from the unrestrained impact of the deflagration front. Diverse protective geometries are employed to protect the parts against inadvertent damage. The structural integrity of the chamber is complemented by the installation of a mixing block. This component enables both homogeneous mixing of the process gases and their controlled introduction into the process chamber. The various gases used in this process include natural gas, hydrogen and oxygen. For reasons of ecological sustainability, hydrogen and oxygen are now primarily used as combustion gases. The ignition of the explosive mixture

is initiated through strategically positioned spark plugs, installed both atop and along the sidewall of the process chamber.

In this research, the deburring process was carried out using hydrogen and oxygen as the process gases. Therefore, a controlled mixture of oxygen and hydrogen gases with a volumetric ratio of $\psi_G = 3{:}1$ was employed. The deburring process was conducted under a vacuum pressure of $P_V = 200$ mbar. Following the establishment of the vacuum, the processing chamber was filled with the process gases at a pressure ranging of 350 mbar $\leq P_I \leq$ 600 mbar. Furthermore, the ignition of the deflagration was initiated from the top of the process chamber. The parts were positioned within a metal plate made of stainless steel type 1.4301 featuring holes with a diameter of $D_H = 10$ mm and a height of $h_H = 40$ mm. This arrangement ensured that the resulting deflagration was directed toward the inner geometry of the components. In addition, parts of the combustion energy E_C could be dissipated to keep the precise strut structures intact. The protective geometry is shown in Figure 2.
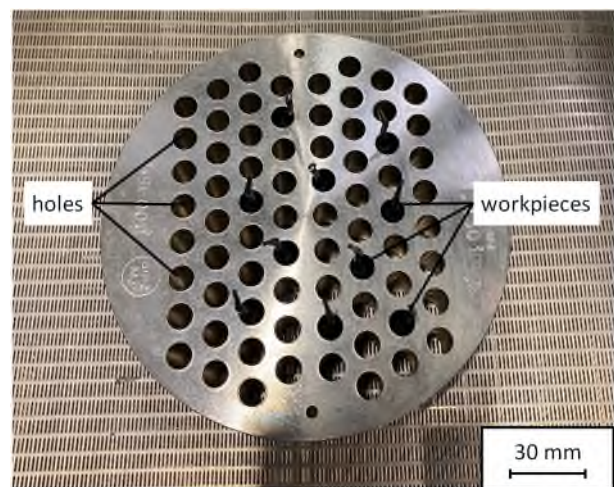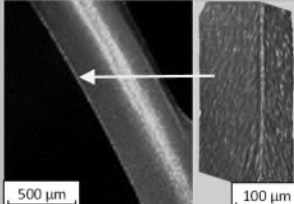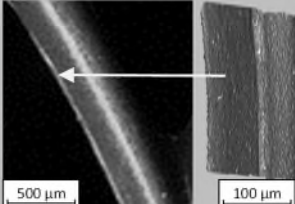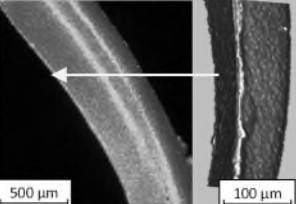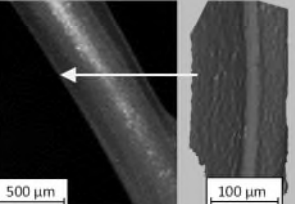
Figure 2. Protective geometry and workpiece holder

In addition to the holes in the thick steel plate, the components were enclosed by a perforated cover. This additional layer of protection served to further dampen and evenly distribute the deflagration. To prevent any displacements of this cover due to the deflagration pressure p_D, the cover was attached to the carrier basket using rods. For a visual representation of this setup, please refer to Figure 3.
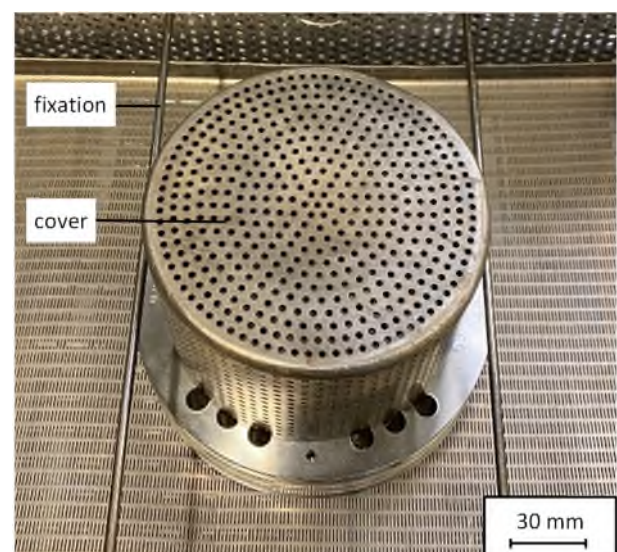
Figure 3. Final protective cover on top of the workpiece holder

	Initial state	Abrasive disc finishing	Abrasive flow machining	Thermal energy machining

	Workpiece:
	High-precision injection-
	moulded medical component
	Material:
	Thermoplastic
	Polyurethane (TPU)
		1. Media: KXMA wet
		   Duration: t_B = 180 min
		   Speed: n_T = 300 1/min
		2. Media: M5/400 dry
		   Duration: t_B = 600 min
		   Speed: n_T = 250 1/min
			Media: SiC F400
			Speed: v_K = 30.0 mm/min
			Pressure: p_A = 12.0 bar
			Cycles: n = 0.5
				Gases: O_2 + H_2
				Gas ratio: ψ_G = 3:1
				Vacuum: p_V = 200 mbar
				Pressure: p_I = 600 mbar
				Cycles: n = 1

	edge rounding r_β = 3 µm	edge rounding r_β = 16 µm	edge rounding r_β = 21 µm	edge rounding r_β = 60 µm

Figure 4. Results of the deburring process using abrasive disc finishing, abrasive flow machining and thermal energy machining

In the comparative assessment of post-processing, additional experiments were conducted using abrasive disc finishing. Therefore, the machine tool CF 2x18 by OTEC PRÄZISIONSTECHNIK GMBH, Straubenhardt, Germany, was applied. The initial processing step involved wet processing for a duration time of t_P = 180 min using fine-grained ceramic particles composed of sintered ceramic type KXMA. Subsequently, a polishing procedure in corn granulate with attached diamond particles classified as media M5/400 was used for a duration time of t_P = 600 min. In addition, the injection-moulded components underwent post-processing through abrasive flow machining, whereby a non-Newtonian fluid containing silicon carbide particles type F400 were pressurised through the components using a hydraulic piston. This procedure was carried out with the machine tool Delta Towers 100D IPC by MICRO TECHNICA TECHNOLOGIES GMBH, Kornwestheim, Germany.

To assess the deburring results, the edges of the components were measured using the focus variation microscope InfiniteFocus by ALICONA IMAGING GMBH, Graz, Austria. The measured data were used to analyse the edge rounding r_β of the machined parts.

3. Experimental Results

Within the investigation of high precision injection-moulded polymer components, three deburring processes in form of abrasive disc finishing, abrasive flow machining and thermal energy machining were applied. The results of the experiments are shown in Figure 4. In their initial state, the components showed an edge rounding of r_β = 3 µm. In the context of a cardiac support system application, this represent a potential risk of damage to blood components or cardiac tissue. Through abrasive disc finishing, the edge rounding could be improved to r_β = 16 µm. However, noticeable inhomogeneities and breakouts were observed along the edges of the machined parts. Due to geometric limitations, only isolated edges could be reached by the processing medium, preventing a homogeneous treatment of all edges. Similar challenges were encountered using the abrasive flow machining, whereby an improvement in edge rounding to r_β = 21 µm was achieved. Nevertheless, the processing results also showed inhomogeneities concerning the machined surfaces and edges. Additionally, the high machining pressure of P_A = 12 bar led to a permanent component deformation, thus compromising the high-precision geometry. By using the thermal energy machining, a homogeneous maximum edge rounding of r_β = 60 µm could be obtained, without any observable breakouts or other irregularities along the edges. To gain extensive knowledge about the influence of the pressure P_I of the used processing gases hydrogen and oxygen, a pressure ranging of 350 mbar ≤ P_I ≤ 600 mbar was analysed. The results are shown in Figure 5.

Measurement device:
InfiniteFocus, Alicona
Workpiece:
High-precision injection-moulded parts
Process parameters:
Gases: O_2 + H_2
Gas ratio: ψ_G = 3:1
Vacuum: P_V = 200 mbar
Cycles: n = 1
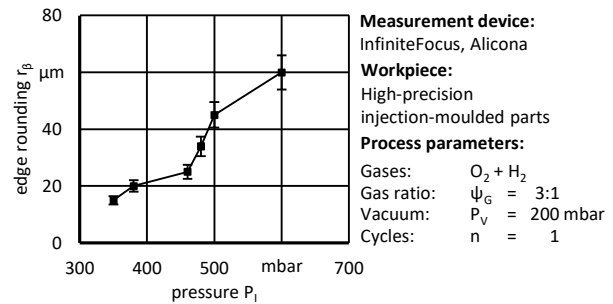
Figure 5. Edge rounding r_β in dependency of the pressure P_I using TEM

As a result of the investigations, an almost linear correlation between the pressure P_I of the gases and the edge rounding r_β could be identified. The application of increased pressures P_I facilitated a greater induction of thermal energies E_T into the component, leading to an increased edge rounding r_β. However, structural damages to the components could be observed at pressures P_I > 600 mbar. Therefore, this also represents the process limitations for the TEM process for the material TPU and the specific component geometry.

4. Simulation

The results presented show the fundamental suitability of the TEM process for deburring high-precision injection molded parts. In addition, TEM is a very experience-based process that requires iterative adjustments to identify the right operating conditions or the need for additional equipment such as flame guide geometries or absorber materials to achieve high-quality deburring results. To avoid these iterative adjustments, numerical simulations are proposed in this study as they provide reliable and condensed spatio-temporal data of chemically reacting flows and conjugate heat transfer challenges between solid and gaseous phases. Therefore, two different transient 2D simulations of the TEM process were performed in this study to demonstrate the ability of high-fidelity simulations to analyze the TEM process:

One combustion simulation within the process chamber (Figure 6a - d) and one simulation of the heat transfer from burnt gases into the cold workpiece (Figure 6e - h). Both simulations are based on a simplified generic process chamber with a dimension of 60 mm x 60 mm that confines two different generic workpieces featuring generic burrs.

The simulation of the combustion process within the chamber was performed with the reactingFoam-solver by the company OPENCFD LTD, Bracknell, UK, that solves the compressible Navier-Stokes equations as well as the governing reaction chemistry. The walls of the process chamber and the boundaries of the workpieces were set as isothermal with ϑ_B = 20°C and no-slip
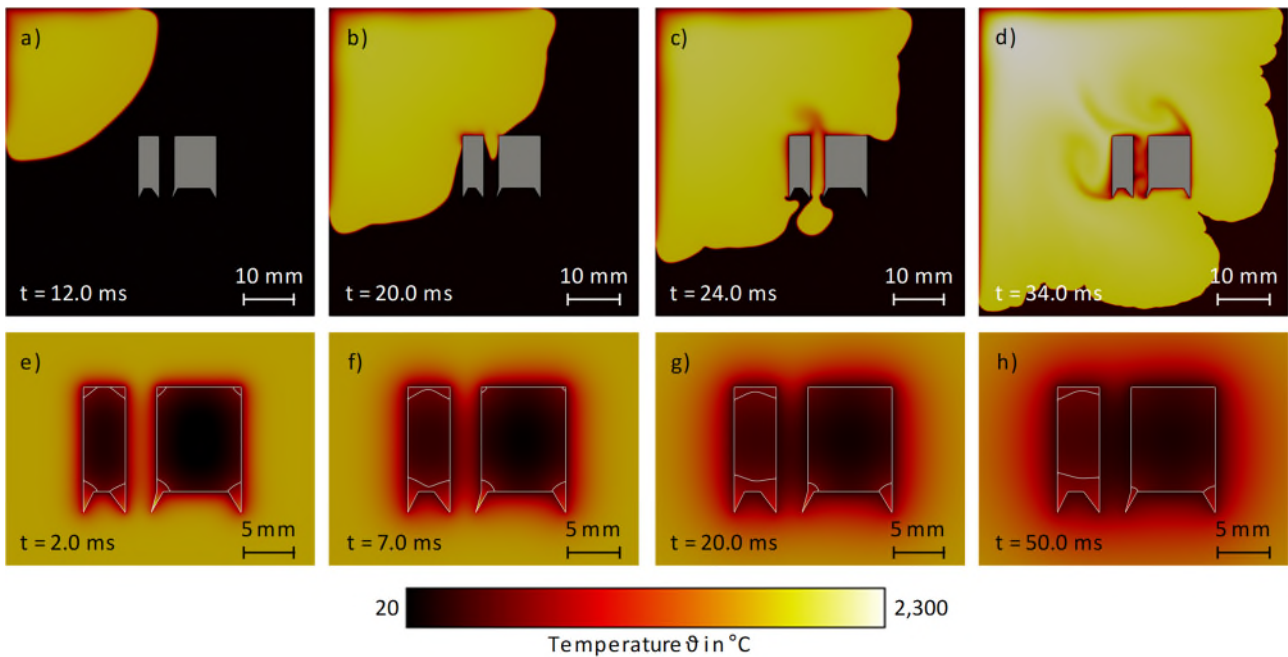
Figure 6. Simulation of the a) - d) flame propagation and the e) - h) heat transfer into the workpiece and the burr (contour line ϑ = 230 °C)

boundary conditions. The resting gasous phase was initialised as a suitable premixed mixture of methane and air with a stochiometric equivalence gas ratio ψ_G at atmospheric pressure p_A and room temperature ϑ_R, which was ignited by a spark in the upper left corner. Figure 6a - d depicts the subsequently ignited mixture that forms a flame front that causes a steep temperature rise, propagating towards the unburnt mixture. While this propagation mostly unperturbed at first (Figure 6a), the flame interacts with the workpieces that cause deflections of the flame front (Figure 6b - c). After a time of t = 34.0 ms, the flame further propagated confining both workpieces with hot burnt gases (Figure 6d). The temperature field that encloses the workpieces exhibits strong inhomogeneities in the vicinity of the workpieces. The temperature ϑ between the workpieces is significantly lower than on the other workpiece surfaces.

The second simulation utilizes the chtmultiregionFoam solver by the company OPENCFD LTD, Bracknell, UK, and governs the heat transfer between the gasous phase and the workpieces. For this purpose, the workpieces were discretised in addition to the gasous phase. While the workpieces were initialised with a temperature of ϑ_{WP} = 20 °C, the gasous phase was set with an average hot gas temperature of ϑ_G = 1.800 °C. Furthermore, the gasous phase was set to the species composition of completely combusted gases corresponding to a stoichiometric methane-air mixture, whereas the workpieces feature the material properties of TPU. After the start of the simulation, the large temperature gradient $\vartheta\Delta$ causes a heat flux from burnt gases into workpieces as shown in Figure 6 e-h, leading to an overall rise of the temperature ϑ in the workpieces, where the burrs display significantly larger temperatures ϑ compared to the remaining parts due to the different surface-to-volume ratios ψ of the burrs. Based on this, the figures with contour lines of ϑ = 230 °C as the melting temperature ϑ_M of TPU show that the smaller workpiece heats up significantly more than the larger one. This indicates that the surface-to-volume ratio ψ is a decisive parameter for the deburring quality. Overall, both simulations depict a high complexity of the TEM process, featuring large spatio-temporal inhomogeneities. While the first simulation indicates a strong interaction between workpiece geometry, flame propagation and the resulting temperature field, the latter highlights the importance of the surface-to-volume ratio ψ for the spatial temperature evolution within the workpiece. However, it is noted that both flame propagation and heat exchange between gasous and solid phase occur simultaneously in reality. This results in further complexities of the TEM process, which will be further addressed in future studies.

5. Conclusion and further investigations

This study adressed post-processing techniques for deburring complex high-precision injection-moulded components. Using TPU workpieces, the TEM process demonstrated superior edge rounding of r_β = 60 µm without irregularities at the surfaces and edges. In contrast, abrasive disc finishing and abrasive flow machining showed uneven results and several deformations. The use of TEM enables an almost linear relationship between the edge rounding r_β and the pressure p of the applied gases hydrogen and oxygen. In addition, initial simulations of flame propagation and heat transfer during the TEM process were carried out. It was found that the TEM process is a highly transient process. Overall, TEM represents a promising post-processing method for deburring of high-precision injection-moulded components made of TPU, demonstrating superior efficiency in achieving homogenous edge rounding r_β. While traditional methods show significantly limitations, TEM is a suitable solution and shows its potential for enhancing safety and performance in critical applications such as cardiac support systems. Future research work will address the more detailed simulation of the TEM process. This will primarily involve a more precise simulation and detailed analysis of the interaction between the flame propagation and the burr geometry in order to achieve a comprehensive model of the TEM process. The fundamental aim is to significantly reduce iterative process adaptations and to develop a detailed scientific knowledge of the TEM process.

References

[1] Wintermantel, E.; Suk-Woo, H.: Medizintechnik - Life Science Engineering. Berlin, Heidelberg: Springer, 2009.

[2] Seul, T.; Roth, S.: Kunststoffe in der Medizintechnik. München: Hanser, 2020.

[3] Uhlmann, E.; Mullany, B.; Biermann, D.; Rajurkar, K.P.; Hausotte, T.; Brinksmeier E.: Process chains for high-precision components with micro-scale features. CIRP Annals – Manufacturing Technology, Volume 65, Issue 2 (2016), p. 549 – 572.

[4] Thilow, A. et. al.: Entgrattechnik – Entwicklungsstand und Problem-lösungen. Kontakt & Studium Band 392. Expert, 2017. p. 122 – 135.

Digital surface shadow for fly-cut surfaces utilizing dynamic axis data

Sabrina Stemmer[1], Lars Schönemann[1,2], Oltmann Riemer[1], Bernhard Karpuschewski[1,2]

[1]Leibniz Institut für Werkstofforientierte Technologien IWT, Laboratory for Precision Machining LFM, Badgasteiner Straße 2, 28359 Bremen , Germany
[2]MAPEX Center for Materials and Processes, University of Bremen, Germany

stemmers@uni-bremen.de

Abstract

The digitalization of manufacturing processes enables the tracing of dynamic influences in the production processes to specific characteristics of the final product. In this case, existing models for surface simulation of ultra-precision fly-cut surfaces were extended to dynamically incorporate acquired axis data of the machine tool to further improve the prediction of the machined surface topography. Therefore, a signal splitter was incorporated into the machine tool's control systems, which allows for a seamless readout of the axes' encoder signals without influencing the control system of the machine itself. The readout of the sensors was referenced to the machine tool and workpiece coordinate system and then fed into the dynamic model, which periodically examines the interaction of tool and workpiece (i.e. the cutting procedure) and calculates the resulting surface geometry, i.e. topography and form.

The topic to be presented is a detailed description of the applied modeling and simulation framework, the integration of the axis data as well as a validation of this approach, which is illustrated by three examples. While the surface roughness comparison showed clear differences, certain characteristics could be found in the corresponding image when comparing the simulated surface features with the actual generated topography.

Precision machining, surface shadow, simulation

1. Introduction

Digitalization has been gaining importance in manufacturing technology for decades and it has become an integral part of modern production environments. Production data and integrated machine data interfaces can be used for a wide variety of purposes, such as process control, maintenance and interruption planning or to make statements about production progress or component quality. The last point in particular is important for precision machining.

Today ultra-precision parts are applied in a widespread field of sectors such as the automotive, fusion, metrology and aerospace industries, in the health sector and in the field of photography to afford very different functions. Therefore the range of parts is diverse and extends from optical components such as flat, pyramidal, spherical and aspherical-mirrors, ellipsoids, toroids, optics, microlenses, spectrometers installed inside satellites, components for vehicle lighting systems, energy conductors e.g. waveguides, air bearing components, lenses for photography and laser applications to ultra-precision tools like mould inserts.

Ultra-precision manufacturing is a time consuming and challenging task, because of the tiny scaled chip removal and the fact that most steps in this process are nearly invisible to the human eye. This leads to the process requiring long machine production times and to a high uncertainty about the quality of the workpiece along the whole process.

In order to make an adequate prediction of the result at the end of the machining process, a simulation of the generated surface is built from axis data of the manufacturing machine. Ideally, the waste of energy, resources, time and costs can be avoided by recognizing critical moments in the production process at an early stage during runtime and taking appropriate countermeasures. The development of this approach is pursued with the help of a digital surface shadow in an ultra-precision fly-cutting process.

1.1. Previous work

In recent decades numerous research projects have been carried out to optimize ultra-precision fly-cutting processes. Several approaches aim the high speed cutting of ultra-precise surfaces in order to reduce the production time [1, 2]. Other approaches investigate the vibration [3] and the prevention of critical machine states or the identification of critical events [4, 5]. Fewer approaches explore the live representation of the surface. A foundation to build up a digital surface twin for fly-cutting processes was laid by the authors in 2022 [6]. Two different models, a numerical height map and a dexel-based simulation model for generating the surface were developed. The incorporation of axis data took place after the machining process. For the dexel approach the surface is split up in dexel and intersection points. The tool engagement is determined as sweep-volume and for the simulation the position data is transformed to a path of the tool-center-point.

For the height map approach the complete surface is tessellated into smaller patches containing height points. The tool engagement apex points, referring to the height, are determined using the process parameters such as feed, raster spacing and fly-cutting radius. To handle overlapping and the failure addition of material the minimum of either the tool footprint or of the existing surface is saved in the height map. Both approaches achieved high accuracy in predicting the surface.

In the presented work the height map approach is extended in order to set up a data interface for axis data, a live data handling and a parallel simulation of the surface while the machine is running.

1.2. Intention

The intention of the presented work is a simulation of the surface, parallel to the machining process utilizing live axis data and static process data. This approach is validated in machine tests and the results of the simulation is compared to the physical surface measured by white light interferometry. Section 2 presents the methodology, describing first in 2.1 the experimental setup and the materials utilized for this purpose. Then in 2.2 the data operations are briefly outlined followed by 2.3 explaining the simulation. Section 3 presents the results of the simulation divided into the presentation of the simulated surface in 3.1 and the measured surface in 3.2. Followed by the comparison of simulated and measured surfaces presented in 3.3 and a disturbance test described in 3.4. Finally, section 4 summarizes the contents.

2. Methodology

The methodology for setting up the surface simulation essentially consists of two main parts: The management of live data and the visualization of the surface. The dynamic axis data is obtained within a fly-cutting process that is depicted in Figure 1.

2.1 Experimental setup and materials

The utilized ultra-precision 5-axis machine tool Nanotech 350 FG is placed in the Laboratory for Precision Machining LFM in Bremen on a marble base in an air-conditioned room in order to eliminate external influences. The material of the workpiece, German silver, which is a Nickel alloy with copper and zinc, was also chosen for this reason. The surface is generated in a fly-cutting process with a fly-cut radius $r_{fly} = 67\ mm$ using monocrystalline diamond as cutting material with a tool nose radius $r_\varepsilon = 0.762\ mm$.

To achieve the axis data during the machine run an interface system EIB 741 (Heidenhain) is used, which splits the axis signal directly from the machine control cabinet into two signals; one for the machine control and one for the laptop input socket. Furthermore a Talysurf CCI HD (Taylor Hobson) while light interferometer is utilized to measure the generated surfaces after machining.
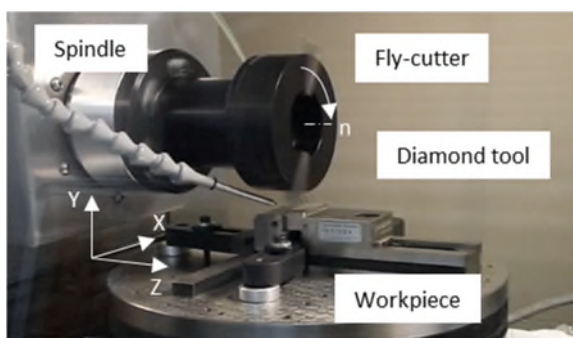
Figure 1. Surface machining of a workpiece with a diamond tool mounted in a fly-cutter on the main spindle

2.2 Axis Data

The data of the machine axis are routed to a software interface where the arranged data packets are streamed into a file. This is done by the signal splitter before the computation job of the machine itself. After that a Python script reads the latest data out of the file and converts the values from the raw format to the actual length scale.

2.3 Simulation

When the simulation starts the current position is saved as reference position and the first tool operation is visible. If the axis data changes, the surface is updated simultaneously. The simulated tool sweep is repositioned periodically as the tool is moved relative to the workpiece.
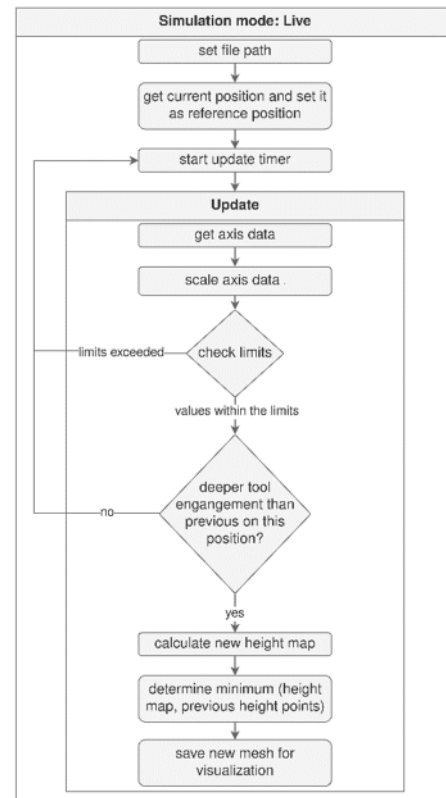
Figure 2. Program flowchart of the live simulation

If the new height is deeper than the current height of this tool position, the mesh is changed and passed to the visualization in order to show the new surface. The calculation of the height points is mainly dependent on the radius of the diamond tool and the fly-cut radius, but also on the feed and the raster space, since they define the tool engagement. An outlined program flowchart is shown in Figure 2.

Although there is a data transition in both processes, the update function of the new height map and the visualization function, can operate independently of each other. While the process is running it is possible to move and zoom the visualization to check the generated surface and stop the machining process when a critical fault is identified. The prerequisite is a suitable choice of the resolution parameter to prevent long calculation times. With the developed graphical user interface a visualization and several options e.g. to save the current mesh and a picture or to edit the reference positions are presented, as shown in Figure 3.
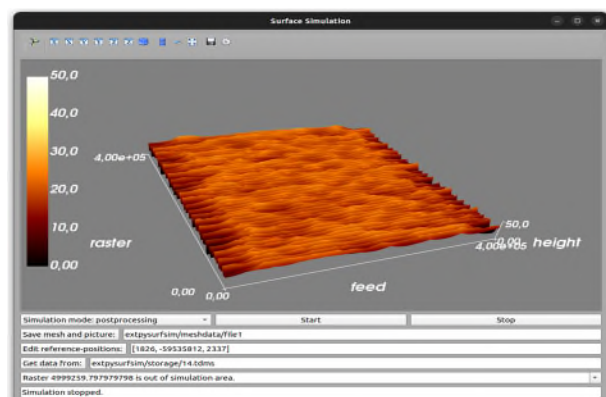
Figure 3. Graphical user interface of the simulation

3. Results

In order to be able to find the section for the measurement, the tool was moved close to the simulation area during tool engagement. This resulted in features at the left and right edge of the section. During machining the simulated surface is visualized and shows these features. In addition the simulation input axis data and the resulting surface could be saved during the machining session.

As the tool path data is handled separately from the visualization, the resulting surface geometry can be repeatedly generated in the post processing mode. This reveals the advantage of a higher resolution and the opportunity to change simulation parameters e.g. the smoothing value.

3.1. Simulated surface
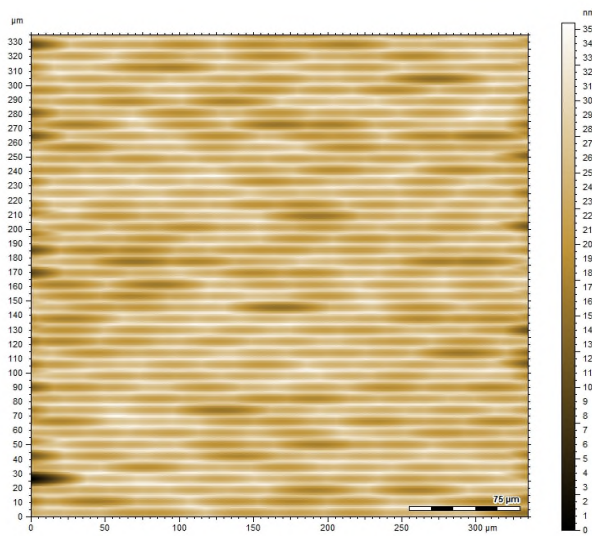
Figure 4. Simulated Surface as a result after the process (sample 5)

The post processed simulated surface from the machine test setup of the presented example is depicted in Figure 4. Conspicuous are the features on the edge; some are more pronounced e.g. the feature near the bottom left corner. The features in the middle are less noticeable.

3.2. Measured surface

Figure 5 shows the measured surface referring to the simulated surface depicted in Figure 4.
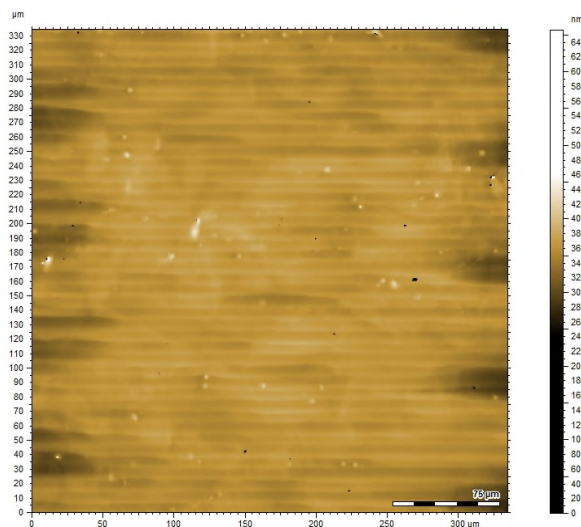
Figure 5. Measurement of the surface (sample 5)

In the measured surface the edge features are also clearly visible, although in a slightly different way. In comparison it looks as if the simulated image has been sharpened. This could be due to the different height scaling. The measured image is displayed on a scale ranging from approx. *250* to approx. *400 nm*, with a maximum range of *650 nm.* On the other hand, the simulated image is displayed on a scale ranging from zero to approx. *35 nm*, utilizing the full range of the scale, although this is dependent on the simulation, the zoom and the scale settings.

3.3. Feature and roughness comparison

In Figure 6 three distinctive features are selected for comparison.
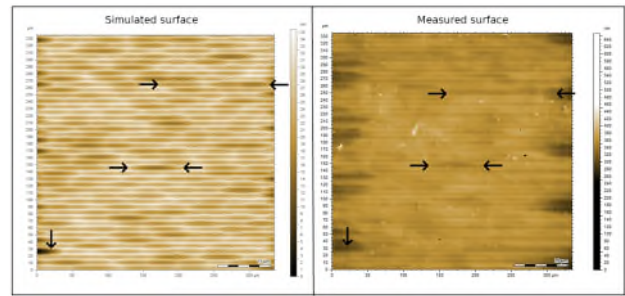
Figure 6. Comparison of the features in the simulated surface and the measurement of the first example (sample 5)

Although there were some matching features, the result is not entirely clear, as not all features were found in the respective comparison image.

The second example presented here also shows ambiguous results, according to Figure 7.
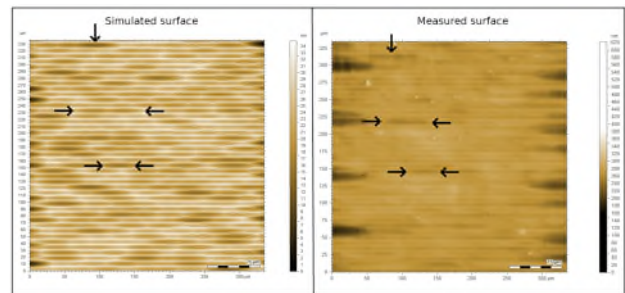
Figure 7. Comparison of the features in the simulated surface and the measurement of the second example (sample 12)

For this reason the roughness values of the surfaces were compared, see Table 1. The comparison shows for the mean arithmetic height clear differences of $\Delta Sa = 6.6\ nm$ between the parallel simulated and the measured surface and for the maximum height $\Delta Sz = 601.75\ nm$. The differences between the post processed simulated and the measured surface vary in the same area. In percentage terms, the *Sa* values of the simulated surfaces are approx. ten times higher.

Table 1. Comparison of the surface parameters

Surface roughness of the second example (sample 12), ISO 25178			
[*nm*]	Parallel simulated surface	**Post processed surface** (higher resolution, generation not in real-time)	Measured surface
Sa	2.18	3.12	8.78
Sz	19.85	34.80	621.60

One reason for the differences may be the mechanism of the simulation, which causes a limitation of height outlier values. This can be seen even more clearly in the disturbance test presented below.

3.4. Disturbance test

The post processed simulated surface of the machine test with introduced disturbances is investigated in the following part.
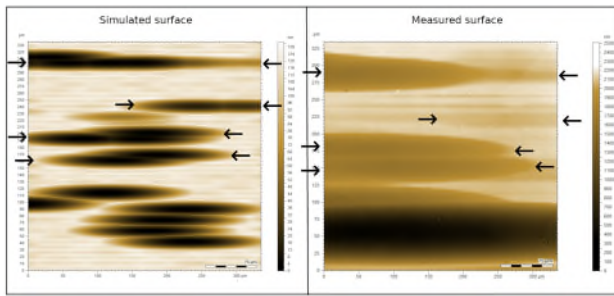
Figure 8. Comparison of the features in the simulated surface and the measurement of the third example (sample 9)

Figure 8 shows the external influences clearly in both the simulated and the measured image. Although the same sharp effects can be observed as in the previous presented samples, a connection of the simulated image with the measured one can be determined.

The surface roughness parameters in Table 2, however show a discouraging result, that does not reflect the real situation. Although the values are higher than for the samples without interference, with differences of $\Delta Sa = 419.28\ nm$ between the parallel simulated and the measured surface and $\Delta Sz = 2462.19\ nm$, they are still far from the values of the measured surface. The Sa values of the simulated surfaces also differ greatly in percentage terms. It should be noted that even the smallest outliers, that occur e.g. due to the material, influence the measurement of the maximum height.

Table 2. Comparison of the surface parameters

Surface roughness of the third example (sample 9), ISO 25178			
[nm]	Parallel simulated surface	**Post processed surface** (higher resolution, generation not in real-time)	Measured surface
Sa	2.72	35.46	422.00
Sz	44.81	130.70	2507.00

4. Conclusion

To summarize, a live axis data stream was implemented and fed into a simulation of the generated surface during the machining process.

The experimental setup and the materials as well as the data operations and the simulation were described. As a result of the simulation the visualization was compared with the measured surface in a qualitative and quantitative way. With a disturbance test the observations could be confirmed.

In conclusion the axis data seem to be a good choice for this purpose, but the evaluation did not reveal a clear result. While a similarity cannot be denied in the image comparison a direct coincidence cannot be ruled out. The surface roughness comparison in particular showed very clear differences. Thus further work in the area of limit data management and resolution improvement is necessary. This work represents preliminary work that can be expanded and utilized for optimizing fly-cutting processes.

References

[1] Brinksmeier E and Schönemann L 2022 Ultra-precision High Performance Cutting: Report of DFG Research Unit FOR 1845 1 10.1007/978-3-030-83765-5

[2] Schönemann L et al. 2020 Synergistic approaches to ultra-precision high performance cutting J. CIRP Journal of Manufacturing Science and Technology 28 p. 38-51 10.1016/j.cirpj.2019.12.001

[3] Ding Y,Rui X,Chen Y, Lu H, Chang Y and Wei W 2022 Theoretical and experimental investigation on the surface stripes formation in ultra-precision fly cutting machining J. The International Journal of Advanced Manufacturing Technology 124 p. 1041-1063 10.1007/s00170-022-10493-9

[4] Wu L, Sha K, Tao Y, Ju B and Chen Y 2023 A Hybrid Deep Learning Model as the Digital Twin of Ultra-Precision Diamond Cutting for In-Process Prediction of Cutting-Tool Wear J. Appl. Science 13 p.6675 10.3390/app13116675

[5] Selvaraj V, Xu Z and Min S 2022 Intelligent Operation Monitoring of an Ultra-Precision CNC Machine Tool Using Energy Data J. International Journal of Precision Engineering and Manufacturing-Green Technology 10 10.1007/s40684-022-00449-5

[6] Schönemann L, Riemer O, Karpuschewski B, Schreiber P, Klemme H and Denkena B 2022 Digital surface twin for ultra-precision high performance cutting J. Precision Engineering. 77 p. 349-359 10.1016/j.precisioneng.2022.06.010

3D measurement vision system using reflection for machine tools

Youngjun Yoo[1], Seungtaek Kim[1]

[1]Industrial Transformation Technology department ,Korea Institute of Industrial Technology

youdalj@kitech.re.kr, stkim@kitech.re.kr

Abstract

The proposed paper introduces a 3D vision system that harnesses the capabilities of mirrors. This visionary system is designed to capture three distinct images, achieved through the strategic arrangement of three cameras and two mirrors. These images are the building blocks for facilitating three-dimensional reconstruction, ushering in a new era of depth perception in imaging technology. The paper also presents the development of a dedicated autofocus stage and a motor control system. The motor control unit is ingeniously built around the Raspberry Pi, showcasing the system's adaptability and versatility. Furthermore, the user interface (UI) is constructed using Node-Red, which offers user-friendly web-based control. The implications of this measurement system have potential applications spanning various industries. One particularly promising application is within the field of manufacturing. This system can measure even the most hidden areas, such as the obscured rear parts of objects, where conventional viewing angles fall short. In manufacturing, precise measurements are paramount, and the proposed 3D vision system, with its multifaceted design and innovative technologies, promises to revolutionize the way these measurements are taken. As this paper and the associated system advance our understanding of 3D imaging, it is clear that the proposed system holds significant potential in improving the accuracy and efficiency of measurements in manufacturing, ultimately contributing to enhanced product quality and process optimization.

Engineering, Measuring instrument, Tool, Visual inspection

1. Introduction

In recent technological advancements, the integration of Computer Numerical Control (CNC) systems in manufacturing processes has significantly contributed to automated machining and production. CNC tools, vital components in these processes, play a crucial role in shaping specific parts with precision and repeatability. However, the use of damaged CNC tools can lead to various problems, including overheating, equipment damage, and errors affecting the entire system. Therefore, it becomes imperative to develop a system that can diagnose tool damage effectively.

This paper introduces a novel 3D diagnostic solution for CNC tools, departing from traditional image-based solutions. While traditional 3D scanners come with a hefty price tag, often exceeding $1000 for industrial-grade equipment, this proposed system offers a cost-effective alternative. The system aims to provide diverse views of CNC tools for precise diagnostic information, overcoming the limitations of existing 3D scanning methods vulnerable to light reflection and refraction.

To address these challenges, the proposed system utilizes a 3D vision system employing mirrors and a sophisticated motor control unit based on Raspberry Pi. The system captures three distinct images through strategic camera and mirror arrangements, enabling three-dimensional reconstruction. The use of mirrors allows the system to measure challenging areas, such as obscured rear parts of objects, which conventional viewing angles struggle to reach. The motor control system, built around Raspberry Pi, ensures adaptability and versatility, while the Node-Red-based user interface offers a user-friendly web-based control mechanism.

The potential applications of this cutting-edge system extend across various industries, with a particularly promising impact on manufacturing. Precision measurements are critical in manufacturing, and the proposed 3D vision system, with its multifaceted design and innovative technologies, promises to revolutionize the way measurements are taken. The use of mirrors for image capture, coupled with Raspberry Pi-based motor control and a web-controlled interface, adds an unprecedented level of flexibility and ease of use to this technology.

As the paper progresses, it delves into the challenges faced by conventional 3D scanning methods, highlighting their vulnerabilities to light reflection and refraction. The paper then introduces the concept of Neural Radiance Fields (NeRF) [1,-6] as a promising alternative due to its ability to depict light reflection accurately. NeRF's advantages, including ease of dataset creation and representation of continuous space for natural view transitions, are discussed. Despite NeRF's longer processing times, the paper proposes a feasible application in the industrial sector for real-time rendering systems.

In summary, this research aims to construct a 3D diagnostic system for CNC tools, utilizing a cost-effective approach with a single manual focus camera and NeRF technology. The proposed system demonstrates commendable performance in analyzing the external state of CNC tools economically and effectively. This approach is anticipated to find practical utility in small-scale manufacturing or environments with budget constraints, providing an innovative solution for CNC tool diagnostics.

2. Proposed Methodology

2.1 Hardware description

The proposed method involves positioning two mirrors and three cameras to obtain images of the unseen areas from the cameras through the reflection in the mirrors. In this setup, cameras with adjustable focal lengths are controlled using DC motors due to the variations in focal length and field of view depending on the camera's position. Figure 1 illustrates the process of measuring a solid end mill, showcasing two mirrors reflecting the top surface of the solid end mill, captured by three cameras in action. This method can find practical applications in tasks requiring high precision measurements. By utilizing mirrors to expand the field of view and capturing images from multiple angles through multiple cameras, it becomes possible to scrutinize detailed information about the target object. This is particularly advantageous for measuring small objects or objectswith intricate shapes. Moreover, the ability to adjust the camera's focus adds flexibility to measurement tasks across various environments. By automatically adjusting the focus using DC motors, users can maintain accuracy in the measurement process while operating efficiently. The hardware is installed in a clean environment and is not integrated into the actual manufacturing system but rather deployed for proof of concept purposes.
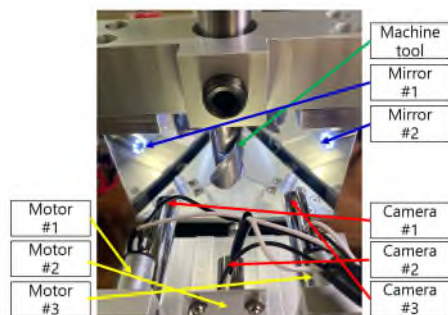
Figure 1. Proposed Hardware (Mirrors, Cameras, DC motors) for test-bed.

2.2. Software description

To establish a seamless integration between the cameras and DC motors, a connection was established with the Raspberry Pi. This intricate setup involved attaching gears to the focus ring of the manual focus camera and the DC motor, enabling changes in the camera's focus with the rotation of the DC motor. The automated focus feature of the DC motor and its impact on the captured images were implemented through Node-Red, as depicted in Figure 2. Utilizing three cameras in tandem allowed the system to acquire three distinct images in a single measurement session, amplifying the efficiency and depth of data collection.
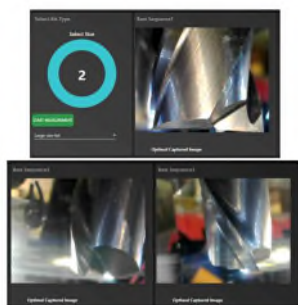
Figure 2. Proposed Software (User Interface with Node-red)

2.3. 3D reconstruction results

Figure 3 depicts the three-dimensional reconstruction results achieved using NeRF. The cost of the applied system, at less than $1000, indicates the feasibility of building an economical and effective 3D diagnostic system. However, the approximately 1-2 minutes required for image pre-processing and 3D rendering pose challenges with performance matric [7-9] for real-time rendering system implementation. The proposed method can help improve product quality by measuring machine tools through 3D Rendering.
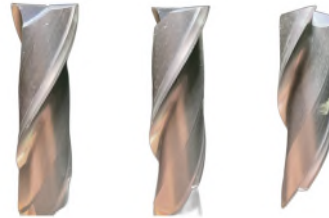
Figure 3. Reconstruction Results

3.Conclusion

This paper introduces an 3D diagnostic system for CNC tools, using mirrors and a Raspberry Pi-based motor control unit to overcome traditional 3D scanning limitations. The system enables precise measurements and three-dimensional reconstruction in challenging manufacturing areas. Exploring NeRF technology as an alternative to conventional 3D rendering, the paper highlights its potential for real-time rendering in industrial applications. The cost-effective approach, employing three autofocus camera and NeRF, performs well in analyzing CNC tool states. In conclusion, this research offers an accessible and efficient solution for CNC tool diagnostics, promising improvements in accuracy and efficiency for manufacturing processes.

References

[1] T. M¨uller, A. Evans, C. Schied, A. Keller 2022, Instant neural graphics primitives with a multiresolution hash encoding, ACM Transactions on Graphics (ToG), **41**, no. 4, pp. 1-15,

[2] Mildenhall, B., Srinivasan, P. P. , 2021, Tancik, M., Barron, J. T., Ramamoorthi, R., Ng, R., "Nerf: Representing scenes as neural radiance fields for view synthesis", Communications of the ACM, **65**, 199-106.

[3] Mildenhall, B., Srinivasan, P. P., Tancik, M., Barron, J. T., Ramamoorthi, R., Ng, R. 2021, Nerf: Representing scenes as neural radiance fields for view synthesis, Communications of the ACM, **41**, no. 1, pp. 99-106.

[4] Jonathan T Barron, Ben Mildenhall, Matthew Tancik, Peter Hedman, Ricardo Martin-Brualla, and Pratul P Srinivasan, 2021. Mip-nerf: A multiscale representation for anti-aliasing neural radiance fields. In Proceedings of the IEEE/CVF International Conference on Computer Vision, pp. 5855–5864.

[6] K. Deng, A. Liu, J. Zhu, D. Ramanan 2022, Depth-supervised nerf: fewer views and faster training for free. In Proceedings of the IEEE/CVF Conference on Computer Vision and Pattern Recognition, pp. 12882–12891,

[7] A. Horé and D. Ziou, "Image Quality Metrics: PSNR vs. SSIM. 2010. 20th International Conference on Pattern Recognition, pp. 2366-2369.

[8] Zhou Wang, A. C. Bovik, H. R. Sheikh, E. P. Simoncelli 2014, Image Quality Assessment: From Error Visibility to Structural Similarity, IEEE Transactions on Image Processing, **13**, no. 4, pp. 600-612,

[9] Zhang, R., Isola, P., Efros, A.A., Shechtman, E., Wang, O. 2018, The unreasonable effectiveness of deep features as a perceptual metric, In Proceedings of the IEEE Conference on Computer Vision and Pattern Recognition, pp. 586–595,

Plasma electrolytic polishing of bulk metallic glasses: what determines success?

Kristina Navickaitė[1,2], Klaus Nestler[2], Jan Wegner[3], Stefan Kleszczynski[3,4], Michael Penzel[1,2,5], Falko Böttger-Hiller[1], Henning Zeidler[1, 2]

[1]Technical University Bergakademie Freiberg, Faculty of Mechanical, Process and Energy Engineering, Institute for Machine Elements, Engineering Design and Manufacturing, Professorship for Additive Manufacturing, Agricolastr. 1, 09599, Freiberg, Germany
[2]Beckmann Institute for Technology Development e.V., Annabergerstr. 73, 09111, Chemnitz, Germany
[3]University Duisburg-Essen, Faculty of Engineering, Institute for Product Engineering, Chair of Manufacturing Technology, Lotharstr. 1, 47057 Duisburg, Germany
[4]Center for Nanointegration Duisburg-Essen (CENIDE), Carl-Benz-Str. 199, Duisburg, 47057, Germany
[5]Plasmotion GmbH, Halsbrücke Str. 34, 09599 Freiberg, Germany

kristina.navickaite@imkf.tu-freiberg.de

Abstract

In this study two types of bulk metallic glasses (BMG) were treated by plasma electrolytic polishing (PEP). Namely Vitreloy 101 with chemical composition Cu-Ti-Zr-Ni and AMZ4 with chemical composition Zr-Cu-Al-Nb. Both types of samples were manufactured by means of a laser powder bed fusion (PBF-LB/M) technology. In addition, AMZ4 samples were prepared using two distinct PBF-LB/M parameter sets. Owing to the similar chemical composition of the BMGs, they underwent the PEP-treatment in the same electrolytes. Surprisingly, different AMZ4 samples responded to it differently, whilst the results obtained on Vitreloy 101 samples were reproducible and predictable when process parameters and/or electrolyte were modified. Furthermore, some AMZ4 samples broke during or shortly after the PEP-treatment as they became more brittle and/or their surface became strongly oxidised. On the other hand, the Vitreloy 101 samples showed no signs of degradation and their surface became more glossy and smooth after the PEP-treatment. Nevertheless, it must be mentioned that for some AMZ4 samples satisfactory results were obtained, as they did not disintegrate during the process and/or did not break immediately after it and their surface became smoother and glossier. This inconsistency in the response to the same treatment of the same material could be attributed to the varying surface oxidation level of the AMZ4 samples and/or not yet properly selected electrolyte(s). The PEP duration varied from $\tau = 300$ s to $\tau = 600$ s with applied voltage between $U = 300$ V and $U = 420$ V. The pH value of the electrolyte varied between 3.4 and 3.8 during the PEP process and the electric conductivity was $\kappa \approx 105$ mS/cm at electrolyte temperature of $t = 75$ °C.

Plasma electrolytic polishing; bulk metallic glasses; additive manufacturing; surface oxidation; hatching strategy

1. Introduction

Material science is on an ongoing quest to develop new more durable, more mechanically stable and/or biocompatible, etc. materials. Recently a metastable austenitic CrMnNi steel was presented that demonstrates both increased yeld and tensile strength and improved ductility at the same time [1], [2]. Bulk metallic glasses (BMGs), however, have been known since 60s'. The vitrification of metals with various chemical compositions were achieved by rapid quenching [3]. The benefits of hardness, increased elastic limits and biocompatibility sparked the intereset for using BMGs for a number of different applications ranging from medical engineering to sports [4]. Recently, successful attempts to produce BMGs, namely Vitreloy 101 and AMZ4, by means laser powder bed fusion (PBF-LB/M) were reported [5]–[9]. It is well known, that the size of BMG parts is constricted by the precise cooling rate of a bulk material at which the vitrification takes place [3], [5]. A successful application of additive manufacturing (AM) technologies in producing BMGs, relaxes this constraint [5].

However, it is well established, that the surface quality of additively manufactured parts is rather poor. This, in many engineering applications, and customary preferences, is a serious drawback limiting parts applicability. Of course, there is

a number of techniques to refine the surface of AM parts, like particle blasting, (dry) electrochemical polishing, mechanical polishing etc. All these methods with greater or lower efficiency can be applied on AM parts made out of conventional material, like steel or titanium alloys [10]–[12]. Yet BMGs like Vitreloy 101 and AMZ4 pose a challenge to all of these polishing methods, especially to those exploiting electrochemistry. The chemical composition of these materials is very complex, thus an electrolyte used in such processes must be well tailored to avoid selective material removal, or other kind of surface damage. Furthermore, the unique material properties vanish upon crystalisation, which limits the temperature window during the post processing. Since cast BMGs typically feature a very good surface finish, and PBF-LB/M just recently emerged, studies on post-treatments are limited to a few exemptions.

Though there is a research gap on polishing BMGs, few studies have emerged reorting the efficiency of successful plasma electrolytic polishing (PEP) of BMGs [13]–[15].

In this study, results on PEP of AMZ4, a Zr-based alloy, and Vitreloy 101, a Cu-based alloy, are presented. The selection of the used electrolyte and PEP process marameters is discussed. The effect of the surface quality, namely the existing oxide film on as-received samples, is determined by the achieved polishing results. The efficacy of the PEP treatment is evaluated in terms of an area surface roughness Sq, a rooth mean square height,

and *Sv*, a maximum pit height, as it is shown to influence the fatigue life of AM parts the most [16].

2. Material and methods

2.1. Plasma electrolytic polishing

A bath-PEP technology where samples are immersed into the electrolyte bath was used for post-processing additively manufactured AMZ4 and Vitreloy 101 samples with different surface quality in as-received condition. The principal scheme of the test rig is presented in [17]. The applied direct voltage, *U*, was varied in the range from 300 V to 420 V. The electrolyte temperature, *t*, was varied from 75 °C to 85 °C. The process time, *τ*, was varied from 300 s to 600 s.

An electrolyte for Zr-based alloys was prepared following the chemical composition of an electrolyte used for polishing Zr-based bulk metallic glasses as reported in [13]. Yet, the Vitreloy 101 samples were also polished in this electrolyte. As it will be discussed later in this article, the polishing results of the AMZ4 samples were not reproducible, thus some additives, e.g., surfacants were added.

Due to the hydrodynamic conditions occurring during the bath-PEP process that is not assisted by an electrolyte stream directed to a specific sample surface, samples might be exposed to a different intensity of the PEP process. In other words, the efficiency of the treatment depends on the sample orientation in the electrolyte. In order to achieve as uniform as possible polishing effect, all samples were polished in two-steps, i.e. after half of the PEP time, *τ*, the samples were rotated by 180° and continued to be polished.

2.2. AMZ4 and Vitreloy 101 samples

Owing to the success of the previous experience in PEP-treating Vitreloy 101+Sn [15], only few test samples out of Vitreloy 101 were used for the PEP treatment in this study. Thus, the main focus of this article is placed on polishing the AMZ4 samples. It is acknowledged that the chemical compositions of AMZ4, which is a Zr-based material, i.e. Zr-Cu-Al-Nb, and Vitreloy 101, which is a Cu-based material, i.e., Cu-Ti-Zr-Ni, are rather different. Yet, the Vitreloy 101 samples were also polished in AMZ4-specific electrolyte(s).

In total four types of the AMZ4 samples were PEP-treated. They are so categorised according to the used PBF-LB/M-parameters and/or additional surface treatment using the particle blasting (PB) technique, which resulted in different surface quality of the analysed samples. Figure 1 shows the characteristic AMZ4 and Vitreloy 101 samples used in this study.
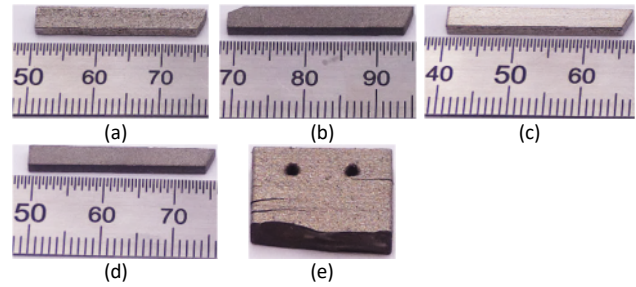
Figure 1. Characteristic AMZ4 samples manufactured using (a) standard PBF-L/M settings, (b) additional contouring strategy, (c) standard PBF-L/M settings with PB, (d) additional contouring strategy + PB and (e) Vitreloy 101 sample in as-received condition.

The characteristic measurements of the samples dimension and mass were taken before and after the PEP process. For these measurements a digital micrometer *BGS technic 8427* (resolution 0.001 mm), a digital electronic calliper (resolution 0.01 mm) and a scale *KERN 572* were used. The surface roughness of the samples before and after the PEP treatment was measured by a confocal microscope *MarSurf CM Explorer*.

3. Results and discussion

The PEP process conditions are listed in Table 1. One can see that the current during the PEP process, when the standard electrolyte was used, is significantly higher compared to the modified electrolyte. This is because the experiments using the basic electrolyte were conducted in a three times lower electrolyte volume. Note that the electric conductivity of both electrolytes was $\kappa \approx 105$ mS/cm at *t* = 75.0 °C.

Table 1 PEP process parameters investigated in this study and resulting surface roughness *Sq* and *Sv*.

Sample No.	Sample class	Electrolyte	PEP time, *τ*, s	Voltage, *U*, V	Current, *I*, A	Temperature, *t*, °C
1	Standard	Base	600	331	4.0	79.4
2			600	328	4.0	79.2
3			600	328	4.0	79.6
4	Contour		600	329	4.0	79.7
5			600	329	4.0	79.4
6			300	330	4.0	77.8
7	Standard	Additives	600	300	2.5	74.6
8			600	300	2.3	74.7
9			600	300	2.5	74.4
10	Contour		600	300	1.5	75.0
11			600	300	3.6	75.4
12			300	300	1.0	84.8
13			600	420	1.1	84.7
14	Standard+PB		600	300	2.1	74.9
15			600	300	2.1	74.6
16			600	300	2.5	74.8
17	Contour+PB		300	300	2.3	74.9
18			300	300	2.5	74.1
19			600	300	2.2	75.3
20	Contour		600	360	1.1	84.2
21			600	360	1.1	84.7

Figure 2 presents the selected samples after the PEP. One can see that the surface of Sample 5, which was treated in a basic electrolyte, was ruined since a dark oxide layer was formed on it during the treatment. Sample 1, on the other hand, which was PEP-treated at the same conditions developed no signs of degradation. Furthermore, the initial surface roughness of both samples, as shown in Figure 3, was comparable. Remarakably, the surface roughness of both samples was reduced by the PEP process, regardless of the developed oxide layer on Sample 5. Note that surface roughness of all the investigated samples was measured on the same sample side, in the middle of the sample in 2.3 × 2.3 mm² area.

From Figure 3, one can see that the surface roughness could consistenly be reduced when samples were polished in a basic electrolyte, while using the modified electrolyte the surface roughness, especially Sv parameter, would increase/decrease unpredictably. One can argue that these results could have been affected by the applied voltage. Indeed, samples polished in a basic electrolyte were exposed to $U \approx 330$ V, while samples polished in the modified electrolyte were exposed to $U = 300$ V,

except a few samples polished at 360 V and 420 V. However, samples that were polished in the basic electrolyte at $U = 300$ V broke, thus they are not further discussed in this article.
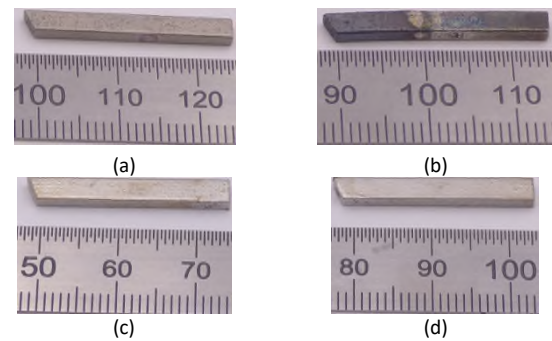
Figure 2. Photographs of (a) Sample 1, (b) Sample 5, (c) Sample 20 and (d) Sample 21 after PEP.
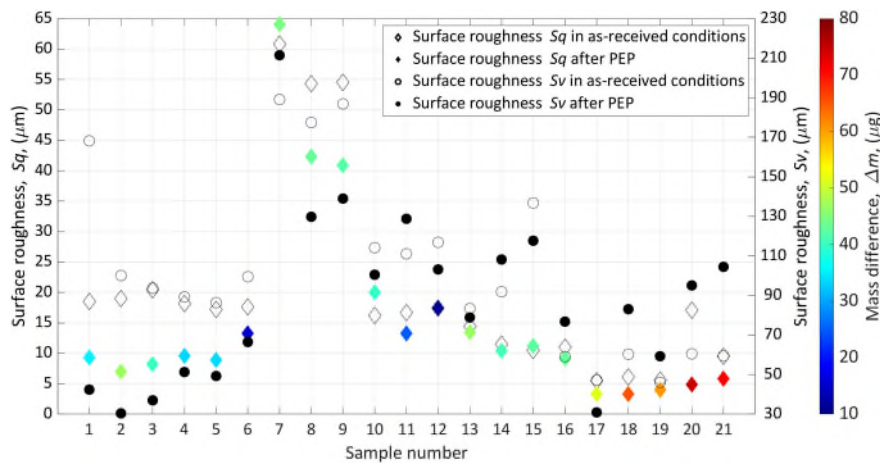
Figure 3. Surface roughness Sq and Sv before and after PEP. The colour scale shows the mass difference before and after PEP.

Further investigation of the surface topography of the samples before and after the PEP revealed that PEP uncovered some defects of the PBF-LB/M process causing artificial increase in surface roughness. These defects, like weld tracks and/or lack of fussion, partly molten particles etc. create artificial surface valleys/peaks that are evaluated as surface roughness. Some examples of such surface defects are highlighted with red arrows in Figure 4. Nevertheless, the duration of the PEP treatment for Sample 9 and other samples, which were manufactured using the standard PBF-LB/M parameters and had higher initial surface roughness compared to those that were produced with contour scanning strategy and/or addtionally particle blasted could have been extended to achieve lower surface roughness. The surface quality of the samples with already low initial surface roughness, on the other hand, was significantly improved in $\tau = 300$ s of PEP.

Finally, it must be reported that multiple samples that were polished in a base electrolyte broke during or shortly after the PEP and/or developed black oxide layer as shown in Figure 2 (b). A very few samples, that are reported in Table 1 were successfully polished in this electrolyte. Initial hypothesis was that the samples had a light oxide layer that prevented a good electrical contact with the power source. Thus a new batch of samples with improved surface quality, i.e. after particle blasting, was produced. Indeed, a light oxide layer on the samples with standard manufacturing parameters was indicated under the microscope. A trial test was performed on one sample

with improved surface quality in the base electrolyte and it was ruined. Thus the initial hypothesis was disregarded and a modified electrolyte was developed and used for polishing the rest of the samples. However, the phenomena of the modified electrolyte was rather temporary. At a certain point, samples polished in this electrolyte also started to develop a black oxide layer. Fortunately, no sample broke during or shortly after the PEP treatment. Despite the continuous modulation of the pH level and the electrolyte conductivity, no successful PEP experiments could be conducted at $U = 300$ V. Thus, several trials at higher applied voltage, as reported in Table 1, were carried out that astonishingly led to positive results. However, the reason behind this is not yet understood. The Vitreloy 101 samples, though, could be successfully polished using both eletrolytes at varying process conditions without any signs of sample degradation.

4. Conclusions

In this study two electrolytes were tested for PEP of AM AMZ4 and Vitreloy 101 samples. The AMZ4 samples were prepared using two distinct PBF-LB/M process parameter sets. Part of these samples were also particle blasted. These samples were PEP-treated using various process settings and the obatined results are summarised as follow:
1. The efficacy of the PEP process on AMZ4 / Vitreloy 101 does not depend on the initial surface oxide layer.

2. The results obtained using the base electrolyte for PEP of AMZ4 are not reproducible.

3. The degeneration of the modified electrolyte was slowed down by added surfactants. Yet, the damage to the surface of the polished AMZ4 samples could be avoided only by modulating the process parameters rather than electrolyte properties.

4. Vitreloy 101 samples could be successfully polished in either of the electrolytes witout any signs of damage to the surface.

Future studies will focus on a wider PEP parameters in terms of electrolyte temperature and applied voltage to determine the right set of parameters for post-processing BMGs materials. The crystallisation of the samples as well as mechanical properties of the PEP-treated AMZ4 samples will be investigated to find out whether PEP influences the material properties.
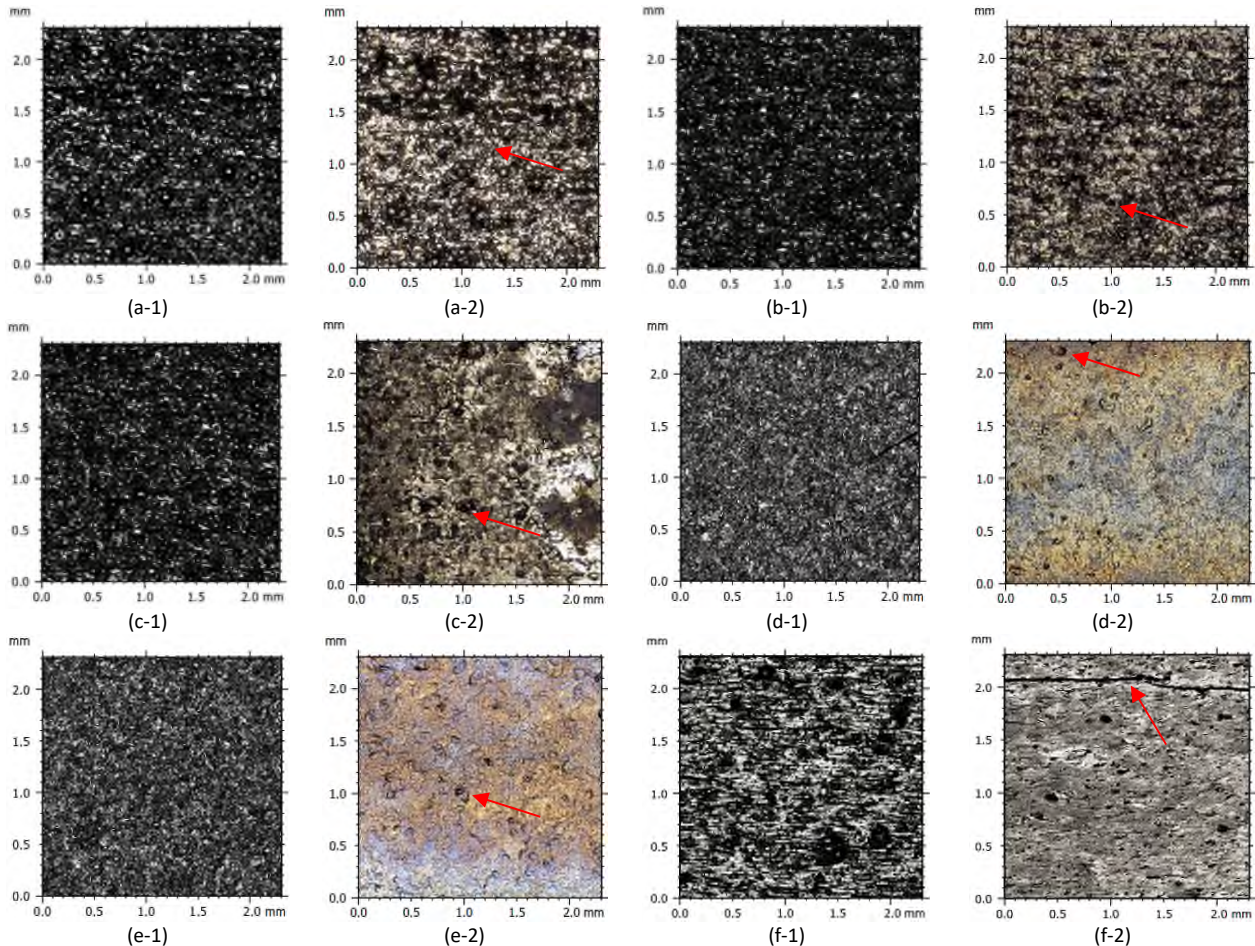
Figure 4. Micrographs of analysed samples in (1) as-received and (2) after PEP conditions: (a) Sample 9, (b) Sample 10, (c) Sample 11, (d) Sample 17, (e) Sample 18 and (f) Vitreloy 101.

References

[1] Schröder C, A Weiß, and O Volkova 2018 *Materwiss. Werksttech.* **49** 577–590

[2] Weidner A, A Glage, and H Biermann 2010 *Procedia Eng.* **2** 1961–1971

[3] Oleszak D and T Kulik 2010 *Mater. Sci. Forum* **636–637** 917–921

[4] Telford M 2004 *Mater. Today* **7** 36–43

[5] Frey M *et al.* 2023 *Addit. Manuf.* **66** 103467

[6] Soares Barreto E *et al.* 2022 *Mater. Des.* **215** 110519

[7] Sohrabi N *et al.* 2021 *Mater. Des.* **199**

[8] Wegner J *et al.* 2021 *Mater. Des.* **209** 109976

[9] Marattukalam J J *et al.* 2020 *Addit. Manuf.* **33** 101124

[10] Parfenov E V., R G Farrakhov, V R Mukaeva, A V. Gusarov, R R Nevyantseva, and A Yerokhin 2016 *Surf. Coatings Technol.* **307** 1329–1340

[11] Мукаева В Р, Е В Парфенов, М В Горбатков, and Р Р Невьянцева 2014 *Вестник Уфимского Государственного Авиационного Технического Университета* **3** 150–157

[12] Jahadakbar A *et al.* 2020 *Metals (Basel).* **10** 151

[13] Wang C *et al.* 2023 *Int. J. Adv. Manuf. Technol.* **124** 2079–2093

[14] Navickaitè K *et al.* in *19th International Symposium on Electrochemical Machining Technology*, Saarbrücken, Germany, 2023.

[15] Navickaitè K, K Nestler, F Böttger-Hiller, M Penzel, and H Zeidler in *euspen 23rd International Conference & Exhibition*, Copenhagen, Denmark, 2023, 2–3.

[16] Lee S, B Rasoolian, D F Silva, J W Pegues, and N Shamsaei 2021 *Addit. Manuf.* **46** 102094

[17] Navickaitè K *et al.* 2022 *Procedia CIRP* **108** 346–351

Root cause analysis in Float-Zone crystal growth production using fishbone diagram and association rule mining

Tingting Chen[1], Guido Tosello[1], Matteo Calaon[1]

[1]*Technical University of Denmark, Produktionstorvet, 2800 Kgs. Lyngby, Denmark*

tchen@dtu.dk

Abstract

Float-Zone (FZ) crystal growth process is a critical process for producing ultra-pure silicon crystal with extremely low impurities, particularly low oxygen level. However, the occasional oxide problem on polysilicon surface acts as a impediment to the process efficiency. Hence, this study aims to address this problem by conducting root cause analysis. Specifically, association rule mining is applied on a dataset with the input identified by a fishbone diagram from different aspects. The results showed that a high moisture level from the early phase could potentially be a critical contributor to the oxide problem, thereby indicating the next step of research – exploring the underlying reasons for the high moisture level.

Float-zone crystal growth; root cause analysis; association rule mining

1. Introduction

It is undisputed that silicon wafers have become crucial to our modern life and the world's commercial and military applications. The demand for silicon wafers has witnessed a substantial surge in recent years, necessitating a substantial increase in productivity. In order to meet these growing demands and enhance the competitiveness of businesses, single crystal growth process as the key process for the fabrication of silicon wafers, has been driven to increase good-for-order single-crystal silicon yield while keeping costs low. Float-Zone (FZ) crystal growth process is a critical process in the production of high-quality single crystals used in various applications, including solar cells, insulated gate bipolar transistors (IGBTs) [1], etc, where there purity of the silicon crystal is essential. The FZ process can allow for producing a higher purity silicon crystal with much lower concentrations of impurities, particularly lower content of oxygen (below 5×10^{15} atom/cm^3 [2]) due to the absence of crucible. However, the high production costs of FZ crystals have been a hindrance for its wider applications, due to the high costs for the feedstock material, polysilicon feed rod [3]. The contribution of the feed rod to the Cost of Ownership (CoO) of the growth process is far more than 50% [3]. Therefore, crystal yield is of great significance for the FZ process. However, the FZ process occasionally suffers from the oxygen contamination, which may disrupting the process efficiency, thus affecting crystal yield. The oxygen contamination can be visually observed in the images captured by the FZ vision system, as seen in Figure 1. To enhance the crystal yield and thus enhance the competiveness of the FZ process, it is essential to optimize the FZ process and achieve consistent quality by mitigating the oxide problem. Therefore, it is desired to discover the root causes of the oxide problem, which motivates this study.

Root cause analysis is a process through which we can understand the fundamental triggers of a problem, thus leading to more effective solutions. Knowledge-driven approaches are widely used in conventional root cause analysis involving domain-specific expertise, and human intuition to identify the underlying causes of issues. Typical examples are fishbone diagram, 5 Why, and FMEA. However, these knowledge-driven approaches are time consuming and inefficient, which becomes particularly evident in the era of big data [5]. The rise in data accessibility, coupled with the increased availability of computational resources, has prompted researchers and practitioners to utilize data-driven approaches such as data mining and machine learning techniques to enhance the efficiency of the root cause analysis process [5].

Hence, this paper aims to improve the FZ process, by conducting root cause analysis for the oxide problem in the FZ process. To this end, association rule mining [6], a data-driven approach would be leveraged for the root cause analysis.
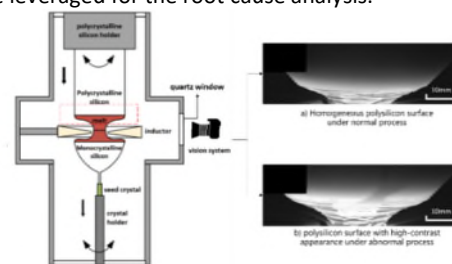
Figure 1. The comparison of normal process and abnormal process with oxygen contamination.

2. Root cause analysis with association rule mining

Association Rule Mining (ARM) [6] is a data-driven approach that can provide quantitative evidence of relationships between variables, allowing for discovering hidden relationships within the data that might have been overlooked. The frequent patterns extracted by ARM are in the form of X → Y The frequent patterns are then examined by a minimum threshold of statistical measures, such as support and confidence and lift. The larger these measures, the more robust the rule is. One only needs to look into the strong rules extracted from ARM, and examine if they are related to the source of the problem using expert knowledge.

However, it should be noted that ARM can only handle binary or categorical attributes, which is not common in manufacturing data. Therefore, if ARM is applied, the manufacturing data should be processed and converted into binary or categorical data. Besides, since the number of rules is highly dependent on support (frequency), some interesting rules might have been filtered due to the rarity. Hence, to assign equal importance to each variety of the oxide, ARM would be applied on each subdataset categorized by the varieties of the oxide.

3. Experiments

Before applying ARM, the relevant data associated with the oxide problem was first identified by a fishbone diagram from 5 aspects: Machine, Process, Ambition, Human, Material, as seen in Figure 2. Several potential factors were identified that may contribute to oxide (see Figure 2).
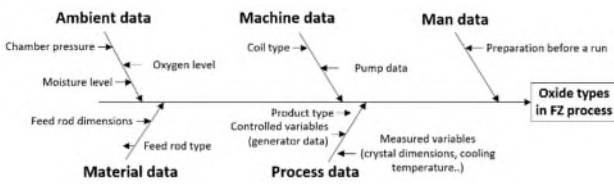
Figure 2. Fishbone diagram for identify potential factors that contribute to the oxide problem.

Subsequently, a total of 387 observations of these potential factors along with FZ images were collected from 387 production runs. These observations were cleaned and transformed to categorical data types. After data-preprocessing, the dataset consists of 387 samples and 135 features along with three oxide types: normal, spot and shadow. Next, FP-Growth from rCBA package in R was applied with a minimum class-wise support threshold of 30% and a maximum length of the itemsets of 3 which is equivalent to considering at most two features. The generated rules were pruned with the absolute confidence threshold of 50% and the absolute lift threshold of 1.2, followed by removing redundant rules that have no positive improvement on confidence and lift measures. Finally, a total of 68 rules were identified, with lift values ranging from 1.2 to 11.88.

The scatter plot for visualizing all rules can be see in Figure 3. As seen, the rules with the highest lift values are concentrated in the bottom left corner of the plot, indicating low support and confidence. In fact, the majority of these rules are linked to the normal type. While these rules may not be very actionable in practice, they offer valuable insights into the optimal conditions for a normal process. Another cluster stands in the upper-right corner of the plot with both a high level of support and confidence, making them particularly interesting. These rules are associated with spot and shadow oxide types. The network graph for the classes of normal, spot and shadow can be seen in Figure 4, 5, and 6, respectively. The highlighted itemsets of each graph are the most commonly occurring itemsets, indicating their great significance. As seen, the spot and shadow are associated with the moisture level from the early while the normal case is associated with high preparation time and low oxygen level. As mentioned in the scatter plot, the priority would be put on the rules of spot and shadow types rather than the the normal. Hence, the subsequent research would be to discover the root cause of high moisture level.

4. Conclusions

In order to identify the fundamental triggers of the oxide problem to improve the FZ process, association rule mining was leveraged for root cause analysis. The results showed that high moisture level from the early phase could potentially contribute to the spot and shadow types. Therefore, the next step of research would be focus on the root cause analysis of high moisture level.
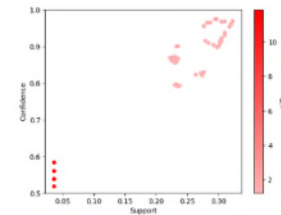
Figure 3. The scatter plot of rules.
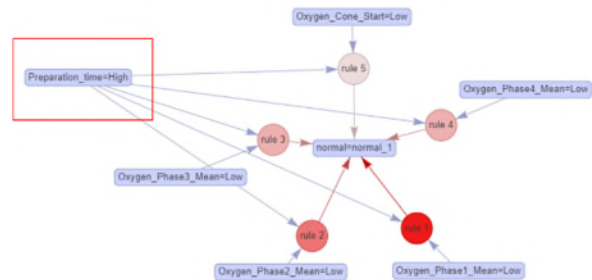
Figure 4. The network graph for normal case.

Figure 5. The network graph for spot case.
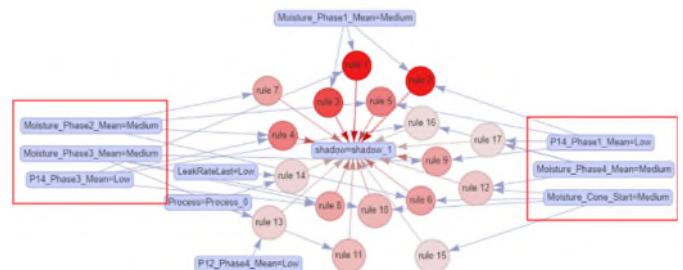
Figure 6. The network graph for shadow case.

References

[1] Kajiwara K, Harada K, Torigoe K and Hourai M 2019 Oxygen Precipitation Properties of Nitrogen-Doped Czochralski Silicon Single Crystals with Low Oxygen Concentration. *physica status solidi (a)*. **216** 1900272.

[2] Kiyoi A, Kawabata N, Nakamura K and Fujiwara Y 2021 Influence of oxygen on trap-limited diffusion of hydrogen in proton-irradiated n-type silicon for power devices. *Journal of Applied Physics*. **129** 025701

[3] von Ammon W 2014 FZ and CZ crystal growth: Cost driving factors and new perspectives *physica status solidi (a)*. **211** 2461-2470.

[4] Muiznieks A, Virbulis J, Lüdge A, Riemann H and Werner, N 2015 Floating zone growth of silicon. *In Handbook of Crystal Growth* 241-279

[5] e Oliveira E, Miguéis VL, Borges JL 2023 Automatic root cause analysis in manufacturing: an overview & conceptualization. Journal of Intelligent Manufacturing. **34** 2061-78

[6] Agrawal R, Imieliński T, Swami A 1993 Mining association rules between sets of items in large databases *In: Proceedings of the 1993 ACM SIGMOD Int. Conf. on Management of data* 207-216

An in-process digital twin and decision support system for additive manufacturing

Cathal Hoare[1], Andrew Parnell[2] & Denis Dowling[1]

[1]*I-Form Centre, School of Mechanical and Materials Engineering, University College Dublin, Dublin, D04 V1W8, Belfield, Ireland*
[2] *Department of Mathematics & Statistics, Maynooth University, Maynooth, Kildare, Ireland*

cathal.hoare@i-form.ie

Abstract

The application of digital manufacturing technologies to additive manufacturing offers significant potential to improve process resilience, sustainability, and productivity. While Machine Learning (ML) is now widely applied in AM, the ability of operators to use and act on predictions from ML approaches in real time has been limited. Factors such as heterogeneity of data, inexpressive data models, timeliness of results, and poor contextualization of ML results have contributed to this limitation. The novel software platform described in this paper addresses this deficit in two parts; first, a digital twin outlined in this paper represents the additive manufacturing process state using a novel data model that collects and fuses various information, including real-time hardware sensor data. The second component is a Decision Support System that captures operator expertise and heuristics in the form of rules. Drawing insights from both successful and unsuccessful print runs, the system continuously learns, enhancing its ability to provide informed recommendations for remedial actions over time. Together, the digital twin and decision support system provide recommendations to operators while a print process is ongoing.

Additive Manufacturing, In-process Monitoring, Digital Twin, Recommender System, Decision Support System, Machine Learning

1. Introduction

Metal Additive Manufacturing (AM) offers significant advantages over traditional subtractive manufacturing, such as enhanced design flexibility, increased sustainability, and shorter product development times [1]. However, AM faces challenges related to process stability and repeatability [2]. In-process analysis during part printing can identify and predict anomalies using machine learning (ML) and other forms of artificial intelligence. To harness machine learning successfully, obstacles like data heterogenization, suboptimal data architectures (especially for real-time analysis), and inadequate data models must be addressed [3]. Digital twins, dynamic virtual copies of physical assets, offer a solution to these challenges, especially when employed in real-time scenarios. However, platforms providing near real-time decision support for AM processes, particularly in sensor fusion and data management applications, are still considered in their early stages [4].

This paper describes a real-time digital twin that informs an in-process decision support system, aiding operators of additive manufacturing equipment in addressing processing issues and thereby improving product quality, production line efficiency, and sustainability. Additionally, we present an example illustrating the application of the digital twin and decision support system in a production environment.

2. Platform Description

The digital twin outlined in this paper represents the additive manufacturing process state using a novel data model that collects and fuses various information, including real-time hardware sensor data. This information populates a data model describing the printing process. Our digital twin enhances the data model by employing machine learning-based analysis on the collected data to gain profound insights into the print's state. It works in conjunction with a rules-based decision support system that assesses the digital twin's described printing process state, providing real-time recommendations to guide manufacturing. These rules are tailored on a per-product basis and can be refined and reused for similar manufacturing processes. The interactions among data sources, the digital twin, and the decision support system for our approach are illustrated in Figure 1.

The digital twin's data model describes a series of tables that can be integrated into other schema, for example the NIST schema [4], to provide support for real-time reasoning about an ongoing build. The data schema is capable of capturing information in fine detail; these data can be aggregated to various levels to provide summary information about individual build layers, the build or collections of builds. Information can be represented in different forms, including image data obtained using optical sensors and camera, measurements derived from in-process data and events such as anomalies reported by analysis modules. Details of the analysis module that generates an event are also captured.

The developed system also incorporates a Recommender System framework that captures operator expertise and heuristics in the form of rules. Drawing insights from both successful and unsuccessful print runs, the system continuously learns, enhancing its ability to provide informed recommendations for remedial actions over time.

The platforms user interface is shown in Figure 2. It displays three key pieces of information. Figure 2 (A) shows summary information about the print and provides an overview of key metrics about the print. Figure 2 (B) shows sensor data,
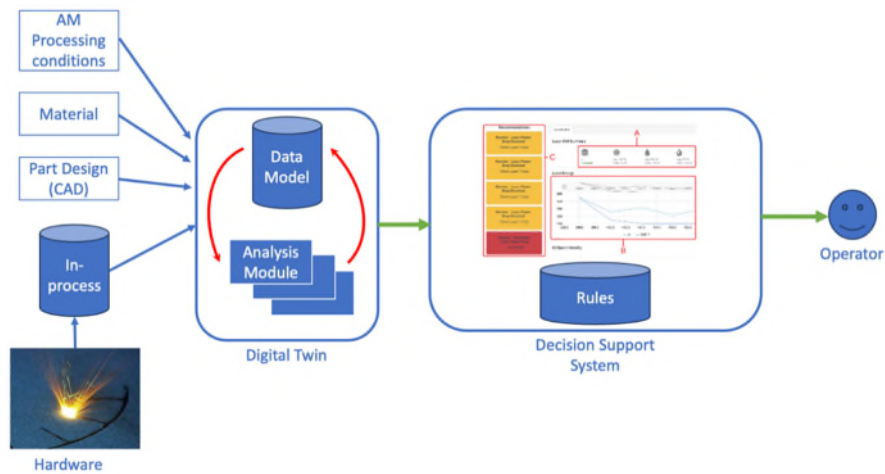
Figure 1. Overview of the I-Form Digital Twin/Decision Support Platform, including data collection, analysis and generation of recommendations.
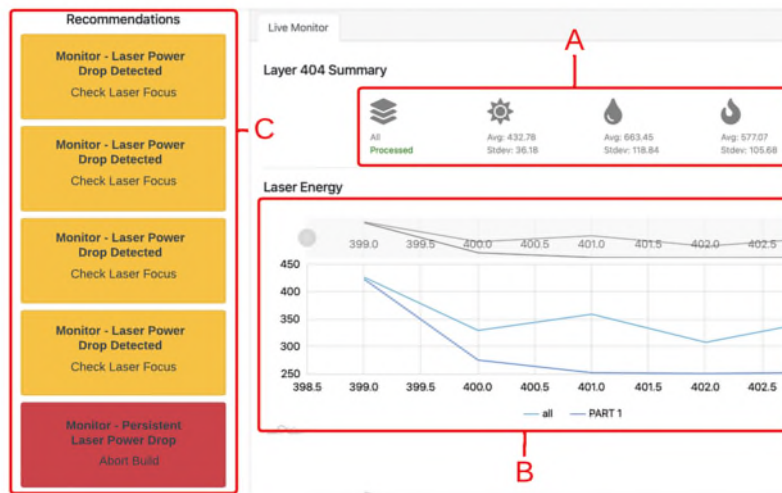
Figure 2. Screenshot of Web-based Decision Support Interface showing (A) a summary of the AM processes' current status (B) Monitor for Laser Energy Output (C) a series of recommendations.

displayed as a series of graphs, displaying aggregated values per layer for the overall build area and each of the observed volumes. In this view of the print, the mean value of the laser output are displayed. The graph of the laser output shows a fall in laser output has occurred. This drop began at layer 400 and continued over three contiguous layers. Figure 2 (C) shows generated recommendations; here analysis modules associated with an observed volume noted the laser power drop for a layer. This triggered a recommendation with advice to check the laser focus. When this anomaly was detected over three layers, the second FSM generated a second recommendation type that advised that the print be abandoned.

The versatility of the developed digital twin and decision support system extends beyond L-PBF processes, making it applicable to a broader spectrum of manufacturing processes. This is attributed to its flexible structure, capacity to consume data from various sources, and the application of diverse analysis methodologies to this data. However, it's imperative to note that, for each process application, defining and applying rules to the outputs of the analysis is essential.

3. Conclusions
In conclusion, the outlined digital twin and decision support platform not only addresses the intricacies of additive manufacturing but also holds promise for broader manufacturing applications, thanks to its adaptable architecture and robust analytical capabilities. Having been successfully deployed in an industry setting, the platform seamlessly processed high-volume and high-velocity sensor data in near real time. For instance, in the L-PBF process discussed in this paper, each print layer generates approximately 450 MB of data. Despite this substantial volume, the system defines and delivers recommendations to operators before the next layer completes. This rapid processing speed coupled with operator decision support represents a distinctive advantage within the realm of AM processing.

References

[1] Atzeni E and Salmi A 2012 Economics of additive manufacturing for end usable metal parts *The International Journal of Advanced Manufacturing Technology*. **62** 9 1147–1155

[2] Grasso M and Colosimo B M 2017 Process defects and in situ monitoring methods in metal powder bed fusion: a review *Meas Sci Technol.* **28** 4

[3] Zhang L *et al.* 2020 Digital Twins for Additive Manufacturing: A State-of-the-Art Review *Applied Sciences*. **10** 23

[4] Razvi S, Feng S, Narayanan A, Lee Y T, and Witherell P 2019 A Review Of Machine Learning Applications In Additive Manufacturing *Proceedings of the ASME 2019 International Design Engineering Technical Conferences and Computers and Information in Engineering Conference*

Adaptive dexelisation approach for material removal simulation in milling

Yigit Ozcan[1,2], Shashwat Kushwaha[1, 2], Jun Qian [1,2], Dominiek Reynaerts[1, 2]

[1]Department of Mechanical Engineering, KU Leuven, Celestijnenlaan 300, Leuven 3001, Belgium
[2]Member Flanders Make, Belgium

yigit.oezcan@kuleuven.be

Abstract

Minimizing lead time without sacrificing accuracy is a major challenge in various industries. In CNC milling, geometrical inspection takes one of the biggest efforts. Process-parallel simulations have the potential to reduce down-time and effort spent in inspection. Especially for real-time workpiece quality estimation, the cutter workpiece engagement methods must be improved to achieve effective computation without sacrificing precision. According to the literature, the dexelisation method is one of the best contenders for high-fidelity material removal simulations.

The literature shows promising results for offline part geometry estimation considering cutting loads. However, academic studies and industrial software tools are scarce for process-parallel material removal simulation. This is due to the need of high computation power. Therefore, in this study, an adaptive dexelization approach for workpiece is proposed. The method is accelerated by using a Ray Tracing algorithm and GPU cores without comprising the accuracy of inspection considering cutting loads. Around five times reduction on computation time has been reached with this method.

Material removal simulation, dexelization, Tridexel, milling, cutter workpiece engagement.

1. Introduction

Currently, the manufacturing field is experiencing the fourth industrial revolution, which enables value-adding interconnected assets to communicate with each other so that digital data can provide greater added value. This digital revolution allows faster reporting and hence efficient and timely decision making and intervention. Like in other manufacturing methods, in CNC milling, there is a trend through the digitalisation of the process to generate a digital model of the physical product [1]. In that sense, virtual machining is critically important to evaluate whether the physical workpiece is in the desired condition during the process.

Three primary methods exist for virtual workpiece representation for milling. (1) Solid Modelling, including Constructive Solid Geometry (CSG) or Boundary Representation (B-rep) [2], uses primitive volumes updated through Boolean operations. However, both CSG and B-rep have limitations; Brep's reliability in updating the workpiece for every cutter location is uncertain, and CSG struggles with supporting free-form objects [3].

(2) Space Partitioning, representing the workpiece through voxels, discrete volume elements defined as binary (1 for material, 0 for empty) [4]. Here the memory allocation is directly proportional to $O(n^3)$, where O is memory allocation, and n is the number of voxels. Dexel method overcomes the memory requirements. Here, the workpiece is represented by vectors, where memory allocation is proportional to $O(n^2)$ [5]. On top, tri-dexel methods address fidelity problems, e.g. on high slope surfaces by sending line segments from three perpendicular axis-aligned planes [6]. The tri-dexelisation can be sped by running ray tracing algorithm on a GPU [7].

Despite progress in virtual workpiece representation for CNC milling, achieving high-fidelity and low-latency in the digital twin context remains a challenge. This study focuses on enhancing Tri-dexel method efficiency by adaptively adjusting dexel density based on known cut regions and their expected tolerance. This step is pre-processing for process-parallel geometry estimation intended to save memory and reducing simulation time while improving the precision at required locations.

2. Tridexel algorithm

2.1. Step -1: Adaptive Workpiece Dexelisation

In this section, details of adaptive Tri-dexel algorithm are given. Our method requires the input of tessellated CAD model of the stock material. The user divides the CAD model into sub-geometries with respect to required tolerances in every x, y, and z directions separately while triangulating the geometry (.STL conversion). Each sub-geometry is to be defined in a specific dexel resolution and corresponding spatial grids are generated along the three axes. From each grid, rays are cast to make intersection with triangles of sub-geometries. This procedure is applied only once before the material removal is calculated. It should be noted that each grid execution is done in one GPU block. The results from every ray-triangle intersection are transferred to the CPU to find the starting and ending points of

Z dexel grids   X&Y dexel grids

Lower Density Grids   Higher Density Grids
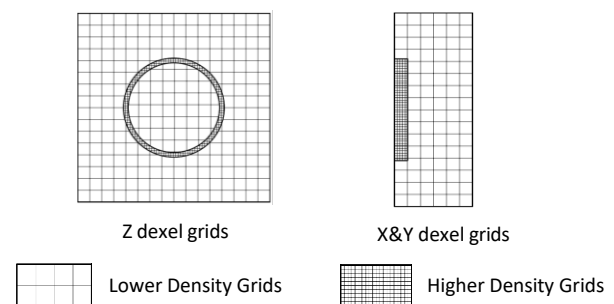
Figure 1. Adapted Grids for WP in X,Y,Z directions

every intersection calculation between ray and triangles. Depending on the intersection distance and grid IDs, the starting and ending points are found by sorting for each grid IDs. In this study, an 80x80x30 mm workpiece material was dexelised adaptively. Referring to Figure 1 the inner 40 mm diameter cylindrical pocket is dexelised with higher density grids. Here a 1 mm from the cylindrical surface is chosen for high density dexels. Similar procedure is applied in X and Y direction independently. In all directions, remaining part is kept with relatively lower grid density, i.e., 0.5 mm grid resolution, which is represented in Figure 1. Regarding to these grids, adaptive dexels in X and Z directions can be seen in the Figure 2. Note that because of the symmetricity, Y dexels are basically the same figure with dexelised workpiece (WP) in X direction.

Dexelised WP in X   Dexelised WP in Z
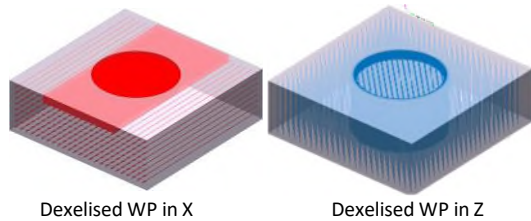
Figure 2. Dexelised WP in X and Z directions.

2.2. Step 2: Finding Axis Aligned Bounding Box (AABB)

At this stage, another improvement on calculation can be done by using an axis aligned bounding box (AABB). First, multiple cutter locations are collected and AABB is calculated by the finding an envelope for the collected cuter locations. The AABB allows to locate the dexels within this envelop. For the material removal simulation to proceed, only the dexels inside the AABB are loaded for further calculations. That means only the rays inside of the extreme point of cutter regions is to be activated for ray to tool geometry intersection. In the Figure 3, the blue lines represent the tool path and corresponding tool locations in grey. By finding the extreme points in XY plane (for Z direction dexel intersection) the AABB is created. In this way, only the dexels that fit into this box are activated for ray-cylinder/tool intersection.
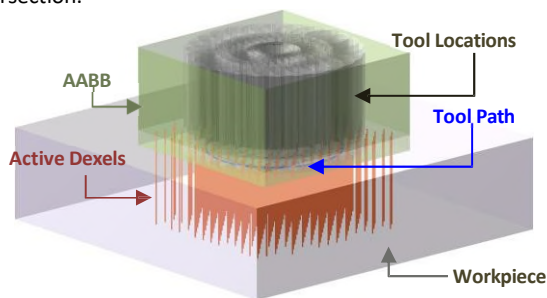
Figure 3. Active Z dexels by finding AABB of tool locations.

2.3. Step 3: Ray-tool intersection

To further simplify the calculations, the tool (end mill) is represented as a cylinder. The ray cylinder intersection calculation was used, which is computationally effective as opposed to intersection problem with a triangulated tool. If the intersection distance is lower than the end point of corresponding active dexel element's end point, then the dexel element end point updated with the intersected point.

The algorithm is developed on MATLAB by using the parallel computing tool of CUDA cores. NVidia GeForce RTX3070 graphics card with 8GB dedicated memory was used for ray-triangle/cylinder intersection. In this simulation a 10 mm flat end tool is selected. Cutter is simulated as a cylinder geometry with total 553 cutter locations for the circular (high density) region as 40 mm diameter and 5 mm depth.
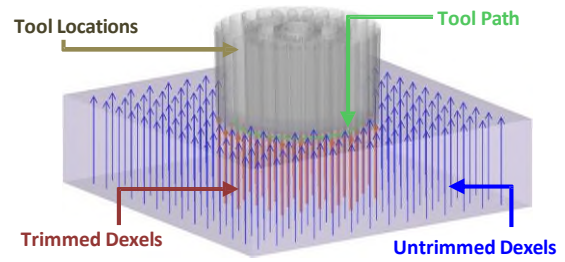
Figure 4. Dexel trimming

3. Results and Conclusion

The comparison of computation time for uniform dexelisation and adaptive dexelisation is shown in Figure 5. The low density region in the adaptive dexelisation case is always set to 0.5 mm. Whereas, the high density region is varied from 15 to 250 μm. On the other hand, for uniform density dexelisation, the whole workpiece is dexelised with the same density. The GPU memory imposed a limit in dexel resolution, at 15 μm uniform density case utilised the whole 8 GB of GPU.

It is seen that at the highest resolution a 5 times simulation time improvement is achieved. The calculation cost is compared based on Step 2 and 3, because adaptive dexelisation (Step 1, pre-process) is a one-time operation and it is not the part of process-parallel geometry estimation during the milling process.
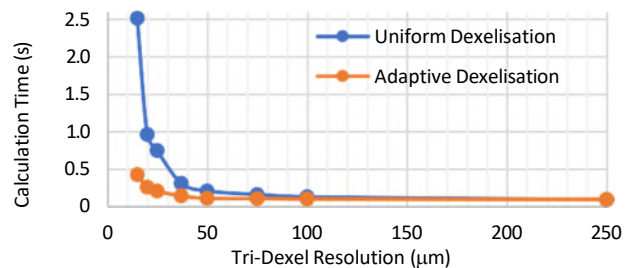
Figure 5. Comparison of uniformly and adaptively WP calculation

As a conclusion, adaptive dexelisation provides a potential use with GPU parallelized dexelisation. Since part geometry features can be read from PMI data of the CAD by using some standardized formats like QIF or STEP 242, these standardised formats allow the user to reach features of the CAD data with their IDs in .xml format. Therefore, finding these regions by using standardized formats for adaptive dexelisation is the potential future study.

References

[1] Frenz W 2022 *Handbook Industry 4.0: Law, Technology, Society*. Springer Nature

[2] Requicha AAG, Rossignac JR 1992 Solid Modeling and Beyond *IEEE Comput Graph Appl* **12**, no. 5,

[3] Benouamer MO,Michelucci D 1997 Bridging the gap between CSG and Brep via a triple ray representation *Proceedings of the Symposium on Solid Modeling and Applications*, pp. 68–79

[4] Miers JC, Tucker T,Kurfess T,Saldana C 2021 Voxel-based modeling of transient material removal in machining *International Journal of Advanced Manufacturing Technology* **116**, no. 5–6, pp. 1575–1589

[5] Altintas Y, Kersting P, Biermann D, Budak E, Denkena B, Lazoglu I, 2014,Virtual process systems for part machining operations *CIRP Ann Manuf Technol* **63**, no. 2

[6] Lee SW,Nestler A 2012 Virtual workpiece: Workpiece representation for material removal process *International Journal of Advanced Manufacturing Technology* **58**, no. 5–8, pp. 443–463

[7] Abecassis F, Lavernhe S, Tournier C, Boucard PA 2015 Performance evaluation of CUDA programming for 5-axis machining multi-scale simulation *Comput Ind* **71**

Data-driven modeling for the correlation of the inputs and outputs in thermoplastic micro injection molding

Alireza Mollaei Ardestani[1]*, Reza Asadi[2], Uma Maheshwaran Radhakrishnan[1], Inigo Flores Ituarte[2], Murat Kulahci[3], Matteo Calaon[1], Jesper Henri Hatel[1], Guido Tosello[1]

[1]Department of Civil and Mechanical Engineering, Technical University of Denmark, 2800 Kgs. Lyngby, Denmark; almoa@dtu.dk ; guto@dtu.dk
[2]Faculty of Engineering and Natural Sciences, Tampere University, Korkeakoulunkatu 6, 33014, Tampere, Finland
[3]Department of Applied Mathematics and Computer Science, Technical University of Denmark, 2800 Kgs. Lyngby, Denmark

* Corresponding author: almoa@dtu.dk

Abstract

This paper explores the application of micro manufacturing in the production of plastic parts, focusing on the widely used injection molding process. The increasing demand for high-quality parts in industrial settings has led to a heightened need for digital twins in micro injection molding. To address this demand, a Data-Driven approach is employed, involving the simulation of process parameters effects in plastic injection molding. The project employs the Design of Experiment (DOE) methodology for a specific geometry, varying three key input process parameters—Melt Temperature, Mold Temperature, and Injection Speed—across different material grades. Responses such as Part Weight, Cavity Injection Time, and Maximum Injection Pressure are simulated using a commercially available Finite Element Analysis (FEA) Simulation software. Data Driven Modelling is achieved by incorporating viscosity and pvT coefficients of each material, along with the specified process parameters. Statistical Analysis, Machine Learning, and Deep Learning methods are employed for the data driven modeling. The results indicate that Part Weight and Maximum Injection Pressure are influenced by all three input parameters, while Cavity Injection Time is primarily affected by the Injection Speed of the machine. Both Statistical and artificial intelligence models demonstrate effective performance with the selected materials. Importantly, these models successfully predict results for materials not initially considered, affirming the achievement of Data Driven Modelling for the specific geometry under investigation.

Keywords: plastic injection molding; design of experiments; machine learning; digital twin; process optimization

1. Introduction

In the modern engineering world, the widespread adoption of algorithms has lead to a transformative era by eliminating additional costs associated with time-consuming and expensive tests in the product design and production development cycle. Contemporary modeling, prediction, and optimization methods have markedly diminished the reliance on traditional experimental trials and measurements for enhancing both product and process. This spectrum of techniques including statistical methods (such as ANOVA), machine learning methods (including artificial neural networks – ANNs), and optimization methods utilizing meta-heuristic algorithms.

In the present context, the integration of Finite Element Analysis (FEA) methods with modern optimization approaches has proven to be effective for manufacturers in identifying optimal levels of input parameters, leading to the production of products of the highest quality. Given the intricate behavior of polymers, especially during injection molding processes, the multitude of parameters influencing product quality underscores the importance of monitoring and controlling each parameter and their interactions. This becomes imperative in the prevention of injection defects.

Many studies have been conducted till now focusing on the application of data analysis in plastic injection molding process. They have used experimental tests and statistical analysis to rank the significance of some process parameters on the quality measures of the product [1,2]. In some other studies, researchers used ML-based techniques on experimental data to create a prediction model for an injection process [3,4,5]. Silva et al. [6] introduced an intelligent method to classify the quality of products. For this purpose, they employed artificial neural networks (ANNs) and support vector machines (SVMs) and a combination of the two methods. The trained models showed a good capability to predict the defects and classify them by type.

Deep Neural Networks (DNNs) are preferred over traditional Artificial Neural Networks (ANNs) due to their increased depth, signifying the presence of multiple hidden layers. This depth allows DNNs to automatically learn hierarchical representations of features, making them highly effective in handling complex tasks such as image processing [7] and other intricate problem domains. The added depth enables DNNs to capture and understand intricate patterns in injection molding data, leading to superior performance compared to shallower networks with fewer layers.

2. Materials and methods

The part under study has a dogbone-shaped geometry with the dimensions of 12×3×1 mm. the total volume of the part is 76.4 mm^3, and the surface of the part is 241.2 mm^2. The mould has 2 cavities (see Figure 1). For this study, 36 different grades of different classes of thermoplastic polymers (both amorphous and semi-crystalline) have been chosen. The list includes ABS (Terluran EGP-7, Novodur E211, ALCOM AWL 10WT 1308-05 LB,

Terluran 2802 TR, Terluran GP 22, Sinkral F332), COPE (Tritan MX731, Eastar DN011), HDPE (Dowlex IP60), PA6 (Ultrmid B3K), PA12 (Grilamid L20L), PC (Iupilon S-2000), PES (Ultrason E2010G6), PET (Petro 140), PMMA (95UX-BK 13, Altuglas drm), POM (Ultraform N2640 E2, Ultraform N2320 003, Ultraform S2320 003), PP (80CM-NC 601, ALCOM PP 6201 WT 0134-05LB, Exxon Mobil PP1013H1), PS (Polystyrol 456M), SAN (Kostil B266), PLA (Natureworks 7000D), PEEK (RTP 2205HF), PBT (Ultradur B4500), PVC (Polyvin 6620), LDPE (Lacqtene 1003 FL 22), PPO (Noryl 731), PPSU (Ultrason P 3010), PEI (Ultem 1000), PSU (Ultrason S 2010), PPS (Fortron 1131L4), LCP (Vectra A430), and PAI (Torlon 5030). In the beginning, the CAD geometry of the part was created. Then the model was transferred to the FEA software, Moldex 3D.
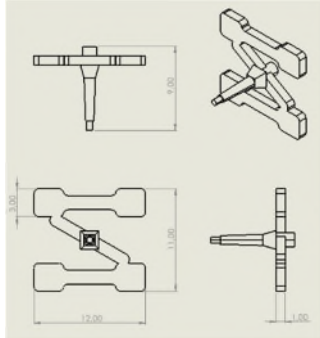
Figure 1. Micro part geometry and dimensions including miniaturized sprue, runners, and gates.

A 3D mesh with the seeding size of 0.2 mm was employed which created 12061 elements on the part. Then, for some materials, a 2-level (with the levels of -1 and +1) and for some others, a 3-level full factorial DOE (with the levels of -1, 0, +1) was employed for the 3 input factors. So, in total, 8 and 27 experiments were designed respectively. The amounts for each input variable (melt temperature, mold temperature, and injection speed) were normalized so that process parameters variations could be computed evenly across all DOEs for all the materials grades. After setting all the experiments in the FEA software, the results (part weight, cavity injection time, maximum injection pressure) were simulated and collected.

Studying and optimizing various parameters in the injection molding process is possible but time-consuming and expensive. To reduce defects, focusing on key parameters such as melt temperature, mold temperature, and injection speed is crucial. The objectives of this study considered to be the part weight, maximum injection pressure, and cavity injection time. Correlating controllable input parameters (melt temperature, mold temperature, injection speed) with output parameters (part weight, cavity injection time, maximum injection pressure) helps in implementing Data Driven Modelling in injection molding.

Every thermoplastic has specific coefficients which represent the materials properties in their respective material models. These coefficients remain constant for every selected material grade, resulting in 36 recorded levels for the corresponding 36 material grades. In this study, viscosity and pvT model coefficients of the materials are extracted from the Moldex3D material database. The list of coefficients can be seen in Table 1. After performing the simulations based on the DOE plan, all the simulated results were collected. Then, Analysis of Variance was applied on the results to provide main effect diagrams of the variables on the results. Finally, a Deep Learning (DL) algorithm was trained based on the input data to allow predictions of the process results.

Table 1 List of coefficients.

Viscosity coefficients		pvT coefficients	
Cross model 2	Cross model 3		
n	n	b1L [cc/g]	b1S [cc/g]
τ* [dyne/cm³]	τ* [dyne/cm³]	b2L [cc/g.K]	b2S [cc/g.K]
B [g/cm.sec]	D1 [g/cm.sec]	b3L [dyne/cm²]	b3S [dyne/cm²]
Tb [K]	D2 [K]	b4L[1/K]	b4S [1/K]
D [cm²/dyne]	D3[cm²/dyne]	b5 [K]	b6 [cm'².K/dyne]
	A1	b7 [cc/g]	b8 [1/K]
	A2b[K]	b9 [cm^2/dyne]	

In this study, two DNNs for the considered material types are provided. Figure 2 illustrates the schematic view of the proposed networks. The DNNs contain 6 hidden layers, which are fully connected to the previous and next layers without any dropout layers. For cross model (2) and cross model (3), 4 and 7 parameters are considered as viscosity parameters respectively and 13 parameters as PVT parameters. Three parameters are considered as uncontrollable parameters. In Table 2, the optimal parameters of the proposed DNN's can be observed.
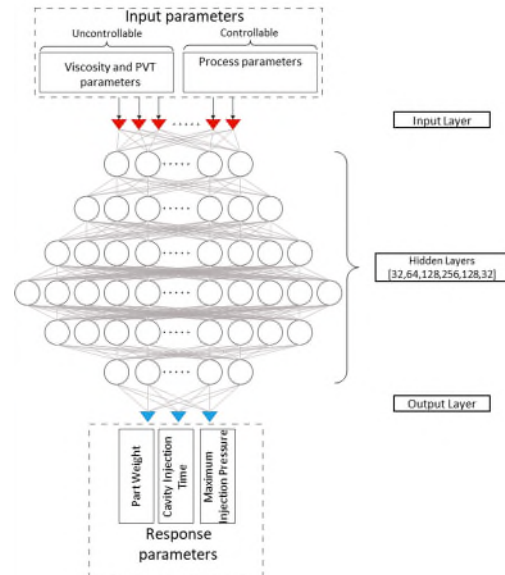
Figure 2. The DNNs architecture considered for the study.

Table 2 DNNs characteristics for Cross model 2 and 3 materials

	Cross model 2	Cross model 3
Number of hidden layers	6	6
Number of neurons in each layer	[32,64,128,256,128, 32]	[32,64,128,256,128, 32]
Loss function	Mean Square Error (MSE) loss	Mean Square Error (MSE) loss
Optimizer	AdamW	AdamW
Activation function of each layer	[GELU, GELU, GELU, GELU, GELU, LeakyReLU]	[ReLU6, ReLU6, ReLU6, ReLU6, ReLU6, LeakyReLU]
Starting learning rate	0.0005	0.0003
Training and validation instances	232	332

3. Results

The results of simulations were analyzed using the ANOVA method. The main effect plots for all the outputs and interaction plots for the part weight can be observed in Figure 3.
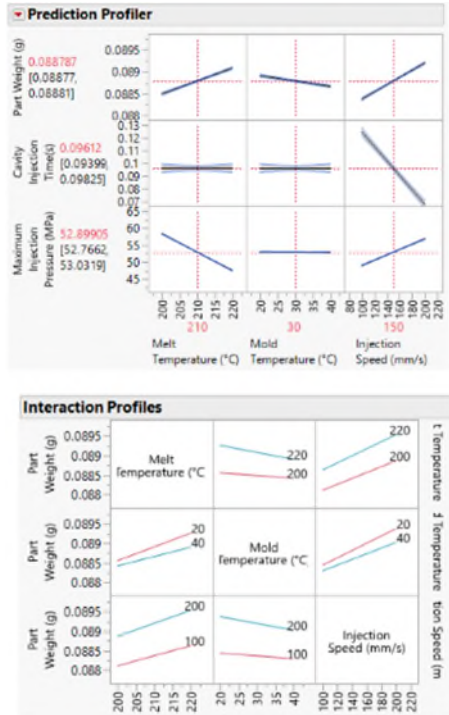
Figure 3. Main effect and interaction plots.

The interaction profiles have also been obtained for the other two output objectives, namely Cavity Injection Time and Maximum Injection Pressure. The main effect summary and the interaction effect summary of the part weight can be seen in the Figure 4. The same responses can also be provided for Cavity injection time and Maximum injection pressure.
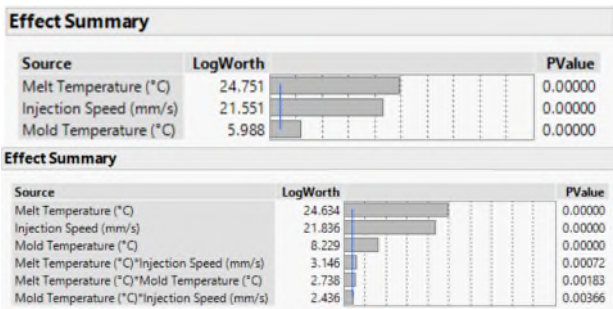
Figure 4. Part weignt main effect and interaction summary

As a result of ANOVA, prediction regression models can be obtained. The general form of these models are as follows:

$M[g]$ = μ+β1 *(A)+β2 *(B)+β3 *(C)+β4 *(A∗B)+β5 *(A∗C)+β6 *(B∗C) (4.1)

$T[s]$ = μ+β1 *(A)+β2 *(B)+β3 *(C)+β4 *(A∗B)+β5 *(A∗C)+β6 *(B∗C) (4.2)

$P[MPa]$ = μ+β1∗(A)+β2∗(B)+β3∗(C)+β4∗(A∗B)+β5∗(A∗C)+β6∗(B∗C) (4.3)

The terms of M, T, and P are representing Part weight, Cavity injection time, and Maximum injection pressure, respectively.

The factors are interpreted as:

- A - Melt Temperature
- B - Mold Temperature
- C - Injection Speed

- AB - Melt and Mold Temperature Interaction
- AC - Melt Temperature and Injection speed Interaction
- BC - Mold Temperature and Injection speed Interaction

β1, β2, β3, β4, β5, β6 are the coefficients of the above-mentioned factors. In the equations above, μ is the mean of responses. For each material grade, all the coefficients were extracted. Since 36 materials were chosen to be investigated, 108 equations to predict the 3 outputs for each material have been extracted. The prediction results of each model are shown in Figure 7.

3.1 DNN model

In Figure 6., the training and validation outcomes of the suggested DNNs for Cross Model (2) and Cross Model (3) are depicted. The red-highlighted area signifies the occurrence of overtraining, prompting the cessation of the training process and the preservation and utilization of optimal coefficients at that point.

Table 3 provides an assessment of the performance of the trained DNNs concerning the loss functions or MSE, and RMSE. Notably, the MSE and RMSE values for Cross Model (2) exhibit a lower magnitude compared to Cross Model (3) across both training and validation datasets. However, it is noteworthy that both sets of values, specifically less than 0.0055 for MSE and 0.075 for RMSE, fall within a range deemed acceptable in the context of the given analysis.
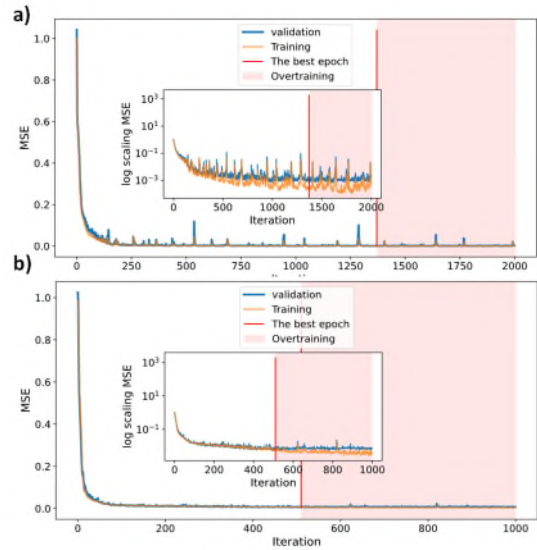
Figure 5. Training and validation loss plots of the modeling performance of a) Cross Model (2) and b) Cross Model (3), including optimal validation epochs and overtraining ranges.

Table 3. Training and validation MSE/RMSE for Cross Model (2) and Cross Model (3)

Model	Training		Validation	
	MSE	**RMSE**	**MSE**	**RMSE**
Cross model (2)	0.00024	0.01547	0.00060	0.02441
Cross model (3)	0.00518	0.07199	0.00538	0.07334

Following the completion of training and validation phases, the testing process is essential. The recommended method involves plotting the fit line between model output (predicted values) and target values (ground truth data). Figure 6 illustrates the fit line alongside the line y=x, depicting optimal results with an R² value of 1. Notably, the fitted lines for all process

responses exhibit R² values exceeding 0.96, with slope values within the range of 0.965 and 1.093, and intercepts below 0.186. These results affirm the efficacy of the training and validation processes, showcasing the model's accuracy in predicting outcomes.
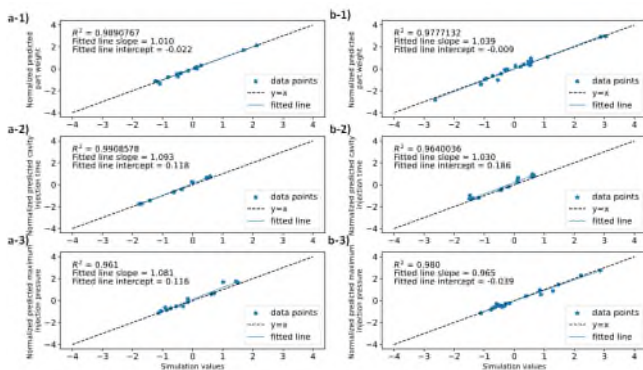
Figure 6. Testing fit lines of DNN models for 1) normalized part weight, 2) normalized cavity injection time, and 3) normalized maximum injection pressure, alongside their comparison with the identity line y=x

In the final analysis, Figure 7 offers a comprehensive comparison between the ground truth values and the predicted values generated by DNNs for Cross Model (2) and Cross Model (3) and predictions made by RSM. Notably, with only minor discrepancies observed in a few instances, where testing data exhibits trivial differences from the ground truth, the networks consistently demonstrate accurate predictions of the trends and values associated with the proposed response parameters.
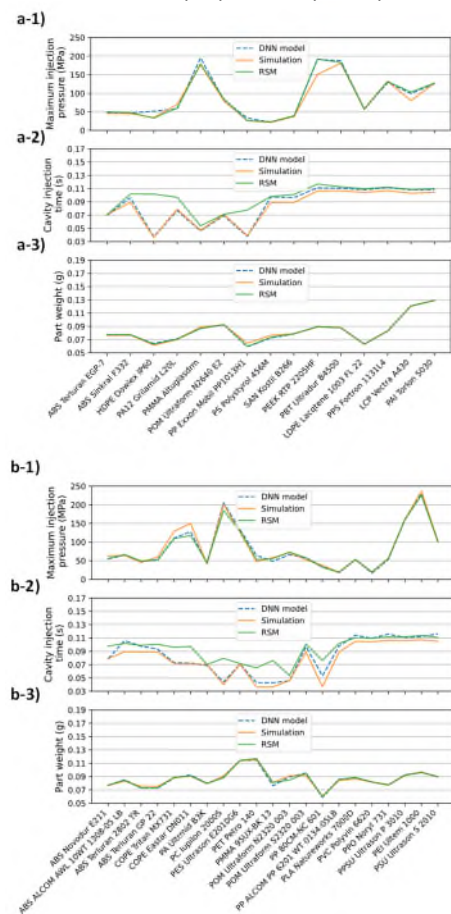
Figure 7. Comparative analysis of ground truth and predicted values by trained DNNs for a) Cross Model (2) and b) Cross Model (3), utilizing testing data alongside predictions made by RSM.

4. Conclusion

This study focused on the investigation of the effect of melt temperature, mold temperature, and injection speed on 3 part quality factors (part weight, maximum injection pressure, injection time). 36 different thermoplastic materials were studied. After performing full factorial DOEs with all materials, two types of models were assembled (based on the materials' specifications). Then, FEA was conducted, and the results were measured. Then a prediction model for each of the outputs of the process for all the 36 materials were extracted (108 in total). To investigate if we can reach higher accuracy prediction models rather than RSM models, a DNN was optimized and trained for each model. At the end, the results of RSM models' predictions were compared to those of the DNN models.

It was observed that the DNN model can predict the results with much higher accuracy compared to RSM model. The prediction accuracy of DNN for part weight, cavity injection time, and maximum injection pressure is 98.9%, 99.1%, and 96.1% for cross model 2 and 97.8%, 96.4%, and 98.0% for cross model 3.

References

[1] Li, Y., Chen, J. C., & Ali, W. M. (2021). Process optimization and in-mold sensing enabled dimensional prediction for high precision injection molding. Int. J. on Interactive Design and Manufacturing (IJIDeM), 1-17.
[2] Asadi, R., Niknam, S. A., Anahid, M. J., Ituarte, I. F. (2023). The use of wavelet transform to evaluate the sensitivity of acoustic emission signals attributes to variation of cutting parameters in milling aluminum alloys. Int. J. of Advanced Manufacturing Technology, 126(7-8), 3039-3052.
[3] Mollaei Ardestani, A., Azamirad, G., Shokrollahi, Y., Calaon, M., Hattel, J. H., Kulahci, M., Tosello, G. (2023). Application of Machine Learning for Prediction and Process Optimization—Case Study of Blush Defect in Plastic Injection Molding. Applied Sciences, 13(4), 2617.
[4] Chen, J. C., Guo, G., & Wang, W. N. (2020). Artificial neural network-based online defect detection system with in-mold temperature and pressure sensors for high precision injection molding. International Journal of Advanced Manufacturing Technology, 110, 2023-2033.
[5] Asadi, R., Queguineur, A., Ylä-Autio, A., Martikkala, A., Wiikinkoski, O., Mokhtarian, H., Ituarte, I. F. (2023, December). Using artificial neural networks to model single bead geometries processed by laser-wire direct energy deposition. In IOP Conference Series: Materials Science and Engineering (Vol. 1296, No. 1, p. 012005). IOP Publishing.
[6] Silva, B., Sousa, J., & Alenya, G. (2021, December). Machine learning methods for quality prediction in thermoplastics injection molding. 2021 IEEE Int. Conf. on Electrical, Computer and Energy Tech., pp. 1-6.
[7] Asadi, R., Queguineur, A., Wiikinkoski, O., Mokhtarian, H., Aihkisalo, T., Revuelta, A., Ituarte, I. F. (2024). Process monitoring by deep neural networks in directed energy deposition: CNN-based detection, segmentation, and statistical analysis of melt pools. Robotics and Computer-Integrated Manufacturing, 87, 102710.

In-process point cloud generation and predictive correction in Selective Thermal Electrophotographic Process

Shuo Shan[1], Hans Nørgaard Hansen[1], Yang Zhang[1], Matteo Calaon[1]

[1]Department of Civil and Mechanical Engineering, Technical University of Denmark, Building 427A, Produktionstorvet, 2800 Kgs. Lyngby, Denmark

sshan@dtu.dk

Abstract

As a novel additive manufacturing technology, Selective Thermal Electrophotographic Process (STEP) draws inspiration from widely used electrophotographic printing techniques, creating possibilities for large-scale additive manufacturing. To obtain real-time dimensional information during manufacturing, this paper proposes a methodology to acquire the in-process point cloud of the printed object by stacking height information from layered scanning. By inferring point-wise deformation vectors and applying corrections to the in-process point cloud, the corrected point cloud is obtained that accurately reflects the shape of the object after cooling, with up to 0.204 mm difference of average length.

Process monitoring, Metrology, Additive manufacturing, Dimensional prediction

1. Introduction

Selective Thermal Electrophotographic Process (STEP) employs the established 2D printing process at a large scale to construct 3D components, bonding layers combining application of heat and pressure [1]. Due to the complex temperature gradients variations and material state changes involved in the STEP printing [2], the possibility to have effective in-process would affect process accuracy and part quality. Figure 1 shows the STEP process and the laser profiler in the printer. For each layer printed, the building plate undergoes one reciprocal motion, which is utilized by the laser profiler to scan the surface and stich the linear profiles into a heightmap [3].
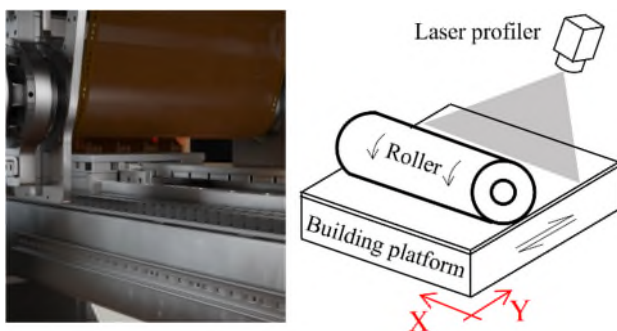
Figure 1. Selective Thermal Electrophotographic Process.

Due to the cooling deformation at room temperature after printing completion, the in-process dimensional information obtained by the laser profiler cannot accurately reflect the final dimensions of the printed components. In this study, the height maps obtained through layer-by-layer scanning are processed and stacked to generate an in-process point cloud synchronized with the printing process. Through a specially designed neural network which is trained to infer the deformation vector on each point, the point cloud corresponding to the cooled state is derieved to describe the expected shape after deformation.

2. Methodology

2.1. In-process point cloud generation by stack of height maps

A matrix consisting of cubes measuring 25 mm × 25 mm × 7.5 mm is printed, and layerwise heightmaps of single cubes are obtained through laser profiler during the printing process.
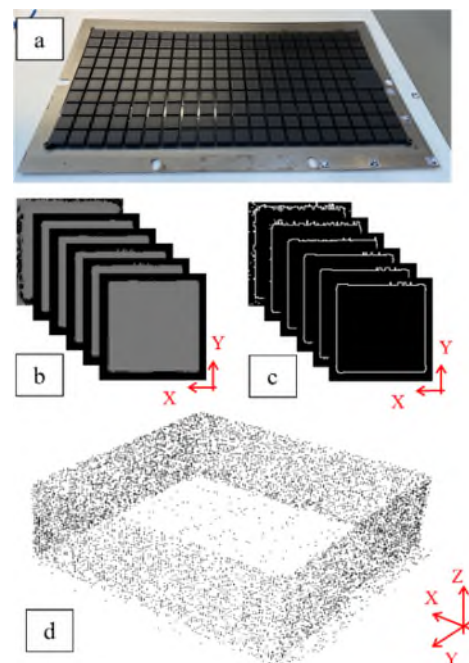
Figure 2. In-process point cloud generation. a. cube matrix; b. example of heightmaps of a cube during printing; c. edges of height maps; d. generated in-process point cloud.

Figure 2 shows the generation of in-process point cloud., The heightmap generated by laser profiler each printed layer undergoes edge detection, where only the outermost pixels are retained and converted from their positions in the image to X

and Y coordinates. The Z coordinates of the pixels are determined based on the current layer of the print and the thickness of each layer. The heightmap of the final layer is not subjected to edge processing but is directly transformed into 3D points overlaid at the top. The purpose of this is to obtain a shell-shaped point cloud that describes the outer contour of the printed object.

2.2. Correction by inferences of cooling deformation

Scanning the object after cooling deformation yields the target point cloud. By comparing the in-process point cloud with the target point cloud, a dataset of deformation vectors is obtained. Specifically, both the target and in-process point clouds are downsampled, with the number of points in the target point cloud significantly exceeding that in the in-process point cloud. In this study, the target point cloud is downsampled to 10,000 points while the in-process point cloud is downsampled to 500 points. For each point in the in-process point cloud, the nearest point is searched in the target point cloud, creating point pairs. This process results in a dataset of vectors pointing from points in the in-process point cloud to corresponding points in the target point cloud, with a total of 500 pairs.
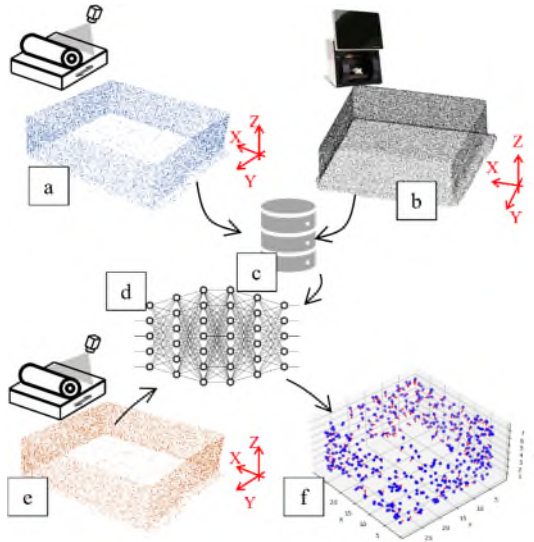
Figure 3. Correction on in-process point cloud. a. in-process point cloud for dataset; b. point cloud of objects after colling deformation; c. deformation vector dataset; d. neural network for deformation vector inference; e. in-process point cloud; f. derieved deformation vector.

As shown in Figure 3, the deformation vector dataset is then employed to train a neural network which infers deformation vectors for each point in the input point cloud. The collection of points at the ends of all deformation vectors forms a set, constituting the corrected point cloud, which describes the shape of the printed object after cooling deformation.

3. Results and analysis

To verify whether the correction on point cloud, dimensions are mearsured on both generated point cloud and the real object.
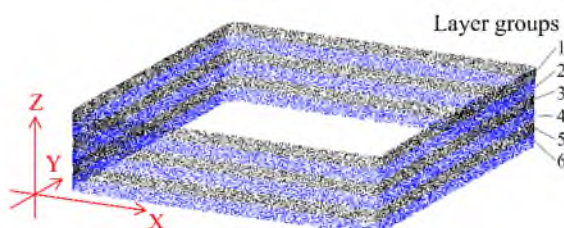
Figure 4. Slices and layer groups to measure.

As shown in Figure 4, point clouds are sliced into 6 layer groups from top to bottom so that dimensions can be obtained at different positions. Figure 5, indacates the comparison of the generated point cloud and the real ones. It can be observed that the dimensions of the point cloud, after correction, align more closely with the actual dimensions.
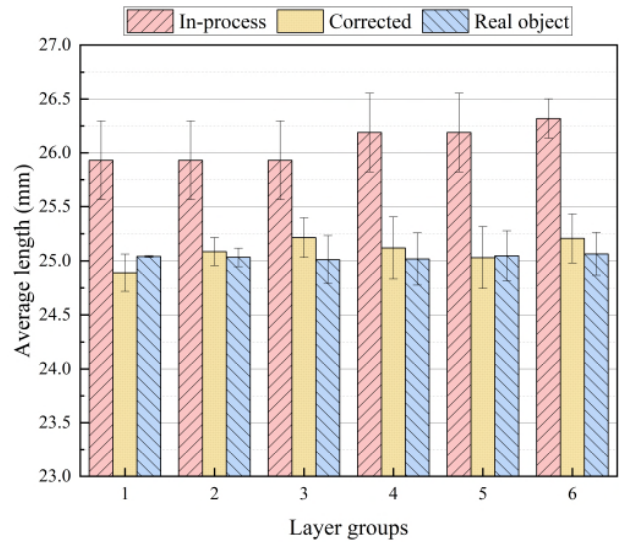
Figure 5. Comparison of dimensions in in-process generated point cloud, corrected point cloud and real object measurement .

Table 1 shows the difference on average lengths between the real objects and corrected point clouds. Despite inconsistency in different layers groups, the maximum difference in the corrected point cloud is up to 0.204mm.

Table 1 Difference on lengths between corrected point cloud and real object, where $\Delta = \overline{L}_{real} - \overline{L}_{corrected}$.

Layer groups	1	2	3	4	5	6
Δ (mm)	0.150	0.052	0.204	0.102	0.016	0.143

4. Conclusion and future works

In this paper we propose a novel in-process poing cloud generation approach in STEP. Laser line profiler is employed to perceive the height maps layer by layer during the process, which are then post-processed and accumulated into point cloud. A neural network is trained to infer the deformation caused by cooling. After the correction the point cloud can faithfully describe the object with maximum 0.204 mm difference on average length. This approach provides real-time measurements as well as final cooling deformation predictions for the STEP process.

References

[1] Yeh HP, Rotari M, Shan S, Meinert KÆ, Hattel JH, Kulahci M et al. Thermo-mechanical model for a selective thermoplastic electrophotographic process for dimensional defects. euspen. 2023. p. 187-188

[2] Yeh HP, Meinert K, Bayat M, Hattel JH. Part-scale thermal modelling of the transfusion step in the selective thermoplastic electrophotographic process. International Journal of Advanced Manufacturing Technology. 2024. doi: 10.1007/s00170-023-12300-5

[3] Shan S, Yeh HP, Rotari M, Meinert KÆ, Hattel JH, Pedersen DB et al. In-process monitoring of selective thermoplastic electrophotographic process by laser profiling system and digital fingerprint. euspen. 2023. p. 181-182

Session 2: Metrology

Mechanical engineering challenges at European XFEL

Daniele La Civita[1], Massimiliano Di Felice[1], Bertram Friedrich[1], Nicole Kohlstrunk[1], Marc Planas[1], Harald Sinn[1], Maurizio, Vannoni[1], Mark Wünschel[1], Fan Yang[1]

[1]European XFEL GmbH, Holzkoppel 4, 22869 Schenefeld, Germany

daniele.lacivita@xfel.eu

Abstract

Research facilities like European XFEL, located in Hamburg, Germany, are innovative hard X-ray photon sources that allow the exploration of previously inaccessible research areas. With the help of the 3.4 kilometre-long, underground machine, the scientists map the atomic details of viruses, decipher the molecular composition of cells, take three-dimensional images of the nanoworld, film chemical reactions, and study processes such as those occurring deep inside planets.

To deliver the X-rays to the experimental stations, the photon beam has to be manipulated by optical elements that have to preserve the unique properties of the photon beam. The optical elements are mounted in Ultra High Vacuum (<10^{-8} mbar) environment, have to be aligned and adjusted with high resolution (below 100 nm) and repeatability. The photon distribution system is 1 km long and the optical element have to drive the photons to the experimental targets with sub-micrometre accuracy. Therefore, mechanical stability and minimization of vibrations are paramount. A small part of the photon beam is absorbed by the optical elements and to avoid thermal drifts and minimize deformation of the perfect optical surface, cooling solutions based on eutectics are implemented. This contribution gives an overview of challenges and solutions for UHV compatible, high precision mechanics that support and remote control cooled optical elements for X-ray transport.

FEL, Synchrotron, SASE, Precision Mechanics, UHV, X-ray

1. Introduction

European XFEL is an X-ray Free Electron Laser research facility located in Hamburg, Germany and operational since 2017 [1,2]. The European XFEL is being realized as a joint effort by 11 European countries: Denmark, France, Germany, Hungary, Italy, Poland, Russia, Slovakia, Spain, Sweden and Switzerland. Since 2018 United Kingdom is also part of the European XFEL Convention.

The Free Electron Lasers produce coherent and intense laser-like radiation by accelerating a beam of electron bunches to relativistic speeds then passing it through a long periodic magnetic structure. As the electrons move through this magnetic field, they undergo periodic oscillations, emitting radiation in the process. Repeated interactions with the electron bunches amplify the emitted radiation, resulting in a high-powered and tuneable laser beam.

The facility is an international scientific infrastructure that generates extremely brilliant, ultrashort pulses of spatially coherent X-rays with wavelength that spans from 300 eV to 25 keV [3]. The high brilliance is enabled by the implementation of superconducting technology in the electron accelerator, while the high degree of coherence and the femtosecond pulses are the result of the self-amplified spontaneous emission (SASE) process that generates the photon beam.

Innovative and cutting-edge scientific experiments in a variety of disciplines spanning physics, chemistry, materials science and biology make use of the peculiar properties of the radiation, in particular in the investigation of ultrafast processes in atoms, ions, simple and very complex molecules, clusters or condensed matter. The high pulse energies allow the collection of meaningful data sets from single pulses, thereby enabling the study of non-reversible processes. Coherence properties are

exploited in imaging techniques that aim to obtain atomic spatial resolution for weakly scattering systems. Finally, the very high X-ray pulse energies in combination with ultrashort pulses produces very high peak powers of up to several tens of GW and this enables the exploration of excited solids through non-linear X-ray scattering [4].

Besides the European XFEL in Germany, Free Electron Laser light sources able to produce hard X-rays also exist in Japan at SACLA [5], South Korea at PAL-XFEL [6], Switzerland at SwissFEL [7], and in the USA at LCLS-II [8]. In China, SHINE is under construction and is foreseen to become operational in 2025 [9]. Table 1 provides an overview and comparison of the main key parameters of the above-mentioned hard X-ray facilities.

In this contribution, following a description of the overall European XFEL facility, the main aspects, requirements, and implemented solutions for the mechanical design of photon devices are discussed. Finally, an outlook about possible future development directions and area of interest for this specific field of application is provided.

2. Layout of the European XFEL facility

The European XFEL facility consists principally of three sections: the superconducting accelerator, the electron and photon transport sections and the experimental hall. The Figure 1 provides an overview of the European XFEL facility.

The general layout of the facility is defined by three main conditions. In order to achieve high photon energy (in the order of 25 keV) and high pulse energy the electrons have to be accelerated up to 17.5 GeV. The average acceleration gradient of the implemented superconducting cavities is 20-25 MeV/m. Therefore, the total length of the acceleration section has to be in the order of 1 000 m.

Table 1 Comparison of main parameters and key figures of hard X-ray FEL facilities worldwide.

	European XFEL	LCLS-II	SACLA	SwissFEL	PAL-XFEL	SHINE
Start of commissioning	2016	2023	2011	2016	2016	2025
Accelerator technology	Super-conducting	Super-conducting	Normal-conducting	Normal-conducting	Normal-conducting	Super-conducting
Total facility length [km]	3.4	3	0.75	0.74	1.1	3.1
Maximum electron energy [GeV]	17.5	5	8.5	5.8	10	8
Maximum pulses per second	27 000	1 000 000	60	100	60	1 000 000
Minimum wavelength [nm]	0.05	0.25	0.08	0.1	0.06	0.05
Number of undulator lines	3	2	3	1	2	3
Number of experimental stations	7	10	4	3	3	10
Peak brilliance [photons/s/mm^2/mrad^2/0.1%BW]	5×10^{33}	2×10^{33}	1×10^{33}	1×10^{33}	1.3×10^{33}	1×10^{33}

The high collimated radiation produced at the end of the undulator sections, to be easily transported and manipulated by the optical systems, and stopped by the photon shutters, has to be of the size of 1 mm. The divergence of the high photon energy beam is in the order of 1 µrad and therefore the total length of the photon distribution system is about 1 000 m. The last condition is about the lateral separation of the experimental stations at the end of the tunnels that is linked to the maximum deflection angle of the electron beam. To achieve a separation of about 17 m among the beamlines, the photon transport system has to span over 1 000 m. Those conditions together with construction, installation, and possible future upgrade conditions bring the total length of the facility, from gun to experimental station, to 3.5 km.

The complete facility is constructed underground, about 25 m to 6 m below the surface. Access to tunnels for personnel and for installation and maintenance of components, is enabled by shaft buildings at the start and end of each tunnel section.

The first main element of the facility is the linear accelerator (linac) that is installed in 5.2 m diameter and about 2 000 m long tunnel. The linac accelerates the electrons to a final energy of up to 17.5 GeV by means of 96 accelerator modules operated at 2.2 K. The design of those superconducting modules was developed by an international collaboration for European XFEL based on the TESLA design [10]. Each module is 12 m long, weighs eight tons and comprises eight nine-cell Nb cavities.

The European XFEL accelerator is operated in the so-called burst mode. As depicted in figure 2, the accelerator delivers up to 2 700 electron bunches or pulses in a pulse train that lasts 600 µs. The repetition rate of the bunch trains is 10 Hz. Inside the bunch train the time distance between two consecutive pulses can be 220 ns, giving the possibility to operate at up to 4.5 MHz inside the bunch train. Electron bunches are converted in photon pulses that are going to be manipulated by the optical elements of the beam transport and then used for the experiments. This peculiar pulse structure provides very high power in the single pulse, exceeding 20 GW in the very short single pulse, but a quite mild, in the order of few watts, average power with respect to similar applications in the X-ray optic field.

At the end of the linac, after a collimation section the electrons enters in the FEL undulator sources where the electron bunches generate laser-like radiation at the X-ray wavelength [11, 12].

The electron and X-ray beam transport system is designed to accommodate up to five FEL sources. Each FEL source has a dedicated photon beam transport section to transport, guide, focus, and diagnose the X-ray beams. Distribution mirrors, installed in each FEL source, allow the delivery of the photon beam up the three experiments. the Figure 3 provides an overview of the complete electron and photon transport system.

Presently only three of the five possible FEL sources are installed and they are denoted SASE1, SASE2 and SASE3. SASE1 and SASE2 provide light in the hard X-ray regime from approximately 3 to 25 keV, while SASE3 is the soft X-ray source that spans from 250 eV to 3 keV. The entire electron and photon transport section is about 1 400 m long and the undulators are installed in a tunnel with diameter of 5.3 m while the photon transport tunnels have smaller diameter (4.6 m) because before those sections the electron beam is already separated from the photon beam and stopped on electron dumps. The undulator line consist of a sequence of 5 m long magnetic structures (NdFeB permanent magnet). Undulators are mechanical devices that can change the distance between the magnetic arrays in order to change the intensity of the magnetic field that is seen by the traveling electron beam and therefore tune the wavelength of the produced radiation. SASE1 and SASE2 are equipped with 35 undulators for a total length of 205 m, while SASE3 has 21 segments and a total length of 121 m.

The X-ray photon beam transport system is 1 000 m long and consists of optical systems to steer, slit, focus, attenuate, and monochromatize the photon beam, of diagnostic devices to characterize the photon beam properties and of shutters that can stop the photon beam to allow access in the downstream tunnel sections or experiments [15-17].

The last section is the experiment hall in which the scientific instruments are located and where the research program is run. The experiment hall has a size of 50 m along the beam direction and 90 m across to install five beam line areas.
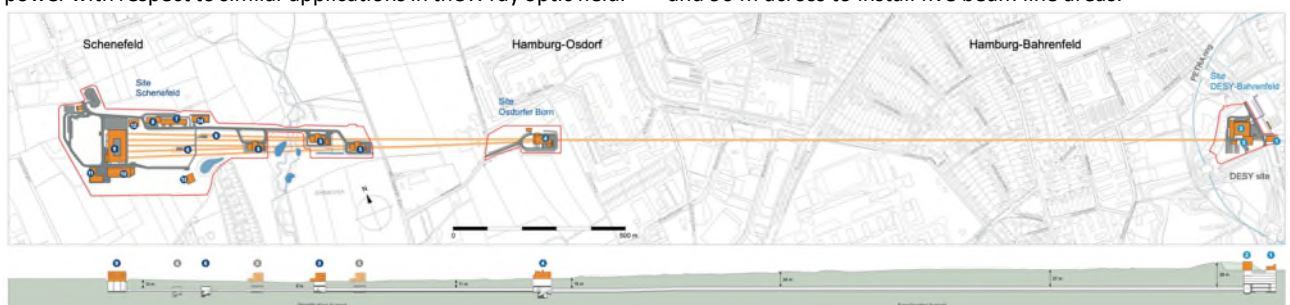
Figure 1. European XFEL facility layout [13].
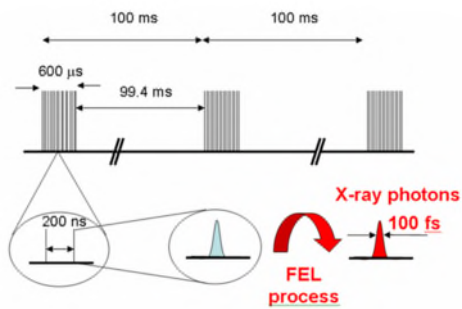
Figure 2. Time structure of the European XFEL accelerator [14].

Presently seven instruments are installed and operational: SPB/SFX and FXE at the end of SASE1, MID and HED at the end of SASE2 and SQS, SCS and SXP in the SASE3 beamline. A new instrument, HXS, located at the end of the SASE2 beamline is currently under design.
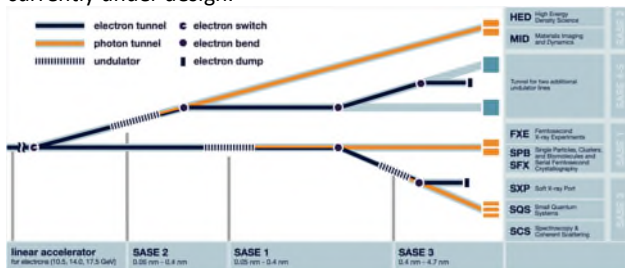
Figure 3. Electron and photon transport layout [13].

3. Challenges in the mechanical design of photon devices

The mechanical devices dedicated to supporting and adjusting the optical elements that manipulate the photon beam present challenging requirement. The complexity of the design comes from the requirement of high ultimate mechanical performance and from the boundary conditions given by the environment where those devices are installed and operated. Finite element analyses are widely used to support the design activity.

3.1. Mechanical requirements

To preserve the outstanding quality of the photon beam, the mirrors that guide and focus the X-rays have a reflecting surface with a maximum error of up to just 2 nm peak-to-valley. The mechanical interfaces have to be carefully designed to preserve the original shape at the nm level. Mirrors are made of single crystal silicon, have the shape of a rectangular parallelepiped and length up to 1 m for a total weight of about 6 kg. Mirror supports are designed as perfectly isostatic supports with three contact points from bottom located at the mirror Bessel points. In the horizontal plane there are three fixed points preloaded by custom designed pushers mounted exactly opposite [18]. In the contact area, the supporting points present spherical shape and are made of soft materials (CuSn6) in order to reduce the Hertzian contact stress. The low roughness (Ra = 0.01), spherical part of the supporting tip minimizes the friction between mirror and support. In this way two goals are achieved: the mirror is free to thermally expand minimizing the possible deformation and also the residual stress due to the mounting is minimized, making the optical metrology and the assembling process reproducible [19]. Special clamping system to transfer moment from motor actuated leaf springs to the mirror itself are designed in the case the mirror has to be bent in order to allow photon beam focusing. The design takes into account the anisotropic properties of the single crystal silicon slab and 17 MPa is considered the safe value for the ultimate tensile strength [20, 21].

The long beamlines and the small beam dimension at the experimental station set the angular stability of the reflective elements to values that are in the order of 0.1 µrad. The need to operate in a quite wide energy range requires adjustments of the optical elements in the 10 mm and 10 mrad range. A lot of effort goes in minimizing the degrees of freedom to the strict operational need and to achieve excellent and predictable mechanical behaviour. The mechanisms need to be, among other things, exactly constrained, free of backlash, extremely stiff and lightweight. Parallel kinematic systems based on flexures can be a viable option to comply to the tight specifications.

Part of the beam energy is absorbed by the optical elements and this generate thermal deformation that has to be minimized. The integrated power to be removed is rather small, in the order of 10 W, with respect to similar application but it is enough to create a thermal bump that spoils the quality of the optical elements. In vacuum and at almost room temperature conditions, the heat transfer is dominated by conduction effects: the mirror has to be connected to a heat sink that consists of a water pipe or an in-air dissipator. Critical is the connection of the cooling system with mirror because any clamping with good thermal conduction deforms the optics. Indium-Gallium eutectic, that is liquid metal at room temperature, is used as medium between mirror and cooling elements: nickel coated copper bars, connected to the heat sink with thermal braids, are immersed in grooves on the mirror that are filled with the eutectic bath.
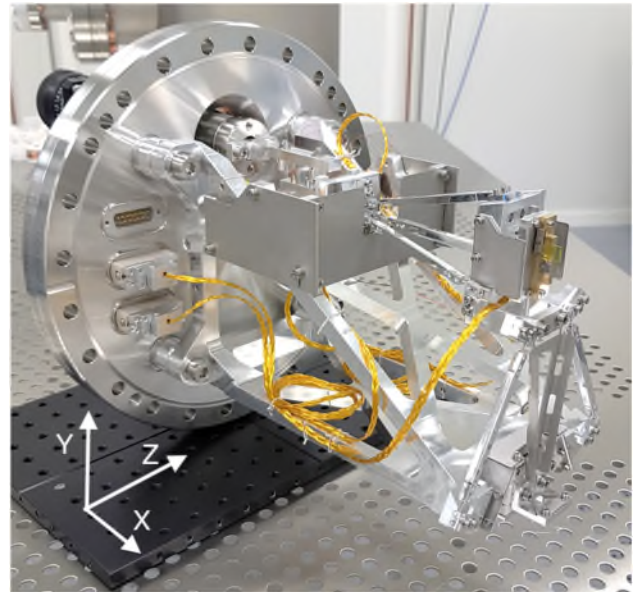
Figure 4. Example of parallel kinematic system for UHV environment.

Figure 4 displays an example of newly developed high-precision mechanics. This system is integral to the XFEL-Oscillator project, which endeavours to establish for the first time ever a laser cavity operating in the hard X-ray regime. The mechanics function to manipulate an HPHT-IIa diamond, used as crystal optics to form the cavity. Table 2 offers a summary of the degrees of freedom and their nominal performance. The motion is driven by piezoelectric positioning stages from SmarAct (SLC-1720 and SLC-2430 models), and the lever arms consist of Ti sheets that have been laser-cut and bent. The design is based on the parallel kinematics concept, realized with flexures made from metallic cables. Short metallic cables were chosen for their favourable ratio between high axial stiffness and limited bending force [22]. Laboratory testing has yielded reliable results to the micrometre level, constrained by environmental limitations. To

verify performance at the nanometre level, commissioning with a photon beam is necessary. This commissioning process is scheduled to commence in spring 2024.

Table 2 Degrees of freedom and nominal performance of the crystal alignment mechanics. Figure 4 shows the cartesian axis convention.

Degree of freedom	Nominal resolution	Travel range
Translation X	1 nm	-8 mm +2 mm
Translation Y	1 nm	± 5 mm
Rotation X	8.3 nrad	± 33.3 mrad
Rotation Y	7.7 nrad	± 30.8 mrad

3.2. Installation and operation environment

The mechanical design has to take into account not only the ultimate performance but also the boundary conditions defined by the environment where the devices operate. The photon tunnels during operation cannot be accessed due to the high level of radiation generated by the traveling X-rays. The devices can be maintained and serviced only every six months. This imposes certain requirements about reliability, durability and remote control of the installed systems. The X-rays travel in an Ultra High Vacuum environment (UHV, $< 10^{-8}$ mbar) and therefore all the elements that interact with the beam have to be compliant to the UHV requirements [23]. The UHV requirements that impact the mechanical design the most are the careful choice of materials and the need to avoid lubricants for motors or linear guides. The design process has to take into account the benefit and the consequences of locating motors and position sensors inside or outside vacuum. To minimize possible optic contamination the cleaning, assembling and installation has to be done in an ISO class 5 or 6, depending of the installation area, particle free environment and this poses additional constraints to the material choices and make the handling and the life cycle of the device more complex. In the case the components are installed in the proximity of the electron beam the additional requirement of low magnetic permeability has to be accomplished [24]. Within 300 mm from the electron beam all the components should have relative magnetic permeability below 1.01 and this requirement restricts further the list of usable material and limits the use of welded solution. The high radiation level environment forces also careful considerations about the implementation of electronic elements in proximity of the electron beam. The main aspects that have to be taken into account are the possible coupling of noise in the reading and the reduced life of components.

3.3. Implementation of numerical computational techniques

Computational techniques, such as finite element analysis (FEA) and computational fluid dynamics (CFD), are widely implemented in various scientific and engineering fields. The main application areas are steady-state and transient thermomechanical simulations of optical elements under photon beam heat load, vibrational analyses, damage simulation due to heat load on solid stopper or gas-based attenuators, optimization of fluid cooling system and characterization of liquid sheet jets for sample delivery system. ANSYS and COMSOL are the commercial software that are used to perform such studies. In the case of thermal simulations that cover a wide temperature range like cryogenic elements or beam stoppers, the thermal properties of materials as function of temperature are a very relevant aspect and they are not easily available in the scientific literature. The material that are subject to the studies are mainly ceramic materials like Boron Carbide (B_4C), diamond, copper, silicon and high quality, low magnetic permeability stainless steels like AISI316LN. The transient analyses are often used to capture the behaviour of the optics under the peculiar

time structure (see figure 2) of the heat load. The complexity of those simulations is given by the different dimensional scale of the elements involved: the timescale of the phenomena is in the in few hundreds of nanoseconds and therefore to satisfy the CFL condition the mesh has to be very small with respect to the beam profile and the area of interest in the optical elements that is in the millimetre scale [25]. Damage simulations allow to predict the damage limit of elements exposed to the beam taking into account a wide number of variables like photon beam size, pulse energy, number of pulses and photon energy that defines the penetration of the beam in the material. Recent developments in damage studies focus on the multiphysics problem of material ablation in the beam stopper [26].

An important topic is the reliability of the simulations and the effort that goes in setting up a systematic verification, validation and uncertainty quantification (VVUQ) process.

4. Outlook and future development direction

There is constant need of further development and innovation in the research facilities in order to enable new experiments. New FEL facilities target beamlines that offer high repletion rate and high pulse energy in a broad photon energy range. The high repletion rate and high pulse energy require more advanced cooling solutions and more careful considerations about the optics and stopper damage. Cryocooling of mirrors is an interesting solution for the thermal issues and it has already been implemented in few installations but for relatively short mirrors. The current understanding of the phenomena involved in the laser cutting technology can help in addressing part of the issues related to the optics damage and therefore a close collaboration with those institutes can be beneficial.

Quality of optics has dramatically improved in the last years and the length of the beamlines is also increased raising the mechanical stability requirements. Active controls together with precision mechanics offer a good prospective to cope with this kind of challenging requirements.

In the field of numerical simulations, the application of artificial intelligence tools and digital twins can improve the understanding of phenomena, reduce significantly the simulation time and support the mechanical design.

References

[1] Decking W et al 2020 *Nat. Photonics* **14**, 391-7
[2] Decking W et al 2017 *Proc of IPAC17 MOXAA1* 1-6
[3] Altarelli M et al 2007 *Rep. DESY 2006-097*
[4] Tschentscher T et al 2017 *Appl. Sci.* **7** 592
[5] Ishikawa T et al 2012 *Nat. Photonics* **6** 540-4
[6] Ko I S et al 2017 *Appl. Sci.* **7** 479
[7] Patterson B D et al 2010 *New J. Phys.* **12**
[8] Galayda J N 2014 *Proc of LINAC 2014*
[9] Liu T 2023 *Front. Phys.* **11**
[10] Brinkmann R et al 2002 *Rep. DESY 2002-167*
[11] Pellegrini C et al 2016 *Rev. Mod. Phys.* **88**
[12] Saldin E 1999 *Springer 1st ed.*
[13] European XFEL online data base: https://media.xfel.eu
[14] Weise H, 2009 *Proc of SRF2009, MOOAAU02*
[15] Sinn H et al 2011 *XFEL.EU TR-2011-002*
[16] Sinn H et al 2012 *XFEL.EU TR-2012-006*
[17] Grünert J 2012 *XFEL.EU TR-2012-003*
[18] Siewert F et al 2012 *Optics Express* **20-4** 4525-36
[19] Schmidtchen S et al 2019 *Proc. SPIE 11109*
[20] Kelez N 2009 et al *Proc of FEL2009 WEPC20*
[21] Hopcroft M 2010 *J. of Microelectromechanical Systems* **19-2**
[22] Noll T 2004 *Doctoral Thesis TU Berlin*
[23] Dommach M 2011 *XFEL.EU TN-2011-001*
[24] Decking W 2010 *DESY int. tech. note*
[25] Dutykh D 2016 *LAMA UMR 5127*
[26] Yang F et al 2021 *Proc of SRI2021*

Mechanical resonance induced measurement uncertainty of ultra-precision on-machine surface measurement system

Maomao Wang, Wenbin Zhong[*], Guoyu Yu, Paul Scott, Xiangqian Jiang, Wenhan Zeng

EPSRC Future Metrology Hub, Centre for Precision Technologies, University of Huddersfield, Huddersfield, HD1 3DH, UK

Corresponding author: W.Zhong@hud.ac.uk

Abstract

Mechanical vibration is an inevitable factor for on-machine surface measurement (OMSM), and it can significantly impact the measurement results, particularly when measuring high-sag surfaces. A great number of OMSM system has been reported in recent decades, however, the contribution of the mechanical resonance on the measurement result has never been revealed. This paper investigates the source of measurement uncertainty arising from mechanical resonance errors in the OMSM system. The system dynamic model of the whole measurement platform is modelled by an equivalent two degree of freedom (2-DOF) oscillating system. The frequency response property of on-machine measurement device fixture is evaluated experimentally by hammer excitation test. A case study on evaluation of large off axis spherical (OAS) with 380 mm diameter aperture is performed. Resonance condition is identified by a joint time-frequency analysis on the slide acceleration and the chromatic sensor displacement. A net-zero-force criteria is applied to locate the moments resonance happens. The on-machine measurement result indicates that time-variant force fluctuation of the precise slide is the major excitation source for the integrated measurement device. It shows that the disturbance induced by system resonance can reach up to 300 nm, which is 100 times greater than the ground truth amplitude in a quasi-static measurement. This research provides a potential solution for evaluating the real-world performance of optical measurement devices integrated with manufacturing equipment.

Keywords: In-process measurement, ultra-precision, uncertainty, vibration

1. Introduction

Integrating surface metrology devices with machining equipment is becoming highly focused in recent decades, as it helps to improve the metrology efficiency and machining quality of components [1]. Integrating a point measurement sensor on the axes of the lathe forming a coordinate measurement machine (CMM) is one of the most feasible solutions for ultra precision surface measurement [2]. It is crucial to perform careful alignment and calibration to get a reliable measurement result.

Attentions have been paid to mitigate the static errors, including axis kinematic errors [3], beam deviation induced errors [4], and temperature fluctuation induced errors [5]. Alignment between the point measurement sensor and the target surface is usually guaranteed by fine adjustment mechanisms [6]. Existing works regard mechanical vibration as a random noise introduced to the system [5]. However, the dynamic interaction between the platform and the integrated measurement device has seldomly been revealed.

In this paper, a system dynamics model is developed for the on-machine measurement system. The contribution of the mechanical resonance to the uncertainty of on machine measurement is studied. A case study of on machine evaluating a large sag off-axis sphere mirror is illustrated.

2. Measurement system and dynamics model

2.1. On machine measurement system

An OMSM system is setup on a diamond turning machine, as shown in Fig 1. The chromatic confocal sensor has nanometre level vertical resolution over 100 μm measurement range. The platform is a Moore Nanotech 650 FG-V2 diamond turning machine. The measurement system and machine control system are synchronized by an in-house developed controller HUD-CNC [7, 8].
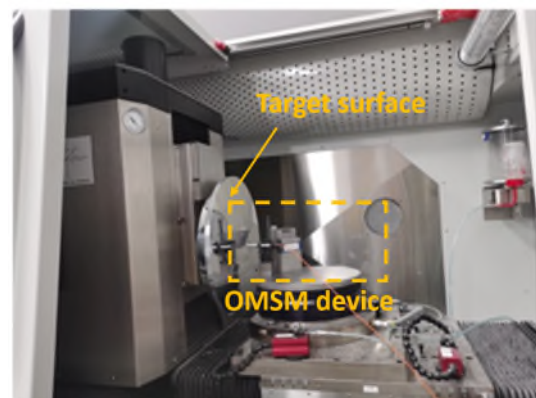
Figure 1. On machine measurement system.

The slide is driven by linear motors with hydrostatic bearings, and the sensor is mechanically coupled to the B-axis by an adjustable fixture. The accurate positions of the slides are measured by linear grating encoders for closed-loop control and large range coordinate measurement.

2.2. Dynamic property identification of OMSM device

The dynamic response of the OMSM unit is evaluated with the hammer impact experiment. The setup of the test system is shown in Fig 2. An impact hammer and an accelerometer are applied for the measurement of the impact input and response. The fixture is attached to a rigid steel bench and the sensitive direction of the accelerometer is in the horizontal plane. The impact signal and the acceleration signal are collected simultaneously by a NI-USB-6211 data acquisition card.
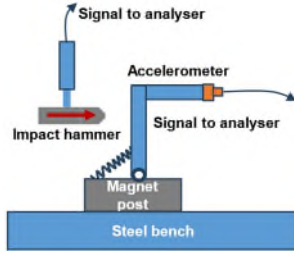
Figure 2. Schematic of nature frequency test of OMSM fixture.

The measured impact signal and response are shown in Fig 3. It can be identified that the first three order nature frequency of the OMSM device is 293Hz, 385Hz, 106Hz.
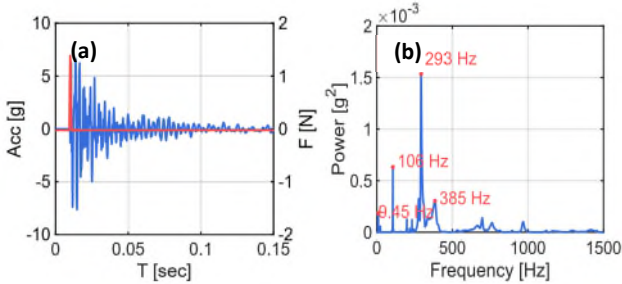
Figure 3. (a) Impact and response of the OMSM fixture, (b) Frequency spectrum of the response signal.

2.3. Dynamic model of the full OMSM system

Resonance of the OMSM system and the platform is a sensitive factor that affects the measurement result as the fixture is not ideally rigid. Dynamics model of the whole system is shown in Fig 4. The sensor is coupled to the stage by a fixture, and the stage is driven by a linear motor, and the corresponding driving force is F_d.
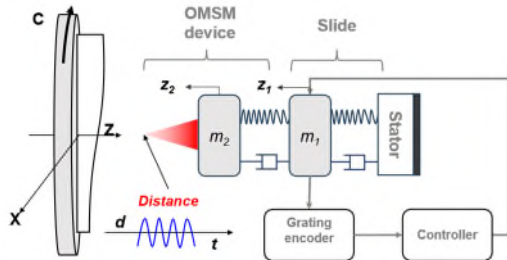
Figure 4. System dynamic model of the OMSM system integrated with diamond turning machine.

The dynamic system is simplified as 2-DOF oscillating system as shown in Fig 4. The state space model of the system is:

$$\dot{x} = Ax + Bu \tag{1}$$

$$\dot{y} = Cx + Du \tag{2}$$

where A, B, C and D are the coefficients determined by the mechanical components of the system, and $\dot{x}$, $\dot{y}$ and u are state variable. The measurement device integrated with the stage is a mechanical system with time-invariant parameters, thus D is zero in this study. The model can be expressed in a form with parameters:

$$\begin{bmatrix} \dot{x_1} \\ \ddot{x_1} \\ \dot{x_2} \\ \ddot{x_2} \end{bmatrix} = \begin{bmatrix} 0 & 1 & 0 & 0 \\ \frac{k_1}{m_1} & \frac{b_1}{m_1} & -\frac{k_1+k_2}{m_1} & -\frac{b_1+b_2}{m_1} \\ 0 & 0 & 0 & 1 \\ -\frac{k_1}{m_2} & -\frac{b_1}{m2} & \frac{k_2}{m_2} & \frac{b_2}{m_2} \end{bmatrix} \begin{bmatrix} x_1 \\ \dot{x_1} \\ x_2 \\ \dot{x_2} \end{bmatrix} + \begin{bmatrix} 1/m_1 \\ 0 \\ 0 \\ 0 \end{bmatrix} F_d \tag{3}$$

$$y = \begin{bmatrix} 1 & 0 & 0 & 0 \\ 0 & 0 & 1 & 0 \end{bmatrix} \begin{bmatrix} x_1 \\ \dot{x_1} \\ x_2 \\ \dot{x_2} \end{bmatrix} \tag{4}$$

where x_1 and x_2 are the absolute position of the slide and the OMSM sensor, respectively. F_d is the driving force from the linear motor. Physical meaning and values of other parameters are listed in the table below. The stiffness of the slide and the mass of the OMSM fixture are explicitly given in the table. Other parameters need to be practically determined. More detailed analysis on the similar system can refer to [9, 10].

Table 1. Parameters of system dynamics.

Parameters		Units	Variable name	Value
Slide	Mass	kg	m_1	*
	Stiffness	N/μm	k_1	200
	Damp	1	c_1	*
OMSM fixture	Mass	Kg	m_2	0.5
	Stiffness	N/μm	k_2	*
	Damp	1	c_2	*
*Parameters practically determined				

The state of the system can be solved numerically with the explicit Runge-Kutta method with all parameters are determined. Here, two major semiquantitative conclusions can be assumed for further analysis of the system:

a) For forced vibration, the system response frequency f is governed by the frequency of the driving force f_d.

b) When mechanical resonance occurs, the force on the slide fulfils the relationship:

$$F_{Net} = F_{21} + F_d = 0 \tag{5}$$

where F_{21} is the interaction force between the slide and the OMSM fixture. As the position of the slide z_1 is measured by a precision grating encoder with very high resolution, thus with the help of Eq (5), we can simplify the analysis by estimating the net force:

$$F_{Net}/m_1 = \ddot{z_1} \tag{6}$$

2.4. Frequency response and uncertainty of the system

The OMSM system is configured with a CMM structure, thus for an ideal measurement:

$$z_1(t) = z_2(t), \; z(t) = d(t) + z_1(t) \tag{7}$$

where $d(t)$ is the true position of the target, considering the error contributed to the vibration of the system:

$$z_2(t) = z_1(t) + \delta(t), \; \overline{z(t)} = d(t) + z_1(t) + \delta(t) \tag{8}$$

where $\delta(t)$ is the relative displacement between the sensor and the slide of the machine. The dynamic effect induced measurement error is defined as:

$$Ez = \overline{z(t)} - z(t) = \delta(t) \tag{9}$$

There is only one active force in the system, the driving force of the motor upon the slide. It can be summarized that variation of the driving force on the slide is the governing factor that affects the measurement error, which causes a forced vibration of the OMSM system. And according to the properties of the forced vibration, two major contributions of the error caused by vibration:

a) Frequency of driving force is close to the nature frequency of OMSM system fixture.
b) Wide bandwidth stochastic background noise exists in the driving force.

3. Case study: On machine measurement of large sag OAS

A large area off axis spherical surface (OAS) is fabricated with the diamond turning machine as shown by Fig 5. The curvature radius is 5000 mm, the aperture diameter is 380 mm, and the sag value is 5 mm. Due to the sag value is much greater than the range of the chromatic confocal sensor, the Z axis of the machine is incorporated to enlarge the measurement range.
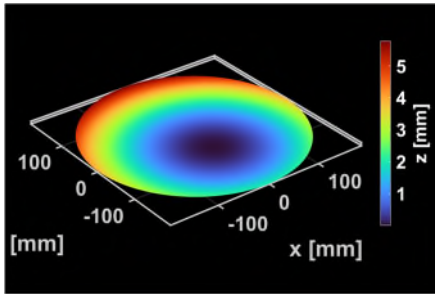
Figure 5. Topography off-axis sphere measured by OMSM method.

3.1 Quasi-static distance measurement

A quasi-static measurement of 30 seconds is performed to identify the background noise of the measurement system when all axis are standstill. The time series measurement result and the power spectral density (PSD) are shown in Fig 6(a) and (b). The absolute amplitude of the noise is about 50 nm. The major components of the measurement results are high frequency noise of 320 Hz with a root means square (RMS) of 3.16 nm. Some minor frequency components are also identified near the 200 Hz and 100 Hz and 50 Hz, respectively. The results indicate that the chromatic confocal sensor integrated with the system is qualified for evaluating surface form, sufficient in most cases to measure waviness, and may not be accurate in roughness evaluation.
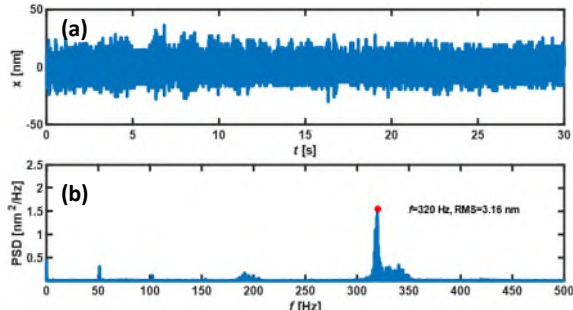
Figure 6. (a) Standstill the measurement result,
(b) PSD of the standstill measurement signal.

3.2 Uncertainty evaluation method

The deviation between the ground truth value and the measured results is given in Eq (9). Due to the ground truth of the on-machine measurement is unknown, the contribution of the vibration is evaluated by:

$$\hat{\delta}(t) = z(t) - z'(t) \tag{10}$$

where $z(t)$ is the original measured profile, $z'(t)$ is the profile filtered by a robust median filter with 32 points fixed bandwidth. Fig 7 (a) shows part of the continuous evaluation profile. The deviation between $z(t)$ and $z'(t)$ changes over the time. It can be identified that the maximum deviation happens at the moment of 1.35 hours.
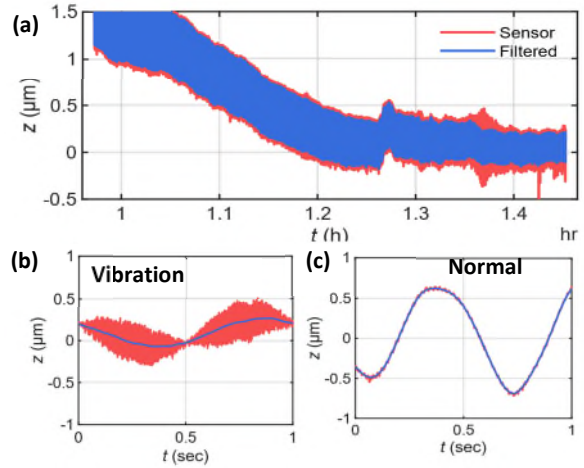
Figure 7. (a) On machine measured profile,
(b) Measured profile with vibration,
(c) Measured profile under normal conditions.

One single circular profile at that moment is extracted in 1 second, the peak-to-valley(P-V) value of the original profile is about 0.8 μm. The P-V value of the filtered high frequency signal is about 0.5 μm, nearly the same level of the surface form, which is far beyond reliable. In comparison with the profile measured at normal condition, the P-V value of the high frequency components is within tens of nanometers, the same level of system background noise. The relative error contributed by the vibration is indicated by:

$$Err = \frac{\mathbf{PV}[z(t)] - \mathbf{PV}[z'(t)]}{\mathbf{PV}[z(t)]} \tag{11}$$

For a frequency component, the absolute contribution of the vibration to the profile is given by:

$$\mathrm{RMS}(f) = \int_{f_1}^{f_2} \frac{\mathrm{FFT}(\hat{\delta}(t))^2}{Bw} \, df \tag{12}$$

where $\mathrm{FFT}(\cdot)$ is the fast Fourier transform spectrum of the separated profile, and Bw is the bandwidth of the filtered profile, which is the range between cutoff frequency f_L to $F_s/2$.

3.3 Full time scope evaluation on vibration

The full scanned profile Z_2 is evaluated with time-frequency analysis method, and the time spectrum is shown in Fig 8. The form is removed with a low pass filter. In total five different time windows, and for each the duration is shown in detail. A background stationary vibration about 50 Hz, 200Hz, and 330 Hz is shown in the chart. The 50 Hz is close to the working current of the motor, and the other two frequencies are located within the range of the nature frequency of the OMSM fixture.

Resonance vibration occurred from 1.1 hour to 1.5 hour. A series of time variant frequency components are identified. Three resonance moments are identified at T_2, T_4, and T_5. The frequencies are 420 Hz, 350Hz, and 180 Hz, respectively. The distortion on the P-V values is 0.02 μm, 0.1 μm, 0.5 μm, respectively. The absolute contribution of the resonance vibration to the overall amplitude of the measurement are: RMS(f_{420Hz})=50 nm, RMS(f_{350Hz})=200 nm, RMS(f_{180Hz})=300 nm. A series of higher order vibration components over 400 Hz is identified after 1.3 hours, limited by the measurement bandwidth of the sensor, these components current is hard to

be interpreted. One major concern of the mode identification problem illustrated here is how to avoid accounting surface waviness in the evaluation results. Here, the analysing technique is referred to as zero-net-force criterium is applied, and the details are shown in the following section.
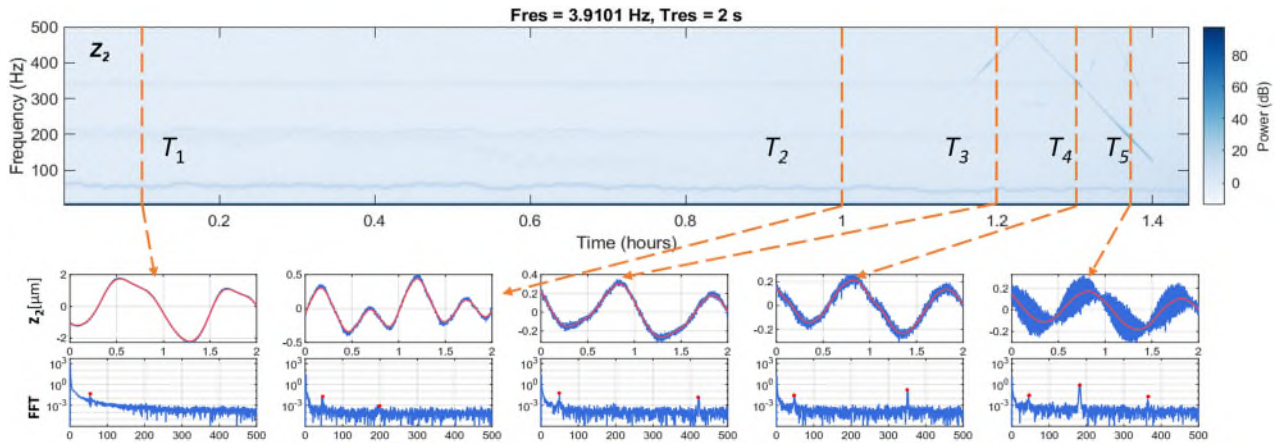
Figure 8. Time-frequency analysis of the full time scope profile measured by OMSM.

3.4 Zero net force criteria for resonance identification

As the conclusion implied by Eq (5) in Sec 2.3, the zero net force criteria are applicable to identifying the moment resonance happens in a forced vibration. Fig 9 shows the time-frequency properties of the net force on the slide, as well as the response of the OMSM sensor. It can be identified from the frequency of response follows the disturbance on the net force. Two notches on the time-frequency diagram of the net force are identified.

Among them, Notch1-Vr1, Notch2-Vr2 are two pairs of resonance modes in the system, which is shown in Fig 9(a) and (b). Vr1 and Vr2 located the frequency of OMSM fixture nature frequency range. Vr3=320 Hz is same as the main frequency components of the background noise of the system.
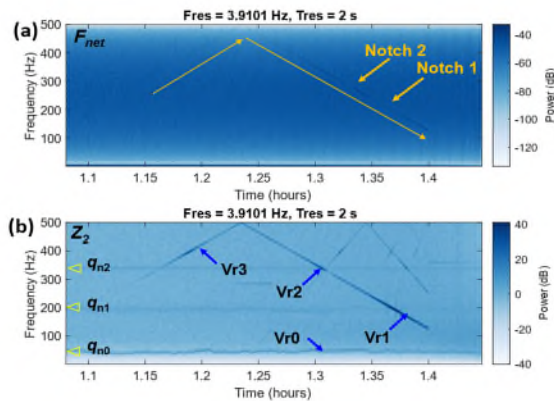
Figure 9. (a) Time-frequency diagram of net force on the slide, (b) Time-frequency diagram of the position of OMSM sensor, q_{n0} is the background noise, and q_{n1}, q_{n2} are the first two order nature frequencies of the OMSM fixture.

4. Summary and conclusions

In this paper, we firstly present the measurement uncertainty caused by mechanical resonance for on machine measurement system. Due to the disturbance of the platform, the result from the point measurement sensor is distorted with an amplitude of 0.5 μm over a millimetre scale surface measurement. The system dynamics model is established to evaluate the contribution of the resonance vibration to the measurement result. The results indicate that the disturbance induced by system resonance can be 100 times greater than the ground truth amplitude in a quasi-static measurement. This research will contribute to a more comprehensive understanding of the performance of optical measurement devices integrated with manufacturing equipment.

References

[1] Li, D., Wang, B., Tong, Z., Blunt, L., and Jiang, X.: 'On-machine surface measurement and applications for ultra-precision machining: a state-of-the-art review', The International Journal of Advanced Manufacturing Technology, 2019, 104, (1-4), pp. 831-847

[2] Rolland, J.P., Davies, M.A., Suleski, T.J., Evans, C., Bauer, A., Lambropoulos, J.C., and Falaggis, K.: 'Freeform optics for imaging', Optica, 2021, 8, (2), pp. 161-176

[3] Li, D., Tong, Z., Jiang, X., Blunt, L., and Gao, F.: 'Calibration of an interferometric on-machine probing system on an ultra-precision turning machine', Measurement, 2018, 118, pp. 96-104

[4] Xi, M., Wang, Y., Liu, H., Xiao, H., Li, X., Li, H., Ding, Z., and Jia, Z.: 'Calibration of beam vector deviation for four-axis precision on-machine measurement using chromatic confocal probe', Measurement, 2022, 194, pp. 111011

[5] Ye, L., Qian, J., Haitjema, H., and Reynaerts, D.: 'Uncertainty evaluation of an on-machine chromatic confocal measurement system', Measurement, 2023, 216, pp. 112995

[6] Wang, S., and Zhao, Q.: 'Development of an on-machine measurement system with chromatic confocal probe for measuring the profile error of off-axis biconical free-form optics in ultra-precision grinding', Measurement, 2022, 202, pp. 111825

[7] Tong, Z., Zhong, W., Zeng, W., and Jiang, X.: 'Closed-loop form error measurement and compensation for FTS freeform machining', CIRP Annals, 2021, 70, (1), pp. 455-458

[8] Zhong, W., Tong, Z., and Jiang, X.: 'Integration of On-machine Surface Measurement into Fast Tool Servo Machining', Procedia CIRP, 2021, 101, pp. 238-241

[9] Altintas, Y., Verl, A., Brecher, C., Uriarte, L., and Pritschow, G.: 'Machine tool feed drives', Cirp Ann-Manuf Techn, 2011, 60, (2), pp. 779-796

[10] Huang, P., Wu, X., To, S., Zhu, L., and Zhu, Z.: 'Deterioration of form accuracy induced by servo dynamics errors and real-time compensation for slow tool servo diamond turning of complex-shaped optics', International Journal of Machine Tools and Manufacture, 2020, 154

OCT system for the detection of Subsurface Damage in glass-substrates

L. Schwörer[1], M. Wagner[1], A. Lichtenegger[2], L. Autschbach[3], D. Ewert[3], J. Mazal[3], R. Börret[1]

[1]Hochschule Aalen für Technik und Wirtschaft, Aalen, Germany
[2]Medizinische Universität Wien, Zentrum für Medizinische Physik und Biomedizinische Technik, Vienna, Austria
[3]Carl Zeiss Jena GmbH, Oberkochen, Germany

lukas.schwoerer@hs-aalen.de

Abstract

The manufacturing process of high-tech optics for semiconductor manufacturing, space or military applications poses many challenges. One of them is a class of hard to detect defects called Subsurface Damage (SSD). This refers to microscopic defects beneath brittle material surfaces, often occurring because of mechanical stresses during manufacturing. Conventional methods, such as microscopy, are inadequate for SSD detection. The prevailing quantification technique [1,2], hydrofluoric acid etching and subsequent microscopy, is destructive and cannot be applied on the original high-value optic.

We propose a non-destructive solution - Optical Coherence Tomography (OCT).[1] OCT is a cross-sectional imaging technique offering high resolution and high sensitivity, presenting an opportunity to replace destructive SSD assessment methods. Our research focuses on enhancing the sensitivity of a high-speed OCT system while preserving rapid imaging capabilities. We conducted multiple experiments to evaluate the sensitivity within the OCT system under different configurations, such as the influence of optical power output and imaging rate. The results of these experiments are promising. Operating at its maximum imaging rate, the system demonstrated a sensitivity of up to 120 dB. This outcome shows the potential of this system as an effective tool for non-destructive SSD detection and quantification in high-value optics. Additionally, it may have the capability to detect other defects such as bubbles or impurities in similar materials.

In summary, our research highlights the necessity for non-destructive SSD detection methods in high-tech optics manufacturing. The development and optimization of our high-speed OCT system showed promising results. Achieving this notable level of sensitivity at a high imaging rate opens new possibilities for elevating the quality and reliability of high-value optics in critical applications such as semiconductor manufacturing and space exploration.

Subsurface Damage (SSD), Optical Coherence Tomography (OCT), Imaging rate, High-sensitivity

1. Introduction

Manufacturing high-technology optics for critical applications, ranging from semiconductor manufacturing to space and military applications, presents many challenges. Among these challenges lies the detection of a particular class of defects known as Subsurface Damage (SSD). SSD refers to tiny faults directly underneath the surface of a material, a consequence of stresses introduced during the mechanical processing of brittle materials such as glass or ceramics. SSD is introduced during most conventional manufacturing methods of modern optics. [2,3]

Understanding and measuring the extent of Subsurface Damage in modern optics is important for several reasons. SSD can exert a significant impact on the performance and longevity of optics. This impact stems from the unique characteristic of SSD to scatter and absorb light, leading to compromised image quality and reduced light throughput. In applications involving high-energy lasers, the presence of SSD can even lead to catastrophic failures of optical components. [4] Accurate measurement of SSD within optics is indispensable for ensuring compliance with industry standards related to reliability and lifespan, ultimately contributing to enhancing of the manufacturing process.

The quest to speed up manufacturing processes forms the core motivation for the high-tech optics industry. The existing challenge lies in the inherently destructive nature of current measurement methods, rendering it impossible to measure optics intended for use in end products. The lack of precise information about the remaining SSD in optics post-grinding necessitates the incorporation of large safety margins during the final polishing phase. The absence of a reliable, non-destructive method for SSD measurement has resulted in prolonged final polishing processes, sometimes extending days or even months.

This gap in knowledge and methodology underscores the critical need for a reliable technique to measure SSD in optics production. Such a method has the potential to accelerate final polishing processes, leading to reduced machining time and costs while simultaneously augmenting throughput.

In this paper, the primary objective is to present a comparison between Optical Coherence Tomography (OCT) and the well-established destructive method of Magnetorheological Finishing (MRF) spot polishing to detect Subsurface Damage (SSD) in optics. The goal is to showcase the development of an OCT system that produces measurements correlating with the outcomes of the established MRF spot polishing method. This comparison aims to highlight the potential of OCT as a reliable and non-destructive tool for SSD characterization, while highlighting the correlation between its measurements and those obtained through the widely used MRF spot polishing method.

2. Materials & Methods

Glass discs composed of the optical material NPK51 (SCHOTT) were chosen as samples for this study. NPK51 was selected based on the fact, that destructively tested glass samples could be supplied by the company Carl Zeiss. The chosen glass discs had a standard diameter of 80 mm and a thickness of 8 mm. To ensure uniformity, the samples underwent a precision grinding process at Zeiss, reducing surface irregularities to ± 1.5 µm. This step was crucial to establish a consistent baseline for subsequent procedures. The NPK51 sample is shown in Figure 1.
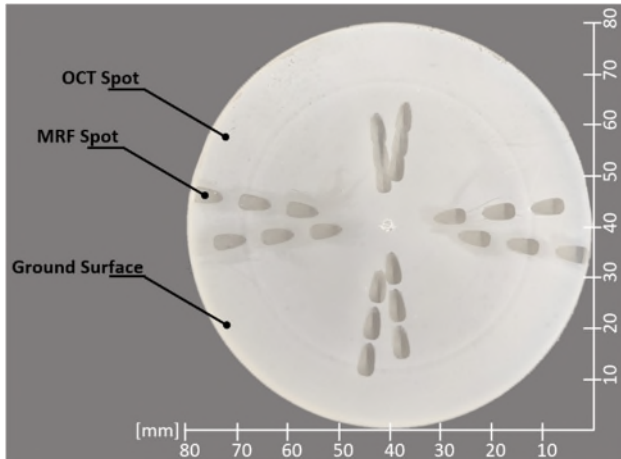
Figure 1. Image of the NPK51 glass sample with polished and etched MRF spots for the SSD analysis.

The reference SSD measurement was conducted using a well-established combination of Magnetorheological Finishing (MRF) polishing and hydrofluoric acid etching. MRF was chosen as the primary polishing technique due to its ability to achieve nanoscale precision and to not introduce additional Subsurface Damage into the sample. With the MRF polishing process, 24 spots were polished into the glass surface, as depicted in Figure 1. The hydrofluoric acid was then applied locally to each spot to preserve portions of the original surface for reference purposes and subsequent Optical Coherence Tomography (OCT) measurements.

For the OCT measurements a custom build system, engineered for the measurement of Subsurface Damage was chosen. Developed in-house, based on previous research, this system offers a lateral resolution of 800 nm, an axial resolution of 1 µm, and a sensitivity of 115 dB.[5] In contrary to the MRF method, this system also offers high-resolution 3D tomographic measurements. The used OCT system, a resolution test as well as an example of a 3D tomographic OCT image are shown in Figure 2.

Post-OCT data acquisition, the obtained raw data was processed to enhance the image quality of the OCT scans. Initially, the OCT data was processed in MATLAB to correct for dispersion and compensate the material refractive index.[6] Correction of the systems dispersion was crucial for minimizing distortions in the acquired data and compensation of the material refractive index was essential for accurate depth profiling.

Subsequently, the processed OCT data was rendered into a high-resolution 3D volume, providing a detailed representation of the internal structures of the modified glass samples. The rendering process allowed for a comprehensive visualization of subsurface features and damage.

The location and depth of subsurface damages was then established using the open source image processing tool ImageJ.[7] This involved an iterative process where cross-sections of the 3D volume were analysed.

These analytical steps were essential to extract meaningful information about the distribution and characteristics of subsurface damage, contributing to a thorough understanding of the effects of the surface modification techniques applied in this study.
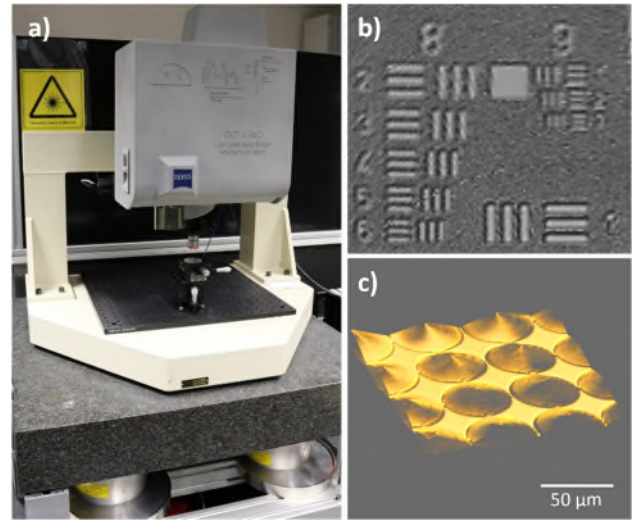
Figure 2. (a) image of the custom build OCT system. (b) OCT measurement of a USAF target showing G9E3 (linewidth 800 nm). (c) 3D OCT image of a microlens array created with a Nano scribe 3D printer (lens height 8 µm, lens diameter 50 µm).

3. Results

The depth profile of Magnetorheological Finishing (MRF) spots was initially measured using an optical profilometer (Taylor Hobsen, Luphoscan 420 HD), providing a baseline for the following SSD analysis. The measured profile is shown in Figure 3

To analyse the Subsurface Damage within the MRF spots, high-resolution images were captured and stitched together using a microscope (ZEISS Axio Imager 2). Figure 3 shows the resulting image of the MRF spot. The SSDs as revealed by etching can be seen as black dots within the MRF spot.

Quantitative assessment of the SSD was achieved by counting the amount of SSDs and mapping them to a depth based on the previous profilometer measurement. The compiled data was organized into a chart (see Figure 4) depicting the amount of SSD per depth.

The analysis of the compiled data revealed a predominant concentration of Subsurface Damage within the initial 10 µm beneath the surface. A subset of damages extended to greater depths, with some reaching as far as 14 µm. The measurement process using the MRF method typically requires approximately 2 hours for both the polishing and etching stages. However, due to limited machine availability, waiting periods of up to 12 weeks are not uncommon.
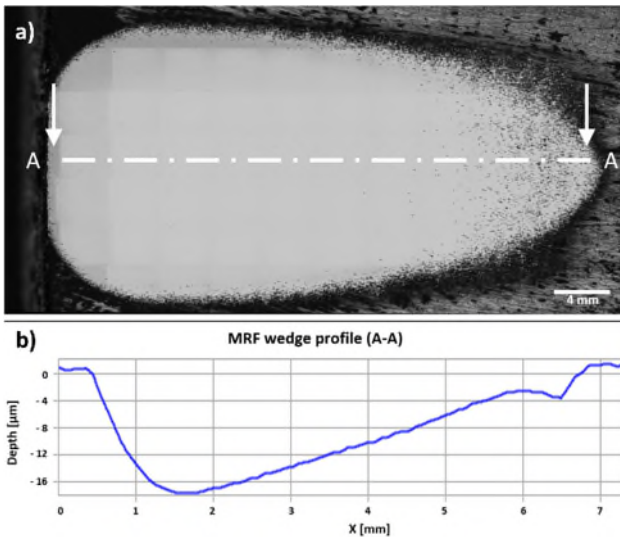
Figure 3. (a) microscopy image of the hydrofluoric acid etched MRF spot. (b) graph showing the depth profile of the MRF spot.
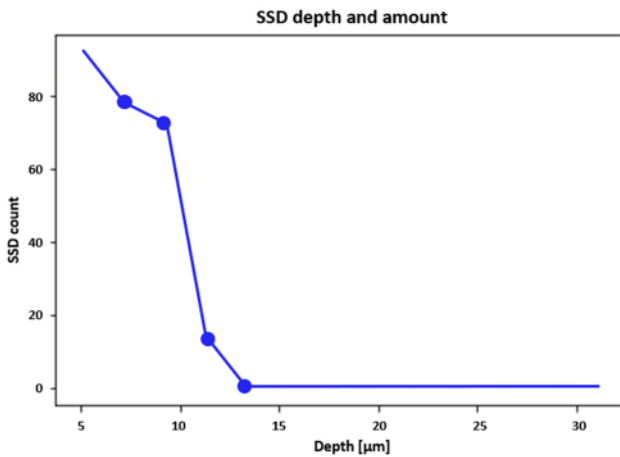
Figure 4. Graph showing the result of the MRF method as SSD amount over the measured depth.

Figure 5. Cross-sectional OCT scan of the NPK51 sample, showing the sample surface and SSD defects up to a depth of 16 μm.
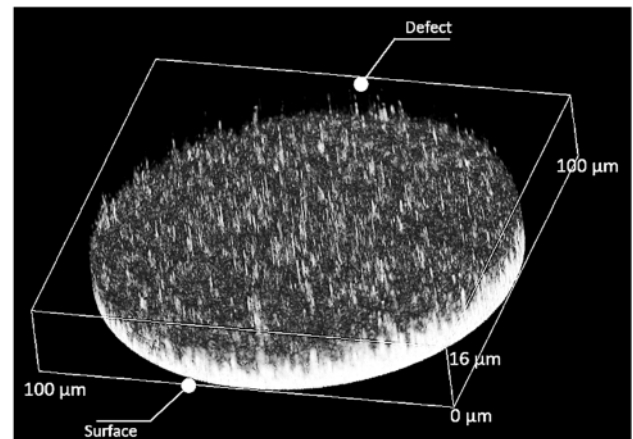
Figure 6. Bottom view of the NPK51 sample rendered OCT data.

The OCT measurement was performed next to the MRF spot on the untreated surface of the NPK51 sample. The acquired data was first analysed in a cross-sectional manner as shown in Figure 5. With this process a maximum SSD depth of 16 μm was measured. Similar to the MRF analysis, the OCT data also showed that the majority of the damages lie within the first 10 μm underneath the surface of the sample. Both the deepest crack with 16 μm as well as the mainly damaged zone from 0 to 10 μm can be seen in Figure 5. The full scan, rendered as 3D volume of the OCT data is shown in Figure 6. This image shows the bottom view of the sample with the SSD protruding in the positive y-direction. This image also shows the deepest damages at a depth of 16 μm. The SSD measurement using OCT including data processing and analysis took only a few minutes.

4. Discussion

The identification of Subsurface Damage (SSD) in glass materials remains a challenging task, with only a limited set of methods available, none of which are non-destructive. In this context, Optical Coherence Tomography (OCT) has emerged as a highly promising technique, offering a non-destructive and contactless way to precisely image SSD in transparent materials.

The conducted research specifically aimed at assessing the capabilities of OCT in detecting SSD within a defined size range, showcases its effectiveness for a size range of up to 20 micrometres. The results highlight OCT's potential as a valuable tool for identifying and characterizing Subsurface Damage in glass materials with a high degree of precision.

One crucial observation from this study is the consistency in results between OCT and the currently established measurement method, such as Magnetorheological finishing (MRF). This agreement between these two distinct techniques strengthens the reliability of OCT in detecting and characterizing SSD.

The small difference in the measured maximum depth may be attributed to the inherent nature of the different measurement methods. OCT, with its non-destructive characteristics, provides detailed volumetric measurements without causing harm to the investigated material. On the other hand, MRF, while effective, only analyses a very small portion of the sample, potentially leading to variations in results. The ability of OCT to capture a full volume of the sample might explain the observed discrepancy in measurements.

5. Conclusion

In conclusion, the research demonstrates the potential of Optical Coherence Tomography (OCT) in detecting Subsurface Damage (SSD) within a specific size range in glass materials. The non-destructive nature of OCT sets it apart from existing methods, providing detailed volumetric measurements without compromising the integrity of the material under investigation.

The agreement in results between OCT and established SSD metrology methods, such as Magnetorheological finishing (MRF), underscores the potential of OCT in SSD detection. While a difference for the maximum SSD depth between the measurements obtained from MRF and OCT is noted, it is hypothesized that OCT's ability to analyse a full volume of the sample contributes to this variance. This distinction highlights the importance of considering the measurement method's characteristics and limitations when interpreting results.

Overall, the findings suggest that OCT could become a cornerstone in the measurement of SSD, potentially establishing itself as the future standard in this domain. Its non-destructive nature, applicability to high-value optics, and independence from reliance on manufacturing samples contribute to its potential as a versatile and reliable method for SSD detection in various glass materials.

Looking ahead, the system will undergo continuous development aimed at further improving image quality, resolution, and imaging speed. Additional experiments will be conducted to generate more data regarding the correlation between OCT measurements and already established SSD measurement methods. Furthermore, it is planned to expand the class of materials the system is capable of measuring, including, for example, polymer optics. These future endeavours aim to enhance the system's capabilities, broaden its applicability, and contribute to the advancements in non-destructive SSD detection.

References

[1]   R. Boerret, T. Hellmuth, K. Khrenikov, 3-dimensional Scanning of Grinded Optical Surfaces Based on Optical Coherence Tomography, Optics and photonics.

[2]   D.S. Anderson, M.E. Frogner, A Method for the Evaluation of Subsurface Damage, Spectra- Physics Inc.1250 W. Middlefield Rd., Mountain View CA 94042.

[3]   G. Schnurbusch, E. Brinksmeier, O. Riemer, Influence of Cutting Speed on Subsurface Damage Morphology and Distribution in Ground Fused Silica, Inventions 2 (2017) 15. https://doi.org/10.3390/inventions2030015.

[4]   Liu Hongjie, Huang Jin, Wang Fengrui, Zhou Xinda, Ye Xin, Zhou Xiaoyan, Sun Laixi, Jiang Xiaodong, Sui Zhan, Zheng Wanguo, Subsurface defects of fused silica optics and laser induced damage at 351 nm, Opt. Express, OE 21 (2013) 12204–12217. https://doi.org/10.1364/OE.21.012204.

[5]   Rainer Boerret, Dominik Wiedemann, Andreas Kelm, Detection of subsurface damage in optical transparent materials using short coherence tomography, 2014.

[6]   X. Attendu, R.M. Ruis, C. Boudoux, T.G. van Leeuwen, D.J. Faber, Simple and robust calibration procedure for k-linearization and dispersion compensation in optical coherence tomography, Journal of biomedical optics 24 (2019) 1–11. https://doi.org/10.1117/1.JBO.24.5.056001.

[7]   C.A. Schneider, W.S. Rasband, K.W. Eliceiri, NIH Image to ImageJ: 25 years of image analysis, Nature methods 9 (2012) 671–675. https://doi.org/10.1038/nmeth.2089.

Innovative measurement methods for 2D and 3D surface acquisition in additive manufacturing technology

Niloofar Kashefpour[1], Alexander Pierer[2], Holger Schlegel[1], Martin Dix[1, 2]

[1]Institute for Machine Tools and Production Processes, Chemnitz University of Technology, Reichenhainer Str. 70, 09126 Chemnitz, Germany
[2]Fraunhofer Institute for Machine Tools and Forming Technology, Reichenhainer Str. 88, 09126 Chemnitz, Germany

niloofar.kashefpour@mb.tu-chemnitz.de

Abstract

This work considers the development of a measuring system for surface quality control, which is presented for quality monitoring of the products of an already developed hybrid polymer-metal extrusion system. The extrusion system is based on wire or filament-shaped starting materials and enables 3D printing of electrical connections, insulation and mechanical protection devices that can be adapted to complex shapes, as well as the repair of conductive and insulation structures on circuit boards. A key aspect of this work is the development of a low-cost measurement system for simultaneous acquisition of 2D and 3D surface data from workpieces. This system uses two optical measurement techniques, laser triangulation for 3D surface acquisition and optical flow for 2D surface acquisition. The goal is to carry out the visual inspection automatically and in real time during production in order to avoid errors and increase the robustness of production. The publication covers the fundamentals of optical metrology, especially laser triangulation and optical flow, as well as the development of the measurement system including hardware and software. In addition, investigations are carried out to evaluate the measuring system and the measuring methods. The results show that laser triangulation is suitable for 3D surface detection, while optical flow provides good results for 2D surface detection. This work provides an insight into the development of advanced manufacturing technologies and the importance of real-time quality control in additive manufacturing.

Visual inspection, quality control, optical flow, laser triangulation, image processing, optical measurement methods, extrusion , process sustainability, defect detection

1. Introduction

Although Advanced Additive Manufacturing (AM) technologies enable flexible production of customized products and offer the possibility of integrating electronic functions into structural components as well as repairing electronic components, this requires the development and updating of appropriate quality control methods and systems.

This work considers the development of a measuring system for monitoring the surface quality of the products of an already developed hybrid polymer-metal extrusion system. The extrusion system is based on wire or thread-like starting materials. This makes it possible to 3D print permanent and stable electrical connections, insulation and mechanical protection devices such as strain reliefs that can be adapted to geometrically complex shapes, as well as repair the conductor tracks and insulation structures on circuit boards. In the first development phase, low-melting tin alloys for the conductor structures and non-polar thermoplastic polymers such as PLA and ABS were investigated. In further development steps, metals with a higher melting point (e.g. copper, aluminum, steel) should also be considered as conductive and support structures or glass as an insulator in the build-up welding process.

A key aspect of optimizing the execution of these tasks is the development of methods and systems for evaluating and quality control of processes/products in real time. This goal is achievable through two main factors, firstly through the correct selection and online correction of manufacturing parameters and secondly through accurate process control or product follow-up. The manufacturing parameters are usually selected regarding to the application to ensure the repeatability of the process and quality of the products. However, unexpected defects such as insufficient bonding or geometric dimensional deviations may occur at any time during the process. Furthermore a research study by Öberg et al. [1] shows the variation of the selected preliminary welding process specifications prepared in five welding shops for the production of the same workpiece, which also results in inconsistent quality of the workpiece and requires the existence of a human factor in the evaluation process which again affects the consistency of the assessment. However, there is a risk that some defects may be overlooked due to fatigue and limited human performance. On the other hand, there is a greater amount of time spent inspecting workpieces in this manner. The consequences are higher costs and increased energy consumption.

The idea of this work is the development of a simple and cost effective measurement system for simultaneous acquisition of 2D or 3D surface data of the workpieces. The system contains a combination of two optical measurement methods; laser triangulation for 3D surface acquisition and optical flow method for 2D surface acquisition, which enables the automation of visual inspection tasks during production in order to avoid corresponding errors and the associated additional costs, material and energy consumption and thus achieving greater robustness and sustainability of production.

The main technical simplification and cost advantage of this system lies in the use of only one industrial camera to capture the 2D image information, the 3D laser profile and the feed movement. The evaluation of the 3D-profile and the feed path as well as feed rate is done by image processing algorithms.Welded workpieces were used to perform the

investigations and consider the functionality of the measurement methods for the intended application.

In the following sections, first the basics of the respective methods as well as the investigations regarding the functionality of the methods are considered and finally a short summary of results as well as a conclusion is given.

2. Optical measuring methods

Methods of optical metrology are developed on the basis of physical reflection and absorption principles. These enable non-contact, fast and full-surface measurement of workpieces. In this work, two optical measurement methods are used to acquire the 2D and 3D surface data of the workpiece. These are considered in the following sections.

2.1. Laser triangulation

Laser triangulation is the most commonly used method for 3D surface measurement, and its performance has been gradually improved by accurate mechanical laser scanning control and high-resolution, high-sensitivity image sensors. There are four main components of a 3D triangulation system: a camera, a projector that is typically laser-based, a mechanism that moves the object or camera-laser system through the imaging system's field of view, and software to process the captured image and accurately convert pixel offsets into height differences [2].

The interaction between laser illumination and object surface results in a distribution of intensity values. This distribution depends on the topography of the surface and the properties of the propagating light. During acquisition, the workpiece is moved under the laser-camera-system. By capturing the intensity distribution and calculating the workpiece profile over time, a three-dimensional geometric reconstruction of the workpiece can be obtained [2,3].

In this work, the reverse arrangement of the camera-laser-system (Figure 1) is used. According to the triangulation principle, based on the known distance of the laser line to the camera axis Δx and the angle α between the projection axis of the laser and the camera axis, the height Δz of the scanned object (Figure 2) can be determined using the following formula:

$$\Delta z = \frac{\Delta x}{\tan \alpha} \qquad (1)$$

This means that the system parameters Δx and α are the decisive factors for determining the sensor properties such as detection range, height or depth resolution, occlusion, and laser reflection. A trade-off between depth or height resolution and detection range is a typical problem of laser triangulation systems. Many commercial solutions have a fixed baseline, so they only work with a fixed resolution and range [4,5].

2.2. Optical flow

The motion of an object in 3D scene is projected into a 2D image by the optics of the image sensor. This is defined as a motion field that cannot be measured directly.

Optical flow is an estimation of the motion field by detecting the motion of brightness patterns using the concept of flow vectors in image sequence. Mathematically, this is referred to as the gradient of the gray values between two images and describes the gray value flow caused by the relative motion of objects and observers to each other [6]. Therefore, it contains information not only about the spatial arrangement of the observed objects, but also about their velocity change.

A detailed mathematical description of the methodology can be found in the works of Agarwal et al. [6] and Rideaux et al. [7].
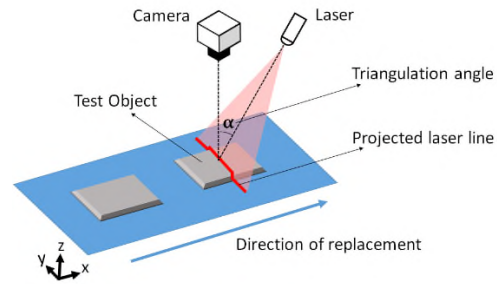
Figure 1. Configuration of laser-camera-system for laser triangulation method: reverse geometry
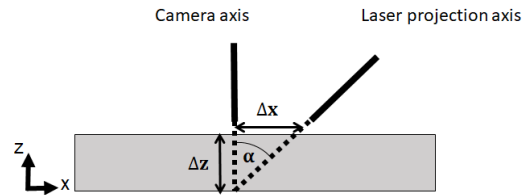
Figure 2. Parameters of the laser triangulation system

3. Development of the measuring system

3.1. Hardware of the system

Two versions of the measurement system were developed, a stationary and a portable measurement setup. The use of a color camera is a special feature of these experimental setups compared to other similar works. By using such a camera, the information concerning the color of the laser line can be acquired. The properties of different color spaces can simplify the detection or acquisition as an additional feature. The characteristic of this feature is described and implemented for example in works of Yin [8] and Breier et al. [9] for inspection as well as 3D profile detection of the printed circuit boards and in a paper of Pierer et al. [10] for inspection of the thickness of paint coating of extruded aluminum parts.

Based on these findings, a stationary measurement setup was constructed. In order to design the system as accurately as possible, the optimal triangulation configuration was calculated. Regarding the measurement system (constant distance between the camera and the laser), the parameter x can be set by adjusting the angle between the projection axis of the laser and the camera axis (α). As a consequence, α is the only free mechanical adjustment parameter that determines the sensitivity of the 3D surface measurement. The DIN 1319 defines it as *"change of value in the output quantity of a measurement device referred to the change of value of the input quantity which causes it"*. In this system, it would be defined as a relation of measured pixel shift of the camera to the height change on the workpiece. According to equation (1) and the fact that the field of view of the camera in which the laser light is visible is a boundary condition for determining the sensitivity range of the sensor, the optimal triangulation angle for 3D surface detection can be determined by looking at the image scale. This is defined by the ratio of image size and object size. The prerequisite for this is that the object lies on a plane parallel to the sensor or camera. In addition, the image scale must be recalculated in case of a change of the distance between the object and the camera.

After preliminary tests with the stationary setup, a portable measurement device with similar components was created. The mechanical components are 3D printed from PLA plastic. The portable measurement system can be moved by hand on the workpiece.

3.2. Software of the system

The algorithms required for the acquisition procedures were implemented in the XEIDANA® framework developed at Fraunhofer IWU (Fraunhofer-Institut für Werkzeugmaschinen und Umformtechnik IWU, Chemnitz, Deutschland) [11]. This framework enables the implementation of complex data analysis tasks by modularization and parallelization of data processing algorithms and sensor fusion. In this work, the data acquired by camera is fused by means of the appropriate modules and used to determine the 3D profile of the workpiece as well as the displacement diagram of its motion.

By using the RGB camera, the bitwise combination of the hue and color saturation of the laser light is used as a strong feature to detect the laser line on the workpiece. This is achieved by converting the RGB image to the HSI color space and decomposing it into the appropriate components. Mathematical transformations between the RGB and HSI color spaces are mentioned in the work of Saravanan et al. [12]. In the process, three new images are obtained in terms of the component's hue (H-image), saturation (S-image) and intensity (I-image).

The combined HS-evaluation can also differentiate reddish, albeit relatively weakly color-saturated, rust spots from the laser line. The average of the segmented laser line (Figure 3-d) is the input image for the triangulation calculations (Figure 3-e).
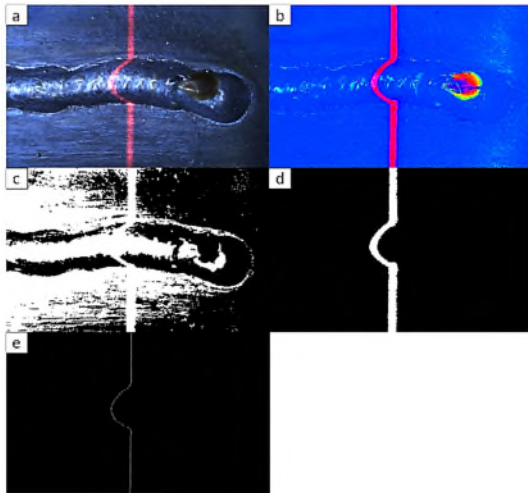
Figure 3. a) Calibrated input image, b) Hue image (H-image), c) Color saturation image (S-image), d) Segmented laser line, e) Average value of segmented laser line.

The 2D surface acquisition module receives two consecutive calibrated RGB images from the camera in the input and calculates the flow vectors of the pixels between these two images. The feed motion results from the conversion of flow vector with the image scale. Whereby the determination of the exposure time of the camera plays an important role in the interference-free acquisition.

3.3. Investigations for evaluation of the system

For the experimental evaluation, investigations were carried out both according to the measurement methods (laser triangulation and optical flow) and measurement systems (stationary and portable measurement systems).

The accuracy and linearity of the measurements of laser triangulation method were considered by means of the measurement of test standards (gauge blocks) with a size of 0.5 to 6 mm.

The investigations according to the application of optical flow for 2D surface measurement were carried out with regard to the

repeatability as well as the linearity of the measurement results and depending on the feed path, feed speed, feed direction as well as surface design of the sample object.

Having established the good functionality of the optical flow method, especially for longer feed paths, the authors compared it with the image registration method. This method evaluates the similarity of two images and calculates a transformation between them. A very robust and well-established image registration method in industrial image processing uses the so-called Enhanced Correlation Coefficient (ECC) [13].

To evaluate the developed measuring system, it was used for surface detection of welded workpieces. During the tests with the stationary measuring system, the workpiece was moved under the laser-camera-system at a speed of 100 mm/min. (Figure 4) Two nuts were placed next to the weld as reference points for the beginning and end of the detection. The smooth, shiny as well as weakly textured surface of the nut resulted in its noisy image on some parts (measurement deviations).
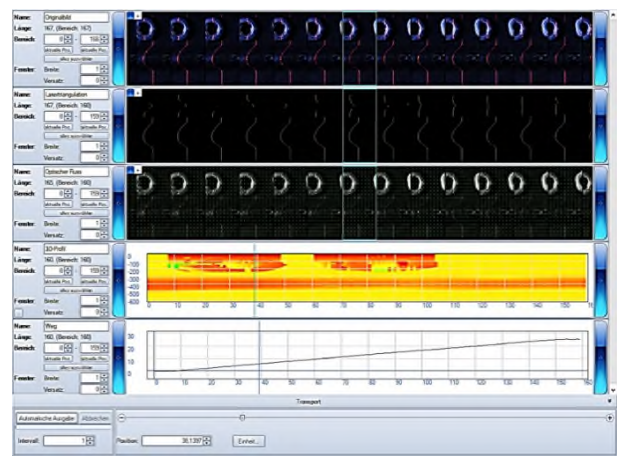
Figure 4. Measurement results of the stationary measurement system (the rows contain respectively: the color image sequence captured by the camera, the segmented images to extract the laser line, the RGB image with the directions of movement measured from the optical flow, the 3D profile of the workpiece, the displacement diagram of the motion)

3.4. Results

For the measurement system, the influencing factors regarding the measurement accuracy can be classified according to its components as follows:

- Camera: reprojection errors, lens aberrations
- Laser: spot size, linearity of the laser line
- Object: speckle noise, occlusion, tilt angle, color anomalies such as rust spots or glossy spots on the workpiece
- Conveyor: vibrations
- Environment: ambient light noise

The measurements of the test standards using laser triangulation resulted in a maximum measurement deviation of 0.11 mm, which is sufficient for fulfilling the requirements of DIN EN ISO 5817 level C ("medium") for permissible dimensions of weld irregularities. This is also suitable for the evaluation of 3D extruded parts, whereby the layer thickness varies between 1 to 3 mm depending on the technology and requirements of the component and an extrusion thickness accuracy of 0.5 mm should be maintained.

It is worth noting that the less fluctuations the segmented line has, the more accurately the profile can be measured. In the system the combination of saturation and hue serves as features

for segmenting the laser line so that in the presence of a suitable additional light source, the variations caused by ambient lighting and/or nature or manufacture of the test object etc. (e.g. rust stain) can be avoided. During the dynamic tests, a correlation between the speed of the conveyor and the measurement resolution was found, whereby the measurement reliability increased as the feed speed of the object on the conveyor decreased. Here, a compromise between the feed speed, the measurement resolution, as well as the acquisition time should be determined. It was also demonstrated that the segmented laser line could be used to monitor or inspect the weld regarding the external/surface anomalies.

When implementing 2D surface detection using the optical flow method, a dependence of the measurement accuracy on the feed motion as well as the motion speed was found, whereby with an increased path and/or feed speed, the measurement deviation and standard deviation of the measured values also increased. In addition, a dependence on the nature of the sample was found, whereby for objects with recognizable textures qualitative good results for the detection of the feed motion are provided. Moreover, the influence of exposure time on the quality of motion detection by method of optical flow is remarkable. The comparison of the measurement results with the results of the ECC method (Figure 5) showed that an increase in the feed path causes a greater reduction in measurement accuracy with the ECC method than with the optical flow. Additionally, the optical flow has shorter calculation times compared to the optical flow.
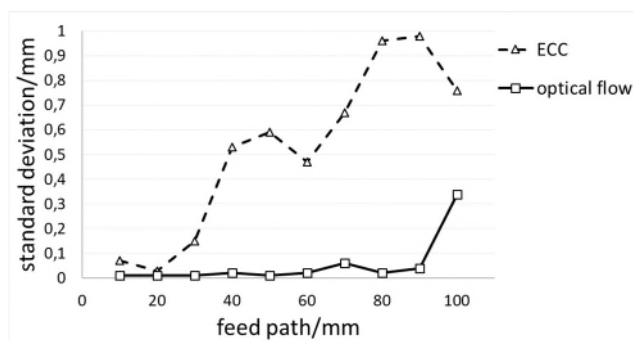
Figure 5. Standard deviation of feed path measurement by optical flow and ECC with a feed rate of $500 \frac{mm}{min}$

In the measurements using the portable measurement system (static object and moving camera-laser-system), the 3D profile of the object has a lower resolution. This can be justified by the variable speed of movement and the inevitably uneven hand guidance of the device.

4. Conclusions

The investigations have impressively shown that the combination of laser triangulation and feed detection by means of optical flow is an extremely promising method, especially in the context of the novel additive manufacturing process that uses hybrid metal and plastic extrusion. This process enables layer-by-layer creation of complex components, using both metals and plastics in a single process. According to the results when the object to be measured has recognizable textures, the optical flow provides high-quality results for the detection of the feed motion. This precision is essential to ensure that the layers are correctly matched during the additive manufacturing process and that high-quality end products can be produced.

Fine-tuning of lighting and camera parameters, including adjustment of lighting color composition, irradiance and optimal choice of camera exposure time, plays a crucial role in optimizing this process for hybrid metal and plastic extrusion. These parameters make it possible to precisely detect the materials and ensure the quality of the printed layers. In addition, it has been shown that the quality of segmentation of the laser line, especially with respect to the nature of the sample surface, has a significant influence on the measurement accuracy of laser triangulation processes. A low variation in the segmented line is essential to accurately perform offset measurements and thus generate accurate profiles for hybrid metal and plastic extrusion.

The results of this work thus lay the foundation for the development of an ergonomically optimized device for the manual inspection of components as a part of the additive manufacturing process. Moreover, they can be integrated directly into automated test systems to support the monitoring and quality assurance of this innovative manufacturing method.

These results are instrumental in increasing the efficiency and quality of hybrid metal and plastic extrusion in the manufacturing industry, and open up exciting possibilities for the wider application of this revolutionary manufacturing process across multiple industries.

References

[1] Öberg A E and Åstrand E 2018 Variation in welding procedure specification approach and its effect on productivity *Procedia Manufacturing* **25** *412–417*

[2] Björk T, Samuelsson J and Marquis G 2008 The need for a weld quality system for fatigue loaded structures *Welding in the World* **52**

[3] Leach R 2020 Advances in optical form and coordinate metrology *IOP Publishing Bristol*

[4] Munaro M, So E W Y, Tonello S and Menegatti E 2015 Efficient completeness inspection using real-time 3D color reconstruction with a dual-laser triangulation system *Integrated Imaging and Vision Techniques for Industrial Inspection 201–225. Springer London*

[5] Donadello S, Motta M, Demir A G and Previtali B 2019 Monitoring of laser metal deposition height by means of coaxial laser triangulation *Optics and Lasers in Engineering* **112** *136–144*

[6] Agarwal A, Gupta S, and Singh D K 2016 Review of optical flow technique for moving object detection *2nd International Conference on Contemporary Computing and Informatics (IC3I) pp. 409-413*

[7] Rideaux R and Welchman A E 2020 But still it moves: static image statistics underlie how we see motion *Journal of Neuroscience* **40**

[8] Yin A 2012 Analysis of optical inspection from AOI and AVI machines

[9] Breier M, Moller P, Li W, Bosling M, Pretz T and Merhof D 2015 Accurate laser triangulation using a perpendicular camera setup to assess the height profile of PCBs *IEEE International Conference on Industrial Technology (ICIT)*

[10] Pierer A, Hauser M, Hoffmann M, Naumann M, Wiener T, de León M L, Mende M, Koziorek J and Dix M 2022 Inline quality monitoring of reverse extruded aluminum parts with cathodic dip-paint coating (KTL) *Sensors* **22** *no.* 24

[11] Putz M, Wiener T, Pierer A and Hoffmann M 2018 A multi-sensor approach for failure identification during production enabled by parallel data monitoring *CIRP Annals* **67** *491–494*

[12] Saravanan G, Yamuna G and Nandhini S 2016 Real time implementation of RGB to HSV/HSI/HSL and its reverse color space models *International Conference on Communication and Signal Processing (ICCSP)*

[13] Evangelidis G D and Psarakis E Z 2008 Parametric image alignment using enhanced correlation coefficient maximization *IEEE transactions on pattern analysis and machine intelligence* **30** *1858–1865*

In-situ surface inspection for roll-to-roll process: Towards responsive manufacturing

Hussam Muhamedsalih[1], Mothana Hassan[1], Prashant Kumar[1], Liam Blunt[1], David Bird[2], Dan Kolb[2], Steven Edge[2], Jonathan Howse[3], Andrew Campbell[3]

[1]EPSRC Future Metrology Hub/ Centre for Precision Technologies (CPT), University of Huddersfield UK
[2] Centre for Process Innovation CPI, UK
[3]Chemical & Biological Engineering/ University of Sheffield UK

h.muhamedsalih@hud.ac.uk

Abstract

Roll to roll (R2R) manufacturing is known as a cost-effective process for mass production of flexible products ranging from papers to flexibles electronic devices such as PV cells and displays. Slot-die coating technologies are widely used in R2R as a simple but effective process to deposit inks on moving substrates to form thin film tracks with high uniformity. R2R utilising slot-die approaches is in need of further refinement to produce defect-free ultra uniform thin films with nano-scale thickness coating capability. This presents a challenge as the current status of slot-die printing is that it is an open-loop manufacturing process without sufficient in-process metrology instrumentation. Monitoring sub-micro scale coating thickness and micro-scale defects on metre-scale substrates (e.g. 0.3 m width) moving at high speeds (e.g. 50m/min) poses a significant obstacle. In this work, the authors are aiming to pave the way for R2R to translate toward responsive (closed loop) mode manufacturing by controlling the operation conditions via two optical metrology approaches that can be used as feedback sensors for close-loop responsive manufacturing. The first optical instrument is an in-situ single shot multi-wavelength polarising interferometer to measure the surface topography of coated film "on the fly" during manufacturing (out of plane). The polarisation serves as an instantaneous phase shifting mechanism and the multi-wavelength is employed to generate a long synthetic wavelength to extend the measurement range beyond $\lambda/4$ limitation. The surface height information, with nano-scale accuracy, can be used as a feedback signal to the manufacturing process. It will be shown that surface topography measurement can directly be linked to one of the operating variables, namely the slot-die pump flow-rate. The second optical instrument is a machine vision senor for edge and defect detection (in plane) using Otsu thresholding algorithms. It is demonstrated in this paper that the edge uniformity along the printed track can be quantified as metric values. The complete system demonstration shows also that track defects, track geometry and track topography (in and out of plane measurement) can be detected and successfully classified in real time. Fluoropolymer, silver, and Carbomer Ethanol Methylene Blue (PAA-C2H6O-MB), printed ink samples on Ti coated polymer substrates and a PTE substrate, have been utilised in this study as an exemplar combination.

Thin film inspection, roll-to-roll printed coating inspection, edge and defect detection, machine vision

1. Introduction

Roll-to-roll coating/printing (R2R) is a viable process for the production of large area flexible devices. R2R has the potential to save production cost if the print operating variables and web (substrate) handing are well controlled and optimised. R2R manufacture has developed capabilities from conventional paper, foil and textile process to high value components such as optoelectronics or graphene-based devices. Such devices have high demands on the precision of the processing to tight manufacturing specification [1]. For example, thin film thickness for flexible electronics applications, such as capacitors films, needs to be controlled to sub-micron level across meter-scale web widths. Slot-die coating technologies are commonly used in R2R to deposit conducting thin film inks to a wide-range flexible substrates. In slot-die coating, the uniformity of thin films is directly linked to the operating variables such as ink pump flow-rate, speed of the web, ink drying, and the gap between the slot-die head and the web [2]. Film defects are mainly related to the web handling [3]. As such, imperfections in R2R operation lead to unwanted thickness/width variation or defects in thin films, resulting in low productivity and large amount of waste. Unfortunately current practice is that R2R processes are forward-loop systems with no feedback to adjust the coating operation. The transition to a close-loop approach is a way forward to upgrade R2R to responsive mode manufacturing and thereby enhancing process productivity.

Real time film surface monitoring providing reliable quantitative information to process controllers is the key to facilitating successful R2R closed loop processes. The present authors have demonstrated static optical surface metrology for thin film inspection [4]. This paper discusses the combination of two real-time (dynamic) surface inspection methods that potentially can be used as feedback sensors. The sensors provide both in plane and out of plane data regarding the R2R coating processes. The first method is a single shot multi-wavelength scanning interferometer (MPI) (out of plane) and the second is a machine vision sensor (MVS) for coat edge monitoring and defect detection.

2. Multi-wavelength Polarising Interferometer MPI (out of plane)

The MPI configuration, shown in Figure 1, consists of a Michelson polarising interferometer and four detection optical arms. Each detection arm has a colour CMOS camera placed after a polarisation arrangement to generate a single RGB interferogram shifted by $\pi/2$ sequentially. Four colour

interferograms are captured at single exposure time (< 1 ms) to negate the surface vibration. The frames are transferred to the computing console for analysis. The system operation principle has been reported in our previous publication [5]. The MPI has been installed onto a R2R production line at the Centre for Process Innovation/UK, see Figure 1.

In the present work, a slot-die printer was used to print Fluoropolymer ink into Ti coated polymer substrate at 1m/min web speed. The MPI was aligned with the edge of the track to measure the ink top surface real time with respect to the substrate, as shown in Figure 2.a. The pump flow rate was then changed from 1500-4000 µl/min incrementally. Based on MPI measurement, shown in Figure 2b, it can been seen that the variation in coating thickness can be measured dynamically during the pump flow-rate change process.
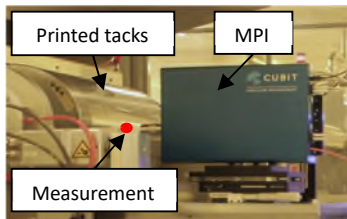
Figure 1. MPI installed onto R2R manufacturing
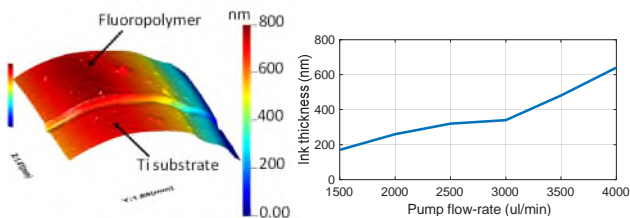
Figure 2. (a) Web real surface measurement (b) film thickness vs pump flow-rate *(Note; curvature dure to roll form)*

3. Machine vision sensor MVS (in of plane)

The MVS, described in [6], was used for in-plane inspection to identify defects and print track edge irregularities on the web that can produced during the slot-die coating process. The edge irregularities/straightness was analysed using the Otsu thresholding algorithm. The foreground and background pixels represented by the ink track and the web substrate were successfully distinguished after tuning the threshold value. As such, the produced segmented results can be used to easily extract the track edge profile. The authors have reported previously that the lateral arithmetic average edge deviation calculation, named as (Ra_{LAT}), can be quantified to indicate the edge quality as shown in Figure 3. In this case Silver Ink on Polyethylene Terephthalate (PET) substrate was used to verify Otsu performance.
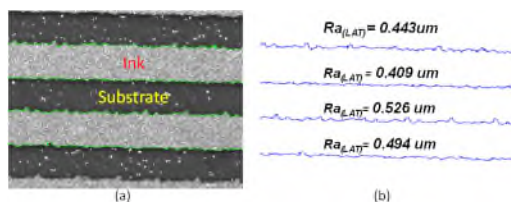
Figure 3. (a) MVS captured image (b) Extracted edge profiles

This MVS work also focused on extracting the presence of defects for classification in order to be linked later to R2R operation conditions. To extract defects, a template image was captured from a defect-free area on the sample. This reference template can be convolved to images captured from the substrate during R2R operation to subtract original features and extract unexpected features (i.e. defects). The defects then can

be further processed by a simulated defects template for classification purposes as described in [7]. This defects analysis concept has been verified by using the MVS to dynamically inspect moving web of PAA-C2H6O- MB/PET. Figure 4 shows defects detection and classification results collected dynamically. The lighter spots in Figure 4a are defects in the ink. It can be seen that this sensor can successfully extract and classify such defects as shown by the yellow frame in figure 4b.
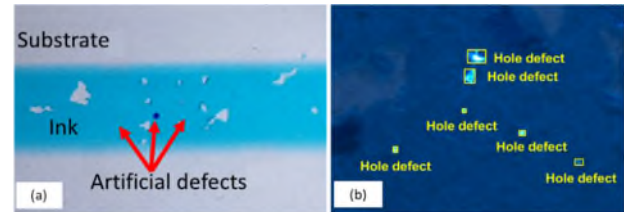
Figure 4. Defects detection; (a) PAA-C2H6O- MB sample (b) MVS results

4. Conclusion

To translate R2R process from forward-loop to close-loop, responsive mode, manufacturing is a core requirement. Consequently the existence of feedback sensors to provide quantitative information is necessary. The two combined optical sensors outlined in this work provide the basis for scale up to a full manufacturing environment where their output is directly linked to the operation conditions. For example, it has been found that surface thickness extracted from the surface topography information measured by MPI can be directly linked to the pump flow rate. As such, any undesirable thickness variation can be measured with nano-scale resolution and fed to manufacturing controller for optimisation. The MVS has also demonstrated an effective methods for defect/edge defection and classification. The metric information for the edge straightness can linked to the web handling such as the web tension or slot die clogging. Research continues to investigate methods for optimising the operation variables and web handling by using manufacturing controllers connected to optical sensors.

References
[1] Lee, J., Byeon, J., & Lee, C. (2020). Theories and control technologies for web handling in the roll-to-roll manufacturing process. International Journal of Precision Engineering and Manufacturing-Green Technology, **7**, 525-544.
[2] Lee, S., & Nam, J. (2015). Response of slot coating flow to gap disturbances: effects of fluid properties, operating conditions, and die configurations. Journal of Coatings Technology and Research, **12**, 949-958.
[3] Roisum, D. R., Walker, T. J., & Jones, D. P. (2021). The Web Handling Handbook. DEStech Publications, Incorporated.
[4] Muhamedsalih, H., Blunt, L., Martin, H., Hamersma, I., Elrawemi, M., & Feng, G. (2015). An integrated opto-mechanical measurement system for in-process defect measurement on a roll-to-roll process. euspen.
[5] Muhamedsalih, H., Al-Bashir, S., Gao, F., & Jiang, X. (2018, August). Single-shot RGB polarising interferometer. In Interferometry XIX (Vol. **10749**, pp. 52-57). SPIE.
[6] Hassan, M., Blunt, L., & Muhamedsalih, H. euspen's 23rd International Conference & Exhibition, Copenhagen, DK, June 2023.
[7] Wu, W. Y., Wang, M. J. J., & Liu, C. M. (1996). Automated inspection of printed circuit boards through machine vision. Computers in industry, **28(2)**, 103-111.

Saturation reduction in fringe projection using polarization sensors and varying light intensities

Mira Sinée[1,2], Han Haitjema[1], Wim Dewulf [1]

[1]Department of Mechanical Engineering, Katholieke Universiteit Leuven, 3001 Leuven, Belgium
[2]Flanders Make, 3001 Leuven, Belgium

mira.sinee@kuleuven.be

Abstract

Fringe projection systems are well established as metrology tools for fast measurements of (large) workpieces. However, as specular surface reflectivity causes camera saturation, the accuracy of fringe projection for (semi-)reflective parts is limited. The use of polarization filters can reduce the effect of this specular reflectivity, but lowers the signal-to-noise ratio (SNR), resulting in lower quality measurements. In this paper, a hybrid method which combines a polarization camera and an adaptive fringe projection technique, is proposed and validated. As four images are captured simultaneously, choosing the most appropriate polarization channel will partly reduce saturation and enhance the pointcloud integrality. To completely eliminate camera saturation in highly reflective areas, an adaptive fringe projection algorithm is moreover used to vary the intensity of the projected light. The hybrid approach proves to be promising as it provides an accurate and complete 3D reconstruction for complex workpieces with a high dynamic range.

Keywords: Optical Metrology, Fringe Projection, Surface Reflectivity, Polarization Camera

1. Introduction

Fringe projection (FP) is an optical measurement technique that uses structured light to capture complex surfaces. Due to its ability to provide high-resolution 3D reconstructions in a non-contact, non-destructive manner; fringe projection has become increasingly relevant in various fields like manufacturing, quality control, aerospace and medicine[1, 2]. However, for many of its applications it can not yet reach its full potential as the state-of-the-art industrial fringe projectors remain unable to (accurately) measure reflective surfaces and high-dynamic-range (HDR) sceneries [2]. A common solution is to spray the surface with an anti-reflective coating, which can be a time-consuming task and may be undesirable for delicate surfaces. Furthermore, the uniformity and thickness of the powder will influence the measurement accuracy [3].

During the measurement of shiny workpieces, saturated pixels caused by specular reflection directed towards the camera, are the main reason for the loss of 3D information. Therefore, Lin et al. developed an Adaptive Fringe Projection (AFP) technique that calculates the optimal pixel-wise projection intensity to avoid camera saturation [4]. This method ensures a high signal-to-noise ratio (SNR), but proves to be less effective when dealing with HDR situations.

Placing a polarization filter in front of the projector and camera of a FP system, can reduce specular reflection and enlarge the dynamic range. However, this approach tends to be rather innefficient and time-consuming. A more recent approach is to use a polarization camera that can capture four images with different polarization directions simultaneously. Salahieh et al. introduced a method where the most appropriate polarization channel is chosen to ensure a better SNR compared to a single polarization image [5]. The four polarization images are used to form one measurement. However, polarization filters can not eliminate reflection caused by external light sources. Additionally, they tend to lower the intensity range. Both AFP and polarization algorithms contribute to image saturatation avoidance, however neither will cause complete elimination.

In this paper, a hybrid method that combines an adaptive fringe projection method and a polarization camera is proposed to enable accurate and complete measurements of complex workpieces with both bright and dark areas. In section 2, the general fringe projection process is described and the methodology of the different experimental methods is given. Section 3 provides a description of the experimental setup. Section 4 compares the proposed methods to a reference dataset and section 5 summarizes our conclusion.

2. Methodology

2.1. N-step phase shifting algorithm

During the fringe projection process, an N-number of sinusoidal fringe patterns are projected onto the workpiece to create a phase map [3]. The intensity I of the fringe patterns can be expressed as:

$$I_i(x,y) = I'(x,y) + I''(x,y) \cos[\phi(x,y) + \delta_i] \qquad (1)$$

where (x,y) is the pixel coordinate of the image plane, $I'(x,y)$ is the average intensity, $I''(x,y)$ is the intensity modulation, $\phi(x,y)$ is the unknown phase value and $\delta_i = 2\pi/N$ is the phase shift between the fringe patterns (with $i = 0, \ldots, N-1$).

A phase map is needed to retrieve the height information of the workpiece. For an N-step phase shifting algorithm [2], the phase is calculated as:

$$\phi(x_c, y_c) = \tan^{-1}\left[\frac{\sum_{n=0}^{N-1} I_i(x_c,y_c) \sin(2\pi n/N)}{\sum_{n=0}^{N-1} I_i(x_c,y_c) \cos(2\pi n/N)}\right] \qquad (2)$$

where $I_i(x_c, y_c)$ is the pixelwise intensity of the captured camera image. Equation (2) results in a wrapped phase map that ranges from $-\pi$ to π. As a continuous phase map is needed, it has to be unwrapped by removing the 2π discontinuities. In this paper, a binary coded pattern [6] will be used to retrieve the absolute phase. From the unwrapped phase, the height information of the workpiece is calculated and a pointcloud is generated.

2.2. Adaptive fringe projection (AFP) method

The amount of camera image saturation is dependent on the exposure time and the intensity of the projected light. While changing the exposure time has a global effect, the projected intensity can be adjusted locally. The optimal pixelwise projection intensity is calculated such that the camera image stays below the saturation limit, while maintaining a decent SNR. The different steps of the AFP method are visually represented in Figure 1 and further described in the next paragraphs.
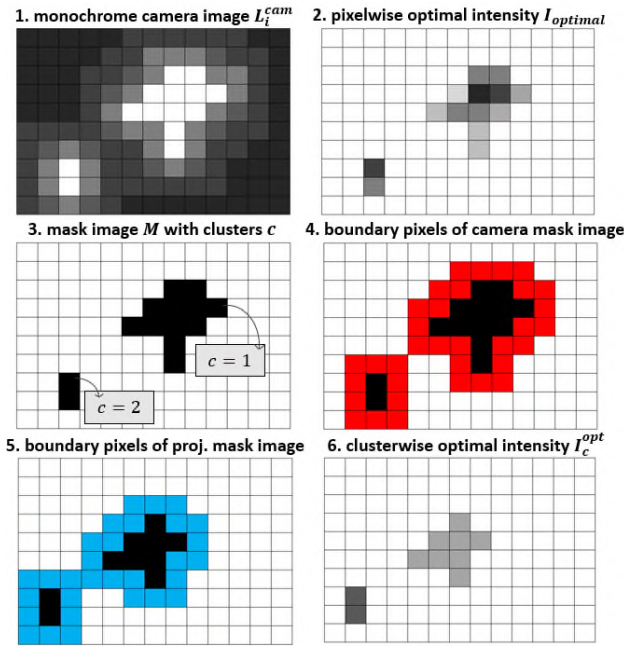
Figure 1: Visual representation of the AFP method

A series of images $L_i^{proj} = \left\{ \frac{255i}{n} \mid i = [1, n] \right\}$ with a uniform intensity are projected onto the artefact to be measured. A corresponding camera image L_i^{cam} is captured for each projected image. For every individual camera pixel, a set $A(x, y) = \{i \; such \; that \; L_i^{cam}(x, y) < 255\}$ is defined. From this, the optimal intensity $I_{optimal}$ is calculated for each pixel position:

$$I_{optimal} = \begin{cases} \max_i \{L_i^{proj} \mid i \in A\}, & if \; A \neq \emptyset \\ 0, & if \; A = \emptyset \end{cases} \quad (3)$$

Once the optimal intensity is known for the camera pixels, their value has to be mapped to the corresponding projector pixels.

By applying the phase shifting algorithm, the correlation between camera and projector image is found. Because the phase value cannot be evaluated correctly for saturated pixels, a camera mask image M^c is created to exclude them:

$$M(x, y) = \begin{cases} 0, & \exists i \in [1, n] \; such \; that \; I_i(x, y) \geq T \\ 255, & otherwise \end{cases} \quad (4)$$

where I_i are the phase shifts captured by the camera and T is the chosen mask treshold, often a bit lower than the saturation threshold of 256 as a safety margin for noise. All pixels for which $M = 0$, are assigned a cluster number c, where the pixels belonging to the same cluster are connected to eachother. For each of the enclosed saturation clusters within the masked image, a global optimal cluster intensity I_c^{opt} is calculated as:

$$I_c^{opt} = \begin{cases} \min_{(x,y) \in c} \{I_{optimal}(x, y)\}, & if \; \overline{I_{optimal}} > 100 \\ 100, & otherwise \end{cases} \quad (5)$$

The optimal intensity clusters can be mapped towards the projector image, using the phase value of the pixels that directly surround the saturated clusters. Their location is found by applying boundary tracing techniques [7] to the mask image. The workpiece is scanned again with the adapted fringe patterns.

2.3. Multi-polarization Fringe projection

A polarization camera has a polarization filter array placed directly on top of the image sensor grid [8]. The array consists of a repeated 2x2 pattern of polarization filters with four different angles (0°, 45°, 90° and 135°) as shown in Figure 2. This enables the camera to capture four polarization images in a single shot. The projected fringes pass through a linear polarizing filter, before falling onto the workpiece. The surface and reflectivity of the workpiece modulate the Degree and Angle of Polarization (DoLP, AoLP), resulting in different behaviour on the four polarized camera images. For each pixel, the most appropriate polarization channel can be selected.
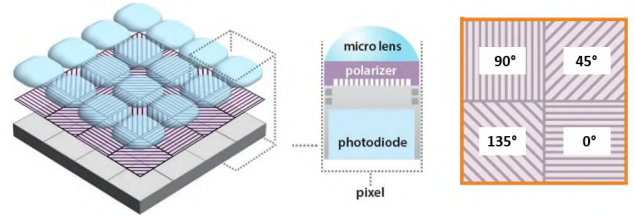
Figure 2: Polarization camera image sensor

The multi-polarization technique in this paper will, for each pixel, select the polarization channel with the highest greyvalue p_{max} that lies below the saturation threshold:

$$p_{max}(x, y) = \max_p \{I_p(x, y) \mid I_p(x, y) < 255\} \quad (5)$$

with $I_p(x, y)$ the intensity of a certain pixel in the polarization images ($p = [1,4]$). When the intensity of a pixel is above the threshold in all polarization channels, a random channel can be selected but no valuable height information will be retrieved.

For all phase shifts, data will be extracted from the optimal channel. This ensures the highest possible intensity range and therefore a better SNR in comparison with using a single polarization filter.

2.4. Hybrid fringe projection method

In our hybrid fringe projection method, adaptive fringe projection and multi-polarization fringe projection are combined consecutively to further eliminate saturation and get more accurate and stable results. To ensure the highest SNR, the fringe pattern is only adapted for pixels that are saturated in all four polarization channels.

3. Experimental setup

The experimental fringe projection setup, as seen in Figure 3, consists of a projector (DLP LichtCrafter 4500 Texas Instruments, 912x1140 pixels), a monochrome camera (Basler Ace acA4024-29, 4024x3036 pixels) and a polarization camera (Blackfly S USB3, SONY sensor Polar-Mono, 2448x2048 pixels). The projector and one camera are installed on a rigid aluminum baseplate, attached to a tripod stand. The cameras can be interchanged and the projector lens can be equipped with a linear polarizing filter. An N-step phase shifting algorithm (N=10) is used to scan one side of an aluminum workpiece (200

mm x 200 mm), produced by incremental sheet forming (see Figure 4). It comprises both convex and concave surfaces.

Five different measurements are performed:

- M0 : reference measurement with anti-reflective spray (monochrome camera)
- M1: normal measurement, without any additional algorithms (monochrome camera)
- M2: AFP measurement (monochrome camera)
- M3: polarization measurement (polarization camera, + linear polarizing filter)
- M4: hybrid measurement (polarization camera + linear polarizing filter)
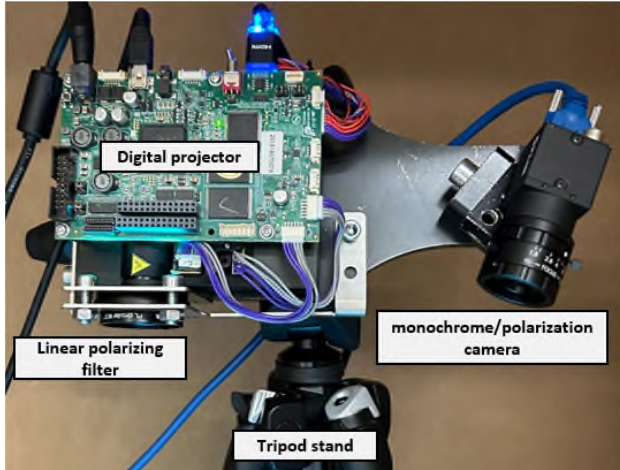
Figure 3: Experimental fringe projection setup
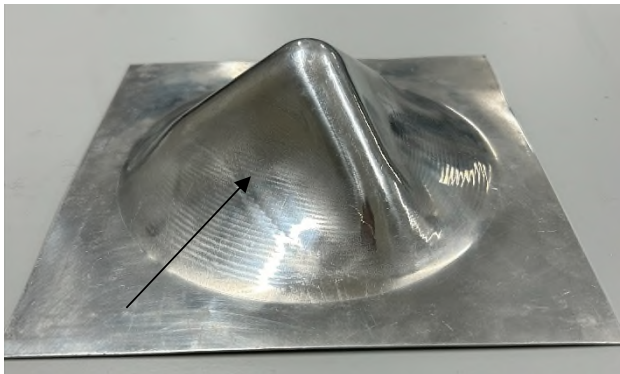
Figure 4: Aluminum workpiece produced by incremental sheet forming, with an arrow indicating the scan direction

4. Results and discussion

The measurement quality of the different 3D reconstructions is determined by two important factors. The point cloud integrality (PCI) serves as a metric for coverage percentage and is the ratio of the number of points in a certain area (M1-M4) and the number of points of the reference measurement with full coverage (no holes, M0) [3]. The topography fidelity measures the bias and standard deviation (std) of the deviation between the measurements (M1-M4) and the reference (M0).

Special attention is given to two surface areas: a bright area where the light is reflected directly to the camera and a dark area where the light is reflected away from the camera. On Figure 5, they are indicated with a red box and green triangle respectively.

It has to be noted that the measurements executed with the polarization camera (M3 and M4) have a lower lateral resolution compared to the monochrome camera(612x512 pixels instead of 4024x3036 pixels for each polarization channel). Also, when

repeating the individual measurements (M0-M4) multiple times, the average deviation between them stays below 0.04 mm.
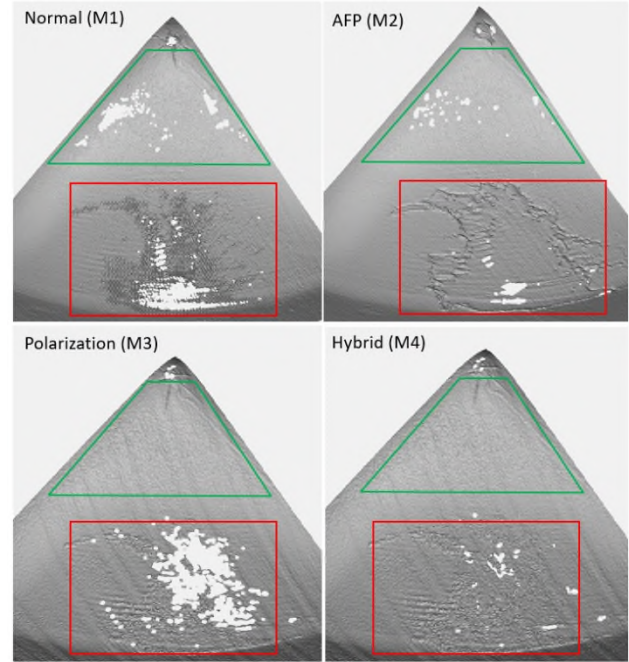
Figure 5: 3D reconstruction of a normal (M1), AFP (M2) , polarization (M3) and hybrid (M4) measurement. The red box and green triangle indicate the reflective and dark areas respectively.

4.1. Reflective area

In Figure 5, the 3D reconstruction of the normal measurement (M1) has a number of holes, as the areas that possess the most reflectivity could not be reconstructed. Meanwhile, areas that suffered from partially saturated pixels, cause a noisy and inaccurate point cloud. This observation is supported by table 1, which shows that the normal measurement deviates 0.223 mm on average from the reference measurement (M0). The large std shows the noisy character.

The AFP method improves both the bias and the integrality of the pointcloud (see Table 1). From Figure 5, it can be observed that the deviations in M2 are mostly situated around the edges of the reflective area. This is due to the sudden intensity change in the adapted fringe pattern that introduces slightly more errors in the phase unwrapping algorithm. The noise due to saturation however, is reduced.

The polarization method does not perform well for very bright areas, with M3 having the lowest PCI of all four. Similar to the normal measurement, the pointcloud is quite noisy with a higher deviation. This is partly due to reflections caused by an external light source, which can not be eliminated by the polarization camera. The PCI is also affected by the saturated areas and the random, sudden changes is the polarization channel surrounding them.

Table 1: Topography fildelity of the four fringe projection methods compared to the reference measurement (reflective area)

Method	PCI in %	Bias in mm	Std in mm
Normal (M1)	78.33	0.223	0.168
AFP (M2)	92.78	0.105	0.096
Polarization (M3)	67.38	0.213	0.175
Hybrid (M4)	96.26	0.116	0.086

The hybrid method produces the most complete pointcloud with 96.26% PCI. M4 has a bias equal to the AFP method, which is very good considering the lower lateral resolution. The

measurement is less affected by the intensity change in the adapted fringe pattern, but shows a bit more general noise. This noise can be explained by the overall fringe intensity reduction associated with polarization filters and the limitations of the camera

4.2. Dark area

The normal measurement of the dark area has the lowest coverage percentage, which is clearly visible in both Figure 5 and Table 2. Especially on the left and right sides of the triangular area, the geometry of the workpiece reflects too much light away from the camera. As the contrast between the fringes is too low, there is no phase information available and no points are generated. Additionally, the presence of extensive clusters of saturated pixels tends to lower the overall intensity of the other pixels. The application of the AFP method addresses this aspect and therefore partly reduces the problem, increasing the PCI by 8% in Table 2.

Both the polarization method and the hybrid method prove to be very effective within the dark area, with a PCI above 99% . If the polarization direction of the incoming light is properly aligned, having four polarization channels ensures there is always one channel that will eliminate specular reflection directed towards the camera; increasing the dynamic range in other areas. The bias of the methods that use the polarization camera does not go below 0.1 mm. However this could be improved with a larger camera resolution.

Table 2: Topography fidelity of the four fringe projection methods compared to the reference measurement (dark area)

Method	PCI in %	Bias in mm	Std in mm
Normal (M1)	78.15	0.103	0.076
AFP (M2)	86.87	0.075	0.026
Polarization (M3)	99.86	0.116	0.091
Hybrid (M4)	99.92	0.113	0.091

4.3. Overall performance

From the results for the reflective and dark area, it is clear that the AFP and polarization technique prove to be most effective in opposing areas. While the AFP technique effectively improves the coverage and accuracy within the reflective area, the polarization technique fails to do so. In the dark area however, the polarization technique outperforms the AFP technique with almost full coverage.

The hybrid method effectively combines the benefits of both methods and provides an overall coverage of 98% with a bias of 0.116 mm. The hybrid methods proves to be highly suitable for workpieces with a high dynamic range and complex forms, which is an improvement compared to the other methods. To further improve this method, a polarization camera with a higher resolution can be used and/or the monochrome camera and the polarization camera can be operated simultaniously to reduce time and complexity.

5. Conclusion

The measurement of reflective objects is still a challenge, especially when they require a HDR due to a complex surface geometry. Adaptive fringe projection performs great in reflective areas, however lacks to provide full 3D reconstruction in areas with low intensity. Polarization filters on the other hand broaden the dynamic range, but still struggle with high reflectivity towards the camera. In this paper, a hybrid method is developed, that effectively combines the benefits of both AFP and polarization filters. It proves to provide (almost) complete 3D reconstruction of complex shaped workpieces with a high dynamic range with an accuracy of 0.1 mm.

References

[1] S.S.Gorthi and P.Rastogi, 2010, "Fringe Projection Techniques: Whither are we", *Optics and Lasers in Engineering 48 133-40*

[2] S.Zhang, 2016, *High speed 3D Imaging with Digital Fringe Projection Techniques*, Boca Raton: CRC Press

[3] J.Sun and Q.Zhang, 2022, "A 3D shape measurement method for high-reflective surface based on accurate adaptive fringe projection", *Optics and Lasers in Engineering,* **153** 12

[4] H.Lin, J.Gao, Q.Mei, Y.He, J.Liu, X.Wang, 2016, "Adaptive digital fringe projection technique for high dynamic range three-dimensional shape measurement", *Optics Express*, **24** 7703-18

[5] B.Salahieh, Z.Chen, J.J.Rodriquez and R.Liang, 2014, "Multi-polarization fringe projection for high dynamic range objects", *Optics Express,* **22** 10064-71

[6] N.J.Cheng and W.H.Su, 2021, "Phase shifted Fringe Profilometry Using Binary-Encoded Patterns", *Photonics*, **8** 362-85

[7] M.A.Ansari, D.Kurchaniya and M.Dixit, 2017, "A comprehensive Analysis of Image Edge Detection Techniques", *International Journal of Multimedia and Ubiquitous Engineering,* **12** 1-12

[8] Lucid Vision Labs, "Beyond Conventional Imaging: Sony's Polarized Sensor, [online], available: https://thinklucid.com/tech-briefs/polarization-explained-sony-polarized-sensor/. [Accessed on 9/11/2023]

Measuring capability of a confocal sensor integrated in a two-stage long-range nanopositioning platform

L.C. Díaz-Pérez[1], M. Torralba[2], J.A. Albajez[1], J.A. Yagüe-Fabra[1]

[1]I3A, Universidad de Zaragoza, Zaragoza, Spain
[2]Centro Universitario de la Defensa, Zaragoza, Spain

lcdiaz@unizar.es

Abstract

The NanoPla is a high precision 2D positioning platform developed, manufactured, and assembled at the University of Zaragoza, offering a large range of 50 mm × 50 mm with submicrometre accuracy. Initially designed for metrological applications, the first prototype integrates a chromatic confocal sensor in its moving platform as the primary measuring instrument. Complementing this, a system of three capacitive sensors is incorporated into the NanoPla to measure parasitic motion along the Z-axis as the platform levitates within its working range, thanks to this system, parasitic motions can be corrected from the confocal sensor measurements. The NanoPla has been designed to measure statically, a procedure in which the levitating platform lands at the measuring point before recording readings. However, it also exhibits dynamic measurement capabilities, allowing for data acquisition while the moving platform is levitating. In this study, two reference artefacts are measured using the NanoPla's confocal sensor, both statically and dynamically. The obtained results are compared with those from other metrological instruments, such as a focus variation microscope, to evaluate the NanoPla's measuring capability.

Nanopositioning stage, confocal sensor, measuring capability.

1. Introduction

Nanotechnology applications such as nanomanufacturing or nanometrology require precise positioning systems serving as supplementary stages for measuring or manipulating samples. Accurate positioning is a critical requirement for applications like scanned probe microscopes, lithography, and surface profilometers. These applications find relevance in various industries, such as electronics, wherein nanostructures and features give rise to objects with dimensions in the centimetre range. Consequently, the demand for accurate, repeatable, and long-travel-range positioning systems is rapidly escalating.

To address this requirement, the University of Zaragoza has developed a large-range nanopositioning stage, called NanoPla, that is able to perform a planar motion along a range of 50 mm × 50 mm with a submicrometre resolution. The NanoPla design and implementation have been subject of previous works [1]. The first prototype of the NanoPla is intended for the metrological characterization of large surfaces at a submicrometre scale. For this purpose, a confocal sensor has been integrated as measuring instrument [2].

Previous works focused on the integration of the measuring instrument in the NanoPla, and the analysis and minimization of the error sources that affect the measuring result. In this work, reference artefacts are going to be measured by the NanoPla in order to assess its measuring capability.

2. The NanoPla as a metrology system

A picture of the actual Nanopla setup is shown in Figure 1. The NanoPla is divided in three parts: an inferior and a superior base that are fixed, and a moving platform that is placed between them. The moving platform levitates thanks to three air bearings, and it is driven by four linear Halbach motors that

perform planar motion. The position feedback in XY-plane is provided by a 2D plane mirror laser system. The positioning system controls the position in the XY-plane and rotation around Z-axis of the moving platform. The position in Z-axis and the rotation around X- and Y-axes are only monitored by a capacitive sensor system, their control is not necessary thanks to the air bearings stiffness (13 N/μm).
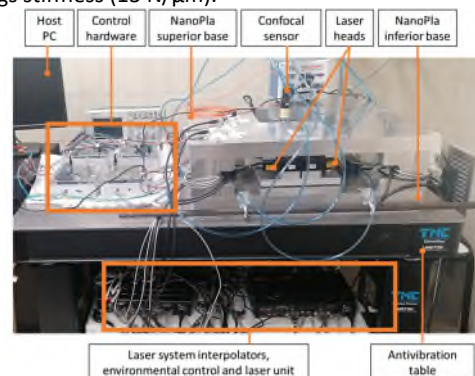
Figure 1. Picture of the NanoPla setup.

As mentioned, a Chromatic Confocal Sensor (CCS) has been integrated in the moving platform of the NanoPla as a measuring instrument. The selected CCS (CL4-MG35, from Stil) is capable of measuring in 1D along the NanoPla Z-axis, in a 4-mm range with a resolution in the measuring axis of 122 nm and a static noise that is dependent on the measuring surface characteristics. The measuring procedure for which the NanoPla was designed is the following: The sample is positioned in a sample holder placed in the fixed inferior base. The levitating moving platform displaces the measuring instrument to the desired measuring position. Once the moving platform has reached the desired position, it lands, and it stays static while the measuring instrument records the measurements. However, the NanoPla also allows to perform a dynamic measurement, that is, the CCS can record the

measurements while the levitating moving platform displaces over the sample, without having to land.

3. Method and materials

In this work, we study the measuring capability of the NanoPla by measuring steps of two different reference artefacts. The NanoPla measurements are compared to the ones performed in other metrological systems. In every case, the steps are measured according to the standard ISO 25178-70:2014.

3.1. Reference artefacts
The first reference artefact is a calibrated contour standard from Alicona, with steps of 100 µm, 500 µm, 1000 µm and 2000 µm. The second artefact has been designed ad-hoc for this project with 10 steps from 250 µm to 3800 µm and manufactured by Electrical Discharge Machining (EDM). The steps of both artefacts have been measured with the calibrated focal variation microscope (FVM) Infinite Focus SL from Alicona, as a reference instrument.

3.2. Confocal sensor measuring capability
The measuring capabilities of the CCS were assessed by measuring the calibrated Alicona contour standard in an external setup, aiming to determine the errors introduced by the CCS as a measuring instrument. The external setup consists of a fixed holder for the sensor, and a commercial linear stage that moves the sample driven by a screw linear stepper motor. The measurements were performed both statically, with the linear stage stopping at every measuring point, and dynamically, that is, recording the measurements while the linear stage was displacing. The static measurements show that the sensor measurements are compatible with the ones provided by the calibration certificate of the standards, with a measuring error lower than 1 µm for every step. Regarding the dynamic measurements, it was observed that the relative speed between sample and sensor does not affect the measurement performance of the sensor. However, due to the sensor sampling frequency, higher speeds result in less measured points, which results in a higher measuring error when calculating the steps height. At speeds lower than 1 mm/s, the results of the dynamic procedure were similar to the ones obtained by the static procedure.

3.3. NanoPla measurements
The reference artefacts have been measured in the NanoPla, following the static and dynamic procedure. In the static procedure, measurements are taken at each measuring position (at intervals of 0.15 mm), providing a snapshot of the height at those specific points (Figure 2a), not allowing to measure roughness. While in the dynamic procedure, height measurements are continuously recorded as the platform moves, offering a more comprehensive view of the height variations throughout the displacement (Figure 2b), and allowing to measure roughness. To minimize the moving platform parasitic motion, the dynamic measurements were performed at a speed of 4 µm/s.
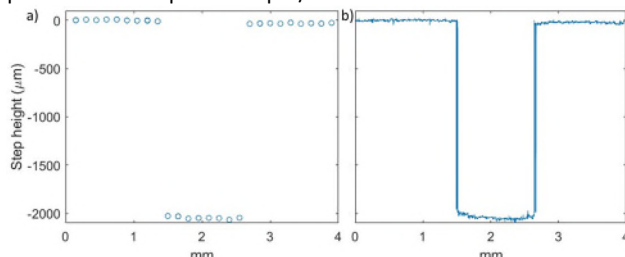
Figure 2. a) 2000-µm step measurement with the static procedure. b) 2000-µm step measurement with the dynamic procedure.

4. Measurement results

The obtained results show that there is compatibility between the NanoPla measurements in the static and the dynamic procedure, and the reference measurements performed in Alicona FVM. As an illustrative example, Figure 3a shows the measurement results of the calibrated standard 2000-µm step, while Figure 3b shows the results of ad-hoc artefact 1000-µm step. In every case, the measurement results are presented with their respective measuring uncertainties (k=2).
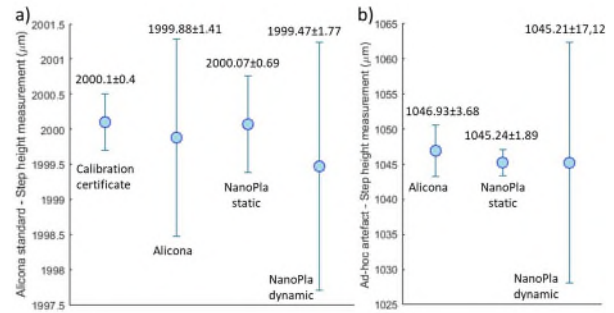
Figure 3. a) Alicona standard 2000-µm step measurement. b) Ad-hoc artefact 1000-µm step measurement.

Considering the measurement uncertainties, the compatibility indexes (E_n), calculated according to ISO 13528:2015, between the reference measurements of Alicona FVM and the NanoPla measurements are lower than 1 (0.41 in the worst case).

The uncertainties of the measurements have been calculated for all the procedures. The NanoPla uncertainty budget was addressed in a previous work [3]. In both, the static and the dynamic procedure, the NanoPla highest measuring uncertainty contribution is the measuring noise recorded by de CCS. This noise is highly dependent on the measured surface, higher roughness results in higher measuring noise. In addition, it is observed that the NanoPla levitation in the dynamic procedure amplifies that noise.

To address the roughness measurements, the Alicona contour standard roughness (ISO 21920-2:2021) was measured in Alicona FVM, the CCS in the external setup, and the CCS integrated in the NanoPla. As shown in Table 1, the dynamic measurement in the NanoPla amplifies the roughness due to the coupling of parasitic motions of the levitating platform.

Table 1. Roughness measurements of the contour standard surface.

Measuring system	Alicona FVM	CCS in external setup	CCS in the NanoPla
R_a (l_n=4mm)	0.28 µm	0.70 µm	8.59 µm

4. Conclusions

The measuring capability of the NanoPla system with a confocal sensor integrated was addressed. Although the NanoPla results are compatible with the reference measurements the NanoPla measuring uncertainty is higher when performing dynamic measurements: the coupling of parasitic motions of the levitating platform amplifies the measuring noise and the roughness measurements. Future works should focus on improving the positioning control system to reduce these parasitic motions.

References

[1] Torralba M, et al 2016 *Measurement*. Large range nanopositioning stage design: A three-layer and two-stage platform **89**, 55–71.

[2] Muro L, Díaz L, Torralba M, Albajez JA, Yagüe JA. 2022 Integration of a piezostage and a measuring instrument in a two-stage long-range nanopositioning platform *22nd euspen International Conference & Exhibition*

[3] Díaz L, Torralba M, Albajez JA, Yagüe JA 2023 *Measurement*. Uncertainty budget of a large-range nanopositioning platform based on Monte Carlo simulation **208**, 112469.

Methodologies for the comparison of gear measurement results using tactile and fibre optic laser interferometry sensors within a Coordinate measuring machine

Denis Sexton[1], Andy Sharpe[2], Robert Frazer[3], Sofia Catalucci[1], Samanta Piano[1]

[1]*Manufacturing Metrology Team, Faculty of Engineering, University of Nottingham, UK*
[2]*Department of Metrology and NDT, Manufacturing Technology Centre (MTC), UK*
[3]*National Gear Metrology Laboratory (NGML) Department of Engineering, Newcastle University, UK*

denis.sexton@nottingham.ac.uk

Abstract

The growth of optical measurement techniques in recent years has introduced the possibility of allowing several alternative methods of non-contact gear measurement to be utilised. Optical methods offer many advantages over tactile ones such as the potential to evaluate delicate surfaces quickly and to measure the whole area of the gear tooth flank at the sub-micron level. However, in order to maximise this potential, the magnitude of error and sources of uncertainty need to be better understood. In order to allow greater confidence in the results obtained from optical measurements, a series of trials was undertaken with a known size artefact. This paper presents results obtained from the Hexagon HP-O optical measurement system when used in conjunction with traditional tactile probing for gear measurement. The use of a series of designed experiments (DOE/DOX) allowed deliberate changes to specific key instrument parameters to be explored. The results presented in this paper are intended as preliminary outcomes of the application of designed experiments as a tool to explore the cause-and-effect influence on predetermined instrument variables. Future work will include experiment campaigns and analysis, planned specifically to further validate the results obtained from the application of the proposed method. The planned gear measurement validation activities will be supported by the UK National Gear Metrology Laboratory (NGML).

Keywords: Optical Gear Metrology, Laser Interferometry, Analysis of Means, Analysis of Range, Orthogonal Array,

1. Introduction

Gear geometry as defined in ISO 1328-1:2013 [1] requires specific elements of the gear (i.e. profile, lead or helix, and pitch) to be considered independently. This ISO standard is used in conjunction with ISO TS 10064-1 [2] which defines approved gear inspection methods. Since the standard does not currently establish any optical technology methodologies to measure gears, these methods remain essentially tactile. Modern optical methods can offer many advantages over tactile, such as the ability to quickly measure the whole area of the gear tooth flank at the sub-micron level. Data extracted may then be used as a predictor model to aid gear design and wear analysis. BS ISO 18653:2003 [3] addresses gear traceability, calibration intervals, and sources of measurement error and uncertainties including mechanical alignment and drift. In order to explore the capabilities of optical techniques for gear measurement, one optical methodology was chosen. Measurement trials were performed to evaluate measurement results against a known size artefact, which in this case was a master gear provided by the UK National Gear Metrology Laboratory (NGML). The information gathered from these measurement trials could assist in defining the highest class of gear which could be evaluated utilising any given optical technology under predetermined conditions. Investigation may provide working models to explore error and uncertainty in other optical measurement systems. It may also be possible to obtain and provide useful information when defining any optical gear instrument suitability with reference to measuring multiple gear features against any specific tolerance classification. One advantage offered by these trials, is that since both sensors exist within the same coordinate measuring machine (CMM) tool rack, any component alignment errors accumulated when moving between instruments are removed. Results from both sensors can also be evaluated directly in real time via Quindos® gear software.

2. Methodology and Gear Setup

A series of trials were planned for a NGML supplied spur gear on a Leitz PMM-C CMM at the MTC. The first series of trials were designed to look at the repeatability of the HPOAL-0010L optical sensor (as shown in Fig 1). In order to set a baseline, the gear was first aligned and measured twice with a conventional tactile ruby sphere of 3 mm diameter [4, 5]. Initial repeatability studies were made with the tactile sensor without the use of the rotary axis, while further tactile run included it. The profile scan speed was set at 2 mm/second with a distance of 0.005 mm between points, while the lead was scanned at 1 mm/second with a maximum distance of 0.0005 mm between points. The order of tooth scan was kept as left flank profile, then left flank lead, then right flank profile followed by right flank lead. Four of the teeth were scanned for each trial of profile and lead, and numbered as 1, 8, 16, and 23. Each sensor was utilised in a single orientation (tactile probe A axis = 0°, B axis = 0° and optical probe A axis = 90°, B axis = 0°). The rotary axis was utilised for all the trials, since it is not possible to utilise the optical sensor without the rotary axis due to indexing head constraints. Due to further constraints with the HPOAL optical sensor, a tactile versus optical comparison was not initially possible for the full depth of the tooth. Profile measurements were taken from the gear

reference diameter (equal to 113.10 mm) to the tip diameter (equal to 120.90 mm). The width of the teeth was 20 mm so an evaluation range of 14 mm was initially chosen for lead measurement, allowing 3 mm of clearance at each end of the tooth flanks. Following successful repeatability trials for both tactile and optical methods, the second phase of the experiments involving the optical scans was undertaken. In this paper the data obtained from the second phase of optical trials is reported.

2.1. Reportable features

The measurement results provided from the CMM gear software consists of various outputs, including those specific gear characteristics which are defined as mandatory reportable features [1]. These include profile (FHα), lead (FHβ), individual pitch (fpi), cumulative pitch (Fpi) and runout (Fri). Profile and lead measurements are completed on both flanks of four of the total (29) teeth as previously identified, and at approximately 90 degrees apart. Individual and cumulative pitch are normally measured across both flanks of all teeth. Runout can be calculated from pitch measurements back to the defined datum axis [1]. Since it was not initially possible to scan the full length of each gear tooth due to specific optical hardware issues, the first trials were planned as a comparison between tactile CMM scanning and the HP-O optical scanning over the same tooth area. Individual pitch error (fpi) on one flank of the spur gear is reported in this paper. The methodology defined here is planned for further tactile and optical measurement studies.
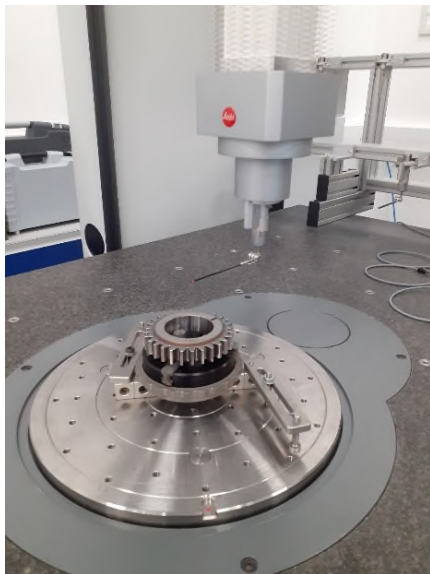
Fig 1. NGML Spur gear measured with the Hexagon HP-O (HPOAL) sensor on a Leitz PMM-C CMM at the MTC

3. Utilising ANOM and ANOR experimental control charts

When we are interested in repeatability (data recorded in time series under the same input settings), we can make use of statistical process control (SPC) charts such as the X -mR chart [6]. However, when we are looking at experimental data, we make use of a particular pair of SPC charts called Analysis of means (ANOM) and Analysis of Range (ANOR) [7]. The detection limits on ANOM & ANOR charts initially look similar to the control limits on a X-mR chart, but they differ slightly. SPC charts are used for data which is characterised by routine. On the other hand, experimental data is characterised by uniqueness. This is why control charts have a potential shortcoming as a tool for analysing experimental data. Industrial experiments will

generally involve the exploratory analysis of a limited amount of data that is, *a priori,* thought to contain real differences. Control charts are set up for the analysis of ongoing streams of data that hopefully contain no real differences. So, if a control chart is used to analyse experimental data, those differences identified as potential signals by the control chart are likely to represent real effects, though some real differences may be missed. In conclusion, the ANOM is different from the control chart for subgroup averages in two physical aspects: (a) ANOM is limited to a finite number of subgroups, and (b) ANOM requires the specification of an overall alpha level for the procedure (in this case 0.1 or 10% for ANOM, and 0.05 or 5% for the ANOR). The first of these differences prevents one from using the ANOM technique with production data. The second of these differences lets the user adjust the sensitivity of the ANOM procedure. ANOM tests whether the treatment means differ from the overall mean (also called the grand average) as will be shown.

3.1. Investigating the instrument variables on a test gear

The maximum individual pitch error (fpi) from the left flanks of a 29 tooth spur gear with a normal module of 3.9 were measured three times on the CMM. The measurements were recorded at two different point densities and at five different scan speeds to evaluate the effects of these changes as observed upon the results. The recorded results were gathered in a randomised fashion and are reported in Table 1 below.

Table 1. Experimental Trial Data

Run Order #	Blocks	Point Density	Scan Speed	fpi (μm)
1	1	B	1	3
2	1	B	2	3.5
3	1	A	1	1.9
4	1	A	5	3.5
5	1	B	5	3.8
6	1	A	3	3
7	1	B	3	3.9
8	1	A	4	3.1
9	1	B	4	3.6
10	1	A	2	2.8
11	2	B	3	3.2
12	2	B	2	4.7
13	2	A	1	1.8
14	2	A	2	2
15	2	B	5	4.6
16	2	A	5	3.9
17	2	A	3	3.1
18	2	B	4	4.4
19	2	B	1	3.8
20	2	A	4	3.7
21	3	B	4	3.9
22	3	A	4	3.6
23	3	A	3	3.3
24	3	A	5	3.6
25	3	B	3	3.8
26	3	B	1	3.1
27	3	B	2	4
28	3	A	2	2.3
29	3	B	5	4.1
30	3	A	1	2.2

3.2. Constructing the ANOM & ANOR charts

A set of three measurements were recorded for each of the ten combinations of point density and scan speed. The first variable, point density, has two levels coded as A and B (where A is higher density), while the second variable, scan speed, had five levels coded as 1,2,3,4, and 5 (where level 5 is fastest). Three questions can be asked:

1. How does the point density affect the results?
2. How does the scan speed affect the results?
3. Does any interaction exist between point density and scan speed (and is it statistically significant)?

Firstly, the data from Table 1 is plotted onto the ANOM control chart as shown in Fig 2. This process is similar to a conventional statistical process control chart, but the constants used for calculating the control limits and the terminology are slightly different. The detection limits are computed in a similar way to the control limits for the individual (X) and moving range (mR) chart. The grand average for all the data in the table is 3.373 μm and the average range is 0.68 μm. With an overall alpha level of 10 percent, the ANOM scaling factor (taken from ANOM statistical tables) for k = 10 subgroups of size n = 3 is 0.893. The ANOM detection limits in microns are calculated thus:

ANOM Detection Limits (LDL & UDL) =

$$\text{Grand Average} \pm ANOM_{.10} \text{ (Average Range)} \quad (1)$$

= 3.373 μm ± 0.893 (0.68) = 2.766 μm (LDL) and 3.981 μm (UDL)
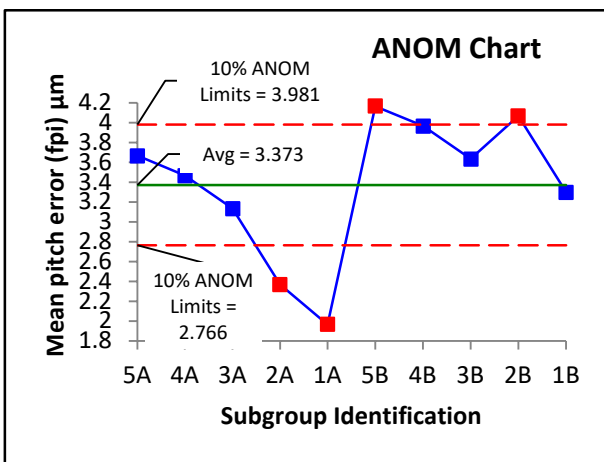
Fig 2. ANOM Chart constructed from data in Table 1
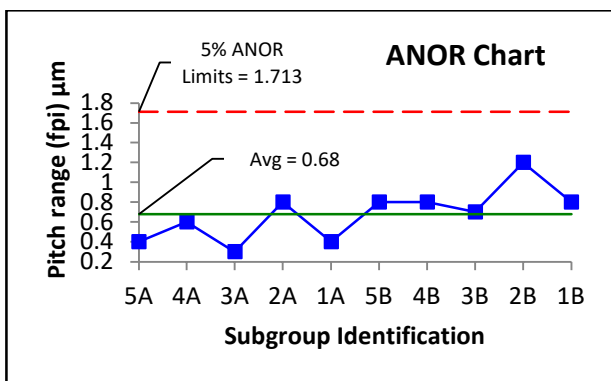
Fig 3. ANOR Chart constructed from data in Table 1

The analysis of ranges (ANOR) proceeds in a similar manner as shown in Fig 3. With an alpha level of 5 percent, and with k = 10 and n = 3, the ANOR scaling factor (taken from ANOR statistical

tables) for k = 10 subgroups of size n = 3 is 2.519. The ANOR detection limits are then calculated thus:

ANOR Upper Detection Limit (UDL) =

$$ANOR_{.05} \text{ (Average Range)} \quad (2)$$

UDL = 2.519 (0.68) = 1.713 μm

There is no lower detection limit (LDL) for this ANOR chart.

3.3. Observations

From the range (ANOR) chart it is possible to observe that each group has similar "within group" variation. Additionally, it can be seen that the point density is significant, as it is shown in the "between group" means (ANOM) chart. Each data point in each chart is the average of the three readings in Table 1. The two groups for point density defined as A and B could not fit on the same ANOM chart. By looking between groups A and B, it easy to see that the values with higher point density (A Group) have lower values and most values come down with lower scan speeds (from 5 to 1). The groups are significantly different. Since there are two predictor variables, one interaction should be checked. This interaction effect can be exploited or avoided as necessary only after it has been visualized. In the ANOM chart, the interaction can be visualised by observing the line between 3A and 2A and comparing it with the line between 3B and 2B. These are almost perpendicular, showing interaction is present. Numerical values (p values) of the statistical significance can be assigned by conducting an ANOVA test (as will be shown in 4.1).

So, in answer to the three initial questions:

Moving from higher (A) to lower (B) point density levels leads to significantly higher values for maximum individual pitch error.

Moving from higher (5) to lower (1) scan speeds levels leads to significantly lower values for maximum individual pitch error.

There is one point of interaction between scan speed and point density, and it occurs between levels 2A and 3A when compared to 2B and 3B.

In order to determine which values are more representative of the "true size" under study, further correlation work would be required by measuring the gear on an instrument with known uncertainties at the NGML. The purpose of this study is simply to determine if point density and scan speed (and their interaction) were statistically significant on the results obtained.

4. Orthogonal screening matrix

The ANOM / ANOR charts test whether the treatment means differ from the grand average or overall mean. When utilising an orthogonal array [8], it is possible to test whether multiple treatment means differ significantly from each other. To explore the effects of changing CMM parameters (or variables) on the measurement results, a factorial design matrix (or array) can be utilised. Since the output results from gear trials include many gear characteristics, the previous maximum individual pitch error (fpi) characteristic shall be considered.

4.1. Analysis via Factorial ANOVA

The matrix shown in Table 1 was generated in Minitab® statistical software. It was only necessary to specify the number of factors, the levels of factors, and the number of replications (in this case 3) for the matrix to be created. Normally, when completing trials in real time, it is recommended to do this in a random order and this order can be generated by the software. This was the case with the presented trials. Measurements were completed in the run order as shown and entered the data in the appropriate cell in the final column of Table 1. An analysis of variance (or ANOVA) test [8] was then conducted on the recorded data. The results of the analysis are shown in Table 2.

Table 2. Analysis of Variance Table for data in Table1

Source	DF	Adj SS	Adj MS	F-Value	P-Value
Model	11	14.5233	1.3203	10.26	0.000
Blocks	2	0.4847	0.2423	1.88	0.181
Linear	5	12.0773	2.4155	18.78	0.000
Point Density	1	6.1653	6.1653	47.93	0.000
Scan Speed	4	5.9120	1.4780	11.49	0.000
2-Way Interactions	4	1.9613	0.4903	3.81	0.020
Point Density*Scan Speed	4	1.9613	0.4903	3.81	0.020
Error	18	2.3153	0.1286		
Total	29	16.8387			

4.2. Observations

The results recorded in Table 1 were obtained from optical measurements when employing the HP-0 system. Analysis in Table 2 shows significant difference (p values < 0.05) for point density, scan speed, and their interaction confirming the findings of the ANOM and ANOR charts. At the time of writing the measurement trials from the optical and tactile studies are still ongoing and the results are far from complete, but the methodology shown demonstrates how results from various measurement methods could be compared. In order to see if the results of the optical and tactile results differ significantly, the graphical and numerical techniques outlined here would be utilised to make this determination. As previously stated, in order to see which methodology gave results closer to the true value, further correlation work would be required with the assistance of the NGML.

4.3. Study limitations

Due to initial hardware constraints, it was not possible to scan the full length of each gear tooth as would be required by the standard [1]. However, the methodology shown here provides a useful comparison between conventional CMM scanning and optical scanning over the same tooth area (as far in as can be achieved within the instrument constraints). This trial made use of the HPOAL sensor, and some results were inconsistent for some output parameters. The HPOAM optical probe may give more consistent results, and this will be the focus of future trials. DOE and ANOM / ANOR charts are able to investigate the effects of how changing any instrument parameters could be utilised to establish boundaries for uncertainty (both for individual sources and their interactions). Designed experiments could be applied to investigate various sources of instrument variation and sensitivity coefficients. DOE/DOX has advantages over the partial derivative method [9] since the various assumptions associated with ANOVA can (and always should) be tested using various *post hoc* analysis options as shown in Fig 4. These assumptions include that the "within group variation" is

homogeneous, no serial correlation is present between means and standard deviations, and that the residuals are normally distributed. These conditions were met during early trials.
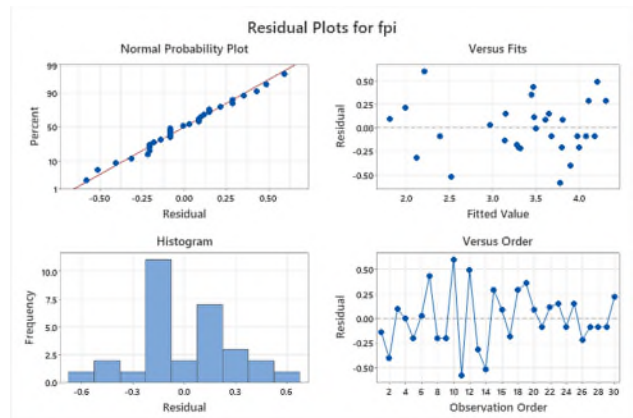
Fig 4. Plot of Residuals to test the assumptions of ANOVA

5. Conclusions

In this paper, the results of the optical gear measurement of individual gear pitch were reviewed. Firstly, the data sets were investigated utilising ANOM and ANOR charts, checking if the scanning speed and point density of the CMM sensor had an influence on the measurement results. It could be seen graphically that both predictor variables had an influence, and interaction was present. This means that both factors could be defined as significant sources of error and should be considered when developing any uncertainty budget [9]. The same data was reviewed in an orthogonal matrix/array, and with the use of modern statistical software it was simple to create the ANOVA table and confirm the graphical findings with numerical p values. All sources of variation (and interactions) not statistically significant (p > 0.05) could be removed from the uncertainty budget, and this would simplify any uncertainty calculation process since if the effects of any specific sources were not significant, then the uncertainty associated with that source could not be significant either. As point density and scan speed are significant, values for them should be defined when developing any part programs for the Coordinate measuring machine (CMM), and for any associated inspection plans.

References

1. BS ISO 1328-1-2013--[2022-03-18--03-04-03 PM]
2. PD ISO-TR 10064-1-2019--[2024-01-23--12-08-31 PM]
3. BS ISO 18653-2003--[2023-07-19--03-11-31 PM]
4. Flack D Good Practice Guide No. 41 CMM Measurement Strategies Issue 2
5. Flack D Good Practice Guide No. 43 CMM Probing Issue 2
6. 2008 *BS 5702-2:2008 Guide to statistical process control (SPC) charts for variables-Part 2: Charts for individual values PERMISSION EXCEPT AS PERMITTED BY COPYRIGHT LAW BRITISH STANDARD*
7. Donald J. Wheeler 1990 *Understanding Industrial Experimentation* Knoxville USA: SPC Press
8. R.J. Del Vecchio 1977 *Understanding Design of Experiments*
9. UKAS M3003:2022 The Expression of Uncertainty and Confidence in Measurement Edition 5

A comparative study of network sensor and laser tracker in establishing digital twin for robotic manufacturing

Zhaosheng Li[1], Francesco Giorgio-Serchi[2], Nicholas Southon[3], Andrew Brown[1], Nan Yu[1]

[1]*Institute for Materials and Processes, The University of Edinburgh, Edinburgh EH8 9FB, UK*
[2]*Institute for Mirco and Nano Systems, The University of Edinburgh, Edinburgh EH8 9FB, UK*
[3]*INSPHERE, Bristol & Bath Science Park, Dirac Crescent, Emersons Green, Bristol, BS16 7FR, UK*

s2137204@ed.ac.uk

Abstract

This study employs network sensors and laser trackers to track a robot's end-effector and assess the performance of network sensors through comparative experimentation. The establishment of a digital twin for robots using network sensors contributes to enhancing the robot's global accuracy. The novel network sensor, IONA, is capable of providing real-time 6DOF data to the robot, thus assisting in improving the robot's global accuracy. To evaluate the tracking capabilities of the network sensor two sets of experiments with different robot motion modes are designed, with a laser tracker serving as the reference benchmark. These experiments encompass linear and circular motions executed by the robot, each repeated multiple time. The robot's motion speed varies across three orthogonal directions, ranging from 0.5 m/s to 0.01 m/s, encompassing six distinct speed levels. The analysis of the collected experimental data sets indicates that the network sensor exhibits a dynamic tracking accuracy of 0.45 mm when the target motion speed is below 0.5 m/s.

Network sensor, laser tracker, robot, global accuracy, dynamic

1. Introduction

In modern intelligent manufacturing systems, robots play a pivotal role in the automation industry due to their cost-effective efficiency in handling repetitive tasks. Notably, the positional repeatability of mainstream 6-axis robots is exceptionally high, ± 0.05 mm. However, their global accuracy (absolute accuracy) exceeds ± 1.0 mm, which is 20 times less accurate than their repeatability [1]. Various factors contribute to this discrepancy in accuracy, such as the stiffness of robot hardware materials, thermal effects, payload effects, and manufacturing tolerances. In scenarios requiring robot interaction with external devices or multi-robot collaboration, enhancing the robot's global accuracy becomes crucial.

Large-volume metrology technology offers a range of solutions to improve the global accuracy of robots. The measurement systems for robots are diverse, including contact-based coordinate measuring machines (CMM), ball-bars, and non-contact optical sensors such as laser scanners, indoor Global Position System (iGPS) and photoelectric sensors [2]. There are also systems measuring robot velocity, acceleration, force, and torque using inertial sensors and piezoelectric strain gauges. Although these varied measurement systems provide flexible and efficient methods for assessing robots' static errors (pose errors) and dynamic errors (path errors), a distributed network sensor system based on photogrammetry principles can provide 6 degrees of freedom (6DoF) in both static and dynamic measurements in the workplace.

This novel network sensor system can provide real-time 6 DoF positional data (detailed in Section 2.1). According to the manufacturing company's data, the accuracy of this system is 210 μm [3]. However, due to its recent introduction and lack of comprehensive literature reviews evaluating its performance,

the measurement accuracy claimed by the manufacturer requires further verification. This paper is designed to experimentally investigate and analyze the dynamic accuracy measurement performance of this network sensor system, comparing it with the performance of a laser tracker under the same experimental conditions.

2. Equipment devices description

The experiment conducted in this paper involves three kinds of equipment: the distributed network sensor IONA produced by Insphere, the Vantage S6 Laser Trackers by FARO, and the UR5e robot from Universal Robots. These three devices are detailed in the following sections.

2.1. Network sensor

This innovative network sensor system, named IONA, is manufactured by Insphere Ltd. It consists of multiple stereo infrared cameras (nodes) arranged around the object to be measured, spherical retro-reflective targets arranged in different configurations called tiles, as shown in Figure 1.
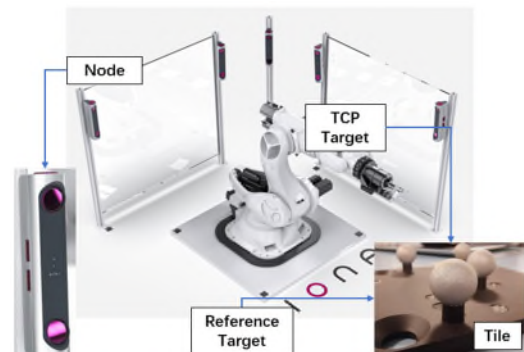
Figure 1. IONA system setup consists of nodes and tiles [4]

In Figure 1, each node of the system is an infrared camera equipped with two wide-angle lenses. These cameras capture images within their field of view and process them accordingly. Due to the retroreflective spheres' high grayscale contrast in the original images, enable the system to determine their positions in 2D images based on stereo imaging principles. Following this, a coordinate transformation process is employed to derive the spheres' 3D coordinates in space [5]. A set of tiles is affixed to the ground or a fixed base where the robot is located, and another set is attached to the robot's end-effector. During high-frequency photography by the cameras, the network sensor system provides real-time coordinates of the Tool Center Point (TCP) relative to the base.

Theoretically, a single camera can determine the coordinates; however, the distributed network's advantage lies in avoiding line-of-sight issues and providing multiple data sets for the same measurement, thereby achieving redundancy. This redundancy is further optimized in data processing, ensuring the final position data is within an acceptable precision tolerance. According to the product technical manual, the accuracy (1σ) of this metrology system is 210 μm and the measurement frequency is 10 Hz [3]. However, this often represents the manufacturer's measurement in ideal conditions. In practical use, uncertainties in this system arise from factors such as the ambient temperature of the environment, background light intensity, reflectivity of the measured object's material, the speed of the target's movement, and the number of sensors involved.

2.2. Laser tracker

The laser tracker is a high-precision 3D metrology system that integrates advanced technologies such as laser interferometry and angular measurement, primarily used in the field of large-volume spatial coordinate metrology. In robotic metrology, it is often considered one of the most reliable metrology methods. Its working principle involves the precise metrology of 3D coordinates through encoder-based angle measurement and laser time-of-flight distance measurement. In the experiment, the FARO Vantage S6 Laser Tracker was utilized, which boasts a single-point angular accuracy (2σ) of 20 μm + 5 μm/m and a distance angular accuracy (2σ) of 16 μm + 0.8 μm/m, operating at a frequency of 50 Hz [6].

2.3. Robot

In the experiment, the 6-axis UR5e robot from Universal Robots was employed to generate dynamic trajectories. This robot facilitates the easy production of trajectories and adjustment of motion speeds. It has a maximum payload of 5 kg, a reach distance of 850 mm, and a maximum tool speed of 1 m/s. The robot's pose repeatability is 0.03 mm [7].

3. Equipment setup

3.1. Equipment layout

The arrangement of the three instruments used in the experiment is depicted in Figure 2. The UR5e robot is mounted on a stable table and positioned in a corner. The network sensor (IONA) is set up in a C-formation around the robot, approximately 1.5 meters away, ensuring that each node's field of view is centered on the robot's end-effector. A set of tiles, serving as the target, is affixed to the table and remains stationary, establishing the base coordinate system reference for the network sensor. Another set of tiles is placed on the robot's end-effector to track its trajectory. The laser tracker is mounted on a tripod approximately 3.5 meters away from the robot. A 1.5-inch spherical mirror reflector (SMR) of the laser tracker is magnetically attached to the robot's end-effector.

The robot performs linear and circular motions in the three directions of the illustrated coordinate system. For each movement, both the network sensor and the laser tracker record the robot's trajectory. The obtained measurement results are compared to verify the dynamic tracking performance of the network sensor.
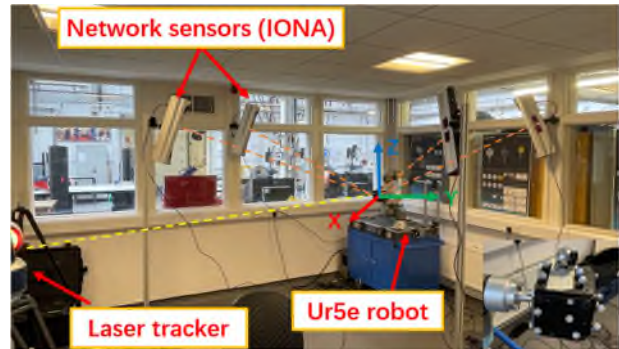
Figure 2. Experiment layout in the laboratory and the end-effector of the robot with tiles and SMR

3.2. Experiment procedure

As shown in Figure 3, the robot was programmed to perform linear reciprocating motions in three mutually orthogonal directions and circular motions on three orthogonal planes. It results in a total of six different movement trajectories, labeled as Trajectories 1-6. The robot conducted experiments at different speeds under these 6 trajectories, with 6 speed gradients ranging from 0.01 m/s to 0.5 m/s, as detailed in Table 1. This gradient of speeds was designed based on the range of tool speeds commonly used in real-world robotic applications.
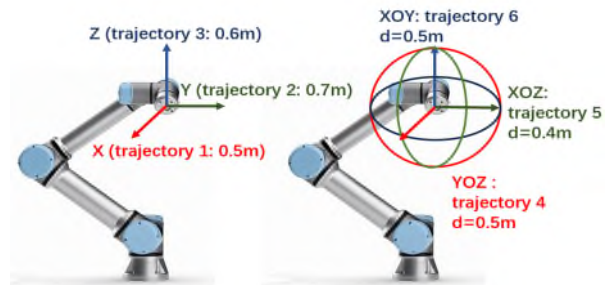
Figure 3. The robot's six motion trajectories and travel distances: Trajectories 1-3 are linear reciprocating movements in three directions, and Trajectories 4-6 are circular movements on three planes.

Table 1 Speed gradients of the trajectories

	Speed gradients from 0.01 m/s to 0.5 m/s					
Speed [m/s]	0.01	0.1	0.2	0.3	0.4	0.5

Due to the limitations of the robot's working space and its maximum reachable range, the sizes of the 6 trajectories are illustrated in Figure 3. For each of the six trajectories, the robot executed movements at six different speeds, yielding a total of 36 sets of experimental data. To minimize randomness in the experiments, the robot performed four reciprocating runs at each speed for every trajectory.

4. Results and discussion

To analyze the results, it is not feasible to directly compare the recorded results of two different metrology methods for the same robotic trajectory. In the network sensor system, the
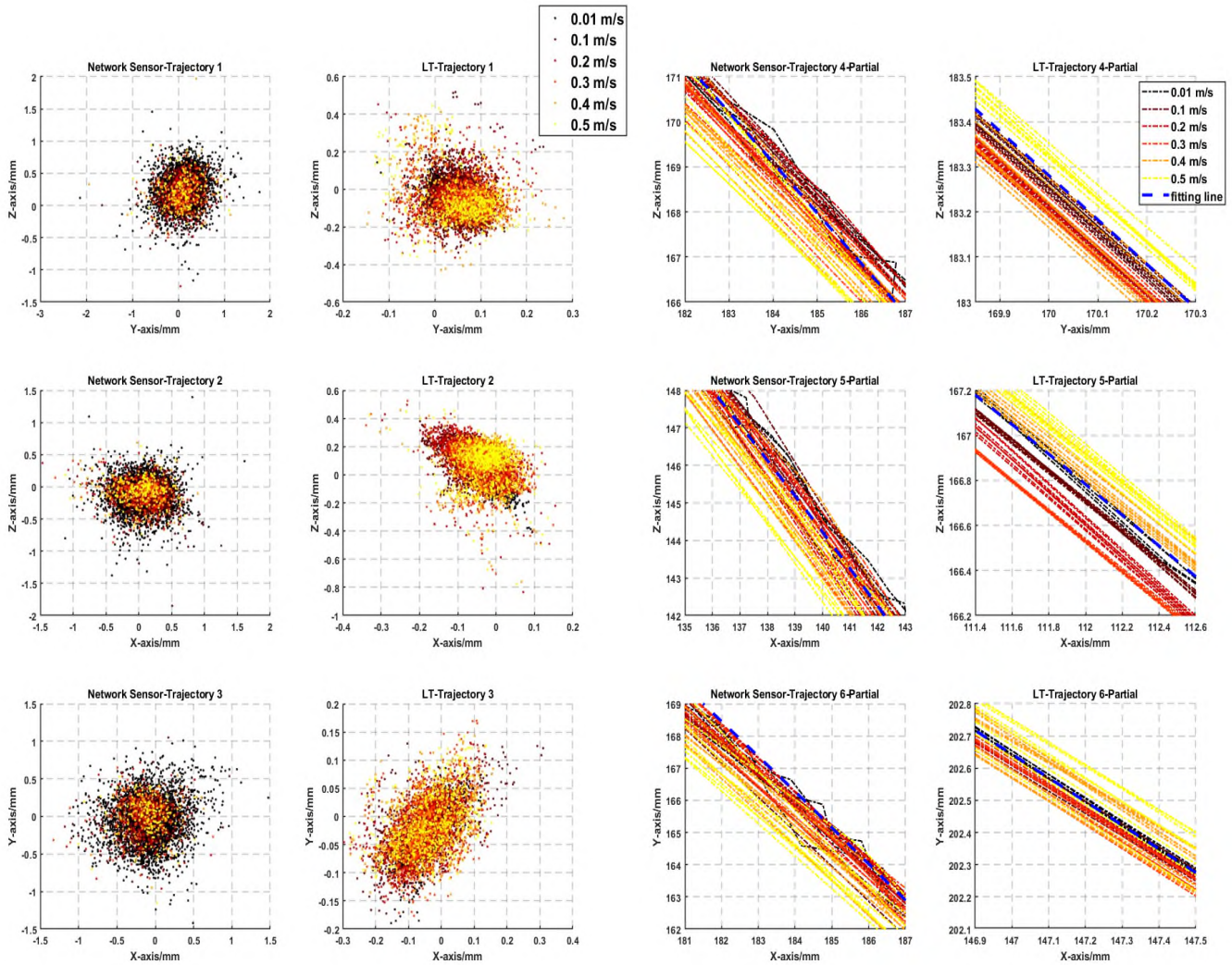
Figure 4. The 2-left columns shown the measurement of Trajectories 1-3 from both the network sensor and laser tracker, projected onto a 2D plane. The origin of each graph is positioned at the location of the fitted line. The 2-right columns display a magnified view of the measurement of Trajectories 4-6 from both the network sensor and laser tracker, projected onto the plane of the fitted circle. This includes a legend for the robot's speed variations and the fitting line.

robot's TCP coordinates are set in the software based on the tiles at the robot's end-effector, and the reference coordinates are set based on the tiles on the table. In contrast, for the laser tracker system, the reference coordinates are based on the tracker's base, and the robot's TCP coordinates are determined using the SMR. To compare the dynamic tracking performance of these two metrology systems, this paper adopts the method of reference line generation proposed by Wang et al [8].

4.1. Reference Line generation

To compare the results of the two metrology systems, the fitting was generated using the data from the six trajectories where the robot's motion speed was lowest (0.01 m/s). The fitted results are considered the actual motion trajectory of the robot in that direction and are used as the reference for comparison. For linear motions, six sets of 0.01 m/s data from both metrology systems can be used to fit six reference lines. Similarly, for circular motion, six reference circles can be fitted. The fitting for linear motion is done using linear least squares. Fitting a spatial circle for circular motion is a relatively complex task, and there are various algorithms for fitting a circle to discrete points in space. However, since the fitting data in this experiment are obtained at an extremely low speed of the robot and the theoretical circle is known, this paper uses Principal

Component Analysis (PCA) to fit the optimal plane, and then projects the point data onto this plane for fitting a planar circle.

4.2. Results analysis

Due to the difficulty of comparing 3D data, this study converted all data from 3D to 2D. In linear motion, the generated reference line in 4.1 is used as the normal vector of a plane, and all point data obtained from that trajectory are projected onto this plane. As shown on the left side of Figure 4, deviations caused by changes in the robot's speed along the same trajectory are all projected onto the plane. In circular motion, the plane where the fitted reference circle lies is used, and all points obtained at different speeds on that trajectory are projected onto this plane. As seen on the right side of Figure 4, data from spatial circular motion is also visualized in a 2D image.

From the linear motion data, it is evident that when measuring the same trajectory, the network sensor data is significantly more dispersed overall compared to the laser tracker, with a higher number of outliers. Furthermore, the data measured by the laser tracker aligns with the expectation that robot repeatability decreases with increased speed; that is, data points are more concentrated near the origin at lower speeds. However, the network sensor data is more scattered, and the effect of robot speed variation is not well-reflected in its data.

Figure 5. Mean of the distance from the measured coordinate data to the fitting trajectories for network sensor and laser tracker
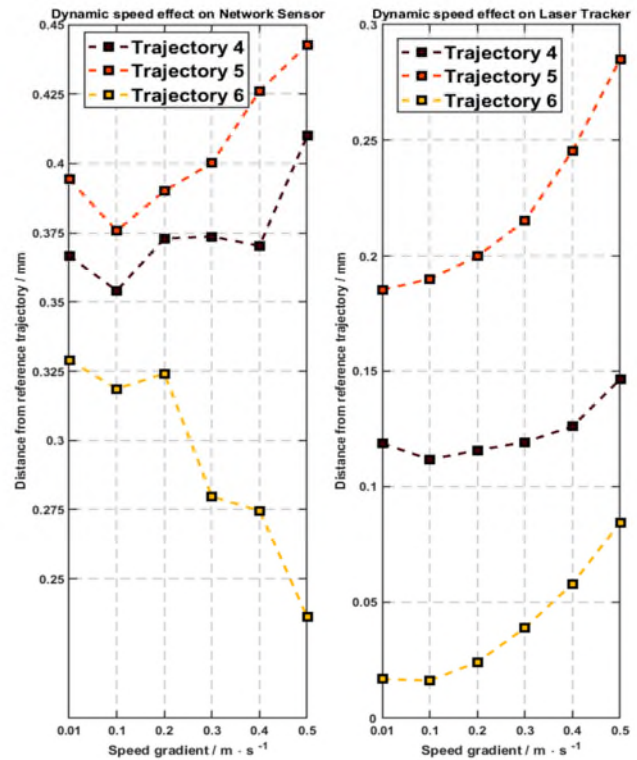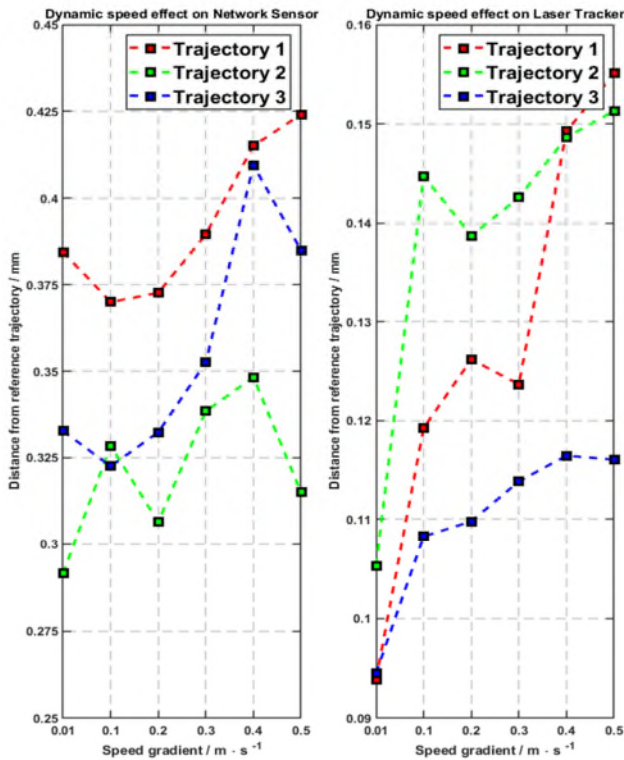
Additionally, with the increase in robot speed, the number of network sensor data samples rapidly decrease, limited by its measurement frequency of 10Hz.

In the circular motion data, a notable difference between the network sensor and laser tracker recorded trajectories is that the position of the trajectory with the lowest speed for the laser tracker is in the middle. The increase in robot speed results in the trajectory data being evenly distributed on both sides of the fitting line. In contrast, for the network sensor, the low-speed trajectory data is distributed externally, shifting towards the circle's center as the speed increases.

Figure 5 quantitatively displays the average distance of each measurement point from the fitting line under its trajectory relative to increasing speed. As the robot's speed increases, the accuracy of both the network sensor and the laser tracker generally decreases. However, the network sensor shows a paradoxical increase in precision at a speed of 0.5 m/s. This abnormal performance is speculated to be caused by the unsatisfactory measurement frequency of the network sensor under high-speed movement, which leads to insufficient sample collection. Additionally, at a speed of 0.01 m/s, the repeatability of the network sensor's measurements does not significantly improve, suggesting that the system's measurement capability cannot be enhanced by reducing target speed when it is already below a certain threshold.

5. Conclusion

In this work, the dynamic tracking performance of an infrared camera-based network sensor metrology system was validated. Linear and circular motions were set up for the robot, using the measurements from the laser tracker as an experimental control. A method of reference line generation was employed to unify the comparison standards between the two metrology systems. It was concluded that the dynamic measurement accuracy of this network sensor system is between 0.3 - 0.45 mm for target speeds below 0.5 m/s.

This novel network sensor system offers potential for robot metrology and its related applications, as well as the establishment of digital twin systems. Currently, further long-term measurements to verify its accuracy are being conducted, and the development of automated manufacturing systems based on robots and this network sensor is underway.

References

[1] Hägele, M., et al. 2016. "Industrial robotics." Springer Handbook of Robotics, 1385-1422.

[2] Norman, A. R., et al. 2013. "Validation of iGPS as an external measurement system for cooperative robot positioning." The International Journal of Advanced Manufacturing Technology **64**, 427-446.

[3] INSPHERE LTD. 2022. "IONA-Brochure_2022." Version 2022. UK: IN SPHERE LTD. Available at: https://insphereltd.com/app/uploads/20 22/06/IONA-Brochure_2022.pdf

[4] Martin, O. 2022. "Confronting the Challenges Associated with Measuring Industrial Robots." Coordinate Metrology Society Conference, 26-28th July, Orlando, USA.

[5] He, B., Chen, Z., and Li, Y. 2012. "Calibration method for a central catadioptric-perspective camera system." J. Opt. Soc. Am. A **29**, 2514-2524.

[6] FARO LTD. " 4862_TechSheet_Vantage_Max_6Probe_LT_ENG." US A: FARO LTD. Available at: https://media.faro.com/-/media/Project /FARO/FARO/FARO/Resources/2_TECH-SHEET/Techsheet_Vantage _Max_6Probe/4862_TechSheet_Vantage_Max_6Probe_LT_ENG.pd f?rev=25b7347cfd304dbd9d386e39cf4bb6d4

[7] UNIVERSAL ROBOT LTD. "ur5e-rgb-fact-sheet-landscape-a4." Denm ark: UNIVERSAL ROBOT LTD. Available at: https://www.universal-ro bots.com/media/1807465/ur5e-rgb-fact-sheet-landscape-a4.pdf

[8] Wang, Z., Mastrogiacomo, L., Franceschini, F., & Maropoulos, P. 2011. "Experimental comparison of dynamic tracking performance of iGPS and laser tracker." The International Journal of Advanced Manufacturing Technology **56**, 205-213.

Resolution enhancement of Fabry-Perot optical fiber probe for microstructure measurement

Hiroshi Murakami[1], Akio Katsuki[2], Takao Sajima[2], and Tatsumi Yoshimatsu[1]

[1]The University of Kitakyushu
[2]Kyushu University

murakami@kitakyu-u.ac.jp

Abstract

In recent years, there has been an increase in the number of devices with fine and high-aspect-ratio microstructures in the fields of semiconductors, optical communications, medicine, biotechnology, Micro Electro Mechanical Systems (MEMS), micromachines, and various nozzle holes. There is an increasing demand for precise, nondestructive measurement of the dimensions and surface roughness of these devices in order to enhance the functionality of products. Therefore, we propose an optical fiber probe to detect contact with a measured surface by incorporating a Fabry-Perot interferometer into an optical fiber tip. This paper describes the configuration of the Fabry-Perot fiber probe for microstructure measurement. Simulation results then confirmed that the wavelength shift corresponding to the measurement resolution was increased by approximately 6.9 times by making a film of the elastic resin of the reference probe 10 μm thicker than that of the measurement probe.

Microstructure measurement; Probe; Optical fiber; Fabry-Perot interferometer, Vernier effect

1. Introduction

In recent years, there has been an increase in the number of devices with fine and high-aspect-ratio microstructures in the fields of semiconductors, optical communications, medicine, biotechnology, Micro Electro Mechanical Systems (MEMS), micromachines, and various nozzle holes. There is an increasing demand for precise, nondestructive measurement of the dimensions and surface roughness of these devices in order to enhance the functionality of products [1-2]. We have developed a measurement system using small diameter optical fiber as probe [3-5]. However, when the diameter of probe shaft is less than a few μm, the laser spot diameter at the laser irradiation point becomes larger than the shaft diameter, which causes diffraction of the laser beam, which results in a problem of reduced sensitivity. Therefore, we propose an optical fiber probe to detect contact with a measured surface by incorporating a Fabry-Perot interferometer into an optical fiber tip. This paper introduces the measurement principle of the probe and simulation results of measurement resolution enhancement using the vernier effect.

2. Measurement priciple

Based on past measurement results, the resolution of probe was about 20 nm. However, some measurement objects require a measurement resolution of 10 nm or less. Therefore, we try to enhance the measurement resolution by using the vernier effect. Figure 1 shows a schematic diagram of the Fabry-Perot optical fiber probe and its optical system. Light I_{in} irradiated from a broadband SLD light source enters the measurement and reference probes with 1:1 light intensity via single-mode fiber and coupler. The fiber probe consists of the gold half mirror SM1, the elastic resin, and the probe tip coated with a gold half mirror SM2, in that order. The reference probe consists of the gold half mirror RM1, the elastic resin, and the glass substrate coated with a gold half mirror RM2, in that order. A Fabry-Perot interferometer is configured between the half-mirrors at the tip. The reflected lights I_{out_S} and I_{out_R} from the Fabry-Perot interferometer of the measurement and reference probes are again received by the spectrum analyzer via the coupler. The spectrum of the interference light received by the spectrum analyzer varies with the thickness of the elastic resin. In other words, the thickness of the elastic resin changes when the probe tip contacts the measured surface, making it possible to detect contact by measuring the spectrum of the reflected light (*e.g.*, the amount of shift in the peak wavelength). The light I_{out_S}, which is the interference light between the light I_{S1} reflected by the half-mirror SM1 and the light I_{S2} reflected by the half-mirror SM2 coated on the probe tip for measurement, and the light I_{out_R}, which is the interference light between the light I_{R1} reflected by the half-mirror RM1 and the light I_{R2} reflected by the half-mirror RM2 coated on the glass substrate for reference, respectively, interfere at the coupler, and the interference light I_{out} is received by the optical spectrum analyzer (OSA).
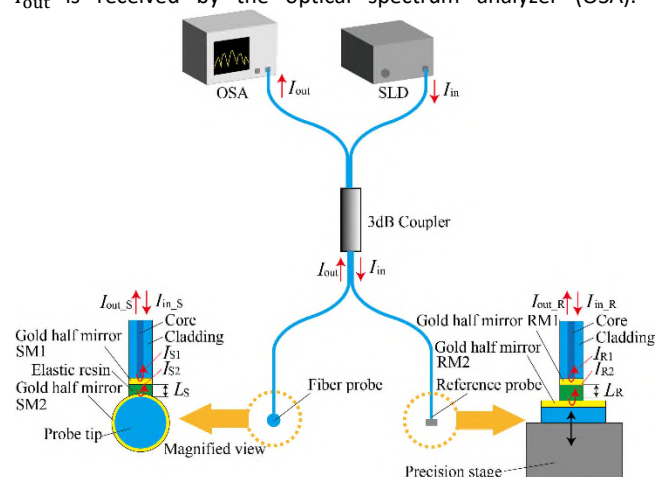
Figure 1. Schematic diagram of the Fabry-Perot optical fiber probe and its optical system.
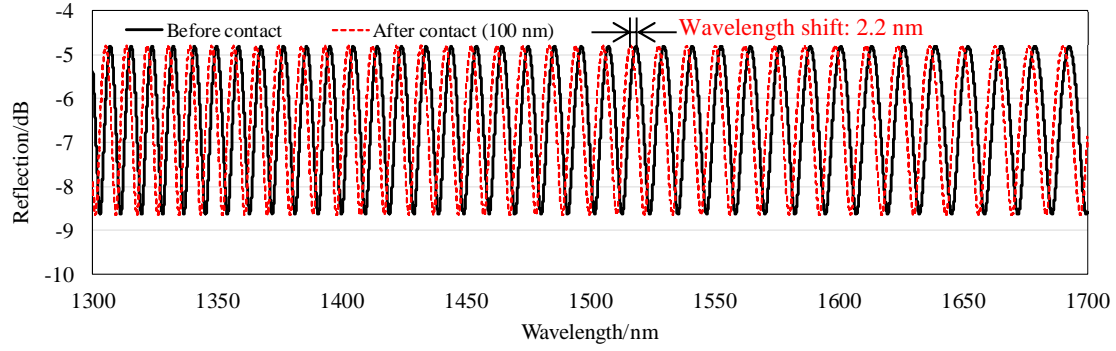
Figure 2. Interference spectra before and after contact without vernier effect.
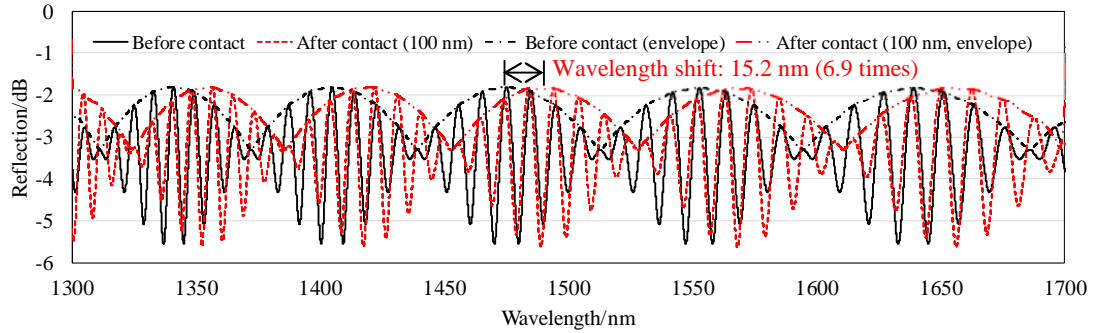
Figure 3. Interference spectra before and after contact with vernier effect (thickness difference: 10 μm).

3. Resolution enhancement using vernier effect

The interference light intensity I_{out} can be expressed by Equation (1).

$$I_{out} = I_{\text{out\_S}} + I_{\text{out\_R}}$$
$$= I_{S1} + I_{S2} + I_{R1} + I_{R2} + 2\sqrt{I_{S1} + I_{S2}} \cos \phi_1$$
$$+2\sqrt{I_{R1} + I_{R2}} \cos \phi_2 \tag{1}$$

λ：Wavelength of incident light, n：Refractive index of elastic resin, L_S, L_R：Film thickness of elastic resin, ϕ_S, ϕ_R：Initial phase of interference

The interference spectrum without the vernier effect, i.e., without the reference probe in Figure 1, is shown in Figure 2. The solid line shows the spectrum when the probe tip does not contact the measured surface, and the dashed line shows the spectrum when the probe tip comes into contact with the measured surface and the elastic resin film thickness then decreases by 100 nm. It can be confirmed that the spectrum is shifted by about 2 nm due to contact. Next, Figure 3 shows the interference spectrum when the vernier effect is utilized with the optical system in Figure 1. The thickness of the elastic resin of the reference probe was 10 μm larger than that of the measurement probe. Similar to Figure 2, the solid line shows the spectrum when the probe tip is not in contact with the measured surface, and the dashed line shows the spectrum when the elastic resin thickness decreases by 100 nm due to contact. The wavelength shift of the envelope of the interference signals reflected from the measurement and reference probes was calculated to be 15.2 nm, which is 6.9 times larger than that without the vernier effect, indicating that the vernier effect is expected to enhance the resolution by improving sensitivity.

4. Conclusions

This paper describes the measurement principle of the probe and simulation results of measurement resolution enhancement using the vernier effect. We confirmed that the wavelength shift corresponding to the measurement resolution was increased by approximately 6.9 times by making a film of the elastic resin of the reference probe 10 μm thicker than that of the measurement probe.

References

[1] Michihata M 2022 Surface-sensing principle of microprobe system for micro-scale coordinate metrology: a review *Metrol.* **2**(1) 46-72

[2] Fang F Z, Zhang X D, Gao W, Guo Y B, Byrne G and Hansen H N 2017 Nanomanufacturing—Perspective and applications *CIRP Ann. - Manuf. Technol.* **66**(2) 683-705

[3] Murakami H, Murakami H, Katsuki A, Sajima T and Uchiyama K 2023 Development of a two-step stylus with elastic hinge for microstructure measurement to improve sensitivity and vibration characteristics *Precis. Eng.* **80** 72-81

[4] Uchiyama K, Murakami H, Katsuki A and Sajima T 2023 Development of a sharp-tipped L-shaped stylus for measurement of nanoscale sidewall eatures *Int. J. Autom. Technol.* **16**(4) 489-96

[5] Murakami H, Katsuki A, Sajima T, Uchiyama K, Yoshida I, Hamano Y and Honda H 2020 Development of measurement system for microstructures using an optical fiber probe: improvement of measurable region and depth *Meas. Sci. Technol.* **31**(7) 72-81

Identification of geometric errors of rotary axes on five-axis machine tools by tactile on-machine measurement

Yue Tang[1], Xiaobing Feng[1], Guangyan Ge[1], Zhengchun Du[1]

[1]*Shanghai Jiao Tong University, Shanghai, China*

xiaobing.feng@sjtu.edu.cn

Abstract

Identification of geometric errors in machine tools is widely deployed to improve machining accuracy. While double-ball bar, R-test, and interferometry-based error calibration techniques are widely used, on-machine measurement (OMM) is increasingly available on machine tools and can be utilized as an alternative technique for calibrating geometric errors. This work proposes a method to calibrate geometric errors of rotary axes on five-axis machine tools using tactile on-machine measurement. The positions of three precision spheres mounted on the rotary table at different heights are measured by a tactile on-machine measurement system while the rotary axis is positioned at various rotational angles. Geometric errors of the rotary axis are then identified based on the measured sphere positions. A validation experiment is conducted to demonstrate the identification accuracy. After correcting for the identified errors, roundness of the circular trajectory of a single sphere mounted on the rotary table is improved by over 50%. Furthermore, the contribution of OMM probing repeatability on the error identification uncertainty is analysed. The proposed geometric error identification method is cost-effective and suitable for periodic verification of geometric errors as outlined in ISO 230-2, enabling continuous monitoring and restoration of machine tool accuracy during manufacturing operations.

Keywords: five-axis machine tools, rotary axes, geometric errors, error calibration, on-machine measurement

1. Introduction

Five-axis machine tools are vital equipment for the production of crucial aerospace components like blades and impellers [1-2]. The high precision required for the manufacture of these parts makes it imperative to maintain the accuracy of the machine tools [3]. The accuracy of machine tools tends to decrease over time due to factors such as component wear. As a result, conducting regular inspections is crucial in ensuring the maintenance of machine tool accuracy. Performing 'periodic verification' is a vital practice in the maintenance of machine tool accuracy, as emphasized by ISO 230-2. Similarly, ISO 10360-1 stresses the importance of carrying out 'interim checks' to maintain the precision of high-precision measuring tools [4]. As periodic verification necessitates more frequent testing compared to acceptance testing, testing efficiency plays a crucial role in achieving production efficiency. Geometric errors on rotary axes are commonly indirectly identified using measurement instruments, including double-ball bar, R-test, and laser interferometer, which require highly skilled operators and expensive equipment. Recently, there has been an increasing focus on applying on-machine measurement technology [5-6] to identify geometric errors. This approach allows for automated periodic accuracy checks of the machine tools. Despite its potential, this method is yet to be commercialized, with no international standards established for its use. This paper proposes a geometric errors identification method of rotary axes on a five-axis machine tool using on-machine measurement. Section 2 describes the method of geometric errors identification. Section 3 describes the geometric error identification experiment and verification. Section 4 concludes the main findings of this work.

2. Method of identification

2.1. definition of geometric errors

The method of identifying the geometric errors in the rotary B- and C- axes in five-axis machine tools is presented. Each rotary axis has six geometric errors that include three linear errors and three angular errors, as shown in Figure 1. During machine operation, the actual position of the workpiece deviates from the nominal position due to these geometric errors, resulting in machining errors in the workpiece. These geometric errors are defined with respect to the machine reference coordinate system, and therefore, the geometric errors of each of the two rotary axes can be identified independently, thus avoiding the coupling effect of the geometric errors on both rotary axes.
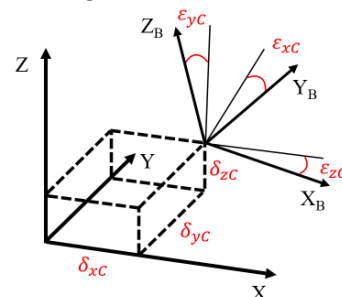
Figure 1. Illustration of geometric errors of the rotary axis

2.2. Geometric errors identification

Geometric errors identification of the C-axis is taken as an example. Three standard spheres are mounted on the rotary worktable at various heights, each positioned at a different radial distance from the rotary axis. The positions of the spheres are measured by a tactile OMM probe as the C-axis is sequentially rotated by an incremental angle. The geometric

errors of the rotary axis can be identified by calculating the deviation between the measured and nominal coordinates:

$$\begin{bmatrix} 1 & 0 & 0 & 0 & {}^M P_{nZ} & -{}^M P_{nY} \\ 0 & 1 & 0 & -{}^M P_{nZ} & 0 & {}^M P_{nX} \\ 0 & 0 & 1 & {}^M P_{nY} & -{}^M P_{nX} & 0 \end{bmatrix} \begin{vmatrix} \delta_{xC} \\ \delta_{yC} \\ \delta_{zC} \\ \varepsilon_{xC} \\ \varepsilon_{yC} \\ \varepsilon_{zC} \end{vmatrix} = \begin{bmatrix} \Delta x \\ \Delta y \\ \Delta z \end{bmatrix}$$

where ${}_A^M T \cdot {}_C^A T \cdot {}^C P = {}^M P_n$, ${}_A^M T$ and ${}_C^A T$ are transformations between coordinate systems. ${}^C P$ represents the coordinate of the sphere when the C-axis is at zero position, while ${}^M P_n$ represents the nominal coordinate of the sphere in the machine reference coordinate system. $[\Delta x \quad \Delta y \quad \Delta z]^T$ is the deviation between the measured and nominal sphere centre coordinates.

3. Experiments and verification

3.1. Experiment of geometric error identification

Figure 2 illustrates three standard spheres placed on the rotary table, each one manufactured with high precision (0.2 μm roundness) to ensure minimal sphericity error. The position of the spheres are measured at 30° incremental rotational angles of the C-axis.
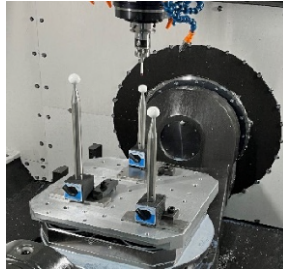
Figure 2. Experimental setup of geometric error identification

The geometric error of rotary axis at any position can be solved given the measured coordinates of the three sphere centres, as outlined in section 2.2. The identified geometric errors are shown in Figures 3 and 4.
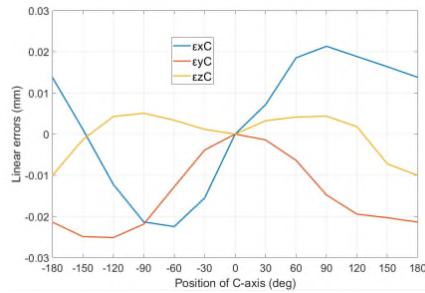
Figure 3. Linear errors identification results of the C-axis
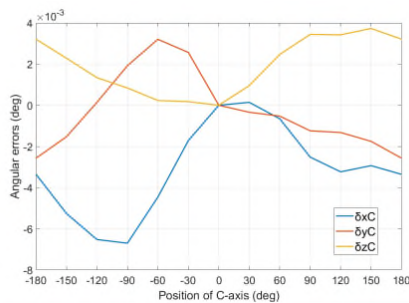
Figure 4. Angular errors identification results of the C-axis

3.2. verification

To validate the identified results, a standard sphere is installed at a new position on the rotary table, and the centre position of the sphere is measured as the C-axis completes a full rotation at an incremental angle of 30°. Roundness of the Gaussian associated circle fitted using the measured sphere centre positions are obtained. The sphere centre coordinates are corrected for the identified geometric errors according to the established error model. After correction, the roundness of the sphere circular trajectory is reduced from 7.2 μm to 3.5 μm, achieving an improvement of over 50% and demonstrating the effectiveness of the proposed identification method.

3.3. uncertainty evaluation

The Monte Carlo method, combined with the error ellipsoid, is employed to evaluate the contribution of OMM probing repeatability on the geometric error identification uncertainty. The single-point probing uncertainty in each direction is obtained by repeatedly probing the workpiece 50 times. The error ellipsoid, as shown in Figure 5, precisely depicts the input probability distribution [7]. The uncertainty in identifying the geometric errors is obtained by a Monte Carlo method that adaptively adjusts the number of simulations to reach convergence [7], which is found to be 2000. The identification uncertainties of the linear errors δ_{xC}, δ_{yC} and δ_{zC} are calculated to be 1.7 μm, 2.1 μm and 2.3 μm, respectively, while the identification uncertainties of the angular errors ε_{xC}, ε_{yC} and ε_{zC} are calculated to be 0.00045deg, 0.00036deg and 0.00034deg, respectively.
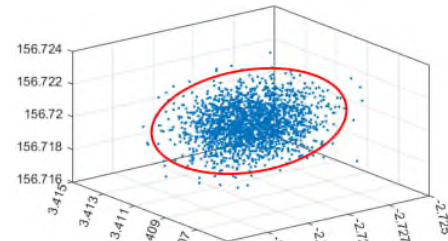
Figure 5. Error ellipsoid of single point probing repeatability

4. Conclusions

This work investigates the calibration of geometric errors of rotary axes on five-axis machine tools by tactile on-machine measurement. Method of identification is established. Experiments are performed to identify the geometric errors using three standard spheres by on-machine measurement. Six geometric errors are identified by the proposed method. The results of identification indicate that the correction effectiveness in on-machine measurement surpasses 50%, validating the identification method. Additionally, the adaptive Monte Carlo method based on the error ellipsoid is utilized to evaluate the identification uncertainty, thereby illustrating the identification outcome's reliability. This approach allows for automated periodic accuracy checks of the machine tools, which enables consistency in machining quality. Future research for improving correction performance will concentrate on identifying position-independent geometric errors caused during machine tool assembly, alongside simultaneous identification of position-dependent and position-independent geometric errors.

References

[1] Ibaraki S and Okumura R 2021 Int J Mach Tools Manuf 163 103702
[2] Lasemi A, Xue D and Gu P 2016 Meas Sci Technol 27 055004
[3] Li H, Zhang P and Deng M 2020 Meas Sci Technol 31 055201
[4] Feng X, Kinnell P and Lawes S 2016 Proc. 16th Int. euspen Conf. Jun
[5] Ge G, Du Z and Feng X 2020 J. Precis. Eng. 63 206-213
[6] Huang N, Zhang S, Bi Q and Wang Y 2016 Int J Adv Manuf Technol 84 505–512.
[7] Tang Y, Feng X, Ge G, Du Z and Lv J 2023 Meas Sci Technol 35 035022

Refraction effects on a Structured Laser Beam as a reference line for alignment

Witold Niewiem[1,2] , Jean-Christophe Gayde[1], Dirk Mergelkuhl[1]

[1]CERN – European Organization for Nuclear Research, Switzerland
[2]ETH Zurich, Switzerland

witold.niewiem@cern.ch

Abstract

A Structured Laser Beam (SLB) is a pseudo-non-diffractive beam characterized by an optical intensity profile resembling a Bessel Beam. SLBs are known for the small divergence of their inner core (i.e., 10 µrad) during long-distance propagation (i.e., 900 m) making them suitable for establishing a reference line for an offset measurement. However, the propagation of laser beams through an inhomogeneous medium causes light path deviation, introducing constraints on reference lines for particle accelerator alignment. Historically, vacuum systems have addressed atmospheric refraction influences, yet their installation poses challenges such as vacuum forces, reflections inside a vacuum pipe and symmetry breaking of an SLB. In addition, the sequential measurement adds other constraints connected to the synchronisation of the multipoint measurement system. This paper investigates atmospheric refraction effects on SLBs in a 140-meter underground laboratory, assessing SLB straightness using the Hydrostatic Levelling System (HLS) and Wire Position Systems (WPS). The results reveal straightness in the horizontal and vertical directions under 400 µm, albeit with the standard deviations reaching 580 µm. These findings provide insights into the feasibility of SLB-based alignment systems for particle accelerators.

Alignment, Laser, Measurement, Positioning

1. Introduction

Particle accelerators impose stringent demands on the alignment of their elements, reaching 20 µm within a length of 200 m [1]. Generally, the techniques used for accelerator alignment refer to either gravity or a straight line.

One of the systems that exploits the gravitational field is the Hydrostatic Levelling System (HLS). The HLS serves as the primary vertical reference at the interaction points for the High Luminosity Large Hadron Collider (HL-LHC). The HLS utilizing capacitive sensors demonstrates a repeatability of 2 µm and an accuracy of 10 µm [2].

Another category of systems involves offset measurement with respect to reference lines in the horizontal or vertical direction, established in space using either a physical object or an optical axis. The Wire Positioning System (WPS) utilizes capacitive sensors for continuous transverse offset measurement relative to a stretched wire, achieving a measurement resolution of 0.1 µm and a sensor accuracy of a few micrometres [3]. The WPS primarily measures the transversal offset but can be used to determine the vertical deviations by combining information acquired by the HLS and the catenary reconstruction [4].

Establishing a straight-line reference for accelerator alignment sometimes involves an optical beam. However, the divergence of light poses limitations on long-distance propagation. To address this, various laser systems have been proposed [5], [6]. The future system based on the Structured Laser Beam (SLB) shows particular advantages in beam divergence.

An SLB represents a pseudo-non-diffracting beam with a transversal intensity profile similar to a Bessel Beam. The transversal intensity profile of an SLB is characterized by a narrow inner core surrounded by concentric rings. The low divergence of the inner core reaching 10 µrad, which was experimentally tested over 900 m is promising for establishing a straight reference line. The generation principle and main properties of an SLB were detailed in the previous work [7].

However, the potential of an SLB for alignment may be limited by the symmetry breaking of the beam. This phenomenon, observed by Polak [8] occurs when the transversal intensity profile is obstructed by an asymmetric obstacle. The influence may be especially detrimental for narrow propagation paths where a large portion of the profile is covered resulting in a transversal change in the inner core position.

Atmospheric refraction is one of the most significant limitations to long-distance optical alignment due to its influence on the alignment reference straightness. In the atmosphere, light bends due to local differences in the refractive index of air. To mitigate the effect of refraction, a vacuum pipe with a pressure of around 0.01 mbar was introduced [5]. Other institutes, inspired by pioneering works at SLAC, installed vacuum systems at KEK [9] and DESY [6].

The objective of this paper is to quantify the influence of refraction on the straightness of the laser beam in the 140 m underground tunnel. The investigation assesses the refraction influence on the SLB in atmospheric pressure based on the WPS and HLS measurements, which was not studied before. In addition, other sources of errors that limit the alignment performance are discussed in the paper together with potential harm reduction measures.

2. Methodology

The long-distance test was conducted in an underground tunnel with a total measurement setup length of 140 m. The setup comprises seven metrological plates made of invar [10].

On each plate, sensors for three different systems (HLS, WPS, and SLB) have been installed, as illustrated in Figure 1.
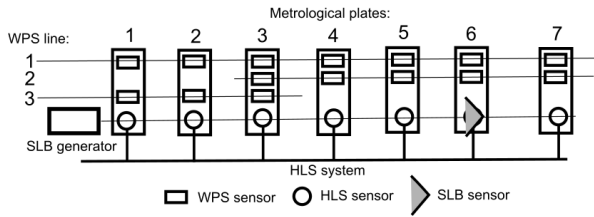
Figure 1. Experimental setup in the 140 m tunnel of HLS, WPS and SLB.

For the free air test, a 3.5-inch modified Taylor-Hobson ball was used as a housing for the camera (Basler a2A5328-15umPRO) with a chip of 14.60 mm x 12.62 mm. The ball was positioned directly on the conical top of the HLS sensors as shown in Figure 2. The perpendicularity of the camera coordinate system with respect to the laser line was ensured using a spirit level mounted on the ball, and a mirror installed in front of the ball was used for autocollimation. The generator for the initial two measurement series was placed at the beginning of the line in front of plate 1, and for the subsequent two measurement series, it was positioned behind plate 7. A single sensor was manually displaced between different metrological plates during the measurement. The typical acquisition period for each position has been 10 minutes with a frequency of 2 Hz. For the analysis, the arithmetic mean has been calculated.

Figure 2. The camera mounted in the Taylor-Hobson ball adapter on the conical top of the HLS sensor (left) and the WPS sensor (right).

The algorithm chosen for the measurement of an SLB in the images was the centre of gravity with gamma correction, as described in [11]. This algorithm enables precise detection of the inner core position while maintaining an appropriate measurement frequency.

3. Results

The transversal intensity profile of an SLB is shown in Figure 2. The two images were acquired using the CMOS chip at the middle plate (number 4) after 70 m and at the last plate (number 7) after 140 m of propagation. In the pictures, the inner core and concentric rings are visible, and the inner core fits well within the camera frame, allowing for the detection of its centre of gravity.
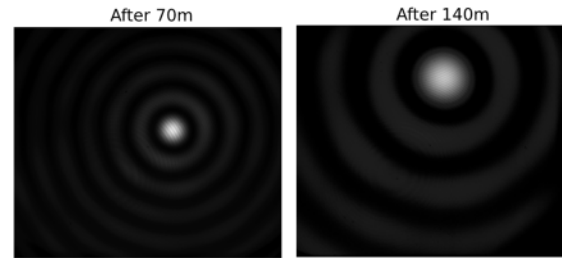
Figure 3. The transversal intensity profiles after 70 m and 140 m of propagation.

In Figure 4, the results of free air propagation along seven metrological plates are presented. The horizontal and vertical offsets of an SLB line with respect to the straight line, measured by WPS and HLS, are displayed. Absolute deviations are comparable in both directions and are smaller than 400 µm. When the distance is limited to 100 m, deviations do not exceed 100 µm. Additionally, the standard deviations of the measured position are provided. The maximum standard deviation of the horizontal position is twice as large as the vertical. The standard deviations across all series of measurements are consistent.
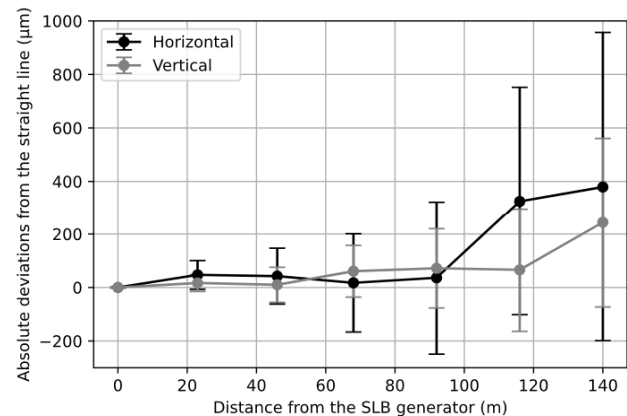
Figure 4. Results of the horizontal and vertical straightness along with the standard deviation of an SLB for 140 m propagation in the tunnel compared to WPS and HLS references.

4. Discussion

The results demonstrate the accuracy of offset measurements based on the SLB laser reference line. An SLB may enable measurements in particle accelerators, depending on a specific alignment task. By leveraging the low divergence of the inner core, the SLB laser line could have various applications, potentially replacing Gaussian beams.

The bending of an SLB propagating in a non-homogeneous medium excludes its exploitation for the most stringent alignment tasks, especially taking into account high standard deviation. The bending of the SLB line is mainly induced by a temperature gradient along the propagation path.

The test tunnel exhibits thermal stability, with a daily temperature variation at 0.005 °C for the base slab and 0.082 °C for the air as reported in previous investigations [12]. Tests conducted at the tunnel during a previous study, using a 2.5 m long rod with six thermometers positioned at 10 locations along the tunnel, suggest air temperature differences reaching up to

3 °C [13], see Figure 5. However, since the gradient was measured using a single rod displaced from one position to another, the results are dynamic in time. The SLB is nearly horizontal as it passes above the HLS conical sockets aligned vertically within a few millimetres. This implies that the effective temperature gradient is even less pronounced.
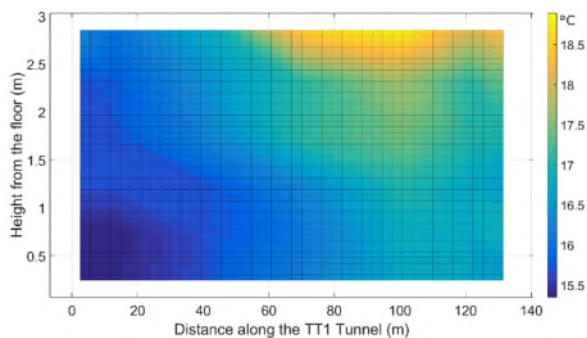
Figure 5. The temperature distribution measured in the test tunnel for another experiment [13].

Despite the excellent thermal stability in the test tunnel, which lacks the active ventilation and electronic systems present in accelerator facilities, it is not sufficient to provide a homogeneous temperature gradient. To utilize an SLB for more challenging tasks, mitigating the effects induced by atmospheric refraction is imperative. While atmospheric modelling seems like an obvious solution, its limited effectiveness has been demonstrated [14]. Refraction dynamically changes over time, and even small deviations can significantly influence the light path, given its considerable length. Monitoring refraction would require a dense grid of temperature sensors along the propagation path, ensuring unbiased readings despite small temperature differences. Ideally, temperature data acquisition would be synchronized with laser data measurements.

The SLB line direction may be unstable over time, potentially due to noise in the power supply or heating of the generator. Similarly, the inclination of the generator, treated as a rigid and constant entity over time, may be induced by vibrations and movements of the Earth's crust. By measuring the position of the inner core at multiple places along the SLB line at the same moment, it becomes possible to mitigate temporal changes in the laser line direction.

Refraction in the tunnel environment presents different characteristics compared to refraction observed in surface measurements. In contrast, as shown in Figure 4, the horizontal deviations are larger than the vertical deviations. The well-known layering of the air, in accordance with the gravitational vector, is recognized as typical behaviour of the temperature gradient in geodetic measurements on the surface. However, in underground tunnels, the effect of layering is not as visible, especially when the laser passes closer to the tunnel walls. Additionally, other air movements exist in the tunnels connected to ventilation that differentiate the atmosphere behaviour underground from that on the surface. Therefore, it cannot be excluded that horizontal errors induced by atmospheric refraction may be more detrimental than vertical ones.

The most well-known solution to reduce refraction in a non-homogeneous medium is to use a vacuum system. While these solutions have proven to be effective, they may face challenges due to the contraction of the vacuum system, impacting the accuracy of the alignment system. The vacuum system shrinks upon reaching operational pressure, posing potential problems for the transfer and stability of relative alignment between the sensor and the measured object. Additionally, vacuum installations must adhere to strict technical conditions of tightness, making them a relatively expensive and fragile part of the alignment system.

The vacuum pipe is typically of limited diameter to reduce costs and avoid reserving large space in the precious underground environment. This limitation brings the problem of symmetry breaking, which can potentially deviate the straight reference line. Moreover, the propagation of an SLB in the steel vacuum pipe may introduce reflections of light, potentially reducing the quality of the detected image due to interference from both direct and reflected light reaching the sensor.

The alternative to the vacuum system may be propagation in a closed pipe under atmospheric pressure. The air inside the pipe can be additionally homogenized using a ventilation system. This approach has the advantage that shrinkage is limited, and expensive equipment is not necessary. However, the problems of symmetry breaking and reflection inside the pipe may still be detrimental to the alignment system. This type of solution has not been used in any accelerator facility yet.

5. Conclusion

The study highlights the straightness of SLB in an underground tunnel of 140 m. The deviations from straightness in the horizontal and vertical directions are under 400 μm, with standard deviations reaching 580 μm, which is considered a large value compared to their magnitude. Although an SLB can be well-suited for diverse applications, challenges arise during free air propagation over hundreds of metres due to atmospheric refraction. To address this issue, the most effective solution appears to be the adoption of a vacuum system. However, potential limitations such as system contractions, symmetry breaking, and light reflections in the vacuum pipe need further investigation, making them crucial areas for subsequent research.

In addition, alternative solutions to the vacuum system should be studied to avoid demanding infrastructure and, in some other way, control the conditions along the propagation path. Such a solution may involve a covered space with additional ventilation to avoid the layering of the air. Another important aspect to increase accuracy is proposing a simultaneous measurement system along the straight line, which would help with laser line drift and changing conditions over time.

The SLB exhibits potential for precise measurements, contingent on the implementation of appropriate strategies to mitigate atmospheric effects.

Acknowledgement

References

[1] Leao R J, Baldo C R, Da Costa Reis M L, Trabanco L A, 2018, Engineering survey planning for the alignment of a particle accelerator: Part {I}. Proposition of an assessment method, DOI 10.1088/1361-6501/aa9dc4
[2] Herty A et al., 2017 Technical challenges for HL-HLC alignment and associated solutions, Copenhagen, Denmark, DOI 10.18429/JACoW-IPAC2017-TUPIK085

[3] Herty A, 2009, Micron precision calibration methods for alignment sensors in particle accelerators, Nottingham Trent University, https://irep.ntu.ac.uk/id/eprint/364*J. Biomech.* 37 1733-41

[4] Fleig L, Herty A, 2022, Vertical shape determination of a stretched wire from oscillation measurements CERN-BE-2023-017

[5] Herrmannsfeldt W B, Linac alignment techniques 1965, IEEE Trans Nucl Sci, vol. NS-12, no. 3, pp. 9–18, 1965, DOI 10.1109/TNS.1965.4323586

[6] Kamtner D and Prenting J, 2006, Straight line reference system (SLRS) for the adjustment of the x-ray free-electron laser (XFEL) at DESY, in 9th International Workshop on Accelerator Alignment

[7] Niewiem W, Polak K, Dusek M, Mergelkuhl D, Gayde JC, Wieser A, and Sulc M, 2023, "Variation of structured laser beam pattern and optimization for an alignment reference line creation," Opt. Express 31, DOI 10.1364/OE.503016

[8] Polak K, Gayde JCH, Sulc M, Structured laser beam for alignment and large-scale metrology, 2022, Euspen's 22nd International Conference & Exhibition, Geneva, CH, May/June 2022

[9] Suwada T, Satoh M, and Kadokura E, 2010, Experimental study of new laser-based alignment system at the KEK B-factory injector linear accelerator, Review of Scientific Instruments DOI 10.1063/1.3504370

[10] Mainaud Durand H, Pfingstner J, Rude V, 2017, Micrometric Propagation of Error Using Overlapping Stretched Wires for the CLIC Pre-Alignment, 8th International Particle Accelerator Conf.

[11] Dusek M, Polak K, Gayde J C, Sulc M, Mergelkuhl D, Niewiem W., 2022, Detection of structured laser beam centroid and its use for alignment, 16th International Workshop on Accelerator Alignment

[12] Azaryan N, Budagov J, Lyablin M, Pluzhnikov A, Gayde J-Ch, Di Girolamo B., Mergelkuhl D, 2017, Physics of Particles and Nuclei Letters DOI 10.1134/S1547477117060206

[13] Nikolitsas K, 2021, A methodology for correcting refraction in vertical angles for precise monitoring in tunnels, Journal of Civil Engineering and Architecture, DOI 10.17265/1934-7359/2021.07.006

[14] Polak K, Gayde J C, Sulc M, 2022, Structure laser beam in non-homogeneous environment, 16th International Workshop on Accelerator Alignment

Calibration of reference spheres by double-ended interferometry

Tillman Neupert-Wentz[1], Guido Bartl[1], René Schödel[1]

[1]*Physikalisch-Technische Bundesanstalt*

Tillman.Neupert-Wentz@ptb.de

Abstract

Reference spheres are a standard tool for the calibration of coordinate measuring machines (CMMs). Typically, the calibration of a reference sphere considers the diameter and the sphericity on the equator. Because spheres in CMMs form the foundation of dimensional 3D metrology, it is important to develop methods that can ensure low uncertainty, easy manipulation and short calibration times with regard to other interferometric calibration techniques, for example those of the Avogadro project [1]. The required improvements are, firstly, to provide a diameter topography, and secondly, to decrease the measurement uncertainty. To fulfil these requirements, a new measurement setup has been proposed. The setup utilises PTB's double-ended interferometer (DEI) which has originally been developed for gauge block calibrations without wringing. By adding focusing optics to the measurement path, measurements on spheres can be done through interference of plane wavefronts.

In this work, the initial implementation of the proposed modifications is presented. First results are validated, and the required measurement uncertainty budget is compiled. Based on the experience of the first measurement campaign, possibilities for improvement are identified and presented.

Interferometry, reference spheres, metrology

1. Introduction

The ever-increasing industrial and scientific requirements for high-accuracy CMMs demand improvement of the calibration of such devices. A major contributor to uncertainty is the calibration of reference spheres. These spheres are used for calibrating CMM styli. To meet those demands, an extension of PTB's double-ended interferometer has been proposed [2]. This new setup aims to decrease the measurement uncertainty of calibration of reference spheres. In addition to the standard calibration data, which contains a diameter and the sphericity along the equator, this setup will provide a diameter topography. In this work, the local topography of the sphere under test (SUT) is measured. The surface covered by the local topography is defined by the system's field of view. Future work

will include a positioning system to cover the whole surface of the SUT.

First the implementation of the DEI with the proposed extension is introduced. The evaluation method is presented. Then measurements on a 30 mm reference sphere are shown and discussed. A lookout on future developments is given, and the results are concluded.

2. Experimental setup

PTB's DEI, which is situated in a temperature-controlled vacuum chamber (ΔT_{24h} = ±5 mK; p = 10^{-4} hPa), consists of two Twyman-Green interferometers that share the same extended collimated light source (diameter = 80 mm). The first beam splitter divides the incident light into two partial beams, one for each interferometer (side A and B, Figure 1). Each side contains
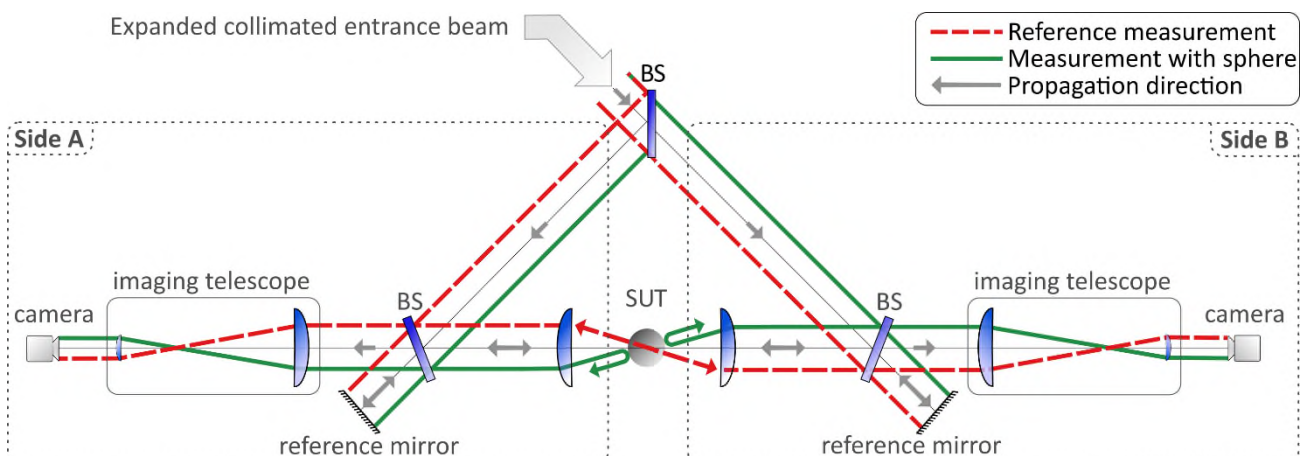
Figure 1. Setup of PTB's DEI with exemplary sections of the beam path. BS: beam splitter, SUT: sphere under test. In reference measurements the sphere is removed from the beam path.

another beam splitter which transmits the beam to the reference mirrors and reflects it towards the SUT, respectively.

Therefore, the measurement paths of each interferometer are on the same optical axis with opposite directions. Focusing optics are in front of the SUT. The centre of the SUT is placed in the coinciding focal point of these optics. Therefore, the focused beams have a right angle of incidence on the SUT. After reflection, the beam is recollimated through the optics. After superimposition with the reference beams, the interference pattern is imaged on CMOS cameras through an afocal optical system. Without the SUT in the measurement path (reference measurement, section 2.1.) this configuration yields a telescope with a magnification of 1.

Plano-aspheric lenses were chosen for this work. With a numerical aperture of 0.14 the chosen lenses provide an angular field of view of 16°. Lens topography measurements were used to select the best lenses from a batch of four. All lenses exhibit manufacturing artefacts typical for aspheric lenses. An example of such topography can be seen in [3]. The peak-to-valley value of the topography ranged from λ/6 to 2λ (at 633 nm).

For phase retrieval a five-step phase shifting algorithm is used [4]. Phase steps are introduced through piezoelectric movement of the reference mirrors.

2.1. Diameter evaluation

The evaluation method is derived in [2]. The calculation of the SUT's diameter requires two measurements: one with the SUT inside the telescope and a reference measurement with the SUT removed from the beam path. The beams then propagate through the empty telescope.
Figure 2 portrays exemplary beam paths to clarify the variables used in the equation below, which apply for the whole aperture. This set of four beam paths is necessary to calculate the diameter.

$$d_{sphere} = \frac{L_{A,ref} + L_{B,ref}}{2} - \frac{L_A + L_B}{2} \qquad (1)$$

With L the corresponding path length, index A/B denoting the two output sides of the interferometer and index ref the reference measurement without the SUT in the beam path.

To increase the unambiguity interval beyond λ/2, the coincidence criteria is applied [5]. Therefore, two iodine-stabilised lasers are used: a frequency doubled Nd:YAG laser (λ = 532 nm) and a HeNe laser (λ = 633 nm). Doing so sets the unambiguity interval to 1.6 μm.
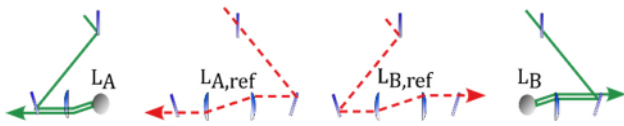
Figure 2. Path length L for sphere and reference measurement for a single diameter. Indices A/B correspond to the output side of the interferometer (Figure 1). Index ref refers to the reference measurement.

3. Measurement results

The SUT is a ceramic aluminium oxide reference sphere with a nominal diameter of 30 mm. Due to the chromatic focus shift of the lenses and a subsequent increase in uncertainty, only data for one wavelength (532 nm) will be presented.

Table 1 compares a tactile measurement of the diameter of the SUT with the result of the interferometric measurement. The tactile measurement was provided by an accredited calibration laboratory. The shown diameter obtained from the

Table 1. Comparison of SUT with tactile and interferometric measurements. The location of the measurements below, is show in Figure 4. Coverage factor k = 1.

	Value / mm	Standard uncertainty / nm
Tactile	29.99274	150
Interferometric	29.99279	190
Difference	0.00005	

interferometric measurement is taken from the centre of the field of view of the lenses. Due to the effects described in the following paragraph, the central diameter is shown instead of the mean diameter over the field of view. The difference to the tactile measurement is 50 nm, which agrees within the measurement uncertainties.

Figure 3 displays the phase topographies of the measurement. Figure 4 shows the diameter topography calculated from the phase topographies in Figure 3 using Equation 1. Note that the average diameter is subtracted from the shown topography for better readability. In this topography, multiple artefacts are visible like the concentric rings that are visible at 2°, 4° and 8°. The shape of theses rings is consistent with the results of the lens topography measurements. Any aberration, including
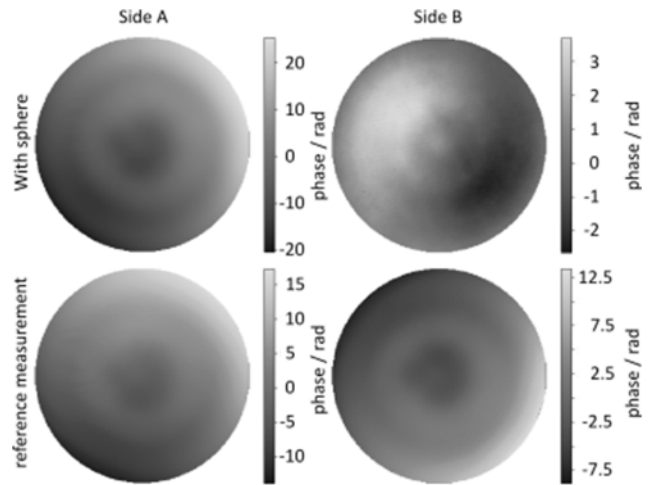
Figure 3. Phase topography of measurement with sphere and reference measurement for each interferometer side.
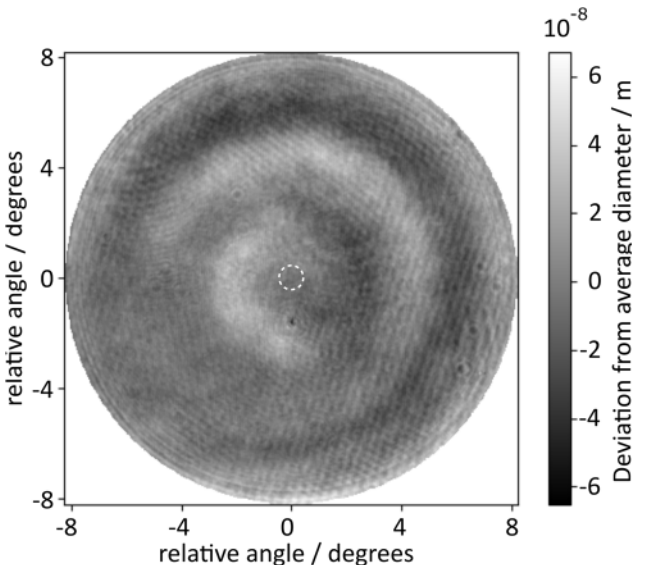
Figure 4. Deviation of the diameter topography from the average diameter within the field of view. The dashed circle marks the target position of the measurements shown in Table 1. Average diameter = 29.99309 mm.

Table 2. Major uncertainty contributions to the interferometric measurement shown in Table 1.

Contribution	Uncertainty	Sensitivity	%	Contribution
Coordinate misallocation	170 nm	1	82	170 nm
Position uncertainty	65 nm	1	11	65 nm
Parasitic reflection side A	0.66 rad	$4.24 \cdot 10^{-8}$	2.2	28 nm
Parasitic reflection side B	0.66 rad	$4.24 \cdot 10^{-8}$	2.2	28 nm
Phase change on reflection and roughness side A	40 nm	0.5	0.6	20 nm
Phase change on reflection and roughness side B	40 nm	0.5	0.6	20 nm

manufacturing artefacts, causes a misallocation of coordinates on the SUT with respect to the coordinates on the camera. This leads to a miscalculation of the diameter. The aberrations are thus transferred to the diameter topography. Furthermore, high frequency periodic structures are visible. These ripples are caused by parasitic reflection within the interferometer, i.e. between the backside of the beam splitters and the surfaces of the aspheric lenses. Every optical component within the interferometer has an anti-reflection coating with a residual reflection below 0.5 % at the relevant wavelengths. Additionally, the bulk material of the beam splitters has a 3 mrad wedge angle. Due to the interaction between two beam splitters and a reference mirror, the angle of certain parasitic reflections to the optical axis becomes zero. Therefore, some reflections from the beam splitters backside reach the camera and cause unwanted interference.

4. Uncertainty

Table 2 contains the major contributions to the measurement uncertainty of the interferometric measurement displayed in Table 1.

The largest contribution is the coordinate misallocation. This contribution is estimated through the residual aberrations after alignment. Therefore, it not only depends on the quality of the lenses but also on the alignment of the system. From the residual aberrations a maximal deviation between diametral points on the SUT is estimated. The difference between the nominal diameter and the chord that connects two deviated points amounts to the uncertainty.

Position uncertainty describes the accuracy with which the position of the measurement on the sphere can be determined. The accuracy is estimated to be ±2.5°. Within this range, the peak-to-valley value is determined which yields the uncertainty value.

Besides the parasitic reflection originating from the beam splitters as described in the previous paragraph, also, the residual reflection of the lens surfaces must be considered. Therefore, three surfaces must be considered of which the backside of the central beamsplitter and one surface of the lens are flat, and the second surface of the lens is curved. For simplicity the aspheric surface of the lens is approximated with a spherical surface that has the same focal length. The amplitude of the beam that is reflected from the curved surface is attenuated by the inverse square law. The orientation of the lenses shown in in Figure 1 indicates that the beam does not hit the flat surface of the lenses perpendicularly. Therefore, the reflected beam is divergent. To determine the influence, the amplitude of each parasitic reflection relative to the amplitude of reference and measurement beam must be evaluated. The relative intensity is determined through the losses inside the beam path and residual reflection of the anti-reflection coatings. The parasitic reflection effects the measurement for both sides of the interferometer independently, hence it must be considered twice.

Phase change in reflection and roughness is a well-known source of uncertainty of double-ended-interferometers in absolute length measurements [6]. The phase change in reflection deviates from 180° for non-dielectric materials. This moves the apparent plane of reflection away from the plane of mechanical contact depending on the complex index of refraction. Similarly, the apparent plane of reflection is moved through surface roughness. The rougher a surface, the deeper light can penetrate the SUT's surface. Hence the interferometric length will appear smaller than the mechanical length. Since no calibration method for phase change and roughness is available, literature values for ceramic gauge blocks where used [7,8]. This can only be a rough estimation but since the contribution is rather small (<1%) even being off by a factor of two, does not affect the result notably. Therefore, this estimation is deemed acceptable as long as other contributions retain their dominant influence. The approximation must be revised when the contribution of the coordinate misallocation is reduced. This effect also occurs on both sides of the SUT, therefore it also has to be considered twice.

5. Conclusion

The measurement setup proposed in [1] has been implemented. These first measurements agree with the calibration diameter within the measurement uncertainty. Although the uncertainty of the new method is still larger than that of the (tactile) calibration, these measurements can be used to identify opportunities for further improvement.

First the sensitivity to manufacturing artefacts or for that purpose all aberrations and their transmission behaviour to the diameter topography are visible. Whilst the lenses used are already the highest quality, that is available off-the-shelf, the topography measurements have shown that there is a wide range of quality. Subsequently a reduction of the influence of manufacturing artefacts can be achieved by sourcing more lenses and picking the best ones.

The influence of the parasitic reflections can be addressed through a reconfiguration of the setup. Instead of using lenses, which always have surfaces that cause parasitic reflections, off-axis-parabolic mirrors could be utilised. This would not only reduce the number of pass-through optical surfaces to zero but also eliminate any chromatic effects within the optical setup.

At last, a positioning unit will be developed that will enable the sphere to be rotated in both axes to be able to measure a full surface topography.

References

[1] Bartl G, Bettin H, Krystek M, Mai T, Nicolaus A, Peter A 2011 Volume determination of the Avogadro sphere of highly enriched 28Si with a spherical Fizeau interferometer *Metrologia* **48** 96-103

[2] Schödel R and Fischedick M 2021 Proposed extension of double-ended gauge block interferometers for measuring spheres *Meas. Sci. Technol.* **32** 084010

[3] El-Hayek N, Nouira H, Answer N, Damak M, Gibaru O 2014 Comparison of Tactile and Chromatic Confocal Measurements of Aspherical Lenses for Form Metrology *Intern. Journ. Of Prec. Eng. And Manufac.* **15** 821-829

[4] Tang S 1996 *Self-calibrating five-frame algorithm for phase-shifting Proc. SPIE* **2860** 91-98

[5] Schödel R 2015 Utilization of coincidence criteria in absolute length measurements by optical interferometry in vacuum and air *Meas. Sci. Technol.* **26** 084007

[6] Fichedick M, Stavridis M, Bartl G, Elster C 2021 Investigation of the uncertainty contributions of the alignment of PTB's double-ended interferometer by virtual experiments *Metrologia* **58** 064001

[7] Shutoh S, Moriyama H, Sawabe M 1998 Phase shift on ceramic gauge blocks *SPIE* **3477** 181-186

[8] Balling P, Ramotowski Z, Szumski R, Lassila A, Křen P, Mašika P 2019 Linking the optical and the mechanical measurements of dimension by a Newton's rings method *Metrologia* **56** 025008

Analysis of the influence of cutting conditions on surface roughness of turning workpieces using a focus variation optical system

Sergio Aguado[1,2], Marcos Pueo[1,2], Raquel Acero[1,2], Ana C. Majarena[1,2], Jorge Santolaria[1,2]

[1]*Department of Design and Manufacturing Engineering department, University of Zaragoza, C\María de Luna3, Zaragoza 50018, Spain*
[2]*Instituto de Investigación en Ingeniería de Aragón (I3A), 50018 Zaragoza, Spain*

Email: saguadoj@unizar.es

Abstract

This work aims to analyse the influence of machining cutting conditions on the surface quality of machined Steel 11SMnPb30 pieces using a CNC parallel lathe. The parameters whose influence is studied are cutting speed (v_c), feed rate (f), and depth of cut (a_p). To achieve this, a series of analysis techniques and a method for constructing statistical models were employed. The measurement of the surface roughness of the machined pieces is performed using a focus variation optical system from the Alicona brand, InfiniteFocusSL model. The surface quality metric used is the average surface roughness (Ra). The influence of cutting conditions on the surface quality metrics is assessed using analysis of variance (ANOVA) or the statistical design of experiments (DOE), studying the machining temperature also as a result of the process. In this context, the Scheffler regression equation is used in an attempt to extrapolate the roughness values of a series of control pieces.

Keywords: focus variation optical system, surface roughness, machining conditions, machining temperature, statistical analysis

1. Introduction

Machining industry demands high quality products. The surface finish and texture of machining pieces have a crucial role in wear and fatigue resistance, lubrication and the external appearance of the parts. Hence, it is crucial to take into account parts' surface roughness. Achieving the required surface roughness values depends on a proper selection of cutting parameters during the machining operation.

Current models for predicting surface quality in machining are divided into four groups [1]: models based on machining theories that consider that surface quality is strongly affected by the geometry of the problem and the associated vibrations [2]; models that examine the effects of different cutting parameters on factors such as residual stresses, microstructure, micro hardness and roughness, by the execution of experiments and analysis of results [3]; models created through Design of Experiments (DOE) [4] or Taguchi techniques [6]; and models developed using artificial intelligence like Fuzzy Logic, Artificial Neural Networks or Genetic Algorithms [5].

This paper aims to analyse the influence of machining temperature and cutting parameters on the surface quality of 11SMnPb30 steel machined parts using a numerical control parallel lathe. Experimental details are presented in the second section, while the third section covers the results and discussion of the empirical real tests.

2. Materials and methods

The details of the methodology followed, experimental conditions, equipment and measurement systems used on the study are presented in this section.

2.1. Workpiece material

Pieces to be machined are made of F-212 steel according to UNE standard, equivalent to 11SMnPB30 on DIN standard. Lead is added to this steel to enhance machinability without affecting the mechanical or metallurgical properties of the base steel. However, it is not suitable for welding. It is commonly used in screws, bolts, bushings, fittings, and washers due to its mechanical properties [7].

2.2. Cutting tool

Experimental tests were carried out using a cutting insert Sandvick CNMG 12 04 08 QF 4025 as cutting tool. It is a hard metal tool used in finishing operations with an effective cutting edge length of 12.096 mm, a tip radius of 0.794 mm, a hole fixing diameter of 5.156 mm, an inscribed circle of 4.762 mm, a CVD coating of TiCN+Al203+TIN, and four cutting edges per insert.

2.3. Machine tool

The machine tool to be used for machining the parts is a manually assisted conventional CNC lathe Pinacho Rayo 180 Ø 360 x 1000 mm with a spindle power of 5.5 Hp, weight capacity of 1.5 Ton, swing over bed of 360 mm, swing over carriage of 198 mm, distance between centres of 1000 mm, a spindle hole diameter of 42 mm and a speed range 100 – 4000 rpm.

2.4. Cutting Conditions

Cutting conditions must be a balance between the cutting conditions provided by the cutting tool, the characteristics of the material to be machined, and the real limitations of the machine tool.

The insert selected is designed to work with materials until 180 HB with a depth of cut (a_p) in range (0.2 – 2.5) mm, feed rate (f) in range (0.11 – 0.38) mm/rev and cutting speed (v_c) in range (320 – 450) m/min. As the material to be machined has a hardness of 140.5 HB, v_c can be increased to (450 – 562)

m/min. The dimensions of the workpiece to be machined are 48 mm diameter and 75 mm length. Facing and turning operations of length 45.5 mm will be carried out.

Considering the specifications of section 2.3, the machine should be able to operate on these ranges without issues. However, preliminary tests showed excessive system vibrations due to structural problems. Therefore, the cutting conditions ranges were adjusted to a_p (0.25 – 1.0) mm, f (0.05– 0.2) mm/rev and v_c (100 – 220) m/min.

2.5 Thermal camera

The camera used to measure the temperature of machining process is a FLIR E60. The measurement conditions employed were emissivity value of 0.6 and reflected temperature 21°C. The camera was used in video recording mode. Both capture and data processing were done using Matlab.

2.6 Surface roughness measurement

The measurements of average surface roughness (Ra) were done on an Alicona InfinityFocusSL optical system using an objective of 10x. The equipment specifications are presented in Table 1.

Table 1 InfinityFocusSL specifications

Objective magnification	10X
Lateral measurement area (X x Y))	4 mm²
Distance of measurement points	1 μm
Calculated lateral optical limiting resolution	1.09
Measurement noise	40 nm
Vertical resolution	100 nm
Finish lateral topographic resolution	2 μm
Vertical measurement range	16 nm
Min. measurable roughness (Ra)	0.3 μm
Min. measurable roughness (Sa)	0.15 μm

The workflow to measure the roughness in the workpieces was the following:
1. Set lateral and vertical resolution as 1.76 μm and 100 μm respectively.
2. Define a measurement area
3. Choose true or polynomial form to remove its influence on the measurement: cylinder on turning operation or plane on facing one.
4. Adjust the reference plane to remove the polynomial form.
5. Define profile width as 5 mm and a lineal path of 4 mm.
6. Define the area of measurement. On the turning surface three measurement areas were defined, rotating the piece 120 degrees among each one. On the facing surface three areas were aleatory defined.
7. Choice Lc filtering as 800 μm for R_a between 0.1 μm and 2 μm and 2500 μm for R_a between 2 μm and 10 μm, according to ISO 4288 [8].
8. Calculate roughness parameter Ra.

2.7. Experimental plan procedure

The impact of cutting conditions on the surface roughness will be studied using two statistical tools. Initially, a three-factor with two-level Design of experiments (DOE), see Table 2,will be conducted, resulting in a total of 8 test, calculating the effect and basic contribution of each factor as well as their interactions. . Each test is replicated seven times with facing and turning operations.

Table 2 DOE d matrix

	Factor 1	Factor 2	Factor 3
Test Id	V_c (m/min)	f (mm/rev)	a_p (mm)
1	100	0.05	0.25
2	100	0.05	1.00
3	100	0.20	0.25
4	100	0.20	1.00
5	220	0.05	0.25
6	220	0.05	1.00
7	220	0.20	0.25
8	220	0.20	1.00

A total of 56 workpieces are machined and six roughness zones are measured on each piece, three for each operation. To eliminate potential outliers, Chauvenet's criterion is applied [9].

After machining the pieces, an analysis of variance technique (ANOVA) is used to determine the parameters that are the most significant in relation to surface roughness.

The F-test or variance ratio is essentially the correlation between the variance of the process parameter and the error. It serves to quantify the significance of the different study factors concerning the overall variance, encompassing all factors, including the error, as shown in equation 1. Where e is the experimental variance error and V is the variance of the parameter analysed.

$$F = \frac{V}{e} \tag{Eq.1}$$

The percentage of influence (P) is the percentage value of influence for each study factor, as defined in Equation 2, where S is the residual sum of squares and ST is the sum of total squareness, as shown in equation 3.

$$P = S \, x \frac{1}{ST} \, x \, 100 \tag{Eq.2}$$

$$ST = S - C * F \tag{Eq.3}$$

The sum of squares (ST) allows quantifying the variability of a dataset by focusing on the difference between each data point and the mean of all points in the set. Where S and $C*F$ are presented in equation 4 and 5, representing y_i the value of R_a for piece i with $i = 1 \ldots 56$.

$$S = \sum_{i=1}^{n} y_i^2 \tag{Eq.4}$$

$$C * F = \left(\frac{1}{n}\right) [\sum_{i=1}^{n} y_i]^2 \tag{Eq.5}$$

Degrees of freedom equations are a measure taken from a certain amount of information, determined based on the number of data. Total degree of freedom (DF_{total}) is defined as number of machined pieces minus one. The parameters' degree of freedom (DF) is defined as the number of level of parameters minus one. The difference between both is defined as the degree of freedom of the error (DFe). These values are used to obtain the variance of the parameter to study VF, given by equation 6, and the variance of the error Ve, shown in equation 7, where j represents the parameter to study a_p , f or v_c.

$$VF = \frac{S}{DF} \tag{Eq. 6}$$

$$Ve = \frac{Se}{DFe} = \frac{ST - \sum_{j=1}^{m} VF_j}{DFe} \tag{Eq. 7}$$

After conducting the ANOVA analysis, a Design of Experiments (DOE) analysis is performed, examining both the main effects and the fundamental contribution of the parameters and their interactions [10].

Additionally, five extra pieces are machined. The machining conditions for these pieces are fixed within the studied ranges. The Scheffler regression equation is used as a tool to predict the roughness of future pieces considering the machining conditions within the ranges established in the experiments [11].

The experiments are carried out in the precision mechanics workshop at the University of Zaragoza, following the set up shown in Figure 1. This set up includes a Flir E60 thermal camera to perform the radiometric measurement.

Figure 1. Set up of machining tests

The measurement of the surface roughness of machined parts is carried out in a metrology laboratory under controlled environmental conditions at 20±1°C using the Alicona InfiniteFocusSL variation equipment, see Figure 2. Before measuring the pieces, they were stabilized for a minimum of one day and a maximum of seven days to prevent issues such as surface oxidation.
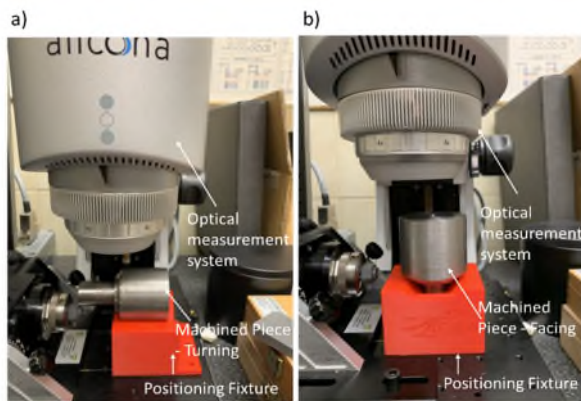
Figure 2. Measurement of roughness a) turning operation b) facing operation

3. Results

Table 3 presents the results of the surface roughness and the temperature measurement of the machined parts. It includes the roughness parameter *Ra* as the most representative one. The mean value and standard deviation of *Ra* are obtained from the measurement of roughness in three positions for each of the seven pieces that were machined on each test. In regard to the temperature values, the maximum value of temperature (Maximum Area), comes from the maximum temperature in the ROI rectangular measurement area shown in Figure 3. The second column (Temperature control point) shows the temperature of the control point located on the piece, Figure 3.

Both rectangular measurement area and control point are the same for all tests and pieces.

Table 3 Experimental results

Test Id	Facing *Ra* (µm)		Turning *Ra* (µm)		Temperature (°C)	
	Average	Std	Average	Std	Maximum Area	Control Point
1	1.08	0.27	1.19	0.17	71.7	29.5
2	1.37	0.30	1.44	0.31	36.4	26.9
3	3.74	1.21	3.46	0.41	52.9	27.9
4	2.80	0.88	2.82	0.88	56.7	30.5
5	1.13	0.19	1.41	0.11	86.9	32.7
6	1.11	0.76	1.70	0.88	115	33.8
7	1.75	0.41	1.88	0.23	60.4	37.1
8	2.89	1.86	1.98	0.23	84.5	39.8

The results obtained show small variations in the surface roughness depending on the measured area and the piece machined. Similarly, if the results of turning and facing *Ra* are compared, see table 3, these provide similar results between facing and turning to the same test, except in the test 8. This discrepancy is attributed to a deflection issue in the tool turret that increase its influence using more aggressive cutting conditions.
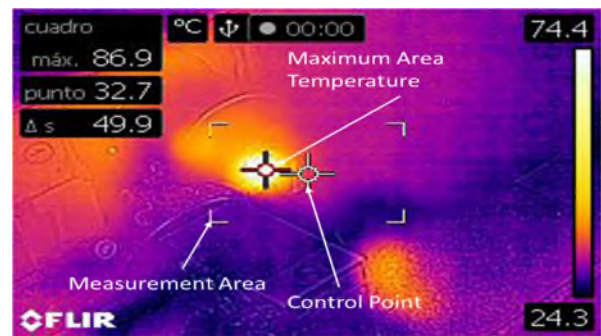
Figure 3. Machining thermal image (area , maximum temperature, and control points)

Temperature results in Table 3 show that changes on cutting conditions affect to machining temperature. However, experimental results show how the maximum temperature value in an area cannot be considered representative of the process due to reflections from older chips, glare or environmental factors. In the temperature of the control point, these influences are reduced. However, it is not possible to isolate the machining process from its surrounding radiation.

Table 4 Summary of ANOVA analysis.

	DF	V (μm^2)	F	% P	S (μm^2)
V_c	1	3.73	4.36	4.33	3.73
f	1	39.26	45.98	45.63	39.26
a_p	1	0.282	0.33	0.33	0.03
Error	52	0.86			
ST Total	55				86.04
C*F = 214.76					

ANOVA analysis results, presented in Table 4, show that the machining parameter with the most significant impact on the surface roughness is the feed rate. It has a Fisher's F test of 45.891 and a percentage of influence of 45.63 %. The second parameter on influence is the cutting speed with a value F of 4.36 and a P value of 4.33%.

The *Ra* analysis carried out through DOE shown in Figure 4, corroborates the results of the ANOVA analysis. It illustrates that higher feed rates lead to an increase in surface roughness. In the same way, a low cutting speed increases *Ra,* contrary to expected results and cut depth effect is negligible. Similarly, Figure 4 shows how the influence of iterations is smaller than individual effect's contribution. The interaction with the greatest influence is the relationship between the cutting speed and the feed rate with a value of -0.73.
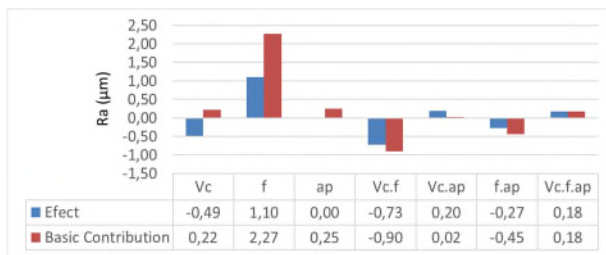
Figure 4. Summary of Ra DOE analysis (influence on surface roughness (Ra) of machining conditions Vc, f and ap)

DOE analysis of the influence of cutting conditions on the control point temperature in the turning process in Figure 5, shows that the parameter with the greatest influence is the cutting speed, followed by feed rate and cut depth. In relation with interaction influence, their influence is similar in value and can not be negligible.
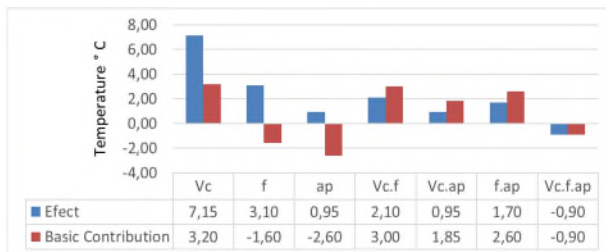
Figure 5. Summary of Control point Temperature °C DOE analysis (influence on the machining control point temperature of machining conditions Vc, f and ap)

Table 4 Adaptation of the Scheffler equation to control components

Piece	V_c (m/min)	f (mm/rev)	a_p (mm)	Measured Ra (μm)	Scheffler Ra (μm)
1	150	0.05	0.70	1.14	1.19
2	210	0.10	0.50	0.81	2.50
3	180	0.20	1.00	1.65	3.13
4	120	0.15	0.25	0.97	2.59
5	220	0.15	0.40	1.02	1.71

Table 4 presents the adequacy of Scheffler regression to predict *Ra* behaviour, using five extra pieces used as control parts with different cutting conditions within the ranges performed in the experimental tests. As can be observed, only the first piece has similar results. Therefore, there is not a linear relationship between *Ra* and cutting conditions. Hence, more complex methods like neural networks are necessary to infer further conclusions among the factors relations.

4. Conclusions

This work provides a generalizable procedure to establish the correlation between cutting conditions with machined part's surface roughness and temperature on machining process.

ANOVA analysis determined that the parameter with the greatest influence on roughness is the feed rate, with an influence percentage of 45.63% followed by cutting speed and cut depth, with influences of 4.33% and 0.33%, respectively.

DOE analysis showed that the surface roughness decreases with increasing cutting speed, especially when interacting with the feed rate, representing the optimal combination of factors. On the other hand, recognizing that the feed rate is the most relevant factor, it can be inferred that higher feed rates result in increased surface roughness. In relation with machining temperature and based on the Scheffler regression equation results, it is concluded that cutting conditions has not a linear relationship with *Ra.*

Based on the results of this work, further exploration will be undertaken to establish the relationship between cutting conditions, temperature, and surface roughness, employing artificial intelligence techniques for this purpose.

References

[1] Benardos P G and Vosniakos G C 2003 Predicting surface roughness in machining: A review *Int. J. Mach. Tools Manuf.* **43** 833–844.
[2] Baek D K, Ko T J and Kim H S2021 Optimization of feedrate in a face milling operation using a surface roughness model *Int. J. Mach. Tools Manuf.* **41** 451–462.
[3] Akkuş H and Yaka H 2021 Experimental and statistical investigation of the effect of cutting parameters on surface roughness, vibration and energy consumption in machining of titanium 6Al-4V ELI (grade 5) alloy *Meas. J. Int. Meas. Confed.* **167**p. 108465.
[4] Venkata Rao K, Suvarna Raju L, Suresh G, Ranganayakulu J and Krishna J 2024 Modelling of kerf width and surface roughness using vibration signals in laser beam machining of stainless steel using design of experiments *Opt. Laser Technol.* **169**, p. 110146.
[5] Huang P, Lee C-H 2021 Estimation of tool wear and surface roughness development using deep learning and sensors fusion *Sensors.* **22**, 6pp.
[6] Nangare K and Chavan S 2023 To predict the surface roughness of Black ABS component with variable parameters by applying the Taguchi method *Mater. Today Proc.* **72**, 706–712.
[7] Grade S Steel Grade 11 SMnPb 28 Chemical information,Mechanical properties. Accessed: Jan. 08, 2024. [Online]. Available: http://www.steel-grades.com/.
[8] ISO 4288:1996 - Surface texture: Profile method - Rules and procedures for the assessment of surface texture. 1998.
[9] Rochim 2016 A Chauvenet ' s Criterion , Peirce ' s Criterion , and Thompson ' s Criterion 2nd Quantitative and Qualitative Analysis Course Homework pp 3-5.
[10] 5.4. Analysis of DOE data." https://www.itl.nist.gov/div898/handbook/pri/section4/pri4.htm (accessed Jan. 10, 2024).
[11] B. L. Iverson and P. B. Dervan 2014 *Applied Linear Regresion.* Sanford Weisberg University of Minnesota.

Evaluation of the measurement uncertainty of a high-precision telescopic instrument for machine tool verification

Francisco Javier Brosed[1,2,3], Juan José Aguilar[1,2], Raquel Acero[1,2], Sergio Aguado[1,2], Marcos Pueo[1,2]

[1]*Department of Design and Manufacturing Engineering, University of Zaragoza, María de Luna 3, 50018 Zaragoza, Spain.*
[2]*Instituto de Investigación en Ingeniería de Aragón (I3A), 50018 Zaragoza, Spain*
[3]*fjbrosed@unizar.es*

Abstract

Precision measuring instruments and the ability to track measurement results to verify production systems in accordance with national and international standards are key tasks in the manufacturing industry. There are instruments on the market that allow the measurement of three-dimensional coordinates using telescopic systems. Typically, from three multi-cycle measurements of the head position, using a single telescopic system, or from a single measurement, using three telescopic systems during a simultaneous measurement process. These are products used to verify the behaviour of machine tools and robots. The work presented in this paper shows the modelling of the measurement system to evaluate its uncertainty and the effect on it of different system configuration options. The measurement system is based on a multilateration process that starts by measuring distances with several telescopic systems simultaneously. The evaluation of the influence of the configuration on the measurement uncertainty will include the distances between the reference points for multilateration and the angles formed by the telescopic systems.

Measurement uncertainty, machine tool multilateration, Interferometric multilateration, Monte Carlo simulation.

1. Introduction

Precision measurements in manufacturing systems are a key factor for advanced technologies [1]. In the optimization process of the manufacturing systems, the verification techniques allow the measurement and compensation of machine tool (MT) errors [2]. Furthermore, the high precision dimensional metrology [3,4] has become essential for the manufacturing industry [5] due to tighter geometric tolerances in the manufactured products. In this frame, the traceability of the measurement results is needed to improve the behaviour of the manufacturing systems and guarantee the quality in the production process [6].

MT verification can be carried out measuring the MT head position with measuring instruments such as interferometers [7], measuring distances following the axis directions of the MT; ball bars [8], measuring circular trajectories of the MT; laser tracers [9] and laser ball bars [10, 11] that measure the distance from a fixed point in the MT table to the MT head running several cycles, varying the position of the fixed point to the MT table, to measure the position of the MT head; and laser trackers [12] using the distance measured to a retroreflector and the angles from its angular encoders to measure the position of the MT head.

The measurement system to be analysed in this paper can be classified in the laser ball bar group, but with the special feature of allowing the measurement of the MT position in a single cycle. The measurement system (Telescopic Simultaneous Ballbar, TSB) uses three telescopic arms to simultaneously measure the distance from three spheres in the MT table to one sphere in the MT head, achieving verification process times similar to those obtained with the use of a laser tracker, but improving the precision of the measurement result compared to the precision obtained with non-simultaneous laser ball bars because the

positioning repeatability of MT will not affect the triangulation calculation as occurs with laser tracers [9].

A calibration and uncertainty budget analysis for the TSB is presented in [13] but an analysis of the variation of the measurement uncertainty in the verification field depending on the spatial distribution of the three spheres fixed to the MT table is needed to assure the traceability of the measurement results obtained with the TSB using different spatial configurations in the MT table.

The main goal of this work is to evaluate the correlation between the measurement uncertainty value of the TSB and the position of the target points (TGs) in the verification volume. To achieve this objective, the behaviour of the TSB has been simulated and its measurement uncertainty has been estimated, with the Monte Carlo method [14,15], for different spatial distributions of the three spheres in the MT table.

The paper is structured as follows: Section 2 describes the TSB and the mathematical model used to estimate its uncertainty. Section 3 details the methodology followed in the analysis and the settings of each test simulated. Section 4 present the uncertainty obtained for each scene simulated. Finally, Section 5 shows the main conclusions of the study.

2. *Measurement system* description

The TSB is a measurement system composed by three telescopic arms. Each telescopic arm measure the distance between two spheres using a laser interferometer integrated in the telescopic arm (measurement uncertainty of the laser interferometer, Attocube IDS3010, with a coverage factor of two is 0.3 μm using an environmental compensating unit). For the measurement of a point in the space (i.e.: the centre of a sphere in the MT head) one end of each of the three telescopic arms is placed on a surface (i.e.: the MT table), so that their relative distances remain constant. This end of each of the telescopic arms is a sphere joined with the surface where is placed through

a kinematic support that allows the rotation of the arm keeping the sphere centre static. The other end of the telescopic arms is a multi-point kinematic coupling especially developed for the TSB [16] that allows the connection of the three telescopic arms with a single sphere simultaneously. This configuration of the TSB enable the calculation of the single sphere centre position using multilateration.
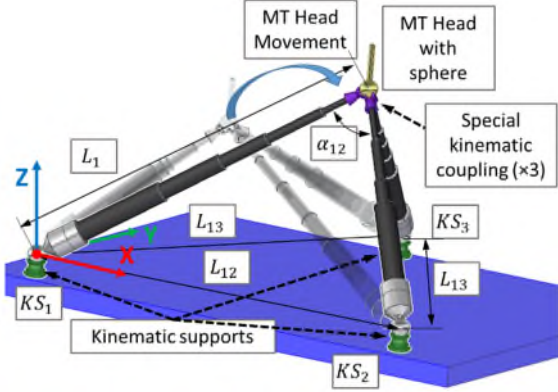
Figure 1. Example of the configuration of the TSB in the position measurement process using multilateration and main parameters of the model. The parameters L_2, L_3, α_{13} and α_{23} have been omitted in the figure to improve the visibility, but can be easily deduced.

The main error sources considered to simulate the behaviour of the TSB are: the geometric error of the TSB spheres, the measurement bias of the telescopic arms with the inclination and the rotation angles, the errors in the compensation of the temperature and the uncertainty of the telescopic arms measuring distances between centres. The measurement uncertainty obtained from this error sources following the methodology explained in [13] for a TSB's telescopic arm measuring distances in workshop conditions is 4 μm (with a confidence level of two, k=2) and the measurement range for each arm goes from 411 mm to 1040 mm. From this input data the simulation tests, explained in the following section, have been carried out.

3. Methodology and simulation test

The measurement of the position of a sphere (generally linked to the MT head) with the TSB requires previously measuring of the distance between each of the three kinematic supports (KS_i, with i from 1 to 3). The three distances, L_{ij}, with i and j from 1 to 3 and $i \neq j$, are the distances with which the reference system is build. This reference system is the one used to express the three dimensional coordinates of the centre of the sphere that are obtained as result of the measurement with the TSB. From L_{ij} the coordinates of each kinematic support, KS_i, can be calculated, equations (1), (2) and (3).

$$X_{KS2} = L_{12} \tag{1}$$
$$X_{KS3} = L_{13} \cdot \cos(\beta_{13}) \tag{2}$$
$$Y_{KS3} = L_{13} \cdot \sin(\beta_{13}) \tag{3}$$

Where β_{13} is the angle between the segment joining KS_1 and KS_2 with the segment joining KS_1 and KS_3. The values of the rest of coordinates of KS_i are zero: The centre of the sphere in KS_1 is defined as the origin of the reference system, KS_2 defines, together with the origin, the X axis and the three KS_i define the XY plane of the reference system.

The coordinates of the centre of the sphere in the MT header are obtained via multilateration as the intersection of three spheres, equations (4), (5) and (6).

$$X = \frac{L_1{}^2 - L_2{}^2 + X_{KS2}{}^2}{2 \cdot X_{KS2}} \tag{4}$$
$$Y = \frac{L_1{}^2 - L_3{}^2 + X_{KS3}{}^2 + Y_{KS3}{}^2}{2 \cdot Y_{KS2}} - \frac{X_{KS3}}{Y_{KS3}} \cdot X \tag{5}$$
$$Z = \sqrt{L_1{}^2 - X^2 - Y^2} \tag{6}$$

Where L_i, with i from 1 to 3, are the distances between spheres measured by the telescopic arm i of the TSB.

From equations (1) to (6) could be seen that the calculation process for obtaining the position of the sphere in the MT Head depends on the length measurement of each telescopic arm of the TSB (L_i and L_{ij}). Therefore, the effect of the measurement uncertainty of the telescopic arms of the TSB is simulated and the uncertainty of the measurement of the position of the sphere in the MT head is estimated using the Monte Carlo Method [15].

A configuration of the supports forming an equilateral triangle has been assumed and the measurement uncertainty has been estimated for different sizes of the triangle. The side of the triangle has been varied from 500 mm in 100 mm increments to a maximum of 1000 mm. A total of six cases, designed with the letters from A to F have been studied, table 1.

Table 1. Sizes of the equilateral triangle formed by the kinematic supports, KS_i. A total of six cases are studied. The values under each letter indicates the size of the triangle side, L_{ij}, and the number of target points, TG.

Case	A	B	C	D	E	F
L_{ij}/mm	500	600	700	800	900	1000
TG	181	208	214	214	214	213

The target points (TGs) in the TSB verification volume have been obtained by varying the lengths of the arms from 500 mm in 100 mm increments to a maximum of 1000 mm so that a representative verification volume of the TSB was covered, figure 2.

The measurement uncertainty of the TSB has been evaluated for the TGs within the verification volume in the six cases (from A to F) recording, in addition to the uncertainty obtained in the X, Y, Z directions of the reference system (U_X, U_Y, U_Z), the position of the TGs and the angles that the arms formed with each other (α_{ij}, with i and j from 1 to 3 and $i \neq j$).
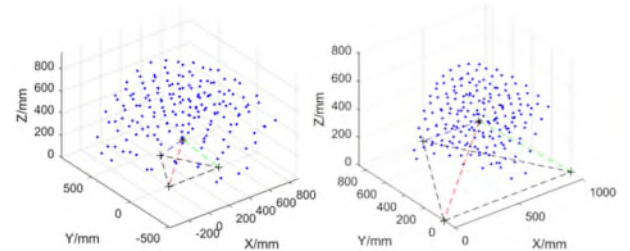
Figure 2. TSB Verification Volume for different sizes (500mm and 1000 mm) of the triangle formed by the kinematic supports (black cross and black dashed line).

The number of iterations is an important parameter of the Monte Carlo simulation. If the number of iterations is low the results obtained diverge when the test is repeated. If the number of iterations is high enough the results converge to the same solution but if the number of iterations is excessively high, the time required to perform the simulation increases, which can result in unfeasible test. From previous works, the Monte Carlo simulation converge using 10^6 iterations [13].

The main results obtained from the simulation tests are the correlation of U_X, U_Y and U_Z with some of the main

configuration and characteristics of the TSB, such as: the distribution of KS_i, the coordinates of the TGs in the verification volume (blue dots in figure 2) and α_{ij}. The variation of the verification volume when L_{ij} changes can also be analysed.

4. Simulation Results

Following the methodology exposed in the previous section the simulation tests have been performed. Running 10^6 iterations for each of the six cases, 120 s for each case were enough to end the simulation with a 2.3 GHz CPU clock speed.

The measurement uncertainty within the verification volume has been estimated using Monte Carlo Method and U_X, U_Y and U_Z for each TG has been obtained.

The uncertainty variation within the verification volume can be observed in figure 3, where the results for the case A with $L_{ij} = 500\ mm$ and case F with $L_{ij} = 1000\ mm$ are shown. These are the cases with the higher values of uncertainty ($L_{ij} = 500\ mm$) and with the lower values ($L_{ij} = 1000\ mm$) of the six cases analysed. In figure 3, the colour of the target point indicates the maximum value of the uncertainty in each TG (max $\{U_X, U_Y, U_Z\}$).
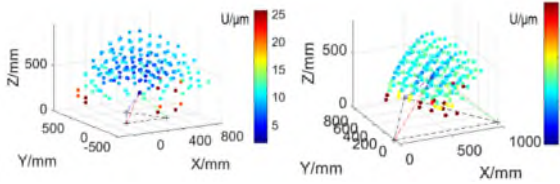
Figure 3. Measurement Uncertainty of the TSB in the verification volume. The maximum value of the uncertainty for each TG (max $\{U_x, U_y, U_z\}$) is represented for case A, $L_{ij} = 500\ mm$, and case F, $L_{ij} = 1000\ mm$.

Despite the difference in scale presented by case A and case F showed in figure 3, that will be further explained with the next figures, similarities can be established between them, which are also applicable to the rest of the cases (from case A to case F). The maximum values of the colormap are reached only by points located in the periphery and in the lower levels of the admissible Z-axis direction. The rest of the TGs within the volume (more than 90% for all the cases) present uncertainty values for any direction, under 10 μm (k=2), for case A, and 6 μm (k=2), for case F. The other four cases (from case B to case E) are between these two values. This point can be corroborated for Cases A and F with figure 4, where the distribution of the uncertainty values are plotted for U_X, U_Y and U_Z.
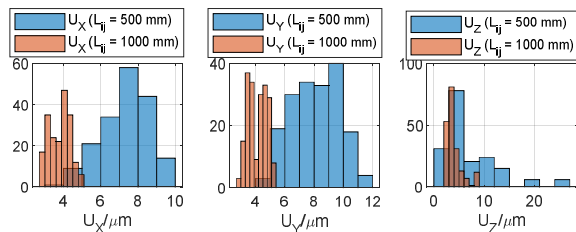
Figure 4. TSB Measurement Uncertainty distribution in X, Y and Z directions for case A ($L_{ij} = 500\ mm$) and case F ($L_{ij} = 1000\ mm$).

The distributions presented in figure 4 have been obtained with the simulation results of 181 TGs in case A and of 213 TGs in case F. First, it is confirmed what appears in figure 3, the measurement uncertainty values of the TSB are higher in case A than in case B. In addition, figure 4 allows to identify the differences between U_X, U_Y and U_Z and evaluate their distributions corroborating what was previously asserted, that

more than 90% of the TGs present measurement uncertainty values for any direction, under 10 μm (k=2), for case A, and 6 μm (k=2), for case F.

By introducing cases B to E into the comparison, it is possible to observe the decrease in uncertainty values as L_{ij} increases, figure 5.

Figure 5, plots the correlation of the measurement uncertainty value (U_X, U_Y, U_Z) with the position of the TG evaluated for the six cases analysed (from case A to F), figure 5(a), and with α_{ij}, from case A to F too, figure 5(b). The first column of graphs in figure 5(a) plots the X-axis coordinate of the TG versus U_X (first row), versus U_Y (second row) and versus U_Z (third row). In the same way, in figure 5(b), the columns of the figure contains the graphs plotting α_{ij} of the TG versus U_X, first row, U_Y, second row and U_Z, third row.
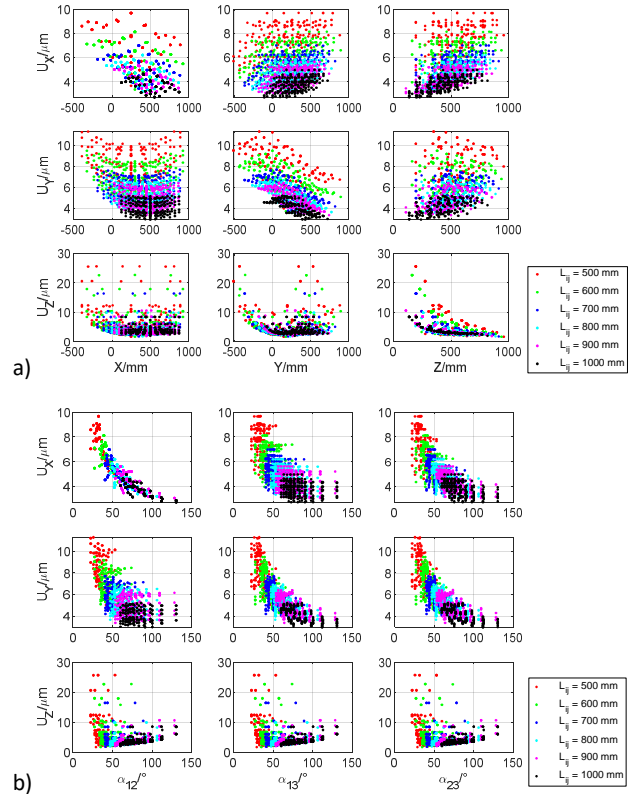
Figure 5. Measurement uncertainty value for the six cases analysed (from case A to F). (a) The coordinates of each TG (X, Y, Z) versus U_X, U_Y, U_Z. X, Y, Z coordinates are plotted in the abscissa of the graphs in the first, second and third column respectively. U_X, U_Y, U_Z uncertainties are plotted in the ordinate of the graphs of the first, second and third row respectively. (b) α_{12}, α_{13}, α_{23} for each TG versus U_X, U_Y, U_Z. α_{12}, α_{13}, α_{23} angles are plotted in the abscissa of the graphs in the first, second and third column respectively. U_X, U_Y, U_Z uncertainties are plotted in the ordinate of the graphs of the first, second and third row respectively.

There are two correlations that appear clearly: U_Z with Z-axis direction in figure 5(a) and U_X with α_{12} in figure 5(b). Although inflection points can be detected in some of the other graphs. From figure 5(a): U_X increases with X and reach a maximum with $X = L_{ij}/2$, decreasing for higher values of X and Increases with Y until reaching a stable value for $Y \geq 0$. U_Y decreases with the increase of X and reach a minimum with $X = L_{ij}/2$, increasing for higher values of X and presents a change in behaviour approximately in $Y = 0$.

In figure 5(b), the correlation between U_X and α_{12} appears clearly because, due to the reference system definition, X-axis coordinate is calculated from L_1 and L_2 and without L_3, equation (4). The correlation shows that U_X decreases when α_{12} increases.

The correlation of U_Z with the Z-axis coordinate is shown in figure 5(a) and indicates that the higher the Z value the lower the uncertainty value. This correlation appears, in a more diffuse way, in the opposite direction between U_X and U_Y and the Z-axis coordinate. This behaviour is related to the angles α_{ij}: for high Z values the angles are smaller allowing, when noise appears in the measurement results, a very precise identification of Z-axis coordinate but a less precise identification for X and Y-axis coordinates. In figure 6, the uncertainty for TGs of case F is plotted with Z-axis coordinate to clearly show this correlation that appears similar in the other cases.
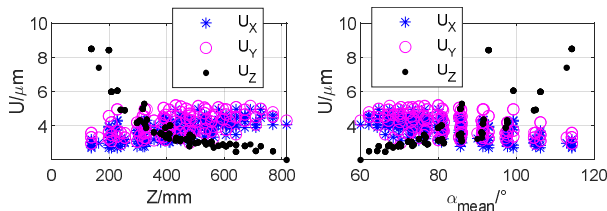
Figure 6. Measurement uncertainty value for case F ($L_{ij} = 1000\ mm$). U_X, U_Y, U_Z versus Z-axis coordinate and U_X, U_Y, U_Z versus the mean value of α_{ij} (α_{mean})

The correlation between U_Z and the angles (α_{ij}) depends on the three angles at the same time. For this reason in figure 6 the uncertainty for TGs of case F is plotted with the mean value of α_{ij} (α_{mean}). The lower values of U_Z are related to low values of α_{mean}, this happens when the target points are located in high Z-axis coordinates ($U_X \leq 4\ \mu m$ if $\alpha_{mean} \leq 80°$ or $Z \geq 500\ mm$).

5. Conclusions

The measurement results of the TSB have been simulated and its measurement uncertainty estimated to evaluate the correlation between the measurement uncertainty value of the TSB and the position of the target point in the verification volume. The measurement system (TSB) and the methodology for the simulation have been presented. The measurement uncertainty of the TSB has been estimated with Monte Carlo simulation using from 181 to 214 TGs depending on the case (six different cases, from A with $L_{ij} = 500\ mm$ to F with $L_{ij} = 1000\ mm$). The simulation with the six cases indicates that the measurement uncertainty decreases when L_{ij} increases. Although, the correlation of U_X, U_Y and U_Z with the position of the TGs and α_{ij}, has been evaluated showing these main results: Several configurations of the KS_i can be found ($L_{ij} \geq 800\ mm$) where the TSB can measure target points with a measurement uncertainty lower than 6 μm ($k = 2$) excluding the target points located in the surroundings of the physical limits of the telescopic arms (10% of the target points). The dependence of U_X and U_Y with X and Y-axis coordinates show inflection points with $X = L_{ij}/2$ and $Y = 0$. The correlation of U_Z with the Z-axis coordinate of the target point can be explained in terms of α_{mean}: for high Z values the angles α_{ij} decreases and the effect of the noise in the measurement results lost weight in the calculation of the Z-axis coordinate ($U_X \leq 4\ \mu m$ if $\alpha_{mean} \leq 80°$ or $Z \geq 500\ mm$ for case F).

As future work could be interesting to evaluate the effect on the measurement results when L_{ij} are dissimilar and implement the methology to the target points of a MT volumetric verification process to optimize the selection of the target points depending on the measurement uncertainty.

References

[1] Kunzmann H, Pfeifer T, Schmitt R, Schwenke H, Weckenmann A 2005 Productive metrology - adding value to manufacture *CIRP Ann.* **54** (2) 155-68 https:// doi.org/10.1016/S0007-8506(07)60024-9.

[2] Schwenke H, Knapp W, Haitjema H, Weckenmann A, Schmitt R, Delbressine F 2008 Geometric error measurement and compensation of machines – An update *CIRP Ann.* **57** (2) 660-75, https://doi.org/10.1016/j.cirp.2008.09.008.

[3] Ferrucci M, Haitjema H, Leach R 2018 Chapter: Dimensional Metrology in: Basics of Precision Engineering (R. Leach, S. T. Smith, R. Leach, S.T. Smith, Boca Raton), CRC Press, 151-203 978-1-4987-6085-0.

[4] De Groot P, Badami V, Liesener J 2016 Concepts and geometries for the next generation of heterodyne optical encoders *Proc. ASPE* (Portland, Oregon) **65** 146–149.

[5] Moona G,Jewariya M, Sharma R 2019 Relevance of Dimensional Metrology in Manufacturing Industries *MAPAN* **34** (1) 97–104, https://doi.org/10.1007/s12647-018-0291-3.

[6] BIPM, IEC, IFCC, ILAC, ISO, IUPAC, IUPAP, OIML 2008 International vocabulary of metrology—Basic and general concepts and associated terms, JCGM 200 Bureau International des Poids et Mesures (BIPM), 2008.

[7] Jiang X, Meng T, Wang L, Liu C 2020 Rapid calibration method for measuring linear axis optical paths of computer numerical control machine tools with a laser interferometer *Int. J. Adv. Manuf. Technol.* **110** 3347-64, https://doi.org/10.1007/s00170-020-05976-6.

[8] Zhong L, Bi Q, Wang Y 2017 Volumetric accuracy evaluation for five-axis machine tools by modeling spherical deviation based on double ball-bar kinematic test *Int. J. Mach. Tools Manuf.* **122** 106-19, https://doi.org/10.1016/j.ijmachtools.2017.06.005.

[9] Zha J,Wang T,Li L, Chen Y 2020 Volumetric error compensation of machine tool using laser tracer and machining verification *Int. J. Adv. Manuf. Technol.* **108** (7- 8) 2467-81 https://doi.org/10.1007/s00170-020-05556-8.

[10] Fan K C, Wang H, Shiou F J, Ke C W 2004 Design analysis and applications of a 3D laser ball bar for accuracy calibration of multiaxis machines *J. Manuf. Syst.* **23** (3) 194-203 https://doi.org/10.1016/S0278-6125(05)00009-9.

[11] Etalon X-AX LASERBAR, https://www.etalonproducts.com/en/products/x-ax_laserbar/, 2021 (Accessed: January 2024).

[12] Aguado S, Samper D, Santolaria J, Aguilar J J 2012 Identification strategy of error parameter in volumetric error compensation of machine tool based on laser tracker measurements *Int. J. Mach. Tools Manuf.* **53** (1) 160-9, https://doi.org/10.1016/j.ijmachtools.2011.11.004.

[13] Brosed F J, Aguilar J J, Acero R, Santolaria J, Aguado S, Pueo M 2022 Calibration and uncertainty budget analysis of a high precision telescopic instrument for simultaneous laser multilateration *Measurement* **190** 110735. https://doi.org/10.1016/j.measurement.2022.110735.

[14] BIPM, IEC, IFCC, ILAC, ISO, IUPAC, IUPAP, OIML 2008 Evaluation of Measurement Data—Guide to the Expression of Uncertainty in Measurement, JCGM 100 Bureau International des Poids et Mesures (BIPM), 2008.

[15] BIPM; IEC; IFCC; ILAC; ISO; IUPAC; IUPAP; OIML 2008 Evaluation of Measurement Data—Supplement 1 to the Guide to the Expression of Uncertainty in Measurement—Propagation of Distributions Using a Monte Carlo Method; JCGM 101 Bureau International des Poids et Mesures (BIPM), 2008.

[16] Acero R, Aguilar J J, Brosed F J, Santolaria J, Aguado S, Pueo M 2021 Design of a Multi-Point Kinematic Coupling for a High Precision Telescopic Simultaneous Measurement System *Sensors* **21** 6365 https://doi.org/10.3390/s21196365.

euspen's 24th International Conference &
Exhibition, Dublin, IE, June 2024
www.euspen.eu

Shape memory alloy mechanical actuator with reduced commutation time

Simón Prêcheur Llarena[1], Loïc Tissot-Daguette[1], Marjan Ghorbani[1], Charles Baur[1], Simon Henein[1]

[1]*École Polytechnique Fédérale de Lausanne, Switzerland*

simon.precheur-llarena@epfl.ch

Abstract

Using shape memory alloys (SMAs) as actuators offers several advantages, including high power density, large stroke capabilities, and friction elimination. These attributes make SMAs suitable for actuating flexure-based mechanisms in a wide array of extreme environments. However, their extended cooling time limits their use for applications requiring a high cadence or fast commutation. This paper presents the design of a novel type of mechanical actuator conceived to address this dynamical performance issue. The proposed mechanism is a bistable switch based on a preloaded buckled beam attached to a flexure pivot. The mechanism is actuated by a set of n individual modules, each powered by an SMA spring. Each module is selectively engaged and disengaged from the switch through a selection gear put in motion by a coupling blade. Since only one module is active at any given time, the others can cool down in the meantime: the commutation time is hence reduced by a factor of n compared to a classical antagonistic-pair SMA design. This solution operates passively: it doesn't require active cooling or any additional energy intake.

This innovative and generic design is intended for use with SMA actuated bistable mechanisms, leveraging their advantages to achieve very high accuracy, precision and repeatability while keeping a highly dynamical performance.

Keywords: Design, Mechanism, Actuator, Shape memory alloy

1. Introduction

Shape Memory Alloys (SMA) are a unique class of materials that can recover their original shape when subjected to certain stimuli. By changing the temperature of thermally responsive SMAs, a thermoelastic solid-solid phase transformation occurs. This reversible and diffusionless transformation happens between the high temperature stable phase known as Austenite, and the low-temperature one named Martensite. SMA springs are small, lightweight, and provide large strokes, which makes them well suited for actuation. However, their long cooling time hinders their use in certain applications. Improving the commutation time of SMA-based actuators would provide them with a whole range of new applications in fields where speed is critical, and where volume, total mass, or cost are not as limiting.

Previous published work on this matter includes the exploration of active cooling strategies or periodic heat sink usage [1]. The achieved improvements through these methods are not sufficient and bring additional multifactorial system level complexities. Because of these limitations, a fully mechanical approach was instead researched, resulting in this work.

This paper presents the mechanical concept and characteristics of this new actuator design, followed by an explanation of its kinematics. Then, an analytical model is established and verified by simulations. Finally, two examples of the realization and performance of a metal-based version are presented.

2. Description of the actuator

2.1. Actuation sequence

The commutation time is defined as the time it takes for the end effector of the bistable mechanism to switch from one stable state to the other. Two commutations correspond to a full cycle.
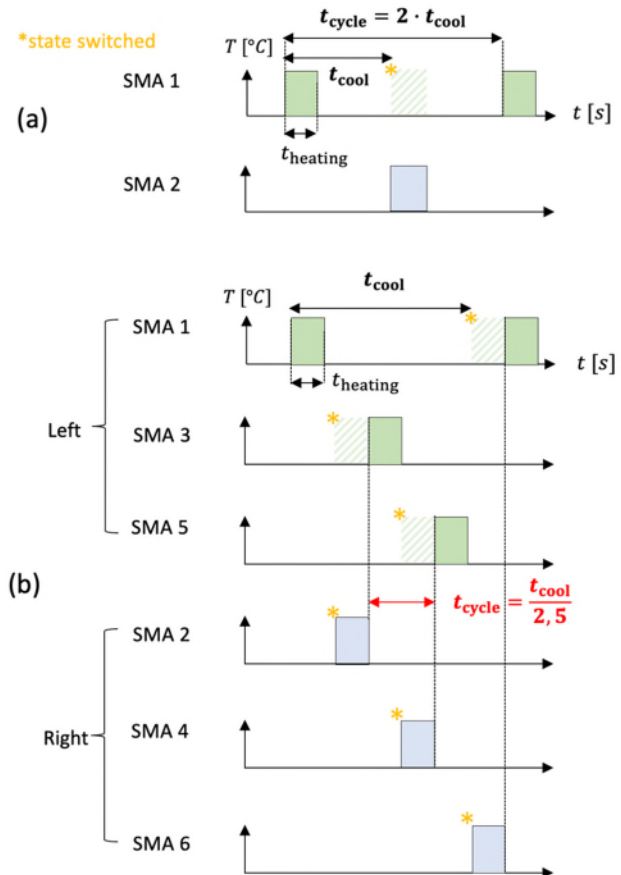
Figure 1. (a) Sequence showing the heating periods (i.e. electrical current delivery) as a function of time in a 2-SMA design. (b) Sequence in a 6-SMA design with the proposed architecture. *Note: The SMAs must be cold and back to the original position when the state switches.

Provided there is no heat convection and good thermal isolation between individual SMA modules, the commutation time t_{commute} is as follows:

$$t_{\text{commute}} = \frac{t_{\text{cycle}}}{2} = \frac{t_{\text{cool}}}{n-1} \qquad (1)$$

where t_{cycle} is the time it takes to perform two commutations (the end effector being back to its initial position), t_{cool} is the time one SMA takes to cool down, and n is the number of SMA modules. Since the state of the system is switched every two commutations, the time is divided by $n-1$.

A two SMA system would yield the control sequence in Fig. 1(a). In comparison, selectively decoupling 6 SMAs results in sequence in Fig. 1(b) instead.

The proposed system requires no additional energy input in order to decouple the SMAs during their cooling periods.

2.2. Actuator kinematics

This actuator is a bistable pivoting mechanism with a tunable stroke. The bistability is provided by the use of a buckled beam preloaded by a displacement. It features two stable positions $\pm\theta_{\text{stable}}$ that can be tuned by adjusting a screw.

A minimum of two SMA modules selectively pull on the bistable part to switch from one stable state to the other. When the SMAs are not active, there is an elastic decoupling between them and the end effector, which ensures the actuator still exerts an almost constant force when a displacement is imposed on it [2]. Otherwise, it remains at a stable position. This behavior makes it ideal for the actuation of grippers, for example.

The use of bistability is required to compensate for the SMAs' lack of repeatability in terms of positional inaccuracy [3]. It also makes it possible to run the system without sensors in an open loop (i.e. without sensors). This makes this mechanism well suited for actuating a variety of systems that already operate using bistability, such as the bistable flexure based gripper seen in section 4.2.

The bistable switch acting as the end effector of the actuator (Fig. 2) is at the heart of the system. A beam of length L is preloaded by a displacement Δl. When a critical angle θ_{in} is applied, the buckled beam snaps through and switches state.
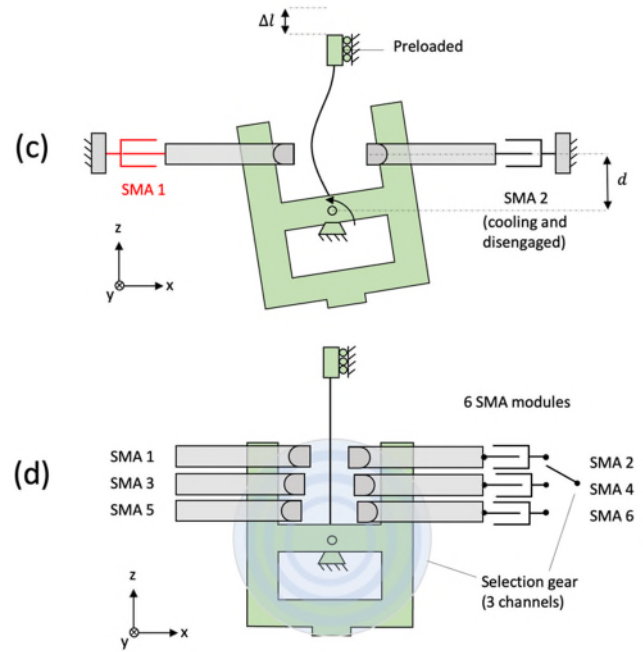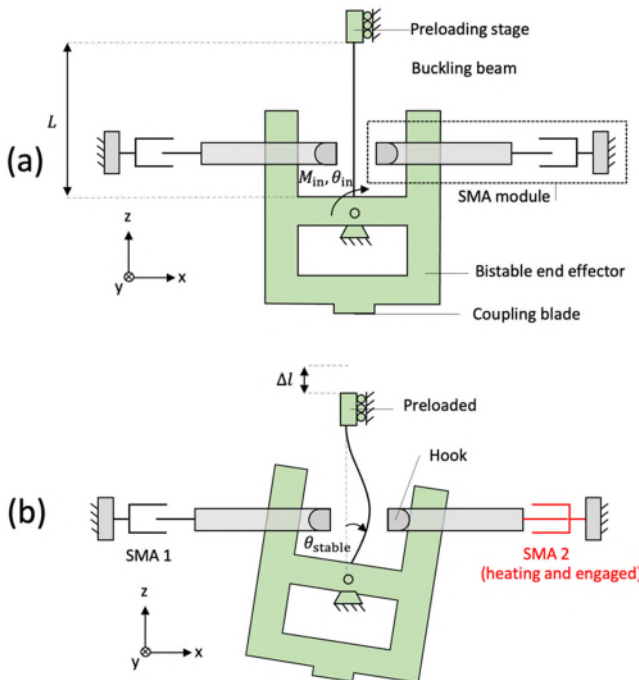
Figure 2. (a) Unloaded bistable stage, (b) Preloaded and actuated on the right, (c) Preloaded and actuated on the left, (d) Version with $n=6$ stacked modules and selection gear.

An "SMA module" is defined as the subsystem comprised of one SMA spring, a parallelogram linkage spring, and finally a hook mounted on a pivot that actuates the end effector (Fig. 3). The parallelogram linkage guides the SMA in translation and returns it back to its modified open shape as it cools down. Eventually, the SMA is ready to be coupled and heated again, returning to its original size.

The selection gear is a ratchet gear. It is held in place by a pawl on one side of its perimeter (Fig. 3), and driven by the coupling blade on the opposite side. The gear has thus several stable angular positions equal to the number of its teeth, which by construction must be a multiple of $n/2$. The front of the selection gear has one or several circumferential channels where pins shaped like arcs are fixed in a fitting pattern. When superposed with its associated hook, the pin exerts a force against the hook's elastic pivot, engaging it with the end effector. The hook is then ready to be pulled by the SMA. When the latter heats and the SMA pulls, a snap-through occurs and the bistable state of the system is switched. When SMAs on the right pull, the coupling blade pushes against the teeth of the gear, which then rotates until the pawl secures it in the next position. Simultaneously, the pin rotates disengaging the aforementioned hook, decoupling it from the end effector, and allowing it to cool down while the sequence continues. When the SMAs on the left pull, the coupling blade is instead retrograded a notch, the pawl securing the gear in position. As such, the selection gear changes state once every two commutations, in a similar fashion to a clock escapement.

The resistance felt by the coupling blade or pawl blade due to the friction force against the selection gear when changing states should be significantly lower than the force the SMAs exert, for the actuator to be efficient.

All ideal joints are implemented by flexures [4]. The input pivot is embodied by a cross-spring flexure pivot, and parallelogram linkages by parallel leaf spring stages. The pawl is replaced by an L-shaped blade. The pivot supporting the hook is replaced by a simple blade. The choice of SMA springs is detailed in section 4.
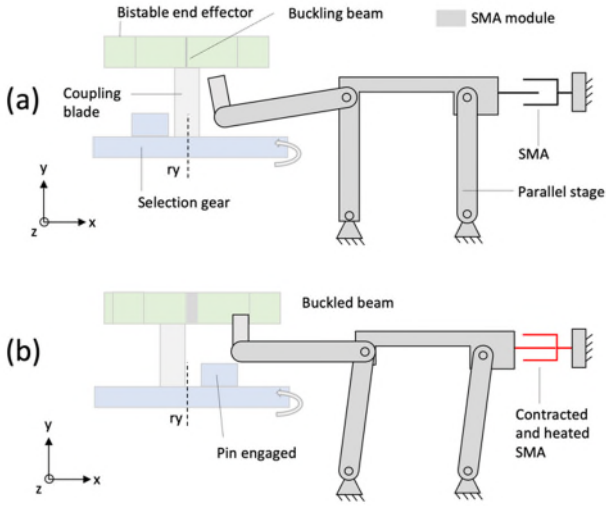
Figure 3. Summarized kinematics of one single SMA module.

2.3. Generalization to multiple SMA modules

When scaling the number of SMA modules up, there is an increase in performance for each additional SMA module at a decreasing marginal cost. Each added SMA module makes the commutation frequency to mass, cost, or volume ratio greater. SMA modules can be added so far as the selection gear's geometrical limitations, and overall volume and mass constraints are met. The theoretical limit to the decrease in commutation time is the time it takes for an SMA to heat and complete a stroke. Therefore, the commutation time will be:

$$t_{\text{heating}} < t_{\text{commute}} = \frac{t_{\text{cool}}}{n-1}, \text{ see Eq. (1)} \tag{2}$$

where $t_{heating}$ is the time required to heat the SMAs to operating temperature.

When scaling up, SMAs must be dimensioned differently according to their actuating distance d from the pivot center of rotation, in order to always achieve the same input torque M_{in}, given by $M_{\text{in}} = d \cdot F_{\text{SMA}}$, where F_{SMA} is the force exerted by the SMA at snap-through angle.

3. Analytical model

An analytical model was established to characterize the behaviour of the mechanism. In a fixed-pinned configuration, the magnitudes of the input angle and torque required to switch the state of a buckled beam are respectively given by [2] as:

$$\theta_{\text{in,lim}} = 1.78 \sqrt{\frac{\Delta l}{L}} \tag{3}$$

$$M_{\text{in,lim}} = 12.90 \frac{EI}{L} \sqrt{\frac{\Delta l}{L}} \tag{4}$$

where EI stands for the flexural rigidity of the buckling beam, L its length, and Δl its shortening. The constants in Eqs. (3) and (4) correspond to limit points in the input moment-angle characteristics of the buckled beam after which snap-through occurs [2]. The whole flexure system resisting the SMA's movement (coupling blade, pawl corner blade, parallel leaf spring stage) shows an equivalent stiffness k_{eq} that acts against the SMA. The linear stroke at which snap-through occurs is [2]:

$$x_{\text{lim}} = d \cdot sin(\theta_{\text{in,lim}}) \tag{5}$$

Therefore, the condition for snap-through is:

$$F_{\text{SMA}} > \frac{M_{\text{in,lim}}}{d} + x_{\text{lim}} k_{\text{eq}} \tag{6}$$

4. Realisation of the design

By adapting the analytical model to the specifications required, all dimensions were computed for the realization of two CAD versions. The chosen SMA has a Kirigami architecture. It is a novel topology inspired by the Japanese paper cutting and folding kirigami art. It features W shaped cutout patterns which increase the stroke and heat dissipation surfaces, both critical in this use case, in comparison to other conventional alternatives such as wires [3]. The material used is NiTiNOL.

4.1. 2-SMA metal prototype

A version using the full kinematics and only 2 SMA modules is proposed (Fig. 4). Its fabrication is intended with the goal of testing the kinematics, and the adequacy of the measurements with the analytical model, without creating a full stack version. The proposed dimensions are: thickness of the buckled beam: 150 μm, thickness of cross spring blades: 100 μm, angle of actuation, $\theta_{\text{stable}} = 12°$, $F_{\text{SMA}} = 3$ N, and a stroke of 4 mm.
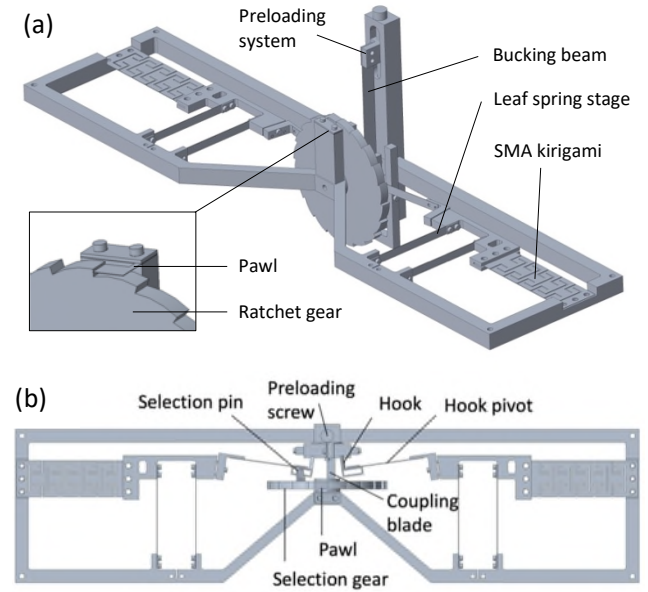
Figure 4. 2 CAD views of a metal 2-SMA prototype. The pawl is shown in the bottom left corner. SMAs are not displayed at the nominal position.
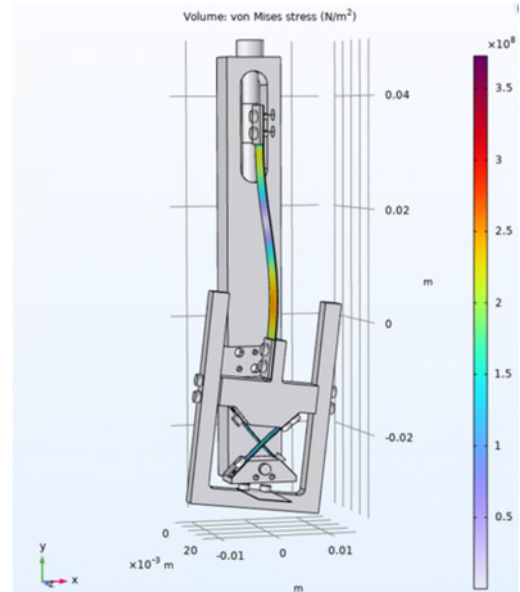
Figure 5. FEM simulations showing von Mises stress for the buckling beam and cross pivot, as well as the end effector in a stable state.

FEM simulations were conducted to validate the design and ensure that stress limits were not surpassed. Fig. 5 shows that stress does not exceed the steel's yield strength at maximum stroke.

4.2. Metal prototype for flexure-based gripper actuation

Fig. 6 shows a concrete use case, where the system was implemented on a bistable gripper flexure based mechanism [5]. This particular design uses 3 SMA modules on each of 4 quadrants, thus a total of $n = 12$ SMAs. The wheel has $n/n_{\text{quadrant}} = 3$ channels. Using properly dimensioned SMAs with $t_{\text{cool}} = 4\ s$, we have $t_{\text{commute}} = \frac{t_{\text{cool}}}{11} = 364\ ms$.
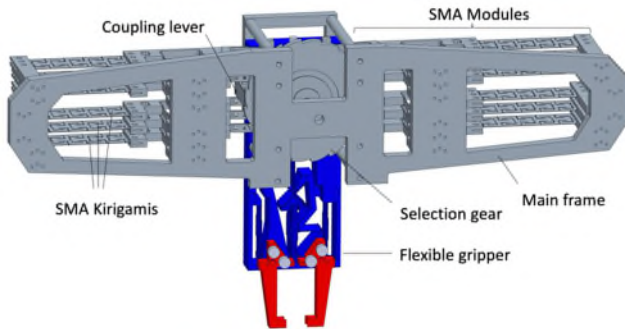
Figure 6. CAD view of a metal 12-SMA prototype mounted on a gripper.

5. Discussion

5.1. Optimization and limits to this design

While lowering the virtual cooling time of SMAs in a fully mechanical way, this approach comes at the expense of volume, mass, and cost. Optimizing the design for reducing these parameters is possible and should be sought in further developments, which are outside the scope of this article. The selected manufacturing process will be critical. Opting for an electro-eroded monolithic design for each module may reduce the costs in comparison to traditional manufacturing techniques requiring assembly. It also requires fewer parts which will reduce mass. Topology optimization can further help in that regard. The choice of materials will also impact mass. Although dense, metal offers great thermal dissipation which is essential to lower SMA cooling times. A proper characterization of the thermal performance will aid in choosing a proper material.

The stacking of SMA sheets might impact the thermal dissipation and thus affect the cooling time of the actuator. The actuation sequence heats the SMAs that are furthest from each other sequentially, which minimizes this effect. Notwithstanding, this effect should be properly estimated and to further mitigate the effect, a thermal insulation layer should be added between the modules, in a material such as a polymer.

5.2. Control and sensors

A current supply and a microcontroller control the n relays that drive the SMA modules, to ensure the right sequence is applied. Current heats the SMA through Joules Effect. It should be noted that the SMA modules should be electrically insulated from the frame to avoid short circuits.

In stable conditions, and given the bistable nature of this actuator, it can safely be used in an open loop, without sensors or encoders. However, proximity sensors can be used to check whether the switches were correctly realised. This would be useful in perturbed environments, to ensure that temperature or humidity do not tamper performance. Furthermore, such a sensor would be useful to run an automatic calibration routine, or to optimize performance dynamically during use.

Finally, it is possible to motorize the screw preloading the buckled beam, so that the stroke and exerted force can be tuned dynamically. In the case of the gripper section 4.2, such a setting would be useful to dynamically adjust the strength of the prehension, modulating the kind of weight that can be carried.

5.3. Dynamical behaviour

Due to the significant mass of the metal moving parts, external acceleration and gravity cannot be neglected. Dynamically balancing the SMA modules would fix that, but at the cost of extra mass and volume. To compensate for gravity without adding mass, both prototypes in section 4 feature horizontal SMA modules. Using a vertical design instead would induce a gravitational force on the SMA equivalent to $P \approx 0.4 \cdot F_{SMA}$. To keep the compensation, the actuator must be mounted on a tool operating with 4 degrees of freedom (three translational and one rotational: x, y, z, r_z). The mechanism would work in all orientations (6 degrees of freedom) if the modules were resized so that the SMAs can exert more force to accommodate gravity. This would rack up some extra mass, volume, and cost.

6. Conclusion

The mechanical concept and the actuator's working principle were described. An analytical model and its associated simulations were presented. Finally, examples for the realization of two metal-based versions were shown.

The potential for mechanical actuators coupling and decoupling several individual actuators was established. This innovative concept is promising in the context of Shape Memory Alloys in order to increases significantly the actuation rate.

Future work includes testing and realizing measurement campaigns on the prototype following its fabrication. Namely, the experimental validation of the analytical model and eventually the development of the device into a more optimized version, with a set of specifications. These elements together will help determine the usability of this system in industrial applications. If successful, this type of device could expand the range of SMA applications to cases where high cadence, performance and repeatability are required, whilst leveraging their compatibility to environments such as clean rooms, vacuums, space, or contamination-free biological applications [6, 7].

References

[1] Lara-Quintanilla A, Bersee H E N 2015 Active Cooling and Strain-Ratios to Increase the Actuation Frequency of SMA Wires *J. Shap. Mem. Superelasticity* **1** 460–467

[2] Tissot-Daguette L, Schneegans H, Thalmann E, Henein S 2022 Analytical modeling and experimental validation of rotationally actuated pinned–pinned and fixed–pinned buckled beam bistable mechanisms *J. Mechanism and Machine Theory* **174** 104874

[3] Ghorbani M, Thomas S, Lang G, Martinez T, and Perriard Y 2023 Fabrication and Characterization of the Kirigami-Inspired SMA-Powered Actuator *IEEE Transactions on industry* applications, **59**

[4] Cosandier F, Henein S, Richard M, Rubbert L 2017 *The art of flexure mechanism design* EPFL Press Lausanne

[5] Tissot-Daguette L, Prêcheur Llarena S, Baur C and Henein S 2024 Fully compliant snap-through bistable gripper mechanism based on a pinned-pinned buckled beam *24th Euspen conference*

[6] Zanaty M, Fussinger, T, Rogg A, Lovera A, Lambelet D, Vardi I, Wolfensberger T J, Baur C, and Henein S 2019 Programmable Multistable Mechanisms for Safe Surgical Puncturing ASME. *J. Med. Devices* **13(2)** 021002

[7] Power M, Barbot A, Seichepine F and Yang G 2023, Bistable, Pneumatically Actuated Microgripper Fabricated Using Two-Photon Polymerization and Oxygen Plasma Etching *J. Adv. Intell. Syst.*, **5** 2200121

Model enhanced paperboard permeability measurement with aerostatically sealed non-contacting instrument

Mikael Miettinen[1], Valtteri Vainio[1], Onni Leutonen[1], Petteri Haverinen[1], Raine Viitala[1]

[1]Aalto University

Mikael.miettinen@aalto.fi

Abstract

Paperboard permeability is a crucial quality parameter for various grades of paper and cardboard. Traditionally, the permeability measurements are conducted offline using contacting devices. The present study delved into a non-contact aerostatically sealed measurement method and device.

The investigated method, previously developed by the authors, was improved by introducing an aerostatic seal flow model into the calculation of sample permeability. This flow model enables the calculation of seal exhaust into the measurement volume, directly influencing the measured flow through the sample. The method was compared to a reference measurement with contacting seals and to the simple method of the previous study.

The results show that the improved method has good accuracy. Furthermore, the influence of seal supply pressure is found to be negligible. Thus, the study provides evidence on the feasibility of the measurement method and device.

Aerostatic bearing, aerostatic seal, in-process measurement, aerostatic seal model

1. Introduction

Paperboard permeability is crucial quality parameter for various paper and cardboard grades, including applications in filter and packaging materials. Furthermore, permeability is closely related to porosity, which is also a quality parameter of interest.

Permeability measurement methods, such as the Bentsen method standardized in ISO 8791-2:2013 [1], typically involve generating a pressure difference across the investigated sample and measuring the flow through it [2, 3]. The maximum feasible pressure difference is limited by the strength of the sample. Therefore, some measurement devices use wire meshes or grids to support the sample, allowing for the application of higher pressure differences [4, 5].

Permeability measurement with a non-contacting method has significant benefits over the contacting methods, one of the most important being the possibility to measure continuously from a fast moving web. This allows online measurement during roll-to-roll processing, while the conventional methods necessitate offline measurements with samples cut from the web.

The present study improves upon previous studies, in which first a two-sided aerostatically sealed measurement device was introduced [6], and later an improved single sided device better suited for online measurements was presented [7]. The current study further enhances these advancements by introducing a seal flow model to the permeability calculation. The flow model establishes a connection between the measured flow rates and the permeability of the sample.

2. Methods

The investigated device consists of porous aerostatic bearing elements, a measurement volume, and a vacuum groove (Figure 1). The vacuum groove is used to preload the measured sample against the aerostatic bearing elements, establishing a seal around the measurement volume. The measurement volume is an 8.2 mm wide and 30 mm long slot. Instrumentation of the seal supply and vacuum connections included flow and pressure sensors. Additionally, the gap height between the sample and the device was measured with a triangulating laser sensor. The measurement setup is presented in Figure 2.
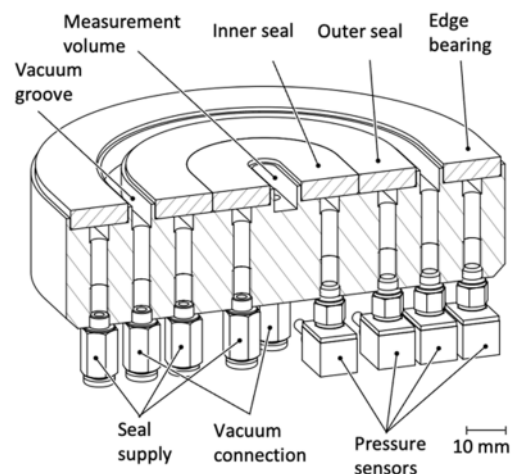
Figure 1. Cross-section of the measurement device.

Tests were conducted with a pressure difference of 1.47 kPa across the paper sample, which is the same pressure difference as in the conventional Bentsen method. The seal supply pressure was varied in the range of 0.15 MPa to 0.25 MPa. Reference tests were conducted with a 31.5 mm diameter measurement area device, that clamped both sides of the sample and sealed with o-rings.

The paper samples used were ordinary printing paper, referred to as sample 1, and coated paper with lower permeability, referred to as sample 2.

Furthermore, the improved calculation method with the flow model was compared to the simpler method utilized in the previous study [6]. In the simpler method, it was assumed that exactly all of the inner seal exhaust flowed into the measurement volume.
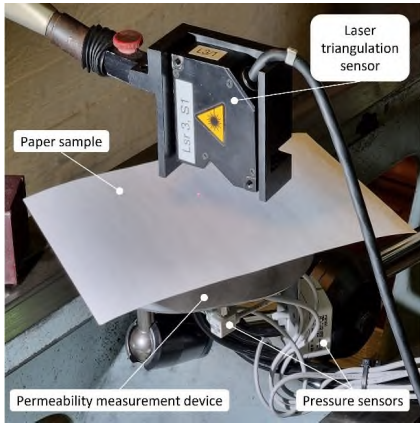
Figure 2. Measurement setup. The laser used in the gap height measurements is positioned between the inner and outer seal elements. [6]

In the flow model, a simplified porosity model was used, assuming unidirectional flow in the restrictor. Furthermore, the opposing surface of the seal was considered impermeable. The flow model is based on the well-known modified Reynolds equation for aerostatic bearings [8, 9]:

$$\nabla \cdot (ph^3 \nabla p) = -\sqrt{\frac{12k_P}{h_P}}\left(p_S^2 - p^2\right)$$

where p is the pressure in the air gap, p_S is the supply pressure, h is the air gap height, k_P is the permeability and h_P is the height of the restrictor.

The boundary conditions of the model, i.e., the supply pressure, pressures in the measurement chamber and vacuum groove, and the gap height, were measured. The model was then used to calculate the flow into the measurement volume. Consequently, the permeability of the paper sheet could be calculated from the measured flow out of the measurement volume and the calculated flow from the seal into the volume:

$$Q = k_Q(Q_{MV} - Q_{SE})$$

where Q is the flow through the sheet (comparable to the Bentsen method), k_Q is an empirically determined coefficient, Q_{MV} is measured flow out of the measurement volume and Q_{SE} is calculated seal exhaust into the measurement volume.

3. Results

The measured permeability values for samples 1 and 2 are shown in Figure 3.
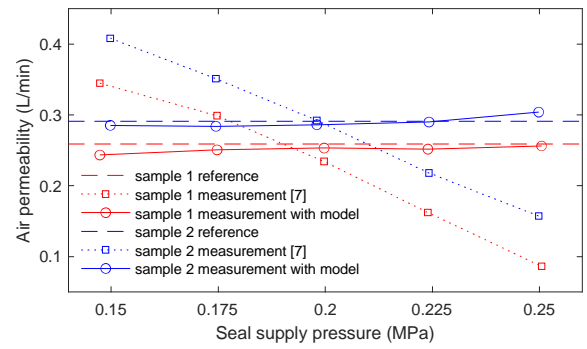
Figure 3. Air permeability of the investigated samples. Measurement [7] is with simpler method, measurement with model is with the improved method and reference value is measured with O-ring seals.

4. Discussion

The findings of this study show that the improved method with the seal flow model significantly improves the accuracy of the measurement in comparison to the simple method of the previous study. Notably, the improved method negated the influence of the seal supply pressure on the measurement result.

The simplifications of the model required the use of an empirically determined coefficient on the flow, k_Q = 0.5. The authors hypothesize that this coefficient may be necessary due to the assumption of the impermeable opposing surface for the seal, while in reality there is flow through the sample. Another potential cause changing the flow behaviour is the deformation of the sample resulting in non-uniform gap height.

Further studies could improve the flow model by implementing a permeable opposing surface for the seal, potentially removing the need for heuristic correction parameters. Furthermore, online measurements at low and high running speeds would be beneficial in further elucidating the method's efficacy.

References

[1] ISO 8791-2:2013 Paper and board — Determination of roughness/smoothness (air leak methods) — Part 2: Bendtsen method.

[2] TAPPI test method T 547 om-07, Air permeance of paper and paperboard (Sheffield method), Tappi Press, Atlanta, GA, USA

[3] M. H. Waller, "On-line Papermaking Sensors: An Historical Perspective," In Sci. Papermak., Trans of the XIIth Fund. Res. Symp. Oxford, 2001. pp. 785–895 doi: 10.15376/frc.2001.2.785.

[4] M. Rasi, "Permeability Properties of Paper," PhD thesis, Department of Physics, University of Jyväskylä, 2013.

[5] T. Kano, A Comparison between Oken Air Resistance-Smoothness Tester and Related Testers in Relation to Measured Values. Japan TAPPI Journal. 2008, 62 (12) p. 84

[6] M. Miettinen, V. Vainio, and R. Viitala, "On-line measurement of paperboard air permeability using aerostatic bearings," in Proc of EUSPEN 2022, Jun. 2022, pp. 187–189.

[7] M. Miettinen, V. Vainio, O. Leutonen, P. Haverinen, T. Tiainen, and R. Viitala, "Aerostatically sealed non-contacting paperboard porosity measurement device," in Proc EUSPEN 2023, euspen, Jun. 2023, pp. 231–232, isbn: 978-1-9989991-3-2.

[8] V. N. Constantinescu, Gas Lubrication, American Society of Mechanical Engineers, 1969.

[9] Farid Al-Bender, Air Bearings - Theory, Design and Applications, John Wiley & Sons, 2021.

Attenuation of thermographic disturbances emitted from a high-sensitivity sensor

HyungTae Kim[1], Kwon-Yong Shin[1], Jun Yong Hwang[1] & Heuiseok Kang[1]

[1]Research Institute of Human-Centric Manufacturing Technology, KITECH, Sangrok, Ansan, Gyeonggi, South Korea

htkim@kitech.re.kr

Abstract

A thermographic image usually provides a large field-of-view (FOV) with high temperature sensitivity; thus it has great potential for the inspection of panel devices such as flat panel displays (FPDs), wafers, and photovoltaic elements. However, the high reflectivity and high sensitivity of panel devices can lead to the shape of the thermal camera itself being detected in the thermographic image. Thus, long-wave infrared rays (LWIR) from the thermal camera should be removed for accurate thermography of reflective devices. This study investigated the attenuation of the LWIR from the front of the reflective surfaces. The proposed structure was similar to the coaxial optics in a microscope, and polished LWIR filters were tested as half mirrors within the coaxial optics. Thermal uniformity in the dark state was considered for the removal of LWIR within the thermal camera, and thermographic images of an ink stain were investigated when an LWIR source was applied.

Image, optical, visual inspection, temperature

1. Introduction

Thermography visualises long-wave infrared rays (LWIR), which exhibits quite different characteristics from visible rays (VIS), being able to penetrate media opaque to visible light. Thus, thermography reveals invisible or hidden phenomena as visible patterns, and has become popular in industrial applications such as the detection of gas leakages and mechanical failure [1].

Thermography is primarily intended to capture the thermal emission of arbitrary objects in the field of view (FOV); however, false images are frequently captured owing to thermal reflection. The LWIR creating these images originates from the surroundings rather than from within the FOV, and is reflected on the surfaces of objects in the FOV. Thermal reflection usually occurs on polished surfaces and is generally stronger than VIS reflection [2]. To address the resultant false images, which cause confusion at industrial sites, the removal of thermal reflection has been discussed in some studies. The simplest method for removing LWIR is background subtraction from time-varying thermal images [3]; background subtraction can be used for surveillance, but is ineffective for stationary objects. Deep learning and artificial intelligence (AI) have also been applied to remove thermal reflections [4]; however, AI requires sample images for training and the removal results are not guaranteed. Thermal camera companies have recognised the problem of reflection: they recommend changing the camera positions and angles when capturing images of reflective objects to prevent direction frontal reflection [5]; furthermore, a frontal image can be synthesised using multiple images from different incidence angles. Polarisation is the most popular method for reflection removal [6]; however, it requires an oblique incidence angle. Thus, the polarisation method is disadvantageous for frontal image acquisition.

Thus, the attenuation of frontal thermal reflection using conventional optical filters was investigated in this study. Briefly, a thermographic image of an ink stain in front of a polished silicon wafer was acquired, and LWIR-pass filters and an LWIR source were placed between the wafer and the camera ,similar

to a half-mirror. The proposed structure is typical of coaxial optics used to bypass the LWIR from a camera.
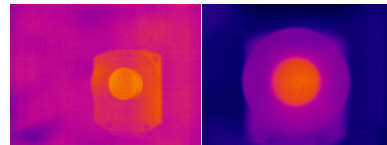
Figure 1. Thermographic images focused on polished surfaces of a silicon wafer (left) and an LWIR-pass filter (right) reflecting a camera.
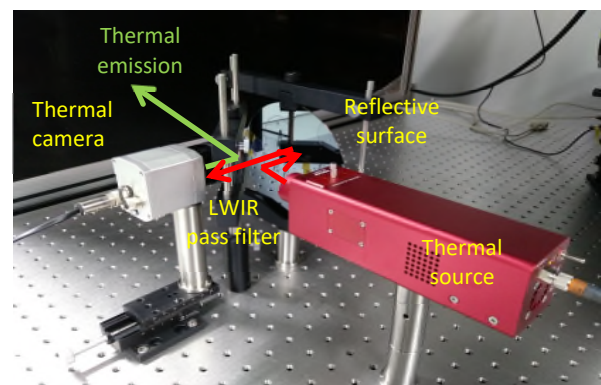
Figure 2. Experimental apparatus to remove thermal reflection.

2. Materials and method

As the thermal sensitivity of a thermal camera increases, thermal reflection becomes important in the inspection of precisely processed products. Figure 1 shows the thermal images from a camera directed at a silicon wafer and a LWIR-pass filter, showing that the thermal emission from the camera is visible due to reflection. The silicon wafer is opaque to LWIR; however, the LWIR-pass filter is transparent according to its specifications. Both surfaces were polished, and thermal reflections were observed in both images, despite the LWIR transparency of the filter. In the case of the LWIR-pass filter, the shapes behind the filter were also captured; thus, the filter can be used as a half-mirror. Figure 2 shows that the structure of the

coaxial optics eliminates unwanted thermal reflection. The emissions from the thermal camera are deflected out of the system by the half-mirror. The thermal radiation from the LWIR source is also deflected by the filter, and reflected from the target surface. Subsequently, the reflected LWIR passes through the filter and arrives at the thermal camera. Thus, the image of the thermal camera is removed from the thermographic image.

In a coaxial structure, the transmissibility and reflectivity of the filter with respect to the LWIR are crucial. The LWIR transmissibility can be obtained from the spectral responses of the material and LWIR reflection is achieved by polishing the surface. After investigating the transmissibility, Potassium Bromide (KBr), Germanium (Ge), Barium Fluoride (BaF$_2$) and Sodium Chloride (NaCl) were chosen as half mirrors. The reflection removal performance can be measured by observing the uniformity of a thermographic image in IR darkness. When inspecting a blank wafer, the uniformity of the image increases when false images are removed, because the deviation among the image pixels decreases. The uniformity can be conventionally calculated using the average (μ) and standard deviation (σ) of the image pixels as follows.

$$\gamma = 1 - \sigma/\mu \qquad (1)$$

3. Experiments

The experimental apparatus was constructed with a thermal camera (Optris PI640, Δ=40mK), an LWIR source (Thorlabs SLS203L), an LWIR-pass filter, an industrial controller (Beckhoff CX2020) and a silicon wafer on an optical table. The surfaces of the filter and wafer were polished. Printed patterns and an ink stain were drawn on the wafer. The camera was placed in front of the wafer and the LWIR source was vertically installed on the right side. The filter was set close to the thermal camera to cover the lens. The filter was attached to a rotatable post to enable adjustment of the incidence angle of the LWIR source and the thermal camera. The filter was transparent under VIS conditions and covered the thermal lens in front of the camera. The materials of the filters in the experiment were selected to have the LWIR transmission range between 8 and 14μm, such as KBr, Ge, BF$_2$ and NaCl. The LWIR from the source was reflected on the back side of the filter, and arrived at the wafer. The reflected LWIR on the wafer passed through the filter and was captured using the thermal camera. Thermographic images were acquired after rotating the filter by 0° and 45°. The source was then activated to investigate the ink stain on the wafer. The thermographic images were stored in an industrial controller and image processing was performed using OpenCV.

4. Results and discussion

Reflection removal was observed when using KBr, Ge, BaF$_2$ and NaCl filters. The float glass filter exhibited no response because of the spectral range of transmission. Figure 3 shows the thermographic images obtained using the Ge filter. When the angle of the Ge filter was 0°, the brightness range owing to reflection became larger than that without the filter. The brightness range decreased when the Ge filter was rotated by 45°. After applying the LWIR source, the line written using ink became conspicuous. This indicates that the LWIR from the camera was bypassed and the ink stain on the wafer became clear. The other filters also exhibited this effect during the experiments. Table 1 lists the variations in uniformity according to the rotation angle and material of the LWIR filters. At 0°, the uniformities with the filters were greater than those without the filters. Because the filters were placed near the camera, the thermal reflection of each filter was stronger than that of the

wafer. After rotating the filters by 45°, the uniformity increased, indicating that the false images were reduced. Therefore, the proposed method is effective in removing thermal reflections when the thermal camera is placed in front of the inspection area. Moreover, thermal inspection of the semiconductor and flat panel displays from the front was possible using the proposed method. Finally, the best results in the removal of thermal reflection were attained using the Ge filter; however, the removal performance could possibly be increased using another material. In the future, we plan to develop new materials for LWIR half-mirrors.
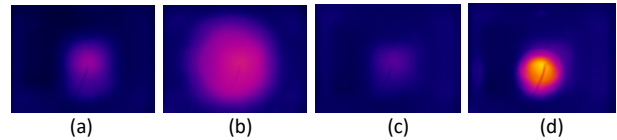
Figure 3. Thermographic images of reflective surface (a) without filter (b) with 0° Ge filter (c) with 45° Ge filter; and (d) with 45° Ge filter and an LWIR source.

Table 1 Uniformity according to rotation and LWIR filters

Angle	Free	KBr	Ge	BaF$_2$	NaCl
0°	0.5561	0.4500	0.5053	0.5287	0.5497
45°	-	0.5812	0.7475	0.6293	0.5871

5. Conclusion

This study presents a method for removing the false image of a thermal camera in front of an inspection target. A false image is created by thermal reflection when a thermal camera is placed in front of a reflective surface. Because this phenomenon disturbs temperature measurement, the false image is customarily removed using conventional coaxial optics. In this study, LWIR filters were applied to the half mirror in a coaxial optics system. The consequent image-removal performance was verified in terms of the uniformity of the thermographic images. The LWIR filters generally reduced the false image from the thermal reflection. The Ge filter exhibited the best removal performance among all filters used in the experiment. The proposed method can be applied to the front thermal inspection of reflective products.

References

[1] Resendiz-Ochoa E, Osornio-Rios R A, Benitez-Rangel J P, Romero-Troncoso R J and Morales-Hernandez L A 2018 Induction Motor Failure Analysis: An Automatic Methodology Based on Infrared Imaging *IEEE Access* **6** 76993-77003

[2] Liu R and Vondrick C 2023 Humans as Light Bulbs: 3D Human Reconstruction from Thermal Reflection *Proc. IEEE/CVF CVPR* 12531-12542

[3] Zeise B and Wagner B 2016 Temperature Correction and Reflection Removal in Thermal Images using 3D Temperature Mapping *Proc ICINCO* **2** 158-165

[4] Batchuluun G, Baek N R, Nguyen D T, Pham T D, and Park K R 2020 Region-based removal of thermal reflection using pruned fully convolutional network *IEEE Access* **8** 75741–75760

[8] Beall E and Prairie E 2018 Systems and approaches for thermal image corrections *United States Patent* 10,129,490 B2

[9] Li N, Zhao Y, Pan Q AND Kong S G 2018 Removal of reflections in LWIR image with polarization characteristics *Optics Express* **26** 16488

The INRIM electrostatic balance to implement the new SI definition of the mass in the milligram range

Milena Astrua[1], Marco Pisani[1], Marco Santiano[1], Fabio Saba[1], Marina Orio[1]

[1]Istituto Nazionale di Ricerca Metrologica, INRIM, strada della Cacce 91 – 10135 – Torino - Italy

m.astrua@inrim.it

Abstract

The realisation of the kilogram in the new SI can be implemented in several ways. The solution proposed by INRIM is based on an electrostatic balance operating in the milligram range. Due to the relative weakness of the electrostatic force compared to the 'magnetic' force (used in the Kibble balance), this type of balance is well suited for measuring small masses. On the other hand, small masses today suffer from a degradation of uncertainty due to the number of steps from the kilogram. For these reasons, there is a strong interest both in the scientific and in the metrological community for the realisation of a balance dedicated to masses below one gram. The electrostatic balance developed at INRIM is based on measuring the capacitance of a parallel plate capacitor to which the mass is hung. The objective of such instrument is to achieve a relative uncertainty of 10^{-4} for masses in the milligram range. Based on the experience gained with a previous prototype, a new mechanical structure of the device has been realised. A software for automating the measurements and the data acquisition has been developed in LabVIEW. A FEM model of the balance allowed to simulate the electric field between the capacitor plates and to obtain the relationship between the capacitance and the electrode distance. The paper describes the new set-up and reports the main results obtained in an intensive measurement campaign.

SI definition of the mass, electrostatic balance, parallel plate capacitor

1. Introduction

The new definition of the kilogram adopted in 2018 [1] is based on fundamental constants and its realization can be implemented in several ways [2,3]. The technique proposed by INRIM is based on an electrostatic balance operating in the milligram range. The paper describes the main aspects of the renewed set-up and its characterization.

2. INRIM electrostatic balance

The first prototype of INRIM electrostatic balance to measure small mass standards up to 1 g is described in [4]. Based on the gained experience, a second set-up based on a state of the art mass comparator and a capacitor made by two gold parallel plates has been realised. The mass comparator is the Ultra-microbalance UMX2 manufactured by Mettler-Toledo (measuring range 2 g, resolution 0.1 μg). The capacitor is made by two parallel plates made of glass: one plate is fixed to the pan of the balance, while the second is fixed to a piezoelectric actuator facing the first plate. In order to reduce the roughness of the plates, a gold film was deposited on the plates by sputtering in INRIM laboratories devoted to nano-fabrication of devices. A picture of the capacitor plates is shown in Fig.1. A portable magnifying camera is used to align the system and to assess the parallelism of the plates.

The working principle of the electrostatic balance is the equivalence between the gravitational force from a test mass, F_g, and the electrostatic force from a capacitor, F_e. Hence, the fundamental measurement equation is

$$F_g = mg \left(1 - \frac{\rho_{air}}{\rho_m}\right) = F_e = \frac{1}{2}\frac{\partial C}{\partial z}V^2 \qquad (1)$$

where m is the mass, g is the gravitational acceleration, ρ_{air} is the air density, ρ_m is the mass density, C is the capacitance, z is the distance between the capacitor plates and V is the voltage difference applied to the plates.
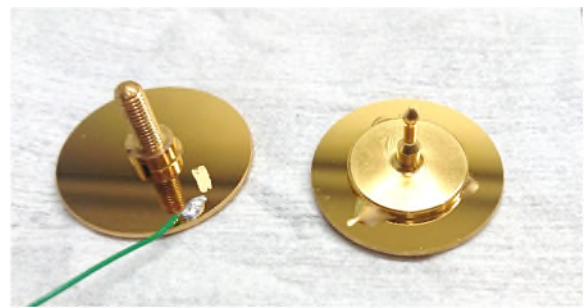
Figure 1. Picture of the capacitor gold plates manufactured in INRIM

The measurement procedure is divided in several steps. The first step is the measurement of the spatial gradient of capacitance, dC/dz, and the calculation of this quantity at a particular distance, d_0. Then the mass to be calibrated is loaded and a voltage is applied to the plate in order to compensate the gravitational force. A high accuracy Andeen-Hagerling 2500A capacitance bridge is used to measure the capacitance between the plates. A linear piezoelectric actuator manufactured by Physik Instrument, model PI-P753.2, is used to set the distance between the plates. The voltage applied to the capacitor is measured by an Agilent 3458A voltmeter. All the measurement are traceable to INRIM standards.

3. Mechanical characterization of the balance

A mechanical characterization of the mass comparator was performed before using it in the electrostatic balance set-up.
First of all, an Attocube laser interferometer was used to characterize the plate displacement caused by the load. The laser beam was directed through a fibre towards the plate fixed to the pan of the balance, as shown in Fig. 2. Then the balance was loaded with increasing mass standards and the corresponding plate displacements were measured by the interferometer. As expected from a good mechanical system, the plate displacement is linearly proportional to the load over the entire measuring range, as shown in Fig. 3.
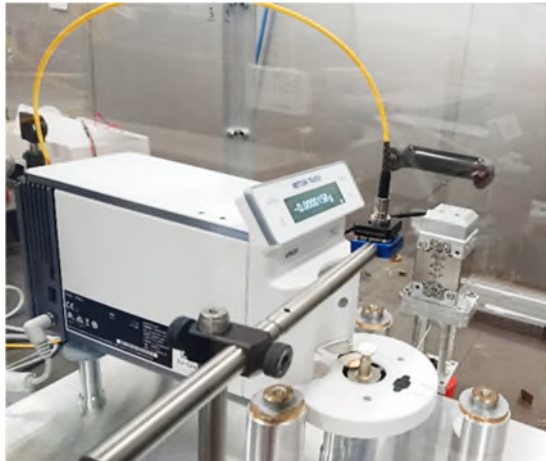
Figure 2. Picture of the interferometric set-up for the characterization of the mechanical properties of the balance
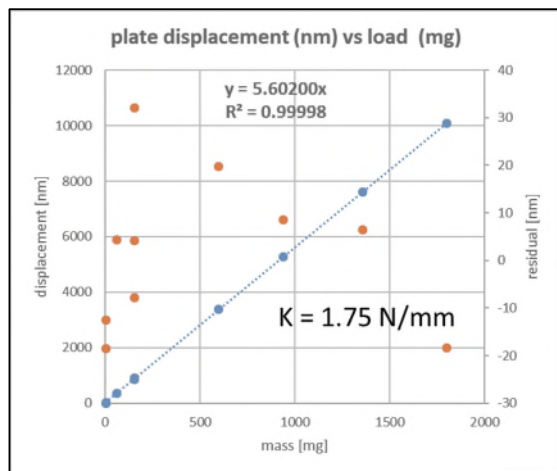
Figure 3. Left axis: linear dependence of the plate displacement on load (blue dots). Right axis: residuals from the linear fit (orange dots)
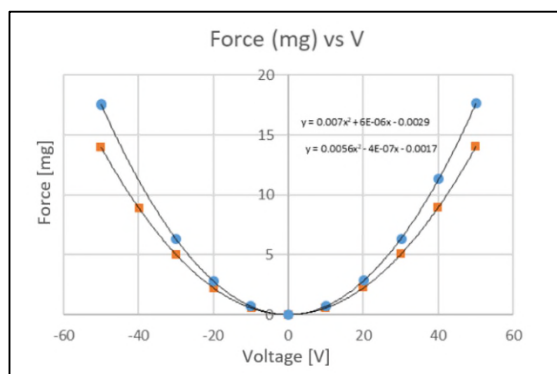
Figure 4. Force values measured by the balance as a function of the voltage applied to the capacitor at two different distances between the capacitor plates

Then the second plate fixed to the piezoelectric actuator is mounted facing the first plate and parallel to it at a distance of about 200 μm to form a capacitor. As second test on the mass comparator, an increasing voltage is applied to the electrodes while the force measured by the mass comparator is recorded. According to theory, the measured force has a second order behaviour with respect to the voltage, as shown in Fig. 4.

4. Measurement automation

In order to avoid the presence of an operator and reduce the thermal drift, a software for automating the procedure and the data acquisition has been developed in LabVIEW.
The program is able to manage the entire measurement cycle. Indeed, it allows to load and unload the mass standard. It communicates with all instruments to acquire data from the balance, the voltmeter and the capacitive bridge.
It allows to drive the piezoelectric actuator in selectable steps in order to measure the capacitance at different distance between the plates and to evaluate the spatial gradient of capacitance, dC/dz, as shown in Fig. 5.
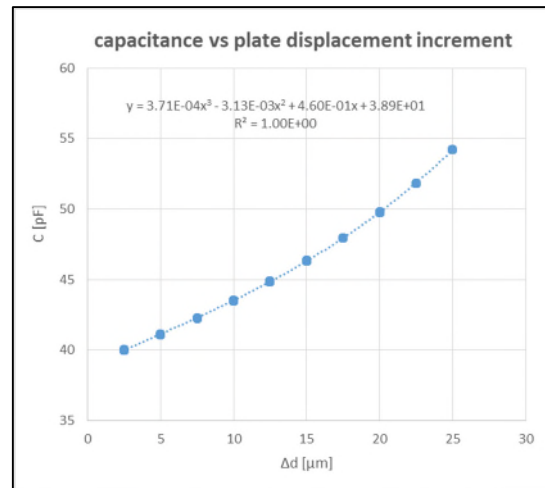
Figure 5. Capacitance values measured as a function of an increment of the distance between the capacitor plates

Finally, it controls a NI daq device USB-6356 to generate an analog voltage which is amplified and sent to one of the capacitor plate to compensate the load with the electrostatic force.
This automation will enable the measurements to be repeated many times in order to lower the statistical uncertainty.

5. Conclusions

A new prototype of an electrostatic balance based on gold parallel plates has been realized at INRIM to measure small mass standards in the milligram range. The mechanical performance of the system was extensively tested and a software for automating the measurement procedure was developed. With this new set-up, we foresee to achieve a relative uncertainty level of 10^{-4} for masses up to 100 mg.

References

[1] Proc. of the 26th meeting of the CGPM (2018)
[2] Robinson I A and Schlamminger S 2016 *Metrologia* **53** no. 5, pp. A46-A74
[3] Fujiiet K et al. 2016 *Metrologia* **53** no. 5, pp. A19-A45
[4] Pisani M, Malengo M, Santiano M, Saba F, Torchio D 2019 *IEEE Trans. Instrum. Meas.* **68** no. 6 pp. 2223-2228

Measuring vibrations in interferometric optical profilometry through imaging fringes at 1kHz

Chaoren Liu, Carlos Bermudez, Guillem Carles, Roger Artigas

Sensofar Tech, S.L., Parc Audiovisual de Catalunya, Ctra. BV-1274, KM 1, 08225 Terrassa (SPAIN)

cliu@sensofar.com

Abstract

Monitoring and controlling vibrations are critical not only for precision manufacturing, but also for high precision optical metrology. There are many sources of vibration that might influence the performance of a system: environmental acoustic noise, seismic vibration, resonances caused by the movement of internal motors, etc. The ability to measure and analyze such vibrations is crucial to evaluate the environment in which the system is installed. This includes the determination of the origin of the vibrations, the assessment of their impact on the performance of the system and, ultimately, the possibility to investigate possible solutions for their suppression. Optical profilometers employing high magnification microscope objectives may be severely affected by vibrations, which introduce jitter or blur in the acquired sequence of input images, depending on the frequency of the vibration. Since processing of such images is used to reconstruct the output topography, this has a serious detrimental effect on the quality of the three-dimensional surface measurements.

In this work, we present a method for obtaining the vibrational information of an interferometric optical profiler. It is based on the acquisition of a time sequence of the interference fringes at a sufficiently high frame rate to enable measurement of vibrations of up to 1 kHz. Because we use the camera of the profiler itself, no additional hardware is required. We demonstrate the approach by computing the vibrational response of a commercial optical profiler to input environmental acoustic noise, at a range of controlled frequencies. The method is readily applicable to any image-based interferometric system, enabling to determine its dynamics, and to use it as a proxy to monitor the surrounding environment. Additionally, it may be used to measure the anti-vibrational performance of isolating platforms which are common components in high-precision optical systems.

Keywords: acoustic, interferometry, metrology, vibration

1. Introduction

Microelectronics have undergone significant development in recent decades, leading to the attainment of sensors with heightened sensitivity and reduced response time. These advancements, coupled with rapidly evolving metrology techniques, have propelled us into the nanometer-scale era. The fabrication and characterization of materials at this scale is very demanding and the ability to monitor the processes and inspect components with high precision has become essential. Optical metrology offers non-invasive and high-performance methods for such tasks. However, the control of vibrations is crucial for high-precision inspection.

Vibrations can introduce jitter or blur to images, depending on the vibration frequency relative to the image sampling rate. Such effects significantly impact techniques such as interferometry. For example, in phase scanning interferometry, vibrations can introduce measurement errors [1]. As a consequence, the accuracy and the repeatability of the metrological system are affected by vibrations. Although the sensitivity to such errors appears to be algorithm-dependent, achieving complete immunity to vibrations remains challenging.

Numerous studies have investigated how vibrations impact metrology system performance, spanning processes related to data acquisition (optical and structural considerations) as well as algorithmic design [2–6]. On the other side, structural mechanical design of the instruments becomes crucial to minimise vibrations. For example, it is important to design the mechanics of the instrument such that the most problematic frequencies are attenuated. Therefore, a method to assess the impact of different sources of vibration directly from the metrological instrument is of great interest. Here, a method to precisely measure these vibrations in an interferometric optical profiler is proposed, by using a simple analysis of image profiles acquired at 1 kHz.

There are various sources of vibrations in manufacturing environments, such as seismic events, passing vehicles or personnel, acoustic noise from the environment, or vibrations induced from moving parts [7]. Controlling noise at a manufacturing site is challenging due to the difficulty in locating the sources and determining the response under such perturbation, especially when dealing with vibrations at the micrometre per second level. Additionally, internal movement within the system like scanning stages, can also introduce vibrations.

Optical tables are commonly employed to isolate vibrations. However, depending on the table's characteristics, some external vibrations may be transmitted, and even resonances may appear in extreme cases. Similar scenarios can occur in the support structures where metrology equipment is placed. For example, a passing staff member may induce vibrations with a frequency matching the pneumatic spring of the workbench [8]
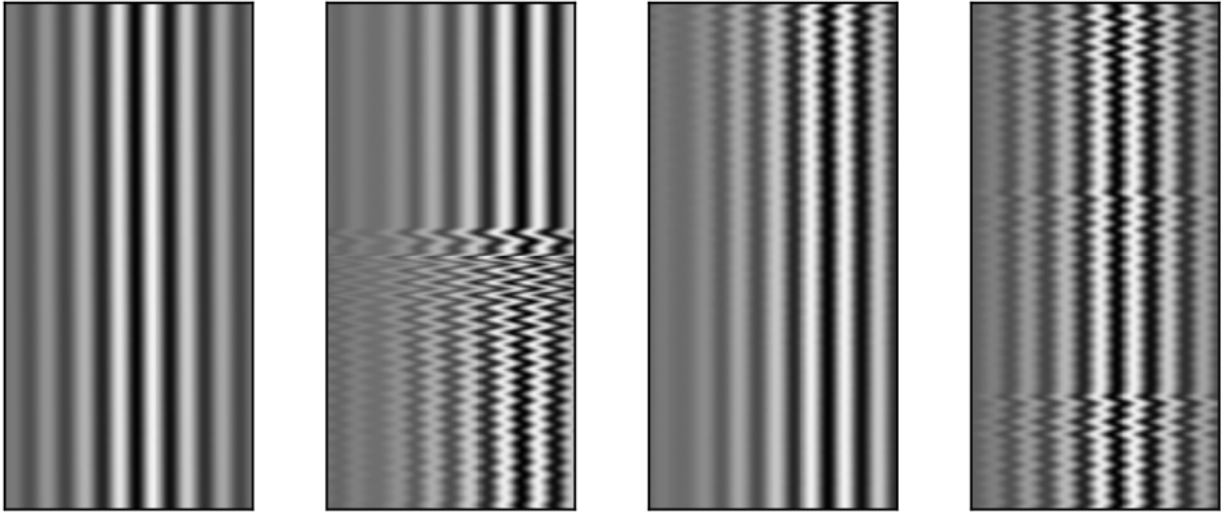
Figure 1. Example of sequence-images obtained from accumulating fringe profiles over time. The horizontal direction captures the fringes generated by the interferometer imaging a tilted mirror. The vertical direction captures the variation over time. The series correspond to a duration of 5 seconds. In the different examples, sporadic knocks on the table induce vibrations that are captured by the sequences, acquired at 1 kHz.

Addressing vibrations involves various strategies depending on the system's damping behaviour, including removing vibration sources, interrupting transmission routes, or altering system characteristics. From a structural designer's perspective, utilizing commercial products like optical tables or active anti-vibration tables, along with established solutions such as anti-vibration legs or constrained layer damping, proves beneficial. In cases where dominant frequency acoustic noise is unavoidable and an acoustic isolation cabinet cannot be installed, structural redesign becomes essential to shift the intrinsic resonance frequency away from identified perturbations.

In all, to mitigate the impact of vibrations, the first step is to identify their characteristics and assessing their impact on system performance. In this study, a straightforward yet efficient method to determine the influence of vibrations directly from the images acquired in an interferometric optical profiler is presented.

2. Methodology

A software module was developed to capture images from an interferometric optical profiler using a camera running at 1000 fps. To achieve such high speed, the stored region-of-interest in the camera was reduced to single-line images of 1×2448 pixels. The system uses a Mirau-type interferometric $10\times/0.3$NA objective. A flat mirror at the sample plane was placed tilted at an angle such that, in the direction of the acquired line-image, interferometric fringes appear. Time sequences of 5 seconds at 1 kHz sampling rate were captured, and so each sequence required to store 5000 time-sequence line profiles in memory. For convenience, such sequences were stored in 2448×5000 images, in which each row contains the captured fringes, and columns capture the variation in time. Example sequence-images are shown in Figure 1.

Note how vibrations are captured directly in this sequence-images because a variation in the axial distance causes a phase shift in the fringes. Such phase shift can be readily detected by measuring the relative horizontal shift in each line. This was done by Fourier transforming each line independently and extracting the phase of the main spatial frequency component, which is readily identified from its high magnitude in the Fourier transform. Finally, the phase of such Fourier component is related to the amplitude of the relative shift by a simple relation: a complete period of 2π radians corresponds to a distance of $\lambda/2$, where λ is the nominal wavelength of the light. In all, the amplitude of vibration over time is computed from each sequence-image, where the displacement:

$$z = \frac{\lambda * \psi}{4\pi} \tag{1}$$

where ψ is the phase of the fringes. Since calculation of displacement (used here to determine the amplitude of vibration) is determined by the physics of light interference, there is no calibration involved and accuracy is intrinsically very high. The main uncertainty for accuracy is the determination of the effective wavelength, which is of course set by the light source but also affected by the numerical aperture of the objective used. Besides this, other sources of error include: the error in identifying the fringe frequency associated with the sample tilt (which is arbitrary), and the error in determining the phase value of the frequency component from each noisy line-image. These sources of error are in practice zero-mean perturbations and affect only the precision of the measurements. We assessed their overall impact directly from measurements: we measured the instrument noise by acquiring sequences of unperturbed samples over time in an isolated environment, such that, variations could be associated only to measurement errors. Such instrument noise was measured to be below 1 nm.
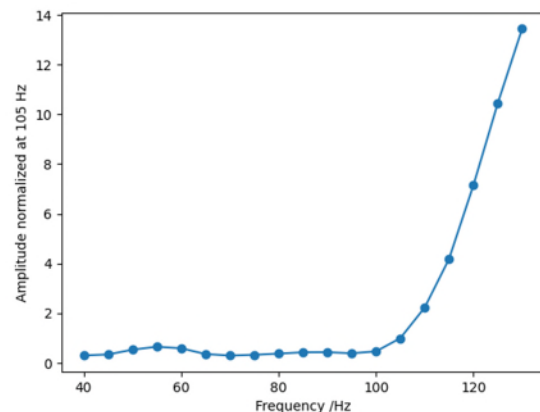
Figure 2. Response of the speaker at different frequencies, measured using a microphone.
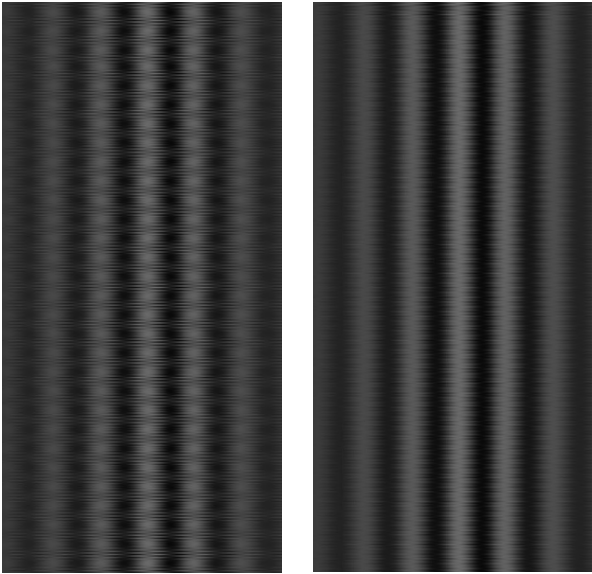
Figure 3. Sequence images obtained for input acoustic excitation at (left) 70 Hz and (right) 75 Hz, as example acquisitions.

Figure 4. The calculated Power Spectral Density of the vibration amplitude induced in the interferometer is shown for the selected excitation frequencies. Blue and red representing with and without active anti vibration table respectively.

For qualitative illustration, the response of the system to external knocks on the optical table was measured, and some examples are shown in Figure 1. It can be visually appreciated how knocking on the table causes a vibration, with particular dominant frequencies, that attenuate over time at a given rate.

Because the aim is to assess the impact of vibrations into the measurements, the time-frequency components of the extracted amplitude sequences were analysed, when the system is perturbated by acoustic input at various frequencies. To do this, the power spectral density (PSD) of the time series was calculated using the Welch method, for each stimulus. Experimentally, the perturbation was applied by playing a pure frequency sound on a 4 inch subwoofer speaker placed close to the optical profiler. Of course, the speaker does not have a constant spectral response, and to have an indication, the response of the speaker using a microphone (Rode, Lavalier) was measured, which is shown in Figure 2 for reference. The microphone has its own spectral response, but vendor specifications indicate that the variation is below 5 dB in the range of 40 Hz to 130 Hz [9].

3. Results

3.1 Vibration induced by knocking the optical table

As mentioned earlier, a qualitative assessment of the method by measuring the vibrations induced by sporadic knock on the optical table was performed. Results are shown in Figure 1, where the impact of vibrations and their attenuation over time is evident. This suggests that the system requires roughly 5 seconds to stabilize.

3.2 Vibration from induced vibration with controlled acoustic input

Here it is analysed how vibrations generated from acoustic input at different frequencies are transferred to the system. This includes how well each input is relatively attenuated and also how other resonant frequencies are excited, as a transmission matrix.
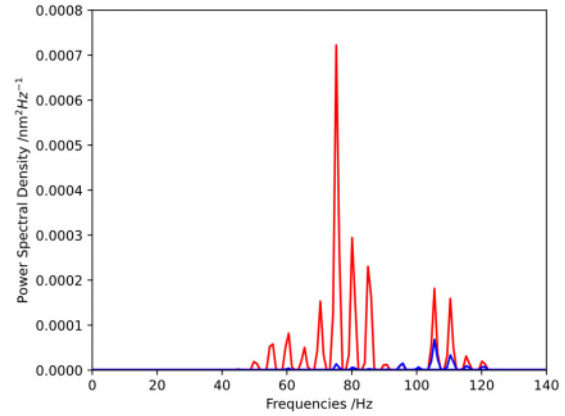
For each specified input frequency within the range of 40 to 130 Hz, a perturbation lasting 5 seconds was introduced, and the corresponding sequence-image was recorded. Examples of sequence images obtained with excitations at 70 Hz and 75 Hz are shown in Figure 3. The experiment was repeated in two different scenarios: with the system directly on an optical table, and with the system installed on an active anti-vibrational table.

Results are shown in Figure 4 and Figure 5, on a linear scale and in a form of a pseudo-coloured transmission matrix, respectively. In the case of pseudo coloured transmission matrix, each row of the matrix corresponds to a single pure acoustic frequency excitation, and the values shown across columns correspond to the impact generated at the images (following a PSD calculation). As expected, the matrix has a strong diagonal, but resonances appearing at harmonics of the excitation frequency also appear. Other intrinsic resonances should appear as vertical features, i.e. that are excited at any (or a range of) frequency. For example, small but detectable perturbations are noted at frequencies close to 30 Hz and 50 Hz.

Secondly, the results were repeated with the system installed on an anti-vibrational table. Active anti-vibrational tables play a crucial role where mitigating vibrations is imperative. In this study, the response of a system was assessed mounted on the Accurion® i4 table, as depicted in Figure 4. Lower PSD values are observed due to the effect of the anti-vibrational table. Results are shown in Figure 4. Similarly, we can observe the appearance of harmonics. Vibrations at 30 Hz and 50 Hz are now more attenuated, arguably through the anti-vibrational table, although the perturbation at 30 Hz is still noticeable, perhaps being associated to another intrinsic vibrational mode of the structure.

4. Conclusions

In this work, an effective method of quantifying the vibration was developed, based on the analysis of the time series of images obtained from Mirau type interferometric objective, with sampling rate of 1 kHz. The instrumental noise of the developed technique was calculated to be below 1 nm in our prototype. Using this method, the transmission matrix that characterises how external perturbations (in this case, in the form of acoustic excitation) are transferred and impact the system was measured.

Various methods are available for monitoring vibrations, with MEMS-based sensors being ideal if sufficient sensitivity is achieved. Other types, such as capacitor-based sensors
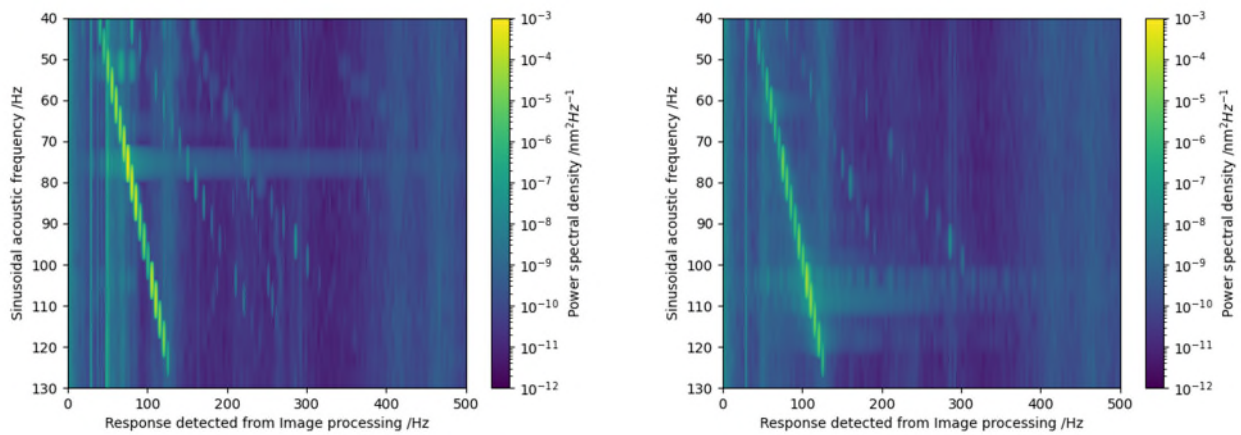
Figure 5. Power Spectral Density calculation of the vibration of the structure under forced vibration by acoustic disturbance for acoustic excitation at the selected frequencies, A false-coloured transmission matrix of the system is shown. (left) highlighting response of the structure, (right) in this case the instrument was installed on an active anti-vibration table.

employed in PIEZO, and external accelerometers with piezo functionality, are also valuable. However, the proposed method provides an alternative approach, efficient and easily implementable in the interferometers without necessitating additional hardware. Furthermore, the measurements are performed directly on the same camera that is used to operate the interferometer.

Using the developed tool, the impact of forced vibration induced by acoustic noise was observed. Notable effects included blurring and jagged fringes, with the resonance amplitude (response to acoustic noise) measuring around 50 nm. The dominant frequencies mirrored the disturbance frequency, exhibiting effects at double and triple frequencies.

The tool offers a straightforward means of determining the adequacy of ambient conditions for metrology measurements. It proves valuable for product development, providing a tool to assess anti-vibration performance effectively. The ease of implementation makes it a practical asset for evaluating the ambient environment's suitability for precise metrological measurements and contributes to the ongoing development of the optical equipment.

Acknowledgement

References

[1] de Groot P J 1995 Vibration in phase-shifting interferometry *Journal of the Optical Society of America A* **12** 354-365

[2] Serbes H and Lehmann P 2023 Investigation of coherence scanning Mirau interferometers with integrated vibration compensation for use in production environments *Technisches Messen* **90** 73–78

[3] Serbes H, Gollor P, Hagemeier S and Lehmann P 2021 Mirau-based CSI with oscillating reference mirror for vibration compensation in in-process applications *Applied Sciences* **11** 9642

[4] Wu D and Fang F 2021 Development of surface reconstruction algorithms for optical interferometric measurement *Frontiers of Mechanical Engineering* **16** 1-31

[5] Liu Q, Li L, Zhang H, Huang W and Yue X 2020 Simultaneous dual-wavelength phase-shifting interferometry for surface topography measurement *Opt Lasers Eng.* **124** 105813

[6] Wiersma J T and Wyant J C. 2013 Vibration insensitive extended range interference microscopy *Appl Opt.* **52** 5957–61

[7] Troutman J, Evans C J, Ganguly V and Schmitz T L 2014 Performance evaluation of a vibration desensitized scanning white light interferometer *Surf Topogr.:Metrol. Prop.* **2** 014011

[8] Amick H and Stead M 2007 Vibration Sensitivity of Laboratory Bench Microscopes *Sound and vibration* 10-16

[9] https://edge.rode.com/pdf/page/297/modules/986/ lavalier_datasheet.pdf Datasheet Lavalier

Study of calibration technique for hybrid structured-light metrology system

Yongjia Xu[1],*, Feng Gao[1], Yanling Li[1,2] & Xiangqian Jiang[1]

[1]EPSRC Future Metrology Hub, University of Huddersfield, Huddersfield, HD1 3DH, UK
[2]School of Mechanical Engineering, Hebei University of Technology, Tianjin 300130, China

*Correspondence: Y.Xu2@hud.ac.uk; Tel.: +44-7510-953359

Abstract

Numerous structured surfaces with composite materials are widely applied in advanced manufacturing. Hybrid structured-light metrology system has been proposed for in-line form measuring of the structured surfaces with both reflective and diffuse characters. A hybrid structured-light metrology system contains a fringe projection profilometry (FPP) subsystem and a phase measuring deflectometry (PMD) subsystem. Each subsystem measures rough surfaces and specular surfaces based on structured-light projection and reflection principle, respectively. Accurate calibration of the system is a challenge and highly influences the data stitching accuracy of the subsystems. In this paper, calibration technique is studied for the hybrid structured-light system to achieve good measurement accuracy. Specific targets are designed and manufactured for the calibration. Novel calibration algorithms are studied based on the calibration targets. Details of the calibration procedure are presented and discussed. Experiments have been conducted and verified the effectiveness of the proposed calibration technique by measuring structured composite samples with a calibrated portable hybrid structured-light metrology prototype. Experimental results demonstrate that the proposed calibration technique can significantly improve the data fusion accuracy and the prototype can achieve good measurement accuracy based on the proposed calibration technique.

Keywords: Optical metrology; Three-dimensional measurement; Structured light technique; Structured composite surfaces; Calibration.

1. Introduction

In-line surface measurement is an important section but still a challenge for precision and ultra-precision machining. Current widely used surface metrology techniques, such as coordinate measuring machine and stylus profilometer are hardly applied in in-line metrology due to their disadvantages of low measurement speed and large volume. By contrast, structured-light metrology techniques, such as fringe projection profilometry (FPP) [1-3] and phase measuring deflectometry (PMD) [4-6] have obvious benefits in fast speed, simple system configuration, and light weight. They are hot-topics in in-line surface form measurements but still have limited measurement ability affected by the reflective properties of the tested surfaces' materials. FPP reconstructs a measured surface's form data based on the scattered structured-light patterns on the surface. Therefore, it can only measure rough surfaces. PMD measures based on structured-light reflection and is only good at measuring specular surfaces.

Hybrid structured-light technique [7-8] has been studied to increase the measurement ability of structured-light technique, which combining the advantages of FPP and PMD. FPP subsystem and PMD subsystem work independently. The reconstruction data from the subsystems can be fused together to generate a completed form of the measured surfaces. Thus, hybrid structured-light technique has obvious advantage in measuring more wider range of surfaces with different reflective characteristics. An accurate data fusion between the subsystems is essential to achieve high measurement accuracy of the hybrid structured-light technique. Martin et al. studied a method to calibrate the subsystems based on a special designed target for a good data fusion [9]. The designed target consists of several specular surfaces and rough surfaces and is difficult to be manufactured. In order to increase data fusion accuracy of the subsystems of hybrid structured-light technique, a flexible calibration technique is investigated based on calibration targets that can be easily manufactured. Details of the calibration algorithms and strategy are also presented.

2. Principle and method

2.1. Measurement principle and system

Figure 1 presents an illustration of a stereo-camera hybrid structured-light metrology system [9]. The system contains two cameras, a projector and a screen. The cameras and the screen form a stereo PMD system, which measures reflective surfaces. Vertical and horizontal phase measuring profilometry (PMP) patterns are generated by a computer, displayed on the screen, and captured by the cameras through the reflection of the measured surfaces. The measured surfaces' form data can be calculated based on the captured fringe patterns. One of the cameras and the projector generate a FPP system, which can measure the form of rough surfaces. PMP patterns generated by the computer are projected by the projector on the measured surface and captured by the camera. FPP reconstructs the 3D data of the measured surfaces based on the captured structured-light patterns. The reconstructed 3D data of PMD and FPP are fused to generate the final output.

In our proposed hybrid structured-light metrology system [9], a plate beam splitter (BS) is applied to fold the optical beam paths to decrease the system volume. Figure 2 illustrates an equivalent configuration of the system.
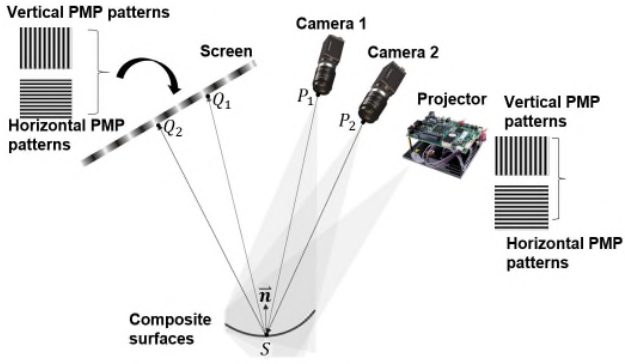
Figure 1. Illustration of the principle of the hybrid structured-light metrology technique
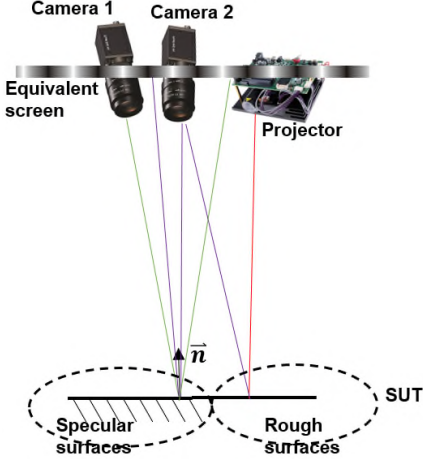
Figure 2. Illustration of configuration of a hybrid structured-light metrology system

2.2. Calibration method
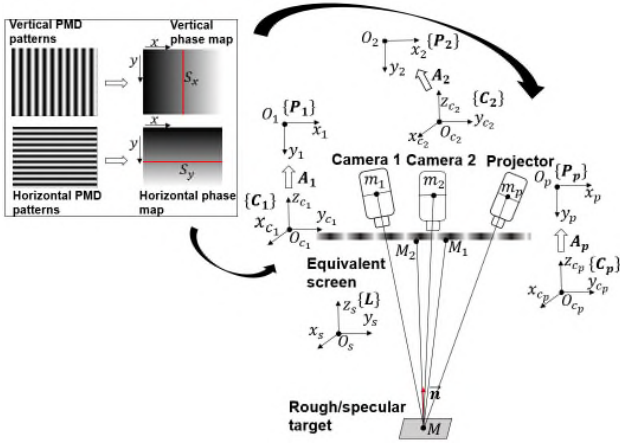
Figure 3. Illustration of the calibration of a hybrid structured-light metrology system
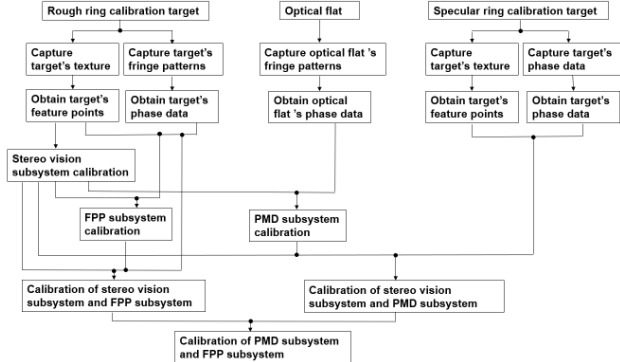
Figure 4. Diagram of the proposed hybrid structured-light metrology system calibration technique

Calibration is an essential process to obtain the imaging parameters of the hybrid structured-light metrology system for the surfaces' form reconstruction. This process also plays an important role in the data fusion between FPP subsystem and PMD subsystem. Figure 3 illustrates the purpose of the calibration process, which is to calculate the imaging parameters of the cameras (denoted as A_1 and A_2, respectively), the relationship between the cameras (using $\{C_1\}$ and $\{C_2\}$ to express the Camera 1 coordinate system and the Camera 2 coordinate system, respectively), the projector's imaging parameter (denoted as A_p), the relationship between $\{C_2\}$ and the projector coordinate system (expressed with $\{C_p\}$), and the relationships between equivalent screen coordinate system (denoted as $\{L\}$), $\{C_1\}$, and $\{C_2\}$. Figure 4 illustrates the strategy of the proposed calibration technique. A rough ring calibration target is placed at several arbitrary positions during the calibration process. The centre of the rings on target can be extracted through imaging processing. The ring centres are used as feature points to obtain A_1, A_2, and the relationship between $\{C_1\}$ and $\{C_2\}$, based on pin-hole model [10]. A_p and the relationship between $\{C_2\}$ and $\{C_p\}$ can be obtained by projecting fringe patterns on the rough ring target [11]. The relationships between $\{L\}$, $\{C_1\}$, and $\{C_2\}$ can be calibrated based on the previous method [12] by using an optical flat. The ring centres of the rough calibration target can be reconstructed with two ways. One is the stereo cameras based on stereo vision algorithm [10]. Another is to calculate the 3D positions of the ring centres by using FPP. Using F to denote as the reconstructed 3D position of the ring centres by FPP, S express the corresponding reconstructed data by the stereo cameras. The relationship between the stereo vision system and the FPP system can be calculated based on Eq. (1).

$$S = R_{F\_S}\,F + T_{F\_S} \qquad (1)$$

where R_{F_S} and T_{F_S} present the transformation relationship from the FPP system to the stereo vision system. A specular ring calibration target is used to obtain the relationship between stereo vision subsystem and PMD subsystem. A specular ring calibration target is applied to obtain the relationship between the stereo cameras system and the PMD system. The ring centres on the specular target can be reconstructed by the stereo cameras system and the PMD system, respectively. Denoting S as the reconstructed 3D data by the stereo cameras and P as the reconstructed data by the PMD, respectively. The relationship between the stereo cameras system and the PMD system can be obtained according to Eq. (2).

$$P = R_{S\_P}\,S + T_{S\_P} \qquad (2)$$

where R_{S_P} and T_{S_P} are the transformation relationship from the stereo cameras system to the PMD system. Equation (3) can be used to conduct the relationship between the FPP system and the PMD system.

$$\begin{cases} R_{F\_P} = R_{S\_P} R_{F\_S} \\ T_{F\_P} = R_{S\_P} T_{F\_S} + T_{S\_P} \end{cases} \qquad (3)$$

where R_{F_P} and T_{F_P} represent the transformation from the FPP system to the PMD system. The reconstructed data from the FPP system and the PMD system can be fused accurately based on R_{F_P} and T_{F_P}.

3. Experiment and results

A hybrid structured-light metrology prototype has been developed and calibrated with the proposed technique. Figure 5 shows pictures of the captured texture of the rough ring calibration target and the extracted feature points. Figures 5(a) and 4(b) are the texture captured by the Camera and the Camera 2, respectively. Figures 5(c) and 5(b) illustrate the extracted feature points on the texture pictures. Calibration results of the

optical parameters of the stereo cameras system is illustrated in Figure 6. Calibration error of the Camera 1 and the Camera 2 in stereo cameras system are demonstrated in Figures 6(a) and 6(b), respectively. The calibration error of the stereo cameras system is within ±1 pixel. Figure 7 displays pictures of the calculated phase data of the optical flat. Figures 7(a) and 7(b) are the phase data obtained by the Camera 1 in horizontal and in vertical, respectively. Figures 7(c) and 7(d) are the phase data calculated by the Camera 2 in horizontal and in vertical, respectively. Figure 8 illustrates calibration results of the PMD system. Figures 8(a) and 8(b) demonstrate the calibration error of the Camera 1 and the Camera 2 in PMD system, respectively. The calibration error of the PMD system is within ±5 pixels. Figure 9 shows pictures of the phase data of the rough ring calibration target obtained from the FPP system. Figures 9(a) and 9(b) are the horizontal and vertical phase data obtained by the Camera 2, respectively. Calibration results of the FPP system is shown in Figure 10. Reprojection error of the Camera 1 and the Camera 2 in FPP system are illustrated in Figures 10(a) and 10(b), respectively. The calibration error of the FPP system is within ±1 pixel. Figure 11 shows pictures of the obtained phase data of the specular ring calibration target. Figures 11(a) and 11(b) illustrate the horizontal and vertical phase data obtained by the Camera 1, respectively. Figures 11(c) and 11(d) demonstrate the horizontal and vertical phase data obtained by the Camera 2, respectively. Figure 12 displays pictures of the captured texture of the specular target and the extracted feature points. The texture captured by the Camera 1 and the Camera are shown in Figures 12(a) and 12(b). The extracted feature points of the texture pictures are illustrated in Figure 12(c) and 12(d). Figure 13 illustrates the calibration results the relationship between the subsystems. Figure 13(a) compares the reconstruction error between the stereo cameras system and the FPP system. Figure 13(b) is a comparison of the reconstruction error between the stereo cameras and the PMD system. The experimental results demonstrate that reconstruction error between the subsystems is decreased to around 50 µm by applying the proposed calibration technique. A structured composite workpiece has been measured by the hybrid structured-light metrology system calibrated by the proposed calibration technique. Figure 14(a) shows the picture of the measured workpiece. The reconstruction data of the workpiece is illustrated in Figure 14(b). The RMS of the reconstruction error of the rough surface and the specular surface are 24.8 µm and 0.4 µm, respectively.
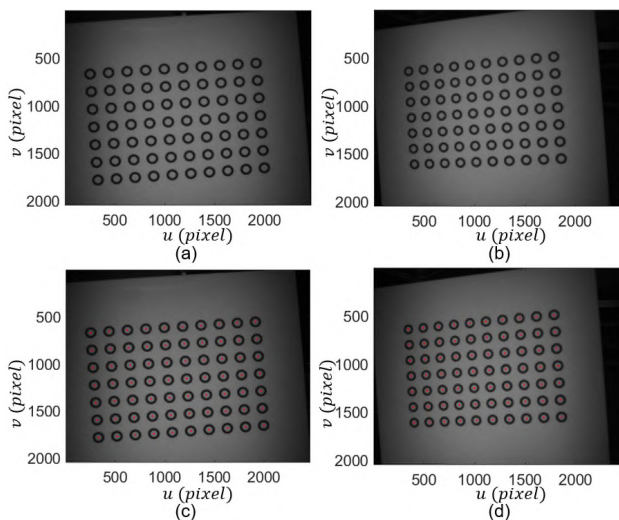
Figure 5. Pictures of the captured texture of the rough ring calibration target and the extracted feature points. (a) The texture captured by the Camera 1; (b) the texture captured by the Camera 2; (c) the extracted

feature points of the Fig. 4(a); (d) the extracted feature points of the Fig. 4(b).
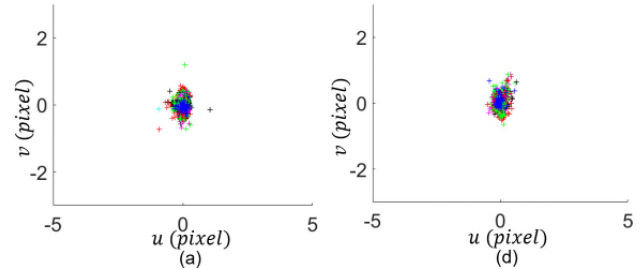
Figure 6. Calibration results of the optical parameters in the stereo cameras system. (a) Reprojection error of the Camera 1 in stereo vision system; (b) Reprojection error of the Camera 2 in stereo vision system
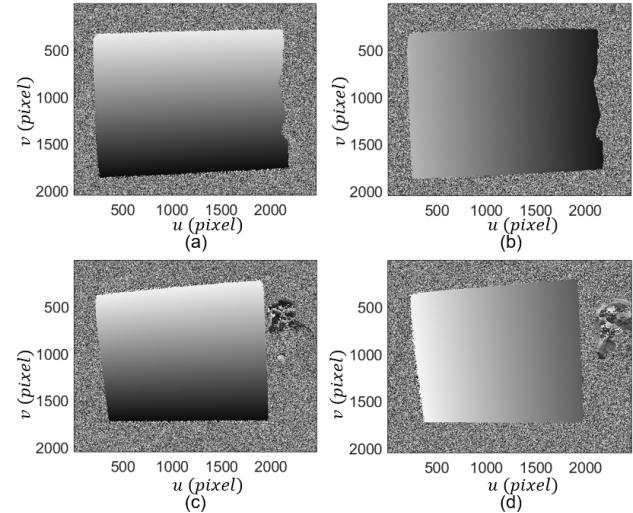
Figure 7. Pictures of the obtained phase data of the optical flat. (a) The phase data in horizontal obtained by the Camera 1; (b) phase data in vertical obtained by the Camera 1; (c) the phase data in horizontal obtained by the Camera 2; (d) phase data in vertical obtained by the Camera 2.
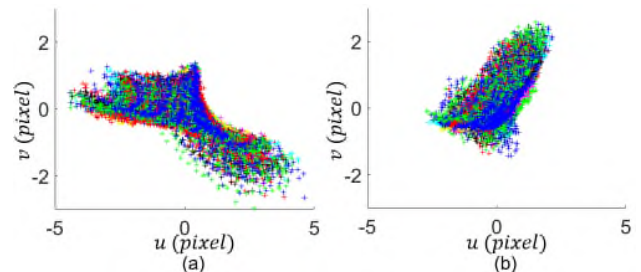
Figure 8. Calibration results of the optical parameters in the PMD system. (a) Reprojection error of the Camera 1 in PMD system; (b) Reprojection error of the Camera 2 in PMD system
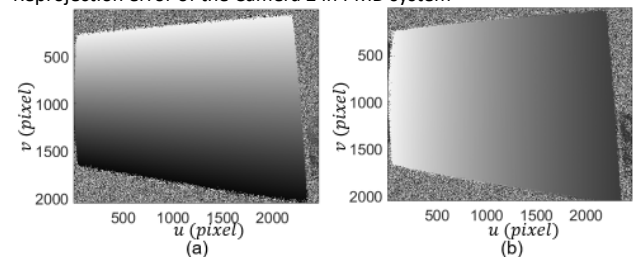
Figure 9. Pictures of the obtained phase data of the rough ring calibration target. (a) The phase data in horizontal obtained by the Camera 2; (b) phase data in vertical obtained by the Camera 2
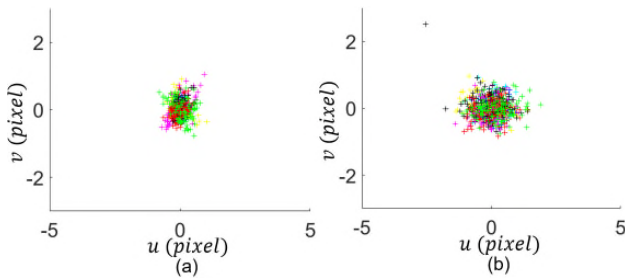
Figure 10. Calibration results of the optical parameters in the FPP system. (a) Reprojection error of the Camera 1 in FPP system; (b) Reprojection error of the Camera 2 in FPP system
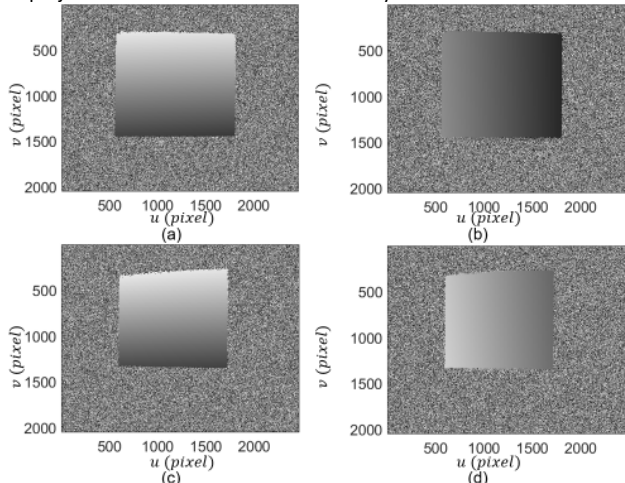
Figure 11. Pictures of the obtained phase data of the specular ring calibration target. (a) The phase data in horizontal obtained by the Camera 1; (b) phase data in vertical obtained by the Camera 1; (c) the phase data in horizontal obtained by the Camera 2; (d) phase data in vertical obtained by the Camera 2.
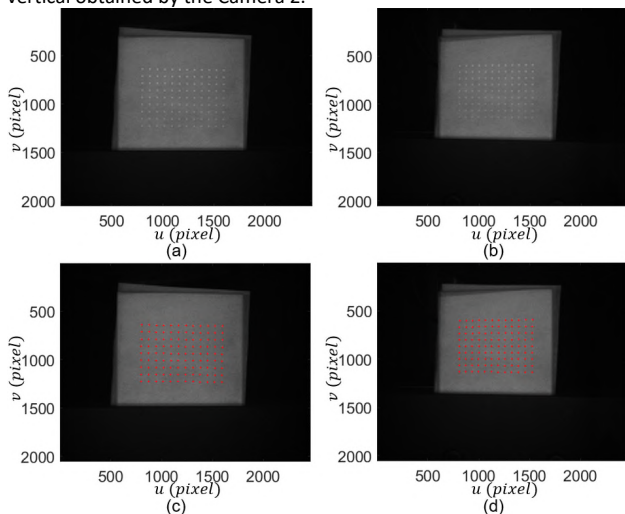
Figure 12. Pictures of the captured texture of the specular ring calibration target and the extracted feature points. (a) The texture captured by the Camera 1; (b) the texture captured by the Camera 2; (c) the extracted feature points of the Fig. 11(a); (d) the extracted feature points of the Fig. 11(b).
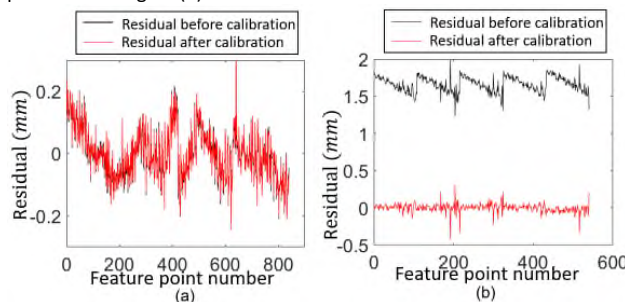
Figure 13. Calibration results the relationship between the subsystems. (a) a comparison of the reconstruction residual between the stereo

vision subsystem and the FPP subsystem; (b) a comparison of the reconstruction residual between the stereo vision subsystem and the PMD subsystem
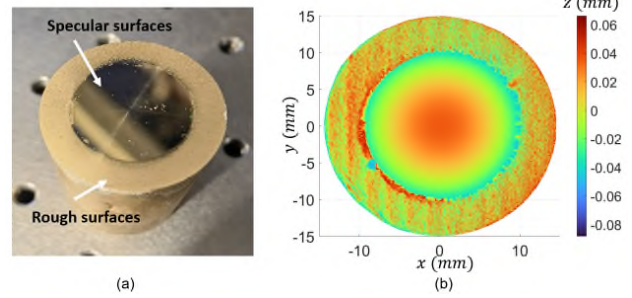
Figure 14. Measurement result of the structured composite workpiece. (a) A picture of the measured workpiece (b) the reconstruction data after data fusion of the subsystems

4. Conclusion

A calibration technique has been studied for hybrid structured-light system. Calibration targets, calibration algorithm, and strategy are described and discussed in this paper. The proposed calibration technique is easily conducted and has good calibration accuracy. More experiments will be conducted to test the calibration technique in the next step.

References

[1] Xu J and Zhang, S 2020 Opt. Lasers Eng. **135** 106193.

[2] Feng S, Zuo C, Zhang L, Tao T, Hu Y, Yin W, Qian J and Chen Q 2021 Opt. Lasers Eng. **143** 106622.

[3] Zhang Z, Xu Y and Liu Y. 2013 In2013 International Conference on Optical Instruments and Technology: Optoelectronic Measurement Technology and Systems **9046** 47-54.

[4] Xu Y, Gao F and Jiang X 2020 PhotoniX **1** 1-10.

[5] Huang L, Idir M, Zuo C and Asundi A 2018 Opt. Lasers Eng. **107** 247-257.

[6] Zhang Z, Chang C, Liu X, Li Z, Shi Y, Gao N and Meng Z 2021 Opt. Eng. **60** 020903.

[7] Liu X, Zhang Z, Gao N and Meng Z 3D 2020 Opt. Express **28**(19) 27561-27574.

[8] Breitbarth M, Kühmstedt P and Notni G 2009 In Optical Measurement Systems for Industrial Inspection **7389** 91-98.

[9] Xu Y, Gao F, Yanling L, Wenbin Z, Yang Y, Duo L and Jiang X 2024 Int. J. Extreme Manuf. Submitted.

[10] Zhang Z 2000 IEEE T. Pattern Anal. **22**(11) 1330-1334.

[11] Zhang S and Huang P S 2006 Opt. Eng. **45**(8) 083601-083601.

[12] Xu Y, Gao F, Zhang Z and Jiang X 2018 Opt. Lasers Eng. **106** 111-118.

Investigation of the filtering effect of virtual image correlation methods in the context of ISO standards

Filippo Mioli[1], Marc-Antoine De Pastre[2], Enrico Savio[1], Nabil Anwer[2], Yann Quinsat[2]

[1]Università degli Studi di Padova, Precision Manufacturing research group, 35131, Padova, Italy
[2]Université Paris-Saclay, ENS Paris-Saclay, LURPA, 91190, Gif-sur-Yvette, France

filippo.mioli@phd.unipd.it

Abstract

Geometrical metrology involves capturing large data sets (point clouds, images, voxels, etc.). From these, pertinent information is extracted. When using imaging sensors and Computed Tomography (CT), a key step is Contour Identification, i.e., the identification of the transition between the workpiece and its surroundings. While several methods can be used for contour identification, most rely on thresholding techniques, but alternative methodologies like Virtual Image Correlation (VIC) are being increasingly studied. This work investigates two VIC methods, focusing on filtration effects embedded in the mathematical definition of the virtual contours. The two methods are based on mode decomposition and B-spline parametric curves. The analysis was conducted on images representing cross-sections of additively manufactured lattice structures. A relation between the curve parameters and the cut-off frequency f_c, as defined in standards, has been proved to be effective. This gives new prospects for implementing emerging methods in relation to filtration as defined in ISO GPS standards and additive manufacturing parts verification.

Additive Manufacturing, Lattice structure, Virtual Image Correlation, ISO GPS standards, Filtration, B-spline, Mode decomposition

1. Introduction

Geometrical Product Specifications and Verification (GPS) standards have been developed over the years to ensure consistent methods to perform feature operations, from design to production up to verification, adapting to diverse functional requirements. Additive Manufacturing (AM), especially in complex design geometries such as lattice structures (LS), introduces new engineering challenges for GPS. Traditional contact measuring systems are impractical for part verification, leading to the use of computed tomography (CT) and other non-destructive measuring technologies for quality control. CT generates voxel-based data, whose values are linked to the density of each point in the scanned volume, requiring contour identification for reconstructing the object's surface. Most methods rely on thresholding [1] (e.g., ISO50%), but new algorithms are being developed exploiting Virtual Image Correlation (VIC) strategies [2][3].

Virtual Image Correlation is a boundary detection process based on creating a virtual image defined by a mathematical parametric equation that will then be deformed to best represent its real counterpart. The deformation is guided by the minimisation of a score function that compares the virtual and the actual images (*Fig. 1*):

$$\{\lambda\} = \arg_{\{\lambda\}} \min \Phi(u) \qquad (Eq.\ 1)$$

$\{\lambda\}$ is the vector of values displacement for each parameter that defines the mathematical contour. The correlation score function, denoted as $\Phi(u)$ in *Eq.1*, is derived by summing the squared differences between corresponding pixels in the virtual and real images across the entire image. A displacement field $u(X)$ is applied to the virtual image g. The optimal value of $\{\lambda\}$

is computed to obtain the deformation field $u(X)$ that minimise the correlation score function Φ.

$$\Phi = \iint_{ROI}[f(X) - g(X + u(X))]^2\ dxdy \qquad (Eq.\ 2)$$

For this work, two VIC methods have been investigated. The first, V2C, developed by De Pastre et al. [3], relies on the modal decomposition of the mathematical contour, i.e., the contour is described as the sum of different vibration modes applied to a circle. The second one, DBACD, part of a work still in progress, describes the contour using a B-spline parametric curve. The working principle is the same as the V2C, but in this case, instead of iteratively changing the amplitude of different modes, the algorithm computes a set of (x,y) displacements for each of the b-spline control points.

(a) (b) (c)
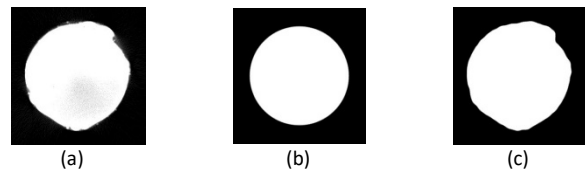
Figure 1. De Pastre et. al [3], Illustration of 2D VIC method applied to a vertical 90° strut: CT measurement image (a), initial virtual shape (b) and correlated final virtual shape (c)

This study focuses on contour analyses of a cylinder section of a lattice structure strut. The evaluation of circular profiles is described in the ISO standards 12181-1/2 [4, 5], to establish the series of operations required. Point filtration is one key step.

In the case of a CT-scanned LS, the contour points of the strut section are extracted with the $ISO_{50\%}$ method. These sections are characterised by geometrically more complex defects if compared with traditionally manufactured cylinders (the relative size of the defects is greater, and in some cases,

undercuts may be detected). Therefore, applying standard algorithms to filter and separate the roughness and waviness profile components is difficult.

This work aims to investigate this *filtration effect* embedded in the mathematical parametrization of the virtual contours and see if there is any relationship between those parameters and the cut-off frequency f_c as defined in ISO 16610-21:2011 [6].

2. Material and Methods

The numerical experiment performed for this research consists of a comparison between the filtered contour according to ISO 16610-21:2011 [6] with the one obtained with the two VIC methods. The contours are extracted from a CT section of a Laser Powder Bed Fusion (LPBF) additively manufactured vertical cylinder, used in previous works [2], with 0.6 mm radii and 5 mm length and produced on an Addup FormUp 350 machine using Inconel 718 powder.
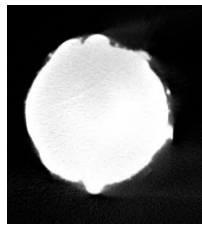
Figure 2. CT measurement section of 90° strut: 0.6 mm in radii and 5 mm in length

The image (*Fig. 2*), extracted from a Computed Tomography volumetric scan, is first analysed with ISO$_{50\%}$ to detect its contour. The (x, y) coordinates from the extracted contour are then processed to remove the undercuts and fulfil the requirement for applying an ISO 16610-21 Gaussian filter. The image is also analysed with the two VIC methods.

The three contours (ISO$_{50\%}$+gaussian, VIC mode and VIC B-spline) are then compared with filtering parameters according to *Eq.3*:

$$f_c = \frac{n_m - 3}{2} = \frac{n_{cp}}{2} \qquad (Eq.\ 3)$$

with n_m number of modes used for V2C and n_{cp} number of control points used to define the B-spline.

This comparison has been run with different values of $f_c =$ [5 15 50] undulation per revolution (upr).

3. Results and Conclusions

In this section, the output of this numerical experiment is reported. In *Fig. 3-4-5, it* is possible to highlight the visual contour comparison for each filtering technique. One can immediately appreciate how the three filtered closed profiles are similar in the representation of geometrical defects, and especially how local differences tend to decrease progressively with increasing f_c. Further investigation could be carried out by testing different cut-off frequencies and sections; quantitative deviation could be plotted. In addition, roundness values could be computed and compared along the different f_c between the three filtration methods. Thanks to the relation described in *Eq. 3*, it becomes feasible to employ VIC methods for extracting contours filtered at a specific f_c, even in the presence of geometries that would typically hinder the use of standard methods. Deviations can subsequently be calculated as the distance between the raw data and the smoothed contour, enabling the extraction of roughness information. This could provide insights for the development/update of GPS standards

applied to lattice structures and, more generally, to additive manufacturing parts.
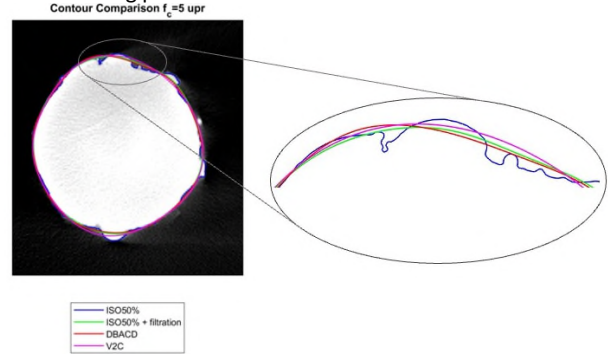
Figure 3. Contour comparison between ISO$_{50\%}$ (blue), ISO$_{50\%}$ + Gaussian filtration (green), DBACD (red) and V2C (magenta) - $f_c = 5\ upr$
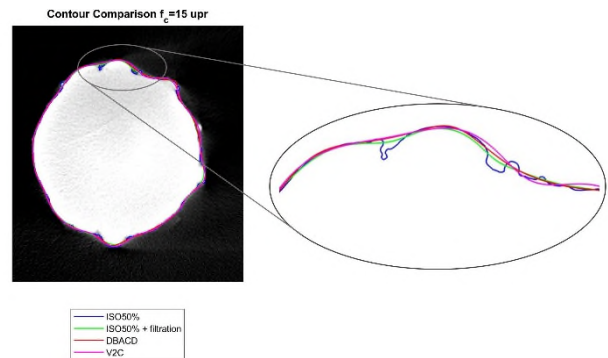
Figure 4. Contour comparison between ISO$_{50\%}$ (blue), ISO$_{50\%}$ + Gaussian filtration (green), DBACD (red) and V2C (magenta) - $f_c = 15\ upr$
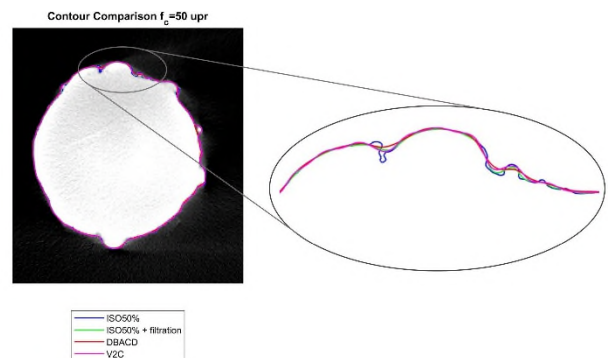
Figure 5. Contour comparison between ISO$_{50\%}$ (blue), ISO$_{50\%}$ + Gaussian filtration (green), DBACD (red) and V2C (magenta) - $f_c = 50\ upr$

References

[1] S. Carmignato, W. Dewulf, and R. Leach, 2017, *Industrial X-ray computed tomography*. Springer International Publishing. doi: 10.1007/978-3-319-59573-3.

[2] M.-A. De Pastre and Y. Quinsat, 2022, "A novel approach for geometrical deviations determination of lattice structures from volumetric data." [Online]. Available: www.euspen.eu

[3] M. A. de Pastre, Y. Quinsat, and C. Lartigue, 2022, "Shape defect analysis from volumetric data - Application to lattice struts in additive manufacturing," *Precis Eng*, vol. **76**, pp. 12–28. doi: 10.1016/j.precisioneng.2022.02.011.

[4] International Organization for Standardization, 2011, *ISO 12181-1:2011-Geometrical product specifications (GPS)-Roundness-Part 1: Vocabulary and parameters of roundness*.

[5] International Organization for Standardization, 2011, *ISO 12181-2:2011-Geometrical product specifications (GPS)-Roundness-Part 2: Specification operators*.

[6] International Organization for Standardization, 2012, *ISO 16610-21:2011-Geometrical product specifications (GPS)-Filtration-Part 21: Linear profile filters: Gaussian filters*.

Visual focusing and levelling towards optical inspection of Mini/MicroLED panels

Hui Tang[1], Yuzhang Wei[2], Xiaoxian Ou[2], Yingjie Jia[2], Yanling Tian[1]

[1]School of Engineering, The University of Warwick; Coventry, UK
[2]Electromechanical engineering, Guangdong University of Technology, Guangzhou, China

Hui.Tang.4@warwick.ac.uk; yzwei@gdut.edu.cn; 2112201468@mail2.gdut.edu.cn; yingjiejia1996@163.com; Y.Tian.1@warwick.ac.uk

Abstract

In order to improve the focus quality and efficiency of Mini/MicroLED chip panel defect detection, we focus our research on visual focusing and levelling techniques. This paper reports on the construction of Image focus evaluation method based on Gaussian fuzzy difference（F-GFD）, and the and the method of focus adjustment and leveling based on ZTTθ leveling and correcting motion stage is also proposed. By optimising and adjusting the parameters, the image focus evaluation method（F-GFD）has a high focus resolution and high sensitivity effect, which has an axial resolution better than 1.25 μm axial resolution. Experiments show that the image focus evaluation method（F-GFD）combined with ZTTθ stage can realize multi-points focus of Mini/MicroLED panel and the leveling process of panel and image plane, which further provides a basis for solving the defocus problem caused by panel warping in the defect detection of Mini/MicroLED chips.

Focusing and leveling；Image focus evaluation; Gaussian fuzzy difference; Mini/MicroLED panels.

1. Introduction

Focusing and leveling is one of the important processes in display semiconductor manufacturing, which can compensate the errors caused by defocusing to ensure the quality of imaging, processing and improve the production yield of the circuit[1].

In the traditional optical system, CCD and laser generator are usually used to measure the height according to the triangle method to determine the defocus amount[2]. In recent years, Jian Wang et al. proposed grating shear interferometry to determine the out-of-focus amount and tangent slope of wafer by measuring the phase difference[3]. Canon and ASML companies used photoelectric detection array, CCD array and other detectors to achieve focusing and leveling measurement in the way of grating array and spot array. Nikon proposed to reduce the ASD error by placing polarizer between the lens and the silicon wafer to improve the process adaptability of the focusing and leveling system, which detects the light intensity of each polarization[4]. The gain coefficient of the focusing and leveling sensor is simulated and tested by the Institute of Microelectronics of the Chinese Academy of Sciences[5]. The results showed that the calibration sensor system can effectively reduce the variation of thickness of different materials of semiconductor panels. Yonghong Wang proposed a new focusing algorithm to complete the focusing process of TFT-LCD panels and improved efficiency[6].

In general, there were two dominant approaches to solving the focus levelling problem, one is the principle based on measuring surface height by optical triangulation and the other is to ensure defocus amount by adding sensors. For the display panels, active focusing or passive focusing is basically adopted for single position focusing, but there are few studies on multi-point focusing or focusing and leveling of the display panel. Therefore, in order to solve the problem of defocusing due to panel warping in Mini/MicroLED chip defect detection, the image focus evaluation method based on Gaussian fuzzy

difference is proposed, and the feasibility of focusing and leveling technology is verified by combining with ZTTθ leveling and correcting stage.

2. Image focus evaluation method based on Gaussian fuzzy difference (F -GFD)

2.1 Fuzzy formation and mechanism of defocusing imaging

In the optical imaging model, the object to be measured will present different clarity basing on its own location in the visual system. With the movement along the direction of the optical axis, there will be sharp to blur with out-of-focus amount changes. The optical imaging simplified model shown in Fig. 1.
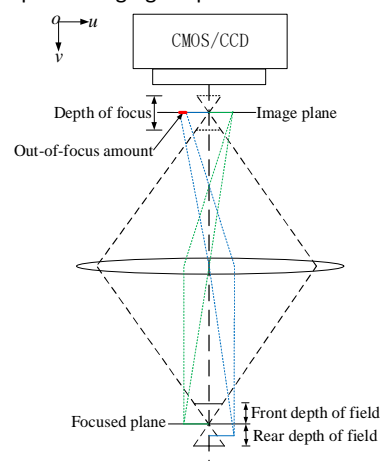
Figure 1. Simplified model of optical imaging

At the same time, the process of focusing to defocusing can be regarded as the process of transforming the focused image through a certain degenerate model. Thus, without considering linear space, the defocused imaging model can be expressed simplistically as:

$$F_i(x, y) = F(x, y) \times h_i(x, y) \qquad (1)$$

From(1), the subscript i is the sequence number corresponding to the position moved along the optical axis direction; $F(x, y)$ is the focused image; $F_i(x, y)$ is the image acquired at the position corresponding to sequence number i; $h_i(x, y)$ is the degenerated model corresponding to $F(x, y)$.

In practice, due to the existence of a certain symmetry between the foreground depth and the background depth, the degenerate model is fitted by a Gaussian function. The degree of degradation is determined by the size of the standard deviation σ_i, so that the larger the standard deviation will have higher degree of fuzzy and degradation. The representation of image is usually a two-dimensional discrete signal, so $h_i(x,y)$ can be represented by a two-dimensional Gaussian function:

$$h_i(x, y) = \frac{1}{\sqrt{2\pi}\sigma_i} \exp[-\frac{x^2 + y^2}{2\sigma_i^2}] \qquad (2)$$

2.2. Addition of Gaussian fuzzy difference

From 2.1, it can be understood that the key of visual focusing technique makes the object under test in the focusing plane so that it can be clearly imaged. Among them, the sharpness evaluation value obtained by the image focus evaluation method will be an important basis for judging whether it is located in the focus plane.

A Gaussian kernel convolution operation with a determined standard deviation is performed on the images acquired by the vision system, in other words, Gaussian blur is added to the original imaging model. Therefore, the image obtained from the out-of-focus imaging model in Section 2.1 by blurring the Gaussian again is $f_i(x, y)$, which can be expressed as[7]:

$$f_i(x, y) = F_i(x, y) \times h(x, y) = F(x, y) \times h_i(x, y) \times h(x, y) \qquad (3)$$

From (3): $h(x, y)$ is the Gaussian kernel convolution whose standard deviation has been determined.

Eq. $h_i(x, y) * h(x, y)$ can be written as an expression in accordance with the principle of multiplication of Gaussian convolution kernel:

$$h_i(x, y) \times h(x, y) = \frac{1}{\sqrt{2\pi} \cdot \sqrt{\sigma_i^2 + \sigma^2}} \exp\left[-\frac{x^2 + y^2}{2(\sigma_i^2 + \sigma^2)}\right] \qquad (4)$$

From (4), the standard deviation of the new Gaussian convolution kernel is $\sqrt{\sigma_i^2 + \sigma^2}$, which can be compared with the standard deviation of the out-of-focus imaging model in (2)and the standard deviation of completely fuzzy imaging model to obtain the magnitude relation , denoted as:

$$\sigma_i \leq \sqrt{\sigma_i^2 + \sigma^2} \leq \sigma_{\dim} \qquad (5)$$

From (5), $\sigma_{\dim}$ is the standard deviation of the Gaussian convolution kernel used to make the focused image $F(x, y)$ completely fuzzy. According to the way of adding the standard deviation of the Gaussian kernel convolution operation, it had already determined the standard deviation of the new Gaussian convolution kernel is $\sqrt{\sigma_i^2 + \sigma^2}$ can only be constantly converged to $\sigma_{\dim}$.
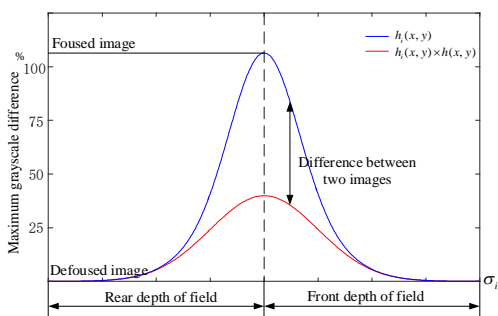
Figure 2. Comparison of grey scale difference between images before and after processing

According to Section 2.1, the larger the standard deviation of the Gaussian convolution kernel is, the more significant the blurring effect on the image. Therefore, for the image joining the Gaussian kernel convolution operation whose standard deviation has been determined, the comparison of grey scale difference values before and after processing will be shown in Fig. 2.

The blue curve in Figure 2 is the expression of the original out-of-focus imaging fuzzy model in the form of grey scale difference, because the change of σ_i makes a series of images in the focusing plane, in the two directions of front and rear depth of field to show a tendency to reduce the value of maximum grayscale difference respectively (have a gradually blurring tendency). The red curve represents the original out-of-focus imaging fuzzy model added to the Gaussian kernel convolution of standard deviation has been determined after the formation of the model, the standard deviation of the standard deviation $\sqrt{\sigma_i^2 + \sigma^2}$ will decide to images in the focusing plane, respectively, the grey scale difference show a similar tendency as blue curve in the two directions of front and rear depth of field.

Combining the equation (5) with the comparison of the red and blue curves, it can be clearly seen that if the acquired image is in-focus, the image after the second Gaussian convolution will have obvious grey value differences (obvious blurring). If the acquired image is out-of-focus, the grey value difference (blurring) of the image after the second Gaussian convolution change less. Therefore, the grey value differences (blurring) decrease with the increase of out-of-focus amount. The difference between the blurred image and the original image can be used as a criterion for sharpness evaluation and as a basis for defining the focus position.

The difference between $F_i(x, y)$ and $f_i(x, y)$ is caused by processing after quadratic Gaussian convolution, so the value of the standard deviation of the Gaussian convolution sum has a close relationship with the sensitivity of the algorithm, and at the same time, in order to satisfy the stability of the Gaussian kernel matrix operation, there is the following relationship between the Gaussian convolution kernel and the mask size[8]:

$$\sigma = 0.3\left[\left(\frac{k_{size} - 1}{2}\right) - 1\right] + 0.8 \qquad (6)$$

From (6), k_{size} is the mask size size, so the value needs to be taken to satisfy that the equation holds.

The difference between $F_i(x, y)$ and $f_i(x, y)$ can be expressed by the difference between the global variance values of the two images, then the clarity evaluation result of a single image can be expressed as:

$$Diff = abs\{\text{cov}[F_i(x, y)] - \text{cov}[f_i(x, y)]\} \qquad (7)$$

From (7), $Diff$ is the difference of the variance value, and also represents the clarity evaluation result of the image; cov(*) means calculating the global variance of the image; abs(*) means taking the absolute value.

According to the relationship between the values of equation (6), if the Gaussian standard deviation is taken as 0.8, 1.1, 1.4, 1.7，the mask size of the Gaussian convolution kernel should be 3*3, 5*5, 7*7, 9*9 respectively. So the completeness of the convolution operation can be guaranteed according to this principle. The difference between the images before and after processing is calculated through the arithmetic relationship of the equation (7) to obtain the clarity evaluation value, and the results for the same set of images processing are shown in Fig. 3.
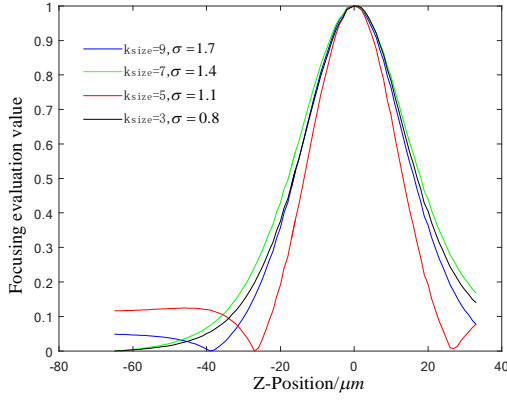
Figure 3. Clarity evaluation results after different Gaussian standard deviation treatments

2.3. Algorithm Effectiveness Validation and Focused Evaluation Metrics

Prior to this, many researchers have proposed spatial domain-based focus evaluation algorithms, including the most common gradient sum-of-squares function (Sobel operator), gradient filtering function (Brenner operator), and Laplace function, and these traditional focus evaluation methods are also the most commonly used in the industry. Therefore, we propose an image focusing evaluation method based on Gaussian fuzzy difference to compare with traditional algorithms by means of quantitative evaluation, highlighting our advantages and indicators. Suppose the image size is m×n:

（1） Gradient filter function (Brenner operator)

$$F_{Brenner} = \sum_{i=1}^{m}\sum_{j=1}^{n}[p(i, j+2) - p(i, j)]^2 \tag{8}$$

（2） Gradient sum-of-squares function (Sobel operator)

$$F_{Sobel} = \frac{1}{m \cdot n}\sum_{i=1}^{m}\sum_{j=1}^{n}\left\{\left[p(i, j) \times G_x\right]^2 + \left[p(i, j) \times G_y\right]^2\right\} \tag{9}$$

$$G_x = \begin{bmatrix} -1 & -2 & -1 \\ 0 & 0 & 0 \\ 1 & 2 & 1 \end{bmatrix} \quad G_y = \begin{bmatrix} -1 & 0 & 1 \\ -2 & 0 & 2 \\ -1 & 0 & 1 \end{bmatrix} \tag{10}$$

（3） Laplace function(Laplacian operator)

$$F_{Laplace} = \frac{1}{m*n}\sum_{i=1}^{m}\sum_{j=1}^{n}\begin{bmatrix} p(i+1, j) + p(i-1, j) + p(i, j+1) \\ + p(i, j-1) - 4 * p(i, j) \end{bmatrix}^2 \tag{11}$$

In accordance with Figure 2 effect comparison, the image focus evaluation method based on Gaussian fuzzy difference selects the fuzzy form with a mask size of 5*5 and a standard deviation of 1.1. The result obtained is plotted as a curve , which compared with the gradient sum-of-squares function, the gradient filter function, and the Laplacian function(as shown in Fig. 5).
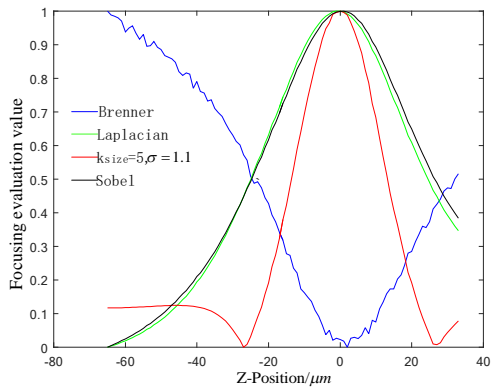
Figure 4. Comparison of the effect of different clarity functions

Based on the statement of the Heisenberg uncertain principle and emulation of the autofocusing uncertainty measure[9],focus resolution can be defined by[10]:

$$\sigma^2 = \frac{1}{\|f\|^2}\int_{-\infty}^{+\infty}\left[(x - x_p) \cdot f(x)\right]^2 dx \tag{12}$$

Conversion of integral form to discrete point superposition form：

$$\sigma^2 = \frac{1}{\|f\|^2}\sum_{i=1}^{n}\left[(i - i_p) \cdot f(i)\right]^2 \tag{13}$$

The computed σ^2 for different clarity functions shown in Figure4 are listed in Table 1. From Table 1, we can clearly see that the σ^2 of Image focus evaluation method based on Gaussian fuzzy difference is significantly lower than other focus functions. This means that Image focus evaluation method based on Gaussian fuzzy difference has higher focus resolutions.

Table 1 Computed focus resolutions for Fig.4

Focus Measure	Sobel	Lapacain	F-GFD
σ^2	425.965	447.542	150.008

3. Mini/MicroLED panels focusing and levelling process implementation

In Mini/MicroLED AOI chip defect inspection and other pan-semiconductor equipment, Mini/MicroLED panels are placed on the fixture and then transported to the workstation. Due to assembly problems and the panel warping phenomenon , Mini/MicroLED panels are not completely in the depth of field range and parallel to the camera's datum surface, which affects the inspection accuracy and efficiency. So it is necessary to adjust so that the panel is parallel to the focal plane.

3.1 Focusing plane positioning accuracy experiment

In order to verify the ability of the image focus evaluation method based on Gaussian fuzzy differences to layer along the optical axis direction (resolution of slice images).

The experimental (Fig. 5) system consists of a vision system with a Z-direction objective displacement stage. The objective lens in the vision system is CCW-10x, which has a magnification of 10, a numerical aperture of 0. 28, and a depth of field of 3.5 μm. Z-axis repeatability is less than ±500nm.
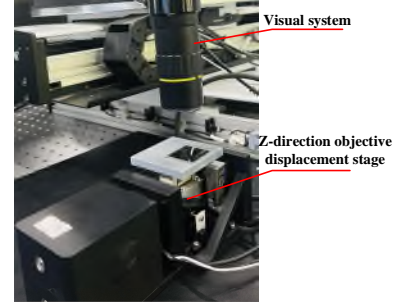
Figure 5. Positioning accuracy experiment

The system performs axial traversal scans and acquires images in 1.25 μm steps over a range of ±20 μm near the plane of focus, followed by resolution performance metrics analysis (Fig. 6).
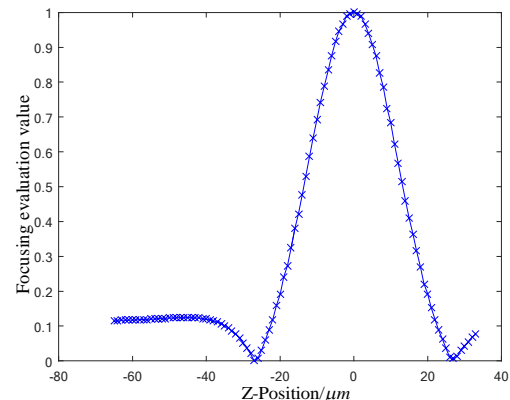
Figure 6. Z-axis resolution performance specification

The results are shown in Fig.6, it can indicate that when axial traversal scanning in the situation of 1.25μm step, the image focus evaluation method （F-GFD） achieves axial position resolution within 20 μm before and after the focusing position. Therefore the axial resolution is considered to be better than 1.25 μm.

3.2 Focusing and levelling process

According to the motion characteristics of ZTTθ levelling and deskewing stage (Fig. 7) and the characteristics of focus levelling, the image focus evaluation method based on Gaussian fuzzy difference proposed in Chapter 2 is combined with ZTTθ levelling and deskewing stage to realise the Mini/MicroLED panel focus leveling process.
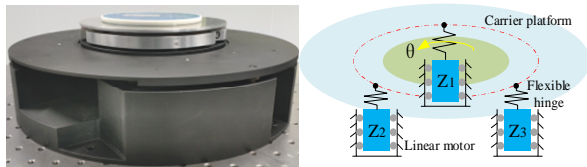
Figure 7. ZTTθ levelling and guiding stage and simple model

As shown in Figure 7, the ZTTθ levelling stage can achieve high-precision pitch and yaw, but it needs to implement the motion strategy in conjunction with vision algorithms （F-GFD） to reduce the influence of coupled and parasitic motions in the focusing and leveling process. This guarantees the completion of accurate focusing and leveling.
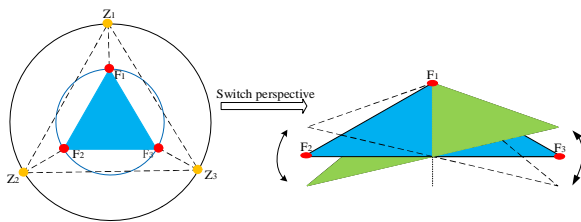
Figure 8. Schematic diagram of ZTTθ stage focusing and levelling movement

As shown in Figure 8, $Z_1Z_2Z_3$ are the support points of the stage (drive point); $F_1F_2F_3$ are the focus points, which located in the same arc and located in the radius of $Z_1Z_2Z_3$. Based on the existing positional relationship, the position height change of $F_1F_2F_3$ can be inverted to solve the pending motion of the support point $Z_1Z_2Z_3$ based on the motion position mapping relation. If F_2 and F_3 do the movement in the opposite direction, the plane composed of $F_1F_2F_3$ is swinging on the axis of the centre line where F_1 is located, theoretically, the position of F_1 can be kept highly unchanged to achieve decoupling. The following movement process and strategy are also developed around this.The specific process is as follows:

1. Firstly, the three-axis synchronised motion is adjusted to achieve the optimum image clarity within the vision system (image clarity evaluation function) to obtain the position F1;

2. Keeping the height of Z_1 unchanged, the system focuses on the F_2 position to achieve optimal clarity through Z_2 and Z_3 for the opposite way of movement (the plane movement state is shown in Fig. 8 on the right). The Z_2 height position is recorded after the focus search was completed;

3. Continue to keep the height of Z_1 unchanged, the system focuses on the F_3 position to achieve optimal clarity through Z_2 and Z3 for the opposite way of movement. The Z_3 height position is also recorded after the focus search was completed;

4. Z_2Z_3 were reached before the recorded position, focusing and levelling process is complete.
By reproducing the above focus levelling strategy in the host computer, the overall process of focus levelling is completed in the experimental system (Fig. 9).
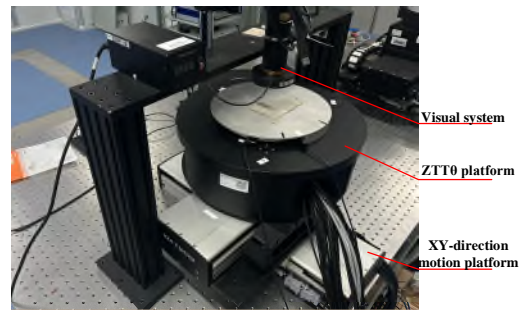
Figure 9. Integral focusing and levelling experiment system construction

From the results, the difference in the sharpness evaluation value of the focusing area $F_1F_2F_3$ is very small and all of them can reach a clear state. Therefore, it is shown that the image focus evaluation method based on Gaussian fuzzy difference （F -GFD） in conjunction with the ZTTθ levelling and deviation correction stage can complete the overall process of focus levelling.

4. Summary

The image focus evaluation method based on Gaussian fuzzy difference （F-GFD） proposed in the paper can achieve axial resolution better than 1.25 μm, and the peak and focus resolution are improved compared with the traditional way. At the same time the focus evaluation method counts with the ZTTθ levelling and deskewing stage in conjunction with the focus leveling technology is able to complete the Mini/MicroLED panel focus leveling process, which provides a certain basis for solving the problem of Mini/MicroLED out of focus due to panel warping. Moreover, it has the advantage of lower cost and simpler operation process than the traditional optical triangulation principle or additional sensors.

Acknowledgment

References

[1] Boef, D. and J. Arie, Optical wafer metrology sensors for process-robust CD and overlay control in semiconductor device manufacturing. *Surface Topography Metrology & Properties*, 2016. **4**(2): 023001.

[2] Huang T , Liu S , Yi P ,et al.Focusing and leveling system for optical lithography using linear CCD[J].Proceedings of SPIE - The International Society for Optical Engineering, 2009, 7160(2):-.

[3] Wang, J., S. Hu and X. Zhu, Measurement of Wafer Focus by Grating Shearing Interferometry. *Applied Sciences*, 2020. **10**(21): p. 7467.

[4] Hidaka, Y., K. Uchikawa and D.G. Smith, Error analysis and compensation method of focus detection in exposure apparatus. Optical Society of America, 2009(1).

[5] Sun, Sangsang, Wang, Dan & Zong, Mingcheng, Process correlation study of gain coefficients of focus levelling sensors. *Journal of Optics*, 2022. **42**(04): p. 109-116.

[6] Wang, Y. H. et al, Research and comparison of auto-focusing algorithms for optical inspection of TFT-LCD panels. *Liquid Crystal and Display*, 2016. **31**(4): p. 8.

[7] David, et al., Blind image blur assessment by using valid reblur range and histogram shape difference. Signal Processing Image Communication, 2014.

[8] Yuan T. et al, A double blur based focus evaluation method for microscopic images. *Journal of Optics*, 2023. **43**(10): p. 63-72.

[9] Yang, G. and B.J. Nelson. Wavelet-based autofocusing and unsupervised segmentation of microscopic images. in IEEE/RSJ International Conference on Intelligent Robots & Systems. 2003.

[10] Zong, G.H., et al., Research on Wavelet Based Autofocus Evaluation in Micro-vision. *Chinese Journal of Aeronautics*, 2006. **19**(3): p. 239-246.

Optimization of symmetrical layers of optical caustic beams generated using cylindrical lenses

Martin Dusek[1, 2], Jean-Christophe Gayde[1], Miroslav Sulc[2,3]

[1]*The European Organization for Nuclear Research (CERN), Geneva, Switzerland*
[2]*Technical University of Liberec (TUL), Liberec, Czech Republic*
[3]*Institute of Plasma Physics of the Czech Academy of Sciences (IPP CAS), Prague, Czech Republic*

martin.dusek@cern.ch

Abstract

Generating symmetrical layers of optical caustic beams using a specific configuration of cylindrical lenses is an innovative technique with potential application in precision alignment and other fields. The technique allows to shape the wavefront to generate a beam, which is layered in a plane creating a specific pattern consisting of different number of lines in a transversal plane, depending on the distance from the generator. Prior methods have produced similar beams using spatial light modulators. However, our approach with cylindrical lenses offers a marked reduction in setup complexity and cost, opening the possibility for new applications. The paper shows the possibilities of adjusting the generator for different applications by changing its parameters. Customization enables tailoring the beam characteristics to meet the unique requirements of different tasks, particularly in alignment.

Non-diffracting Beams, Accelerator Alignment, Caustic Beams

1. Introduction

Optical caustics is a well-known phenomenon present in everyday life every time light is reflected or refracted by curved surfaces [1, 2]. Similarly, Optical Caustic Beams (OCB) are characterized by wavefronts by which the rays of light are strongly focused, creating characteristic patterns and beam trajectories, due to the interference.

The discovery of Airy Beams (AiB), characterized by cubic phase, hence with odd symmetry, started the growing research field of caustic beams. This led to the discovery of Symmetric Airy Beams (SAB) [3] and Symmetric Pearcey Gaussian Beams (SPGB) [4]. All symmetric beams, characterized by the absolute valued cubic phase in the case of the SAB and quadratic phase in the case of the SPGB, are generated by phase profiles with even symmetry. OCB has application potential in particle manipulation [5], acceleration [6], or material processing [7].

The state-of-the-art for generating the mentioned beams uses a spatial light modulator (SLM) with the encoded Fourier spectrum of the desired beam and a lens that performs a spatial Fourier transformation [3, 4]. Numerous other generation principles employ specialized off-shelf components [8, 9]. The possibility of a simple generation principle of non-symmetrical AiB using on-shelf cylindrical lenses was reported in multiple works [10, 11].

At CERN, non-diffractive beams are subject to intensive research regarding their useableness for the alignment of accelerator parts [12] and particle acceleration [13]. The OCBs have potential to be used as a reference for alignment thanks to their unique properties, mainly thanks their low divergence.

Due to the vast size of the CERN accelerator complex a simple, scalable, and inexpensive solution for generating such beams is desired. In this work, we present the possibility of generating layers of OCB with even symmetry of the phase using plano-convex cylindrical lenses, which would comply with the set requirements. We will be referring to these beams as Layer Beams (LB). The possibility of tailoring the beam properties for specific applications by varying the parameters and position of cylindrical lenses is also shown. To our best knowledge, this way of generation has never been considered.

2. Methodology

The LB is generated by using a set of cylindrical lenses (Fig 1). The first lens (phase lens - PhL) is illuminated by a Gaussian beam. This lens functions as a phase modulator similar to SLM. Hence, the phase of the light is modulated in such a way that it has even symmetry. This phase modulation occurs in a specific interval of distances behind the PhL, which is different for each lens. This interval is characterized by the fact that local phase profiles have even symmetry and are convex after unwrapping. These phase profiles are not the same in each plane. An example of the wrapped and unwrapped phase modulation can be seen in Fig. 2. Note that the focal length of the PhL needs to be relatively short to achieve the desired phase modulation.
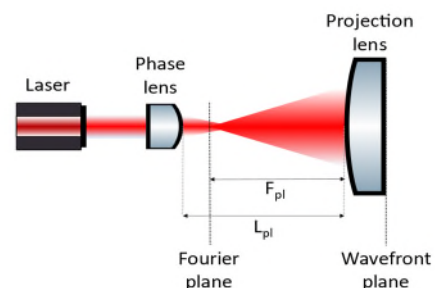
Figure 1. Layer Beam generator

One can also analyse the wavefront in a plane directly behind the PL. This wavefront is convex and has even symmetry, similar to the phase behind the PhL. The local slope of the wavefront defines the caustic properties, meaning how the rays are focused.

The projection lens (PL) is used as a spatial Fourier transforming element. The phase in the focal distance (F_{pl}) from the PL is Fourier transformed, and the LB is consequently generated. This means that changing the distance between the lenses (L_{pl}) affects the plane position from which the phase profile will be transformed. The focal length of the PL affects the Fourier transformation's spatial scaling, hence the beam's properties.

Altering the L_{pl} distance affects the position of the beam's focus and beam curvature. Changing the PL's focal length affects the beam's spatial parameters. Using the long focal length generates a smaller focus, meaning thinner lines in the transversal profile (Fig. 4).

3. Results

The simulation of the LB generated using on-shelf PhL Thorlabs LJ1918L1 with a focal length of 5.79 mm together with PL Thorlabs LJ1703RM with a focal length of 75 mm was done in VirtualLab Fusion©. The L_{pl} distance was 82 mm. Fig. 2 shows the wrapped and unwrapped phase behind the PhL.
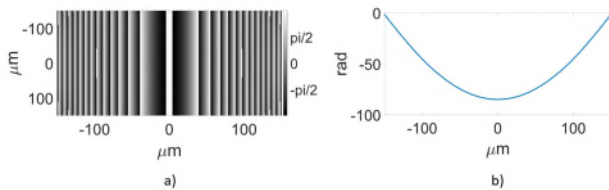
Figure 2. a) Wrapped phase behind the PhL, b) Line-profile of an unwrapped phase behind the PhL

The longitudinal profile can be seen in Fig. 3. Shortening the L_{pl} will decrease the beam curvature. Hence, the beam focus will be shifted at a longer distance from the generator. Shortening the focal length of the PL causes the beam waist to be smaller and the beam focus to be thicker. These effects are due to the changes in the wavefront slope behind the PL.

Notice that LB has a finite distance. Once the L_{pl} becomes too short, the phase profile changes. The wavefront's line-profile behind the PL will have local minima and maxima shaped like a "Sombrero." Once this happens, LB will travel for unlimited distance having similar properties to a so-called Structured Laser Beam (SLB). Note that SLB has a rotational symmetry [13].
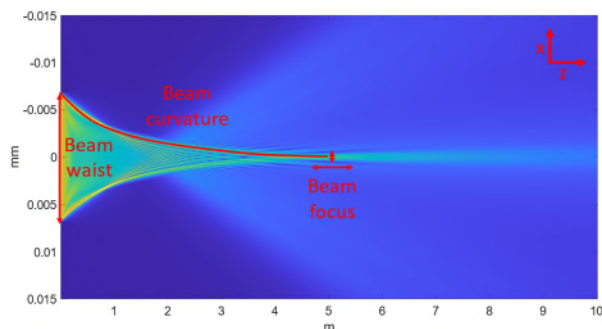
Figure 3. Longitudinal profile of the LB

The transversal profiles in 1, 3, and 5 meters can be seen in Fig. 4. They consist of different number of parallel lines. As mentioned previously, their thickness can be altered by changing the focal length of the PL.
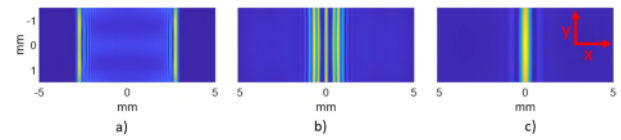
Figure 4. Transversal profile of the LB a) 1 m, b) 3m, c) 5m

4. Conclusion

The method for generating Optical Caustic Beams, namely Layer Beams, using a set of cylindrical lenses, has been presented with examples of how the generator can be tuned to reach the desired properties of the beam.

LB has potential to be used in the context of accelerator alignment, where they can serve as a reference line. One can use the center of symmetry of the pattern as a reference plane. Changing the focal length of the PL to 500 mm can lead to creating a line with a thickness under 10 mm in the LB's focus after propagating over 140 meters. This would mean that the generated line can fit on a regular CMOS chip, and later, the misalignment of the CMOS with respect to the line can be detected.

References

[1] Yu. A. Kravtsov and Yu. I. Orlov, Caustics, Catastrophes and Wave Fields, 2nd ed. (Springer-Verlag, Berlin, 1999).

[2] J. F. Nye, Natural Focusing and Fine Structure of Light Caustics and Wave Dislocations (Taylor & Francis, Philadelphia, 1999).

[3] Vaveliuk, P., Lencina, A., Rodrigo, J. A., & Matos, O. M., "Symmetric airy beams," Optics letters 39(8), 2370–2373 (2014).

[4] WU, You, et al. Symmetric pearcey gaussian beams. Optics Letters, 2021, 46.10: 2461-2464.

[5] Zhang, P., Prakash, J., Zhang, Z., Mills, M. S., Efremidis, N. K., Christodoulides, D. N., & Chen, Z., "Trapping and guiding microparticles with morphing autofocusing Airy beams," Optics letters 36(15), 2883–2885 (2011).

[6] Li, J. X., Fan, X. L., Zang, W. P., & Tian, J. G., "Vacuum electron acceleration driven by two crossed Airy beams," Optics letters 36(5), 648–650 (2011).

[7] Papazoglou, D. G., Panagiotopoulos, P., Couairon, A., & Tzortzakis, S., "Materials processing using abruptly autofocusing beams," CLEO.

[8] Wang, J., Bu, J., Wang, M., Yang, Y., & Yuan, X., "Generation of high-quality Airy beams with blazed micro-optical cubic phase plates," Applied optics 50(36), 6627–6631 (2011).

[9] Yalizay, B., Soylu, B., & Akturk, S., "Optical element for generation of accelerating Airy beams," JOSA A 27(10), 2344–2346 (2010).

[10] Z. Cao, C. Zhai, J. Li, F. Xian, and S. Pei, "Light sheet based on one-dimensional airy beam generated by single cylindrical lens," Opt. Commun. 393, 11–16 (2017).

[11] D. Papazoglou, S. Suntsov, D. Abdollahpour, and S. Tzortzakis, "Tunable intense airy beams and tailored femtosecond laser filaments," Phys. Rev. A 81, 061807 (2010).

[12] W. Niewiem, K. Polak, M. Dusek, D. Mergelkuhl, J.-C. Gayde, A. Wieser, and M. Sulc, "Variation of structured laser beam pattern and optimization for an alignment reference line creation," Opt. Express (to be published) (2023)

[13] K. Polak, J. Gayde, S. M. Sulc et al., "3D Polarisation of a Structured Laser Beam and Prospects for its Application to Charged Particle Acceleration," in Proceedings of 14th International Particle Accelerator Conference (IPAC'23), (2023), pp. 1444–1445.

Motion stage technology for large size OLED flat panel inkjet printing equipment

Li Qi[1], Cao Donghao[1], Zhou Chuanyan[1], Wang Guanming[1], Zhou Zhi[1], Wang Shuhui[1]

[1]*Ji Hua Laboratory, Foshan, China*

liqi@jihualab.com

Abstract

In order to adapt to the accuracy requirements of high-resolution OLED RGB inkjet printing equipment, a new type of ultra-precision large-stroke motion stage was developed. Mechanically, both the stepping axis and the scanning axis adopt linear motor direct drive and air bearing guidance, and use a multi-degree-of-freedom fine-motion stage to compensate for the horizontal straightness error and yaw angle error of the scanning axis guide rail. In terms of measurement, multiple sets of laser interferometers are relied upon to provide real-time feedback on the position and attitude of the substrate stage. Through experimental data, the motion stage can achieve sub-micron accuracy. This precision lays a solid foundation for wet film formation in the OLED RGB printing process, effectively guarantees subsequent dry film formation, and achieves mura free for large-size panels.

Keywords: OLED inkjet printing process, Coarse-fine motion stage, Precision measurement

1. Introduction

In manufacturing processes such as OLED inkjet printing, TFT lithography, panel inspection and repair, the size of the substrate becomes larger and larger from G1 to G8.5, or even G10.5 (see Figure 1 for specific dimensions), and the substrate stage's moving range also increases at the same time. In terms of accuracy, with the improvement of substrate resolution, higher requirements have been put forward for parameter indicators such as the positioning accuracy of the substrate stage. Taking G4.5 inkjet printer as an example, the positioning accuracy of the workpiece motion stage can reach 1 micron or even sub micron. In the field of inkjet printing, several companies have done a lot of exploratory work.

David Albertalli [1] of Litrex Company proposed a conceptual design drawing of the G7 inkjet printer for the large-panel industry. The article briefly introduced the drop watcher and printhead module system, but did not describe
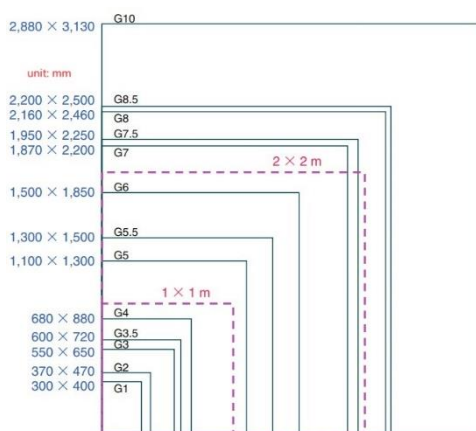
Figure 1. Dimensional drawings of substrates of each generation

the mechanical structure of the printer's motion stage in detail. Also from Litrex Company, Tianzong Xu et al. [2] introduced two types of inkjet printing equipment, G2 and G5,

summarized the error sources that affect the accuracy of inkjet printing placement in the moving platform, and conducted a detailed study of the compensation methods for various error sources. Jun H. Souk et al. [3] from Samsung Electronics have developed a color filter inkjet printing equipment for TFT-LCD panels, with a panel size of G8. The article contains design drawings and physical drawings of the inkjet printing equipment. The maximum printing speed of the equipment reaches 600mm/s, the droplet placement accuracy is ± 15 microns (1 mircron = 1μm), and it is equipped with 24 printheads. The time to complete the full-page printing is 180 seconds.
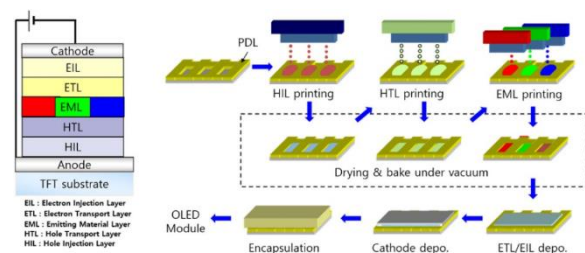
Figure 2. OLED device structure and its inkjet printing process flow [4]

2. OLED inkjet printing process and accuracy analysis

2.1 OLED inkjet printing process

Inkjet printing (IJP) technology is a process that can directly pattern deposit thin films and can achieve efficient patterning processing on flexible and large-area substrates. Inkjet printing technology has the advantages of high resolution, high degree of automation, low cost, simple manufacturing process, high material utilization, low environmental pollution, and is suitable for large-size screen production. The application of inkjet printing technology to OLED flat panel displays has great potential.

Nowadays, the OLED production process is usually prepared by the evaporation method. The organic material is heated in a vacuum environment to evaporate it and deposited on a glass substrate covered with a mask to form a film.

OLED technology	Printing	Evaporation	
	RGB SBS	RGB SBS	White OLED + CF
Overview			
Structure			
Quality	Fair → Good	Good	Fair
Resolution	Fair → Good	Excellent	Excellent
Scalability	Excellent	Bad	Good
Advantages	High material usability Metal mask-less	-	Not fine metal mask
Issues	Material performance Process stability	Large FMM	CF necessity

Figure 3. Comparison between printing process and evaporation process [5]

2.2 Printing accuracy analysis

The inkjet printing comprehensive accuracy depends on the accuracy of the printhead, the accuracy of the motion stage and the accuracy of the substrate [3]. The error tree of comprehensive accuracy is shown in Figure 4. The height between the printhead and the substrate affects the accuracy of the droplet placement, so the printing height (print gap) is listed as the printhead accuracy.

The accuracy of the printhead consists of two parts. One is the geometric accuracy of the nozzle in the printer. During the printing process, there is a six-degree-of-freedom error regardless of whether the printhead is stationary or moving. As shown in Figure 5, the machine tool slide moves linearly
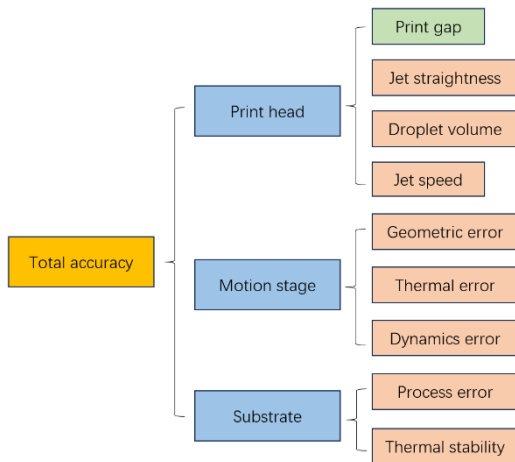
Figure 4. Inkjet printing comprehensive accuracy error tree

along the z-axis guide rail. The silder has three translation errors: positioning error EZZ, horizontal straightness error EXZ, vertical straightness error EYZ, and three rotation errors: roll ECZ, pitch EAZ, yaw EBZ. The second is the physical performance parameters of the printhead: jet straightness, droplet volume/diameter and jet speed.

The accuracy of the motion stage mainly includes the geometric accuracy, thermal error and dynamic error of the printer's motion axis. Since thermal errors are difficult to evaluate and build models for compensation, this article only considers the geometric accuracy of the printer's main motion axes. Like the motion axis of the printhead, the motion axis of the substrate stage also has six degrees of freedom errors. The substrate accuracy consists of the processing accuracy of the previous process and the thermal
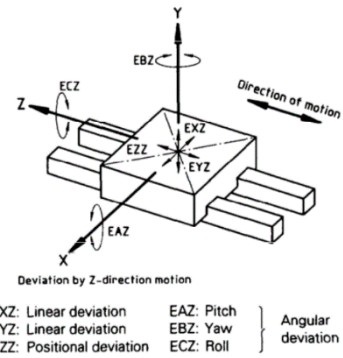
Figure 5. Schematic diagram of the six-degree-of-freedom error of the machine tool slide [6]

deformation of the substrate. To ensure high-quality inkjet printing, substrate accuracy must be strictly controlled.

Jet straightness directly affects the placement accuracy of ink droplets. The ink droplet can be regarded as an ideal sphere during flight, and the diameter of the ink droplet can be calculated according to the formula of the ink droplet volume. Substrate pixel density ppi (pixels per inch) represents the number of pixels per inch. The higher the ppi value, the smaller the pixel size. For example, the sub-pixel width of a 202ppi substrate is 34.5μm, while the sub-pixel width of a 300ppi substrate is 20.8μm.

Assuming the droplet physics parameters such as volume and jet speed are under good control, and jet straightness is zero, the primary error is positioning error. However, the droplet jet straightness can not be ignored, the print height multiplied by the tangent value of jet straightness is equal to the droplet placement accuracy. Therefore, in this article, the positioning accuracy of the motion stage and the static placement accuracy of ink droplets are the main sources of error.

As shown in 6a (left), the sub-pixel pitch corresponding to 202ppi is 42μm, the diameter of the 7pl ink droplet jetted from the printhead is 23.7μm, the sub-pixel slot width is
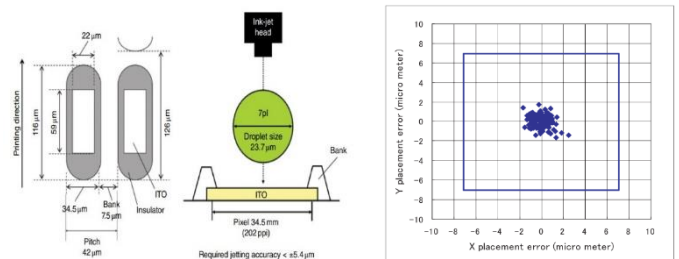
Figure 6. Printhead, ink droplets and sub-pixel slots [7][8][9]

34.5um, and the ink droplet placement accuracy is required to be ±5.4μm.

The ink droplets fall vertically into the sub-pixel slot in the ideal state, without considering the error caused by the straightness of the ejection. Under normal circumstances, there is a jet straightness error when ejecting ink droplets from a nozzle, and this error conforms to a normal distribution. Assume that the ink droplet jet straightness of a certain nozzle is θ and is 3mrad, satisfying the normal distribution 3 sigma, the height h_g from the printhead to the substrate is equal to 500um, and the placement accuracy δ = $h_g \tan θ$. The calculated result of δ is 1.5μm. The accuracy of the placement is distributed in two-dimensional space, as shown in Figure 6b (right). The ink droplet placement is in the xy two-dimensional coordinate system, $δ_x = δ_y = ±1.5μm$. Nozzles that exceed this error range are closed by the

printhead control board. Otherwise, ink droplets risk flying out of the sub-pixel slots, causing printing defects [10].

3. Motion stage structure

3.1 Current status of large-size panel motion stage

In the past two decades, with the popularity of LCD TVs, the large-size flat panel industry has developed rapidly. Starting in 2000, the substrate size was only 700mmx900mm. By 2018, the G10.5 generation panel size reached 2940mmx3370mm. The panels are getting larger and larger, and the stroke and accuracy of the substrate carrier and motion stage are increasing at the same time.

In flat panel exposure machines, large-stroke high-precision motion stage are widely used [11][12]. Nikon officially released new FPD exposure equipment corresponding to G10.5 glass substrates in 2018. Compared with the existing G10 exposure equipment, the G10.5 exposure equipment has improved exposure and calibration sequences to achieve faster and more precise exposure.

3.2 Inkjet printer motion stage design
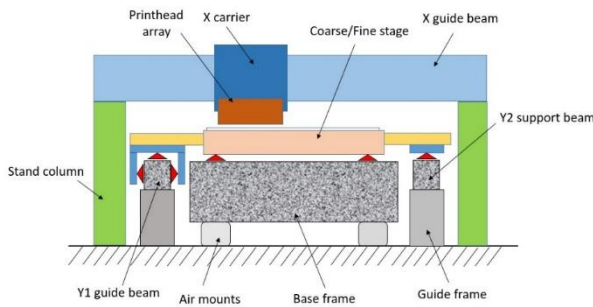
Figure 7. Main structure of inkjet printer motion stage

Design a motion stage that covers the printhead array sliding stage and the glass substrate carrier. The substrate size is 920mm×730mm (G4.5). The printhead array slide stage makes a stepping movement along the X-axis guide rail with a stroke of 1500mm; the glass substrate stage makes a scanning movement along the Y-axis guide rail with a stroke of 2200mm. As shown in Figure 7, the inkjet printing equipment mainly consists of a base frame, guide frame, printhead array, glass substrate stage, air mounts, etc. The glass substrate stage includes a dual-drive servo-controlled coarse stage and a multi-voice coil motor servo-controlled fine stage. The total weight of the substrate stage is 1.2t, the maximum movement speed is 500mm/s, and the positioning accuracy is ±3μm.

3.3 Multi-degree-of-freedom substrate stage

When the coarse motion stage moves along the Y-axis guide rail, there are positioning errors, angular errors and straightness errors. The positioning accuracy of the coarse motion stage can reach 1 micron using laser interferometer measurement data compensation. Angle error (Yaw error) and horizontal straightness error can be measured with a laser interferometer. For a guide rail with a length of about 3 meters, the horizontal straightness error reaches tens of microns. To achieve high-quality printing, improve the placement accuracy of ink droplets, and allow large amounts of ink droplets to be accurately and stably ejected into designated sub-pixel slots, a fine-motion stage mechanism is required to compensate for errors in real time. In addition, the fine-motion stage mechanism is required to correct the
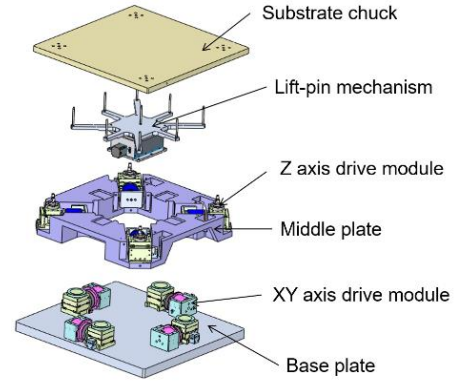
Figure 8. Schematic diagram of fine-motion stage mechanism

angle deviation of the substrate caused during the substrate loading process.

The fine-motion stage can complete six degrees of freedom micro-movement. As shown in Figure 8, the six-degree-of-freedom fine-motion stage is composed of upper and lower fine-motion mechanisms connected in series. The upper fine-motion mechanism is divided into a substrate suction plate, an intermediate drive plate and a Z-direction drive module. Four independently controlled Z-direction drive modules support the substrate suction plate, and use the middle drive plate as a reference object for relative movement to realize Z, θ_x , θ_y micro-movements of the substrate suction plate along the Z axis and around the X/Y axis. Four XY-direction drive modules are installed on the base. The middle drive plate uses the base as a reference object to make relative movements to achieve X, Y, and θ_z micro-movements along the X/Y axis and around the Z axis. There is also a Lift-pin mechanism inside the micro-motion stage. When the glass substrate is loaded and unloaded, the Lift-pin mechanism rises. When printing, the Lift-pin mechanism is in a contracted state.

3.4 Measuring system
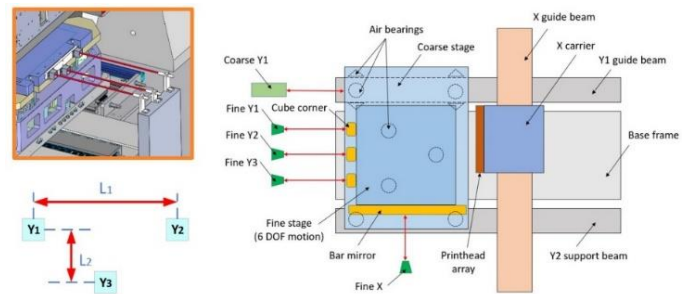
Figure 9. Coarse-fine stage measurement system. The upper left figure shows the spatial geometric position relationship between the three-way laser interferometer and the substrate chuck, and the lower left figure shows the plane geometric position relationship of the three corner cubes.

Precise measurement to realize the precise positioning of the coarse-fine-motion stage in the printing equipment. The coarse-motion stage moves along the guide rail Y1, and the laser interferometer Y1 measures the position of the coarse-motion stage in real time, and feedback the position signal to the motion controller, so as to realize the uniform speed control of the coarse-motion stage.

The attitude of the fine-motion stage in the inkjet printer space coordinate system is obtained by measuring the laser interferometers Y1, Y2, and Y3. Three corner cube prisms are
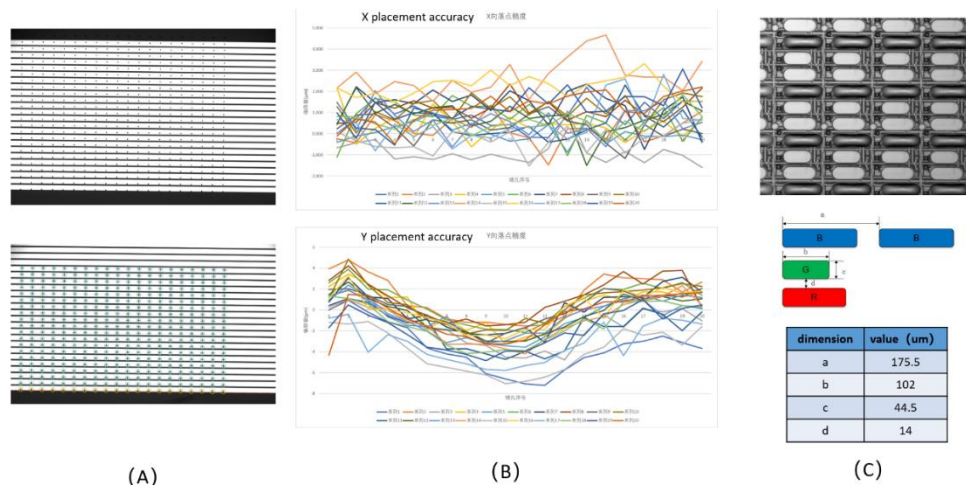
Figure 10. OLED ink printing test results

fixed on one end of the upper plate (substrate chuck) of the fine-motion stage. Details are shown in Figure 9. Real-time measurement of Y axis positioning accuracy、yaw error around Z axis and pitch error around the X axis. Combining forward and inverse kinematics, the adjustment parameters of the fine-motion stage can be obtained. The specific calculation formula is as follows:

$$y = (Y_1 + Y_2)/2 \qquad (1)$$

$$\Theta_z = \arctan\left[(Y_1 - Y_2)/L_1\right] \qquad (2)$$

$$\Theta_x = \arctan\left\{\left[\frac{Y_1+Y_2}{2} - Y_3\right]/L_2\right\} \qquad (3)$$

In formula (1), y represents the positioning of the fine-motion stage along the Y axis, and Y1 and Y2 represent the length measurement values of the laser interferometers Y1 and Y2 and the corresponding corner cubes. In formula (2), L1 represents the horizontal distance between corner cube Y1 and Y2. In formula (3), Y3 represents the length measurement value of the laser interferometer Y3 and the corresponding corner cube, and L2 represents the vertical distance between the corner cube Y1 and Y3.

4. Measurement data and print test

The inkjet printing equipment printed substrates at 80ppi, 137ppi, and 144ppi in the clean room of the laboratory. In Figure 10 (A) shows ink droplet placement accuracy test board and image processing software which can calculate the ink droplet's placement accuracy. There are a total of 20 columns of ink droplets in each image, which means that 20 nozzles participate in scanning printing, and each nozzle jets 20 droplets. From the figure, it can be seen that the ink droplets accurately placed in the test area.

Figure 10 (B) shows accuracy curve of ink droplet placement. Top figure shows the placement accuracy of ink droplet in X-direction, with a maximum error is 4.664 μm. Minimum error is -1.597μm. Down figure shows the placement accuracy of ink droplet in Y-direction, with a maximum error 4.845 μm. Minimum error is -7.212μm. The volume of ink droplets used for testing is 3.7pL, and the diameter of ink droplets is 19.2μm. According to the placement accuracy of the Y-direction, ink droplets can accurately fall into the R/G/B sub pixel slots.

In Figure 10 (C), the top figure shows the printing results observed by a high magnification CCD camera. From a local perspective, the ink droplets have accurately and evenly fallen into the R sub pixel slot. The middle figure shows the 144ppi substrate pixel map. The down figure shows the pixel size table of the 144ppi substrate.

5. Conclusion

In this paper, we developed a new type of motion stage whose performance parameters meet the requirements of high-resolution OLED substrate inkjet printing process. The key axis positioning accuracy of the motion stage is ±1 μm, and the repeatable positioning accuracy is ±0.8 μm. The accuracy of ink droplet placement is better than 3 μm.

References

[1] David Albertalli. Gen 7 FPD Inkjet Equipment – Development Status. SID 2005 DIGEST.
[2] Jun H. Souk et al. Inkjet Technology for Large Size Color Filter Plates. SID 2008 DIGEST.
[3] Tianzong Xu et al. Achieving High Accuracy and Precision Inkjet Drop Placement Using Imperfect Components in an Imperfect Environment. IMID/IDMC 2006 DIGEST.
[4] Kye-Si Kwon et al. Review of digital printing technologies for electronic materials. Flexible and Printed Electronics. 5 (2020)
[5] Toshiaki Arai. Innovative Technologies for OLED Display Manufacturing. AM-FPD 2018.
[6] ISO 230-1:2012 Test code for machine tools. Part 1: Geometric accuracy of machines operating under no-load or quasi-static conditions.
[7] Tadashi Gohda. 202-ppi Full-Color AMPLED Display Fabricated by Ink-Jet Method. Sharp Corportation, Japan 2006.
[8] Mitsuhiro Koden. OLED Displays and Lighting[M]. John Wiley & Sons, Ltd. 2016.
[9] Komatsu Katsuaki et al. Development of New Inkjet Head for the Display Panel Industry. 2008
[10] Yixin Wang et al. A high-adaptability nozzle-array printing system based on a set covering printing planning model for printed display manufacturing. Scientific Reports. 2023 13:156
[11] Wesselingh, J. Contactless Positioning using an Active Air Film. 2011.
[12] FX-1035S FPD Lithography System. www.nikon.com/company/technology/stories/1909_fpd.

Single-shot transmission Differential Interference Contrast Microscopes using LC Savart prism as the shear device

Shyh-Tsong Lin* and Ting-Yu Chien

Department of Electro-optical Engineering, National Taipei University of Technology, 1, Sec.3, Chung-Hsiao East Road, Taipei 10608, Taiwan

Corresponding author e-mail address: f10402@ntut.edu.tw

Abstract

Four types of Differential Interference Contrast Microscopes (DICMs) have been verified feasible, the first one uses a pair of Normaski prisms, the second utilizes a Savart prism, the third adopts a cyclic apparatus, and the fourth employs a pair of twisted nematic liquid-crystal cells as the shear device; however, they all require a mechanical movement to switch shear directions; consequently their inspection throughput is decreased in case shear direction switching is necessary during the inspections. An innovative transmission DICM is therefore proposed in this research. It is the same as a single-shot phase-shifting polarizing microscope except it has a liquid-crystal Savart prism inserted in between the objective and sample, and it possesses the advantages of switching shear directions non-mechanically and completing the inspection in a single-shot time. This paper is to introduce the configuration, examination theory, and experimental setup of the DICM; it also exhibits the experimental results from the uses of the setup; the results confirm the function and advantages of the DICM.

Keywords: Differential Interference Contrast Microscope (DICM); liquid-crystal Savart prism; single-shot phase-shifting polarizing microscope

1. Introduction

We have already known that optical microscopy for enhancing image contrast can be implemented using Dark-Field Microscopes (DFMs), Phase-Contrast Microscopes (PCMs), and, DIfferential Interference Contrast Microscopes (DICMs), where DICMs are with the advantage of revealing more sample features (e.g. surface roughness, slope, etc.). Up to date, four types of DICMs have been verified feasible, the first one [1-7] uses a pair of Normaski prisms, the second [8-10] utilizes a Savart prism, the third [11-12] adopts a cyclic apparatus, and the fourth [18] employs a pair of twisted nematic Liquid-Crystal (LC) cells as the shear device; however, they all require a mechanical movement to switch shear directions; consequently their inspection throughput is decreased in case shear direction switching is necessary during the inspections.

An innovative DICM is therefore proposed in this research. It is the same as a single-shot phase-shifting polarizing microscope except that it adopts a novel LC Savart prism, inserted in between the objective and sample, as the shear device, it switches the shear directions by just adjusting the driving voltage of the LC Savart prism, and it is able to achieve living-sample inspections. This paper sequentially introduces the configuration, examination theory, and experimental setup of the proposed DICM, in addition to the experiments and experimental results conducted by the experimental setup. This paper then concludes the research by summarizing the inspection performance of the proposed DICM.

2. The proposed DICM

As that shown in Fig. 1(a), the proposed DICM is composed of a broad-band light source (BLS), polarizer (P) with its transmission axis at 45° measured from the x-axis, color filter (CF), condenser lens (C) with a small numerical aperture, reflecting mirror (M), objective (O), tube lens (TL), quarter-wave plate (QWP) with its fast axis at 45° measured from the x-axis, and CMOS sensor equipped with an analyzer composed of repeated arrays of 2×2 pixelated polarizers. In addition, an LC Savart prism (LCSP) is placed between the objective and sample (S). A magnified 3D drawing of the LC Savart prism is exhibited in Fig. 1(b), it demonstrates that the prism is made up of two anti-parallel alignment LC cells (LC$_x$ and LC$_y$), which are with their respective driving powers and their principal sections (plane containing prism surface normal and optic axis) parallel to x-z and y-z planes, respectively.
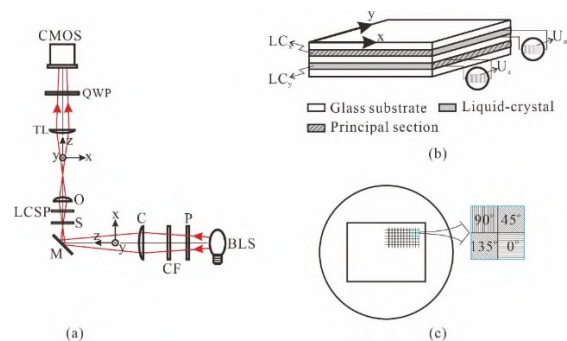
Figure 1 (a) Schematic of the proposed DICM; (b) 3D drawing demonstrating the LC Savart prism; (c) CMOS sensor viewed along the z-axis, where the polarizers of one array are marked to indicate their respective transmission axis orientations.

The optics pertaining to uniaxial birefriengent crystals has been analyzed in detail in Refs. [13, 14], by which the effects of each LC cell of the LC Savart prism on an incident ray are summarized and interpreted as follows. As that shown in Fig. 2(a), when LC$_x$ is driven by an AC voltage with an amplitude of U$_a$ (e.g. U$_a$ = 3.5 V), its optic axis (i.e. the long axis of the LC molecules) moves to a direction having an angle β with respect

to the cell surface normal [15, 16], it can therefore shear an incident ray with a small incident angle into two rays (o- and e-rays), whose propagation direction is parallel to that of the incident ray and whose shear direction is along the x-axis, having a shear distance and Optical-Path-Difference (OPD) of

$$\Delta x = t \frac{(n_o^2 - n_e^2)\sin\beta\cos\beta}{A} \qquad (1)$$

and

$$\Lambda_0 = t\left(\frac{n_o n_e}{A^{1/2}} - n_o\right), \qquad (2)$$

respectively; where **t** represents the thickness of the LC layer, n_o and n_e are the ordinary and extraordinary refractive indices, respectively, of the LC material, and

$$A = n_o^2 \sin^2\beta + n_e^2\cos^2\beta . \qquad (3)$$

Nevertheless, as the phenomenon demonstrated using Fig. 2(b), when the amplitude of the driving voltage increases to an adequately high value (e.g. $U_a \geqq 10$ V), the optic axis displaces to the direction parallel to the cell surface normal (i.e. $\beta \approx 0^\circ$), accordingly the shear distance disappears and the corresponding OPD becomes zero.

Figs. 2(a) and 2(b) are respectively called the turned on and turned off states of the LC cell and represented as $LC_x=1$ and $LC_x=0$ hereafter.
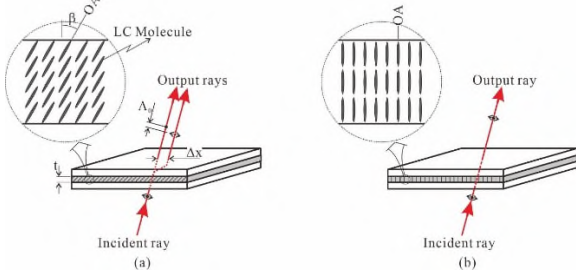
Figure 2 (a) Turned on and (b) turned off states of LC_x; where.and $\leftrightarrow$ represent o- and e-rays, respectively.

Like LC_x, the turn on and turn off states of LC_y are represented as $LC_y=1$ and $LC_y=0$, respectively.The effects of LC_y on an incident ray are the same as those of LC_x except that its shear direction is along the y-axis. By using the above-described effects, the inspections using the proposed microscope are demonstrated as follows. Referring to Fig. 1(a) again, where the polarizer and color filter convert the light beam from the light source into a linearly polarized and adequately band-narrowed beam, the condenser collects the beam emerging from the color filter to illuminate the sample and then pass through the LC Savart prism, and the objective collects the light beam emanating from the LC Savart prism to propagate through the tube lens and quarter-wave plate to generate an image on the CMOS sensor.
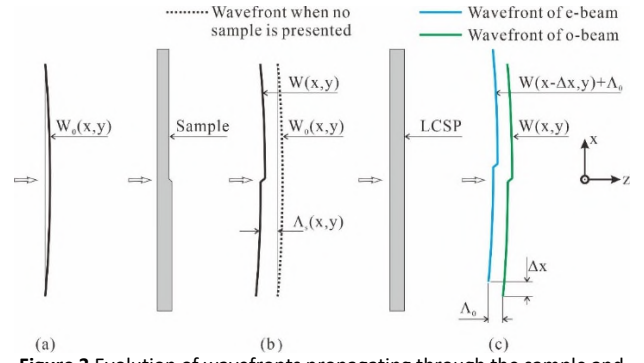
Figure 3 Evolution of wavefronts propagating through the sample and then LC Savart prism.

As $LC_x = 1$ and $LC_y = 0$, the image on the CMOS sensor can be illustrated via Fig.3; where (a) shows the wavefront, i.e. $W_0(x, y)$, of the beam incident on the sample; (b) presents the wavefront, i.e. W (x, y) which is the superposition of $W_0(x, y)$ and $\Lambda_s(x,y)$, of the beam emerging from the sample; and (c) depicts the wavefronts, i.e. W (x-Δx, y)+Λ_0 and W (x, y), of the sheared beams emanating from the LC Savart prism, the lateral shear, Δx, and longitudinal lag, Λ_0, are due to the above-mentioned effects contributed by LC_x. Fig. 3 gives that the sheared beams are with an OPD of

$$\Lambda = W(x,y) - [W(x - \Delta x, y) + \Lambda_0] \qquad (3a)$$

or, since W (x, y) = $W_0(x, y)$ + $\Lambda_s(x,y)$,

$$\Lambda = \Delta W_0(x,y) + \Delta\Lambda_s(x,y) - \Lambda_0 ; \qquad (3b)$$

where $\Lambda_s(x,y)$ stands for the Optical Path Length (OPL) of the sample, $\Delta W_0(x,y) = W_0(x,y) - W_0(x - \Delta x, y)$, and

$$\Delta\Lambda_s(x,y) = \Lambda_s(x,y) - \Lambda_s(x - \Delta x, y) \qquad .$$

Correspondingly, the image on the CMOS sensor has an interference intensity of

$$I = I_0[1 + \cos(\frac{2\pi}{\lambda}\Lambda + 2\alpha)], \qquad (4)$$

where λ represents the central wavelength of the light beams and α denotes the transmission axis angle of the analyzer where the interference beams pass through [17, 18]. Substituting Eq. (3b) into Eq. (4) leads to

$$I = I_0[1 + \cos(\Delta\phi + \tau + 2\alpha)], \qquad (5)$$

where

$$\Delta\phi = \frac{2\pi}{\lambda}\Delta\Lambda_s(x,y) \qquad (6)$$

and

$$\tau = \frac{2\pi}{\lambda}[\Delta W_0(x,y) - \Lambda_0]. \qquad (7)$$

Eq. (5) agrees that the configuration of Fig. 1(a) is a DICM, since its phase is a function of OPL variation of the sample. The only difference of this equation from that of conventional DICMs is the existence of phase τ, which is independent of the sample and can be eliminated using the subtraction method.

When $LC_x = 0$ and $LC_y = 1$, the image on the CMOS sensor can also be interpreted via Fig.3, and a derivation gives an image intensity the same as Eq. (5) except that the lateral shear is along the y-axis.

The images corresponding to Eqs. (5) and (6) are referred to as the Differential Interference Contrast (DIC) image and phase-DIC image, respectively. Be aware that, as that demonstrated in Fig. 1 (c), a single-shot image grabbed by the CMOS sensor can be separated into four DIC-images with $\alpha=0^\circ$, 45°, 90°, and 135°, respectively; by which, the phase-DIC image can be obtained using the four-step phase-shifting technique [19, 20] incorporated with the subtraction method, i.e.,

$$\Delta\phi = a\tan 2\left(\frac{I_4 - I_2}{I_1 - I_3}\right) - \tau ; \qquad (8)$$

where I_1, I_2, I_3, and I_4 stand for the DIC images with $\alpha=0^\circ$, 45°, 90°, and 135°, respectively, and τ is pre-determined by the same four-step phase-shifting technique when no sample is presented.

.

3. Experimental setup

To implement the proposed DICM, a setup comprising the proposed DICM and a control and image processing system was installed, where the control and image processing system comprised a dual-channel function generator, DG 1022 from RIGOL Technologies, Inc., China, and a personal computer.

In the DICM, the light source was a halogen lamp, the condenser had a numerical aperture of 0.05, the color filter output a red-light beam with a central wavelength of 648nm, the objective was CFI Plan Flour ELWD 20xC (NA = 0.45, cover glass compensation: 0-2.0 mm) from Nikon Corp., Japan, the tube lens was MT-1 from Nikon Corp., Japan, the quarter-wave plate was of a broadband type obtained from the Photoelastic Division of Measurements Group, Inc., USA, the CMOS sensor was BFS-U3-51S5P-C from FLIR Integrated Imaging Solutions Inc., Canada, and the LC Savart prism was fabricated at the liquid crystal lab of the authors' department.

In the control and image processing system, the two channels of the function generator were utilized as the driving powers of the LC Savart prism, and each of them exported a one kHz rectangular-wave voltage with U_a = 3.5 V/ 10.0 V to turn on/ off its corresponding LC cell; the computer executed three programs: image grabbing, evaluation, and display. The image grabbing involved acquiring the DIC images on the CMOS sensor and storing them in the memory of the computer; the evaluation extracted the phase-DIC images by the uses of Eq. (8) and the stored images; and the display exhibited the obtained DIC and phase-DIC images on the computer monitor.

4. Experimental results

To verify the proposed DICM, two experiments were carried out. The first conducted the setup to inspect a 2-D rectangular grating made of quartz. The DIC images grabbed as LC_x = 1 and LC_y = 0 are illustrated in Fig.4 (a). The phase-DIC image calculated using the DIC images of Fig. 4(a) and Eq. (8) is presented in Fig. 4(b). The DIC images captured as LC_x =0 and LC_y =1 are exhibited in Fig.5 (a). And the phase-DIC image determined using the DIC images of Fig. 5(a) and Eq. (8) is revealed in Fig. 5(b). Figs. 4 (b) and 5(b) confirm the function of the proposed DICM, since they are consistent with the predicted x- and y-shearing phase-DIC images, respectively, of the 2-D rectangular grating. According to Eq. (6), the x-shearing phase-DIC image of the 2-D rectangular grating is predicted to be with positive and negative phases at vertical low-to-height and high-to-low edges, respectively; whereas the y-shearing image is predicted to be with positive and negative phases at horizontal low-to-height and high-to-low edges, respectively.
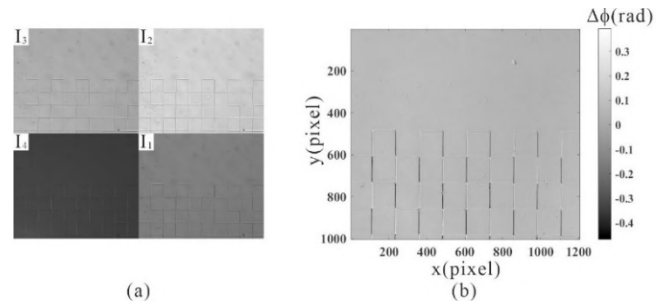
Figure 4 Inspection results when LC_x = 1 and LC_y = 0. (a) Grabbed DIC images; (b) calculated phase-DIC image; where each image is with a size of 1224×1024 pixels, and each pixel represents a length of 0.348 μm.
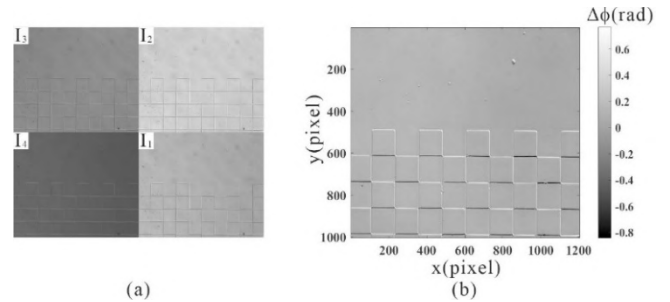
Figure 5 Inspection results when LC_x =0 and LC_y =1. (a) Grabbed DIC images; (b) calculated phase-DIC image.

The second experiment was to examine an unstained onion epidermal tissue, sandwiched in between a slide and a cover slip. The obtained x- and y-shearing phase-DIC images are shown in Figs. 6 (a) and (b) respectively, illustrating the proposed DICM is capable of retrieving more detailed images/features of the sample than the equivalent bright-field image shown in Fig. 6(c). On examining these images, Figs. 6 (a) and (b) clearly exhibit the tissue's nuclei, however Fig. 6 (c), the bright-field image of the same sample, fails to distinguish the nuclei.
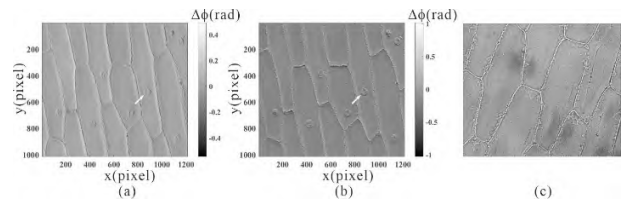
Figure 6 (a) X-shearing phase-DIC image, (b) y-shearing phase-DIC image, and (c) bright-field image of an onion epidermal tissue. The white arrows direct to a nucleus of the tissue; the field of (c) is not the same as that of (a) and (b)

5. Discussions

Furthermore, the above experiments verify that the proposed DICM can not only switch the shear directions by adjusting the driving voltage of the LC Savart prism, but also obtain the phase-DIC image by using a single-shot image; the latter endows the DICM with the ability of living-sample inspections. To verify this ability, an experiment conducting the setup to examine a paramecium solution sandwiched in between a slide and a cover slip was accomplished, where the computer recorded the images on the CMOS sensor for 2 seconds at 25fps and then converted the recorded images into their respective phase-DIC images. 6 images of the obtained y-shearing phase-DIC images are exhibited in Fig. 7, confirming the living-sample inspection ability of the proposed DICM.

Referring to Fig. 1 again, the DICM can be enhanced by inserting a beam-splitter between the objective and tube lens, and placing a module composed of a broad-band light source, polarizer, color filter, and condenser lens on the right-hand side of the beam-splitter. With this enhancement, the DICM will be capable of both reflection and transmission inspections. The authors are now installing a setup implementing this enhancement.
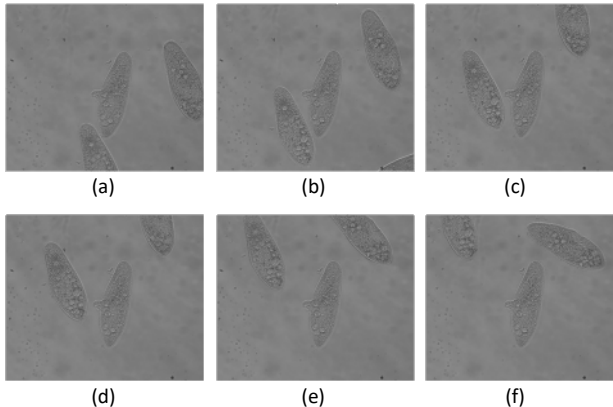
Figure 7 (a)-(f) y-shearing phase-DIC images of a paramecium solution.

6. Conclusions

An innovative transmission DICM using LC Savart prism as the shear device has been developed for retrieving images with OPL variation information. In addition to the intended advantage of switching the shear directions without mechanical movements, it also provides a superior ability over conventional DICMs of living-sample inspections. This paper has introduced the detail of the DICM, exhibited the setup for implementing the DICM, and performed the experimental tests and assessed the results achieved; which not only confirmed the intended functionality but also its additional advantages achieved.

Acknowledgments

References

[1] D. L. Lessor, J. S. Hartman, and R. L. Gordon, "Quantitative surface topography determination by Nomarski reflection microscopy. I. Theory," J. Opt. Soc. Am. 69, pp. 357-366 (1979).

[2] J. S. Hartman, R. L. Gordon, and D. L. Lessor, "Quantitative surface topography determination by Nomarski reflection microscopy. 2: Microscope modification, calibration, and planar sample experiments," Appl. Opt. 19, pp.2998-3009 (1980).

[3] J. S. Hartman, R. L. Gordon, and D. L. Lessor, "Nomarski differential interference contrast microscopy for surface slope measurements: an examination of techniques," Appl. Opt. 20, pp.2665-2669 (1981).

[4] S. N. Jabr, "Surface-roughness measurement by digital processing of Nomarski phase-contrast images," Opt. Lett. 10, pp. 526-528 (1985).

[5] T. R. Corle and G. S. Kino, "Differential interference contrast imaging on a real time confocal scanning optical microscope," Appl. Opt. 29, pp.3769-3774 (1990).

[6] S. V. King, A. Libertun, R. Piestun, C. J. Cogswell, and C. Preza, "Quantitative phase microscopy through differential interference imaging," J. Biomed. Opt. 13, pp. 024020 (2008).

[7] A. Serrano-Trujillo, A. Nava-Vega, and V. Ruiz-Cortez, "Development of a polarimetric experimental setup for surface profiling based on a microscopy application," Proc. SPIE 9598, pp.

95981H (2015).

[8] M. Françon, "Polarization apparatus for interference microscopy and macroscopy of isotropic transparent objects," J. Opt. Soc. Am. 47, pp. 528-535 (1957).

[9] H. X. Trịnh, S. T. Lin, L. C. Chen, S. L. Yeh, and C. S. Chen, "Differential interference contrast microscopy using Savart plates," J. Opt. (United Kingdom) 19, pp. 045601 (2017).

[10] S. T. Lin, H. X. Trinh, Z. W. Chen, and T. H. Lee, "Phase-shifting differential interference contrast microscope with Savart shear prism and rotatable analyser," J. Microsc.272, pp.79-84 (2018).

[11] S. Chatterjee and Y. P. Kumar, "White light differential interference contrast microscope with a Sagnac interferometer," Appl. Opt. 53, pp.296-300 (2014).

[12] S. Chatterjee and Y. P. Kumar, "Un-polarized light transmission DIC microscope," J. Opt. (India) 45, pp. 297-301(2016).

[13] M. Francon and S. Mallick, Polarization interferometers, Wiley-Interscience, New York, 1971.

[14] L. Wu, C. Zhang, Y. Yuan, and B. Zhao, "Exact calculation of lateral displacement and optical path difference of Savart polariscopes," Acta Optica Sinica 25, pp. 885-890 (2005).

[15] P. D. Berezin, I. N. Kompanets, V. V. Nikitin, and S. A. Pikin, "Orienting effect of an electric field on nematic liquid crystals," Sov. Phys.-JETP 37, pp. 305-308 (1973).

[16] E. Hecht, Optics, 5th Ed., Pearson, New York, 2017.

[17] S. Suja Helen, M. P. Kothiyal, and R. S. Sirohi, "Achromatic phase shifting by a rotating polarizer," Opt. Commun. 154, pp. 249–254(1998).

[18] S. Mukhopadhyay, S. Sarkar, K. Bhattacharya, and L. Hazra, "Polarization phase shifting interferometric technique for phase calibration of a reflective phase spatial light modulator," Opt. Eng. 52, pp. 035602 (2013).

[19] J. Millerd, N. Brock, J. Hayes, B. Kimbrough, M. North-Morris, and J. C. Wyant, "Vibration insensitive interferometry," Proc. SPIE 10567, pp. 105671P (2006).

[20] J. W. Jeon and K. N. Joo, "Single-shot imaging of two-wavelength spatial phase-shifting interferometry," Sensors 19, pp. 5094 (2019).

Realization of a uniform magnetic field for the KRISS Kibble balance II

MyeongHyeon Kim[1], Dongmin Kim[1], Minky Seo[1], Sung Wan Cho[1], Jinhee Kim[1] and Kwang-Cheol Lee[1]

[1]Quantum Mass Metrology Group, Quantum Technology Institute, Korea Research Institute of Standards and Science (KRISS) 267 Gajeong-ro, Yuseong-gu, Daejeon 34113 Republic of Korea

mhkim@kriss.re.kr

Abstract

The Korea Research Institute of Standards and Science (KRISS) is currently in the process of creating a magnetic system intended for the KRISS Kibble balance II. In this engineered magnet system, two circular permanent magnets are employed. These permanent magnets are encased by a yoke, ensuring the establishment of a consistent magnetic field across the specified air gap. The air gap's width measures 15 mm, and its length, maintaining a uniform magnetic field, spans 40 mm. Through meticulous design optimization, the resulting magnetic field strength exceeds 0.4 T, and the uniformity is maintained at less than 20 ppm. Actual magnet fabrication was conducted based on the optimized design. To minimize temperature effects, special materials were employed for the magnets, and a detachable upper and lower structure was implemented to facilitate the insertion of the main coil into the air gap. The performance of the ultimately fabricated magnet system is assessed.

Kibble balance, Kibble balance magnet, planck constant, mass measurement

1. Introduction

The Kibble balance experiment is a methodology employed for the realization of the kilogram in the updated SI [1]. This experimental approach involves the comparison of mechanical and electrical power. Establishing traceability of mass standards to the Planck constant is made possible through the utilization of quantum electrical standards.

Typically, the realization of the kilogram using the Kibble balance experiment involves two modes: the moving mode and the weighing mode. Enhanced performance is achieved with a larger area featuring a uniform magnetic field. For this purpose, several magnet systems have been developed [2-4]. In pursuit of improved performance, KRISS initiated the development of the second model of the KRISS Kibble balance (KRISS KB-2). The magnet system to be applied to KRISS KB-2 aims for a target magnetic field of 0.4 T and a magnetic field uniformity of 100 ppm.

2. Design constraints of the magnet system
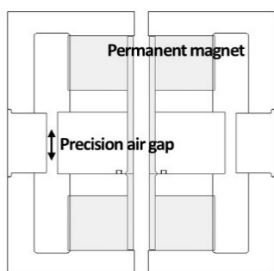
Figure 1. Structure of magnet system for KRISS KB-2

In Fig. 1, a schematic illustration of the magnet system for KRISS KB-2 is presented. During the moving mode, the main coil is designed to operate within a range of ±10 mm. The air gap's width at the designated coil position is 15 mm, and the length of the precision air gap, crucial for achieving a uniform magnetic field, is set at 40 mm, accounting for a safety factor.

The magnetic field is susceptible to temperature-induced changes, making the selection of magnet materials with low temperature coefficients a crucial factor in enhancing the performance of the Kibble balance. The EEC 2:17-TC16 provided by EEC is an excellent magnet material with a reversible temperature coefficient of -0.001 %/°C. This is utilized in the creation of permanent magnets.

3. Analysis and optimization for the magnetic field

3.1. Design parameters

Several variables, such as the thickness of the magnet and the size of the cavity formation entrance, are defined to design the magnet system. Based on these specified parameters, a magnetic field finite element method (FEM) simulation is conducted.

3.2. Optimization and results

The magnetic field intensity and uniformity within the cavity are optimized by iteratively adjusting the defined variable values. Considering a target magnetic field of 100 ppm and accounting for a safety factor, the simulation's uniformity must exceed the actual target. Table 1 and 2 presents the finalized results of the optimized design.

3.3. Modification for the vertical magnetic field

To minimize changes in the vertical magnetic field within the air gap, the heights of the inner yoke and outer yoke are asymmetrically adjusted [5]. Through several optimization iterations, it was observed that a height difference of 1 mm minimized the magnetic field variations.

Table 1 Dimension of the magnet system

Assembly size/mm³	Magnet size/mm³	gap/mm
360(OD)×25(ID)×360(H)	190(OD)×35(ID)×75(H)	15

Table 2 Magnetic field simulation results

Field strength [T]	Field uniformity [ppm]	ΔBz [G]
0.4167	19	0.6

Figure 2 presents the uniformity results of the radial magnetic field through magnetic analysis. Figure 3 represents the intensity of the vertical magnetic field.
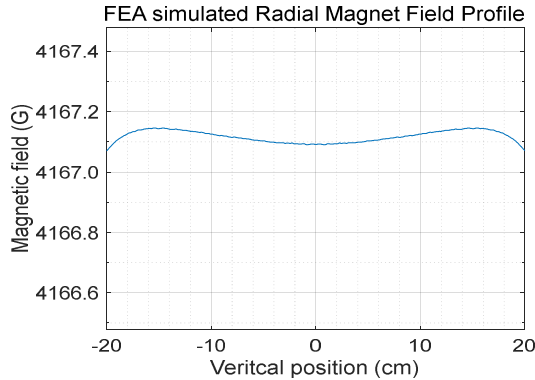
Figure 2. Radial magnetic field according to vertical position
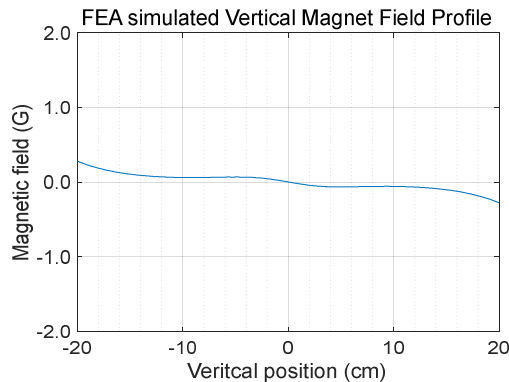
Figure 3. Vertical magnetic field according to vertical position

4. Manufactured magnet system

Based on the final design, the actual fabrication of the magnet was performed. The magnet has a total height of 360 mm and a diameter of 360 mm. There are 9 holes on the upper and lower parts, serving as optical paths for the laser interferometer to measure the motion of the coil and for the suspension of the coil to be inserted later. The entire upper yoke of the coil can be separated. For repetitive assembly and disassembly, guide pins are incorporated. Figure 4 shows manufactured magnet system.
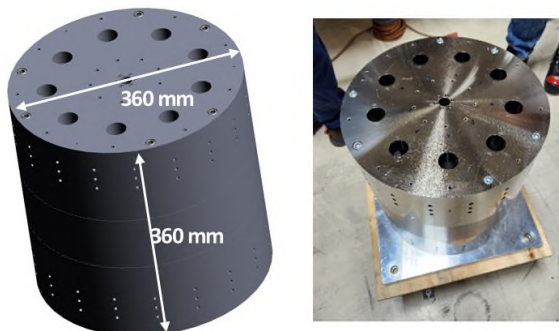
Figure 4. Modeling and manufactured magnet system

5. Magnetic field measurement

The magnetic field of the final polished magnet is measured, and its uniformity is analyzed. The uniformity of the magnetic field is the foremost performance goal in this fabrication. The uniformity measurement is also conducted through the 9 holes, where the average magnetic field values are measured by moving vertically based on the average values in a single plane. The figure below depicts the resulting values.
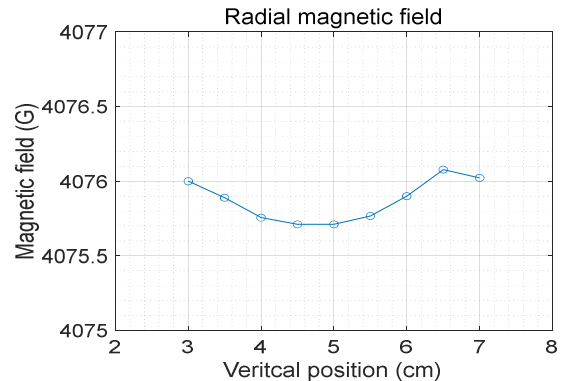
Figure 5. Measured uniformity of the magnetic field

The uniformity of the magnetic field measurement results shows ±45 ppm within a 40 mm range. This performance meets the initial goal and represents a world-class level of uniformity.

6. Conclusion

A magnet system design was undertaken for the KRISS KB-2. Design objectives were established, and parameters influencing performance were identified. Optimal values were determined through parameter analysis. The yoke height was optimized to minimize variations in the vertical magnetic field. In the specified region, achieving a magnetic field uniformity of less than 20 ppm and a magnetic field strength of approximately 0.4 T or higher, the design goals have been successfully met. Based on this, actual fabrication was carried out, and real magnetic field measurements were also conducted. As a result, a magnet system with outstanding uniformity of approximately ±45 ppm has been successfully implemented, and this will be utilized for the KRISS Kibble balance II.

References

[1] I. A. Robinson, "Towards the redefinition of the kilogram: a measurement of the Planck constant using the NPL Mark II watt balance", *Metrologia* **49**, 113–56, 2012.
[2] M.Kim et al, "Design of Magnet System for the KRISS Kibble Balance II", *2022 Conference on Precision Electromagnetic Measurements (CPEM)*, 2022.
[3] Rafael R. Marangoni et al, "Magnet system for the Quantum Electro-Mechanical Metrology Suite", *IEEE Transactions on Instrumentation and Measurement*, **69**, 5736-5744, 2020.
[4] Shisong Li, Michael Stock and Stephan Schlamminger "A new magnet design for future Kibble balances", *Metrologia* **55**, 319–325, 2018.
[5] Q. You, J. Xu, Z. Li, and S. Li, "Designing model and optimization of the permanent magnet for joule balance NIM-2," IEEE Trans. Instrum. Meas., vol. **66**, no. 6, pp. 1289 – 1296, June 2017.

Detecting microscale impurities on additive surfaces using light scattering

Ahmet Koca[1], Helia Hooshmand[1], Mingyu Liu[2], Richard Leach[1]

[1]*Manufacturing Metrology Team, Faculty of Engineering, University of Nottingham, Nottingham, UK*
[2]*School of Engineering, University of Lincoln, Lincoln, UK*

Ahmet.Koca@nottingham.ac.uk

Abstract

Additive manufacturing (AM) is a fast-growing method that allows the production of complex geometries by reducing the need for traditional cutting tools and fixtures. A common metal AM technique, known as laser-based powder bed fusion (PBF-LB), uses laser beams to melt and fuse powder layer-by-layer into 3D parts. Despite efforts to improve the process, achieving consistency and reliability in PBF-LB remains a challenge, necessitating the development of comprehensive quality assessment systems tailored to PBF-LB. Microscale impurities that are formed on individual layers can significantly impact the overall part quality, and are the most common features across various materials. Hence, there is a need to establish a measurement system for their detection to create a quality assessment method for PBF-LB. This research introduces a light scattering technique designed for the detection of microscale surface impurities on PBF-LB components. Following the design of the experimental setup, a corresponding scattering simulation model, which is based on the Beckman-Kirchhoff approximation, has been developed to simulate the experimental conditions. This simulation model can be utilised for future use in generating scattering data faster and simpler than through experimentation. The paper presents preliminary results of both the experimental setup and simulation model. Our findings affirm that the proposed methodology, utilising both experimental and simulated approaches, can be used to detect microscale surface impurities. This advancement contributes to the establishment of a quality inspection system for the overall part assessment of PBF-LB.

Keywords: Laser-based powder bed fusion, light scattering, surface impurity detection

1. Introduction

Additive manufacturing (AM) is the method of building three-dimensional (3D) components by depositing materials such as metals, polymers and ceramics in a layer-by-layer fashion [1]. Among metal AM techniques, laser-based powder bed fusion (PBF-LB) stands out as the most widely used and developed technique [2]. It employs a high-power laser source to selectively melt and fuse layers of powdered material based on the geometric specifications of the parts.

Despite advancements in PBF-LB, determining the optimal process parameters for a specific material and geometry remains challenging due to insufficient stability, robustness and repeatability in the manufacturing processes [3]. This challenge can result in anomalies, defects and non-uniformities during fabrication, emphasising the need to assess fabrication quality to ensure product quality.

The assessment of PBF-LB fabrication quality can be achieved through measurement and monitoring methods utilising in-situ and ex-situ approaches [4]. This paper proposes an ex-situ inspection method, which holds potential applicability as an in-situ approach with further improvements, within both experimental and simulation frameworks.

The proposed approach utilises a light scattering technique for the detection of microscale surface impurities that may detrimentally impact the overall quality of the fabricated part. This method offers notable advantages, such as a rapid processing speed and the capability to detect impurities smaller than 100 µm in our case. Although the simulation model will be further utilised in subsequent research, this paper presents the outcomes of both approaches and validates their alignment.

In section 2, the experimental setup and simulation model to obtain the scattering pattern are detailed. Section 3 then presents the outcomes obtained through these methodologies. Section 4 provides a summary of the paper and the future work.

2. Methods

In this work, the surface is illuminated with a laser light source, and the resulting scattered light generates a distinct scattering pattern on a plane/screen. The surface topography determines the angle of the scattered light, and as a consequence, the scattering pattern contains information about surface topography, enabling impurity detection and surface quality evaluation [5].

The experimental setup (Figure 1) used in this study includes a diode laser with a central wavelength of 635 nm to illuminate the surface. The beam diameter of the laser source was reduced from the initial size of 1.1 mm to around 90 µm by a converging lens (with a focal length of 75 mm and a diameter of 50.8 mm) to enhance the detection capability of microscale impurities. The scattered light projected onto a screen is recorded by a digital single-lens reflex camera (with a field of view of (160 × 106) cm and a (6000 × 4000) pixels sensor). A microscopy system is used to confirm the illuminated area. Figure 2 a) and b) display microscopy images highlighting circular areas depicting illuminated regions with and without impurities, respectively.
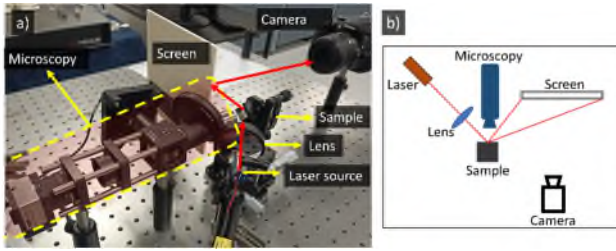
Figure 1. a) Experimental setup of the light scattering technique and its b) schema.

For simulation of the experimental results, the Beckman-Kirchhoff theory of scattering [6] is employed. The simulation model reproduces the scattering patterns from the surface topographies obtained by a surface topography measuring instrument based on the coherence scanning interferometry (CSI) technique (Zygo Nexview NX2). The measured surface topographies cover an area of approximately (90 × 90) μm. Figure 2 c) and d) showcase examples of surface topographies of the PBF-LB surfaces with and without impurities, respectively. The PBF-LB parts examined in this study were produced from titanium alloy powder using a Renishaw 500Q machine.
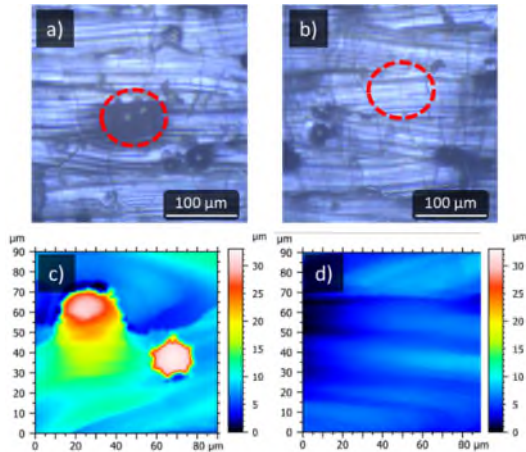
Figure 2. Example microscopy images of the PBF–LB surface a) with and b) without surface impurities. Example surface topographies of the PBF-LB surface c) with and d) without surface impurities obtained by the CSI instrument.

3. Results

Figure 3 and 4 present randomly selected scattering patterns derived from surfaces with and without impurities. Each figure displays two rows, with the top row showing experimentally acquired scattering images, and the bottom row presenting simulated scattering images. The images in Figure 3 demonstrate that surfaces with impurities produce randomly distributed scattered light patterns, whereas those in Figure 4 show that surfaces without impurities generate curved-like scattered light patterns. The observed distinction in scattering patterns produced by surfaces with and without impurities can be used for detecting such impurities, thereby affirming its potential utility in assessing surface quality.

4. Conclusion

In summary, this paper proposes a light scattering method within an experimental and simulation framework to detect microscale surface impurities. Surfaces containing impurities produce similar scattering patterns, as do surfaces without impurities. However, there are notable distinctions in the scattering patterns of surfaces with and without impurities. This indicates that the proposed method is applicable for detecting micrometre-scale surface impurities, allowing for the assessment of the quality of components produced by PBF-LB.
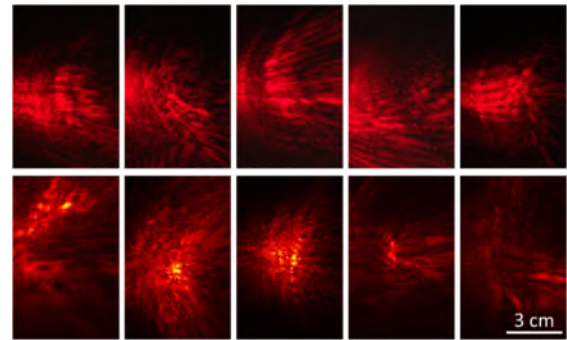
Figure 3. Scattering patterns of surfaces with impurities from the experimental (top) and simulation (bottom) models.
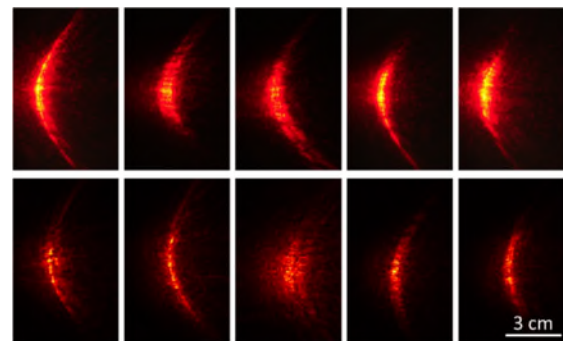
Figure 4. Scattering patterns of surfaces without impurities from the experimental (top) and simulation (bottom) models.

For future work, our plan involves training a machine learning algorithm to detect impurities from scattering images. The training process requires a substantial dataset, and the collection of a large volume of experimental data may prove challenging and time-consuming. Therefore, the simulation model emerges as a viable alternative, allowing for the generation of ample data in a more efficient and expeditious manner compared to the experimental setup.

Acknowledgement

References

[1] Gibson I, Rosen D, Stucker B 2015 Additive *Manufacturing Technologies: 3D printing, Rapid Prototyping, and Direct Digital Manufacturing* (Springer New York)
[2] Leach R K, Carmignato S 2020 *Precision Metal Additive Manufacturing* (CRC Press New York)
[3] Everton S K, Hirsch M, Stavroulakis P I, Leach R K, Clare A T 2016 Review of in-situ process monitoring and in-situ metrology for metal additive manufacturing *Mater. Des.* **95** 431–445
[4] Grasso M, Remani A, Dickins A, Colosimo B M, Leach R K 2021 In-situ measurement and monitoring methods for metal powder bed fusion: An updated review *Meas. Sci. Technol.* **32** 112001
[5] Liu M, Senin N, Su R, Leach R K 2022 Measurement of laser powder bed fusion surfaces with light scattering and unsupervised machine learning *Meas. Sci. Technol.* **33** (7)
[6] Su R, Coupland J, Sheppard C, Leach R K 2021 Scattering and three-dimensional imaging in surface topography measuring interference microscopy *J. Opt. Soc. Am. A* **38** A27–A42

Simulation-based approach on relative intensity effect in multi material X-Ray computed tomography evaluation

D. Gallardo[1], L.C Díaz-Pérez[1], J.A. Albajez[1], J.A. Yagüe-Fabra[1]

[1]I3A, Universidad de Zaragoza, Zaragoza, Spain

dgallardo@unizar.es

Abstract

Evaluation of multi material parts by means of X-ray computed tomography (XCT) remains as a challenge in terms of dimensional measurements. Several factors (differences in material density, gap between parts, etc.) may affect the characterisation of an assembly, creating the need of an adjustment in the XCT settings to reduce artifacts. A key parameter is the relative intensity (I/I_0) registered in the detector, which is an indicator of the attenuation of the X-rays. In this paper, a metrological study of the effects of the variation in the I/I_0 registered is presented. A simulation-based experiment is conducted with a metal-polymer test object, using the thickness of the outer part as a variable to modify this I/I_0 value. Results confirm a correlation between dimensional accuracy on polymeric features and higher I/I_0 values, as well as in the contrast-to-noise ratio (CNR); however, significant differences are found between scenarios with similar I/I_0 values but different metals, indicating that results could not be automatically extrapolated.

Keywords: X-ray computed tomography, Multi material, Simulation.

1. Introduction

The use of X-ray computed tomography (XCT) in metrology for the evaluation of industrial parts has increased recently due to its ability to non-destructively characterize both inner and outer geometries. It is able to measure macro and micro geometries, being an innovative technique for dimensional metrology [1].

However, as a new technology in industry, it still has several limitations. XCT is based on the X-ray penetration of the object, producing a grayscale histogram that varies depending on the beam intensity received by the detector. X-ray attenuation is directly related to the density of the material, so settings should be adjusted for each part [2]. In case of multi material parts, it could result in defects, such as noise and artifacts, consequently creating measurement errors. This becomes more evident if the difference in density between materials is elevated.

Here, an important indicator to consider is the relative intensity (I/I_0) between the beam emitted and received by the detector. This coefficient is directly related to the energy of the beam source [3], the penetration length and the attenuation coefficient of the material. Theoretically, the lower the relative intensity that reaches the detector, the poorer is the quality of the tomography and, hence, more defects will appear.

In this paper, a preliminary study of the effects of I/I_0 variation in a multi material test object is presented. An ad hoc artefact is designed, including a polymeric low-density measurand and outer metallic hollow cylinders made by aluminium (Al) and steel (St) with different thicknesses to create a range of I/I_0 values. XCT simulations have been performed, evaluating dimensional characteristics and contrast-to-noise ratio of the tomographies.

2. Design and methodology

2.1. Attenuation curve

First step has been to calculate the attenuation curve for the materials selected for the experiment, Al and St (Figure 1). Attenuation can be described by Beer-Lambert law [3] in Eq.1:

$$I(x) = I_0 \cdot e^{-\mu x} \quad (1)$$

Where I = intensity received by the detector, I_0 = intensity emitted and μ = linear attenuation coefficient of the material.
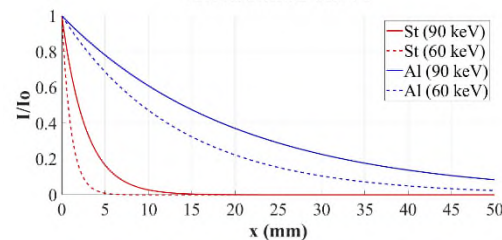
Figure 1. Attenuation curve for X-ray beams of different energies.

Curve is different depending on the average energy (E_{av}) obtained from the characteristic energy spectrum of the tube. Spectrums have been obtained using software SPEKTR 3.0 [4].

2.2. Test object

To conduct the experiment, an ad hoc test object has been designed. It consists in an outer metallic hollow cylinder and an inner polymeric part, with 4 polymeric cylinders (nominal diameters of Ø12 mm, distances between cylinders of 12 mm) for dimensional evaluation. Rest of dimensions of relevant features are shown in Figure 2.
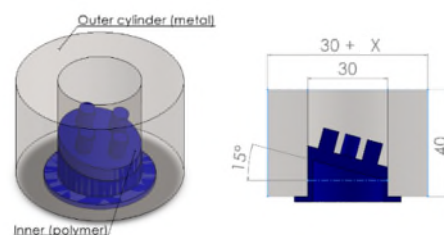
Figure 2. General assembly (left), relevant dimensions (right)

Outer diameter of the metallic cylinder is modified for each scenario, considering its thickness as the variable to calculate

I/I_0 (Figure 1). The target has been to obtain values of $I/I_0 \approx 0.50 - 0.08$. Ranges used in the experiment are shown in Table 1.

Table 1. Penetration length and relative intensity for each material.

Material	X [mm]	I/I_0
Aluminium	10 - 40	0.472 - 0.093
Steel	2 - 8	0.471 - 0.081

2.3. Simulations and evaluation

XCT simulations have been performed by software aRTist 2.12 (BAM, Germany). One simulation has been done for each scenario, including the case with no metal. Settings have been optimized for each scenario, aiming for the most uniform configuration in terms of voltage and physical filter. Post processing has been done by software VG Studio Max 3.4.2, extracting contrast-to-noise ratio (CNR) by gray value difference between material and background [5] and a dimensional evaluation of the cylinders. CNR is relevant as an indicator of the quality of the image: better contrast in tomographies of the same part is correlated with lower noise. Regions of interest (ROI) have been created for each material for proper CNR study.

3. Results

3.1. CNR comparison

In Figure 3, the relationship between CNR and I/I_0 for each scenario (Al-St) and each ROI (metal/polymer) is shown.
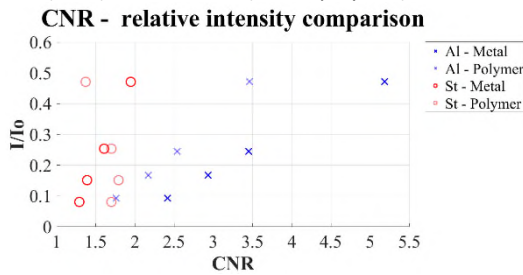
Figure 3. CNR comparison for each scenario and each ROI.

Although in general CNR increases for cases with higher relative intensity, it is shown that trend is not always followed and values do not agree for Al and St scenarios with same I/I_0. An XCT slice from scenarios with similar I/I_0 is shown in Figure 4 and their gray values histogram is shown in Figure 5.
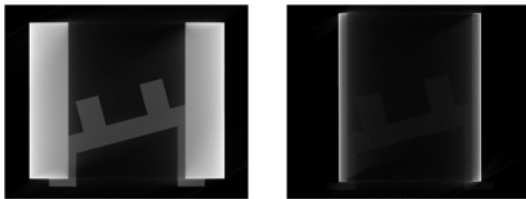
Figure 4. XCT 2D slices. Al 20 mm (left), St 4 mm (right).
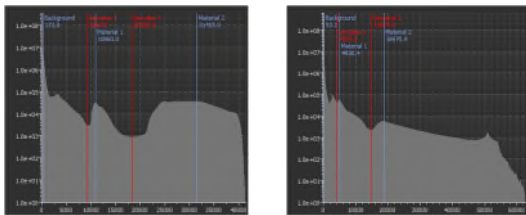
Figure 5. Gray values histograms. Al 20 mm (left), St 2 mm (right).

3.2. Dimensional measurements

Diameters, form error and distances between elements have been extracted from the cylinders. Absolute form error of the cylinders for each scenario is shown in Figure 6.
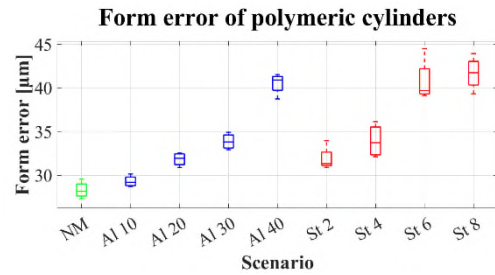
Figure 6. Absolute form error of polymeric cylinders for each scenario.

A trend is followed for both Al and St scenarios, obtaining higher form errors in scenarios with lower I/I_0 values; however, Al results are more stable (less standard deviation) and closer to no metal (NM) scenario. In Table 2, diameter and distances mean deviations from NM values are shown.

Table 2. Mean deviation in same-material scenarios from NoMetal XCT.

Material	Diameters [μm]	Distances [μm]
Aluminium	3.25	0.19
Steel	-3.81	-9.69

Significant differences have been found between Al and St scenarios. Noise present in St tomographies difficult a proper characterization of the cylinders, modifying the points extracted and consequently the diameter and the central axis. This becomes more evident in the higher deviation in distances.

4. Conclusions and future work

A simulation-based analysis of the effect caused by variations of relative intensity in metal-polymers assemblies is presented. Experiments show that results obtained in different metals could not be extrapolated. Trends are followed in most cases, as CNR values and dimensional measurements improve as I/I_0 increases; however, higher deviations are shown in steel scenarios, where also CNR values are significantly lower than Al scenarios with same I/I_0, suggesting that this parameter cannot be considered alone as an indicator. As results are only extracted from virtual simulations, future work should focus on obtaining experimental results from real XCT measurements to validate the simulations and corroborate the hypothesis here presented.

References

[1] Villarraga-Gómez H, Herazo E, and Smith S 2019 X-ray computed tomography: from medical imaging to dimensional metrology *Precis. Eng.* **60** 544–569

[2] Schmitt R H, Buratti A, Grozmani N, Voigtmann C and Peterek M 2018 Model-based optimisation of CT imaging parameters for dimensional measurements on multimaterial workpieces *CIRP Annals* **67**(1) 527–530

[3] Villarraga-Gómez H, Körner L, Leach R and Smith ST 2020 Amplitude-wavelength maps for X-ray computed tomography systems. *Precis Eng.* **64** 228–42.

[4] Punnoose J, Xu J, Sisniega A, Zbijewski W, Siewerdsen JH 2016 Technical Note: spektr 3.0-A computational tool for x-ray spectrum modeling and analysis. *Med Phys.* Aug **43**(8):4711.

[5] Kyuseok K and Youngjin L 2021 Improvement of signal and noise performance using single image super-resolution based on deep learning in single photon-emission computed tomography imaging system. *Nuclear Eng and Tech.* **53**(7) 2341-2347.

Enhancing single camera calibration results using artificial bee colony optimisation within a virtual environment

Mojtaba A. Khanesar[1], Luke Todhunter[1], Vijay Pawar[2], Hannah Corcoran[2] Lindsay MacDonald[2], Stuart Robson[2], Samanta Piano[1]

[1]_Faculty of Engineering, University of Nottingham, NG8 1BB, Nottingham, UK_
[2]_Faculty of Engineering Science, University College London, WC1E 6BT UK_

Mojtaba.ahmadiehkhanesar@nottingham.ac.uk

Abstract

Close range photogrammetry is among the top candidates for non-contact metrology in high precision applications. It is frequently used within industrial environments for high precision measurement, automation, and control tasks. When using off-the-shelf cameras for such applications it is necessary first to understand how image content influences the image measurements made and in turn what effects this has on estimating imaging geometry. A virtual environment involving camera and digital objects may be used for testing the efficacy of machine learning algorithms. In this paper, enhancement of a single pose camera calibration process utilising a virtual environment and images taken with different lighting directions is investigated. The algorithm used for enhancing the calibration process is Artificial Bee Colony (ABC), a metaheuristic optimisation method. Multiple single image camera orientations are tested in this paper resulting in different extrinsic camera parameters. From multiple tests using different camera orientations, we observe that it is possible to enhance the calibration efficacy in terms of reprojection error using artificial bee colony when compared to an established two step Levenberg Marquardt (LM).

Vision sensor, artificial bee colony, central perspective camera, calibration, virtual environment, Blender, MATLAB, metrology

1. Introduction

Non-contact vision-based metrology is the process of performing measurements without physically contacting the object using imaging sensors [10, 11]. A range of metrology equipment within this category is routinely utilised within aerospace industries, automotive industries, and manufacturing environments [10, 11]. Photogrammetry [12, 13] and structured light metrology [12, 13] are typical techniques of non-contact vision-based metrology. However, the usage of cameras for measurements introduces systematic errors due to practical lens and sensor designs having significant non-linear distortions from the ideal central perspective projection [14]. Camera lens distortions and network solutions for multi-camera imaging geometries have been studied over many years, but it is only more recently that surface illumination and reflectance variations over the surfaces to be measured.

Use of a virtual environment to implement and test vision sensors and algorithms for manufacturing purposes is highly desirable [1-3]. In such an environment, designs for system configurations, algorithms, and sensors can be tested with high precision before practical implementation. A key task within a virtual manufacturing environment is evaluating optical metrology sensor placement under varying illumination conditions in order to estimate performance. In the work described in this paper, we are evaluating virtual environments able to simulate a multi-illumination dome imaging system. The system uses a single camera to take a sequence of images of a surface. Each image in the sequence is taken under point source illumination from different lighting directions. The resulting image stack is then used to estimate a pixel-by-pixel normal map based on knowledge of the sensing and illumination geometry.

Blender software with its ability to represent optical surface properties and light paths has been used for vision process simulation in medical environments [4, 5], for electrical component identification [6], in manufacturing environments [7, 8], and for educational purposes [9]. Drawing on Blender's OpenCV functionality and MATLAB integration, camera geometry including position and orientation, and internal optical parameters representing optical distortions can be modelled as an integral part of the virtual environment.

In this paper, images of a checkerboard calibration pattern, often used with OpenCV, and MATLAB, and representing a planar surface to be measured are synthesised. The image geometry is based on a perspective camera model with point source illumination provided by each of 64 different lighting orientations. Different lighting conditions result in different images of the checkerboard squares. The geometric effect of these variations can be usefully investigated as part of the least squares network adjustment process to estimate discrepancies between ideal and measured image coordinate reprojection residuals.

In the MATLAB environment [6], the camera was first calibrated using a two-step Levenberg Marquardt (LM) algorithm [15]. The calibrated parameters were then enhanced to determine if improvements were possible using an artificial bee colony (ABC) approach. The performance improvement of the proposed approach over two-step LM method is investigated under different orientations for the camera. It is shown that using the ABC algorithm results in enhancement of the camera calibration performance in terms of reprojection error.

The paper is organised as follows. Camera parameters including intrinsic and extrinsic parameters are explained in Section II. The basic camera calibration procedure using a checkerboard calibration board is discussed in Section III. ABC algorithm for enhancing camera calibration is summarised in Section IV. Overall multi-illumination dome system setup is presented in Section V. Simulation results, and conclusion remarks are presented in Sections V, and VI, respectively. Acknowledgements are given in Section VII.

2. Camera model: intrinsic and extrinsic parameters

2D imaging is the projection process of the real world in 3D onto a 2D image. The position of the features within the 2D image depend upon their real-world position and also on the camera parameters [17, 18]. Within OpenCV, and MATLAB machine vision toolbox, the overall projection process is formulated as follows,

$$
\begin{bmatrix} p_u \\ p_v \\ 1 \end{bmatrix} = \underbrace{\underbrace{\begin{bmatrix} f_x & \theta & c_x \\ 0 & f_y & c_y \\ 0 & 0 & 1 \end{bmatrix}}_{\substack{intrinsic \\ matrix}} \underbrace{\begin{bmatrix} R_{xx} & R_{xy} & R_{xz} & T_x \\ R_{yx} & R_{yy} & R_{yz} & T_y \\ R_{zx} & R_{zy} & R_{zz} & T_z \end{bmatrix}_w}_{\substack{extrinsic \\ matrix}}}_{\substack{projection \\ matrix}} \begin{bmatrix} P_x \\ P_y \\ P_z \\ 1 \end{bmatrix}_w \quad (1)
$$

where (p_x, p_y, p_z) are the position coordinates of the point in real world, (p_u, p_v) are the corresponding coordinates of the point in the image in pixels, f_x and f_y are the camera intrinsic parameters such that $f_x = FS_x$, and $f_y = FS_y$, and $S_x(\frac{pixel}{mm})$, and $S_y(\frac{pixel}{mm})$ are the sensor's scale factors within x-coordinate, and y-coordinate, respectively. The parameter θ is the skew. The parameters $R_{ij}, i, j = x, y, z$ form the rotation matrix and $T_i, i = x, y, z$ form the translation matrix.

The radial distortion can be modelled as a polynomial function of the radius from the lens centre. The mathematical model of the distortion is as follows [19]:

$$
x_u = p_u\big(1 + k_2 r_d^2 + k_4 r_d^4 + \cdots\big)
$$
$$
y_u = p_v\big(1 + k_2 r_d^2 + k_4 r_d^4 + \cdots\big) \quad (2)
$$

where (x_u, y_u) are the coordinates of the points within the image as distorted by radial distortion function.

3. Camera calibration algorithms

The camera calibration application within MATLAB software [20] is used in this paper for calibration of the camera within Blender. The algorithm is summarised in this section. The assumptions are that:

1. the field of view for camera is no more than 95°.
2. the camera is modelled by a pinhole model.

To perform camera calibration identification, the following matrix equation is used within MATLAB:

$$
w \begin{bmatrix} p_u \\ p_v \\ 1 \end{bmatrix} = K[R \quad T] \begin{bmatrix} P_x \\ P_y \\ P_z \\ 1 \end{bmatrix}_w \quad (3)
$$

where w is an arbitrary scaling factor, the matrix K is the camera intrinsic matrix, R presents the rotation matrix, and T presents

the translation matrix. In the first step of the algorithm, the corners of squares within the calibrating checkerboard are identified using image processing methods. Using the identified corners of squares and realistic corners from real-world, intrinsic and extrinsic parameters are estimated assuming that there exists no distortion using the algorithm given in [15]. The algorithm uses the LM Algorithm [21] as implemented in `Minpack` to find the projection matrix as well as intrinsic and extrinsic matrixes [22]. In the next step, considering the initial values for the distortion parameters as equal to zero and the distortion model of (2), a LM algorithm is applied on the overall camera projection process including the distortion parameters to estimate the overall parameters [23, 24].

4. Enhancement using artificial bee colony

To enhance the calibration results in terms of reprojection error, a meta-heuristic optimisation algorithm of artificial bee colony (ABC) is used. The objective is to find the optimal deviation of camera parameters from the calculated values from 2-step LM algorithm [15]. To perform such an optimisation, a cost function is defined as the difference between the projected real-world points to the image coordinate and the detected points on the image. The ABC algorithm is used to find the optimal deviation of the parameters with respect to the calculated values from LM algorithm optimisation method over all calibration images. This procedure is performed by optimising the cost function associated with the reprojection error.

This ABC algorithm employs swarm based optimisation which imitates the honeybee foraging behavior[25]. The optimal solution to this algorithm is the high dimensional position of the food source. Pseudocode of the ABC algorithm is given as follows [25]:

1. randomly initialise population $x_i, i = 1, \ldots, SN$,
2. evaluate the population against the cost function,
3. the next few steps are repeated until convergence:
   a. a new set of calibration parameters is generated using the employed bee as $v_{ij} = x_{ij} + \varphi_{ij}(x_{ij} - x_{kj}), k \in 1, \ldots, SN, j \in 1, \ldots, D$, where $\varphi_{ij}\epsilon[0,1]$ is a uniform random number,
   b. the fitness function is evaluated for each solution $f(x_i)$ as the reprojection error between reprojection points from (3) using estimated camera parameters with the real points within the image.
   c. for each solution $f(x_i)$, its probability is given by:

$$
p_i = \frac{f(x_i)}{\sum_{i=1}^{SN} f(x_i)} \quad (4)
$$

   d. new solutions v_i for the onlooker bees are generated and evaluated from the solutions x_i selected depending on p_i,
   e. A greedy selection procedure is applied to select onlookers which ensures a new candidate is chosen based on its fitness compared to the current ones.
   f. Replace possible abandoned food sources with new food source using $x_{ij} = x_{i,min} + r_j(x_{i,max} - x_{i,min})$. The random parameter $r_j\epsilon[0,1]$ is a uniform random number.
   g. The overall best solution is updated by comparing the best solution in the iteration with the overall best solution.
   h. Terminate the algorithm if termination criteria are met, otherwise iterate the algorithm.

5. System Setup, image generation and processing

The imaging setup considered in this paper involves a fixed camera on the top of a dome, and 64 light sources located on the inside of the dome at fixed locations providing illumination geometry to take multiple images of the static object under the dome [26]. Figure 1 shows the CAD model of the system. Within this image, the position of the light sources is indicated by yellow, camera is positioned on top of the dome, and the dome with 1m radius is rendered in grey.
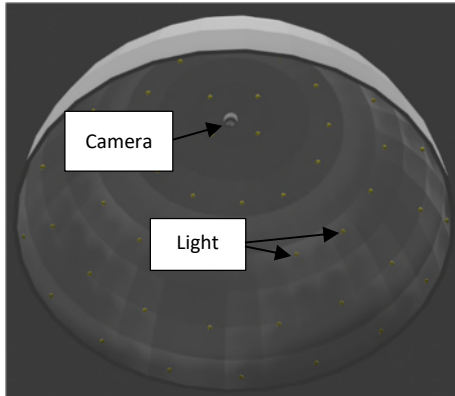
Figure 1. The CAD model corresponding to the dome, light sources, and camera on top.

To perform calibration, a checkerboard (Figure 2) is designed and imported into the Blender environment, centred in x-y plane. A camera is positioned 1 metre up the z-axis directly above the board with its Euler rotation angles being equal to (180, 0, -90). A total of 64 different light sources with beam angle of 15 degrees are used within this simulation environment, each facing towards the centre of the checkerboard. The light sources are turned on sequentially and synchronised with the camera shutter, resulting in 64 different images. Groups of images and real-world checkerboard corners are processed first with the 2-step LM method and then utilising the output extrinsic and intrinsic parameters as starting values with the ABC method.

6. Simulation results

A sample result from the calibration when the camera Euler rotation angle around axis is [-179.9141, 0.1432, -118.0724] is depicted in Figure 3. As can be seen, the reprojected points are very close to the originally detected square corners within the image. Reprojection errors in terms of pixel error values are shown in Figure 4. It is observed that the reprojection errors for the enhanced calibration using ABC algorithm are an order of magnitude smaller than those for the 2-step LM method. Table 1 presents the calibration results for 20 different camera orientations around the perpendicular downward direction. For each camera calibration, statistical results are given for 2-step LM algorithm and its enhanced version using ABC in terms of reprojection errors. As can be seen from this table, by using ABC algorithm the mean reprojection error decreases by 66.1% in comparison with 2-step LM method. Figure 5 presents the reprojection error versus orientation of the light sources in polar coordinates when camera Euler angle is equal to [-179.9141, 0.1432, -118.0724]. These figures clearly demonstrate that the calibration error using ABC algorithm is enhanced for images taken with light sources in most angles. Finally, the convergence graph for the ABC optimisation algorithm for the camera Euler angle is equal to [-179.9141, 0.1432, -118.0724] is illustrated in Fig. 6. This graph shows that the optimisation algorithm converges after more than 80 iterations.

Table 1 Reprojection error values

	Mean reprojection error (pixels)	Standard deviation of reprojection error (pixels)
Reprojection error values for checkerboard (pixels)	0.046	0.0712
Reprojection error values after ABC enhancement (pixels)	0.0156	0. 0178
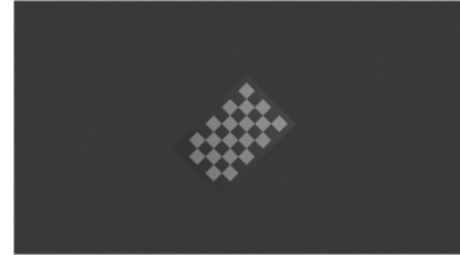
Figure 2. Sample checkerboard calibration image.

Figure 3. Detected points versus reprojected points from enhanced calibration using ABC.
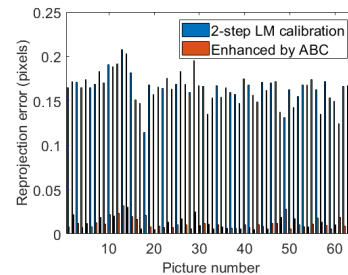
Figure 4. Reprojection error obtained from checkerboard calibration.
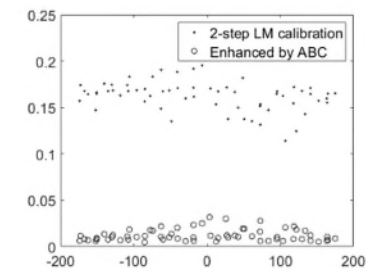
Figure 5. reprojection error values as a function of θ.
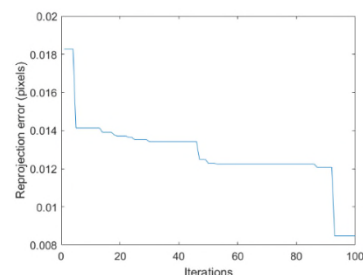
Figure 6. The convergence graph for ABC optimization algorithm.

7. Conclusions

In this paper, the Blender environment is used to make some initial vision simulation tests for an experimental imaging system. The work is part of an initial study to evaluate the metrology potential for simulating light sources, light surface interaction and camera geometry within a wider environment which might contain multiple objects with their reflections and occlusions. The basic simulation created in this software includes a camera mounted on top of a checkerboard and 64 light sources with 15 degrees beam angle facing towards the centre of the checkerboard. These light sources are turned on sequentially resulting in 64 different images of the checkerboard from a single camera pose. A cost function based on the mean reprojection error for the images is defined to optimise the camera parameters. ABC enhancement is shown to be an effective enhancement to a two-step LM algorithm calibration method. To show the effectiveness of this optimisation method, 20 different random camera orientations are used for calibration purposes. Comparison between the reprojected image from the image to the real world with and without enhancement are presented. Whilst these simulation results are limited to a single camera view, it is concluded that the ABC optimisation algorithm is worth pursing further to evaluate its effectiveness in both virtual and practical camera systems designed for non-contact metrology tasks.

Exploration of the camera pose and calibration determination within the virtual Blender environment has highlighted the value of further exploration for surface metrology applications. Further work will seek to better understand how such environments can support decisions on camera selection, machine learning method selection and implementation across different optical surfaces and geometries.

Acknowledgment

References

[1] T. H.-J. Uhlemann, C. Lehmann, and R. Steinhilper, "The digital twin: Realizing the cyber-physical production system for industry 4.0," *Procedia Cirp,* vol. 61, pp. 335-340, 2017.

[2] M. Ericsson, X. Zhang, and A.-K. Christiansson, "Virtual commissioning of machine vision applications in aero engine manufacturing," in *2018 15th International Conference on Control, Automation, Robotics and Vision (ICARCV)*, 2018: IEEE, pp. 1947-1952.

[3] J. Nilsson, M. Ericsson, and F. Danielsson, "Virtual machine vision in computer aided robotics," in *2009 IEEE Conference on Emerging Technologies & Factory Automation*, 2009: IEEE, pp. 1-8.

[4] J. Cartucho, S. Tukra, Y. Li, D. S. Elson, and S. Giannarou, "VisionBlender: a tool to efficiently generate computer vision datasets for robotic surgery," *Computer Methods in Biomechanics and Biomedical Engineering: Imaging & Visualization,* vol. 9, no. 4, pp. 331-338, 2021.

[5] A. Munawar *et al.*, "Virtual reality for synergistic surgical training and data generation," *Computer Methods in Biomechanics and Biomedical Engineering: Imaging & Visualization,* vol. 10, no. 4, pp. 366-374, 2022.

[6] C. Wu *et al.*, "MotorFactory: A Blender Add-on for Large Dataset Generation of Small Electric Motors," *Procedia CIRP,* vol. 106, pp. 138-143, 2022.

[7] H. B. Lisboa, L. A. R. de Oliveira Santos, E. R. Miyashiro, K. J. Sugawara, P. E. Miyagi, and F. Junqueira, "3D virtual environments for manufacturing automation," in *22nd International Congress of Mechanical Engineering (COBEM 2013), University of São Paulo, Brazil November*, 2013, pp. 3-7.

[8] W. S. Harrison III and F. Proctor, "Virtual fusion: state of the art in component simulation/emulation for manufacturing," *Procedia Manufacturing,* vol. 1, pp. 110-121, 2015.

[9] M. Matys, M. Krajčovič, G. Gabajová, B. Furmannová, and P. Bubeník, "Integration of Virtual Reality into Teaching Process for Design of Manufacturing Systems," in *INTED2021 Proceedings*, 2021: IATED, pp. 190-198.

[10] M. A. Khanesar, M. Yan, M. Isa, S. Piano, and D. T. Branson, "Precision Denavit–Hartenberg Parameter Calibration for Industrial Robots Using a Laser Tracker System and Intelligent Optimization Approaches," *Sensors,* vol. 23, no. 12, p. 5368, 2023.

[11] S. Catalucci, A. Thompson, S. Piano, D. T. Branson III, and R. Leach, "Optical metrology for digital manufacturing: a review," *The International Journal of Advanced Manufacturing Technology,* vol. 120, no. 7-8, pp. 4271-4290, 2022.

[12] S. Catalucci, N. Senin, D. Sims-Waterhouse, S. Ziegelmeier, S. Piano, and R. Leach, "Measurement of complex freeform additively manufactured parts by structured light and photogrammetry," *Measurement,* vol. 164, p. 108081, 2020.

[13] A. Thompson *et al.*, "A single-click automated metrology demonstrator."

[14] R. Swaninathan, M. D. Grossberg, and S. K. Nayar, "A perspective on distortions," in *2003 IEEE Computer Society Conference on Computer Vision and Pattern Recognition, 2003. Proceedings.*, 2003, vol. 2: IEEE, pp. II-594.

[15] Z. Zhang, "A flexible new technique for camera calibration," *IEEE Transactions on pattern analysis and machine intelligence,* vol. 22, no. 11, pp. 1330-1334, 2000.

[16] F. Itami and T. Yamazaki, "An improved method for the calibration of a 2-D LiDAR with respect to a camera by using a checkerboard target," *IEEE Sensors Journal,* vol. 20, no. 14, pp. 7906-7917, 2020.

[17] F. Bottalico, C. Niezrecki, K. Jerath, Y. Luo, and A. Sabato, "Sensor-Based Calibration of Camera's Extrinsic Parameters for Stereophotogrammetry," *IEEE Sensors Journal,* vol. 23, no. 7, pp. 7776-7785, 2023.

[18] P. Sturm, "Pinhole Camera Model," in *Computer Vision: A Reference Guide*, K. Ikeuchi, Ed. Boston, MA: Springer US, 2014, pp. 610-613.

[19] I. Enebuse, M. Foo, B. S. K. K. Ibrahim, H. Ahmed, F. Supmak, and O. S. Eyobu, "A comparative review of hand-eye calibration techniques for vision guided robots," *IEEE Access,* vol. 9, pp. 113143-113155, 2021.

[20] (25/1/2024). *Camera calibration - Matlab R2023* [Online]. Available: https://uk.mathworks.com/help/vision/camera-calibration.html.

[21] M. A. Khanesar, E. Kayacan, M. Teshnehlab, and O. Kaynak, "Levenberg marquardt algorithm for the training of type-2 fuzzy neuro systems with a novel type-2 fuzzy membership function," in *2011 IEEE symposium on advances in type-2 fuzzy logic systems (T2FUZZ)*, 2011: IEEE, pp. 88-93.

[22] J. J. Moré, "The Levenberg-Marquardt algorithm: implementation and theory," in *Numerical analysis: proceedings of the biennial Conference held at Dundee, June 28–July 1, 1977*, 2006: Springer, pp. 105-116.

[23] J. Heikkila and O. Silvén, "A four-step camera calibration procedure with implicit image correction," in *Proceedings of IEEE computer society conference on computer vision and pattern recognition*, 1997: IEEE, pp. 1106-1112.

[24] G. Bradski and A. Kaehler, *Learning OpenCV: Computer vision with the OpenCV library.* " O'Reilly Media, Inc.", 2008.

[25] D. Karaboga, B. Gorkemli, C. Ozturk, and N. Karaboga, "A comprehensive survey: artificial bee colony (ABC) algorithm and applications," *Artificial Intelligence Review,* vol. 42, no. 1, pp. 21-57, 2014.

[26] L. W. MacDonald, A. H. Ahmadabadian, and S. Robson, "Determining the coordinates of lamps in an illumination dome," in *Videometrics, Range Imaging, and Applications XIII*, 2015, vol. 9528: SPIE, pp. 156-167.

Stereo camera calibration with fluorescent spherical marker and laser interferometer

Kenji Terabayashi[1], Kazuya Ogasawara[2], Yuuki Hamamoto[2], Takaaki Oiwa[2], Tohru Sasaki[1]

[1]Graduate School of Science and Engineering, University of Toyama
[2]Department of Mechanical Engineering, Shizuoka University

tera@eng.u-toyama.ac.jp

Abstract

Stereo vision is an image measurement system that acquire three-dimensional information of a target without contact. One of the most important applications of stereo vision is a motion capture system measuring three-dimensional positions of multiple moving targets. In this presentation, we propose a calibrator with fluorescent spherical marker and laser interferometer for improving accuracy of stereo vision system. In conventional calibration of stereo camera, check pattern on a plane is usually used as a calibrator. The conventional calibrator has relative accuracy of about 10^{-3} to its size and can be detected in a captured image with accuracy of about 0.1 pixels. In contrast, the proposed calibrator has relative accuracy of about 10^{-6} and can be detected in a captured image with accuracy of about 0.001 pixels. In displacement measurement of 180 mm with fluorescent spherical marker as a measuring target, RMSE of the proposed and conventional methods were 1.57 μm and 232.84 μm respectively. The standard deviation of both methods was 0.45 μm. These results show the proposed method improved trueness of stereo vision system about 100 times higher than the conventional one.

Fluorescence, Spherical Marker, Calibration, Stereo Camera

1. Introduction

Stereo camera systems are calibrated with geometrical information obtained from a calibrator. The most famous calibrator is two-dimensional grid pattern on a plane like a chessboard [1-4]. In this calibrator, control points are expressed as corner points [1, 2] or circle centers [3, 4] and can be detected in a captured images with about 0.1 pixel precision. Relative shape accuracy of this calibrator to its size is about 10^{-3}.

A sphere is used as three-dimensional stereo vision calibrator [5, 6]. Retroreflective spherical markers are widely used in a motion capture system and are installed on a calibrator. This marker can be detected in a captured images with about 0.01 pixel precision [6, 7]. Fluorescent spherical markers can be detected more precisely than the retroreflective ones [8, 9].

In this paper, we propose a stereo vision calibration with fluorescent spherical marker and laser interferometer for high-accuracy image measurements. The proposed method improves the camera parameters obtained from a conventional calibration method.

2. Stereo camera calibration

2.1. Fluorescent spherical marker

Fluorescent spherical markers are optical ones for precise image measurement [8, 9]. Precision of the marker detection is about 0.001 pixels, which is milli-pixel marker detection. This marker has a potential of improving stereo camera calibration.

Fluorescent spherical markers excited by a UV light are captured by a camera with UV-cut filter. This leads to high contrast between the marker and background in the captured image. Image edges on the high contrast contour can be detected precisely. The position of this marker is calculated as a center of the circle fitting to the edges [8, 9].

2.2. Calibrator with fluorescent spherical marker and laser interferometer

In this paper, we propose a calibrator for stereo camera calibration with a fluorescent spherical marker and laser interferometer as shown in Figure 1. The fluorescent spherical marker is installed on a moving stage and captured by a stereo camera system for calibration. Relative accuracy of displacement measurement by the laser interferometer is about 10^{-6}.

Displacement of the marker is measured by both of the stereo camera system and the laser interferometer. Parameters of the stereo camera system are estimated as minimizing the difference between these measured displacements by Levenberg-Marquardt algorithm:

$$\boldsymbol{p}^* = \underset{\boldsymbol{p}}{\arg\min} \sum_{i=1}^{n} \left(x_{\mathrm{C},i}(\boldsymbol{p}) - x_{\mathrm{L},i} \right)^2,$$

where $\boldsymbol{p}$ is the vector of camera parameters which are same as described in [1], x_{C} is measured displacement by the stereo camera, x_{L} is measured displacement by the laser interferometer, and n is the number of calibration data.
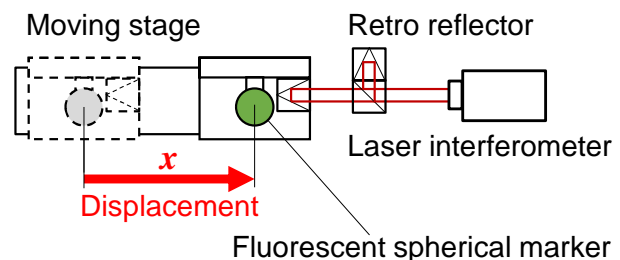
Figure 1. Proposed calibrator with fluorescent spherical marker and laser interferometer.

2.3. Calibration procedure

The proposed calibration method consists of two-step calibrations. The first step is conventional calibration using grid-pattern calibrator [1], which is pre-calibration. The second step is calibration with the proposed calibrator.

The purpose of the second step is to improve the camera parameters. In the calculation of the second step, camera parameters estimated in the first step are used as a initial values in optimization of the second step.

3. Displacement measurement by calibrated stereo vision

Accuracy of calibrated stereo camera system was evaluated in displacement measurement as shown in Figure 2. Measurement error was calculated by subtracting displacement measured by a laser interferometer from one measured by the camera system. Measured errors were compared between conventional (1-step) and proposed (2-step) calibrations.

3.1. Experimental equipment

Two cameras of AVT Prosilica GX6600 with lens of AI AF Nikkor 50mm f/1.8D were placed on a vibration-isolated table. The optical axes were parallel, and the baseline was 125 mm.

A fluorescent spherical marker of 25.4 mm diameter was installed on a moving stage. Distance between the moving axis and optical centers of the camera system was 800 mm.

UV-ring lights were placed in front of the camera system. The peak wavelength of the lights was 375 nm. The fluorescent spherical marker was excited by the lights and captured by the camera system with UV-cut filter of 410 nm cut-off wavelengths.

A laser interferometer of Renishaw XL-80 measured displacement of the moving marker as ground truth.

3.2. Stereo camera calibration

As the first step calibration, the stereo camera system was calibrated by conventional method [1] with grid pattern shown in Figure 3. The number of stereo image pairs for this calibration was 20. Estimated camera parameters were used as the initial values in optimization calculation of the second step calibration.

In the second step calibration, the fluorescent spherical marker was moved 180 mm in 20 mm steps. At the each position, the marker was captured 30 times by the stereo camera system as calibration data.

3.3. Displacement measurement

The fluorescent spherical marker was moved 200 mm in 20 mm steps. At each position, the marker was captured 5 times by the stereo camera system as evaluation data.

Figure 4 shows the comparison of measurement error between conventional (1-step) and proposed (2-step) calibrations. The proposed calibration reduced the RMS error of measured displacement by more than 99%. Relative accuracy and precision of the proposed method was 7.9×10^{-6} and 2.3×10^{-6}, respectively.

4. Conclusion

This paper proposes a stereo calibration method with fluorescent spherical marker and laser interferometer. In displacement measurement of 200 mm, RMS error of displacement measured by calibrated stereo camera system was reduced by more than 99% compared with conventional calibration method.

Acknowledgment
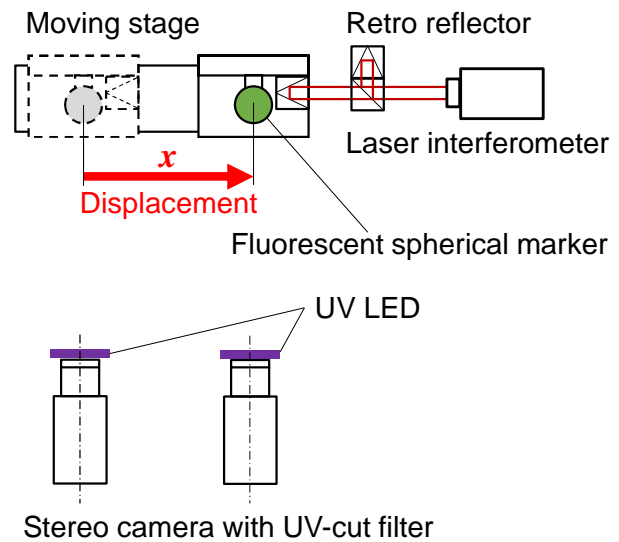
Figure 2. Experimental setup for displacement measurement by stereo camera system with a fluorescent spherical marker.

Figure 3. Grid pattern for conventional camera calibration.
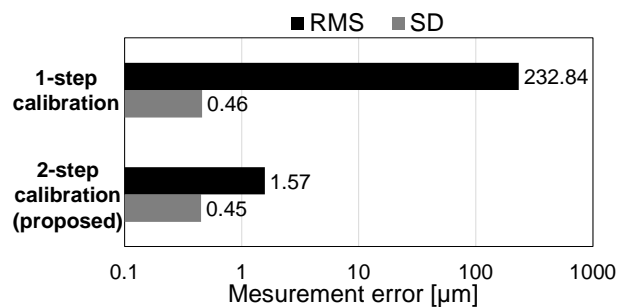
Figure 4. Comparison of measurement error between conventional and proposed calibration methods.

References

[1] Zhang Z Y 2000 *IEEE Transactions on Pattern Analysis and Machine Intelligence* **22** 11 1330-1334

[2] Ha J E 2007 *Optical Engineering* **46** 10 107203

[3] Heikkilä J 2000 *IEEE Transactions on Pattern Analysis and Machine Intelligence* **22** 10 1066-1077

[4] Rudakova V and Monasse P 2014 *Proc. of 2014 Canadian Conference on Computer and Robot Vision* 195-202

[5] Hui Z, Wong K Y K, and Guoqiang Z 2007 *IEEE Transactions on Pattern Analysis and Machine Intelligence* **29** 3 499-502

[6] Summan R, Pierce S G, Macleod C N, Dobie G, Gears T, Lester W, Pritchett P, and Smyth P 2015 *Measurement* **68** 189-200

[7] Zhuang W, Dong M L, Sun P, and Wang J 2013 *Proc. SPIE* **8916** 89161G

[8] Ogasawara K, Terabayashi K, and Oiwa T 2016 *Proc. of the 16th International Conference on Precision Engineering* P02-8109

[9] Terabayashi K, Hamamoto Y, Ogasawara K, Oiwa T, and Sasaki T 2021 *Proc. of the 21st International Conference of the European Society for Precision Engineering and Nanotechnology* 535-536

Development of a multi-configuration support for the comparison of X-ray computed tomography and optical profilometry surface texture measurements

Filippo Mioli[1], Nicolò Bonato[2], Simone Carmignato[2], Enrico Savio[1]

[1]*Università degli Studi di Padova, Department of Industrial Engineering, Padova, Italy*
[2]*Università degli Studi di Padova, Department of Management and Engineering, Vicenza, Italy*

filippo.mioli@phd.unipd.it

Abstract

The comparison of measurements from different instruments is an increasingly common task in advanced metrology. One case in point is the calibration of measuring machines using task-specific calibration artefacts. Another example is when two different measurement technologies are combined, e.g., to emphasise their strengths and mitigate their weaknesses. The study presents a practical case where design for metrology principles were applied to create a versatile additively manufactured support for test specimens. This support, compatible with both X-ray computed tomography and optical profilometry, not only serves the purpose of holding the specimen in place but it is also designed to include specific common features to assist in the subsequent data alignment operations, that would be otherwise challenging due to the high complexity of AM surface topography.

Design for Metrology, Surface Texture, X-ray Computed Tomography, Optical Profilometry, Additive Manufacturing

1. Introduction

When deciding which measurement strategy and instrument to adopt to perform a specific metrology task, several factors must be considered. These include the metrological characteristics of the measuring instrument and the geometrical complexity of the measurement to be performed [1]. In addition, the type of features and/or materials to be measured must also be taken into account. There is no such thing as an omnivalent measuring instrument, and very often, one has to compromise between the advantages and drawbacks of different techniques. Sometimes, the choice is relatively straightforward, while for other measuring tasks, an obvious solution seems to be lacking due to the limitations of the available measuring systems. In such cases, the solution frequently lies in merging the results of measurements from different measuring instruments to enhance their strengths and compensate for their weaknesses.

To this aim, appropriately referencing of measurements originating from different instruments is an important step. When dealing with surface texture measurements, previous works in the literature show the challenges linked to the comparison of results obtained using different measuring systems [2-3]. Among the most difficult surfaces to be evaluated, additively manufactured (AM) as-built surfaces are peculiar due to their inherent complex texture showing high roughness values [4], which also manifest significant variability depending on both process conditions and fabricated features [5]. Furthermore, the presence of re-entrant features makes effective measuring tasks challenging, thus motivating the use of X-ray Computed Tomography (XCT) to overcome the inherent limits of line-of-sight measuring instruments. On the other hand, instruments such as those based on Optical Profilometry (OP), are ideal for performing surface texture measurements with more than adequate resolution, but struggle with the identification of steep slopes and undercuts.

This work aims to exploit design for metrology principles to devise a measurement setup enabling the comparison of surface texture measurements in additively manufactured test specimens (e.g., for tensile testing), carried out using XCT and OP. The proposed approach can potentially be leveraged to provide more accurate and reliable surface texture measurements resulting from a fusion of data obtained with different instruments.

2. Specimen holder design methodology

Establishing functional requirements or limitations is paramount before proceeding with the design of any support equipment. This paper selected a specific sample with rotationally symmetric geometry. The first requirement relies on the need to collect information across the entire surface of the central portion of the test specimen shown in *Fig. 1*, where its main dimensions are reported.
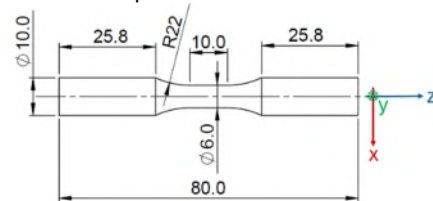
Figure 1. Test specimen geometry (dimensions are in mm).

Furthermore, the specimen holder should enable the comparison between surface texture measurements obtained using XCT and OP. Measurements should be repeatable also after the specimens are tested and the references must be preserved. To measure with OP, the specimen should be housed horizontally. The support should allow the user to place the specimens repeatedly in the same position. To do so, the holder should be able to lock the three linear translations ($\vec{x}, \vec{y}, \vec{z}$) and two of the three rotations ($\vec{r_x}, \vec{r_y}$), allowing the specimen to rotate only around the generative axis ($\vec{r_z}$). In addition, to capture the whole surface and label each patch, the rotation axis should have a reference system with its zero and some discrete controlled positions. Regarding XCT scans, the specimen should

be oriented vertically, and only the zero reference for the $\vec{r_z}$ rotation should be collected, since the entire specimen volume of interest is acquired. Therefore, as opposed to OP, the need for labelling each patch does not apply to XCT measurements. However, depending on the system's properties and on the desired magnification, the volume acquired during a circular scan has fixed dimensions. Hence, the zero mark should also be comprised in the scanned volume to be acquired with the specimen. *Tab. 1* summarises the functional requirements and limitations considered within the design for metrology workflow.

Table 1 Functional requirements and limitations for the specimen holder

	OP	XCT
1	Reproducibility	
2	Horizontal support to lock ($\vec{x}$, $\vec{y}$, $\vec{z}$) translations and ($\vec{r_x}$, $\vec{r_y}$) rotations	Vertical support to hold up the specimen
3	Zero reference system on axial rotation $\vec{r_z}$	Zero reference system for the specimen axial rotation $\vec{r_z}$ comprised in the XCT scanning volume
4	Stepped control on axial rotation $\vec{r_z}$	

Considering the specifications listed above, a design solution for multi-purpose support has been developed. The proposed specimen holder designs are shown in *Fig. 2,* for the XCT and OP configurations, respectively.
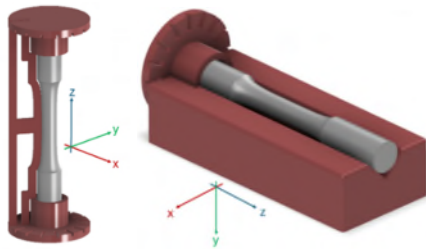
Figure 2. Specimen holder in XCT configuration (left) and OP configuration (right).
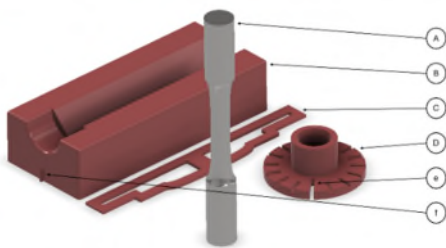
Figure 3. Proposed solution: (A) specimen, (B) V-shape support, (C) zero flap, (D) base disc, (e) zero notch, (f) coupling protrusion.

The two configurations share the base disc (*Fig. 3.D*) as a common component. This base disc, unequivocally interlocked with the specimen (*Fig. 3.A*), has *n* notches to mark different angular positions. The zero notch (*Fig. 3.e*) is the only one passing through the whole disc thickness, therefore easily recognisable. For the OP configuration, the specimen is placed on top of a V base support (*Fig. 3.B*) that locks two rotations ($\vec{r_x}$, $\vec{r_y}$) and two linear translations ($\vec{x}$, $\vec{y}$). To stop the last translation ($\vec{z}$), the base plate is brought up against a wall of the V-shaped base where, thanks to the coupling of a protrusion (*Fig. 3.f*) with the notches, the rotation can be controlled.

For the XCT configuration, a second disc is mounted on the other specimen gripping section, which presents a pass-through zero notch as well. Thus, a lightened flap (*Fig. 3.C*) is vertically mounted using the zero notches on each disc and it will appear inside the scanned volume to serve as the zero reference. Therefore, thanks to the notches the OP acquired patches will have consistent overlapping regions, thus facilitating the stitching. The zero flap, on the other end, will provide a common reference system between the two scanned surfaces.

3. Realisation and future works

The support has been fabricated in Polylactic Acid (PLA) using a Raise3D Pro3 (Raise3D, CA) system, applying a material extrusion (MEX) layer-wise manufacturing approach. The specimen holder has been tested in both the proposed configurations and it has proven to be successful in facilitating the comparison of data of corresponding regions between OP and XCT. *Fig. 4* shows the prototype used for OP (a) and for XCT scans (b).

Future works will focus on developing smart algorithms to stitch the *n* surface patches obtained using OP into a single surface that can then be compared and fused with the data coming from XCT. This approach has the potential to allow for more comprehensive surface texture data enhancing the knowledge on the AM surfaces and mechanical properties.
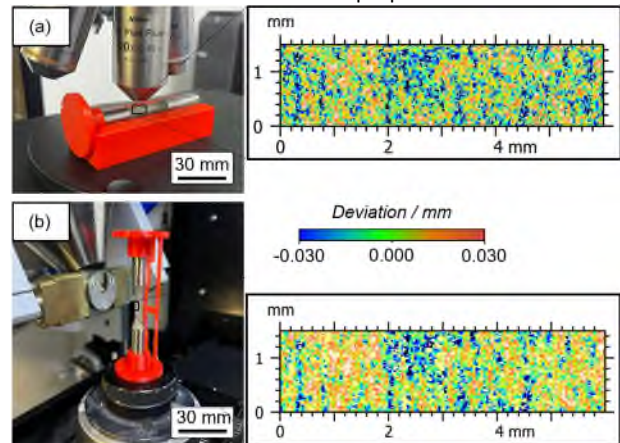
Figure 4. Specimen holder prototype used to measure an AM specimen using OP (a), and XCT (b). Insets show the corresponding respective measured surface topographies.

References

[1] F. Zanini, M. Sorgato, E. Savio, and S. Carmignato, 2021, 'Dimensional verification of metal additively manufactured lattice structures by X-ray computed tomography: Use of a newly developed calibrated artefact to achieve metrological traceability', *Additive Manufacturing*, vol. **47**, p. 102229, doi: 10.1016/j.addma.2021.102229.

[2] A. Townsend *et al.* , 2018, 'An interlaboratory comparison of X-ray computed tomography measurement for texture and dimensional characterisation of additively manufactured parts', *Additive Manufacturing*, vol. **23**, pp. 422–432, doi: 10.1016/j.addma.2018.08.013.

[3] F. Zanini, L. Pagani, E. Savio, and S. Carmignato, 2019, 'Characterisation of additively manufactured metal surfaces by means of X-ray computed tomography and generalised surface texture parameters', *CIRP Annals*, vol. **68**, no. 1, pp. 515–518, doi: 10.1016/j.cirp.2019.04.074.

[4] J. C. Snyder and K. A. Thole, 2020, 'Understanding Laser Powder Bed Fusion Surface Roughness', *Journal of manufacturing science and engineering*, vol. **142**, no. 7, doi: 10.1115/1.4046504.

[5] S. Rott, A. Ladewig, K. Friedberger, J. Casper, M. Full, and J. H. Schleifenbaum, 2020, 'Surface roughness in laser powder bed fusion – Interdependency of surface orientation and laser incidence', *Additive Manufacturing*, vol. **36**, p. 101437, doi: 10.1016/j.addma.2020.101437.

Sub-minute measurement times in inline-CT: development of a fast data acquisition pipeline

N. Kayser[1], G. Dürre[1], A. Tsamos[1], C. Bellon[1], C. Hein[1]

[1]*Fraunhofer Institute for Production Systems and Design Technology IPK, Germany*
[2]*Bundesamt für Materialforschung und -prüfung, Unter den Eichen 87 12205 Berlin, Germany*

nicolas.kayser@ipk.fraunhofer.de

Abstract

As the healthcare and life sciences sector plays an essential role in driving the rapidly expanding micro injection molding market, companies are faced with the challenge of maintaining rigorous quality control standards. Despite available non-destructive testing technologies permitting the precise measurement of internal defects, they are severely limited by their speed. A novel and scalable fast data acquisition pipeline for non-destructive testing is presented, enabling a 100 % inline-inspection of injection molded parts. The pipeline includes a robot-based radiographic measurement system and an AI model for defect detection. With only 6 to 14 required projections, measurement times of 30 s ± 3 s were achieved. Defect detection is performed by an AI model directly on the 2D projections. Initial performance of the AI model is promising with further development focused on eliminating false positives.

Projection analysis, Inline-CT, Acceleration of measurement, Neural networks

1. Introduction

Despite recent advancements, prolonged measurement times remain a significant barrier to widespread adoption of non-destructive testing (NDT) technologies for the 100% inline-inspection of injection molded parts. Current quality control systems primarily focus on monitoring weight, surface geometry, and surface quality, thus limiting defect detection to externally observable factors and necessitating destructive testing for internal defect identification [1, 2, 3]. To address this challenge, a novel data acquisition pipeline was developed, integrating a custom robot-based x-ray computed tomography system and a specialized AI model for defect detection.

While existing research emphasizes the development of faster sensors and algorithms to expedite individual projection acquisition and image reconstruction, these approaches still require several hundreds to thousands of projections, posing limitations for inline inspection in micro injection molding [4, 5, 6]. For instance, Murtaza et al. implemented a radiographic system capable of rapidly scanning additively manufactured components, capturing 720 radiographs in 36 seconds. However, the system's reliance on high frame rates and moderate resolutions limits its suitability for defect detection in larger components requiring higher spatial resolution [7].

The subsequent chapters detail the experimental setup, the data acquisition pipeline, and methodology for data acquisition and defect detection. Furthermore, the reduction in the number of required projections and resulting measurement times are presented, along with an initial assessment of the AI model's performance. The paper concludes with an overview of the findings significane for injection molding.

2. Methodology

Conventional x-ray based non-destructive testing methods need at minimum several minutes to capture the required measurement data. The following chapter present a scalable, fast data acquisition pipeline which performs everything from image capture to defect detection in less than a minute.

2.1. Setup

The radiographic measurement system, depicted in Figure 1, integrates a 6-axis robotic manipulator at its core. This industrial robot maneuvers a bespoke C-arm, housing both an X-ray source and detector, facilitating projections from diverse angles and positions in 3D space. All pre-computation steps, encompassing trajectory planning to data acquisition, are centralized on a control PC, serving as a Single Point of Control (SPOC).
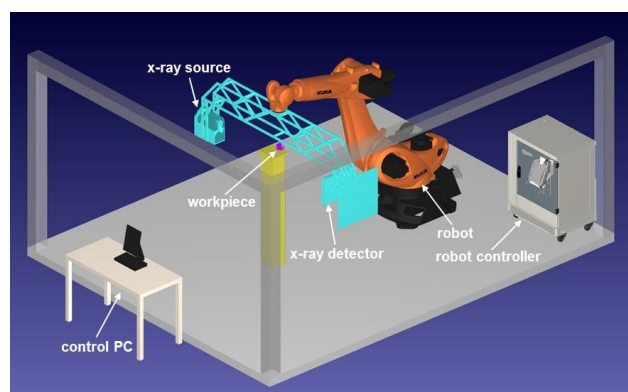
Figure 1. Setup of the radiographic measurement system for the measurement of arbitrary projection poses

The system is capable of inspecting components as small as 5 mm, achieving magnifications in the range of x1.36 to x61.44.

It is possible to scale the system for the non-destructive testing of smaller or larger components up to 225 mm but the maximum available magnification decreases with increasing object size.

2.2. Pipeline

The presented pipeline is based on the hypothesis, that each projection contains information on the location, shape and size of all defects present in a workpiece. Since all information is contained within the projection data, no 3D reconstruction is necessary for defect detection. Thus, it is possible to perform defect detection with an arbitrary number of projections, with each additional projection providing diminishing information. Consequently, by using a small number of projections data acquisition can be reduced by multiple magnitudes. A pipeline was implemented on this basis, as can be seen in Figure 2.
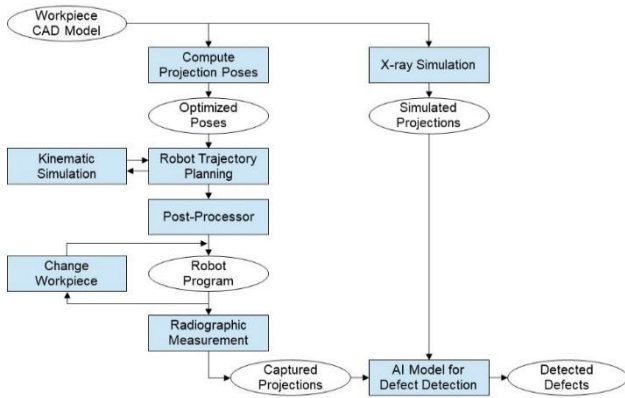
Figure 2. Sub-minute data acquisition pipeline

The Fraunhofer developed FLUX framework is used to conduct an x-ray simulation using 3D CAD models of the specimen with varied defect populations to generate synthetic projection data for a large number of projection poses and defect variations. These are used to train the AI model prior to data acquisition.

The inspection process starts by computing the optimal projection poses for a predefined number of projections. To evaluate the information contained in a specific set of projection poses, the 3D CAD model without defects is evaluated with two metrics. The first metric measures the standard deviation of the model thickness for every projection angle in 3D space. The second metric measures measures the geometric independency of projection poses. An optimal projection pose is the combination of a high standard deviation of the model thickness and high geometric independency.

Subsequently the trajectory planning for the robot is conducted with the help of a collision simulation using RoboDK. Robot program code is generated from the found trajectory and loaded onto the robot. After placing a workpiece in the system, a completely automatic inspection cycle is perioremd. Following the measurement program, the acquired projection data is automatically evaluated by the AI model and all identified and localized defects returned via the graphical user interface (GUI).

3. Results

The number of required projections was successfully reduced to 6 to 14 images in 3D space, signifying a reduction in projection data by a factor of 90 to 160 compared to conventional systems. The entire radiographic measurement of a component can be completed within less than a minute. When using 8 projection poses, a complete measurement cycle was completed within 30 s ± 3 s, excluding workpiece handling.
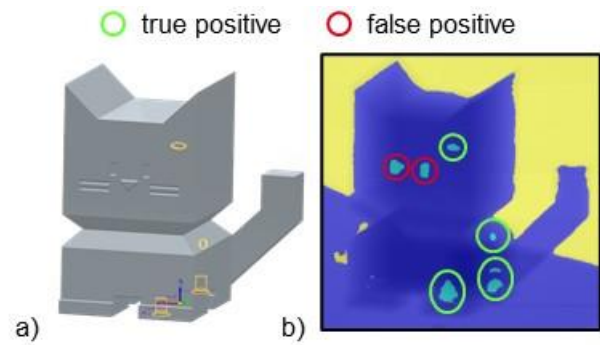
Figure 4. Example of AI-based defect detection using raw 2D projection data from an uncalibrated detector **a)** CAD model of the specimen with defects outlined in orange **b)** Identified defects with correct identifications marked in green and false identifications marked in red

Both internal and external defects in components are identified and localized by the defect detection AI model. The model finds all four of the existing defects in the specimen, for every of the four preliminary defect variations. From the seven small-scale geometry features, two are misclassified as false positives. While the model finds all of the existing defects in the specimen, individual geometry features, s.a. the eyes, tend to be misclassified as false positives, as seen in figure 4. Given the state of AI development this falls within expectations and current efforts are focused on remedying this problem.

		Actual	
		Positive	Negative
Predicted	Positive	**TP** 4	**FP** 2
	Negative	**FN** 0	**TN** 5

Table 1. Confusion matrix for the defect detection seen in Figure 4

4. Conclusion

In conclusion, the presented fast data acquisition pipeline represents a significant advancement in non-destructive testing for injection molding. By shortening measurement times, this approach enables a 100% inline inspection of injection molded parts with a radiographic measurement system for the first time. Through the adaptation of projection reduction and AI defect detection, measurement times were reduced to 30 s ± 3 s. While initial results are promising, ongoing efforts are aimed at further optimizing the system and improving defect detection capabilities. These advancements possess the potential to transform quality control across the injection molding sector.

References

[1] Wang B, Zhong S, Lee T-L, Fancey K S, Mi J 2019 *Adv. in Mech. Eng.* **12** 1-28
[2] Zwanenburg E A, Williams M A, Warnett J M 2021 Meas. Sci. and Tech. 33 012003
[3] Lagerwerf M J 2021 *Mach. Learn.: Sci. Technol.* **2** 015012
[4] Gülcür M, Wilson P, Donnelly M, Couling K, Goodship V, Charmet J, Williams M A, Gibbons G 2023 *Materials & Design* **227** 111741
[5] Cakmak E, Bingham P, Cunningham R W, Rollett A D, Xiao X, Dehoff R R 2021 Mat. Char. 173 110894
[6] Hampel U et al. 2022 Sensors 22
[7] Murtaza H et al. 2023 Cellulose 30 6173-6185

Versatile high precision synchrotron diffraction machine

G. Olea, N. Huber, J. Zeeb, R. Schneider

HUBER Diffraktionstechnik GmbH & Co. KG, Rimsting, Germany

go@xhuber.com

Abstract

A newly developed instrument intended to be used for advanced experimental investigations in a modern upgraded synchrotron research facility has been recently completed and delivered. The dedicated diffraction machine (diffractometer), working on X-ray diffraction principle consists of a basic structure with five circles 5C(2D+3S) geometry. By adding some specific components related with the enlargement of functional spectrum, as different techniques (polar dependent spectroscopy and magnetic scattering) applied on various samples (such as magnets and thin films), the machine became a complex research instrument, including the rigorous requirements of precision. In this respect, two interchangeable positioning modules have been provided, opening the way of comparing the results of various samples with the same technique, avoiding the associated errors related with their transfer (reproducibility). A stiff alignment base (B) supports a heavy dovetail detector (D) and sample (S1, S2) modules, each including several high precision positioning units (Pu) with linear and/or rotational motions (goniometers/translational) stages. (S1) includes a stiff high precision customized Euler cradle (Ec) for positioning of a magnet (2T) and (S2) several precision gonios (G), together with a nano positioning piezo device. The paper gives a complete final view of this versatile instrument, including the proposed kinematic structure, design concept selected solutions, together with an analysis of precision data collected during the final tests.

Synchrotron, diffractometer, positioning, kinematics, design, precision

1. Introduction

Synchrotron radiation is one of the most powerful investigative tools available today for exploring the internal structure of various matter states. It is expected that in the future, advanced research will be based not only on newly built or, improved (upgraded) modern facilities with increased functional beam parameters, but on new dedicated instruments /machines, working inside for specific applications [1].

A consistent upgradation process started few years ago at Advanced Photon Source (APS-U) [2]. After that, the primary characteristics of the beam e.g., emittance, coherence, etc will be improved and several new beam lines will be constructed. As such, the afferent instruments in the experimental hutches will be new ones or partially renewed.

Several beamlines from the X-ray Science (XRS) division have been allocated for the Magnetic Materials (MM) group investigations. Here, 4-ID (POLAR) beamline will be focused on emergent topic of electronic/magnetic effects of inhomogeneities in magnetic and/or ferroelectric materials relevant to actual quantum and energy requests. In this purpose, several techniques will be used, as X-ray spectroscopy (XRS) and/or X-rax magnetic scattering (XRMS) [3].

For one of the experimental stations, hutch (G) a request to develop a dedicated machine, called diffractometer (Dm) has been released [4]. Based on this, the new (Dm) intended to be used has to be adapted for horizontal scattering (Q-range) access, using both heavy load (superconducting magnets) and low vibration smaller samples, under extreme conditions (low temperature, high pressure) investigations. (Dm) has to offer not only the possibility of using the above-mentioned X-ray techniques for a single sample, but to be prepared for high precision (interchangeable) working capabilities of the samples.

A short overview, including the main features of the final instrument (prototype), during its finalized process have been revealed [5]. However, here more details are to be presented, especially taking into account the relevant challenging and solutions aspects related with its precision based on raw collected data in the final step of tests.

2. Diffractometer

For a relative long time, diffractometers have been one of the key research instruments in any synchrotron facility. Based on X-ray diffraction principle and using well-known classic or modern specific techniques [6,7], various types have been developed since their first proposal. Actually, there are several well-known companies producing them; see, for example [8].

2.1. Geometry

Generally, Dm(s) include two types of geometrical configurations, in which various actuated rotation stages, called circles (C) are arranged relative to their motion axes.

In the first group (orthogonal), the basic types include machines with four to six circles (Dm-nC, n=4-6) arranged at the right angles (α=90°). However, (n) can increase, depending on the number of auxiliary devices, and sample manipulation setups, reaching eight (n=8), or more (n>8). As the actual tendency is to use – a) several X-ray techniques to investigate b) different types of samples in the same place, the number and complexity of (Dm) machines constantly increased. Note that the working precision didn't change, but even decreased. In the second group (Kappa), each axis of the circles is arranged in an angular way (α=50°-60°), as Kappa letter. Mainly, the (Dm) working principle consists of a corelated motions of detector and sample circles, relative to a fixed beam (X-ray), based on diffraction law (Bragg) principle.

Based on the specificity of ID-4G beamline [9], the new requested diffractometer was necessary to be able to use two – spectroscopy (polarized dependent resonant) and magnetic scattering X-ray techniques. In addition, it has to provide the possibility to manipulate - a) heavy cylindrical (200x400) mm 2T magnet (120kg) and b) smaller (30, 2, 0.2 kg) samples under extreme conditions– high pressure (HV) and/or low temperature (cryostat) devices. A 2D pixel array detector (5kg), together with the afferent vacuum tube (12kg) and polarization analyser (15kg) with optics devices, totalling (100kg) must be manipulated, as well.

Following these, and others explained further, the POLAR-Dm machine was proposed on a basic five circles (n=5) orthogonal geometry, Dm-5C(2D+3S), where C_i, i=2 for detector (D) and C_i, i=3 for the sample (S). However, by the intention to use two sets of sample manipulators (S1, S2), each with additional circles (C_i, i=6), together with those included in the auxiliary devices (polar analyser) the subsequent total number of circles became much more (C_i, i=9), as Fig. 1 shows. Thus, the (POLAR-Dm) machine, belongs to a complex multi-circles (Dm) family. More details featuring the chosen kinematic structure are given below.

2.2. Kinematic structure

From the kinematic (K) point of view, a (Dm) structure results from the selected geometry and the auxiliary devices necessary to be used. Each of the components from inside must fulfil the required functional and precision working parameters, e.g., range, accuracy, etc of motions. The type of their arrangements (serial and/or parallel) has also a significant importance.

In the POLAR-Dm case, the proposed structure consists of a combination of three main kinematic chains (K$_i$, i=1,2,3), corresponding to detector (D), sample (S) and base (B) manipulation subsystems (modules), Fig. 1.
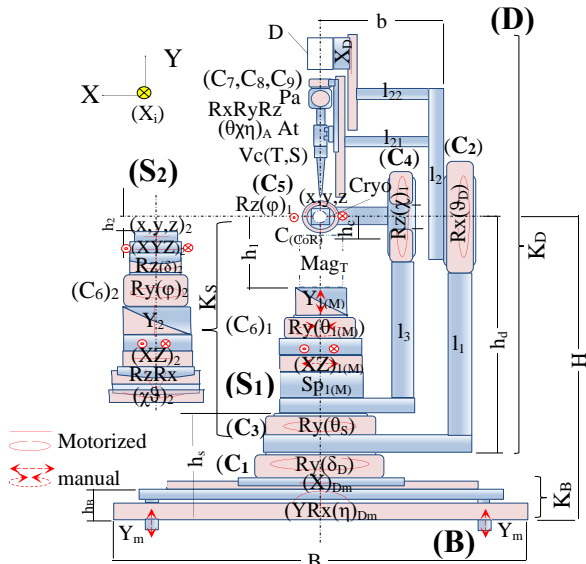
Figure 1. Kinematic structure (K)

The first kinematic chain (K$_D$) of the (D) manipulator consists of two active rotational joints (circles) –$C_1(\delta_D=\pm180°)$ and $C_2(\vartheta_D=-30°+180°)$ orthogonally linked together by an arm (l_1). In addition, arm (l_2) is supporting two linear guides (L$_1$, L$_2$) to accommodate with the use of a detector (D) and optics, as the polar analyser (An), attenuator (At) and vacuum tube (Vc) to catch the scattered X-rays. (An) is based on a combination of three orthogonal circles - $C_7(\theta_X=\pm5°)$, $C_8(\chi_Y=\pm5°)$ and $C_9(\eta_Z=+30°-110°)$. Basically, a detector point performs a spherical motion around the fixed point of the machine, called center of rotation

(CoR), which in turn, coincides with beam line (sectional) center. The (D) nominal position ($\delta_D=\vartheta_D=0°$), otherwise when the polar analyser arm is collinear with the beam.

The kinematic chains of the sample manipulation (Ks) afferent of two types of manipulators (S1, S2) consist of various in-series (stacked) arranged actuated devices, performing rotation or translational motion, with $C_3(\theta_S=\pm180°)$, as a common base.

In its first configuration (S$_1$), two orthogonal circles $C_4(\chi)$ and $C_5(\phi)$ form the Euler cradle (Ec) mechanism. (Ec) is providing an enlarged access (setup, maintenance) to the samples, especially for the large sample (magnet). It includes also a small translational motion (X=Y=±2, Z=±3) mm device, holding the cryostat. Nominal position, χ=0° when $C_5(\phi)$ along X(+). A separate support (Sp), and two (manually) driven translational (XZ=±10, Y=±5) mm and rotational $C_6(\theta_{1M}=\pm180°)$ devices performing the alignment of (M), will be sometimes removed.

In the second configuration (S$_2$), several motion devices are stacked one after the another, starting with one performing arc circles RzRx $(\chi=\vartheta)_2=\pm7°$, following the translational (X$_2$=Z$_2$=5, Y$_2$=2.5) mm ones. On top of these, performing full $C_6(\phi_2=\pm180°)$ and partial Rz$(\delta_2=\pm7°)$ circular motions, carrying a course (X$_2$=Z$_2$=5, Y$_2$=2.5) mm and fine $(xyz)_2$=0.1 mm translational motions devices is forming the precision gonio (Pg) mechanism.

An alignment base (B) subsystem has to support the entire machine structure, providing reliable stability and short motions - (X,Y)$_{Dm}$= 20 mm and Rx$(\eta)_{Dm}$=±0.5° for the rough alignment toward X-ray beam longitudinal axis. (K$_B$) was chosen as a four legged (quatro) in-parallel mechanism (PKM) [10], from which two pairs of them are actuated. (Y$_m$) are manually driven feet are short motions levelling with the floor.

The main motion parameters, as the range – stroke (St) and precision -repeatability (Rp), resolution (Rs) required for the basic circles are included in Table 1. The indicated values are the lowest (highest) allowed ones. A short simulation video of the motions can be seen [6].

Table 1 Dm basic motions parameters

Circles (C$_i$)	St (°)	Rp* (")	Rs (")
$C_1(\delta_D)$	±180	8	3.6
$C_2 (\vartheta_D)$	-30+180	8	3.6
$C_3 (\theta_S)$	±180	0.5	0.36
$C_4(\chi_S)_1$	±100	8	3.6
$C_5(\phi_S)_1$	±180	8	0.36

* Bidirectional

The O-XYZ reference system is a right-handed set of orthogonal axes, with the origine in CoR point (O=C); the positive orientation of Z being along the incoming X-rax beam and Y vertically upward.

2.3. Design concept

Following the kinematic structure, a design process [11] started to select the suitable components, based on load supported, actuation type, shape and precision criteria. Most of them are standard with modified/improved features in-house manufactured. The resulted concept (layout) is shown in Fig. 2.

As a modular design approach has been applied, the entire machine architecture has been divided into three main positioning modules (Pm$_i$, i=1,2,3), each of them built from a serial and/or parallel combination of multiple positioning units (Pu$_i$, i=1,...,n) (Pu$_i$), performing basic rotational/translational motions. (n) varies from module to module, being in a strong correlation with the motion actuated axis A$_i$ (i=1,...,n). In addition, there is a fourth module (Pm$_4$), dealing with the wire/cable manipulation.

Mainly, the first positioning module (Pm$_1$), corresponds to the detector manipulator (D) includes two powerful motorized Pu goniometers (G) linked with two stiff arms. (Pm$_1$) was built for

the first time on two heavy load and high precision gonios (G480) able to work in both – horizontal (W1) and vertical (W2)
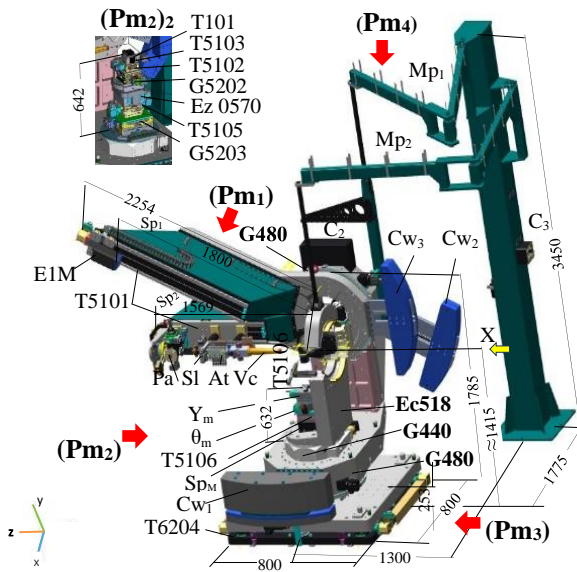
Figure 2. Design concept (CAD)

This extreme solution was adopted based on the fact that the (D) arm must carry several heavy instruments at an appreciable distance (2m) and apart (0.63 m) from the machine center point. Thus, it must provide the necessary actuation moment (force) carrying a) detector (EIGER1M) and b) Polar analyser (customized), pneumatic attenuator (3002.60M), slit (IB-C30-HV) and vacuum tube (Vc), together with their supports (linear stages). In this purpose, a dovetail concept including two stiff, but light spacers (Sp) from sheet metal (welded) was provided. And, for the static balance three counterweights (Cw_i, i=1,2,3), as well. (Pa) was built on a combination of two gonios (G410A, G409 - XEW2), one linear (X5101/XE) and head (H1005).

The positioning module $(Pm_2)_1$, corresponding to (S_1) configuration consists of a customized Euler cradle (Ec518), combining a stiff base and carrier, holding a translational stage (5106), which must carry the cryostat (ARS DE-202G).

The positioning module $(Pm_2)_2$ corresponding to the second configuration of the sample manipulator (S_2) is a high Precision gonio (Pg) system built on a (gonio) segment (S5203) with required precision (XE), supporting a standard XYZ translation stage (T5105) on which a high precision air bearing stage (EZ 0570) is located. On top of them, a segment (gonio) stage (S5202) is fixed where a combination of two linear stages (X5101/T5102) and a nano(piezo) positioning stage (TRITOR 101 CAP, JENA) are supported. $(Pm_1)_2$ and $(Pm_2)_2$ modules are moved by a common precision gonio stage (G440, X2W2).

The alignment base (B) module (Pm_3) was designed on a standard table type (T6207), providing stiff and stable support of loads (<1000 kg) and precision motions for all the necessary working modules above it. An overview of selected (Pu) types, together with their available loads and precision provided Tab.2.

Table 2 Dm design parameters

Axis (A_i)	Modules (Pm_i)	Units (Pu_i)	Load (H/V)	Prec. (X)
A_1	Pm_1	G480	W2V	XE
A_2	Pm_1	G480	W2H	XE
A_3	$(Pm_2)_{1,2}$	G440	W2V	XE
A_4, A_5	$(Pm_2)_1$	Ec518	H&V	XE

As precision was also one of the main requirements, modelling and simulations have been performed, using finite element analyse (FEA).
The estimation of the deformations (deflections) and stresses (von Misses) helped a better design. By improving the stiffness, the deformation causing the geometric errors of positioning was reduced, or even totally eliminated. (D) and (Ec) components were identified as the critical ones, and the process focused mainly on them. An example is given in Fig. 3 for (D) deformation, where (ε_2) must be less than 0.02 mrad around Z

b) (D) arm vertical $D_a(V)$

a) (D) arm horizontal $D_a(H)$
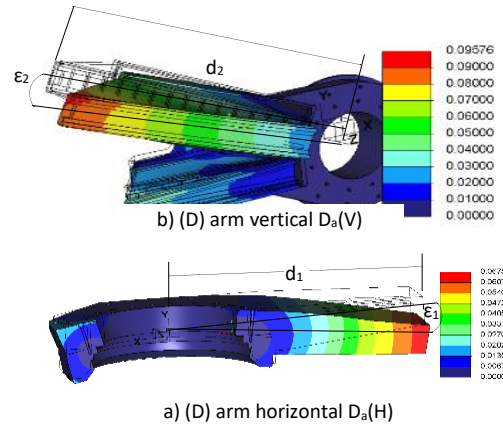
(θ_z), at d=2m and with ϑ_D=0-30°.

Figure 3. Modelling and simulation (FEA)

(Dm) machine design included not only an appreciable number of motorized circles, but the linear ones, as well. The total amount of axes reaching a high number (A_i, i=1,...,30). Generally, from the control of motion point of view, this multi-axes machine is driven by commercially available stepping motor (VEXTA/ORIENTAL, PK/P), gears boxes and incremental encoders (VIONICS/RENISHAW, RKLC/RESM). In addition, four power drives (POWERPACK) and two driving (SMC9300) electric /electronic boxes have been provided for basically, a closed loop approach applied. As expected, the management of the appreciable number of the cables from the actuated axis- wires (electric) and pipes (air), together with their necessary length for the roof (>10m) was an issue. To solve it, a specific design of a manually actuated (planar) manipulator (Pm_4) was provided. (Pm_4) mainly consists of two Brinkman incorporated manipulation components – one for detector (Mp_1) and other for Euler cradle (Mp_2), respectively. In addition, the connections have been performed through three main connexion boxes - $(Cb)_i$, i=1,3. Sleep rings were sometimes used, and the wires directed through central holes of the components. Additionally, for preventing any crushing hazards of large components in motion, electric warning stickers have been included, as well.

2.4. Precision

Precision positioning is a permanent concern in the synchrotron industry. The successful management involves not only knowledge and extensive expertise from several fields (mechanics, electric, metrology), but a permanent control (tests) during the entire manufacturing process.

Based on the above design considerations and the final adopted solutions, a first POLAR-Dm instrument (prototype) has been manufactured. It is shown in Fig. 4 (left), about to undergo the last round of motion errors tests. Fig. 4 (right) includes the measurements setups details, for both (Ec) and (Pg), submodules. However, it does not include the real cryostat device (Ec) and nor the piezo units (Pg) in order to make possible the process. In addition, the slits and vacuum tubes were already

shipped before to the facility. All functional and precision motion parameters were tested at factory premises and then included in a report [12] issued to the facility. For the measurements purpose several instruments (interferometers, autocollimator, dial gages) and auxiliar devices (dummies, calibrated balls) have been used.
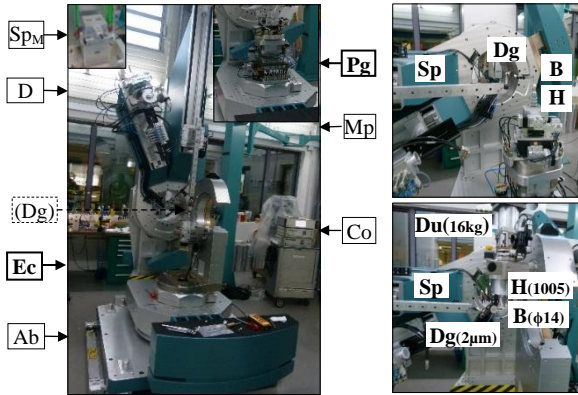
Figure 4. Prototype and measurements (SoC)

Sphere of Confusion (SoC) parameter is a global indicator of the accuracy of positioning of any (Dm). It takes in to account all types of geometric errors during the complex motion of (D) and (S). However, from practical point of view, the separate partial values - $(SoC)_D$ and $(SoC)_S$ or even those of individual axis $(SoC)_i$ could be from real interest. The required values for POLAR-Dm are displayed, Table 3.

Table 3 Runout errors (Max)

C_i [i=1,5]	$C_1(\delta_D)$ [μm]	$C_2(\vartheta_D)$ [μm]	$C_3(\theta_S)$ [μm]	$C_4(\chi_S)$ [μm]	$C_5(\phi_S)$ [μm]
$(SoC)_i$	15	50	5	50	5

As easy can be seen from the table, the maximum values must be less than fifty micrometers. In addition, as specified the value of reproducibility, following the interchangeable actions of individual and/ or combined modules (Ec)/(Pg) should comply with fifty microns interval (Rpr<50 μm). At a short survey, these values are qualifying the instrument, as with high precision one.

For the detector module (Ci, i=1,2), the error determination consisted in the measurements of radial (ε_r) and axial (ε_a) runout values in the two cases, with following conditions: a) (Ec) - ϕ_S=0°, χ_S=90° and b) (Pg) – χ_2=υ_2=ϕ_2=0°, through the basic gonio stage (θ_S=0°). In the first case (a), the horizontal arm performing full rotations (δ_D=±180°), and the second arm being vertical (ϑ_D=295°), the max/min values reached: a) $\varepsilon_r \in$ (-3,3) μm and b) $\varepsilon_r \in$ (0,8) μm intervals. Note, that ε_a=0 μm. When the second arm performs partial rotations (ϑ_D=-180°+30°), and the horizontal arm fixed (δ_D=25°), the obtained values were: a) $\varepsilon_r \in$ (-25,8) μm and b) $\varepsilon_r \in$(-13,0) μm and $\varepsilon_a \in$(-20,18) μm and b) $\varepsilon_a \in$(-25,12) μm.

For the sample module (Ec) with (Ci, i=3,5), the same type of errors has been collected, under the condition of the detector arm being horizontal (δ_D=25°), in two cases of payloads: a) 5 kg and b) 16 kg, Fig. 4(right). Thus, for the first case of the motion (χ_S=±100°), with (ϕ_S=0°), the obtained values were: a) $\varepsilon_r \in$(-5,7) μm, $\varepsilon_a \in$(-6,6) μm and b) $\varepsilon_r \in$(-13,12) μm, $\varepsilon_a \in$(-10,11) μm. Note: For the second determination, (ϕ_S=±180°) all the errors fall inside $\varepsilon_r \in$ (0,2) μm and ε_a=0 μm, identically with the individual gonio stage values. The graphical representation is given (Fig. 5.)

The measurements in the case of basic gonio (θ_S=±100°), for both types of sample (sub)modules – (Ec) and (Pg), the values reached: a) $\varepsilon_r \in$ (-4,0) μm and b) $\varepsilon_r \in$ (0,4) μm intervals, with (χ_S=90°), (ϕ_S=0°) and the detector arm vertical (ϑ_D=295°).
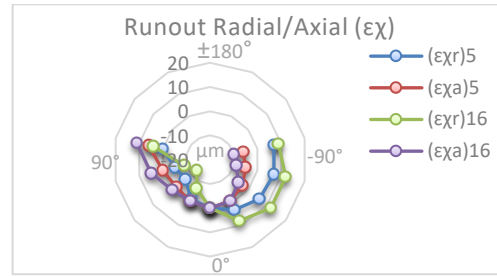
Figure 5. Positioning errors (Ec)

The max values from all measurements above are summarized in Table 4.

Table 4 Runout errors (Max)

S_i (i=1,2)	$C_1(\delta_D)$ ε_r[μm]	$C_2(\vartheta_D)$ $\varepsilon_r/\varepsilon_a$[μm]	$C_3(\theta_S)$ ε_r[μm]	$C_4(\chi_S)$ $\varepsilon_r/\varepsilon_a$[μm]
S_1(Ec)	6	25/38	5	25/21
S_2(Pg)	8	13/33	4	-

Shortly analysing the obtained results and to corroborate with the specificity of measurement conditions, qualifying us to affirm that the complex multi-axes (Dm) machine was able to deliver an outstanding precision, overall SoC<50μm.

3. Conclusion

A dedicated diffractometer (Dm-POLAR) with flexible research investigation capabilities to work in an upgraded 4th generation synchrotron facility has been developed. Able to support different types of X-ray techniques applied on large spectrum of (electromagnetic) materials, under extreme conditions (pressure and temperature), the machine has resulted, as a successful combination of commercial and customized components improving a basic structure. Two selective chosen specific precision modules for samples are preserving the necessary accuracy during the interchangeable process. Based on its specific features and precision data obtained, during the tests, we are entrusted to believe that a versatile high precision diffraction machine has been produced, expecting to enhance the experimental synchrotron investigation capabilities in the aforementioned fields.

References

[1] Lightsources 2023 https://lightsources.org
[2] APS Upgrade Project 2019 *Final Design Report* APSU-2.01-RPT-003 ANL USA
[3] Hettel R. 2023 Status of the APS-U Project *Proc. IPAC2021* Campina BR 7-12
[4] Stremfer J. 2022 4-ID-G Diffractometer *Statement of work APS Upgrade* ANL US
[5] Olea G. et al. 2023 POLAR synchrotron *diffractometer Proc. MEDSI2023* WEPPP009 Beijing CN
[6] Klug H. P. 1974 X-ray diffraction procedures: For polycristaline and amorphous materials *John Wiley & Sons 2nd ed*. ISBN: 978-0471-49369-3
[7] Seek O.H. and Murphy B.M. 2015 X-Ray Diffraction: Modern Experimental Techniques *CRC Pres* ISBN 9789814303590
[8] HUBER Diffraktionstechnik GmbH&Co.KG 2023 *https:// www. xhuber.com*
[9] Stremfer et al. 2022 Possibilities at Polar beamline with APS-U SRI2021 *J. Physics* 2380 (012038) 1-7
[10] Merlet J-P. 2006 Parallel Robots *Springer* 2 ed. ISBN-10-1402041322
[11] CREO9 Design Package 2023 *https:// www.ptc.com/en/ products/ creo/package*
[12] POLAR synchrotron diffractometer- Factory Acceptance Test (FAT) 2023 *Technical Report* HUBER Diffractionstechnik, DE

EURAMET's European Metrology Network for Advanced Manufacturing

Anita Przyklenk[1], Alessandro Balsamo[2], Harald Bosse[1], Alex Evans[3], Daniel O'Connor[4] and Dishi Phillips[5]

[1]Physikalisch-Technische Bundesanstalt (PTB), Braunschweig, Germany
[2]Istituto Nazionale di Ricerca Metrologica (INRIM), Torino, Italy
[3]Bundesanstalt für Materialforschung und -prüfung (BAM), Berlin, Germany
[4]National Physical Laboratory (NPL), Teddington, United Kingdom
[5]European Society for Precision Engineering and Nanotechnology (euspen), Cranfield, UK

anita.przyklenk@ptb.de

Abstract

Advanced manufacturing has been identified by the European Commission as one of the key enabling technologies (KET). These KETs are predicted to increase industrial innovation by addressing societal challenges and creating innovative and sustainable economies. Developments in the field of advanced manufacturing are progressing rapidly, particularly accelerated by digitalisation technologies, demanding appropriate evaluation methods, measuring devices, guidelines and standards for quality control of manufacturing processes and products in multiple industries. The metrology needs of these industry sectors are regularly surveyed on workshops by the European Metrology Network (EMN) and prioritised according to the advice of the EMN's Stakeholder Council, which is currently consisting of 13 industry representatives. These metrology needs are published in the Strategic Research Agenda (SRA) and are regularly revised to address the most recent metrology requirements in the field of advanced manufacturing. The SRA serves as a guide for decision-makers from industry and politics, and scientists who apply for funding of their research. This article introduces the purpose of the SRA and a new approach for a planned ongoing survey of stakeholder needs on the EMN website.

Advanced manufacturing, metrology, European Metrology Network (EMN), Strategic Research Agenda (SRA), stakeholder

1. Who we are

Advanced manufacturing requires new and enhanced metrology methods to assure the quality of manufacturing processes and the resulting products. The European Metrology Network (EMN) for Advanced Manufacturing drives the high-level coordination of the metrology community in this field with the aim of promoting the impact of metrology developments for advanced manufacturing.

The network is operated by national metrology institutes and designated institutes in close cooperation with stakeholders from academia, industry, and international initiatives with an interest in advanced manufacturing (Table 1).

Table 1 Overview of active EMN members

Members with active role in the EMN	No
Metrology institutes and designated institutes	18
Primary contacts	18
Cross-sectional experts	15
Advanced materials experts	17
Smart manufacturing systems experts	14
Manufactured components & products experts	15
Partner expert	1
Stakeholder council members	13
International associations/organisations	5

1.1. Our Vision

The EMN's Vision is to establish a self-sustainable interactive network of experts and an infrastructure to support metrology for advanced manufacturing in Europe. The EMN strives for being the primary contact point for metrology challenges in the advanced manufacturing industry.

1.2. Our Mission

The EMN has the mission of supporting competitiveness and innovation of the European advanced manufacturing industry by further developing a metrology infrastructure in cooperation with stakeholders, providing access to metrology research, services, and knowledge transfer. The realisation approach of these actions is described in detail in Przyklenk et al., 2021 [2].

1.3. Our Objectives

The EMN has identified the following main areas to support advanced manufacturing technologies (Figure 1) by

- continued stakeholder dialogue - supported by high-level experts of the EMN stakeholder council - targeting future metrology needs to be addressed in joint research projects,
- regular interaction with existing and upcoming European Partnerships and other international organisations to identify future needs for providing metrology-related input for research programmes,
- developing and providing specific metrology knowledge transfer to the European advanced manufacturing industry and stakeholders,
- representing European interests in standardisation and regulation committees that are relevant for advanced manufacturing, and
- coordinated approach to further develop and maintain a European metrology infrastructure of measurement capabilities and metrology services to support the competitiveness of the European advanced manufacturing industry.

Figure 1 Objectives of the EMN for Advanced Manufacturing.

2. Strategic Research Agenda

The purpose of the strategic research agenda (SRA) is to collate and highlight the key measurement challenges and opportunities for metrology in the field of advanced manufacturing. Thus, the SRA is intended to facilitate coordination and prioritisation of advanced manufacturing metrology research and development activity in Europe and acts as a reference document for the wider metrology and advanced manufacturing community. The SRA focusses on the cross-cutting topics listed in Table 1. Additionally, the 13 key industry sectors of the EMN are addressed [2, 3]. The SRA content is available in compressed form on the EMN website [3]. The next update is planned in mid-2024.

3. Metrology needs in Nano- and Microelectronics

The metrology challenges for Nano- & Microelectronics were discussed in an Open Consultation, organised by EURAMET and the EMN on 8th July 2022 with contributions from major European companies addressing their metrology needs. Additional input was provided from other sources, such as the Chips Joint Undertaking [4] and the International Roadmap for Devices and Systems [5]. In the following, one of the identified needs is assigned to a cross-cutting topic as an example, so that the needs are represented along the entire production chain:

(i) Intelligent product design: Full and fast characterization of functional 3D nanostructures (dimension, materials/composition, dopants, strain, optical and electrical properties) for new device technologies (compound semiconductors, micro-LED, power electronics and vertical-cavity surface-emitting lasers)

(ii) Advanced materials: Larger components in lithography machines may cause drift issues, for drift compensation near ideal raw materials and accurate methods for material property qualification are needed.

(iii) Smart manufacturing systems: In-line capabilities of metrology methods are needed, e.g. to measure carrier mobility.

(iv) Quality control and testing: Metrology to support introduction of high NA EUV lithography in high volume manufacturing.

(v) Digitalisation and vertical metrology integration: Integrating metrology tools along the whole semiconductor manufacturing lines (Industry 5.0).

(vi) Legislation and standardisation: Easy to use, time-stable industrial calibration standards to cover the whole parameter ranges of instruments and measurands.

(vii) Health and safety, environment and sustainability: Developing improved characterisation methods for carbonaceous materials and composite/multi-component substances.

(viii) Knowledge-transfer and accessibility: Pooling good practice guides from NMIs on EMN website.

4. Outlook – Stakeholder contact through a long-term survey

Staying in contact with stakeholders is a tremendously important task to know the latest trends and to predict future metrology requirements in advanced manufacturing accordingly. This exchange is currently realised through regular workshops. Supplementing these by a long-term stakeholder survey is planned. The idea is to investigate metrology requirements in various areas by means of indicating catchy adjectives, such as *precise*, *easy*, *safe* or *sustainable*, to permanently rank stakeholder needs of a wide metrology and manufacturing community.

Table 2 shows the planned survey as a prefilled table. The results of the survey will be updated and displayed as a cumulative graphic on the future EMN website.

Table 2 Content of a planned long-term online stakeholder survey.

	Intelligent product design	Advanced materials	Smart manufacturing & assembly	Quality control & testing	Digitalisation & vertical integration of metrology	Legislation & standardisation	Health & safety, environment & sustainability	Knowledge-transfer & accessibility
Cross-Cutting Topics								
Precise	●	▽	▲	▲	●	●	▽	--
Traceable	●	●	●	▲	●	●	▲	--
Fast	▲	--	▲	▲	▽	--	▽	●
Easy	●	●	▲	▲	▲	--	▲	●
Cheap	●	●	●	●	▲	▽	▽	▲
Safe	▲	▲	▲	▽	●	▲	▲	▽
Sustainab.	▲	▲	▲	▽	--	▲	▲	--

▲ Very limiting   ● Limiting   ▽ Not limiting   -- Not applicable

Acknowledgements

References

[1] Bosse H *et al* 2023 *Euspen 23rd ICE Proceedings*
[2] Przyklenk A *et al* 2021 *Meas. Sci. Technol.* **32** 111001
[3] https://www.euramet.org/european-metrology-networks/advanced-manufacturing/strategic-research-agenda
[4] https://www.chips-ju.europa.eu/
[5] https://irds.ieee.org/

Session 3: Advances in Precision Engineering

Design of electrical contact surfaces for fast charging systems

Lars Kanzenbach[1], Sebastian Wieland[1], Jörg Schneider[1], Jan Edelmann[1]

[1]*Fraunhofer Institute for Machine Tools and Forming Technology IWU, Chemnitz, Germany*

lars.kanzenbach@iwu.fraunhofer.de

Abstract

E-mobility is of high interest for the energy transition and the achievement of climate targets. Nevertheless, this forward-looking technology still has a number of drawbacks. One example is the very long charging time of battery systems. To counteract this, an innovative fast charging system using a face contact instead of classic plug-in contacts is being developed that significantly reduces conventional charging times. To enable this, an electrical contact surface is functionalized in such a way that, on the one hand, the contact resistance is reduced and, on the other hand, the thermal as well as mechanical properties are improved. This can be achieved by a special design of the microstructure of the electrical contact surface. In the following, the procedure is described in detail. First, a single microcontact is designed to break up the oxide layers and minimize the constriction resistance. The thermal, mechanical and the electrical properties are described and optimized using analytical and numerical methods. Special attention must be paid to the heating of an a-spot during current flow. Then, the single microcontact is multiplied to exploit the principle of a parallel connection. This can significantly reduce the constriction resistance. Finally, this designed microstructure is manufactured and tested in experiments. Consequently, high charging currents can be transmitted via a face contact on a relatively small contact area.

Keywords: electrical contact, contact resistance, face contact, numerical analysis, FEM

1. State of the art of charging systems

E-mobility is a key technology for managing a successful energy transition and to transform the mobility sector. In order to make this forward-looking technology practicable, new methods of energy transmission up to the megawatt range must be found. Classic plug-in contacts, which are commonly used, are limited in the normal force due to their manual operability. This leads to a comparatively small contact surface and thus a limitation in the transferable electrical load to avoid overheating. To overcome this, the principle of face contacting is operated mechanically, which offers up to 20 times higher contact normal forces and therefore significantly higher transmittable power as well as greater thermal stability. This is achieved by increasing the current-carrying surface area of a given contact surface, ensuring the necessary wear protection and the mechanical-electrical development of the face contact with optimal heat conduction, taking into account the clearance and creepage distances.

2. Basics and design approach of electrical contact surfaces

In this section, the basics and the design approach for the electrical contact surfaces are presented. First, the basic relationship of the contact resistance is explained. The contact resistance $R_{contact}$ is made up of the sum of the resistance of the base material R_B, the constriction resistance R_c and the external layer resistance R_L, see [1-2].

$$R_{contact} = R_B + R_c + R_L \qquad (1)$$

The basic idea behind the electrical contact surfaces is that, on the one hand, face contacting of the microstructure breaks up the oxide layers and, on the other hand, the microstructure leads to the lowest possible constriction resistance, which

enables higher transmittable power. Therefore, the design of the microstructure plays a very important role. As a consequence, the initial focus is on the design of a single microcontact (also known as an a-spot). The resistance of a single circular microcontact can be determined via the constriction resistance, see [1-4].

$$R_c = \frac{\rho(T)}{2\,r_K} \qquad (2)$$

Here, ρ describes the specific electrical resistance and r_K the radius of the microcontact or the radius of the a-spot. Figure 1 shows two constriction resistance curves for two different radii of curvature R_K, each with flat counter body. Note that different radii of curvature lead to different contact radii r_K and thus to different constriction resistances for the same normal force F_N.
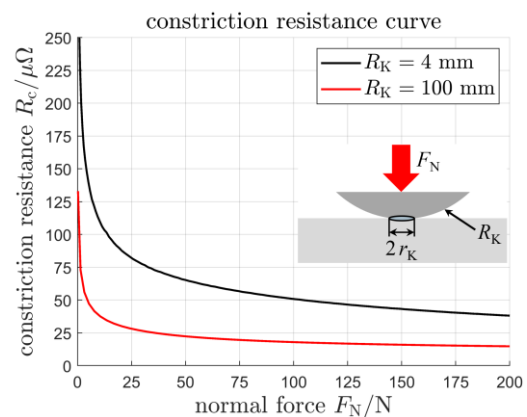
Figure 1. Constriction resistance curves for two different radii of curvature

Figure 1 shows that a certain normal force is required to significantly reduce the constriction resistance. The simulations

were carried out with Tribo-X. Furthermore, it can be observed that no significant improvement occurs with increasing normal force. In direct comparison, $R_K = 4$ mm shows a higher constriction resistance due to the smaller contact area. In the following, a relationship between mechanical, thermal and electrical variables is derived, which enables a targeted design of the microstructure. It is obvious that the radius and the temperature T of the microcontact as well as the current flow I_K influence each other. Based on the approach of an ellipsoid model, a relationship can first be established between the maximum temperature T_{max} in the a-spot, the temperature of the boundary surfaces T_1 and the contact voltage U_K, see [2, 4].

$$T_{max} = \sqrt{\frac{U_K^2}{4L} + T_1^2} \tag{3}$$

Here, L describes the Lorenz number. Using Ohm's law, the current strength and the resistance can be built in and above this the radius of the a-spot. As a result, we obtain an evaluation equation, which shows the correlation of all important influencing variables.

$$T_{max} = \sqrt{\frac{\rho^2 I_K^2}{16 L r_K^2} + T_1^2} \tag{4}$$

It should be noted that the investigations carried out here were performed for copper, more precisely Cu-ETP (CW004A). In addition, the temperature dependence of the specific electrical resistance $\rho(T)$ was taken into account. Finally, Figure 2 shows the 3D-plot of the maximum temperature in dependence of the current strength and the radius of the a-spot, which can be used to dimension the microstructure.
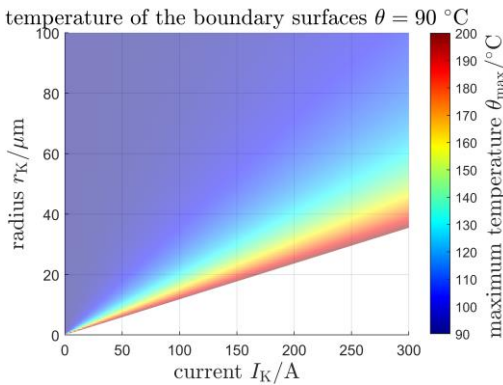
Figure 2. 3D-plot of maximum temperature in dependence of current strength and radius of a-spot

The figure clearly shows that there is a very sensitive relationship between the radius of the a-spot, the current flow and the maximum temperature in the a-spot. Consequently, the microstructure of the electrical contact surface cannot be made infinitely small. For example, if a current of $I_K = 300$ A is to be transmitted without a significant increase in temperature, the microstructure should have a radius of more than 80 µm. This radius or the resulting contact area must therefore be present when the normal force is applied. Our design approach is that no significant increase in temperature can be reached for the developed microstructure. After dimensioning a single microcontact, the structure is multiplied to utilize the principle of parallel connection [5].

$$R_c = \frac{1}{n} \frac{\rho(T)}{2 r_K} \tag{5}$$

For this, the constriction resistance R_C is shown as a function of the normal force F_N and the number of a-spots n. Figure 3 shows that the constriction resistance decreases very fast with increasing normal force and increasing number of a-spots. Additionally, it should be mentioned that the constriction resistance curve from Figure 1 ($R_K = 4$ mm) represents the limit curve in Figure 3 for one a-spot.
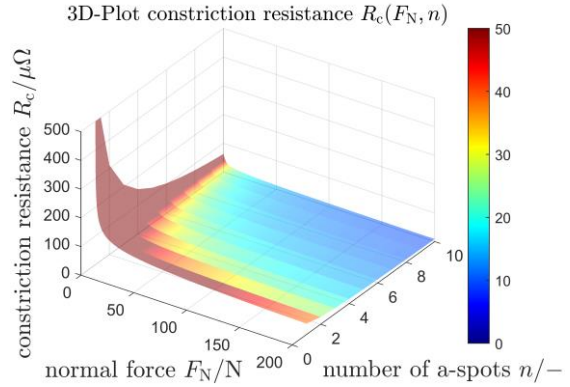
Figure 3. 3D-plot of constriction resistance in dependence of normal force and number of a-spots

It can be observed that just a few microcontacts (a-spots) are sufficient to reduce the constriction resistance significantly. In contrast, it should be taken into account that the effective contact radius also decreases with a large number of microcontacts since the normal force is evenly distributed among them. For a first prototype, a face contact with five microcontacts is designed. This setup offers the best compromise in terms of constriction resistance and available normal force. Figure 4 (left) depicts the contact surfaces with five microstructures.

3. Simulation with COMSOL Multiphysics

In this section, the current flow and the heat distribution are simulated for the previously designed prototype, consisting of a face contact with microstructure and a flat face contact. In [6], similar investigations were carried out for a multi-spot contact, but at very low currents (200 mA). The numerical calculations were performed using the finite element method (FEM) in COMSOL Multiphysics. A step file of a CAD model was used to create the finite element model. For the electrical boundary condition, a current density of $J = I/A = 5.9683 \cdot 10^6$ A/m^2 was specified (with $I_K = 300$ A and $D = 8$ mm). In addition, copper ETP was used for material characteristics and material properties. Figure 4 shows the FE-model (left) and the current flow (right).
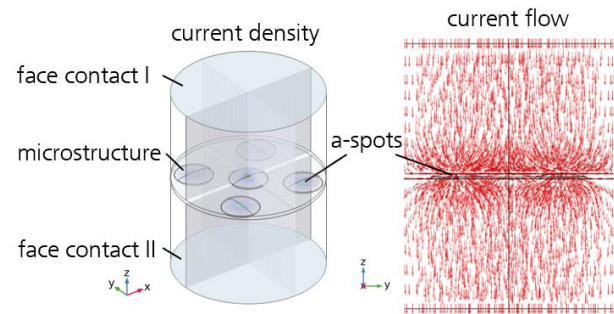
Figure 4. Face contact with five microstructures – display of current flow

As illustrated, the narrowing and subsequent widening of the current flow at the contact points (a-spots) can be seen very clearly. This is the cause of both the increase in resistance, which is introduced as constriction resistance and the increase in temperature. As a result, the electrical current transmission can be mapped physically. It should be noted that the influence of oxide layers caused by oxidation of the surface is not simulated here. Experimental tests will be carried out later to investigate their influence and their break up through face contact.

In the following, the maximum temperature in an a-spot from COMSOL Multiphysics is validated with the analytical design approach. For this, the maximum temperature of an a-spot is evaluated for an effective radius of 60 μm. The results are shown in Figure 5.
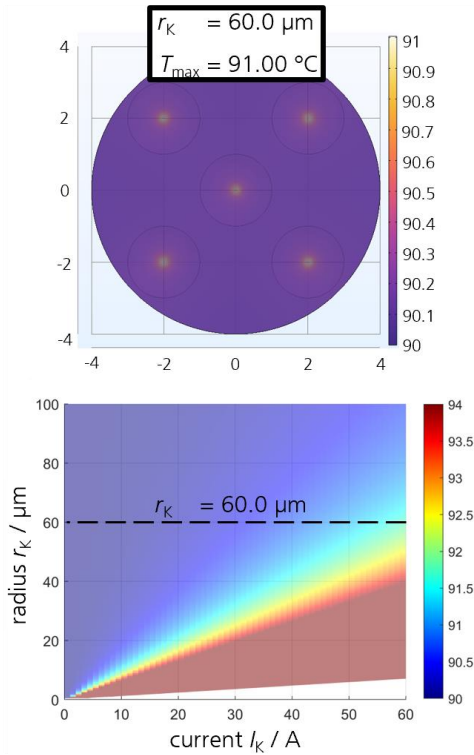
Figure 5. Comparison of the maximum temperature in an a-spot. Results from COMSOL Multiphysics (top) and results from analytical design map (bottom)

It can be stated that the FE-simulation leads to a maximum temperature of 91.0 °C and the analytical design approach to 91.5 °C. The temperature of the boundary surfaces is 90.0 °C. Consequently, the design approach can be verified. In addition, investigations were also carried out into the mutual influence of the a-spots. It was found that the distances between the microcontacts are so large that no interaction takes place. This can also be confirmed by analytical approaches, see [5].

$$l > 20 \cdot r_K \tag{6}$$

Here, l describes the average distance between the a-spots and r_K, as already mentioned, the current a-spot radius.

4. Manufacturing of the microstructure

After dimensioning the face contact with microstructure, manufacturing is carried out using laser ablation. This production process is ideally suited for manufacturing prototypes with high accuracy. For the patterning experiments, an Nd:YVO$_4$-doped picosecond laser with a wavelength of 532 nm and a maximum average output power of 8 W was used. The linearly polarized Gaussian laser beam was focused to a focal diameter of 11 μm using a f-θ lens array with a focal length of 100 mm. The workpiece was microstructured using Direct Laser Writing (DLW).

As a result, Figure 6 shows the manufactured face contact with five microstructures. The microstructure was applied to a cylinder with a diameter of 8 mm (see Figure 4). The counter body is a flat cylinder with a diameter of 8 mm. It should be noted that the face contacts will later be provided with a special coating to minimize wear. These coatings are developed by the Fraunhofer Institute for Surface Engineering and Thin Films IST.
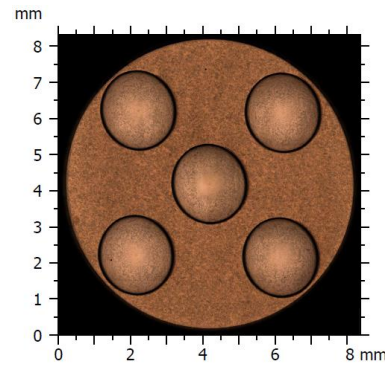
Figure 6. Face contact with five microstructures – surface manufactured by laser ablation

5. Surface measurement of the microstructure

Finally, the finished surface with five microstructures is measured using a confocal microscope MarSurf CM mobile from Mahr. Figure 7 shows a perspective view of face contact II.
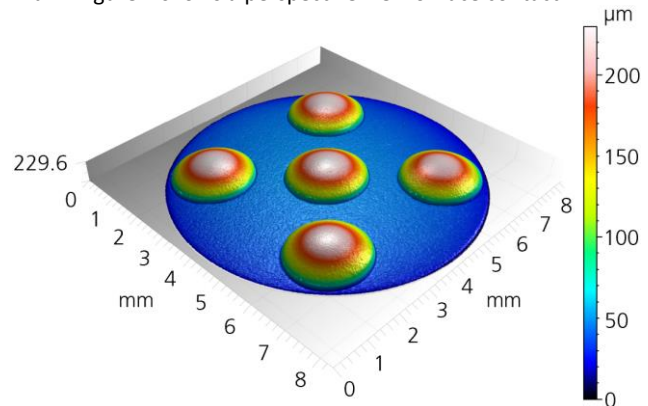
Figure 7. Face contact with five microstructures (perspective view) – surface measured with confocal microscope (Mahr)

A visual inspection already indicates a high quality regarding the geometry of the microstructures as well as their surface roughness. In the next step, they should be evaluated using a geometry and roughness analysis. For this, a profile cut is made first through three of the microcontacts and then evaluated (see Figure 8).
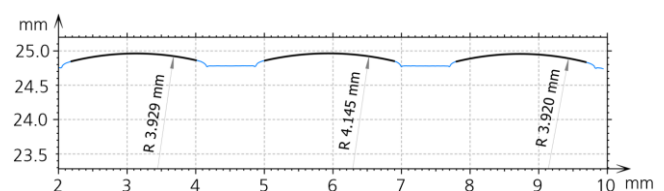
Figure 8. Evaluation of the surface profile – surface measured with confocal microscope (Mahr)

As can be seen from the diagram, the profile curve is well reproduced. The maximum deviation from the specified contour ($R_K = 4$ mm) is $f = 3.625$ % (average radius deviation). In the following, roughness evaluation is focused at the central microcontact. Surface roughness values according to DIN EN ISO 25178 and roughness derived from 10 single profiles are evaluated, see Table 1. Therefore, the spherical shape was eliminated and filtering was carried out.

Table 1 Roughness evaluation according to DIN EN ISO 25178 and DIN EN ISO 21920 of the central microstructure

DIN EN ISO 25178, $\lambda_c = 0.8$ mm	
S_a [µm]	0.267
S_k [µm]	0.830
S_{pk} [µm]	0.411
S_{vk} [µm]	0.450
DIN EN ISO 21920, $\lambda_s = 2.5$ µm, $\lambda_c = 0.8$ mm	
R_z [µm]	1.672
R_a [µm]	0.244

The high surface quality previously assumed visually is confirmed by the low roughness values. Consequently, the laser ablation process is very suitable for producing microstructured face contacts.

For later series production or volume production, a forming or replication process must be developed after completion of the prototype development.

6. Conclusion and Outlook

This paper describes a design approach that enables the dimensioning of electrical contact surfaces for fast charging systems. The aim is to design a face contact in such a way that a high current flow can be transmitted. The designed microstructure of spherical segments was optimized with regard to the constriction resistance and the maximum temperature occurring at the a-spot. After the analytical design, the face contact with microstructure was validated in COMSOL Multiphysics. The following results were obtained:
i. The physical principle of face contacts can be confirmed.
ii. The required current flow leads to identical maximum temperatures as in the analytical design.
iii. There are no interfering interactions between the microcontacts.
After the design, the face contact with microstructure was manufactured by laser ablation. The subsequent measurement with a confocal microscope shows that this method leads to very good surface quality and geometry.

In further investigations, the manufactured face contacts with microstructure will be tested experimentally. On the one hand, the functional principle should be checked and, on the other hand, the actual contact resistance should be determined. Therefore, a special test bench will be developed and equipped with appropriate measurement technology. Cyclic tests, tests at different current levels and wear tests will also be carried out.

After completion of all developments, a demonstrator of a fast charging system will be introduced together with the Fraunhofer Institute for Transportation and Infrastructure Systems IVI as well as the Fraunhofer Institute for Surface Engineering and Thin Films IST, which will enable energy transmission up to the megawatt range.

References

[1] Holm R 1967 Electric Contatcs: Theory and Application *Springer*: *Berlin/Heidelberg*
[2] Leidner M 2009 Kontaktphysikalische Simulation von Schichtsystemen *Darmstadt*
[3] Greenwood J A 1966 Constriction resistance and the real area of contact *BRIT. J. APPL. PHYS.* **17** 1621-32
[4] Israel T 2020 Verhalten von Hochstrom-Steckverbindungen mit Kontaktelementen bei kurzer Strombelastung *Dresden*
[5] Schlegel S 2019 Stromführende Verbindungen und Leiterwerkstoffe der Elektroenergietechnik *Dresden*
[6] Dankat G G and Dumitran L M 2022 Computation of the Electrical Resistance of a Low Current Multi-Spot Contact *Mater.* **15** 2056-69

Off-Axis Fast-tool-servo diamond turning of customized intraocular lenses from hydrophobic acrylic polymer

W. Wang[1], O. Riemer[1,2], K. Rickens[1], T. Eppig[3,4], B. Karpuschewski[1,2]

[1]*Laboratory for Precision Machining LFM, Leibniz Institute for Materials Engineering IWT, Germany*

[2]*MAPEX Center for Materials and Processes, University of Bremen, Germany*
[3]*AMIPLANT GmbH, Germany*
[4]*Institute of Experimental Ophthalmology, Saarland University, Germany*

wang@iwt-bremen.de

Abstract

Intraocular lenses (IOLs) are small optical devices for implantation into the human eye to substitute the opacified natural crystalline lens (cataract). The requirement for such cataract surgery arises when the opacification significantly impedes vision in order to prevent blindness. To date, apart from moulding, the prevailing method for manufacturing IOLs is single-piece on-axis diamond turning especially for small batch production and product variability as in toric lenses. In the scope of this project, an exploration of alternative techniques, i.e. off-axis diamond turning with fast-tool-servo (FTS), will be undertaken to increase the productivity and to manufacture highly customized lenses; a vacuum clamping device aiming to enable the simultaneous processing of multiple pieces will be developed. Specifically, hydrophobic acrylic polymer where cooling is required, rather than hydrophilic materials, will be used as raw materials, in order to meet the increasing market demand for hydrophobic IOLs.

The primary objective is to improve production efficiency by realizing faster, more resource-efficient, and ultimately more cost-effective manufacturing processes. In this contribution, principal process designs for FTS machining including vacuum clamping of hydrophobic blanks are discussed and particular solutions are demonstrated; the collected manufacturing data using FTS off-axis diamond turning are analysed.

Manufacturing (CAM); Material; Turning; Ultra-Precision

1. Introduction

In progressed age, the transparency of the natural lens gradually decreases, i.e. cataract, and vision deteriorates, which can even lead to blindness without treatment. The only known effective treatment for cataract is to surgically substitute the cloudy lens with an intraocular lens (IOL) [1]. In Germany, about 800,000 cataract surgeries are conducted annually [2]. The productivity of customized IOLs is yet limited to maximal 4,000 pieces per machine per year, which is much lower than the need. A potential solution to increase the productivity is parallelized processing with FTS, whose application in optical surface manufacturing has been proved [3].

Standard foldable IOLs are made of hydrophilic or hydrophobic acrylic polymer. Compared to the IOLs made of hydrophilic polymer, hydrophobic ones are advantageous for preventing the after-cataract - an excessive growth reaction of remaining epithelial cells of the natural lens after surgery [1]. However, since the glass transition temperature T_g of available hydrophobic acrylic polymer is distinctly lower than room temperature, it can only be continuously manufactured with in-process cooling.

In this paper, we discuss the principal process designs of alternative techniques for customized hydrophobic IOL production, i.e. off-axis diamond turning with FTS, including vacuum clamping device and embedded in-process cooling function. This process design aims at increasing the production efficiency of IOLs by parallelized processing.

2. Principle process designs for FTS off-axis turning

The simultaneous diamond turning of multiple free-form surfaces is only possible with the additional degree of freedom offered by FTS.
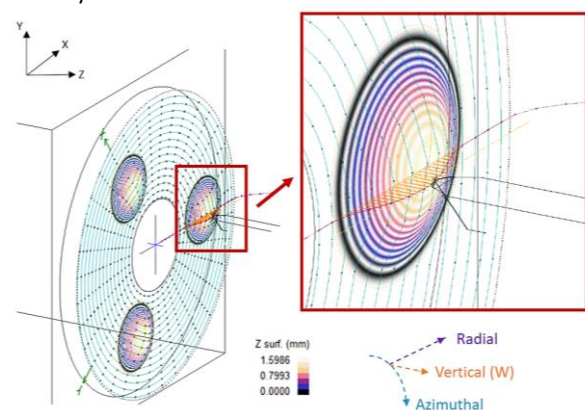
Figure 1. CAM simulated tool path in azimuthal, radial and W directions; Sample IOLs with cutting path area (D = 50 *mm*, blue) and lens geometry (d = 6 *mm*, coloured)

Figure 1 shows the simulated diamond tool path in the CAM software Precitech/Ametek Diffsys, where the point cloud above the three IOLs (coloured) and the entire clamping device represents the information for the computer numerical control (CNC). In contrast to conventional on-axis turning, for off-axis turning with FTS, the diamond tool exhibits not only radial motion but also expeditious perpendicular movement

concerning the clamping device in vertical direction, while the clamping device rotates in azimuthal direction.

Two prerequisites must be satisfied to transition from simulation to processing: clamping device that can concurrently secure three IOLs while facilitating in-process cooling, and assessing the feasibility of using FTS for polymer processing.

3. Clamping device and embedded in-process cooling

The three vacuum fixing positions align with the relative positions of the sample IOLs in figure 1, forming a rotational symmetric distribution on the clamping device with an included angle of 120°. The upper side of figure 2 depicts air evacuation from the backside through vacuum channels, ensuring uniform pressure dispersion across the polymer blank's surface via a porous vacuum insert to prevent localized pressure damage. To maintain blank temperature below the T_g, continuous cooling is applied through a ribbed structure, with cold air injected at the rear and exiting at the front (lower side of figure 2).
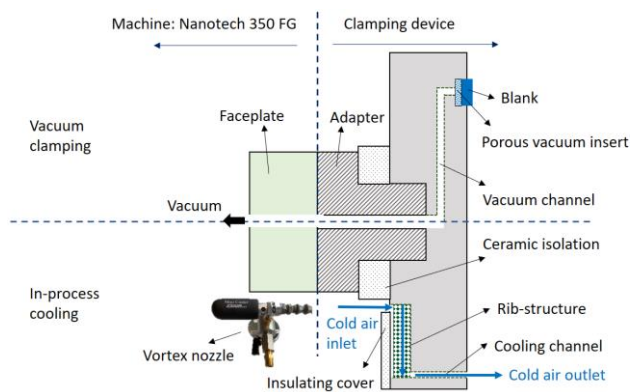
Figure 2. Design of vacuum clamping device (upper) and embedded in-process cooling function (lower)

A simplified vacuum clamping device (figure 3) was used for testing the cooling effects statically. A vortex nozzle, at 8 *bar* pressure, 200 *l/min* flow, and 20℃ starting temperature, was employed. This includes porous vacuum inserts of three materials (aluminum with pore diameters of 15 *μm* and 400 *μm*, poroplastic with a pore diameter of 10 *μm*) paired with blanks of two materials (polymethylmethacrylate (PMMA) and steel).
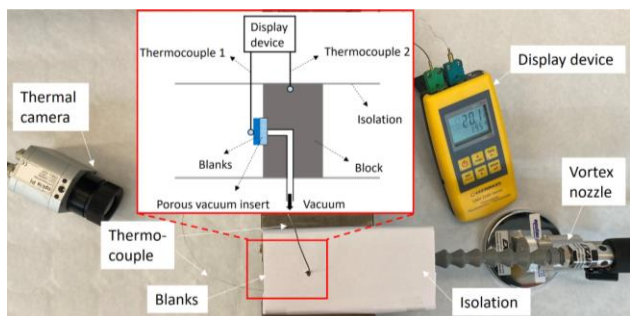
Figure 3. Experimental setup for the cooling performance test

As can be seen from figure 4, the porous vacuum insert made of aluminum with pore diameters of 15 *μm* has the best thermal conductivity; at the same time, smaller pores are advantages for protecting the optical surfaces. Overall, aluminum with pore diameters of 15 *μm* is the best suited of the three materials. Yet the lowest temperature (10℃) with vortex nozzle is still higher than T_g (7℃), and a cooling device with higher power is inevitable.
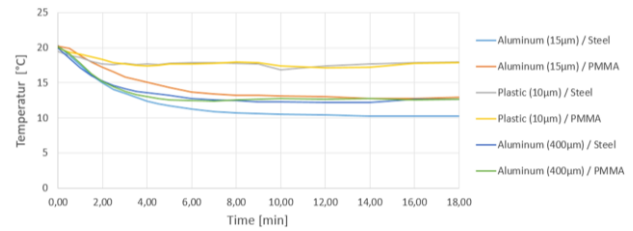
Figure 4. Cooling performance test results under different material combinations, legend: porous vacuum insert / blank.

4. Diamond turning of PMMA with FTS

Since hydrophobic materials must be cooled to be machined precisely, PMMA, which is common for IOL manufacturing, was chosen to test machinability with FTS. On the surface of a 60 *mm* diameter PMMA blank, a lens array composed of four concave lenses with diameter of 4.5 *mm* was processed using a machine tool 350 FG and NFTS 6000 from Moore Nanotechnology Systems (figure 5).
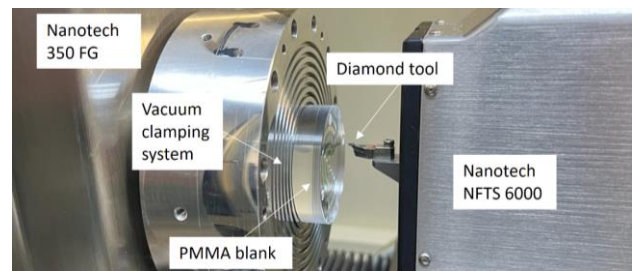
Figure 5. Experimental setup for the machinability test of PMMA

With the depth of cut a_p of 50 *μm*, feed rate v_f of 2 *mm/min*, turning speed *n* of 100 *1/min* and tool's corner radius r_ε of 0.5 *mm*, the above mentioned lens array is successfully processed with a rough surface quality, indicating principally the machinability of PMMA using FTS.

5. Conclusion and future work

We introduced the principle process design for off-axis diamond turning with FTS for the manufacture of hydrophobic IOLs. Two key aspects are addressed: testing materials for the porous vacuum insert and evaluating FTS feasibility for polymer processing. Experimental results favour porous aluminum (15 *μm*) for the vacuum insert, and FTS proves effective with PMMA. Future research will concentrate on developing and testing the complete off-axis clamping device with in-process cooling. We will investigate the processing parameters for machining hydrophobic polymer under cooled condition.

Acknowledgements

References

[1] Kohnen T, Baumeister M, Kook D, Klaproth O K and Ohrloff C 2009 Cataract surgery with implantation of an artificial lens *Dtsch. Arztebl. Int.* **106** 695-702

[2] Wenzel M, Pham D T, Scharrer A, Schayan-Araghi K and Klasen J 2009 Outpatient Intraocular Surgery: Outcome of the 2008 Survey by BDOC, BVA and the DGII – Review of the past 20 years *OPHTHALMO SURGER* **21** 199-211

[3] Boinski A-K, Riemer O, Kapuschewski B, Schneider M, Guttmann M and Worgull M 2022 Fast tool machining and hot embossing for the manufacture of diffractive structured surfaces *Precision Engineering* **74** 12-9

Fully compliant snap-through bistable gripper mechanism based on a pinned-pinned buckled beam

Loïc Tissot-Daguette[1], Simón Prêcheur Llarena[1], Charles Baur[1] and Simon Henein[1]

[1]Instant-Lab – IMT – STI – EPFL

loic.tissot-daguette@epfl.ch

Abstract

This paper presents a new planar flexure-based bistable two-jaw parallel gripper mechanism. The bistability of the mechanism is enabled by a pinned-pinned buckled beam suspended onto two cross-spring pivots. External energy is required only during the switching between the two stable states: open and closed jaws. This is particularly advantageous in gripping applications where power consumption is a limiting factor. Since it is based exclusively on flexure elements, this gripper mechanism is free from friction, wear and lubricant and is well suited for cleanroom environments, biomedical applications, or space environments. Another key feature is that the jaw opening/closing motion is based on fast snap-through transitions of the buckled beam, relying on an actuator motion which can be comparatively slow. This is highly beneficial for high-speed pick-and-place applications. Furthermore, the elastic decoupling between the actuator and the jaws allows the gripper to safely apply a limited output force to the grasped object, regardless of the force supplied by the actuator. In this article, the nonlinear load-deformation behaviors of the gripper are analytically modeled using Euler-Bernoulli beam theory and validated using finite element modeling. A prototype of the gripper mechanism with an external size of 10 mm x 35 mm x 85 mm was monolithically manufactured out of steel using wire electrical discharge machining. A voice coil actuator is integrated for actuation. The load-deformation characteristics, as well as the time to switch state, were measured on the prototype using a dedicated testbed. The experimental data are in good agreement with the theoretical models. The results show a stable gripping force of 1 N, a maximum stroke per jaw of 1.7 mm, and a state switching time (i.e., snap-through time) below 7 ms demonstrating high-speed gripping performances in comparison to state-of-the-art grippers.

Gripper, Mechanism design, Compliant mechanism, Flexures, Beam buckling

1. Introduction

Bistable grippers have the benefit of not requiring power to maintain the gripping and open states. This ability is extremely valuable in applications where energy consumption must be minimized and if the gripper may remain in closed or open state for extended periods of time, e.g., for drone perching [1] or for space applications [2]. Furthermore, if made fully compliant, bistable grippers are free from friction, wear and lubricant, and can thus be conveniently utilized in cleanroom or surgical environments [3].

In this work, a novel planar parallel fully compliant bistable gripper based on pinned-pinned buckled beam is presented. This bistable gripper exhibits rapid state switching created by snap-through. Thanks to the elastic decoupling between the actuation input and the jaws, the gripping output force is limited to a specific value. This is highly beneficial for preventing the damage of the grasped object [4]. The work will, first, describe the working principle of the gripper mechanism. Next, based on analytical modeling, a prototype is designed and fabricated. Experiment is then conducted to validate the design and modeling. Finally, a linear voice coil actuator is integrated to the bistable gripper to evaluate its dynamic performances.

2. Description and working principle

The ideal kinematics of the gripper mechanism is presented in Fig. 1a. Two parallelogram linkages are implemented to guide the jaws in translation. Both jaws are linked by an reverse-motion linkage to ensure that the jaws translate in opposite direction with the same displacement magnitude x_{out}. The rotating lever of the reverse-motion linkage is attached to a pin joint (called *output pivot*) and is connected to one extremity of an initially straight buckling beam. At its other extremity, the buckling beam is attached to a lever which is free to rotate around a second pivot joint (called *input pivot*). The two pinned extremities of the buckling beam can be brought togther by a displacement Δl using a preloading stage which is guided by a parallelogram linkage. This displacement causes the buckling beam to buckle, allowing the mechanism to exhibit a bistable behavior. When the gripper is in a stable position (open or closed), the gripper output state is maintained without requiring additional energy. The gripper state can be switched by actuating the input pivot. At specific values of the input angle θ_{in}, the mechanism reaches a snap-through instability where the output angle θ_{out} suddenly varies to close or open the jaws.

In order to make the gripper structure fully compliant, to be fabricated monolithically, the ideal joints in Fig. 1a are implemented by flexures, as seen Fig. 1b. The input and ouput pivots are embodied by cross-spring flexure pivots and parallelogram linkages by parallel leaf spring stages. The connecting rods of the reverse-motion linkage are replaced by simple blades. The precompression displacement Δl can be adjusted using a preloading screw (Fig. 1c). This adjustement can be used to tune the output jaw stroke x_{out} and the gripping force F_{out}. Furthermore, a lateral screw can be used to limit the jaw stroke to a specific value (see Figs. 1c and 1d). As we will see in Sec. 7.2, this second screw is used to reduce the vibration of the jaws.
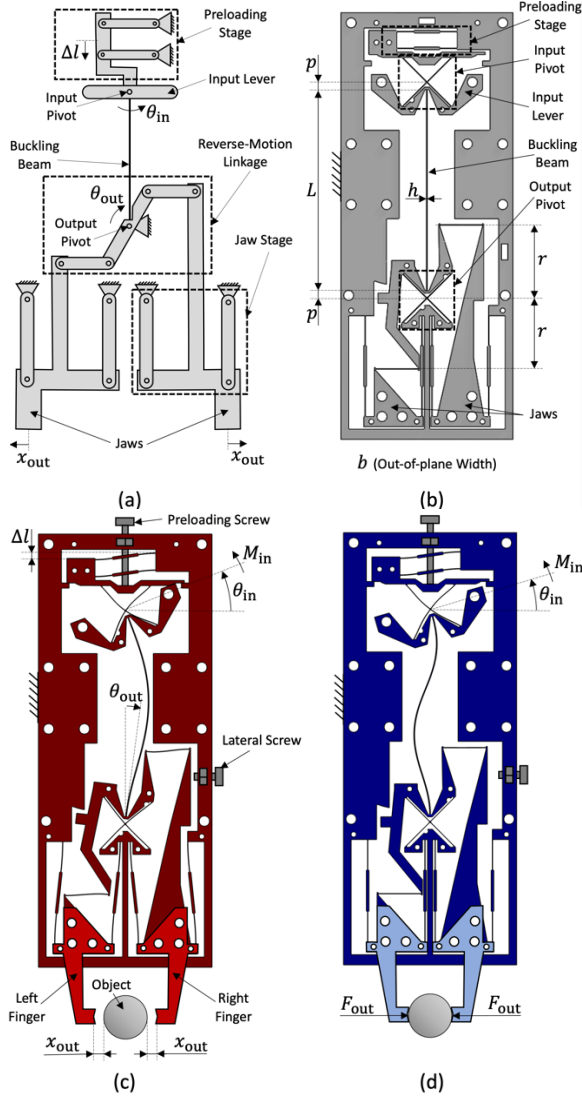
Figure 1. (a) Ideal kinematics of the gripper mechanism. Flexure-based gripper mechanism (b) in its fabricated position, (c) in open stable state and (d) in closed unstable state.
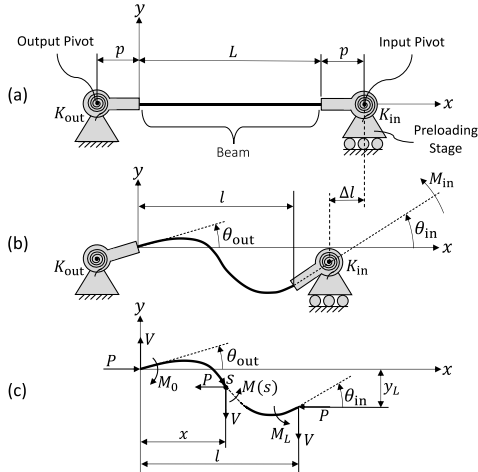
Figure 2. (a) As-fabricated, (b) deformed and (c) free-body diagram of the buckling beam.

3. Analytical model

A theoretical model is derived in order to characterize the nonlinear actuation behaviors of the gripper. To achieve that, the load-deflection characteristics of the buckling beam is first computed, then the gripping force and the jaw displacement are derived.

3.1. Buckled beam load-deflection characteristics

The schematic view of the buckling beam deflection is presented in Fig. 2. In this simplified schematics, the torsional springs K_{in} and K_{out} correspond to the equivalent angular stiffnesses resulting from the flexures at the input and output pivots, respectively. The buckled beam has a flexural rigidity EI and an initial length L. The distance p between the center of rotation of the pivots and the beam extremities is considered. Using the same modeling approach as in [5], the generic deflection y of a buckled beam can be expressed by:

$$y(s) = A\sin(ks) + B(\cos(ks) - 1) + Cs \qquad (1)$$

where $k = \sqrt{P/EI}$ and s is the arclength position. After integrating the boundary conditions, i.e., $y'(s = 0) \cong \theta_{out}$, $M_0 \cong K_{out}\theta_{out} + Vp - Pp\theta_{out}$, $y(s = L) \cong -p(\theta_{out} + \theta_{in})$ and $y'(s = L) \cong \theta_{in}$, in Eq. (1), the deflection parameters A, B and C are respectively given by:

$$A = \frac{-L\theta_{in}\big((1 + 2\bar{p})(kL)^2 + \varepsilon_{out}(\bar{p}kL\sin(kL) + 1 - \cos(kL))\big)}{kL\Big(((\bar{p} + \bar{p}^2)(kL)^2 - \varepsilon_{out} + 1)kL\sin(kL) - ((kL)^2 + 2\varepsilon_{out})\cos(kL) + 2\varepsilon_{out}\Big)} \qquad (2)$$

$$B = -\frac{M_0}{P} = \frac{-L\theta_{in}\big((\bar{p} + 2\bar{p}^2)(kL)^3 + \varepsilon_{out}(\bar{p}kL(\cos(kL) - 1) - kL + \sin(kL))\big)}{kL\Big(((\bar{p} + \bar{p}^2)(kL)^2 - \varepsilon_{out} + 1)kL\sin(kL) - ((kL)^2 + 2\varepsilon_{out})\cos(kL) + 2\varepsilon_{out}\Big)} \qquad (3)$$

$$C = \frac{V}{P}\frac{l}{L} \cong \frac{V}{P} = \frac{-\theta_{in}\big((\bar{p}^2(kL)^2 - \varepsilon_{out}\bar{p} - 1)kL\sin(kL) + (-2\bar{p}(kL)^2 + \varepsilon_{out})\cos(kL) - \varepsilon_{out}\big)}{((\bar{p} + \bar{p}^2)(kL)^2 - \varepsilon_{out} + 1)kL\sin(kL) - ((kL)^2 + 2\varepsilon_{out})\cos(kL) + 2\varepsilon_{out}} \qquad (4)$$

where $\bar{p} = p/L$ and $\varepsilon_{out} = K_{out}/(EI/L)$. The end-shorting can be approximated with the following equation:

$$\Delta l \cong \frac{p}{2}\big(\theta_{in}^2 + \theta_{out}^2\big) + \int_0^L \frac{y'(s)^2}{2}ds = H(kL)\,L\theta_{in}^2 \qquad (5)$$

where from [5]:

$$H(kL) = \frac{(\bar{A}^2 + \bar{B}^2)(kL)^2}{4} + \frac{(\bar{A}^2 - \bar{B}^2)kL\sin(2kL)}{8} + \frac{\bar{A}\bar{B}kL(\cos(2kL) - 1)}{4} + \bar{A}\bar{C}\sin(kL) + \bar{B}\bar{C}(\cos(kL) - 1) + \frac{\bar{C}^2}{2} + \frac{\bar{p}}{2}((\bar{A}kL + \bar{C})^2 + 1) \qquad (6)$$

where the deflection parameters are normalized as follows: $\bar{A} = A/(L\theta_{in})$, $\bar{B} = B/(L\theta_{in})$ and $\bar{C} = C/\theta_{in}$. By rearranging Eq. (5), the input angle can be evaluated as a function of kL:

$$\theta_{in} = \pm\sqrt{\frac{\Delta l}{L}}\sqrt{\frac{1}{H(kL)}} \qquad (7)$$

The input moment can be written as follows:

$$M_{in} \cong M_L + Vp - Pp\theta_{in} + K_{in}\theta_{in} = \frac{EI}{L}((kL)^2(\bar{p}(\bar{C} - 1) - \bar{A}\sin(kL) - \bar{B}\cos(kL)) + \varepsilon_{in})\theta_{in} \qquad (8)$$

where $M_L = EIy''(s = L)$ and $\varepsilon_{in} = K_{in}/(EI/L)$ is the relative input stiffness.

3.2. Output force-displacement characteristics

Considering that the reverse-motion linkage has a lever length r (see Fig. 1b), the force-displacement characteristics of the jaws is related to the moment and angle of the buckling beam output pivot as follows:

$$F_{\text{out}} = \frac{M_0 - Vp}{2r} = -\frac{EI}{L} \frac{(\bar{B} + \bar{C}\bar{p})(kL)^2 \theta_{\text{in}}}{2r} \tag{9}$$

$$x_{\text{out}} \cong r\theta_{\text{out}} = r(\bar{A}kL + \bar{C})\theta_{\text{in}} \tag{10}$$

Note: While the gripper is in closed and open states, F_{out} and x_{out} are respectively assumed to be null.

4. Prototype design

Using the analytical model, a flexure-based mesoscale embodiment of the compliant structure was designed and manufactured with wire-cut electrical discharge machining (EDM) process. The selected material of the compliant structure is steel (Böhler K390), with a yield strength $\sigma_y = 2300$ MPa and Young's modulus $E = 220$ GPa. The cross-spring pivots at the input and output of the buckling beam have equal dimensions. Their angular stiffness can be calculated from [6] as $K_{\text{p}} = 2Ebh_{\text{p}}^3/(3L_p)$, where h_p is the thickness and L_p is the total diagonal length of the crossed blades. The input angular stiffness K_{in} is simply equal to K_{p}. In open state, the output angular stiffness constant $K_{\text{out,open}}$ is evaluated from Finite Element Method (FEM), to make modeling simpler. In closed state, $K_{\text{out,closed}}$ tends to infinity assuming that the object and the fingers are considerably stiff. The parameters of the fabricated gripper mechanism are summarized in table 1.

Table 1 : Design parameters (see Figs. 1 and 2)

	Parameter	Value
Mechanism width	b	10 mm
Preloading stage	Δl	1.25 mm
Buckling beam	h	150 µm
	L	40 mm
	p	2 mm
Cross-spring pivots	h_{p}	60 µm
	L_{p}	11.2 mm
Reverse-motion linkage	r	14 mm
Equivalent angular stiffnesses	K_{in}	28.3 Nmm/rad
	$K_{\text{out,open}}$	211 Nmm/rad

5. FEM and experimental characterization

A 2D static FEM study is carried out on Comsol Multiphysics 5.4 to verify the analytical model and the gripper design. The nonlinear load-deformation characteristics of the gripper are simulated by varying the input pivot angle θ_{in}. Deflection solutions of the study are illustrated in Figs. 1c and 1d and the FEM data are reported in Sec. 7.1.

The load-deformation characteristics of the gripper prototype are experimentally evaluated using a dedicated test bench, see Fig. 3. The setup includes a manual micrometer linear stage to push the mechanism input lever by an angle θ_{in} through a force sensor (Kistler Model 9207) in order to measure the applied input torque M_{in}. The angle θ_{in} and the displacement x_{out} of one of the jaws are recorded by laser displacement sensors (Keyence Model LK-H082). A second identical force sensor placed in-between the two jaws measures the gripping force F_{out}. The mechanism is characterized, for both opening and closing transitions, from the corresponding stable state until snap-through. Data acquisition is performed after each increment of the linear stage position when the system is steady in order to assess quasi-static measurements.
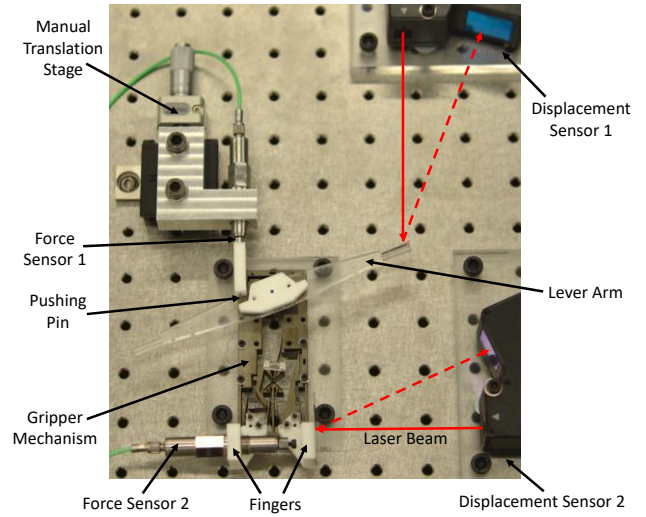
Figure 3. Test bench used to characterize the gripper mechanism.

6. Actuator integration

Based on the gripper actuation requirements obtained from the models and the experiment, we have selected a linear voice coil motor (Moticont LVCM-025-022-01) for the actuation of the gripper input pivot (Fig. 4). A 3D-printed monolithic compliant coupling mechanism is based on a parallel leaf spring stage to guide the coil holder with respect to its fixed frame. A flexure-based connecting rod and a lever arm are used to convert the linear motion of the coil into a rotation to angularly actuate the input pivot. The proposed control strategy consists in applying a constant electrical current in the voice coil such that the applied moment exceeds the opening and closing critical moments (Fig. 5) in order to switch the gripper states.
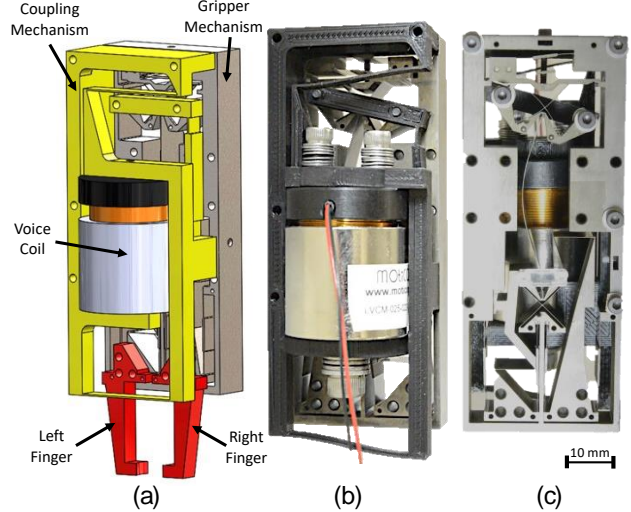
Figure 4. Assembly of the bistable gripper with voice coil actuator. (a) Schematic (with mounted fingers), and photographs with (b) front and (c) back views.

7. Results and discussion

7.1. Actuation characteristics

The analytical results of the actuation characteristics as well as the ouput force and displacement are illustrated in Fig. 5 (where the blocking effect of the lateral screw is not taken into account). Using Eqs. (7)-(10), the analytical parametric curves are traced out as the parameter kL ranges from 1.4π (near the closed stable state) to 2.4π (at the unstable position) and from 1.3π (near the open stable state) to 2.2π (at the unstable position) for the closed and open gripper states, respectively. The FEM and experimental data are added in Fig. 5 to evaluate the

accuracy of the analytical model. Since the error between the analytical and FEM models is bounded within 5%, the analytical modeling derived in Sec. 3 is validated. Some discrepancies between the experimental data and the models (15% maximum difference) are assumed to be due to manufacturing tolerances and measurement errors.
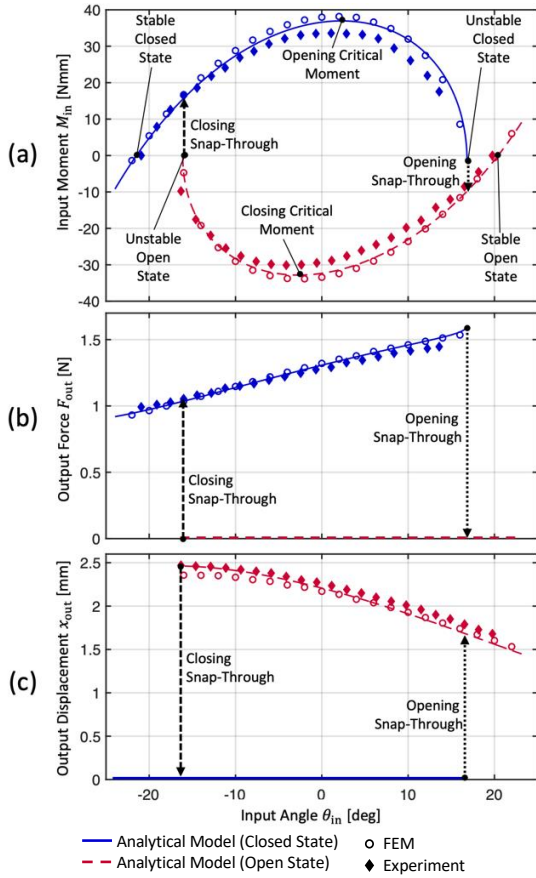
Figure 5. (a) The input moment, (b) the output force and (c) the output displacement as a function of the input angle.

As can be observed in Fig. 5(a), the gripper is in a stable equilibrium at $\theta_{in} = 20°$ and $\theta_{in} = -21°$ and reaches unstable states at $\theta_{in} = -16°$ and $\theta_{in} = 17°$, when open and closed, respectively. When the unstable gripper states are outreached, snap-through under angle control occurs. This causes hysteresis in the actuation. During both closing and opening sequences, the input moment M_{in} reaches a maximum magnitude, see Fig. 5(a). In order to switch the gripper state, the actuator must hence be able to apply these critical moment values. The snap-through transitions lead to discontinuous changes at the gripper output as can be see in Figs. 5b and 5c. In stable closed and open states, F_{out} and x_{out} are constant and equal to 1 N and 1.7 mm, respectively. During actuation to switch the gripper state, F_{out} and x_{out} increase until they reach a limited value, just before snap-through, of 1.6 N and 2.5 mm, respectively. This shows that the gripper has force limitation properties and that the gripper will continuously apply a force on the gripping part during the opening, and will always be open during the closing transition.

7.2. Dynamic behavior

The dynamic response of the gripper prototype actuated by the voice coil is recorded with a high-speed camera (IDT NX4-S3) at a frame rate of 5000 Hz. Based on the video frames and timing, table 2 reports the durations of the *actuation* (when the actuator starts to move until snap-through occurs), *snap-through* (until the gripper reaches its final state), and *stabilization* (until the gripper is stable within 10% error with respect to its final state). The video of the dynamic testing is

available here: https://youtu.be/LWhnJjIXFwo. In this experiment, the lateral screw is used to limit the jaw displacement to $x_{out} = 1.4$ mm. Without the lateral screw, the opening stabilization time is in the order of 1 s, which is impractical for high-speed pick-and-place applications. Indeed, the jaws would oscillate around the stable open position with low energy disspation (due to the absence of solid friction in flexure mechanisms). Even when the lateral screw is used, some vibrations of the flexures remain at the output. To further reduce the stabilization time, damping systems would need to be added to the gripper output.

Snap-through allows the gripper to advantageously, change states rapidly. Yet, impacts on the object to be grasped might be relatively important. For brittle objects, one could consider adjusting the compliance of the fingers to limit the shock level.

Because the gripper input and output are substantially decoupled until snap-through (see Fig. 5), the operations can be cascaded. For instance, the actuation can begin before the jaws are fully stabilized.

Table 2 : Time durations of the gripper actuation sequences

	Sequence	Time [ms]
	Actuation	21.6
Opening	Snap-through	5.4
	Stabilization	28.8
	Actuation	26.4
Closing	Snap-through	6.6
	Stabilization	4.2

8. Conclusion

This work presents a novel fully compliant parallel gripper based on pinned-pinned buckled beam to achieve bistability. This bistable gripper, powered by a voice coil, demonstrates rapid opening and closing motions while requiring no additional energy to maintain its open or closed state. Thanks to the elastic decoupling between the actuation and the jaws, the gripping force is advantageously limited. In this paper, an EDM-wire cut monolithic gripper is designed, modeled and fabricated. Experimental results are in good agreement with the established models, and exhibit a maximum total jaw aperture of 3.4 mm and stable gripping force of 1 N. Dynamic testing shows a snap-through time in the order of 7 ms for both closing and opening sequences. Future work will include designing and integrating Shape Memory alloy (SMA) actuators to actuate this gripper with minimized time response and compact volume.

References

[1] Zhang H, Lerner E, Cheng B and Zhao J 2021 Compliant bistable grippers enable passive perching for micro aerial vehicles *IEEE ASME Trans. Mechatron.* **26** 2316-2326

[2] Zhang Y, Quan J, Li P, Song W, Zhang G, Li L and Zhou D 2023 A flytrap-inspired bistable origami-based gripper for rapid active debris removal *Adv. Intell. Syst.* **5** 2200468

[3] Lassooij J, Tolou N, Tortora G, Caccavaro S, Menciassi A and Herder J 2012 A statically balanced and bi-stable compliant end effector combined with a laparoscopic 2DoF robotic arm *Mech. Sci.* **3** 85-93

[4] Liu Y, Zhang Y and Xu Q 2017 Design and control of a novel compliant constant-force gripper based on buckled fixed-guided beams *IEEE ASME Trans. Mechatron.* **22** 476-486

[5] Tissot-Daguette L, Schneegans H, Thalmann E, Henein S 2022 Analytical modeling and experimental validation of rotationally actuated pinned–pinned and fixed–pinned buckled beam bistable mechanisms *Mech. Mach. Theory* **174** 104874

[6] Cosandier F, Henein S, Richard M, Rubbert L 2017 *The art of flexure mechanism design* EPFL Press Lausanne

Highly efficient flattening and smoothing process for Poly Crystalline Diamond substrates by combining laser-trimming and plasma-assisted polishing

Sota Sugihara[1], Dong Jiayuan[1], Sun Rongyan[1], Yuji Ohkubo[1], Kazuya Yamamura[1]

[1]Research Center for Precision Engineering, Graduate School of Engineering, Osaka University, Osaka, Japan

yamamura@prec.eng.osaka-u.ac.jp

Abstract

Semiconductor power devices are expected to be applied to electric vehicles and power generation technology because of their high energy efficiency. However, performance degradation due to self-heating is a serious problem. Therefore, it has been proposed to bond a power device to a diamond substrate, which has the highest thermal conductivity in all materials can improve the heat extraction from power device and lower temperature of the device. To bond a diamond substrate and a power device, it is necessary to polish the diamond substrate to an atomic level smoothness. However, diamond is the hardest material and a surface of diamond substrate after CVD growth has large waviness, so it requires a very long polishing time. Therefore, we applied a laser-trimming process to remove large waviness efficiently. In this process, a Poly Crystalline Diamond (PCD) substrate whose shape has been measured in advance is subjected to numerically controlled processing for each contour line in units of ablation depth to remove the undulations and flatten the substrate. By applying laser-trimming, we succeeded in reducing the low-frequency waviness component of approximately 150 µm p-v existed on the surface of the PCD substrate to approximately 50 µm p-v. Then, we smoothed the PCD substrate after the laser-trimming by plasma-assisted polishing (PAP). As a result, the PCD substrate, which was Sa 9.6 µm after CVD growth, was polished to less than Sa 11 nm. It was also confirmed that the surface layer that had been graphitized by laser-trimming was removed by PAP. In this paper, we report the results of our work on a planarization and smoothing process for PCD substrates by combining laser-trimming and PAP.

Keywords: Diamond, Finishing, Laser, Polishing

1. Introduction

Poly crystalline diamond (PCD) has very high thermal conductivity and high mechanical strength. In addition, it is cheaper than single-crystal diamond and can be easily made into large size. To bond a power device to a PCD for heat dissipation, the PCD surface must be made atomically smooth. Currently, Scaife polishing and CMP are widely used for diamond polishing, but Scaife polishing involves high polishing pressure, which introduces damage to the surface. On the other hand, CMP requires a long process time due to its low polishing rate. In addition, the slurry used in CMP is very costly. Therefore, a highly efficient damage-free polishing technique that does not use slurry is desired. Plasma-assisted polishing (PAP), a dry polishing technique that combines surface modification by plasma irradiation and removal of the modified layer by ultra-low pressure or using polishing plate, has been successfully applied to polish difficult-to machine materials such as SiC, GaN, and SCD [1-3]. However, since the PCD substrate produced by CVD growth has a very large waviness component, a very long polishing time is required even if PAP is applied.
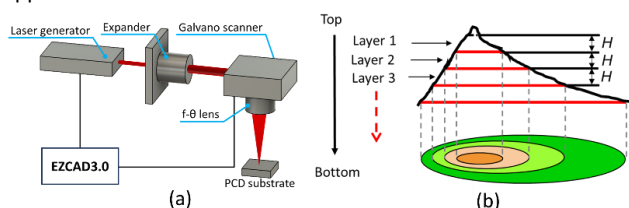
To solve this problem, laser-trimming, which removes the waviness component of the substrate by laser ablation, was introduced as a pre-polishing process. In this report, we present the results of smoothing of PCD substrates synthesized by CVD growth by laser-trimming and then applying PAP to the substrates.

2. Experimental Setting

2.1. Laser-trimming

Figure 1(a) shows the schematic of laser trimming setup. It is mainly consisted of a laser generator, a beam expander, a Galvano scanner, an f-theta lens, and software EZCAD3.0 for controlling laser scanning path. A fiber laser with a 1064 nm wavelength and a constant pulse duration of approximately 100 ns, supplied by Raycus Co. Ltd, was used in the following experiments. The following is an overview of the laser trimming process. First, the 3D shape of the PCD substrate was measured with SWLI (SWLI, NewView 8300 Zygo). Next, a 2D contour map was created from the measured 3D shape image using EZCAD3.0. An appropriate reference at the top areas is set and the points with H from the reference are connected to form a closed curve, which is the contour of the first layer of laser trimming (Layer 1), where H is the depth to be removed by the laser irradiation. The points with 2H from the reference are connected to form a closed curve, which is the contour of the second layer of laser-trimming (Layer 2), and so on, until the suitable points at bottom areas. Then, the substrate is flattened by removing each layer divided by the laser. Table 1 shows the parameters of laser-trimming of this experiment.

Figure 1. Schematic of laser-trimming setup

Table 1 Experimental parameters of laser-trimming

Power density	9.1 W
Spot size on target	40 μm
Repetition frequency	80 kHz
Scanning speed	600 mm/s
Filling space	7.5 μm
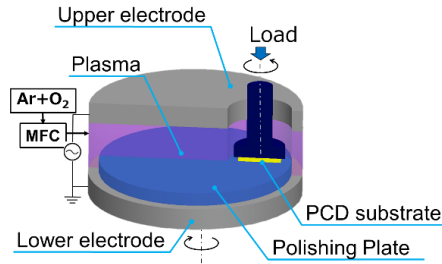
Figure 2. PAP experimental setting

2.2. Plasma-assisted Polishing

Figure 2 shows a schematic diagram of the PAP setup. It is composed of plasma generation and mechanical removal parts. Both parts are installed in a vacuum chamber, where the process gas composition and pressure are controlled. Plasma generation part is consisted of an upper electrode and lower rotary table, both made of aluminum alloy. The polishing plate made of quartz glass is fixed on a rotary table and PCD substrate is fixed on a rotating sample holder. The experimental parameters are shown in Table 2.

Table 2 Experimental parameters of PAP

Rotation speed	PCD substrate: 26 rpm, Polishing plate: 300 rpm (until 19h), 200 rpm (after 19h)
Polishing pressure	224 kPa
Flow rate	Ar: 200 sccm, O_2: 30 sccm
Chamber pressure	7 torr
RF power	100 W

3. Results and discussion

Figure 3 shows the scanning white light interferometer (SWLI) image and its cross-sectional profile of the entire PCD substrate before and after laser trimming. The initial shape of the PCD substrate was a concave shape with a p-v of about 150 μm in the cross section A1-A1'. By applying laser trimming for 1 m 59 s, the PCD substrate was flattened, and the p-v value was reduced to 50 μm. However, the surface of the PCD substrate turned into graphite, and high-frequency roughness component remained.

Next, we applied PAP to remove graphite component and high-frequency roughness component on the PCD substrate. PAP was performed on PCD substrates without and with laser trimming. Figure 4 shows the transition of the SWLI image of the surface when PAP was applied to PCD substrate without laser trimming and with laser trimming. Comparing Fig. 4(b) and (d), the PCD substrate without laser trimming had deep depressions after 26
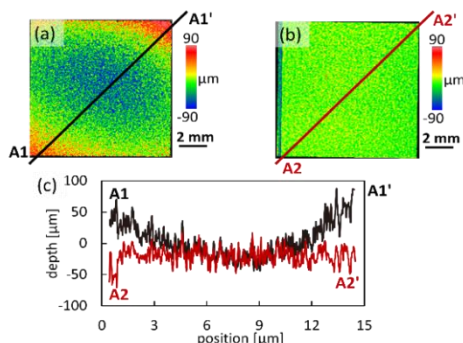
Figure 3. (a)(b) SWLI image of entire PCD substrate (a) initial (b) after laser-trimming, (c) cross-section of A1-A1' and A2-A2'.

hours of PAP (Fig. 4(b)). On the other hand, when applying laser trimming, the depressions disappeared at 26 hours of PAP (Fig. 4(d)). In addition, the surface was successfully improved from Sa 9.6 μm to Sa 11.0 nm after laser trimming (Fig. 4(c)(d)). These results indicate that the combination of laser trimming, and PAP is very useful for highly efficient smoothing of PCD substrates.

Figure 5 shows the results of Raman spectroscopy evaluation of the crystal structure of the PCD substrate in its initial state, after laser trimming, and after 26 hours of PAP after laser trimming. Initially, a peak around 1332.5 cm^{-1} was observed, indicating the presence of a diamond structure. As a result of the graphite phase transition on the surface of the PCD substrate caused by laser irradiation, the peak of the diamond structure weakened, and a peak at 1580 cm^{-1} appeared, indicating the graphite structure. On the other hand, no graphite peak was observed on the PCD substrate after PAP, and only a diamond structure peak was observed. These measurement results suggest that laser trimming does not affect the polishing of the PCD substrate because the graphite layer is completely removed by PAP.
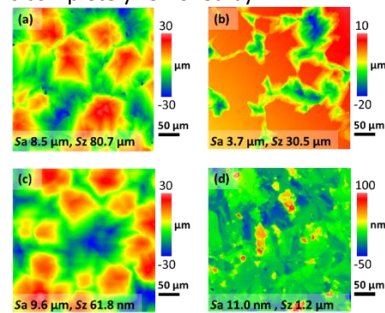
Figure 4. SWLI images of PCD surface (a) initial surface (b) surface after PAP for 26 h w/o laser-trimming, (c) surface after laser-trimming, (d) surface after 26 h of PAP w/ laser-trimming.
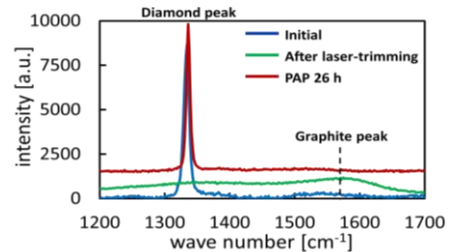
Figure 5. Raman spectra of the PCD surface of initial, after laser-trimming and after 26 h of PAP.

4. Conclusions

In this report, the following conclusions were obtained.

1) The p-v value was reduced from about 150.0 μm to 50 μm by applying laser-trimming for 1 m 59 s to a 10 mm square PCD substrate.

2) Plasma-assisted polishing was applied to 10 mm square PCD substrates that had been roughly flattened by laser-trimming. Comparison with untreated substrates showed that the time required for planarization and smoothing of PCD substrates was significantly reduced by the application of laser-trimming.

References

[1] Deng H, et al. (2013) Atomic-scale flattening mechanism of 4H-SiC (0001) in plasma assisted polishing. CIRP Annals 62(1) 575.

[2] Deng H, et al. (2015) Plasma-assisted polishing of gallium nitride to obtain a pit-free and atomically flat surface. CIRP Annals 64(1) 531.

[3] Yamamura K et al., (2018) Damage-free highly efficient polishing of single-crystal diamond wafer by plasma-assisted polishing. CIRP Annals 67(1) 353.

Investigation of the interfacial damping characteristics of passively damped components in ultrasonic frequency range

E. Uhlmann[1,2], M. Polte[1,2], T. Hocke[1], J. Tschöpel[1]

[1]*Institute for Machine Tools and Factory Management IWF, Technische Universität Berlin, Germany*
[2]*Fraunhofer Institute for Production Systems and Design Technology IPK, Germany*

julius.tschoepel@iwf.tu-berlin.de

Abstract

Machining components made of brittle materials with the highest requirements in terms of form and surface tolerances represents a technological challenge in industrial environment. Ultrasonic vibration-assistance in milling processes is one of the most promising approaches. According to the current state of the art, vibrations are transmitted to the machine system, which reduces the service life of the applied spindle bearings. To reduce the expansion of these high-frequency vibrations in the machine system, numerous solutions were developed, which can only be integrated into rotating machine components to a limited extent. This study shows an innovative approach to vibration damping based on the integration of inserts into the base material of the machine component. For this purpose, cylindrical damping inserts made of EN-GJL-250 were installed into test specimens. Based on their frequency responses, the damping properties were determined. Furthermore, the effects of the surface pressure of the inserts on the overall damping behaviour were investigated by varying the geometric interference. As a result, it was shown that the damping ratio can be significantly increased by targeted use of interface damping.

Keywords: high-precision machining, ultrasonic vibration-assisted machining, structural damping, material damping

1. Motivation

The machining of high- and ultra-precision components, whether for direct use or for replication using injection moulding processes, results in high demands on the machining setup. Undesired vibrations of the tool or machining system are one of the most significant factors affecting machining results in high- and ultra-precision machining. For this purpose, the aim of this work is to investigate a passive vibration damping method that optimises structural damping by integrating cylindrical inserts into components of the machine structure. The basic dependencies of the surface pressure p_s and the surface roughness Ra with the damping characteristics are analysed below.

2. Material and structural damping

The damping of solid-state vibrations is fundamentally caused by the dissipation of energy from the vibrating system. Damping effects can be divided into external and internal damping. In external damping, the energy is dissipated into the surrounding atmosphere, e.g. in the form of sound waves. The inner energy dissipation ΔE leads to an increase in the vibrating systems temperature ϑ_{vib} due to internal friction effects [1]. However, the effects of internal damping are only effective if a relative movement takes place between two or more surfaces. These displacements can occur at dislocations and defects in the crystallographic structure or at micro-cracks within the material structure (material damping). It should be noted that material damping should not be considered as a material constant due to its strong dependence on ageing effects [2]. In addition, relative movements can also be present at interfaces of component assemblies (structural damping). Figure 1 illustrates these key damping mechanisms schematically.
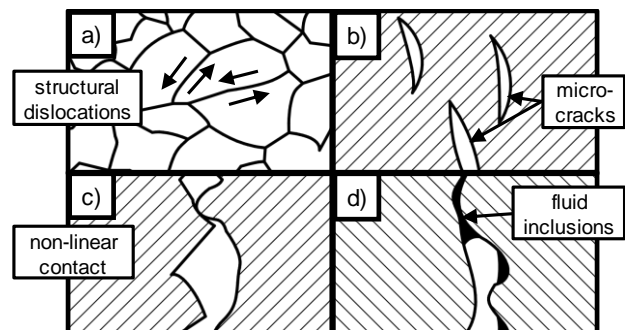
Figure 1. Main damping causes a) dislocations in crystal structure; b) micro-cracks; c) irregular interface conditions; d) fluid inclusions at the interface

In 1957, LÖWENFELD [3] demonstrated that the connections between machine components exert a more significant impact on an assemblies overall damping than the material damping of individual components. For this reason, the damping effects occurring at bolted, riveted or welded joints were investigated in numerous scientific studies. PETUELLI [4] examined the influence of joint surface pressures p_s on damping characteristics and found that an increase in surface pressure p_s substantially hinders relative movements, resulting in a reduced damping behaviour. The investigations by BRENDEL [5] showed that the damping significantly increased by filling the joints with liquid. Consequently, the use of interface damping through the targeted introduction of precisely defined separation and joining points represents a promising approach to the damping of high frequency vibrations on machine components.

The main factors influencing the damping properties are the surface pressure p_s and the surface roughness Ra, which are analysed in more detail [3, 4, 6].

3. Specimen Design

In order to record the interface damping independently of the material damping, test specimens were produced using same materials and same base geometries. Therefore, the variations of the specimens only affected the design of the interfaces in terms of surface roughness Ra and surface pressure p_s. The main bodies of the test specimens were made of C45 steel blocks, each with five holes drilled with a diameter of D = 10 mm. As damping inserts, cylindrical pins from grey cast iron type EN-GJL-250 with a length of l = 30 mm and a diameter of D = 10 mm were manufactured. In order to realise different surface pressures p_s between the main body and the cylindrical inserts, the holes in the main body are manufactured slightly smaller with defined diameter undersizes D_{uz}. To investigate the influence of the surface roughness Ra, the bores in half of the specimens were additionally reamed, which resulted in an improvement in surface roughness of Ra = 12 μm (drilled) to Ra = 2 μm (reamed). The damping inserts were integrated in advance by heating the main bodies to ϑ = 600 °C, which resulted in a widening of the holes due to thermal expansion. Based on this, the resulting surface pressure p_s at the interface was determined by calculation, which is also shown in Table 1 [6].

Table 1. Overview of the specimens' interface conditions

No.	Surface roughness Ra in μm	Diameter undersize D_{uz} in μm	Surface pressure p_s in N/mm²
1	12	40	306
2	12	70	608
3	2	40	342
4	2	70	645
5	Reference - no damping inserts		

4. Modal- and Frequency Response Analysis

The vibration characteristics of the specimens were analysed using modal analysis and frequency response analysis. The modal analysis provides information on the natural vibration behaviour of the specimens, while the frequency response analysis shows the specimens behaviour under forced vibration excitation. The modal analysis was carried out using an impulse hammer excitation type 9722A of the company KISTLER AG, Winterthur, Switzerland. The vibration response of the specimens caused by the impulse excitation was measured using a triaxial accelerometer type HT356A44 of the company PCB PIEZOTRONICS, Depew, USA. The resulting damping ratio D was determined using the half-power bandwidth method, analogue to [7]. As part of the frequency response analysis an ultrasonic transducer with an excitation frequency of f_{ex} = 40 kHz was used. It was bolted to one side of the test specimen. The amplitude a_{in} of the input vibration was measured using a laser-doppler-vibrometer type OFV-503 of the company POLYTEC GMBH, Waldbronn, Germany. The resulting vibration amplitude a_{out} was measured at the opposite side of the ultrasonic transducer. The degree of damping was represented by the amplitude reduction Δa, calculated as Δa = a_{out} - a_{in}. Consequently, the damping ratio D and the amplitude reduction Δa can be considered as comparable measures of the damping properties of the specimens, each for a natural and a forced vibration.
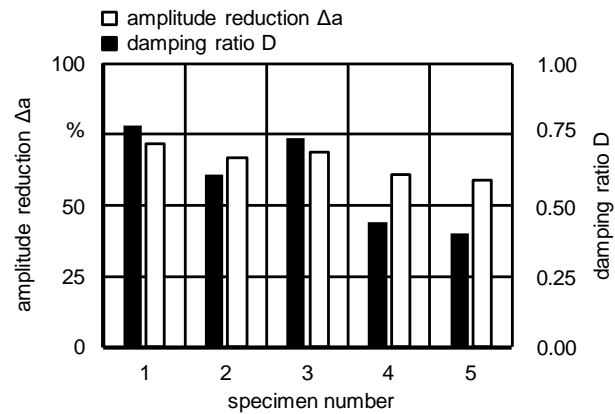
Figure 2. Results of the modal analysis (damping ratio D) and the response analysis (amplitude reduction Δa)

5. Experimental Results

Figure 2 summarises the experimental results, which could be obtained. The amplitude reduction Δa and the damping ratio D could be increased in all cases by installing damping inserts. Specimen No. 1 showed the largest amplitude reduction of Δa = 78 % and the highest damping ratio of D = 0.78. The smallest increase in amplitude reduction Δa and damping ratio D was observed for specimen No. 4. The improvements in damping found are significantly more pronounced in the natural frequency range than for forced vibrations with f_{ex} = 40 kHz. On average, the damping ratio D could be increased by 60 % for all samples compared to the reference specimen No. 5 (natural vibration), but the amplitude reduction only by Δa = 8 % (forced vibration) with f_{ex} = 40 kHz (Figure 2).

6. Conclusion

The described correlations between surface pressure p_s, surface roughness Ra and damping properties are consistent with established theoretical models. They are describing a reduction in the possible relative displacements at the interface and consequently a reduction in the damping properties. It could be shown that the ability of the specimens to dampen vibrations decreases with increasing surface pressure p_s. Furthermore, it could be determined that a lower surface roughness Ra shows a negative effect on the damping properties. Using this approach, vibrations in the machine structure can be specifically damped without adding an external energy.

References

[1] Frank, M.; Jaeger, M.; Groschup, B.; Hameyer, K.: Strukturdynamische Werkstoffdämpfung von Blechpaketen elektrischer Maschinen. Elektro- und Informationstechnik 193 (2022), S. 167 - 175.

[2] Bangsong, Y.; Xuanpu, D.; Rong, M.; Shuqun, C.; Zhang, P.; Hongjiang L.: Effects of heat treatment on microstructure, mechanical properties and damping capacity of Mg–Zn–Y–Zr alloy. Mat. Science and Engineering 594 (2014), S. 168 – 177.

[3] Löwenfeld, K.: Die Dämpfung bei Werkzeugmaschinen. Der Maschinenmarkt 63, 1957.

[4] Petuelli, G.: Theoretische und experimentelle Bestimmung der Steifigkeits- und Dämpfungseigenschaften normalbelasteter Fügestellen. Aachen, RWTH Aachen, Diss., 1983.

[5] Brendel, H.: Zur Schwingungsdämpfung von Fugenverbindungen. München, TU München, Diss., 1990.

[6] DIN 7190-1, Teil 1, (02.2017), Berechnungsgrundlagen und Gestaltungsregeln für Pressverbände. Berlin: Beuth.

[7] Beards, C. F.: Structural Vibration: Analysis and Damping. Oxford: Butterworth-Heinemann, 1996.

Nano- to microscale experimental characterisation of the tribological behaviour of Al$_2$O$_3$ thin films via lateral force microscopy

Marko Perčić,[1, 2] Saša Zelenika,[1, 2] and Martin Tomić [1]

[1]*University of Rijeka, Faculty of Engineering, Laboratory for Precision Engineering, Vukovarska 58, 51000 Rijeka, CROATIA*
[2]*University of Rijeka, Centre for Micro- and Nanosciences and Technologies & Centre for Artificial Intelligence and Cybersecurity - Laboratory for AI in Mechatronics, Radmile Matejčić 2, 51000 Rijeka, CROATIA*

szelenika@uniri.hr

Abstract

Stochastic frictional phenomena in mechanical contacts are an aggravating challenge in controlling precision mechanical systems, highly dependent on the involved physical origins and scales of the applied forces. The fundamental insights into this complex phenomenon can be beneficial for the design and development of new precision equipment or the optimal selection of functional coatings. Novel experimental findings about the scaling effects at the nano- to microscales of normal forces exerted on a single asperity contact are described in this work. The study is conducted via the scanning probe microscope (SPM) in the lateral force microscopy measurement mode, allowing quantitative measurements of single asperity frictional forces between the SPM silicon nitride probe and the surface of Al$_2$O$_3$ thin film samples. The measurements are structured to cover normal forces ranging from a few nN to 2.8 μN by using two different SPM probes. To achieve precise quantitative results, the used probes are carefully calibrated.

Nano- and microtribology, lateral force microscopy, scaling effects, thin films, experimental measurements

1. Introduction

Precision positioning systems face a significant design challenge due to the negative effects that occur in the mechanical contacts of sliding bodies. Frictional phenomena as a major disturbance in these systems, are currently being extensively researched. Such studies pose a modelling and prediction challenge due to their inherent stochastic nature, which is influenced by factors such as material type, contact area, normal loads, sliding velocities, temperature, and the complex interplay of other physio-chemical effects and interactions at different scales [1]. To gain insights into such phenomena, tribological experimental measurements are conducted in this work at the nano- to microscale of normal loads with the aim to determine the frictional interactions occurring under single asperity contact conditions.

2. Experimental methodology

The investigation of single asperity frictional phenomena is based in this study on an approach that relies on experimental measurements carried out via the Bruker Dimension Icon scanning probe microscope (SPM) in the lateral force microscopy (LFM) configuration, which represents a cutting-edge technique for quantifying nanometric frictional phenomena, while approximating the conditions of a single asperity contact [1, 2] (Figure 1). A silicon nitride (Si$_3$N$_4$) microcantilever probe moves herein laterally, while continuous contact is maintained between its tip and the surface of the studied alumina (Al$_2$O$_3$) thin film samples deposited on Si wafer substrates by using the atomic layer deposition (ALD) technique. Al$_2$O$_3$ thin films have, in fact, favourable properties as coatings due to their high hardness, wear resistance, non-reactivity, etc. The Si$_3$N$_4$ probes apply here a constant normal load on a 500 x 500 nm^2 scanning area of the sample with a set scanning resolution of 512 lines per scan.
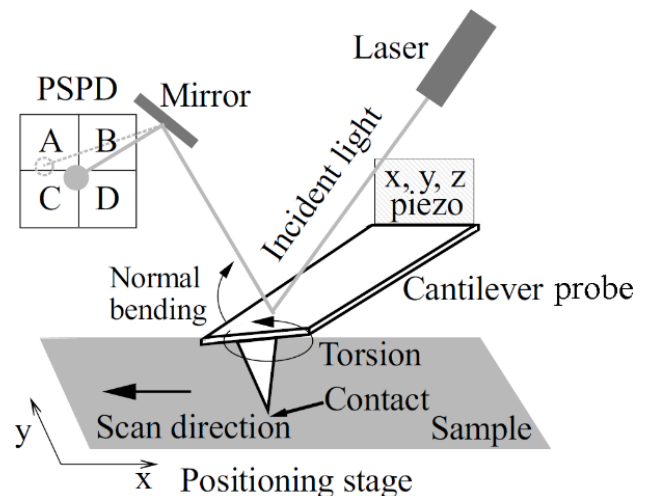
Figure 1. Scheme of the used LFM measurement configuration [3]

To obtain a precise value of the forces in the normal (exerted load) and in the lateral (frictional) directions, prior to the measurements each probe is calibrated in terms of its normal and lateral sensitivity [3]. To cover the normal force ranges from nano- to microscales, six different probes, each with a different geometry, are selected: Bruker MSNL-10 E & F [4], BudgetSensors AiO-Al A, B & C [5], and Nanosensors PPP-LFMR [6]. The calibration of probes' normal and lateral sensitivity yields, thus, their stiffness and resonant frequencies.

The achievable normal force values F_N for the calibrated probes with respect to the set-point voltage V_{SP} of the z-axis piezoelectric actuator are shown in Figure 2. Based on these results, probes of type AiO-Al A & B are hence selected for the measurements in the nano- and micro-ranges, respectively. In fact, for the AiO-Al A probe the F_N range for nanotribology measurements is from ca. 4 to 470 nN, while the AiO-Al B probe is used in the F_N range from 235 nN to 2.8 μN.

The lateral calibration of the selected probes is carried out at different F_N values by employing the calibration grating TGF11 and using Varenberg's method [7]. The obtained lateral calibration constants for the AiO-Al A & B probes is thus determined to be 0.184 μN/V and 1.192 μN/V, respectively, with a standard deviation of ~ 13 %.

The LFM measurements are conducted next on the 500 nm scan size of the surfaces of the Al_2O_3 thin film samples in a 21 °C temperature-controlled environment with a constant scan rate of 1 Hz, resulting in a 1 μm/s sliding velocity.
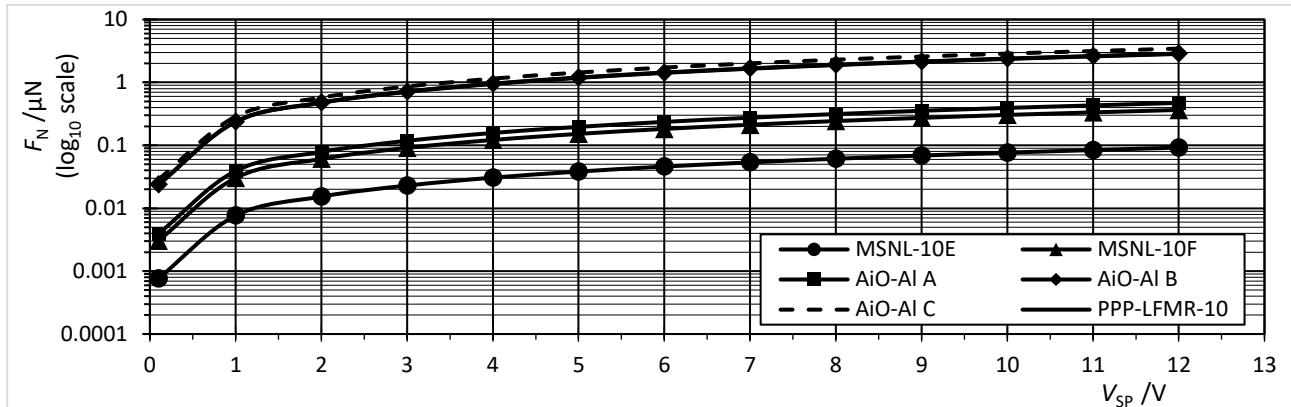
Figure 2. F_N values achieved for each of the studied probes at different set-point voltages V_{SP} of the z-axis piezoactuator

3. Results and discussion

The measured LFM voltages for all F_N values are hence processed with the lateral calibration constants so as to obtain the values of the frictional force F_f in the nN to μN range of normal loads, as shown in Figure 3. The expected quasi-linear trend is visible for both curves, while the transition between the nN and μN ranges shows some discrepancies. What is more, the values in the higher μN range exhibit some non-linearities, which is a sign of an enlargement of the surface area of the tip of the probes due to wear. This effect is tendentially rather high for large normal loads, giving rise to an enlargement of the adhesion force in the contact region between the tip of the probes and the samples' surface.

The instabilities visible for the higher nN and μN F_N ranges can, in turn, be an indication that the deformation limit of the selected probes is reached, implying that future measurements should be carried on with more probes that would enable covering the complete range of the foreseen normal loads.
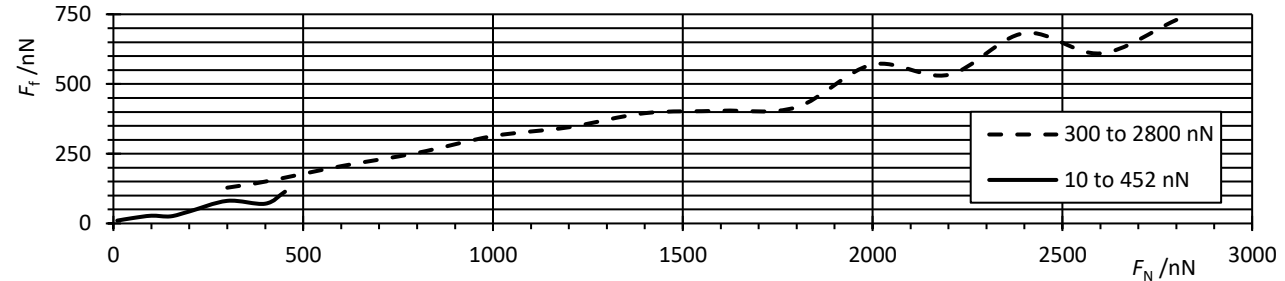
Figure 3. F_f values on the Al_2O_3 thin film samples vs. the variable normal load F_N in the nN to μN range

4. Conclusions and outlook

The performed study into the multiscale tribological properties of the studied Al_2O_3 thin film material allows establishing that, although the general trends of the frictional force variability for normal loads in the nano- to microscales show the expected quasi-linear behaviour in line with the conventional frictional models, the transitional and higher-value ranges of F_N require further in-depth and structured studies to determine all the involved coupled effects. Additional experimental studies of the influence of the probes' tip wear with the resulting adhesion effects, as well as probes' deformation limits are, therefore, needed to fully understand the frictional scaling phenomena, thus providing the necessary insights for the development of predictive tribological models as well as of the corresponding compensation typologies.

References

[1] Bhushan Bh (ed.) 2001 *Fundamentals of Tribology and Bridging the Gap Between the Macro- and Micro/Nanoscales.* (Dordrecht, NL: Springer)
[2] Bruker Dimension Icon (Billerica, MA, USA: Bruker) www.bruker.com/en/products-and-solutions/microscopes/materials-afm/dimension-icon-afm.html
[3] Perčić M, Zelenika S et al. 2020 *Friction* **8**(3) 577-93
[4] Bruker MSNL-10 Sharp Nitride Lever Probes (Billerica, MA, USA: Bruker) https://www.brukerafmprobes.com/p-3710-msnl-10.aspx
[5] BudgetSensors All-In-One-Al multipurposeAFM probes (Sofia, Bulgaria) https://www.budgetsensors.com/multipurpose-afm-probe-aluminum-all-in-one-al
[6] NanoSensors PointProbe Plus AFM Probes (Neuchatel, Switzerland) https://www.nanosensors.com/pointprobe-plus-lateral-force-microscopy-reflex-coating-afm-tip-PPP-LFMR
[7] Varenberg M, Etsion I and Halperin G 2003 *Rev Sci Instrum* **74**(7) 3362-7

Ultra-precision cutting of graphite materials for air bearing applications using single crystal diamonds

E. Uhlmann[1,2], M. Polte[1,2], T. Hocke[1,2], F. Felder[1]

[1]*Institute for Machine Tools and Factory Management IWF, Technische Universität Berlin, Germany*
[2]*Fraunhofer Institute for Production Systems and Design Technology IPK, Germany*

fabian.felder@iwf.tu-berlin.de

Abstract

In the field of non-contact bearing motor spindle systems for ultra-precision machining, graphite materials are increasingly focused for the use in complex aerostatic bearing components. The material-specific porosity of graphite enables the consistent distribution of air pressure throughout the bearing surface, which increase the axial and radial load-bearing capacity and stiffness. In order to ensure the functionality of the bearing components, low surface roughness values Ra ≤ 200 nm are essential. Based on the state of the art, uncoated tungsten carbide (WC) tools and polycrystalline Chemical Vapour Deposition (CVD) diamonds are conventional used cutting materials. However, these are characterised by high rounded cutting-edge radii and maximum chipping of the cutting-edges, which lead to increased surface roughnesses. For this purpose, single crystal diamonds (SCD) were used as a solution approach to enable the manufacturing of aerostatic bearing components made of graphite concerning the described requirements. Using SCD with rounded cutting-edge radii r_β ≤ 50 nm leads to tensile stresses in surface-near boundary layers. Induced tensile stresses in brittle materials result in crack formation, which requires extensive investigations using SCD. In this study, the cutting behaviour of SCD for cutting of graphite materials concerning crack formation and breakout behaviour were analysed. Specific turning tests based on statistical DoE using an ultra-precision machine tool were carried out to analyse and quantify the impact of cutting speed, cutting depth, feed rate and rake angle on the surface roughness. First results show the influence of the selected process parameters in dependency to surface roughness as well as the potential of SCD tools for the machining of graphite. In this context, a lower surface roughness could be achieved compared to conventional used cutting materials made of tungsten carbide and CVD diamonds.

Keywords: graphite, single crystal diamond, ultra-precision machining

1. Introduction

Spindle technologies in machine tools based on aerostatic bearing systems show great potential for high- and ultra-precision manufacturing. This non-contact bearing technology is characterised by utilising a thin film of pressurised air in bearing gaps of s_g < 10 µm to ensure high rotational speeds s, dynamic stiffness and load capacity c_l. Therefore, components made of porous graphite are increasingly being used to provide a stable air flow through the bearing face and to distribute a constante pressurised air film. According to state of the art, uncoated tungsten carbide (WC) tools and poly-crystalline Chemical Vapour Deposition (CVD) diamonds were applied for machining graphite [1,2]. The use of these tools results in increased tool wear due to the abrasive effect of the graphite agglomerates [2]. In order to overcome the current challenges in the machining of graphite and to meet the requirements in manufacturing of air bearing components, the use of single crystal diamond (SCD) tools represents a promising approach due to its specific geometric and material properties. To gain fundamental knowledge for the machining of graphite using SCD, specific turning tests were carried out to identify suitable parameters and to compare the cutting performance with WC and CVD.

2. Experimental Setup

In order to identify the potential of SCD in graphite machining, experimental turning tests were carried out on the five-axis ultra-precision machine tool Moore Nanotech 350 FG of Moore Nanotechnology Systems, Swanzey, USA. The used materials were isotropic fine-grained graphites EDM-200, EDM-3 and EDM-AF5 of Poco Graphite, INC., Decatur, USA, which are widely used in electrical discharge machining (EDM) but can also be suitable for the use in aerostatic bearing components due to their permeability and specific properties (Table 1).

Table 1. Specific properties of the graphite materials

Parameter	EDM-200	EDM-3	EDM-AF5
Average grain size g_s	10.0 µm	< 5.0 µm	< 1.0 µm
Flexural strength σ_{bB}	55.8 MPa	91.7 MPa	99.9 Mpa
Compressive strength σ_d	96.5 MPa	124.8 Mpa	152.4 MPa
Shore hardness H_s	68.0	73.0	83.0

The used graphite specimen are characterised by a diameter of D = 50 mm and a height of H = 10 mm. For the turning tests, SCD tools with a corner radius r_ε = 0.8 mm, a rounded cutting edge radius r_β ≤ 50 nm and a clearance angle α_0 = 10° of Contour Fine Tooling B.V., Valkenswaard, the Netherlands, were applied. The CVD tools type DCMW11T308 with a corner radius r_ε = 0.8 mm were provided by Mössner GmbH, Pforzheim, Germany. The WC tools type DCGT11T308-FN HU7315-1 with a corner radius of r_ε = 0.8 mm were purchased by Hoffmann SE, Munich, Germany. The surface roughness Ra was measured with a chromatic white light sensor MicroProf100 of Fries Research & Technology GmbH, Bergisch Gladbach, Germany.

3. Experimental investigations and results

In this study, the single-point turning of fine-grained graphite materials EDM-200, EDM-3 as well as EDM-AF5 using SCD were investigated. Subsequently, further tests were carried out to compare the cutting performance of SCD to conventionally used cutting materials such as uncoated WC and CVD diamonds.

3.1. SCD cutting experiments

To gain fundamental knowledge of the potential of SCD, a full factorial design of experiments was used to identify reliable parameters for achieving low surface roughness values Ra. The factor levels (Table 2) were aligned to conventionally used cutting parameters of roughing and finishing processes in ultra-precise SCD machining according to the state of the art [3].

Table 2. Factor levels for specific turning tests on graphite with SCD tools

Parameter	Factor levels		
Cutting speed v_c	1 m/min	$\leq v_c \leq$	240 m/min
Feed rate f	2 µm	$\leq f \leq$	45 µm
Depth of cut a_p	1 µm	$\leq a_p \leq$	25 µm
Rake angle γ_0	-40°	$\leq \gamma_0 \leq$	8°

The test series were split in pre- and main-tests. The pre-tests were applied to identify the significance of each parameter and a suitable type of the investigated graphite materials. In the main-tests, suitable parameter ranges were achieved for a process-reliable manufacturing of graphite materials in terms of surface roughness Ra. The pre-tests showed that the surface roughness Ra is significantly dependent on the grain sizes g_s of the graphite materials used due to the random orientation of the agglomerates. Therefore, a high variation in mechanical strength could be proven [1,2]. These characteristics lead to an asymmetric breakout behaviour and reduced surface qualities. Based on this, EDM-AF5 with an average grain size of $g_s \leq 1$ µm could be identified as a suitable graphite material for further evaluations. The results of the main-tests show a significance for all analysed cutting parameters, whereby a major impact for feed rate f on the surface roughness Ra was determined (Figure 1). This correlates with previous research works [1,2,5].
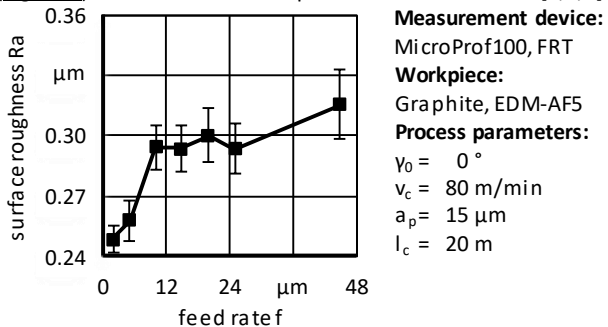
Figure 1. Surface roughness Ra as a function of different feed rates f

The results show that an increased feed rate f results in high surface roughnesses Ra. The lowest value of Ra = 0.249 µm was determined at the minimum investigated feed rate of f = 2 µm, whereby a roughness of Ra = 0.315 µm was identified for a maximum feed rate of f = 45 µm within the analysed process area. In a feed range of 5 µm ≤ f ≤ 10 µm, the surface roughness increased quite intensely by 12.3 % to a value of Ra = 0.294 µm. For feed rates between 10 µm ≤ f ≤ 25 µm, the roughness values remain constantly in a range of 0.293 µm ≤ Ra ≤ 0.300 µm. In comparison to this, the surface roughness Ra within a range of 2 µm ≤ f ≤ 5 µm shows a sligth incline of 3.5 %. The findings reveal that the surface roughness Ra decreased, as the ratio of chip thickness to cutting edge radius is reduced towards $h(\varphi)/r_\beta \sim 1$. This can be attributed by the characteristic behaviour of brittle materials regarding the occurrence of micro-cracks in surface-near boundary layers due to induced tensile stresses σ [4]. Using SCD with a low cutting edge radius of $r_\beta \leq 50$ nm with decreasing feed rates f lead to reduced tensile stresses σ. Based on this, cracking effects only occur in the area of the cutting depth a_p used. Furthermore, it could be proven that a cutting speed of v_c = 80 m/min, a rake angle of γ_0 = 0 ° as well as a depth of cut of a_p = 15 µm lead to the lowest surface roughness Ra in the investigated process area (Figure 1). According to the results of the pre- and main-tests, these parameters in terms of a feed rate of f = 2 µm were used for further evaluation of the cutting performance using SCD.

3.2. Comparison to conventional cutting materials

In further tests, the cutting performance of SCD in turning EDM-AF5 was compared to the cutting materials CVD and uncoated WC in two test series. Firstly, specific parameters for CVD and uncoated WC according to the state of the art were applied [1,2]. In this process a minimum surface roughness of Ra = 0.390 µm for WC and Ra = 0.348 µm for CVD were identified. For the second test series, a direct comparison between the cutting materials was carried out using the same parameters and thus the same theoretical surface roughness depth R_{th} (Figure 2) [4,5].
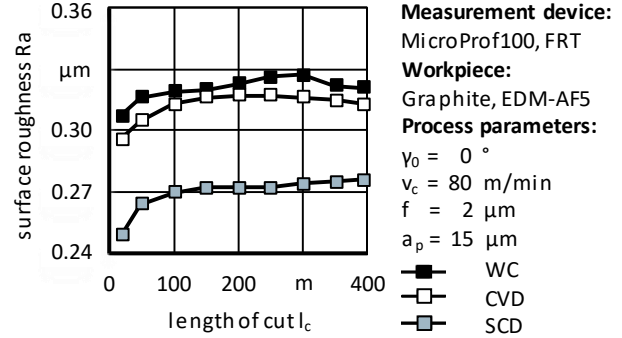
Figure 2 Surface roughness Ra as a function of constant cutting conditions for uncoated WC, CVD and SCD

The used parameters result in surface roughness values of Ra = 0.307 µm for WC and Ra = 0.296 µm for CVD after a cutting length l_c = 20 m compared to the parameters chosen according to the state of the art. However, a surface roughness of Ra = 0.249 µm was identified for SCD after l_c = 20 m. The findings show the differences in the performance of the used cutting materials regarding the machined surface roughness Ra. Using SCD for the machining of EDM-AF5 leads to a marginal increase of 7.3 % over a total cutting length of l_c = 400 m. This correlates to a decrease of 18.4 % in comparison to uncoated WC and of 14.8 % to CVD in terms of surface roughness Ra.

4. Conclusion and further investigations

The findings show that the surface roughness Ra significantly depends on the grain size g_s of the used graphite materials due to material specific properties. In this study, the lowest surface roughness of Ra = 0.249 µm was achieved by using SCD in turning fine-grained graphite type EDM-AF5. Therefore, a cutting speed v_c = 80 m/min, a feed rate f = 2 µm, a cutting depth a_p = 15 µm and a rake angle γ_0 = 0 ° were determined by statistical evaluation. The feed rate f was identified with a major effect on the surface roughness Ra, whereby the use of small feed rates f is recommended in turning of fine-grained graphites using SCD. It could be further proven, that the use of SCD in turning of EDM-AF5 allows the manufacturing of surface roughnesses Ra ≤ 0.249 µm and is potentially able to substitute conventionally used cutting materials such as WC and CVD. Further investigations address the optimisation of the process limits and the analysis of the wear behaviour of SCD. This work was funded by the GERMAN RESEARCH FOUNDATION DFG.

References

[1] König M 1998 Fräsbearbeitung von Graphitelektroden *Diss. RWTH Aachen*.

[2] Almeida F.A, Sacramento J, Oliveira F.J, Silva R.F 2008 Micro- and nano-crystalline CVD diamond coated tools in the turning of EDM graphite *J. Surface & Coatings Technology* **203** 271-276

[3] Uhlmann E, Polte M, Rolon D.A., Kühne S 2019 Ultra-precision-milling of silicon by means of single crystal diamond tools *Euspen 19th international conference and exhibition*

[4] King, R. F, Tabor, D,The strength properties and frictional behavior of brittle solids *Proceed. of the Royal Society of London* **223** 225-238

[5] Brammertz P.H. 1961 Die Entstehung der Oberflächenrauheit beim Feindrehen. *Industrie-Anzeiger* 25-32

Waste heat energy harvesting system for winter monitoring of honeybee colonies

Petar Gljušćić[1, 2] and Saša Zelenika[1, 2]

[1]University of Rijeka, Faculty of Engineering, Precision Engineering Laboratory, Vukovarska 58, 51000 Rijeka, Croatia
[2]University of Rijeka, Centre for Micro- and Nanosciences and Technologies, Radmile Matejčić 2, 51000 Rijeka, Croatia

szelenika@uniri.hr

Abstract

As the most commonly managed bee in the world, the European honeybee significantly impacts agriculture via crop pollination. The increasing occurrence of weather extremes caused by climate change, together with diseases and human activity, provoke the winter loss of numerous colonies of managed bees in Europe and around the world. This work proposes an autonomous system aimed at monitoring managed honeybee colonies to estimate the size and strength of the winter cluster. The system comprises temperature sensors strategically placed within the hive, as well as a communication module allowing data transfer, and it is powered by using the energy harvesting approach, i.e., a thermoelectric generator (TEG) able to utilize the temperature gradient between the hive interior and the environment. All the system components in direct contact with the colony are to be designed in such a way that their impact on the colony is minimised, as well as by respecting the so called "bee space". Initial measurements in a conventional Langstroth hive, combined with a validated finite element TEG model, have clearly shown the possibility of generating a sufficient amount of electrical energy to power the foreseen design setup.

Energy harvesting, thermoelectric generator, hive monitoring, autonomous sensors

1. Introduction

The European honeybee (*Apis mellifera*) represents the most commonly managed bee in the world, with a significant impact on agriculture (crop pollination). With growing effects of climate change, new pests and diseases as well as human activity, about 10 % of managed bee colonies in Europe succumb to winter losses each year [1–3]. In fact, in a cold winter environment the colony has to maintain the individual bee's body temperature of at least 16 °C, while the temperature of the brood needs to be around 35 °C [4, 5]. To achieve such conditions, a considerable metabolic production of energy is needed, with honey reserves being utilized by the bees as the primary energy source. The cluster should be warm enough to enable the colony enough mobility to defend itself, as well as to reach the honey stores.

Figure 1. A honeybee colony in a winter cluster [5]

The colony forms therefore a tight cluster within the hive, as shown in Figure 1, typically ranging from ~ 100 up to ~ 240 mm in diameter, corresponding to approximately 3 - 7 standard Langstroth frames. The colony also has to manage its food stores in order for them to last until spring [3, 4].

Generally, if a colony declines or dies out during winter, a considerable amount of time may pass before it is noticed by the beekeeper (typically upon the first spring inspection), and by that time clues to the causes of such events are lost [1]. To determine the causes, the timely sampling and analysis of honeybee colonies is, therefore, required.

2. Hive monitoring

In the last decade there was a significant increase in the use of electronic systems aimed at monitoring the state of honeybee colonies. These systems, both commercially available as those under development, most commonly measure temperature and humidity in a single point within and outside the hive. To perceive soon enough the nectar flow in spring, in some specific cases additional parameters are also monitored, e.g. the presence of the queen, brood temperature or the mass of the hive [6–8]. Such systems are almost exclusively powered by conventional batteries, which necessitate periodical human intervention inside the hive, disturbing thus the microclimate within it, particularly during the winter. What is more, batteries have a significant impact on the environment due to their production process as well as their disposal [9, 10].

An autonomous system aimed at colony strength monitoring is thus suggested in this work, comprising several temperature sensors placed in the hives, enabling the estimation of the winter cluster size and strength, as well as a suitable communication module. The overall sensor node is designed to utilize the waste heat produced by the colony, transducing it into electricity via a thermoelectric generator (TEG).

In fact, as a honeybee colony overwinters within a tight cluster, the size of which corresponds to the strength of the colony [11], a measurable temperature difference occurs between the zone of the hive occupied by the cluster and the

remaining zones without bees [12, 13]. Due to hot air rising to the top of the hive, a temperature map can then be obtained by strategically placing temperature sensors above the frames. Such a map would reflect the size of the cluster, and thus the strength of the colony itself.

To assess the viability of such an approach, a finite element (FE) heat transfer simulation is carried out using ANSYS® Workbench 18.0 [14, 15], where three different cluster sizes are considered, i.e., clusters occupying 3, 5 and 7 hive frames. The maximal temperatures occurring within the cluster are set according to available literature [3, 14], while the ambient temperature is set at 1°C, thus emulating average winter conditions in the considered environment in the inland of the Istrian peninsula in Croatia. The resulting temperature maps above the clusters for each of the studied case are displayed in Figure 2, where a clear difference in the distribution of temperature can be observed for different cluster sizes.
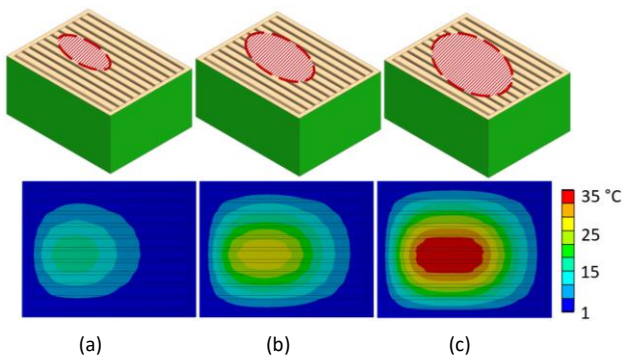
Figure 2. FE simulations of heat transfer within a beehive containing a winter cluster occupying 3 (a), 5 (b) and 7 frames (c)
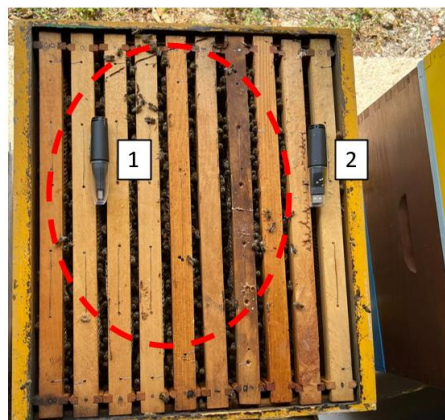
(a)
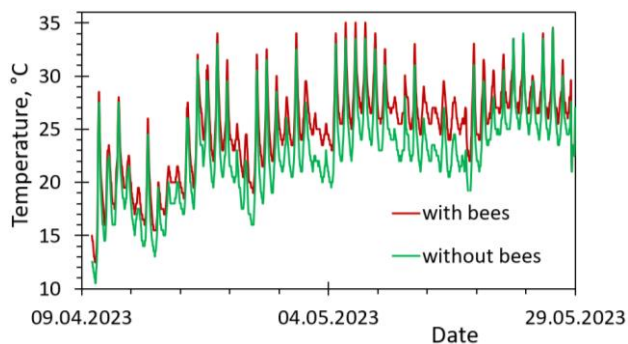
(b)

Figure 3. Honeybee colony inner temperature measurements [9]

What is more, to initially assess the temperature differences between areas with and without bees, measurements are performed on a colony in a period from early to late spring by placing 2 sensors above (1) and away (2) from the bee cluster (Figure

3a), resulting in an average 2 °C temperature difference (Figure 3b) [9]. Both studies indicate, therefore, the feasibility of the above-described monitoring approach based on temperature difference to estimate the size and strength of the colony.

3. Hive waste heat energy harvesting

For the ideated system, there are several potential power supply options that can be considered, e.g. batteries or solar power. In this case, when an autonomous system aimed at winter monitoring is being studied, an energy harvesting (EH) approach based on thermoelectric waste heat is proposed instead, with the goal of utilizing the metabolic heat generated by the honeybee colony and typically lost through the hive walls [3, 16]. The EH approach [17, 18] is selected here to minimise the mentioned drawbacks related to battery usage [9, 10]. The possibility to use photovoltaics is, in turn, limited due to short and typically cloudy or foggy days in the considered region, though it could be considered as an addition to the TEG energy production, forming thus a hybrid EH system [18].

To assess the possibility of using thermoelectric EH as a power source, temperatures within and outside a standard wooden Langstroth beehive are measured next during the winter period in the studied environment. The measurements are performed by placing one data logger inside the hive, above the cluster of bees, while the other is placed on top of the hive roof. The thus obtained data shown in Figure 4 provide the input parameters, i.e., the thermal gradient between the maximum and minimum temperature, required for analysing the potential power generation. A fairly consistent thermal gradient, with an average temperature difference of about 21.3 °C, is hence obtained.
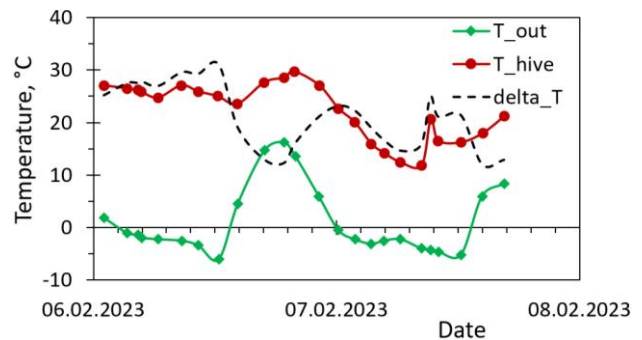
Figure 4. Honeybee temperature measurements at the actual beehive placement location during the winter - inner vs. ambient temperature

To utilize the available temperature gradient, a Tecteg® TEG2-126LDT thermoelectric generator [19] is considered in this frame. Firstly, an experimentally validated FE model of the considered TEG is developed by using ANSYS® Mechanical 18.0 [20], with the respective boundary conditions simulating the real working conditions with the average inner and outer measured temperatures of T_{out_av} = 0.9 °C and T_{in_av} = 22.3 °C. The maximum determined voltage and power outputs, at a load resistance of 4 Ω, are, thus, P_{max} = 38.6 mW and U_{max} = 0.39 V.

A prototype energy harvesting device, able to utilize the determined temperature gradient, is designed next. The harvester, depicted in Figure 5a, comprises an inner heatsink (1), heated by the hot air above the bee cluster, the chosen TEG2-126LDT thermoelectric generator (2), two QG-IF-A6-1X3 aluminium heat pipe interface blocks (3 and 5), three QY-SHP-D6-400SA sintered copper heat pipes with ultrapure water, enabling an efficient heat transfer from the hive interior (4) and the outer heatsink (6), able to dissipate the heat into the environment. This harvester assembly in then integrated into a standard 5 frame Langstroth (LR) nucleus hive (Figure 5b) and tested in laboratory conditions by imposing different

temperature gradients comparable to those occurring in a real hive housing of a honeybee colony.

(a)

(b)
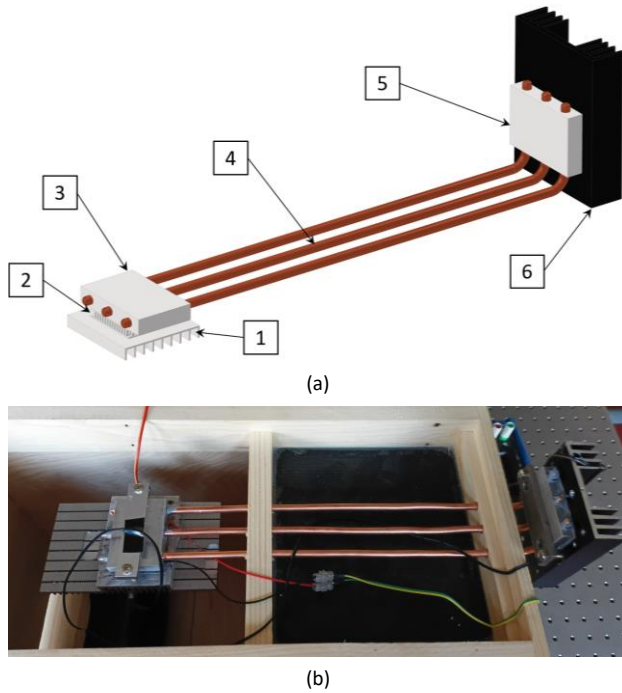
Figure 5. CAD model of the waste heat harvester prototype (a) and the harvester integrated into a nucleus hive (b)

As shown in Figure 6, the performance of the harvester is assessed by heating the air within the hive (1) comprising the integrated harvester (2) by using a digitally controlled conventional KLW-007E1-EU400 ceramic (PTC) heater (3) placed within the hive. The voltage generated by the TEG is routed via a TE 1051 [21] variable resistance box (4) to the National Instruments MyRIO® device (5) [22] serving as a DAQ system, connected to a LabVIEW® control virtual instrument (VI) [23] running on a PC (6). Along with the generated voltage, the temperatures on both the inner and outer heatsink are also monitored by using sensors connected to the DAQ device.
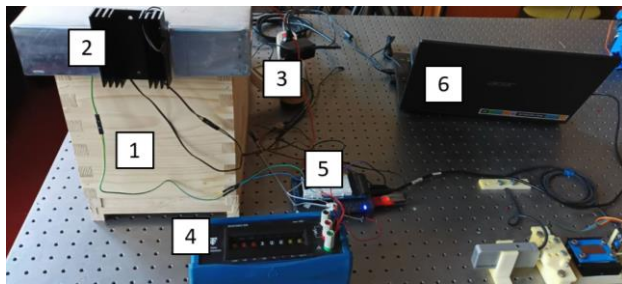
Figure 6. Experimental setup for testing the waste heat energy harvester

3.1. Results

The voltage generated by the harvester for different temperature differences is used to calculate the power output, both in relation to the load resistance values R (Figure 7a), as well as the current I (Figure 7b). Maximum power outputs ranging from P = 3.5 to 9.7 mW can be observed at the optimal resistances of R_{load} = 8 – 10 Ω. The respective voltages generally range from U = 0.25 to 0.32 V. During the measurements it was determined that a more efficient outer heatsink is required at the cold end, enhancing thus heat dissipation, and, finally, increasing the thermal gradient, i.e., the temperature difference at the TEG itself. This would, in turn, result in an increased power output of the overall system. What is more, the inner heatsink also needs to be carefully designed in terms of the so called "bee

space", i.e., by respecting the requirement that all gap sizes are to be held between 6 and 9 mm to keep the colony from filling them up with propolis resin or wax comb, thus minimizing the intrusion into the colony itself.

(a)

(b)
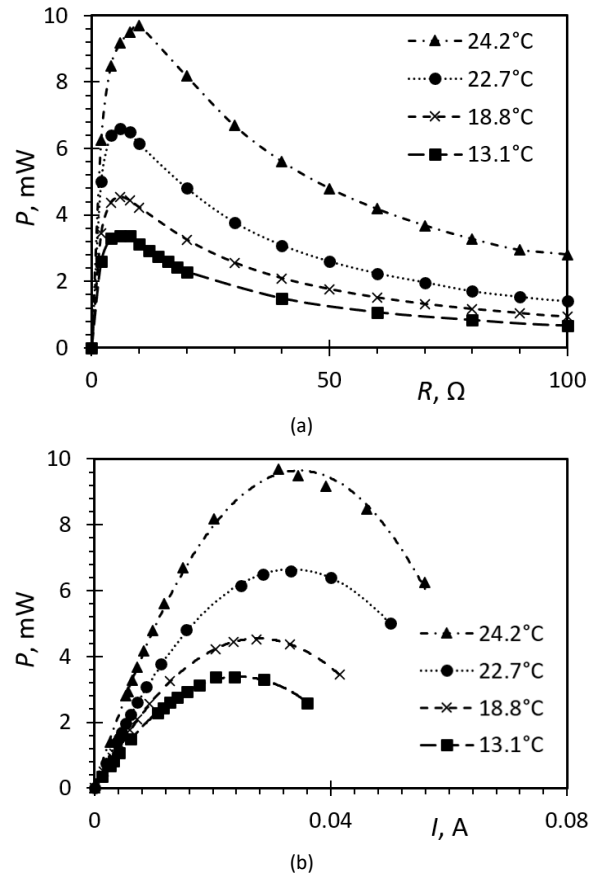
Figure 7. Experimentally assessed power outputs P of the waste heat energy harvester at different temperature gradients vs. load resistance R (a) and current I (b)

What is more, possibilities to develop design configurations comprising a larger number of TEG transducers and/or heatsinks, such as that of Figure 8, are also being explored [24].
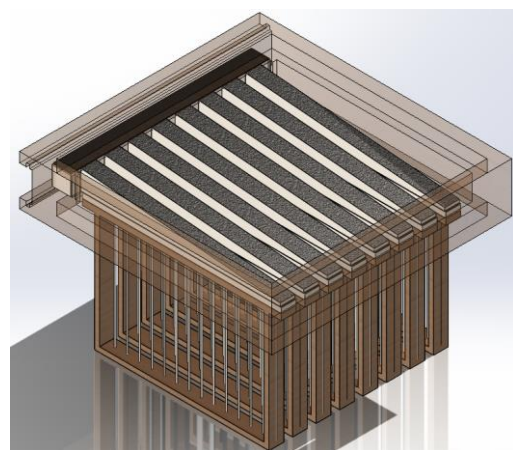
Figure 8. Design configuration with several heatsinks in the hive [24]

3.2. Hive monitoring system

As it is schematically depicted in Figure 9, the final integrated autonomous hive monitoring system, intended to be used during winter conditions, comprises then an array of ultra-low power temperature sensors, e.g. the MCP9700 low-power linear active thermistor [25] (a possibility of using other sensor principles, such as ultra-low power IR cameras, could also be

237

considered), combined with AD converters as well as ultra-low power CPU and communication modules. These components are to be powered by the energy stored in a supercapacitor, which is in turn charged via the TEG, exploiting the thermal gradient present between the colony and the environment. To utilize the power generated by the harvester for powering this system and successfully charge the supercapacitor, the low generated voltages would need to be increased via a step-up DC-DC converter. To manage the power distribution within the system, a suitable power management module is also needed. Additionally, by employing smart duty cycles, i.e., by limiting the operational time of components with large power requirements (especially the communication module), the overall power consumption of the system could be significantly reduced.
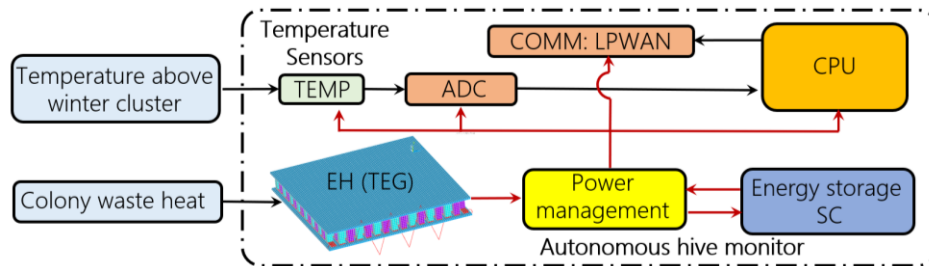
Figure 9. Schematic representation of the suggested autonomous hive monitoring system [14]

4. Conclusions and outlook

After a short introduction into managed honeybee colonies, with an emphasis on the issues of overwintering and the potential benefits of hive monitoring, an innovative autonomous hive monitoring system is proposed in this work. The system is to be powered by a novel approach based on thermoelectric EH principles able to utilize the thermal gradient between the honeybee colony and the surrounding environment.

An original method of assessing the size and strength of the colony by obtaining the temperature map above the cluster is suggested next, along with heat transfer simulations and temperature measurements supporting its viability. The possibility of practically utilizing the thermal gradient is discussed next, supported by data collected from a honeybee colony itself. Based on the data collected in the hive, a suitable TEG is numerically modelled by using ANSYS®, allowing to estimate a power generation of 38 mW.

A prototype energy harvester assembly is then designed and constructed, based on the same TEG, and comprising two heatsinks and heat pipes used to dissipate the heat generated by the colony into the environment. The harvester is integrated into a hive nucleus and tested in laboratory conditions by producing a thermal gradient comparable to that found in the actual colony. It is established that at different thermal gradients and with connected electrical load resistances of 8 - 10 Ω, the harvester is able to generate voltages ranging from 0.25 - 0.32 V and power outputs ranging from 3.5 to 9.7 mW. This is lower than the values calculated via FE simulations; the difference could be attributed to the fact that in the FE model the thermal gradient is applied directly at the hot and cold ends of the TEG, simulating an ideal case, while the temperatures during the experiment (ambient temperatures inside and outside the hive) are measured at the heatsinks, resulting in a thermal gradient at the TEG that is significantly lower than that in the FE model.

The essential components of the suggested hive monitoring system are finally described, considering also, to keep power consumption as low as possible and thus extend the autonomy of the proposed system, power management and duty cycles.

Further studies are required to develop a fully functional device. The development of suitable heatsinks, both inner and outer, is herein of crucial importance in terms of heat dissipation efficiency as well as of minimizing the intrusion into the honeybee colony while considering bee space. Moreover, a suitable step-up DC-DC converter needs to be paired with the harvester and the supercapacitor. What is more, the sensor array also needs to be designed and tested in combination with the CPU and the communication system, enabling thus a more exact assessment of the overall power requirements. Finally, the harvester needs to be tested on a factual hive containing a honeybee colony during winter conditions. The integration of additional EH principles, e.g. photovoltaics, will also be considered, constituting thus a novel hybrid EH approach to hive monitoring.

References

[1] van Engelsdorp D, Meixner M D 2010 *J. Invertebr. Pathol*. **103**:80-95
[2] Van Dooremalen C, Van Langevelde F 2021 *Agriculture* **11**:529
[3] Döke M A, Frazier M, Grozinger C M 2015 *Curr. Opin. Insect. Sci.* **10**:185-93
[4] Cushman D: www.dave-cushman.net (accessed 24 October 2023)
[5] Oliver R: scientificbeekeeping.com (accessed 24 October 2023)
[6] Cecchi S et al. 2020 *Sensors*, **20**(9):2726
[7] Zacepins A et al. 2016 *Biosyst. Eng.* **148**:76–80
[8] Gil-Lebrero S et al. 2016 *Sensors* **17**(1):55
[9] Prpić M. 2023 B.Sc. thesis, University of Rijeka, Croatia, Faculty of Engineering
[10] Melchor-Martínez E M 2021 *CSCEE* **3**:100104
[11] Nasr M E et al. 1990 *J. Econ. Entomol*. **83**:748-54
[12] Stabentheiner A et al. 2003 *J. Exp. Biol.* **206**:353-8
[13] Ocko S A, Mahadevan L 2014 *J. R. Soc. Interface.* **11**:20131033
[14] Gljušćić P, Zelenika S 2023 Proc *2nd Int. Conf. Mach. Des.* 70
[15] Ansys Workbench: https://www.ansys.com/products/ansys-workbench (accessed 8 January 2024)
[16] Fahrenholz L, Lamprecht I, Schricker B 1989 *J. Comp. Physiol. B* **159**:551-60
[17] Prya Sh, Inman D J 2009 *Energy harvesting technologies* (New York, NY, USA: Springer)
[18] Tan Y K 2013 *Energy Harvesting Autonomous Sensor System* (Boca Raton, FL, USA, CRC Press)
[19] TEG2-126LDT: https://tecteg.com/product/teg2-126ldt-body-scavenger (accessed 8 January 2024)
[20] Ansys Mechanical: https://www.ansys.com/products/structures/ansys-mechanical (accessed 8 January 2024)
[21] TE 1051: https://www.timeelectronics.com/decade-boxes/1051-8-decade-resistance-box/ (accessed 11 November 2021)
[22] NI MyRIO 1900: https://www.ni.com/en-rs/support/model.myrio-1900.html (accessed 18 January 2022)
[23] NI LabVIEW: https://www.ni.com/en-rs/shop/labview.html (accessed 18 January 2022)
[24] Julien L, Kladarić M, Emerencienne M 2024, Student project, University of Rijeka, Croatia, Faculty of Engineering
[25] MCP9700: https://www.microchip.com/en-us/product/mcp9700 (accessed 28 December 2023)

The evolution and future trends of the mounting of high-performance optics

Marwène Nefzi[1], Jens Kugler[1]

[1]*Carl ZEISS SMT GmbH, Oberkochen, Germany*

marwene.nefzi@zeiss.com

Abstract

High-performance projection optics must meet very tough specifications since the early phase of the development of semiconductor manufacturing machines. One key issue has always been the mounting of optical elements. The last three decades witnessed continuous evolution in the technologies used in this context. Whereas the first successful ideas consisted in clamping the optical elements to the housing aiming at a rigid connection and small relative motions within the projection optics, later approaches rely on controlling the position and orientation of kinematically determined parallel manipulators holding the optical elements. For understanding this evolution and anticipating future trends, a review of different mounting technologies together with the increasing demands to high-performance optics is essential. To this end, this paper revisits some mounting technologies and recalls the basic kinematic principles needed to understand these technologies.

Three phases can be distinguished in the evolution of the mounting of optical elements. Correspondingly, this paper is divided into three sections. The first section outlines the very first mounting solutions that were used in projection optics. The second section emphasizes the reasons that lead to the use of manipulators. The last section addresses further challenges and proposes kinematically over-determined manipulators to meet the requirements expected in future developments.

Keywords: Semiconductor Manufacturing, Mounting Technologies, Optomechanics, Optics, Kinematics

1. Introduction

The mounting technologies of high-performance optics evolved in three phases. In the first phase, passive mounting technologies were dominant. Later, kinematically determined monipulators become the state-of-the-art. In the near future, it is expected that kinematically over-determined manipulators are needed to cope with the increasing demands. But first, it is important to recall the fundamental problem of mounting optical elements. It is generally required that optical elements, often made of glass, are mounted inside a housing, often made of metal, that isolates the optical elements from different environmental disturbances, like shocks, vibrations, thermal disturbances etc. One crucial task consists therefore in solving the problem of fixing the optical elements to the housing. The first section revisits the passive mounting of optical elements. The second section emphasizes the need of using manipulators to enable high-accurate alignment of the optical element. The third section proposes kinematically over-determined manipulators to meet the requirements expected in future developments.

2. Passive mounting of optical elements

The first phase of the mounting of high-performance optics relies on axial and radial clamping [1]. As the requirements become tougher, decoupling the optical elements from the housing gains in importance. Elastic hinges are then necessary and must be designed to decouple the optical element from its environment.

2.1. Clamping and adhesives

The most intuitive way of mounting an optical element to the housing is clamping it. Hard clamping, as depicted in **Figure 1(a)**, is clearly simple and cost-effective. If the available volume for the mounting is limited, adhesives, as depicted in **Figure 1(b)**, are often used to fix the optical element to the housing [2]. Morevover, both clamping and glueing allow for a radial mouting of the optical element. It induces however more mechanical stress and surface distortions. The result is often poor optical performance, especially when the system is subject to thermal and mechanical disturbances.
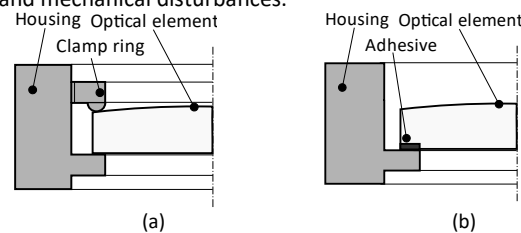
Figure 1. First mounting solutions rely on clamping and adhesives

The increasing demands and the sensitivity of larger optical elements to disturbances compel engineers to design a better decouping of the optical element. One decisive idea is the use of elastic hinges.

2.2. Use of elastic hinges

Figure 2 depicts an optical element mounted on flexure hinges. Each elastic hinge has 2 degrees of freedom allowing therefore each mounting point of the optical element to move in a horizontal and vertical direction. In this way, thermal and mechanical disturbances coming from the housing are attenuated and don't induce mechanical stresses in the optical element.
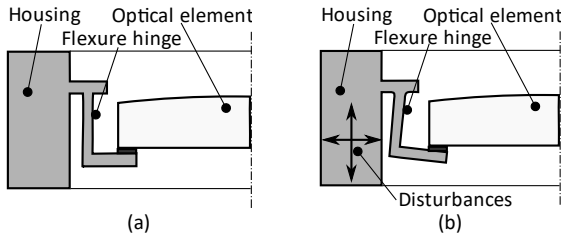
Figure 2. Elastic hinges for decoupling optical elements

The main drawback of passive mounting is the fact that an alignment of the optical element is challenging and time-consuming, since it is achieved by means of machine tolerances of the components and shims [2]. A more adequate way of aligning the optical element is to use a manipulator. The next section addresses this issue.

3. Kinematically determined manipulators

A manipulator consists of several links connected with hinges. In this context, the fixed frame corresponds to the housing, and the moving platform corresponds to the optical element. Such a system must first ensure that the desired number of degrees of freedom (DoF) needed for alignment is met. To this end, the mobility of the manipulator is investigated in the first subsetion. The second subsection addresses parasitic forces and moments that arise from the manipulation of the optical element.

3.1. The mobility of a manipulator

Figure 3(a) depicts an optical element that is connected by means of six links to a fixed frame. Clearly, the optical element is the moving platform of this manipulator. One crucial issue in designing such a manipulator is to find out the degrees of freedom needed in each link so that the whole mechanism is kinematically determined. The Grübler formula [3] can be used for this purpose. For simplicity of exposition, each limb is replaced by a subset of links and elastic hinges as shown in Figure 3(b). The final system has one fixed frame, one moving platform and six joints. By means of the Grübler formula, it is now possible to find out the number of degrees of freedom for each subset

$$F = 6(n - 1 - j) + \sum_j f_j$$

The final mechanism is kinematically determined, if the mobility number F equals zero. Referring to Figure 3(b), the number of parts building up the manipulator is $n = 2$, i.e. the fixed frame and the moving platform, the number of subsets is $j = 6$. Hence, the sum of all degrees of freedom needed in the six subsets is $\sum_j f_j = F - 6(n - 1 - j) = 30$ for having $F = 0$. In other words, the number of degrees of freedom in each subset should be five, if a kinematically determined manipulator is aimed at.
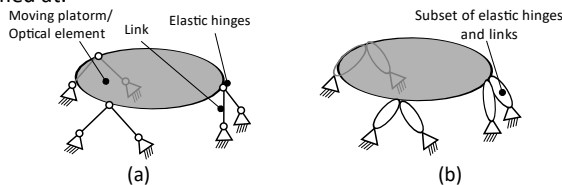
Figure 3. Kinematically determined manipulator

An alignment of the optical element can be carried out by actuating the limbs depicted in Figure 3(a). Six actuators will add six degrees of freedom to the platform so that the optical element can be positioned and oriented in the 6-dimenstional space in order to achieve the desired alignment. After the alignment, the actuators are locked, the mobility number is zero again $F = 0$.

3.2. Parasitic forces and moments

As seen in Section 2.2, elastic hinges are often used. Although the manipulator is kinematically exactly constrained, the hinges, when deformed, react with internal forces and moments that are transmitted to the optical element according to Figure 4(a). These forces and moments are called parasitic and lead to distortions of the optical surface. This, in turn, causes optical aberrations. Figure 5 shows the impact of a tangential moment on the optical element.
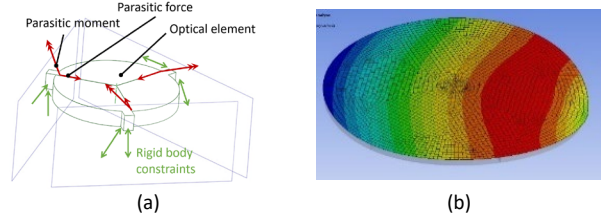
Figure 4. (note: larger figures can be set over 2 text columns)

Consequently, even if a kinematically determined manipulator is properly designed, distortions of the optical surface cannot be prevented, especially when alignment is needed and elastic hinges are used. As the demands to the optical surface increase, parasitic forces and moments become a challenge. So, reducing them is a key issue in further devolpments of high-precision manipulators. Kinematically over-determined manipulators are therefore more in the focus.

4. Kinematically over-determined manipulators

As seen in the previous section, it is not sufficient to ensure that the manipulator is kinematically determined for minimizing the distortions of the optical surface. A reduction of parasitic forces and moments is necessary in order to obtain better optical performance.

If the optical element is moved for alignment purposes, parasitic forces and moments arise according to Figure 5(a) and deform the optical surface. As far as radial forces are concerned, additional radial actuators can be added to the manipulator according to Figure 5(b). These exert forces that counteract forces going through the optical element. Hence, parasitic radial forces and thereby the distortions of the optical surface can be minimized. Although six DoFs are needed for the alignment process, more than six actuators are used. This redundancy is used to minimize the forces on the optical element and to improve the optical performance.
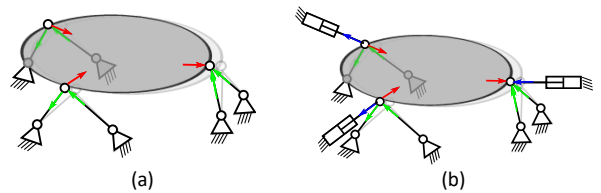
Figure 5. Motivation for using over-determined manipulators

5. Conclusion

This paper addresses the evolution of the technologies used in the mounting of optical elements. Kinematically over-determined manipulators are expected to gain in importance, as the demands for accurate manipulators increase.

References

[1] Yoder, Paul R. *Opto-Mechanical Systems Design*. Marcel Dekker, Inc. 1986.

[2] Leach, R., & Smith, S.T. (Eds.). Basics of Precision Engineering (1st ed.). CRC Press. 2018.

[3] Grübler, Martin. *Getriebelehre. Eine Theorie des Zwangslaufs und der ebenen Mechanismen*. Berlin: Verlag Julius Springer. 1917.

Three-dimensional observation and morphological analysis of inclusions in a Ni-Co-based superalloy using the serial sectioning method

Yuki Aida[1,2], Ryoma Suzumura[1,2], Norio Yamashita[2], Shinya Morita[1,2], Toru Hara[3], Toshio Osada[3], and Hideo Yokota[2]

[1]*Nano Precision Manufacturing Laboratory, Tokyo Denki University, Japan*
[2]*RIKEN Center for Advanced Photonics, RIKEN, Japan*
[3]*National Institute for Materials Science, Japan*

yuuki.aida@riken.jp

Abstract

In this study, we observed the microstructural defects of inclusions and pores in a relatively large volume of a Ni-Co-based superalloy, TMW-4M3, including more than one hundred thousand inclusions using the serial sectioning method with precision cutting and optical microscopy, and analyzed their statistical morphology. First, we applied ultrasonic elliptical vibration cutting (UEVC) to the Ni-Co-based superalloy, a difficult-to-cut material, to obtain a mirror cross-section suitable for observation. Cutting conditions of a depth of cut of 1 μm, a cutting speed of 120 mm/min, and an elliptical vibration amplitude of 1.5 μm_{p-p} resulted in the best surface roughness (Ra 10.3 nm). Next, we performed serial sectioning of the superalloy with 105 and 1000 cross-sections under these conditions. Here, image tiling was also applied to obtain large volumes of 12.2 × 11.7 × 0.105 mm and 12.2 × 11.7 × 1 mm. Finally, the inclusion regions were extracted and their number, volume, and equivalent diameter were calculated. Histograms of the 3D features of nearly 140,000 inclusions were obtained. This statistical morphological information will contribute to the safe design of high-temperature components with stringent safety requirements.

Keywords: Ni-Co-based superalloy, inclusion, Elliptical vibration cutting, Precision cutting

1. Introduction

Ni-Co-based superalloys designed based on a combination of a Ni-based superalloy and a Co-based alloy, both with γ-γ' two-phase structure, are attractive materials for turbine disks in jet engines operating in high-temperature and high-pressure environments [1]. The evaluation of the material properties and reliabilities requires an assessment of the shape, distribution, and number of micron-sized microstructural defects in the inclusions and pores that act as crack initiation sites of fatigue failure. However, this is based on previous 2D observations, which is not always sufficient for statistical evaluation [2]. Therefore, it is necessary to perform highly efficient 3D observations over a wide area of millimeters with submicron-high resolution to obtain information on the spatial distribution, number of such objects, and morphology. One such method is serial sectioning, which removes thin layers and acquires a series of cross-sectional images [3]. Polishing methods are commonly used to remove thin layers. However, a highly efficient method using precision cutting has been proposed [3], which has the advantage of less processing time and controllability of the amount of removal. In this study, a large amount of inclusion information of Ni-Co-based superalloy was obtained using the serial sectioning method with precision mirror cutting and subsequent morphological analysis. Using the cutting condition from several cutting experiments, a volume from 105 slices of images were obtained. The inclusions were segmented from the images and histograms of the volume and equivalent diameter of the inclusions were created for statistical evaluation. Since further accumulation of data is required for material fatigue statistics, we demonstrated 1000 slices imaging, and also assessed the life of the cutting tools, which often limits the imaging volume.

2. Research methods

First, suitable cutting conditions were searched using ultrasonic elliptical vibration cutting (UEVC) [4] to create a mirror surface via precision cutting, considering those for Inconel 718 [5], which is likely to have similar machinability to that of a Ni-Co-based superalloy. Thin layer removal and continuous cross-sectional image acquisition via image tiling were performed, and 3D images containing numerous inclusions were reconstructed. We used MATLAB (R2022b, R2012a) for image tiling and statistical evaluation of inclusion morphology. The inclusion regions were segmented by binarization of the image and labeled according to their 3D connections, and their number, volume, and equivalent diameters were calculated. The filtered results were also calculated, excluding those with fewer than three voxels of connection in the Z-direction, such as chips, dust, or too small.
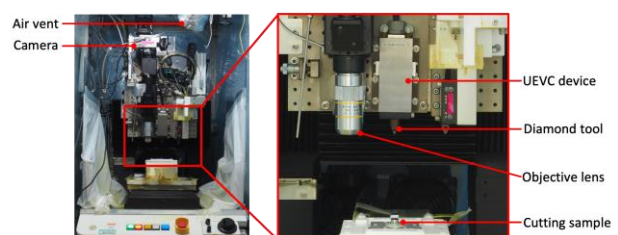
Figure 1. 3D internal structure microscope

3. Experimental device and Cutting sample

We used the UEVC device (EL-50Σ, Taga Electric Co., Ltd., Japan) to precisely cut the Ni-Co-based superalloy. The device was mounted on a 3D internal structure microscope (Riken Micro Slicer System: RMSS-005 [6], Japan) equipped with an epi-illumination imager as shown in Figure 1. An NC milling machine (MULTIPRO MP6 series, Takashima Sangyo Co., Ltd., Japan), a single-crystal diamond tool (UPC, A.L.M.T. Corp., Japan), and objective lens (M Plan Apo HR 10×, Mitutoyo Corp., Japan) were installed to enable fully automated cutting and observation. It uses planar cutting with a tool with a flat cutting edge of 1 mm, as shown in Figure 2. A single stroke can generate a mirror-like cross-section of the tool width. Shifting the cutting paths generates a wide cross-section. The sample material was TMW-4M3 [2], which was created at NIMS using the same casting and forging process as the turbine disk. This part was prepared as a cylindrical sample with a diameter and height of 10 mm.

4. Experimental results

4.1. Precision cutting condition search and surface roughness

The sample surfaces were polished beforehand. Precision cutting was performed under six conditions: cutting speeds of 30, 60, 90, 120, 150, and 180 mm/min at a tool width of 1 mm, depth of cut of 1 μm × 10 times, and elliptical vibration amplitude of 1.5 $μm_{p-p}$. A mirror surface with a roughness of approximately Ra of 10 nm was created under all conditions. The roughness values of the polished and cut surfaces at a cutting speed of 120 mm/min are shown in Figure 3. Their surface roughness values were Ra = 20.1 nm and 10.3 nm, respectively. The UEVC achieved sufficient surface roughness for observation, and we selected 120 mm/min for subsequent experiments.

4.2. Continuous 105 cross-section 3D observation

3D observation of 105 continuous cross-sections was performed using precision cutting. Each cross-section was obtained as 54 tiling images (9 in the x-direction and 6 in the y-direction) with a voxel pitch of 0.391 × 0.391 × 1 μm and an optical resolution of 0.6 μm at high resolution. The total observation time was approximately 10.5 h.

4.3. Inclusion morphology analysis using 3D data of 105 continuous cross-sections

The volume and equivalent diameter of each inclusion were calculated assuming that they were spherical. Figures 4 (a) and (b) show histograms of the volume and equivalent diameter of the inclusions in a double-logarithmic graph, respectively. The red bars are from all the inclusions, whereas the blue bars are from those filtered, which connect more than three continuous cross-sections. The filtering was to exclude the cutting chips and those that were too small. The number was approximately 140,000 prior to filtering. After filtering, those with more than 10 $μm^3$ and the largest volumes were 8583 and 7027 $μm^3$,
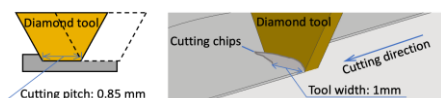
Figure 2. Creation of observation surface by precision cutting process
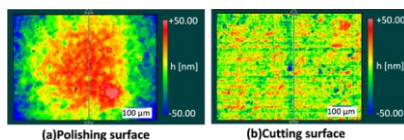
Figure 3. Surface roughness (120 mm/min)
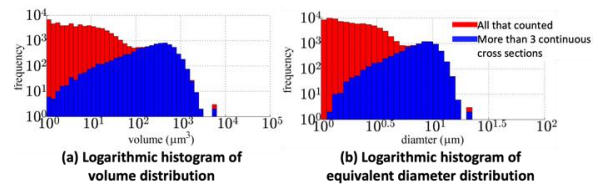
Figure 4. Histogram of volume and equivalent diameter of inclusions

respectively. Therefore, our method demonstrated a statistical evaluation of the inclusion size and percentage of their existence.

4.4. Continuous 1000 cross-section 3D observation

A 3D observation of 1000 continuous cross-sections was performed using the same precision cutting and observation conditions. Approximately 100 h of automated observation was conducted to obtain a total of 31083 × 30025 × 1000 voxels. Figure 5 shows a 2D cross-sectional image (12.2 × 11.7 mm) and a 3D image of a part of the sample (2346 × 1564 × 1000 μm). The spatial distribution and various sizes of the numerous inclusions were confirmed in the volume. Future analyses of the data will provide a more precise statistical inspection of the inclusion morphology.
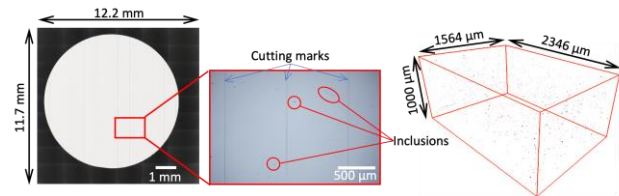
Figure 5. Cross-sectional image by precision cutting and 3D image

5. Conclusion

(1) We proposed a statistical evaluation method for 3D morphology of many inclusions in the Ni-Co-based superalloy by serial sectioning using UEVC and morphological analysis.
(2) We found a suitable UEVC speed for mirror surface generation of TMW-4M3 with a surface roughness Ra of 10.3 nm.
(3) 3D observation of TMW-4M3 with 105 and 1000 cross-sections were demonstrated to obtain large volumes, 12.2 × 11.7 × 0.105 and 12.2 × 11.7 × 1 mm, respectively, with a voxel pitch of 0.391 × 0.391 × 1 μm.
(4) Approximately 140,000 inclusions were evaluated from the 3D image with 105 sections, and those with more than 10 $μm^3$ and the largest volumes were 8583 and 7027 $μm^3$, respectively.

Our statistical inclusion evaluation method based on a large 3D imaging will contribute to advanced material development.

References

[1] Gu Y, Harada H, Cui C, Ping D, Sato A and Fujioka J 2006 *Scripta Materialia*. **55** 9 815-818
[2] Kobayashi S, Ono Y, Osada T, Ii S, Kawagishi K, Date M and Ohno T 2019 *Proc. Int. Gas Turbine Congress 2019 Tokyo*. IGTC-2019-172
[3] Fujisaki K, Yamashita N and Yokota H 2012 *Precis. Eng.* **36** 2 315-321
[4] Jung H, Shamoto E, Chin H and Anh N V 2016 *Proc. J. Japan Soc. Precis. Eng.* 153-154
[5] Kawasaki S, Yamashita N, Morita S and Yokota H 2022 *Proc. the 19th Int. Conf. on Precis. Eng.*, C255
[6] Suzumura R, Yamashita N, Morita S and Yokota H 2022 *Proc. Int. Symp. Adv. Abrasive Tech.*, 618-624

Design and manufacture of face grinding wheels with micro-structured channels

Lukas Steinhoff[1], Emma Tubbe[1], Folke Dencker[1], Tim Denmark[2], Lars Kausch[2], Marc Christopher Wurz[1]

[1]*Institute of Micro Production Technology (IMPT), Garbsen, Germany*
[2]*Schmitz Schleifmittelwerk GmbH, Remscheid, Germany*

steinhoff@impt.uni-hannover.de

Abstract

In this study, we demonstrate the design and manufacture of face grinding wheels with micro-structured fluid channels for the uniform distribution of cooling lubricant in the tool working zone. For this purpose, the effect of different channel geometries on the flow velocity and the pressure exerted by the fluid on the channel wall is tested simulatively. To ensure effective heat exchange between the coolant and the workpiece, the channel geometry was designed to achieve a large contact area between the fluid and the ground material. Here, the tested curved channel geometries showed to have about 5 % more area than straight channels. However, the higher influence here is exerted by the number of channels. The produced curved channels further showed a direct influence on the flow rate of the cooling lubricant depending on the direction of rotation of the grinding wheel. This allows slowing down the flow rate by 2 % or increase it by up to 18 % compared to straight channels. We observed a beneficial influence to the flow rate and thus also the heat exchange without changing the pump parameters of the fluid. Prototype grinding wheels were produced by microsystem technology. For this purpose, silicon carbide is mixed as an abrasive into a photosensitive polymer (flexible binding matrix) and applied to a steel substrate. Structuring takes place by using photolithography. The unexposed areas can be cleared using developer solution. These form the channel structures. The cooling lubricant, for which water was selected, is supplied via the spindle and thus via the tools centre. The achievable minimum channel width is 200 μm or greater with a depth of 50-60 μm. First grinding tests resulted in roughness values of $R_a = 0.07 \pm 0.03$ μm and $R_z = 3.38 \pm 1.96$ μm for dry machining and $R_a = 0.08 \pm 0.03$ μm and $R_z = 1.92 \pm 0.20$ μm for machining with water as cooling lubricant. Temperature measurements proofed that the temperature increase of around $8*10^{-4}$ °C/s could be decreased to around $2*10^{-4}$ °C/s by use of water als cooling lubricant.

Keywords: micro grinding, micro production technology, precision engineering, lubricant distribution

1. Introduction

Grinding as a mechanical machining process is an important step in achieving the required surface quality as well as dimensional accuracy of a component and is often used as finishing process in different fields, like automobile or aerospace [1]. However, the process harbours challenges that can prevent the required surface quality. Grinding burn is one of them [2]. Excessively high temperatures in the grinding zone can lead to damage to the material surface e.g. high residual stresses. A reduction in friction and reduction of the genereated heat can be achieved through the application oriented use of cooling lubricants (CL) [3]. The reduction in temperature can be maximised by guiding the CL through the tool directly into the contact zone between tool and workpiece. This continues to be an issue in the field of toolmaking and the associated research. Therefore, there are already some approaches to solving the problem. One group constructed a peripheral grinding wheel from a sandwich system consisting of several layers into which channels for the distribution of CL were inserted [4]. Another approach shows a face grinding wheel with an interrupted abrasive layer and guided cooling lubricant feed via the spindle [5].

This paper presents the process of manufacturing a grinding wheel for achieving high surface qualities with a structured grinding layer using photolithography. For this purpose, a polyimide with embedded abrasive grains (silicon carbide, SiC) is used as a binding matrix, which has already been shown as a suitable combination for production of micro grinding tools [6]. Sufficient CL distribution should be achieved by creating fluid channels in the grinding layer, through which the CL can flow from the centre of the tool. Hereby, photolithography offers the advantage of variable channel geometry. After production, initial grinding tests should demonstrate the functionality of the tools.

2. Experimental procedures

The following section describes the simulation based design of the grinding wheel, the manufacturing process and its structuring by photolithography as well as the first grinding experiments.

2.1. Simulation-based design of the grinding wheel geometry

The aim of this research is to design and manufacture a face grinding wheel with a size of 100 mm, which should feature photolithographically structured fluid channels. The channel width should be in the range of a few hundred micrometres, while the channel depth should correspond to the grinding layer height. Various geometries were therefore created as 3D models using *SolidWorks*. Straight and curved channels as well as angular and radius channel transitions are tested. The pressure distribution on the channel walls through the CL during rotation of the grinding wheel was simulated using *Ansys Fluent*. The pressure distribution serves as a decision criterion here. The aim is to achieve the smoothest possible transition with homogeneous pressure distribution, to minimise the risk of the

abrasive layer detaching from the substrate due to excessive pressure peaks. A rotational speed of 4,000 rpm and a mass flow of 0.0004 kg/s were defined as parameters, as these could become possivle grinding parameters for the tool. The pressure distribution on the channel wall and the velocity distribution of the fluid within the channel were extracted as a result of the simulation.

2.2. Manufacturing and characterisation process of micro-grinding tools

Micro-technical structuring using photolithography was chosen for the production of the grinding discs. This allows various geometries and customisations to be realised. The abrasive layer is produced from the photosensitive polyimide LTC9320 (Fujifilm) and SiC abrasive grains (grain size distribution 4-6 μm). Both components are mixed in a glass container to form a homogeneous polyimide abrasive solution (PAS) (Fig. 1a). Steel wafers (1.4301) with a diameter of 100 mm are used as a substrate to produce the grinding tools. The PAS is applied to this by means of spin coating. After a two-part softbake (70 °C for 10 min, 100 °C for 10 min), the grinding wheels are slowly cooled to room temperature. The PAS is then exposed for 250 s using a glass mask to produce the channel geometries. Subsequent development takes place in a 3-stage immersion bath in cyclopentanone, propylene glycol methyl ether acetate (PGMEA) and isopropanol (Fig. 1b). In total, the process from mixing to developing, including handling, takes around two hours. Finally, the grinding wheels cleaned with DI water are baked in an N_2 gas atmosphere at 350 °C for 60 min. The fluid channels are analysed for residues of PAS using light microscopy and the layer thickness is measured using tactile profilometry. In a post-processing step, a 4 mm hole is drilled in the centre of the grinding wheel for the CL connection (Fig. 1c).
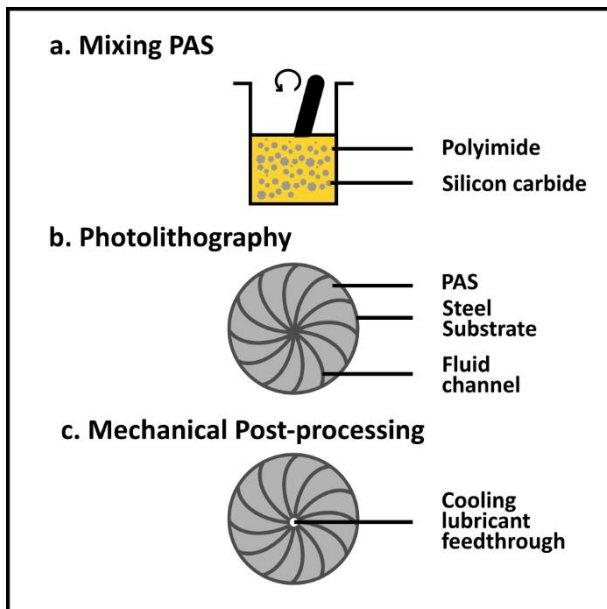
Figure 1. Schematic of the manufacturing process. It is divided in the mixing process of the PAS (a.), the structuring of the fluid channels by photolithography (b.) and the mechanical post-processing (c.).

2.3. Grinding experiments with temperature measurement

In order to ensure a supply of CL through the grinding wheel for the grinding tests, a test setup was designed. The schematic cross-section and a photo of the setup are shown in Fig. 2. The grinding wheel is attached to the grinding wheel mounting using adhesive film. The mounting offers nine places on top for the placement of weights in order to set a defined contact pressure

of approximately 625 Pa and 1,250 Pa for the experiments. The CL is supplied via a tube that is connected to the grinding wheel via a swivel joint. The tube is also hung in a reservoir of the used CL, which is supplied by a peristaltic pump. Mass flow rates of 150 ml/min and 300 ml/min were selected. The grinding wheel is driven by a toothed belt, which is moved by a DC motor. A rotation speed of 80 rpm has been set for the grinding wheel as working speed, which is limited by the motor. As CL water is chosen, whereas dry machining is chosen as comparison.

Stainless steel with a diameter of 130 mm was chosen as the material to be machined. In order to make a statement about the resulting temperatures and the cooling capacity of the cooling medium, temperature sensors of type Pt1000 were attached to the rear of the workpiece in milled pockets with a distance of 300 μm to the front side (see Fig. 2a). A total of three sensors were attached, each at a distance of 20 mm, 30 mm and 40 mm from the centre. This array allows an in situ monitoring of the temperature homogeneity.. The measurement data was recorded continuously for 10 min during grinding using a QuantumX measurement amplifier from HBM. Ten measured values were recorded per second. In order to make a statement about the cooling performance, the gradients of the temperature curves were compared with each other. Furthermore, images of the ground surface were taken using confocal laser scanning microscopy in order to assess the surface roughness values R_a and R_z and therefore the grinding performance of the tools. Surface roughness values were obtained over an area of 200 x 200 μm².
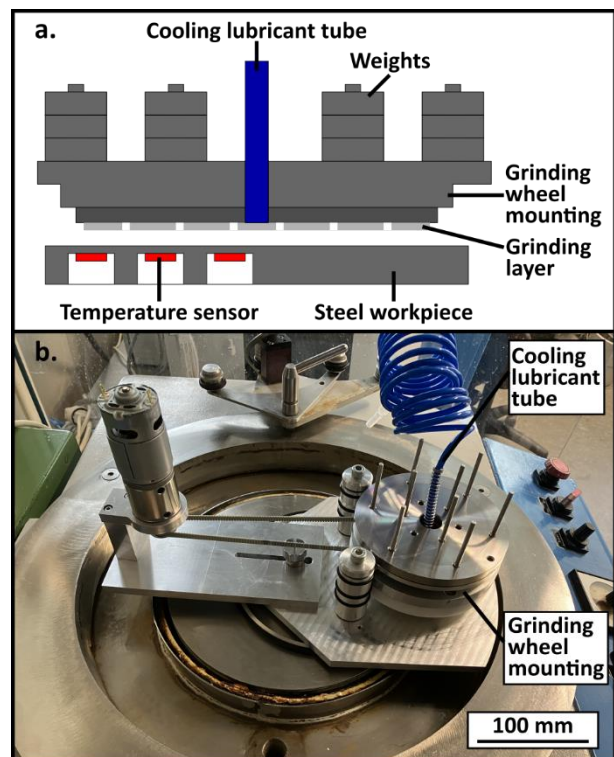
Figure 2. Illustration of the experimental setup for carrying out grinding tests with temperature measurement. A schematic cross-section with the position of the temperature sensors (a.) and a real image of the assembled test stand (b.) are shown.

3. Results and discussion

3.1. Design and manufacturing

In the simulation, the first aim was to investigate two different transitions between the connection of the grinding wheel to the cooling lubricant feed line and the microstructured cooling

channels. As shown in Fig. 3, an angular transition (Fig. 3a) and a radius transition (Fig. 3b) are compared. A normalised pressure decrease distribution is shown. The radius transition shows a much more homogenous and in total lower pressure decrease. Here, the pressure drops very evenly over a longer distance than with the angular transition. In this case, there is a concentrated load directly at the transition, which could lead in the worst case to delamination of the grinding layer.
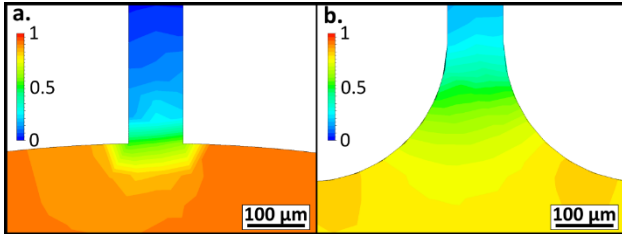
Figure 3. Illustration of the simulation results for comparing an angular transition (a.) and a radius transition (b.). The normalised pressure distribution from the fluid to the solid materials is shown.

Furthermore, straight channels were compared with curved ones. The flow velocity within the channels is used as comparison. The aim is to achieve a high flow velocity for a constant supply of fresh CL. Both types showed an increase in speed from the beginning to the end of the channel. However, the curved channels showed a dependence on the direction of rotation. If the curves of the channel are the opposite direction to the direction of rotation of the tool, the speed is decreased by about 2 % in comparison with straight channels. In numbers it is 21.3 m/s at the end of straight channels and for curved channels around 20.9 m/s. If the rotation direction is in the same direction, an acceleration can be detected by around 18 % (25.1 m/s). This has the advantage that more fresh CL is fed over the grinding zone, resulting in a greater temperature gradient between the workpiece and CL. Another, bigger advantage of the curved channels is the contact surface between the fluid and the workpiece. Due to the channel layout, this is about 5 % larger with curved channels (5.1 mm²) than with straight ones (4,9 mm²), which results in more surface area for heat exchange. This is further increased with the number of channels, which applies for both geometries. Based on these results, the design of the first grinding wheels with radius transitions and 36 curved channels is created.
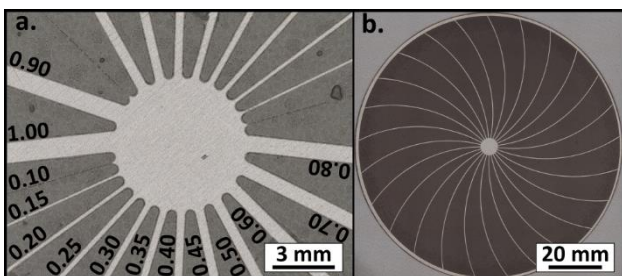
Figure 4. Illustration of the photolithographically structured grinding wheels. The results of a test on the feasible channel width are shown on the left (a.). Above the channels, the channel width from 0.10 mm to 1.00 mm is marked. A grinding wheel with a channel width of 300 μm is shown on the right (b.).

The channel width was evaluated in a feasibility experiment. The aim was to find a compromise between small channels with good manufacturability. The results are shown in Fig. 4. The smallest channels with a width of 100 and 150 μm still showed residual material within the channel structures even after a

longer development time with simultaneous ultrasonic support while at some points over development could already be detected. The 200 μm wide structures could be developed well (Fig. 4a). With regard to the later transfer to larger grinding wheels with thicker grinding layers, a slightly larger channel geometry was chosen. The channel width was therefore set to 300 μm. The first face grinding wheels with the set parameters were then produced with a layer thickness of approx. 50 μm (Fig. 4b).

3.2. Grinding experiments

The grinding wheels produced and shown in Fig. 4b were then used in grinding tests in the setup shown in Fig. 2. The recorded temperature curves were analysed and the resulting temperatures were evaluated for the different CL used. A comparison between dry machining (red) and machining with water as CL (blue) is shown in the following Fig. 5 for the outermost sensor. The range in which the temperature gradient was calculated is also shown as an example.
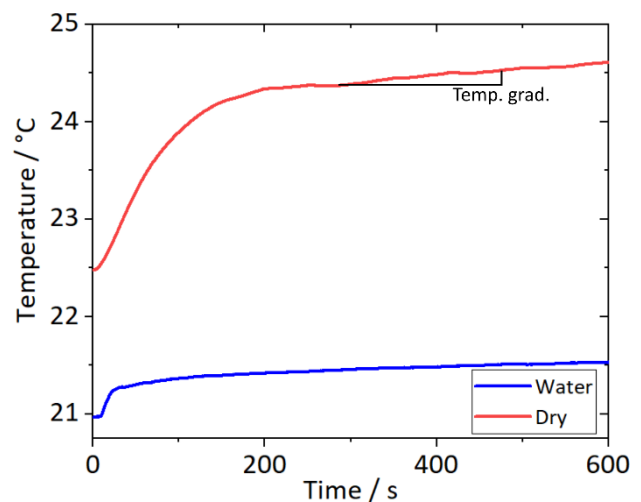
Figure 5. Exemplary evaluation of the recorded temperature during a grinding test. Both curves were recorded by the outermost sensor (40 mm). The tests were carried out at a contact pressure of 1,250 Pa. The CL feed rate was 150 ml/min. The determined temperature gradient for the subsequent comparison of the individual grinding tests is shown.

The temperature development in the first few seconds is significantly higher in most tests, as this is when the workpiece has the highest roughness, the lubricant has not yet been fully distributed and the tool is conditioned in the first few seconds. The abrasive grains can be covered with bond matrix after the manufacturing process, which is why the cutting effect is low but the friction is higher. As soon as the bonding matrix has reset and the abrasive grains can penetrate the workpiece with their cutting edges, the friction is reduced. Furthermore, the absolute initial temperature is not comparable, as this is related to the laboratory conditions and the cooling time of the workpiece between the individual grinding tests. The temperature gradient was therefore selected as the comparison factor. In all tests, an approximately linear curve was obtained after the initial time. It could be observed that the gradient depends on whether CL is used or not. The results are listed in Fig. 6 below. The gradients are small in both cases. This is partly due to the position of the temperature sensors, as the heat must first be conducted through the residual material to the sensor surface and part of it is already dissipated via the remaining workpiece. Furthermore, the rotational speeds and contact pressures are low due to the test setup. Nevertheless, a difference can be observed between dry machining and the use of CL. In dry

machining, the values are approx. 3 times higher than in wet processing with water. It can also be seen that the temperature rises more in the outer machining area than in the inner area. In the case of dry machining, the temperature gradients from sensor to sensor (inside to outside) are each 10 % higher. As both the workpiece and the tool are not moved in a plane, the cutting speed increases due to the increasing radius at a constant speed, resulting in more mechanical interaction. The higher layer thickness results in a higher contact pressure in specific area with the same effective weight. A significant difference between the selected CL quantities could not be determined. However, the resulting absolute temperatures are still very low. At higher cutting speeds and higher contact pressures and thus higher temperatures, the use of cooling lubricant and in particular the quantity will play a greater role than with the process parameters selected in this study.
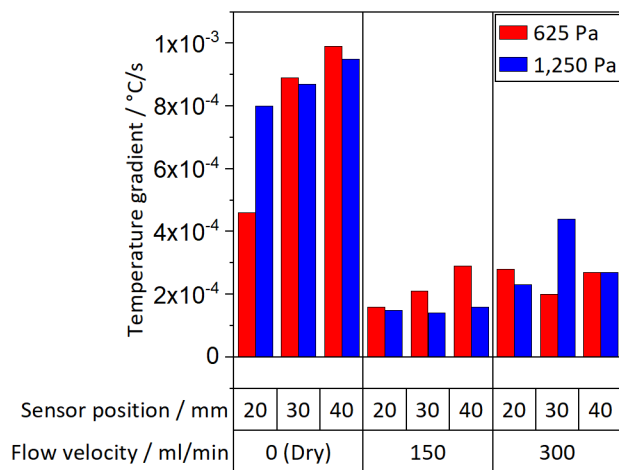
Figure 6. Illustration of the temperature gradients from the grinding tests as a function of the selected cooling lubricant and the grinding parameters used. Red represents the used contact pressure of 625 Pa and blue the used contact pressure of 1,250 Pa.

Fig. 7 shows a comparison of the workpiece surface before and after dry machining for 10 min. For the most part, homogeneous grinding marks can be seen on the machined surface and less heterogeneously distributed scratch marks than on the unmachined surface.
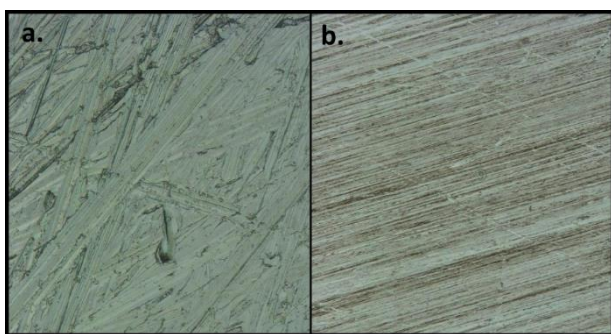
Figure 7. Comparison of the workpiece surface before grinding (a) and after 10 min dry grinding (b).

This is also reflected in the roughness values. Before grinding, the roughness values were $R_a = 0.29 \pm 0.08$ µm and $R_z = 5.37 \pm 0.91$ µm, which then decreased after machining to $R_a = 0.07 \pm 0.03$ µm and $R_z = 3.38 \pm 1.96$ µm. With regard to the surface roughness achieved, 10 min machining with water lead to roughness values of $R_a = 0.08 \pm 0.03$ µm and $R_z = 1.92 \pm 0.20$ µm.

4. Conclusion

In this work, a process for the manufacturing of grinding wheels using microsystems technology with a photolithographically structured grinding layer was demonstrated. The design was created by testing different geometries in a simulation, making it possible to demonstrate the effects of changes in geometry. A radius transition of the CL inlet led to a more homogeneous pressure distribution compared to an angular transition. Furthermore, curved channel structures showed the advantages of reduced flow velocity (-2 %) and a larger contact surface (+5 %) with the workpiece compared to straight channels. After the first design evaluation, a further check by means of finer geometry modifications, like radius of the curved channel or the channel transitions, can be useful for optimization. A test of the possible minimum channel width showed that channels with a width of 200 µm or greater can be produced using microsystem technology with SiC as abrasive grains and polyimide as binding matrix. In the first grinding tests, it was shown by measuring the resulting temperature that the temperature increase during dry machining is approx. 3 times higher than when machining with water as CL. In dry machining, an increase in surface quality to roughness values of $R_a = 0.07 \pm 0.03$ µm and $R_z = 3.38 \pm 1.96$ µm was achieved. After wet machining surface roughness values of $R_a = 0.08 \pm 0.03$ µm and $R_z = 1.92 \pm 0.20$ µm could be measured. The first grinding tests with the manufactured grinding wheels were therefore already successful. Further investigations into tool wear and optimised machining strategy and machining parameters must now follow in order to determine the performance of the grinding wheels. Other CL are also to be investigated and compared with the previous water cooling system. Furthermore, other structuring methods such as moulding or stamping processes for structuring are to be tested.

References

[1] Kishore K, Sinha M K, Singh A, Archana, Gupta M K, Korkmaz M E 2023 A comprehensive review on the grinding process: Advancements, applications and challenges *J Mechanical Engineering Science* **236** 10923-10952

[2] Irani R A, Bauer R J and Warkentin A 2005 A review of cutting fluid application in the grinding process *Int. J. Mach. Tool. Manu.* **45** 1696-1705

[3] Yang K Z, Pramanik A, Basak A K, Dong Y, Prakash C, Shankar S, Dixit S, Kumar K, Vatin N I 2023 Application of coolants during tool-based machining – A review *Ain Shams Eng. J.* **14** 101830

[4] Nadolny K 2015 Small-dimensional sandwich grinding wheels with a centrifugal coolant provision system for traverse internal cylindrical grinding of steel 100Cr6 *Journal of Cleaner Production* **93** 354-363

[5] Peng R, Huang X, Tan X, Chen R, Hu Y 2018 Performance of a pressurized internal-cooling slotted grinding wheel system *Int J Adv Manuf Technol* **94** 2239-2254

[6] Steinhoff L, Ottermann R, Dencker F, Wurz M C 2023 Detailed characterisation of batch-manufactured flexible micro-grinding tools for electrochemical assisted grinding of copper surfaces *Int. J. Adv. Manufact. Technol.* **128** 2301-2310

Superhydrophobic surfaces for polymers with micro and sub-micro scale structure via Two-Photon Polymerization

Kai Liu[1], Marco Sorgato[1], Enrico Savio[1]

[1]*Department of Industrial Engineering, University of Padua, Padova 35131, Italy*

Kai Liu, Email: kai.liu@phd.unipd.it

Abstract

Due to surface functionalities such as self-cleaning, anti-fogging, and oil-water separation, superhydrophobic surfaces are attractive in many industrial fields. Contact angles greater than 150° can be achieved by fabricating micro-nanostructures and modifying surface energy. Additive manufacturing allows us to overcome the limitations of traditional manufacturing methods in terms of geometrical complexity. This paper reports an investigation on Two-Photon Polymerization (TPP), focusing on the influence of the surface structure types on the wettability performance. Moreover, the micro-structure and sub-micron surface morphology of eggbeater's structure after TPP were also investigated.

Keywords: Superhydrophobic surface, Two-Photon Polymerization, Polymers, Surface structure

1. Introduction

Superhydrophobic surfaces with self-cleaning functionality, oil-water separation capability, anti-fogging, and anti-fouling properties play crucial roles across various industries such as automobile, aerospace, shipbuilding, and medicine [1]. Contact angle (CA) measurements are commonly employed to assess surface wettability. A contact angle higher than 150° typically indicates a superhydrophobic surface. A superhydrophobic surface is attained by either structuring a surface in a hydrophobic base material or modifying the surface chemistry within a micro-nanostructured surface. Developing a universally applicable method to transform a hydrophilic flat surface into a superhydrophobic surface across various materials poses a significant challenge. While several manufacturing techniques exist for creating structured surfaces - including cutting, abrasive machining, beam-based processes, electrical machining, and chemically assisted manufacturing - most struggle to achieve the complexity and high accuracy required for structured surfaces [2]. The emergence of two-photon polymerization (TPP) for crafting sub-microscale 3D structures has opened new avenues for fabricating highly adaptable functional surfaces [3], circumventing the constraints encountered in traditional manufacturing methods when dealing with intricate shapes. This study delves into TPP on the correlation between diverse surface structured shapes and surface wettability and achieves a shift from a hydrophilic with the plat surface to superhydrophobic surfaces with structure solely through alterations in surface structure.

2. Principle

TPP uses pulsed high-energy femtosecond laser beams in a small area [4]. As shown in Figure 1(a) and (b), the resin in the focus plane solidifies when the photoresin molecules simultaneously absorb the energy of two photons. Due to the significant threshold of two-photon polymerization, the rest of the resin can not absorb photons and solidify itself, which means that TPP

has high resolution and spatial selectivity [5]. With the movement of the laser focusing point and the stage, the micro and sub-micro scale surface structures are fabricated by curing layer by layer at the desired location.
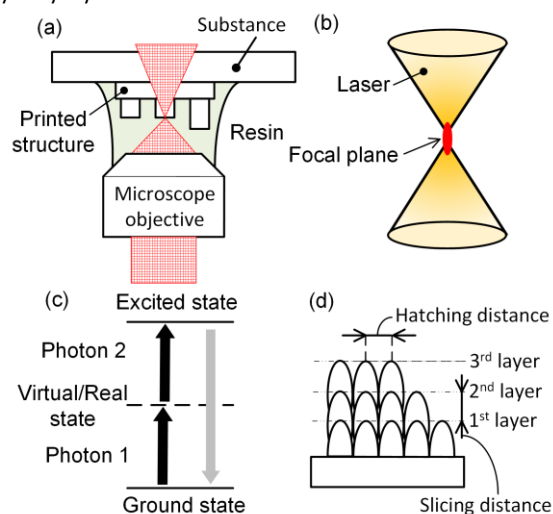
Figure 1. Schematic of two-photon polymerization

3. Experimental details

3.1. Experimental setup

A commercial two-photon polymerization equipment (Nanoscribe Photonic Professional GT) was employed to manufacture structured surfaces, utilizing a maximum power supply of 50 mW. The materials utilized included IP-S Photoresist and glass substrates measuring $25 \times 25 \times 0.7$ mm^3, featuring a one-sided conductive and optically transparent Indium tin oxide (ITO) coating. The surface topography was analyzed using confocal microscopy (Sensofar Neox). Cross-sectional scanning electron microscopy (SEM, FEI QUANTA 450) was employed to visualize the structured surfaces. Surface contact angle was determined by imaging using a Nikon D5300 camera equipped with micro-lens and evaluation through ImageJ software.

3.2. Experimental conditions

The different types of surface structure designs were built as STL, post-processed using DeScribe software, and fabricated using the parameters reported in Table 1. The samples produced through the TPP process underwent a sequential treatment: initially immersed in Propylene glycol monomethyl ether acetate (PGMEA) for 20 minutes, followed by a 5-minute ethanol cleansing stage to eliminate residual resin. Subsequently, the samples were exposed to UV light for 20 minutes to ensure complete curing. Contact angles were obtained as an average of five separate tests, aiming to minimize random errors.

Table 1 The details of experimental parameters

Parameter	Value
Slicing distance	1 μm
Hatching distance	0.5 μm
Laser Power	50 mJ
Scanning speed	100 μm/s
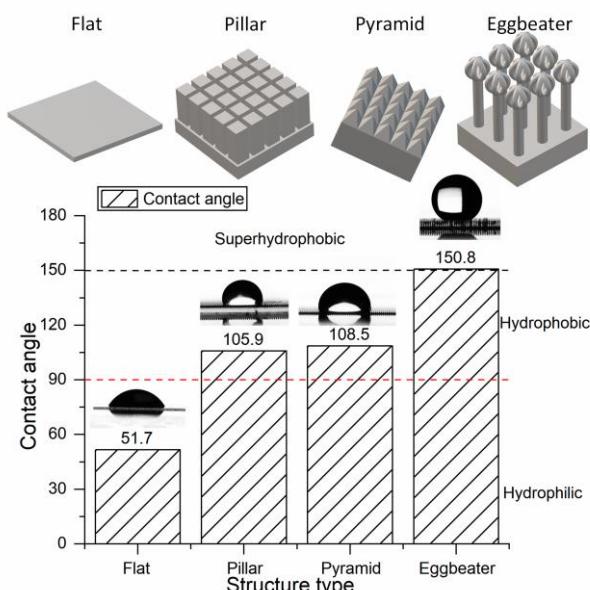
Figure 2. Effect of structure type and contact angle

4. Result and discussion

Figure 2 depicts the relation between various surface structures—Flat, Pillar, Pyramid, and Eggbeater—and their respective contact angles. As per the wettability definition, surfaces exhibiting contact angles exceeding 150° are categorized as superhydrophobic, those below 90° as hydrophilic, and those falling in between as normal hydrophobic surfaces [1]. The contact angle measured for the flat surface registered at 51.7°, characteristic of hydrophilic surfaces. In contrast, both the pillars, measuring 120 μm in height and 45 μm in width, and the pyramid, standing at 50 μm with a width of 50 μm, notably elevate the contact angle. This elevation effectively transforms the wettability from hydrophilic to hydrophobic compared to the flat surface. The base pillar of the eggbeaters exhibits a 20 μm diameter and stands at a height of 120 μm. The top arms comprise 10 μm circles encircling a 40 μm circle. Diverging from pillars and pyramids, the eggbeater-type surface structure achieves a superhydrophobic state. The upper structure of the eggbeater maintains a thin air layer spanning from its base to the top and the droplet is also fixed on the top of the eggbeater structure with hydrophilic surface wettability, demanding greater energy for water to breach this well-defined area [6].

Figure 3 shows the scanning electron microscopic morphologies and surface topography of the eggbeater's structured surfaces. The surface structure has good dimensional accuracy, while the underside of the structure needs to be spliced and fabricated due to the limitations of the lens range. The surface topography and line profile of the top structure after form removal are shown in Figures 3(d) and (e). The structured surface is not completely smooth, but sub-micron structures are created, which is attributed to the slicing distance and hatching distance during the TPP process, as shown in Figure 1(d).
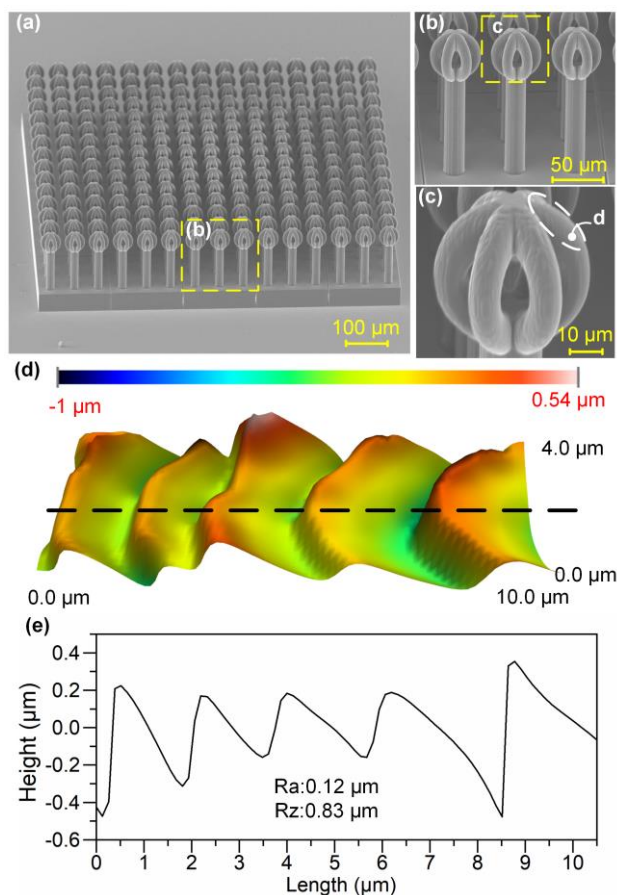
Figure 3. The eggbeater surface structure of SEM Micromorphology (a-c), topography (d), and profile (e).

5. Conclusion

Transforming a hydrophilic flat surface into a superhydrophobic one using typical pillar and pyramid structures presents challenges. Conversely, the eggbeate's structures demonstrate greater ease in achieving superhydrophobicity. The versatility of two-photon polymerization enables enhanced fabrication of intricate three-dimensional structures. Moreover, the sub-micron scale surface morphology is significantly influenced by process parameters, indicating its pivotal role in surface modification.

References

[1] Moghadam S G, Parsimehr H and Ehsani A 2021 *Adv. Colloid Interface Sci.* **290** 102397.
[2] Brinksmeier E, Karpuschewski B, Yan J and Schönemann L 2020 *CIRP Ann Manuf Technol* **69(2)** 717-739.
[3] Zhang S, Li S, Wan X, Ma J, Li N, Li J and Yin Q 2021 *Addit Manuf* **47** 102358.
[4] Maruo S, Nakamura O and Kawata S 1997 *Opt. Lett* **22(2)** 132-134.
[5] LaFratta C N, Fourkas J T, Baldacchini T and RA Farrer 2007 *Angew. Chem. Int. Ed.* **46(33)** 6238-6258.
[6] Barthlott W, et al. 2010 *Adv. Mater.* **22(21)** 2325-2328.

In-situ fine adjustment system for in-vacuo weighing cells

Mario André Torres Melgarejo, René Theska

Technische Universität Ilmenau, Department of Mechanical Engineering
Instute for Design and Precision Engineering, Precision Engineering Group

mario.torres@tu-ilmenau.de

Abstract

For traceable determination of mass, mass comparators and precision balances with a weighing cell as core unit are used. A further reduction of the measurement uncertainty is achieved by operation in a hermetically sealed chamber under vacuum conditions. The adjustment of the weighing cell required for high-resolution measurements is currently carried out manually under atmospheric conditions. This limits the achievable adjustment quality since the verification of the adjusted state is only possible under working conditions in the closed chamber.

This paper presents a novel system that enables the in-situ adjustment of high-precision weighing cells. The result of the adjustment can be directly controlled in a closed loop, thus fulfilling the conditions for a determined fine adjustment. The required high sensitivity of the moving parts of the weighing cell to be adjusted demands the minimization of disturbing influences to the largest possible extent. Based on a systematic investigation, sources of disturbances are eliminated and unavoidable residual systematic deviations are significantly reduced. The adjustment is performed by high-resolution actuators integrated directly into the moving elements. Power is supplied exclusively during the adjustment process via highly flexible electrical wires, which are connected via a separate rack-mounted drive system with low disturbances. The contact is released before the actual measuring process. Therefore, disturbances by the adjustment system are completely avoided during the measurement process. With the novel low-disturbance in-situ adjustment system, a significant increase in the performance of high-precision weighing cells can be achieved.

Keywords: weighing cell, in-situ adjustment, adjustment system, disturbance effects

1. Introduction

Comparison between mass standards at the top end of the dissemination chain demands mass measurements with highest resolution and least possible uncertainty. State-of-art mass comparators and precision balances use force-compensated weighing cells as core unit [1,2]. A monolithic linkage with filigree flexure hinges serves as mechanical structure to achieve highest sensitivity and repeatability. To avoid deviations from external sources, such devices are often operated in hermetically sealed vacuum chambers. Measurement uncertainty is further reduced by compensating remaining systematic deviations through fine adjustments of movable elements of the mechanism [3].

Fine adjustments are carried out on the arrested weighing cell using manually-driven built-in mechanisms under atmospheric conditions [4]. However, the adjusted state can only be verified under working conditions inside the vacuum chamber. Due to the large adjustment loop, an ex-situ adjustment is associated with a high uncertainty. The achievable performance of the device is, thus, limited. Conventional remotely-controlled drives cannot be integrated due to the highly unstable mechanical disturbances brought by their electric cables.

The following contribution presents a novel system for the in-situ adjustment of high-precision weighing cells. The system achieves the adjustment inside the sealed vacuum chamber with minimal disturbances and without arresting the weighing cell. Any sources of disturbance are eliminated from the weighing cell after the adjustment process, allowing for high stability of the adjusted value.

2. Adjustment of weighing cells

Figure 1 shows the functioning principle of a weighing cell based on the principle of electromagnetic force compensation. The weight force of the measurand induces a deflection of the compliant mechanism, which is detected by a position indicator at point M. Then, the force of the voice coil actuator at point K is regulated to compensate the deflection. The electric current required by the actuator is used as indirect measure of the mass of the measurand. A compensation mass is often built on the balance beam (GK) to reduce the electromagnetic compensation force and its associated disturbances.
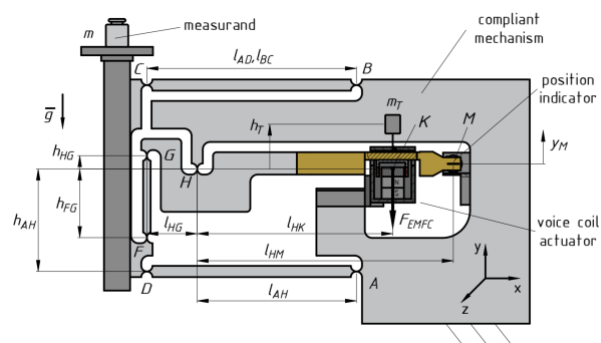
Figure 1. Functioning principle of a weighing cell based on the principle of electromagnetic force compensation

The inherent mechanical stiffness of the compliant mechanism C limit the achievable measuring resolution of the weighing cell,

i.e. $r_m = C \cdot g^{-1} \cdot r_{y_M}$. Furthermore, restoring forces due to residual deflections u_{y_M} around the zero position represent a major source of uncertainty, i.e. $u_{m,y_M} = C \cdot g^{-1} \cdot u_{y_M}$. Thus, the stiffness of the system must be adjusted to an approximate zero value for maximum performance. Height-adjustable trim masses are built on movable elements of the mechanism for this purpose [3]. Highest sensitivity is achieved with adjustments on the balance beam, see Figure 1. The variation in stiffness ΔC as a function of the vertical position h_T of the trim mass m_T can be approximated by the following equation:

$$\Delta C \approx -\frac{m_T \cdot g \cdot h_T}{l_{HG} \cdot l_{HM}} \qquad (1)$$

While other adjustments, e.g. tilt and corner-load sensitivity, are required maximize performance, this contribution focuses solely on the adjustment of the mechanical stiffness. Subject of this investigation is a weighing cell mechanism widely treated in previous works [3-6]. Table 1 shows the the parameters of the compliant mechanism. Due to its high sensitivity, it is a suitable application example for the targeted adjustment system.

Table 1 Ideal parameters of the weighing cell

Parameter	Value	Parameter	Value
Young's modulus E	71 GPa	length l_{HG}	27 mm
Poisson's ratio ν	0.33	length l_{HK}	105 mm
Density ρ	2.8 g/cm^2	length l_{AD}	112.5 mm
gravity acceleration g	9.81 m/s^2	length l_{BC}	112.5 mm
min. hinge height h	0.05 mm	length l_{HM}	137.5 mm
hinge radius R	3 mm	length l_{AH}	85.5 mm
hinge width w	10 mm	height h_{AH}	55 mm
height h_{HG}	3.15 mm	height h_{FG}	40 mm

Figure 2 shows the adjustment behavior of the investigated weighing cell according to equation 1, finite element simulations as well as measurements on a prototype. The finite element model is constructed as suggested in previous works [3,6]. The adjustment on the prototype is realized manually on the arrested weighing cell by means of built-in screws. The results are in good accordance with each other. The adjustment sensitivity amounts to $dC/dM = -0,2369$ N/m/Nmm, where the momentum is defined as:

$$M = m_T \cdot g \cdot h_T \qquad (2)$$
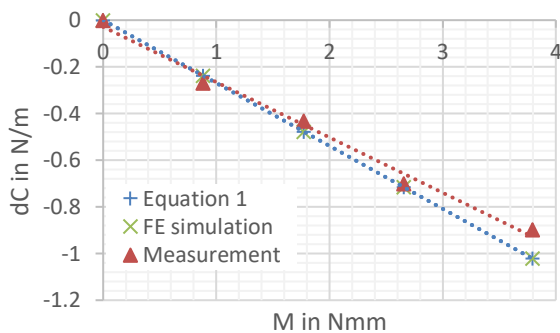
Figure 2. Stiffness adjustment of weighing cell according to analytical and finite element models as well as measurements on prototype.

On the current prototype, the stiffness can be adjusted to a value of $C < 0.01$ N/m. This corresponds to a contribution to the measurement uncertainty of $u_{m,C} < 1$ ng for an error of the position sensor of $u_{y_M} = 1$ nm [7]. To further increase the performance, the novel in-situ adjustment system must realize an adjustment of the momentum better than 4,21 mNmm. Due

to the high sensitivity of the mechanism, disturbances introduced by the fine adjustment system on the adjustment location (point K in Figure 1) require special consideration.

3. Behavior regarding disturbances

A previous investigation in [6] shows that mechanical and thermal disturbances on the adjustment location must be completely avoided during the measurement process. Limiting these down to acceptable values regarding the admissible mass measurement deviation may not be technologically possible. However, the püermissible limit values regarding the admissible stiffness deviation during the adjustment are orders of magnitude higher. Disturbances could be, therefore, tolerable only during the adjustment process and must be eliminated afterwards.
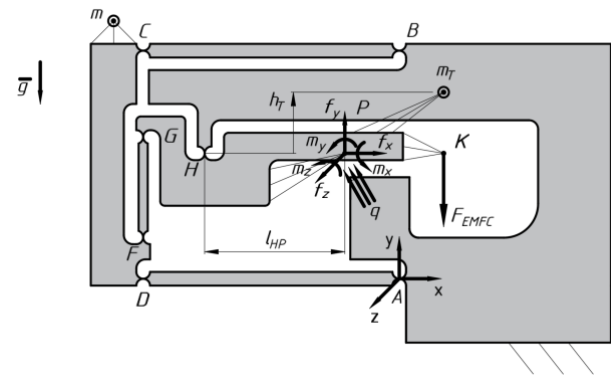
Figure 3. Model of the weighing cell for investigation of disturbance sensitivities and their application point

To further reduce the influence of disturbances by the adjustment system, the investigation based on the finite element model is extended to find a location on the balance beam with minimum sensitivity (see Figure 3). Figure 4 shows the variation of the critical disturbance sensitivity to the forces in x-direction f_x due to the position l_{HP} in x-direction of the application point relative to the main pivot H. A strong reduction can be observed as the application point P tends towards H, $l_{HP} \longrightarrow 0$. This is due to the reduction of the deflection-dependent lever arm, and thus, of the torque.
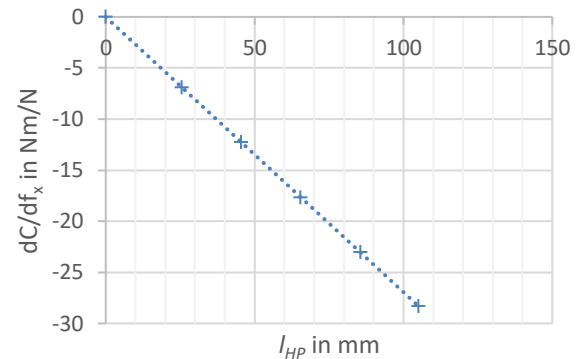
Figure 4. Variation of sensitivity of the stiffness to parasitic force f_x due to the application point l_{HP}.

On the contrary, the sensitivity to forces in y-direction f_y increases as its application point approaches the main pivot H (see Figure 5). This is due to the effective centre of rotation of the balance beam not coinciding with the geometric centre of the flexure hinge, where the load is applied. Thus, an effect similar as the one described in Equation 1 occurs. Further

investigations have shown that the sensitivity to f_y is dependent on the loading of the weighing cell (m and m_T), which induces an displacement of the effective centre of rotation. The sensitivity to forces on the z-direction f_z decreases progressively as l_{HP} reduces to zero. Other sensitivities do not show any change in behavior.
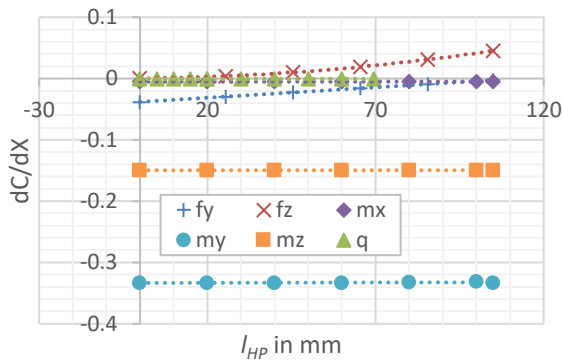
Figure 5. Variation of sensitivity of the stiffness to parasitic forces f_y, $f_z = 0,1$ N , parasitic torques $m_x, m_y, m_z = 10$ Nmm and heat $\dot{q} = 10$ W due to the application point l_{HP} (linearized values)

Based on the sensitivities on the main pivot H, new limit values for the disturbances during the adjustment are derived. These are presented in Table 2. A maximum deviation of the stiffness of 0,1 mN/m is used to set the limit values. Whereas the allowable forces in the x- and z-directions can be significantly increased, allowable forces in the y-direction are highly critical.

Table 2 Disturbance sensitivities of the weighing cell and limit values on the adjustment location K and main pivot H

X	Disturbance sensitivity			Limit value		
	point K	point H	unit	point K	point H	unit
fx	2,8E+01	4,6E-03	N/m/N	3,5E-06	2,2E-02	N
fy	2,6E-03	3,8E-02	N/m/N	3,9E-02	2,6E-03	N
fz	3,0E-03	1,9E-05	N/m/N	3,3E-02	5,4E+00	N
mx	5,0E-03	5,0E-03	N/m/Nm	2,0E-02	2,0E-02	Nm
my	2,2E-02	2,2E-02	N/m/Nm	4,6E-03	4,6E-03	Nm
mz	4,3E-01	4,3E-01	N/m/Nm	2,3E-04	2,3E-04	Nm
q	1,1E-02	1,1E-02	N/m/W	9,0E-03	9,0E-03	W

4. Design of in-situ adjustment system

A novel concept for an in-situ adjustment system is developed based on the knowledge gained from the investigation in Section 3. The main idea of the system design is the reduction of the influence of parasitic loads during the adjustment by purposely locating them in the least sensitive spot on the balance beam. Figure 6 shows an scheme of the concept system.
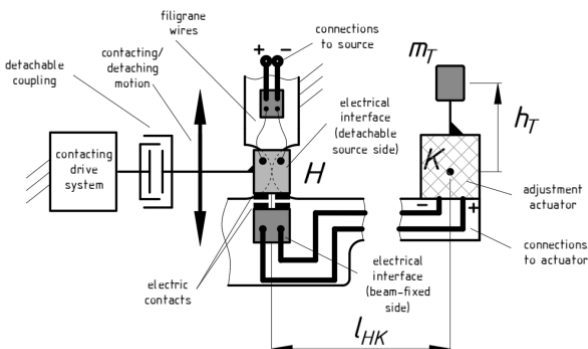
Figure 6. Schematic representation of concept for the fine adjustment system.

Since critical mechanical loads are mainly introduced through the electric connections for energy transfer to the adjustment actuator built on the balance beam, these are laid out as filigrane wires and short-circuitted through the main pivot H. Gold-plated copper wires with a diameter of 50 μm are used due to their very low stiffness. To minimize the number of wires, a drive element with two lines is selected. The adjustment actuator stays on point K and energy is transferred from point H through electrical connections fixed on the balance beam. A detachable electrical interface is required to eliminate the mechanical coupling between the source and the balance beam after the adjustment. A separate rack-mounted drive system is used to realize the contacting and detaching motion.

Particular focus lies on the design of the detachable electrical interface. The interface must enable an electric connection between the electric cables of both sides with least electrical resistance. The weight of the source side also is the main source of parasitic mechanical loads during the adjustment, particularly f_y. A change in stiffness is produced after it is detached, leading to a different adjusted state. Thus, the mass of the source side must be as low as possible and the centre of mass must accurately coincide with the centre of rotation of the balance beam (point H). In addition, a mechanical interface is required for its manipulation with the contacting drive system.

(a)

(b)
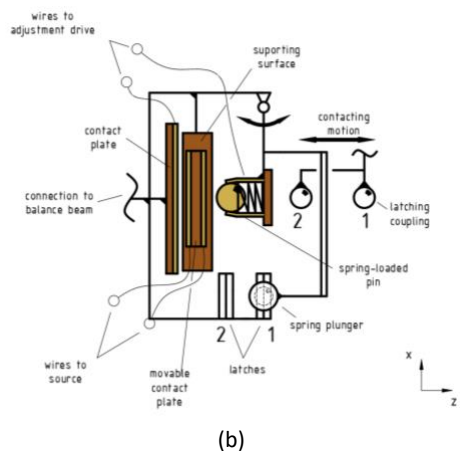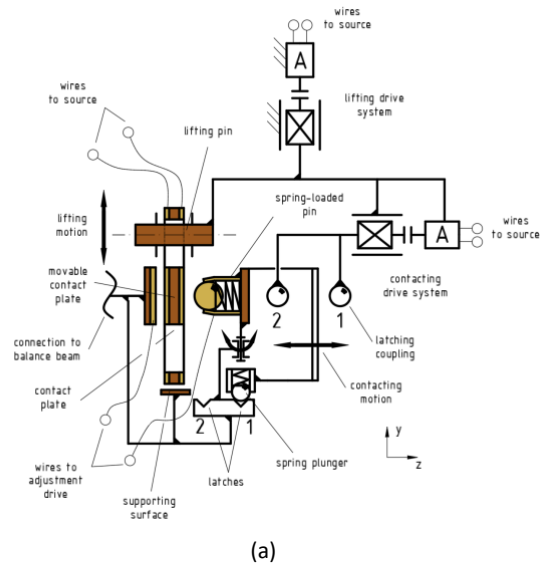
Figure 7. Functioning principle of detachable electrical interface: (a) in yz-plane, (b) in xz-plane. Gold color indicate conducting elements, brown color indicate insulating elements. Dimensions are not proportional.

Figure 7 shows the functioning principle of the detachable electrical interface. A movable contact plate based on a double-sided gold plated substrate is transported in the y-direction

(gravity vector direction) using an lifting mechanism. The mechanical coupling is done via a form contact pairing with an insulated pin on the lifting mechanism. Clearance is necessary to allow self-aliment of the contact plate. Stops on the pin avoid excessive lateral motions. A supporting flat surface on the beam side of the interface defines the position of the centre of mass in y-direction to avoid the stiffness variation. The contact plate is designed symmetrical for a better definition of its centre of mass, see Figure 8. When the contact plate touches the locating surface, mechanical coupling with the lifting mechanism is interrupted. Thus, no forces in y-direction are transmitted. The pin stays in its position without mechanical contact until the adjustment is done and the contact plate can be retired.
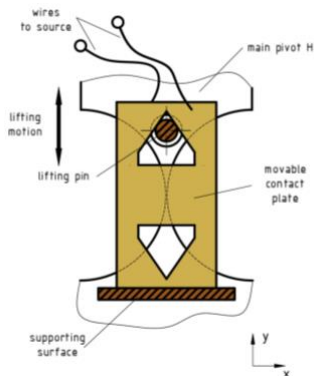
Figure 8. Positioning of contact element relative to main pivot H in xy-plane. View during contact with supporting surface without beam-fixed contact plate.

To mechanically secure the contact plate and ensure the electrical connection, a contacting drive system mounted on the lifting mechanism pushes the movable plate against the contact plate fixed on the balance beam. The contacting mechanism mounted on the balance beam composes of a latching lever with two secured positions: open (1) and closed (2). On the lever there is a spring-loaded electrical pin which is used to push the movable contact plate. The spring-loaded pin forms with the double-sided contact plate the other electrical connection with the adjustment actuator. The motion of the lever from position 1 to 2 and viceversa by introducing external forces in the stiff z-direction via ball-plane contact pairings with the contacting mechanism. Actuation of the contacting mechanism in this direction allows for higher forces to be used for establishing the electrical connection. The latching coupling can move in one direction until a position (1 or 2) is secured, then move in the other direction to eliminate the contact. To avoid any influence on the stiffness, the position of the centre of mass of all components of the beam side of the interface in y-direction does not change between position 1 and 2.

A two line linear actuator (built on the balance beam) is required for producing the in-situ adjustment motion. The actuator must be able to maintain the adjusted position after the energy supply has been interrupted as well as to limit heating nor magnetic fields. Piezoelectric actuators store the electrical energy while also convert it into deformation. They can hold the adjusted position for relatively long periods of time. In addition, in quasistatic applications, current requirements and heat losses are very low. A vacuum-compatible piezoelectric stack actuator from Physik-Instrumente GmbH [7] was used in a preliminary investigation on the unconstrained weighing cell. Due to its high resolution, a theoretical resolution of the stiffness adjustment better than 0,1mN/m is possible with a 100g trim mass. After separating the electrical contact, the adjusted position varies over time slightly due to the self-discharge of the actuator. This voltage loss is also problematic for readjustments

due to the difference between the voltage of the source and the actuator, which produce current peaks during coupling. These problems could be avoided using long-term stable piezoelectric actuators, which maintain their position at 0V [8].

5. Conclusions and outlook

This contribution presents a novel concept for an in-situ fine adjustment systems on highly sensitive movable elements of weighing cells inside hermetically sealed vacuum chambers. The system is designed to produce minimal disturbances during the adjustment process and completely avoid them afterwards. Thus, a highly accurate and stable adjustment can be produced. The adjustment can be achieved without arresting the weighing cell, further increasing its performance.

Disturbances by the adjustment system are mainly introduced by the electric cables for energy transfer to the actuator built on the balance beam. These are designed as detachable filigrane wires purposely connected to the frame through the least sensitive location of the balance beam. The electric interface is securely connected and detached via a contacting system which introduces forces only in the stiff z-direction of the weighing cell. The only significant parasitic effect to stiffness adjustment is due to the momentum of movable contact plate, which is kept minimal and its application point on the centre of rotation with its embodiment design. To minimize heat generation, while simultaneously maintaining the adjusted position, a built-in high-resolution piezoelectric actuator is used for the in-situ adjustment. A theoretical stiffness adjustment resolution better than 0,1 mN/m is possible with the aforementioned system.

Experimental validation of the system represent the ongoing work. In addition, further geometry and material optimization of the electric interface is required to reduce the weight and to ensure a secure electric contact with low disturbances.

References

[1] Fehling F, Fröhlich T and Heydenbluth D 2009 Design and Performance of the New Sartorius 1kg-Mass Comparator for High Precision Mass Determination and Research Application *Transverse Disciplines in Metrology: Proceedings of the 13th International Metrology Congress* 657-668
[2] Shaw G, Sterling J, Kramar J, Moses A, Abbot P, Steiner R, Koffman A, Pratt J and Kurabych Z 2016 *Metrologia* **53** A8
[3] Darnieder M, Pabst M, Wenig R, Zentner L, Theska R and Fröhlich T 2018 *J. Sens. Sens. Syst.* **7** 587–600
[4] Darnieder M, Pabst M, Fröhlich T, Zenter L and Theska R 2019 Mechanical properties of an adjustable weighing cell prototype *Proceeding of euspen's 19th International Conference and Exhibition* 86-89
[5] Pabst M, Darnieder M, Theska R and Fröhlich T 2022 *J. Sens. Sens. Syst.* **11** 109–116
[6] Torres Melgarejo, M A, Wittke M and Theska R 2023 Investigation of the sensitivity of a high-precision weighing cell to disturbances caused by the adjustment system *Proceeding of euspen's 22nd International Conference and Exhibition* 223-224
[7] Physik-Intrumente (PI) GmbH & Co. KG 2017 PI887.91 *Broschure PICMA Stack Multilayer-Piezoaktoren*
[8] Marth H, Reiser J and Bach M 2018 PIRest Actuators – Active Shims with Long-Term Stability and Nanometer Resolution *Proceeding of euspen's 18th International Conference and Exhibition*

Impact of higher-order surface imperfections on the stiffness of flexure hinges

Martin Wittke, Maria-Theresia Ettelt, Matthias Wolf, Mario André Torres Melgarejo, Maximilian Darnieder, René Theska

Technische Universität Ilmenau, Department of Mechanical Engineering, Institute for Design and Precision Engineering, Precision Engineering Group

E-Mail: martin.wittke@tu-ilmenau.de

Abstract

Compliant mechanisms composed of stiff links and concentrated compliances are frequently used in high-precision force metrology. Low bending stiffness and minimum parasitic motions are often desired. Since the elasto-kinematic behavior of these systems is predominantly defined by the flexure hinges, they are implemented with high aspect ratios and minimum thicknesses down to about 50 µm. An unexpectedly strong deviation of the elasto-mechanic behavior of manufactured prototypes compared to the theoretical models was found. First investigations in the state of the art show that even minor deviations from the ideal hinge geometry can lead to a significant change in the properties. For first-order form deviations, the hinge thickness has been identified as the main impact factor. However, second and higher-order form deviations can also lead to a non-negligible thickness change in the flexure hinges significant region, but have not been investigated.

For this reason, this work deals with the impact of the waviness and periodic roughness on the stiffness of a semi-circular flexure hinge. Modeling and simulation of the hinges with a sinusoidal notch surface showed that an increasing amplitude and a decreasing wavelength lead to a decrease in stiffness. By increasing the wavelength of the sinusoidal function, an increasing scatter range resulting from the phase shift of the two opposed hinge sides has been identified. Combining the results of waviness and periodic roughness for measured specimens' parameters leads to a maximum deviation of approximately 17.5 % from the ideal stiffness. A variation in the shape parameters of the flexure hinge showed that smaller hinge thicknesses increase the influence of higher-order form deviations. In future work, the investigations will be extended to several hinge contours and compared to measured specimens.

Keywords: compliant mechanism, flexure hinge, bending stiffness, finite element method, surface topography, geometric deviations

1. Introduction

In precision force measurement devices, the kinematic structure is often implemented as a compliant mechanism with concentrated compliances [1-3]. Advantageous properties are zero backlash of the mechanism, highest reproducibility of the motion, a highly accurate motion behavior, and an extreme sensitivity in a dedicated direction due to the low bending stiffness. The latter is achieved by reducing the hinge thickness of the frequently used semi-circular flexure hinges (Figure 1) down to the technologically feasible minimum of about 50 µm [4]. However, prototypes showed crucial differences in the calculated stiffness values driven by manufacturing-related form deviations [5, 6]. Investigations of dimensional deviations were already carried out in the state of the art [7, 8]. The results reveal that the bending stiffness C_ϕ of a semi-circular flexure hinge has the highest sensitivity to the deviation of the thickness t. Deviations of the radius R and the width w are almost negligible. This can be explained considering the parameter coefficients in the mathematical equation (1) for the stiffness of a single semi-circular flexure hinge [9] and the large relative deviation of the thickness due to the manufacturing at the technological limit.

$$C_\phi = \frac{2 \cdot E \cdot w \cdot t^{2.5}}{9\,\pi \cdot \sqrt{R}} \qquad (1)$$

Notch surface deviations like waviness or roughness also lead to a non-negligible change of the minimal thicknesses in the significant region. Since this influence has not been addressed in the state of the art, this work deals with the modeling and simulation of semi-circular flexure hinges with surface waviness and roughness. Initially, a suitable approach for implementing the surface topography is selected. Systematic studies are then carried out to conclude for measured profile parameters.
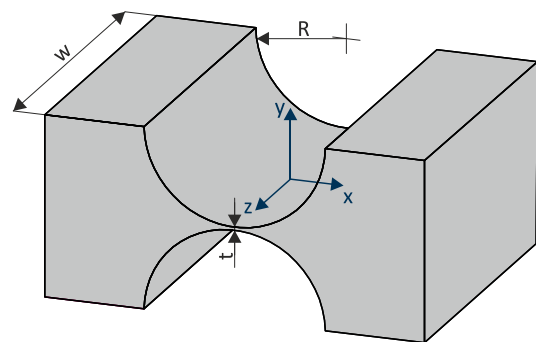
Figure 1. Geometry parameters of the semi-circular flexure hinge.

2. Finite element model of the flexure hinge

The basis for this work is the significant region of a state-of-the-art finite element model of an ideal semi-circular flexure hinge [5]. Its geometric and material parameters are shown in Table 1. The selection of a mathematical approach for manufacturing-related surface deviations and the adaptation and optimization of existing solutions for surface modeling [11, 12] enable the development of a suitable tool.

Table 1. Geometry and material parameters of the ideal flexure hinge.

Parameter	Symbol	Value	Unit
Thickness	t	50	µm
Radius	R	3	mm
Width	w	10	mm
Young's modulus	E	71	GPa
Poisson's ratio	υ	0.33	-

2.1. Mathematical approach for manufactured surfaces

DIN 4760 [10] divides the form deviations into different orders. The effects of dimensional deviations (1st order) on the stiffness can be investigated directly by changing the geometric parameters of the hinge. For deviations of a higher order, a suitable mathematical approach has to be found. Since the waviness (2nd order) and the periodic roughness (3rd order) occur regularly, sine functions according to equation (2) are used.

$$f(x) = a \cdot \sin\left(\frac{2\pi}{\lambda} \cdot x + \phi\right) \qquad (2)$$

For this approach, the total height of the waviness Wt and the mean roughness depth Rz are selected as twice the amplitude a. The waviness spacing WSm and the mean peak width RSm define the wavelength λ [13]. The phase shift φ is random for both effects. However, the approach is limited by the need to average the locally differing parameters of waviness and periodic roughness.

The form deviations of the 2nd and 3rd order are considered solely along the semi-circular contour. In this case, the modeling of the surface approach leads to a change in the thickness of the hinge over the entire width, to which the stiffness shows the highest sensitivity. Since the significance of the change in thickness for the stiffness decreases with increasing thickness, a high change in stiffness is to be expected due to the heights and depths in the center of the flexure hinge. In the direction of the width, a surface topography according to the approach would lead to neighboring heights and depths in the center. The influences of these heights and depths on the thickness would almost cancel each out due to a high width-wavelength ratio of at least 40. Thus, the bending stiffness remains nearly unaffected.

4th- and higher-order form deviations are also expected to have a negligible impact on the properties of the flexure hinge since they occur only locally on the surface. The influence on the bending stiffness also decreases the higher the order of the form deviation.

2.2. Characterization of the approach parameter ranges

To specify the definition ranges for the parameters to be investigated, the notch surfaces of five milled semi-circular flexure hinge specimens were characterized using a white light interferometer. The primary profiles were measured ten times per notch across an area of (250 x 250) µm² in the direction of the semi-circular contour (Fig. 2 a)). The cut-off wavelength λ_C was set to 25 µm.

The measured primary profile of each measurement run was filtered and split into the contour with superimposed waviness and roughness (Fig. 2 b). This enabled an evaluation according to ISO 21920-2 [13] and thus a direct determination of the parameters Wt, WSm, Rz, and RSm intended for the approach. The minima and maxima of all measurements specify the definition ranges (Table 2).
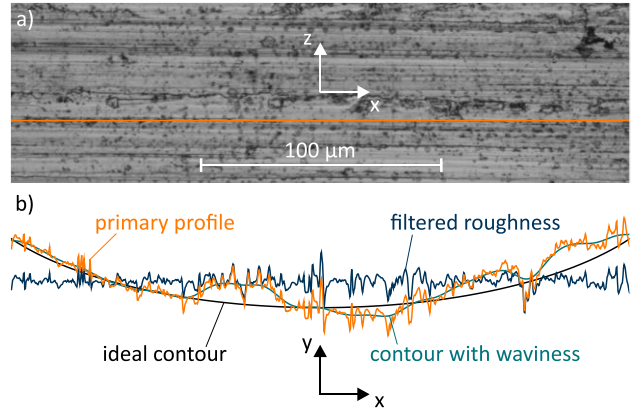
Figure 2. Characterization of the definition ranges of the approach parameters. a) Section of the measured area of the notch surface of a hinge specimen. b) Primary profile of the surface section and application of filters to determine the profile parameters.

Table 2. Ranges of the notch surface profile parameters for λ_C = 25 µm.

Parameter	Symbol	Minimum	Maximum	Unit
Total height of the waviness	Wt	2.39	7.24	µm
Waviness spacing	WSm	20.00	225.02	µm
Mean roughness depth	Rz	0.67	4.37	µm
Mean peak width	RSm	3.62	8.49	µm

2.3. Setup of the finite element model

The state-of-the-art significant region finite element model of the semi-circular flexure hinge [5] is to be enhanced to integrate manufactured notch surfaces according to the approach described in Chapter 2.1 for the profile parameter ranges defined in Chapter 2.2. However, existing concepts for generating the surface topography [11, 12] proved to be inappropriate, as fine meshing along the semi-circular contour is required. For this, the nodes of the ideal hinge are not moved to implement the surface topography. They are set directly to the intended position during the buildup of the model. The desired position p for each node is determined mathematically using equation (3) for the x-coordinate and equation (4) for the y-coordinate. It depends on the notch surface side, the radius R of the flexure hinge, and the angular position α on the contour.

To ensure consistent meshing of the model, the sections between the surfaces are each divided into elements of equal length. Single nodes, which are connected to the significant region model, are located at both ends. One of these nodes has a degree of freedom of 0 and defines the frame. At the other node, a rotation of α = 1° is initiated and the required moment is evaluated.

$$p_{x,i}(\alpha,r) = \left(r + a \cdot \sin\left(\frac{2\pi}{\lambda} \cdot r \cdot \alpha + \phi\right)\right) \cdot \cos(\alpha) \qquad (3)$$

$$p_{y,i}(\alpha,r) = \left(r + a \cdot \sin\left(\frac{2\pi}{\lambda} \cdot r \cdot \alpha + \phi\right)\right) \cdot \sin(\alpha) \pm \left(r + \frac{t}{2}\right) \qquad (4)$$

The optimum between realizable profile parameter ranges and computing time was then determined by performing a mesh convergence analysis. For the final model (Figure 3), amplitudes of a maximum of 5 µm and wavelengths of at least 100 µm can be investigated.
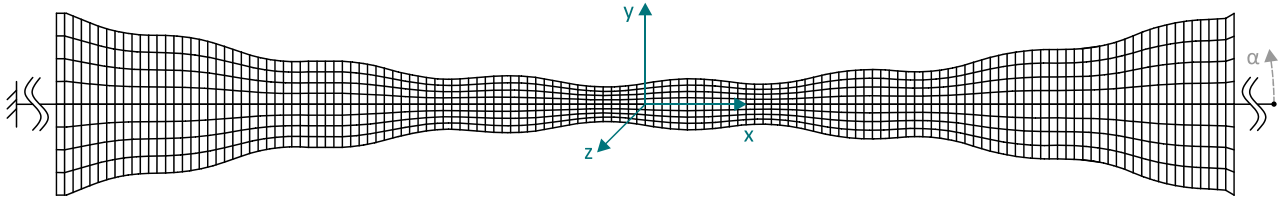
Figure 3. Significant region finite element model of the flexure hinge with manufactured notch surfaces.

3. Stiffness sensitivity to the approach parameters

Due to the wavelength limitation of the model, it is not possible to implement the total definition ranges of the waviness spacing and the mean peak width. For this reason, the investigations are initially carried out using the general approach from equation (2). The definition ranges for the approach parameters are derived from the measured profile parameters ranges from Table 2 (Table 3). In the overall assessment, conclusions for the measured specimen will be drawn.

When developing the design of experiments, it is determined that the amplitude a can be considered individually, as it is a pre-factor of the sine function. The relation between wavelength and phase shift is still unknown. For this reason, they are considered in combination.

Table 3. Definition ranges of the approach parameters.

Parameter	Symbol	Minimum	Maximum	Step size
Amplitude	a	0 µm	5 µm	0.5 µm
Wavelength	λ	100 µm	300 µm	50 µm
Phase shift	φ	0	2π	π/4

3.1. Amplitude

By setting the amplitude to zero, the stiffness of the ideal flexure hinge was determined in the first step. It amounts to $C_{\phi,0} = 18.23$ N mm/rad. To investigate the impact of the superimposed amplitude, the phase shift of the sine functions of both surfaces was set to a constant value of zero. Simulation runs were carried out to determine the stiffness $C_{\phi,i}$ of the flexure hinge in dependency of the amplitude for different wavelengths.
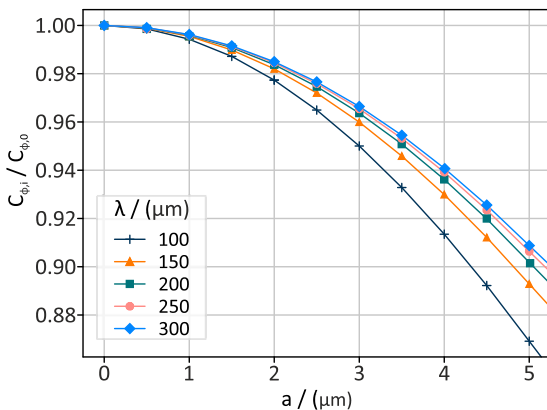
Figure 4. Stiffness amplitude diagram for different wavelengths with the phase shifts set to a constant value of zero.

The stiffness amplitude diagram (Figure 4) reveals first of all that 2nd- and 3rd-order form deviations are always leading to a reduction in stiffness. The stiffness decreases significantly more for larger amplitudes, in the worst case of up to 13 %. It can also be observed that the sensitivity of the stiffness to the amplitude

depends on the wavelength. The shorter the wavelength, the larger the reduction of the stiffness for each amplitude value.

3.2. Wavelength and phase shift

To characterize the sensitivity of the stiffness to the wavelength and the phase shifts, the wavelength was set initially to a constant value and the phase shifts were varied.
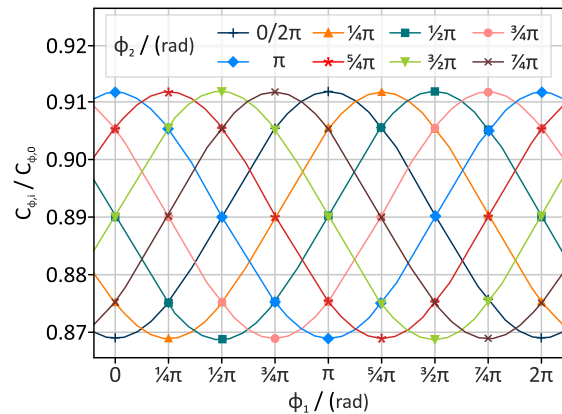
Figure 5. Stiffness phase shift diagram for different phase shifts of the opposite notch surface with a constant wavelength of 100 µm and an amplitude of 5 µm.

The stiffness phase shift diagram for 100 µm wavelength (Figure 5) shows that the phase shifts of the two opposite sides lead to a non-negligible scattering of the stiffness. Contrary to expectations, the maximum stiffness in the scattering area does not occur when the thickness is at its maximum in the middle of the hinge. The maximum is reached when the difference of the phase shifts is a multiple of π. This means the minimum hinge thickness is constant at 50 µm. If both phase shifts have the same value, the stiffness is at its lowest. This is the case for both, the minimum and maximum thickness in the center of the hinge. It becomes clear that not only the center of the hinge is relevant for its stiffness, but the entire significant region.
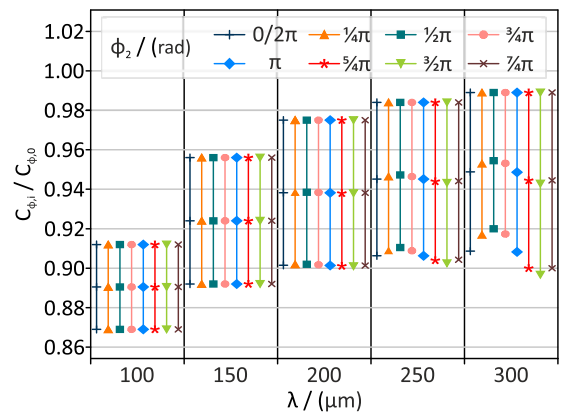
Figure 6. Stiffness scatter ranges resulting from the range of ϕ_1 for different phase shifts ϕ_2 and wavelengths.

Extending the investigations to the entire wavelength range (Figure 6) makes clear that the scatter range increases and the

offset of the mean stiffness decreases with the wavelength. For longer wavelengths, it is also noticeable that the stiffness scattering no longer depends only on the wavelength, but also on the phase shift. To ensure that this effect was not caused by the significant region model, the simulation results were validated for a wavelength of 300 μm with the overall model of the flexure hinge. The occurring variance of the scatter range can be explained by considering the geometric dimensions of the flexure hinge. For longer wavelengths, the material distribution in the stiffness-defining areas around the center of rotation is more asymmetrical compared to shorter wavelengths.

3.3. Surface topography impact for varying geometry

Since higher-order form deviations only occur together with shape deviations (1st order), the influence of the notch surface topography on the stiffness is also considered for a slightly varying geometry. To be able to evaluate the filtered surface impact, the hinge stiffness $C_{\phi,si}$ with notch surface topography was put into relation to the stiffness $C_{\phi,s0}$ of the ideal hinge with varied geometric parameters. All investigations were carried out for constant surface parameters with an amplitude of 5 μm, a wavelength of 200 μm, and phase shifts of 0.

The relations between the stiffness change and the change of the geometric parameters (Figure 7) show, that a varying thickness significantly changes the impact of the notch surface topography on the stiffness. In contrast, changing the width and radius has no significant impact.
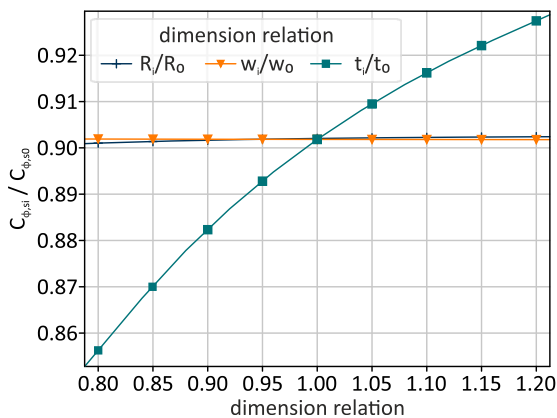
Figure 7. Stiffness dimension change diagram for constant notch surface topography parameters.

4. Conclusions

To be able to evaluate the findings and relate them to the measured specimens, it is necessary to differentiate between the parameters of the approach that can be controlled during manufacturing and those that cannot. The phase shift causing the scatter range of the stiffness is a random value parameter. However, the amplitude and wavelength can be controlled by manufacturing parameters. The amplitude is more critical in terms of stiffness. If the amplitude increases, the stiffness scatter and the mean offset of the stiffness increase. For the wavelength, a distinction must be made. Longer wavelengths lead to a lower mean stiffness offset, but the scattering range of the stiffness is larger. For shorter wavelengths, the effect is reversed. Considering the calculations of the measured specimens (Table 4), it can be seen that the maximum total deviation is almost the same for the measured wavelength range. For shorter wavelengths, however, the scattering range is only half as large. Although the mean stiffness deviation is larger in this case, it can be taken into account during the development of a mechanism or corrected by an oversizing of the hinge

thickness. For the periodic roughness, a large average peak width should be aimed for. The reason is that the scatter range hardly changes and the total offset can therefore be reduced.

Overall, the maximum deviation with the measured profile parameters compared to the ideal hinge is approximately 17.5 %. However, it should be noted that additionally occurring 1st-order form deviations can significantly increase this value.

Table 4. Estimated stiffness deviation for the maximum amplitude in the measured wavelength ranges of the waviness and periodic roughness.

	Wavelength	Mean stiffness reduction	Stiffness scattering
Waviness	20.00 μm	9.01 %	2.03 %
	225.02 μm	6.98 %	4.08 %
Roughness	3.62 μm	7.20 %	0.41 %
	8.49 μm	6.73 %	0.43 %
Combined maxima		16.21 %	4.51 %

5. Outlook

In future work, a calculation model is to be developed to characterize the overall stiffness scatter range of a semi-circular bending hinge, taking into account manufacturing-related form deviations of 1st to 3rd order. This will improve the development of compliant mechanisms. The need to integrate adjustment devices to achieve the desired properties can also be predicted more accurately based on this. The investigations of this work will also be done for other hinge contours. All the obtained results will then be compared to measured hinge prototypes.

Acknowledgment

References

[1] Darnieder M, Wittke M, Pabst M, Fröhlich T, Theska R 2023 *Engineering for a changing world: 60th ISC, Ilmenau Scientific Colloquium* Article 1.4.112
[2] Wittke M, Torres Melgarejo M A, Darnieder M, Theska R 2023 *Engineering for a changing world: 60th ISC, Ilmenau Scientific Colloquium* Article 1.3.017
[3] Keck L, Seifert F, Newell D, Schlamminger S, Theska R, Haddad D 2022 *EPJ Techniques and Instrumentation* 9 Article 7
[4] Bacher J P, Joseph C, Clavel R 2002 *Ind. Robot* 29 349–353
[5] Torres Melgarejo M A, Darnieder M, Linß S, Zentner L, Theska R 2018 *Actuators* 7 (4) 86
[6] Darnieder M, Harfensteller F, Schorr P, Scharff M, Linß S, Theska R 2020 *Microactuators, Microsensors and Micromechanisms* 15-24
[7] Ryu J W, Gweon D-G 1997 Precision Engineering 21 (2-3) 83-89
[8] Shen J Y 2013 *Applied Mechanics and Materials* 302 343-346
[9] Paros J, Weisbord L 1965 *Machine Design* 25 151–156
[10] Deutsches Institut für Normung 1982 DIN 4760 – Gestaltabweichungen; Begriffe, Ordnungssystem
[11] Thompson M K 2006 Methods for Generating Rough Surfaces in ANSYS *International ANSYS Users Conference & Exhibition*
[12] Wittke M, Melgarejo M A, Darnieder M, Theska R *Proceedings of the 23rd International Conference EUSPEN Copenhagen* 71-72
[13] International Organization for Standardization 2021 ISO 21920-2 – Geometrical Product Specifications (GPS)

Orientation-dependent behavior of miniaturized compliant mechanism for high-precision force sensors

Matthias Wolf, Mario A. Torres Melgarejo, Martin Wittke, René Theska

Technische Universität Ilmenau, Institute of Design and Precision Engineering, Precision Engineering Group

matthias.wolf@tu-ilmenau.de

Abstract

Traceable measurement and application of forces with nanonewton resolution and lowest measurement uncertainties over large measurement ranges are fundamental for high precision technologies such as nanofabrication. To increase the range of applications, the main target of this work is a gravity orientation-independent working principle. Furthermore, a miniaturization of the mechanism is being investigated, as it is advantageous due to reduced inertia.The resolution of the measurement in load cells based on compliant mechanisms with concentrated compliance is mainly limited by the stiffness of the hinges, which depends on the hinge geometry. Due to the limits in the manufacturing of the hinge thickness, the geometrical scaling leads to a higher stiffness of the overall mechanism. To achieve lowest stiffness and to avoid parasitic deflections due to the orientation in the gravitational field, the mechanism needs to be further optimized. The investigation has shown that the use of corner-filleted hinge contours results in much lower bending stiffnesses compared to the widely used semi-circular hinge contours. By changing length and corner fillet radius, the hinges are optimized in terms of low bending stiffness and high cross stiffnesses. This provides a compromise between the resolution of the measurement and the amount of parasitic displacements driven by the tilting to the field of gravity. The findings of the investigation were summarised in optimization approaches and verified in a FE Analysis. The result of the tilting analysis shows that an orientation-independent working principle is possible with the optimized mechanism.

Keywords: Force measurement, geometric scaling, gravity independent, compliant mechanism, stiffness

1. Introduction

Orientation-independent, traceable measurement and application of forces with nanonewton resolution are fundamental for high-precision technologies, e.g. nanofabrication. Due to numerous advantages, the use of electromagnetic or electrostatic force-compensated weighing cells based on compliant mechanisms is state-of-the-art for high-resolution force measurement with low uncertainty [1]. However, in weighing systems, even the slightest tilt of the load cell leads to measuring deviations caused by mismatch of the center of mass and the main pivot point H (Figure 1). It causes an astatic state of the stiffness of the mechanism. To achieve the lowest uncertainty, the tilt sensitivity of the load cell has to be compensated. For the typicaly small tilt angles of less than 1° this has been done by means of dead weights [2,3]. A universally
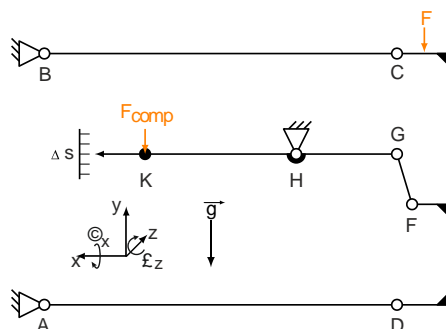
applicable principle has to avoid deviations in the measured value even with large angular deflections.

2. Goals and approaches

The tilt compensation with dead weights needs to be replaced by a more orientation-independent operating principle. The miniaturization of the mechanism will help to reduce the inertial masses. In addition, a more compact design will help to facilitate integration into existing systems. As described in [3], point K (Figure 1) is crucial because it serves as the application point of the compensation force and the position measurement. Any displacement of point K caused by deflections directly influences the relative position of the fixed and moving components of the actuator and sensor located there. To ensure constant properties, these deviations must be minimized by enhanced cross stiffnesses of the overall mechanism. In the previous investigation [4] the behavior of the stiffness of a miniaturized mechanism was considered. The resolution of the force measurement is limited by the bending stiffness of the hinges. A further reduction in the thickness of the bending hinges would be helpful, but is not achievable from a technological point of view, so that the stiffness of the mechanism increases with the degree of miniaturization. Therefore, the miniaturized mechanical structure needs to be optimized for inherently low stiffness in the direction of the force measurement and high cross stiffness avoiding displacements due to tilting. In [4] the scaling behavior of miniaturized hinges was investigated using an FE analysis. It was shown that corner-filleted hinges provide low bending stiffness and high cross stiffnesses even with an increasing grade of miniaturization. The results obtained are used for ongoing optimization approaches.

Figure 1 The principle design of the load cell is based on a compliant mechanism. The measured force is applied at the linkage between C and D. Point K serves as the compensation point where the compensation force is applied and controlled using a position sensor.

3. Mechanical model and simulation setup

In the first approach, a 3D FE model was developed and parameterized with the geometrical values from the scaling study in [4]. To simulate gravity, an acceleration was applied to the center of mass. It was divided into the x, y, and z components and was calculated using the amount of gravity and the roll around the x-axis Φ_x and pitch around the z-axis Θ_z. To simulate the position control of point K, it is fixed in the y-direction and the reaction force was observed.

3.1. Simulation results and optimization approaches

The diagrams in Figures 2 and 3 show the results of tilting. Rolling around Φ_x leads to a linear displacement in the z-direction and a negligible displacement in the x-direction. The reaction force is symmetrical to the roll angle Φ_x.
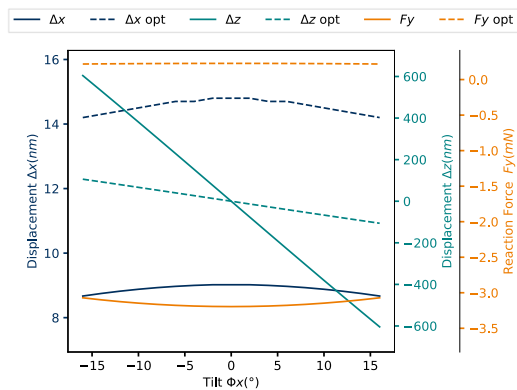
Figure 2 Resulting displacements and reaction force of point K due to tilting the mechanism to gravity around Φx.

Pitching around Θ_z leads to a linear displacement in the x-direction and a negligible displacement in the z-direction. The reaction force is unsymmetrical to the pitch angle Θ_z.
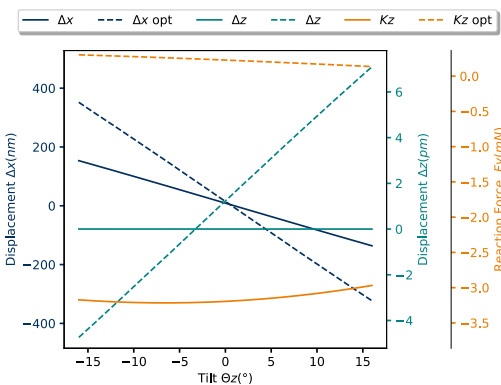
Figure 3 Resulting displacements and reaction force of point K due to tilting the mechanism to gravity around Θz.

The displacement in the z-direction driven by the roll around Φ_x is higher, compared to the x-direction. The behavior of the reaction force can be traced back to the center of gravity, which is not in the center of the pivot point H. This results in a gravity-intended astatic adjustment of the stiffness by tilting.

To provide the tilt-insensitive behavior the following **optimization approaches** were derived:

- expand the structure in z-direction
- place symmetrical cut-outs in the middle to separate the hinges
- reduce the mass of moving parts
- decouple parasitic displacements of the parallel spring guide from the load beam
- place the center of mass of the load beam into the center of pivot H

3.2. Simulation results with geometry optimization

Based on the optimization approaches obtained from the previous analysis, a mechanism with optimized geometry was developed (Figure 4). The load beam (2) and the parallel spring guide (3) are now optimized in terms of mass. The center of mass of the load beam is now located at the pivot point H. In addition, the parallel spring guide and the load beam were decoupled in z-direction, using additional flexure hinges (1).
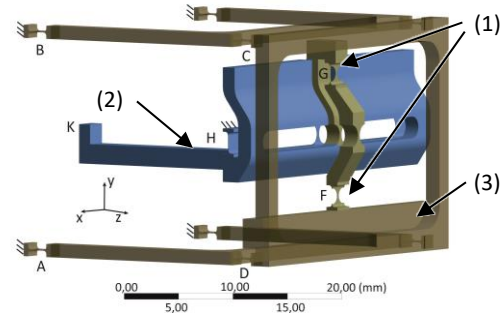
Figure 4 Optimized mechanism with additional hinges (1) to decouple the loadbeam (2) from the parallel spring guide (3)

The mechanism was expanded to 30 mm x 30 mm x 20 mm to enhance the cross stiffnesses while the bending stiffness was reduced by symmetrical cut-outs separating the hinges. The results of the FE-Analysis are shown as the dashed lines in Figure 2 and Figure 3. By decoupling the load beam and the parallel spring guide, the displacement in the z-direction could be reduced by a factor of six. The reduction of the masses, the positioning of the center of mass to pivot point H, and the cut-outs of the hinges led to a reduction of the tilt intended reaction force by almost 30 times. The cut-outs also led to increase the displacement in x-direction by a factor of 2. Tilting around Φ_x has a negligible influence on the reaction force of point K.

4. Conclusion

The investigation showed that the original mechanism is very sensitive to tilting. The defined optimization approaches led to a significantly reduced tilting sensitivity. When tilted by Φx, the reaction force at point K shows a tilting sensitivity close to zero. In addition, the displacements between the fixed and moving components of the actuator and the sensor to the tilting can be neglected. For the further development of the force sensor, a working principle based on tilting around the x-axis and rotating around the gravitational axis is recommended to achieve all force vectors in space.

References

[1] Marangoni R.R., 2019. Traceable Multicomponent Force and Torque Measurement. diss., Technische Universität Ilmenau

[2] Darnieder M., Pabst M., Zentner, L., Fröhlich T., Theska, R., 2019. Mechanical properties of an adjustable weighing cell prototype. *In Proc. 19th Int. Conf. Eur. Soc. Precision Eng. Nanotech.*

[3] Dannberg, O., 2020. Entwicklung eines Prüfstandes zur rückführbaren Kalibrierung von Cantilevern. diss., Technische Universität Ilmenau

[4] Wolf M., Wittke M., Torres Melgarejo M.A., Theska R., 2023. Scaling of a compliant mechanism for high-precision force measurement applications. *In: Engineering for a changing world: Proceedings : 60th ISC, Ilmenau Scientific Colloquium, Techn. Universität Ilmenau*

Positioning and alignment strategy in freeform mirror-based systems

Sumit Kumar, Wenbin Zhong, Shan Lou, Paul Scott, Xiangqian Jiang, Wenhan Zeng

EPSRC Future Metrology Hub, Centre for Precision Technologies, School of Computing and Engineering, University of Huddersfield, Huddersfield, HD1 3DH, United Kingdom

Sumit.Kumar@hud.ac.uk

Abstract

System performance in optical, optomechanical, and optoelectronic systems is directly dependent on the precision level of positioning and alignment of the components. The location-specific placing of the optics plays a crucial role in limiting the energy loss in the Head-up display (HUD) system. The requirements for positioning and optical alignment become more stringent as the freeform optical elements, their functional and mounting surfaces with size and orientation become complicated along with the packaging restrictions get more severe. A simple sequential positioning and alignment technique that maintains the performance of HUD systems as per the required level is outlined. Three processes are involved in controlling the precision level i.e., (1) string-based mapping that provides accuracy upto 100's μm, (2) coordinate-measuring machine-based adjustments that offer position accuracy under 10's μm and (3) laser-based approach to maintain sub-micron positional accuracy. In spite of having certain challenges in terms of component handling and fixturing, this newly developed sequential stationing method (SSM) opens up new research directions that are inevitable for small-, mid-, and large-scale system integration.

Keywords: Alignment; Coordinate Measuring Machine (CMM); Laser; Positioning

1. Introduction

For building precision optical systems – especially for freeform reflective mirror-based systems, every single component is essential to be positioned with extreme accuracy to achieve high-quality imaging that corresponds to the optical design data. In the research and development phase of the optical, optoelectronic, and optomechanical instruments, a variety of certain errors can arise during the positioning and alignment of the components in the system. Besides the deviation in the form of each freeform optical surface, surface quality, and integrity, the physical and mechanical placement of each non-symmetrical optic could be the cause of degradation of imaging quality. The computational, mathematical i.e., positional data conversion, and mechanical errors such as the centration and tilt errors concerning the fiducials planes, zenith point, and form error deviations along the optical axis need to be considered for the better functioning of the system.

The optical component has a specified axis by default since it is often defined as a portion of a rotationally symmetric "parent" element. Although a more accurate view would refer to the off-axis component as the "child" element, historically often referred to the symmetric curve as the "parent" curve and the off-axis portion as the "daughter" element [1]. The "flare spot" alignment method was a simple optical system tilt and decenter detection with low powered laser [2]. Systems containing freeform surfaces mostly adapt to the off-axis portion.

Freeform optics stands different from conventional spherical, aspherical, and conics in terms of functionality and additional features that come with compact size and minimum complexity in system integration [3]. The challenges in the development of freeform optical systems are not only in design, fabrication, measurement, and surface integrity but also in the positioning and alignment of the components for functional testing and complete utilization.

When performing aligning operations in an optical system with rigid supports and depending on the mechanical and optical measurements of the precision surfaces, new difficulties emerge [4, 5]. The capacity to put the optical component in the desired location, knowledge of the optical properties owing to measurement machine error, and damage to the optical surfaces are a few critical challenges in the positioning and alignment of freeform optical systems.

A point of symmetry about a reference axis should be defined in order to measure a Centering error. The measurement process is referred to as "Measurement in Reflection" when the optical surface's radius of curvature is used to calculate centration errors [6]. Due to the non-symmetrical nature of the freeform surface, it becomes tedious to eliminate or control these mechanical errors. Therefore, multiple referencing with fiducials (i.e., planes and points) must be considered for the positioning and alignment. With this approach, the system integration can be done accurately but consumes more time than the systems with conventional optics. Thus, there is a need for a simple, fast, step-step approach that sequentially improves the precision level of the placement of the optical components for high performance in the HUD system. In this research work, an SSM is provided utilizing multiple platforms to limit the mechanical errors in a freeform optical system and avoid direct or indirect contact damage to the functional/active aperture of the optical components and fixtures.

In view of this, the following structure and methodology were chosen: In section 2 the basic concept and strategy are presented especially the approach developed to position the freeform optics HUD system. A description of the SSM along with the design, manufactured product, and fixturing for the functional testing is revealed in Section 3. The results in terms of positional and angular errors of each component with different approaches are provided in Section 4. Based on this research carried out, succinct research conclusions are given in Section 5.

2. Methodology

Precise positioning and alignment of the optical components and the optical beam is critical for imaging performance in HUD systems. To achieve optimum optical performance for the HUD image projection, it is essential to design a precise position and alignment scenario, including transverse alignment, and longitudinal alignment through measurements. The basic concept of the SSM for components in HUD systems is:

- String-based mapping for the initial placement of the freeform optics and devices as per the design data to detect the chief ray.
- Coordinate metrology-based placement of the components for improved precision level of positioning in a system.
- Laser-based positioning to precisely control the centration and tilt errors.
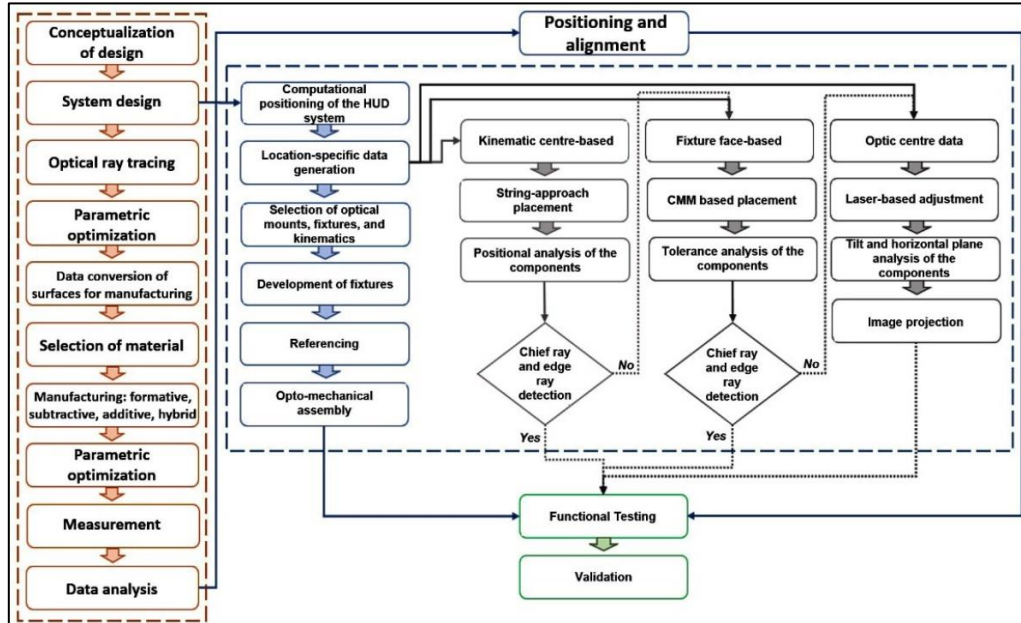
Figure 1. Strategy for positioning and alignment of optical components in HUD system.

The novel stationing strategy combines both mechanical (i.e., contact measurement feedback) and optical (i.e., non-contact measurement) modes for locating the precision components held on fixtures and kinematics. In this method, three different phases are sequentially implemented to avoid any chance of surface imperfection such as scratches, digs, etc. on the clear apertures of the freeform mirrors. Because manufacturing the complex freeform mirror requires more time and money than producing the symmetric optical components. Not only manufacturing and metrology are critically difficult for such surfaces but handling these optics is a significant obstacle to a product's sustained life. Therefore, a methodical strategy is presented that comprises two stages of contact referencing. The first stage involves a string-based technique for kinematics placement, followed by coordinate metrology for bringing the active aperture into the micron-level range concerning the design data coordinates. The final phase is the laser-based non-contact alignment which precisely balances the components in the systems. Figure 1 illustrates the complete developmental process route for the HUD systems, however, only position and alignment strategy are expanded in this research.

3. Strategy for positioning and alignment of freeform optical components

In the development of the freeform optical system, all phases under production are dependent on the design data. A few common challenges for open system testing include (1) freeform surface referencing; (2) sufficient space for fixtures and mounts to hold the delegate optics while adhering to design data coordinates; (3) external temperature fluctuations; and (4) type of environment. Implementation of SSM in HUD testing and final assembly may also have certain risks including surface contamination, dust particle deposition on the active surface, collision, and collapsible fixtures and components. In this

Section, different modes to position and align the component and optical beam are described.

3.1. Design data

Typically, a system's design data is obtained as coordinates that are subsequently separated into many subsets for the independent construction of subsystems. On the other hand, an increase in reference points, planes, and data conversion could further complicate the process of assembling and testing a system for optomechanical engineers. The first step is to designate a single element in a system as the referenced point of the plane. In this case, the centre of the Eyebox serves as the pivot point for the sub-systems and is represented as a constant point in Figure 2(a). The current HUD system contains two freeform mirrors for directing the light beam toward the Eyebox via. Windscreen. Referencing facilitates the quick identification of the chief and edge rays of various freeform optics and eases the mathematical calculation of the remaining optical component placements.
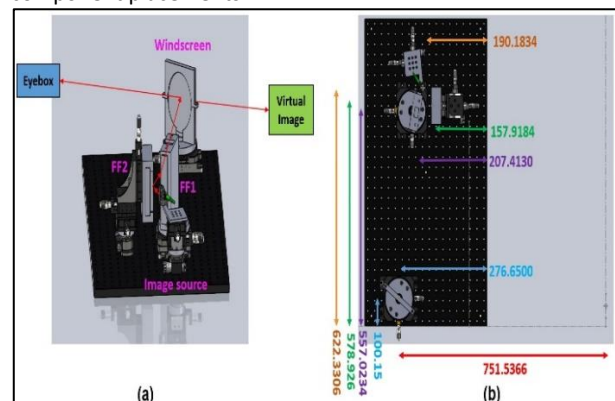
Figure 2. Freeform HUD system, (a) 3D model including the schematics of chief ray and (b) kinematic centre-based coordinates from referenced Eyebox centre.

Table 1 Position of the components of HUD system design obtained through multi-parameter optimization.

Components	Description (Clear aperture)	Dimension (mm)	Angle (°)		Position (mm)	
			H*	V^	H*	V^
Eyebox	Rectangle	130 X 130	093.000	003.000	0	0
Windscreen	Circle	88 Ø	134.860	044.860	757.5366	009.8609
Freeform mirror 1	Rectangle	90 X 100	52.8155	37.1845	682.3179	466.5543
Freeform mirror 2	Rectangle	60 X 80	70.3155	19.6845	632.8050	488.4569
Image source	Rectangle	35.04 X 28.03	59.3155	30.6845	665.0700	531.8615

H* – Horizontal

V^ – Vertical

For ease in calculation, the design data coordinates of components in the sub-system are converted in terms of the position and angle with respect to 90° horizontal and 90° vertical imaginary planes as listed in Table 1. The simplification of the element's location in the sub-system reduces the actual time for the assembly and optical testing. Also, it adds referencing coordinates for the freeform system which is predominantly required for complex highly valuable systems with multiple components.

3.2. Kinematic centre-based

Kinematics plays a critical role in the system testing at the R&D phase. For successful testing of freeform optical systems, precise movements of the components in required degrees of freedom are essential. Initially, the kinematic mounts and reflecting optics are placed with fixtures on the testbed using a manual placement technique, which is referred to as a string-based method. This technique is more advantageous than the single ruler and scale as the intersection of the strings gives the actual center of the kinematics. The plane that passes through the optic's centre is then further adjusted using the first referenced point, or the Eyebox centre point, as indicated in Figure 2(b), or the length of the kinematic side face. The problem with this method is that it cannot support an off-axial mount or optics on a kinematic mount. To increase the degrees of freedom for optics, multiple mounts are often tightened, either on the base kinematics mount or one above the other. In this instance, the string-based method provides the first marking, and the other adjustments are made by the computation that determines the optics centre plane using trigonometric functions. When the system design has optics location coordinates in proximity to other components, then off-axial fixturing is recommended.

3.3. Fixture referenced approach

Once the freeform optics and devices are positioned close to the required coordinate (with the highest manual adjustment precision level) then the Coordinate Measurement Machine (CMM) is utilized for further reduction in the closeness to the nominal value calculated from the design data. The measurement values are obtained from the side face of the kinematic mounts, and as Figure 3 illustrates, a CMM (ZEISS PRISMO ACCESS) can achieve a measurement accuracy of 1 μm. However, the true component placement is close to the machine's measurement repeatability. Geometric inaccuracies in the mounting, fixturing, and manufacturing process of these components may result in substantial variations in measurement results. The main challenges with this technique are; (1) long tracing path setup time, (2) maintaining stable temperature, (3) contact type measurement which may induce surface imperfection on the precision freeform optics, (4) sufficient gap between the components for clean travel of the probe, and (5) proper handling of the measurement probe tip. Also, a quick solution in terms of measuring the sub-system's positional coordinates would be laser and computed

tomography scanning as the capturing points are exceptionally more than the points obtained from the tactile CCM technique. The CT scan provides quick solutions for part analysis, however, when the large-sized (i.e., centimeter- and meter-class) systems with large spacing between components the CMM is preferred due to low instrument cost.

Figure 3. Coordinate metrology-based positioning and alignment of the freeform mirror-based HUD system.

3.4. Optics centre data

Detection of the chief ray for symmetrical optical objects such as spheres, conic, and aspheres is widely implemented by controlling mechanical errors such as centration and tilt. However, the centration error is not observed in open system testing and assembly. The presence of tilt on freeform optics is the prime focus to control with a Laser-based approach. There are three objectives for adapting this technique for the freeform optical HUD system i.e., (1) detection of chief ray, (2) control over tilt and tip of the non-symmetrical surfaces, and (3) functional testing. Functional testing of the HUD system is performed by projecting the laser and capturing it in the required magnified form. The beam spot diameter is calculated theoretically and compared with the captured image of spots at the entrance pupil diameter of 8 mm. The optical fibre diameter is selected as per the pixel size in real image projection in 2D image simulation.
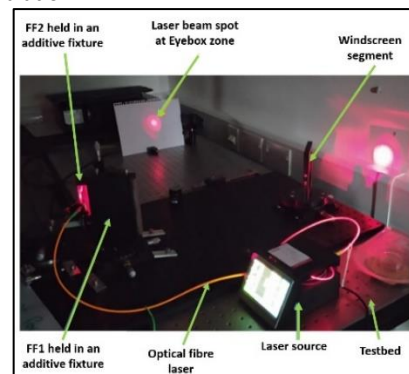
Figure 4. Laser-based alignment for HUD system.

The optical alignment and the functional testing of the freeform mirror-based HUD system using the low-powered laser as shown in Figure 4. Initially, in this experimental research, the tilt is removed by comparing the laser beam spot from different

field angles. The projection was performed for the laser source and freeform mirror 1 due to their off-axial mountings on the kinematics.

4. Results

To demonstrate the novel SSM for the freeform HUD system, a few positional results are presented in Table 2. The positional errors are obtained from string-based and CMM approaches to put the components in the desired place. The optical components are stationed more systematically with string-based in the range of 100's μm precision and further reduced to 10's μm with the Coordinate metrology-based approach.

After the placement of the optical component with the best achievable human and mechanical machine ability, the next phase is the optical alignment of the elements in the HUD system. The alignment and the testing of the freeform HUD system using the low-powered laser are described in Figure 5. The magnification factor and measurement of the laser beam spot diameter are reported in Table 3.

Table 2 Positional values of the fixture face-based components in the HUD sub-unit system measured using CMM.

Components	X (mm)				Y (mm)				α_x (°)			
	(A)	(B)	(C)	(E1)	(A)	(B)	(C)	(E1)	(A)	(B)	(C)	(E1)
Windscreen	276.6500	276.7480	276.6381	0.012	-100.1500	-100.2149	-100.1528	0.0028	134.8600	135.1850	134.7270	0.133
Freeform mirror 1	230.1609	230.2395	230.1903	-0.0294	-574.3027	-574.2791	-574.3024	-0.0003	52.8155	52.1265	53.0001	-0.1846
Freeform mirror 2	80.4702	080.3838	80.4647	0.0055	-551.2191	-551.1722	551.2000	-0.0191	70.3155	71.0365	70.1065	0.209
Image source	211.6641	211.6048	211.6728	-0.0087	-700.4909	-700.4544	-700.4908	-0.0001	59.3155	59.8105	59.1423	0.1732

(A) - Nominal

(B) - Measurement readings from String-based method

(C) - Measurement readings from Coordinate metrology-based method

(E1) - Error = **(A)** – **(C)**
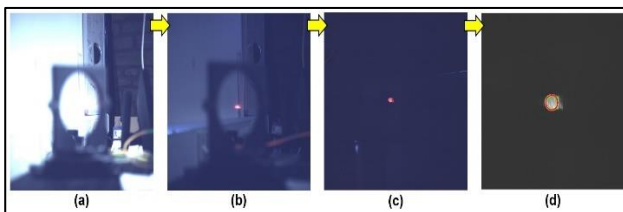
Figure 5. Laser-based alignment and functional testing of HUD system, (a) focus with lens at 3000 mm, (b) laser beam at centre of the windscreen, (c) laser spot at 0,0 field angle captured with an entrance pupil diameter of 8 mm, and (d) equivalent circular diameter of the original image.

Table 3 Laser-based alignment and functional testing with beam spot diameter at (0,0) field angle.

Image name	ECD (Pixels)	Image Pixel size	Beam Diameter (μm)	
			Theoretical	Experimental
O	51.6	4.179	75.7	215.6364
O1	50.6	4.179	75.7	211.4574
O2	48.1	4.179	75.7	201.0099

ECD – Equivalent circular diameter

5. Conclusions

The proposed strategy can be applied to various optical, mechanical, and electrical systems at the R&D phase as well as for the system functional testing. The major contribution of our approach for positioning and alignment finds potential relevancy in precision system development and has great potential in aspects of rapid, preventive, and optimistic freeform optical system integration for different applications. Some of the key features of the SSM are as follows,

- String-based placement of the components results in a precision level 100's μm.
- Coordinated metrology-based positioning is capable of further improving the precision level under 55 μm of the component placement in the system assembly and optical functional testing.
- Laser-based approach to control the alignment and position of the freeform components tilt under 0.0138 degrees and centration in submicron precision level.

The SSM strategy reduces the number of collisions and collapsibility of optical components and fixtures required for positioning and alignment to a minimum or negligible in complex optical systems. While fewer mechanical adjustment devices are needed, the cost of system development decreases. Also, it reduces processing time and improves accuracy in a step-by-step manner which gives numerous opportunities for different applications depending upon the level of precision required. Future work includes optimization of SSM for various precision settings.

References

[1] K. R. Castle, "Introduction to optical alignment techniques: a long-running SPIE short course," in *Proc. SPIE 10747, Optical System Alignment, Tolerancing, and Verification XII*, San Diego, California, United States, 2018, doi: https://doi.org/10.1117/12.2321326.

[2] N. D. Haig, "A simple technique for accurate optical alignment," *Journal of Physics E: Scientific Instruments,* vol. 6, no. 6, p. 516, 1973, doi: https://doi.org/10.1088/0022-3735/6/6/007.

[3] S. Kumar, Z. Tong, and X. Jiang, "Advances in the design and manufacturing of novel freeform optics," *International Journal of Extreme Manufacturing,* vol. 4, no. 3, p. 032004, 2022, doi: https://doi.org/10.1088/2631-7990/ac7617.

[4] M. Aliverti, G. Pariani, M. Riva, B. Saggin, and M. Tarabini, "Mechanical alignment of optical systems: practical limits and accuracy estimation," in *Proc. SPIE 10706, Advances in Optical and Mechanical Technologies for Telescopes and Instrumentation III, 107064L*, Austin, Texas, United States, 2018, vol. 10706: SPIE, doi: https://doi.org/10.1117/12.2313819.

[5] M. Aliverti, G. Pariani, M. Riva, B. Saggin, and M. Tarabini, "Mechanical alignment of optical system: CMMs forces and damages on optical elements," in *Proc. SPIE 10706, Advances in Optical and Mechanical Technologies for Telescopes and Instrumentation III, 107064M*, Austin, Texas, United States, 2018, vol. 10706: SPIE, doi: https://doi.org/10.1117/12.2313833.

[6] P. Langehanenberg, J. Heinisch, and D. Stickler, "Smart and precise alignment of optical systems," in *Proc. SPIE 8884, Optifab 2013, 88842E*, Rochester, New York, United States, 2013, vol. 8884: SPIE, doi: https://doi.org/10.1117/12.2034592.

Influence of binder content on the wear behaviour of carbide milling tools in high-precision machining of injection moulds made of AlMgSi1

E. Uhlmann[1,2], M. Polte[1,2], T. Hocke[1,2], N. Maschke[1]

[1]*Institute for Machine Tools and Factory Management IWF, Technische Universität Berlin, Germany*
[2]*Fraunhofer Institute for Production Systems and Design Technology IPK, Germany*

maschke@tu-berlin.de

Abstract

Injection moulding is the most commonly used process for the high-volume production of plastic components. To meet the increasing demands on surface quality and dimensional accuracy of these components, the preparation of the corresponding injection moulds made of AlMgSi1 requires technological research on innovative cutting materials in the development process. In industrial environment, uncoated and diamond coated tungsten carbide-cobalt (WC-Co) cutting tools are conventionally used for machining AlMgSi1-alloys. However, milling of AlMgSi1-alloys is characterised by increased temperature development during the cutting process, whereby a significant tool wear occurs. This results in an early elution of the binder phase and a fast chipping of the coating, which leads to a destabilisation of the cutting material structure and reduces the economic efficiency for the manufacturing process of components made of AlMgSi1. Using binderless WC-Co tools as cutting material for machining AlMgSi1-alloys represent a promising approach to overcome the present state of the art challenges. The binderless WC-Co material shows a great potential to avoid an early tool failure as the structural cohesion is archieved by the chemical bonding of the individual grains rather than by the binder phase. For this purpose, this study investigated the influence of different binder contents C_{Co} on the wear development concerning abrasion and surface attrition. Silicon carbide abrasives were used in blasting tests at various blasting angles α_S. Furthermore, cemented carbide materials with different binder contents of C_{Co} = 13 %, C_{Co} = 3 % and C_{Co} = 0.9 % were applied. Initial results show that wear resistance significantly improves with decreasing binder content C_{Co} and the potential of binderless WC as a cutting material for the production of AlMgSi1-alloys could be proven.

Keywords: abrasive tool wear, binderless tungsten carbide, AlMgSi1 cutting

1. Introduction

To enhance surface quality and precision in high-volume plastic component production via injection moulding, ongoing research on cutting materials is crucial, especially for injection moulds made of AlMgSi. Conventional tungsten carbide-cobald (WC-Co) cutting tools, whether uncoated or diamond-coated, encounter high challenges such as elevated temperatures ϑ and substantial wear when milling AlMgSi1 alloys. A promising approach to significantly decrease the tool wear is the use of binderless carbide tools with a binder content of $C_{Co} < 1$ %. The cobalt phase in the material structure represents a weak point that is susceptible to an early elution and followed by fast chipping, according to UHLMANN and POLTE [1,2]. Binderless WC milling tools with increased hardness and no binder phase show a high potential to prevent an early tool failure. Previous studies [3,4] showed that a binder content range of 0.25 % < C_{Co} < 6.00 %, with decreasing binder content C_{Co}, leads to an improvement in wear resistance. However, understanding specific and isolated wear mechanisms in relation to binder content C_{Co} remains incomplete. For this purpose, the ongoing study analyses abrasive wear and surface attrition in WC-Co cemented carbide tools with binder contents between 0.9 % < C_{Co} < 13.0 %.

2. Material specification

For the investigations of abrasive wear and surface attrition on prospective rake and flank surfaces, three specimen with different WC-Co configurations A1, BL130 and BL100 from the company SUMITOMO ELECTRIC INDUSTRIES, Itami, Japan, were analysed. The cemented carbide specimen A1 and BL130 feature an average grain size of d_g = 0.7 µm and BL100 with d_g = 0.4 µm.

The specific material characteristics are shown in Table 1. Although BL100 has a binder content of C_{Co} = 0.9 %, it is described as a binderless carbide material.

Table 1 Characteristics of the different tungsten carbide-cobalt materials

Abbreviation	Composition	Hardness HV30
A1	WC-13Co	1,423
BL130	WC-3Co	2,117
BL100	WC-0.9Co	2,473

The abrasive used to analyse the wear behaviour is silicon carbide (SiC) type F220 with an average grain size of d_g = 50 µm, supplied by HAUSEN GMBH, Telfs, Austria. The SiC-particles used for blasting tests represent the carbides that occur as a result of tribological effects during machining of AlMgSi1 alloys.

3. Experimental method

In this study, the wear mechanisms concerning abrasion and surface attrition were characterised by analysing the mass losses m_l and by optical examination of the machined surfaces. The experimental setup and the parameters used were chosen in accordance with the blasting tests carried out by POLTE [2] as well as the standard testing method ASTM G76-18 [5]. For abrasion, a blasting incident angle of α_S = 30 ° was choosen, since the degradation mechanism occurs through shearing processes with micro-cutting and ploughing of the matrix, resulting in spalling of the carbide phase [2-4]. The surface attrition experiments were carried out at a blasting incident angle of α_S = 90 °, as the particle indentation induces stresses σ, causing micro-cracks and pitting [2,6]. This demonstrates the material's ability to resist fatigue from overlapping

tangential stress τ and normal stress σ in the machining process, particularly in interrupted cutting [2,6]. Each specimen was studied by particle irradiation for different blasting times of $t_B = 30$ s, $t_B = 60$ s, $t_B = 90$ s and $t_B = 120$ s. The tests were repeated twice and the results were averaged. For partical blasting tests the air blast machine FSA-1 of the company SABLUX TECHNIK AG, Bachenbülach, Switzerland with a blasting pressure of $p_b = 0.5$ N/mm² was used. The nozzle, directing particles onto the surface, consists of a diameter $D_d = 0.8$ mm and is positioned at a distance of $D_D = 10.0$ mm. The respective mass losses m_l are determined as a function of the blasting time t_B with a precision scale PLS 1200 from KERN & SOHN GMBH, Balingen, Germany. To evaluate the wear mechanisms in relation to the binder content C_{Co}, the LEO 1455 VP SEM scanning electron microscope from LEICA ELECTRONIC OPTICS, Wetzlar, Germany, with a magnification of $M_A = 5,000$x and acceleration voltage of $V_{||} = 15$ kV was used.

4. Experimental investigations and results

Figure 1 illustrates the wear behaviour concerning abrasion and surface attrition for the three carbide types used. The isolated abrasive wear at an impact angle of $\alpha_S = 30°$ reveals a direct correlation between binder content C_{Co} and wear in terms of mass loss m_l. The wear rates m_l for all specimens show an almost linear progression, indicative of stable plastic deformations. In general, WC-13Co shows a total mass loss of $m_l = 1.18$ %, WC-3Co a mass loss of $m_l = 0.8$ % and BL100 a mass loss of $m_l = 0.17$ % after a blasting time of $t_B = 120$ s. Based on the results, it could be demonstrated that an improvement in abrasive wear of 86 % was achieved for binderless WC and 32 % for WC-3Co compared to specimen type A1.

Measurement device:
Blasting machine FSA-1 of SABLUX TECHNIK AG
Weight scale:
Precision scale PLS 1200 of KERN & SOHN GMBH
Process parameter:

Blasting pressure	P	= 0.5	N/mm²
Nozzle diameter	d_d	= 0.8	mm
Nozzle distance	d_D	= 10	mm
Blasting angle	α_S		°
Abrasive SiC-grain size	d_k	= 220	µm

▲ WC-13Co   ■ WC-3Co   ◆ WC
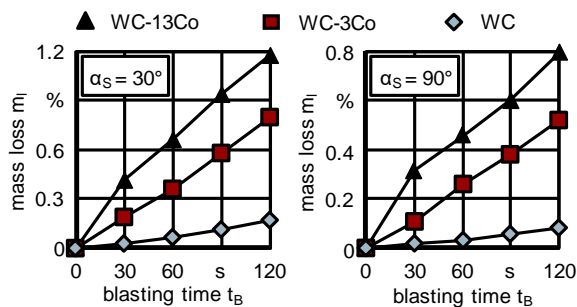
Figure 1. Wear of different binder contents C_{Co} and impact angles α_S

At an impact angle of $\alpha_S = 90°$ to investigate the surface attrition, WC-13Co shows the highest mass loss of $m_l = 0.77$ % after $t_B = 120$ s. In comparison, WC-3Co is characterised by a mass loss of $m_l = 0.52$ % and WC demonstrates the lowest mass loss of $m_l = 0.08$ %, indicating reductions of 32 % as well as 90 %, respectively. In general, all investigated specimen show the lowest mass loss m_l at an impact angle of $\alpha_S = 90°$, suggesting a greater resistance to surface attrition than abrasion wear.

Figure 2 presents additionally SEM images of the surfaces related to the machined specimen concerning abrasive wear behaviour and surface attrition. The specimens of type WC-13Co (A1) show a recognisable wear behaviour, which is characterised by pronounced cutting and ploughing grooves (2a). In contrast, the specimens of type WC-3Co (Figure 2b) showcases a reduced wear but lip formations were detected, which could be attributed to plastic deformations. Based on the investigations

of the binderless WC (Figure 2c), a minimum topographical wear could be determined, which corresponds to the results of the quantitative analyses in Figure 1. As a result, the binderless WC shows no typical characteristics of a brittle material.
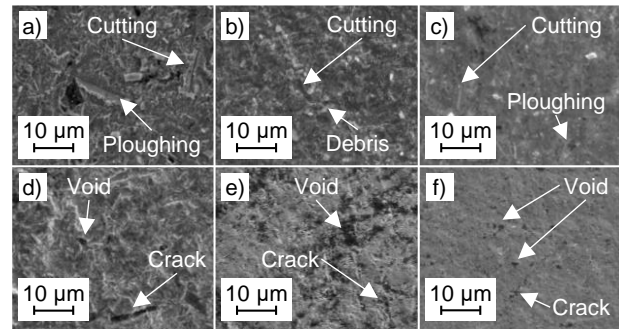
Figure 2. Surfaces of all investigated specimen after $t_B = 120$ s. a) A1, $\alpha_S = 30°$; b) BL130, $\alpha_S = 30°$; c) BL100, $\alpha_S = 30°$; d) A1, $\alpha_S = 90°$; e) BL130, $\alpha_S = 90°$; f) BL100, $\alpha_S = 90°$

Examinations into surface attrition for WC-13Co unveil the presence of voids and an expansion of pits attributed to crack propagation, accompanied by ploughing traces (Figure 2d). In the case of WC-3Co (Figure 2e), substantial lip formations and debris are observed, while process-dependent hole expansions are noted to a lesser degree than in specimens with a binder content of $C_{Co} = 13$ % (WC-13Co). Significantly, binderless WC (Figure 2f) shows a low topographic wear, featuring well-defined fractures and pronounced surface craters compared to the other investigated specimens. The binderless WC demonstrates the lowest abrasive wear and surface attrition, while the specimens with a binder content of $C_{Co} = 13$ % exhibits the highest wear behaviour in terms of abrasion and surface attrition.

5. Conclusion and further investigations

This study established that binder content C_{Co} in cemented carbide affects abrasive wear and surface attrition. The results support the theories of various research studies [3-5]. With decreasing binder content C_{CO}, the material separation remains plastic during abrasion and surface attrition. Specimens made of binderless WC show the most potential for milling AlMgSi1 alloys, demonstrating superior resistance to tensile stresses σ and shear stresses τ compared to the investigated specimen in an binder content area of 0.9 % < C_{Co} < 13.0 %. Further research works will explore the wear behaviour of innovative binderless WC configurations with binder contents between 0.25 % < C_{CO} < 1.00 % to fully understand the impact of the cobalt binder C_{Co} in material structure. Examining the performance of cutting tools made of binderless WC under different machining conditions will enhance their applicability, particularly in scenarios involving the manufacturing of injection moulds made of AlMgSi1 alloys. This work was funded by the GERMAN RESEARCH FOUNDATION DFG.

References

[1] Uhlmann, E; Polte, M; Oberschmidt, D; Polte, J; Löwenstein, A: Werkzeugkonzept zum Mikrofräsen mit superharten Schneidstoffen. Diamond Business (2014) 03/2014, S. 24 – 29.

[2] Polte, J: Kubisch-kristallines Bornitrid ohne Bindephase als Schneidstoff in der UP-Zerspanung. Berichte aus dem PTZ Berlin. Hrsg.: Uhlmann, E. Stuttgart: Fraunhofer IRB, 2016.

[3] Gee, M.G.; Phatak, C; Darling, R: Determination of wear mechanisms by stepwise erosion and stereological analysis. Wear (2005) 258(1–4). S. 412 – 425.

[4] Beste, U; Hammerström, L.; Engqvist, H.; Rimlinger, S.; Jacobson, S.: Particle erosion of cemented carbides with Low Co content. Wear (2001) 250(1–12). S. 809 – 817.

[5] ASTM G76-18, (2018) Standard Test Method for Conducting Erosion Tests by Solid Particle Impingement Using Gas Jets, West Conshohocken, USA: ASTM International.

[6] Czichos, H.; Habig, K.-H.: Tribologie-Handbuch. Wiesbaden: Vieweg + Teubner, 2010. S. 133 – 140.

Modelling and analysis of cutting forces in ultraprecision diamond turning of freeform surfaces and their assessment

Shangkuan Liu[1], Kai Cheng[1] and Joe Armstrong[2]

[1]Department of Mechanical and Aerospace Engineering, Brunel University London, Uxbridge, London, UK
[2]Polytec GmbH, Polytec-Platz 1-7, 76337 Waldbronn, Germany

Emails: Shangkuan.Liu@brunel.ac.uk; Kai.Cheng@brunel.ac.uk; j.armstrong@polytec.de

Abstract

In the realm of ultraprecision manufacturing freeform surfaced optics and devices, the ultraprecision diamond turning process holds significant prominence. While cutting force, a pivotal physical parameter in the machining process, has received substantial attention in R&D and machining practices, scant emphasis has been placed on elucidating the nuances of cutting forces and the associated cutting dynamics in ultraprecision diamond turning of freeform surfaces particularly through fast and/or slow tool servo (FTS / STS) modes. In this paper, theoretical analysis on the cutting force and its modelling are presented in the ultraprecision diamond turning of freeform surfaces, particularly considering constant variations of cutting forces along the freeform surface curvature and the increasingly stringent requirement on high precision optical surface finishing. The cutting forces modelling is based on integration of Akins model with the influence of shear angles varying constantly on the freeform surface conduction. Based on the toolpath data of the cutting process at the freeform surface, the depth-of-cut (DoC) of the surface, curvature variations, and shear angle variations throughout the process are meticulously analysed. Subsequently, a cutting force model is developed to discern the nuances of the cutting motion by analysing the cutting toolpath, and then consequently enabling the prediction of cutting forces variation during orthogonal cutting motion with a round-edged diamond cutting tool. Finally, an integrated approach for examining the correlation between cutting forces and the analysis of surface texture and texture aspect ratio should be developed and further investigated, particularly on the functionality of a freeform surface and its generation in ultraprecision machining.

Keywords: Cutting force modelling; ultraprecision diamond turning; freeform surfaces; micro cutting mechanics; surface texture aspect ratio; freeform optics.

1. Introduction

The fast-/slow-tool servo (F-/STS) diamond turning process, known for its high determinism, has seen significant success in producing micro-structured functional freeform surfaces and been widely introduced into the area with high requirement of high customization and nanometre's level surface roughness in recent years. The fundamental kinematic feature in cutting motion between the fast and slow tool servo systems exhibits similarities: the workpiece follows the spindle in rotational movement, while the diamond tool tip cutter moves uniformly along the x-axis at the centre height of the spindle and precisely follow the designed micro-structure and moved in the z-direction. Eventually the desired freeform surface can be produced with high quality promised. The technique ensures the surface roughness quality of the product surface, achieving as low as 1-10 nm.

In the last three decades, there is a large amount of research and efforts in diamond turning machine development, in ultraprecision cutting, single-point diamond turning (SPDT) stands out as the primary method for achieving surface roughness at the nanometer level [1]. In SPDT machining process, the cutting tool material consists of a single-crystal diamond with a small diameter cutting edge. This nanoscale cutting edge facilitates the production of smooth surfaces with minimal damage to the top surface [2]. Apart from traditional slow tool servo cutting technology, fast tool servo cutting is employed to achieve high accuracy on complex non-spherical surfaces and microstructures [3]. Furthermore, due to the rapid development and widespread application of freeform surfaces, optimizing freeform surface toolpath generation has become increasingly vital in the state-of-the-art ultra-precision machining field [4][5]. In the Single Point Diamond Turning (SPDT) process, research has been conducted to explore the capabilities in different materials [6][7] and shapes [8]. In addition, some integrated research explores such as Macro-micro dual -drive technology, contributing to the advancement of both ultra-precision systems and macro–micro dual-drive technology [9].

The cutting force holds paramount significance in the single-point diamond turning machining process as it reflects the direct interaction between the cutter and the workpiece. Leveraging the wealth of information derived from the toolpath data, which is intricately linked to the designed freeform surface, cutting force modelling emerges as a highly promising approach for ensuring the quality control of the designed surface. Over the past decade, extensive research has been conducted on cutting force in single-point diamond turning machining processes. This research encompasses areas such as cutting force prediction, analysis of cutter kinematic motion, including cutting force tracking and prediction [10], cutting force control for improved surface results, and the investigation of the relationship between chip loads and cutting force fluctuations [11], etc. The anticipation of required cutting forces in advance serves as the foundational element for linking resulting surface quality to the cutting process."

In the SPDT machining process, the fabrication of freeform surfaces presents a notable challenge due to the continuous changes in surface curvature. These dynamic alterations correspondingly lead to variations in cutting angles during the machining process. The inherent changes in curvature directly influence both the cutting angles and the depth of cutting (DoC) of the cutter, consequently affecting the cutting forces throughout the machining operation. Through an analysis of the toolpath file and the prediction of variations across the entire cutting loop, it becomes possible to examine the positional relationships among each cutter location point. This analysis aids in identifying problematic or challenging areas on the designed surface. From an industrial perspective, the utilization of toolpath analysis serves a dual purpose. Firstly, it provides the means to retrospectively trace the cutting process, enabling the identification of factors that may have contributed to the production of faulty parts. Secondly, this retrospective analysis serves as a valuable tool for preventing similar challenges in subsequent production cycles, contributing to enhanced efficiency and product quality.

This paper is focused on the cutting force variances with the height position changes in the z-axis, which leads to the varies DoC and angles of kinematics. It aims to investigate the relationship between the designed freeform surface curvature changes, 3D surfaces parameters analysis of the surface, and the resulting cutting force to enhance the precision and quality of microstructured surfaces.

2. Methods
2.1. STS process toolpath interpretation and analysis
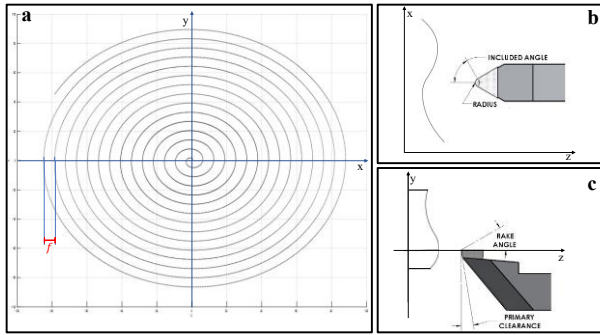
Figure 1. Schematic of cutting kinematics of diamond turning machining. a) the toolpath of the surface in the XOY plane; b) the tooltips and surface relationship at the top view and c) the lateral view of the cutting process.

As depicted in Fig.1(a), the trajectory of the machine tool in STS mode can be conceptualized as the Archimedes spiral pattern motion of the cutter within the $O - X\theta Z$ cylindrical coordinate system. In this system, the XOY plane is aligned parallel to the spindle surface. On this plane, the cutter's movement follows a linear motion with uniform speed along the X-axis direction (either from the center to the edge or vice versa). This motion is coordinated with the rotational movement of the spindle in the C-axis. As a result, an Archimedean spiral pattern is generated, with a predetermined distance between each point and a specified feed rate. These parameters significantly influence the number of points in each circle and the number of circles the cutter needs to traverse, which, in turn, has a substantial impact on the resulting quality and processing time of the machine. The specific values of these parameters are generally dependent on the tool radius.

The YOZ plane runs parallel to the plane defined by the cutting edge of the tool, while the XOZ plane illustrates the correlation between the tool radius and the movement along the x-direction. Both planes collectively portray the motion of the cutter along the Z-axis direction. Understanding and optimizing these

trajectories are crucial for achieving precise and efficient machining, considering the interplay between tool geometry and the chosen toolpath strategy.

2.2. Cutting force and shear force
The cutting force model developed in this study is grounded in Atkins' model [12]. Simultaneously, we consider the direction of the cutting force and the practical DoC. In instances where surface work plays a substantial role in steady deformation, several internal works are identified: (i) plasticity along the shear plane; (ii) friction along the underside of the chip at the tool interface; and (iii) formation of a new cut surface [12]. All these work components are externally provided by the FC component of the tool force moving along the machined surface's toolpath file.

2.3. Cutting force model in STS process
To estimate the practical cutting force based on the toolpath data, the practical shear direction needs to be first been calculated below:

$$\phi = \frac{\pi}{4} - \frac{\beta - \alpha}{2} \tag{1}$$

In this scenario, where β represents the friction angle along the rake face, and α is the tool rake angle. Simultaneously, with the cutter transitioning from the (i-1)-th to the i-th point, the relative distance between these two location points can be calculated using the following function [13]:

$$d = \sqrt{f^2 + (z1 - z2)^2} \tag{2}$$

where f represents the feed rate along the X-axis of the cutting process, and z1 and z2 are the positional data along the Z-axis. The included angle α_0 between these two points can be expressed by

$$\alpha_0 = \arctan\left(\frac{z1 - z2}{f}\right) \tag{3}$$

The coordinates of the intersection point A (Xa, Za) between the cutter edge at the previous (i-1)-th point and the current i-th point can be calculated by

$$\begin{cases} x_a = -\frac{1}{2}f - \sqrt{r^2 - \left(\frac{d}{2}\right)^2}\sin(\alpha_0) \\ z_a = \frac{1}{2}(z1 + z2) - \sqrt{r^2 - \left(\frac{d}{2}\right)^2}\cos(\alpha_0) \end{cases} \tag{4}$$

The coordinates of the intersection points B (Xb, Zb) and C (Xc, Zc), corresponding to the cutter edge at the preceding (i-1)-th point and the current i-th point, with the uncut surface, can be calculated by

$$\begin{cases} x_b = \sqrt{r^2 - (z1 - h_0)^2} - f \\ z_b = z_c = h_0 \end{cases} \tag{5}$$

Where h_0 is the height of the uncut surface in the toolpath data. And the relative angle between the i-th point to point A, B, and C respectively can be obtained as

$$\begin{cases} \theta_a = \arcsin\left(\frac{x_a}{r}\right) \\ \theta_b = \arctan\left(\frac{x_b}{z2 - h_0}\right) \\ \theta_c = \arcsin\left(\frac{x_c}{r}\right) \end{cases} \tag{6}$$

Accordingly, the practical DoC can be calculated by using the equations (7) below.

$$\begin{cases} DoC = \frac{1 - \cos(\alpha_0 + \theta_i + \alpha_1)}{\cos(\alpha_0 + \theta_i)}, \text{where } \theta_a \le \theta_i < \theta_b \\ DoC = r\cos(\alpha_0) - \frac{z2 - h0}{\cos(\theta_i)}\cos(\alpha_0), \text{where } \theta_b \le \theta_i < \theta_c \end{cases} \tag{7}$$

With the help of Atkins' model, the overall main cutting force can be obtained as follows:

$$F_c V = (\tau_y \gamma)(t_0 w V) + [F_c \sec(\beta - \alpha) \sin \beta] \frac{V \sin \phi}{\cos(\phi - \alpha)} + R w V \quad (8)$$

where V is the cutting velocity, F_c is the horizontal component of the cutting force, τ_y is the (rigid-plastic) shear yield stress, γ is the shear strain along the shear plane, given by $\gamma = \cot\varphi + \tan(\varphi - \alpha) = \cos\alpha / \cos(\varphi - \alpha)\sin\varphi$; t0 is the uncut chip thickness, w is the width of the orthogonal cut, φ is the orientation of the shear plane and R is the specific work of surface formation (fracture toughness). The constant parameters using for calculation have been listed in the Table 1.

Table 1 Constant parameters using in the calculation

Parameters	Definition	value
Vr	(r/s) Spindle rotation speed	3000
τ_y	(Mpa) Shear yield stress	55.2
μ	The coefficient of friction	0.583
r	(mm) Tool radius	0.35
D	(mm) Objective surface diameter	78
α	(mm) Tool rake angle	0

3. Results and discussion

3.1 Experiment setup

Fig. 2(a) illustrates the cutting motion in the process, highlighting the mirror surface machining procedure that employs a carrier disk. As depicted in Figure 2(b), the diameter of the disk is 290mm, and the capacity of the carrier disk allows the machine to work on six mirrors simultaneously. The distribution of mirrors is symmetrical from left to right, with two mirrors allocated on the top and bottom, and one each on the left and right. The cutter works concurrently on six mirrors within the container, continuously transitioning between kinematic motion and movement toward the next surface.

3.2 Modelling results and discussion

The estimated primary cutting force is depicted in Fig. 3. The selected estimated cutting force corresponds to the tool movement along the X-axis, spanning from 18.76 cm to 18.9 cm (utilizing 206,460 cutter location points). The illustration demonstrates a commendable accordance, perfectly reflecting the variations in cutter kinematics as it moves between each surface without any cutting progress.

To provide a more detailed insight into the characteristics of cutting force changes during the cutting progress, a specific loop was selected when the cutter's location on the X-axis ranged between 18.86cm and 18.87cm, with a focus on material removal from the surface. A clear periodicity is observed in this motion, with the estimated minimum cutting force occurring when the cutter is positioned at 18.8642 along the X-axis. At this point, the cutting force is recorded as 0.0120778 N.

As illustrated in Fig. 4, as the practical shear angle decreases, the rising trend of the cutting force becomes negative, eventually showing a decline. As the cutter moves into the material removal area, the changes in shear angle become more frequent but remain subtle. Notably, the cutting force exhibits a similar trend of change. These findings indicate that the developed model adeptly captures the cutter's location based on the toolpath data and process parameters associated with material removal in the diamond turning machining process.
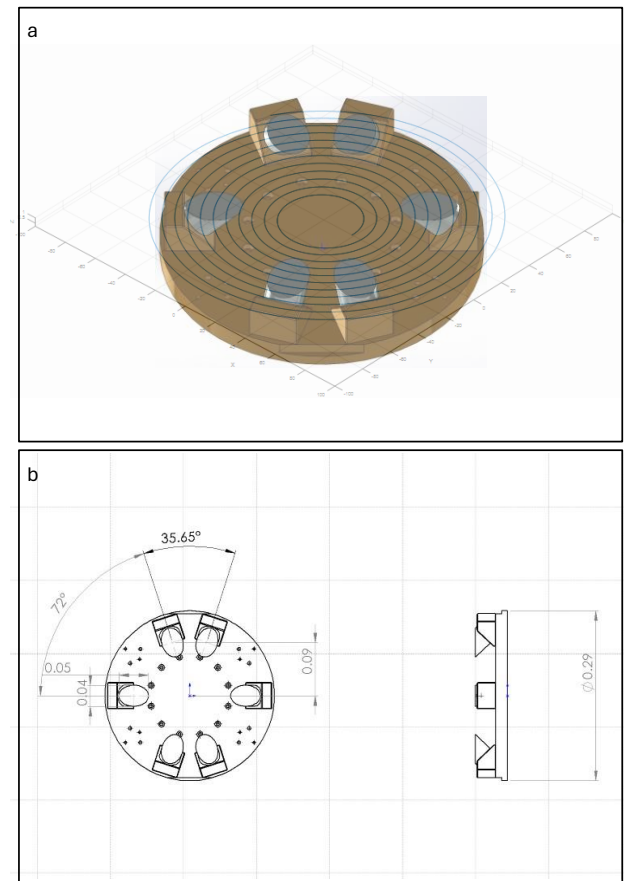
Figure 2. a) Cutting motion in the process and mirror surface machining procedure with a carrier disk. b) Parameters and spread of the workpieces on the carrier disc
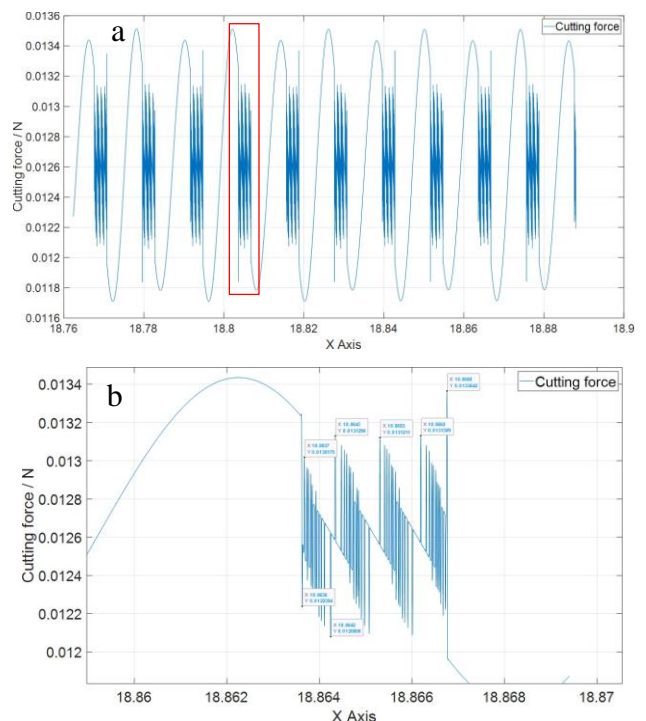
Figure 3. Characteristics of the estimated cutting force. a) the cutting force from 18.76 cm to 18.9 cm, b) the cutting force plot only focus on the red frame part (from 18.86cm to 18.87cm).

Figure 5 illustrates a 3D surface topography obtained after SPDT machining process. Stitched profilometer image of 3 mm area from a curved surface area with form removed using software showing machine tool travel across the surface with numerical

texture 2D and 3D areal parameters. 2D profile lines are in line with the tool path direction.
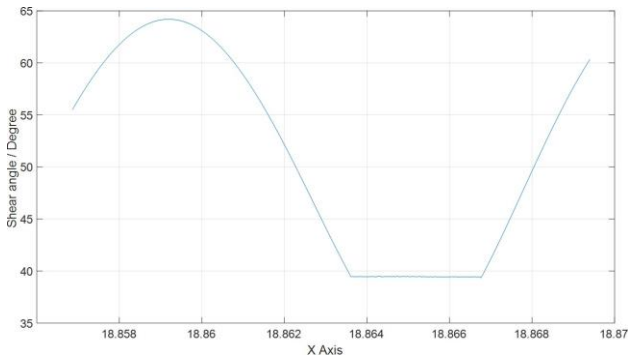
Figure 4. The practical shear angle.
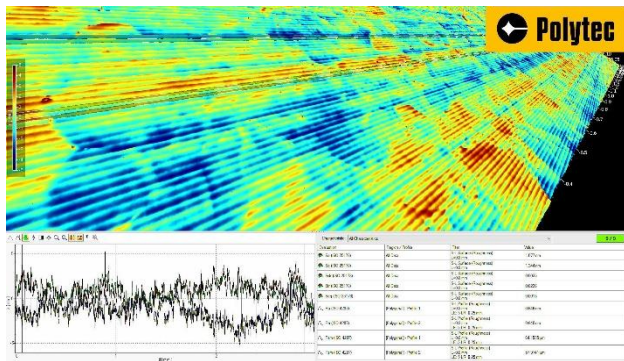
Figure 5. The 3D surface topography assessment result of machined surface by using white light interferometers.

4. Conclusions

In this research, we developed a cutting force model that considers the influence of cutting angles and the corresponding DoC, utilizing machine toolpath data. To achieve this, we extracted and thoroughly investigated the machine toolpath. Calculated the practical shear angle, relative distances between each cutter location point, and the practical Depth of Cut. These parameters were then incorporated into the final cutting force calculations. In future work, the current model lacks control interfaces, making it unable to directly import toolpaths. Secondly, the model currently lacks comparative data for expanded parameters such as residual height and the relationship between cutter radius and cutting force. Lastly, ongoing efforts involve the comparison of the model's predictions with real-world data. The surface of toolpath file has been machined, and observations have been conducted using a white light interferometer. The current phase involves the organization and analysis of the collected data.

Nomenclature	
STS	Slow-tool servo diamond turning process
SPDT	Single-point diamond turning machining process
DoC	Depth of cutting
ϕ	Practical shear direction
β	Friction angle along the rake face
α	Tool rake angle
d	the relative distance between two continues location points
f	Feed rate of the cutter in the machine process
z1 z2	the two positional data of the cutter along the Z-axis
α_0	The practical included angle of the cutter in the process

x_a, x_b, x_c	The location data in the X-axis at the intersection points between the cutter edge at the (i-1)th point and the (i)th point.
z_a, z_b, z_c	The location data in the Z-axis at the (i-1)th and (i)th intersection points between the cutter edge and the uncut surface.
h_0	Height of the uncut surface in the toolpath data
$\theta_a, \theta_b, \theta_c$	Relative angle between the (i) point to point A, B, and C
F_c	Cutting force
V	Cutting velocity
τ_y	Shear yield stress
t_0	Uncut chip thickness
w	Width of the orthogonal cut
γ	Shear strain along the shear plane
φ	Orientation of the shear plane
R	Fracture toughness

References

[1] Yip, W. S., To, S., & Zhou, H. (2022). Current status, challenges and opportunities of sustainable ultra-precision manufacturing. Journal of Intelligent Manufacturing, 1-13.

[2] Yip, W. S., Yan, H. E., Zhang, B., & To, S. (2024). The state-of-art review of ultraprecision machining using text mining: Identification of main themes and recommendations for the future direction. Wiley Interdisciplinary Reviews: Data Mining and Knowledge Discovery, 14(1), e1517.

[3] Gong, Z., Huo, D., Niu, Z., Chen, W., & Cheng, K. (2022). A novel long-stroke fast tool servo system with counterbalance and its application to the ultra-precision machining of microstructured surfaces. Mechanical Systems and Signal Processing, 173, 109063.

[4] Cheng, K. and Huo, D. (Editors), Micro Cutting: Fundamentals and Applications, John Wiley & Sons, Chichester, October 2013.

[5] He, S., Xuan, J., Du, W., Xia, Q., Xiong, S., Zhang, L. & Shi, T. (2020). Spiral tool path generation method in a NURBS parameter space for the ultra-precision diamond turning of freeform surfaces. Journal of Manufacturing Processes, 60, 340-355.

[6] Mukaida, M. & Yan, J. (2017). Ductile machining of single-crystal silicon for microlens arrays by ultraprecision diamond turning using a slow tool servo. International Journal of Machine Tools and Manufacture, 115, 2-14.

[7] Sawangsri, W. & Cheng, K. (2016). An innovative approach to cutting force modelling in diamond turning and its correlation analysis with tool wear, Proceedings of the IMechE, Part B: Journal of Engineering Manufacture, 230(3), 405-415.

[8] To, S., Zhu, Z., & Wang, H. (2016). Virtual spindle based tool servo diamond turning of discontinuously structured microoptics arrays. CIRP Annals, 65(1), 475-478.

[9] Yang, M., Gui, H., Zhang, C., Zhao, S., Han, F., Dang, M., & Zhang, B. (2023). Recent development for ultra-precision macro–micro dual-drive system: A review. Machines, 11(1), 96.

[10] Chen, Y. L., Cai, Y., Tohyama, K., Shimizu, Y., Ito, S., & Gao, W. (2017). Auto-tracking single point diamond cutting on non-planar brittle material substrates by a high-rigidity force controlled fast tool servo. Precision Engineering, 49, 253-261.

[11] Zhou, X., Wang, R., & Liu, Q. (2017). Study on suppressing cutting force fluctuations based on chip loads for turning optical freeform surfaces. The International Journal of Advanced Manufacturing Technology, 90, 2037-2046.

[12] Atkins, A. G. (2003). Modelling metal cutting using modern ductile fracture mechanics: quantitative explanations for some longstanding problems. International journal of mechanical sciences, 45(2), 373-396.

[13] Zhu, Z., To, S., Zhu, W. L., Huang, P., & Zhou, X. (2019). Cutting forces in fast-/slow tool servo diamond turning of micro-structured surfaces. International Journal of Machine Tools and Manufacture, 136, 62-75.

Temperature-dependent modification of gallium nitride using vacuum hydrogen plasma

Tong Tao[1], Yuya Onishi[1], Rongyan Sun[1], Yuji Ohkubo[1], and Kazuya Yamamura[1]

[1]Research Center for Precision Engineering, Graduate School of Engineering, Osaka University, 2-1 Yamadaoka, Suita, Osaka 565-0871, Japan

t-tao@nms.prec.eng.osaka-u.ac.jp

Abstract

Gallium nitride (GaN) is considered to be one of the most promising materials for applications such as light-emitting diodes, and high-power, high-frequency electronic devices, owing to its excellent mechanical and electrical properties. However, machining GaN poses challenges due to its high hardness and chemical inertness. To achieve high-efficiency and damage-free finishing of GaN, plasma-assisted polishing (PAP), which combines surface modification by hydrogen plasma irradiation and removal of the modified layer using soft abrasives, was proposed. In the PAP process, the modification rate was the crucial limiting factor for the polishing rate. Since substrate temperature significantly influenced the modification process. In this study, the correlation between temperature and modification characteristics of GaN was explored.

Gallium nitride, hydrogen plasma, temperature, modification characteristic

1. Introduction

Due to its superior properties, such as wide bandgap, high thermal conductivity, and high electron mobility, Gallium nitride (GaN) has become increasingly pivotal in the fabrication of high-frequency and high-power electronic devices. To fully harness these excellent characteristics of GaN, a damage-free atomically smooth GaN surface is required. However, GaN is a difficult-to-machine material with high hardness and chemical inertness. For the final finishing of GaN, the commonly used process is chemical mechanical polishing (CMP), using a suspension containing chemicals, such as alkali, known as slurry, along with abrasives [1]. However, when applying the CMP process, which can achieve a high polishing rates for Si substrates, to GaN substrates, the polishing rate was extremely low, typically at 77 nm / h or less. This low polishing rate necessitates a significant improvement. Furthermore, the processing cost and environmental load when purchasing and disposing of the slurry are also large. Additionally, the epitaxial growth GaN film often contains numerous dislocations, leading to the formation of a large number of etch pits on the GaN surface due to the alkaline component in the slurry [2].

For the flattening of some difficult-to-machine materials such as GaN, SiC, and diamond, a dry polishing process named plasma-assisted polishing (PAP), which combines surface modification by plasma irradiation, and removal of modified layer conducted by applying ultra-low polishing pressure or polishing using soft abrasive, was proposed by our research group [3]. In our previous research, it has been demonstrated that PAP, using atmospheric CF_4 plasma, can achieve atomically smooth GaN surfaces with a well-ordered step-terrace structure [4]. However, a primary limitation of PAP, especially when applied to GaN, is its slow modification rate, posing an efficiency challenge in GaN semiconductor manufacturing. To overcome this limitation, the use of vacuum hydrogen plasma to replace atmospheric CF_4 plasma in PAP for GaN was proposed. In the reaction between GaN and hydrogen plasma, the reaction rate of nitrogen (N) with hydrogen (H) radicals, forming NH_3, was faster than that of gallium (Ga) in GaN, leaving Ga on the GaN surface. This selective interaction was crucial for the plasma-assisted modification process. Hydrogen has shown potential for faster reaction rates of GaN compared to traditional reactive gases like CF_4. Nevertheless, even with the adoption of hydrogen plasma, the quest for optimizing the modification speed continues. According to the Arrhenius equation:

$$ln\ k = -\frac{E_a}{RT} + lnA$$

(*k* is the rate constant; *T* is the absolute temperature)
It gives the dependence of the rate constant of a chemical reaction on the absolute temperature. So it is concluded that temperature could play a critical role in further enhancing the reaction rate of hydrogen plasma. In this study, plasma modification experiments were conducted under different temperature conditions to explore the relationship between temperature and the modification characteristics of GaN in hydrogen plasma.

2. Experimental setup

Figure 1 shows the experimental setup for plasma modification used in this study. A GaN substrate was fixed on the lower stage, which can be heated up to 500°C. A mixture of Ar and H_2 was supplied from the side of the vacuum chamber, maintaining a constant of 40 torr by controlling the pumping rate with a dry pump. Besides, to control the hydrogen concentration below 4% (burst point), the gas flow rates (Ar: 200 sccm, H_2: 5 sccm) were controlled by mass flow controllers (MFCs). By applying radio frequency (RF) (*f*=13.56 MHz) power on the upper electrode, plasma was generated in the area between the upper electrode and GaN substrate.

Figure 2 shows the optical emission spectroscopy (OES) spectrum of the Ar-based hydrogen plasma generated during the plasma irradiation. Optical emission from H (656.9 nm) was confirmed from the spectrum.
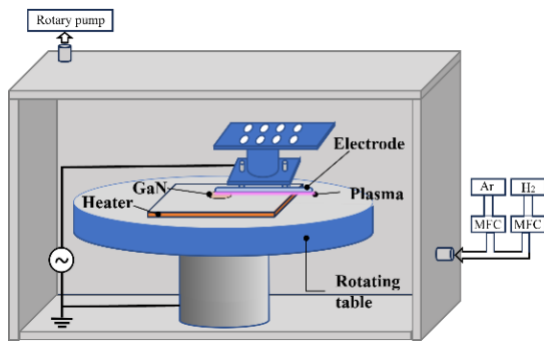
Figure 1. Schematic of the experimental setup.
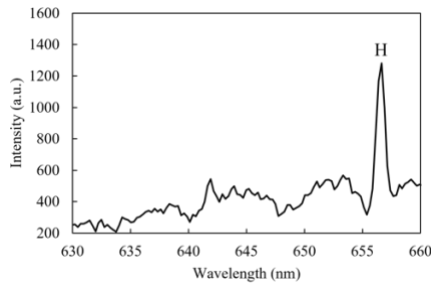
Figure 2. OES spectrum of the Ar-based vacuum hydrogen plasma.

Figure 3. Ga2p XPS spectrum of the GaN surface (a) before plasma irradiation (b) after plasma irradiation under room temperature (c) after plasma irradiation under 100℃ (d) after plasma irradiation under 500℃.

Figure 4. SEM image of GaN surface (a) before plasma irradiation (b) after plasma irradiation under 100℃ (c) after plasma irradiation under 500℃.

3. Results and discussion

To investigate the impact of substrate temperature on the plasma modification characteristics of GaN in vacuum hydrogen plasma, plasma irradiation experiments were conducted for 30 mins under room temperature, 100°C and 500°C through substrate heating. Before plasma irradiation, GaN substrates were cleaned using SPM & HF solutions. The surface composition change of GaN substrate was analysed by X-ray photoelectron spectroscopy (XPS) before and after hydrogen plasma irradiation. As shown in Fig.3(a), only Ga-N peak was observed in the Ga2p spectrum of the GaN surface before plasma irradiation. After 30 mins of plasma irradiation at room temperature (without heating), a weak peak corresponding to Ga-Ga was observed, as shown in Fig. 3(b). This result suggested that the modification rate at room temperature was very low due to the low density of H radical. Fig. 3(c) shows the Ga2p spectrum of GaN surface after plasma irradiation at 100°C. According to the Arrhenius equation, the modification reaction rate can be increased by raising the temperature, a stronger Ga-Ga peak was observed. However, when the sample temperature was increased to 500°C, the peak of Ga-Ga did not continue to rise; instead, it disappeared. This implies that at 500°C, the modification rate did not follow the equation's increase but rather decreased.

Moreover, the surface morphology changes of GaN substrates before and after plasma irradiation was also measured using scanning electron microscope (SEM). As shown in Fig.4(a) and 4(b), after hydrogen plasma irradiation at 100°C, the surface morphology did not change significantly, while a Ga modification layer was formed. However, as shown in Fig.4(c), after plasma modification at 500 °C, there was a substantial change in the surface morphology, particularly with the observation of numerous hexagonal etching pits. Combining the results from XPS, it can be inferred that in a hydrogen plasma, below a certain temperature, the modification rate on the surface of GaN fellow the Arrhenius equation, where the modification rate increased with the rise in temperature. However, at excessively high temperature (500°C), intense surface thermal motion made it
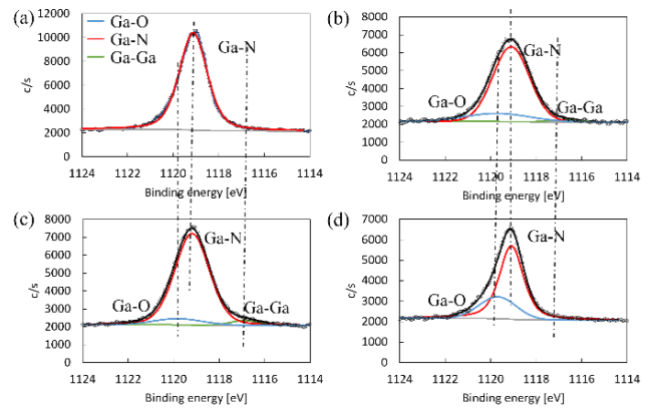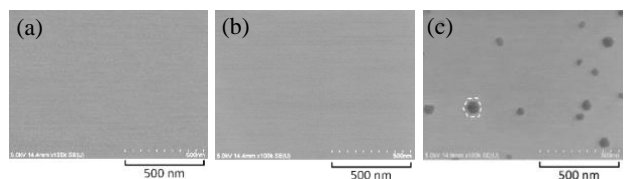
difficult for H radicals to adsorb onto the GaN surface and enhanced desorption from the surface. This led to a decrease rather than an increase in the modification rate. Additionally, the reduction in the adsorption of H radicals caused the preferential reaction of defect sites on the GaN surface, believed to be the reason for the formation of etching pits.

4. Conclusions

In this study, the correlation between temperature and modification characteristics of GaN was explored. Within a certain temperature range, raising the substrate temperature can effectively increase the modification rate. However, at excessively high temperature, particularly at 500°C, the modification rate decreased and led to the formation of etching pits on the surface. This result indicated that by optimizing the modification temperature, a high modification rate could be achieved while ensuring surface quality without the formation of etching pits.

References

[1] Li C, Zhang F, Ma Z. *Proceedings of the Institution of Mechanical Engineers, Part B: Journal of Engineering Manufacture*, 2018, **232**(11): 1986-1995

[2] Aida H, Kim S, Suzuki T, et al. *ECS Journal of Solid State Science and Technology*, 2014, **3**(5): P163

[3] K. Yamamura, K. Emori, R. Sun, Y. Ohkubo, K. Endo, H. Yamada, A. Chayahara, Y. Mokuno 2018 *CIRP Annals*, **67**(1), 353

[4] Deng, H., Endo, K., & Yamamura, K. 2015 *CIRP Annals*, **64**(1), 531-534.

The anisotropy of deformation behaviors of MgF₂ single crystal

Yinchuan Piao[1,2], Xichun Luo[2], Chen Li[1], Qi Liu[2], Feihu Zhang[1]

[1]School of Mechatronics Engineering, Harbin Institute of Technology, Harbin, China
[2]Centre for Precision Manufacturing, DMEM, University of Strathclyde, Glasgow, UK

Yinchuanpiao@outlook.com

Abstract

Anisotropy of deformation behaviors limit the high surface quality of Magnesium fluoride (MgF_2) components. Cleavage factor have the relationship with the anisotropy of deformation behaviors of Magnesium fluoride (MgF_2) single crystal, which can influence the manufacturing efficacy and component quality. To determine the reveal anisotropy mechanism of deformation behaviors of the MgF_2 single crystal, the nanoindentation tests were systematically performed on different crystal planes. Besides, the hardness, displacement-load curves, the SEM images of the surface morphologies and cleavage factors under different experimental conditions were obtained. According to compared the experiment results and the cleavage factors under different experimental conditions, the cleavage factor can be used to reflect the activation of the plastic deformation and reveals the anisotropy of deformation behaviors. The theoretical results consisted well with the experimental results, which can improve the manufacturing efficacy and component quality in the manufacturing process of the MgF_2 components.

Anisotropy, Single crystal, Deformation behavior, Cleavage factor

1. Introduction

Magnesium fluoride (MgF_2) single crystal is widely used as infrared optical components because of the extraordinary infrared optical characterization and excellent mechanical strength. However, MgF_2 single crystal is the typical hard-to-machine materials due to the high brittleness, high hardness and anisotropy. Huang et al. carried out the nano scratch tests and found the obvious brittle damage on the surface of the MgF_2 single crystal [1]. Min et al. determined that the ductile-to-brittle depth of MgF_2 single crystal was affected by the crystal orientations [2]. Liu et al. developed an innovative ultrasonic-assisted cutting technology to manufacture the MgF_2 single crystal and obtained the MgF_2 components with high efficacy and high quality. Although numerous researchers have analyzed the mechanical properties and developed the manufacturing technologies, fewer studies focus on revealing the anisotropy of deformation behaviors of the MgF_2. Revealing the anisotropy of deformation behaviors of the MgF_2 can determine the optimal crystal orientation of manufacturing, however, the anisotropy of deformation behaviors mechanism for MgF_2 single crystal is unclear.

The nanoindentation tests can be used to analyze the deformation behaviors. Li et al. conduced the nanoindentation tests and obtained the hardness, elastic modulus, fracture toughness and maximum elastic recovery rate of YAG crystal [4]. According to nanoindentation tests of the Si single crystal, the significant amorphous and nano-crystalline damage in the subsurface region were observed by Yan et al [5]. Zhang et al. conduced the nanoindentation tests to analyze the deformation behaviors of KDP crystal and found that the creep was induced by the dislocation motion [6]. For the single crystal, the cleavage factor is used to estimate the degree of the cleavage fracture. High cleavage factor is more prone to generate the cleavage fracture. Therefore, plenty of studies determined that cleavage

factor is related with the anisotropy of the deformation behaviors. Mizumoto et al. carried out the orthogonal cutting experiments of CaF_2 single crystal and determined that the variation of critical cutting depth is consisted with the variation of cleavage factor [7]. Kwon et al. conduced the scratch experiments of sapphire and analyzed the anisotropy of crack initiation by the cleavage factor [8]. Mizumoto et al. discussed the anisotropic ductility of monocrystalline sapphire by the cleavage factor [9]. Although, numerous researches have discussed and analyzed the cleavage factor, fewer studies deeply introduce the cleavage factor into the anisotropy of deformation behaviors.

This study focuses on the revealing the anisotropy mechanism of deformation behaviors of MgF_2 single crystal by cleavage factor. In this work, the nanoindentation tests were carried out on (001) crystal plane, (010) crystal plane and (110) crystal plane to obtain the displacement-load curves and calculate the hardness. Besides, the surface morphologies of nanoindentation tests on (001) crystal plane, (010) crystal plane and (110) crystal plane are measured by the SEM (Scanning Electron Microscope) to analyzed deformation behaviors, and the cleavage factor under different experimental conditions were calculated to analyze and illustrate the anisotropy of the deformation behaviors. This paper reveals the anisotropy mechanism of the deformation behaviors of MgF_2 single crystal, which can provide the theory to suppress the brittle damage and improve the manufacturing efficacy.

2. Experimental methods and simulation models

2.1. Materials and methods

The displacement-load curve can be used to analyze the deformation behaviors. In order to analyze the anisotropy of the deformation behaviors of MgF_2 single crystal, the nanoindentation tests were carried out on the (001) crystal

plane, (010) crystal plane and (110) crystal plane to obtain the displacement-load curves. As shown in the Figure. 1, the Berkovich indenter was used to obtain the displacement-load curves under different displacement depth. The dimensions of the workpiece were 10×5×2 mm.
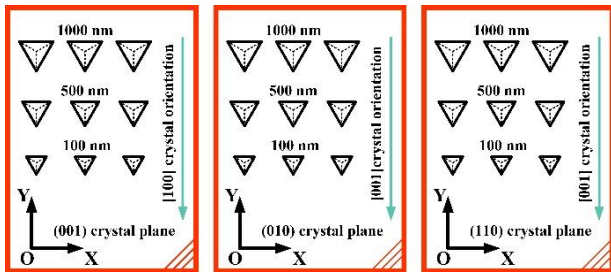
Figure 1. Schematic diagram of the nanoindentation tests on the different crystal planes

The damage of the workpiece surface has a significant effect on the deformation behaviors. Therefore, the chemical-mechanical polishing technology was used to obtain the workpieces with damage-free surface. The quasi-static mode can be used to get the hardness during the nanoindentation tests. The detailed experimental conditions of the nanoindentation tests were listed in Table 1. Each test was repeated three times to confirm the accuracy of the experimental results. Indentation morphologies were observed by the Scanning Electron Microscope (SEM, SUPRA55 SAPPHIRE, Germany).

Table 1 Experimental conditions.

No.	Crystal plane	The maximum Indentation displacement h
1-3	(001)	100 nm, 500 nm, 1000 nm
4-6	(010)	100 nm, 500 nm, 1000 nm
7-9	(110)	100 nm, 500 nm, 1000 nm

2.2. The calculation of Hardness and cleavage factors

Hardness is the key mechanical parameter which can reflect the characteristic of the resistance to the deformation. Therefore, the hardness can be used to analyze the anisotropy of the deformation behaviors. The hardness $H=P_m/A_s$, where P_m is the maximum load during the nanoindentation test, and A_s is the contact area between the indenter and workpiece under the P_m. The Berkovich indenter shapes as the triangular pyramid. The angle between the perpendicular line and the edge line is 77.05° and the angle between the perpendicular line and the pyramid plane is 65.3°. According to the geometry of the Berkovich indenter, the $A_s=3\sqrt{3}(h\tan65.3°)/2$。cleavage factor can be used to represent the degree of the slip motion and cleavage fracture. As shown in the Figure 2, during deformation behaviors of MgF_2 single crystal, the cleavage fracture was induced by the tensile stress σ_k which along the cleavage plane. The higher the cleavage factor is, the more easily the cleavage fracture occur. The cleavage factor $m=\cos^2\alpha$，Where α is the angle between the cleavage plane and the force P.
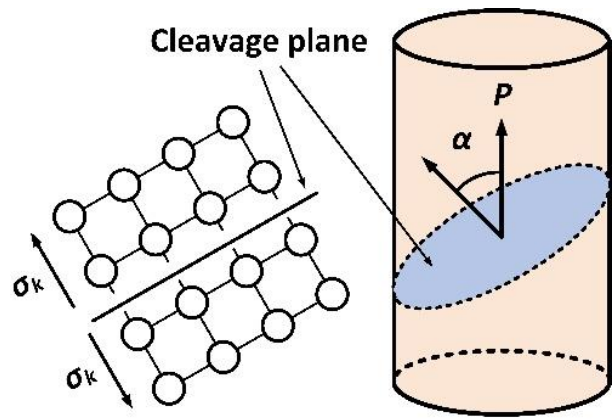
Figure 2. The cleavage fracture

3. Results and disucssions

3.1. Deformation behaviors of MgF₂ single crystal

The hardness curves of (001) crystal plane, (010) crystal plane and (110) crystal plane are shown in Figure 3. Due to the size effect, the hardness H increases initially and then decrease with the depth of indentation h increasing. When depth of indentation h higher than 600 nm, the hardness value turns to be stable. It is clear that the hardness of (001) crystal plane is lowest and the hardness of (110) crystal plane is highest, which indicates that the plastic deformation is most prone to occur on (001) crystal plane and brittle fracture most easily generates on (110) crystal plane.
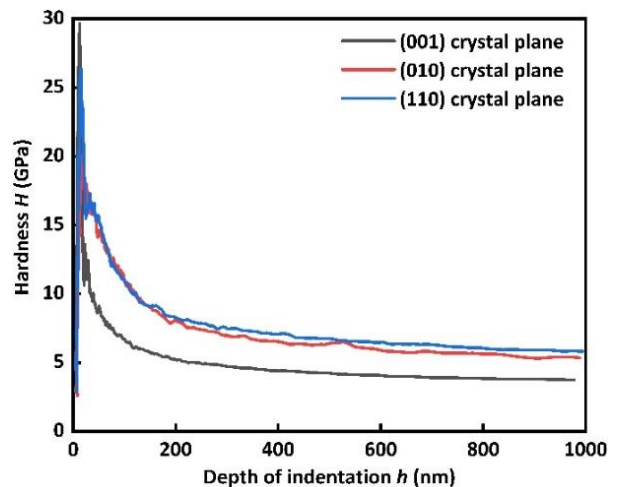
Figure 3. Hardness curves of (001) crystal plane, (010) crystal plane and (110) crystal plane.

The displacement-load curves are shown in the Figure 4. Under the same depth of indentation h, the load values of (001) crystal plane, (010) crystal plane and (110) crystal plane are significantly different. the maximum loads of (001) crystal plane, (010) crystal plane and (110) crystal plane are approximately 79.1 mN, 102.1 mN and 112.5 mN, respectively. Compared with the max loads under the same displacement depths, the loads of (001) crystal plane is lowest. Besides, according to the Figure 4 (d)-(f), the "pop-in" which is symbol of the elastic-to-plastic transformation can be observed. However, the depths of "pop-in" occurrence for (001) crystal plane, (010) crystal plane and (110) crystal plane are approximately 14.5 nm, 39.4 nm and 72.8 nm, respectively. Compared with the loads of the "pop-in" occurrence, the loads of (001) crystal plane is lowest. lower the depth of "pop-in" and the loads under the same depth are, the more easily the plastic deformation occur.

The results of the hardness, the load values of the first occurrence of 'pop-in' and max loads of the indentation displacement under the same depth of the displacement can reflect the plastic deformation behaviors. The lower the hardness, the load value of the first occurrence of 'pop-in' and the load under the same indentation displacement are, the more the plastic deformation is prone to generate. Therefore, the plastic deformation is most prone to occur on (001) crystal plane and least prone to occur on (110) crystal plane for MgF$_2$ single crystal.
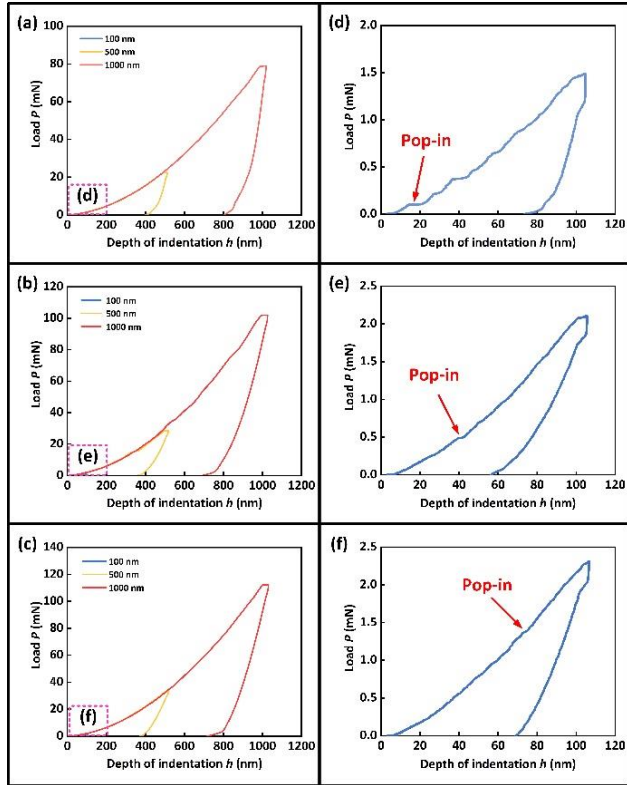
Figure 4. The displacement-load curves of (a) (001) crystal plane, (b) (010) crystal plane and (c) (110) crystal plane. The enlarge displacement-load curves of (d) (001) crystal plane, (e) (010) crystal plane and (f) (110) crystal plane when h=100 nm.

3.2. Cleavage factor of different crystal planes

The surface morphologies of (001) crystal plane, (010) crystal plane and (110) crystal plane are shown in the Figure 5. For (001) crystal plane, there are not distinct cracks, which indicates that the plastic derformation play the domain role during the nanoindentation tests. For (010) crystal plane, the cracks are generated when the max depth is 500 nm. With the depths increasing, the cracks propagate. However, the cracks only appear on the one side. For (110) crystal plane, the cracks are generated when the max depth is 500 nm like (010) crystal plane. And the crack appears on the three areas of the surface. Compare with the SEM image of surface morphologies, the cracks of the (110) crystal plane is most severe, and the plastic deformation in most prone to generate on (001) crystal plane.
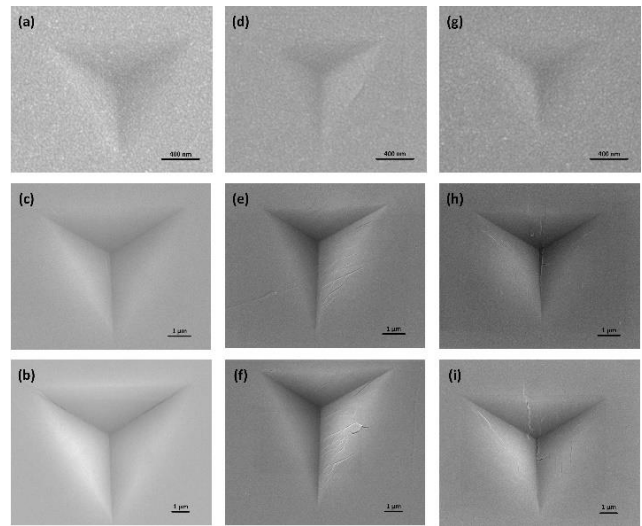
Figure 5. (a), (b) and (c) are the SEM image of surface morphologies on (001) crystal plane under 100 nm, 500 nm and 1000 nm. (d), (e) and (f) are the SEM image of surface morphologies on (010) crystal plane under 100 nm, 500 nm and 1000 nm. (g),(h) and (i) are the SEM image of surface morphologies on (110) crystal plane under 100 nm, 500 nm and 1000 nm.

The higher cleavage factor is, the more cleavage fracture prone to occur. For MgF$_2$ single crystal, the cleavage plane are (110) crystal plane and ($1\bar{1}0$) crystal plane [10]. During the nanoindentation tests, only the normal force work on the workpiece. Based on the space and geometric conditions, the cleavage factors under different experimental conditions are calculated and listed in the Table 2. For (001) crystal plane, the cleavage factors of (110) cleavage plane and ($1\bar{1}0$) cleavage plane are 0, which indicates the cleavage fracture is hard to generate on the (001) crystal plane during the nanoindentation. However, the cleavage factors of (110) cleavage plane and ($1\bar{1}0$) cleavage plane are 0.5 for (010) crystal plane, which means the degree of the cleavage fracture for (110) cleavage plane and ($1\bar{1}0$) cleavage plane is same on (010) crystal plane. Besides, for (110) crystal plane, the cleavage factors of (110) cleavage plane is 1, but the cleavage factors of ($1\bar{1}0$) cleavage plane is 0, which indicates the cleavage fracture of (110) cleavage plane is mainly activated. Compared with the results of the three crystal planes, the cleavage factors for (110) crystal plane are maximum and the cleavage factor for (001) crystal plane is minimum, indicating the (001) crystal plane is most prone to occur the plastic generation, and the cleavage fracture is easiest to generate on (110) crystal plane, which consists with the experimental results. Therefore, the hardness of the (110) crystal plane is highest and the hardness of the (001) crystal plane is lowest. The plastic deformation is most prone to occur on (001) crystal plane, and the cleavage fracture is easiest to generate on (110) crystal plane.

Table 2 The cleavage factor of different crystal plane.

Crystal plane	Cleavage factor of (110) cleavage plane	Cleavage factor of ($1\bar{1}0$) cleavage plane
(001)	0	0
(010)	0.5	0.5
(110)	1	0

4. Conclusion

In this work, the nanoindentation tests of MgF$_2$ single crystal were systematically carried out on different crystal planes. The hardness, displacement-load curves, the SEM images of the surface morphologies and cleavage factors under different experimental conditions were obtained to analyze the anisotropy of the deformation behaviors of MgF$_2$ single crystal. According to the experiment results, the plastic deformation is most prone to occur on (001) crystal plane, and the cleavage fracture is easiest to generate on (110) crystal plane. In addition, the cleavage factors were calculated to analyze the anisotropy of the deformation behaviors. The cleavage factors of (001) crystal plane is 0. However, the maximum cleavage factor is calculated on (110) crystal plane. It is obvious that the activation degree of cleavage fracture is highest for (110) crystal plane and lowest for (001) crystal plane. The cleavage fracture is hard to occur on (001) crystal plane and easy to generate on (110) crystal plane. Therefore, the plastic deformation is easiest to occur on (001) crystal plane.

References

[1] Huang W, Yu D, Zhang M, Cao Q and Yao J. 2018 *Int. J. of Adv Manuf. Tech.* **98** 781-790

[2] Min S, Dornfeld D, Inasaki I, Ohmori H, Lee D, Deichmueller M, Yasuda T and Niwa K. 2006 *CIRP Ann-Manuf. Techn.* **55** 103-106.

[3] Liu X, Yu D, Chen D, Yang S, Wen Y and Xiao Y. 2021 *Precis. Eng.* **72** 370-381

[4] Li C, Zhang Q, Zhang Y, Zhang F, Wang X and Dong G. 2020 *Ceram. Int.* **46** 3382-3393

[5] Yan J, Takahashi H, Gai X, Harada H, Tamaki J I and Kuriyagawa T. 2006 *Mat. Sci. Eng. A-Struct.* **423** 19-23

[6] Zhang Y, Hou N, and Zhang L C. 2018 *Adv. in Manuf*. **6** 376-383

[7] Mizumoto Y and Kakinuma. 2018 *Precis. Eng.* **53** 9-16

[8] Kwon S B, Nagaraj A, Yoon H S and Min S. 2020 *Nanotechnology and Precision Engineering* **3** 141-155

[9] Mizumoto Y, Maas P, Kakinuma Y and Min S. 2017 *CIRP Annals*, **66** 89-92

[10] Fujii S, Hayama Y, Imamura K, Kumazaki H, Kakinuma Y and Tanabe T. 2020 *Optica*. **7** 694-701.

New shape profiling polishing method for diffuser microstructured surface

Pengfei Zhang[1], Zhao Jing[1], Linguang Li[1], Saurav Goel[2], Jiang Guo[1]*

[1]*State Key Laboratory of High-performance Precision Manufacturing, Dalian University of Technology, Dalian, 116024, China*
[2]*School of Engineering, London South Bank University, London, SE10AA, UK*

guojiang@dlut.edu.cn

Abstract

Diffusers are integral components in projection, lighting, and imaging systems, prized for their superior beam diffusion capabilities. Polishing is a critical process for enhancing the performance of diffusers by removing tool marks on the mold surface. However, traditional polishing methods often struggle to improve surface quality without compromising shape accuracy. Addressing this challenge, this study introduces a novel non-contact shape profiling polishing method utilizing non-Newtonian fluids, designed for ultra-precision processing of array microstructured surface molds. Our findings demonstrate that this innovative polishing method significantly enhances diffuser performance, achieving remarkable improvements in mold precision. Notably, after the application of this polishing method, the surface roughness of the diffuser mold sees a remarkable reduction from an initial roughness average Ra of 164.2 nm to a mere 8.1 nm, concurrently preserving shape accuracy to an exceptional degree of less than 0.8 μm.

Keywords: Microstructud surface; Diffusers mold; Shape profiling polishing; Tool mark removal; Shape accuracy

1. Introduction

Diffusers play an important role in optical lighting, projection, and imaging systems [1], mainly used for diffusing and unifying point laser sources, improving the brightness, color, and light source uniformity of projection and LCD backlight module systems [2].

In order to meet the requirements of mass production of diffusers, injection molding technology is generally used for manufacturing. As the core component in the injection molding process, the shape accuracy and surface quality of the mold have a crucial impact on the optical performance of the diffusers. At present, high-quality diffusers molds mainly rely on single point diamond turning technology (SPDT)for manufacturing. Guo et al. used SPDT technology to prepare V-shaped groove microstructure surfaces. [3]. However, due to cutting, it is inevitable to produce defects such as tool marks and burrs on the surface of the mold, which seriously affects the performance of the replicated optical components.

Polishing is the main way to improve the surface quality after machining. However, existing polishing methods for micro structured surfaces have certain limitations. The contact polishing method is prone to poor surface quality of the workpiece due to direct contact between the tool and the workpiece [4]. Jet or magnetic field assisted polishing methods are affected by the fluid flow state, which can lead to poor shape accuracy and ultimately affect the performance of the terminal components [5,6]. Non-contact polishing methods leveraging shear thickening principles have gained prominence for their process flexibility, ease of setup, and cost efficiency. Li et al. [7] achieved Ultra-precision polishing using a weak chemical shear thickening polishing (STP) process. Additionally, Zhang et al. [8] established a damping tool specifically for polishing aspherical surfaces that achieved very low surface roughness on nickel-phosphorus (NiP) alloy surfaces. Leveraging non-Newtonian fluids' flexibility enhances polishing of microstructured surfaces, necessitating approaches for sub-10 nm roughness and shape accuracy due to unique geometric characteristics.

To address the issues of suboptimal surface quality and inaccuracies in the shape of polished array microstructured surface, this research presents a solution through the implementation of a non-contact profiling polishing technique, specifically tailored for the conformal polishing of diffuser molds. The efficacy and superior performance of this innovative processing method were validated via a series of meticulous polishing tests, underscoring its capability to enhance the quality and precision of microstructured surfaces significantly.

2. Method and principle

This study utilizes the shear thickening effect of non Newtonian fluid polishing solution to shear remove the surface material of the mold by forming particle clusters wrapped in abrasive particles, achieving the polishing effect (Figure 1). In order to achieve uniform polishing of the mold surface, a contour polishing tool is prepared using the principle of film replication. The base of the profiling tool is cylindrical in shape, with a diameter of 30 mm. The height of the profiling part of the tool is 380 μm. In order to enhance the shear thickening effect of the polishing solution, the damping polishing pad is adhered to the surface of the non-contact profiling tool.
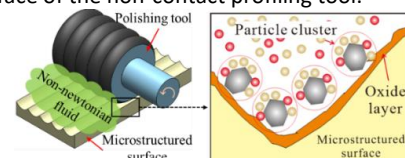
Figure 1. Diagram of the non-contact shape profiling polishing method

3. Experimental details

3.1 Workpiece

In this study, the microstructurd surface mold samples used for polishing were obtained through the previous ultra precision milling process, and the mold material was nickel phosphorus alloy. The mold is 15 mm long and 16.9 mm wide, with 13 grooves arranged on the surface. As depicted in Figure 2, the initial state of the mold sample, which was utilized in the

polishing test, is presented. Figure 2(a) shows the mold obtained by ultra precision milling, and Figure 2(b) shows the measured geometric dimension of the mold.
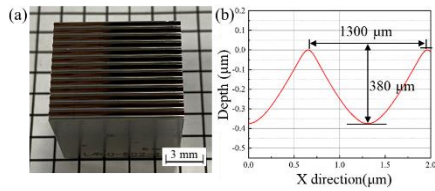
Figure 2. The diffuser mold (a) sample and (b) geometric dimension

3.2 Experimental setup

The polishing experiment is carried out on a custom-developed 5-degree-of-freedom precision machining platform, as illustrated in Fig. 3. During polishing, the tool axis is aligned parallel to the workpiece surface, then adjusted to maintain a 0.2 mm gap above the workpiece for the profiling procedure. The tool position can be adjusted by setting the profile damping tool to the same 0.2 mm gap above the workpiece. The slurry utilized for this experiment is a mixture of non-Newtonian fluid and silica sol. Specifically, the non-Newtonian slurry is composed of a polyhydroxyl polymer and deionized water, with SiO_2 abrasive particles having a size of 50 nm and a concentration of 10% by weight.
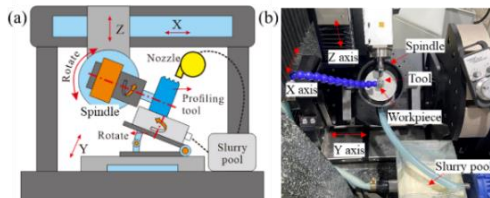
Figure 3. Experimental setup (a) diagram and (b) practical device

Figure 4 shows the prepared profiling damping tool. The tool consists of a tool base, a duplicated film and a damping pad. The duplicated film is made by replicating the contour of the workpiece surface, and the damping pad is to better drive the polishing fluid.
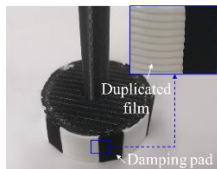
Figure 4. The profiling damping tool developed for polishing experiments

4. Results and discussion

4.1 Surface defects

Figure 5 shows the surface morphology results of the array microstructure mold before and after polishing. Figure 5(a) and (b) respectively show the surface morphology of the workpiece before and after polishing. It can be seen from the images that there are more defects such as spiral tool marks and burrs on the surface of the mold before polishing, and most of defects on the surface after polishing are eliminated.
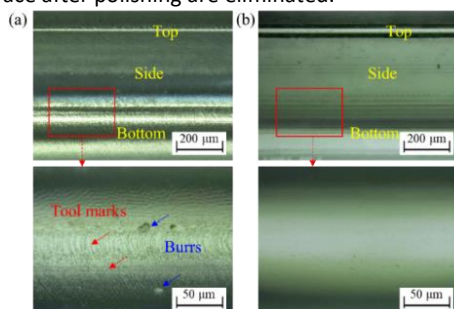
Figure 5. Comparison of the surface defects (a) before and (b) after polishing

4.2 Surface roughness

Figure 6 shows the results of diffuser mold surface roughness before and after polishing. It can be seen from Figure 6 that the surface roughness before polishing is 164.2 nm Ra, and the surface roughness converges to 8.1 nm Ra after polishing for 1 h. The rough peak of the mold surface is effectively eliminated after polishing, and the surface becomes smooth.
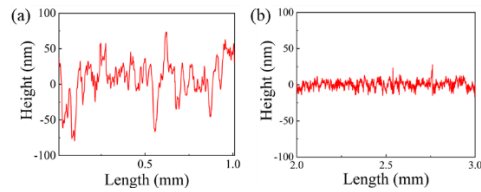
Figure 6. The rough peaks distribution (b) before and (c) after polishing

4.3 Shape accuracy

Figure 7 provides an analysis of the diffuser mold's shape change before and after polishing. The figure reveals that the most significant material removal occurred at the top of the mold groove, with minimal material removal at the bottom. The experimental results indicate the shape change is 0.8 μm.
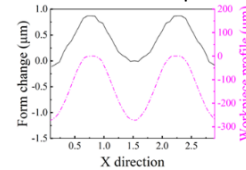
Figure 7. Surface shape change of diffuser after polishing

5. Conclusions

In this study, we present a non-contact profiling polishing method that utilizes non-Newtonian fluid, achieving conformal polishing of the diffuser mold. The key findings can be summarized as follows:

1. The polishing process successfully eliminates tool marks and burrs from the diffuser mold, thereby rendering the surface of the mold significantly smoother.

2. The surface roughness significantly decreases from an initial value of Ra 164.2 nm to 8.1 nm, effectively eliminating the rough peaks on the mold.

3. The geometry and depth of the mold features are preserved with high fidelity, with the form error resulting from the polishing process maintained below 1 μm.

Reference

[1] Zhang W, Liang C Z, Li J, et al. Design of Optical Elements for Beam Shaping and Uniform Illumination in Laser Digital Projection Display System. Acta Optica Sinica, 2015, **35**(08): 44-9.

[2] Chen E, Xie H, Huang J, et al. Flexible/curved backlight module with quantum-dots microstructure array for liquid crystal displays. Optics Express, 2018, **26**(3): 3466-82.

[3] Guo, J, Zhang, J, Wang, H, et al. Surface quality characterisation of diamond cut V-groove structures made of rapidly solidified aluminium RSA-905. Precision Engineering, 2018, **53**: 120-133.

[4] Brinksmeier E, Riemer O, Stern R. Machining of precision parts and microstructures. Initiatives of Precision Engineering at the Beginning of a Millennium. Springer, 2002, 3-11.

[5] Wang C, Zhang Z, Cheung C F, et al. Maskless fluid jet polishing of optical structured surfaces. Precision Engineering, 2022, 73(270-83).

[6] Guo J, Kum C W, Au K H, et al. New vibration-assisted magnetic abrasive polishing (VAMAP) method for microstructured surface finishing. Optics Express, 2016, **24**(12): 13542-54.

[7] Li M, Song F Z, Huang Z R. Control strategy of machining efficiency and accuracy in weak-chemical-coordinated-thickening polishing (WCCTP) process on spherical curved 9Cr18 components. Journal Of Manufacturing Processes, 2022, **74**: 266-282.

[8] Zhang P F, Li L G, Yang Z, et al. Achieving sub-nanometer roughness on aspheric optical mold by non-contact polishing using damping-clothed tool. Optics Express, 2022; **30**: 28190-28206.

Session 4: Mechanical Manufacturing Processes

Real-time motion error compensation in optical surface fabrication using a 2-DOF linear encoder

Yan Wei[1,3], Shinya Morita[1,3], Masahiko Fukuta[2], Toru Suzuki[2], Takanobu Akiyama[2], Yutaka Yamagata[3], Takuya Hosobata[3]

[1]*Department of Advanced Machinery Engineering, Graduate School of Engineering, Tokyo Denki University, Japan*
[2]*Machine Tools Company, Shibaura Machine Corp., Japan*
[3]*RIKEN Center for Advanced Photonics, RIKEN, Japan*

yan.wei@riken.jp

Abstract

Recent optical components and molds for high-grade camera lenses, x-ray and neutron optics with aspherical or free-form surfaces demand form accuracy of a few nanometers. Optical performances of such high-grade optics are often compromised by surface waviness with short spatial period that introduces significant slope errors. Traditional polishing techniques prove ineffective for mitigating these errors, especially when the waviness have spatial frequencies ranging from 0.1 mm^{-1} to several mm^{-1}. These deviations are largely attributed to motion inconsistencies such as minute waviness in stage motion straightness and rotational motion errors. To address this issue, we introduce a novel position detection and compensation method implemented on an ultra-precision machine tool equipped with dual 2-DOF (degrees of freedom) linear encoders. The uniquely designed encoder, resembling a fish-bone pattern, is crucial for capturing positional changes in two orthogonal directions on a horizontal plane. By introducing the 2-DOF linear encoders, in-plane positioning errors can be compensated in a straightforward manner. To validate the efficacy of our approach in reducing minute waviness and slope errors, a machining experiment was conducted by single crystal diamond turning of a spherical surface of 200 mm in radius made of electroless nickel phosphate plating on aluminum substrate. The result shows about 49% reduction of minute waviness and slope errors by compensation.

Keywords: Compensation, Diamond Turning, Ultraprecision Machining, Optics manufacturing

1. Introduction

With a rising demand for ultraprecision optical elements, addressing micro waviness on optical surfaces is a key challenge. These waviness patterns, typically spanning 0.1 mm to several millimeters in wavelength, significantly degrade optical performance. Traditional polishing methods struggle to efficiently remove this waviness [1], often attributed to machine tool motion errors during the optical surface machining process, caused by machine-related issues, which significantly impact form accuracy [2].

To tackle this challenge, Shibaura Machine Corp. has developed an innovative compensation system for an ultra-precision machine tool. This system employs a novel 2-DOF linear encoder to detect straightness errors [3]. In this paper, we introduce this system and present the results of a diamond turning experiment conducted on two identical optical surfaces. Our aim is to evaluate the extent to which this system improves the mitigation of waviness resulting from machine tool motion errors.

2. Compensation System with 2-DOF Encoder

2.1. Features of 2-DOF Encoder

Machine tool motions are tracked by encoders. Standard 1-DOF linear encoders, as seen on the X-axis in **Figure 1**, detect forward shifts but not lateral ones. Lateral shifts are often due to guide rail waviness, affecting workpiece accuracy.

For simultaneous X and Y detection, a 2-DOF linear encoder is essential. Traditionally, it uses two scales on X and Y axes, but precise straightness on a long Y-scale is challenging and affects accuracy.

To solve this, we've developed a fish-bone 2-DOF linear encoder, detecting X and Y motions using a short scale tilted ±45°. Position shifts are calculated with these equations:

$$\text{(1)}$$
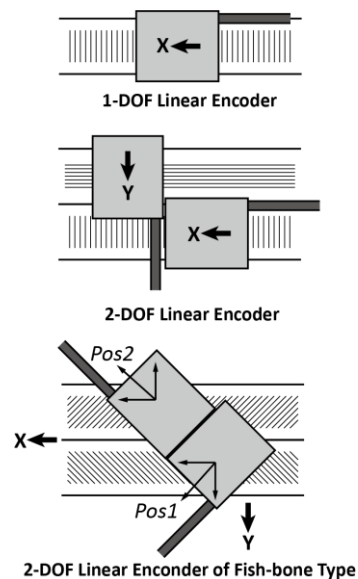
Figure 1. Linear Encoder with Multi Degrees of Freedom.
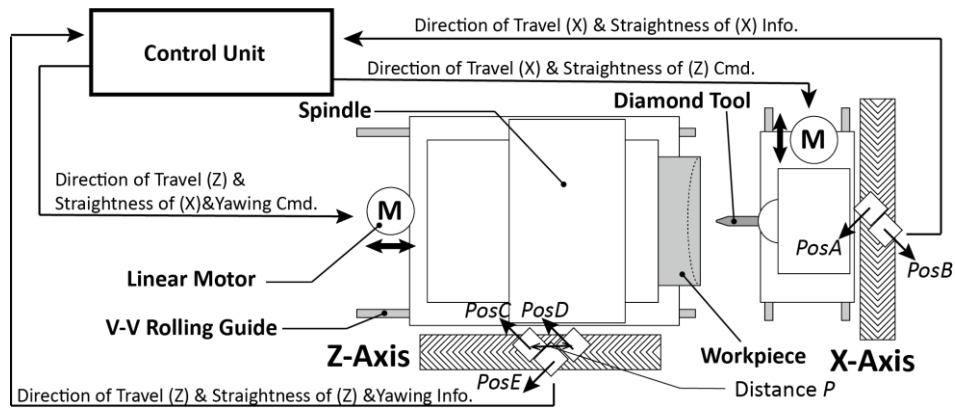
Figure 2. Configuration of Compensation System featured with 2-DOF Linear Encoders.

$$X = \frac{\sqrt{2}}{2}(Pos1 + Pos2)$$

$$Y = \frac{\sqrt{2}}{2}(Pos1 - Pos2) \tag{2}$$

By applying the fish-bone type of 2-DOF encoders to the machining axis, we can capture orthogonal position shifts on the guide way. This makes it easier to compensate for motion errors in real-time, leading to improved machining precision.

2.2. Configuration of Compensation System

The machine system configuration equipped with 2-DOF encoders is depicted in **Figure 2**. In this system, the X-axis represents the feed axis of the machine tool, while the Z-axis represents the cutting axis on the spindle. The X-axis is equipped with a 2-DOF linear encoder to detect the straightness error of the motion in the X-direction. Meanwhile, the Z-axis is equipped with three detection unit to measure not only the straightness error but yawing motion error. The yawing angle θ can be calculated using Equation (3).

$$\theta = \frac{\sqrt{2}}{2}\left(\frac{PosD - PosC}{P}\right) \tag{3}$$

By providing feedback regarding the position shifts of both the X and Z axes to each other, most of motion errors on horizontal plane can be corrected. This system was integrated into the ultraprecision lathe turning machine tool (ULC-100F(S); Shibaura Machine Corp.), which is equipped with V-V roller guides driven linear motors and pneumatic spindle with porous restrictor.

3. Turning of Optical Surfaces with Real-time Compensation

3.1. Diamond Turning of Optical Spherical Surfaces

We conducted a diamond turning experiment to assess the effectiveness of the compensation method using 2-DOF encoders on workpiece accuracy. Two identical workpieces were prepared, consisting of Al-Mg alloy substrates plated with Ni-P. These workpieces had 100 mm diameter optical surfaces, which were shaped into spheres with a 200 mm curvature radius using a diamond tool with a 1.0 mm cutting edge radius. The surfaces were then machined to achieve a theoretical roughness of 0.125 nm (P-V) by running the spindle at 1000 min^{-1} and feeding at 1 mm/min. During this process, one surface incorporated the compensation system, while the other did not.

3.2. Evaluation of Optical Spherical Surfaces

To assess the form accuracy of the optical surfaces we fabricated, we employed a laser interferometer (Verifire QPZ; Zygo Corp.) to measure the slope error of the waviness present on the surfaces. We removed profile errors of long wavelengths by subtracting profile fit data consists of quartic plane curve, then waviness errors along diameter direction is integrated through 180 degree by step of 5 degrees and average was
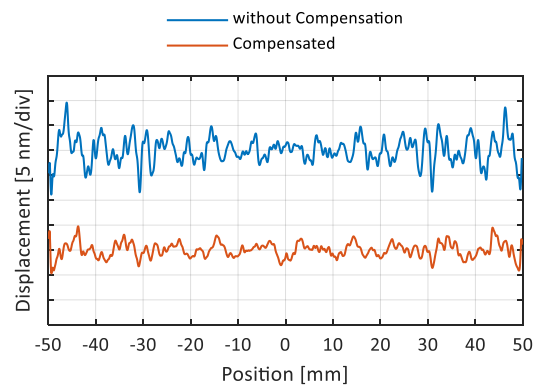
Figure 3. Form Displacement of Diamond Turned Optical Surfaces.

calculated. In addition, wavelengths above 10 mm were filtered out to enhance the distinction of waviness. As shown in **Figure 3**, a noticeable distinction in waviness was evident along the line segment stretching from the sphere's center to its periphery when comparing the compensated and non-compensated surfaces. The amplitude of waviness on the compensated surface was approximately ±4.7 nm p-v (peak-to-valley), while the non-compensated surface exhibited an amplitude of around ±9.2 nm p-v, representing a reduction about 49%. Furthermore, the slope error for each optical surface measured 7.88 μrad p-v with compensation and 12.50 μrad p-v without compensation, representing a substantial 43.3% reduction. This significant decrease in slope error underscores the effectiveness of the compensation system in mitigating waviness on the optical surface.

5. Summary

A novel compensation system for the ultra-precision lathe turning machine equipped with 2-DOF linear encoders is introduced and a diamond turning experiment was conducted. Two sphere optical surfaces were fabricated while one with compensation and the other without. Results showed a significant improvement in reduction of waviness and slope errors, which indicates the accessibility of this new compensation system.

References

[1] Hosobata T, Yamada N L, Hino M, Yoshinaga H, Nemoto F, Hori K, Kawai T, Yamagata Y, Takeda M and Morita S 2019 *Opt. Express* **27** 26807-20
[2] Duan H, Morita S, Hosobata T, Takeda M and Yamagata Y 2021 *J. Adv. Mech. Des. Syst. Manuf* **15** 4
[3] Suzuki T, Fukuta M 2023 *Proc. JSPE Conf.* **2023A** 219 (In Japanese)

Precision plunge grinding with coarse-grained diamond grinding wheel

Barnabás Adam[1,2], Oltmann Riemer[1,2], Kai Rickens[1], Carsten Heinzel[1,2]

[1]Leibniz Institut für Werkstofforientierte Technologien IWT, Laboratory for Precision Machining LFM, Badgasteiner Straße 2, 28359 Bremen, Germany
[2]MAPEX Center for Materials and Processes, University of Bremen, Germany)

adam@iwt.uni-bremen.de

Abstract

Economic machining of brittle materials is enabled by ultra-precision grinding. A ductile material removal mechanism in precision grinding allows the generation of high surface qualities, low subsurface damage and tight tolerances.

For precision grinding of brittle materials, fine-grained grinding wheels are commonly used, as they reduce the maximum chip thickness and support ductile material removal. However, a disadvantage of fine-grained grinding wheels with soft bonds is their susceptiality to wear, which reduces efficiency and can lead to form errors. These disadvantages could be solved by coarse-grained grinding wheels with hard bonds. However, the application of coarse-grained grinding wheels is challenging due to the process design based on the critical and maximum chip thickness.

In this research, the applicability of a coarse-grained diamond grinding wheel with a grain size of D301 for ductile precision grinding of grooves in BK7 glass is investigated. For this purpose, the active grains on the circumference of the grinding wheel were identified and the expected material removal mechanism was calculated based on Malkin's maximum chip thickness equation. Cross grinding experiments with in-process force measurement were carried out to investigate the influence of feed rate and cutting speed on the material removal mechanism and surface generation. The evaluation of the prevailing material removal mechanism was assessed by surface texture and surface roughness, measured by white light interferometry.

Based on the results, it can be shown that ductile and ductile-brittle material removal occurs with the investigated grinding wheel. Feed rate and cutting speed have only limited influence on the material removal mechanism and the generated surface roughness. Furthermore, the force measurements show that not only individual grains are engaged during the grinding process, but rather clusters of grains.

Precision grinding, coarse-grained diamond grinding wheels, surface roughness, material removal mechanism

1. Introduction

Ultra-precision grinding enables the economical machining of optical and precision components made of brittle-hard materials. High surface qualities, low subsurface damage and tight tolerances can be achieved through ductile material removal [1, 2].

Fine-grained grinding wheels are generally used for precision grinding, as they reduce the maximum chip thickness and enable ductile material removal. However, fine-grained grinding wheels with soft bonds are susceptible to severe wear, which reduces the overall efficiency and productivity of the grinding process. Coarse-grained grinding wheels can be a solution to this problem, as they are less susceptible to wear due to their grain size and generally hard bond. However, the challenge when using coarse-grained grinding wheels is the process design based on the critical chip thickness [1,3].

In precision grinding of brittle-hard materials, the material removal mechanisms are crucial in generating the surface of the workpiece. According to Bifano, the material-dependent critical chip thickness $h_{cu,crit}$, as shown in (1), describes the maximum tolerable chip thickness, which in this context causes a ductile material removal mechanism and enables the machining of high surface qualities.

$$h_{cu,crit} = 0.15 * \left(\frac{E}{H}\right) * \left(\frac{K_c}{H}\right)^2 \qquad (1)$$

E describes the modulus of elasticity, H the hardness and K_c the fracture toughness of the material; the factor 0.15 is a constant determined experimentally by Bifano et al. [4].

Exceeding the critical chip thickness leads to the formation of cracks and chipping as well as damage to the subsurface [4]. When designing grinding processes, the decisive parameter for calculating the transition from ductile to brittle machining is the maximum chip thickness $h_{cu,max}$, which has to fall below the critical chip thickness $h_{cu,crit}$ in order to machine ductilely [5]. The calculation of $h_{cu,max}$ according to Malkin requires the determination of the active cutting edge number C_{kin} and the grain shape factor r, as shown in (2) according to [5]. Other influencing variables are the feed rate v_w, the cutting speed v_c, the depth of cut a_e and the grinding wheel diameter d_s.

$$h_{cu,max} = \left(\frac{4 \cdot v_w}{v_c \cdot C_{kin} \cdot r} \sqrt{\frac{a_e}{d_s}}\right)^{1/2} \qquad (2)$$

Based on Malkin's formula, the number of active cutting edges per surface and the grit size have an effect on the maximum chip thickness $h_{cu,max}$ and thus on the dominant material removal mechanism [5]. For this reason, fine-grained grinding wheels are generally used for precision grinding. They have a high grain density i.e. a high number of active cutting edges C_{kin} and small grain diameters which, according to (2), lead to a reduction in the maximum chip thickness and thus favour a ductile material removal mechanism. Furthermore, the stochastic distribution of the grains promote the applicability of the described calculation

formula. For example, with a high grain density, deviations of individual grains from the average grain form used in the formula are not significant. However, it is questionable whether this applies to coarse-grained diamond grinding wheels. Compared to fine-grained grinding wheels, coarse-grained grinding wheels have a low grain density and a stochastic distribution of the abrasive grains is only given to a limited extent. This has already been shown in earlier research work [6]. Based on the results shown in [6], a more detailed investigation of the application of a coarse-grained grinding wheel is to be carried out, focussing on the characteristics of the grinding wheel topography and detecting individual grain engagement in the force measurement. The aim is to gain a better understanding of the material removal mechanism.

2. Experimental setup, machining and analysing methods

In this research, plunge grinding experiments are carried out on BK7 glass with a coarse-grained diamond grinding wheel of grain size D301 with varying cutting speed v_c and feed rate v_w. The objective was to investigate to which extent ductile material removal can be realised with the coarse-grained diamond grinding wheel and whether individual grain impacts are recognisable in the force measurement in order to gain a better understanding of the process.

The grinding wheel applied is a galvanic bonded tool with blocky diamond grains, which was manufactured using reverse plating. According to the manufacturer, the envelope curve deviation is therefore less than 2 μm. The wheel has a radius of 40 mm and a spherical segment shape, which radius is also 40 mm.

To design the grinding experiments, the previously described formula for maximum chip thickness according to Malkin is applied. Therefore, it is necessary to determine grain density and active number of cutting edges respectively number of grains. This is carried out using a Keyence VHX-6000 digital microscope. The entire circumference of the grinding wheel is mapped. The area with a width of 2.2 mm of the grinding wheel that will later be in contact with the workpiece is then considered. This contact area was determined by the geometric contact conditions as well as previous work and is shown in Figure 1.
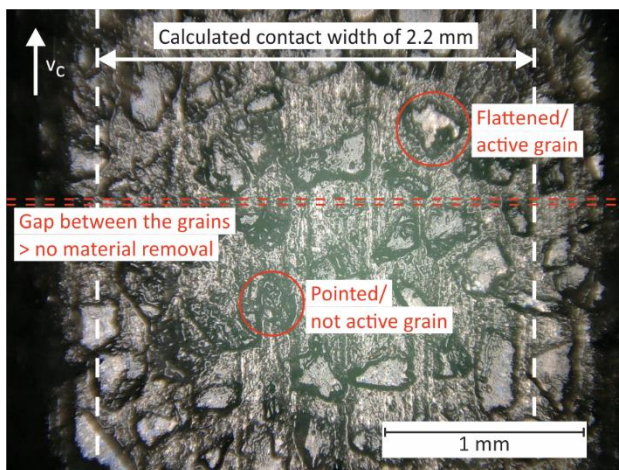
Figure 1. Exemplary digital microscopic measurement of the grinding wheel circumference with flattened and pointed grains

Within this area, the flattened grains are counted at four different positions in order to determine the grain density and the active grains. This is done under the assumption that flattened grains come into contact with the workpiece during

the experiments and remove material. Pointed grains are assumed to be lower and thus non-active grains as they have not been flattened by the manufacturer's dressing process and are therefore not expected to come into contact with the workpiece. Based on the grinding wheel circumference it was furthermore be determined that the grains are grouped in a way that they overlap in a tangential direction and several grains will be engaged. However, there are also gaps between these grain clusters. No active grains can be found here and it can be assumed that material removal is not to be expected here. There are a total of four of these gaps on the grinding wheel circumference.

A grain density of 10.75 grains/mm² is determined. With the process parameters shown in Table 1, this results in a maximum chip thickness of 11.35 nm to 26.7 nm, depending on the selected parameter variation. As the specimens have a tip tilt of less then 4 μm for clamping reasons and in order to ensure full tool engagement after touching procedure, several grinding steps are carried out. At a feed rate v_w = 10 mm/min, three grinding steps with a depth of cut a_e of 2 μm are carried out first, followed by a grinding step with a_e = 3 μm. The last grinding step represents the actual experiment. The parameters are also listed in Table 1. In the experiments with a feed rate v_w of 15 mm/min, the specimens could be aligned more precisely. Therefore, only two grinding steps with an a_e of 2 μm are carried out first and then the final grinding step with a_e = 3 μm. The last grinding step again represents the actual experiment. The individual parameter combinations are each carried out three times in order to obtain a sufficient number of experiments for the evaluation and to be able to identify outliers. The kinematics of the grinding experiments are shown in Figure 2.

Table 1 Process parameters

Machine: Cranfield Precision TTG 350 Twin Turret Generator	
Material: N-BK7 glass	
Process: Plunge grinding	
Parameters:	
v_w = 10 mm/min	v_w = 15 mm/min
v_c = 30 ; 60 m/s	v_c = 30 ; 60 m/s
$a_{e,\,cut\,1-3}$ = 2 μm	$a_{e,\,cut\,1-2}$ = 2 μm
$a_{e,\,cut\,4}$ = 3 μm	$a_{e,\,cut\,3}$ = 3 μm
$h_{cu,max}$ = 20.01 ; 11.35 nm	$h_{cu,max}$ = 26.7 ; 15.07 nm
Grinding fluid: Emulsion	
Tools: Coarse-grained diamond grinding wheel, D301 (reverse plated)	
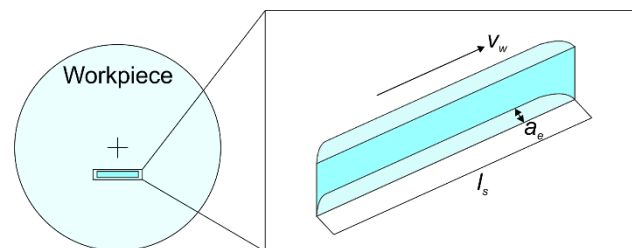
Figure 2. Kinematics of the plunge grinding experiments

Grinding experiments were performed on a Cranfield Precision TTG 350 Twin Turret Generator. The experimental setup is shown in Figure 3. A workpiece with a diameter of 50 mm and a thickness of 10 mm is mounted on a dynamometer type 9119AA1 from Kistler, which is clamped in the main spindle. The tool is located on the vertical grinding spindle. The process forces are measured at a measuring frequency of 50,000 Hz using inhouse software MesUSoft.
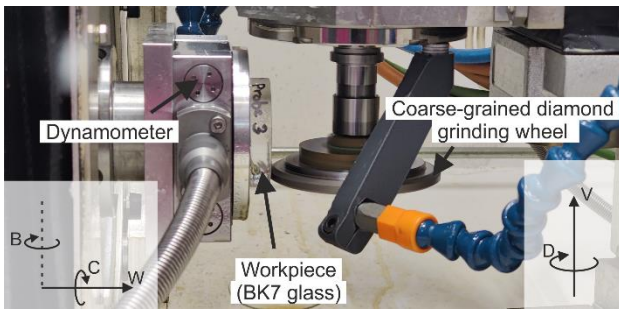
Figure 3. Experimental setup for plunge grinding experiments

The generated surface topography is measured using white light interferometry (WLI). A lens with 50x magnification and a measuring area of 0.34 mm x 0.34 mm is applied for topography characterisation. The generated depth of cut a_e is also measured using WLI. Here, a lens with 20x magnification and a measuring area of 0.84 mm x 0.84 mm as well as stitching is applied. Three measurements are carried out for each groove. The measurements are analysed using the commercial software Mountains 9.

3. Results and Discussion

As described in section 2, one machining step was omitted in the experimental sequence with v_w = 15 mm/min, as the specimens were already well aligned. The total depth of cut was determined to ensure that the depth of cut was achieved and that further evaluation of the experiments was reasonable. The depth of cut should be 9 µm at v_w = 10 mm/min and 7 µm at v_w = 15 mm/min. The results of the measurements are shown in Figure 4. The bars represent the mean value of all measurements and the error bars represent the minimum and maximum measured depth of cut. It can be seen that the intended depth of cut could be obtained with deviations. These deviations are shown by the error bars, which represent the maximum and minimum measured depth of cut of the grooves. The indicated deviation can be explained by two effects. Foremost, the specimens have a tip tilt due to the clamping technique, which can affect the actual depth of cut. Furthermore, a touching procedure is carried out before machining each groove to determine the surface of the samples. As this is done manually, there may also be slight deviations that affect the overall depth of cut. Except with the parameter combination with v_c = 30 m/s and v_w = 10 mm/min. However, the depth of cut of the final grinding step could also be realised in all experiments. It can therefore be assumed that the last grinding step of experiments were carried out with the intended set of parameters.
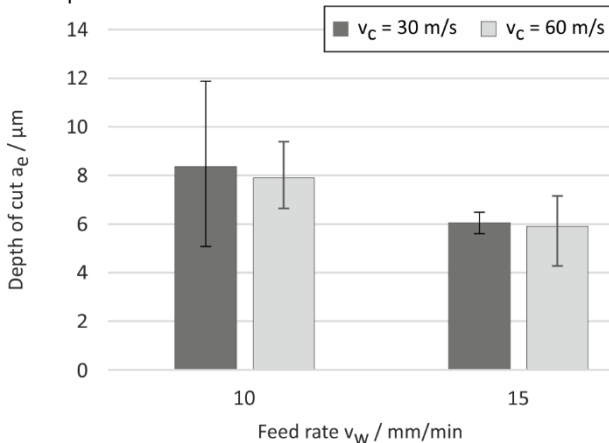
Figure 4. Generated depth of cut a_e

The generated surfaces are measured as described using WLI. The tip-tilt of the measurements is removed by alignment and a cut-off wavelength of 80 µm is used to separate waviness from roughness.

The mean arithmetic height of the generated surfaces and their deviation is shown in Figure 5. Roughness Sa between 55 nm and 88 nm generated. The lowest roughness Sa occured at v_w = 15 mm/min and v_c = 60 m/s. However, there is no recognisable significant influence of the feed rate and cutting speed on the generated surfaces. The measured surface roughness is similar and the areas of deviation partially overlap. This could be due to brittle breakout during machining, as shown in Figure 5. This is particularly noticeable at v_c = 60 m/s and v_w = 15 mm/min. Although the lowest mean arithmetic height Sa is measured here, the highest deviation is present once again.
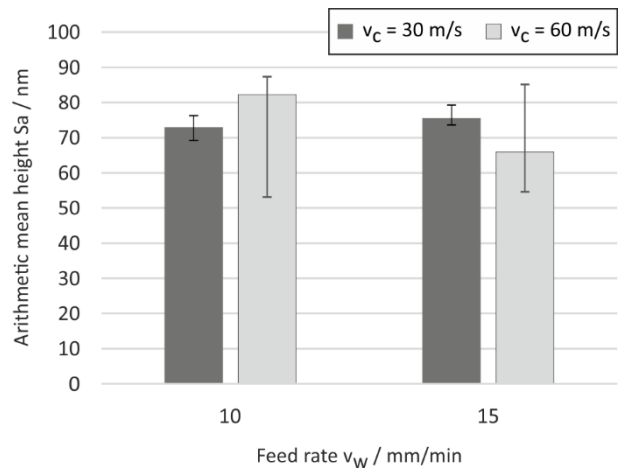
Figure 5. Measured arithmetic mean height Sa

Based on the qualitative analysis of the generated surfaces, which is shown exemplarily in Figure 6, it can be seen that the dominant material removal mechanism was ductile or ductile-brittle. There is only isolated brittle breakout visible. With a cutting speed v_c of 30 m/s, almost entirely ductile material removal was realised. At a cutting speed of 60 m/s, a ductile-brittle material removal mechanism occurs. There are large areas that indicate a ductile material removal and also smaller areas with brittle breakout and irregular surface morphology, which indicate a rather brittle material removal mechanism. This also explains the described deviation of the determined arithmetic mean height Sa.
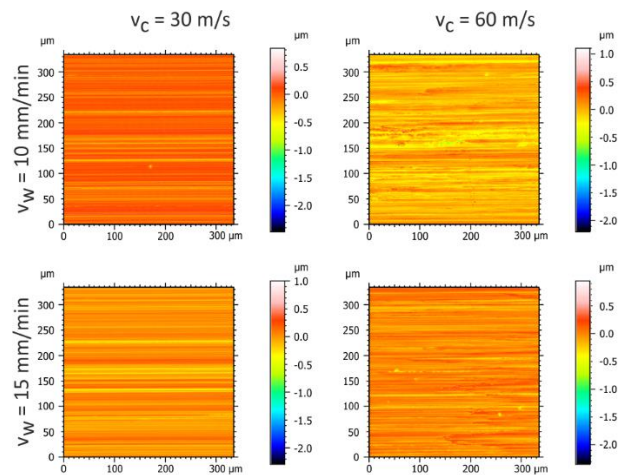
Figure 6. Qualitative comparison of the generated surfaces

Figure 7 shows the mean normal forces F_N that occurred during the experiments. The deviation is not shown in this figure, because dynamic effects with high deviations from the mean value occurred in some cases, which do not allow a reasonable representation. Figure 6 shows a clear influence of the cutting speed vc on the normal force F_N. With a higher cutting speed, significantly lower normal forces occur. This can be explained by the decrease in the maximum chip thickness, which is given by a higher cutting speed. The influence of feed rate, on the other hand, is marginal and does therefore not allow any clear conclusions to be drawn.
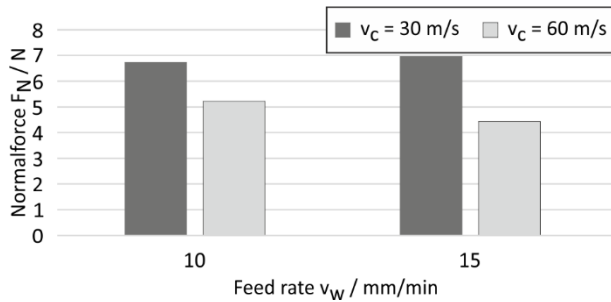
Figure 7. Mean normal force F_N of the grinding experiments

Figure 8 shows an example of the force measurement of four grinding wheel rotations in an experiment with a cutting speed v_c of 30 m/s and a feed rate v_w of 15 mm/min. It can be seen that the normal force is almost identical for all four grinding wheel rotations and it can therefore be assumed that the contact conditions remain the same. The figure shows furthermore the dynamic effects not previously shown in Figure 6, which in some cases lead to very high normal forces. This can be attributed to individual grains that protrude slightly further from the bond and therefore remove more material. It is also noticeable that the normal force F_N falls back to 0 N four times, which indicates an interrupted cut. The number of these interruptions corresponds with the number of gaps between the grain clusters of the grinding wheel, which were described in section 2. Furthermore, the individual high peaks indicate single-grain interactions, but these do not correspond to the number of single grains present in the grain clusters. Instead, several individual grains appear to overlap, so that only isolated single-grain interactions can be recognised.
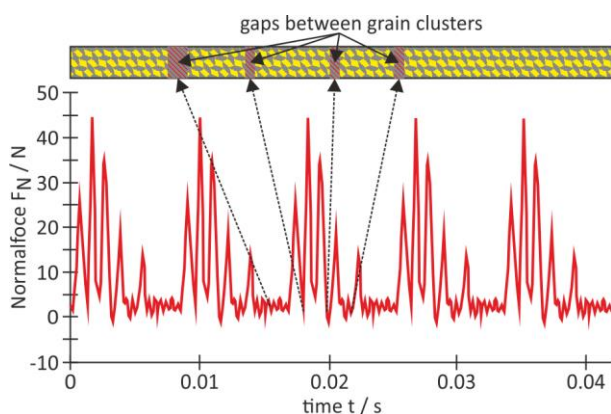
Figure 8. Force measurement of four grinding wheel rotations in an experiment with a cutting speed v_c of 30 m/s and a feed rate v_w of 15 mm/min

4. Summary and conclusions

With a coarse-grained diamond grinding wheel relatively low roughness below 100 nm can be generated in BK7 and mainly ductile and ductile-brittle material removal is present. However, the generated surface roughness is too high for ultra-precision applications and therefore further finishing process steps are required.

A significant influence of the cutting speed v_c and the feed rate on the generated surface roughness could not be determined.

When analysing the normal forces F_N, no detectable influence of the feed rate v_w on the forces and their characteristics could be determined either. However, an influence of the cutting speed v_c on the normal forces is detectable and manifests itself in decreasing normal forces with increasing cutting speed. This can be explained by the decreasing chip thickness with increasing cutting speed or rotational speed of the grinding wheel.

A more detailed examination of the force measurements and the normal forces occurring for each of four grinding wheel rotations shows that the force is almost identical for each rotation. Furthermore, there are points in the force curves where the normal force drops to 0 N. The number of these points coincides with the previously determined gaps between the grain clusters on the grinding wheel circumference. Furthermore, only isolated single grain interactions can be detected in the force, which do not correspond to the expected number of engagements. It is therefore assumed that several individual grain engagements are superimposed and that a single grain analysis is not sufficient to make further conclusions about the material removal mechanism. Rather, another approach must be found to assign the occurring forces to the material removal mechanism and the contact conditions between the grinding wheel and the workpiece.

5. Future work

Current work is focussing on the analysis of additional coarse-grained grinding wheels up to a grain size of D1001. The aim here is no longer to analyse individual grains but to measure the grinding wheel circumference in order to determine the grinding wheel topography. Using the height information obtained and high precision force measurements, the objective is to determine the load stresses in the contact zone.

Acknowledgements

References

[1] Brinksmeier E, Mutlugünes Y, Klocke F, Aurich J C, Shore P, Ohmori H 2010 Ultra-Precision Grinding CIRP Ann. 59 P 652-671
[2] Wang, J; Li, Y; Han, J; Xu, Q; Guo, Y Evaluating subsurface damage in optical glasses In Journal of the European Optical Society – Rapid Publications, 2011, 6/11001; S1-16
[3] Brinksmeier E, Riemer O, Rickens K, Berger D 2016 Application potential of coarse-grained diamond grinding wheels for precision grinding of optical materials. Prod. Eng. 10 P 563–573
[4] Bifano T G, Dow T A, Scattergood R O 1991 Ductile-regime grinding: a new technology for machining brittle materials. Trans. o. t. ASME, Journal of Engineering for Industry 113 P 184–189
[5] Malkin S 1989 Grinding Technology - Theory and Application of Machining with Abrasives, Ellis Horwood Ltd
[6] Adam, B., Riemer, O., Rickens, K., Heinzel, C. 2023. Precision grinding of BK7 glass with coarse-grained diamond grinding wheels. euspen – ICE 2023, Copenhagen, DK, P 501-502.

Effect of different cutting environments on surface integrity and wear resistance properties of Incoloy 925

Shravan Kumar Yadav[*], Sudarsan Ghosh, Aravindan Sivanandam

Mechanical Engineering Department, Indian Institute of Technology Delhi, New Delhi, India-110016

Submitting author, email: shravanyadav1444@gmail.com

Abstract

Ideally, machining is the final manufacturing process for the product; however, surface integrity (SI) produced by it, especially for Ni-based alloys, is a primary concern for the manufacturer. Induced surface integrity can influence the mechanical properties of the material. In order to improve the surface properties of the machined component, in this study, nano-metallic copper (Cu) based nanofluid (dispersed Cu in coconut oil) is used as a cutting environment and compared with dry machining and pure oil-based MQL (minimum quantity lubrication) condition. Further, its consequences on the wear resistance of machined components are studied with the help of ball-on-disc in reciprocating mode. Results show that dry machining produces poor surface integrity (in terms of surface roughness, surface topography, and microhardness) due to lack of lubrication and cooling, consequently, leads to higher wear of material for the machined component as compared to components machined in MQL and n-MQL (nanofluid-based minimum quantity lubrication) conditions.

Keywords: Incoloy 925, n-MQL, Surface integrity, Surface wear resistance

1. Introduction

Incoloy 925, one of the advanced versions of Ni-based alloys, is extensively used in the oil and gas industry owing to a combination of high strength and superior resistance to sulfide stress cracking and stress corrosion cracking [1]. However, Ni-based alloys are often difficult to machine and show poor machinability and machining-induced surface integrity, which results in a decline in the functional performance of the material when it is in use [2]. The relationship between mechanical cutting and functional performance is significant, which is why several studies have been done to improve the machining-induced surface integrity and wear resistance of the machined surface. Furthermore, wear (a progressive loss of materials) causes significant financial losses and possible failures [3]. Wear accounts for one-third of primary energy use and almost 60 % of mechanical component failure [4]. Grain refinement, hardness increase, and surface roughness reduction are common ways to improve the machining-induced surface integrity and wear resistance of machined surfaces [5,6]. Within the domain of mechanical cutting, the approaches utilized to enhance the wear resistance and surface integrity of machined surfaces are primarily classified as (i) Unconventional machining techniques (such as thermally aided machining, ultrasonic vibration assisted machining, and abrasive water jet machining), (ii) Advancement and optimization of cutting tools (such as coatings, micro-textures, and geometric parameters), and (iii) Cutting-edge lubrication and cooling methods include minimum quantity lubrication (MQL), nanofluids, cryogenic cooling, high pressure cooling (HPC), and hybrid cooling. Unconventional techniques utilize high specific energy. Hence, conventional machining (like turning and milling) is still attractive for machining superalloys.

However, because nickel alloys have low thermal conductivity, heat builds up, and temperatures rise at tool surfaces, compromising the integrity of the surface in terms of microstructural changes, thermo-mechanical stresses, and mechanical property changes. Hence, cooling and lubrication are needed to dissipate heat from the cutting zone. Several researchers [7,8] have reported that the surface integrity of rigid materials is significantly impacted by cooling and lubrication during the machining process. On the other hand, conventional lubrication raises the cost of machining and frequently leads to excessive lubricant wastage. Furthermore, traditional cutting fluids harm the environment and people [9]. Considering the present climate change condition and the exhaustion of natural resources, it is recommended to avoid using the traditional lubricating approach. Thanks to nanotechnology helped to develop cutting-edge fluid (called nanofluid), showing excellent properties to conventional cutting fluid, which has been proven to be an efficient cutting fluid when it is used under the minimum quantity lubrication (MQL) technique [10,11]. From the previous research investigations, it is observed that most of the research is focused on improving the surface integrity of superalloys, and very limited work is available on relating the surface integrity to functional performance (such as tribological performance) of machined components. Hence, this work investigates the influence of different sustainable cutting environments on microstructure evolution and wear resistance properties of one of the advanced superalloys (Incoloy 925).

2. Materials and methods

Alloy 925, also known as Incoloy 925, was chosen as the workpiece and vertical milling center as a machine (model, VMC 600 II, Hardinge), whereas TiAlN/TiN PVD coated carbide, grade of KCSM40 inserts (ISO EDPT10T312PDERHD) with a 0.8 mm nose radius made by Kennametal with indexable shoulder end mill as a tool holder (ISO 16A02R025A16ED10) were used. Machining parameters were chosen according to the manufacturer's suggestion for the cutting tool. These parameters included a cutting speed of 60 meters per minute, a

feed rate of 0.075 millimeters per tooth, an axial depth of cut 0.4 millimeters, and a radial depth of cut 16 millimeters. Optimized MQL parameters in a previous study [12] such as nozzle pressure of 6 kg/cm², a nozzle distance of 30 mm, a nozzle angle of 30° from vertical, and a flow rate of 150 ml/hr were used to supply the nanofluid that was prepared using two steps technique [13] in which 0.1 Vol.% Copper (Cu) nanoparticles with an average size of 80 nm were dispersed in coconut oil (having superior lubricity and excellent thermal oxidation resistance owing to almost 90 % saturated fatty acids (more details of pure coconut oil can be found in previous report [1])) using 30 minutes magnetic stirrer (1000 rpm) and 1-hour ultra-probe sonication (20 kHz).
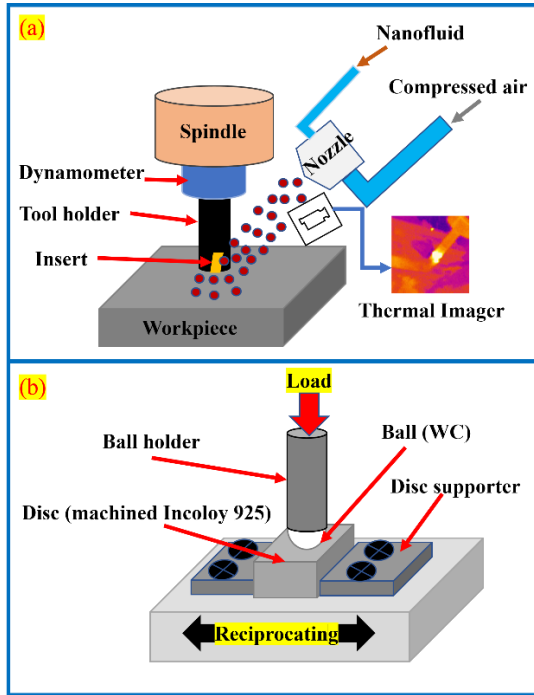
Figure 1. Schematic sketch of :(a) Machining setup and (b) Tribological testing

A dynamometer (model: RCD 9170A, Kistler) was used to record the cutting force signals (F_x, F_y, and F_z), and the resulting cutting force (F) was computed using Equation (1), whereas cutting temperature was measured using thermal camera (model: TIM 8, Epsilon, Germany).

$$F = \sqrt{F_x^2 + F_y^2 + F_z^2} \qquad (1)$$

With an optical profiler (Lambda-2), the surface topography of machined samples was captured. A metallurgical optical microscope (model: Leica ICC50 HD) was used to take micrographs of machined samples (cross-section) after they had been polished to a mirror finish using various grades of SiC paper and alumina slurry followed by etching using HCl + H_2O_2. Using a micro-Vickers hardness tester (model: HMV-G, Shimadzu), microhardness was measured on a polished cross-section of a machined surface at different positions with a 50 g load and a 12-second holding period.

A 6 mm tungsten carbide ball against 30 mm x 8 mm x 15 mm machined samples was used for the tribological test in the reciprocating mode of a multi-functional tribometer (model MFT 5000, R-tec instruments with an integrated Lambda-2 optical profiler) with a 5 N load, 2 mm stroke, 2 Hz frequency, and a sliding duration of 15 minutes. The details of the

machining setup are displayed in the sketch (Figure 1 (a)), while the schematic drawing for tribological testing is displayed in Figure 1(b).

3. Results and discussion

3.1. Surface roughness and topography

Surface roughness and topography of components play an important role in the tribological performance. Hence, its characterization is essential. The 3D topography (Figure 2) of machined components shows that the highest variation in roughness (peaks and valleys) is found in dry cutting. In contrast, the lowest variation is observed in nanofluid-based minimum quantity lubrication (n-MQL) assisted machining due to adequate lubrication compared to dry cutting. Further, from Figure 3, it is observed that areal surface roughness parameters, Sa (average roughness) and Sq (root mean square roughness), are found lowest in n-MQL assisted machining, followed by MQL (pure oil-based minimum quantity lubrication) and dry cutting.
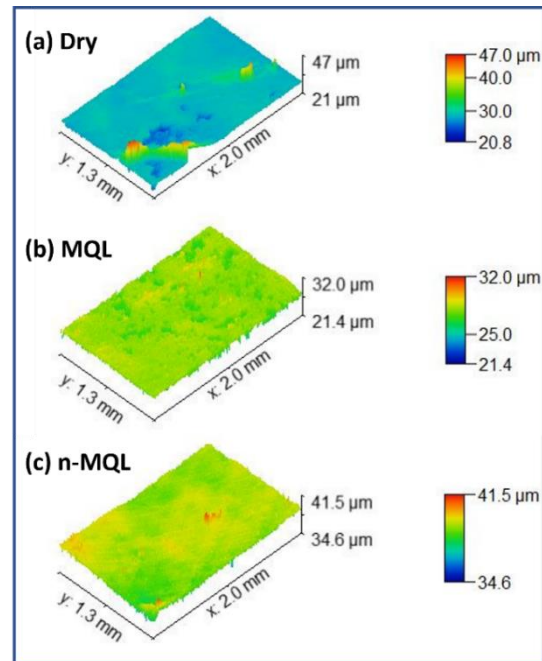
Figure 2. Surface topography of machined components under different cutting environments
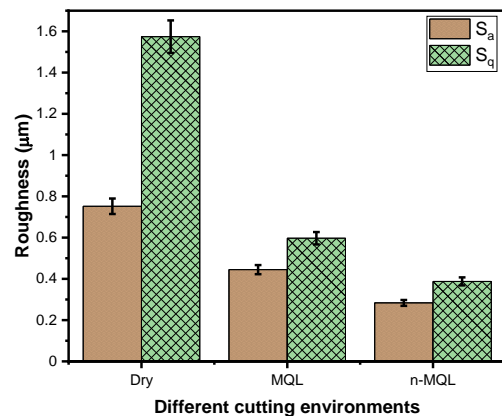
Figure 3. Areal surface roughness of machined components under different cutting environments

3.2. Microstructure and microhardness

All the mechanical properties of components depend on the microstructure of the material. Figure 4 shows the optical micrograph of cross-section of the machined surface under different cutting environments. It is observed that within a certain limit of depth from the machined surface, deformation of grain has occurred for all the cutting environments, possibly due to thermo-mechanical effect [9]. Figure 5 shows that heat generation and cutting force are higher in dry cutting. In the case of MQL assisted machining, heat generation and cutting force are lower due to reduced coefficient of friction caused by lubrication effect which reduces tool wear and result in lower deformation, whereas, in the case of n-MQL assisted machining, it is further reduced due to combination of nanoparticles and oil which enhances lubrication and heat transfer as compared to MQL and dry conditions.
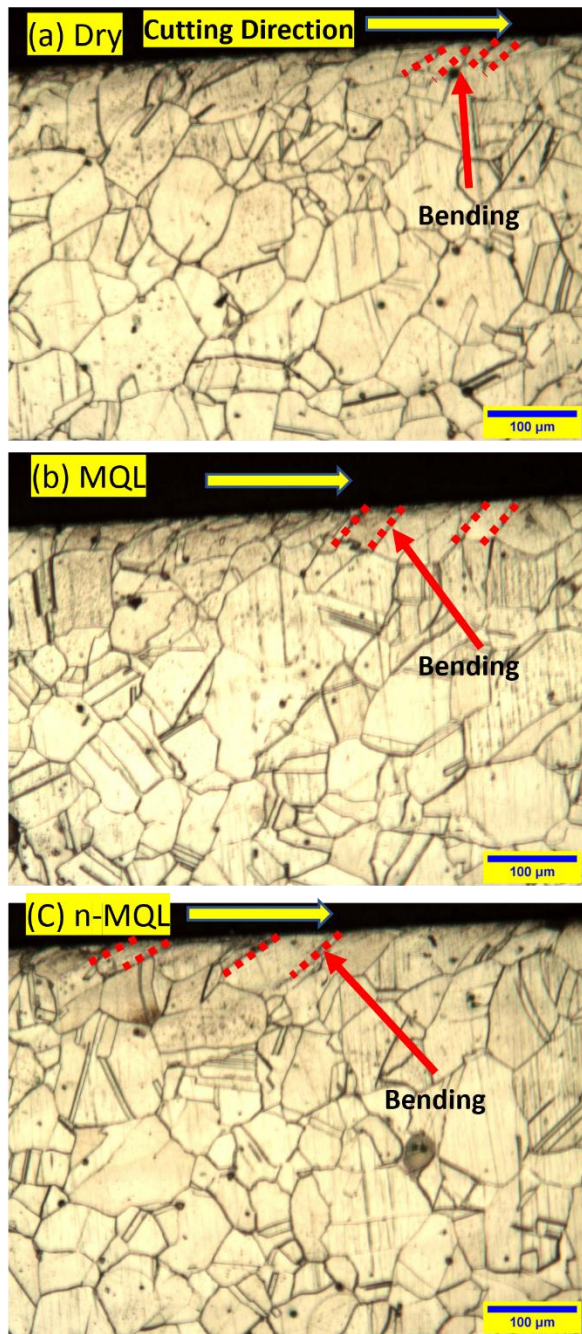
Figure 5. Cutting force and Cutting temperature for different cutting environments

Further, Figure 6 shows that microhardness is the highest in the case of dry cutting, followed by MQL and n-MQL assisted machining, possibly due to plastic deformation caused by the thermo-mechanical effect, as discussed previously. However, the increment in micro-hardness is limited to a certain depth from the machined surface for all the components machined under different cutting environments, possibly due to the reduction of the thermo-mechanical effect as the depth increases from the machined surface.
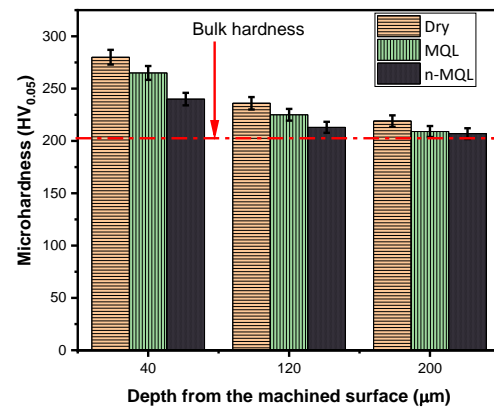
Figure 6. Microhardness of machined components(cross-section) under different cutting environments

3.3 Tribological performance

A ball-on-disc-based tribological test in reciprocating mode under dry conditions has been performed to correlate the tribological performance of machined components with surface topography, microstructure, and microhardness. From Figure 7, it is observed that the sample machined under dry cutting gives the highest coefficient of friction although having the highest hardness (see Figure 6) as compared to other samples machined under MQL and n-MQL conditions, which is possibly due to the domination effect of surface roughness parameters (see Figure 3). Further, Figure 8 shows that the wear (degradation of material) of the sample machined under dry cutting is higher than those machined under MQL and n-MQL conditions, confirming that surface roughness dominates over microhardness for tribological performance. A similar phenomenon was reported by Yuan et al. [14].

Figure 4. Microstructure of machined components (cross-section) under different cutting environments
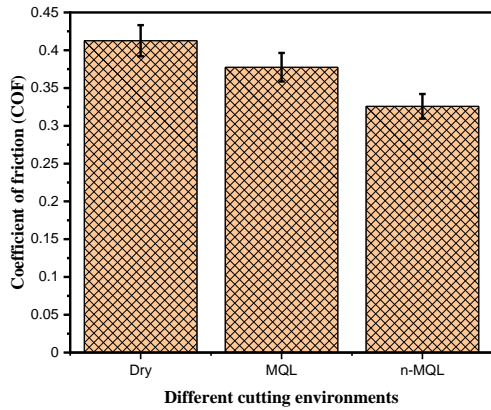
Figure 7. Coefficient of friction of machined components under different cutting environments
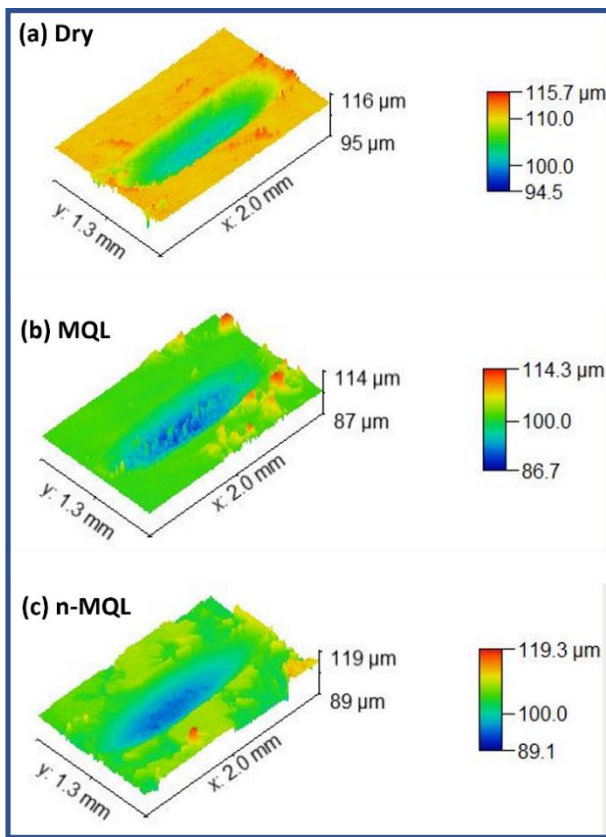
Figure 8. Wear topography of components machined under different cutting environments

5. Conclusion

The effects of surface characteristics processed by machining under different cutting environments on the tribological performance of Incoloy 925 have been investigated. The following key conclusion can be drawn out:

- Nanofluid-assisted machining gives the best topography with a reduction in areal surface roughness, Sa (average roughness), and Sq (root mean square roughness) by 62 % and 75 %, respectively, compared to dry cutting due to enhanced lubrication and heat transfer properties.
- The coefficient of friction for the sample processed with n-MQL-assisted machining is lower by 21 % and 13.7 % compared to dry cutting and MQL-assisted

machining, respectively, due to lower areal surface roughness.

- Although microhardness for the sample processed with n-MQL assisted machining is lower than that of samples processed with MQL and dry conditions, it gives lower wear of the material, possibly due to the domination effect of surface roughness over microhardness.

References

[1] Yadav, S. K., Ghosh, S., and Sivanandam, A., 2023, "Surfactant Free Enhancement to Thermophysical and Tribological Performance of Bio-Degradable Lubricant with Nano-Friction Modifier for Sustainable End Milling of Incoloy 925," J. Clean. Prod., **428**(October), p. 139456.

[2] Peng, Z., Zhang, X., Zhang, Y., Liu, L., Xu, G., Wang, G., and Zhao, M., 2023, "Wear Resistance Enhancement of Inconel 718 via High-Speed Ultrasonic Vibration Cutting and Associated Surface Integrity Evaluation under High-Pressure Coolant Supply," Wear, **530–531**(May), p. 205027.

[3] Khonsari, M. M., Ghatrehsamani, S., and Akbarzadeh, S., 2021, "On the Running-in Nature of Metallic Tribo-Components: A Review," Wear, **474–475**(December 2020), p. 203871.

[4] Yi, S., Chen, X., Li, J., Liu, Y., Ding, S., and Luo, J., 2021, "Macroscale Superlubricity of Si-Doped Diamond-like Carbon Film Enabled by Graphene Oxide as Additives," Carbon N. Y., **176**, pp. 358–366.

[5] Bruschi, S., Bertolini, R., Medeossi, F., Ghiotti, A., Savio, E., and Shivpuri, R., 2018, "Case Study: The Application of Machining-Conditioning to Improve the Wear Resistance of Ti6Al4V Surfaces for Human Hip Implants," Wear, **394–395**(October 2017), pp. 134–142.

[6] Duncheva, G. V., Maximov, J. T., Anchev, A. P., Dunchev, V. P., Argirov, Y. B., and Kandeva-Ivanova, M., 2022, "Enhancement of the Wear Resistance of CuAl9Fe4 Sliding Bearing Bushings via Diamond Burnishing," Wear, **510–511**(July), p. 204491.

[7] Chen, S., Yan, P., Zhu, J., Wang, Y., Zhao, W., Jiao, L., and Wang, X., 2023, "Effect of Cutting Fluid on Machined Surface Integrity and Corrosion Property of Nickel Based Superalloy," Materials (Basel)., **16**(2).

[8] Wang, Y., Ren, Y., Yan, P., Li, S., Dai, Z., Jiao, L., Zhao, B., Pang, S., and Wang, X., 2023, "The Effect of Cutting Fluid on Machined Surface Integrity of Ultra-High-Strength Steel 45CrNiMoVA," Materials (Basel)., **16**(9).

[9] Singh, R., and Sharma, V., 2022, "Machining Induced Surface Integrity Behavior of Nickel-Based Superalloy: Effect of Lubricating Environments," J. Mater. Process. Technol., **307**(April), p. 117701.

[10] Peng, R., He, X., Tong, J., Tang, X., and Wu, Y., 2021, "Application of a Tailored Eco-Friendly Nanofluid in Pressurized Internal-Cooling Grinding of Inconel 718," J. Clean. Prod., **278**, p. 123498.

[11] Sinha, M. K., Kishore, K., and Sharma, P., 2023, "Surface Integrity Evaluation in Ecological Nanofluids Assisted Grinding of Inconel 718 Superalloy," Proc. Inst. Mech. Eng. Part E J. Process Mech. Eng.

[12] Yadav, S. K., Ghosh, S., and Aravindan, S., 2023, "Study on Atomization Characteristics of Droplet of Bio-Degradable Oil for End-Milling of Incoloy 925," Manuf. Technol. Today, **22**(4), pp. 45–51.

[13] Yadav, S. K., Vasu, V., and Paliwal, U. K., 2019, "Experimental Study on Thermo-Physical Properties of Nano-Fluids Based on Copper Nanoparticles," *Materials Today: Proceedings*, pp. 525–532.

[14] Yuan, C., Yan, X., Liu, D., Yang, J., Li, S., Huang, C., and Wan, M., 2024, "Optimizing Tribological Property by Inducing the Gradient Microstructure and Surface Topography in Martensite Stainless Steel," Mater. Today Commun., **38**(October 2023), p. 107699.

Thermomechanical impact of the cutting edge microgeometry on the surface properties in turning of aluminium alloys

Thomas Junge[1], Thomas Mehner[2], Andreas Nestler[1], Andreas Schubert[1], Thomas Lampke[2]

[1]*Micromanufacturing Technology, Chemnitz University of Technology, Reichenhainer Str. 70, 09126 Chemnitz, Germany*
[2]*Materials and Surface Engineering, Chemnitz University of Technology, Erfenschlager Str. 73, 09125 Chemnitz, Germany*

thomas.junge@mb.tu-chemnitz.de

Abstract

In machining with tools exhibiting geometrically defined cutting edges their microgeometry has a significant influence on the surface properties. The process-adapted design of cutting edges enables a targeted modification of the thermomechanical load during machining as well as the resulting surface layer properties. In order to increase the fatigue strength of the machined parts and to enhance their application performance, low surface roughness values and strong compressive residual stresses are aspired. Hence, for the experimental investigations, the cutting edge geometry of cemented carbide indexable inserts is modified. The size and the orientation (form factor $K_S < 1$, $K_S > 1$) of the cutting edge rounding are changed by brushing. In the experimental investigations, the cutting speed (50 m/min and 550 m/min) and the depth of cut (0.4 mm and 0.8 mm) are varied, while the feed is kept constant. For an evaluation of the resulting thermal load in turning of the aluminium alloy EN AW-2017, the temperature is measured by a tool-workpiece thermocouple. Additionally, the components of the resultant force are recorded by a dynamometer.

The results show an enlargement of the tangential residual stresses with an increasing cutting edge radius due to rising temperatures in the cutting zone. Nevertheless, the selection of a low cutting speed and a high depth of cut combined with an appropriate orientation of the cutting edge rounding allows for strong compressive residual stresses. In-process monitoring of the cutting temperature and the force components enables a better comprehension of the thermomechanical impact. Although not all effects of the cutting edge geometry on the residual stresses can be explained by the results of the in-process measurements, the findings contribute to a tailored cutting edge design and selection of the machining parameters in regard to the desired surface properties.

Keywords: Aluminium, Cutting edge geometry, In-process monitoring, Surface properties, Turning

1. Introduction

The cutting edge microgeometry describes the transition area of the cutting edge from the rake face to the flank face. It can be modified by various processes (e.g. grinding, brushing, laser machining, etc.). The VDI Standard VDI/VDE 2654 Part 2 defines various cutting edge parameters for this purpose. Commonly, the cutting edge radius r_β is used for the characterisation of the edge rounding. The form factor K_S has been introduced to describe the orientation of the edge rounding towards the flank face ($K_S < 1$) or the rake face ($K_S > 1$). It is calculated by the division of the projected rounding on the rake face (S_γ) and flank face (S_α). Overall, the defined cutting edge design can have different purposes like the reduction of cutting edge chipping, the improvement of cutting edge stability and the enhancement of coating adhesion. However, modifying the cutting edge geometry is also accompanied by a change in machining conditions, in particular the thermomechanical load in the cutting zone. [1]

According to Bassett et al. [2], the cutting and feed forces increase significantly due to the intensification of friction and ploughing as a result of an increase in S_α as well as the average radius. In contrast, an orientation of the cutting edge rounding towards the rake face has hardly any influence on the forces. A high cutting edge radius especially for $K_S > 1$ can lead to the formation of a stagnation zone in the area of the cutting edge, similar to a sharp one, where the relative velocity between the tool and the workpiece material is temporarily equal to zero.

This effect particularly applies for machining of aluminium where a stable built-up edge can influence the forces considerably [3]. Shen et al. [4] conclude that the resulting intensification of the ploughing effect can increase the absolute values of the compressive residual stresses in the material.

Bergmann [5] measured the temperatures inside the indexable insert with an embedded thermocouple during dry orthogonal turning of C45N, Ti6Al4V, and EN AW-2007. In contrast to C45N and Ti6Al4V, where the measured thermal load increased with a larger cutting edge radius ($K_S = 1$), there was no significant temperature rise (5%) measurable for the aluminium alloy. However, an empirically calculated temperature field showed that the temperature at the flank face rises with an increase in S_α. According to the FEM model by Bergmann et al. [6] for the simulation of the thermomechanical during machining, the increased friction in the transition area to the flank face is the main reason for that.

In milling, Denkena et al. [7] investigated the influence of the cutting edge radius on the resulting residual stresses of the aluminium alloy EN AW-7449 in milling. On the one hand, they observed stronger compressive residual stresses beneath the surface with an increasing cutting edge radius. On the other hand, the tensile residual stresses at the surface rose simultaneously.

Considering the influence of the cutting edge microgeometry on the surface roughness, inconsistent findings can be observed. In this regard, the ratio of undeformed chip thickness to cutting edge radius must be taken into account. The smaller the ratio, the higher the ploughing effect, which increases the material

flow along the flank face and thus could lead to a deterioration of the surface roughness. [1]

The state of the art in science and technology shows that the modification of the cutting edge microgeometry can change the thermomechanical load and therefore the resulting surface properties during machining. Nevertheless, the impact is strongly related to the material properties, e.g. the thermal conductivity and strength [6]. In this context, there has been no comprehensive experimental investigation in machining of aluminium alloys up to now. Therefore, the object of this study is the characterisation of the thermomechanical impact during machining of EN AW-2017 with different cutting edge microgeometries and its influence on the surface properties with special emphasis on the residual stresses. It is of high interest if the modification of the cutting edge microgeometry can contribute to the enhancement of the fatigue strength of finish machined aluminium parts.

2. Materials and Methods

2.1. Specimens and cutting tools

In the experimental investigations, cylindrical specimens of the aluminium alloy EN AW-2017 (T4) with a total length of 80 mm were used. The specimens were stepped and had a diameter of 28 mm for a length of 60 mm. For the remaining part of the length, the diameter amounted to 25 mm. The side with the smaller diameter was utilised for clamping applying a dead-length collet chuck.

In the finish machining experiments, uncoated cemented carbide indexable inserts of the type CCMT 09T304 were used. They were characterised by a tool included angle of 80°, a clearance angle of 7°, a rake angle of 0°, and a corner radius r_ε of 0.4 mm. In combination with the tool holder used, the nominal tool cutting edge angle of the major cutting edge was 95°. After grinding, the cemented carbide indexable inserts were characterised by a cutting edge rounding r_β of 7 μm (tool type 1) with a form factor K_S of 0.8. For a variation of the cutting edge microgeometry the tools were modified by brushing. Afterwards the cutting edges were measured by an optical coordinate measuring machine (Bruker alicona μCMM). The cutting edge radius and form factor were evaluated by the Alicona Edge Master Module by extracting 50 orthogonal profiles each in the area of the tool corner and the major cutting edge. Table 1 shows the average values of four tools with the same cutting edge characteristics and their mean absolute deviations.

Table 1 Measured cutting edge radius r_β and form factor K_S of the applied cutting tools and their mean absolute deviations

Tool type	Cutting edge radius r_β / μm	Form factor K_S
1	7.3 ± 0.1	0.80 ± 0.02
2	14.4 ± 1.5	0.73 ± 0.06
3	28.6 ± 3.2	0.98 ± 0.04
4	15.6 ± 1.2	1.75 ± 0.04

Comparing the orientation of the cutting edge rounding of tool type 1 to 3, it can be seen that the reproducibility of the same form factor is difficult to achieve for different cutting edge roundings. The rise of the mean absolute deviation of r_β from tools type 1 to type 3 results from the brushing process and can be explained by the increasing deviation between r_β in the area of the corner radius and the main cutting edge. Figure 1 shows a modified cutting edge microgeometry in comparison to a tool after grinding captured by 3D laser scanning microscopy using a Keyence microscope type VK-9700.
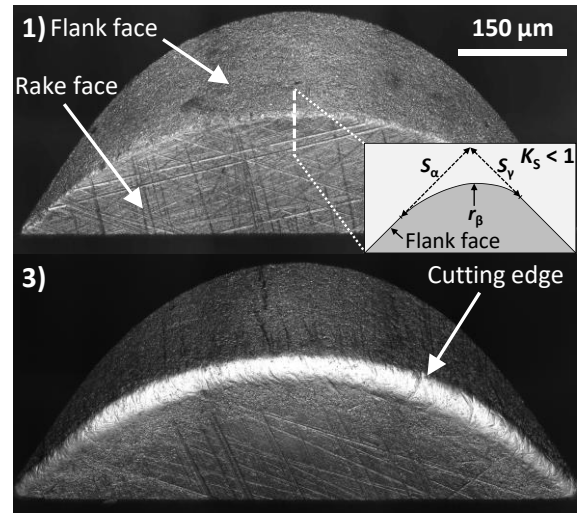
Figure 1. Microscope images of the cutting edges of tools type 1 and type 3 in the area of the tool corner as well as a schematic depiction of a form factor $K_S < 1$ ($S_\alpha > S_\gamma$)

2.2. Measurement principles and implementation

For the acquisition of the mechanical load the tool holder was mounted on a three-axis dynamometer type 9257 A (Kistler), which was connected to a charge amplifier type 5070 A (Kistler). Therefore, the cutting force F_c, the feed force F_f, and the passive force F_p could be recorded separately during machining.

The evaluation of the thermal load close to its point of origin was realised by the application of a tool-workpiece thermocouple. It is similar to a conventional thermocouple except for the fact that workpiece and tool form a natural thermocouple. The measured thermoelectric voltage corresponds to the average temperature at the interface of the tool and the specimen [8]. The complete setup of the tool-workpiece thermocouple and its integration into the lathe are described and visualised in detail in [9].

2.3. Machining experiments

The experimental investigations were conducted on a precision lathe of the type SPINNER PD 32. For pre-machining of the specimens, an indexable insert comprising a CVD diamond tip was used. The applied machining parameters were constant (feed $f = 0.1$ mm, depth of cut $a_p = 0.1$ mm, and cutting speed $v_c = 150$ m/min). To avoid a significant heating of the specimen, it was cooled applying a cold-air nozzle. After pre-machining, the specimens had a diameter of 27.8 mm.

During finish machining experiments, the tools listed in Table 1 were used. The thermal load was altered by choosing cutting speeds of 50 m/min and 550 m/min due to the direct correlation between the cutting speed and the process temperature. Furthermore, a change in the cutting edge length in contact with the workpiece material was obtained by selecting two different depths of cut of 0.4 mm and 0.8 mm. The feed was kept constant at 0.04 mm. For each combination of cutting speed and depth of cut, two specimens were machined with one tool. All experiments were performed with emulsion flood cooling in an air-conditioned laboratory.

2.4. Evaluation of surface properties

The geometrical properties of the machined surfaces were measured using a stylus instrument type Mahr LD 120. The stylus was characterised by a spherical radius of 2 μm and an included angle of 90°. After finish machining, the surface roughness of all specimens was measured in the direction of feed motion. Three measurements, each with an evaluation length of 4 mm, were taken at different positions along the circumference at the

beginning and at the end of the specimen. Filtering of the profiles was done in accordance with DIN EN ISO 21920-3.

Residual stresses σ were measured on the specimen surface by X-ray diffraction (XRD) using the $\sin^2\psi$ method. One specimen was measured for each parameter set. A diffractometer D8 Discover (Bruker) with a Co anode (parameters 35 kV, 40 mA), a 0.5 mm pinhole aperture, and a 1D detector LYNXEYE XE-T has been utilised. The tilt angles ψ were selected in such a way that their spacing on the $\sin^2\psi$ scale is 0.1 (between 0 and 0.8 – both in positive and negative tilt direction). Rotation angles φ 0°, 45°, and 90° were used. The measurements were performed using the {311} peak of Al with the lattice-specific elastic constants Young's modulus $E^{\{311\}} = 69.3$ GPa and Poisson's ratio $\nu^{\{311\}} = 0.35$ [10].

3. Results and discussion

3.1. Thermomechanical process conditions

In a first step, the thermomechanical impact of the form factor $K_S < 1$ (tool type 2) and $K_S > 1$ (tool type 4) was compared for similar cutting edge radii. Regarding the tool-workpiece interface temperature no significant change was visible as the highest temperature difference amounted to only 11.6 K ($v_c = 550$ m/min, $a_p = 0.4$ mm). The same result could be obtained for the measurement of the components of the resultant force, where the maximum force difference due to a higher form factor amounted to 1.5 N for F_c, 1.8 N for F_f, and 1 N for F_p over all experimental tests. Consequently, the variation of the form factor in the range from 0.7 to 1.8 had no measurable influence on the thermomechanical load.

In a second step, the effect of an increasing cutting edge radius on the thermomechanical impact was analysed for similar form factors. Figure 2 shows the tool-workpiece interface temperature T for tools of type $1 - 3$ in dependence of cutting speed and depth of cut. The diagram displays the mean values of the measurements calculated from two equivalent tests and the standard deviations over the course of the measurements.
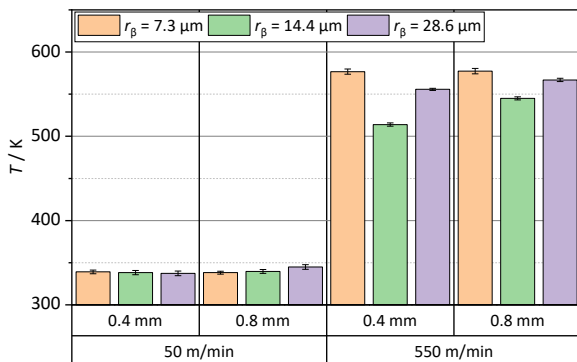
Figure 2. Influence of the cutting edge radius r_β on the tool-workpiece interface temperature for different v_c and a_p

Since the majority of the mechanical energy supplied to the cutting process is converted into thermal energy, there is a significant growth of the interface temperature with increasing cutting speed. On the one hand, there is no temperature change visible in regard to different cutting edge radii for the low cutting speed. On the other hand, high cutting speeds lead to lower temperatures for tools of type 2 and type 3 in comparison to tool type 1, but there is no clear tendency concerning the cutting edge radius.

Figure 3 illustrates the average values of the components of the resultant force calculated from two similar experiments. The error bars represent the mean standard deviation over the course of the measurements.
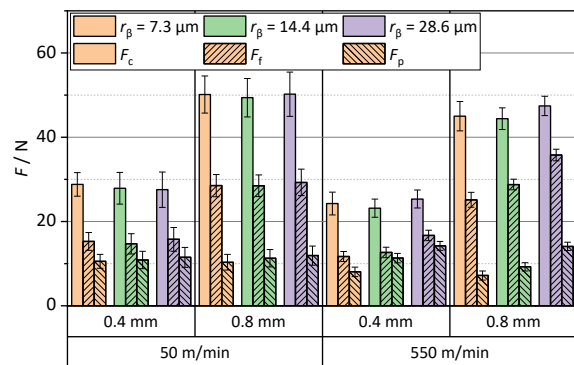
Figure 3. Influence of the cutting edge radius r_β on the components of the resultant force for different v_c and a_p

The increase in depth of cut leads to an enlargement of the cross-sectional area of the undeformed chip. Hence, the work required for elastic and plastic deformation of the material increases and enlarges the cutting and feed forces. However, with a higher cutting speed the cutting force slightly decreases due to the material strength reduction resulting from higher temperatures. For $v_c = 550$ m/min the feed and passive forces rise steadily with an enlargement of the cutting edge radius. This force enhancement could result from increased material flow towards the flank face (ploughing) and intensified squeezing of the material in the shear zone. Surprisingly, this mechanical impact of the cutting edge radius is not visible for lower cutting speeds. This behaviour could be attributed to increased built-up edge (BUE) formation at low temperatures, illustrated in Figure 4.
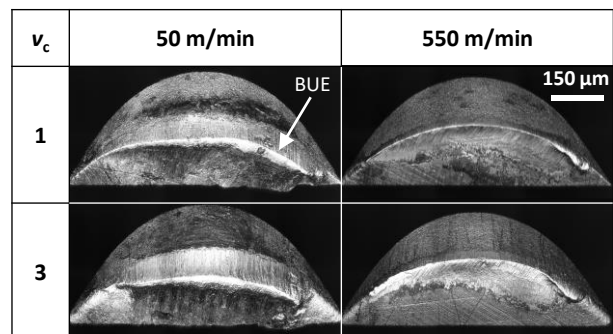
Figure 4. Microscope images of the cutting edges of tools of type 1 and type 3 in the area of the tool corner after machining for $a_p = 0.4$ mm

Due to strain hardening the deposited aluminium material is harder than the specimen material and thus it takes over the function of the cutting edge. The temporarily changed cutting edge microgeometry has a different cutting edge radius and a higher rake angle of up to 25°. Therefore, the BUE alters the material flow and counteracts the force enhancing effect by an increased cutting edge radius.

3.2. Surface properties

Independent of the cutting edge radius, the surface roughness values varied between 1.3 μm − 2.1 μm for Rz and 0.16 μm − 0.34 μm for Ra across all experimental tests. However, no consistent trend or significant change in surface roughness was observed that could be explained by the modification of the cutting edge rounding. Therefore, it is not considered in detail in this study.

Different cutting edge microgeometries and machining parameters change the residual stress distribution in axial and tangential direction (Figure 5). These stress modifications depend on the components of the resultant force and the cutting temperature.
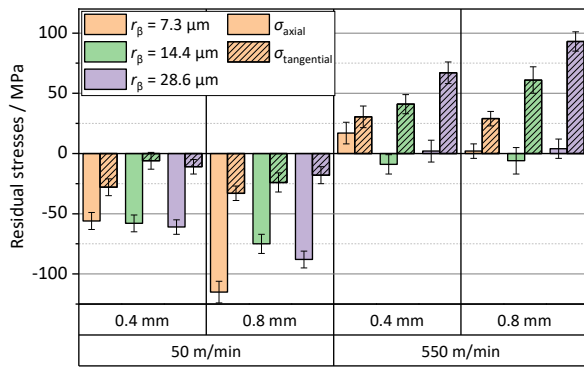
Figure 5. Influence of the cutting edge radius r_β on on the residual stresses in the axial and the tangential direction for different v_c and a_p

For low cutting speeds compressive residual stresses are dominant due to the overall minor temperature changes of the specimens. They become even stronger by an increase of the cutting and feed forces as a result of higher plastic deformation. In contrast, this mechanical impact is not visible for the higher cutting speed as the thermal influence increases.

In reference to [2] and [6] a higher cutting edge radius in combination with a form factor $K_S \leq 1$ leads to an increase in the contact surface between the tool and the specimen material in the area of the flank face. Furthermore, the rise of the sliding friction work between tool and workpiece contributes to a rise of the frictional heat. Finally, the enlarged contact surface in the tertiary shear zone favours the heat transfer into the specimen and therefore leads to an increase in the residual stresses in the tangential direction with rising cutting edge radius (see Figure 5). Since the cutting speed is significantly higher than the feed velocity, this effect is not observed in the axial direction, where no significant influence of the cutting edge rounding is evident. The described local increase of the thermal load cannot be seen in Figure 2 because the tool-workpiece thermocouple only measures the average temperature of the contact surface between the tool and the specimen. Since the tool-specimen contact surface on the rake face is larger than the contact surface in the area of the flank face a temperature change in the tertiary shear zone can hardly be measured.

Despite there were no significant measurable differences of the thermomechanical load during machining with tools comprising different orientations of the cutting edge rounding, tangential residual stresses changed (Figure 6).
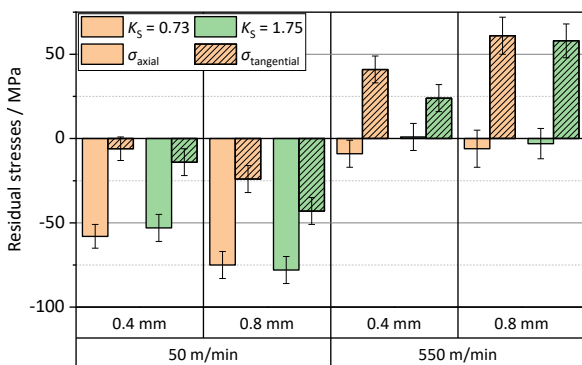
Figure 6. Influence of the form factor K_S on on the residual stresses in the axial and the tangential direction for different v_c and a_p

With the enlargement of the form factor tangential residual stresses decrease. The more the cutting edge rounding is orientated towards the rake face ($K_S > 1$), the smaller the contact surface between tool and specimen. This leads to a reduced heat input into the specimen resulting in enhanced compressive or lower tensile residual stresses in the tangential direction, respectively. Additionally, the surface roughness values for Rz were reduced slightly in experimental tests by up to 0.4 µm.

5. Summary and conclusions

Different cutting edge geometries are evaluated concerning their thermomechanical influence on the surface properties in turning of EN AW-2017. The experimental findings reveal a significant dependency from the cutting speed. Low process temperatures lead to increased built-up edge formation, that counteracts the force enhancing effect of an increased cutting edge rounding. However, the enlargement of the mechanical load for higher cutting speeds shows no clear effect on the residual stresses as its influence is suppressed due to the more dominant thermal influence. Overall, the results confirm that low temperatures favour the generation of compressive residual stresses. In this context, the modification of the residual stresses by the changed cutting speed could be explained as a result of the global thermomechanical load. However, the local thermal impact of the cutting edge geometry cannot be depicted by the tool-workpiece thermocouple as the increase of the contact surface between the tool and the specimen due to a larger cutting edge radius is too small in relation to the overall size of the contact surface.

It can be assumed that the enlarged heat transfer into the specimen leads to a rise of tangential residual stresses. Consequently, it is not recommended to apply a tool with a large cutting edge radius and a form factor $K_S \leq 1$ for machining of aluminium parts with a desired high fatigue strength. Nevertheless, compressive residual stresses can be obtained by applying a low cutting speed and a higher depth of cut. In terms of tool design, a slight reinforcement of the compressive residual stresses in the tangential direction can be achieved by a form factor $K_S > 1$.

Further investigations should examine in more detail the local heat input in the tertiary shear zone by the application of FEM simulations leading to better comprehension of the thermomechanical impact of the cutting edge microgeometry.

References

[1] Denkena B and Biermann D 2014 Cutting edge geometries *CIRP Annals* **63**(2) 631-653
[2] Bassett E et al. 2012 On the honed cutting edge and its side effects during orthogonal turning operations of AISI1045 with coated WC-Co inserts *CIRP J. Manuf. Sci. Technol.* **5**(2) 108-126
[3] Waldorf D J et al. 1999 An Evaluation of Ploughing Models for Orthogonal Machining ASME *J. Manuf. Sci. Eng.* **121**(4) 550-558
[4] Shen Q et al. 2018 Effects of Cutting Edge Microgeometry on Residual Stress in Orthogonal Cutting of Inconel 718 by FEM *Materials* **11**(6) 1015
[5] Bergmann B 2017 Grundlagen zur Auslegung von Schneidkantenverrundungen (PhD) Hannover: *TEWISS* **IFW 9/2017**
[6] Bergmann B et al. 2021 FE-Simulation Based Design of Wear-Optimized Cutting Edge *Roundings J. Manuf. Mater. Process.* **5**(4) 126
[7] Denkena B et al. 2008 Machining induced residual stress in structural aluminum parts *Prod. Eng. Res. Devel.* **2** 247–253
[8] Stephenson D A 1993 Tool-Work Thermocouple Temperature Measurements: Theory and Implementation Issues ASME *J. Ind. Eng. Int.* **115** 432-437
[9] Junge T et al. 2024 Methodology for soft-sensor design and in-process surface conditioning in turning of aluminum alloys *Prod. Eng. Res. Devel.* **18** 267-287
[10] Eigenmann B and Macherauch E 1996 Röntgenographische Untersuchung von Spannungszuständen in Werkstoffen (Teil 3) *Mater. Werkst.* **27** 426-437

Benchmarking rapidly solidified aluminium alloys for ultra-precision machining of ultra-violet mirrors and diffractive optical elements

D.A. Rolon[1,2], F. Hölzel[2], J. Kober[1], S. Kühne[1], M. Malcher[1], T.K. Naderi, [1], T. Arnold[2], D. Oberschmidt[1]

[1]Technishce Universität Berlin, department of Micro and Precision Devices MFG, Germany
[2]Leibniz Institute of Surface Engineering (IOM), Germany

rolon@mfg.tu-berlin.de

Abstract

Only few materials are suited for the manufacturing of diffractive gratings or mirrors designed for the ultra-violet (UV) range. In recent years, research has been undertaken to identify materials capable of supporting microstructures created by ultra-precision machining while possessing the surface roughness required for mirror applications in the UV range. Rapidly solidified aluminium alloys (RSA) have emerged as promising candidates due to their micrometre sized grain and desirable optical properties. Since certain characteristics of common industry-standard alloys limit their use in UV optics, developing new and improved alloys holds significant potential. This paper benchmarks aluminium alloys RSA-6061-T6, RSA-902, RSA-7034-T6, and RSA-501. A series of ultra-precision shaping experiments with facetted single crystal diamond (SCD) tools were conducted to manufacture diffractive grating structures. Flat surfaces were polished to produce optical surfaces. The results obtained through white light interferometry (WLI) and atomic force microscopy (AFM) measurements indicate that RSA-6061-T6, RSA-902, and RSA-501 are promising candidates for mirror applications. Root-mean-square surface roughness Sq < 10 nm during the experiments were achieved. Moreover, besides RSA-501, RSA-7034-T6 is considered a candidate for diffractive optical elements for its capability to support microstructures. WLI measurements indicate that the constrains on achieving low surface roughness in ultra-precision shaping processes are predominantly driven by the size and - to a lesser degree - the composition of precipitates within the material. It is important to highlight, the impact precipitations have on surface formation during cutting. These precipitations due to its mechanical properties result in the random distribution of defects on the surface. Furthermore, flake structures over the RSA-501 and RSA-902 are possible to be observed, however no correlation with defects was found.

RSA-alloys, Mechanical Manufacturing, Ultra-precision machining

1. Introduction

Aluminium alloys have gained in importance for optical system applications in the past years [1-3]. Among their desirable characteristics, mechanical properties like elastic modulus, hardness, density, and, in some cases, the thermal expansion coefficient, are crucial for the application and machinability of these alloys. Naturally, high reflectivity across a broad range of the electromagnetic spectrum including UV, is essential for optical applications. Innovative methods to produce these alloys attract the attention of optical system manufacturers towards materials. For instance: The melt-spinning process has proven to be an effective method to produce the RSA-501 alloy with an average grain size $d_g \leq 1$ μm [2]. The literature shows that the reduced grain size enables achieving optical surfaces with Sq < 10 nm by means of ultra-precision shaping [2]. Literature concerned with inhomogeneities in these alloys' textures and the resultant influence on their machinability is scarce.

The aim of this investigation is to analyse the feasibility of recently developed RSA-902, RSA-6061-T6, RSA-7034-T6, RSA-501 for the manufacturing of optical elements. The T6 heat treatment indicates that the alloy was heat treated and aged at 150 °C to hardened precipitations and increase the mechanical properties of the alloy. In order to give a step forward to find aluminium alloys suitable for further improvement of the surface roughness by means of UP-machining and ion beam etching. The texture of the above-mentioned alloys must be first analysed. The first hypothesis to be tested is the existence of a flake structure generated from the production process of RSA-alloys. Since they may incur in surface damage during cutting. Secondly, the correlation between the flake structure and surface formation during the cutting of mirrors and structured surfaces is examined.

During the melt-spinning process the alloys are rapidly cooled in less than a second, resulting in the formation of thin ribbons. The primary characteristic of this process is its ability to prevent grain growth, thereby generating very fine oversaturated crystals. After solidification, these ribbons are chopped and subjected to hot isostatic pressing (HIP) before being extruded at 300°C [3]. The fine grain structure facilitates smooth surfaces and is of advantage for other finishing processes such as ion beam etching.

For achieving the required surface roughness for UV-applications, aluminium alloy substrates can be machined by ultra-precision machining resulting in a suitable surface quality for ion beam processing. Mechanical polishing process of UP-machined aluminium alloy substrates often results in undesirable form deviations. With ion beam etching no such deviations are created. Ion beam etching is proven to reduce surface roughness [3]. However, the presence of precipitations and inhomogeneities within the alloys and their influence on surface formation during cutting and etching is not discussed conclusively.

In ultra-precision machining with diamond tools, the above-mentioned precipitations can be directly responsible for tool wear. Also, such precipitations are responsible for the formation

of voids or pits along the material surface during cutting, limiting the attainable roughness [3]. In ion beam etching processes, such precipitations and polycrystalline grain structures, can be responsible for different etching rates. Therefore, increasing the surface roughness instead of reducing it. Within the realm of ion beam etching, different strategies can be pursued to diminish the influence of the grain orientation by forming a passivation layer using O_2 gas [3]. However, inhomogeneities within the material must be first understood, the defects origin must be found, then a proper method to deal with them can be suggested.

2. Equipment and method

RSA-6061-T6, RSA-902, RSA7034-T6, and RSA-501 were metallographically prepared, considering the extrusion direction. The dimensions of the samples for the analysis are 15 mm x 15 mm x 10 mm, with each sample cut either in the longitudinal or transverse direction. Similar samples, were used for the ultra-precision shaping experiments.

For the ultra-precision shaping experiments, faceted diamond tools with a setting angle χ'r = 1° were used. The experiments were conducted in a modified machine tool MMC1100 by LT-ULTRA TECHNOLOGY GMBH, Germany. The cutting strategy used is previously described by Rolon [2] and Steinkopf [4]. The strategy consists of orienting the stepover direction of cutting towards the short grating size. The main reason for using this strategy is its capability to achieve constant cutting conditions and to avoid collisions of the tool with the tip of the blaze structure.

The metallographic preparation was conducted using slurries with abrasive grains ranging from 1 µm ≤ d_g ≤ 3 µm. The alloys were etched using a 10 % concentration of NaOH.

For the electron backscatter diffraction (EBSD) measurement, samples were prepared with a vibration polishing process using diamond grains with d_g = 0.5 µm. Measurements of the prepared samples was performed in a scanning electron microscope DSM 982 GEMINI by CARL ZEISS AG, Germany. For the calculation of grain size, the calliper method provided by the MTEX toolbox in a self-developed script in MATLAB, from MATHWORKS, USA, was used following the method described by Rolon, et. al. [2]. The etched samples were analysed using a light microscope DM6 by LEICA MICROSYSTEMS GMBH, Germany. Topography measurements from the machining experiments were conducted with a white light interferometer (WLI) Wyko NT1100 by VEECO, USA, and an atomic force microscope (AFM) Nanite by NANOSURF AG, Switzerland.

3. Results

3.1. Polishing

All materials were polished using the same parameters and steps. Figure 1 shows WLI measurements of the surface and Figure 2 the achievable surface roughness measured in 5 different areas over the surface.
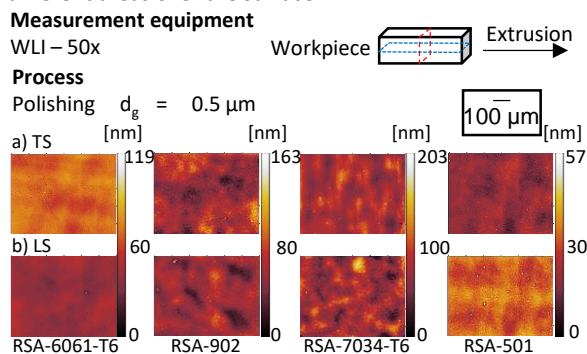
Figure 1. WLI measurement of RSA-6061-T6, RSA-902, RSA-7034-T6, and RSA-501
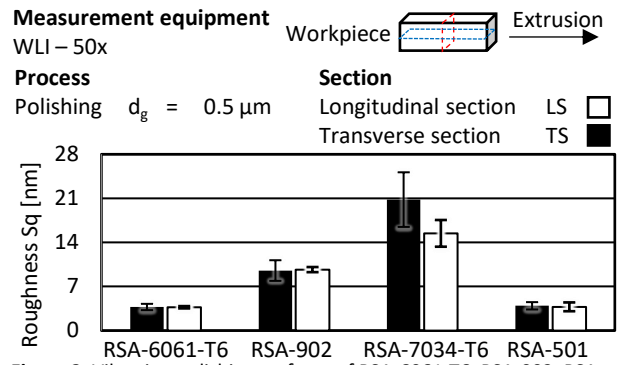
Figure 2. Vibration polishing surfaces of RSA-6061-T6, RSA-902, RSA-7034-T6, and RSA-501

3.2. Texture characterisation of RSA-alloys

By metallographic preparing the above-mentioned alloys, and etching them using NaOH 10% flake structure and precipitation becomes evident. The flake structure indicates areas with different grain sizes or concentration of precipitations. Figure 3 shows the result of the chemical etching using 10% NaOH.
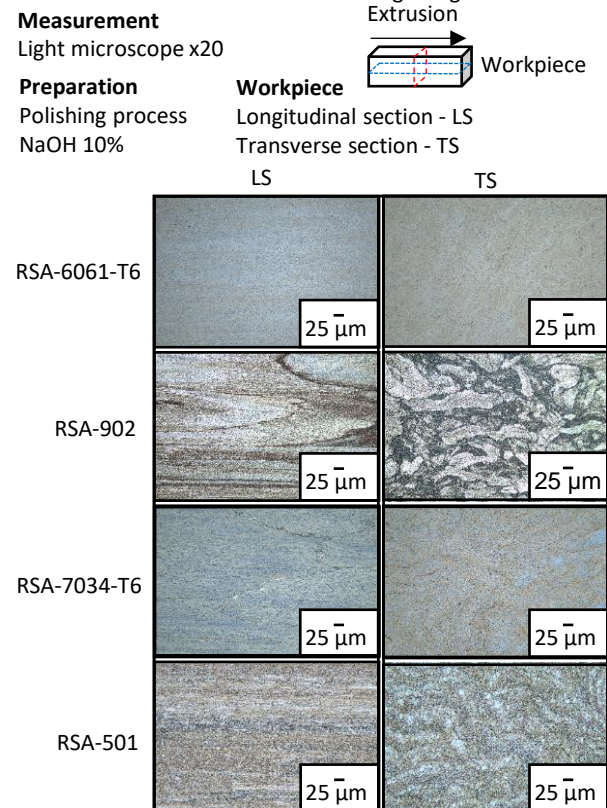
Figure 3. Light microscope measurements of RSA-6061-T6, RSA-902, RSA-7034-T6, RSA-501 regarding the longitudinal and transverse section of each alloy

After preparing the alloy, EBSD measurements were taken and grain sizes of the aluminium phase were measured. Figure 4 shows the EBSD-measurements of RSA-6061-T6, RSA-902. RSA-7034-T6, and RSA-501 along the transversal and longitudinal section. Figure 4 shows the histogram of grain size distribution for each alloy and section. In Table 1 the calculated mean grain size based on the grain distribution provided by the Calliper method of the MTEX MATLAB tool box is presented.

Measurement | **Section**
EBSD | Longitudinal section | LS
Preparation | Transverse Section | TS
Polishing

BE
RSA-alloy
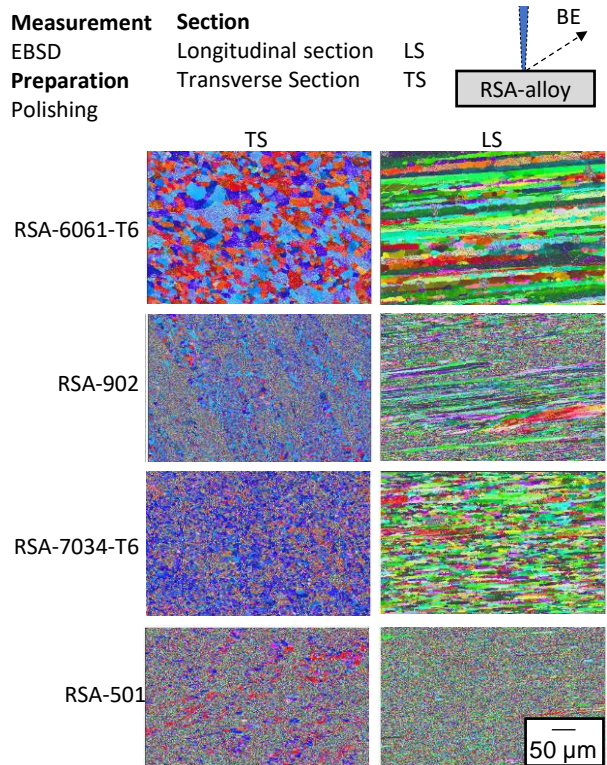
Figure 4. EBSD measurements of RSA-6061-T6, RSA-902, RSA-7034-T6, RSA-501 regarding the longitudinal and transverse section of each alloy.

Measurement | **Section**
EBSD | Longitudinal section | LS ☐
MTEX | Transverse section | TS ■
Preparation
Polishing

d_g
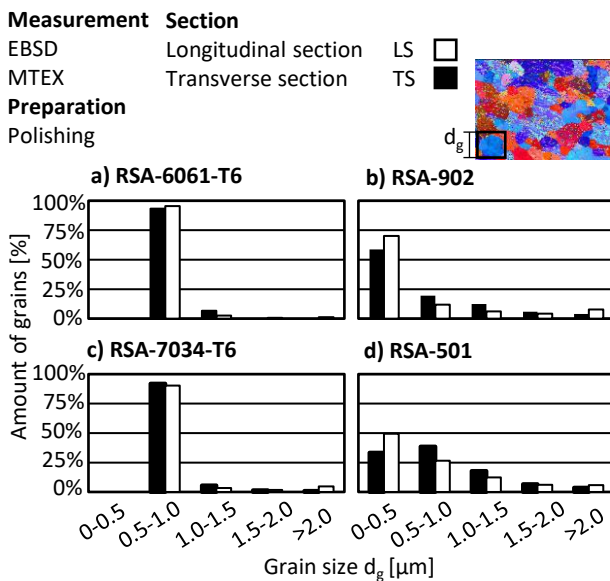
Figure 5. Distribution of grain size along the material texture

Table 1 Average grain size calculation for each alloy

	Average grain size d_g			
Section	RSA-6061 T6	RSA-902	RSA-7034 T6	RSA-501
	[μm]	[μm]	[μm]	[μm]
TS	0,80 ± 0,11	0,77 ± 0,88	0,86 ± 0,92	0,90 ± 1,01
LS	1,01 ± 7,18	0,80 ± 2,20	1,22 ± 3,80	1,01 ± 0,90

3.3 Ultra-precision shaping surfaces

Ultra-precision shaping experiments were conducted according to the description in section 2. The only varied variable was the alloy. In this experiment, RSA-6061-T6, RSA,902, RSA-7034-T6, RSA-501 were structured using a facetted single crystal diamond tool. Figure 6a) shows the results obtained within the

experiments. Figure 6b) presents the profiles of representative defects of the machined surfaces.

Material
RSA-501
Transverse section
Process
UP-shaping
χ′r = 1 °
V_c = 1000 mm/min
a_p = 1 μm

Equipment
WLI – 50x
Tool   Workpiece

a)

b)
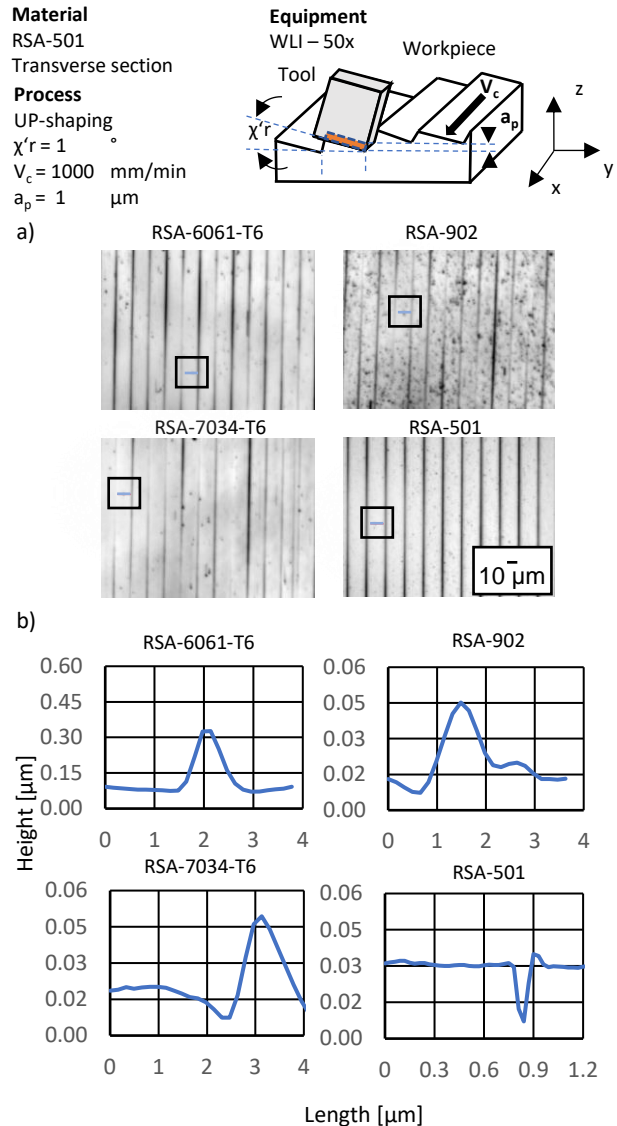
Figure 6.a) Grey scale images of UP-shaped surfaces of the RSA-alloys.
b) Profile of exemplary defects.

4. Discussion

Analysis of the chemically etched structures in Figure 3 reveals areas with a pattern on the material texture. These patterns are more evident in RSA-902 and RSA-501 and less evident in RSA-6061-T6 and RSA-7034-T6. Furthermore, the shape of these patterns is strongly related to the direction of extrusion. Therefore, such patterns on the material texture are characterized as flake structures. The hypothesis based on this observation is that these structures is formed due to two distinct mechanisms. The first mechanism is the reaction of the etching media with precipitations within the material, implying that the precipitations are concentrated in specific areas. The second possible mechanism considers the crystallization effects following the rapid cooling during the alloy's production. Specifically, during the ribbon formation process, prior to the hot isostatic pressing (HIP). During the production of the alloy, the molten alloy is poured on a rotating cooling copper wheel as illustrated in Figure 7 b). Depending on the pressure and speed of this wheel, ribbons with a specific thickness are rapidly created. The area of the initial contact of the molten alloy with the cooling copper wheel crystallises almost immediately.

It it is proven that the contact area with the wheel has smaller grains compared to the outer region of the ribbon in such rapid cooling processes [5]. What supports these mechanisms is that RSA-6061-T6 and RSA-7034-T6 do not show evident flake structures. The reason could be related to the post process heat treatment T6 on the alloy, in which the alloy is heat treated and aged at 150 °C. Therefore, the grains are allowed again to grow and to be more homogenous on the material texture. While the flake structures may seem not relevant for conventional or micro-machining processes, they are critical in ultra-precision machining. In processes where chip thickness can be in the sub-micrometre range, it is assumed that the non-uniform texture of the material will have different reaction during cutting. Therefore, generating defects over the surface of the material. Investigation concerning the influence of such flakes during cutting are still ongoing. To test this hypothesis, different material batches must be tested and more machining experiments are required.
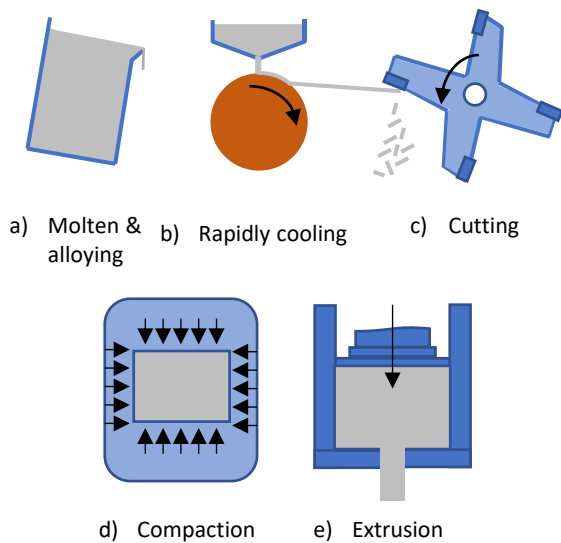
Figure 7. Production process chain of RSA-alloys.

At the polishing experiments, since the abrasive grain trajectory is not conducted in a definable path, it is expected that the cutting process occurs in all possible directions. Therefore, the influence of the achievable surface roughness regarding cutting orientation was not significantly different. The average grain size deviation between transversal and longitudinal direction were not significantly different from another. This experiment indicates the type of surfaces that can be achieved during a mechanical manufacturing process. However, there is still room for improvements of certain surface properties. Especially for RSA-902 further experiments must be conducted in order to assess the influence of the cutting parameters during the polishing process on surface formation.

Ultra-precision shaping experiments with relatively small undeformed chip thickness indicate the possibility to manufacture grating structures using RSA-501, RSA-7034-T6, and, to some extent, RSA-6061-T6. However, the inhomogeneities themselves still present a challenge for the cutting process with facetted diamond tools. Especially precipitations found within the alloys may cause hill-like ruptures. This phenomenon is observed more frequently in RSA-902. Flake structure and surface damage during cutting using facetted diamond tools cannot be correlated yet. However, it is expected that material textures with more concentrated precipitations would result in more defects during material removal. Also, considering the second supposition, areas of increased grain heterogeneity may lead to higher surface roughness by forming a step at the grain's borders. Literature

indicates this phenomenon is observed while machining aluminium AA6061-T6 [6].

5. Conclusion

The texture characterization of the investigated alloys reveals insights into potential undesired inhomogeneities within the alloys. Notably, the presence of flake structures and varied grain sizes could be limiting factors in achieving desired surface roughness through mechanical manufacturing processes. However, further experiments are necessary to substantiate this hypothesis.

Alloys developed by RSP Technology are emerging as promising candidates for use in the optical manufacturing industry. Of the optical materials studied, RSA-6061-T6 and RSA-902 demonstrate favourable surface properties for mirror applications. RSA-902 exhibits a higher roughness compared to RSA-6061-T6 and RSA-501, but there is potential for process optimization to enhance its surface property. Particularly in RSA-902, the presence of precipitations limits the attainable surface roughness in ultra-precision shaping processes. Detailed assessments of its precipitations' stoichiometry are needed for optimization. Employing ion beam etching techniques could potentially yield improved surface roughness compared to current results as shown by Hölzel, et al. [3].

In the category of high-strength alloys, RSA-501 stands out as a versatile material suitable not only for structured surfaces but also for mirror manufacturing. Its surface quality is comparable to that of RSA-6061. Additionally, in ultra-precision (UP) shaping processes.

6. Outlook

For further experiments, ribbons prior to the HIP process, and resultant alloys after HIP will be further analysed using the same methods as the ones discussed in this paper. The aim is to correlate grain size to ribbon thickness and its relation to flake structures appearance observed in this paper. This approach will allow the customization of RSA-alloys to improve the surface characteristics of these alloys.

Acknowledgements

References

[1] T. Newswander, B. Crowther, G. Gubbels, and R. Senden 2013 *Aluminum alloy AA-6061 and RSA-6061 heat treatment for large mirror applications*, Proc. SPIE 8837, Material Technologies and Applications to Optics, Structures, Components, and Sub-Systems, **883704**.

[2] D.A. Rolon, et al. *Suitability of Aluminium RSA-501 for manufacturing diffractive optical elements by shaping processes*. 2023 at 23st International Conference, EUSPEN.

[3] F. Hölzel, et al. 2023. Reactive ion beam smoothing of rapidly solidified aluminum (RSA) 501 surfaces for potential visible and ultraviolet light applications. Surfaces and Interfaces **38,** 102784.

[4] R. Steinkopf, et al. Optimization of diamond machined gratings for low light scattering and highest diffraction efficiencies. 2023 at 23st International Conference, EUSPEN.

[5] F. Palm, R. et al. Scalmalloy® = A Unique High Strength AlMgSc Type MaterialConcept Processed by Innovative Technologies for AerospaceApplications. PM2010 World Congress. PM Aluminiumn and Magnesium 2. 2010-

[6] R. G. Jasinevicius, et al. *Size effects in ultraprecision machining of aluminum alloys: Conventional AA6061-T6 and RSA 6061-T6*. 2021 in Journal of Manufacturing Processes **68**, Part B, 136-157.

Effect of electric fields on micro-scratching of calcium fluoride

Yunfa Guo[1], Jiaming Zhan[1]

[1]Department of Mechanical Engineering, College of Design and Engineering, National University of Singapore

guo.yunfa@u.nus.edu

Abstract

Electric field assistance has shown positive effectiveness in facilitating the machining of conductive materials (e.g., metals and alloys). However, the electric field effect on the manufacturing performance of non-conductive materials is less studied. In this study, an external electric field is employed in micro-scratching of a non-conductive ceramic material, single-crystal calcium fluoride (CaF_2). The electric field effect on the machinability of non-conductive CaF_2 was assessed by characterizing scratched surface morphology, critical load, scratch profile, and acoustic emission (AE) signals. Compared to conventional scratching, the scratched surface quality was improved with fewer cracks and surface defects after applying the electric field. The critical load that quantitatively identifies the position of ductile-brittle transition and crack formation was larger with the electric field. A smoother cross-sectional scratch profile and larger residual depth were observed with the assistance of an electric field. The lower AE amplitude with the electric field further suggests that the application of the electric field can effectively suppress brittle material removal of single-crystal CaF_2 in micro-scratching. The mechanism responsible for enhanced machinability of CaF_2 in the presence of an electric field was discussed based on the theory of electro-plasticity and further revealed by molecular dynamics simulations. This study deepens the comprehension of electric field-assisted machining technology in non-conductive materials and opens a novel path for improving the manufacturing efficiency of ceramic components.

Keywords: electric field, non-conductive materials, calcium fluoride, machinability, micro-scratching

1. Introduction

The machining efficiency is significantly influenced by the unique properties of workpiece materials, such as excessive plastic deformation in ductile metals [1,2] or high brittleness in ceramics and glasses [3,4]. These distinct material characteristics impose significant limitations on the machinability of materials with specific properties, hampering their broader application. Physical field-assisted machining provides a way to augment the machinability of difficult-to-machine materials by inducing targeted modifications in material properties and deformation behaviours. Typical physical fields employed in machining include electric field [5], magnetic field [6,7], and thermal field [8,9]. Compared to thermal field assistance, electric field and magnetic field can be readily implemented and controlled in existing machine tools, contributing to both improved processing revenue and a more environmentally friendly machining environment. In this paper, we conducted an original investigation to estimate the effectiveness of electric field assistance in micro-scratching of non-conductive ceramic material.

Electric field assistance has been successfully employed in various manufacturing processes for conductive metal alloys, which include wire drawing [10], sheet forming [11], sintering [12], forging [13], material joining [14], and rolling [15]. Positive improvements were observed in these manufacturing processes, e.g., reduction in forming and cutting forces, weakened elastic recovery, quicker ageing and recrystallization, increased formability, and lower specific energy for deformation. However, the advantages of electric field assistance have not been fully harnessed in the machining of non-conductive ceramics, let alone in the realm of precision micro-scratching. Furthermore, the thermal effects induced by electric current, such as joule heating, thermal softening, and thermal expansion, continue to be significant considerations in the study of conductive materials [16]. The existence of thermal effect makes it challenging to ascertain the role of the electric effect in the improvement of machining performance during machining of metals and alloys.

The literature on the positive impact of the electric field on conductive materials offers a potential application for the assistance of the electric field to enhance the machinability of non-conductive ceramics. Therefore, load-varying micro-scratching tests with and without the assistance of an electric field were performed in this paper. This work focuses on the influence of an electric field on non-conductive calcium fluoride (CaF_2) crystal during the scratching process, which is unlikely to involve thermal effects that potentially affect the results of the investigation. The electric field effect on the machinability of non-conductive CaF_2 crystal was assessed by characterizing scratched surface morphology, critical load, scratch profile, and acoustic emission (AE) signals. Subsequently, the material removal mechanism in electric field-assisted scratching of non-conductive CaF_2 was uncovered by the electro-plasticity theory and molecular dynamics (MD) simulations.

2. Methodology

2.1. Micro-scratching tests with electric field

Micro-scratching tests were carried out on an Anton Paar Step 300 - MCT³ Micro Combi Tester, as shown in Figure 1. A non-conductive ceramic material, (111) single-crystal CaF_2, was chosen as the case material to eliminate the thermal effects. The sample of (111) CaF_2 crystal was purchased from Latech Singapore with dimensions of 10 mm × 10 mm × 2 mm. Load-

varying micro-scratching tests, with and without the assistance of an electric field, were performed using a Rockwell indenter with a 100 μm radius. During scratching, the applied normal force increased linearly from 0.03 N to 1 N over a length of 1 mm, with a constant speed of 10 mm/min. The scratching direction was along the [11$\bar{2}$] crystallographic orientation of (111) CaF$_2$ crystal. A direct current (DC) power source generated the electric field, with an intensity set at 10 V/cm and aligned with the scratching direction.

Scratched surface morphology and scratch profiles were analyzed using the Olympus LEXT OLS5500 laser confocal microscope. The critical normal load, indicating the position of the ductile-brittle transition and the initiation of the first crack, was determined using integrated analysis software in the Micro Combi Tester. Additionally, AE signals during the scratching process were recorded with an AE sensor integrated into the Micro Combi Tester.
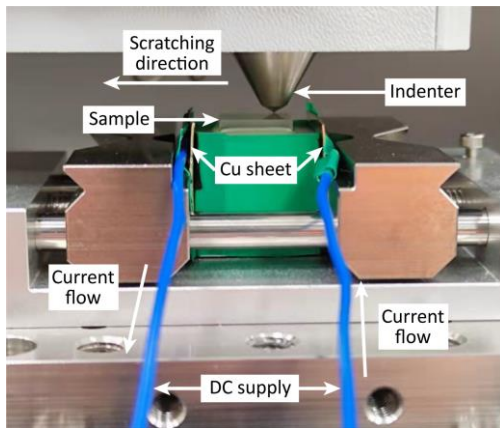
Figure 1. Electric field-assisted micro-scratching setup.

2.2. Molecular dynamics simulations

MD scratching simulation with the influence of electric field was conducted on CaF$_2$ crystal using the Large-scale Atomic/Molecular Massively Parallel Simulator (LAMMPS). Figure 2 displays the MD simulated scratching model of CaF$_2$ with a dimension of 50 nm × 23 nm × 13 mm along [11$\bar{2}$], [$\bar{1}$10], and [111] directions, respectively. The diamond indenter (spherical cap with a 12 nm radius of sphere) first penetrated the (111) surface of CaF$_2$ crystal. After the penetration depth reached 0.7 nm, the indenter maintained the depth for scratching along [11$\bar{2}$] direction with a constant speed of 100 m/s over a distance of 30 nm. During MD simulations, the Buckingham interatomic potential and Lennard-Jones potential [17,18] were respectively used to model the workpiece atom interaction and indenter-workpiece interaction. The external electric field was applied in MD simulated scratching in the form of Coulomb force ($F = qE$). In MD simulations, the electric field intensity and direction were defined as 1 V/nm and aligned parallel to the scratching direction. The discrepancy in electric field intensity between MD simulations and experimental results is attributed to the size effect and geometric factors [17].
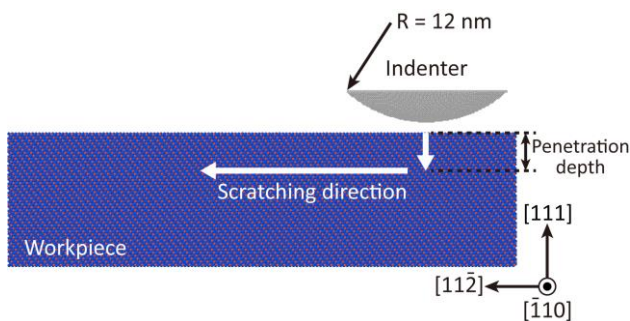
Figure 2. MD simulated model of scratching of CaF$_2$ crystal.

3. Results

3.1. Scratched surface morphology

Figure 3 shows the scratched surface morphology of CaF$_2$ crystal without and with the assistance of an electric field. The scratched surface was firstly covered with a damage-free region, i.e., ductile-removal region. With increasing normal load, defects and cracks started to appear on the scratched surface, i.e., the brittle-removal region. The brittle-removal region without the assistance of an electric field exhibited three types of defects: material peeling, lateral crack, and radial crack. It can be seen from Figure 3 that the application of the electric field enlarged the range of the ductile-removal region and delayed the crack formation (especially the material peeling) during the brittle-removal region.

As displayed in Table 1, the application of the electric field also increased the critical load for ductile-brittle transition and the first crack formation in micro-scratching of CaF$_2$ crystal. The critical load for the transiting point of the ductile-brittle region showed an increase of 52%, ranging from 630 mN without an electric field to 958 mN with the electric field. The critical load for the initial lateral crack rose from 949 mN to 958 mN with the introduction of an electric field. Similarly, the application of an electric field resulted in an escalation of the critical load for the first radial crack, increasing from 974 mN to 1000 mN. These results quantitatively indicate that electric field-assisted machining can significantly enhance the machining efficiency in achieving damage-free surfaces during micro-scratching of non-conductive brittle ceramics.
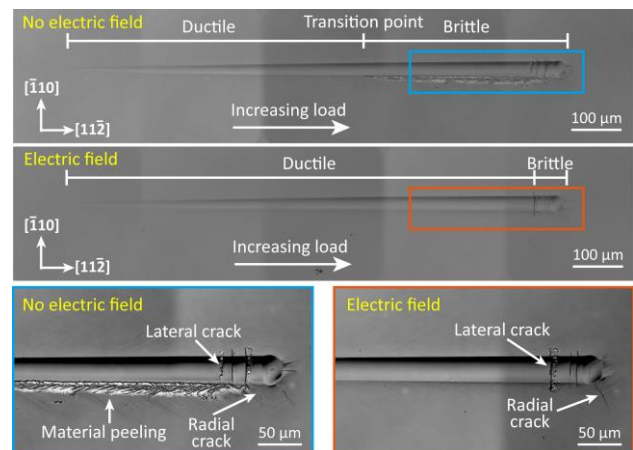
Figure 3. Scratched surface morphology without and with electric field.

Table 1 Critical load (mN) for ductile-brittle transition and the first crack formation without and with electric field.

Position	Critical load (mN)	
	No electric field	Electric field
Ductile-brittle transition	630 mN	958 mN
The first lateral crack	949 mN	958 mN
The first radial crack	974 mN	1000 mN

3.2. Scratch profile

Figure 4(a) presents the height image of residual scratch after micro-scratching under no electric field and electric field. As shown in Figure 4(a), cross-sectional scratch profiles were measured at three positions with different normal loads (400, 630, 900 mN), which respectively represent the positions of ductile removal, ductile-brittle transition, and brittle removal at electric-free condition. Figure 4(b) shows the distribution of cross-sectional scratch profile at three different normal loads without and with electric field. At the position with the applied load of 400 mN, smooth scratch profiles were observed

regardless of electric field conditions. When the applied normal load increased to 630 mN, the scratch profile without an electric field showed significant fluctuation at one side, which is attributed to the material peeling on the scratched surface. The fluctuation of the scratch profile at electric-free conditions increased at the higher normal load (900 mN). Conversely, the cross-sectional scratch at all three normal loads exhibited a smooth and stable profile with the electric field. The residual depth is an indicator of the plastic deformation degree. As recorded in Table 2, the cross-sectional residual depth increased with the electric field at all three normal loads. It suggests that the application of an electric field can augment the plastic deformation of CaF$_2$ crystal.
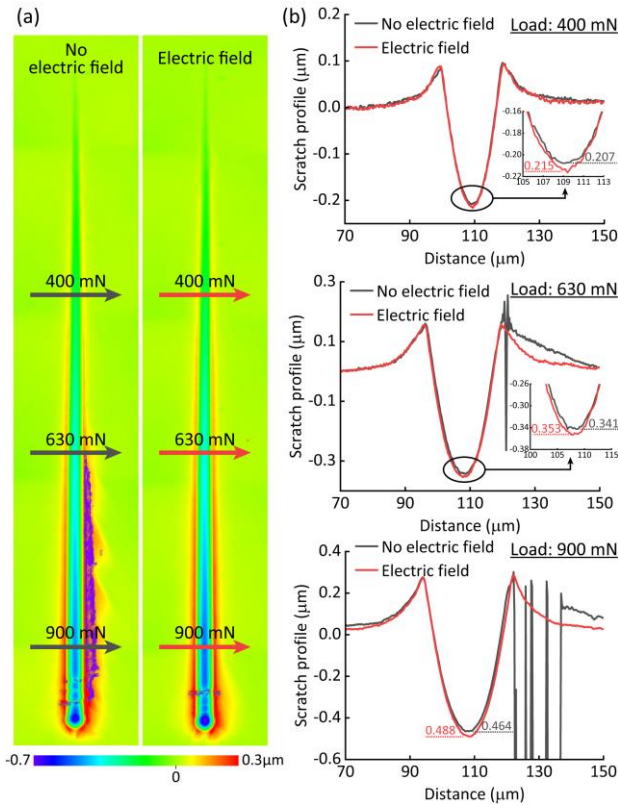
Figure 4. Scratch profile without and with electric field.

Table 2 Residual depth (μm) without and with electric field.

Applied normal load (mN)	Residual depth (μm)	
	No electric field	Electric field
400	0.207	0.215
630	0.341	0.353
900	0.464	0.488

3.3. Acoustic emission signals

The AE sensor is capable of capturing signals corresponding to the energy dissipated during the generation of a new surface, as defects and cracks form on both the surface and subsurface during micro-scratching [19]. Therefore, the amplitude of the recorded AE signals reveals the degree of crack formation in micro-scratching. Figure 5 illustrates the recorded AE waveforms without and with electric fields. The percentage of AE voltage in Figure 5 was determined by computing the ratio of the measured voltage to the fixed electronic circuit voltage within the AE sensor system, reflecting the amplitude of AE signals. As illustrated in Figure 5, the introduction of an electric field resulted in a reduction in AE amplitude (AE voltage). It further indicates that the electric field assistance can suppress crack formation and brittle material removal during micro-scratching of CaF$_2$ crystal.
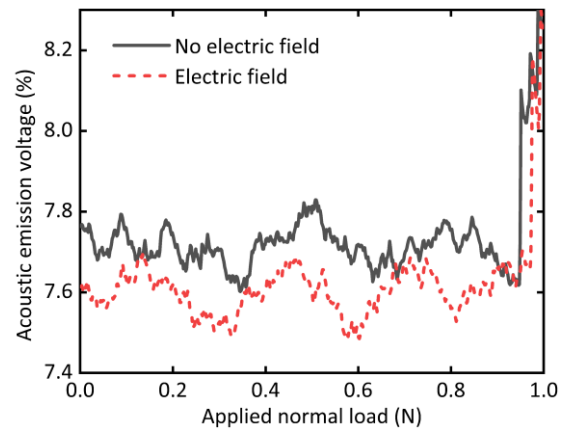
Figure 5. Acoustic emission waveforms during scratching without and with electric field.

4. Material removal mechanism

4.1. Electro-plastic effect

The ductile removal of crystalline ceramics in micro-scratching is governed by dislocation-dependent plastic deformation. Hence, the observed extension in the ductile removal region during scratching of CaF$_2$ crystal is believed to result from enhanced dislocation plasticity under an electric field. According to Conrad [20], the application of an electric field has shown a favourable potential to increase the plasticity of materials, even in non-conductive ceramics, which is defined as the electro-plastic effect or electro-plasticity. Two potential scenarios were used to expound the electro-plastic effect on dislocation plasticity [20]. On one hand, the application of an external electric field induces a force on charged dislocations via electrostatic Coulomb interaction. This, in turn, enhances the mobility of dislocations, enabling them to surmount obstacles that impede deformation. On the other hand, as illustrated in Figure 6, charged barrier-dislocation radical pairs can also be reoriented to a uniform orientation where the radical pairs transit from singlet state to triplet state under an electric field, which would lower the pinning force between barriers and dislocations to decrease the resistance for dislocation motion. As a result, improved dislocation motion under an electric field promotes plastic deformation, which further lowers stress concentration and suppresses crack formation for extending the ductile removal region and increasing the ductile-brittle transition in scratching of CaF$_2$ crystal. The results of MD simulations discussed in the next section will be employed to confirm the theory of electro-plasticity.
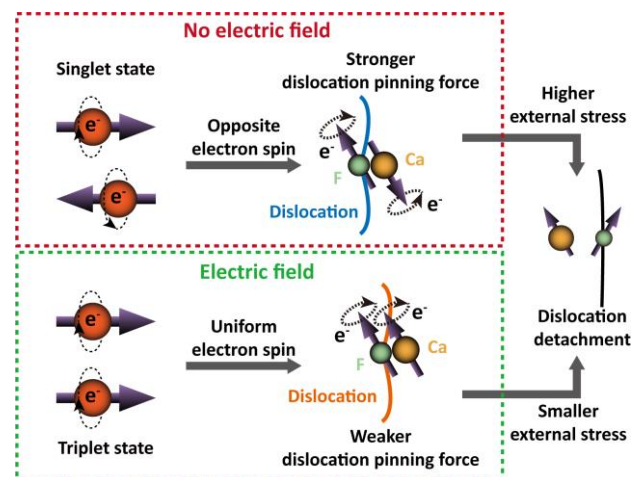
Figure 6. Enhanced dislocation movement due to the spin conversion of charged barrier-dislocation radical pairs under an electric field.

4.2. MD simulated material removal behaviours

Figure 7 presents the influence of the electric field on dislocation distribution at different scratching distances. During MD simulated scratching, dislocations mainly propagated along the penetration direction and scratching direction, which is governed by the primary dislocation slip systems {100} <110> of CaF$_2$ crystal [21]. The application of the electric field had a slight effect on the direction of dislocation propagation. Oppositely, the dislocation distribution range is significantly affected by the applied electric field. It is evident in Figure 7 that a larger range of dislocation distribution was observed during scratching with the assistance of an electric field. The result suggests that the applied electric field can promote the dislocation movement and plastic deformation of CaF$_2$ crystal. In addition, the total dislocation line length was also measured in Figure 8. The dislocation line length increased with increasing scratching distance regardless of electric field conditions, which is attributed to dislocation accumulation with new dislocation formation during scratching. Compared to the electric-free condition, the applied electric field increased the length of dislocation lines during the total scratching process, which reconfirms the enhanced plasticity with an electric field.
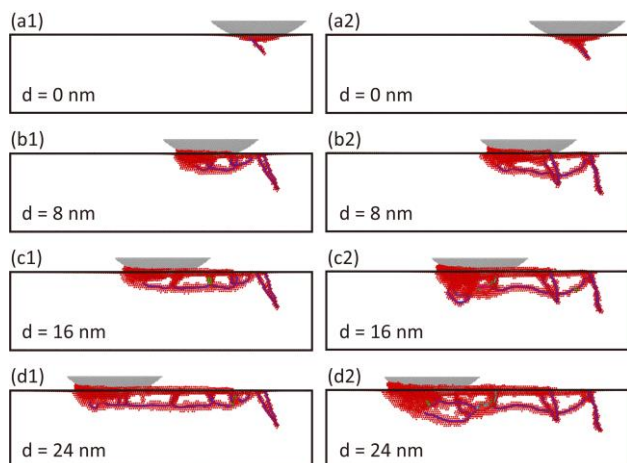
Figure 7. Representative MD snapshots of dislocation distribution at different scratching distances without electric field (a1-d1) and with electric field (a2-d2). The letter 'd' represents the scratching distance.
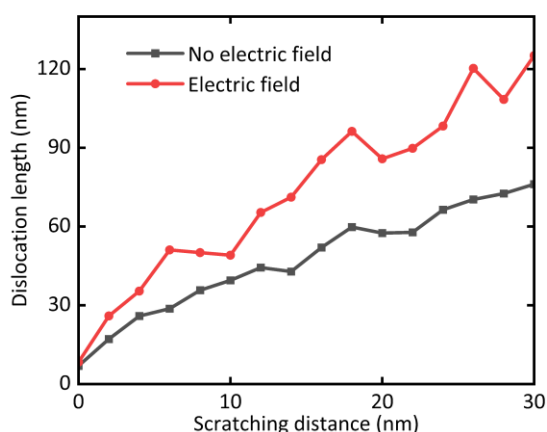
Figure 8. Dislocation line length during scratching without and with the electric field.

5. Conclusions

In this work, electric field-assisted micro-scratching tests and MD simulations were conducted to investigate the potential of electric field to enhance the machinability of a non-conductive ceramic material, single-crystal CaF$_2$. The contributions of this study are highlighted as follows:

(1) The application of electric field can result in a substantial reduction in surface damage and up to a 50% increase in damage-free machining load (i.e., ductile-brittle transition load) in micro-scratching of non-conductive CaF$_2$ crystal.

(2) The increased residual depth under the influence of an electric field signifies heightened plastic deformation in the CaF$_2$ crystal. The reduced AE amplitude with electric field suggests suppressed brittle fracture of CaF$_2$ crystal in micro-scratching.

(3) Based on the electro-plastic effect, electric field assistance facilitates the machinability of CaF$_2$ crystal by the electric field acting as a mediator that improves dislocation mobility through the Coulomb interaction and spin conversion.

(4) MD simulated scratching of CaF$_2$ crystal showed a broader distribution of dislocations and an augmented length of dislocation lines after applying the electric field. It provides additional support for the theory of enhanced dislocation mobility under the electric field effect (i.e., electro-plasticity).

The experimental and theoretical studies of the electric field effect on scratching of non-conductive CaF$_2$ crystal will provide guidelines for better design and development of precision machine tools equipped with a well-designed electric field environment for the efficient manufacturing of ceramics.

References

[1] Guo Y, Lee YJ, Zhang Y and Wang H 2022 *J. Mater. Sci. Technol.* **124** 121–134
[2] Chaudhari A, Soh ZY, Wang H and Kumar AS 2018 *Int. J. Mach. Tools Manuf.* **133** 47–60
[3] Guo Y, Lee YJ, Zhang Y, Sorkin A, Manzhos S and Wang H 2022 *J. Mater. Sci. Technol.* **112** 96–113
[4] Lee YJ, Kumar AS and Wang H 2021 *Int. J. Mach. Tools Manuf.* **168** 103787
[5] Bilal A, Jahan M, Talamona D and Perveen A 2018 *Micromachines* **10** 10
[6] Guo Y, Zhan J, Lee YJ, Lu WF and Wang H 2023 *Int. J. Mech. Sci.* **249** 108272
[7] Guo Y, Zhan J, Lu WF and Wang H 2024 *Int. J. Mech. Sci.* **263** 108768
[8] Wang H, Senthil Kumar A and Riemer O 2018 *Proc. Inst. Mech. Eng. Part B J. Eng. Manuf.* **232** 1123–1129
[9] Chua J, Zhang R, Chaudhari A, Vachhani SJ, Kumar AS, Tu Q and Wang H 2019 *Int. J. Mech. Sci.* **159** 459–466
[10] Tang G, Zhang J, Yan Y, Zhou H and Fang W 2003 *J. Mater. Process. Technol.* **137** 96–99
[11] Fan G, Gao L, Hussain G and Wu Z 2008 *Int. J. Mach. Tools Manuf.* **48** 1688–1692
[12] Langer J, Hoffmann MJ and Guillon O 2009 *Acta Mater.* **57** 5454–5465
[13] Jones JJ, Mears L and Roth JT 2012 *J. Manuf. Sci. Eng.* **134**
[14] Skovron JD, Ruszkiewicz BJ, Mears L and Abke T 2016 *Proceedings of the ASME 11th International Manufacturing Science and Engineering Conference*
[15] Li X, Wang F, Li X, Zhu J and Tang G 2017 *Mater. Sci. Technol.* **33** 215–219
[16] Dimitrov NK, Liu Y and Horstemeyer MF 2020 *Mech. Adv. Mater. Struct.* **29** 705–716
[17] Zhan J, Guo Y and Wang H 2024 *Int. J. Mech. Sci.* **261** 108693
[18] Zhan J, Guo Y and Wang H 2024 *J. Eur. Ceram. Soc.* **44** 1795–1805
[19] Gu X, Zhao Q, Zhang J, Guo B and Wang H 2020 *Ceram. Int.* **46** 26085–26099
[20] Conrad H 2000 *Mater. Sci. Eng. A* **287** 276–287
[21] Wang H, Riemer O, Rickens K and Brinksmeier E 2016 *Scr. Mater.* **114** 21–26

Advancing sustainable and efficient industrial cleaning: CO₂ snow jet blasting for residue-free surface cleaning

E. Uhlmann[1,2], J. Polte[1,2], P. Burgdorf[1], W. Reder[2], J. Fasselt[1]

[1]*Fraunhofer Institute for Production Systems and Design Technology IPK, Germany*
[2]*Institute for Machine Tools and Factory Management (IWF), Technische Universität Berlin, Germany*

philipp.burgdorf@ipk.fraunhofer.de

Abstract

Through the increase in importance of environmental consciousness due to legislature and social awareness, efficient though sustainable manufacturing processes are gaining in popularity. CO_2 snow jet blasting is a widely used technology for industrial cleaning and allows for sustainable cleaning in comparison to established traditional methods which often necessitate the use of water, chemicals or abrasive material leading to hazardous waste products. In contrast CO_2 snow jet blasting is a dry and residue-free cleaning process. The presented investigations examine the efficacy of CO_2 snow jet blasting in removing a reference contamination consisting of a mixture of grinding oil and abrasive borcarbide particles from 316L stainless steel and tungsten carbide surfaces. The influence of three process parameters was investigated, stand off distance s, jet angle α and traversing speed v_f. The cleaning performance was evaluated based on residual filmic and particulate contamination.The results show the capability of CO_2 snow jet blasting for industrial cleaning applications by removing of up to 99 % of contaminations.

Keywords: cleaning, CO_2, snow jet blasting, residue-free, sustainable cleaning,

1. Introduction

As a process variant of blasting with solid CO_2, CO_2 snow jet blasting is a dry and residue-free cleaning method. Currently only approximately 6 % of blast cleaning method users utilize CO_2 snow jet blasting, despite it being viewed, by users and suppliers, as a process with clear future potential. Furthermore many blast cleaning applications require a substrate drying process which is considered to be an important technological and economical aspect. This drying step can be entirely circumvented by CO_2 snow jet blasting [1]. During CO_2 snow jet blasting, liquid carbon dioxide is released from a nozzle at high pressure p and room temperature θ. The sudden drop in pressure Δp when exiting the nozzle causes a phase transition in which the liquid CO_2 converts into a mixture of gaseous CO_2 and solid CO_2 snow particles [2]. To increase the cleaning effect the CO_2 snow particles are further accelerated by a pressurised air stream with higher pressures equating to increased cleaning capabilities [3]. Some current cleaning methods necessitate the usage of various chemicals including ecologically harmful ammoniac solutions [4]. By reusing the CO_2 produced as a waste product in the chemical industry for the purpose of a cleaning medium and utilizing the resulting cascade, no new CO_2 is produced [5]. For a more environmentally friendly cleaning process the removal of a mixture of grinding oil and borcarbide abrasive from differing metal surfaces using CO_2 snow jet blasting was tested under experimental conditions. Generally cleanliness results should be evaluated regarding the necessary technical cleanliness of components or assemblies rather than cleaning as clean as possible, in order to reduce resource usage [6]. CO_2 snow jet blasting is often used to clean bonding and functional surfaces. Due to the low abrasiveness of the CO_2 snow particles, it is also suitable for cleaning finely structured and highly sensitive components in microelectronics and optics [7]. This paper presents the initial findings using CO_2 snow jet blasting for the cleaning of a reference contamination of a grinding process from 316L stainless steel and tungsten carbide metal surfaces. The used reference contamination consisted of a mixture of grinding oil and borcarbide particles of the size F320 and F1200. A cobalt bonded tungsten carbide was used within this paper with a cobalt content of $w_{CO} = 10$ wt. % and a grain size of $0.5 \, \mu m \le d_K \le 0.8 \, \mu m$. The influences of various process parameters are presented and their implications discussed based on the experimental data.

2. Methodology

Both examined materials were cleaned simultaneously to avoid possible errors and random influences. A consistent and defined movement of the nozzle was achieved by using a robot. The design and analysis of the experiments were done in Minitab.

2.1. Devices and setup

The CO_2 snow jet blasting was carried out using a single two-component concentric nozzle supplied with blasting media by the JetWorker system of the firm acp systems AG, Zimmern ob Rottweil, Germany, mounted to a six-axis robotic arm for routing purposes of the firm KUKA AG, Augsburg, Germany, of the type KR 10 R900-2. For the detection of residual surface contaminations, a fluorescence detector of the firm SITA Messtechnik GmbH, Dresden, Germany, of the type SITA CleanoSpector was used to detect filmic residues. Furthermore, a grazing light system of the firm PMT Partikel Messtechnik GmbH, Heimsheim, Germany, of the type PartSense 2.0 was used to detect particles left over after the cleaning process. The cleanliness of the substrate is classified based on two variables: the removed filmic contamination f_r and the removed particles p_r. The removed filmic contamination f_r is given in comparison to samples cleaned in an ethanol ultrasonic bath. The removed particles p_r are calculated in relation to the initial contaminated state. On average the contaminated samples

showed a Component Cleanliness Code (CCC) according to ISO 16232 of A(B18/C18/D19/E16/F11/G9/H10/I9/J9) for stainless steel and A(B19/C19/D19/E15/F12/G11/H12/I10/J9) for tungsten carbide before cleaning.

2.2. Design of experiments

To achieve an efficient cleaning process, multiple process parameters were held constant, including air pressure p, capillary diameter d_k, and path spacing a. The air pressure p and capillary diameter d_k were set to the corresponding maximum settings to achieve a strong cleaning effect, increasing both the mechanical and thermal influence of the CO_2 snow jet blasting on the contamination and substrate [2]. The path spacing was set to a = 3.5 mm. The varied process parameters include the nozzles stand off distance s, the jet angle α and the traversing speed v_f. The process parameters and routing of the cleaning nozzle are shown in figure 1. Based on the different settings, a full factorial design was created encompassing a total of 18 runs for each material. The experiments were repeated 2 times leading to 108 runs.
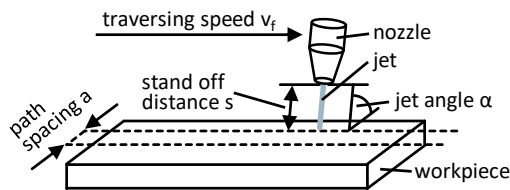
Figure 1. Experimental setup and procedure

3. Results and discussion

Figure 2 shows the removed filmic contamination f_r in correlation with the jet angle α. The results indicate a significant increase in cleanliness by up to 10 % through adjustment of the jet angle from α = 90° to α = 45°. It is important to note that the jet angle is not tilted along the path, pushing contamination ahead but rather perpendicular to the path line, as displayed in figure 1. The disparities in results between carbide and stainless steel might be due to differing surface structures or adhesion capabilities of the substrate.
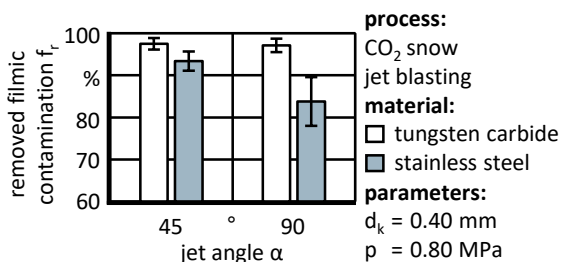
Figure 2. Results of the removed filmic contamination f_r in correlation with the jet angle α

Figure 3 shows the removed filmic contamination f_r corresponding to the the stand off distance s. A matching correlation between the filmic contamination f_r and the stand off distance s is not apparent for the investigated materials.
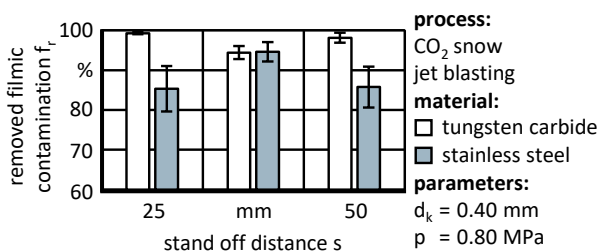
Figure 3. Results of the removed filmic contamination f_r in correlation with the stand off distance s

Figure 3 shows a convex curve of the removed filmic contamination f_r over the stand off distance s for carbide and a concave curve for stainless steel. The correlation between the removed particles p_r and the traversing speed v_f, shown in figure 4, indicates an increase in cleaning capabilities through decreasing the traversing speed v_f. Lower traversing speeds v_f equate to extended exposure durations of substrate and contamination to the CO_2 snow jet. While the averaged measured data between maximal and minimal settings only varies by approximately 2 % a trend is observable. Through increasing the step size between settings of the traversing speed v_f larger influences should become apparent.
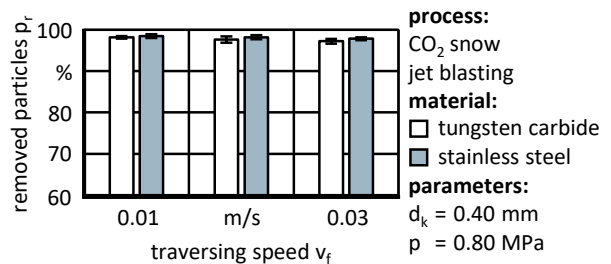
Figure 4. Results of the removed particulate contamination p_r in correlation with the traversing speed v_f

4. Conclusion

For all parameter combinations, 83 % - 99 % of filmic and particulate contaminants were removed. When only considering the parameter combinations with v_f = 0.01 m/s and α = 45° an averaged CCC for particulate contaminations according to ISO 16232 of CCC = A(B14/C13/D12/E7) was achieved for stainless steel and CCC = A(B12/C12/D12/E10/F6/G5/H7) for tungsten carbide surfaces. The investigations show that CO_2 snow jet blasting is suitable for the different material/contaminant combinations, although the process parameters must be adjusted according to the combination. The influence and interaction of contaminant and material need to be analysed in further studies. Many machining processes lead to grease, oil and particulate residues on the substrate surface. This necessitates cleaning steps after machining to not influence further manufacturing steps or the functionality of the final product. For this CO_2 snow jet blasting can be a valid alternative to common chemical cleaning methods, as shown in this paper. The cleaning of other surface level filmic and particulate machining residues should be further investigated, to provide functional alternatives to common, environmentally harmful, cleaning methods.

References

[1] Rögner F, Pfeilschifter M, 2021 Markt- und Trendanalyse in der industriellen Teilereinigung. Geschäftsbereich Reinigung bei Fraunhofer.

[2] Kretzschmar M, 2017 CO2-Schneeentstehung und deren Wirkung auf die Effekte beim CO2-Schneestrahlen. Berlin, Fraunhofer Verlag.

[3] Uhlmann E, Hollan R, 2015 Blasting with Solid Carbon Dioxide – Investigation of Thermal and Mechanical Removal Mechanisms. Procedia CIRP 26 (2015) 544 – 547.

[4] Sareminia G, Zahedi F, Eminov S, Karamian A, 2011 Cleaning method of InSb [$\overline{1}\overline{1}\overline{1}$] B of n-InSb [111] A/B for the growth of epitaxial layers by liquid phase epitaxy.

[5] Uhlmann E, Polte J, Burgdorf P, Reder W: Nachhaltige Oberflächenbehandlung und Präparation. VDI-Z (2024) Edition: 01/02-2024, 43–45.

[6] Tammer C, Schießl T, Burgdorf P, 2023 Brennstoffzelle – wie sauber muss es sein? JOT Journal für Oberflächentechnik 60 – 61.

[7] Krieg M, 2008 Analyse der Effekte beim Trockeneisstrahlen. Berlin, Fraunhofer Verlag.

Influence of drilling depth and feed per tooth on burr formation when micro drilling

Sonja Kieren-Ehses[1], Felix Zell[1], Benjamin Kirsch[1], Jan C. Aurich[1]

[1]Institute for Manufacturing Technology and Production Systems, RPTU Kaiserslautern, Gottlieb-Daimler-Str., 67663 Kaiserslautern, Germany

sonja.kieren-ehses@rptu.de

Abstract

Micro drilling is a common process to manufacture micro holes. However, micro drilling is characterized by burr formation at the drill entry and exit. Deburring is not possible or only possible with great effort. For this reason, burr formation must be avoided or minimized by appropriate selection of the process parameters.

In this paper, the burr formation when micro drilling is investigated. Micro drilling tests were carried out using uncoated cemented carbide micro drills with a diameter of 100 μm. When machining brass, the drilled hole depth and feed per tooth were varied. Burr formation and manufacturing accuracy were analyzed. In particular, the burr height, the burr width, and the diameter-deviations of the hole were considered. The results are discussed and recommendations for micro drilling of brass are given to enhance the process efficiency and the functionality of the components.

Micro drilling, manufacturing accuracy, burr formation

1. Introduction

Micro drilling is widely used in industrial applications [1]. In many cases, the quality of the micro drilled holes determines the functionality of the components. Micro drilling is characterized by burr formation at the drill entry and exit [2]. Due to the high cutting edge radius r_β to chip thickness h ratio (r_β/h ratio), drilling with these tool sizes is characterized by squeezing and friction processes [3], which result in burr formation. Subsequent deburring is not possible or only possible with high efforts. This results in the need for knowledge of chip and burr formation as a function of the process influencing variables (e.g. cutting edge radius, chip thickness/feed per tooth) to reduce burr formation and finally increase the hole quality.

This paper focuses on the investigation of the influence of the parameters drilling hole depth and feed per tooth on the burr formation and the diameter of micro holes when using micro drills with a diameter of 100 μm.

2. Experiments

2.1. Experimental setup, tools, and workpiece material

The tool used for the micro drilling tests was a single edged uncoated micro drill made of cemented carbide with a diameter of 100 μm (manufacturer: Prestera[1]). The micro drill had a drill-point angle of 120°, a helix angle of 0° and a flute length of 700 μm. SEM images of the tool used is shown in Figure 1.

The micro drilling tests were carried out on the micro milling center (MMC), a desktop sized machine tool developed at the Institute for Manufacturing Technology and Production Systems at the RPTU Kaiserslautern. The air-bearing spindle (spindle speed range 10,000 rpm-125,000 rpm) has a maximum run-out of 2 μm at the applied spindle speed of 30,000 rpm.

The workpiece material used for the micro drilling experiments was brass (CuZn39Pb2) with a size of 10 mm x 20 mm x 3 mm. Prior to micro drilling, the workpiece was face milled with an end mill with a diameter of 3 mm.
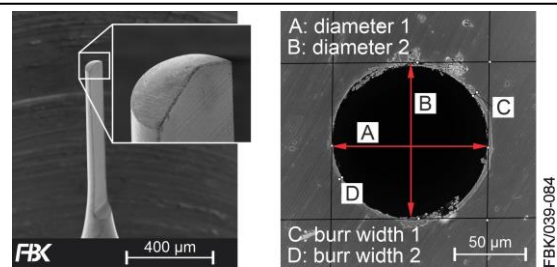
Figure 1. Micro drill with a diameter of 100 μm used for the experiments and exemplary evaluation of a drilled hole.

2.2. Cutting parameters

In the experiments the drilled hole depth and the feed per tooth were varied each at three levels: the drilled hole depths 50 μm, 100 μm, and 150 μm and the feed per tooths (f_z) of 0.05 μm, 0.5 μm, and 1 μm were considered. The spindle speed of 30,000 rpm was kept constant. Each parameter combination was repeated three times. The order of the tests was randomized. All tests were carried out with one tool. The tool was not unclamped during the experiment, which means that the influence of the clamping error on the run-out and therefore the effective diameter of the tool is constant. This allows to analyze the influence of the varied parameters on the burr formation and the diameter of the hole in the best possible way. Due to the in total very short feed travel, a significant influence of abrasive wear on the process results can be excluded.

2.3. Experimental procedure

First the spindle was warmed up for 10 minutes. The feed travel of the micro drill inside the workpiece is composed of the distance until the drill tip completely entered the workpiece and the drilling depth itself. The movement of the micro drill outside the workpiece was chosen sufficiently long to ensure that the acceleration of the axis is completed when the micro drill enters the workpiece.

2.4. Measurement technology

To analyze the burrs and the diameter of the drilled hole, confocal microscope images were taken using a Nanofocus[1]

OEM microscope. A 60x objective lens with a numerical aperture of 0.9 was used. The measuring field was 268 µm x 268 µm.

The width and height of the burrs and the diameter of the hole were analyzed using the software MountainsMap[1]. The diameter was measured in X- and Y-direction (see Figure 1). Out of these two values the mean value and the deviation to the nominal diameter of 100 µm was calculated. The burr height is the maximum burr height. The burr width, which represents the uniform bead around the drilled hole, was measured at two different points. As for the diameter, a mean value out of these two values was calculated.

3. Results and discussion

3.1. Burr height and width
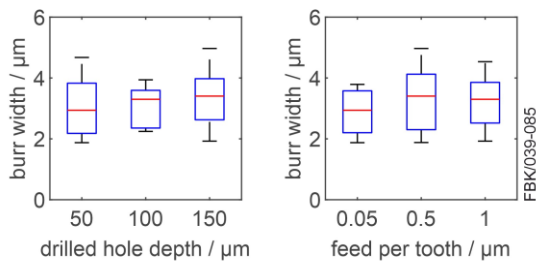
Figure 2. Burr width depending on drilled hole depth and feed per tooth.

Figure 2 shows that there is only a slight increase in burr width with increasing drilled hole depth. The median increases from 2.9 µm at a drilled hole depth of 50 µm to 3.4 µm at a drilled hole depth of 150 µm. However, the scatter of the measured values remains the same. The feed per tooth has no notable influence on the burr width.
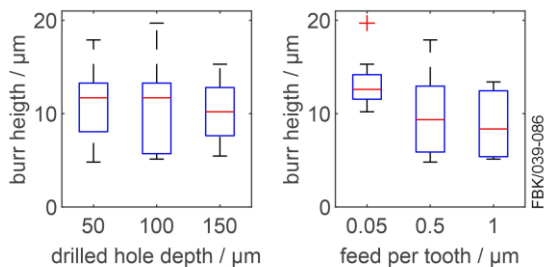
Figure 3. Burr height depending on drilled hole depth and feed per tooth.

Figure 3 shows that the drilled hole depth only has small influence on the maximum burr height. The median decreases from 11.7 µm (50 µm) to 10.2 µm (150 µm). However, a clear impact of the feed per tooth is recognizable in the burr height. The median of the maximum burr height decreases from 12.6 µm to 9.4 µm (f_z = 0.05 µm increased to 0.5 µm), which corresponds to a reduction of 25 %. At the same time, the scatter of the values has increased. Between 0.5 µm and 1 µm there was a further slight reduction in the median of the burr height. The reason for the reduction in burr height is probably the exceeding of the minimum chip thickness between a feed per tooth of 0.05 µm and 0.5 µm, which results into a better chip separation and less ploughing.

3.2 Diameter deviation

Figure 4 shows that there is an increase in the scatter of the measured values of the diameter deviation with increasing drilled hole depth. In contrast, the median stays at the same level (7.5 µm) from a depth of 50 µm to 100 µm and increases at 150 µm to 12.0 µm. In general, it can be observed that the measured diameters are higher than the nominal diameter of

100 µm. This deviation cannot be attributed to the run-out of the spindle.

As the drilling depth increases, more chips must be removed out of the hole. Since the tool has no helix, it is possible that the chips are not removed out of the hole sufficiently fast, resulting in squeezing processes on the circumference of the drill and increasing temperatures. This could lead to built-up edges resulting in an increase in the effective diameter.
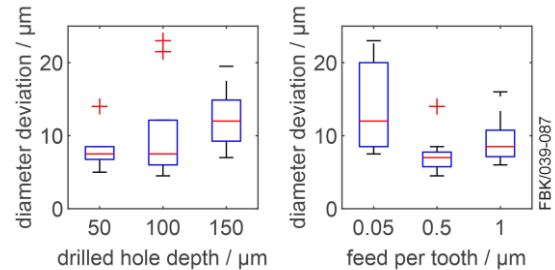
Figure 4. Diameter deviation depending on drilled hole depth and feed per tooth.

In contrast to the drilled hole depth, the scatter of the measured values of the diameter deviation decreases with increasing f_z. The lowest median with 7.0 µm was achieved with the central f_z of 0.5 µm. The highest median with 12.0 µm occurred at f_z = 0.05 µm. The reduction in diameter deviation is probably due to the lower amount of ploughing at 0.5 µm compared to 0.05 µm, which results in less adhering material at the tool. With a further increase of f_z to 1 µm, the chip cross-section is further increased, which leads to a higher load on the micro drill.

4. Conclusion and outlook

In this paper, micro drilling with a single-edged 100 µm diameter tool was examined. The focus was on burr formation and diameter deviations when machining brass. The drilled hole depth and the feed per tooth were varied each at three levels.

The results show that the drilled hole depth has no influence on the burr formation, but on the diameter variation. The feed per tooth has no influence on the burr width, but on the burr height. The diameter deviation was positively influenced by rising feed per tooth.

These first studies show that the hole quality in micro drilling can be improved by adjusting the drilling parameters. In further studies, the parameter field will be extended and also through-holes as well as drilling cycles will be examined.

Acknowledgements

[1] "Naming of specific manufacturers is done solely for the sake of completeness and does not necessarily imply an endorsement of the named companies nor that the products are necessarily the best for the purpose."

References

[1] Yoon H-S, Moon J-S, Pham M-Q, Lee G-B and Ahn S-H 2013 Control of machining parameters for energy and cost savings in micro-scale drilling of PCBs *Journal of Cleaner* Production **54** 41–48

[2] Bhandari B, Hong Y-S, Yoon H-S, Moon J-S, Pham M-Q, Lee G-B, Huang Y, Linke B S, Dornfeld D A and Ahn S-H 2014 Development of a micro-drilling burr-control chart for PCB drilling *Precision Engineering* **38** 221–229

[3] Klocke F, Gerschwiler K and Abouridouane M 2009 Size effects of micro drilling in steel *Prod. Eng. Res. Devel.* **3** 69–72

Comparison of different approaches towards measuring cutting edge radius and geometry on ultra sharp diamond and cbn tools

Jindrich Sykora[1, 2], Marvin Groeb [2]

[1]*Department of Machining Technology, University of West Bohemia, CZ [2] Kern Microtechnik GmbH, DE*

sykora@fst.zcu.cz

Abstract

To achieve high quality surface finishes, cutting tools with low cutting edge waviness and sharp cutting edges are needed. Commonly, polished monocrystalline diamond tools are used. The size of the optimal cutting edge radius (RE) and micro geometry is highly dependent on the material to be machined. Generally, a smaller RE is suitable for soft materials like copper or aluminium,but brittle materials require a higher value which ensures effective negative rake. Furthermore, the actual RE value is a critical component for setting up process parameters when brittle materials are machined. Currently, the measurement of the RE of ultra sharp tools remains challenging. Ordinarily, the values of RE fall within the range of tens to hundreds of nanometres. Measurement using optical methods is not viable as the diffraction criteria of visible light limits the resolution to effectively larger values than the RE to be measured, while the reflectivity and transparency of polished diamond hinder effective confocal measurements. Consequently, tool manufacturers are generally unable to provide an RE value for a given tool. The current state of the art approach for the measurement is a reversal method. For this, an impression of the cutting edge in a soft material (i.e. copper) is created using a dedicated device and the reverse artefact of the cutting edge is analysed. Currently, the measurements are conducted using atomic force microscopy (AFM). The indentation depth and sidewall angles that can be measured with this approach are limited. In this research, a high precision machining centre is used to generate the reverse artefact, allowing for simple industrial implementation of this technique. Furthermore, additional methods for indentation measurements are explored. These include a combination of focused ion beam (FIB) milling, scanning electron microscopy (SEM) evaluation and direct SEM evaluation of a platinum sputter coated cutting edge. Cutting edge radii with double digit nanometric dimensions have been successfully evaluated using this novel approach.

diamond tool, tool geometry, cutting edge, measurement, scanning electron microscope (SEM), atomic force microscopy (AFM)

1. Introduction

For high quality surface finishes, polished tools with a low cutting edge waviness are needed. Traditionally, these tools are crafted from monocrystalline diamond (MCD); however, alternative materials such as binderless polycrystalline diamond (BL-PCD) or cubic boron nitride (CBN) are increasingly being utilized [1], [2]. Generally, the cutting edge radius (RE) of polished MCD tools falls within the 20-200 nm range and they generally have a 0° rake angle.

To achieve sufficient surface quality when machining hard and brittle materials such as monocrystalline silicon or silicon carbide, it is essential to operate within the ductile cutting regime [3]. This regime is achieved as a combination of hydrostatic pressure, sheer strain and elevated temperature in the cutting zone (primary deformation zone) [4]. The nature of this state is a direct result of tool geometry and mostly the effective rake angle. Which typically has to have a negative value [5], [6].

The effective negative rake can be either generated by an actual rake angle or by selecting an appropriate combination of RE and maximum chip thickness (Hm) value [7]. Therefore, in the context of machining hard and brittle materials in a ductile cutting regime, accurate knowledge of the cutting edge radius of a tool is imperative for the proper configuration of machining parameters, with particular emphasis on the Hm [8], [9], [10]. For these reasons, the evaluation of the cutting edge radius of the cutting tool is a critical factor.

The state-of-the-art approach uses direct and indirect atomic force microscopy (AFM) measurement of the RE. The direct AFM measurement requires a laborious alignment process and the risk of cantilever tip damage is significantly high. Hence, the indirect approach (reversal method) is being explored. The cutting edge of the tool is indented into a soft and ductile workpiece and the resulting indentation is analysed. [11], [12]

Direct optical measuring methods cannot be used due to the optical diffraction limit of light used in the measuring devices. This limits the lateral resolution to 10 nm which is insufficient considering the typical RE values of the evaluated tools [12]. Moreover, the spatial resolution, restricted by the Abbe limit, is also inadequate. The reflectivity and transparency of polished diamonds hinder effective confocal measurements.

This study investigates the feasibility of measuring RE in ultra sharp polished cutting tools using diverse methodologies. The assessment involves SEM techniques and the application of a reversal method. The outcomes obtained from the reversal method are further analysed through AFM and a combination of FIB cutting and SEM analysis.

2. Materials and methods

Two distinct approaches were used to measure the RE in this work. Initially, the possibility of evaluating the tool directly using SEM was explored. The MCD tools were coated with 20 Å of platinum and subsequently analysed. Firstly, the ball milling tool was angled in a 5-axis SEM so that the electron beam was tangent to the analysed section of the cutting edge.

Consequently, the focal plane was adjusted to the point where the electron beam tangentially intersected with the ball mill (see Figure 1). Secondly, a direct cutting edge analysis was carried out of a damaged section of the tool. A chip in the cutting edge effectively provides a cross section of the tool.
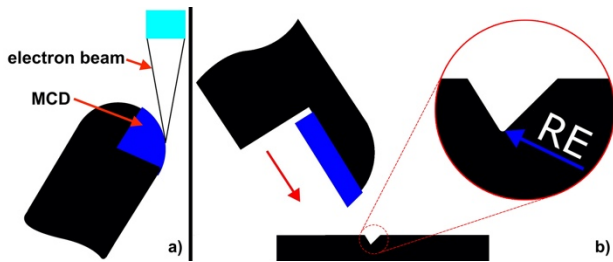
Figure 1. a) Setup of the tangential direct SEM measurement and b) schematic diagram of the indentation procedure – the red arrow shows the feed motion

Subsequently, a reversal method is investigated. The cutting edge of a stationary tool is pressed into a soft workpiece, similar to indentation hardness tests. The tools were indented into a 99% pure copper workpiece with an indentation depth of 5 μm. This material has a combination of high density, large Young's modulus and low yield strength, which is a favourable combination of characteristics for this purpose [13]. As a result, the elastic deformation after the indentation will be minimal [13]. Drawing upon the research conducted by Zhang et al., the impact of elastic deformation on measurement results falls within the low single-digit nanometer range. They found that for indentation depths larger than 200 nm the elastic recovery can be ignored [12]. Furthermore, the chemical interaction between the tool and the copper workpiece should be minimal.

Prior to the indentation procedure, the face of the part was fly cut with an MCD tool to achieve a single digit nanometric surface. The indentations were performed on a Kern Micro HD precision CNC machining centre, which provides a positioning accuracy to within 1 μm. All of the evaluated tools have a flat rake (i.e. no helix) and a single flute and were held in the spindle in a standard powRgrip holder. The length of the tools was set using a Blum laser tool setter and finetuned by milling a flat surface at a location measured by a touch probe. The spindle angulation was found using a dial test indicator swept over the rake and the position held through the NC control. The indentation was performed at a speed of 5 mm/min with a 1 s dwell time at the final depth. The cutting edges of all the tools were inspected pre and post indentation and process induced damage was not found.

Three specific tools were evaluated: tool A ('Standard') was an MCD tool which was a 6.206 mm MCD ball mill with a 0° rake from Contour Fine Tooling BV; tool B was a new, 6 mm MCD ball mill with a -30° negative rake and a chemically assisted rake finishing process from Edge Technologies; and tool C was a new, 2 mm BL-PCD ball mill with a 0° rake and polished rake and flank from SUMITOMO ELECTRIC Hartmetall GmbH. Because the evaluated tools are ball mills, the resulting reverse artefact to be evaluated is a V groove (see Figure 2), which gets gradually shallower towards one end. Therefore, the depth of the indentation can be in the range of μm at the tip even if the depth requirement for the evaluation is in the tens of nanometres range.
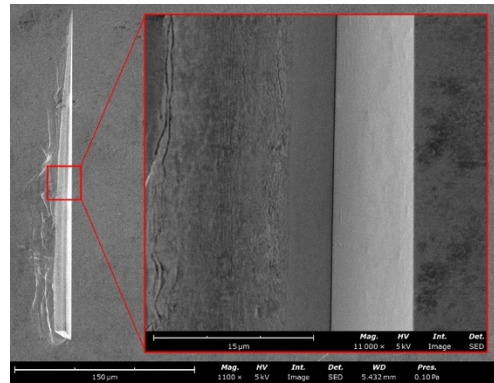
Figure 2. Top view of the indentation made with tool A

The AFM measurement of indentations is done using the Park Systems NX20 in non-contact mode. The lateral imaging resolution was set to 4.88 nm. The AMF probe limitation has to be taken into account for cutting tools with a 0° rake angle either by measuring indentations shallower than the RE or indenting the workpiece at an angle. Here the cutting tools with a 0° rake angle were indented with a B axis angulation of 35°, while the spindle was oriented appropriately as shown in Figure 2 b). As a result, the indentation features walls angled over 90° from the top face, allowing access for the AFM probe tip.

The second approach to evaluating the indentations was a combination of FIB milling and SEM imaging using the In-Beam SE detector. The analysis was done on a Tescan XEIA3. Before the FIB milling the area was coated with platinum to reduce process-induced damage of the surface as well as the curtaining effect. Figure 3 shows the entire sequence of steps where the surface is firstly coated with platinum and subsequently the FIB cut is made at a specified location.
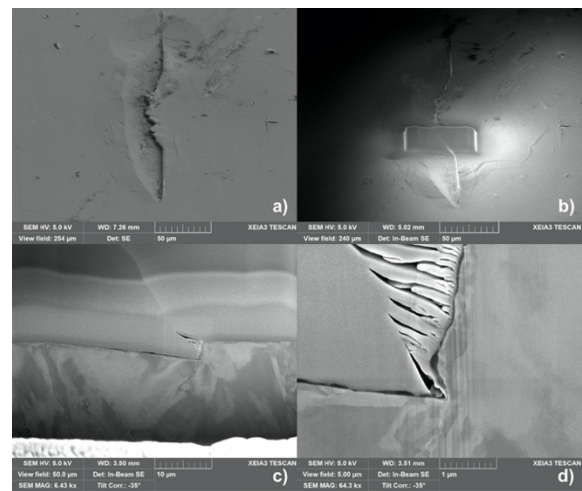
Figure 3. The sequence of the SEM analysis: a) the raw indentation in the workpiece, b) coated with platinum, c) a side view of the indentation and d) a micrograph of the cutting edge with a view field of 5 μm. Note that this analysis method is not limited by the geometry of the indentation.

3. Results and discussion

3.1. Direct measurement of MCD

Using the direct SEM approach has a smaller risk of damaging the cutting tool during the analytical process. Apart from manipulation, coating and the electron beam, there is no interaction with the tool. The results from the direct SEM analysis with the tangent approach are displayed in Figure 4. The mean RE value measured with this method was 146 nm with standard deviation (SD) of 7 nm at a point 30° from the tool rotation axis. However, this approach has several drawbacks. Precision is crucial in placing the focal plane precisely where the

electron beam is tangential to the cutting edge, which is a task heavily reliant on the operator's precision and highly susceptible to human error. The rotation of the tool along its axis is another critical step, greatly dependent on the operator and impactful on the results. Furthermore, the section of the cutting edge above the focal plane causes blurring due to electron beam blockage, diminishing the clarity of the measured feature.

This method is straightforward in terms of preparatory steps, but its precision and repeatability are constrained because the correct focal plane setting which affects the results is susceptible to operator error. Therefore, all the samples should be analysed by the same person with meticulous care to ensure the validity of the results. This method is better suited for comparing several significantly different tools rather than for precise measurements.
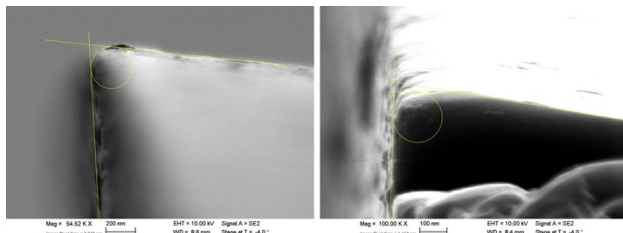
Figure 4. a) Direct measurement of the RE using the SEM beam tangent to the ball mill and b) direct measurement of the RE at a chipped section of the cutting edge – tool A.

SEM imaging of a section of the cutting edge damaged by chipping offers a clear visual representation of the cutting edge shape (effectively a cross section), and finding the correct focal plane is more straightforward with this method. However, it is only suitable for the analysis of used and damaged tools. Additionally, the section of the cutting edge that is to be analysed cannot be freely selected. Any measurement results will have to be corrected if the imaged plane is not normal to the cutting edge.

The direct RE measured at the chipped section (see Figure 4 b)) of a used MCD tool (tool A) was 89 nm with SD of 3 nm. This value aligns with the edge reversal method (FIB-SEM) in which the same section of the cutting edge was measured, yielding a value of 88 nm with SD of 2 nm. In the same setup, this approach can be employed for comprehensive wear analysis of tools, as wear marks (e.g. VB wear, chipping of the cutting edge) are visible and measurable. Larger sections of the cutting edge can be evaluated than the single cross section in the FIB-SEM reversal method.

3.2. Measurement using the reversal method

3.2.1. Evaluation of RE using AFM

The combination of the indentation method and AFM measurement as demonstrated by Zhang et al. and Chen et al., involves a dedicated nanoindentation device with a depth setting below 200 nm [9], [10]. One of the disadvantages of measuring deep indentations is that AFM probes with a high aspect ratio need to be used and that a significant height difference between the original surface and the indentation might influence the result and cause damage to the probe. Therefore, here a shallow section of an indentation left by a circular cutting edge is scanned.

Even with a shallow section the material displaced around the indentation and the resultant burrs (see Figure 2) hinder the measurement process. The resulting scans do not follow the expected shape of the indentation and show a significantly higher RE than the other methods (leading to improbable values). It was also found that this measurement method is sensitive to the meticulous alignment of the sample as well as its cleanliness. Future research should focus on resolving the deficiencies in the current understanding of RE AFM measurement, specifically its process parameters, challenges, and optimal settings. Owing to these complexities, further exploration of this method was not pursued.

3.2.2. Evaluation of RE using FIB-SEM combination

Evaluation of the cutting edge radius combining the reversal method and FIB with SEM imaging provides a clear image of the micro geometry for a given cross-section. The procedure is definitive and replicable. This method can be used for any tool material and the precision of the edge radius is limited only by the SEM resolution. Unlike AFM this measurement is not constrained by the geometry of the indentation. For instance, tool C underwent indentation with a rake face perpendicular to the top surface of the copper workpiece, and the corresponding evaluation is depicted in Figure 5 b).
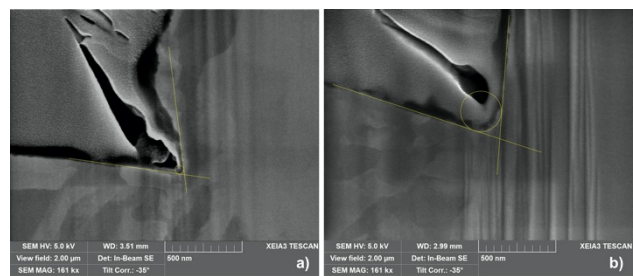
Figure 5. Evaluation of the RE of a) tool A and b) tool C with rake face indented perpendicular to the top face of the copper workpiece

It is worth noting that only a single cross-section of the cutting edge can be imaged at a time. This limitation restricts the possibility of averaging, a common practice in standard RE evaluation with optical methods. In further research a series of FIB cuts and SEM measurements could be done to achieve the averaging effect and obtain a more comprehensive analysis of a cutting edge section. Furthermore, the observation of tool wear is not as straightforward as other methods, even though the change in the rake angle caused by VB tool wear is still clearly noticeable (see Figure 6).

All three tools are assessed with this method, with tool A intentionally evaluated at a spot where a significant portion of the cutting edge is chipped away. This spot exhibits the smallest RE, allowing for the evaluation of the resolution limit of this method. The resulting RE 27 nm with SD of 3 nm for tool A at this specific section, can be determined from Figure 5 a).
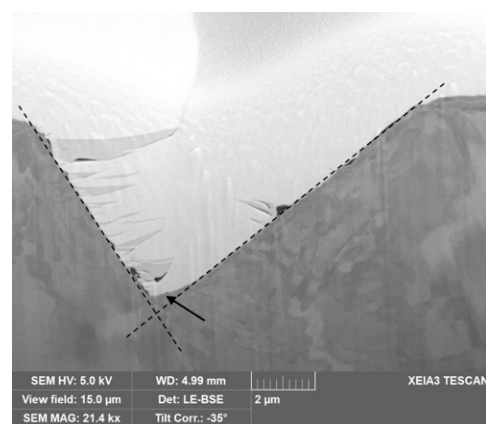
Figure 6. The arrow indicates VB tool wear on the flank face of an MCD tool.

Tools B and C were measured using the same approach, and the resulting RE for tool C was 126 nm with SD of 5 nm. However, achieving precise measurements for tool B proved challenging due to the excessive curtaining effect near the RE area (see Figure 7). This limitation highlights a potential pitfall of the measurement method. Curtaining in each sample must be assessed, and appropriate FIB milling parameters need to be established to minimize the associated effect, along with thorough cleaning of the sample before the FIB-SEM process.
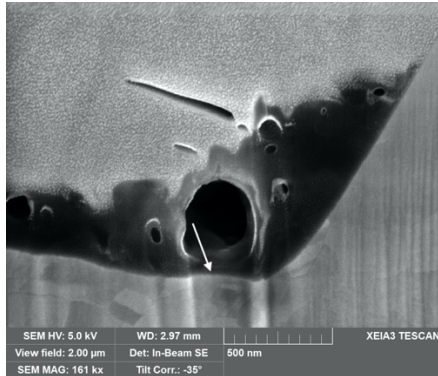
Figure 7. Analysis of indentation created by tool B, with the arrow indicating a feature (wave) resulting from the curtaining effect, which hinders effective RE measurement.

4. Conclusion

This work presents existing and novel approaches, all of which are viable for the measurement of cutting edge geometry and RE in ultra-sharp cutting tools.

Direct SEM – This method consists of direct observation of a tool using an SEM. It is a valid option which gives accurate results for the assessment of damaged tools that effectively have a physical cross section (i.e. chipping) of the cutting edge. In addition, the tool wear can be analysed. The application of this technique on new tools is constrained due to the tangential approach of the electron beam. This approach complicates the identification of the correct focal plane and results in blurring in the measured area.

AFM reversal method – The cutting tool is indented into a soft ductile workpiece and the reverse artefact is scanned using AFM, from which the RE is measured. As demonstrated in prior research, this method is viable. Here it was found that it is sensitive to material displacement around the indentation and requires meticulous sample preparation for successful outcomes. A notable gap in the current literature is the lack of detailed descriptions of the AFM measurement process, its parameters, and potential challenges, which future studies should aim to address.

FIB-SEM combination – This novel method also relies on analysis of the reverse artefact of the cutting edge. Using FIB milling a cross section of the indentation is revealed with minimum process induced damage, and this is subsequently imaged by SEM. It can be reliably used for RE measurement of ultra sharp cutting tools. Additionally, there is no restriction of the indentation geometry. This analysis can be hindered by the curtaining effect caused by FIB milling, which needs to be monitored. Future work should focus on a reduction of the curtaining effect, ensuring accurate and repeatable results.

References

[1] H. Sumiya and K. Harano, 'Innovative ultra-hard materials: Binderless nanopolycrystalline diamond and nano-polycrystalline cubic boron nitride', Apr. 2016, [Online]. Available:sumitomoelectric.com/sites/default/files/2020-12/download_documents/82-04.pdf

[2] M. Groeb, Y. Zecha, J. Groeb, M. Fritz, and W. Ensinger, 'Ductile cutting regime in ball milling of single crystal silicon', in *euspen's 22 nd International Conference*, 2023.

[3] M. Groeb, M. Fritz, J. Groeb, and W. Ensinger, 'Ductile cutting regime in diamond milling of monocrystalline silicon', *American society for precision engineering.* Annual meeting. 36th 2021.

[4] K. Liu, H. Wang, and X. Zhang, 'Ductile Mode Cutting Characteristics', in *Ductile Mode Cutting of Brittle Materials*, in Springer Series in Advanced Manufacturing. , Singapore: Springer, 2020, pp. 39–53. doi: 10.1007/978-981-32-9836-1_3.

[5] X. Gu, H. Wang, Q. Zhao, J. Xue, and B. Guo, 'Effect of cutting tool geometries on the ductile-brittle transition of monocrystalline sapphire', *International Journal of Mechanical Sciences*, **vol. 148**, pp. 565–577, Nov. 2018, doi: 10.1016/j.ijmecsci.2018.09.015.

[6] D. A. Lucca, P. Chou, and R. J. Hocken, 'Effect of Tool Edge Geometry on the Nanometric Cutting of Ge', *CIRP Annals*, **vol. 47**, no. 1, pp. 475–478, Jan. 1998, doi: 10.1016/S0007-8506(07)62878-9.

[7] X. Wu *et al.*, 'Experimental Study on the Minimum Undeformed Chip Thickness Based on Effective Rake Angle in Micro Milling', *Micromachines*, **vol. 11**, no. 10, Art. no. 10, Oct. 2020, doi: 10.3390/mi11100924.

[8] F. Z. Fank and G. X. Zhang, 'An experimental study of edge radius effect on cutting single crystal silicon', *The International Journal of Advanced Manufacturing Technology*, **vol. 22**, doi: https://doi.org/10.1007/s00170-003-1593-2.

[9] K. Liu, X. P. Li, M. Rahman, K. S. Neo, and X. D. Liu, 'A study of the effect of tool cutting edge radius on ductile cutting of silicon wafers', *The International Journal of Advanced Manufacturing Technology*, **vol. 32**, no. 7, pp. 631–637, Apr. 2007, doi: 10.1007/s00170-005-0364-7.

[10] S. Arefin, X. P. Li, M. Rahman, and K. Liu, 'The upper bound of tool edge radius for nanoscale ductile mode cutting of silicon wafer', *The International Journal of Advanced Manufacturing Technology*, **vol. 31**, no. 7, pp. 655–662, Jan. 2007, doi: 10.1007/s00170-005-0245-0.

[11] Y.-L. Chen, Y. Cai, M. Xu, Y. Shimizu, S. Ito, and W. Gao, 'An edge reversal method for precision measurement of cutting edge radius of single point diamond tools', *Precision Engineering*, **vol. 50**, pp. 380–387, Oct. 2017, doi: 10.1016/j.precisioneng.2017.06.012.

[12] K. Zhang, Y. Cai, Y. Shimizu, H. Matsukuma, and W. Gao, 'High-Precision Cutting Edge Radius Measurement of Single Point Diamond Tools Using an Atomic Force Microscope and a Reverse Cutting Edge Artifact', *Applied Sciences*, **vol. 10**, no. 14, Art. no. 14, Jan. 2020, doi: 10.3390/app10144799.

[13] X. P. Li, M. Rahman, K. Liu, K. S. Neo, and C. C. Chan, 'Nano-precision measurement of diamond tool edge radius for wafer fabrication', *Journal of Materials Processing Technology*, **vol. 140**, no. 1, pp. 358–362, Sep. 2003, doi: 10.1016/S0924-0136(03)00757-X.

Tool wear in drilling using cutting fluid diluted with alkaline aqueous solutions

Hideo TAKINO[1], Souta KASHIWA[1], Yuki HARA[1], and Motohiko HAYASHI[2]

[1]Chiba Institute of technology, Japan
[2]Maruemu Shoukai Co.,Ltd., Japan

takino.hideo@it-chiba.ac.jp

Abstract

For precision drilling, it is important to reduce tool wear. Thus, in this study, we investigated tool wear in drilling conducted by supplying a water-soluble cutting fluid diluted with an alkaline aqueous solution. Through-holes with a diameter of 5 mm were drilled while supplying a water-soluble cutting fluid diluted with potassium hydroxide (KOH) or sodium hydroxide (NaOH) aqueous solution. Workpieces were flat plates made of non-heat-treated tool steel, and drills were made of heat-treated high-speed steel. The drilling was conducted at a constant feed rate. The cutting fluid was applied to a machining point at a constant flow rate. After drilling, the top of a drill was photographed with a digital microscope. From the obtained photographs, the wear length of the outer corner was measured. For comparison, through-holes were also drilled while supplying a water-soluble cutting fluid diluted with tap water. Experimental results indicate that the use of an alkaline aqueous solution for dilution is effective for inhibiting the outer corner wear of the drill. The wear was inhibited in the drilling of up to at least 150 holes when the initial pH of the cutting fluid was approximately 12. The length of the outer corner wear when using the KOH aqueous solution was almost the same as that when using the NaOH aqueous solution. It was considered that the wear was inhibited by the passive film generated on the tool surface in the alkaline aqueous solution, which protected the tool surface.

Keywords: Drilling, Cutting fluid, Alkaline aqueous solutions, Tool wear, Tool steel, Potassium hydroxide, Sodium hydroxide

1. Introduction

In recent years, some researchers have investigated the tool wear reduction caused by using a cutting fluid mixed with strong alkaline water produced by electrolysis [1–5]. On the other hand, in our present study, we investigated tool wear in a process by supplying a water-soluble cutting fluid diluted with an alkaline aqueous solution that was not produced by electrolysis. Producing strongly alkaline water by electrolysis requires an electrolysis apparatus and a long time. In contrast, our method only requires the dissolution of granules, making it easy to prepare strongly alkaline water. For precision drilling, it is important to inhibit tool wear. The inhibition of tool wear also allows the increase in productivity because the number of times of changing tools is reduced.

Thus, in the present study, we drilled a steel flat plate while supplying a cutting fluid diluted with potassium hydroxide (KOH) or sodium hydroxide (NaOH) aqueous solution. The wear of the outer edge of the drill was examined. A drill used in this study was made of heat-treated high-speed steel, which was coated with (Al, Ti) N. Such drills are widely used in the manufacturing industry for drilling holes in steel. Therefore, it is industrially valuable to reduce the wear of such tools in a drilling process.

2. Experimental

2.1 Experimental apparatus and material

Figure 1 shows the experimental apparatus, which mainly consists of a drilling machine and a circulation system for the cutting fluid. The drilling machine has an automatic spindle feed function. On the worktable of the drilling machine, the x–y stage and the vessel are fixed. A workpiece is set in the vessel. The cutting fluid is supplied to a machining point through a tube at a constant flow rate. The cutting fluid is allowed to flow from the vessel to the fluid reservoir and is then circulated to the machining point by the pump.

A drill was made of heat-treated high-speed steel coated with (Al, Ti) N, whose diameter was 5 mm. Workpieces were flat plates with a thickness of 7 mm made of non-heat-treated tool steel. The hardness of each workpiece was measured to be 333 HV using a micro Vickers tester.
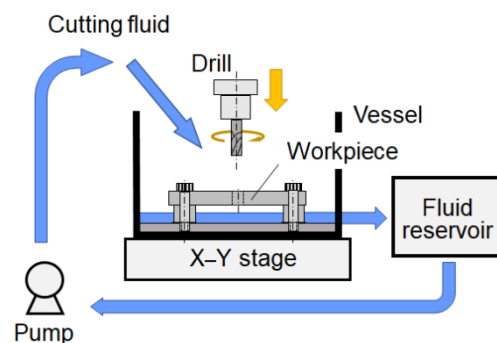
Figure 1. Experimental apparatus.

2.2 Experimental method

Through-holes with a diameter of 5 mm were drilled in each workpiece using the drilling machine. The number of revolutions of the drill was 750 rpm and the feed rate of the drill was 0.07 mm/rev.

KOH and NaOH aqueous solutions were prepared by dissolving their powder in tap water. The cutting fluid was water-soluble and diluted with KOH or NaOH aqueous solution. The cutting fluid was applied to a machining point at a flow rate of approximately 100 ml/min. The pH of the cutting fluid was measured with a glass electrode pH meter.

After drilling several holes, the drill was removed from the machine, and the drill tip was photographed with a digital microscope to evaluate tool wear. In general, flank wear is evaluated to determine tool life in normal drilling operations. The flank wear is greatest at its outer edge, which dominates the drill life. Thus, in this study, we measured the wear length of the outer edge from the obtained photographs. Figure 2 shows an example of the drill tip. The length of the wear of the outer edge was calculated from the change in angle θ on the basis of the initial angle θ_0 as a reference.
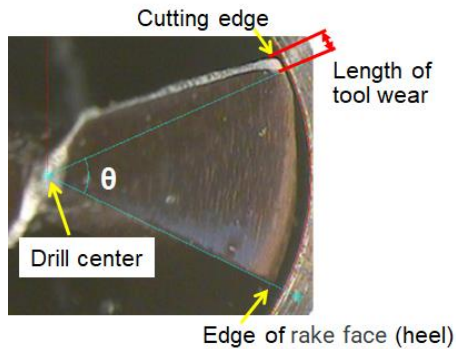
Figure 2. Photograph of the top of drill.

3. Experiment using cutting fluids prepared by diluting the concentrate with KOH and NaOH aqueous solutions

By using the water-soluble cutting fluid prepared by diluting a concentrate (NEOS Company Limited, CFS-100) with the KOH aqueous solution, we drilled through-holes: the pHs of the KOH aqueous solution and the resulting cutting fluid were 12.5 and 11.7, respectively. For comparison, drilling was also conducted using the cutting fluid prepared by diluting the concentrate with tap water: the pHs of the tap water and resulting cutting fluid were 8.3 and 9.5, respectively.

Figure 3 shows increase in the length of the tool wear with the number of drilled holes. In Fig. 3, the length of the tool wear is the average of three replicates. As shown in Fig. 3, the tool wear was inhibited by using the KOH aqueous solution.

Next, by using the water-soluble cutting fluid prepared by diluting the concentrate, which is the same concentrate as that described above, with NaOH aqueous solution, through-holes were drilled: the pHs of the NaOH aqueous solution and the resulting cutting fluid were 12.5 and 12.0, respectively. Experimental results are also shown in Fig. **3,** showing increase in the length of the tool wear with the number of drilled holes. As shown in Fig. 3, the tool wear was also inhibited by using the cutting fluid prepared by diluting the concentrate with the NaOH aqueous solution. Moreover, it was found that the tool wear when using the NaOH aqueous solution is almost the same as that when using the KOH aqueous solution. This result indicates that the cutting fluid prepared by diluting the concentrate with the alkaline aqueous solution inhibitions tool wear.

Figure 4 shows the change in the pH of the cutting fluid sampled from the fluid reservoir during with the number of holes. As shown in Fig. 4, the pHs of the cutting fluid prepared using the KOH and NaOH aqueous solutions after drilling 150 holes reached 11.0 and 11.1, respectively. Thus, the cutting fluid maintains alkalinity during the process.

One reason for the inhibition of the wear is the passive film generated on the tool surface in the alkaline aqueous solution, which protected the tool surface. Generally, passive films can be formed on Fe in an alkaline aqueous solution. Therefore, it is possible that tool wear is reduced by using other alkaline aqueous solutions.
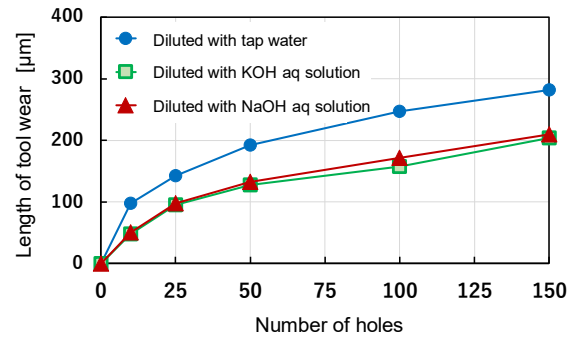
Figure 3. Increase in length of tool wear when using KOH and NaOH aqueous solution with the number of holes.
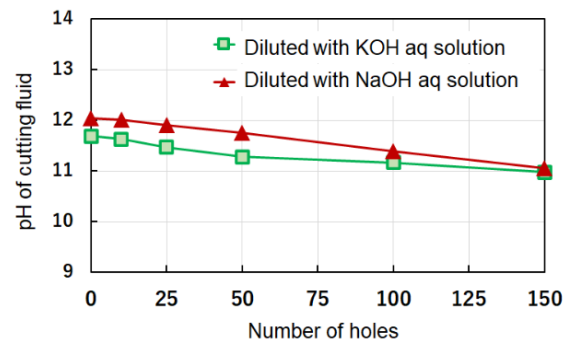
Figure 4. Change in pH of cutting fluids with the number of holes.

4. Conclusions

We investigated tool wear in drilling conducted by supplying a water-soluble cutting fluid diluted with an alkaline aqueous solution, such as KOH or NaOH aqueous solution. As a result, we found that tool wear was inhibited by using a cutting fluid prepared by diluting a concentrate with an alkaline aqueous solution.

In this study, we used only KOH and NaOH, but there are a variety of alkalis. Further cutting experiments using different alkaline solutions are required to select an optimum alkali.

References

[1] Tanabe I, Da Cruz R J, Soe Y H, Tomioka K and Takahashi S 2013 Drilling technology using strong alkali water with micro-bubble, *Transactions Japan Society of Mechanical Engineers Series C*, 79, 748-758. (in Japanese)

[2] Iwai M, Hashimoto H, Yamada M, Sato T and Suzuki K 2014 Machining property by strong alkaline ionized water, *JSPE spring conference*, 1171-1172. (in Japanese)

[3] Iwai M, Hashimoto H, Yamada M, Yamada H and Suzuki K 2014 Performance of strong alkali ion water in cutting and grinding applications, *Advanced Materials Research*, 1017, 298-303.

[4] Nakai H, Iida Y, Sasaki S, Kudoh K, Kasuga D, Ogata K, Ishikawa F, Sawa T and Anzai M 2017 A study on drilling method of SCM435 steel with alkali water, *JSPE spring conference*, 918-919. (in Japanese)

[5] Da Silva P, Tanabe I, Junior D. C. R and Takahashi S 2018 The analysis of environmental and human impacts of using strong alkaline water for cooling during machining, *J. Machine Engineering*, 18, 1, 32-44.

Mechanical machining of a Ni-Mn-Ga alloy with magnetic shape memory effect

E. Uhlmann[1,2], J. Polte[1,2], B. Hein[1], Y. Kuche[2]

[1]*Fraunhofer Institute for Production Systems and Design Technology IPK, Germany*
[2]*Institute for Machine Tools and Factory Management IWF, Technische Universität Berlin, Germany*

benjamin.hein@ipk.fraunhofer.de

Abstract

Actuator elements are essential components of micro-mechanical systems with application areas in the automotive industry, medical technology or mechanical and plant engineering. Magnetic shape memory alloys (MSMA) based on the alloying elements Ni-Mn-Ga offer an industrial alternative to piezo actuators, but are cost-intensive to manufacture. They react sensitively to higher machining temperatures and pressures, which makes it difficult to mechanically produce the required final contours. This article shows that, under certain conditions, grinding and lapping enable the production of flat surfaces and surface roughnesses of Rz ≤ 0.1 µm can be realized.

Keywords: magnetic shape memory, double face grinding, lapping, mechanical machining

1. Introduction

Against the background of short switching times t_s, high energy densities, low wear and without direct electrical contact, actuators with magnetic shape memory effect are relevant for a variety of applications [1, 2, 3]. One specific magnetic shape memory alloy (MSMA) consist of nickel (Ni), manganese (Mn) and gallium (Ga). The alloy can be manufactured with a single crystalline martensite structure with distinct twin boundaries, shown in Figure 1a. When a magnetic field is applied, the lattice is displaced and the motion of the twin boundaries results in magnetic field-induced strains (MFIS) [4, 5].

For use as actuators, the MSMA must be processed into small rectangular sticks. Due to its physical properties, however, both higher temperatures ϑ and pressures p are critical for producing the final contours and ensuring high dimensional accuracy. Depending on the material composition, higher temperatures ϑ during processing can lead to a transformation from martensite to austenite. Furthermore, increased pressures p during mechanical processing or clamping of the semi-finished products lead to the indication of cracks and also an offset of the twin boundaries, shown in Figure 1b [6]. Machining processes such as milling, grinding or lapping offer an economical series production of the sticks if a precise production of functional final contours with high plane parallelism and low edge layer damage can be achieved. In this paper, different approaches for one-sided grinding and lapping of the MSMA are presented and discussed.

2. Experimental setup

For the investigations, sticks of MSMA were prvided by the company ETO GRUPPE TECHNOLOGIES GMBH, Stockach, Germany. The sticks have a length of l = 15 mm, a width of b = 3 mm and a thickness of t = 2 mm. As can be seen in Figure 1a, the sticks supplied have no damaged edge zones due to electro-chemical pre-treatment, which makes the individual twin boundaries of the alloy visible.
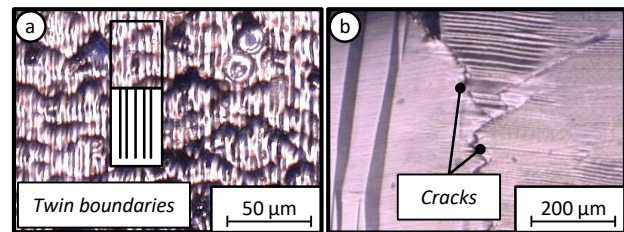
Figure 1. a) Visible twin boundaries on the top of a Ni-Mn-Ga stick; b) Cracks after mechanical processing.

A Saphir 360 E disc grinding machine tool was used for the grinding experiments. A speed of n = 150 rpm was specified. Furthermore, silicon carbide-based abrasive paper of the types P1.200, P2.500 and P4.000 was used. Due to the decreasing material removal rate Q_w with the grain size d_s used in the abrasive papers, the processing time t had to be successively increased, whereby a processing time of t = 2.0 min was set for the use of P1.200, t = 10.0 min for P2.500 and t = 15.0 min for P4.000. For the machining process, the sticks were fixed on a sample holder and pressed onto the grinding surface with a homogeneous contact force of approximately F ≈ 5 N using the weight m of the holder.

Furthermore, a single disc lapping machine tool of the type 4R40GR from the company WENTZKY, Stuttgart, Germany, was used. A speed of n = 60 rpm was specified for the experiments. A lapping oil of the type OL 20 PLUS from the company FLP MICROFINISH GMBH, Zörbig, Germany, was used. The lapping mixture consists of the lapping powder and the lapping oil, whereby four different lapping powders with different grain size d_s were used in accordance with Table 1. The MSMA sticks were centred by a guide system on the lapping disc and a surface pressure of p = 0.03 N/mm^2 was achieved using a defined weight m.

Table 1. Abrasive powder for investigation of the lapping process

Abrasive powder	SiC F500	SiC F1.200
Grain size d_s	6 µm ≤ d_s ≤ 8 µm	2 µm ≤ d_s ≤ 4 µm
Abrasive powder	Tetratbor Boron carbide F500	Tetratbor Boron carbide F1.200
Grain size d_s	5 µm ≤ d_g ≤ 25 µm	1 µm ≤ d_g ≤ 7 µm

The processed Ni-Mn-Ga sticks were analysed tactilely using a HOMMEL nanoscan 855 measuring system from Jenoptik Industrial Metrology GmbH, Jena, Germany, and optically using a JCM-5000 NeoScope scanning electron microscope (SEM) from the company Jeol Ltd, Akishima, Japan. A VHX-5000 digital microscope from the company KEYENCE Deutschland GmbH, Neu-Isenburg, Germany, was also used.

3. Results and discussion

Figure 2 and Figure 3 show the results of the roughness measurements using the arithmetical mean deviation Ra and the mean roughness depth Rz. The two graphics above show the results of the single-sided lapping process, while the graphs below show the results of the grinding experiments.

The results of the roughness measurements of the MSMA sticks processed by lapping show an increase in the roughness values compared to the initial state. In some cases, considerable grooves were detected, which had a particularly strong influence on the measured values of the mean roughness depth Rz. In contrast to grinding, lapping results in non-directional grain movement, which has an effect on the grinding pattern of the machined surfaces. In combination with the process parameters and lapping grains used, it was not possible to produce polished surfaces and visualise the twin boundaries.

Machine tools:
Saphier 360 E, 4R40GR

Measurement device:
HOMMEL nanoscan 855

■ -
◻ SiC F800
◼ SiC F1.200
◼ Boron carbide F500
◼ Boron carbide F1.200
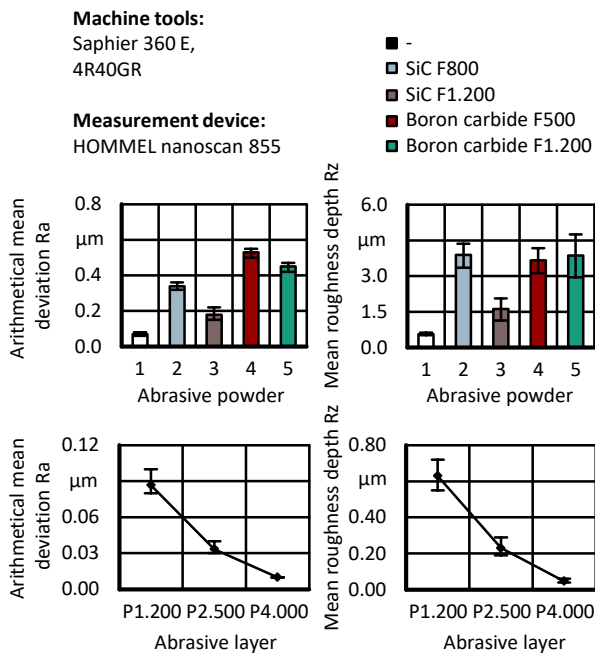
Figure 2. Surface roughness of the machined Ni-Mn-Ga sticks

The roughness measurements after grinding the NiMnGa alloys show surface improvements with reduced abrasive grain size d_s. A high surface quality with a arithmetical mean deviation of Ra = 0.08 µm and a mean roughness depth of Rz = 0.62 µm was achieved, even when using the coarser grain with P1200 abrasive paper. With decreasing grain size d_s and increased processing times t, the surface quality can be further improved, whereby the grinding grooves are only very slightly pronounced when using the P4.000 abrasive paper and the twin boundaries are easily recognisable. This indicates that with a very low mechanical load and corresponding process conditions similar to polishing, it is possible to reduce mechanically impaired edge zones by grinding. At the same time, however, the selection of different processing surfaces was observed along the machined stick surface, which suggests a geometric change in the sticks during the process and thus fluctuating grinding conditions. The

boundaries between dissent areas were identified as being susceptible to cracking and therefore a challenge for homogeneous mechanical processing.
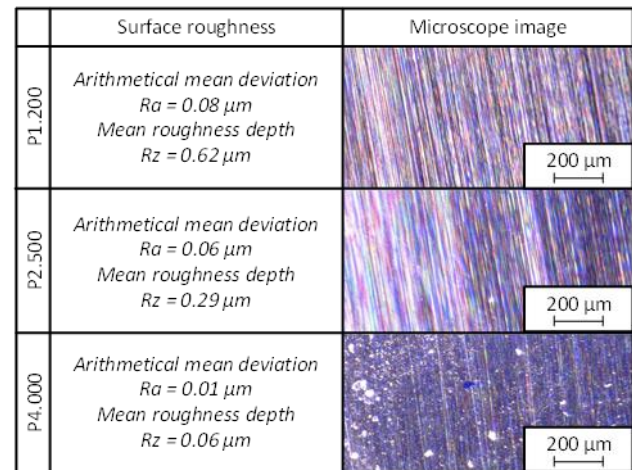
Figure 3. Images of the surfaces of grinded Ni-Mn-Ga sticks

4. Conclusion

Optical analyses and roughness measurements show that high surface qualities with roughness values of Rz ≤ 0.1 µm can be achieved and mechanical machining is basically possible. On the one hand, the results demonstrated the careful mechanical processing of the Ni-Mn-Ga alloy, which can be used as a basis for future process design. At the same time, however, the generation of cracks in the edge zone and the development of individual machining areas on the flat surfaces of the sticks could also be observed, which significantly compromises the stability of the sticks and impairs their function. In future, these must be further analysed during mechanical processing and avoided when establishing the processes for manufacturing the Ni-Mn-Ga sticks.

Acknowledgements

References

[1] Gabdullin, N.; Khan, H.: Study of Non-Homogeneity of Magnetic Field distribution in Single-Crystal Ni–Mn–Ga Magnetic Shape Memory Element in Actuators Due to Its Anisotropic Twinned Microstructure. IEEE Transactions on magnetics, vol. 53, No. 3, 03/2017.

[2] Hutter, M.; Raab, M.; Kazi, A.; Wolf, F.; Gundesweiler, B.: Magnetic Flux Control through Magnetic Shape Memory Alloys in Reluctance Actuators. ETG-Fachbericht 159: IKMT 2019, p. 58 – 63.

[3] Ullakko, K: Magnetically controlled shape memory alloys: a new class of actuatormaterials, J. Mater. Eng. Perform. 5 (1996), p. 405 – 409.

[4] Dunand, D.C.; Müllner, P.: Size Effects on Magnetic Actuation in Ni-Mn-Ga Shape-Memory Alloys. Advanced Materials 23 (2010) 2, p. 216 – 232.

[5] Sozinov, A.; Lanska, N.; Soroka, A.; Zou, W.: 12% magnetic field-induced strain in Ni-Mn-Ga-based non-modulated martensite. Applied Physics Let-ters 102(2013).

[6] Chmielus, M.; Witherspoon, C.; Ullakko, K.; Müllner, P.; Schneider, R.: Effects of surface damage on twinning stress and the stability of twin microstructures of magnetic shape memory alloys. Acta Materialia 59 (2011) 8, p. 2,948 – 2,956.

Monitoring and prediction in centering process of optical glass lenses using long short-term memory with acoustic emission sensor

Shiau-Cheng Shiu[1], Yu-Chen Liang[1], Chun-Wei Liu[1]

[1]*Department of Power Mechanical Engineering, National Tsing Hua University*

s109033802@m109.nthu.edu.tw

Abstract

To proactively address the occurrence of these issues, the monitoring and prediction methodology of centering process within batch production was developed in this study. The experimental phase encompassed the utilization of 20 quartz lenses for centering batch production, with real-time monitoring of material removal employing an acoustic emission (AE) sensor. Based on the AE signal processing, the long short-term memory (LSTM) algorithm was applied to forecast the trajectory of AE signal trends. Moreover, convolutional neural network (CNN) was integrated into LSTM (CNN-LSTM) to enhance the prediction speed. By virtue of this predictive capability, an assessment of the future conditions within the centering process was made feasible. The analysis of more than 32,000 data points was derived from batch production. A highly accurate predictive model was built in this study, as indicated by coefficient of determination (R^2) 0.9067, root mean square error (RMSE) of 0.0577, and mean absolute error (MAE) of 0.0400. By establishing appropriate thresholds and calculating deviations between real AE signals and predicted values, the defects within the centering process can be effectively detected.

Keywords: centering process, optical glass lens, acoustic emission sensor, long short-term memory(LSTM)

1. Introduction

Optical positioning accuracy is critical to the manufacturing of nanometer scale semiconductors. To achieve such feat, high performance optical glass lenses with excellent optical quality are required. Glass lenses normally go through a key manufacturing process known as centering to optimize optical positioning accuracies.

It is common for glass lenses that came off of surface grinding with their optical axis and geometric center axis misaligned. Thus, centering is crucial step in correcting optical axis error. However, the batch production of centering process is affected by the operators fixing the lenses, the original dimensions of lenses or the stability in machine working. These uncertain factors would randomly cause unexpected defects such as edge cracks. The further negative effect would be on the lens appearance and optical performance.

Acoustic emission (AE) sensors are proven useful in monitoring the status of a manufacturing process. D. Choi et al. created a real time monitoring system that used AE signal during cutting to identify tool breakage [1]. It is found that a drop in AE signal can be tied to tool breakage. Z. Wu et al. experimented with multi-sensor signals including AE signal to identify features related to tool wear [2]. From experiment, AE sensor combined with accelerometer sensor provided the best accuracy to tool wear prediction. W. N. Lopes proposed a method to monitor the dressing operation of aluminum oxide grinding wheel [3]. T. Segreto at al. proposed a method of using AE and other sensors to monitor a robot-assisted polishing process for online assessment of workpiece surface roughness [4]. This study not only used AE sensor to monitor the centering condition of hard-and-brittle material, but also predict the AE signal to forecast the process condition.

In the research of processing prediction, it can be seen that different models will be selected according to different situations. Based on the time series forecasting model of the wavelet process neural network, Bitzel Cortez et al. used the long short-term memory (LSTM) model and other machine learning models to compare the accuracy of emergency event prediction, and found that LSTM is more accurate than the machine learning model in time series prediction [5]. Combining convolutional neural network (CNN) with other algorithms can significantly reduce model computation time and improve overall efficiency. R. Yan et al. built a multi-time and multi-site prediction model, which compared CNN-LSTM with other algorithms [6]. X. Shao et al. proposed a novel domain fusion deep model based on CNN, LSTM, and discrete wavelet transform (DWT) [7]. M. F. Alsharekh et al. developed a residual convolutional neural network (R-CNN) structure and combined it with a multi-layer-LSTM architecture to create an innovative prediction framework [8]. In consideration of the strict changes in the short-time AE signal, this study tried LSTM to predict the AE signals in centering process. Furthermore, CNN was integrated into LSTM to improve the prediction efficiency.

In this study, LSTM was used with AE sensor to monitor and predict the condition of optical glass lens centering process.

2. Methodology

2.1. Centering process

Centering process aligns the geometrical axis to the optical axis by alignment and edge grinding. After fixing the glass lens between two bell-shaped clamps and aligning the optical axis to the rotary axis, the edge of optical glass lens is ground to adjust the size and align the geometrical axis, as shown in Figure 1.
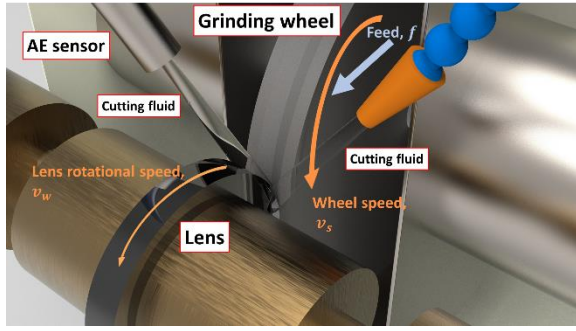
Figure 1. Mechanism of centering process

Centering is cylindrical grinding process of hard-and-brittle material. The material removal rate (MRR) is derived by the following equation:

$$MRR = dWv_w = dW\omega_w(r_w + \tfrac{1}{2}ft) \qquad (1)$$

where d is the depth of cut that changes over time t due to feed rate f, W is the width of cut, v_w is the speed of grinding point on the lens, ω_w is the rotation speed of the lens and r_w is the lens radius.

During centering process, the grinding energy is a key factor affecting the quality of a glass lens's edge. The specific energy is related to the grinding power P and can be calculated using the following equation [9]:

$$u = \frac{P}{MRR} = \frac{F_t v_s}{dW\omega_w(r_w + \tfrac{1}{2}ft)} \qquad (2)$$

where u is the grinding energy, F_t is the tangential grinding force, v_s is the grinding wheel speed.

During centering process, the grinding energy is transmitted from the grinding wheel through grinding force to the lens edge, resulting in material removal. Furthermore, while the microstructure of material is broken, the grinding energy dissipates into the enviroments as heat and wave. AE signal is the stress wave that mainly transferred from the grinding energy. It is assumed to be related to the amount of grinding energy.

2.2. Acoustic emission (AE)

AE signal is elastic stress wave which is generated from irreversible structural changes. It is high-frequency signal and indicates the condition of a material.

A hydrophone AE sensor was adopted in this study to monitor the grinding point in centering process. It was installed in the outlet of the cutting fluid. The AE signal was collected through cutting fluid instead of mechanical contact. The vibration of working machine was then isolated from the sensor. On the other hand, the flow of cutting fluid influenced the noise of signals.

2.3. AE signal process for real-time monitoring

The frequency band of AE sensor was set 300-350 kHz, which was the most sensitive band to centering process. To process and analyze the data in real time, the sampling rate of raw AE signal was limited in 20Hz.

To catch the trend and seanal features of the AE signals more efficiently, The data collected without centering processing was cut away. Only the AE signals of centering processing were fed into the following prediction models.

2.4. Long short-term memory (LSTM)

LSTM is a type of time recurrent neural network suitable for processing manufacturing processes with longer prediction time intervals. Data with indefinite time length can be memorized by LSTM. The proposed model comprises three LSTM layers, each of which includes 128 hidden units. Moreover, a dense layer

with hidden units equivalent to the length of the prediction horizon is appended as the final layer.

To reach the required computation speed and accuracy in real-time monitoring of real manufacturing process, convolutional neural network (CNN) was employed to improve the computation efficiency. CNN is a feedforward neural network. It can effectively read and classify the signal features. By integrating CNN into LSTM, the features in AE signals are extracted in a short time and treated as references for further signal prediction.

In the hybrid model, CNN consists of two convolutional layers with 64 filters and a max-pooling layer with a pool size of 2, as shown in Figure 2. The activation function used is the ReLU function, which makes the model computationally simple and fast.
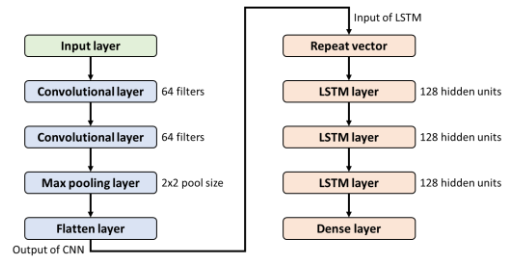
Figure 2. Structure of proposed CNN-LSTM

Each prediction model was trained and verified on sets of preprocessed signals. Three metrics—the coefficient of determination (R^2), RMS error (RMSE), and mean absolute error (MAE)—were used to evaluate model accuracy.

3. Experimental setup

BE-WF-502N horizonal centering machine from Shonan Optics was used in this study. The machine was equipped with a #230 and 150-mm diameter single-layer electroplated diamond grinding wheel. 20 quartz lenses with diameters of 39 mm were randomly chosen from a batch of 300 lenses on a production line. The industrial computer with CPU 4-core i5-7500, RAM 16GB and SSD 256GB was adopted as edge computing to execute AE signal collection, data preprocess and prediction. The experimental setup is depicted in Figure 3.
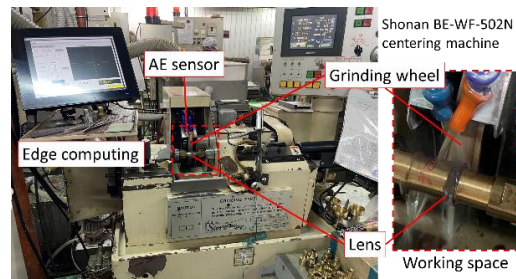
Figure 3. Experimental setup of centering process

A lens in centering process was ground for totally 75 seconds, including 45 seconds of feeding and 30 seconds of spark out. During centering process, the feed rate was 0.02 mm/s in feeding stage and 0 mm/s in spark out stage. The grinding wheel rotational speed was 3,000 rpm and the lens rotational speed was 2 rpm.

The AE signal collected from the centering process of a glass lens is shown in Figure 4.
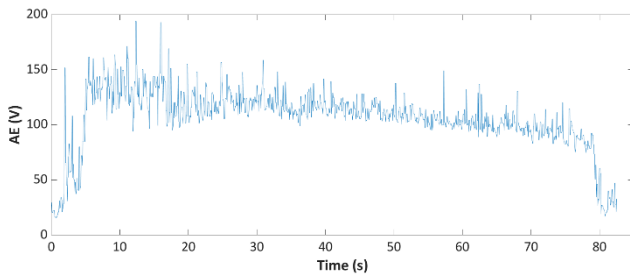
Figure 4. AE signal of a glass lens centering process

4. Results and discussion

According manual inspection, the lenses corresponding to the signals with these features were scraped due to defects. Signal feature 1 was a momentary spike in the signal's amplitude. Correspondingly, an edge crack occurs as the grinding stress concentrates on the corner between the edge and surface. An obvious edge crack was on the corresponding lens. Signal features 2 and 3 were substantially higher signal amplitudes than typical with a clear decrease in gradient as processing continued. The corresponding lenses had poor circularity but no edge cracks. This phenomenon may be caused by the large blank sizes of these lenses before processing. Signal feature 4 was a momentary decrease in the signal amplitude and corresponded to a small edge crack on the lens. Unlike signal feature 1, feature 4 was found to appear when the grinding wheel reached an existing crack instead of when it generated a new crack. Signal features 5 was momentary spikes in the signal. Multiple fine edge cracks were on the corresponding lenses.
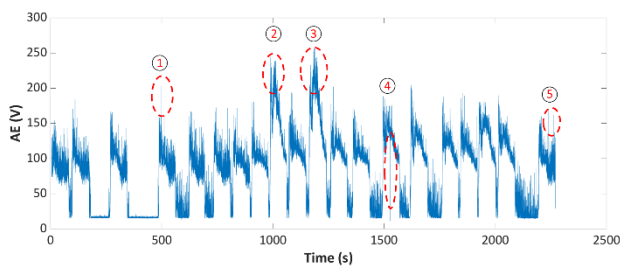
Figure 5. The AE signals from the centering process of 20 quartz lenses

After data process, the overall 30,000 AE signals, collected from centering processes of the 20 quartz lenses were used to train LSTM and CNN-LSTM prediction models. The signals were normalized and divided into training (20%) and testing (80%) sets; after training, the models were evaluated. The results are presented in Table 1.

The prediction accuracy of LSTM was higher, with an R^2 of 0.956660, RMSE of 0.039323, and MAE of 0.022571. On the other hand, the calculation speed of CNN-LSTM was higher than did LSTM and an acceptable R^2 of 0.906716. In steady-state processing, 20 data points are generated per second. The LSTM model required 300 s per calculation. This indicates that LSTM model predicts the next AE signals of 300 s for 300 s. The objective of applying prediction model can not be realized. The CNN-LSTM model required only 20 s. Hence, CNN-LSTM is more suitable for manufacturing processes with short cycle times.

The training and testing results of CNN-LSTM is presented in Figure 2.

Table 1 AE signal prediction results of LSTM and CNN-LSTM

Model	R^2	RMSE	MAE	Time
LSTM	0.9566	0.0393	0.0226	300 s
CNN-LSTM	0.9067	0.0577	0.0400	20 s
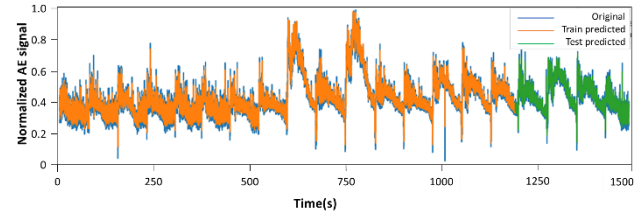
Figure 6. Prediction result by CNN-LSTM compared with original signal

Figure 7 is the graphical user interface (GUI) of the monitoring and prediction system developed in this research. The system has been applied in the actual production line.
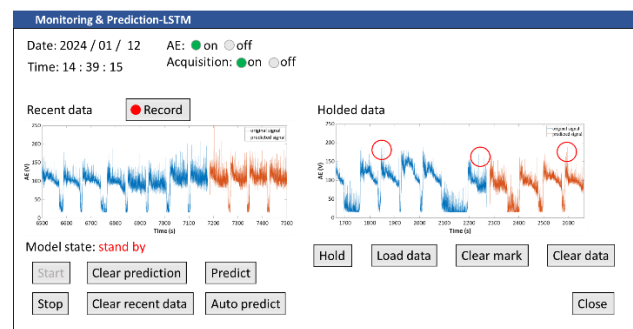
Figure 7. GUI of monitoring and prediction system

Finally, a batch production was carried out to verify the monitoring and prediction system. 50 quartz lenses were prepared for the centering processes. The system kept recording with the AE signals collected during batch production. The defects of the lenses, including edge cracks and circularity errors, were then inspected after processes. During the process, the AE signal features that indicated lens defects were recorded to compare with the actual defects. The prediction result is depicted in Figure 8.

Figure 8. Prediction result of lens defects by monitoring system

According to the results, the defects can be well detected by AE signal features in time. The misidentified defects were predicted by the model with AE rms or slopes closed to the boundary of detection, as shown in Figure 9. The edge cracks and circularity errors were respectively predicted by the rms and slope of the AE signal. An edge crack with depth over 0.1 mm was identified as the AE rms was larger than 20 V, and circularity error over 0.1 mm was identified as the AE slope was larger than 1.5 V/s.
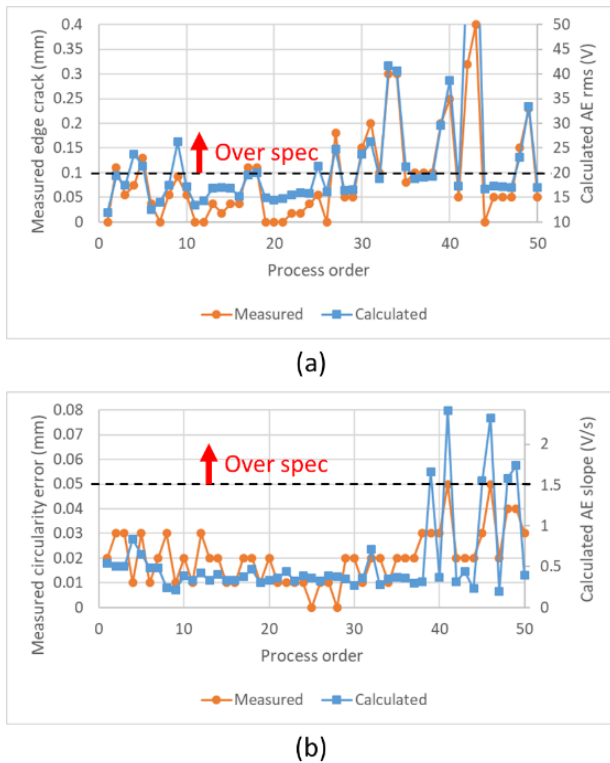
Figure 9. Comparison between calculated results and measured results

To verify the effectivity of the system, the method proposed by this study and the traditional method were defined and conducted. In the proposed method, the AE signal features were recorded, and the features were compared with the lens defects after all the centering processes and inspections were done. In the traditional method, inspection is conducted once after processing every 5 lenses and takes 10 minutes.

If a signal feature was marked in the proposed method, or lens defects were found once in traditional method, the total production time adds 2 minutes that represent an process adjustment. The results of comparison between the proposed method and the traditional method were shown in Table 2.

Table 2 Performance evaluation of monitoring system compared with traditional method

Method	This study	Traditional method
Total marked lenses / total scraped lenses	22	20
Marking accuracy	72%	-
Yield rate	88%	60%
Production time	90 mins	
Inspection time	-	100 mins
Process adjusting time	44 mins	20 mins
Total production time	134 mins	210 mins

Consequently, the proposed monitoring and prediction system in this study can effectively improve the yield rate and reduce the production time. Based on the verification results, the use of monitoring system enhanced the yield rate from 60% to 88% and reduced the total production time by 36.2%. Without batch inspection, much time was saved. Though the adjusting time in the proposed method was more than in the traditional method, the overall yield rate and production time were much better.

5. Conclusion

This study presented a real-time centering process monitoring system by analyzing signal trend and actual manufacturing condition. The real-time monitoring system predicts AE signal trends during centering and triggers fault to allow for parameter change, grinding wheel change or machine fault. The early warning prevents loss from damage to products, such as crack or circularity error, causing scrap. The algorithms LSTM and CNN-LSTM were applied to train an AE signal predicting model, whilst comparing the algorithms for their accuracy and computational time. Results show that LSTM has the highest accuracy at R^2 = 0.95666, but each prediction requires 300 seconds. On the other hand, CNN-LSTM only requires 20 seconds for each prediction while still maintaining an accuracy of R^2 = 0.906716. Compared to other algorithms, CNN-LSTM possesses the most suitable characteristic for real-time centering process monitoring with its short computational time.

A verification including 50 centering processes of quartz lenses was conducted. Based on the results, the proposed monitoring system by this study was evaluated and can effectively improve the yield rate and reduce the production time. The proposed monitoring and prediction system showed an improvement in yield rate from 60% to 88% and reduced the total production time by 36.2%.

This study proves the concept that it is possible to monitor and predict the grinding condition of centering process in real-time. It's a major step towards future smart machining in the glass lens grinding industry as machines will be able to deduce errors autonomously, moving the industry one step forward towards Industry 4.0. Further research on model optimization and implementation on CNC machines will be studied in the distant future.

References

[1] Choi D, Kwon WT, Chu CN 1999 Real-Time Monitoring of Tool Fracture in Turning Using Sensor Fusion. The International Journal of Advanced Manufacturing Technology **15** 305–10

[2] Wu Z, Lu J, Li Y, Chen Y, Feng J, Ma J, et al. 2022 Tool wear prediction under missing data through prioritization of sensor combinations. The International Journal of Advanced Manufacturing Technology **120** 2715–29

[3] Lopes WN, Junior POC, Aguiar PR, Alexandre FA, Dotto FRL, da Silva PS, et al. 2021 An efficient short-time Fourier transform algorithm for grinding wheel condition monitoring through acoustic emission. The International Journal of Advanced Manufacturing Technology **113** 585–603

[4] Segreto T, Karam S, Teti R 2016 Signal processing and pattern recognition for surface roughness assessment in multiple sensor monitoring of robot-assisted polishing. The International Journal of Advanced Manufacturing Technology **90** 1023–33

[5] Cortez B, Carrera B, Kim Y-J, Jung J-Y 2017 An architecture for emergency event prediction using LSTM recurrent neural networks. Expert Systems with Applications **97** 315–24

[6] Yan R, Liao J, Yang J, Sun W, Nong M, Li F 2020 Multi-hour and multi-site air quality index forecasting in Beijing using CNN, LSTM, CNN-LSTM, and spatiotemporal clustering. Expert Systems with Applications 114513

[7] Shao X, Pu C, Zhang Y, Kim CS 2020 Domain Fusion CNN-LSTM for Short-Term Power Consumption Forecasting. IEEE Access **8** 188352–62

[8] Alsharekh MF, Habib S, Dewi DA, Albattah W, Islam M, Albahli S 2022 Improving the Efficiency of Multistep Short-Term Electricity Load Forecasting via R-CNN with ML-LSTM. Sensors **22** 6913

[9] Li P, Chen S, Jin T, Yi J, Liu W, Wu Q, et al. 2020 Machining behaviors of glass-ceramics in multi-step high-speed grinding: Grinding parameter effects and optimization. Ceramics International **47** 4659-73

Validation of the cutting equation by accurate orthogonal cutting experiments

Hiroo Shizuka[1], Katsuhiko Sakai[1], Jinya Yoshida[1], Kenichi Ishihara[2], Yoshihiro Kawakami[2]

[1]*Shizuoka University,3-5-1 Johoku Naka-ku Hamamatsu Shizuoka 432-8561 Japan*
[2]*Johoku Industrial Co.Ltd, 1092 Kamiarayacho Higashi-ku Hamamatu Shizuoka 435-0053 Japan*

shizuka.hiroo@shizuoka.ac.jp

Abstract

This study focuses on accurately measuring orthogonal cutting experimental values to validate cutting equations. Attempts were made to measure these values using a newly developed dedicated orthogonal cutting machine to validate previously proposed cutting equations. The experiment involved selecting a workpiece material that would generate continuous chips without forming a built-up edge or burr under a range of cutting conditions. This material was then used to conduct orthogonal cutting experiments. The experimental values obtained in this study were found to be relatively close to previous experimental values at high cutting speeds but deviated significantly at low-speed and micro cutting conditions. The dependency of experimental values on cutting speed was noted, highlighting the necessity of considering this factor in establishing accurate cutting equations.

Orthogonal cutting, cutting theory, cutting equation, shear surface theory

1. Introduction

When studying cutting phenomena, it is crucial to understand the chip formation mechanism. To address this, many studies have investigated mechanical solutions using orthogonal cutting models, and cutting theories, particularly shear plane models, have been developed since the 1930s. The primary purpose of shear plane theory is to calculate the shear angle, and numerous cutting equations have been proposed to date. Although these equations qualitatively display trends similar to experimental values, large quantitative errors are often noted [1]. Additionally, various issues have been raised concerning the experimental values used to validate theory. These include inadequate implementation of precise orthogonal cutting, deviation of cutting conditions from those used in actual machining, and many experiments being conducted several decades ago with measurement accuracy problems. Therefore, the need to validate the accuracy of experimental values is evident. In response, some studies have reported the development of a orthogonal cutting machine for use in relevant experiments [2]. However, many such experimental devices struggle with issues related to cutting speed and device rigidity, hindering the achievement of accurate orthogonal cutting under general conditions. Hence, this study developed a new orthogonal cutting machine to obtain precise experimental values. This device was initially used to select a workpiece material that would produce continuous chips without forming a built-up edge across a broad range of cutting speeds, from ultra-low to high, thereby facilitating the validation of shear plane theory. Subsequently, experimental values for orthogonal cutting were measured using this material and compared with previously reported values. Additionally, various cutting equations were evaluated against these experimental values to ascertain the accuracy of the cutting equations.

2. Experimental setup

In this study, a orthogonal cutting machine (Figure 1: left) was built for accurate orthogonal cutting. This device had two linear motors and was capable of machining and cutting speeds of 0.001 m/min–180 m/min (±0.5%) with full feedback control using a linear scale. The device also had a rigidity that could withstand over 1000 N in both the cutting force direction and thrust force direction. The tool holder has a drive mechanism with planetary gears and a vernier that enables fine adjustment of the depth of cut. Cutting force can be measured using a dynamometer (Kistler type9601A) built into the tool holder, as shown in Figure 1 (right), and temperature can be measured with the tool-workpiece thermocouple method using the workpiece material and wiring attached to the tool. Furthermore, the cutting points can be freed to enable observation using a high-speed camera.

Figure 1. Orthogonal cutting machine

3. Selection of workpiece material

Selecting a workpiece material that avoids built-up edges or burrs during machining and can generate continuous chips under a wide range of cutting conditions is crucial for obtaining accurate experimental values to validate cutting equations. Consequently, cutting experiments were conducted using eight types of aluminum alloys listed in Table 1 at cutting speeds ranging from 0.01 to 180 m/min. Materials that met the above criteria were selected. Figure 2 shows an example of the experimental results at a rake angle of 5°. The figure illustrates that 5052 (180 m/min), 5083 (10 m/min), and 6063 produce built-up cutting edges, shear-type chips, and burrs. Table 2 summarizes these findings. ANP79 exhibited no built-up edge at cutting speeds ranging from low to high and generated

continuous chips. Based on these results, ANP79 (7075T651) was selected as the workpiece material.

Table 1 Cutting conditions

Work material (AISI)	2017, 2024, 5052, 5083, 6061, 6063, 7075T651 (ANP79), 7075
Cutting speed *V* [m/min]	0.01, 0.1, 1, 10, 180
Depth of cut[mm]	0.10
Cutting width[mm]	2
Rake angle[°]	-10, -5, 0, 5, 10

B.U.E   Shear type chip   Burr
A5052,180m/min   A5083,10m/min   A6063,180m/min
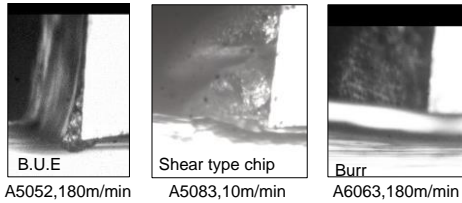
Figure 2. View of the near cutting point using a high-speed camera

4. Validation of experimental values for orthogonal cutting

Merchant, Shaw, and Oxley equations are particularly well-known among the various cutting equations proposed to date, and they have all evaluated the accuracy of their equations by comparing them with their experimental values [3]. As Figure 3 illustrates, the results were categorized into two groups: the 100–200 m/min cutting speed conditions by Merchant et al. and the ultra-low speed conditions of 0.01–0.02 m/min by Shaw, Cook, and Finnie, as well as by Oxley et al. However, the accuracy of these experimental values has been questioned due to outdated machine tools and measuring instruments, necessitating further validation. Figure 3 also presents the results of cutting experiments conducted using the newly developed orthogonal cutting machine across ultra-low to high-speed conditions. The figure shows that, despite a change in cutting speed by a factor of 10,000, the measurement results were consistently within a close range, aligning with the values from Merchant and Lapsley et al. Conversely, the experimental results from the present study differed significantly from those of Shaw, Cook, and Finnie or Oxley et al. This discrepancy is likely attributed more to the cutting environment than the cutting speed, given that the experiments were conducted in an SEM with micro cutting conditions such as depth of cut. Furthermore, it is widely known that the experimental values are distributed

Table 2 Relationship between cutting conditions and chip formation

m/min AISI	180	100	10	1	0.1	0.01
2017	B.U.E.					
2024	○	B.U.E.				
5052	B.U.E.			Burr		
5083	B.U.E.		Shear type chip			
6061	○	B.U.E.				
6063	Burr					
ANP79	○	○	○	○	○	○
7075	○	B.U.E.				
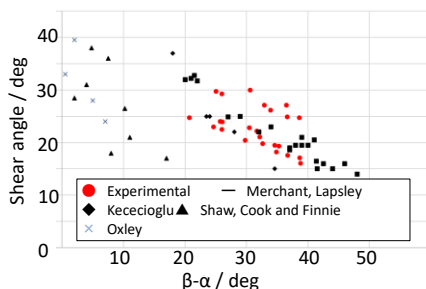
Figure 3. Comparison of experimental values for several orthogonal cutting

around the middle of the Merchant and Lee-Shaffer cutting equations. However, focusing on the experimental results of this study, as depicted in Figure 4, it is evident that the values were categorized into two groups: one with cutting speeds of 100 m/min or higher, and another with speeds of 10 m/min or less. This distinction is attributed to the fact, as illustrated in Figure 5, that the temperature remained close to room temperature at cutting speeds of 1 m/min or less, while the cutting temperature significantly increased at speeds of 100 m/min or higher. Mechanical properties such as tensile strength and fracture toughness of 7075 have temperature and strain rate dependence [4]. This is considered to be the reason why the cutting forces showed a speed dependence. This observation suggests the need to incorporate a temperature term into the cutting equation. Additionally, it was observed that the values closely matched the Merchant and Krystof equations at cutting speeds of 100 m/min or higher.
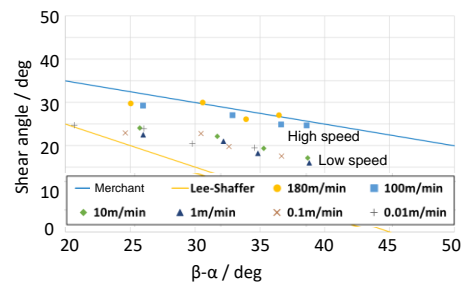
Figure 4. Relationship between cutting speed and shear angle
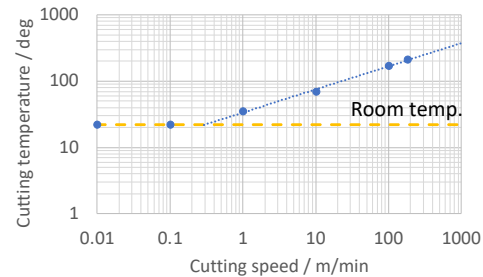
Figure 5. Cutting speed and cutting temperature

5. Summary

This study aimed to accurately measure orthogonal cutting experimental values, necessary for validating cutting equations, using a newly developed orthogonal cutting machine. The results demonstrated that a material capable of producing continuous chips without forming a built-up edge or burrs could be selected, even when significantly altering the cutting speed. Additionally, when conducting orthogonal cutting experiments with this material, it was found that the Merchant experimental values were more accurate compared to the various reported experimental values. It was also found that the obtained experimental values were dependent on the cutting speed, and therefore, the temperature dependency should be considered in the cutting equation.

References

[1] Molinari A., Moufki A.J. 2008 Mech. Sci. **50** 124
[2] Thimm B. et al. 2019 Procedia CIRP **82** 98
[3] Kalpakijan S. 2002 Manuf. Prcess for Eng. Mater.
[4] Pandya S., Roth C., Mohr D. 2020 Int. J. Plasticity **135** 5

Precision cutting of Ni-P plated large mold for X-ray mirror - The effect of tool positioning error on the workpiece form deviation

Hirofumi Suzuki[1], Tatsuya Furuki[1], Katsuhiro Miura[1], Yoshiharu Namba[1], Hisamitsu Awaki[2], Shinya Morita[3] and Akinori Yui[4]

[1]Chubu University, 1200, Matsumoto, Kasugai, Aichi, 487-8501, Japan
[2]Ehime University, 10-13, Dogohimata, Matsuyama, Ehime,790-0825, Japan
[3]Tokyo Denki University, 5, Senjuasahi, Adachi, Tokyo, 120-0026, Japan
[4]Kanagawa University, 3-27-1, Rokkakubashi, Kanagawa, Yokohama, Kanagawa, 221-8686, Japan

[1] suzuki@isc.chubu.ac.jp

Abstract

Precision molds of electroless Ni-P plating are required to mold a Walter-type cosmic X-ray telescope to observe unknown astronomical phenomena such as supernova explosions and the formation of black holes. Conventional X-ray mirrors were made of resin, and they had low strength and low stiffness. In this study, therefore thin mirrors made of CFRP is proposed to overcome those problems. The target value of the maximum size is Φ400 mm, that of the form accuracy is less than 1 µm P-V and that of surface roughness is less than 10 nm Rz. In the cutting experiments, a mold of electroless Ni-P was turned with a single crystalline diamond tool using a vertical type ultraprecision lathe. After cutting, the mirror form accuracy was measured using a capacitive displacement sensor on the machine. In the measurement experiments, the effects of the sensor positioning deviation on the measured accuracy was simulated and the sensor position was compensated in axial and circumferential directions. In the experiment, an accurate mirror could be machined using the developed machining/measurement system.

Precision cutting, electroless Ni-P, X-ray mirror mold, on-machine measurement

1. Introductions

Large reflecting mirrors of high accuracy are used for X-ray telescopes in astronomical spaces to clarify the mechanisms of extremely high energy celestial events. X-ray radiations are is created in space by extremely high energy celestial events, including supernova explosions, the destruction of positrons, the creation of black holes, and the decay of radioactive matter. A number of large parabolic thin mirrors are installed in the Wolter type X-ray telescope where the mirrors are produced by a molding process with ultraprecision diamond-turned and polished molds made of electroless nickel (Ni-P) [1, 2]. To produce high accurate mirrors, it is necessary to measure accurate shape to cut the mold with compensations. In this study, an on-machine form measurement method was developed on the vertical lathe. Form measurement deviations due to sensor positioning deviations were simulated and corrected for position.

2. X-ray mirror for space telescope

High energy rays, such as X-rays, cannot be reflected or refracted with conventional mirrors and instead, X-rays can be reflected by super-smooth surfaces at very small incidence angles. Based on this phenomenon of "grazing incidence," the most practical X-ray telescope was proposed by Wolter, and it comprised a number of optical configurations with the use of confocal parabolic mirrors to focus X-ray radiations as shown in Fig. 1.
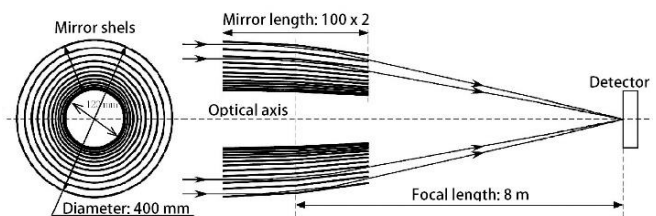
Figure 1. Optical system of an X-ray telescope

The mirrors require a surface roughness of 0.5 nm Ra and a form accuracy of 0.1 µm P-V. In the conventional fabrication process, X-ray mirrors are fabricated using the molding process of the replication method as shown in Fig. 2 (a). The Ni-P layer plated on the base material of harden stainless steel or aluminium was turned ultra-precisely and polished with fine abrasives. Finally, the mirrors of rein were molded with the electroless Ni-P mold, and the replica mirrors were separated and assembled. However, this conventional mirrors had a form deviation based on the high thermal expansion of the mold, and the strength and stiffness of the molded replica mirrors were low.

The proposed process is shown in Fig. 2 (b). Invar having a low thermal expansion was used as the base mold to reduce the form deviation based on the thermal expansion. In addition, CFRP will be molded to increase a specific strength, and to reduce the total mirrors weight.

(1) Cutting of aluminium   (2) Ni-P Plating   (3) Cutting and polishing

(4) Resin molding   (5) replica removal   (6) Assembly

(a) Conventional molding process

(1) Cutting of invar   (2) Ni-P Plating   (3) Oblique cutting

(4) CFRP molding   (5) Replica removal   (6) Assembly

(b) Proposed molding process
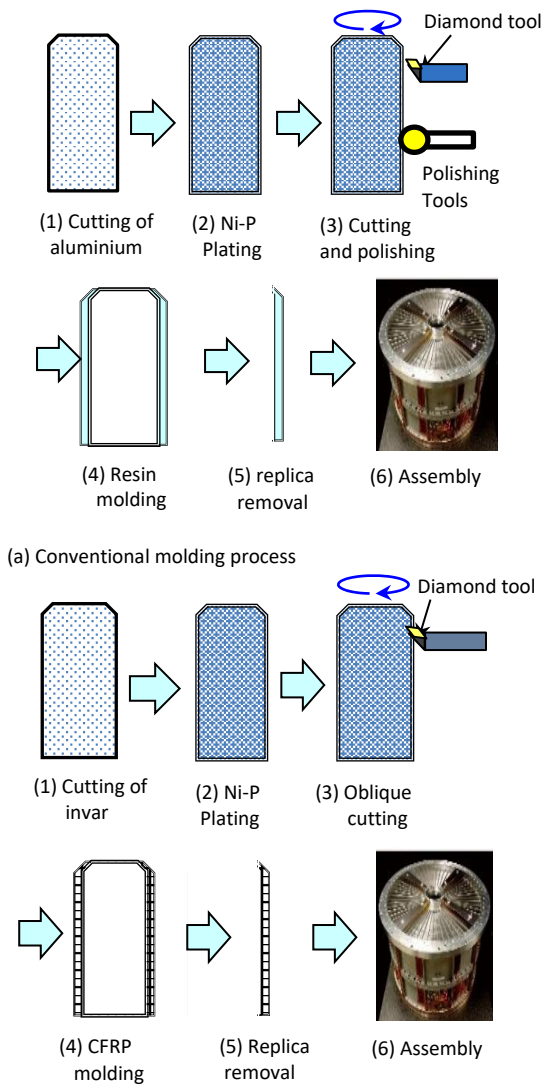
Figure 2. Fabrication process of X-ray mirrors
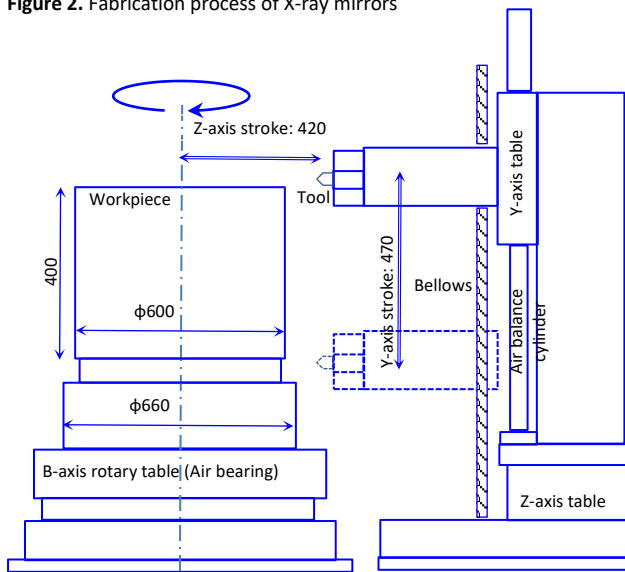
Figure 3. Schematic of ultra-precision machine

3. Experimental set-up and method

A large ultraprecision lathe, UTD-600A (Shibaura machine Co.Ltd.) was used for the X-ray mirror cutting experiments in this study. A schematic illustration of the turning machine is shown in Fig. 3 and, its specifications are shown in Table 1. The diamond tool was mounted on the ultraprecision machine, and the capacitance sensor was mounted 30 mm below the tool as shown in Fig. 4(a). The cutting conditions for the X-ray mirrors are shown in Table 2. The mold surface was plated with 100 μm of Ni-P on the base mold metal of invar. The invar base was used to decrease the thermal expansion of the mirror. The depth of cut was 2 μm and the feed rate was varied from 1 - 2 mm/min.

After cutting, the capacitance sensor was equipped onto the tool holder near the cutting tool, and the form deviations from the designed form were measured by the Capacitance sensor on the machine, and the form deviation profiles were calculated and plotted.

Table 1. Specifications of ultra-precision machine

Y- axis	Stroke	420 mm
	Driving system	Linear motor drive
	Positioning resolution	1 nm
Z-axis	Stroke	420 mm
	Driving system	Linear motor drive
	Positioning resolution	1 nm
B- axis	Maximum rotation	500 min^{-1}
	Stroke	360 deg.
	Bearing system	Air bearing
	Positioning resolution	1/10000 deg.

(a) View of cutting

(b) On-the-machine measurement sensor
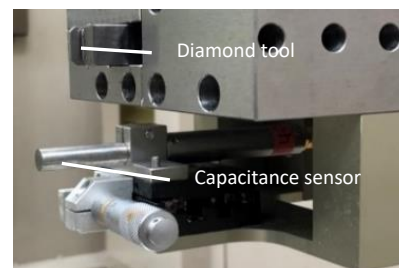
Figure 4. Views of cutting machine and on-machine measurement set-up

Table 2. Cutting conditions for X-ray mirror

Tool material	Natural monocrystalline diamond
Cutting edge radius	5.0 mm
Mold metal	Invar
Plating material	Electroless Ni-P
Plating thickness	100 μm
Maximum diameter	200 mm
Rotation	500 min^{-1}
Depth of cut	2.0 μm
Cutting times	4 times
Feed rate	1.0, 2.0 mm/min
Coolant	White kerosene mist

4. Effects of sensor positioning deviation on the measurement form accuracy

A calculated form deviation of the mold radial direction on the thrust position, ΔZ, is expressed as follows;

$$\Delta Z = Z(Y) - Z'(Y) \tag{1}$$
$$Z'(Y) = (Z(Y)^2 - \Delta X^2)^{0.5} \tag{2}$$

Where, Y is the thrust (vertical) coordinate of the mold, Z(Y) is the radial coordinate on the position of Y, ΔX is a deviation on the sensor position of the X-direction, and Z'(Y) is a radial value with the deviation of ΔX in the X-direction.
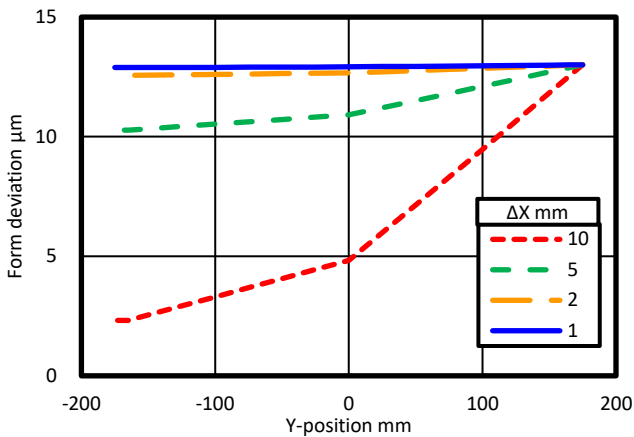
Figure 5. Form deviation curve with the positioning deviation in the X-direction
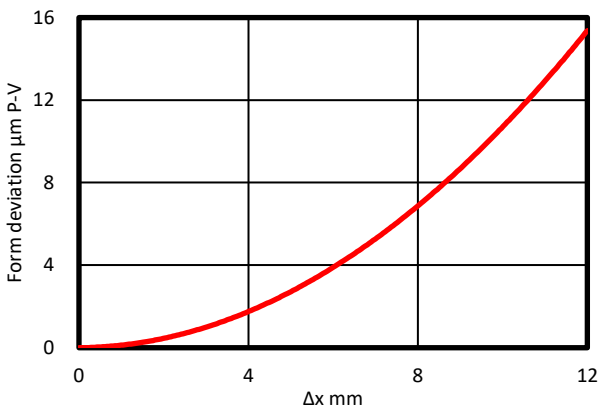
Figure 6. The effect of positioning deviation in X-direction on measured form accuracy

The mold height was 350 mm in the Y-direction and the diameter is was approximately Φ200 mm at the top, and Φ195 mm at the bottom. When there was a tool positioning deviation in the X-direction, the simulated workpiece form deviation curve was calculated using eq. (1) as shown in Fig. 5. The deviation curve increased with the mold radius. Based on these results,

the effect of the tool positioning deviation ΔX in the X-direction on the machining accuracy is shown in Fig. 6.

5. Experimental results

Cutting experiments were performed and the effects of the positioning deviation, deviation in the X-direction on the measured form accuracy were tested. In the cutting of the mirror, ΔX was adjusted to 0, and the mirror of electroless Ni-P was turned at a feed rate of 2.0 mm/min. Fig. 7 shows the change of the experimental form accuracy with the X-axis deviation of the capacitance sensor. The form accuracy became minimum at the range of ΔX =0 - 1 mm, and however, the experimental deviations were too large compared to the calculated ones shown in Fig. 6.

Finally, the tool position and the sensor position were adjusted based on the simulated results in Figs. 5 and 6, and the mold of the electroless Ni-P was machined and measured. The machined and measured form deviation profiles of the X-ray mirror mold were shown in Fig.8. The form deviation of the diamond-turned mold was 2 μm P-V and was not enough for the X-ray mirror mold. This seems to be based on the tool wear because the workpiece size was too large and cutting distance was so long. The deviation will be decreased by using much higher diamond tool such as nanopolycrystalline diamond (NPD) tool and the tool wear prediction.

The surface roughness of the large mirror could not be measured using the white light surface roughness interferometer. However, from the cutting experiment of a small dummy workpiece of electroless Ni-P, the surface roughness of less than 10 nm Rz was obtained.
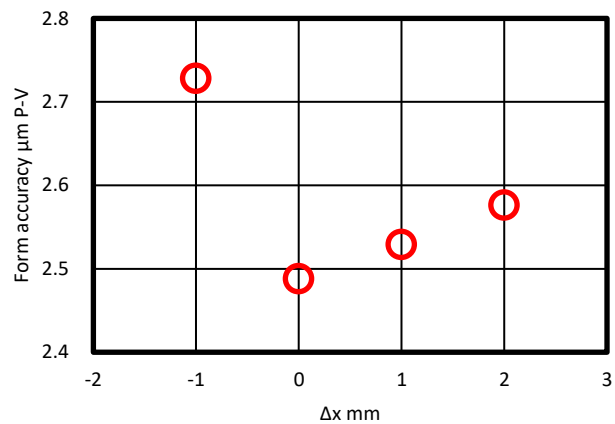
Figure 7. Changes of machined form accuracy with X-axis deviation of the capacitance sensor
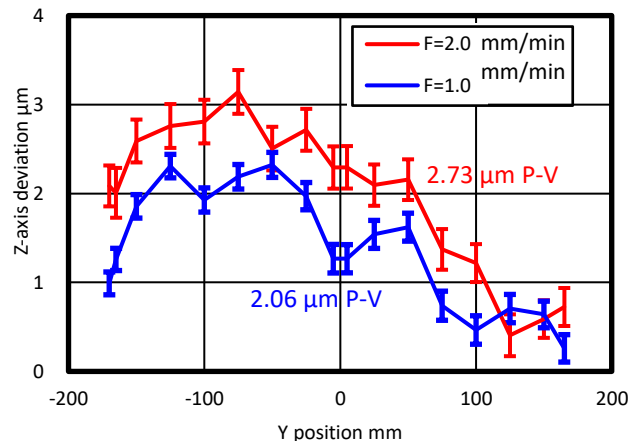
Figure 8. Machined and measured form deviation profile of X-ray mirror mold

6. Conclusions

In this study, a vertical turning system for a large mold and an on-machine form measurement system using a capacitance sensor were developed, and form measurement deviations due to sensor positioning deviations were simulated and corrected for the position in the experiments. In the experiments, the form deviation of the diamond-turned mold was about 2 μm P-V and was not enough for the X-ray mirror mold. The deviation will be decreased by using much higher diamond tool and the tool wear prediction.

References

[1] Wolter H, Mirror systems with grazing incidence as image-forming optics for X-rays, *Annals of Physics*, **6**, 10 1952 94–114.
[2] Suzuki H, Okada M, Masuda Y, Namba Y, Miura K, Morita S, Yamagata Y, Ultraprecision cutting of Ni plated mold for X-ray mirror, *International Journal of Automation Technology*, **10**, 4 2016 624-631.

CAD geometry preparation issues effecting FE simulation accuracy

Thomas Furness, Simon Fletcher, Andrew Longstaff

The University of Huddersfield, Queensgate, Huddersfield, HD1 3DH

T.furness@hud.ac.uk

Abstract

When generating a design for a complex assembly, large amounts of detail are produced in the CAD model. Whilst this level of detail is paramount in generating a Bill-Of-Materials (BOM) and visualising mechanical conformance, it can be detrimental to additional finite element (FEA) operations. Complex CAD-centric assemblies must be prepared for FEA, such as removing unwanted parts, and part geometry defeaturing. Part defeaturing can be considered the most important step in CAD FEA preparation as it can be the largest error contributor. However, the removal of certain features has the potential to create artificial stress risers in the part, that can result in false positive FEA solutions. Additionally, if bulk material is added/removed by defeaturing, structural and thermal properties of the parts can be greatly altered leading to inaccurate solutions.

Conversely, if these features are left in, they can lead to poor quality mesh that can lead to inaccurate results, non-converging solutions, excessive computing time and power requirements.

From discussions with industry partners, the main barriers to them using FEA effectively are the issue around proper defeaturing to ensure accurate results, and the time needed to perform model preparation. The work presented here is aimed at understanding and defining the effects that changes in geometry and mesh attributes can have on simulation results. Certain solutions which have already been evaluated, such as rapid part removal for assembly preparation, are also included. Additionally, this work highlights how current automated defeaturing solutions are not suitable for more complex FEA simulation preparations.

Keywords: CAD, FEA, Mechanical design, defeaturing

1. Introduction

Finite Element Analysis (FEA) has many uses in mechanical engineering. Numerous applications require an in depth understanding of a component or assembly's solid body mechanics, stress distribution, natural frequencies etc.

Because raw material costs are increasing [1,2], and supply chains are being stretched, older practices of over engineering are become less financially viable than they once were. Manufacturers who may have forgone the use of FEA in the past are now starting to review its viability within their business practices. However, the completed CAD-centric model for manufacturing, including a comprehensive bill on materials (BOM), is not always suitable for additional FEA simulations. A complete BOM CAD model may consist of thousands of individual components, many of which might not be required for the simulation at hand. Leaving such components in the simulated assembly model will require additional computing power and can take considerably more time to solve [3]. Therefore, it is important to remove components that are not inherent to the desired solution, in efforts to reduce solver time, and remain in budget. Yet here can be seen the contradiction. Is time to be spent removing unwanted parts for the assembly, or during simulation time?

In addition to the removal of unwanted parts, individual part geometry needs to be considered. FEA generates a mathematical representation of the component under scrutiny. The model is made up of a series of elements connected by nodes that represents the geometry of the component. This process takes irregular shapes of the model and breaks them down into a series of recognisable volumes called elements [4]. The meshing of the components is one of the most important steps in FEA, as it can have a great effect on simulation accuracy or can lead to false-positive results. An understanding of mesh principles and their effects on simulation results is critical to performing accurate FEA simulations. It is important to understand that the act of meshing a component changes the geometry of the model based on size of type of meshing element used [5]. If the ratio of component size to element size is low, the computational time will be quicker but the resultant mesh will be rough and can oversimplify the component's geometry. Conversely, a high ratio will produce a much more accurate representation of the component's geometry due to the small element size, but the mesh could consist of thousands if not millions of elements, that will take a long time to solve, requiring more computing power. Therefore a balance must be struck between accuracy, computing requirements, and time when selecting an element size.

In addition to element size, element quantity also is critical to ensuing simulation accuracy. Certain CAD features can lead to mesh irregularity. Geometric details necessary for manufacture such as holes, slots, radii, indents, and sharp corners, can result in localised smaller element sizes, leading to mesh transition irregularities, and poor mesh quality [6]. Whilst the removal of small holes and slots, etc, is necessary to improve mesh uniformity, their removal from the FEA-abstracted model will change the model geometry increasing uncertainty in the estimated simulation. Additionally, the presence of sharp corners (from the removal of radii) can lead to the introduction of false positive stress rises, or stress singularities [7].

Whilst there are numerous defeaturing methods and analysis techniques to estimate the effect feature removal will have on simulation accuracy [8,9,10], there is no standardised approach to this issue.

An additional barrier to the use of FEA in industry is the standard tools available in typical CAD packages. Most packages defeaturing techniques are too aggressive and offer little or no control over the automated processes for the abstracted model generation. This leaves manual adjustment as the only model manipulation option to ensure the most accurate solution. This in turn increases the number of man-hours and therefore the cost.

The ultimate aim of this work package is to review the defeaturing techniques and disseminate them into a usable CAD package add-on that industry can use. One that can offer the versatility in defeaturing needed to ensure that FEA simulation results are viable, and that error source generation is identifiable. The work presented here highlights some of the issues currently faced with using typical CAD automated defeaturing techniques, and how the incorporation or exclusion of features can affect mesh generation, and result accuracy.

2. Mesh size effects

As said above mesh quality and size are two of the most important factors when consideration simulation accuracy. Figure 1 shows an example CAD-centric design of a machine tool structure.
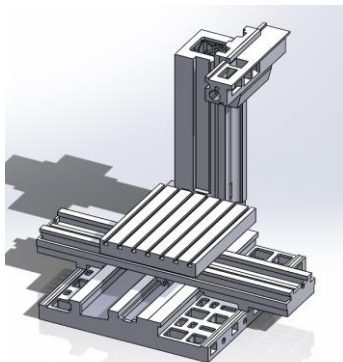
Figure 1. example CAD model of a machine tool structure

Ignoring all other factors, the following shows how element size can affect FEA model geometry, solver time, and solution variance. This model has external dimensions of 3400 mm x 3400 mm x 2740 mm. A modal analysis was performed of this model, with results for the first 5 natural frequencies resolved. (All simulations were run on an 11th gen Intel i9-11900K with 64GB of RAM utilizing 8 cores). Figure 2 shows the element size used, and resultant number of elements in the model, and the time it took to solve the simulation.
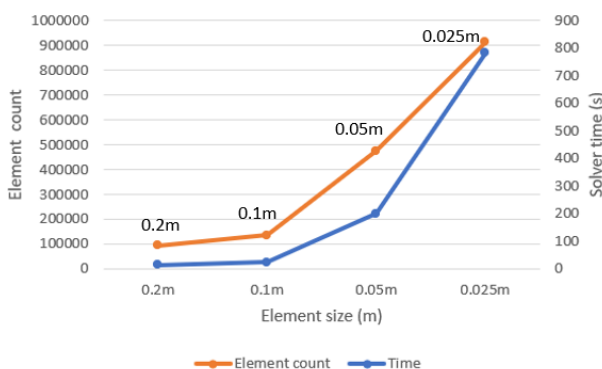
Figure 1. how element size effects element count and solver time.

As can be seen, adjusting the element size and thus the element count can greatly affect the time taken to solve the simulation. With regards to the effect that element size has on accuracy figure 3 shows the results for the first 5 natural frequencies of

the model when simulated with element sizes of 0.2m, 0.1m, 0.05m and 0.025m.
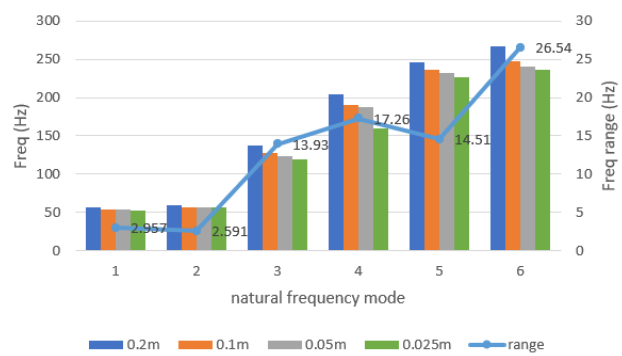
Figure 3. Frequency difference due to changing element size.

As can be seen in figure 3 simply changing the element size does influence the model's natural frequency ranging from 1 or 2 Hz to over 25 Hz. The lower element size allows for the inclusion of more elements within the model, which in turn increases the number of nodal interactions allowing for more degrees of freedom. This reduction in constraint reduces the perceived natural frequency of the model as the model has more flexibility. This is more noticeable at the higher mode numbers which generate more dynamic responses. That said the natural frequency of the fifth mode is a localised deformation in which increasing the nodal count has less of an effect.

2.1. Mesh quality

Changing the element size also affects the quality of the mesh. Ideally the mesh structure needs to be as unform as possible throughout the model. A poor structure can affect the model's stiffness characteristics as the element nodes become less effective. To combat this, the software might either adjust the volume of the models as can be seen in Figure 4 or will automatically add in smaller elements to fill gaps where the larger element cannot be fitted. This in turn can affect the dynamics of the model due to non-uniform loading of the nodes.
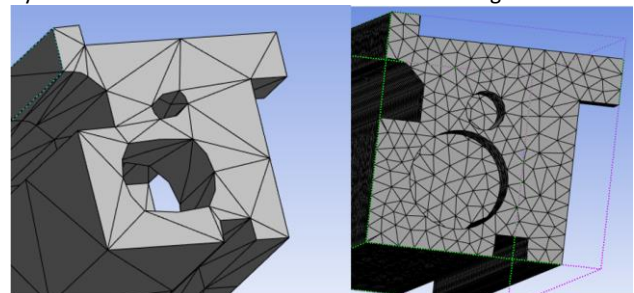
Figure 4. effects of geometry due to element size L- 0.15m, R-0.25m

As can be seen in figure 4 using an element size of 0.15 m has resulted in the geometry of the part being deformed, as compared to the model using 0.025 m element size which has a more uniform mesh with no deformity.

3. Geometric Defeaturing

As previously stated, to take a CAD-centric model, to an abstracted FEA model will require the removal of parts not required for the FEA dynamics, and the geometric defeaturing of parts to remove undesirable features.

3.1. Part removal

Part removal is necessary in FEA model preparation as it can substantially reduce the number of elements in an FEA model. Parts that do not have a role in the desired simulation will simply take up computational resource and elongate the solver time.

Additionally, items such as fasteners, that are needed for the BOM in the CAD model, should also be removed. This is because simplified threads in CAD models often cause interference, as only the drill size is used in the CAD not the thread size leading to an overlap in geometry. When meshed, the interference between the bolt and the holes can lead to severe mesh irregularities.

The removal of these parts is generally straightforward but can be time consuming in its preparation. The CAE engineer will review the CAD-centric model, manually removing the unwanted parts. This can result in many hours of work as complex assemblies can have thousands of parts that need reviewing.

A solution to this is to tag induvial CAD parts within the assembly in which it is being designed. All CAD parts will have part specific user defined properties, such as material, finish, supplier, who designed it etc. By adding an additional custom variable to the part properties that can flag the part for removal, when the design is ready to be defeatured a simple macro can be run that will group these parts together for suppression. Figure 5 shows a completed CAD design for a machine tool base used as an example.
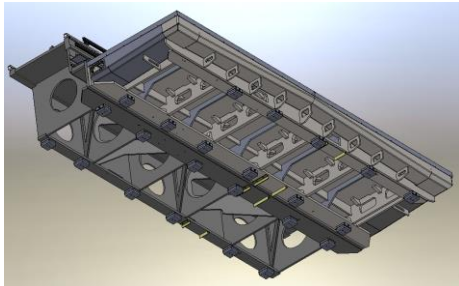
Figure 5. Holistic CAD model of a machine tool bed

All the parts in this assembly shown in figure 5 have had a part property field added named "remove". The parts that need removing have the *remove* field checked, and the parts to remain have the field unchecked. A macro was written for use in Solidworks® that when used will review the status of the *remove* property for all parts in that assembly. If the field is checked, the associated parts are grouped together and highlighted as shown below in figure 6.
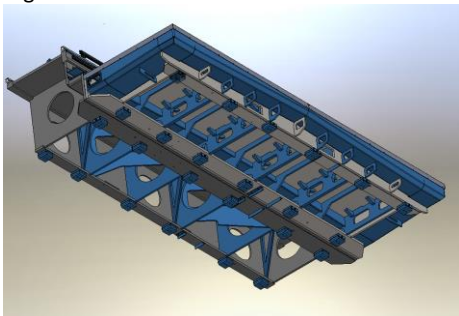
Figure 6. CAD model of a machine tool bed, with parts highlighted for removal.

The macro then generates a new file configuration within the CAD assembly. Within this new configuration all the parts returned with the *remove* field checked are suppressed, leaving the down selected model, as shown below in figure 7.
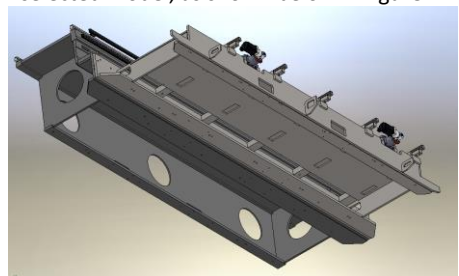
Figure 7. resultant down selected CAD model.

Suppressing the parts in this way allows the user to switch between the CAD-centric model and the new down abstracted model with-in the same file directory resulting in better traceability.

Providing the designer checked the *remove* field during the design process when individual parts were added to the assembly, this method of part removal can result in an abstracted model generated in minutes as opposed to the many hours it would take to do it manually and retrospectively.

3.2. Geometry defeaturing

Geometry defeaturing of CAD parts is the removal of unwanted features from individual parts. As previously stated, features such as, radii, holes, slots etc, will cause mesh irregularities that can alter the FEA model's dynamics. Whilst defeaturing is necessary to ensure the best mesh structure possible, care must be taken not to defeature the part to the extent that the part is no longer representative. Additionally, the removal of certain features will potentially create artificial stress rises, that the removed curved feature would have controlled.

Currently, to ensure optimum part defeaturing, manual intervention is almost always required, and the man-hours dedicated to part defeaturing can be high, especially if the assembly is extensive and consists of many parts.

Most CAD packages have a part-automated defeature or simplification tool, that can speed up this process. Certain CAD software can successfully return a comprehensive defeatured assembly, that maintains part individuality and retains the part relationships. However, the techniques used in most cases can be overly aggressive and lack any comprehensive feature-based control. For example, a popular CAD software commonly used in industry only has two forms of defeaturing large assemblies. The first is a silhouette-based result that removes all features and returns the assemblies' outline shape. For the assembly shown in figure 1, the result of this process is shown in figure 8.
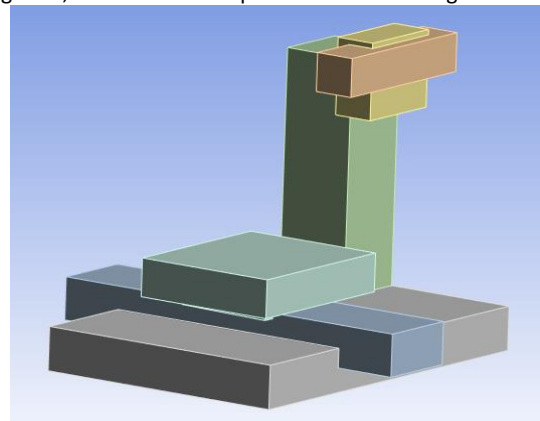
Figure 8. silhouette of machine tool structure.

As seen in figure 8 this level of detail is far removed from the level of detail in figure 1 and bares very little representation of the original CAD model. The second mode of assembly defeaturing in this software does allow for feature selection, however, this feature-based process does not allow for the removal of individual features, but removes all related features. For example, the radii of a square hole cannot be removed in isolation, the entire hole must be removed. Additionally, to perform accurately, selection must be done manually, again increasing the input time. When running the process automatically, the control of what features to keep or remove is rudimentary allowing very little control over the result. An example of this is shown in figure 9.
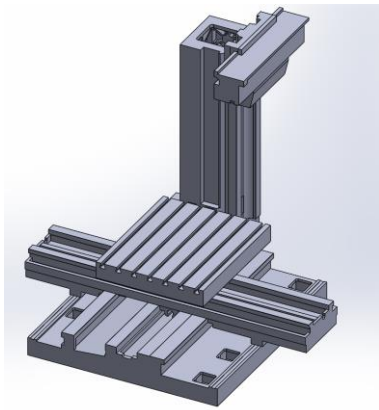
Figure 9. partial defeature of machine tool structure.

As can be seen in figure 9 the defeaturing process has left in several features that should have been removed, namely holes in the base and the detail inside the column. To further remove these features additional process such as extrusions or subtractions will be needed to finalize this model for FEA.

4. *Geometry defeaturing effects*

As geometric defeaturing will have an effect on the model's geometry, it is important to understand how this will affect the FEA simulation results, especially when using pre-defined automated procedures. The models in figures 1 and 6, were subjected to a modal and thermal simulation. In the thermal simulation heat was applied to the back of the column, with results being taken over the column length to show how the temperature of the column varied.

The modal results are shown in figure 10 and the thermal results are shown in figure 11. As can be seen there a marked variation in the two sets of results. In the thermal result the heat transfer is far lower in the nominal model than in the defeatured one. This is due to the removal of the air gap in the defeatured model. In the model results, the frequencies changes for every mode varying from a few hertz to over a hundred. Again, this is due to the change in geometry and thus the change in mass and dynamics.
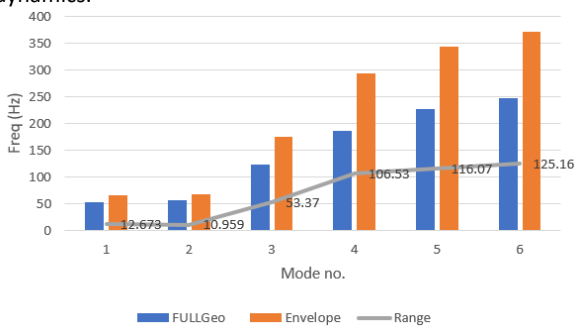
Figure 10. frequency response from the nominal and defeatured models
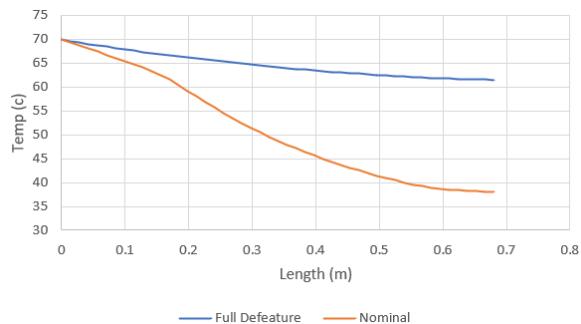
Figure 11. thermal response from the nominal and defeatured models

Whilst this is an extreme case of variance due to the effects of geometry change it highlights the issues that can arise in simulation accuracy when automated defeaturing procedures are used with no regard for their affect.

5. Conclusion

The work presented here highlights how changing FEA variables can affect simulation accuracy. As FEA is being applied more frequently in industry by companies that have never previously used it, it is important for them to understand how small changes in mesh, and geometry can have large effects on result accuracy. It is also important for them to be aware that greater accuracy does come at the price of longevity and man-hours involved, which will incur greater cost.

The ultimate aim of this work package is to generate automated adaptive model preparation techniques that can provide FEA results efficiently and accurately. This will involve automated feature-based defeaturing that can be adaptive to the CAD involved. Part of this work has already been highlighted here. By simply incorporating a custom property into the part design, unwanted parts can simply and quickly be excluded from the model, without the need of manually selected them.

The work for automatic geometric assembly defeating is ongoing with the results to be published in due course.

References

[1] Aluminium, trading economics, https://tradingeconomics.com/commodity/aluminum, accessed sept 2023.

[2] Steel, trading economics, https://tradingeconomics.com/commodity/steel, accessed Sept 2023.

[3] Defeaturing CAD Models: Different Strokes for Different Folks, K. Wong., Jan 2018, www.digitalengineering247.com, accessed sept 2023

[4] The Fundamentals of FEA Meshing for Structural Analysis, Ansys Blog, Apr 2021, https://www.ansys.com/en-gb/blog/fundamentals-of-fea-meshing-for-structural-analysis, accessed sept 2023.

[5] Beall, M. W.; Walsh, J.; Shephard, M. S.: Accessing CAD Geometry for Mesh Generation, In IMR, 2003, pages 33–42.

[6] Quadros, W. R.; Owen, S. J.: Defeaturing CAD models using a geometry-based size field and facet-based reduction operators, Engineering with Computers, 28(3), 2012, 211–224. http://dx.doi.org/10.1007/s00366-011-0252-8

[7] Pike, M., Feng, F., Myres, M., Shrinkwrap geometry defeaturing for finite element analysis for a wheel and hub model, COMPUTER-AIDED DESIGN & APPLICATIONS, 2016, VOL. 13, NO. 3, 295–308

[8] Li, M.; Gao, S.; Zhang, K.: A goal-oriented error estimator for the analysis of simplified designs, Computer Methods in Applied Mechanics and Engineering, 255, 2013, 89–103. http://dx.doi.org/10.1016/j.cma.2012.11.010

[9] Turevsky, I.; Gopalakrishnan, S. H.; Suresh, K.: Defeaturing: a posteriori error analysis via feature sensitivity, International Journal for Numerical Methods in Engineering, 76(9), 2008, 1379–1401. http://dx.doi.org/10.1002/nme.2345

[10] Li, M.; Gao, S.; Martin, R. R.: Engineering analysis error estimation when removing finite-sized features in nonlinear elliptic problems, Computer-Aided Design, 45(2), 2013, 361–372. http://dx.doi.org/10.1016/j.cad.2012.10.019

Analysis of effects of mechanical properties on ductile-to-brittle transitions at nano-scale mechanical machining

Doo-Sun Choi[1], Dong-Hyun Seo[1,2], Eun-Ji Gwak[1], Jun Sae Han[1], Joo-Yun Jung[1], Eun-chae Jeon[#,3]

[1]Dept. of Nano-Manufacturing Technology, Korea Institute of Machinery & Materials, Daejeon, 34103, Republic of Korea
[2]Major of Mechanical Engineering, University of Science and Technology, Daejeon, 34113, Republic of Korea
[3]School of Materials Science and Engineering, University of Ulsan, Ulsan, 44610, Republic of Korea

jeonec@ulsan.ac.kr

Abstract

Single-crystal materials, characterized by their uniform atomic structures and properties, find extensive applications across various industrial sectors, including electronics, optics, and displays. While lapping or polishing of single-crystal materials is a widely employed technique in industries, mechanical machining for patterning is not commonly applied due to their brittle fracture characteristics. Although some previous research has demonstrated the possibility of mechanically machining these materials at ultra-low forces on the nano-scale, estimating the critical thrust force at the ductile-to-brittle transition remains challenging. Furthermore, it is unclear how much plastic deformation affects ductile machining on the nano-scale, as analysing nano-sized chips is inherently difficult. To address these issues, our research focuses on analysing how mechanical properties influence the critical thrust force at the ductile-to-brittle transition during nano-scale mechanical machining using a few single-crystal materials. We also proposed a quantitative method for determining plastic deformation by measuring volume changes in this study. We utilized a nanoscratch tester equipped with a diamond machining tool, which closely resembles an ultra-fine machining system, to measure ultra-low thrust forces during nano-scale machining. We successfully created V-grooved nano-patterns on silicon, germanium, and gallium arsenide and determined the critical thrust force. Our analysis, considering several mechanical properties, revealed that the critical thrust force correlates with hardness and elastic modulus, which are key mechanical parameters influencing plastic deformation and material fracture. The volume change was measured by AFM(Atomic Force Microscope) after machining, the amount of plastic deformation could be successfully calculated without observation of chips.

Ductile-to-brittle transition, Mechanical machining, Nano-scale, Critical thrust force, Plastic deformation

1. Introduction

Single-crystal materials are commonly perceived as difficult-to-cut due to their brittle characteristics. However, previous studies [1,2] have demonstrated that these materials can be mechanically machined with ultra-low forces, exhibiting a phenomenon known as 'ductile machining.' This occurs at forces lower than the critical thrust force determined in earlier research. The ductile machining of single-crystal materials by diamond turning was investigated in previous researches, however, there was limited research on quantitative analysis of thrust force of nano-scale planing. Recent research [3] has revealed that the critical thrust force for single-crystal silicon varies with the applied force per unit, indicating it is an experimental parameter rather than an inherent material property. Moreover, distinguishing whether ductile machining is based on cutting or plastic deformation remains challenging due to the inherent difficulty in analyzing nano-sized chips. Therefore, this study investigates the variation in material mechanical properties affecting the critical thrust forces for selected single-crystal materials and proposes a quantitative method for elucidating the mechanism of ductile machining by measuring volume changes.

2. Experimental methods

We selected three types of single-crystal materials—silicon(001), GaAs(001), and Ge(001). The critical thrust force for each material was determined following the methodology proposed in recent research [3]. A nanoscratch tester (Anton Paar) equipped with a diamond machining tool with a 90-degree shape angle, resembling an ultra-fine machining system, was employed as shown in Fig. 1. All scratching experiments were performed along [110] crystallographic direction on the three single-crystal materials. The critical thrust force, marking the ductile-to-brittle transition, was confirmed by SEM (Scanning Electron Microscope) observation. Mechanical properties were measured using the nanoindentation method [4]. Volume changes after ductile machining were measured using an AFM (Atomic Force Microscope), calculating changes in the volumes of the machined V-groove and pile-ups.
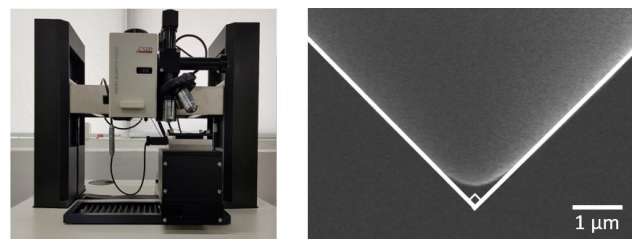
Figure 1. A nanoscratch system(left) and a diamond machining tool(right)

3. Results and discussion

Figure 2 presents ductile machining and brittle fracture of a single-crystal silicon. The ductile machining was observed at much low force as previous researches, and then the ductile-to-brittle transition was observed. The critical thrust force was defined as the force at which the first brittle fracture occurred. To ensure the reliability of our findings, we conducted five repetitions of the same experiments on a single material, demonstrating high repeatability. The critical thrust forces for silicon, GaAs, and Ge were approximately 17 mN, 27 mN, and 8 mN, respectively. The critical forces showed a similar tendency to the results of the previous research [5]. Minomura et al. found that the ratios of the pressure to make phase transition of silicon, GaAs and Ge are about 1:1.25:0.62,respectively. The exact pressure values and further crystallographic analysis are needed in a future study.
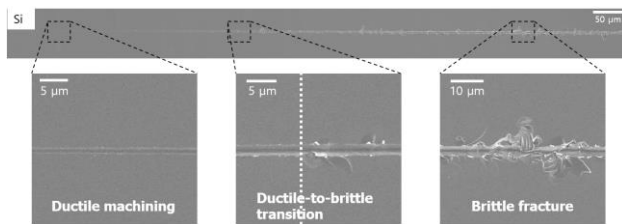
Figure 2. Ductile machining and brittle fracture occurred in a single-crystal silicon

Since ductile and brittle characteristics are clearly related to elastic and plasitic properties of a material, we chose elastic modulus (E) and hardness (H) as representative mechanical properties for studying the ductile-to-brittle transition. Among several combitions of E and H, Tsui et al. [6] proposed that H^3 over E^2 was a parameter of the critical force of plastic deformation in nanoscratch tests. H^3 over E^2 exhibited a robust positive relationship with the critical thrust forces in this study. Though the physical meaning of H^3 over E^2 should be addressed in further study, it can be used for predicting the critical thrust force of a machined material.

Figure 3 shows AFM profiles of silicon and GaAs. The profiles were measured at five machined V-grooves, and they were overlapped much well. We calculated the decresed area of a V-groove and the increased area of pile-ups around the surface of a V-groove. Since we could assume that the V-groove and the pile-ups had the same length, the ratio between the two calculated area should be same to the ratio of the volumes. If the ductile machining is based on plastic deformation, the volume change would be zero theoretically, which means the decreased volume and the increased volume would be same or their ratio would be one. Conversely, if the ductile machining is based on cutting, the decreased volume would be significantly larger than the increased volume, or the volume of the pile-ups would be considerably smaller. Examination of Fig. 3 reveals similar volumes for two V-grooves, yet differing volumes for pile-ups. The volume ratios of pile-ups over V-groove of silicon and GaAs were approximately 0.36 and 1.05, respectively. This allows us to infer that the ductile machining of silicon is based on cutting, while GaAs exhibits characteristics indicative of plastic deformation. Hokkirigawa et al. [7] proposed that the parameters which could predict ploughing(plastic deformation) and cutting in scratch tests Our calculations using these parameters placed GaAs closer to ploughing than silicon, corroborating our experimental findings.
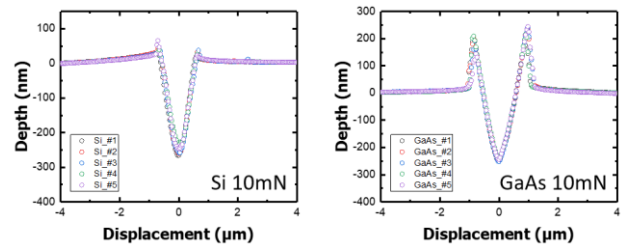
Figure 3. AFM profiles of V-groove of silicon and GaAs

4. Conclusions

We analysed the relationship of material mechanical properties and the the critical thrust forces of three single-crystal materials, and suggested a quantitative parameter for determining the mechanism of ductile machining in this study. The details are written below.

1) The critical thrust force which makes the first brittle fracture was largest in GaAs(001)[110], followed by silicon(001)[110] and Ge(001)[110]. .

2) H^3 over E^2 exhibited a strong positive correlation with critical thrust forces (H: Hardness, E: Elastic modulus).

3) The volume ratio of the V-groove and the pile-ups can be used as a parameter for determining the mechanism of ductile machining of each single-crystal materials.

Acknowledment

References

[1] Shimada S and Ikawa N 1995 *CIRP. Ann.* **44** 523-526
[2] Arif M, Xinquan Z, Raman M and Kumar S 2013 *Int. J. Mach. Tool. Manuf.* **64** 114-122
[3] Choi D H, Lee J R, Kang N R, Je T J, Kim J Y and Jeon E 2017 *Int. J. Mach. Tool. Manuf.* **113** 1-9
[4] Oliver W C and Pharr G M 1992 *J. Mater. Res.* **7** 1564-1583
[5] Minomura S and Drickamer H G 1962 *J. Phys. Chem. Solids* **23** 451-456
[6] Tsui T Y, Pharr G M, Oliver W C, Bhatia C S, White R L, Anderrs S, Anders A and Brown I G 1995 *MRS Online Proceedings Library* **383** 447-452
[7] Kokkirigawa K and Kato K 1988 *Tribology Inter.* **21** 51-57

Porous chuck without vacuum for wafer grinding and polishing

Kenichiro YOSHITOMI[1], Atsunobu UNE[1]

[1]National Defense Academy of Japan

yokken@nda.ac.jp

Abstract

In the grinding and polishing processes for thin substrates such as wafers, a chucking system is essential for a high-precision machining. Vacuum porous chucks are generally used for the grinding and polishing of wafers. However, their surfaces easily wear and they are difficult to clean inside. Additionally, the thinner the wafer, the more difficult it is to clamp without causing deformation above each pore of the porous chuck owing to the vacuum pressure. Therefore, a water-film chuck that does not allow direct contact between the wafer and the chuck has been developed. Our previous study showed that a water film with a size below 0.3 μm was required to obtain a lateral restraint force applicable to polishing. This paper describes a new chucking system that uses a water-film porous chuck without a vacuum. The adoped porous material has considerably smaller grains than those used in a standard porous chuck. Porous materials facilitated the formation of ultrathin water films. In addition, an ultrathin and uniform water film was formed via control of the atomizer application time. According to the experimental results, this chucking system generated a lateral restraint stress greater than 25 kPa, and could be used for polishing at the pressure of 30 kPa.

Keywords: grinding and polishing, porous chuck, water film, lateral restraint stress, sapphire wafer

1. Introduction

A vacuum porous chuck is a standard devices for clamping of a wafer for processing. The vacuum pressure generates a sufficient uniform clamping force over the entire wafer. The use of vacuum also facilitates the wafer attachment and detachment. However, the porous chuck suffers from surface wear owing to repeated contact with the wafers and it is difficult to clean the dust inside. Therefore, the chuck must be replaced. Additionally, the vacuum pressure causes deformation of the areas of the wafer located above in each pore of the porous chuck, as the wafers are expected to become thinner. Therefore, a chucking method without a vacuum is required.

This study describes a new chucking system using a water-film porous chuck, its clamping characteristics, and the results of a polishing experiment on a sapphire wafer.

2. Water-film porous chuck

To overcome the problems related to the vacuum porous chuck, a water-film chuck, which uses the adsorption of an ultrathin water film and does not allow a direct contact between the wafer and chuck, was developed as a unique clamping method without a vacuum. A thinner water film provides larger vertical and lateral restraint stresses that are attributed to the meniscus force generated by the water film [1–3]. When the thickness of the water film is less than 0.3 μm, the lateral restraint stress is above 30 kPa. However, thinning of the water film and detachment of the wafer are not straightforward because the chuck surface is a high-precision flat surface that is mirrored. These issues are caused by the difficulty of moving water in the water film within the small gap between the wafer and chuck, and supplying air between the wafer and chuck for detachment of the wafer. Therefore, we propose a water-film porous chuck with improved practicality compared to a water-film chuck.

2.1. Porous material

The porous material used in this experiment was manufactured via sintering $3.5 - 4.5$ μm alumina ceramic grains and had the porosity of 40%. In addition, the diameter of the material was 100 mm with thickness of 5 mm. The material surface was mirror-polished to a flatness of 0.7 μm over its entire surface and roughness of lower than 10 nm (Ra) on the grain surface. Figure 2 shows a magnified image and calculated contact area (green area) of the porous material surface. The contact ratio was calculated by the height distribution measured by a laser scanning confocal microscope assuming that the area within 0.4 μm from the top of the grain surface contacts the wafer. The minimum size of the pores was 2 μm. This is considerably smaller than that of a standard vacuum porous chuck. The contact ratio calculated as 35.4%.
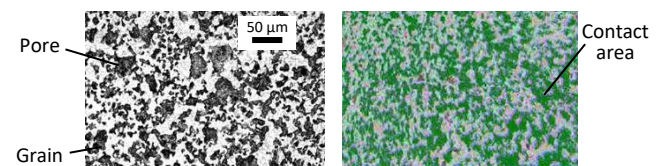
Figure 1. Magnified porous surface and calculated contact area.

2.2. Ultrathin water film formation method

A small amount of water supply is required for the water film formation method. An atomiser that generates mist water containing water particles ($4 - 11$ μm) was used in this experiment. Water mist was applied to the surface of the rotating wafer. A water film was formed after placing the wafer on the porous material and pressing it at the pressure of 7.5 kPa. Finally, a thinner water film forms as the water moves into the pores of the porous material via capillary action. The thickness of the water film could be adjusted based on the application

time of the mist water. Figure 2 shows the sapphire wafers with diameters of 100 mm clamped using a water film under a white-light-emitting diode (LED). In Figure 2(a), interference fringes are observed when the amount of water applied is excessively large. As shown in Figure 2(b), no interference fringes were observed over the entire wafer surface. The water film thickness in this case was smaller than 0.3 µm, as measured by the thin-film thickness measuring instrument. This clamping state was maintained for at least 2 h without drying out.

During grinding and polishing, the lateral restraint stress of the chucking system must be larger than the friction stress generated between the wafer and the grinding wheel or the polishing pad. Figure 3 illustrates the measurement instrument for the lateral restraint force. In the experiment, an optical flat with the thickness of 10 mm was used to avoid cracking, and the maximum load was limited to 200 N. This corresponds to 25.5 kPa for a wafer with a diameter of 100 mm. Figure 4 presents the measurement results for the water-film porous chuck and vacuum porous chuck. For the water-film porous chuck, the lateral restraint force was 197 N, which was almost at the measurement limit. The clamping force for a standard thickness wafer is expected to be considerably larger because its deformation follows the chuck surface profile. In contrast, the lateral restraint force of the vacuum porous chuck, whose frictional force was determined by the friction coefficient and real contact area, was 90 N corresponding to 11.5 kPa.

(a)   (b)
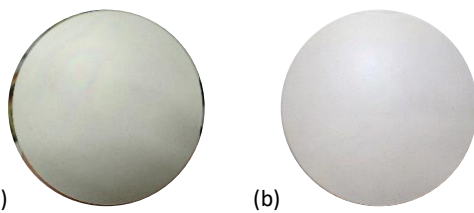
Figure 2. Interference fringe images of sapphire wafers clamped by the water-film porous chuck.
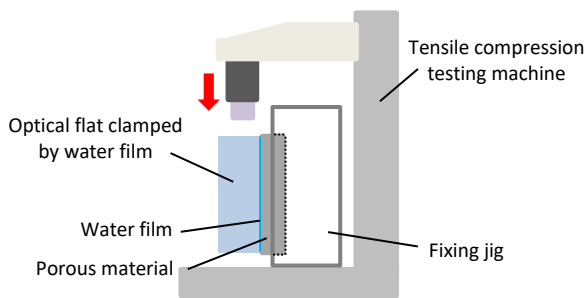
Figure 3. Measurement apparatus for the lateral restraint force.
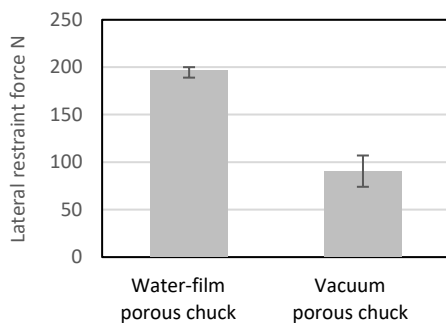
Figure 4. Lateral restraint forces generated by the water-film porous chuck and vacuum porous chuck.

3. Polishing experiment

A polishing experiment using the porous material mentioned above as a water-film porous chuck was conducted under the conditions listed in Table 1. The initial roughness of the wafer was 0.67 µm (Ra). Figure 5 shows the variation in the horizontal load applied to the polishing head over time. The water film exhibited sufficient clamping performance against the frictional force generated by the polishing. The periodic change in the load was caused by the oscillating motion of the polishing head. The average horizontal load was 242 N, which was greater than the lateral restraint force obtained in the experiment. The roughness of the polished wafer was 0.33 µm (Ra). According to the observation after polishing, the slurry did not seep between the wafer and the chuck. Therefore, the water-film porous chuck can polish a wafer without causing wafer detachment under standard polishing conditions.

Table 1 Polishing conditions.

Polishing machine	Fujikoshi Machinery Corp., SLM-140CY	
Wafer	Sapphire wafer	
Polishing pad	NITTA DuPont Inc., MH-S15A	
Rotational speed	Wafer	100 min^{-1}
	Polishing pad	100 min^{-1}
Polishing pressure	30 kPa	
Oscillation speed	60 mm/min	
Slurry	Colloidal silica, 50 mL/min	
Polishing time	60 min	
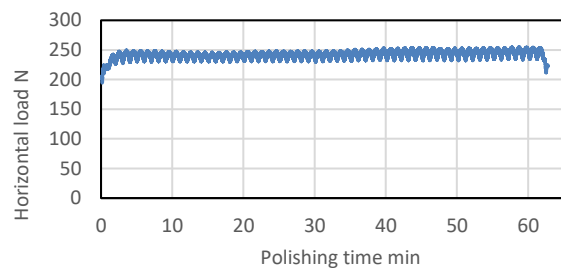
Figure 5. Variation in horizontal load of polishing head during polishing.

4. Conclusion

To overcome the problems related to the vacuum porous chuck, a water-film porous chuck that clamps a wafer without a vacuum was proposed. The main characteristics of the chucking system are the usage of the porous material with pores of 2 µm minimum and forming method of a thinner water film using the mist water. According to the experimental results for the optical flat with diameter of 100 mm, the formation of the water film with a size below 0.3 µm was achieved, and a lateral restraint force of approximately 200 N was obtained. Furthermore, the water-film porous chuck can polish a wafer at the pressure of 30 kPa. Future studies should aim to clarify the grinding and polishing characteristics of the thinning process using this chucking system.

References

[1] Israelachvili J N 1991 Intermolecular and surface forces Academic Press
[2] Yoshitomi K, Une A, Ogasawara N, Mochida M, and Yamamoto E Fundamental characteristics of a water-film chuck 2013 *Proc. 13th euspen* 30–34
[3] Yoshitomi K, Une A, Bando T, and Yamamoto E Development of a water-film chuck (2nd Report) 2019 *J. JSPE* **85** 787–792

Relationship between phase transformation pressure and shear stress in the machining of semiconductor crystals

Marcel Henrique Militão Dib[1], Alessandro Roger Rodrigues[2], Renato Goulart Jasinevicius[2]

[1]Inst. Federal de Educ. Ciência e Tecnologia de São Paulo, CEP 14801-600 Araraquara – SP, Brazil

[2]Depto Eng. Mecânica, EESC, USP, C.P. 359, CEP 13566-590, São Carlos, São Paulo, Brazil

marceldib@ifsp.edu.br

Abstract

In diamond tool turning of semiconductor crystals, the phenomenon of ductility emerges at submicrometric cutting thickness. This is attributed to the complex tool-material interaction, where the pressure in the contact region between the cutting edge and the material can reach levels comparable to the phase transformation pressure of the machined material. Ductile removal varies with the crystallographic orientation and negative rake angle tools, particularly around -37.5°, enhance the ductile response during cutting. Cutting forces decrease as the machining direction transitions from the harder [100] to the softer [110]. This study investigates the shear stress variation with different rake angles in machining semiconductor crystals (Si) oriented along the (001) plane. Results show a clear correlation between increased shear stress and improved material removal efficiency, providing clear-sightedness on the effect of ductility for precision machining in semiconductor manufacturing.

Monocrystalline Silicon; Diamond tool; Transition pressure; Rake angle

1. Introduction

Transition pressure plays an important role in addressing the issue of fragile to ductile behavior in monocrystalline semiconductor materials under loading [1]. Indentation is a commonly employed technique to illustrate pressure-induced phase transformations. It relies on the interaction between the indenter and the material, controlling the dynamic displacement of the indenter into the surface [2]. In materials such as Si and GaAs, specifically on the (100) orientation plane, the [100] direction is anticipated to be the hardest, in contrast to the softer [110] direction [3]. During indentation, the [100] direction exhibits brittle behavior, while the [110] direction demonstrates ductile behavior [4]. However, under the influence of loads from the cutting process, there is an inversion in the brittle and ductile behavior. The [100] direction becomes ductile, while the [110] direction becomes brittle [5]. One explanation for this phenomenon concerning cutting is related to the compression of the tool on the material, which increases the shear stress. This increase in shear stress may be responsible for the inversion of behavior, changing from brittle and ductile during indentation to ductile and brittle during cutting. To clarify this, the specific objective of this study was to demonstrate the effect of shear stress on monocrystalline Si (100) during ultraprecision turning with a diamond tool for different rake angles.

2. Material and Methods

We used single crystal silicon in ultra-precision machining with a circular tip diamond tool. The specimens (20 × 20 mm) were cut from silicon wafers with (100) surface orientation, 1 – 10 Ω.cm resistivity, P-type (Boron concentrations: 10^{15} - 10^{16} atoms cm^{-3}), 55 mm diameter and 500 µm thick.

Commercial diamond tools were used for the experiment with monocrystalline diamond with a nose radius of 762 µm and 100 µm, cutting edge radius of 40 nm, clearance angles of 10º and rake angles of 0º.

Single point diamond turning experiments were carried out on a commercially available diamond turning machine, the Aspheric Surface Generator Rank Pneumo ASG 2500. This is a very rigid system with a T-base carriage configuration and carriages (hydrostatic bearing, driven with pulse-width-modulated DC servomotors, rotary-to-linear motion through 5 mm pitch ballscrews and position feedback using laser interferometer) that had a 10 nm positioning accuracy.

We used cutting forces data to determine the value of shear stress during machining. An acquisition system was assembled to measure the machining forces, consisting of an acquisition plate (400 kHz), a multi-channel load amplifier, and a piezoelectric dynamometer Kistler, model 9652C2 (0 to 250 N; natural frequency of 2 kHz), all commercial. The forces were recorded at a sampling frequency of 130 kHz for each force. The positioning of the dynamometer was established in such a way that the x-axis provided the thrust force (Ft), and the y-axis provided the cutting force (Fc). A device with rotating capability was designed and manufactured to vary the tool's rake angle (Figure 1). This device consisted of an angled base and a tool holder. The angular base was attached to the dynamometer, and the tool holder was attached to the angular base in the position corresponding to the desired rake angle.

Figure 1. Device for changing rake angle.

The shear stress (τ_s) was estimated using measured cutting forces, as proposed by Merchant [6]. It was determined by the decomposition of thrust and cutting forces into the normal and friction forces to the tool face (F and N), as well as the friction force (F_s) in the shear plane. These forces are distributed in the shear plane (As), which is related to the shear angle (φ) and friction angle (β), expressed by the following equations:

$$F = Fc.\sin(\alpha) + Ft.\cos(\alpha)$$
$$N = Fc.\cos(\alpha) - Ft.\sin(\alpha) \quad\quad (1)$$
$$F_s = F_c.\cos(\varphi) - F_t.\sin(\varphi)$$

$$\varphi = 45 + \frac{\gamma}{2} - \frac{\beta}{2} ; \quad \beta = \tan^{-1}\left(\frac{F}{N}\right) \quad\quad (2)$$

$$\tau_s = \frac{F_s}{A_s} ; \quad A_s = \frac{f.ap}{\sin|\varphi|} \quad\quad (3)$$

f: tool feedrate per revolution; ap: depth of cut; α: tool rake angle.

To determine the Vickers Hardness in each direction, we employed a durometer with loads ranging from 1 gf to 2 kgf for indentation tests on silicon (100).

3. Results and Discussion

Figure 1 presented the results of Vickers hardness testing, revealing a notable brittleness along the [100] direction, characterized by more pronounced fractures and propagation of cracks.
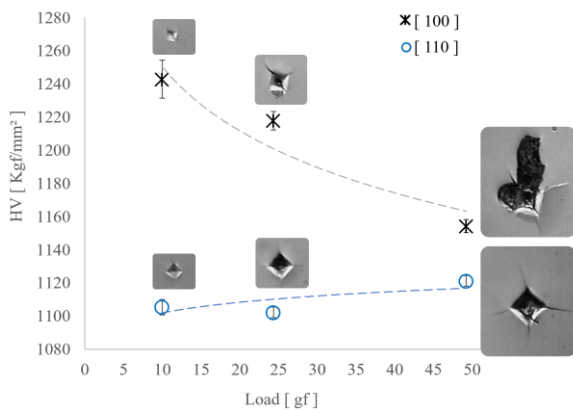
Figure 2. Vicker Hardness on silicon (100).

Figure 3 shows the shear stress results in turning and the influence of tool angle rake, demonstrating an increase in shear stress as it becomes more negative, thereby improving ductile response.
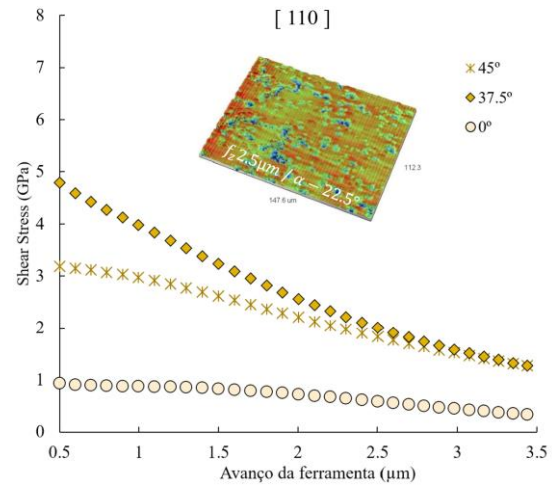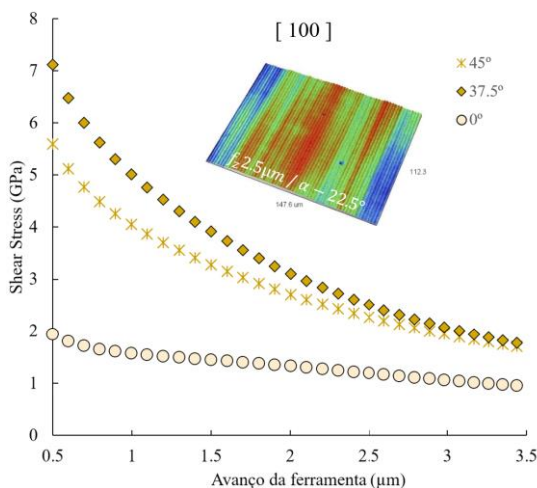
Figure 3. Shear stress in (100) silicon cutting.

However, the peak performance occurs around -37.5°; beyond this angle, the shear stress diminishes once again. This phenomenon was also noted by Lai et al. [7].

In the context of machining, there is a reversal in the brittle and ductile behavior compared to indentation. Unlike in indentation, where the [100] direction shows greater fragility, machining reveals that the [110] direction exhibits more pronounced fractures and crack propagation. This characterizes the beneficial effect of the increased shear stress generated during machining, particularly when the [100] direction attains higher shear stress values, promoting a more ductile behavior.

4. Conclusions

This study evaluated the ductile response of single crystal silicon, considering the influence of shear stress in ultraprecision turning. Contrary to the expected brittleness in the [100] direction of silicon (100) under loading, the turning process reveals a reversal in behavior as shear stress increases, promoting a more ductile behavior of the [100] direction during the cutting.

References

[1] Budnitzki M, Kuna M. Stress induced phase transitions in silicon. Journal of the Mechanics and Physics of Solids 2016;**95**:64–91.

[2] Domnich V, Gogotsi Y. Pressure-Induced Phase Transformations In Semiconductors Under Contact Loading. Frontiers of High Pressure Research II: Application of High Pressure to Low-Dimensional Novel Electronic Materials 2001:291–302.

[3] O'Connor BP, Marsh ER, Couey JA. On the effect of crystallographic orientation on ductile material removal in silicon. Precision Engineering 2005;**29**:124–32.

[4] Gao R, Jiang C, Dong K, Lang X, Jiang J, Huang P. Anisotropy mechanical behavior of crystals based on gallium arsenide cleavage processing. Ceramics International 2021;**47**:22138–46.

[5] Mukaida M, Yan J. Ductile machining of single-crystal silicon for microlens arrays by ultraprecision diamond turning using a slow tool servo. International Journal of Machine Tools and Manufacture 2017;**115**:2–14.

[6] Merchant ME. Mechanics of the Metal Cutting Process. II. Plasticity Conditions in Orthogonal Cutting. Journal of Applied Physics 1945;**16**:318–24.

[7] Lai M, Zhang X, Fang F, Bi M. Effects of crystallographic orientation and negative rake angle on the brittle-ductile transition and subsurface deformation in machining of monocrystalline germanium. Precision Engineering 2019;**56**:164–71.

Mechanized adhesive applying for porous aerostatic bearings

Onni Leutonen[1], Valtteri Vainio[1], Luke Harding[1], Petteri Haverinen[1], Mikael Miettinen[1], Raine Viitala[1]

[1]Aalto University

onni.leutonen@aalto.fi

Abstract

Aerostatic bearings based on porous restrictors commonly consist of two components: the bearing body and the restrictor. The bearing body is usually steel or aluminium, and the restrictor is often graphite or some other porous material. The porous restrictor and the body are bonded together with adhesive. Aerostatic bearings are commonly utilized in precision engineering applications which require narrow manufacturing tolerances and a highly repeatable manufacturing process. The adhesive application in the assembly process of aerostatic bearings is vulnerable to variations, as the adhesive bonding process is sometimes carried out by hand. Thus, variances in the operation have effect on the final product's quality. This study presents a system for mechanized adhesive application for manufacturing of aerostatic bearings. The presented system was developed for mechanized adhesive application using a standard 50 ml handheld, two-component epoxy cartridge. A six-axis robotic arm was utilized to dispense and direct the bead of epoxy in a specified pattern, and a statistical inspection of this method's repeatability is performed. The study investigates the repeatability of this type of automated adhesive application, aiming to minimize the risk of poorly bonded restrictors in future studies.

Aerostatic bearing, adhesion, robot

1. Introduction

Aerostatic bearings are categorized according to the air feeding structure. Nozzle type bearings are common and widely adopted in the industry. Meanwhile, porous material bearings are also favoured in several industrial applications. The structure of porous material bearings commonly consists of a metal body and a porous material restrictor jointed to the body. Illustration of a porous aerostatic bearing structure is presented in Figure 1. The porous material restrictor not only limits the air consumption but also increases the stiffness of the air film compared to other type of aerostatic bearings [1]. Synthetic graphite is a common material utilized as the porous restrictor; however, it can have significant variation in its material properties [2].
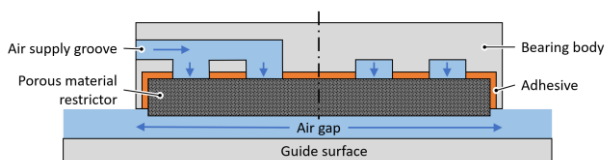
Figure 1. Simplified cross-section of circular porous aerostatic thrust bearing. Restrictor is adhesively mounted to the body.

In addition to the varying material properties of graphite, the adhesive bonding process between the graphite restrictor and the bearing body may introduce inconsistencies [3]. An excessive amount of adhesive may cover the open pores of the graphite or fill the air supply grooves. This can reduce the area of the air passages in the bearing body and limit airflow to the graphite restrictor. Additionally, an insufficient amount of adhesive may cause air leaks or a failure of the adhesive bond. Limited, uneven, or obstructed airflow to the restrictor causes losses in performance due to the uneven pressure distribution in the air gap.

Repeatable adhesive application process can be achieved with volumetric dispenser [4]. Dispensing unit can be mounted to an automated multi-axis machine, for example 6-axis robots are used in automotive industry [5]. This allows the adhesive to be applied in specified patterns and amounts. In cases where small series of bearings are manufactured, manual adhesive application may be required. Manual adhesive application leads to inconsistent dispensed pattern shape and the amount of applied adhesive. In attempts to eliminate any human error in the adhesive application process, this study introduces a simple, automated, and low-cost method of applying the adhesive by means of a robotic arm, two component epoxy cartridge, and a custom dispensing system.

The goal of this study is to validate only the repeatability of the mass of the adhesive bead applied to the bearing body. The data collected in this study demonstrates satisfactory levels of repeatability and this system may be suitable for use in future aerostatic bearing research endeavours. In future studies the adhesive target mass will be defined.

2. Methods

2.1. Machinery

The machinery consisted of UniversalRobots UR10 robot and a custom epoxy dispensing system. The epoxy dispensing system utilized a standard 50 ml handheld, two-component epoxy cartridge. The dispensing system is presented in Figure 2. A NEMA 17 stepper motor was connected through a 10:1 ratio planetary gearbox to a lead screw which actuated the piston pressing the adhesive cartridge pistons. The stepper motor was controlled to operate with constant rotational speed and thus maintained constant volumetric flow of the adhesive.

The mixing of the two epoxy components was performed with a 151 mm long, 21-element static mixing nozzle with an inner diameter of 6.3 mm. The cross section of the nozzle is circular, and the mixing elements are attached to each other only from the middle in a helical pattern thus reducing the possibility of air remaining in the nozzle. Air trapped in the nozzle will be compressed during the process, and after dispensing, the expanding air will cause undesirable flow from the nozzle. A 0.84 mm diameter 13 mm long stainless-steel dispensing needle was mounted to the tip of the static mixing nozzle. The dispensing needle enabled more accurate application of the adhesive bead, although the thin needle increases the pressure in the mixing nozzle and increases the force required to apply the adhesive from the cartridge.
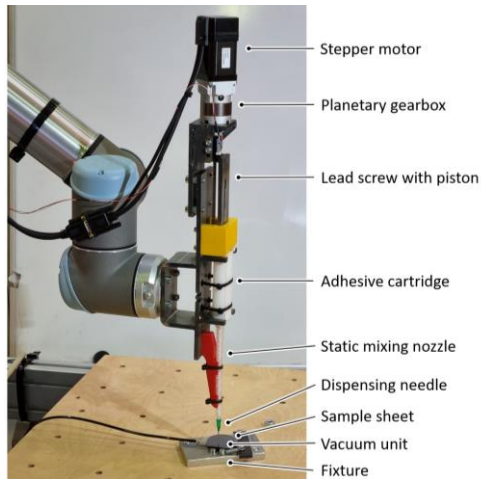
Figure 2. Adhesive dispensing system mounted to a robotic arm.

2.2. Test procedure

The test procedure consisted of the application of adhesive to plastic sheets with a controlled pattern identical to the one used in bearing manufacturing. During the measurements, the bearing body was replaced with a vacuum unit to hold the plastic sheets in place during the dispensing of the adhesive. The mass of each plastic sheet was measured before adhesive application. After dispensing, the adhesive was allowed to cure completely and the sheets with the adhesive were weighted.

2.3. Dispensing procedure

The system was initialized by extruding the adhesive to the mixing nozzle while the nozzle pointed upwards. Extrusion speed during the initialization was extremely slow due to the high viscosity of the adhesive. Filling the nozzle upwards with slow speed minimizes the amount of trapped air in the mixing nozzle. After the nozzle was filled, the first test extrusions were performed. According to the test extrusion results, the robot and extrusion speeds were adjusted. The final tool speed was 10 mm/s. All samples were extruded in one batch with a 35 s cycle time including the sheet changing time. A sample is presented in Figure 3.

Figure 3. Adhesive applied to plastic sheet with the same pattern utilized in the aerostatic bearing manufacturing process.

3. Results

The measurement results are presented in Figure 4. During the adhesive application, it was visually observed that approximately 10 consecutive samples were required before the extrusion results became uniform between samples. The same conclusion can be made from the data in Figure 4. Therefore, the last 30 consecutive samples were selected for analysis. The average mass of the adhesive of the selected samples was 406.15 mg, and the standard deviation was 4.84 mg (1.19 % of the average).
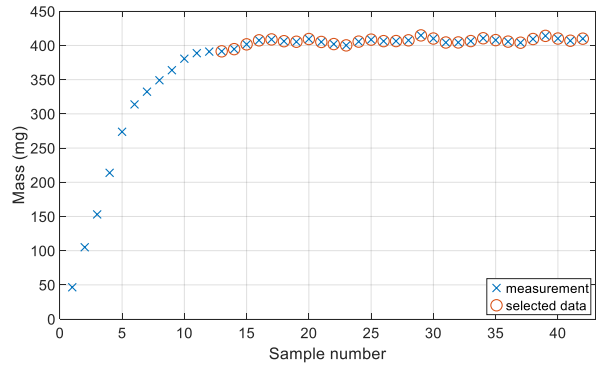
Figure 4. Dispensed adhesive mass. Initial gradient was excluded from statistical analysis.

4. Discussion

The system presented in this study reached an adequate level of accuracy and repeatability. The level of repeatability compared to commercially available solutions is in the same range. The system provided by Techcon reaches ±1 % level of accuracy according to the manufacturer [6]. Most of the commercial solutions are based on volumetrically adjusted dispensing which is a more accurate system by principle.

The main effect on the accuracy of the system originates from excess adhesive dripping from the needle between dispensing events as the pressure is released from the nozzle. To increase accuracy of the system, the authors suggest utilization of a shorter mixing nozzle and a pneumatically operated dispensing valve placed before the dispensing needle. The dispensing valve allows for a higher constant pressure applied in the cartridge without pressure loss between dispensing events. This stabilizes the flow properties and increases repeatability.

References

[1] A. H. Slocum, "Precision Machine Design", Prentice Hall, 1992. 750 p. ISBN: 0-13-690918-3.

[2] W. H. Rasnick, T. A. Arehart, D. E. Littleton and P. J. Steger, "Porous graphite air-bearing components as applied to machine tools," Oak Ridge Y-12 Plant, United States, 1974.

[3] O. Leutonen, "Porous aerostatic bearing graphite restrictor adhesive bonding to aluminium," Bachelor's thesis. Aalto University, School of Engineering. Espoo, 2023.

[4] R. Burga and A. Tausek, "Control of adhesive dispensing parameters during transition from research to production environments," *in Proceedings of the 5th Electronics Packaging Technology Conference* (EPTC 2003), 2003. doi: 10.1109/eptc.2003.1271604

[5] Springer Fachmedien Wiesbaden, "Precise bonding, sealing and insulating: Use of robots in automobile production," Adhesives&Sealants, **11**, pp. 30-33, 2014. doi: 10.1365/s35784-014-0262-1

[6] Techcon, "Accurately Dispense Two Component (2K) Material with Micro-Meter Mix / Dual PC Pump," 21.11.2022. [Online]. Available: https://www.techcon.com/dispensing-valves-and-controllers/accurately-dispense-two-component-2k-material-with-micro-meter-mix-dual-pc-pump/.

Investigating the application of semiconductor manufacturing technology to sealing stainless steel plates in high temperature reforming devices

Ian G. Lindberg[1], Alexander H. Slocum[1]

[1]*Massachusetts Institute of Technology*

ilndbrg@mit.edu

Abstract

The creation of high-performing and durable seals which can join stainless steel parts together is critical for applications such as reforming processes. While ferritic stainless steel is an exceptionally good choice of material for high temperature processes due to its manufacturability, cost effectiveness, and continued resistance to corrosion at high temperatures, it is also difficult to create seals which act as electrical insulators. Many insulators and dielectric materials with suitable high-temperature characteristics, such as glass, are unable to form a performant and durable seal due to the large difference in coefficients of thermal expansion (CTE). The discrepancy in expansion and contraction during heating and cooling cycles can lead to delamination from the stainless-steel substrate or fractures within the seal itself, either of which would render the equipment containing said seal inoperable and potentially causing further damage.

This paper explores methods for sealing stainless steel plates by leveraging technology from the semiconductor industry. Development of a multi-layered composite sealing and bonding method will be accomplished using equipment designed for handling and processing silicon wafers. By layering several coatings to form a seal, properties such as resistivity, adhesion, overall CTE, and self-healing properties will be able to be finely tuned to suit specific applications. Beginning with an assessment of spin-on glass, the use of fabrication methods originally developed for the semiconductor industry is investigated for the production of these composite high-temperature seals.

Reforming, High-Temperature Sealing, Semiconductor Fabrication, Wafer Bonding, Bonding, Composite Seals, Manufacturing

1. Introduction

In high temperature processes such as reforming operations, ferritic stainless steel is an exceptionally good choice of material for processing equipment due to its manufacturability, cost effectiveness, and resistance to corrosion at high temperatures. However, creating seals which can bond ferritic stainless-steel parts and act as electrical insulators, crucial for processes where generating a voltage differential is necessary, is difficult due to the extreme conditions this equipment is exposed to. Many existing insulators and dielectric materials with suitable high temperature characteristics are unable to function effectively as seals due large differences in coefficients of thermal expansion between the seal and the stainless-steel substrate. To overcome these issues, development of a composite seal which can self-heal during thermal cycling and is able to be tuned for physical and electrical properties is necessary. The development of this composite seal leverages fabrication techniques originating in the semiconductor industry, where uniform material deposition to form thin films is commonplace.

Previous work on the development of sealing methods for stainless-steel interfaces has focused on characterizing the mechanical and chemical interfacial mechanics between substrate and homogeneous sealing glass[1,2]. Meanwhile, work on thin layer deposition to stainless-steel substrates using semiconductor fabrication techniques have concentrated on thin layer characterization and interfacial characteristics[3–6]

rather than practical application in the fabrication of high-temperature seals.

The research described in this paper utilizes these semiconductor fabrication techniques in conjunction with interfacial analysis and testing within both mechanical and electrical regimes.

2. Methodology

To develop a composite sealing method, methods originating in the semiconductor manufacturing industry for thin layer deposition will be independently assessed for suitability and compatibility with stainless-steel substrates. Evaluation is carried out using test samples fabricated from AISI 430 stainless-steel, chosen as a representative ferritic stainless-steel due to cost effectiveness and availability. Results from electrical and mechanical testing of individual thin layer deposition methods will be leveraged to determine material and fabrication method choices for a composite seal.

2.1. Sample Preparation

Test samples were fabricated from AISI 430 stainless-steel sheet 0.5mm thick purchased from McMaster-Carr (P/N: 3803T18). As the material was received in a roll form, it needed to be flattened before individual test samples could be cut from it. This was accomplished by cutting the sheet metal into rectangular sections approximately 50mm wide and 150mm long. These sections were then flattened by heating them between two alumina slabs approximately 200mm square and

25mm thick which were ground to a flatness of less than 5μm. A thermocouple was also placed between the alumina slabs adjacent to the stainless-steel sheet to monitor the temperature at the centre of the "sandwich".
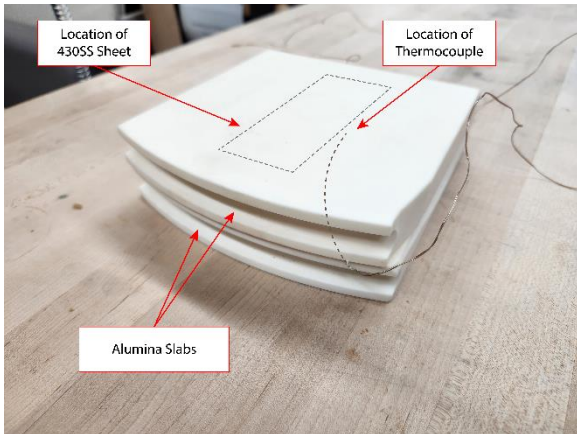
Figure 1. Alumina Slab "Sandwich" with Thermocouple

The flattening procedure was based on guidelines provided for annealing 430 stainless-steel by one of its major manufacturers[7]. The furnace used for the flattening process, a Vulcan A-550 Box Furnace (Fig. 2) was preheated to 760°C before the alumina slab "sandwich" was inserted into the furnace. After the core of the "sandwich" reached 760°C, this temperature was held for 20 minutes before the furnace was switched off and its contents were allowed to cool to room temperature.
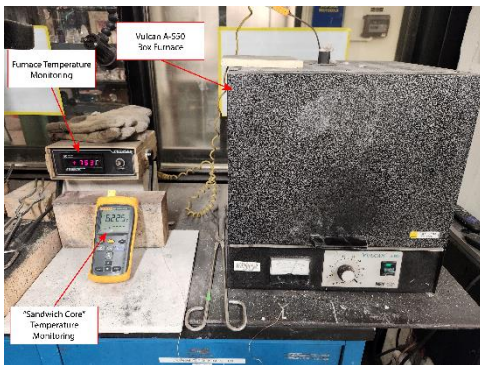
Figure 2. Vulcan A-550 Box Furnace Used for Sample Preparation

After the flattening process was completed, individual test samples in the form of 20mm diameter discs with two tabs for handling (Fig. 3) were cut from the sheet using a fibre laser. These samples were then polished on a Struers RotoPol grinding machine to a mirror finish, corresponding to an Ra of approximately 5μm.
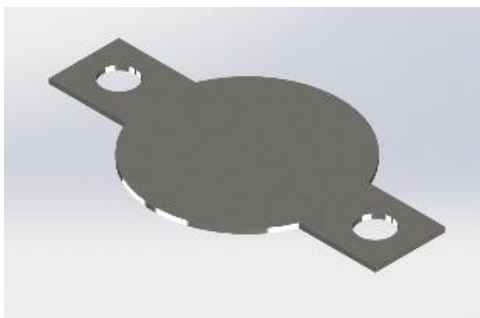
Figure 3. Computer Model of 430 Stainless-Steel Test Sample

2.2. Fabrication

Spin-on glass (SOG) has been selected as the initial material for consideration. Applied as a liquid to a substrate on a spinner table, SOG offers good planarization and insulation characteristics; the thickness of the layer deposited is determined by the rotational speed of the spinner table (Fig. 4). Following this deposition in liquid form, the SOG is baked to form a material with similar properties to SiO_2. Density of the cured SOG is determined by the temperature of the bake, allowing another degree of tunability.[8]

The SOG compound used is Desert Silicon NDG-7000R, a non-doped formulation specified to provide a cured film thickness of 7000 Å when applied with a spin speed of 4000 RPM.[9]
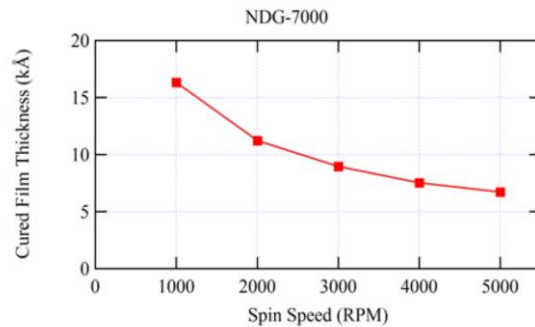
Figure 4. Cured Film Thickness vs. Spin Speed for NDG-7000R[9]

The spin-on glass is applied and processed using procedures common in the semiconductor industry with the ultimate goal of bonding two test samples together for mechanical and electrical characterization (Fig.5).
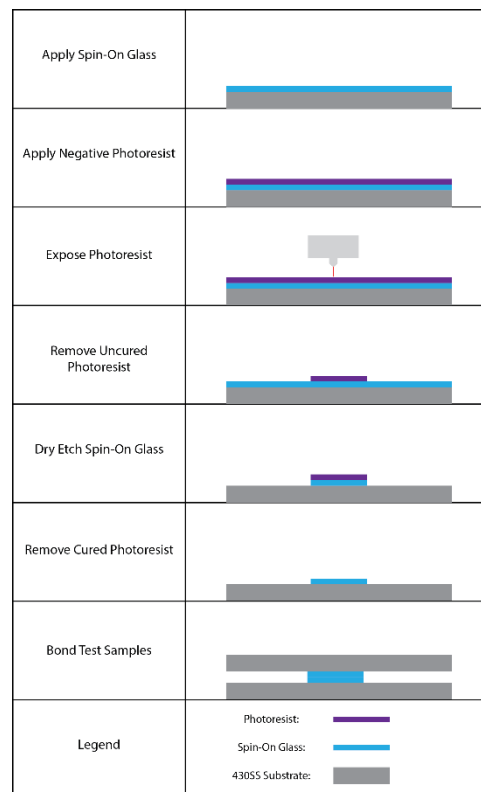
Figure 5. Spin-On Glass Processing

2.2.1 SOG Application

After each sample was cleaned with acetone, they were individually placed on a vacuum chuck spinner and approximately 0.25mL of Desert Silicon NDG-7000R was deposited on the centre of the sample using a micropipette. After ensuring that the sample was correctly centred and fully constrained by the vacuum chuck, the spinner was run at a speed of 1000 RPM for 120 seconds to yield a film thickness of approximately 1.5μm. The test sample was then immediately transferred to a hotplate and baked at 225°C for 240 seconds to cure the spin-on glass.

2.2.2 Photoresist Processing

After the test samples cooled, they were transferred to another spinner for photoresist application. Similarly to the previous processing step, each test sample was individually placed on the spinner and retained using a vacuum chuck. Approximately 0.25mL of AZ nLOF 2020, a negative photoresist[10], was deposited on the sample. The spinner was then run at a speed of 3000 RPM for 120 seconds to yield a thickness of 2μm. After completion of the spinning, each sample was transferred to a 110°C hotplate for a 120 second pre-exposure bake.

The next step in the photoresist processing was to expose the photoresist. As negative photoresist was used, the section which needed to remain behind after development was the region of the wafer which was exposed. This was accomplished using a Heidelberg Instruments MLA 150 Advanced Maskless aligner. A 5mm diameter circular region at the centre of each test sample was exposed using the recommended parameters for nLOF 2020. Following the exposure, the samples were transferred to a 110°C hotplate for a 120 second post-exposure bake.

Following the exposure and post-exposure bake, the photoresist was developed. Each sample was immersed in AZ 726 MIF developer [11] for 60 seconds while being agitated, after which they were removed and rinsed in four consecutive baths of deionized water.

2.2.3 Etching

Following photoresist processing, the samples were dry etched to remove the spin-on glass surrounding the central area where photoresist remained. Multiple test samples were etched simultaneously for 10 minutes with CH_4 plasma using a Samco RIE-230iP Plasma Etching System. This etching cycle would be expected to etch SiO_2 on an Si substrate at a rate of 130nm/min for a total material removal of 1.3μm.

2.3. Testing

To verify the concept of using spin-on glass as an insulating layer, the resistivity of the 2μm layer of Desert Silicon NDG-7000R was measured using a Fluke 117 True RMS Multimeter. With one probe contacting the bare steel underside of a test sample and the other probe contacting the side where spin-on glass was deposited, the multimeter read open loop, indicating that the glass layer was successfully acting as an insulator.

3. Results

Deposition of the Desert Silicon NDG-7000R spin-on glass was successful, with an even layer applied across the entire surface of the stainless-steel test sample. While the surface of the glass remained planar, inspection under an optical microscope revealed that the spin-on glass had fractured into micron-scale pieces (Fig. 6).
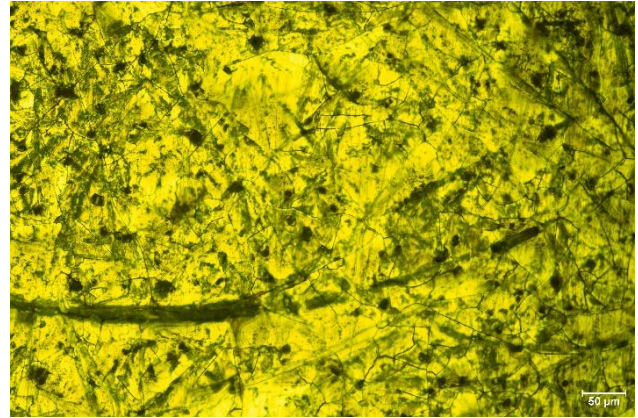
Figure 6. Test Sample Surface After Spin-On Glass Deposition

Apparent adhesion of the spin-on glass to the stainless-steel substrate was good, with the surface undamaged after measurement with an optical profilometer. This profilometer testing yielded an Ra of approximately 5μm, similar to that of the mirror-polished stainless-steel substrate.

Photoresist processing of the samples was also successful. After the exposure and development steps, a 5mm diameter region of cured photoresist remained at the centre of the test sample (Fig. 7)

Figure 7. Test Sample After Photoresist Processing

From imaging performed using an optical microscope, it was observed that the edge of the cured photoresist region had good definition with vertical sides that were not affected by any fractures in the spin-on glass surface below it (Fig. 8)
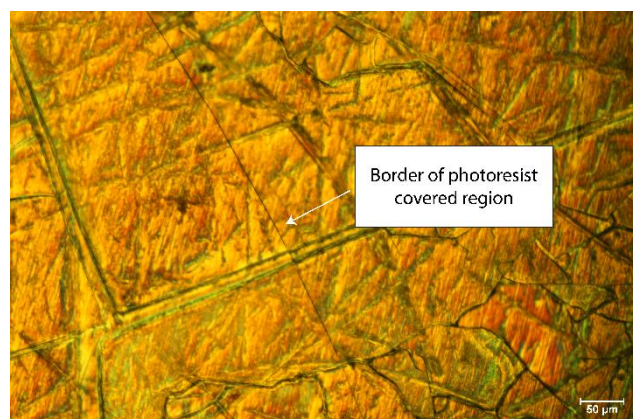
Figure 8. Test Sample Surface After Photoresist Processing

Following the dry etching process, the samples were again imaged using an optical microscope. Spin-on glass remained in the circular region which had been covered by the cured photoresist and the surrounding area had the majority of the spin-on glass previously present removed (Fig. 9). The same fracture pattern which had appeared when the spin-on glass was originally deposited remained, and the edge profile of the glass closely followed the shape of the photoresist pattern.

Figure 9. Test Sample Surface After Dry Etching

The next step taken was measurement characterization of the spin-on glass region using a stylus profilometer. It became apparent at this point that the dry etching process had caused the spin-on glass to delaminate from the stainless-steel substrate, as the stylus dislodged individual segments of glass and made measuring the profile of the spin-on glass impossible. Additionally, further review of the images previously taken revealed that the dry etching process had removed significantly more material than anticipated, with the entire cured photoresist layer removed. This indicates that the etching rate achieved was much higher than that expected for the same process carried out on a silicon substrate.

4. Summary & Conclusions

So far, this investigation of using semiconductor manufacturing methods for fabrication of high-temperature seals has determined that spin-on glass has promise as a material option due to its high electrical resistivity, ease of application, and compatibility with ferritic stainless-steel. However, the difficulties encountered during the dry etching process indicates that some semiconductor manufacturing processes must be adapted for use on a ferritic stainless-steel substrate and cannot simply be used as they are with silicon wafers. Once necessary adaptations are made though, these manufacturing methods which are already widely used and well understood in the semiconductor industry have the potential to be used in the fabrication of high-performance composite seals.

5. Future Work

For continuing development of a composite sealing method, tuning of processing methods such as dry etching for use on ferritic stainless-steel substrates will be necessary. Through this tuning process, an understanding of why the substrate material has such a significant effect on processing results will also be established.

In parallel with this tuning process, spin-on glass will continue to be testing, specifically as a bonding layer. As part of this process, test samples will be bonded together, and the bond will be mechanically characterized using a tensile testing machine.

For continuing development of a composite sealing method, assessment of additional thin layer materials and bonding techniques will be necessary. Physical vapour deposition (PVD) and chemical vapour deposition (CVD) will be investigated for suitability in fabrication of high-temperature seals, with Silicon nitride and metals such as aluminium and titanium being potential options using these methods.

To more closely simulate the conditions seals would be exposed to within a reforming stack or other high temperature processing equipment, mechanical and electrical testing at high temperatures, as well as temperature and load cycling. This high temperature testing will also be useful for determining whether the fracturing behaviour encountered in spin-on glass.

Following the development of a composite seal using these methods, testing in scaled systems which emulate reforming stacks will likely be the next step taken.

Acknowledgements

References

[1]   Haanappel, V. A. C., Shemet, V., Gross, S. M., Koppitz, Th., Menzler, N. H., Zahid, M., and Quadakkers, W. J., 2005, "Behaviour of Various Glass–Ceramic Sealants with Ferritic Steels under Simulated SOFC Stack Conditions," Journal of Power Sources, **150**, pp. 86–100.

[2]   Hu, K., Li, S., Fan, Z., Yan, H., Liang, X., Cai, Y., Zhu, Q., and Zhang, Y., 2021, "Contributions of Mechanical Bonding and Chemical Bonding to High-Temperature Hermeticity of Glass-to-Metal Compression Seals," Materials & Design, **202**, p. 109579.

[3]   Jeng, M.-J., Lai, W.-J., Chang, B.-Z., and Hu, S.-C., 2012, "Insulation and Diffusion Barrier Characteristics of Spin-on-Glass Layer on a Stainless Steel Substrate," Journal of Renewable and Sustainable Energy, **4**(1), p. 011603.

[4]   Lampert, F., Jensen, A. H., Din, R. U., Gonzalez-Garcia, Y., and Møller, P., 2018, "Properties and Performance of Spin-on-Glass Coatings for the Corrosion Protection of Stainless Steels in Chloride Media," Materials and Corrosion, **69**(9), pp. 1279–1291.

[5]   Zhang, Y., Wu, W., Han, Y., Wu, X., Cheng, Y., and Liu, L., 2020, "Adhesion Analysis of Silicon Nitride Film Deposited on Stainless Steel Surface by Adding Transition Layer," Nanotechnology, **31**(21), p. 215711.

[6]   Suganuma, K., Okamoto, T., Koizumi, M., and Shimada, M., 1985, "Effect of Thickness on Direct Bonding of Silicon Nitride to Steel," J American Ceramic Society, **68**(12), p. C-334-C–335.

[7]   1986, "CarTech 430 Stainless Technical Datasheet."

[8]   Peterson, R. J., 2016, *Literature Review of Spin On Glass*, LA--UR-16-21332, 1240802.

[9]   "Spin-on Glass NDG-7000R" [Online]. Available: https://desertsilicon.com/wp-content/uploads/Data-Sheet-NDG-7000R-1.pdf.

[10]   2021, "AZ nLOF 2000 Series Technical Datasheet."

[11]   2021, "AZ Organic Developers Technical Datasheet."

Nanopolycrystalline diamond for precision machining of binderless cemented carbide

E. Uhlmann[1,2], J. Polte[1,2], T. Hocke[1], C. Polte[1]

[1]*Institute for Machine Tools and Factory Management IWF, Technische Universität Berlin, Pascalstr. 8-9, Berlin, 10587, Germany*
[2]*Fraunhofer Institute for Production Systems and Design Technology IPK, Pascalstr. 8-9, Berlin, 10587, Germany*

c.polte@tu-berlin.de

Abstract

In a broad range of industrial applications, the technical importance as well as the demand for the hard-brittle material binderless cemented carbide is increasing due to special material properties. Due to its high wear resistance, binderless cemented carbide is used in industries like tool and mould making, optics as well as for forming and punching dies. However, because of the brittle material properties, the machining of this material with geometrically defined cutting edges is limited by the current state of the art due to considerable tool wear. An innovative approach for machining of binderless cemented carbide is the use of binderless nanopolycrystalline diamond (NPD) as a cutting material for precision turning. As part of these investigations, the use of NPD as cutting material was examined in detail by means of extensive turning tests, starting from the basic machining phenomena. Turning tests were carried out with cemented carbide samples with a cemented carbide content of $C_C = 99.5\%$, a cobalt content of $C_{Co} = 0.5\%$ and a grain size of $d_g = 0.3\,\mu m$. Prior to the basic turning tests, specific spiral cutting tests were carried out to identify the ductile-brittle transition and the minimum chip thickness as a function of the feed. Within subsequent turning tests the influence of the cutting depth, feed, cutting speed and the use of coolant was investigated. Surface topography, roughness characteristics, chip formation and process forces were used as process criteria. The potential of the innovative cutting material NPD could be demonstrated in the course of the investigations.

Keywords: binderless cemented carbide; nanopolycrystalline diamond; turning

1. Introduction

Binderless cemented carbide is used in a wide range of applications. At state of the art, binderless cemented carbide is mainly processed using grinding or electrical discharge machining technologies. However, conventional machining results in increased tool wear and surface cracks in the component surface. Due to the hard-brittle material characteristics and the considerable tool wear, the machining of binderless cemented carbide using geometrically defined cutting edge processes is significantly limited by the current state of the art. Due to its hardness H and grain size d_g the use of binderless nanopolycrystalline diamond (NPD) as a cutting material for precision turning represents an innovative approach to overcome the current challenges. As part of the present investigations, the use of NPD as a cutting material was used to analyse fundamental machining phenomena and for extensive turning tests. The investigations were carried out with a binderless cemented carbide, which is characterised by a tungsten carbide content of $C_C = 99.5\%$, a cobalt content of $C_{Co} = 0.5\%$ and a grain size of $d_g = 0.3\,\mu m$. As part of the investigations into the fundamental cutting mechanisms, scratch tests were carried out as a function of the depth of cut a_p and spiral tests were varied as a fuction of the feed f in order to determine the ductile-brittle transistion and the minimum chip thickness h_{min}.

As part of the subsequent turning tests, the influence of the cutting speed v_c, the depth of cut a_p, the feed f and the cooling lubricant were analysed. The surface topography, roughness characteristics, the chip formation and process forces F_p were analysed in more detail as process criteria.

2. Experimental Setup

To overcome the challenges of the state of the art, the SUMITOMO ELECTRICAL HARDMETAL CORPORATION, Itami, Japan, developed the NPD using a dedicated sintering process and a technology with a pressure of $p \geq 15\,GPa$ as well as a temperature of $\vartheta \geq 2.200\,°C$ to convert graphite directly into diamond. The novel NPD cutting material shows a polycrystalline structure with a hardness of $H = 150\,GPa$ and isotropic properties without any binder phase [1]. The macro- and micro geometries of the novel NPD were analysed by measurements prior to testing.

The macro-geometry of the cutting edge, which was ground and polished, is characterised by a value of $r_\varepsilon = 800\,\mu m$ with a rake angle of $\gamma = 0\,°$ and a clearance angle of $\alpha = 15\,°$. Laser machining was employed for customizing the micro-geometry of the cutting edge due to the exeptional hardness of the NPD material. The micro-geometry of the cutting-edge was examined utilising the optical measurement device InfiniteFocus, manufactured by ALICONA IMAGING GMBH, Graz, Austria. The analysis revealed a cutting-edge radius of $r_\beta = 11.13\,\mu m \pm 1.54\,\mu m$, a K-factor of $K = 0.989$ and a maximum chipping of the cutting edge radius of $R_{S,max} = 0.164\,\mu m \pm 0.023\,\mu m$. The surface roughness parameters of the machined workpiece surfaces were measured in terms of surface roughness Ra and Rz using the white light interferometer NewView 5010 from ZYGO CORPORATION, Middlefield, USA, with a measuring length of $l_m = 1.25\,mm$. Figure 1 shows an example of a NPD turning tool used. A scanning electron microscope (SEM) from LEICA ELECTRON OPTICS, Wetzlar, Germany, was used to take the SEM-images for further optical evaluation.
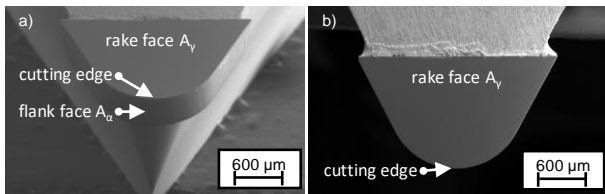
Figure 1. NPD turning tool with
a) overall view and b) view of the rake face A_γ

3. Cutting results

Prior to the spiral cutting tests, scratch tests were performed to get first insights into minimum chip thickness h_{min} and the transistion point from ductile to brittle material behaviour. These tests were carried out by varying the depth of the cut a_p or the feed f to acquire comprehensive insights into the fundamental cutting mechanisms employed in the machining of cemented carbide using binderless NPD. To identify the fundamental cutting mechanisms, comprehensive turning tests of hard-brittle binderless cemented carbide were carried out on the Nanotech 350 FG of the company MOORE NANOTECHOLOGY SYSTEMS, LLC, Swanzey, USA. Fundamental cutting mechanisms could be identified with a minimum chip thickness h_{min} at a depth of cut of $a_p = 2.4$ µm and a feed of $f = 2.7$ µm. The ductile regime was observed in a range of $3\,µm \leq a_p \leq 8\,µm$ and $3\,µm \leq f \leq 8\,µm$, whereas a transition to hard-brittle material behaviour is $a_p \geq 9.5\,µm$ and $f \geq 8.7\,µm$. Force measurement ranging between $19\,N \leq F_p \leq 30\,N$.

Owing to the prevalent carbide content C_{Co}, cemented carbide commonly exhibits brittle characteristics during the cutting process, leading to associated elevated tool wear. The hydrostatic pressure condition is a requirement during machining facilitates ductile cutting of cemented carbide. This hydrostatic pressure condition can be generated by utilising an effective negative rake angle γ, defined by a ratio of the chip thickness to the cutting edge radius $(h / r_\beta) < 1$, throughout the cutting process.

In the spiral tests, a great chip formation with a dominant cutting mechanism could be observed for a ratio of chip thickness to cutting edge radius in a range of $0.269 \leq h/r_\beta \leq 0.718$. Figure 2 shows the chips during the spiral tests in ductile condition (Figure 2a) as well as in hard-brittle condition (Figure 2b).
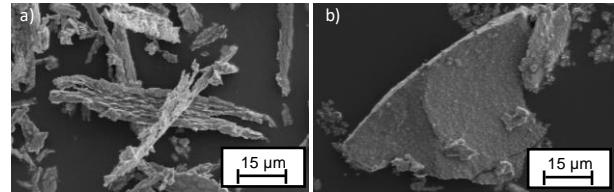
Figure 2. Chips a) finish cut and b) material breakage

The subsequent cutting experiments were conducted in accordance to design of experiments (DoE), utilising an experimental plan 2^{4-1} as illustrated in Table 1.

Table 1 Investigated process parameters for turning

Process parameter	Set 1		Set 2	
cutting speed v_c	50	m/min	200	m/min
depth of cut a_p	3	µm	8	µm
feed f	3	µm	8	µm
cooling lubricant	ISOPAR H		dry	

Figure 3 shows the main effect of the DoE study concerning the surface roughness Ra and Rz. The results show that the feed f has major influence on the surface roughness Ra and Rz with statistical relevance. By increasing the feed f, a significant increase in surface roughness could be demonstrated. The cutting speed v_c as well as the used cooling lubricant also show an influence, especially on the surface roughness Ra. Lowest surface roughness values of Ra = 11.0 nm and Rz = 71.7 nm could be achieved using a cutting speed of $v_c = 50$ m/min, a depth of cut of $a_p = 3$ µm and a feed of f = 3 µm with Isopar H as cooling lubricant.

Figure 3. Cutting results, main effects of the DoE study

4. Conclusion

The results show investigations based on spiral tests and subsequent turning tests. With a fully characterised macro- and micro-geometry of the used NPD tools, the fundamental cutting mechanisms for the machining of binderless cemented carbide could be identified by specific spiral tests. With regard to the micro-geometry of the cutting edge, an industrially relevant range of $3\,µm \leq a_p \leq 8\,µm$ for ductile cutting was observed. Fundamental cutting mechanisms were identified by scratch tests with a minimum chip thickness h_{min} at a depth of cut of $a_p = 2.4$ µm and a transistion to hard-brittle material behaviour for $a_p \geq 9.5$ µm. From a ratio of chip thickness to cutting edge radius of $h / r_\beta \geq 0.718$, surface cracks and brittle material behaviour could be observed. Surface roughness Ra and Rz were further analysed during subsequent turning tests. Based on the results, the feed f showed a major impact on the surface roughness Ra.

The lowest surface roughness of Ra = 11 nm could be identified at a cutting speed of $v_c = 50$ m/min, a cutting depth of $a_p = 3$ µm and a feed of f = 3 µm. In further investigations, the influential process parameters that affect the machining results will be comprehensively researched. Additionally, the wear behaviour of the NPD tools will also be investigated in detail in future research works. This work was funded by the GERMAN REASEARCH FOUNDATION DFG.

References

[1] Uhlmann, E.; Sturm, H.; Polte, M.; Hocke, T.; Polte, C.; Polte, J.: Charakterization and investigation of binderless nanopolycrystalline Diamond turning tools for precision machining, euspen´s 22nd International Conference & Exhibition, Geneva, CH, 2022.

[2] Uhlmann, E.; Oberschmidt, D.; Löwenstein, A.; Polte, J.; Gonia, D.: Binderless-PCD as cutting material for micro milling of cemented carbide moulds. Euspen´s 15th International Conference & Exhibition, Leuven, Belgium, 2015.

Study of sub surface damage in preparation of freeform glass optics using laser assisted single point diamond turning

Sai Kode[1], Jonathan D. Ellis[1], Daniel Ewert[2] and Felix Zeller[2]

[1]Micro-LAM, Inc. 5960 S Sprinkle Rd, Portage, Michigan 49002, United States
[2]Carl Zeiss Jena GmbH, Standort Oberkochen, Carl-Zeiss-Straße 22 73446 Oberkochen, Germany

sai.kode@micro-lam.com

Abstract

Freeform optics are a lucrative choice for optical designers looking to further enhance high end optical systems and reducing commonly known optical aberrations. A rotationally non-symmetric surface poses manufacturing challenges where a multi-axis CNC machine is required to produce such a surface. The real challenge, however, lies in polishing the surface from this state. An ultra-fine generation tool may still induce 20 – 60 µm of sub-surface damage. The process of removing the full extent of sub-surface damage using a sub-aperture tool is time consuming and induces undesirable mid spatial frequencies. Laser assisted single point diamond turning of amorphous glass is shown to exhibit merely 3 – 5 µm of sub-surface damage while maintaining accurate form. A custom Optical Coherence Tomography (OCT) instrument developed by ZEISS will be used to quantify sub surface damage in diamond turned and CNC generated freeform glass optics. This study will illustrate the differences in sub surface damage and resultant form produced using different manufacturing processes, including laser assisted diamond turning.

Laser assisted machining, diamond turning, OPTIMUS, sub surface damage, glass freeform, freeform optics, precision polishing, Optical Coherence Tomography (OCT)

1. Introduction

Freeforms optics are defined by rotationally non-symmetric surface shapes with little to no axis of symmetry. This makes the fabrication of such surfaces challenging because of the additional complexity required in manufacturing techniques/axis, as well as the specialized metrology equipment required to analyze such surfaces. The advent of ultra-precision machines (diamond turning machines) has allowed manufacturing of freeforms for several years in materials like Aluminum, Brass, Plastics, and even Infrared materials like Silicon or Germanium. The primary techniques used in ultra-precision machining are turning, grinding, and milling. Each fabrication technique has its advantages and disadvantages; however abrasive subtractive processes such as milling and grinding suffer from significant sub-surface damage (SSD) these processes impart beneath the surface. It is important to carefully control the amount of SSD, and use successive polishing strategies to smoothen/polish the freeform within the desired optical specification [1]. This paper will focus on examples of directly turning optical glass using micro laser assisted machining in being able to significantly reduce sub surface damage in freeforms. The two examples covered in this paper are round mild freeforms described as an Alvarez lens and phase plate.

2. Micro laser assisted machining process

Micro laser assisted machining was popularized by Ravindra *et al*. for the machining of hard and brittle materials such as Silicon [2]. The success seen in machining Silicon was later realized in several other diamond turnable materials such as Zinc Sulfide, Zinc Selenide and Calcium Fluoride. The laser had varying degrees of improvement dependent on material. There is an improvement in speed and yield on materials like Silicon and Germanium, whereas Zinc Sulfide and Zinc Selenide may see improved quality and yield with similar cutting speeds.

Tungsten carbide is conventionally not diamond turnable, however with the invention of micro laser assisted machining, it is possible to use an ultra-precision lathe to machine smooth optical surfaces for use in precision glass molding.

A 1064 nm continuous wave laser is delivered through the rear face of a diamond cutting tool and aligned such that the zone of contact between the workpiece material and diamond cutting edge is preferentially heated. This promotes increased ductility. In the case of conventional machining, most of the energy required in machining comes from a mechanical process. Using laser energy offsets mechanical energy required and augments this with photon absorption. A schematic of the laser assisted process is shown below in Figure 1 with the region of enhanced ductility highlighted in red. Lastly, the energy imparted by the laser into the workpiece material is immediately removed in the forms of chips. Therefore, the bulk material property remains unaffected.
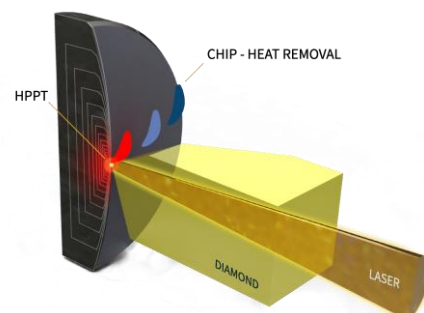
Figure 1. Micro laser assisted machining process cut away section view

Optical glasses such as fused silica and Schott N-BK7 are also not conventionally diamond turnable. However with micro laser assisted machining, it is possible to shape lenses to desired surfaces namely: spherical, aspherical, or even freeform using an ultra-precision lathe. The resultant SSD is 3 – 5 µm versus upto 60 µm with precision grinding. The total SSD induced prior to polishing is necessary to be removed by the polishing process. For aspherical and freeform polishing, sub aperture polishing techniques must be used which induce mid-spatial frequencies. A visual representation of the sub surface damage generated using grinding versus diamond turning with laser assisted machining is shown below in Figures 2 and 3. Figure 3 illustrates difference in appearance of 'gray' using different grits of grinding versus diamond turned.

| Rough Generate | DT with LAM | Freeform Polish |
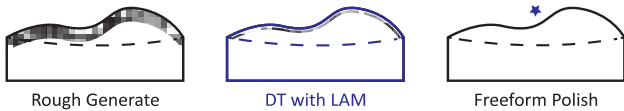
Figure 2. Process chain including laser assisted machining for the manufacture of freeform optics.

Figure 3. Visual comparison of 'grayness' of generated (D64 & D20) versus laser assisted diamond turned sample (right).

3. Freeform design and metrology

The design characteristics for the two freeforms presented in this paper are outlined in Table 1 below. These designs are examples of mild freeforms capable of being machined using slow tool servo on an ultra-precision machine. A slow tool servo process is where the Z-Axis is traversed in an out of the lens in conjunction with the rotary position of the C-Axis while also traversing along the lateral axis (X-Axis) [3].

Table 1. Freeform design and description.

	Units	Design 1	Design 2
Material	-	Schott N-BK7	Fused Silica
Sag range	mm	0.161	0.544
Diameter	mm	28	28
Edge Slope	deg	1.9	7
Slope Range	deg	2	11

3.1 Surface Roughness

The average surface roughness (Sa) obtained for the precision freeforms range from 20 – 80 nm. A comparable surface directly from a generator using a D20 wheel would be near 300 nm. Figure 4 shows the measured average surface roughness for the different regions on the lens.
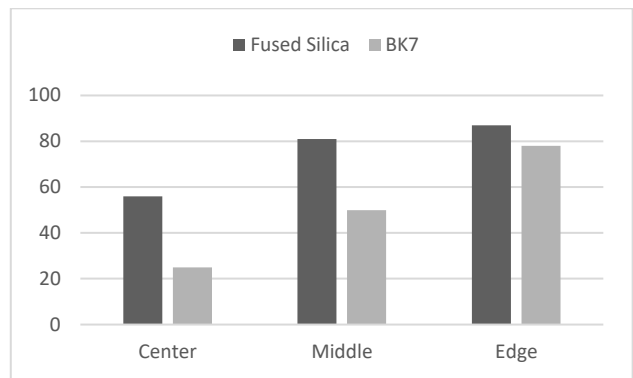
Figure 4. Average surface roughness of fused silica Alvarez lens and BK7 phase plate directly after diamond turning. (20X Objective, 10th order form removed)

3.2 Surface figure

The Schott N-BK7 phase plate is depicted in Figure 5 with the total sag range of 161 µm.
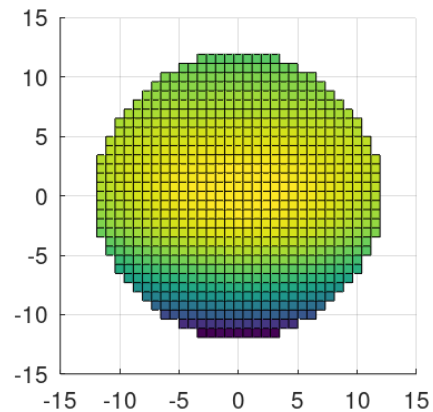
Figure 5. Schott N-BK7 phase plate freeform 3D sag map

As shown in Figures 6 and 7, there is still some deviation of the machined form. This is explainable due programming differences between the designed and machined part. Future efforts will negate this effect, by correcting the tool path adjusted to the measurement after the first run.
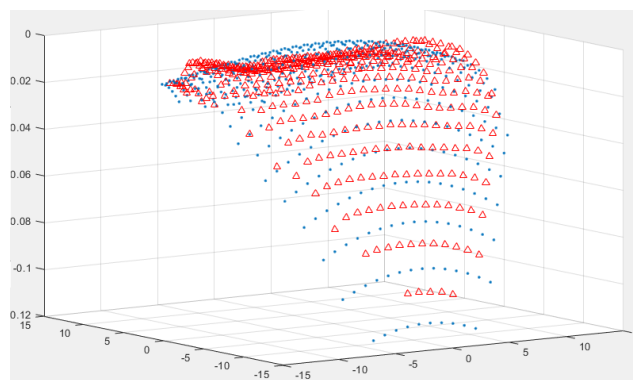
Figure 6. N-BK7 CMM measurement. Theoretical surface (blue), measured surface (red).
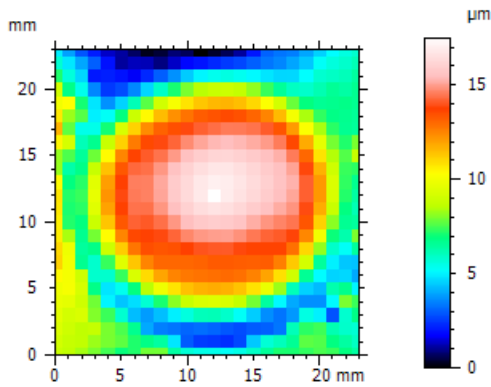
Figure 7. N-BK7 form deviation map. PV Irregularity: 17.48 µm.

The Fused Silica Alvarez design is depicted in the map of Figure 8 with the total sag range of 544 µm.
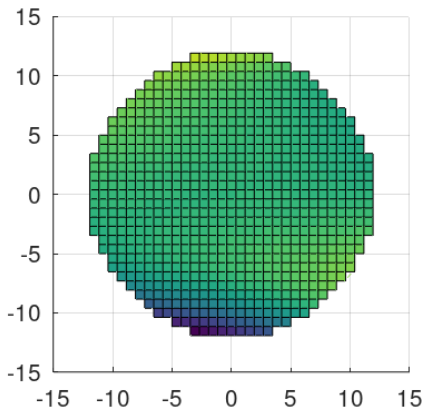
Figure 8. Fused silica alvarez freeform 3D sag map

Similar to the BK7 phase plate, there is also some form deviation of the fused silica Alvarez plate due to programming limitations. The measuerement of this optic is depicted in Figures 9 and 10. The first figure shows a comparison measurement versus model data and in the second figure the deviation map shows just the amount of deviation.
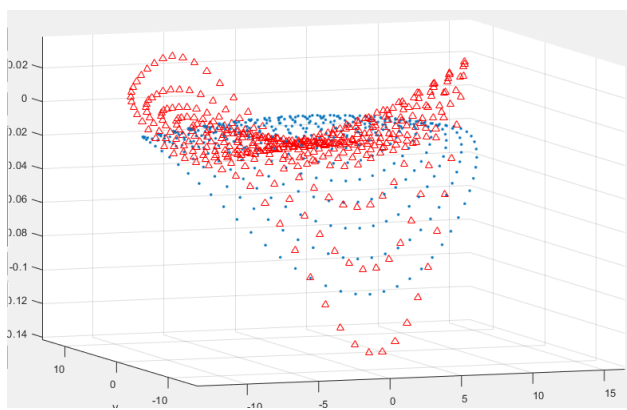
Figure 9. Fused silica alvarez CMM Measurement. Theoretical surface (blue), measured surface (red).
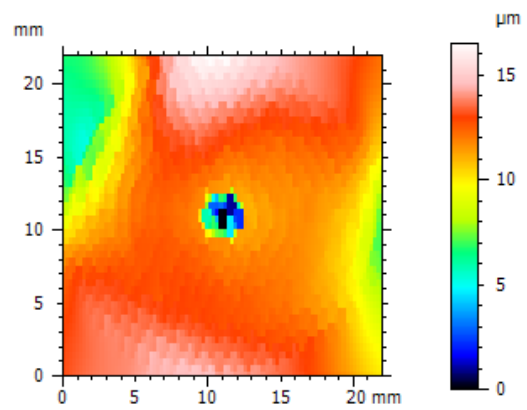
Figure 10. Fused silica form deviation map. PV Irregularity: 16.490 µm.

3.3 Sub-surface damage

One of the defining characteristics of glass machining processes is the amount and depth of sub-surface damages (SSD) the process induces into the machined surface. These are unavoidable because of the brittle behaviour of these materials. But since these SSDs absorb and scatter light, they reduce the quality of the optical element. If these optics are used for high energy laser applications, SSDs are able to absorb high amounts of energy, which can lead to the destruction of the optical element.

The classic approach for measuring SSDs is to polish a ramp of several micrometers into the surface, etch the surface with hydrofluoric acid, to open even tiny invisible cracks and then evaluate the visible cracks. An example of past plano samples that were measured in this way are depicted in Figures 11 and 12. Figure 11 shows the measurement of the whole surface for referencing the depth analysis of the polished ramps. Figure 12 shows the microscopic image of one of the ramps. This method is time consuming and destructive. Nonetheless all initial evaluation processes in the past were performed in this way.
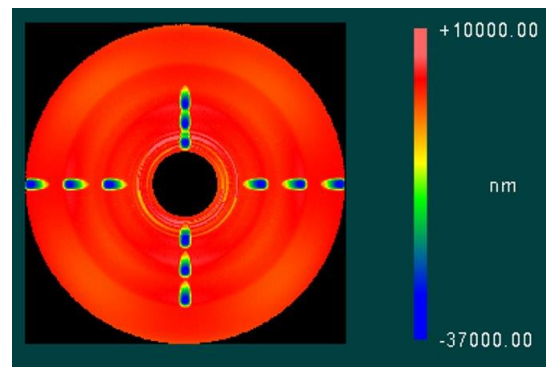
Figure 11. Surface measurement of a plano test sample with several polished ramps for SSD analysis.
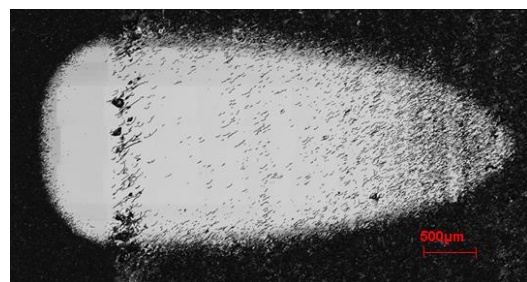
Figure 12. Microscopic image of a polished ramp with visible cracks (SSD).

To improve the measurement speed and process, a non-destructive SSD analysis method was developed, which was used for later SSD measurements of the optics introduced in this paper. The OCT measurement system was introduced by Schwoerer *et al*. [4].
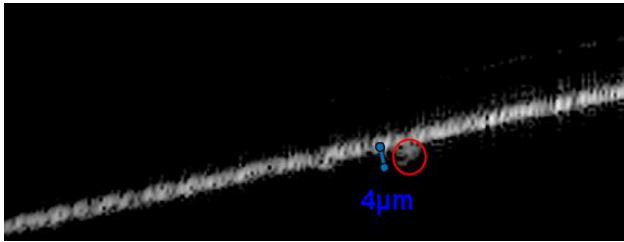
Figure 13. OCT Measurement, one scanning line of the BK7 optic. All SSDs are <4 µm, SSDs are depicted as grey dots below the white surface.
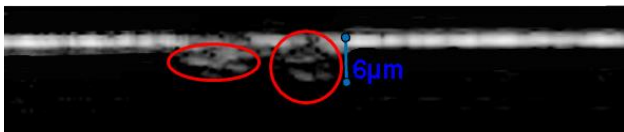
Figure 14. OCT Measurement, one scanning line of the fused silica optic. All SSDs are <6 µm, SSDs are depicted as grey dots below the white surface.
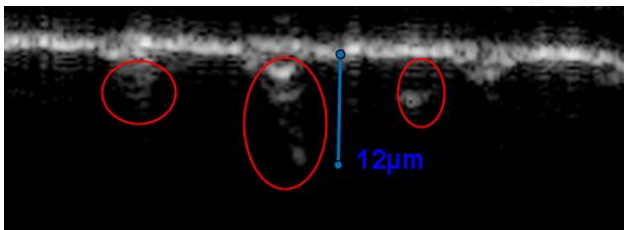
Figure 15. OCT Measurement, one scanning line of the fused silica optic that was fine ground. All SSDs are <12 µm, SSDs are depicted as grey dots below the white surface.

Even though the setup is still in an experimental state, comparative measurements show the great potential of this system. The intensity plots show a greyscale picture. Two examples of measurements of the discussed freeform optics are shown in Figures 13 and 14. Most of the intensity comes from the surface of the measured optic, so it is represented as a white line. Some grey lines or blobs, that go over into the material represent the measured SSDs. Via greyscale analysis the amount and depth of the SSDs is evaluated. The process presented in this paper leaves only SSDs of less than 4 µm in BK7 material and less than 6 µm in fused silica material respectively. These are very good results compared to grinding and even fine grinding of optics of these materials. Figure 16 shows a OCT Measurement of a fine ground freeform optic. The amount of SSDs are higher and the SSDs are up to 12µm deep.

3.4 Visual aesthetics

Both freeform designs appear to be transparent/clear to the naked eye when machined using laser assisted machining. The visual appearance of the freeform surfaces are shown in Figure 16.

Figure 16. Schott N-BK7 (left), Fused Silica (right)

In Figure 17 there is a comparison of microscopic images of a glass surface "cut" by diamond tunrning without laser assistance on the one hand and the glass surface of the fused silica freeform on the other hand. Without the laser there is no defined cutting process visible. At the surface level there are just glass chunks torn out of the surface. The laser assisted diamond turned surface is a lot smoother. There are still surface damages visible, but they are a lot smaller in size. These are the defects that are measured by the OCT. In the OCT measurement in Figures 13 and 14 there are both little dents in the surface as well as some cracks that lead from those dents.
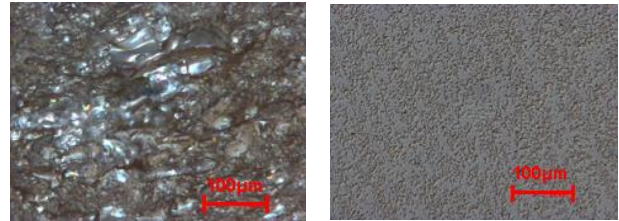
Figure 17. Microscopic images of glass surfaces. To the left diamond turned surface without laser assistance, to the right laser assisted diamond turned surface.

5. Conclusion and discussion

Laser assisted machining of optical glass could be an important avenue in the fabrication of precision freeforms with the aid of an ultra-precision CNC machine. Previous examples in the use of laser assisted machining technology for infrared materials as well as fabrication of precision glass aspheres have shown tremendous promise. This paper has demonstrated the capability and need to extend the capability further to freeforms. An optimized form irregularity of 16 µm was readily obtained without the ability to further correct because of the lack of on site 3D freeform form metrology. A future study shall be conducted with the ability to measure and correct form during diamond turning. We hypothesize the ability to correct measured form will result in being able to generate a total form deviation <1 µm. This paper also demonstrates the quality of the optical surface after laser assisted machining. Surface roughness values below 90 nm and SSDs below 6 µm were readily produced on two different glass types, which only need limited polishing to be finished. Since polishing usually is a process step that enhances surface quality but loses form accuracy, reducing polishing time produces optical surfaces with higher form accuracies.

References

[1] Kumar S, Tong Z and Jiang X 2022 Int. J. Extrem. Manuf. **4** 032004
[2] Mohammadi H, Ravindra D, Kode S, Patten J 2015 J. of Manufacturing Processes **19** 125
[3] Rolland J, Davies M, Suleski T, Evans C, Bauer A, Lambropoulos J and Fallagis K 2021 Freeform optics for imaging Optica **8** Issue 2 161
[4] Schwörer L, Wagner M, Lichtenegger A, Autschbach L, Ewert D, Mazal J, Börret R 2024 euspen international conference, "OCT system for the detection of Subsurface damage in glass-substrates"

A study of surface residual stress and crystal quality during ultra-precision diamond cutting of ZnSe crystals

Chi Fai Cheung[1,2] and Huapan Xiao[1,2]

[1]State Key Laboratory of Ultraprecision Machining Technology, Department of Industrial and Systems Engineering, The Hong Kong Polytechnic University, Hung Hom, Kowloon, Hong Kong, China
[2]The Hong Kong Polytechnic University Shenzhen Research Institute, Shenzhen 518057, China

Benny.Cheung@polyu.edu.hk

Abstract

In this paper, single-point diamond cutting experiments were conducted on soft-brittle ZnSe crystals, and the residual stress and crystal quality of cut surfaces are investigated. The results show that it is possible for negative compressive stress and positive tensile stress to coexist in the cut surfaces. The cut surface exhibits residual compressive stress ranging from tens to several hundreds of MPa. The residual stress and crystal damages of cut surfaces increase with increasing tool feed rate, while they almost remain unchanged with the cutting depth. The interaction effect of cutting parameters on residual stress and crystal quality is minimal. Moreover, a response surface model is developed to determine the residual stress with cutting parameters. This study will provide a reference for the defect-free ultra-precision machining of ZnSe crystals.

Ultra-precision machining, defect-free diamond cutting, ZnSe crystal, residual stress, crystal quality

1. Introduction

ZnSe crystal has stable physical and chemical properties, and it exhibits good transmission performance within a wavelength range from 0.5 µm to 22 µm, which basically cover the visible and infrared bands. It can be made into the fundamental elements for optical detection devices, nonlinear optical devices, and semiconductor lasers, etc [1, 2]. Single-point diamond turning enables efficient and mass production of precision elements, making it to be the most widely used method for processing ZnSe crystals [3, 4]. However, due to the high brittleness, low fracture toughness, and grain anisotropy of ZnSe crystals, various common damages inevitably arise, including fractures, cracks, and pits [5]. These damages greatly limit the utilization of the fabricated elements due to increased absorption or scattering. How to remove these common damages has been a hot research topic [6-8]. However, with the increasing demand for better surface quality of ZnSe crystals in the semiconductor and high-power laser fields, the research is no longer limited to the common damages. Nowadays, the research needs to encompass more subtle damages, especially residual stress and crystal disorder/damage of ZnSe crystals.

Few researchers have publicly reported on the residual stress and crystal quality of the machined ZnSe crystals. Sotillo et al. [9] investigated the residual stress distribution around Vickers indentation on the surface of ZnSe crystals. It is found that the compressive stress occurred inside the indentation, while the tensile stress appeared at the periphery of the indentation. Shojaee et al. [10] were the first to study the residual stress and crystal quality of ZnSe crystals after diamond turning. They identified the tensile stress, and demonstrated that a higher tensile stress and more severe lattice damages generally occurred with increasing feed rate. In the latest research, Huang et al. [11] believed that the stress in ZnSe crystals beneath the cutting tool could be decomposed into the hydrostatic stress caused by tool compression and the deviatoric stress applied by tool friction, with the former being dominant. Obviously, it is still unclear when tensile stress or compressive stress appears and what the magnitude of compressive stress is. The interaction effect of cutting parameters has never been reported.

In this paper, single-point diamond cutting experiments were conducted on ZnSe crystals under different cutting conditions. Raman spectroscopy is used to evaluate the residual stress and crystal quality of cut surfaces. The main and interaction effects of cutting parameters on residual stress and crystal quality are analyzed. Moreover, a response surface model is developed to determine the residual stress. This study will provide a reference for the defect-free machining of ZnSe crystals.

2. Experimental work

One ultra-precision polished ZnSe crystal (Φ25 ×1 mm) was prepared for the single-point diamond cutting experiments by Moore Nanotech 350FG, as shown in Fig. 1(a). The material properties of ZnSe crystal are shown in Table 1. As shown in Fig. 1(b), two groups of surfaces, i.e., Group A above and Group B under the horizontal line, were obtained by plunge cutting. Within each group, there are sixteen cut surfaces. Among them, one half on the left of vertical line was cut by tool 1, and the other half on the right of vertical line was cut by tool 2. The size of each cut surface was 2 mm × 2 mm, and the interval of adjacent cut surfaces was 0.5 mm. The geometrical parameters of tool 1 and tool 2 are shown in Table 2. The cutting parameters for Group A and Group B were determined using random and optimal Latin hypercube designs, respectively, as shown in Table 3. Group A and Group B were performed at different positions of ZnSe crystal. The values or ranges of cutting speed (v), feed (f), and cutting depth (a_p) were 800 mm/min, 0.5–5.0 µm/rev, and 0.5 µm –5.0 µm, respectively. A laser micro-Raman spectrometer (HR-800) was utilized to measure the residual

stress and crystal quality of cut surfaces. Before the measurement, all cut surfaces were cleaned with alcohol, acetone, and deionized water for at least 5 min in an ultrasonic cleaning machine.
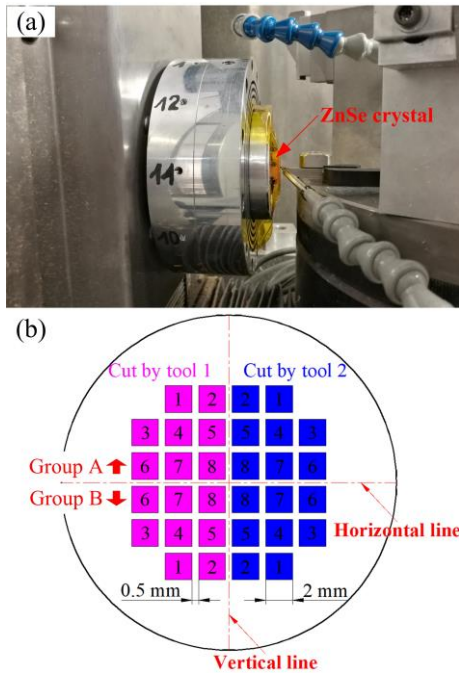
Figure 1. (a) Experimental setup for single-point diamond cutting experiments; (b) two groups of cut surfaces by tools 1 and 2, i.e., group A above and group B under the horizontal line.

Table 1 Material properties of ZnSe crystal

Young's modulus (GPa)	Density (g·cm^{-3})	Poisson ratio	Vickers hardness (GPa)	Fracture toughness (Mpa·m$^{1/2}$)
70.3	5.3	0.3	1.5	0.9

Table 2 Geometry parameters of tool 1 and tool 2

Tool No.	Nose radius (mm)	Nominal rake angle (°)	Clearance angle (°)	Cutting edge radius (nm)
1	1.004	0	12	≈ 25
2	0.201	−25	12	≈ 20

Table 3 Groups A and B of cutting parameters

No. of cut surfaces	Group A		Group B	
	Tool Feed rate f (µm/rev)	Cutting depth a_p (µm)	Tool Feed rate f (µm/rev)	Cutting depth a_p (µm)
1	1.1	0.5	3.1	2.4
2	2.4	1.1	1.1	1.8
3	5.0	1.8	2.4	0.5
4	1.8	2.4	0.5	3.7
5	0.5	3.1	4.4	1.1
6	4.4	3.7	1.8	5.0
7	3.7	4.4	3.7	4.4
8	3.1	5.0	5.0	3.1

3. Results and discussions

Fig. 2 shows a typical Raman spectrum of an uncut surface. The transverse-optical (TO) and longitudinal-optical (LO) modes are centered at 205.6 cm^{-1} and 252.4 cm^{-1}, respectively. The third peak located at 140.3 cm^{-1} corresponds to the second order transversal acoustic (2TA) phonon mode. The Raman spectrum is sensitive to strain, and consequently, the residual stress can be measured by the shift of Raman peaks. A shift of Raman peaks towards a lower wavenumber indicates residual tensile stress, whereas the opposite shift indicates residual compressive stress. Fig. 2 also displays a Raman spectrum of a cut surface. A slight shift of Raman peaks towards a higher wavenumber reveals residual compressive stress in the cut surface. Shojaee et al. [10] reported that the residual stress in the diamond-turned ZnSe surface was tensile. Whether it is compressive or tensile stress depends on various factors, especially tool rake angle [12].
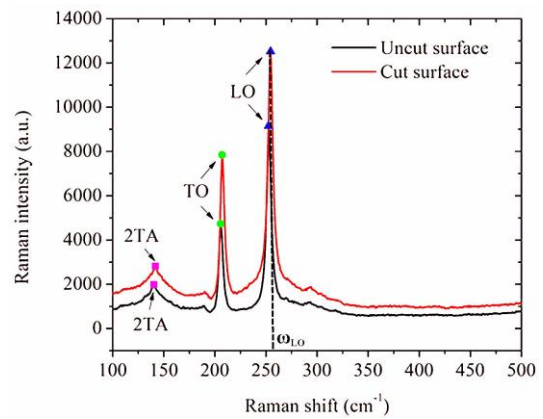
Figure 2. Raman spectrum of an uncut surface and a randomly selected cut surface.

Assuming that the cutting tool can be considered as a conical indenter, the indenter's half-apex angle is related with the tool rake angle and undeformed chip thickness. An analytical model of elastic stress field has been established for the scratching of brittle materials [13, 14]. The maximum principal stress around a scratch groove can be determined with the model. Fig. 3(a) and Fig. 3(b) show the normalized maximum principal stress around a scratch groove on ZnSe surface when the indenters with half-apex angles of 30° and 60° are used. It can be observed that the stress changes from negative to positive as the indenter is approached gradually, indicating the coexistence of compressive and tensile stresses in ZnSe cut surfaces. It provides a reasonable explanation for the possibility of detecting either compressive or tensile stresses when different process parameters are used.
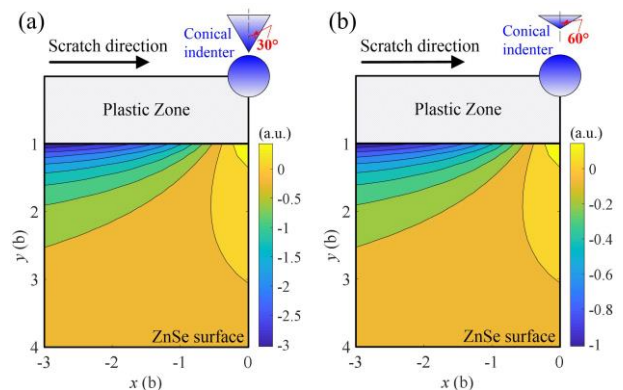
Figure 3. Normalized maximum principal stress around a scratch groove on ZnSe surface with indenter's half-apex angles of (a) 30° and (b) 60°.

LO mode is used to evaluate the residual stress and crystal quality (crystal disorder/damage) of cut surfaces. The residual stress (p) can be expressed as [15]:

$$p = \frac{\omega_{LO} - 252.6}{3.14} \qquad (1)$$

where ω_{LO} indicates the peak position of LO mode. The crystal quality is evaluated based on the peak width of LO mode, which can be determined by fitting the peaks to a Gauss-Lorentz type curve. An increasing peak width indicates a decrease in crystal quality. Five measuring points are selected randomly from each cut surface, and their corresponding residual stress and peak width are measured by laser micro-Raman spectrometer. Fig. 4(a) and Fig. 4(b) show the residual stress and peak width for each cut surface, respectively. It can be observed that the residual stresses range from 0 MPa to 510 MPa, and the peak widths range from 7.4 cm⁻¹ to 8.6 cm⁻¹. The residual stress and peak width for cut surfaces by Tool 2 are generally larger than those by Tool 1. Tool 2 has a negative rake angle compared to Tool 1. Zhang et al. [12] found that a higher hydrostatic compressive stress was generated with a larger negative rake angle, and the stress value reduced as the negative rake angle decreased. This is consistent with the experimental results.
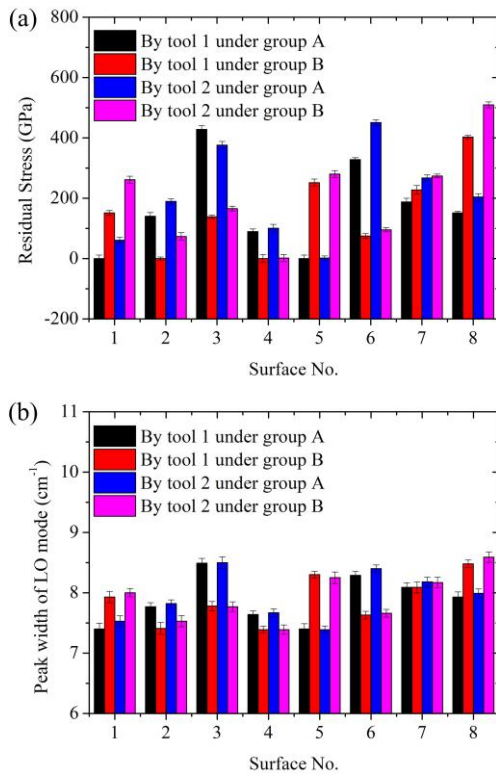
Figure 4. (a) Residual stress and (b) peak width of LO mode for cut surfaces.

As shown in Fig. 5 and Fig. 6, the effects of cutting parameters on residual stress and crystal quality of cut surfaces are investigated. The "Levels of factors" in Fig. 5(a) means that the cutting parameters are normalized to the range of [1.0, 2.0]. It can be found from Fig. 5(a) and Fig. 6(a) that the residual stress and peak width increase as the tool feed rate f transitions from low to high level, while they almost remain unchanged with the cutting depth a_p. This indicates higher residual stress and more severe crystal damages at higher too feed rate. The cutting depth has little effect on the crystal quality. Fig. 5(b) and Fig. 6(b) indicate a small interaction effect of cutting parameters on residual stress and crystal quality. Furthermore, the residual

stress of cut surfaces is modelled with cutting parameters. The response surface model, known as the fitted second order polynomial regression model [16], is built as follows:

$$p = e_0 + e_1 f + e_2 a_p + e_{11} f^2 + e_{22} a_p^2 + e_{12} f a_p \qquad (2)$$

where all coefficients e_0, e_1, …, e_{12} are obtained in Table 4 according to the values of residual stress. The coefficients of determination (R-square) are larger than 0.95, revealing that the fitting can describe the deviation in residual stress up to an extent of 95.0%.
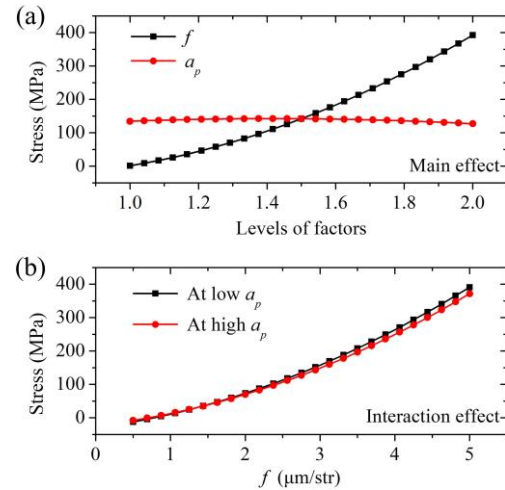
Figure 5. (a) Main and (b) interaction effects of cutting parameters (f: feed; a_p: cutting depth) on the residual stress of cut surfaces.
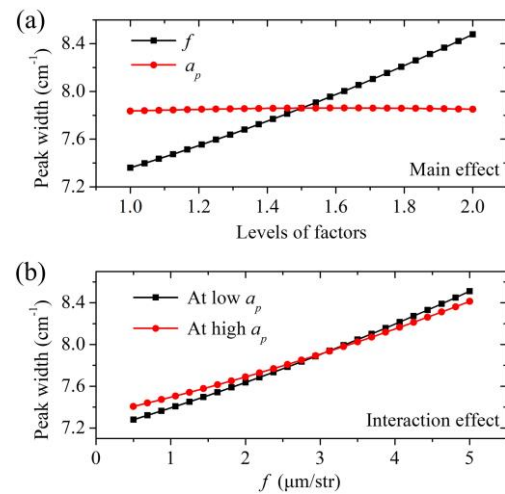
Figure 6. (a) Main and (b) interaction effects of cutting parameters (f: feed; a_p: cutting depth) on the peak width of LO mode for cut surfaces.

Table 4 Coefficients for the response surface model.

	e_0	e_1	e_2	e_{11}	e_{22}	e_{12}
Tool 1	−35.8	30.1	13.2	11.0	−2.1	−1.2
Tool 2	28.6	24.8	11.6	5.2	−9.1	15.1

4. Conclusions

This paper presents an experimental investigation of the residual stress and crystal quality of diamond cut ZnSe surfaces. The conclusions are summarized as follows:
(i) The cut surface exhibits residual compressive stress ranging from tens to several hundreds of MPa;

(ii) The residual stress and crystal damages of cut surfaces increase the with increasing tool feed rate, while they almost remain unchanged with the cutting depth. The interaction effect of cutting parameters on residual stress and crystal quality is minimal;

(iii) A response surface model is developed to determine the residual stress of cut surfaces with cutting parameters, with an R-square value greater than 0.95.

Acknowledgement

References

[1] Yudin N, Antipov O, Balabanov S, Eranov I, Getmanovskiy Y and Slyunko E 2022 Effects of the processing technology of CVD-ZnSe, Cr2+:ZnSe, and Fe2+:ZnSe polycrystalline optical elements on the damage threshold induced by a repetitively pulsed laser at 2.1 μm *Ceramics* **5** 459-71.

[2] Gavrishchuk E M, Kurashkin S V, Savin D V and Timofeev O V 2022 Effect of magnetorheological polishing on laser-induced damage in ZnSe and ZnSe:Cr polycrystals *Appl Phys B* **129** 1.

[3] Geng R, Yang X, Xie Q, Zhang W, Kang J, Liang Y and Li R 2021 Ultra-precision diamond turning of ZnSe ceramics: Surface integrity and ductile regime machining mechanism *Infrared Phys Technol* **115** 103706.

[4] Yin S, Xiao H, Kang W, Wu H and Liang R 2022 Shoulder damage model and its application for single point diamond machining of ZnSe crystal *Materials* **15** 233.

[5] Xiao H, Liang R, Spires O, Wang H, Wu H and Zhang Y 2019 Evaluation of surface and subsurface damages for diamond turning of ZnSe crystal *Opt Express* **27** 28364.

[6] Xiao H, Yin S, Cheung C F, Zhang F, Cao H and Wang C 2023 Material removal behavior analysis of ZnSe crystal during side-forward nanoscratching *Int J Mech Sci* **241** 107968.

[7] Huang W and Yan J 2021 Chip-free surface patterning of toxic brittle polycrystalline materials through micro/nanoscale burnishing *Int J Mach Tool Manu* **162** 103688.

[8] Huang W and Yan J 2023 Effect of tool geometry on ultraprecision machining of soft-brittle materials: a comprehensive review *Int J Extrem Manuf* **5** 012003.

[9] Sotillo B, Escalante G, Radoi C, Muñoz-Sanjosé V, Piqueras J and Fernández P 2019 Correlative study of structural and optical properties of ZnSe under severe plastic deformation *J Appl Phys* **126** 225702.

[10] Shojaee S A, Harriman T A, Qi Y, Lucca D A, Dutterer B S, Davies M A and Suleski T J 2014 Spatial variations in stress and crystal quality in diamond turned ZnSe surfaces measured by Raman spectroscopy *Manuf Lett* **2** 35-39.

[11] Huang W and Yan J 2020 Surface formation mechanism in ultraprecision diamond turning of coarse-grained polycrystalline ZnSe *Int J Mach Tool Manu* **153** 103554.

[12] Zhang S, Zhang H and Zong W 2019 Modeling and simulation on the effect of tool rake angle in diamond turning of KDP crystal *J Mater Process Technol* **273** 116259.

[13] Xiao H, Yin S, Cheung C F and Wang C 2024 Cracking behavior during scratching brittle materials with different-shaped indenters *Int J Mech Sci* **268** 109041.

[14] Xiao H, Zhang F, Yin S, Cheung C F and Wang C 2023 Subsurface damage model in single and double scratching of fused silica with a blunt indenter *Int J Mech Sci* **250** 108309.

[15] Lin C-M, Chuu D-S, Yang T-J, Chou W-C, Xu J-a and Huang E 1997 Raman spectroscopy study of ZnSe and Zn0.84Fe0.16Se at high pressures *Phys Rev B* **55** 13641-46.

[16] Xiao H, Chen Z, Wang H, Wang J and Zhu N 2018 Effect of grinding parameters on surface roughness and subsurface damage and their evaluation in fused silica *Opt Express* **26** 4638-55.

Milling-induced damage characteristics of 70wt% Si/Al alloy

Lianjia Xin[1,2*], Guolong Zhao[2], Shashwat Kushwaha[1,3], Liang Li[2], Jun Qian[1,3], Dominiek Reynaerts[1,3]

[1]Department of Mechanical Engineering, KU Leuven, Heverlee 3001, Belgium
[2]College of Mechanical and Electrical Engineering, Nanjing University of Aeronautics and Astronautics, Nanjing 210016, P. R. China
[3]Member Flanders Make, Belgium

lianjia.xin@student.kuleuven.be; lianjia.xin0308@gmail.com

Abstract

High-mass fraction silicon-aluminium (Si/Al) alloy (mass fraction of Si is larger than 30wt%), renowned for its excellent thermal conductivity and soldering performance, finds extensive application in the encapsulation shells of electronic components. However, the main challenges in machining Si/Al alloys stem from their high hardness, brittleness, and heterogeneity, resulting in poor surface quality and significant tool wear. In this work, milling-induced damages of 70wt% Si/Al were analyzed. K9 glass was selected as a reference group to reveal the damage characteristics caused by the heterogeneous of Si/Al alloy. In addition, the cutting force and machined surface roughness were investigated. The results show that brittleness and plasticity coexist in Si/Al alloy. The brittleness of silicon particles leads to the formation of pits and cracks on the machined surface, while the high ductility of aluminium contributes to the occurrence of burr defects. With the increase of feed rate, machined surface roughness of Si/Al alloy initially decreases and then increases. This study provides a technical guidance for the efficient machining of heterogeneous brittle materials.

Keywords: 70 wt% Si/Al alloy, heterogeneous brittle material, milling-induced damage, cutting force, surface roughness

1. Introduction

There is an ever increasing demand for electronic packaging materials exhibiting high thermal conductivity, low expansion coefficient, and excellent soldering characteristics [1]. 70wt% Si/Al alloy is well-suited to meet the exacting packaging requirements. However, the widespread application of 70wt% Si/Al alloy faces considerable impediments due to severe damage incurred during machining, primarily attributed to the substantial presence of high-hardness and brittleness silicon particles within the material. The microstructure of 70wt% Si/Al is shown in Fig. 1.
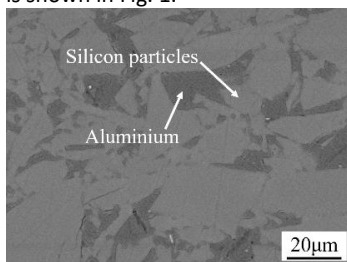
Figure 1. Microstructure of 70wt% Si/Al alloy

70wt% Si/Al alloy is a perfect example of a heterogeneous brittle material prone to diverse forms of machining damage under the ultrahigh stress-strain conditions inherent during milling processes. Niu et al. [2] involved Hopkinson bar tests, demonstrating the material deformation process under one-dimensional stress conditions and establishing a constitutive equation, thereby laying a theoretical foundation for the cutting of Si/Al alloy. In addition, Zhao et al. [3] explored the influence of cutting edge on the machining damage of the 70wt% Si/Al alloy, furnishing valuable technical guidance for tool selection.

While research on hard particle-reinforced aluminium-based materials has garnered significant attention, there remains a notable lack of comprehensive investigations into the intricate damage mechanisms specific to the high-mass fraction Si/Al material. This study adopts a comparative approach, utilizing a homogeneous brittle material—glass as a reference group, to analyze the influence of feed rates on the cutting forces and surface roughness of 70wt% Si/Al alloy. In addition, the milling-induced damages arising from the inherent heterogeneity of the 70wt% Si/Al alloy material was investigated.

2. Experimental configuration

In this work, 70wt% Si/Al alloy samples of dimensions 40 mm × 30 mm × 10 mm were selected as workpieces. K9 glass with the same size were set as the reference group. The milling tool with cutting-edge radii of 15 μm were homemade double-flute polycrystalline diamond (PCD) flat-end mills. The detailed parameters of the tool are listed in Table 1.

Table 1. Detail parameters of the milling tool

Diameter d (mm)	Radial rake angle γ (°)	Radial clearance angle α (°)	Helix angle h (°)
6	3	10	0

The schematic of the experimental setup is shown in Figure . Dry milling experiments were carried out on a three-axis high-precision machining centre (MMP 2522, Kern, Germany), and all the experiments were down-milling. In addition, according to previous cutting tests, the feed rate plays an important role in affecting the quality of the machined surface in milling of 70wt% Si/Al. The detailed cutting parameters are listed in Table 2.
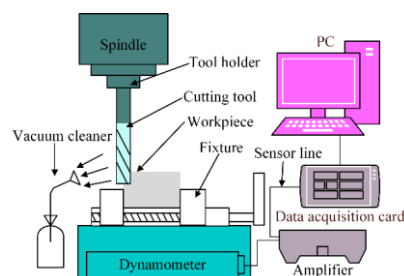
Figure 2. Schematic diagram of experimental setup

In addition, a dynamometer (9119AA1, Kistler, Switzerland) was utilized to measure the cutting force signal, recorded using cDAQ system of Nation Instruments. The machined surface roughness was measured by a three-dimensional profilometer (S neox, Sensofar, Spain). The morphologies of machined surface were observed by an optical microscope (Discovery. V20, Zeiss, Germany).

Table 2. Detailed cutting parameters

Cutting speed v (m/min)	Radial depth of cut a_e (mm)	Axial depth of cut a_p (mm)	Feed per tooth fz (mm)
150	1	1.5	0.001, 0.003, 0.01, 0.02, 0.04, 0.08

3. Results and discussion

3.1. Cutting force

During the cutting of K9 glass and 70wt% Si/Al alloy, the average cutting force exhibited different variations. As shown in Fig. 3, the changes in cutting forces with varying feed rates are depicted. Due to the large amount of Si particles in the workpiece, the cutting-edge is subject to high-intensity impacts during milling, resulting in significant fluctuations of cutting force. In milling of 70wt% Si/Al alloy, the cutting force initially decreased and then increased. Specifically, within the feed rate range of 0.001 – 0.003 mm/z, the cutting force decreased. This phenomenon was attributed to the feed rate being smaller than the cutting-edge radius, causing the aluminium in the Si/Al alloy to undergo ploughing with the cutting-edge. With an increase in feed rate, the ploughing effect diminished, leading to a gradual reduction in cutting force. The minimum cutting force of 47.6 N was reached at a feed per tooth of 0.003 mm. Beyond a feed per tooth of 0.003 mm, the cutting force increased with the feed rate. The ploughing effect became insignificant. Since there was no ductile material in K9 glass, no ploughing phenomenon occurred during its machining [4]. In addition, when milling K9 glass, abrupt fluctuations in cutting force occurred due to the brittle fracture of the material. In the case of Si/Al alloy, the minimum cutting force fluctuations appeared in the feed per tooth of 0.02 mm. Significant abrupt fluctuations in cutting force were observed when the feed per tooth exceeded 0.02 mm, as the high ductility of aluminium reduced the occurrence of brittle fracture in the material.
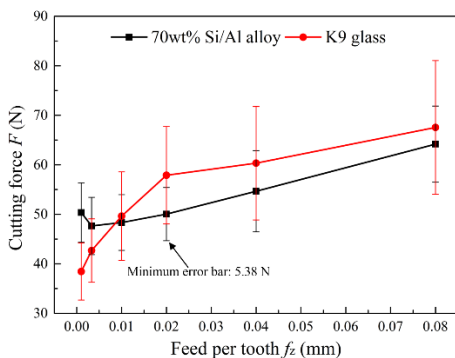
Figure 3. Variations of cutting force with feed rates

3.2. Milling-induced damage characteristics

As depicted in Fig. 4, the three-dimensional topography of the machined surfaces of K9 glass and 70wt% Si/Al alloy are illustrated. In comparison with K9 glass, the machining damages in Si/Al alloy also included pits and crack defects typical of brittle materials. The two kinds of damage were generated by the breakage of the high hardness silicon particles. In addition,

owing to the heterogeneity of Si/Al alloy, the machined surface of 70wt% Si/Al alloy exhibited various forms of damages distinct from those observed in homogeneous brittle materials, such as burrs and scratches. Also, the variations of surface roughness with different feed rates are exhibited in Fig. 5. With an increase in feed rate, the machined surface roughness of 70wt% Si/Al alloy initially decreased and then increased, reaching its minimum (1.5 μm) at a feed rate of 0.02 mm/z. At feed rates below 0.02 mm/z, severe burrs cause larger surface roughness. Above 0.02 mm/z, increased pits and cracks lead to more roughness. In contrast, the machined surface roughness of K9 glass consistently increased with the feed rate, and catastrophic edge breakage started appearing in K9 glass beyond a feed per tooth of 0.01 mm.
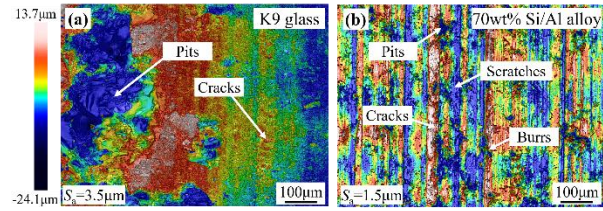
Figure 4. Machined surface topographies of K9 glass (a) and 70wt% Si/Al alloy (b)
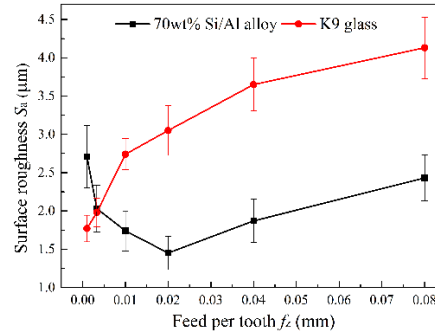
Figure 5. Variations of machined surface roughness with feed rates

4. Conclusions

Milling experiments were conducted to analyze the damage characteristics of 70wt% Si/Al alloy. The 70wt% Si/Al alloy material exhibits the characteristics of both brittle and ductile materials. The milling-induced damage includes pits and cracks caused by the breakage of hard silicon particles. There are also damages such as burrs and scratches generated by the excessive deformation of ductile aluminium.

Feed rates play an important role on machining damages in milling of 70wt% Si/Al alloy. The minimum surface roughness (S_a = 1.5 μm) achieved at a feed per tooth of 0.02 mm. When the feed rate below it, the plastic characteristics of the material dominate. Ploughing occurs during cutting, resulting in the high cutting force (51 N) and generation of many burrs and scratches. When the feed per tooth is larger than 0.02 mm, the brittle characteristics become dominant. The ploughing phenomenon diminished, but brittle fracture during machining increased, which leads to abrupt fluctuations in cutting force and deteriorated machining quality.

References

[1] Liu T S, Zhu L, Yang H Y, Cui H Y, Meng J, Qiu F, Dong B X, Shu S L, Jiang Q C and Zhang L C 2024 *Compos. B. Eng.* **271** 111138

[2] Niu Q L, Li S, Chen Y N, Li C P, Li S J, Ko T J, Li P N, Chen M and Qiu X Y 2022 *J. Mater. Sci. Eng. A.* **836** 142762

[3] Zhao G L, Xin L J, Li L, Zhang Y and Hansen H N 2023 *Chinese J. Aeronaut.* **36** 114-28

[4] Fang F Z and Chen L J 2000 *CIRP Ann – Manuf. Technol.* **49** 17–20

Experiments on micro-milling of cemented carbide with extremely sharp diamond micro mills

Yang Wu[1, 2*], Ni Chen[2], Shashwat Kushwaha[1, 3], Ning He[2], Jun Qian[1, 3], Dominiek Reynaerts[1, 3]

[1]Department of Mechanical Engineering, KU Leuven, Heverlee 3001, Belgium
[2]College of Mechanical and Electrical Engineering, Nanjing University of Aeronautics & Astronautics, Nanjing 210016, China
[3]Member Flanders Make, Belgium

yang.wu@student.kuleuven.be

Abstract

Cemented carbide is extensively used in molding process of miniature components due to its excellent properties. It is difficult to obtain high-quality machined surface by micro-milling of cemented carbide, due to its high hardness and brittle property. The self-fabricated diamond micro mills with extremely sharp edges have been utilized to carry out the micro-milling experments on cemented carbide. The cutting force was measured and the roughness Ra of the machined surface was detected. Based on the analyzing of impact of cutting parameters on peak-valley value of feed force and surface roughness Ra, the feed rate of 0.06 µm/tooth which is the half of cutting edge radius was found to guarantee the occurrence of cutting and shearing instead of ploughing in this condition. Meanwhile the minimal peak-valley (P-V) value of feed force and roughness Ra can be obtained using the feed rate of 0.06 µm/z in micro-milling of cemented carbide with the self-fabricated diamond micro mills.

Keywords: Cemented carbide, micro-milling, sharp diamond micro mills, size effect

1. Introduction

Micro mold technology is an important production method of numerous miniature components in civil fields. Cemented carbide has been widely applied as mold materials as it offers excellent desired properties such as high hardness, high temperature resistance, and corrosion resistance. More and more molds are made of cemented carbide instead of steel to fulfill the demands of long mold life and high product quality [1].

Micro-milling can produce miniature parts with three-dimensional features such as narrow grooves, microcavities, and aspheric surfaces [2]. Due to the high hardness of cemented carbide, only diamond micro mills can meet the requirements of machining cemented carbide. Suzuki [3] utilized the homemade single crystalline diamond (SCD) micro mills to fabricate the aspheric micro molds made of cemented carbide. Zhan [4] studied the impact of cutting parameters on the surface quality and tool wear in micro-milling of cemented carbide with polycrystalline diamond (PCD) micro mills. Wu [5] analyzed different material removal mechanisms and obtained ductile removal by parameter optimization in micro-milling of cemented carbide.

However, these researches are still on the exploratory stage, and the mechanism study is also limited due to the blunt cutting edge of dimond tools. In this paper, the self-fabricated extremely sharp diamond micro mills (edge radius of 0.12 µm) have been used to study the surface formation mechanism by changing feed per tooth at nanoscale for obtaining better surface quality in micro-milling of cemented carbide.

2. Experimental details

The micro end milling experiments were conducted on a 3-axis milling machine (MMP 2522, Kern, Germany) which is illustrated in Fig. 1(a). It is equipped with three linear axes of X, Y, Z and a high-speed spindle. The maximal rotation speed of the spindle is 40000 r/min and its runout is less than 1 µm. The self-fabricated PCD micro mill [6] with single tooth, rake angle of 0° and relief angle of 12° (γ_1) was utilized in the experiments, as depicted in Fig. 1(b) and (c). The diameter of the micro mill is 400 µm and its cutting edge radius is measured as 0.12 µm with Atomic Force Microscope (AFM). The two edges participating in micro milling are the side edge (Es) formed with rake face (Rf) and flank face 1 (Ff$_1$), and the end edge (Ee) formed with rake face and flank face 2 (Ff$_2$). The angle γ_2 is the relief angle of end edge which is designed as 6°, the angle γ_3 is machined to avoid interference. A cuboid block of cemented carbide (WC) was employed as workpiece, which is composed of 85 wt% WC and 15 wt% Co (binder), the average grain size of WC particles was 4-6 µm.
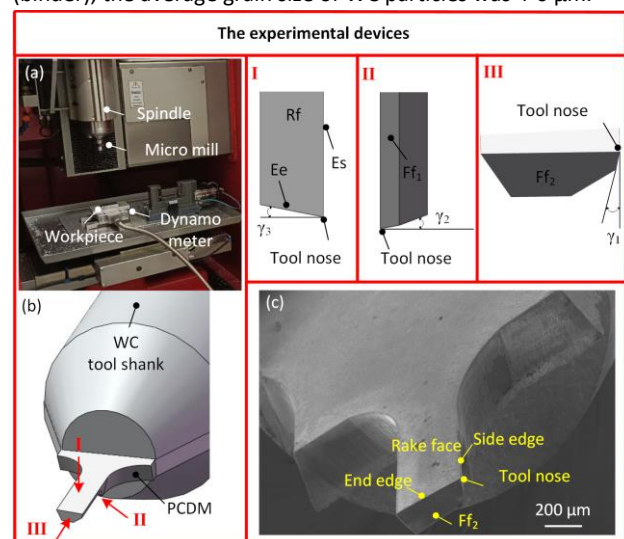
Figure 1. The experimental devices: a) milling machine, b) and c) self-fabricated diamond micro mill.

For the purpose of studying the impact of cutting parameters on the machined surface quality and cutting force, the micro-milling experiments were designed as shown in Table 1. The micro slots were macnined with these parameters to analyze their effect on cutting force and machined surface quality. The feed rate was mainly focused due to its vital impact on size effect, the parameters of feed rate were chosen according to different ratios of cutting edge radius (0.25~1 of 0.12 μm). The cutting force was measured by a dynamometer (Kistler, 9119AA1, Switzerland) with the threshold of 2 mN. The force signals were recorded with the sampling frequency of 30 kHz and processed by second-order high-pass filter with cut-off frequency of 1875.38 Hz to remove the noise. The morphology of the machined grooves were observed by using a surface profilometer (S neox, Sensofar, Spain) and it was also used to obtain the roughness value Ra of the machined groove surface.

Table 1 The detailed cutting parameters in the experiments

Depth of cut a_p(μm)	Spindle speed n (10^4 r/min)	Feed rate f (μm/tooth)
2	2	0.03, 0.04, 0.05, 0.06, 0.07, 0.08, 0.1, 0.12
4	2	0.03, 0.04, 0.05, 0.06, 0.07, 0.08, 0.1, 0.12

3. Results and discussion

In the micro-milling experiments, three dimensional cutting force was measured by the dynamometer with different cutting parameters. In this study, the impact of feed per tooth on cutting force and surface formation mechanism was mainly focused, and the feed force and cross-feed force showed the same trend with the variation of feed rate. To avoid redundant description, only the feed force was analyzed. Moreover, since the feed force exists in two exact opposite directions, the positive and negative values were both recorded. In order to better describe the variation of feed force and to compare its values under different cutting parameters, the peak-valley (P-V) value of feed force was calculated to do the characterization. The P-V value was reffered to the amplitude between the maximal and minimal values within a spindle rotation, and in this study, it was averaged over 200 rotation.
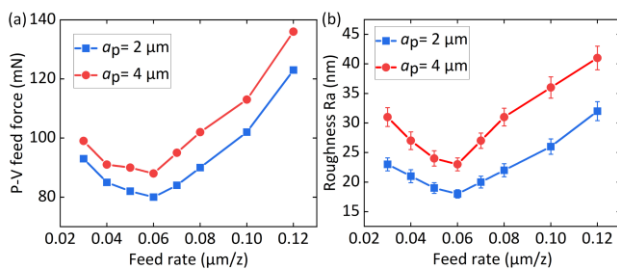
Figure 2. Impact of feed rate on (a) P-V feed force and (b) machined surface roughness Ra.

It can be seen from Fig. 2, both of the two curves have local minimal values of P-V feed force with the feed rate of 0.06 μm/z, which is the half of the cutting edge radius. The reason is that size effect occurs when the feed rate is below 0.06 μm/z, under this circumstance, the cutting thickness is too small to guarantee the occurrence of cutting behavior. The cutting edge keeps ploughing and squeezing the material rather then cutting off the material, in this way the material cannot be removed smoothly leading to the increment of P-V feed force. As the feed is increased the ploughing effect decreases and vanishes until 0.06 μm/z, at this moment, the real cutting behavior occurs and chips are generated, thus the minimum value of P-V feed force is formed. Subsequently, the P-V feed force continues to increase due to the growth of chip thickness.

The topology of machined micro grooves was observed and the roughness value Ra of these machined surface was also detected along the line profile shown in Fig. 3 by the profiler. It can be seen from Fig. 3a, convex contours and unremoved material formed on the machined surface, indicating that the ploughing effect dominated during machining with feed rate of 0.03 μm/z. Thus the machined surface has a relatively larger Ra. When the feed rate increased to 0.06 μm/z which is the half of cutting edge radius, the tool path on the machined surface is clearly visible as shown in Fig. 3c. The shearing effect replaced ploughing effect and the material was removed by cutting off under this condition, so the roughness Ra decreased to a local minimal value as depicted in Fig. 4. However, as the feed rate continued to increase, the surface quality decreased due to the enlargement of cutting thickness, meanwhile, the roughness Ra also increased.
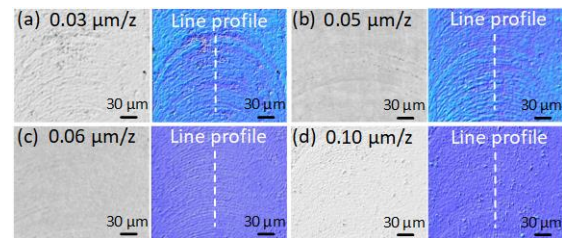
Figure 3. The morphology and outline topography of machined surface with feed rate of a) 0.03 μm/z, b) 0.05 μm/z, c) 0.06 μm/z and d) 0.10 μm/z.

4. Conclusions

Micro-milling experiments on cemented carbide with extremely sharp diamond mills have been conducted and the cutting force as well as the machined surface roughness Ra have been also measured. By analyzing the variation of P-V feed force and roughness Ra along with the cutting parameters, the feed rate of 0.06 μm/tooth which is the half of cutting edge radius was recommended due to the occurrence of cutting and shearing instead of ploughing in this condition. Meanwhile the minimal P-V feed force and roughness Ra can be obtained in this way. Further research is to study the surface formation mechanism in ploughing, shearing and brittle machining of cemented carbide.

References

[1] Guo B, Zhang L, Zhang T, Jiang F and Yan L 2018 *J. Mater. Process. Tech.* **255** 426–433.
[2] Wu Y, Chen N, Bian R, He N, Li Z and Li L 2020 *Int. J. Mech. Sci.* **185** 105884.
[3] Suzuki H, Okada M, Fujii K, Matsui S and Yamagata Y 2013 *CIRP Ann. Manufact. Technol.* **62**(1) 59-62.
[4] Zhan Z, He N, Li L, Shrestha R, Liu J and Wang S 2015 *Int. J. Adv. Manuf. Technol.* **77** 2095-2103.
[5] Wu X, Li L, He N, Zhao G and Shen J 2019 *Int. J. Refract. Met. Hard Mater.* **78** 61-67.
[6] Wu Y, He N, Chen N, Polte J, Yan B, Li L and Uhlman E 2022 *Int. J. Mech. Sci.* **231** 107584.

Experimental investigation of micro-milling of selective laser melted and wrought titanium alloys

Muhammad Rehan[1], Wai Sze Yip[1], Sandy Suet To[1]

[1]*State Key Laboratory of Ultra-precision Machining Technology, Department of Industrial and Systems Engineering, The Hong Kong Polytechnic University, Hung Hom, Kowloon, Hong Kong*

muhammad.rehan@connect.polyu.hk

Abstract

Selective laser melting (SLM) is commonly used for Ti6Al4V parts because it allows for more complex shapes. This study uses micro-milling of SLM Ti6Al4V to investigate surface characteristics, tool wear, and chip morphology. The results of SLM Ti6Al4V are compared with those of wrought Ti6Al4V. SLM titanium alloys achieve surface roughness of 25nm, which is 37.5% lower than wrought Ti6Al4V. However, the tool processed with SLM Ti6Al4V showed higher wear than the tool for micro milling wrought Ti6Al4V. Surface roughness increased in direct proportion to the depth of cut. The chips produced by SLM Ti6Al4V are long and continuous, as opposed to wrought Ti6Al4V, which is discontinuous. This study compared the micro-milling results of SLM Ti6Al4V and wrought Ti6Al4V, demonstrating the influences of micro milling on surface features, tool wear, and chip morphology.

Selective laser melting; Additive machining; Titanium alloys; micro-milling; precision machining

1. Introduction

Selective Laser Melting (SLM) is a cutting-edge technique in the field of Additive Manufacturing (AM), known for its precision and adaptability in producing intricate metallic components with high structural integrity. Machining AM metallic parts presents more formidable challenges than wrought alloys, owing to the intricate dynamics entailed by interactions between the powder bed, molten pool, powder, and laser beam inherent in AM processes [1, 2]. These complexities impede a thorough understanding of the thermophysical and metallurgical phenomena occurring within AM. Subsequent post-processing of metallic AM parts becomes extremely complex, especially in the context of micromachining. Micromachining must contend with factors such as tool-workpiece interactions, machine tool vibrations, and the size effect [3, 4]. The unique characteristics of SLM technology cause the formation of elongated columnar grains oriented in the build-up direction within AMed materials. In addition to the inherent challenges of AM parts, micromachining processes are influenced by the size effect, machine tool vibrations, tool-workpiece interactions, and chip formation, all of which have a significant impact on their behavior [5, 6]. According to the research findings, SLM Ti6Al4V responds differently than conventional Ti6Al4V during micro-machining. There is very little research available comparing SLM Ti6Al4V to wrought Ti6Al4V for micro-milling. The goal of this work is to close this gap. This study examines the micro-milling of SLM Ti6AL4V in terms of surface roughness and topography. Furthermore, tool wear and chip morphology are studied. The results are compared to wrought Ti6Al4V.

2.Methodology

Experiments were conducted on two types of specimens: 3D printed (fabricated using SLM) and wrought titanium alloys. The SLM part was generated using powder particles sized between 15-53μm, with process parameters including a laser power of 340W, scanning speed of 1250mm/min, hatch spacing of .3mm, and layer thickness of 60μm. Experiments were conducted using the high-precision five-axis Toshiba UVM-450C(V2) machine, as shown in Figure 1. This machine has extremely precise movements at increments as fine as 0.01μm along the X, Y, and Z axes. To investigate the machinability of SLM Ti6Al4V, a series of micro-grooves measuring 10 mm in length and matching the tool diameter were machined. Micro-slots were generated at varying depth of cut (20μm ,35μm, 50μm) whereas spindle speed and feed rate are kept constant i.e., 60k rpm and 3μm/flute respectively. The experiments were conducted using two fluted CBN micro-flat end mill cutters with a cutting diameter of 900μm and a length of 1.5mm each. Each sample was treated with a new tool to ensure consistency and precision. Prior to the micro-milling experiments, the workpiece was plane milled with a standard 2mm diameter, two-fluted end mill cutter to ensure precise depth of cut and removal of the oxide layer. Lubrication during experimentation was provided by Klubercut CO (6-102), a biodegradable vegetable oil. Assessment of surface roughness and topography was performed using an optical profiling system (Zygo NexviewTM), while a Hitachi tabletop microscope (TM3000) was utilized for the analysis of tool wear and chip morphology.
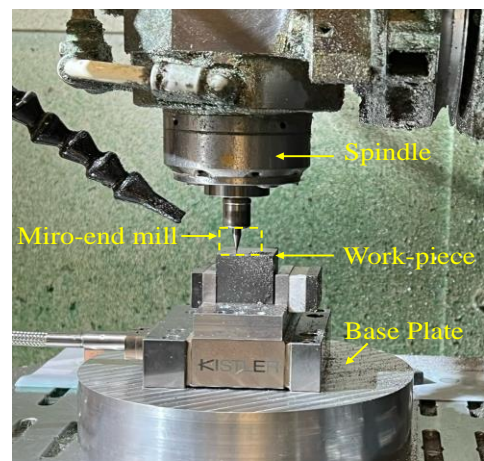
Figure 1. Micro-milling experimental setup

2. Results and Discussions

2.1. Surface Roughness

Exploring surface roughness in the micro-milling of SLM Ti6Al4V provides essential insights crucial for comprehending material behavior and machining effectiveness. The identification and examination of surface roughness are pivotal in evaluating the excellence and accuracy of machined parts [7, 8]. Micro-milling, particularly on intricate materials such as SLM Ti6Al4V, poses distinct challenges influenced by a myriad of parameters. Factors like tool geometry, cutting conditions, material properties, and machining dynamics intricately collaborate to define the ultimate surface finish [9, 10]. Five readings of surface roughness (R_a) were taken along the central line of machined surface, and the average values are shown in figure 2. For each trail, SLM Ti6Al4V has a lower surface roughness than wrought Ti6Al4V. Wrought Ti6Al4V is more ductile; during cutting, the heat generated causes more plastic flow of material than harder SLM Ti6Al4V, resulting in a rougher surface [11]. At a cut depth of 20μm, SLM Ti6Al4V has a 37.5% lower surface roughness than wrought material. As the depth of cut increased, the surface roughness increased. Surface topography is primarily captured from the center of each slot. Figures 3a,b, and c show the surface topography for SLM Ti6Al4V, whereas the peaks in wrought Ti6Al4V are dense and numerous, whereas the surface produced by SLM Ti6Al4V is less dense and far fewer in number. Figures 3c&f show dense marks and more peaks. It can be said that as the depth of cut increased, the surface degraded due to increased heat generation caused by excessive material removal.
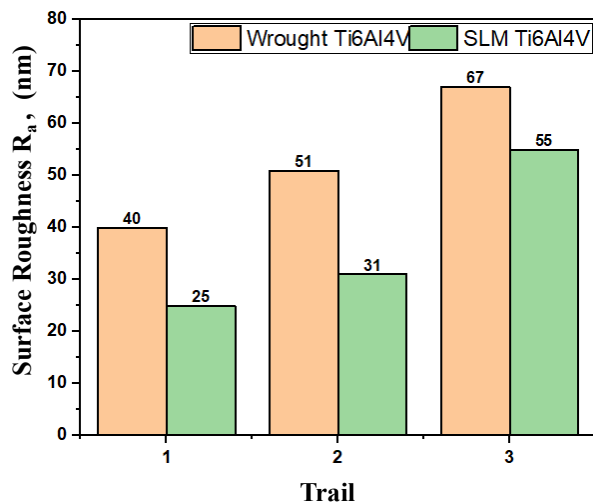
Figure 2. Comparison of surface roughness between SLM Ti6Al4V and Wrought Ti6Al4V

2.2. Tool Wear

The influence of tool wear on the micro-milling process of Ti6Al4V represents a pivotal determinant affecting machining efficiency and surface integrity. This phenomenon emerges as a result of the continuous engagement of the cutting tool with the workpiece, gradually experiencing wear under high loading and unloading machining conditions. The ramifications of tool wear are substantial, notably impacting critical aspects of the machining process, including alterations in cutting forces, chip formation dynamics, and surface quality. As tool wear progresses, discernible changes in tool geometry ensue, leading to notable variations in fundamental cutting parameters, encompassing cutting forces, surface roughness characteristics, and chip morphology [12, 13]. Figure 4 shows the post-machining condition of the tool face. SLM Ti6Al4V shows more wear having adhesive wear and micro chips welded on cross

section as compared to wrought Ti6Al4V, showing no prominent adhesive wear, due to a variety of factors. Differential micro-hardness between the materials plays a significant role, with SLM Ti6Al4V having a higher hardness, resulting in increased cutting forces and tool wear. The non-uniform microstructure amplifies the effects of fatigue loading during micro milling, resulting in increased wear. Furthermore, higher ultimate tensile strength and yield influence the tool-workpiece interaction, resulting in plastic deformation. This accelerates plowing force and promotes tool wear in SLM Ti6Al4V when compared to wrought Ti6Al4. Sharma and Meena [11] discovered a strong correlation between work material microstructure and tool degradation during micro-scale machining. Because of its laminar grains, SLM Ti6Al4V has a higher hardness and lower ductility.
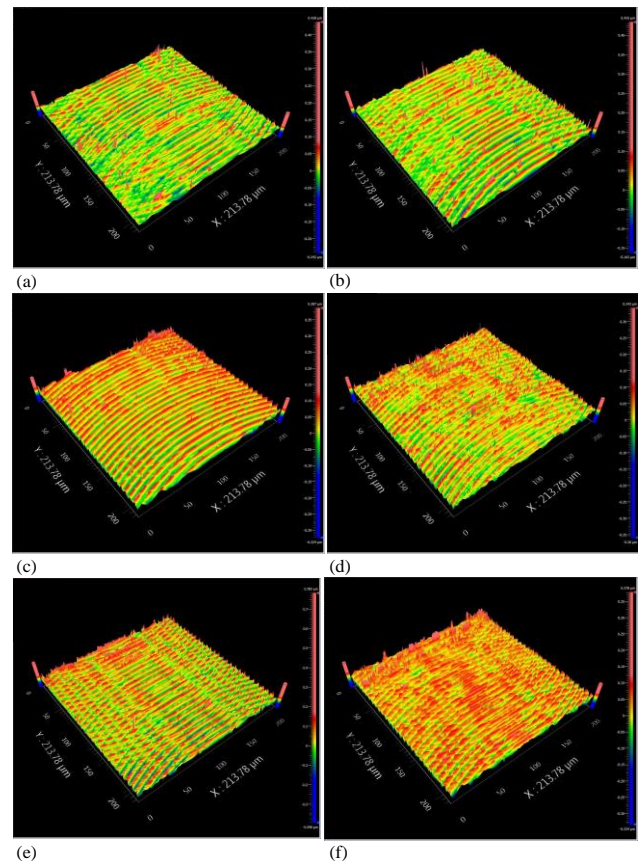
Figure 3. Surface Topography of SLM Ti6Al4V (a)20μm (b) 35μm (c) 50μm; and, wrought Ti6Al4V (d)20μm (e) 35μm (f) 50μm
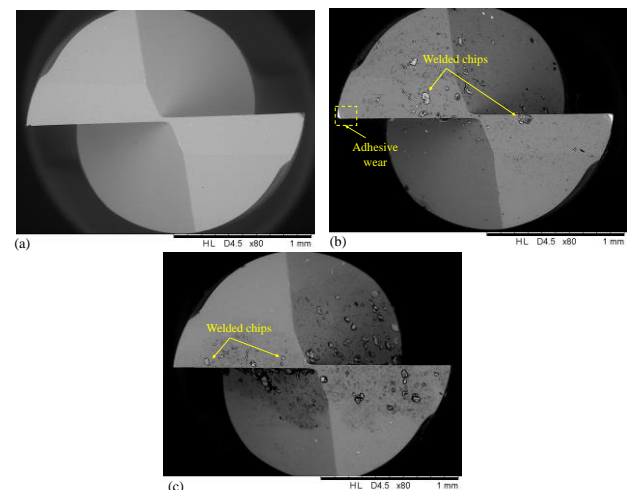
Figure 4. Tool cross section; (a) new tool, (b) tool processed on SLM Ti6Al4V, (c) tool processed on wrought Ti6Al4V

2.3. Chips Morphology

The characteristics of the chips generated during the cutting process serve as the foundation for evaluating micro-machining performance. Chip morphology reflects surface quality, tool wear, and cutting forces. Chip geometry and morphology in micromachining is dependent upon a mechanism involved in the cutting process i.e., when the uncut chip thickness is lower than critical chip thickness, the plowing dominates the shearing and vice versa [14]. Figure 5 compares the chips produced during micro-groove milling of SLM Ti6Al4V and wrought Ti6Al4V at increasing depths of cut. The two materials exhibit distinct differences in chip morphology. The micro-milling process produces spiral-shaped chips in both materials; however, SLM Ti6Al4V chips have a larger radius of curvature than wrought Ti6Al4V chips, which have a smaller radius. Furthermore, the chips from SLM Ti6Al4V (Figure 5a, b, c) appear longer and continuous, whereas those from wrought Ti6Al4V (Figure 5d, e, f) appear shorter and discontinuous. The observed figures show two distinct sides of the chips: the contact side, which is relatively flat and slides over the tool edge, and the free side, which has a scaly lamella structure. This morphological difference can be attributed to material properties, specifically the brittleness of wrought Ti6Al4V versus the greater hardness of SLM Ti6Al4V [15, 16]. The scaly pattern results from large plastic strain during micro-milling, which causes segment sliding and detachment in both Ti6Al4V due to higher material hardness [12, 17]. Notably, SLM Ti6Al4V chips are broader, which can be attributed to the higher cutting temperature, which causes greater plastic deformation and chip softening[11]. As a result, the welded fragments shown in Figures 5a and 5b are caused by increased heat, which causes chip fragments to adhere to the surface.
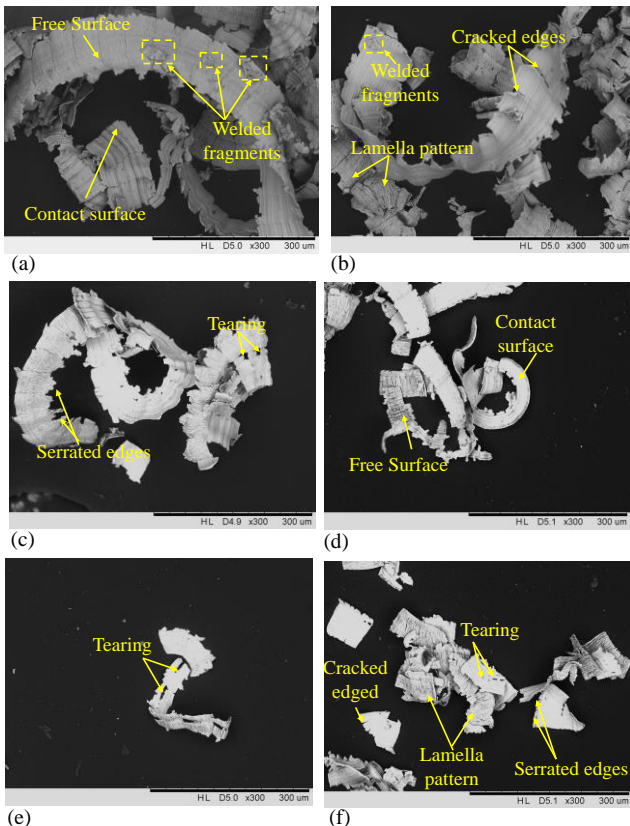
Figure 5. Chip morphology of SLM Ti6Al4V doc(a) 20μm,(b) 35μm, (c) 50μm; and, wrought Ti6Al4V (d) 20μm,(e) 35μm, (f) 50μm

3. Conclusion

This This study is carried out to investigate the micro milling of SLM Ti6Al4V and comparison experimentations were made with the wrought Ti6Al4V using CBN micro end mills. The following conclusions are drawn:

1. At various cut depths, SLM Ti6Al4V had lower surface roughness than wrought Ti6Al4V. A surface roughness of 25nm was achieved at 60K rpm spindle speed, 3μm/flute feed rate, and 25μm depth of cut, a significant 37.5% reduction compared to wrought Ti6Al4V. Surface topography analysis showed fewer defects and peaks in SLM Ti6Al4V, especially at deeper cuts.

2. Machine parameters and material manufacturing methods affect tool wear. Tool wear causes welded fragments on tool surfaces, affecting machined surface quality and tool lifespan, especially when processing softer wrought Ti6Al4V at high cutting temperatures.

3. SLM and wrought Ti6Al4V micro-milled chips show differences. SLM Ti6Al4V produced longer, continuous chips with wider profiles than wrought chips.

Declaration of competing intrest

The authors declare that they have no competing interests.

References

1. Gomes, M.C., et al., *Micro-machining of additively manufactured metals: a review.* The International Journal of Advanced Manufacturing Technology, 2021: p. 1-20.
2. Airao, J., H. Kishore, and C.K. Nirala, *Measurement and analysis of tool wear and surface characteristics in micro turning of SLM Ti6Al4V and wrought Ti6Al4V.* Measurement, 2023. **206**: p. 112281.
3. Li, G., et al., *Machinability of additively manufactured titanium alloys: A comprehensive review.* Journal of Manufacturing Processes, 2022. **75**: p. 72-99.
4. Airao, J., H. Kishore, and C.K. Nirala, *Tool wear behavior in μ-turning of nimonic 90 under vegetable oil-based cutting fluid.* Journal of Micro-and Nano-Manufacturing, 2021. **9**(4): p. 041003.
5. Wang, Z., et al., *The role of annealing heat treatment in high-temperature oxidation resistance of laser powder bed fused Ti6Al4V alloy subjected to massive laser shock peening treatment.* Corrosion Science, 2022. **209**: p. 110732.
6. Carroll, B.E., T.A. Palmer, and A.M. Beese, *Anisotropic tensile behavior of Ti–6Al–4V components fabricated with directed energy deposition additive manufacturing.* Acta Materialia, 2015. **87**: p. 309-320.
7. Rehan, M., et al., *Experimental investigation of the influence of wire offset and composition on complex profile WEDM of Ti6Al4V using trim-pass strategy.* The International Journal of Advanced Manufacturing Technology, 2023. **127**(3): p. 1209-1224.
8. Khalil, A.K., et al., *A novel magnetic field assisted diamond turning of Ti-6Al-4 V alloy for sustainable ultra-precision machining.* Materials Today Communications, 2023. **35**: p. 105829.
9. Khaliq, W., et al., *Tool wear, surface quality, and residual stresses analysis of micro-machined additive manufactured Ti–6Al–4V under dry and MQL conditions.* Tribology International, 2020. **151**: p. 106408.
10. Liang, X., Z. Liu, and B. Wang, *Multi-pattern failure modes and wear mechanisms of WC-Co tools in dry turning Ti–6Al–4V.* Ceramics International, 2020. **46**(15): p. 24512-24525.

11. Sharma, S. and A. Meena, *Microstructure attributes and tool wear mechanisms during high-speed machining of Ti-6Al-4V.* Journal of Manufacturing Processes, 2020. **50**: p. 345-365.

12. Airao, J., C.K. Nirala, and N. Khanna, *Novel use of ultrasonic-assisted turning in conjunction with cryogenic and lubrication techniques to analyze the machinability of Inconel 718.* Journal of Manufacturing Processes, 2022. **81**: p. 962-975.

13. Jun, T.-S., et al., *Local deformation mechanisms of two-phase Ti alloy.* Materials Science and Engineering: A, 2016. **649**: p. 39-47.

14. Vipindas, K. and J. Mathew, *Wear behavior of TiAlN coated WC tool during micro end milling of Ti-6Al-4V and analysis of surface roughness.* Wear, 2019. **424**: p. 165-182.

15. Airao, J., H. Kishore, and C.K. Nirala, *Comparative analysis of tool wear in micro-milling of wrought and selective laser melted Ti6Al4V.* Wear, 2023. **523**: p. 204788.

16. Keist, J.S. and T.A. Palmer, *Development of strength-hardness relationships in additively manufactured titanium alloys.* Materials Science and Engineering: A, 2017. **693**: p. 214-224.

17. Shunmugavel, M., et al., *Chip formation characteristics of selective laser melted Ti–6Al–4V.* Australian Journal of Mechanical Engineering, 2017.

Precision polishing platform based on a flexure-based constant force mechanism

Tinghao Liu[1], Guangbo Hao[1*]

[1]School of Engineering and Architecture, University College Cork, College Road, Cork, Ireland

*Corresponding author: Dr Guangbo Hao   G.Hao@ucc.ie

Abstract

This work presents a precision polishing platform inspired by constant force mechanisms, aimed at enhancing precision and stability in polishing processes. Traditional platforms often struggle with maintaining consistent force application, leading to variations in surface finish and dimensional accuracy. Our solution addresses this challenge by providing a constant reaction force, ensuring constant polishing force distribution even amidst external force fluctuations on the workpiece. Notably, the platform's constant force region exhibits significant large deformation relative to its own geometric size, amplifying its ability to sustain consistent pressure across the polishing surface. Additionally, the platform offers simplicity in structure and ease of manufacture, facilitating cost-effective production and widespread adoption. Its adaptability enables accommodation of diverse workpiece types under specific conditions, adding versatility and flexibility to various polishing applications. Leveraging an energy method based on the smooth curvature model, the constant force mechanism ensures reliable and efficient operation. The optimal inclined angle is 58.7550 degrees with a beam length of 100 mm. The constant force region extends up to 28.8% of the beam's length (28.8 mm). With potential applications in optics, semiconductors, and medical devices, this platform provides an alternative solution for industries requiring precise surface finishing.

Keywords: Manufacturing, Polishing, Precision

1. Introduction

Precision polishing platforms hold a pivotal position across various industries, particularly in fields like optics and semiconductors, where they wield a direct influence on the ultimate quality of end products. Previous research has emphasized the significance of delving into polishing technologies [1-4]. The innovative concept of flexural constant force mechanisms emerges as an alternative approach to enhance the performance of these precision polishing platforms.

Flexural mechanisms offer unique advantages in precision engineering due to their ability to transmit precise motion and force through the predictable deformation of flexural elements, such as beams or flexures [5]. A novel large XY parallel manipulator based on flexural beams was proposed in [6], which is utilized for high-precision motion stages. The application of flexural beams eliminates the need for complex assembly mechanisms, reduces lubrication requirements, and minimizes wear. By leveraging flexural mechanisms, researchers aim to streamline the design and manufacturing process of vibration isolators while maintaining or improving performance. Prior research has convincingly showcased the successful implementation and efficacy of constant force mechanisms within precision polishing platforms. A polishing force control system is developed in [7] to improve the polishing stability, which achieved constant-force polishing through dynamically control the load. Besides, a polishing end-effector is proposed in [8], which achieves regulating the contact force passively. In addition, a parallel polishing machine is proposed in [9], which achieves higher polishing precision. Another polishing platform based on constant-force mechanism is introduced in [10], which

addressed the challenge of controlling constant force in industrial deburring operations. The previous mentioned polishing platforms enable the attainment of precise control over the applied force during the polishing process, culminating in elevated surface quality and heightened processing accuracy.

The precision polishing platform delineated in this study possesses several notable advantages: Firstly, it exhibits a considerable deformation range relative to its geometric dimensions. Secondly, the consistent application of force to the workpiece ensures the maintenance of high precision during the polishing process. Thirdly, its structural simplicity facilitates ease of manufacture. Lastly, the platform's adaptability and passive provision of constant force support obviate the reliance for force sensors or closed-loop control systems.

Flexural constant force mechanisms showcase ongoing technological advancements and hold potential for optimizing precision polishing platforms. As technology evolves, these platforms are set to play a more indispensable role, offering new opportunities and challenges in related fields. The synergy between technological innovation and platform adaptability creates a landscape, promising novel opportunities for advancement.

The structure of this paper is as follows: In Section 2, the design of the constant force polishing platform is presented. Section 3 discusses the energy method utilized for modeling large deformation flexural beams, along with the optimization objective. The final section provides a summary of the content.

2. Design of a constant force polishing platform

Our constant force polishing platform, inspired by constant force mechanisms, provides an innovative solution to challenges posed by traditional fixed or spring-supported platforms. Unlike conventional approaches requiring meticulous force control during polishing, our design ensures precision by delivering a consistent reaction force within the constant force realm. This stability allows our platform to maintain a reliable polishing force, even amidst external force fluctuations on the workpiece, enhancing polishing effectiveness for consistent and precise workpiece processing.

Moreover, the structure of our platform is simple and easy to manufacture, allowing for cost-effective production and widespread adoption. Its adaptive nature enables it to accommodate different types of workpieces under certain conditions, providing versatility and flexibility in various polishing applications. This adaptability not only enhances the platform's usability but also increases its value proposition for industries seeking tailored solutions for precise surface polishing.

The working principle of proposed precision polishing platform can be found in Figure 1.
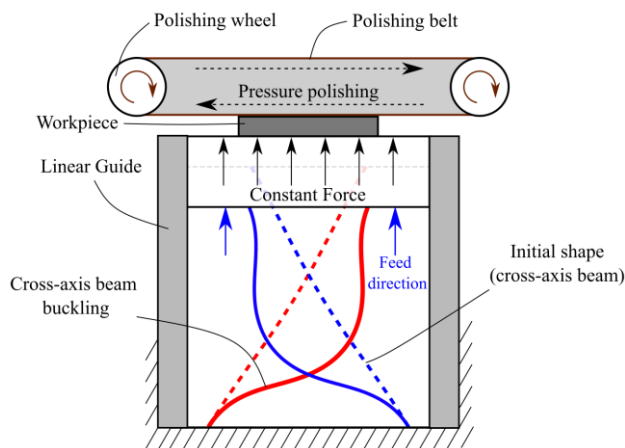
Figure 1. Working principle of precision polishing platform

The precision polishing platform can be used to polish the surfaces of a variety of materials, including metal, plastic, and glass. The proposed precision polishing platform operates by moving the polishing belt past the surface of the workpiece. The polishing wheel rotates and the polishing belt abrades the surface of the workpiece. The constant-force support platform ensures that the workpiece remains in constant-force contact with the polishing wheel at all times and thus ensures high polishing precision. The polishing platform consists of a constant-force support platform and a pressure polishing system.

Constant-force support platform: The constant force mechanism is a single-degree-of-freedom (DOF) mechanism that moves vertically. This mechanism is composed of a pair of cross-axis inclined compliant beams. The flexural beam with initial shape and buckling shape can be seen in Fig.1. Besides, a linear guide is fixed to the ground to ensure the platform moves along vertical direction as a single DOF mechanism. The platform is compact due to the cross-axis design based on the position-space method. By utilizing this flexural mechanism as the support of the polishing platform, the platform can achieve constant-force support within a specific range of movement.

Pressure polishing system: The pressure polishing system relies on removing materials from the surface using abrasives, resulting in a

smooth, polished surface. A polishing belt is affixed to the polishing wheel. As the polishing wheel rotates, the rotational movement is converted to linear movement by the polishing belt. Through the relative motion between the workpiece's surface and the polishing belt, the workpiece is polished as required.

The polishing process primarily relies on pressure polishing, where pressure is applied to the polishing surface to enhance abrasion and eliminate surface defects. A polishing belt is mounted on two rotating wheels, allowing it to glide over the polishing surface. By utilizing four flexural beams on the moving platform, a constant force is exerted on the workpiece, ensuring consistent pressure on the polishing surface. This results in a uniform distribution of force within the constant force region, maintaining its stability throughout the process.

For the proposed precision polishing platform, any workpiece with a thickness smaller than that of the constant force region can undergo polishing. This constraint ensures adequate contact between the polishing belt and the workpiece. The polishing process necessitates no fixture adjustments and can passively provide constant force support. Consequently, it is also deemed adaptable to workpieces of various heights.

The inspiration for constant force polishing platform stems from the need for enhanced precision and stability in polishing processes, particularly in industries where surface quality is paramount. Traditional polishing methods often struggle to maintain consistent force application, leading to variations in surface finish and dimensional accuracy. With our platform, we aim to overcome these limitations by ensuring a constant polishing force throughout the process. This not only improves the overall quality of the polished surfaces but also enhances the efficiency and reliability of the polishing operation, leading to reduced scrap rates and increased productivity.

In addition to its immediate applications in precision polishing, our constant force polishing platform holds promise for advancements in various fields requiring controlled material removal and surface refinement. By providing a stable and predictable polishing force, our platform opens doors for new possibilities in manufacturing processes, such as optics, semiconductors, and medical devices. Furthermore, the adaptability of our platform allows for customization to suit specific industry requirements, offering a versatile solution for a wide range of polishing applications.

3. Flexural constant force mechanism

This section introduces the modelling process of the constant force mechanism, highlighting the advantageous features of our modelling approach. Our method brings notable benefits, particularly in the modelling of large deformation flexural beams. It demonstrates a high level of efficacy in accurately capturing the intricate nonlinear behaviour of such beams.

3.1. Modelling methodology: SCME method

Our previous work introduces the energy method based on the smooth curvature model (SCME method), which aims to effectively model the complex nonlinear post-buckling behavior of inclined flexural beams. This method is grounded in the principle of minimum strain energy, implying that the equilibrium configuration corresponds to the minimum total strain energy. To accurately capture the bending strain energy of large deformation beams, the high-order smooth curvature model is adopted. The Lagrange multiplier method is then

utilized to determine the minimum strain energy and corresponding tip loads simultaneously. Additionally, the SCME method allows for determining the deformation shape and maximum stress using the smooth curvature model. Notably, the proposed SCME method is capable of modelling flexural beams with inclined angles ranging from 0 to 90 degrees. The accuracy of the SCME method has been validated through finite element analysis and experimental tests. In the SCME method, the approximated curvature of deflected beam is expressed in Eq. (1):

$$\omega(\boldsymbol{\alpha}, s) \approx \frac{1}{L} \sum_{n=0}^{N} \alpha_n \varphi_n(s) \qquad (1)$$

where $\boldsymbol{\alpha} = (\alpha_0, \alpha_1, \alpha_2, \cdots, \alpha_N)^T$ is a vector that contains the generalized coefficients an $\varphi_n(s)$ represent the shifted Legendre polynomials. Based on the equation (3.1), the expression of bending strain energy can be formulated using Eq. (2):

$$U_b = \frac{1}{2} \int_0^L EI\omega(\alpha, s)^2 \, ds \qquad (2)$$

Simultaneously, the beam tip position and orientation can be determined through integration from $s = 0$ to $s = L$. The expressions for the beam tip position and orientation are provided in equations (3-5):

$$\varphi_{tip}(\boldsymbol{\alpha}) = \varphi(\boldsymbol{\alpha}, L) = \alpha_0 \qquad (3)$$

$$x_{tip}(\alpha) = \int_0^L \cos\big(\varphi(\boldsymbol{\alpha}, s)\big) \qquad (4)$$

$$y_{tip}(\alpha) = \int_0^L \sin\big(\varphi(\boldsymbol{\alpha}, s)\big) \qquad (5)$$

To determine the minimum bending strain energy, the Lagrange multiplier method is applied to minimize the strain energy under the equation constraint, as expressed in Eq.(6):

$$\mathcal{L}(\boldsymbol{\alpha}, \boldsymbol{\lambda}) = U_b(\boldsymbol{\alpha}) + \begin{bmatrix} \lambda_1 & \lambda_2 & \lambda_3 \end{bmatrix} \begin{bmatrix} x_g - x_{tip} \\ y_g - y_{tip} \\ \varphi_g - \varphi_{tip} \end{bmatrix} \qquad (6)$$

Where the x_g, y_g and φ_g are given trajectory points. By utilizing the SCME method, we can derive the corresponding force at beam tip as:

$$F_x = -\lambda_1 \cos\theta + \lambda_2 \sin\theta \qquad (7)$$

$$F_y = -\lambda_1 \sin\theta - \lambda_2 \cos\theta \qquad (8)$$

Where θ is the inclined angle of complaint beam. In addition, the SCME method can also derive the maximum stress during the deformation process. The stress evaluation considers the axial stress since the axial stress contribute additionally and is not negligible. Hence the stress is evaluated as:

$$\sigma_{\max} = \sigma_{\text{bending}} + \sigma_{\text{axial}}$$

$$= \frac{Et\omega(s)}{2} + \frac{\sqrt{F_x^2 + F_y^2} \cos\big(\varphi_{\text{tip}}(\alpha) - \varphi_s(\alpha)\big)}{Wt} \qquad (9)$$

The above process briefly reviews the modeling process of the constant force mechanism, and we intend to incorporate the SCME method into the optimization algorithm.

3.2. Optimization strategy

Optimization strategies can be applied to determine the constant force mechanism with the longest constant force region, denoted as Ω. This could help to optimize the performance of the precision polishing platform. This region Ω is defined as follows: the forces within Ω fluctuate above and below the buckling force by no more than a specific percentage ξ of the buckling force. Once the force exceeds the predefined constant force range, it marks the end of the constant force region. Therefore, all the forces within the constant force region can be expressed as:

$$\left| F_y^\Omega - F_{bl} \right| \leq \xi \cdot F_{bl} \qquad (10)$$

where F_y^Ω represents the force in the constant force region, F_{bl} is the buckling force, ξ is the tolerance coefficient. The optimization objective is:

$$Maxmize: \ \Omega(\theta)$$

$$\text{Subject to: } \sigma_{max} \leq \sigma_{yield}$$
$$50° \leq \theta \leq 80°$$

The optimization process can be implemented in MATLAB. The suggested optimization algorithm is the genetic algorithm. Genetic algorithms are heuristic global optimization techniques inspired by the principles of natural selection and genetics. They involve evolving solutions to complex problems over successive generations, utilizing techniques such as selection, crossover, and mutation to search for optimal or near-optimal solutions.

3.3. Case study

In this section, we will undertake a case study utilizing the proposed modeling and optimization method. The case study will focus on examining a small-scale constant force mechanism. Details regarding the mechanical properties and determined geometric dimensions can be referenced in Table 1 and Table 2.

Table 1. Mechanical properties of flexural beams.

Material	Tough PLA
Young's Modulus	2800 MPa
Yield Strength	45 MPa
Poisson Ratio	0.35

Table 2. Determined geometric dimensions.

Beam length	100 mm
Beam Thickness	0.5 mm

The optimization process has been conducted. The tolerance coefficient ξ is selected to be 2%. The optimal result obtained is:

$$\theta = 58.7550°$$

$$\sigma_{\max} = 44.9470 \, MPa \ \leq \ \sigma_{yield}$$

$$\Omega = [0, 28.8mm]$$

According to the optimal outcome, the proposed constant force mechanism has a total height of 51.87 mm, with the constant

force region measuring 28.8 mm. This optimal constant force region occupies 55.5% of the structure's height, highlighting its characteristic of being a large constant force region. The force-displacement relationship based on the optimal result can be referred to Figure 2.
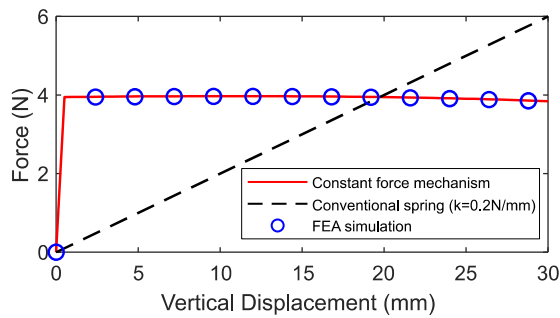
Figure 2. The force-displacement relationship of constant force mechanism and spring. The modeling result is verified using FEA simulation, which is conducted in Strand7.

In Figure 2, a comparison is presented between the force-displacement relationships of a constant force mechanism and a conventional spring with a stiffness of 0.2 N/mm. It is evident that as the vertical displacement increases, the reaction force applied to the workpiece surface increases linearly when a spring is utilized as a feed mechanism. Conversely, with the implementation of the proposed constant force mechanism, the force remains consistently around a specific value. This stability enhances the polishing process by mitigating the impact of fluctuations in force.

4. Conclusion

In conclusion, this study introduces a precision polishing platform with a flexural constant force mechanism, ensuring a constant polishing force for improved precision. The modelling process, utilizing the SCME method, effectively captures the nonlinear behaviour of large deformation flexural beams. Future research could involve exploring the modelling and analysis of shear forces on the platform and conducting experimental validations to assess its stability. These efforts would contribute to advancing our understanding and optimizing the design of precision polishing platforms.

Reference

[1] Ma, G., Li, S., Liu, F., Zhang, C., Jia, Z., & Yin, X. (2022). A review on precision polishing technology of single-crystal SiC. Crystals, 12(1), 101.

[2] Xia, Z., Fang, F., Ahearne, E., & Tao, M. (2020). Advances in polishing of optical freeform surfaces: A review. Journal of Materials Processing Technology, 286, 116828.

[3] Julong, Y., Zhe, W. U., Ducnam, N. G. U. Y. E. N., Huizong, L. U., & Ping, Z. H. A. O. (2012). Review on ultra-precision polishing technology of aspheric surface. Journal of Mechanical Engineering, 48(23), 167-177.

[4] Wu, Z., Shen, J., Peng, Y., & Wu, X. (2022). Review on ultra-precision bonnet polishing technology. The International Journal of Advanced Manufacturing Technology, 121(5-6), 2901-2921.

[5] Howell, L. L. (2013). Compliant mechanisms. In *21st Century Kinematics: The 2012 NSF Workshop* (pp. 189-216). London: Springer London.

[6] Hao, G., & Kong, X. (2012). A novel large-range XY compliant parallel manipulator with enhanced out-of-plane stiffness. Journal of Mechanical Design, 134(6), 061009.

[7] Guo, J., Suzuki, H., Morita, S. Y., Yamagata, Y., & Higuchi, T. (2013). A real-time polishing force control system for ultraprecision finishing of micro-optics. Precision Engineering, 37(4), 787-792.

[8] Wei, Y., & Xu, Q. (2022). Design of a new passive end-effector based on constant-force mechanism for robotic polishing. Robotics and Computer-Integrated Manufacturing, 74, 102278.

[9] Li, B., Li, G., Lin, W., & Xu, P. (2014, April). Design and constant force control of a parallel polishing machine. In 2014 4th IEEE International Conference on Information Science and Technology (pp. 324-328).

[10] Ding, B., Zhao, J., & Li, Y. (2021). Design of a spatial constant-force end-effector for polishing/deburring operations. The International Journal of Advanced Manufacturing Technology, 116, 3507-3515.

Session 5: Non-Mechanical Manufacturing Processes

AFM-ECM: Electrochemical micro/nano machining on an AFM platform

Krishna Kumar Saxena[1], Muhammad Hazak Arshad[1], Dominiek Reynaerts[1]

[1]Micro -& Precision Engineering Group, Manufacturing Processes and Systems (MaPS), Department of Mechanical Engineering, KU Leuven, Leuven – 3001, Belgium | Member Flanders Make

krishna.saxena@kuleuven.be, dominiek.reynaerts@kuleuven.be

Abstract

Fabrication of micro/nanostructures on difficult-to-cut materials is still a challenge and availability of fabrication technologies outside cleanroom is limited. The trend for tip-based nanomanufacturing has attracted research interest as a potential method to address this challenge. Atomic force microscope (AFM) tip based scratching and nanoindentation are steps in this direction. Electrochemical machining (ECM) has the potential to be downscaled as the process is non-contact in nature and dissolution occurs at atomic level. By control and localisation of material removal through downscaling of tool and ultrashort voltage pulses, micro/nanomachining can be realized on difficult-to-cut materials. This work describes the integration of the ECM process on an AFM platform, referred to as AFM-ECM. Through a dedicated AFM tip and short pulsed voltage, micro/nano-machining can be realised. This technology will enable micro/nano-machining, patterning and characterisation on the same AFM platform. The hardware specifications of a prototype desktop AFM-ECM setup and process details are presented. Test experiments are conducted to demonstrate the feasibility of the proposed technology.

Keywords: Electrochemical machining, ECM, micro-ECM, AFM-ECM

1. Introduction

Surface micro/nano-structuring on difficult-to-cut materials with feature size less than 50 μm is still a challenge in the micromanufacturing research community driven by the introduction of novel materials such as cermets and superalloys. Electrochemical micromachining (ECMM) [1] has been widely researched as a fast and force-free process to manufacture components at smaller scales. Since the process involves material removal by anodic dissolution, the surface quality is much higher and microstructure as well as material properties are preserved. Due to non-contact nature of the process and atomic scale dissolution, ECMM process can be further downscaled [2]. By control and localisation of material removal through downscaling of tool and ultrashort voltage pulses [3] on AFM platform, micro/nano electrochemical machining can be realized on difficult-to-cut materials.

This work therefore, focuses on fundamental research on the integration of the ECM process on an AFM platform, referred to as AFM-ECM, focussing on downscaling of tool-based electrochemical micromachining process towards micro/nano structuring of difficult-to-cut workpieces e.g. Inconel IN718.

2. AFM-ECM process

AFM-ECM process implies electrochemical micro/nanomachining on an AFM platform. This facilitates closed loop nanodimensional positioning and accurate interelectrode gap setting (Z piezo stage with 0.06 nm resolution and 30 μm stroke). Figure 1 depicts a process schematic of AFM-ECM process where downscaling of feature dimensions is achieved by using nanosecond voltage pulses and a tungsten tip (~50 nm tip radius) attached to a tuning fork is used as a tool with cathodic polarity. The nanosecond voltage pulses and small interelectrode gaps (≤ 1 μm) facilitate process localisation through the double layer effect (capacitive behaviour of ionic layers near the tool and workpiece). The electrolyte (μL) is supplied in the form of a droplet. The setup allows electrochemical micro/nano machining as well as AFM surface measurement on the same platform with an intermediate cleaning step. The surface measurement is performed by using tungsten tip with tuning fork (resonance frequency ~ 30.233 kHz and quality factor of 988) in self oscillation mode and probe can be controlled by phase lock loop (PLL) in constant signal mode. The use of tuning fork resonant probe eliminates the problems encountered with AFMs using laser based displacement measurements as the hydrogen gas bubbles interfere with the laser spot on the AFM tip.
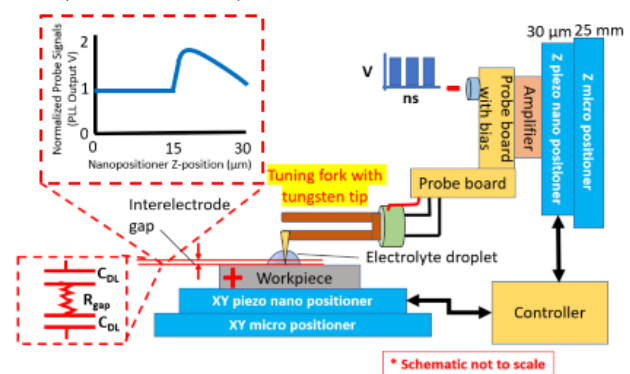
Figure 1. Process schematic of AFM-ECM.

3. AFM-ECM: Experimental setup

Figure 2 provides an overview of the actual AFM-ECM 3-axis experimental setup with major peripherals. The nm resolution position control along with required stroke is realized by superimposing nanopositoning stages on micropositioning

stages. The nanosecond pulses are generated by a function generator (Output 10 Vpp at pulse frequency of 25 MHz for a load of 50 ohm) and output voltage pulses were acquired by an oscilloscope (2 GS/s, 300 MHz, rise time 1.2 ns). The interelectrode gap (1 μm) is set by detecting the surface (resonance frequency shift due to tip-sample interaction tracked by PLL) with the tuning fork tip and retracting the tip by moving micropositioner with a resolution of 95 nm.
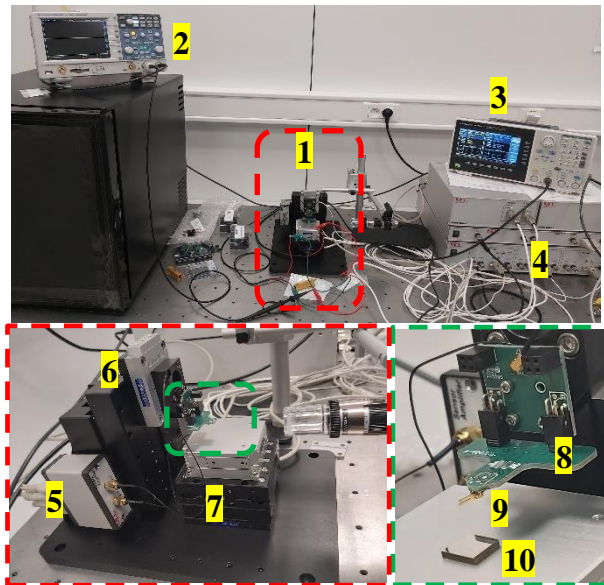
Figure 2. Overview of experimental setup - 1. AFM-ECM platform 2. Function generator, 3. Oscilloscope, 4. Controllers (motion and PLL), 5. Amplifier, 6, 7. Piezo Nanopositioner stages (Z, X-Y) superimposed over micropositioner stages, 8. Probe board, 9. Tuning fork with tungsten tip as ECM tool, 10. Workpiece.

4. Experimental tests and results

Figure 3(a) shows a mirror-finish Inconel IN718 workpiece sample polished with diamond paste (Struers®) of different grain sizes in a decreasing order from 9 μm to 3 μm to 1 μm, and then a final step of polishing with a SiO_2 polishing suspension. Figure
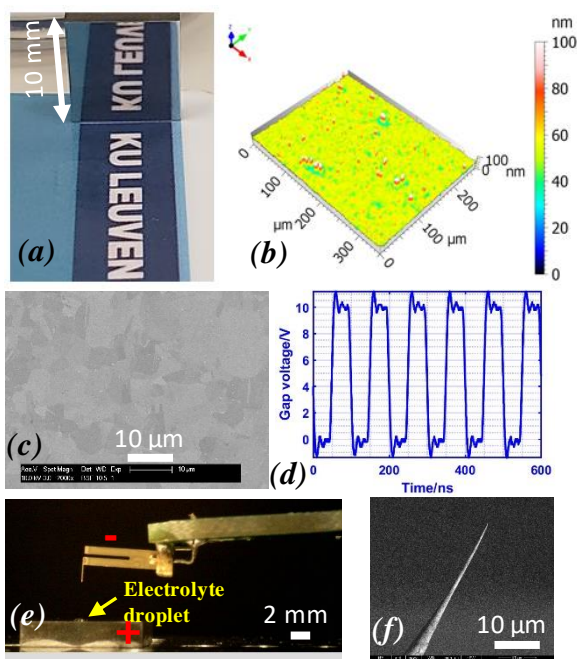
Figure 3. (a) A mirror polished Inconel IN 718 workpiece (b) 3D roughness profile of workpiece (c) SEM image of workpiece (d) Voltage pulses of 100 ns duration and 50 % duty cycle (e) Close-up view of setup with gold coated tungsten tip used as an ECM tool (f) SEM image of tungsten tip used as an ECM tool.

3(b) depicts a 3D roughness profile of the workpiece measured using Sensofar® Neox profiler with Sa 4.74 nm and Sq 10.53 nm (Measurement parameters: 50x lens, L-filter 25 μm, blue LED with 3% light level) and Fig 3(c) shows SE micrograph of the polished workpiece used in the experiments. To achieve process localisation by exploiting double layer effect, nanosecond voltage pulses exemplar output is shown in Fig. 3(d) with an amplitude of 10 V, pulse duration of 100 ns and duty cycle of 50%. To downscale the process and confine the electrochemical reactions, a tungsten tip was employed. Figure 3(e) depicts a gold coated tungsten tip of 2 mm length and 50 nm tip radius (Fig. 3(f)) mounted on the tine of tuning fork which was employed as cathode. To achieve electrical insulation between the tuning fork circuitry and tip while supplying electric current to perform ECM, an intermediate dielectric layer was deposited on the tuning fork followed by final layer of gold coating. A droplet electrolyte was supplied using a pipette. Figure 4 depicts a footprint of AFM-ECM process fabricated by anodic dissolution by virtue of Faraday current flowing between the tip and the workpiece for 10 s. The image is obtained from AFM along with the cross-sectional profile. The experimental parameters used to obtain this nanostructure were voltage 10 V, pulse duration 100 ns and duty cycle 50% (Fig. 3(d)), interelectrode gap 1 μm. A droplet of electrolyte (*aq.* $NaNO_3$) with conductivity of 52.5 mS/cm was used in a humidity rich (RH 70%) environment.
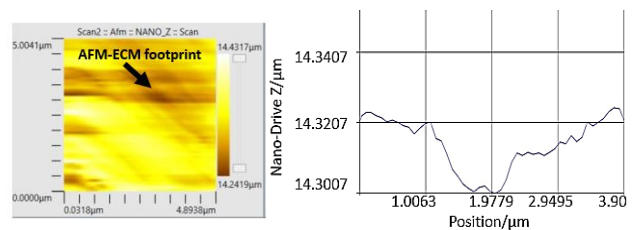
Figure 4. AFM image of an ECM footprint (left) and cross-sectional profile of this footprint (right).

5. Conclusions

This work presented an ECM process on an AFM platform, referred to as AFM-ECM. Through a dedicated AFM tip and short pulsed voltage, micro/nano electrochemical machining of difficult-to-cut materials (e.g. Inconel IN718) can be realised. The process and hardware specifications of a prototype desktop AFM-ECM setup are presented. Proof-of-concept experiments are conducted to demonstrate the feasibility of the proposed technology. The results indicate that by employing ultrashort pulses and downscaled tools on AFM platform, it is possible to fabricate micro/nano structures below 50 μm thereby surpassing the limits of tool and beam based techniques. This technology will enable micro/nano-machining, patterning and characterisation on the same AFM platform.

References

[1] K. K. Saxena, J. Qian, and D. Reynaerts, "A review on process capabilities of electrochemical micromachining and its hybrid variants," *Int. J. Mach. Tools Manuf.*, vol. **127**, pp. 28–56, 2018.

[2] A. P. Malshe *et al.*, "Tip-based nanomanufacturing by electrical, chemical, mechanical and thermal processes," *CIRP Ann. - Manuf. Technol.*, vol. **59**, no. 2, pp. 628–651, 2010.

[3] R. Quan, H. Tong, and Y. Li, "Ns-pulsewidth pulsed power supply by regulating electrical parameters for AFM nano EDM of nm-removal-resolution," *Nanotechnology*, vol. **32**, no. 34, 2021.

Zinc nano-powder mixed electrical discharge machining for antibacterial surface modification

Viet D. Bui[1*], Thomas Berger[1], André Martin[1], Andreas Schubert[1,2]

[1]Chemnitz University of Technology, Professorship Micromanufacturing Technology, Reichenhainer Str. 70, 09126 Chemnitz, Germany
[2]Fraunhofer Institute for Machine Tools and Forming Technology, Reichenhainer Str. 88, 09126 Chemnitz, Germany

* Corresponding author. Email address: duc-viet.bui@mb.tu-chemnitz.de

Abstract

Powder mixed electrical discharge machining (PMEDM) using silver nano-powder has proven its capability in modifying implant surfaces to achieve excellent antibacterial properties along with good biocompatibility. However, the widespread of bacterial resistance to silver in clinical has been reported. In addition, for implantable devices, further enhancement of biocompatibility of the modified surface is required. Zinc is known as a strong antibacterial agent and a biocompatible element to the human body. Consequently, in this study, Ti6Al4V surfaces are modified using the PMEDM milling operation process with zinc powder admixed to the hydrocarbon-based dielectric fluid. The powder with nano-sizes from 40 nm to 60 nm and different powder concentrations up to 15 g/L is utilised. Ti6Al4V sheet tool electrodes with a length of 6 mm and different thicknesses of 0.2 mm and 0.12 mm are used, while discharge energy is varied from 10 μJ to 125 μJ. The workpiece is stimulated by an ultrasonic vibration frequency of 22.3 kHz and an amplitude of 2.5 μm. Results show that the deposited zinc content is homogeneously distributed over the modified surface. Powder concentration, discharge energy, and tool thickness significantly affect the zinc deposition and surface roughness. PMEDM using zinc nano-powder shows a promising potential for antibacterial surface modification of the implantable devices.

Keywords: powder mixed EDM, zinc deposition, antibacterial effect, biocompatibility

1. Introduction

The demand for medical implants has been rapidly increasing. The global market was valued at 5.7 billion USD in 2022 and is predicted to reach more than 24.8 billion USD in 2031 [1]. However, implant-associated infections still pose a major challenge for the implantable device industry. For example, the incidence of prosthetic joint infection and failure in the subsequently prosthesis revision is up to 3 %, as reported in [2].

PMEDM using silver nano-powders has been studied for ablative shaping of medical implants and concurrently forming antibacterial layers on the implant surfaces. The surfaces integrated with silver exhibited long-term antibacterial properties both *in vitro* and *in vivo* while optimizing bone ingrowth of endoprosthesis [3]. The content of deposited silver significantly affects the bacterial colonization on the modified surfaces, whereby an increase of the silver content resulted in a reduction of the bacterial number [4]. However, in clinical, the widespread of bacterial resistance to silver has been reported with various kinds of the bacteria, such as *Pseudomonas aeruginosa*, *Acinetobacter baumannii*, *Staphylococcus aureus, Klebsiella pneumonia, Escherichia coli*, and *Enterobacter cloacae*, etc [5]. The use of high silver contents increases the antibacterial effect, nevertheless it leads to toxicity to human cells. In addition, it has been found that silver showed a weaker antibacterial effect on gram-positive bacteria compared to its effect on gram-negative strains [6].

Zinc, a vital element for multiple biochemical functions of the human body, is a strong antibacterial agent. In contradiction to silver, zinc exhibited a higher susceptibility against gram-positive bacteria, whereas its antibacterial effect is reduced on gram-negative bacteria [6]. Additionally, literature showed that, as a biodegradable element, zinc has a better biocompatibility than silver [7]. And it can be realized that until now there was no challenge related to Zn-resistant bacteria in clinical.

Zinc powders were used in the PMEDM process for modifying AZ31 magnesium alloy surfaces. A study using zinc powder concentration in the dielectric medium up to 3 g/L to modify magnesium alloy showed that the corrosion rate of the PMEDM surfaces was significantly lower than the surface modified without powder. And the lowest corrostion rate was obtained at 2 g/L zinc powder concentration [8]. The enhancemences of microhardness and cytocompatibility were found when mixing zinc powder into the dielectric fluid to modify Ti6Al4V surfaces. The formation of zinc oxide was assumed as its reason [9]. Effects of the powder material on machining efficiency were also investigated, whereby zinc, cobalt and molybdenum powders with different concentration were mixed into the hydrocarbon-based dielectric fluid to machine a nickel-based superalloy. It was found that the highest material removal rate was achieved by using zinc powder, whereas molybdenum powder provided the smoothest surface [10].

It can be realized that zinc is a promising potential agent for antibacterial surface of the implantable devices. Consequently, in this study, PMEDM using zinc nano-powder is investigated for antibacterial surface modification of titanium alloy. This study focuses on the content and distribution of deposited zinc on the modified layer, which is very important for antibacterial capability of the implant surface as well as for homogeneous antibacterial properties over its entire surface.

2. Methodology

In order to provide the homogeneous distribution of deposited zinc over the surface, the homogeneous distribution

of zinc nano-particles in the spark gap is vital [3,4]. Additionally, the narrow spark gap, from approx. 5 µm to approx. 10 µm, leads to challenges for transporting the suspended powders through the gap. In this study, thin Ti6Al4V sheets were therefore used as tool electrodes for modifying the Ti6Al4V surfaces.

To reduce the spattering of materials on the modified surface and support the transportation of zinc powder though the machining gap, the workpiece was stimulated by a Hielscher UIP250 ultrasonic vibration system, which was integrated with a PMEDM circulation system as shown in Figure 1.
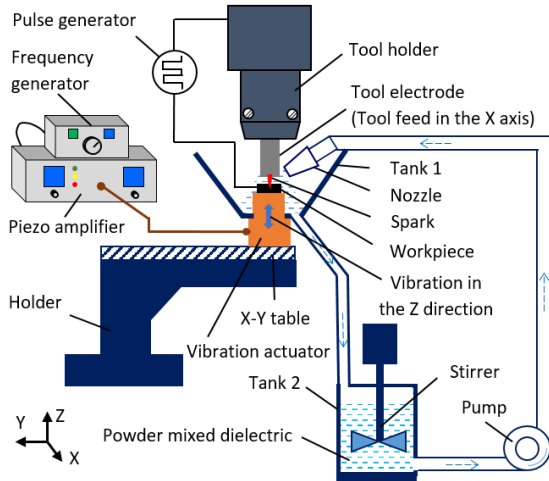
Figure 1. Schematic showing the experimental setup.

The vibration frequency and amplitude were measured by a Polytec OFV-505 Laser Vibrometer and a Polytec OFV-5000 controller. The applied experimental conditions are given in Table 1.

Table 1 Experimental conditions

Parameter	Value
Machine	Sarix T1T4 µ-EDM machine
Workpiece	Material: Ti6Al4V
Tool electrodes	- Length: 6.0 mm - Thickness: 0.2 mm and 0.12 mm - Material: Ti6Al4V
Dielectric fluid	HEDMA111 oil
Discharge energy	10 µJ, 55 µJ and 125 µJ
Polarity	Negative tool electrode
Zinc powder	- Size: 40-60 nm - Concentration in dielectric: 5 g/L and 15 g/L
Ultrasonic vibration	- Frequency: 22.3 kHz - Amplitude (a_{p-p}): 2.5 µm

For each machining condition, three samples were prepared, whereby a (5 x 6) mm^2 area with a depth of 45 µm was machined on each one as shown in Figure 2. After machining, an ethanol filled ultrasonic bath was used to clean each sample. The elemental composition of the modified surfaces was analysed using energy dispersive X-ray spectroscopy (EDS), whereby a spectrum of approx. (3 x 3) mm^2 was analysed at the center of each surface to analyse the average deposited zinc content in the modified layer. To evaluate the distribution of zinc contents over the modified surface, 10 smaller EDS spectra numbered from 1 to 10 were analysed perpendicularly to the tool feed direction as represented in Figure 2. Scanning electron microscopy (SEM) was used to analyse the surface topography. In addition, the modified surfaces were scanned by a Keyence VK9700 confocal 3D laser-scanning-microscope, then MountainsMap 7.4 scanning topography software was utilised to analyse the roughness values.
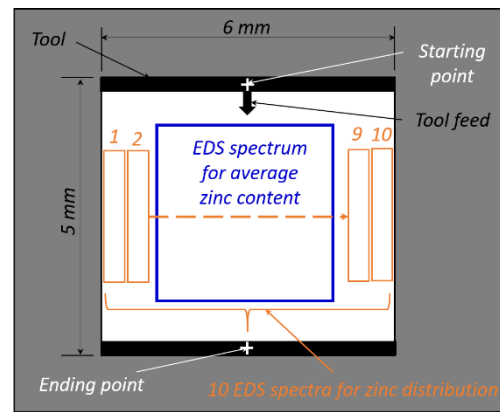
Figure 2. Schematic showing the geometry of the modified area and EDS spectra for analyses of the zinc content and zinc distribution

3. Results and discussions

In this section, the content and distribution of deposited zinc as well as roughness of the modified surface will be represented and discussed. It focuses on effects of powder concentration, discharge energy and tool thickness when applying the PMEDM process using sheet tool electrode on the targeted results.

3.1. Averaged content of the deposited zinc

Figure 3 shows the content of deposited zinc dependent on the concentration of zinc nano-powders mixed in the dielectric fluid and the thickness of tool electrode.
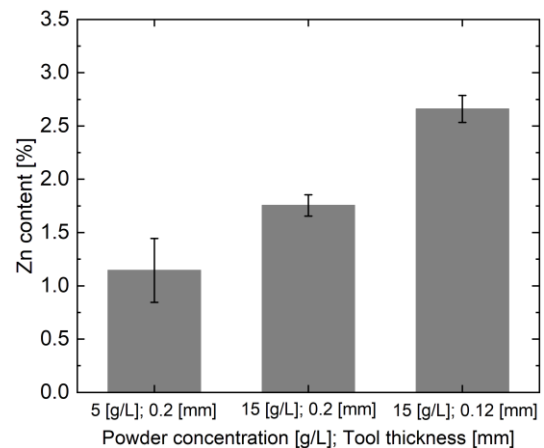
Figure 3. Effects of powder concentration and thickness of the sheet tool electrode on the averaged zinc content (55 µJ discharge energy)

It is clear that an increase of powder concentration increases the deposited zinc content. The addition of more powder to 15 g/L results in a slight improvement of the deposited zinc content to approx. 1.8 % from approx. 1.2 % when using 5 g/L powder. However, zinc nano-powders seem to still face challenges to flow through the spark gap, when applying a 0.2 mm tool thickness and side flushing with ultrasonic vibration assistance. The zinc deposition was also investigated when using a 0.2 mm tool thickness, 5 g/L powder and without vibration assiatance. EDS results show that the content of deposited zinc is reduced to approx. 0.84 $^{±0.3}$ %. Therefore, the assistance of ultrasonic vibration also significantly increases the amount of zinc particles in the gap. However, it can be realised that the efficiency of the PMEDM process on transferring zinc to the modified layer is still low in comparison to the transfer of silver [3]. The reason is not understood well. Nevertheless, low melting and boiling points of zinc are assumed to be a main reason.

The utilisation of a thinner tool electrode with thickness of 0.12 mm can solve the challenge for powder transportation through the machining gap, whereby the content of deposited zinc is remarkably increased to approx. 2.7 % with mixing 15 g/L powder into the dielectric fluid. However, It can be realised that delivering powder particles into the machining gap still faces difficulties when utilising side flushing. Therefore, other flushing stratergies should be investigated in further studies.

Influence of discharge energy on the deposited zinc content is shown in Figure 4.
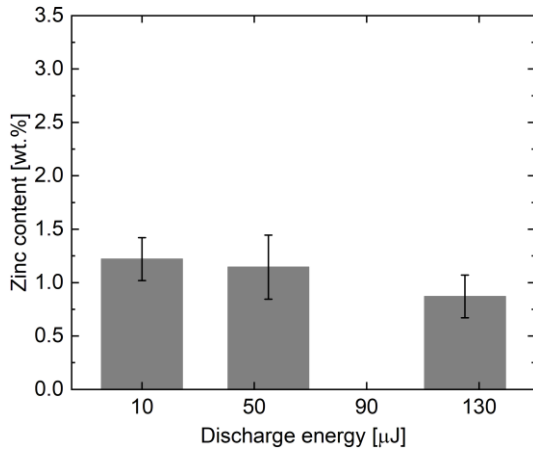
Figure 4. The deposited zinc content on workpiece surfaces for different discharge energies (5 g/L powder, 0.2 mm tool thickness)

Results show that the application of a higher discharge energy leads to a reduction of the deposited zinc. The increase of discharge energy leads to a higher heat, which causes a stronger evaporation of zinc. Therefore, it decreases the amount of zinc re-solidified into and onto the modified layer.

3.2. Distribution of the deposited zinc

Since the content of antibacterial agent plays a vital role in the antibacterial property, therefore a homogeneous deposition over the modified surface is a very important prerequisite for the homogeneous antibacterial effect of the surface. Providing a uniform distribution of zinc powder over the machining gap, which significantly affects the homogeneous deposition of zinc, is the aim of using sheet tool electrodes. Results from Figure 5 indicate that the deposited zinc is quite uniformly distributed

over the modified surface in all cases. Especially when using a 0.12 mm tool thickness, the zinc content distributes in a range of 2.7 $^{\pm 0.17}$ %. This result shows a potential of applying the sheet tool electrode for providing the homogeneous distribution of the antibacterial agent over the big surfaces by the PMEDM process.
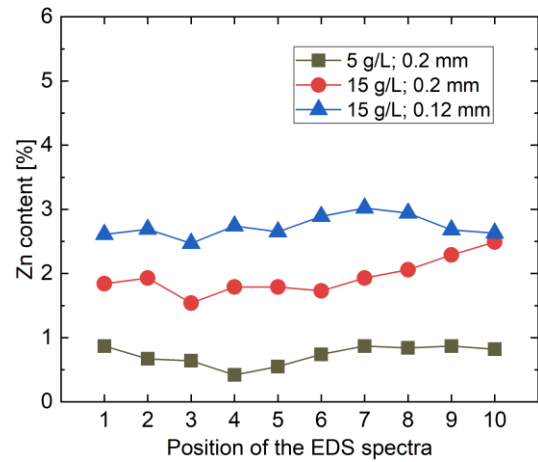
Figure 5. Distribution of deposited zinc over the modified surfaces when using different powder concentrations (g/L) and tool thicknesses (mm) at a discharge energy of 55 µJ

SEM images of the surfaces modified using different machining conditions are represent in Figure 6. It can be observed that the modified surface is formed by overlapping craters. The crater size is mainly affected by discharge energy as can be seen in Figure 6(a-c). The crater sizes are approx. 10 µm, 15 µm, and 40 µm with applying 10 µJ, 55 µJ and 125 µJ discharge energies, respectively. By visualizing backscattered electrons in the SEM analysis, spattered materials containing a large amount of zinc are depicted as a bright color on the surface due to the strong interaction. The use of a higher energy leads to a reduction of the spattered material. This is also one of the reasons for decreasing the deposited zinc content when applying a high energy. However, micro-cracks can be observed with using discharge energy of 55 µJ and especially at 125 µJ.

The amount of spattered materials is remarkably increased with adding more powder into the dielectric fluid as can be seen in Figure 6(d-e). This is due to the fact that a higher powder concentration facilitates the formation of more molten
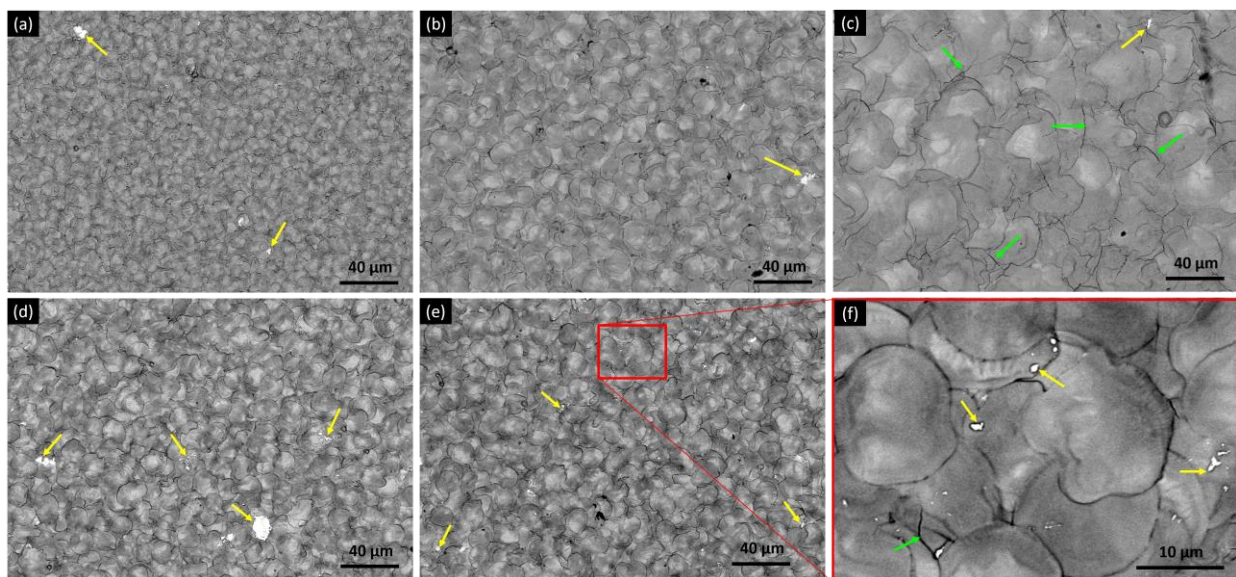
Figure 6. Backscattered electron images of the surfaces modified by the PMEDM process using: (a-d) 0.2 mm tool thickness with (a) 5 g/L, 10 µJ; (b) 5 g/L, 55 µJ; (c) 5 g/L, 125 µJ; (d) 15 g/L, 55 µJ; (e-f) 0.12 mm tool thickness and 15 g/L powder concentration (orrange arrows point on spattered material, green arrows point on micro-cracks)

materials. Additionally, the zinc powders seem to be agglomerated when utilising the 0.2 mm tool electrode (Figure 6(d)), whereby big spattered particles can be found on the surface.

3.3. Surface quality

Figure 7 displays roughness values of the surfaces modified by EDM without powder and with different powder concentration.
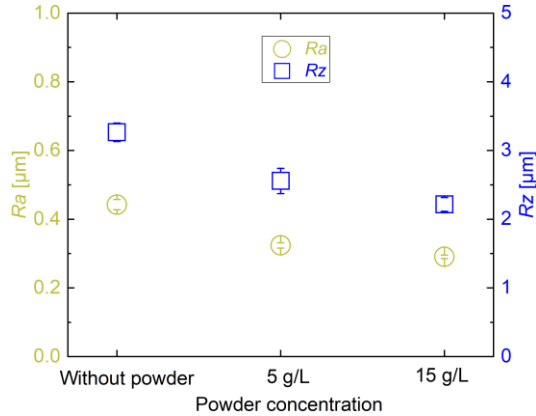
Figure 7. Influence of powder concentration on surface roughness (55 µJ discharge energy)

It can be realised that powder concentration plays a very important role on surface roughness. The addition of powder into the dielectric fluid significantly reduces the roughness of modified surface. Simultaneously, an increase of powder concentration leads to generate a smoother surface. Topography of the surface was also analysed by MountainsMap 7.4 scanning topography software, as shown in Figure 8.
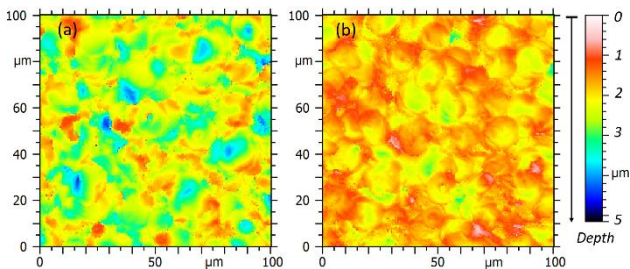
Figure 8. Topography of the surfaces modified by EDM (a) without powder and (b) with 15 g/L powder (55 µJ discharge energy)

It can be observed that shallower craters are formed by EDM with powder addition. An enlargement of the spark gap is assumed as a main reason.

Discharge energy also affects the surface roughness remarkably, which is illustrated in Figure 9. This is clear due to the significant increase of the crater size as illustrated in Figure 6.
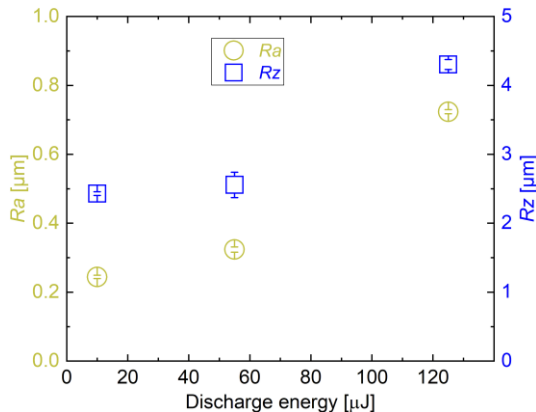
Figure 9. Roughness values of the surfaces modified by PMEDM with 5 g/L powder and different discharge energies

4. Conclusion

In this study, zinc nano-powder has been mixed into the hydrocarbon-based dielectric fluid to modify Ti6Al4V surfaces. Sheet tool electrodes were used, while powder concentration, discharge energy, and tool thickness are varied. Additionally, ultrasonic vibration has been introduced to the Ti6Al4V workpiece during the machining process. From the results, the following conclusions can be drawn:

- Powder concentration, discharge energy and tool thickness significantly affect the integrity of modified surface.
- The content of deposited zinc is increased by adding more powder into the dielectric fluid, reducing the tool thickness, or introducing ultrasonic vibration to the workpiece. However, it is decreased by using a higher discharge energy.
- By utilising the sheet tool, the deposited zinc over the surface is homogeneous, especially when applying a 0.12 mm tool thickness.
- Mixing zinc nano-powder into the dielectric results in smoother surfaces due to the generation of shallower craters.
- PMEDM with zinc nano-powder shows a promising potential for antibacterial surface modification of the implantable devices.

References

[1] Smart medical implants market, 2023, URL: https://www.transparencymarketresearch.com/smart-medical-implants-market.html

[2] Gemmel F., et al.: Prosthetic joint infections: radionuclide state-of-the-art imaging. In *EUR J NUCL MED MOL I*, vol. 39, 2012, pp. 892-909

[3] Bertrand J., et al.: Silver-Integrated EDM Processing of Ti6Al4V Implant Material Has Antibacterial Capacity While Optimizing Osseointegration. In: *Bioact. Mater.*, vol. 31, 2024, pp. 497-508

[4] Bui V.D., et al.: Antibacterial coating of Ti-6Al-4V surfaces using silver nano-powder mixed electrical discharge machining. In: *Surf. Coat. Tech.*, vol. 383, 2020, pp.125254

[5] Mona T.K., et al.: The increasing threat of silver-resistance in clinical isolates from wounds and burns. In: *Infect. Drug. Resist.*, 2019, pp. 1985-2001

[6] Sanjay M., et al.: Hollow mesoporous silica capsules loaded with copper, silver, and zinc oxide nanoclusters for sustained antibacterial efficacy. In: *J. Am. Ceram. Soc.*, vol. 105(3), 2022, pp. 1685-1696

[7] Shimabukuro M.: Antibacterial property and biocompatibility of silver, copper, and zinc in titanium dioxide layers incorporated by one-step micro-arc oxidation: a review. In: *Antibiotics*, vol. 9(10), 2020, pp. 716

[8] Razak M.A.: Controlling corrosion rate of Magnesium alloy using powder mixed electrical discharge machining. In: *IOP Conf. Ser. Mater. Sci. Eng.*, vol. 344, 2018, pp. 012010

[9] Rahul D.: Enhanced micro-electric discharge machining-induced surface modification on biomedical Ti-6Al-4V alloy. In: *J. Manuf. Sci. Eng.*, vol. 144(7), 2022, pp. 071002

[10] Jenarthanan, M.P.: Investigation of powder mixed EDM of Nickel-based superalloy using Cobalt, Zinc and molybdenum powders. In: *Trans. Indian Inst. Met.*, vol. 74, 2021, pp. 923-936

Application of in-situ process monitoring to optimise laser processing parameters during the powder bed fusion printing of Ti-6Al-4V

John J. Power[1], Mark Hartnett[2], & Denis P. Dowling[1]

[1]*I-Form Centre, School of Mechanical and Materials Engineering, University College Dublin, Dublin, D04 V1W8, Belfield, Ireland*
[2]*Irish Manufacturing Research, Block A, Collegeland, Rathcoole, Co. Dublin, D24 WC04, Ireland*

john.power1@ucdconnect.ie

Abstract

This study evaluates the use of in-situ process monitoring feedback as an approach to help reduce print defects such as porosity, during the laser powder bed fusion (L-PBF) of Ti-6Al-4V overhang structures. During initial printing trials it was observed in the region around the print overhang structure that increased porosity levels were present with a volume fraction of up to 0.08% compared with <0.02% in the bulk alloy. It is hypothesized that the increased porosity is associated with the excess heat generated in the overhang region due to the decreased thermal conductivity of the unmelted powder beneath the print layers compared with the solid alloy. Additionally, excess porosity and inclusions were observed in the regions adjacent to the overhang melt pool and attributed to spatter ejection from the overhang melt pool. In-situ process monitoring data obtained from the melt pool infrared emissions was correlated with the properties of the printed parts. This in-process data was then used to assist in selecting optimal laser processing conditions to prevent the melt pool from overheating at the overhang region. By systematically controlling the laser energy while printing the first fifteen layers over the overhang structure, the bulk alloy's porosity level was reduced to <0.02%. There was also an associated reduction in the roughness (Ra) of the overhang itself, with its Ra decreasing from 62.4±7.3 to 7.5±1.9 μm.

Laser powder bed fusion, In-situ process monitoring, Titanium, Porosity, Roughness

1. Introduction

Additive manufacturing (AM) can create complex geometries and features that conventional formative and subtractive manufacturing cannot readily produce. For this reason, AM has seen an increased use in the biomedical [1] and aerospace sectors [2]. However, one of the critical limitations of AM is the ability to control the level of porosity [3] and the as-built surface quality of printed parts [4].

Examples of porosity defects in Ti-6Al-4V alloy parts fabricated using L-PBF include lack of fusion (LOF) and keyhole (KH) [3]. Incomplete melting of the powder due to rapid scanning speeds or low power can result in small irregularly shaped pores, referred to as LOF pores. In contrast, excessive laser power or slower scanning speeds can cause KH pore formation, vaporising the material in the melt pool. This vapour is trapped in the resolidifying alloy, resulting in bubble-like cavities after solidification [5]. This over-melting of the powder bed significantly affects the incorporation of unmelted powder, leading to the formation of voids and porosity.

Relatively high roughness levels observed at the downskin or overhang surfaces of L-PBF parts are another common print defect [6, 7]. Several print parameters can affect the formation of rough surfaces, including laser power and scanning speed [8, 9]. Excess heat in the liquid melt pool can cause surface tension gradient-driven flow inside the melt pool, known as Marangoni convection. This Marangoni convection can lead to instability in the melt pool and affect the shape and formation of the downskin surfaces.

Overhang surfaces challenge the capabilities of the L-PBF process in terms of heat distribution [10] and control over melt pool dynamics [11]. The adverse defects observed in overhang structures fabricated using LPBF are thought to be induced by the difference in absorbed energy into the melt pool at the powder-supported zone versus the solid-supported zone. In-situ process monitoring has seen increased use with the L-PBF process. It can detect defects, including those associated with overhang structures. Optical emission spectroscopy and thermal monitoring are among the in-process monitoring techniques used to monitor L-PBF printing [12-17]. These in situ techniques have also been used by a small number of authors to investigate the laser melt pool during the printing of overhang structures [11, 14, 18]. For example, Egan et al. [14] used process monitoring data obtained from an in situ optical emission spectroscopy setup during L-PBF printing (Renishaw RenAM 500M) to monitor the processing of the first layer printed above an internal cavity. Compared to the solid alloy, the poor thermal conductivity of the alloy powder resulted in an increased melt pool size and temperature. This increased temperature, arising from a decrease in thermal conduction away from a melt pool generated in an overhang, may have resulted in larger thermal gradients, which can, in turn, destabilize the melt pool.

As detailed above, the challenges of fabricating parts with overhangs are well documented in the literature. There have been limited studies on optimising processing parameters for overhang structure printing. The objective of this study is to establish the effects of the overheating that occurs at overhang layers compared to the bulk Ti-6Al-4V alloy. This evaluation will be based on comparing the changes in porosity and roughness. Additionally, the use of in-situ process monitoring to help select optimal processing parameters for overhang structures will be investigated. The goal is to achieve a higher level of homogeneity between the porosity and roughness in the regions around the overhang and the bulk Ti-6Al-4V.

2. Materials and methods

2.1. Materials and processing parameters

Extra-low interstitial Ti-6Al-4V (Grade 23, ELI-0406) powder, with particle size in the 10–45 μm range, was sourced from Renishaw Plc [19]. This printing study was conducted on a Renishaw RenAM 500M system operating under an inert gas atmosphere. Additionally, this AM system has an in situ processing monitoring (PM) system called InfniAM Spectral [20]. The latter system uses several photodiodes to gather data relating to the thermal and optical emissions (in the near-infrared range) from the laser melt pool created during the build process and provide feedback on the laser energy output from the machine [21].

As the objective of this study was to evaluate if in-process monitoring could be used to select optimised process parameters for the printing of overhang structures, the Ti-6Al-4V test sample was designed to simulate a flat overhang structure. Figure 1 shows the design of the test piece used in this study, with the overhang region highlighted by dashed lines in the plan and side view of the drawing schematic.
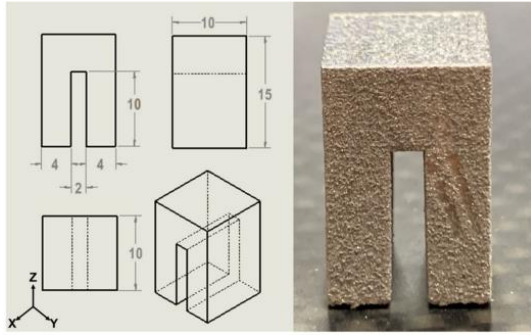
Figure 1. Overhang test piece: **left** design and dimensions (in mm) and **right** photograph of the printed Ti-6Al-4V alloy part.

μm hatch distance using a meander zigzag scan strategy, rotated 67° degrees between each layer, a spot size of 80 μm, layer thickness of 30 μm, and point distance of 75 μm. The delay time between each recoating of the powder was approximately 30 s, and a gas flow rate (Ar) of roughly 29 m³/h was used during printing.

2.2. In-situ process monitoring data analysis

A series of experiments was proposed to help identify the processing conditions which would yield a more homogeneous overhang melt pool temperature profile comparable with that obtained within the bulk alloy. A Box-Behnken design was used to alter three parameters: the laser power and laser exposure time in steps of 5.0%, 12.5%, or 20.0% in either one, eight, or fifteen layers above the overhang. For example, test condition 6 involved a laser power reduction of 5% over eight layers. This involved printing the first overhang layer with 66% of the laser power (133W), which was used to print the bulk alloy. Each subsequent layer was then printed with an increase of laser power of 5% from the previous layer until the laser power reached nominal laser power (200W). The parameter changes are only applied to melt tracks printed directly onto the 2×10 mm overhang region in the centre of the part after layer 464 for one, eight, or fifteen layers. The approach resulted in thirteen print experiments, with three replicants: in all, thirty-nine overhang samples were printed and investigated, as detailed in Table 1. Each sample's volumetric energy density (VED) was calculated using Eq. 1 [22].

$$VED = \frac{Pe_t}{hd_pd_h} \left[\frac{J}{mm^3}\right]$$

Equation 1: Volumetric energy density formula for parts printed using modulated wave laser [22].

Table 1: Processing conditions investigated. Detailed are the percentage reductions in laser power and the exposure time reduction, which indicates the percentage change between subsequent layers until parameters are returned to nominal levels. Also included are the number of layers the laser processing parameters were altered. The average VED column indicates the overall level of laser energy reduction.

Test Condition	Power Reduction (%)	Exposure Time Reduction (%)	No. of gradient layers	Average VED for the 15 layers above overhang (J/mm³)
1	12.5	5	1	67.6
2	5	12.5	1	67.6
3	5	20	1	67.3
4	20	5	1	67.3
5	20	20	1	66.7
6	20	20	8	39.8
7	5	5	8	55.5
8	12.5	12.5	8	45.0
9	20	5	15	14.2
10	12.5	20	15	10.6
11	5	5	15	33.1
12	20	12.5	15	10.6
13	5	20	15	14.2

The first overhang layer was deposited directly onto the unsolidified powder material below without part supports after 10 mm (464 layers) of powder material had been deposited and melted to form the solid leg structures. The overhang area of the test piece was 2 × 10 mm. For non-overhang regions, a laser power of 200 W, exposure time of 50 μs and a modulated 10 ms delay between exposures was used, as recommended by the printer manufacturer for Ti-6Al-4V alloy. For the overhang region, these parameters varied, as detailed in the next section. The alloy samples were built using a pulse laser mode with a 65

Where P (W) is the laser power, e_t (μs) is the laser exposure time, h (μm) is the layer thickness, d_p (μm) is the point distance, and d_h (μm) is the hatching distance. The VED for the non-overhang regions of the build was calculated as 68.4 J/mm³. Table 1 details the average VED for the overhang region over fifteen layers above the overhang.

To evaluate the success of each set of processing conditions, the melt pool emissions in the overhang regions were compared with those in the non-overhang regions in the same print layer. This was done by comparing the in-process monitoring IR

photodiode readings. The pixel intensity associated with each part measured using the PM software was obtained by taking images of the 2D reconstructions of each layer and analysing them using ImageJ software. This analysis of the IR emission data allowed for samples that had not experienced overheating at the overhang to be identified. The in situ data was then correlated with the overhang roughness and porosity data obtained for each print sample.

2.3. Porosity and roughness measurements

Part porosity was evaluated using a GE Phoenix Nanotom M microcomputed tomography (μCT) system, operating at 150 kV and 200 μm, with a scan time of approximately 10 minutes [23]. The resolution of each scan was 12 μm, defined as the smallest detectable pore size in the sample. The μCT scans were analysed using the porosity/inclusion analysis (PLA) module in VGStudio Max version 3.5 [24]. Optical microscopy (OM) was also carried out using an Olympus GX51 optical microscope at 10x magnification. The size and shape of pores at the overhang surface were analysed to determine the type of porosity present. Porosity was evaluated in the solidified alloy directly above the overhang and in the entire structure to compare the effect the overhang had on porosity formation.

Overhang roughness measurements were obtained based on the μCT measurements using an approach previously applied to AM-printed porous structures [25]. The roughness of the overhanging edge was determined based on the profile lines taken from 2D cross-sectional images of the overhang. The overhang profile line was extracted using an ImageJ script written by the first author. This script analyses the pixels along the overhanging edge within a user-selected region of interest. It measures the edge roughness in correspondence with ISO 21920-2:2021. The average roughness (Ra) was determined for each test sample using Eq. 2. Five measurements were taken from five different cross-sections of each sample.

$$ R_a = \frac{1}{l_e} \int_0^{l_e} [z(x)] \, dx $$

Equation 2: The arithmetic mean of the absolute values of the ordinate values [26].

3. Results and discussion

The objective of this study is to identify the laser processing conditions that minimized the measured porosity and roughness. Assessment of overheating in the overhang region is based on photodiode intensity measurements. The Ti-6Al-4V overhang samples printed using the processing conditions detailed in Table 1 were cross-sectioned, mounted, ground, polished, and examined using optical microscopy. LOF porosity large irregular pores with sharp corners and edges, was present in samples were insufficient fusion of metal powder occurred. The presence of LOF pores highlights that simply reducing the level of laser energy used to print the overhang can result in different defect types, compared with those obtained when excess laser energy is used.

Keyhole pores formed in the layers closer to the powder bed in each sample. The poor thermal conductance of the powder bed below the overhang and the initial layers deposited onto the powder bed to form the overhang would have led to an increase in the local melt pool temperature, increasing the chance of material vaporization and keyhole formation. Keyhole porosity was the most common type of porosity observed in samples printed with a higher laser energy.

Increased porosity was observed in the print layers immediately above the overhang, up to 0.08% volume fraction.

This was substantially higher than the level of porosity observed in the bulk alloy regions, which averaged less than 0.02% for all samples. Samples printed with lower laser energy density (test conditions 6, 9, 10, 12, and 13) exhibited higher levels of porosity. This was attributed to pore formation in the area laterally of the overhang regions, figure 2, likely due to spatter ejection from the unstable melt pool [27].
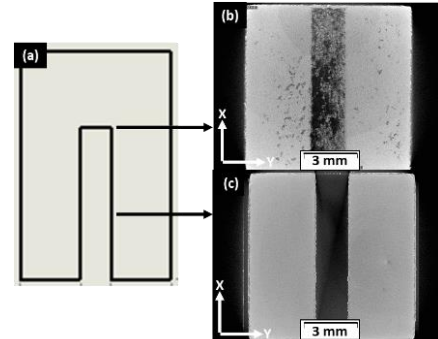
Figure 2. (a) Schematic showing the front view of the overhang test piece. The arrows indicate the approximate location of the layer views from the μCT scans shown. (b) μCT scan images showing the first overhang print layer (layer 464) with an increased level of porosity visible (dark patches) in the non-overhang regions of the part. (c) μCT scan showing print layer (layer 250) which was located away from the overhang and exhibited no visible porosity.

Figure 3 shows the Ra roughness measurement for test samples along with the average IR photodiode measurement for the overhang melt pools. This demonstrated a broad correlation between the intensity of the laser energy used to print the sample and the (Ra) roughness measurements obtained from the CT scans. This figure also includes the associated photodiode measurements . When higher photodiode measurements were recorded, associated with higher melt pool energy, there was generally an associated increase in roughness. However, this correlation was not observed for all overhang samples, e.g. sample 11. A reduction in laser power, and therefore melt pool temperature, has previously been linked to reduced surface roughness [4].
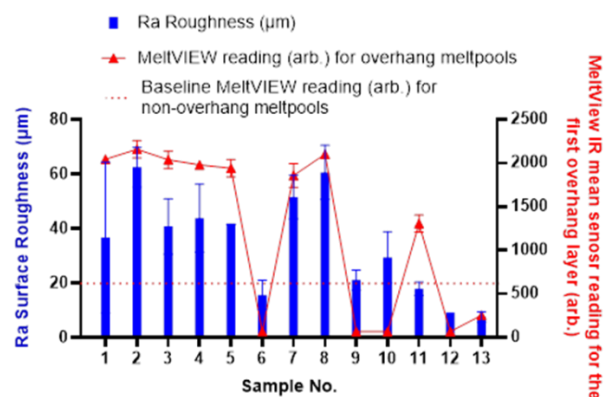
Figure 3. Ra roughness of overhang surface graphed with the average IR photodiode sensor reading (arb.) for the first overhang layer melt pool.

4. Conclusions

Overhang structures in printed alloy structures can create difficulties due to variations in the melt pool temperature, due to decreased thermal conductivity of the powder immediately below the printed overhang layers. In this study a design of experiments was carried out and the results were in-formed

based on in-process monitoring (photodiode measurements) of the melt pool temperature. By tailoring the laser processing conditions for the first 15 layers over the overhang localised overheating was minimised. the level of porosity was significantly reduced. Porosity levels (volume fraction) of up to 0.08% in the overhang region were reduced to the <0.02% obtained for the bulk alloy. There was an associated reduction of up to 88% in the roughness (Ra) of the overhang itself.

References

[1] L. E. Murr *et al.*, "Microstructure and mechanical behavior of Ti–6Al–4V produced by rapid-layer manufacturing, for biomedical applications," *Journal of the Mechanical Behavior of Biomedical Materials,* vol. 2, no. 1, pp. 20-32, 2009/01/01/ 2009, doi: https://doi.org/10.1016/j.jmbbm.2008.05.004.

[2] R. Liu, Z. Wang, T. Sparks, F. Liou, and J. Newkirk, "13 - Aerospace applications of laser additive manufacturing," in *Laser Additive Manufacturing*, M. Brandt Ed.: Woodhead Publishing, 2017, pp. 351-371.

[3] H. Gong, K. Rafi, H. Gu, T. Starr, and B. Stucker, "Analysis of defect generation in Ti–6Al–4V parts made using powder bed fusion additive manufacturing processes," *Additive Manufacturing,* vol. 1, pp. 87-98, 2014.

[4] J. C. Fox, S. P. Moylan, and B. M. Lane, "Effect of Process Parameters on the Surface Roughness of Overhanging Structures in Laser Powder Bed Fusion Additive Manufacturing," *Procedia CIRP,* vol. 45, pp. 131-134, 2016/01/01/ 2016, doi: https://doi.org/10.1016/j.procir.2016.02.347.

[5] G. Kasperovich, J. Haubrich, J. Gussone, and G. Requena, "Correlation between porosity and processing parameters in TiAl6V4 produced by selective laser melting," *Materials & Design,* vol. 105, pp. 160-170, 2016.

[6] S. Rahmati and E. Vahabli, "Evaluation of analytical modeling for improvement of surface roughness of FDM test part using measurement results," *The International Journal of Advanced Manufacturing Technology,* vol. 79, no. 5, pp. 823-829, 2015.

[7] C. Qiu, C. Panwisawas, M. Ward, H. C. Basoalto, J. W. Brooks, and M. M. Attallah, "On the role of melt flow into the surface structure and porosity development during selective laser melting," *Acta Materialia,* vol. 96, pp. 72-79, 2015.

[8] J. Gockel, L. Sheridan, B. Koerper, and B. Whip, "The influence of additive manufacturing processing parameters on surface roughness and fatigue life," *International Journal of Fatigue,* vol. 124, pp. 380-388, 2019/07/01/ 2019, doi: https://doi.org/10.1016/j.ijfatigue.2019.03.025.

[9] D. Wang, Y. Yang, Z. Yi, and X. Su, "Research on the fabricating quality optimization of the overhanging surface in SLM process," *The International Journal of Advanced Manufacturing Technology,* vol. 65, no. 9, pp. 1471-1484, 2013.

[10] A. Ashby *et al.*, "Thermal history and high-speed optical imaging of overhang structures during laser powder bed fusion: A computational and experimental analysis," *Additive Manufacturing,* vol. 53, p. 102669, 2022/05/01/ 2022, doi: https://doi.org/10.1016/j.addma.2022.102669.

[11] Q. Han, H. Gu, S. Soe, R. Setchi, F. Lacan, and J. Hill, "Manufacturability of AlSi10Mg overhang structures fabricated by laser powder bed fusion," *Materials & Design,* vol. 160, pp. 1080-1095, 2018/12/15/ 2018, doi: https://doi.org/10.1016/j.matdes.2018.10.043.

[12] S. Clijsters, T. Craeghs, S. Buls, K. Kempen, and J.-P. Kruth, "In situ quality control of the selective laser melting process using a high-speed, real-time melt pool monitoring system," *The International Journal of Advanced Manufacturing Technology,* vol. 75, pp. 1089-1101, 2014.

[13] T. Craeghs, S. Clijsters, J. P. Kruth, F. Bechmann, and M. C. Ebert, "Detection of Process Failures in Layerwise Laser Melting with Optical Process Monitoring," *Physics Procedia,* vol. 39, pp. 753-759, 2012/01/01/ 2012, doi: https://doi.org/10.1016/j.phpro.2012.10.097.

[14] D. S. Egan, K. Jones, and D. P. Dowling, "Selective laser melting of Ti-6Al-4V: Comparing μCT with in-situ process monitoring data," *CIRP Journal of Manufacturing Science and Technology,* vol. 31, pp. 91-98, 2020/11/01/ 2020, doi: https://doi.org/10.1016/j.cirpj.2020.10.004.

[15] C. S. Lough *et al.*, "Local prediction of Laser Powder Bed Fusion porosity by short-wave infrared imaging thermal feature porosity probability maps," *Journal of Materials Processing Technology,* vol. 302, p. 117473, 2022/04/01/ 2022, doi: https://doi.org/10.1016/j.jmatprotec.2021.117473.

[16] D. Alberts, D. Schwarze, and G. Witt, "In situ melt pool monitoring and the correlation to part density of Inconel® 718 for quality assurance in selective laser melting," in *2017 International Solid Freeform Fabrication Symposium*, 2017: University of Texas at Austin.

[17] S. Berumen, F. Bechmann, S. Lindner, J.-P. Kruth, and T. Craeghs, "Quality control of laser-and powder bed-based Additive Manufacturing (AM) technologies," *Physics procedia,* vol. 5, pp. 617-622, 2010.

[18] L. Scime and J. Beuth, "Using machine learning to identify in-situ melt pool signatures indicative of flaw formation in a laser powder bed fusion additive manufacturing process," *Additive Manufacturing,* vol. 25, pp. 151-165, 2019/01/01/ 2019, doi: https://doi.org/10.1016/j.addma.2018.11.010.

[19] Renishaw-PLC. "Ti6Al4V ELI-0406 powder for additive manufacturing." Renishaw PLC. https://shorturl.at/bJQW9 (accessed Jan 10th, 2023).

[20] Renishaw-PLC, "InfiniAM Spectral - Energy Input and Melt Pool Emissions Monitoring for AM Systems," 2017.

[21] D. S. Egan and D. P. Dowling, "Correlating in-situ process monitoring data with the reduction in load bearing capacity of selective laser melted Ti–6Al–4V porous biomaterials," *Journal of the Mechanical Behavior of Biomedical Materials,* vol. 106, p. 103723, 2020.

[22] G. Repossini, V. Laguzza, M. Grasso, and B. M. Colosimo, "On the use of spatter signature for in-situ monitoring of Laser Powder Bed Fusion," *Additive Manufacturing,* vol. 16, pp. 35-48, 2017.

[23] "Phoenix Nanotom M 180 kV / 20 W X-ray nanoCT® system for high-resolution analysis and 3D metrology," ed. Cincinnati, Ohio, 2021.

[24] VGStudio, "VGStudio Max 2.2 Reference Manual," ed. Heidelberg, Germany: VGStudio, 2012.

[25] G. Kerckhofs, G. Pyka, M. Moesen, J. Schrooten, and M. Wevers, "High-resolution micro-CT as a tool for 3D surface roughness measurement of 3D additive manufactured porous structures," in *Proc iCT*, 2012, pp. 77-83.

[26] *ISO 21920-2:2021 Geometrical product specifications (GPS) - Surface texture: Profile - Part 2: Terms, definitions and surface texture parameters*. Geneva: International Organization for Standardization, 2021.

[27] S. Keaveney, A. Shmeliov, V. Nicolosi, and D. P. Dowling, "Investigation of process by-products during the Selective Laser Melting of Ti6AL4V powder," *Additive Manufacturing,* vol. 36, p. 101514, 2020/12/01/ 2020, doi: https://doi.org/10.1016/j.addma.2020.101514.

High-efficiency fabrication of functional structured array surface on hard metallic ceramic materials by a novel magnetic field-assisted self-assembly electrode

K.S. Li[1], C.J. Wang[1*], C.F. Cheung[1], F. Gong[2]

[1]State Key Laboratory of Ultra-precision Machining Technology, Department of Industrial and Systems Engineering The Hongkong Polytechnic University, Hong Kong, China
[2]Shenzhen Key Laboratory of High Performance Nontraditional Manufacturing, College of Mechatronics and Control Engineering Shenzhen University Shenzhen, Guangdong, China

chunjin.wang@polyu.edu.hk (corresponding author)

Abstract

Hard metallic ceramic materials such as silicon carbide (SiC) and Tungsten carbide (WC), have been widely used in many important industrial applications attributing to their high hardness and stable material properties. Electrical discharge machining (EDM) is one of the effective methods to fabricate the functional structured surfaces on these materials. However, serious electrode wear together with a complicated electrode replacement process leads to high fabrication costs and low production efficiency. Hence, EDM with a self-assembly electrode was proposed for the fabrication of the functional structured array surface on metallic ceramic materials. Based on the discrete design concept, we designed a magnetic field-assisted self-assembly electrode (MASAE). The MASAE is made up of an array of ferromagnetic metallic balls attracted together under the guidance of the magnetic field generated by a permanent magnet. By adjusting the position, number, and size of the metallic balls, different MASAEs can be prepared. After the EDM process, different structured surface arrays on the metallic ceramic materials can be fabricated. The shape evolution and surface quality of the EDMed structure arrays were measured and analysed by ContourGT-X 3D optical profile and scanning electron microscope (SEM). The composition and phase changes of the EDMed surface were characterized by energy-dispersive X-ray spectroscopy (EDS) and Raman. Compared with the traditional integral electrodes made by milling or turning, the MASAE has a great advantage in preparation time, cost-effectiveness, and replaceability. The proposed manufacturing strategy provides an effective way for the design and manufacturing of functional structured surfaces on metallic ceramic materials.

Metallic ceramic materials; structured array surface; electrical discharge machining; self-assembly electrode

1. Introduction

Hard ceramic materials, such as binderless tungsten carbide (WC) and silicon carbide (SiC), are widely used in applications requiring high endurance and high temperature, such as semiconductor electronics devices, car parts, cutting tools, and moulds [1-3]. The effective machining of superhard ceramic materials is one of the research highlights for industry and academia. At present, energy-assisted precision cutting and grinding are two major traditional methods to fabricate functional structured array surfaces on metallic ceramic materials [4]. However, tool wear during the machining process strongly affects the manufacturing accuracy and surface integrity of the machined workpiece. Compared to traditional machining technology, electrical discharge machining (EDM) is one of the non-contact and non-traditional methods and has great advantages in machining hard and brittle materials [5-7].

In the EDM process, the design and development of the electrode is a crucial technique to improve manufacturing efficiency and fabricate a functional structured array surface. Xu et al. [8] used a micro-double-staged laminated object manufacturing method to prepare 3D micro-electrodes for micro-EDM. Yan et al. used a wheel-shaped rotary cupronickel electrode to complete the fabrication of a microstructure array on the polycrystalline diamond. Lei et al. [9] fabricated the deep-narrow blind microgroove array by EDM with a long-laminated electrode. Takino et al. [10] machined the spherical lens array by EDM with a ball-type electrode. Gu et al. [11] proposed a bundled die-sinking electrode to improve the machining efficiency of Ti6Al4V alloys. By designing and optimizing the electrodes during the EDM process, high-effeciency fabrication of functional structured array surfaces can be completed.

In this study, a novel MASAE is proposed for manufacturing of functional structured array surface on metallic ceramic materials. This MASAE is created by using a magnet to adsorb discrete balls. By adjusting the size of the magnet and balls, electrodes of different scales can be prepared. This flexibility in size customization allows for the fabrication of electrodes tailored to specific applications or machining requirements. Larger magnets and balls may be used to create electrodes suitable for machining larger workpieces or producing features on a macro scale. Conversely, smaller magnets and balls can be employed to fabricate electrodes for micro or nano-scale machining tasks. Furthermore, the shape evolution, removal rate, and surface quality of the WC and SiC surface after EDM with a MASAE are investigated. The composition and shape evolution of the EDMed surface are characterized. Finally, functional structured array surfaces with different shapes and sizes are fabricated.

2. Methods

2.1. Design and manufacture route

Based on the discrete design concept, we proposed a MASAE, as shown in Fig. 1(a). A self-assembly ball electrode is made up of magnet spheres with the help of the magnetic force of the permanent magnet. By tuning the arrangement and size of the balls, different self-assembly electrodes can be prepared. Fig. 1(b) shows the optical images of the SiC and WC structure array surface. By adjusting the position and number of magnetic balls, different ball array electrodes can be prepared. After the EDM process, different structured surface arrays on the superhard ceramic materials can be fabricated. Fig. 1(c) shows the SEM image and surface morphology of the EDMed structured surface.
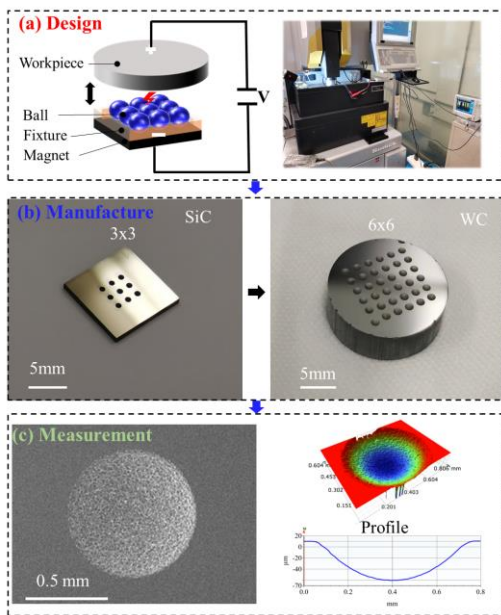
Figure 1. (a) The design principal of EDM with magnetic field-assisted self-assembly electrode, (b) The optical images of the SiC and WC structure array surface, (c) The measurement results of surface morphology.

2.2. Experimental section

Experiments were conducted on a Sodick electrical discharge machine (model AP1L) with three axes. Tungsten carbide (100 wt% WC, 0 wt% Co) and single-crystal 4H-SiC are chosen for the workpiece. By applying pulse energy between the electrodes and the workpiece, the surface structures of the self-assembly electrodes are transferred to the machined workpiece. The EDM conditions and properties of the electrodes are summarized in Table 1.

Table 1 EDM conditions

Conditions		Value
Processing parameters	Input current (A)	1
	Pulse width (μs)	1/5/10
	Pulse interval (μs)	10
	Open voltage (V)	105
	Dielectric fluid	Discharge oil
Tool electrodes	Tool diamater (mm)	1/2.4/3.2
	Resistivity (Ω.m)	2×10^{-7}
	Magnet (T)	1.1

2.3. Measurement and characterization

The surface roughness and shape evolution of the structured surface were measured by ContourGT-X 3D optical profiler (Bruker, Germany). The surface evolution of the structured array was observed using a scanning electron microscope (SEM, FEI, QUANTA FEG 450). The composition and phase changes of the EDMed surface were characterized by energy dispersive X-ray spectroscopy (EDS, FEI, QUANTA FEG 450) and Renishaw micro-Raman spectroscopy system (50 ×objective, laser beam size <10μm).

3. Results and discussions

3.1. Shape evolution and surface quality

Fig. 2 shows the surface morphology of the structured array made by EDM with a self-assembly ball electrode. The diameter and depth of the WC microlens array after EDM are about 450 μm and 47 um, respectively, as shown in Fig. 2(a). Fig. 2(b) shows the surface morphology of the SiC microlens array made by EDM with a self-assembly ball electrode. The diameter and depth of the SiC microlens array are about 425 μm and 50 μm, respectively. The difference in geometry size is due to the machining difficulty of different raw materials. The boiling points of WC and SiC are about 6000 ℃ and 2830 ℃, respectively. During the discharge process, the ablation local temperature can reach as high as 10000 K, significantly higher than the vaporization point of WC and SiC. Compared to the WC, the melting temperature of SiC is low, which affects the material removal rate during the EDM process.
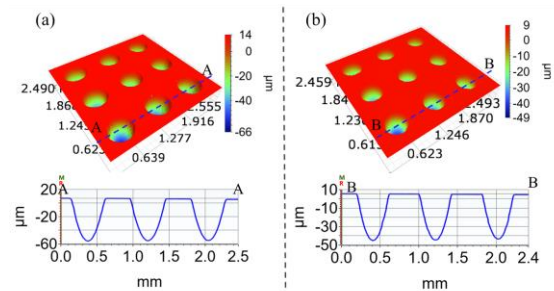
Figure 2. (a) The surface morphology of the EDMed WC surface, (b) The surface morphology of the EDMed SiC surface.

Fig. 3 shows the material removal rate (MRR), and tool wear ratio (TWR) during the EDM process. The MRR and TWR at different pulse widths when machining the WC substrate are shown in Fig. 3(a). When pulse widths are 1, 5, and 10 μs, the MRR are about 0.022 mm³/min, 0.037 mm³/min, and 0.052 mm³/min under a constant pulse current of 1 A and pulse interval of 10 μs. In certain cases, the MRR and TWR increase as the pulse width increases. Fig. 3(b) shows the MRR and TWR at different pulse widths when machining the SiC substrate. It can be found that the rule of MRR in the machining process of SiC is similar to that of WC. However, the TWR in machining the SiC is less than that of WC. The maximum TWR when machining SiC substrate is less than 0.002 mm³/min. The difference in TWR is also due to the differences in machining difficulty of different metallic ceramic materials.
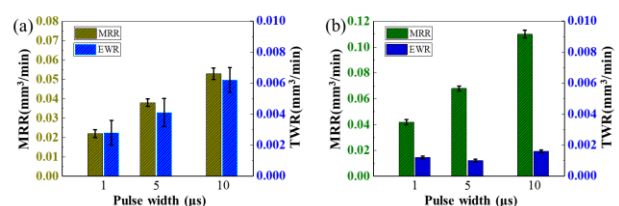
Figure 3. The MRR and TWR during EDM process (a) WC, (b) SiC.

Fig. 4 shows the SEM images of the EDMed surfaces. During discharge process, the interface between the workpiece and electrode forms a plasma channel and produces ultra-high instantaneous temperature, resulting in the melting and vaporization of the workpiece. After the EDM process, lots of ablation craters were formed in the EDMEd surfaces, as shown in Fig. 4(a). The micro-craters forming on the SiC surface affect the surface quality of the EDMed workpiece. Fig. 4(b) shows the SEM images of the WC structured array surface made by EDM with a self-assembly electrode. But unlike the SiC surface, lots of discharge micro-craters and microcracks can be observed on the EDMed WC surface. The tensile stress that occurs during rapid cooling is present in the resolidified layer of the WC surface, leading to the formation of microcracks.
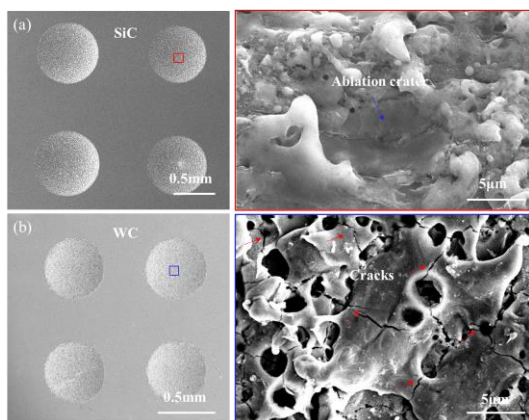
Figure 4. (a) The SEM images of the EDMed SiC surface, (b) The SEM images of the EDMed WC surface.

Fig. 5(a) shows the surface morphology of the EDMed SiC surface before and after curvature tilt. The surface arithmetic roughness (Sa) of the EDMed surface at different conditions is shown in Fig. 5(b) and (c). As the pulse width increases, larger micro-craters form on the fabricated surfaces, resulting in increased surface roughness. When the pulse width, interval, and current are 10 μs, 10 μs, and 1 A respectively, the Sa value of the EDMed WC surface approximates to 1.05 μm. Compared to the EDMed WC, the Sa of the EDMed SiC surface is larger. The maximum Sa of the EDMed SiC surface is about 1.23 μm. It is observed that the size of the discharge-induced craters on the SiC surface is larger than those on the WC surface, given the same discharge parameters. This explains why the surface roughness of the EDMed SiC surface is larger.
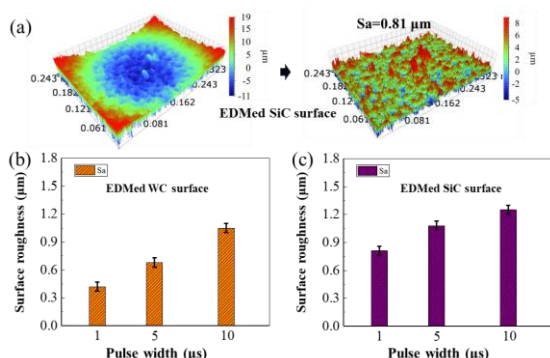
Figure 5. The surface quality after the EDM process (a) The surface morphology of the EDMed SiC surface, (b) The surface roughness of the EDMed WC at different pulse widths, (c) The surface roughness of the EDMed SiC at different pulse widths.

3.2. Composition and phase changes

Fig. 6 shows the SEM image and element distribution mapping of the EDMed SiC surface. It can be found that the C intensity of the C atom in the EDM region is stronger than that of the heat-affected region. The atom percentage of C is about 62%. After EDM, a small amount of O element can be observed. The atom percentage of O is about 2.7%. The formation of oxides during the EDM process is due to the high-temperature ablation effect. The oxides and carbonaceous are also found in the WC machining process [12]. During the vaporization-condensation process of SiC/WC, SiC/WC decomposes into Si/W and C and re-coagulates as separate elements.
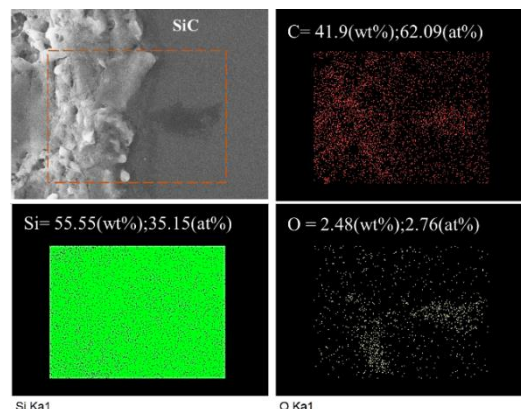
Figure 6. The composition and element changes of the EDMed SiC surface

Fig. 7 shows the Raman spectra in the 200-3200 cm^{-1} range obtained from the surfaces of WC and SiC before and after EDM. The D-band peaks at 1350 cm^{-1}, G-band peaks at 1587 cm^{-1} peaks and 2D-band peaks at 2700 cm^{-1} are detected after materials experience high-temperature discharge ablation. The D and G peaks are related to vibrations of carbon in the sp^2 and sp^3 bonds. The G-band is attributed to the stretching vibration of sp^2 atoms in rings and chains, while the D-band is associated with the breathing mode of sp^2 atoms in rings, and indicates the presence of disorder and defects in the hexagonal sp^2 structure. In Fig. 7(a), the D- and G-bands have not been found in the initial WC substrate. After EDM, very strong D- and G-band peaks are very apparent at the EDMed surface. Besides, graphene structure can also be detected, as shown in the insert image 2 of Fig. 7(a). The formation of carbon is due to the decomposition of WC.

Fig. 7(b) shows the Raman spectra and optical images of SiC surface before and after EDM. Before EDM, the SiC presents distinctive Raman peaks at 778 cm^{-1} and 971 cm^{-1}. After EDM, Raman peaks at 778 cm^{-1} and 971 cm^{-1} disappear, and a new peak at 521 cm^{-1} occurs, indicating the formation of crystalline SiC. Besides, very strong D- and G-band peaks can be found after EDM. The presence of Si and C implies the decomposition of SiC into Si and C. The intensity of the D-, G-, and 2D-bands serves as a measure to evaluate the degree of disorder in the graphitic structure. The EDMed SiC surface is a mixture of crystalline/amorphous Si, amorphous carbon and graphite/graphene. It can be concluded that due to the ultra-high temperature that occurred in the EDM process, SiC decomposes into Si and C, and re-coagulates as separate substances. The phase of carbon in the EDMed surface has graphite and amorphous structures. The phenomenon is similar to the structural changes of WC, but there are a few small changes.
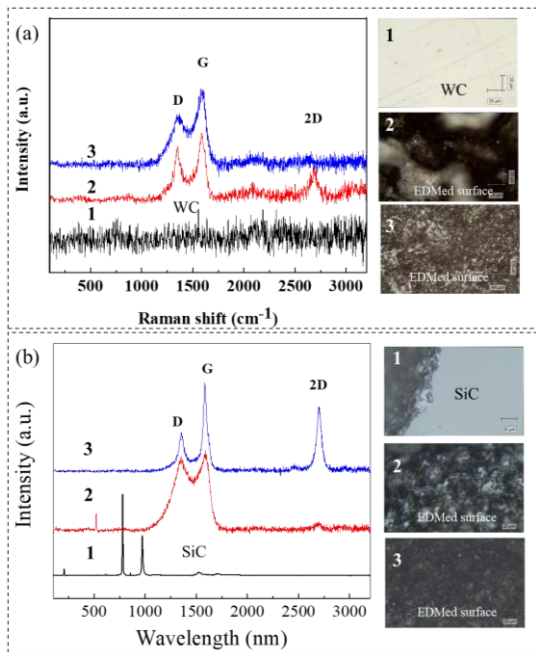
Figure 7. (a) The Raman spectrum and optical images of WC surface before and after EDM, (b) The Raman spectrum and optical images of SiC surface before and after EDM.

3.3. Different geometries of the structured array surfaces

Different depths and shapes of structured array surfaces on metallic ceramic materials can be fabricated by arranging the spherical balls in different arrays and controlling the discharge conditions. Fig. 8 (a) shows the different depths and diameters of structured array surfaces machined by self-assembly ball electrodes. The diameters of the structured array surfaces are about 0.3 mm, 1.2 mm, and 1.3 mm, respectively. Different diameters and depths of structured arrays on the WC and SiC are easily manufactured by adjusting the size of spherical balls and discharge parameters. Thus, self-assembly ball electrodes can be used to fabricate different kinds of freeform surface arrays.

Fig. 8(b) shows the structured array surfaces machined by self-assembly sheet electrodes. By adjusting the thickness and distance of the strip sheet, microstructure arrays with different sizes and shapes can be flexibly fabricated. In sum, the proposed EDM method is very convenient for the replacement of the electrode tool, which is cost-effective for the fabrication of structured array surfaces.
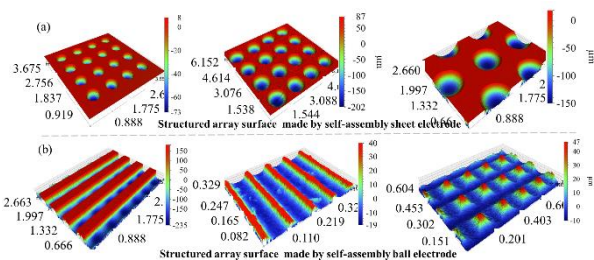
Figure 8. Functional structured array surface on metallic ceramic materials made by EDM with magnetic field-assisted self-assembly ball/sheet electrodes, (a) self-assembly ball electrodes, (b) self-assembly sheet electrodes.

4. Conclusions

In this paper, a novel MASAE for EDM of the structured array surfaces on metallic ceramic materials is presented. Compared

with the traditional integral electrode made by milling or turning, MASAEs have a great advantage in fabricating the structured array surface on the SiC/WC substrates. Higher pulse energy can improve the machining efficiency and MRR during the EDM process, but it would induce the formation of larger craters, leading to increased surface roughness. Besides, SiC and WC decompose into Si/W and C, and then re-coagulate as separate substances due to the ultra-high temperatures generated during the EDM process. The EDMed surface is a mixture of carbon, oxides, and amorphous/crystalline substances, which changes the surface energy of initial materials. In conclusion, the work paves a new path for the design and fabrication of functional structured array surfaces on hard metallic ceramic materials.

References

[1] Sun J, Zhao J, Huang Z, Yan K, Shen X, Xing J 2020 A Review on Binderless Tungsten Carbide: Development and Application *Nano-Micro Lett.* **12** 13-37.

[2] Zhao K, Fang P, Tan J, Zhong W, Liu J, Liu D 2023 A new route to fabricate high-performance binderless tungsten carbide: dynamic sinter forging *J. Am. Ceram. Soc.* **106** 3343-50.

[3] Nakamura D, Gunjishima I, Yamaguchi S, Ito T, Okamoto A, Kondo H, Onda S, Takatori K 2004 Ultrahigh-quality silicon carbide single crystals *Nature* **430** 1009–12.

[4] Liang X, Zhang C, Cheung CF, Wang C, Li K, Bulla B Micro/nano incremental material removal mechanisms in high-frequency ultrasonic vibration-assisted cutting of 316L stainless steel *Int. J. Mach. Tool. Manu.* **191** 104064.

[5] Ming WY, Xie ZB, Du JG, Zhang GJ, Cao C, Zhang Y 2021 Critical review on sustainable techniques in electrical discharge machining *J Manu. Process.* **72** 375-99.

[6] Jithin S, Joshi SS 2021 Surface topography generation and simulation in electrical discharge texturing: A review *J Mater. Process. Tech.* **298** 117297

[7] Philipp N, Richard L, Frank K, Rainer G 2015 Electrical discharge machining of metal doped Y-TZP/TiC nanocomposites *J. Eur. Ceram. Soc.* **35** 4031-7.

[8] Xu B, Wu X, Lei J, Cheng R, Ruan S, Wang Z 2015 Laminated fabrication of 3D micro-electrode based on WEDM and thermal diffusion welding *J. Mater. Process. Tech.* **221** 56-65.

[9] Lei J, Wu X, Zhou Z, Xu B, Tang Y 2021 Sustainable mass production of blind multi-microgrooves by EDM with a long-laminated electrode *J. Clean. Prod.* **279** 123492.

[10] Takino H, Hosaka T. 2016 Shaping of steel mold surface of lens array by electrical discharge machining with spherical ball electrode *Appl. Optics.* **55** 4967-73.

[11] Gu L, Li L, Zhao W, Rajurkar KP. 2012 Electrical discharge machining of Ti6Al4V with a bundled electrode *Int. J. Mach. Tool. Manu.* **53** 100-6.

[12] Li K, Wang C, Gong F, Cheung CF. 2023 Facile and flexible fabrication of structured array surfaces on binderless tungsten carbide by using electrical discharge machining with a novel self-assembly ball electrode *J. Am. Ceram. Soc.* **106** 7386-99.

Influence of plasma-electrolytic rounding on chemical composition, roughness and cutting edge radius of cemented carbide cutting tool inserts

André Martin[1,*], Susanne Quitzke[1], Kevin Eberhardt[2], Andreas Schubert[1]

[1]*Chemnitz University of Technology, Professorship Micromanufacturing Technology, Reichenhainer Str. 70, 09126 Chemnitz, Germany*
[2]*Eberhardt GmbH, Eichendorffstr.5, 91586 Lichtenau, Germany*

[*]*email address of the submitting author:* andre.martin@mb.tu-chemnitz.de

Abstract

The shapes of the cutting edges of cutting tool inserts (CTI) have an essential influence on the machining results and economic aspects. Well-defined rounding and slight chipping of the cutting edges are aspired to achieve high surface qualities and to assure long tool life. Until now, cutting edge preparation is usually realized by mechanical grinding or by laser ablation processes. Both processes require precise alignment of the CTI against the grinding tool or the laser treatment zone, respectively. Moreover, the respective mechanical or thermal impacts might lead to negative influences through an increase in brittleness of the CTI material. Using a plasma-electrolytic process offers the possibility for rounding cutting edges without mechanical impact and low thermal influence by immersion into an electrolyte basin. Previous analyses in plasma-electrolytic rounding (PeR) of a CTI made of WC-TiC-TaC-Co indicated that an aqueous electrolyte based on sodium carbonate and voltages between 240 V and 400 V represent applicable parameters for successful process initiation.

In this study, influences of the PeR process on the chemical material composition and the roughness of the CTI surfaces are analyzed. In addition, different orientations of the relevant cutting edges are investigated with respect to the resulting radii after the rounding experiments. The results of energy dispersive X-ray analyses indicate an increase in oxygen content due to anodic oxidation effects. A preferred removal of tungsten is detected, while cobalt is hardly dissolved in the alkaline solution. A certain increase in surface roughness was detected due to the inhomogeneous elemental dissolution. However, the cutting edge radii with initial values between 18 μm and 26 μm were increased, which represents very promising results regarding the aspired maximum target radius of 30 μm.

Keywords: cutting edge preparation, cemented carbide tools, plasma-electrolytic rounding

1. Introduction

The cutting edges of cutting tool inserts influence in a high degree the surface properties resulting from cutting processes. Precise preparation with high accuracy is a prerequisite to realize high surface qualities [1]. In addition, tool life, which is influenced by thermal and mechanical impacts during cutting, can be increased by cutting edges with slight chipping, which can help save costs [2].

Currently, cutting edge preparation is mainly carried out by grinding or laser-ablative processes. On the one hand, precise alignment of the cutting edges is necessary for both processes. And on the other hand, thermal or mechanical impacts need to be considered. Thermal impacts of the laser process might negatively influence the mechanical characteristics of the surficial edge zones. This can be avoided by ultra-shortly pulsed laser ablation, but results in significant increase in processing time. The mechanical impact from conventional grinding might lead to deviations especially on very sharp edge radii and cause micro cracks that can reduce tool life.

Plasma-electrolytic rounding (PeR) is an innovative ablation process that offers removal with negligible mechanical forces at electrolyte temperatures below their boiling point of approximately 100°C. In addition, there is no need for precise alignment. The setup is comparable to electrochemical polishing with the specifications of plasma-electrolytic polishing (PeP). I.e., the basic principle is an electrochemical cell with initial electrolyte temperatures of (70…90) °C and maximum DC-voltages of 400 V. Usually, environmentally friendly electrolytes with low salt concentration and only low-acidic or low-alkaline pH are applied [3].

On the one hand, sufficient power needs to be provided by sufficiently high voltage in combination with a heated electrolyte temperature to create boiling effects and the formation of a plasma-gas layer that covers the workpiece by means of a closed envelope. This is realized by transfer of electric energy [4] and results in significantly lower electric current density compared to electrochemical machining. But on the other hand, too high voltages need to be avoided, since increasing numbers of electrical discharges result in negative influences of the part's surfaces. Hence, thorough investigation of applicable process parameter combinations is essential to assure reliable initiation and retention of a plasma-electrolytic process with the individual electrolyte composition in combination with the present workpiece material.

Characteristic correlations of the average electric process current as function of the applied voltage are a useful method to investigate applicable voltages for successful initiation of the PeP process [5]. According to [4] it can be assumed that comparable voltages are applicable for PeR to round edges of cutting tool inserts. Hence, a similar strategy was successfully carried out in a previous investigation indicating that PeR is feasible with the analyzed voltages and electrolyte composition [6]. A cutting tool inserts (CTI) made of WC-TiC-TaC-Co was machined with an aqueous electrolyte based on sodium

carbonate at voltages between 240 V and 400 V, which represents applicable PeR parameters.

2. Experimental

Indexable insert types of MI-MPMW090308 UTi20T from Mitsubishi Materials Corp. were chosen as demonstrative CTI. They provide a sufficiently simple setup for basic analyses, since they are not equipped with specific chip guiding shapes nor any coatings that could influence the PeR process or reduce electrical conductivity. Laser markings were applied by means of one and two circular spots to be able to retrace the orientation the symmetric CTI after PeR as shown in Figure 1.
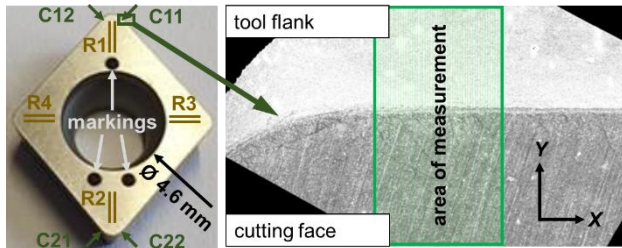
Figure 1. Top view image of a CTI with laser markings, black lines at positions R1…R4 indicate roughness measurements and C11…C22 cutting edge radii measurements (left), microscope image with green-colored measuring lines for cutting edge detection with a lateral distance of 10 µm (right)

Optical measurements were carried out with a Keyence VK-9700 confocal laser scanning microscope with an objective magnification of 50. The roughness values were investigated using MountainsMap7.2 analysis software. The linear roughness values Ra and Rz were analyzed before and after PeR for comparison at the four measuring positions R1…R4 to investigate influences of the CTI orientation in the electrolyte bath. Two measuring lines were arranged at each position and the average values were determined.

The measuring positions C11 and C12 indicate the positions for measuring the cutting edge radii on the side marked by one laser spot, while C21 and C22 refer to the side marked by two laser spots, respectively. The cutting edge radii were measured using a Bruker alicona µCMM optical coordinate measuring machine, as shown by the green-colored measuring lines in the exemplary microscope image. For the evaluation of each radius, 50 individual measurements in Y-direction with a distance of 10 µm in X-direction were arranged orthogonally to the cutting edge and their average value was determined.

The chemical composition of the CTI was detected before and after PeR for comparison via energy dispersive X-ray (EDX) analyses using a scanning electron microscope (SEM) Zeiss EVO 25. SEM images were captured with the same setup to examine the micro-structure of the initial state of the CTI as shown in Figure 2.
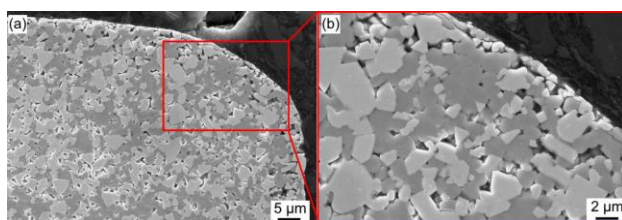
Figure 2. SEM images of grain structure from cross-sectional cut sample, top view (left) and detailed view (right) of the cutting edge

The indexable inserts were cleaned with acetone in an ultrasonic bath and then rinsed with deionized water. Before the experiments, the initial weight of the indexable inserts was determined using a Sartorius ME36S precision microbalance.

The laboratory setup for experimental analyses on PeR is shown in Figure 3.
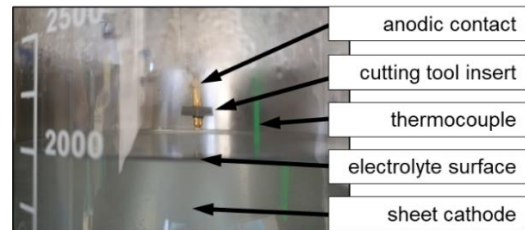
Figure 3. Photograph of the laboratory setup with electrical contacts and a CTI with downward orientation of the cutting edge before immersion into a 2000 ml electrolyte reservoir pre-heated in a beaker glass

The mechanical fixture and electrical contact were realized via the CTI's bore using a bunch plug. To assure chemical resistance, a gold-coated bunch plug was selected. No material removal of the gold-coating was detected after the experiments, which proves its applicability. A linear stage was used for full immersion of the CTI into the electrolyte, approximately 10 mm below the 2000 ml calibration mark. The electrolytes were heated to a temperature of 70 °C and the CTI were immersed for ten seconds before starting the experiments for pre-heating. After the immersion procedure, the voltage was switched on and the current transients were detected via a NI USB-6215 multi-functional device used as a digital multimeter in this case with a sampling rate of 3 Hz. The electric power was provided by a Keysight N8762A energy source.

3. Process parameter investigations

Initial investigations were carried out to analyze applicable electrolyte compositions in combination with useful voltages from the characteristics of the average process current over the whole PeR process [6]. The results showed that aqueous electrolytes of sodium carbonate (Na_2CO_3) with weight concentrations of 5 % and 10 % of the conducting salt is applicable with a processing voltage of 300 V. Experiments were carried out with fully submerged CTI and a processing time of 20 s based on own preliminary experiments, where edge rounding with only negligible influences on the remaining shape of the parts were realized.

3.1. Influence of cutting edge orientation

Figure 4 shows the electric current transients recorded during the PeR experiments with an electrolyte of 10 % of Na_2CO_3.
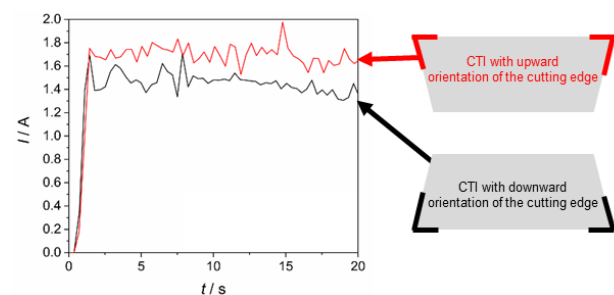
Figure 4. Current transients for cutting edge orientation downward (black line) and upward (red line) during PeR in a 10% Na_2CO_3 electrolyte

The current peak at process initiation with a duration of a few milliseconds is not displayed here since the focus was on investigations of the current development over the whole PeR process with a low sampling rate of 3 Hz. Average processing

currents were between 1.3 A and 2.0 A during the PeR processes. Approximately (10...20) % higher current values were measured when the cutting edge was oriented upward compared to the downward orientation. As a reason, it is expected that the larger horizontal surface oriented downward in the latter case leads to accumulation of more gas bubbles, while for the upward orientation, a larger amount of gas bubbles is released, which results in a lower electric resistance. Influences of the differing current transients on the machining results are discussed in the following sections.

3.2. Electric charge efficiency

The electric charge exchange was integrated from the electric current values over time using trapezoidal calculation. The average current density was calculated from the average electric current over the whole process divided by the surficial area of the CTI, which was 0.603 cm² constantly. The dissolved material weight was measured by differential weighing. The results are shown in Table 1.

Table 1 Dissolved material weight, exchanged electric charge and average current density of PeR experiments with different orientation of the cutting edge (OCE: U...upward / D...downward) and electrolyte concentration

OCE	Concen-tration [%]	Dissolved material weight [mg]	Exchanged electric charge [C]	Current density [A/cm²]
U	5	4.31 ± 0.1	13.56 ± 1.74	1.1 ± 0.3
D	5	4.41 ± 0.5	8.29 ± 2.65	1.7 ± 0.2
U	10	3.91 ± 0.1	10.34 ± 0.86	0.9 ± 0.1
D	10	3.74 ± 0.5	6.98 ± 0.58	1.3 ± 0.2

Both electrolyte concentrations 5 % and 10 % of Na_2CO_3 were investigated. The initial CTI weight was 2957.148 mg measured before PeR as an average of 30 samples. The dissolved material weight is almost comparable for upward orientation and downward orientation of the cutting edge in each single electrolyte. But less material weight was dissolved in the higher concentrated solution. The reason is that significantly lower electric charge was exchanged in the higher concentrated electrolyte, which is also cognizable from the lower average current density values. In both electrolytes, downward orientation of the cutting edge results in significantly lower current density and charge exchange.

The charge effectivity was calculated from the dissolved weight divided by the electric charge exchanged. The highest charge effectivity of 0.54 mg/C was determined with 10% Na_2CO_3 and downward oriented cutting edge, which should be preferred with respect to prospective economic applications focusing on high energy efficiency and short processing times. Hence, this electrolyte was chosen for further investigations. The comparative result for the same electrolyte with 10% concentration and upward orientation is 0.38 mg/C. For the lower concentrated electrolyte of 5%, 0.53 mg/C was measured in downward orientation and 0.32 mg/C in upward orientation. In summary, downward orientation with both the 10% and 5 % electrolyte solutions show the highest charge efficiency with comparable values, which appears useful in an economic point of view but might result from unwanted removals in regions outside from the desired rounding regions.

4. Machining results

The surfaces of the machined CTI were analyzed and compared to the initial surfaces, which are characterized by typical grinding marks from mechanical pretreatment as shown in the microscope image of Figure 5 (a).
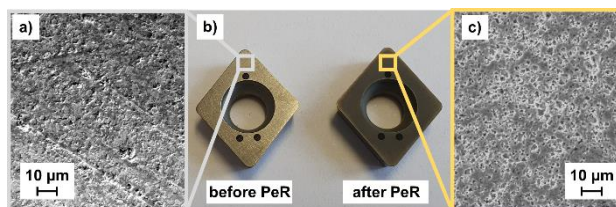
Figure 5. Top view photograph of two CTI, one before (initial) and one after PeR in a 10% Na_2CO_3 electrolyte (b), detailed microscope images of the surface before (a) and after PeR (c)

The grinding marks were smoothened by the PeR process as cognizable from the comparative microscope image in Figure 5 (c). After PeR, the surfaces of the CTI appeared uniformly darker than before as visible in Figure 5 (b). Surficial pores with estimated diameters of ≤ 3 µm already cognizable on the initial surface were exposed by the PeR process.

4.1. Chemical composition

The change of the chemical composition as a result from the PeR process was investigated by EDX analysis. The result is shown in Table 2.

Table 2 Chemical composition of a CTI surface before PeR (bP) and after PeR (aP) in a 10% Na_2CO_3 electrolyte, values in percentage of atoms

	C	O	Ti	Co	Nb	W	Na	Ca
bP	9.9	2.0	7.9	5.3	7.5	67.5	-	-
aP	8.3	9.9	12.3	25.4	9.4	33.9	0.6	0.2

The CTI with WC-Co as basic material composition mainly consist of tungsten (W) and carbon (C) as well as other alloying elements such as niobium (Nb) and titanium (Ti) in addition to the metallic cobalt (Co) binder, which corresponds to the manufacturer's information. The comparative analysis show that mainly the mass fraction of tungsten was decreased, which indicates that tungsten carbide was dissolved preferably, which is also cognizable from the slight carbon reduction. It should noted that the carbon reduction is less significant, since it is overlayed by an accumulation of carbon from the electrolyte. Similar effect is cognizable for small residues of sodium (Na). And negligible residues of calcium (Ca) are cognizable that result from the final flushing process with water.

All the remaining elemental contents were increased. While the oxygen content raised as expected due to anodic oxidation, especially the significant increase of the cobalt content indicates a certain homogeneity in the dissolution of the basic material.

4.2. Surface roughness

The bar charts in Figure 6 show the results of the comparatively measured linear roughness values Ra and Rz before (light gray, dark gray) and after PeR (green, yellow). The exemplary results of two CTI represent cutting edges oriented upward and downward, which were measured before and after machining with a 5% Na_2CO_3 aqueous electrolyte.

As can be seen, all roughness values were increased. The initial values of Ra of (0.1...0.2) µm were increased to (0.3...0.4) µm and the initial Rz values of (0.7...1.3) µm were increased to (3.0...4.0) µm after PeR. The reason is the preferred dissolution of tungsten carbide as discussed before, while the dissolution rate of cobalt was significantly lower, which led to a more uneven surface topography.

The results of the four measuring positions show comparable values after PeR, which indicates an even distribution of the process. In upward orientation, the relative roughness increases are slightly stronger than in downward orientation due to easier gas bubble release. Also, at positions R1 and R3 slightly stronger increases were detected, which results from a slight inclination

of the immersed sample in relation to the electrolyte surface and stronger impacts on these regions. The results achieved with lower concentrated electrolyte revealed comparable changes of the surface roughness.
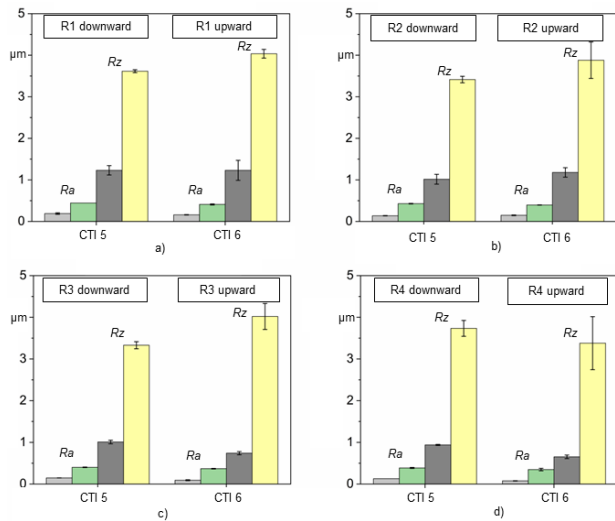
Figure 6. Linear roughness values *Ra* (light gray / green) and *Rz* (dark gray / yellow) detected at the measuring positions R1…R4 of two exemplary CTI with different cutting edge orientations before (gray) and after PeR (green, yellow) with an electrolyte of 10% of Na_2CO_3

4.3. Cutting edge radius

Analyses results of 30 CTI before PeR led to an average initial cutting edge radius of (24.1 ± 2.9) µm. A comparison of the single initial cutting edge radii (gray) and the radii after PeR (orange) is shown exemplarily in Figure 7.
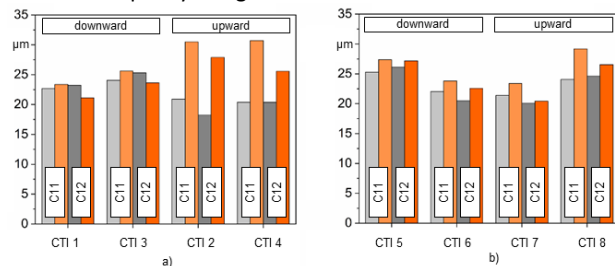
Figure 7. Radii of the cutting edges at positions C11 and C12 of a CTI, initial values (gray) and values after PeR (orange) in aqueous solutions with concentrations of 5% (a) and 10% of sodium carbonate (b)

As cognizable from the results, most of the radii were increased. CTI 2 and CTI 4 machined with the 5% electrolyte solution and upward orientation, which is shown by the two right-handed results of Figure 7 (a), indicate the most significant increase in cutting edge radius between 5 µm and 10 µm. Consequently, the targeted cutting edge radius of 30 µm was realized on initial values of approximately 20 µm at positions C11 on both samples, and only slightly missed at positions and C12.

Also, with upward orientation on sample CTI 8, which was machined in the higher concentrated electrolyte, the target radius was realized. However, the remaining samples show only slight rounding, especially in downward orientation. On the two samples CTI 1 and CTI 3, even a slight radius reduction of approximately 2 µm was detected, which can be attributed to measuring errors. Consequently, upward orientation of the cutting edges appears to be most applicable to realize sufficient rounding.

5. Conclusion and Prospects

The results show that PeR with a voltage of 300 V in electrolytes of Na_2CO_3 at weight concentrations of 5 % and 10 % of the conductive salt was successful. The lower concentrated electrolyte should be preferred in further investigations since it offers the highest charge efficiency and the best rounding results.

However, inhomogeneous dissolution of the single elements of the basic work piece material was detected, which led to significant increase of the surface roughness, regardless of the measuring position and the electrolyte concentration. Hence, the process parameter combination of electrolyte composition and voltage should be analyzed more in detail in future investigations.

For the targeted cutting edge radius of 30 µm, the orientation of the CTI during PeR should be upward, to assure sufficient release of gas bubbles and avoid too strong gas bubble accumulation in the near of cutting edges, which reduces rounding effects.

External longitudinal turning experiments are planned to prove the applicability of the rounded CTI and to assess their tool life in comparison with CTI not treated with PeR.

References

[1] Denkena B and Biermann D 2014 Cutting edge geometries *CIRP annals* **63** 631-653

[2] An S, Foest R, Fricke K, Riemer H, Froehlich M, Quade A, Schaefer J, Weltmann K-D and Kersten H 2021 Pretreatment of cutting tools by plasma electrolytic polishing (PEP) for enhanced adhesion of hard coatings *Surface and Coatings Technology* **405** 126504

[3] Schulze H-P, Zeidler H, Kroening O and Herzig M 2022 Process analysis of plasma-electrolytic polishing (PeP) of forming tools *Intern. Jour. of Mat. Forming* **15** 6

[4] An S, Hansen L, Wolf T, Foest R, Froehlich M, Quade A, Stankov M and Kersten H 2023 Energetic characterization during plasma electrolytic polishing of cemented tungsten carbide *J. Appl. Phys.* **134** 033305

[5] Kellogg H H 1950 Anode effect in aqueous electrolysis *J. Electrochem. Soc.* **97** 133

[6] Quitzke S, Martin A, Eberhardt K and Schubert A 2023 Development of a suitable electrolyte and voltage for plasma electrolytic rounding of cutting edges on cemented carbide tools *Proceedings of the 19th International Symposium on Electrochemical Machining Technology* 86-91

Laser cutting and structuring for processing aluminium nitride chips for optical clocks

Rudolf Meeß, Daniel Albrecht, Carsten Feist

Physikalisch-Technische Bundesanstalt (PTB), Bundesallee 100, 38116 Braunschweig, Germany

rudolf.meess@ptb.de

Abstract

Ultrashort-Pulse (USP) lasers are the state-of-the-art tools for the precise processing of sensitive, even coated workpieces. In this study, laser cutting, and laser micro-structuring processes are presented as steps in the manufacturing chain for gold coated aluminium-nitride (AlN) chips. The results of processing with a laser with a pulse width of 20 ns and a wavelength of 355 nm (UV) are compared with the results with a USP laser system with wavelengths of 1030 nm (IR), 515 nm (VIS) and 343 nm (UV). The choice of the laser source and of the process parameters affect the quality of the edges, the amount and mechanism for creating aluminium on processed surfaces and the existence and treatment of melted material and thus the entire manufacturing chain. It is shown that the use of USP exhibits several advantages and thus minimizes the complexity of the manufacturing chain.

Development, Laser beam machining, Manufacturing, Processing

1. Introduction

Optical clocks are operated using trapped ions. A single ion is trapped in ultrahigh vacuum in an oscillating electric field and laser cooled to near zero temperature. External influences are suppressed, and atomic transition frequencies are essentially unperturbed, thus facilitating atomic clocks with relative uncertainties in the range of 10^{-18}.
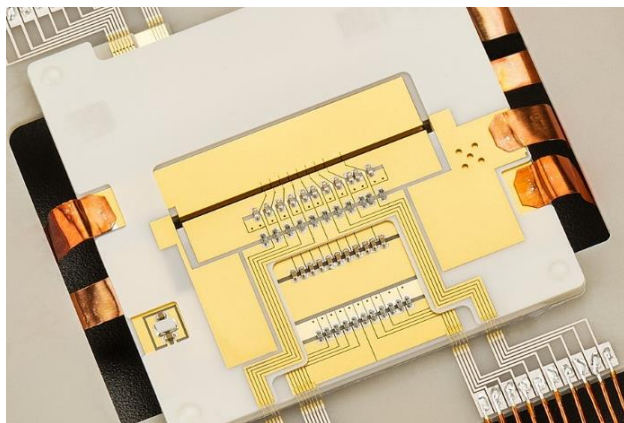
Figure 1. Electrically and thermally connected and assembled ion trap on AlN carrier-frame (Photo: PTB)

At that level of accuracy optical clocks can serve as quantum sensors to measure gravitational potentials with a height resolution in the cm range above the geoid. Fundamental theories such as Einstein´s general relativity theory can be tested in this range [1].

An optical clock for this study is realized by means of a stack of four gold coated and structured aluminium nitride (AlN) chips, which are bonded in a certain distance to each other with spacers at the edges. The AlN chips have a thickness in the range from 120 µm up to 1 mm.

Table 1 Material properties

	AlN	Au
Heat conductivity	175 W/mK	320 W/mK
Thermal expansion	$4.6 \times 10^{-6} K^{-1}$	$14.2 \times 10^{-6} K^{-1}$
Extinction coefficient @ 1030 nm / 515 nm / 343 nm, Absorption depth	Absorption depths 10 nm / 30 nm / 15 nm	6.7038 / 2.0225 / 1.8708[1]
Melting point / decomposition temperature	2.200 °C [4[– 2300 °C [3]	1064.18°C

The gold coating to be structured is applied onto the AlN chips on both sides by means of physical vapour deposition (PVD) and has a thickness of approx. 5 µm. An assembled and connected device in an additional laser-processed AlN frame structure can be seen in Figure 1. The size of the chips is approx. 50 mm × 50 mm.

Laser machining is an appropriate method for structuring a gold plating and for cutting an AlN substrate. The ablation mechanisms of the laser depend on the laser's wavelength, the optical features of laser beam, and the pulse width regime as well as the optical, thermal, and mechanical properties of the substrate and additional factors (see Figure 2).

Processing aluminium nitride with lasers is unique in that aluminium can potentially form on the surface as a result of thermal decomposition (see table 1). This conductive layer is not intended for the design of the ion traps and must be removed or its formation prevented. This task has been the subject of research for more than 30 years, as this ceramic is used in the manufacture of printed circuit boards.

---

[1] Source: https://refractiveindex.info/?shelf=main&book=Au&page=Johnson
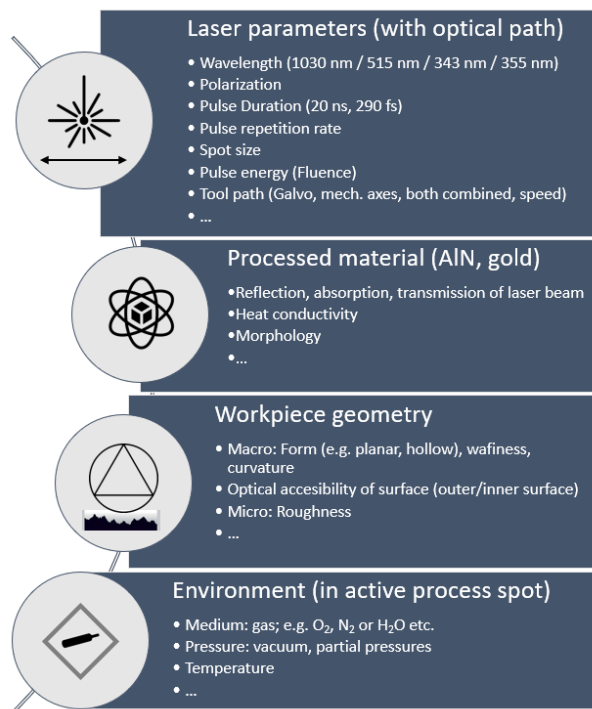
Figure 2. Sketch of influencing variables of laser processing materials

Many theoretical descriptions have been developed to generalize the very complex stages of laser processing. This study cannot claim to analyse all reasonable parameter sets for processing AlN and gold, neither in theory nor in the experiment.

Thus, as a simple and broad approach, in this feasibility study different examples machined with four different beam characteristics are presented and compared.

2. Methods

The thermal conductivity of sintered AlN is about ten times that of alumina, which is the primary reason for its selection here. This high thermal conductivity makes it difficult to machine with a laser because the material can absorb considerable incident energy without melting or vaporizing. Furthermore its transmission is high for the UV wavelength. Process settings that produce good results with alumina, for example, are not suitable for AlN. It is therefore necessary to identify different and appropriate parameters for aluminium nitride.

Processing the gold coating used in some optical clock designs is challenging. A large amount of the gold coated surface must be masked and/or gold must partially be removed after sputtering (see Figure 1). In the uncoated areas, care must be taken to ensure complete electrical insulation over the entire surface in order to avoid electrically undefined charges on metallized islands. For this reason, the surface laser ablation process must also tolerate fluctuations in the thickness of the gold coating sufficiently.

A purpose-built ns laser setup [2] is used in this study to serve as a comparison. The specifications of the Coherent company laser source are shown in table 2, column a. The laser processes are very stable and repeatable. For beam actuation, a galvanometer scanner with F-theta lenses is used. The process chain has remained unchanged over the production of several batches of chips for different generations of ion traps.
Due to the 20 ns pulse length of the AVIA source, thermal influences and debris cannot be avoided during the

manufacturing processes. A protective coating is thus used [2] to prevent adhesion of melted material and debris. Furthermore, the coating protects the functional surfaces during the etching process which must be carried out to remove the aluminium surface and oxide layers after laser processing.

Table 2 Laser specifications

	a	b
Laser	Coherent company: AVIA 355-10-20	Light Conversion company: Pharos
Source	3ω Nd:YVO4	Yb:KGW
Wavelength	355 nm	1030 nm / 515 nm / 343 nm
Pulse length	20 ns	290 fs
Pulse energy	Max. 300 µJ	Max. 400 µJ
Repetition rate	10 Hz – 100 kHz	1 kHz – 1 MHz
Beam quality	$M^2 \leq 1,3$ @ TEM_{00}	$M^2 \leq 1,2$ @ TEM_{00}

Aluminium is a product of laser processing AlN [3-6]. Besides the oxides of AlN, aluminium is observed on the surface due to the nanosecond laser induced thermal decomposition of the polycrystalline sintered material at high temperatures [6] in air. The decomposition temperature is approx. 2200°C [4] to 2300°C [3]:

$$AlN_{(solid)} + h\upsilon \rightarrow Al_{(solid)} + N_{(gas)}$$
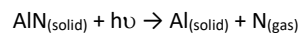
The aluminium layer and the oxides need to be removed here after the chip and coating have been ablated with the ns UV-laser in air. A standard aluminium etchant for use on silicon devices and other microelectronic applications is used here. This appropriate etching procedure is part of the complex and sensitive manufacturing chain as shown in Figure 3.
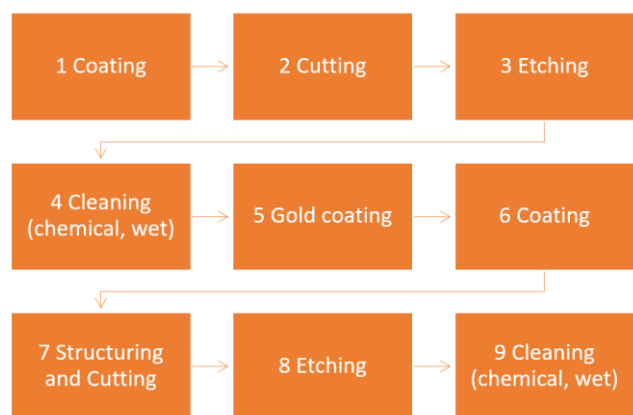
Figure 3. Sketch of the complex process chain with etching processes

Figure 3 does not list the necessary control steps in the process chain. However, the manual operations involved are time consuming. And as the number of necessary processes and control steps increases, the likelihood of damage to the chips and therefore the occurence of rejects – also increases. Therefore, reducing the number of process steps not only saves time in the overall process time per chip and trap, but also valuable working and machining time. This, in turn, decreases the number of semi-finished parts and rejects.
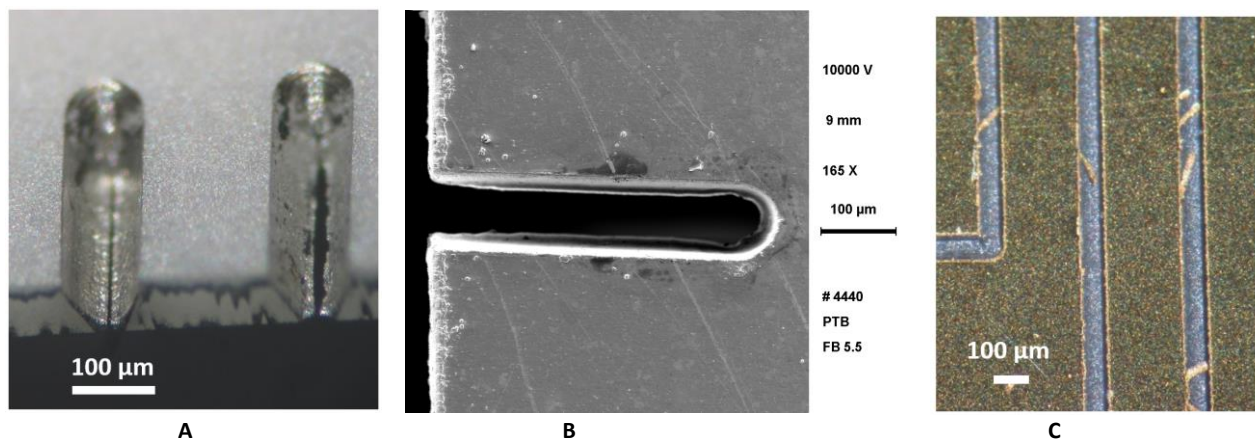
Figure 4. Experimental results of laser processing with 355 nm wavelength and 20 ns pulse length
A: Photo of aluminium layers on AlN surfaces, width of cut on top surface approx. 200 µm; B: Scanning electron microscopy (SEM) image top view of typical cut edge with burr and wavy flanks; C: Photo of typical micro-burr of gold film after simple structuring, gap width of structuring approx. 100 µm

To overcome the nanosecond laser-induced thermal decomposition of the AlN chip, a multi-wavelength USP laser system is applied. The GL.evo laser machining centre of the GFH GmbH company has five axes of motion and is equipped with a Pharos laser system of the Light Conversion company. The specifications of the laser system are shown in table 2 b. The use of USP can reduce the thermal effects in the workpiece.

As stated above, this study cannot claim to be exhaustive as it was not possible to analyse all of the reasonable parameter sets for AlN and gold processing. However, in the context of this feasibility study, meaningful parameter combinations are selected based on experience of working with the laser systems and on approaches that can be found in the literature [5,6]. The burst mode with repetition rates up to the MHz range is not used in this study.

Not all components of the optical path for laser processing are suitable for all wavelength ranges in the GL.evo machine. For this reason, processing with UV is carried out with a fixed optic. In doing so, the possible speed of the beam on the workpiece is reduced, as the mechanical linear axes are used for the relative movement between the two.

The position of the focal plane is a crucial parameter for the quality and efficiency of laser ablation [10]. In this study, the focal plane is selected in such a way that the topography of the cut edge is as homogeneous as possible with the inclined cut surface having a small taper angle. This angle must not be zero due to the constraints of the coating process.

3. Results

Figure 4 shows typical results of processing coated chips with the 20 ns UV laser. Typical aluminium films can be seen on the cut surfaces in the first photo (A). The irregular taper and burr can be seen in photo B. Finally, the burr of the gold can be clearly recognized in the third photo (C). Figure 5 shows a micrograph of a shading on the gold film for marking the chips. No melted edges are visible, even at higher resolution, and due to the very reproducible ablation process, it is possible to partially ablate the 5 µm thick gold film. This avoids isolated islands that could lead to electrostatic charges in the experiment. The lettering is easily recognizable to the naked eye in daylight at any angle of incidence and the numbers are clearly legible.
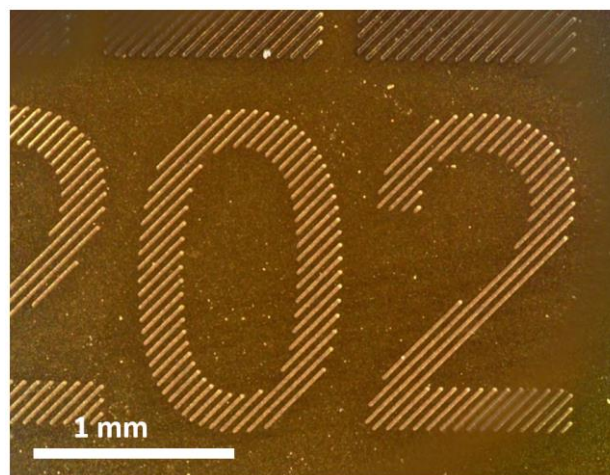
Figure 5. Photo of shading on gold film for marking. The 5 µm thick gold layer is not completely ablated.

With the results of the study, a downsized process chain can be proposed as shown in Figure 6.
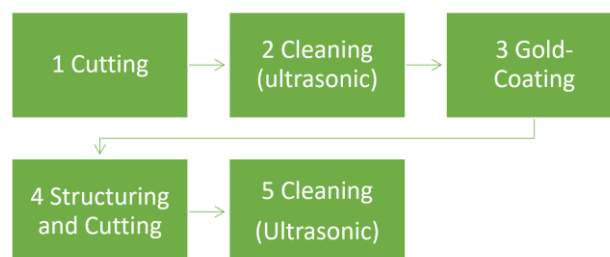
Figure 6. Sketch of novel process chain with reduced number of steps

Wet chemical cleaning steps are no longer necessary, and no etching processes are required. This drastically reduces the number of critical manual operations and the working time per piece.

Figure 7 shows scanning electron microscopy (SEM) images of chips after processing with the USP laser at different wavelengths. The improvements can be clearly seen. No melting of the edges is visible. This means that the thermal effect of the laser radiation is very low.
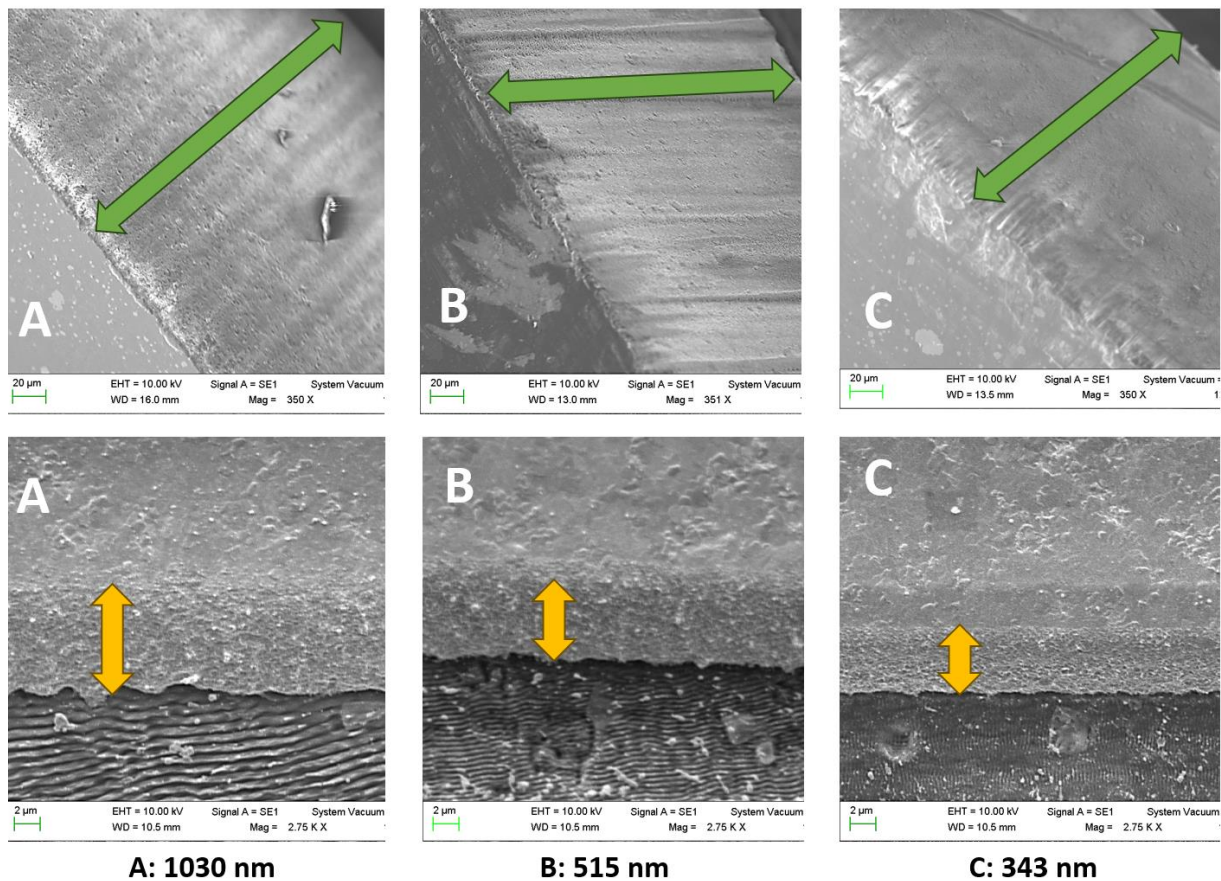
Figure 7. SEM scans of experimental results of USP laser processing at different wavelengths; A: 1030 nm, B: 515 nm and C: 343 nm. Cut surfaces marked with arrows. AlN (green, AlN top surfaces left) and structured gold coating (yellow, Au coating on upper surfaces)

4. Discussion and Outlook

This feasibility study reports on the laser processing of gold coated AlN chips. The results of processing with light pulses in the UV, VIS, and IR wavelength ranges with a duration of 290 fs at frequencies of 30 kHz to 100 kHz for ablating the gold layer and cutting the ceramic are presented. The results are compared with the results of a laser source with a wavelength of 355 nm and a pulse duration of 20 ns and a repetition rate of 20 kHz. It can be shown that the thermal effects on the gold and the AlN can be significantly reduced when processing with ultrashort pulses. First, the melted edge of the gold layer is missing after ablation with the USP laser. Secondly, no aluminium is visible in the cut of the AlN chips. This indicates that the temperature of approx. 2300°C, which is required for decomposition of aluminium nitride, is not reached during laser cutting.

The decreased influence of thermal effects alone makes it possible to drastically reduce the number of process steps and thus the processing time required to produce of chips for use in optical clocks (see Figure 3 and Figure 6 for comparison).

In a next step, the parameter field will be extended to optimise the process further and shorten the process time. Known engineering optimization techniques may be considered here [8] as well as the use of support through artificial intelligence [9].

Finally, the importance of the binder phase in the sintered AlN during laser processing requires further investigation, especially concerning the high transparency of AlN for the UV wavelength.

References

[1] Herschbach N, Pyka K, Keller J and Mehlstäubler T E 2012 *Appl. Phys. B* **107** 891–906

[2] Meeß R, Löffler F and Hagedorn D 2010 Laser cutting of thin gold foils, in: H. Spaan (Ed.), *Proceedings of the 10th International Conference of the European Society for Precision Engineering and Nanotechnology,* Bd. 2, Bedford: Euspen, 33-36.

[3] Zheng H Y, Phillips H M, Tan J L and Lim G C 1999 Laser-induced conductivity in aluminum nitride *Proc. SPIE 3898, Photonic Systems and Applications in Defense and Manufacturing*,

[4] Kozioł P E, Antończak A J, Szymczyk P, Stępak B and Abramski K M 2013 Conductive aluminum line formation on aluminum nitride surface by infrared nanosecond laser *Applied Surface Science*, **287**, 165-171, ISSN 0169-4332,

[5] Kim S H, Sohn I B and Jeong S 2009 Ablation characteristics of aluminum oxide and nitride ceramics during femtosecond laser micromachining, *Applied Surface Science*, **255**(24) 9717-9720, ISSN 0169-4332.

[6] Hirayama Y, Yabe H and Obara M 2001 Selective ablation of AlN ceramic using femtosecond, nanosecond, and microsecond pulsed laser. *J. Appl. Phys.* 1 **89**(5): 2943–2949.

[7] Loebich O 1972 The optical properties of gold. *Gold Bull* **5**, 2–10

[8] Gadallah M H and Abdu H M 2015 Modeling and optimization of laser cutting operations. *Manufacturing Rev.* **2**(20)

[9] Bakhtiyari A N, Wang Z, Wang L and Zheng H 2021 A review on applications of artificial intelligence in modeling and optimization of laser beam machining, *Optics & Laser Technology* **135** 106721

[10] D. Sola et al *2011* Laser ablation of advanced ceramics and glass-ceramic materials: Reference position dependence *Applied Surface Science* **257** 5413–5419

Numerical and experimental investigation of deposition accuracy in GTAW-based additive manufacturing

Masahiro Kawabata[1] and Hiroyuki Sasahara[1]

[1]*Tokyo University of Agriculture and Technology, Japan*

kawabata@st.go.tuat.ac.jp, sasahara@cc.tuat.ac.jp

Abstract

In gas tungsten arc welding (GTAW)-based additive manufacturing (AM), directional dependence of the deposition process may lead to a shift in the deposition position, and non-uniform bead shapes. In this study, the deposition accuracy in GTAW-based AM was investigated by simulation using a particle method and experiment. In the particle method simulation, heat input due to the arc, phase change, heat conduction, and surface tension were considered. As the simulation result, in the side-feed condition, the deposition position shifted compared with other feed conditions. In addition, under the back-feed condition, when the wire was fed to a position slightly off the torch center, the molten pool that interfered with the wire flowed in a direction that avoided the wire, resulting in a bead position deviation. These tendencies were also observed in the experiments, and the results suggest that particle method simulation is useful for predicting deposition accuracy and examining appropriate deposition conditions.

Keywords: Gas tungsten arc welding (GTAW), Additive manufacturing (AM), Particle method, Moving particle simulation (MPS) method

1. Introduction

Wire and arc additive manufacturing (WAAM), in which welding wires are melted and stacked by arc discharge, has attracted widespread attention because of the advantages of relatively high deposition efficiency and low equipment and material costs. Especially in WAAM using gas tungsten arc welding (GTAW), an arc discharge is generated between a tungsten electrode and an object, and a wire supplied from the side is melted and deposited for three-dimensional fabrication. Therefore, the heat input and material input can be controlled independently, allowing high flexibility in deposition conditions. However, because the wire is fed from a fixed lateral direction relative to the central arc heat source, the wire feed conditions will change, such as front-feed, back-feed, and side-feed, relative to the torch travel direction. Although accurate fabrication of 3D shapes is required in AM, this directional dependence of the deposition process may lead to a shift in the deposition position, and non-uniform bead shapes.

Previous studies showed experimentally that GTAW causes a deviation of bead position depending on the wire feed direction [1]. Wang et al. [2] proposed a simplified model to simulate the wire melting position and showed that the deposition conditions could be optimized based on it. In contrast, to simulate the welding process more accurately, numerical methods are needed, such as calculating the molten pool flow. However, few studies have examined in detail the issues and mechanisms of deposition accuracy in GTAW using numerical simulation. Therefore, in this study, the deposition accuracy in GTAW-based AM was investigated by numerical simulation using a particle method and experiment.

2. Numerical and experimental method

In this study, a moving particle simulation (MPS) method [3] was used and heat input and pressure due to the arc, phase change, heat conduction, and surface tension were considered

to simulate the deposition process. The fluid flow is calculated according to the following Navier-Stokes equations (1).

$$\frac{d\boldsymbol{u}}{dt} = -\frac{1}{\rho}\nabla P + \mu\nabla^2\boldsymbol{u} + g + \frac{1}{\rho}F_s \qquad (1)$$

where $\boldsymbol{u}$ is the velocity, ρ is the density, P is the pressure, g is the gravity acceleration, μ is the dynamic viscosity, and F_s is the surface tension. The gradient and Laplacian operators are discretized by the general particle interaction model of the MPS method, and the particle motion is computed. In addition, the surface tension was calculated by the following equation (2).

$$F_s = -\sigma\kappa\delta\boldsymbol{n} + \frac{d\sigma}{dT}\delta(\nabla T - (\nabla T \cdot \boldsymbol{n})\boldsymbol{n}) \qquad (2)$$

where σ is the surface tension coefficient, κ is the curvature, $\boldsymbol{n}$ is the normal vector of the interface, T is the temperature, and δ is a delta function considering that the surface tension was only applied to the interface particles.

As the deposition process to be investigated, three different wire feed conditions: front-feed, back-feed, and side-feed were set up. In addition, the back-feed condition is considered to decrease deposition accuracy due to interference between the wire and the molten pool. To confirm this wire interference effect, a condition in which the wire feed position was shifted in the back feed was also investigated.

In the experiments and simulations, SUS304 was used as the base plate and wire material. Table 1 shows the physical properties of SUS304 used in the simulation. Figure 1 shows a simulated deposition process under the front wire feed condition as an example. The size of the base plate was 40 × 15

Table 1 Physical properties of SUS304

Density	kg/m³	7930
Kinematic viscosity	m²/s	5.04×10^{-7}
Specific heat	J/(kg·K)	590
Thermal conductivity	w/(m·K)	$0.0148T+10.271$
Latent heat	J/kg	2.67×10^{5}
Melting point T_m	K	1727
Surface tension at T_m	N/m	1.872
Surface tension gradient	N/(m·K)	-4.3×10^{-4}

× 5 mm, and 30 mm bead-on-plate deposition was performed. The particle size was set to 0.3 mm basically, and only the particle size at the bottom of the base plate was set to 0.5 mm to reduce calculation time. The time step of the simulation was set to 0.1 ms. As deposition conditions, the wire diameter was 1.2 mm, the wire feed speed was 2.5 m/min, and the torch travel speed was 200 mm/min. In the experiment, the current value was set to 150 A. In the simulation, the arc heat input was assumed to follow a Gaussian distribution, with a total heat input of 1400 W and a heat input radius of 3 mm.
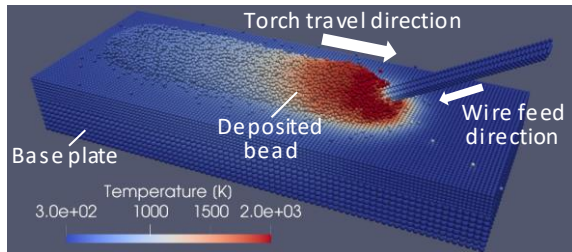
Figure 1. Bead deposition in particle method simulation

3. Results and discussion

3.1. Wire feed conditions and deposition accuracy

Figure 2 shows the deposition state and bead cross-section under each wire feed condition. The red line in the figure shows the center position of the torch (arc heat source). In front-feed and back-feed conditions, the wire was fed to the torch center, and the beads were deposited without deviating from the torch center. In contrast, under the side-feed condition, the position at which the wire was completely melted shifted from the torch center in the wire-feeding direction, and as a result, the bead position also deviated in the same direction. Figure 3 shows the deposition state and the bead cross-section under the side-feed condition in the experiment. The torch center position in the bead cross-section was calculated based on a reference bead previously welded by scanning only the arc without wire material. Figure 3(a) shows that the wire melt position was shifted from the torch center in the experiment as well. In addition, Fig. 3(b) shows that the bead position deviated about 0.3 mm in the wire feeding direction. Therefore, the numerical model using the particle method was able to simulate the same
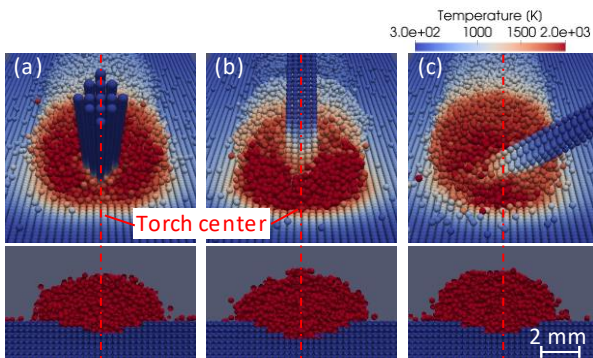
Figure 2. Deposition state and bead cross-section under each wire feed condition: (a) front-feed, (b) back-feed, and (c) side-feed
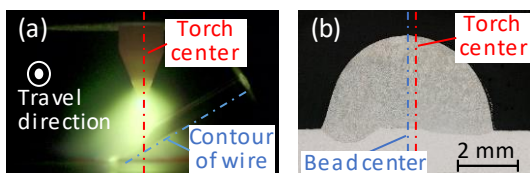
Figure 3. Experimental results under the wire side-feed condition: (a) deposition state and (b) bead cross-section

tendency and the same degree of bead position deviation as in the experiment.

3.2. Effect of interference between wire and molten pool

Figure 4(a) shows the simulation results when the wire feed position was offset from the torch center by 0.6 mm under the back-feed condition. The offset of the wire feed position caused the molten pool to flow in a direction that avoided the wire, and as a result, the bead position was deviated. Figures 4(b) and (c) show experimental results with offset and correct wire feed positions. When the wire feed position was offset, the bead was deposited in a displaced position in the direction to avoid the wire, similar to the simulation results. In this study, the wire feed position was intentionally offset, but in WAAM, the wire aiming position sometimes shifts due to the curvature of the wire. From these results, it can be assumed that the accuracy of GTAW-based AM could be decreased due to such wire curvature, especially under the back-feed condition. Moreover, AM needs to be able to accurately fabricate not only straight paths but also curved paths such as circular arcs. In the case of such a curved path, even if the wire feed position is not misaligned, interference between the molten pool and the wire could cause the bead deviation from the desired position. In contrast, the problem of deposition accuracy due to wire interference seems to be suppressed by changing the wire feed angle and the heat input. In the future, it is necessary to consider deposition accuracy in curved paths and appropriate deposition conditions.
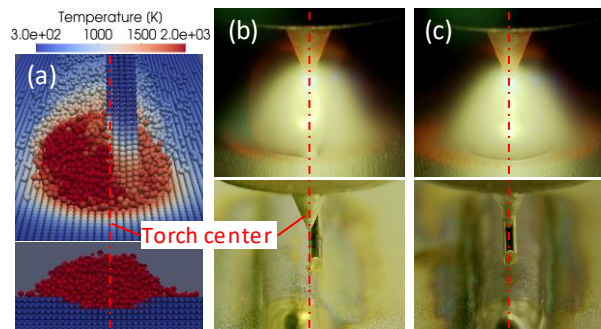
Figure 4. Relationship between wire feed and bead position under the back-feed condition: (a) simulation result with offset wire feed position and experimental result with (b) offset wire feed position and (c) correct wire feed position

4. Conclusion

In this study, the deposition accuracy in GTAW-based AM was investigated by particle method simulation and experiment. As a result, experiments and simulations showed that the bead position deviated under the side wire feed condition and the back-feed condition with offset wire feed position. The numerical model could simulate the experimental results well, which suggests that particle method simulation is useful for predicting deposition accuracy and examining appropriate deposition conditions.

References

[1] Kapil S, Kulkarni P, Joshi P, Negi S and Karunakaran K P 2019 Retrofitment of a CNC machine for omni-directional tungsten inert gas cladding Virtual Phys Prototype **14** 293–306

[2] Wang X, Wang A and Li Y 2020 Study on the deposition accuracy of omni-directional GTAW-based additive manufacturing J Mater Process Technol **282** 116649

[3] Koshizuka S and Oka Y 1996 Moving-Particle Semi-Implicit Method for Fragmentation of Incompressible Fluid Nuclear Science and Engineering **123** 421–434

Design of a low-cost, high-precision rolling nanoelectrode lithography machine for manufacturing nanoscale products

Zhengjian Wang[1], Xichun Luo*,[1], Rashed Md. Murad Hasan[1], Wenkun Xie[1], Wenlong Chang[2], Qi Liu[1]

[1]*Centre for Precision Manufacturing, DMEM, University of Strathclyde, United Kingdom*
[2]*Innova Nanojet Technologies Ltd., Glasgow G1 1RD, United Kingdom*

zhengjian.wang@strath.ac.uk

Abstract

This paper presents the design of a low-cost, high-precision rolling nanoelectrode lithography (RNEL) machine, addressing the growing demand for cost-effective and high-precision nanomanufacturing processes for next-generation nanoproducts. Unlike plate-to-plate methods, the rolling stamp ensures uniform contact pressure across the entire surface of the 8-inch substrates, simplifying the separation process. However, achieving precise positioning between the rolling stamp and substrate during RNEL operations is essential, as even slight deviations can lead to significant defects in fabricated nanostructures. This poses a considerable challenge in developing an affordable, high-precision RNEL machine that meets the requirements for high-yield production, especially for SMEs. The final design adopts a four-axis fixed-gantry configuration where the X- and Y-axes are mounted separately, chosen from four candidates for the superior overall performance. The machine employs a step-and-repeat mechanism using three low-cost ball-bearing linear slides. Additionally, a flexure-based passive tilting stage with nanometre resolution is integrated into the roller unit, promoting high alignment accuracy and uniform contact. In simulations, a 5 N load at the rolling stamp's edge causes a rotation of about 0.00022 radians with only a tiny lateral deformation of 4.9 nm. While the current design achieves an RSS error of approximately 10 μm, attaining the desired sub-micron positioning accuracy requires further developments, particularly in compensating for geometric and thermal errors. Addressing these issues is the next step in our research, aiming to fulfil the precision demands of RNEL operations.

Keywords: Rolling nanoelectrode; Lithography machine; Flexure tilting stage

1. Introduction

The demand for next-generation nanoscale products, such as photonic integrated circuits and heat-assisted magnetic recording disks, is rapidly increasing. These products require high-precision nanostructures with diverse functionalities to meet varied user needs. Consequently, there is a growing need for low-cost, high-precision nanomanufacturing processes and machines, especially for rapid prototyping to reduce time-to-market.

Rolling Nanoelectrode Lithography (RNEL), a recent innovation from the University of Strathclyde, offers a promising solution in nanofabrication [1]. This technique leverages anodic oxidation confined spatially between a conductive rolling stamp and the substrate surface to create nanostructures (see Figure 1). RNEL offers high production efficiency and great flexibility in manufacturing various nanostructures by controlling processing parameters, such as applied voltage, rolling speed, and humidity, without changing stamps [2].

In this context, this paper aims to design a low-cost, high-precision RNEL machine. This design incorporates a rolling stamp, ensuring uniform contact pressure across the substrate, which simplifies the separation process. Even minor misalignments can lead to significant defects in the resulting nanostructures, presenting considerable challenges in developing an affordable, high-precision RNEL machine suitable for high-yield production at costs feasible for SMEs. These issues will be considered in the design process, which is the focus of this paper.
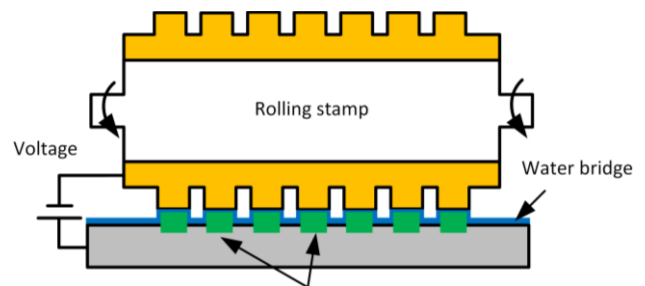
Figure 1. Working principle of RNEL

In this paper, Section 2 introduces the selection process for the RNEL machine's configuration, including analyses of the error budget, static and dynamic characteristics to assess maximum geometric errors, thermal sensitivity and vibrational modes. Section 3 presents the design of a flexure-based passive tilting stage, aiming to enable precise alignment and uniform contact distribution between the rolling stamp and substrate.

2. Machine configuration and performance analysis

The materials of the substrate are silicon or silicon carbide; the maximum size of the workpiece is 8 inches (approximately 200 mm) in diameter. Table 1 displays the specifications of the RNEL machine, which are designed based on the substrate specifications. A four-axis configuration was chosen, utilising three low-cost ball-bearing slides as the X-, Y-, and Z-axes to move the rolling stamp toward the substrate. The rolling stamp's effective length was designed to be 90 mm, which is

nearly half the diameter of the 8-inch substrate, reducing manufacturing difficulties and costs associated with the rolling stamps. The proposed RNEL machine performs the step-and-repeat action to generate nanostructures on the 8-inch wafers.

To achieve nanometer-level motion accuracy, a novel air-bearing rolling stamp unit was designed to hold and rotate the rolling stamp.

Table 1. Specifications of the RNEL machine

Axis number	Type	Stroke	Drive system	Motion accuracy	Resolution
X-axis	Ball-bearing	250 mm	Linear motor	<2 µm	5 nm
Y-axis	Ball-bearing	200 mm	Linear motor	<2 µm	5 nm
Z-axis	Ball-bearing	60 mm	Linear motor	<0.5 µm	1 nm
B-axis	Air-bearing	360°	Direct drive torque motor	<2 arcsec	0.02 arcsec

Four roll-to-plate machine configurations were proposed during the conceptual design stage, as shown in Figure 2.
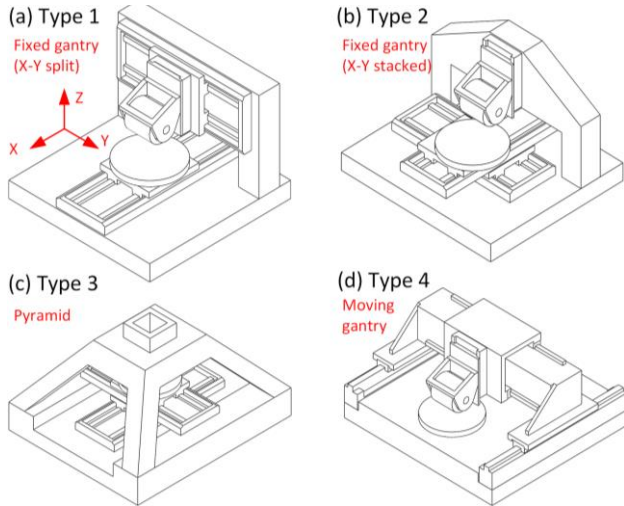
Figure 2. Four candidate configurations of the RNEL machine: (a) Type 1; (b) Type 2; (c) Type 3; (d) Type 4

The error budget estimates potential errors within a machine axis, resulting in deviations from the intended motion. It is utilised as a method for evaluating the capacity of a proposed machine configuration to fulfil the desired specifications [3]. It is an effective tool for predicting the geometric error of a machine system. Figure 3 and Figure 4 illustrate the error budget of Type 1 and Type 4 machine configurations, respectively.

Axis	Feature	Value	Abbe offset	Error (µm)		
X	Pitch	9.3 arcsec	45 mm	2.03		
	Yaw	9.3 arcsec	100 mm	4.51		
	Roll (Y)	9.3 arcsec	45 mm		2.03	
	Roll (Z)	9.3 arcsec	100 mm			4.51
	Straightness	±3 µm			6.00	
	Flatness	±3 µm				6.00
Y	Pitch	8.2 arcsec	130 mm		5.17	
	Yaw	8.2 arcsec	110 mm		4.37	
	Roll (X)	8.2 arcsec	130 mm	5.17		
	Roll (Z)	8.2 arcsec	110 mm			4.37
	Straightness	±2.5 µm		5.00		
	Flatness	±2.5 µm				5.00
Z	Pitch	10 arcsec	59 mm			2.86
	Yaw	5 arcsec	135 mm		3.27	
	Roll (X)	10 arcsec	42.5 mm	2.06		
	Roll (Y)	10 arcsec	59 mm		2.86	
	Straightness	±1.5 µm			3.00	
	Flatness	±1.5 µm		3.00		
B	Radial error (X)	1 µm		1.00		
	Axial error (Y)	1 µm			1.00	
	Radial error (Z)	1 µm				1.00
	Tilt error (X)	2 arcsec	42.5 mm	0.41		
	Tilt error (Y)	2 arcsec	45 mm		0.44	
			Total error	23.18	28.14	23.74
			RSS error	9.52	10.73	10.47

Figure 3. Error budget of Type 1 machine configuration

Axis	Feature	Value	Abbe offset	Error (µm)		
X	Pitch	15 arcsec	20 mm	1.45		
	Yaw	15 arcsec	42.5 mm	3.09		
	Roll (Y)	15 arcsec	50 mm		3.64	
	Roll (Z)	15 arcsec	107.5 mm			7.82
	Straightness	±3 µm			6.00	
	Flatness	±3 µm				6.00
Y	Pitch	15 arcsec	110 mm		8.00	
	Yaw	15 arcsec	185 mm		13.45	
	Roll (X)	15 arcsec	110 mm	8.00		
	Roll (Z)	15 arcsec	185 mm			13.45
	Straightness	±3 µm		6.00		
	Flatness	±3 µm				6.00
Z	Pitch	10 arcsec	75 mm			3.64
	Yaw	5 arcsec	150 mm		3.64	
	Roll (X)	10 arcsec	42.5 mm	2.06		
	Roll (Y)	10 arcsec	75 mm		3.64	
	Straightness	±1.5 µm			3.00	
	Flatness	±1.5 µm		3.00		
B	Radial error (X)	1 µm		1.00		
	Axial error (Y)	1 µm			1.00	
	Radial error (Z)	1 µm				1.00
	Tilt error (X)	2 arcsec	42.5 mm	0.41		
	Tilt error (Y)	2 arcsec	45 mm		0.44	
			Total error	25.02	42.80	37.91
			RSS error	11.23	18.19	18.12

Figure 4. Error budget of Type 4 machine configuration

Following the same fashion, the root sum square (RSS) error of Type 2 and Type 3 configurations is obtained and presented in Table 2.

Table 2. RSS error of Type 2 and 3 configurations

Configuration	RSS error (X)	RSS error (Y)	RSS error (Z)
Type 2	9.52	11.31	11.73
Type 3	9.35	11.21	11.52

Figure 3 reveals that the RSS error of Type 1 configuration in each direction is approximately 10 µm. This suggests that geometric error compensation is necessary for nanomanufacturing manipulation, a task that will be addressed in future work by the authors.

It's worth mentioning that the first three configurations exhibit minimal error differences due to the similarity in specifications and the dimensions of the components. Type 4 configuration has the largest RSS error because of the low-stiffness nature of the moving gantry.

The modal analysis is conducted to assess the dynamic performance of the proposed configurations, and the results are presented in Figure 4. Spring-damper elements were employed to model the dynamic behaviour of the ball bearings.
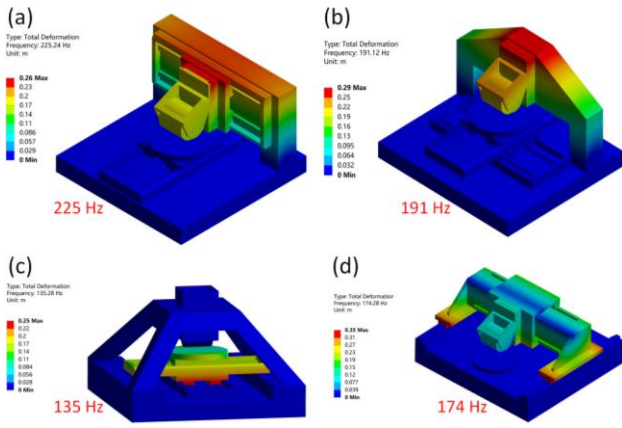
Figure 5. Dynamic performance analysis

The simulation results indicate that the pyramid type exhibits the worst dynamic performance at 135 Hz, whereas the fixed gantry with an X- and Y-axis split design (Type 1) demonstrates the best dynamic performance at 225 Hz.

Since the roller unit operates at extremely low rotation speeds, a large amount of heat is generated during its operation. Therefore, thermal performance analysis is essential to enhance the machine's efficiency, durability, and overall reliability for every candidate configuration. The thermal sensitivity of each configuration is assessed The performance indicator is the deformation between the rolling stamp and the substrate as the ambient air temperature increases from 20 to 21 °C. The results are illustrated in Figure 6.
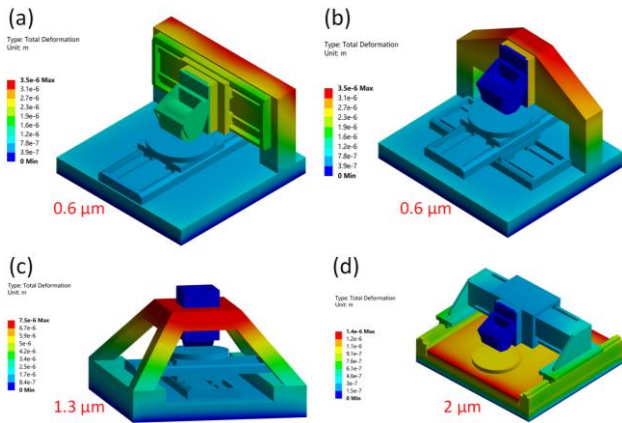
Figure 6. Dynamic performance analysis

It can be concluded that the moving-gantry type is the most vulnerable configuration to temperature fluctuation, with thermal deformation reaching up to 2 µm. In contrast, the fixed gantry type is less sensitive to thermal variation, exhibiting a deformation of only 0.6 µm.

Ultimately, when summarising the results of all performance analyses, it is determined that Type 1 is the best machine configuration, so it was adopted as the configuration for the proposed machine.

3. Flexure-based passive tilting stage

The seamless and uniform contact between the rolling stamp and substrate is a prerequisite for manufacturing consistent nanostructures with high resolution. For instance, there may be an angular misalignment α (see Figure 7) between the template and substrate when they are not parallel.
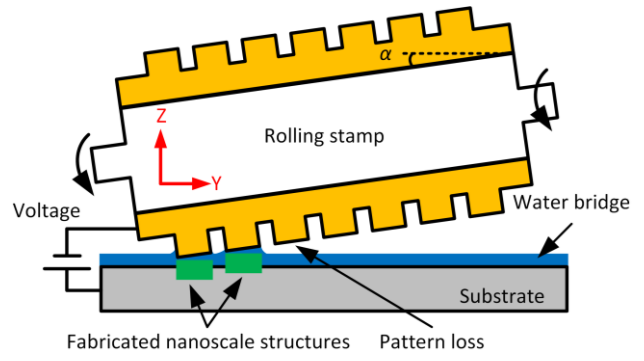
Figure 7. Angular misalignment between stamp and substrate

An excessive misalignment will prevent the electrochemical reaction from occurring uniformly across the entire touched area, leading to pattern loss. An angle compensation remains far from the success of high-accuracy nanopatterning. This is because when the rotation axis of the tilting motion is not on the surface of the stamp, the coupled lateral displacement will increase the overlay error [4, 5]. A four-bar flexure-based tilting stage with semi-circular notches will be introduced to hold the rolling stamp with an angle compensation mechanism to address the above issues. Also, the centre of rotation was designed to coincide with the centre of the rolling stamp's outer edge to control its lateral displacement and prevent slippage between the stamp and substrate.

The semi-circular notches were designed so that when a 5 N load is applied to the edge of the rolling stamp, the roller rotates about 0.00025 radians. After sufficient calculations, the key dimensional parameters of the semi-circular notches, denoted as R and t (as illustrated in Figure 8), were confirmed as 3.7 mm and 0.4 mm, respectively. The material chosen for manufacturing the notches is 7075 aluminium alloy.
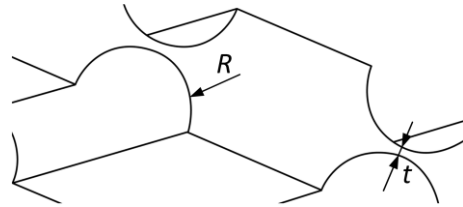
Figure 8. Semi-circular notches

The static analysis was then conducted to evaluate the tilting performance, and the results are shown in Figure 9. A deformation in the Z-direction of about 10 µm can be observed on both sides of the rolling stamp, indicating a rotation angle of 0.00022 radians. Most importantly, as illustrated in Figure 9(b), the rolling stamp moves laterally by only 4.9 nm, demonstrating excellent alignment accuracy.
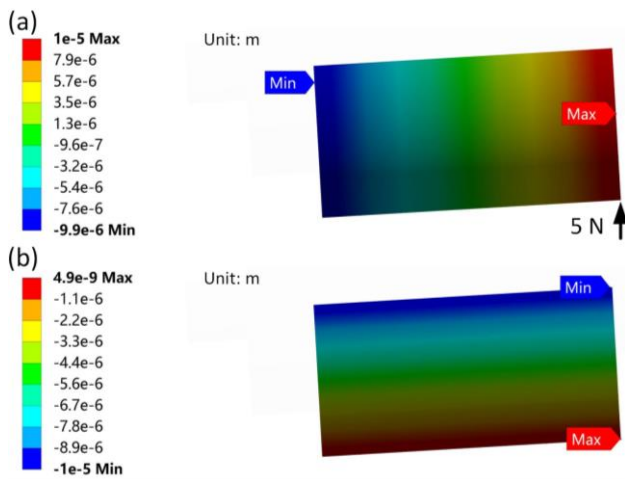
Figure 9. (a) Simulated tilting deformation under an external force of 5 N; (b) simulated lateral deformation.

4. Conclusion

This study presents the design of a low-cost, high-precision rolling nanoelectrode lithography (RNEL) machine. After thoroughly evaluating four machine configuration candidates, the selected configuration emerged as remarkable, excelling in dynamic and thermal performance while minimising geometric errors. A key feature of our design is the incorporation of a flexure-based passive tilting stage within the roller unit, achieving high alignment accuracy and ensuring consistent contact between the rolling stamp and substrate. Simulation results demonstrate that under a 5 N load applied at the edge of the rolling stamp, the roller rotates about 0.00022 radians with a minimal lateral deformation of 4.9 nm. However, the integration of cost-effective ball-bearing linear stages resulted in an RSS error of approximately 10 μm in each direction. This deviation is significant for RNEL operations. The next phase of our research will involve the development and implementation of advanced geometric and thermal error compensation techniques to bridge the gap between the current capabilities and the desired sub-micron positioning accuracy.

References

[1] Hasan R M M, Luo X and Sun J 2020 Micromachines **11** 656
[2] Hasan R M M, Politano O and Luo X 2019 Appl. Surf. Sci. **496** 143679
[3] Chen W, Luo X, Su H and Wardle F 2016 Int. J. Adv. Manuf. Technol. **84** 1177
[4] Lim H, Jung S, Ahn J, Choi K B, Kim G, Kwon S and Lee J 2020 Materials (Basel) **13** 1938
[5] Choi B J, Sreenivasan S V, Johnson S, Colburn M and Wilson C G, 2001 Precis. Eng. **25** 192

Compensation of structure distortion in nonisothermal hot forming of laser structured thin glass

Martin Kohse*[1], Constantin Meiners[1], Denys Plakhotnik[2], Paul-Alexander Vogel[3], Robin Day[1], Tim Grunwald[1], Thomas Bergs[1,4]

[1]Fraunhofer Institute of Production Technology
[2]ModuleWorks GmbH
[3]Vitrum Technologies GmbH
[4]RWTH Aachen University

*martin.kohse@ipt.fraunhofer.de

Abstract

Modern automotive industry employs a variety of complex shaped glass components, from touchscreen displays, dashboard screens, weather resistant windshields to tinted sunroofs. Currently around 50% of these components are functionalised by adding microstructures in a process based on etching or replication processes with structured forming tools, which are neither environmentally nor economically friendly. We present a new approach to functionalise such surfaces by direct laser structuring of glass substrates, thereby reducing costs and energy consumption by up to 60% and avoiding harmful chemicals compared to conventional processes. Current developments in high-power laser-beam sources and laser system technology enable low cycle time direct structuring of glass substrates. Laser-based direct structuring can generate a large portfolio of functional structures of different sizes which we showcase in haptic, hydrophobic and anti-glare structures. The downstream forming of structured glass interferes with high demands of the automotive industry due to shape distortions and positional distortions of the structure. Therefore, we developed a FEM-based predistortion method to adjust the laser trajectory, compensating for the influence of 2D glass moulded into a 3D shaped product. The compensation method was validated by conducting hot forming experiments with different laser-induced geometries on one-dimensional curved forming tools. We were able to reduce the distortion error by more than 90%.

Hot forming, thin glass, laser structuring, green production

1. Introduction

Glass is an indispensable material for numerous components in electronics, the semiconductor industry and sensor technology. The potential of the material lies in its properties: It is light, scratch-resistant, temperature-resistant and very stable. With a thickness of only a few millimitres, such thin glass is the preferred material for high-quality automotive interiors, such as centre consoles, rear-view mirrors, door elements and speedometer units. In more than 50 percent of all thin-glass components, the glass surfaces are functionalised by introducing micro- and nanostructures. These modifications are various: from improved haptics to anti-fogging surfaces to anti-glare and anti-reflection properties [1,2].

Industrially established methods for functionalising such thin glass are either chemical etching or replicative moulding. These methods are inefficient in terms of their carbon footprint, raw material consumption, energy consumption and manufacturing costs. In the context of green transformation of industry it is necessary to develop new approaches for the production of functionalised glass [3,4].

We propose a new process chain that can process functionalised thin glass ecologically and economically. This is achieved by combining laser material processing of the semi-finished glass and the subsequent nonisothermal hot forming. Current industrial ultra-short pulsed laser beam sources provide sufficient energy to process semi-finished glass economically for mass production [5]. In addition, nonisothermal glass forming offers a number of advantages over competing moulding processes thanks to its long tool life and low cycle times [6].

To implement the proposed process chain, several challenges need to be addressed. Firstly, laser structures must be developed and the high-speed laser processing of glass investigated [7]. Furthermore, the forming of a planar semi-finished product into a 3D part results in geometric distortions of the induced laser texture.

These shape and positional distortions of the structure interfere with high demands of the automotive industry. Therefore, we developed a finite element method (FEM)-based predistortion procedure to adjust the laser trajectory and compensate for the influence of 2D glass moulded into a 3D shaped product.

2. Methodology

In order to implement the proposed process chain, laser trajectories for the respective functionalisations must be generated on the basis of the final 3D glass geometries and then adapted for processing on 2D glass.

To allow this adaption, the forming process needs to be predicted using FEM simulations. On this basis, a deformation field linking positions on the 2D to the 3D glass can be generated. Using the 3D position information of the laser structure and the deformation field, the generated laser trajectories can be compensated for the processing of the 2D glass. In order to validate the proposed method, equidistant circular ring segments are simulated on a 2.5D (bending around one axis) deformed glass, and corresponding compensated laser

trajectories are textured into the 2D glass before hot forming (see Fig. 1). The distances between the ring segments on the 2D glass should therefore no longer be equidistant.

Following the hot forming process the distances between each circular ring are measured and validated against simulations.

Expected 2.5D glass   Inital 2D glass

a)   b)
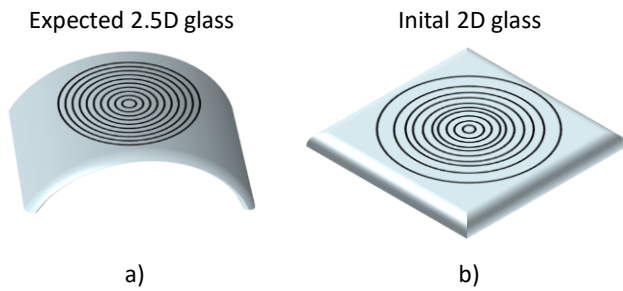
Figure 1. a) Expected 2.5D formed glass with equidistant circular rings. Based on this model the proposed distortion method generates 2D laser trajectories based on FEM simulations with b) deformed ring geometries on the initial 2D glass, which is then hot-formed.

2.1 FEM Simulation of nonisothermal hot forming process

Fraunhofer IPT uses FEM simulations to describe the behaviour of the glass during forming in order to optimise the forming process. This is achieved with material models developed in-house that describe the highly non-linear, visco-elastic behaviour of glass. The model is composed of a mechanical and a thermal model [8]. In particular, the models take glass flow and the thermally induced shrinkage into consideration. Based on this data, an optimised tool design can be derived, thus improving the final shape accuracy. In addition, FEM simulations can be used to predict the macro- and micro-scale distortions caused by the forming process due to compression and tension of the laser structures applied to the glass [9]. These distortions are described by distortion vectors used for the suggested predistortion method. Therefore, a nonisothermal gravity slumping process with a 2.5D deformation (bending around one axis) was simulated using the generalised Maxwell model with 156 meshed elements for the glass and 96 elements for the mould. The forming tool with a bending radius of 100 mm had an initial temperature of 450 °C and the glass (B270i, soda-lime glass) was heated up to 700 °C (see Fig. 2). By simulating viscosity induced deformations over time the resulting shape accuracy of the formed glass and the shape deviation can be predicted [10]. Subsequently, a 30 minutes cooling phase was simulated in order to cool the glass to room temperature (25°C). The result (see Fig. 2) indicates a spring-back phenomenon at the glass edges. Eventually this effect leads to glass shrinkage. This process-specific challenge is known in nonisothermal hot forming and can be reduced by adjusting the process parameters, especially in the cooling phase [11]. The influence of shrinkage is not considered for the described feasibility study.
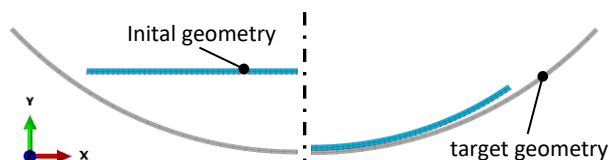
Figure 2. Initial undeformed glass of the simulation at time t=0 (left) and fully deformed glass after forming process at time t=end (right). The deformed glass shows shrinkage in the edge area which leads to deviations from the target geometry.

The overall accuracy of the simulation depends on many factors. For example, to obtain sufficiently accurate information about the macro- and microscopic distortion of the structures, temperature-dependent and glass-specific properties such as stress and structural relaxation values are required. In addition, material heat transfer coefficients are crucial for the accuracy of the simulations. [8] Those values were determined at Fraunhofer IPT for B270i soda-lime glass.

2.2. Predistortion method

The results of the FEM simulation can be used not only for predicting the shape of glass after hot forming but also for generating geometries of pre-deformed structures that later could be hot formed into the designed shape. Intrinsically, FEM simulation results have no temporal nature. Therefore, if structures, geometries and their respective positions are known for the 3D part, inverting the simulation can be a tool to derive positions and distortions for a 2D surface. The idea of applying inverse transformation relies on mapping points on the initial un-deformed (2D) and deformed (3D) surface. Basically, the position of each point marked on the flat glass can be paired with a spatial position of this marker on the deformed glass, since modelling of the deformed geometries in FEM-based simulations is performed in a discrete piecewise manner. Figure 3 illustrates the case of forming a quarter hemisphere. Orange points on the 2D surface (before forming) are connected with blue points after forming. The points are distributed mostly evenly in a rectangular grid. The positional data was acquired from FEM simulation results. The set of points represent a displacement field that is used to derive a deformation field.

The arrangement of structures on the glass is designed with 3D curves on top of CAD surfaces of the formed glass. To map 3D curves onto the displacement field, deformation vectors at arbitrary 3D curve-points need to be interpolated. This is achieved by barycentric coefficients within grid points found in the vicinity of 3D curvature points. Based on the analysis of the deformation field, it is possible to derive a local deformation (elongation, stretching, shear). This information is used to adjust pre-planned 3D laser trajectories onto a 2D surface.
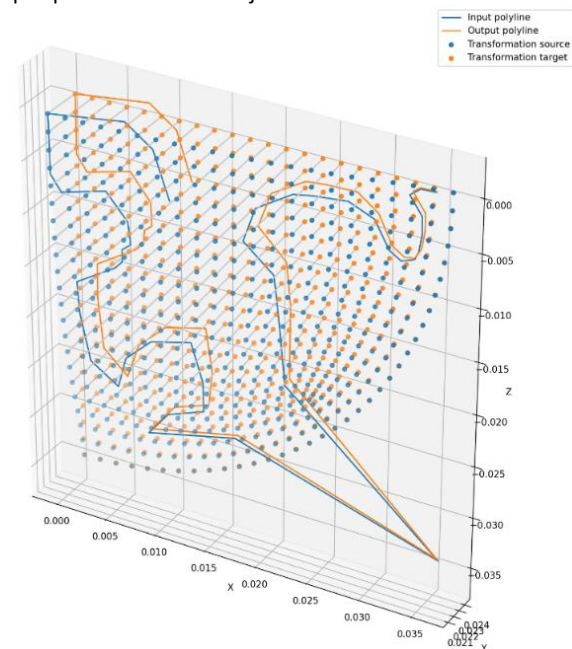
Figure 3. Deformation field between a 2D surface and a 3D quarter hemisphere. The position of a polyline before and after deformation is shown

3. Glass processing

Due to availability Panda-MN228 float glass was used for laser ablation and subsequent hot forming instead of B270i soda-lime glass. Equidistant ring geometries with a spacing of 2 mm (see Fig. 1) were compensated using the described approach in

Chapter 2. The resulting deviation for each circular ring radius used for the compensation of laser trajectories is shown in Figure 4. Using the compensated laser trajectories, the 2D glass was textured with ring segments. The laser-treated 2D glass was then nonisothermally hot formed into a 2.5D shape with a bending radius of 100 mm.
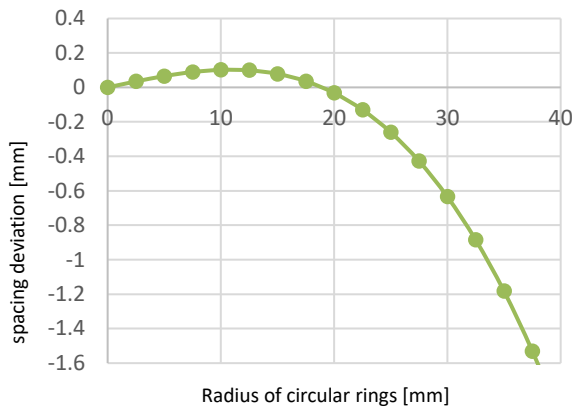
Figure 4. Simulated deviation of the 3D equidistant circular spacing on 2D glass per mm.

3.1 Laser ablation

An ultrashort pulsed Trumpf (model Tru Micro 2230) laser source provides collimated pulsed laser radiation (350 fs) with a maximum power of 10 W and pulse energies up to 25 µJ at a central emission wavelength of 532 nm with a Gaussian intensity distribution. The raw beam (3.8 mm) passes through a liquid crystal polariser into an optical z-axis (varioScan20i_de) with a beam expansion factor of 2.5. Using the optical z-axis, the laser beam can be focused in 3D from the working plane by +-6 mm in the z-direction. A galvanometer scanner (excelliScan14) was used for lateral beam deflection with high precision repeatability (< 1 µm) followed by a telecentric f-theta lens with f = 100 mm focussing the laser onto the glass with a spotdiameter of d_s = 8.5 µm.

A clamping system designed and manufactured at Fraunhofer IPT was used to prevent laser reflections into the glass by clamping the glass only at the edges and thus transmitting the laser beam into air after passing through the glass (see Fig.5).
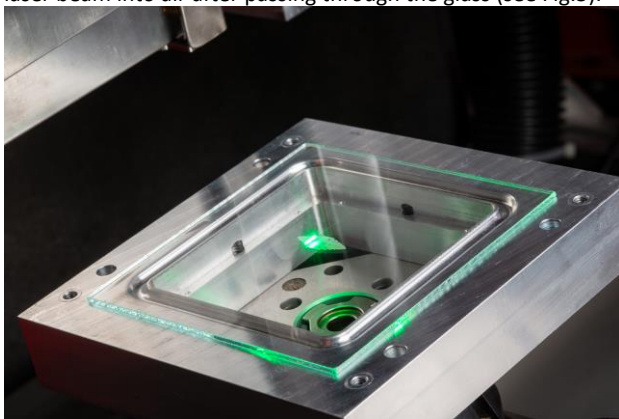
Figure 5. Laser ablation of 100x100 mm floatglass. Using the clamping system for processing laser radiation is transmitted through glass to prevent back-reflections into the glass.

For this system, suitable process parameters were determined to introduce required textures or markings into the glass. Thus, the following process parameters were varied in a full factorial experimental study: (i) laser power, (ii) laser frequency (iii) pulse overlap, (iv) laser bursts and (v) hatching. Results indicate parameter sets for high throughput laser ablation with ablation

rates up to 0.06 mm^2/min and corresponding roughness of S_a =0.15 µm.

Using the predistortion method (see Fig 3), laser trajectories were generated with varying spacing (see Fig 1b) and subsequently textured onto the 2D glass for downstream hot forming.

3.2 Hot forming

A nonisothermal thin glass forming machine (NI-TG Forming Machine) (see Fig 6) from the manufacturer Vitrum Technologies was used for the hot forming experiments.
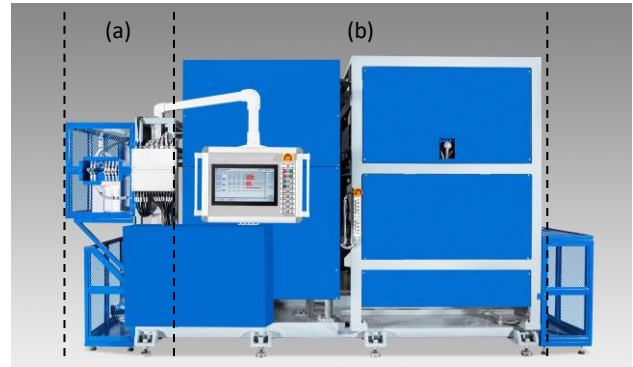
Figure 6. Vitrum Technologies´ non-isothermal thin glass forming machine (NI-TG Forming Machine) with a loading station (a) and several oven chambers (b).

The machine is equipped with several oven chambers offering a temperature range limit of up to 1300 °C and several high-precision movement axis with a position repeatability of < 1 µm. All actuators (axis, valves, heating systems) can be controlled via an intuitive human machine interface (HMI). As a result, the machine is well suited for the development of new glass hot forming processes. All sensor data, actuator positions, movements and energy consumption of the machine are provided with marker signals and time stamps. All data is written into a database every 15 ms using an internal clock signal. This provides the prerequisites for a digital twin model and alignment with the FEM simulations of Fraunhofer IPT.

The machine features four types of thin glass forming processes (i) gravity slumping, (ii) vacuum-assisted slumping, (iii) press bending and (iv) deep drawing.

This publication focuses on gravity slumping with no additional forces applied during the forming process. Without external forces applied, any kind of temperature phenomenon has a major impact on the hot forming result. For this reason the furnace system was calibrated to achieve highest temperature accuracy of < 1 K.

The laser structured glass is loaded onto the mould system by a robot handling system and then transported into the furnace unit. The temperature of the glass and the mould are both monitored during the process. The machine operator is able to observe the process through a view port.

Once the glass has completely fallen into the mould cavity, the mould and glass are transported automatically to the loading area to be unloaded.

During the process development, parameters were optimised systematically based on three fundamental methods: (a) based on experience, the operator chooses sensitive parameter and ranges, (b) temperature and process time prediction based on FEM simulations, (c) using trained machine learning tools to solve non-linear optimisation problems in glass hot forming. A combined approach of the methods (a) and (b) was sufficient to determine the process parameters of these experiments.

4. Results
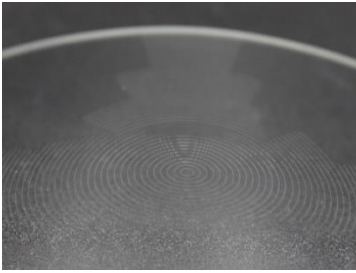
Figure 7 Photograph of the formed glass with compensated ring structures on the surface

The ring segments of four formed glass components were measured up to a radius of r = 48 mm using confocal micros-copy. The respective radius of each circular ring was determined. The measurements were conducted in the bending direction (x - direction) and along the y-direction.

Each measured radius was compared with the expected target radius and plotted (see Fig. 8). No distortions in the y-direction were identified due to a 2.5D bending radius in the x-direction. However, deviations from the expected position were measured for compensated ring segments in the direction of curvature (x-direction). The deviation within the radius interval from 1 mm to 14 mm is smaller than 10 μm. The data then shows a significant deviation of up to 140 μm in the radius interval of 14 mm to 22 mm. The deviation then decreases again for a radius of 22 mm before linearly increasing for larger radii.

x-direction: Measured compensated spacing deviation on 3D glass [mm]

y-direction: Measured compensated spacing deviation on 3D glass [mm]
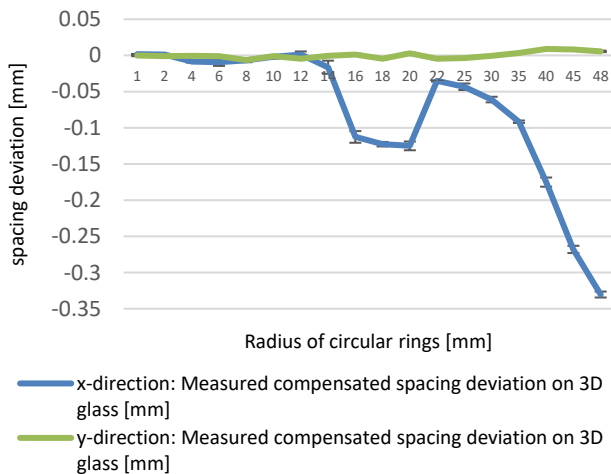
Figure 8. Deviation of compensated circular ring segments with regard to the targeted ring position

The significant increase in positional deviation of ring segments can be explained by comparing the simulated glass bending radius with the actual glass bending radius. Based on the confocal 3D data, the bending radius of the glass was determined to be 93 mm. This deviates by 7 mm from the simulated bending radius (100 mm). This could indicate a possible deformation of the sheet mould during the forming process. Therefore, compensated laser trajectories are based on a differing simulated bending radius.

According to the simulation (see Fig. 4), a zero crossing of the deviation is expected at 21 mm. This means that laser trajectories for this ring radius were not compensated.

For the measured actual bending radius of 93 mm, the zero crossing shifts to a radius of 18 millimetres. This results in a faulty deviation compensation for radii of 16 to 22 mm leading to a subsequent deviation compensation error for larger radii.

Nevertheless, compared to an uncompensated ring geometry on a formed glass, the accuracy for the areas outside the specified error range (16 mm to 22 mm) could be increased by 75% to 99% (see Fig.9).
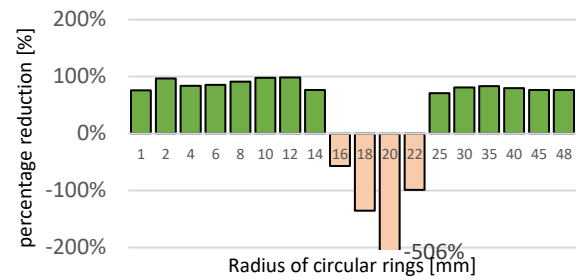
Figure 9. Percentage reduction of formed uncompensated circular rings compared to compensated rings

5. Conclusion and outlook

When 2D glass is formed into a 3D shape, there are positional deviations and shape distortions of a texture introduced beforehand. We validated a new approach to reduce these distortions by up to 90%. The method and results indicate a significant advancement towards an economical series production of functionalized glass, addressing e.g. automotive industry. To even reduce current distortions further we will introduce forming tools made of high-alloy, temperature-resistant stainless steel in the future leading to constant bending radii in the glass.

Acknowledgements

References

[1]	marketsandmarkets.com: Display Market by Product, Technology, Panel Size, Industry, and Geography – Global Forecast 2024. URL: https://www.marketsandmarkets.com /Market-Reports/display-market-925.html, 22.03.2024.

[2]	Obilor, A.F., Pacella, M., Wilson, A., Silberschmidt, V.V., 2022. Micro-texturing of polymer surfaces using lasers: a review **120**, p. 103.

[3]	Zhou, T., He, Y., Wang, T., Zhu, Z. *et al.*, 2021. A review of the techniques for the mold manufacturing of micro/nanostructures for precision glass molding **3**, p. 42002.

[4]	Spierings, G.A.C.M., 1993. Wet chemical etching of silicate glasses in hydrofluoric acid based solutions **28**, p. 6261.

[5]	Kaierle, S., Heinemann, S.W., Editors, 2019. *High-Power Laser Materials Processing: Applications, Diagnostics, and Systems VIII*. SPIE.

[6]	Vu, A.T., Vogel, P.-A., Dambon, O., Klocke, F., 2018. Vacuum-assisted precision molding of 3D thin microstructure glass optics, in *Fiber Lasers and Glass Photonics: Materials through Applications*, SPIE, p. 11.

[7]	John Wallace, 2017. Photonics Products: Laser Scanning: Polygon beam scanners enable essential applications., p. 31.

[8]	Vu, A.T., Vu, A.N., Grunwald, T., Bergs, T., 2020. Modeling of thermo-viscoelastic material behavior of glass over a wide temperature range in glass compression molding **103**, p. 2791.

[9]	Rojacher, C., Vu, A.T., Grunwald, T., Bergs, T., Precision glass molding of infrared optics with anti-reflective microstructures, Optical Manufacturing and Testing XIII, SPIE, p. 30.

[10]	Vogel, P.-A. *Entwicklung eines Prozessmodells für die nicht-isotherme vakuumunterstützte Dünnglasumformung,* 1st edn.

[11]	Vogel, P.-A., Vu, A.T., Mende, H., Grunwald, T. et al., Approaches and methodologies for process development of thin glass forming, Optifab 2019, SPIE, p. 68.

Recycling of erosion sludge particles for laser beam direct energy deposition

Oliver Voigt[1], Moritz Lamottke[2,*], Marco Wendler[3], Henning Zeidler[2], Urs Peuker[1]

[1]Institute of Mechanical Process Engineering and Mineral Processing, Technische Universität Bergakademie Freiberg, Agricolastr. 1, 09599 Freiberg, Germany
[2] Institute for Machine Elements, Engineering Design and Manufacturing, Technische Universität Bergakademie Freiberg, Agricolastr. 1, 09599 Freiberg, Germany
[3]Institute of Iron and Steel Technology, Technische Universität Bergakademie Freiberg, Leipziger Straße 34, 09599 Freiberg, Germany

correspondence *: moritz.lamottke@imkf.tu-freiberg.de & oliver.voigt@mvtat.tu-freiberg.de

Abstract
Waste sludges from electro discharge machining were collected from the bottom of the machining basin. These contain eroded metallic particles, which are suitable for processes in additive manufacturing regarding their size ranges, shape and bulk powder properties. After cleaning and classifying, these particles with high carbon contents were used to clad beads and layers via laser beam direct energy deposition, where defect free structeres could be obtained. These were analyzed regarding their dilution ratio, microstructure and hardness. Microstructures featuring pearlite, austenite, martensite and cementite due to mixtures of high carbon particles and low carbon substrate were observed. The beads and layers show overall high hardness of 700 HV10 to 960 HV10.

Keywords: Additive Manufacturing, Laser Beam Direct Energy Deposition, Recycled Particles, Microstructure, Hardness, Electro Discharge Machining

1. Introduction

The production of metal powders for additive manufacturing (AM) by gas atomization is an energy- and cost-intensive process. Therefore, it is indispensable to focus on alternatives for providing powders. One possibility seems to be waste sludge from electro discharge machining (EDM), which is accumulating at the bottom in machining basins and can be collected. In die-sink EDM, the material gets molten and vaporized by conversion of electrical into thermal energy. Removed material solidifies in the surrounding dielectric fluid (oil). The resulting particles achieve key size, shape and flowability parameters similar to AM powders [1].

A common AM-technique is laser beam directed energy deposition of metal powders (DED-LB/M). This process uses a laser to weld gas guided powder streams layer by layer to a substrate material. Narrow distributed and spherical particles with good flowability are necessary for successfully deposited beads [2]. Influenced by several operational settings and materials, different microstructures and mechanical properties can be achieved. In this study, recycled EDM particles are processed via DED-LB/M to show a use case for recycling EDM sludges. Investigations regarding microstructure and hardness of deposited structures are presented.

2. Materials and Methods

2.1. EDM Particles

Waste sludge was collected from a mold production company, where commercial H11 alloy was EDM-machined with a graphite electrode in a synthetic hydrocarbon-based dielectric with unkown settings. The oily phase was dissolved in acetone and metallic particles dried overnight. Fractions were obtain by sieving. Particles of the size range 20 µm to 63 µm were used for DED-LB/M. Particle sizes and shapes were investigated via laser diffraction and dynamic image analysis. Chemical compostion was measured via ICP-OES and C-S-O analyzer. Hausner ratio was determined by measuring bulk and tap densities.

2.2. Specimen Prodution in DED-LB/M

Deposited beads (B1-B3) and layers (L1+L2) were created of pure EDM particles in a DED-LB/M device LV Midi (Laservorm GmbH, Germany) with a fibre laser source of maximum 1.5 kW. Used parameters are a laser power P of 1.4 kW, laser scan speeds v between 5 mm/s (B1+B2) and 50 mm/s (B3, L1, L2), powder flow rates of 7.91 g/min (B1+B2) or 15.87 g/min (B3, L1+L2), spot size of 0.9 mm, defocus between 15 mm and 30 mm and gas purge flows of 8 l/min (particles) and 16 l/min (inside). A mild construction steel was used as substrate. The dilution ratio α (Eq. 1), whereas d is the height of the deposited bead and h the depth of the molten pool, and linear heat input H (Eq. 2) were calculated for evaluating the deposition result. Values were obtained Fiji ImageJ software.

$$\alpha = \frac{d}{h+d} \times 100 \qquad (1)$$

$$H = \frac{P}{v} \qquad (2)$$

2.3. Microstructure Analysis and Hardness Measurement

The deposited beads, layers and substrate microstructure was examined via light microscopy. Samples were embedded in Polyfast matrix and cut in half. Afterwards, the surfaces were ground with SiC paper, polished with diamond suspension and colloidal silica and etched in Nital. Hardness values of minimum five locations per bead and layer were measured according to Vickers method HV10 with 10 kP for 10 s on the surfaces used for microstructure analysis. A device KB 30 S was used with settings with KB Hardwin XL software.

3. Results and Discussion

3.1. Particle Properties

After sieving, the recycled EDM particles show a narrow particle size distrubtion (table 1). The size parameters are compared to commercial H11 particles. The circularity is on a similar high level ensuring a good flowability, which is confirmed in the determined Hausner ratios. These do not show a

significant difference, whereas the tap and bulk densities are different by approx. 5 %.

Table 1: Characteristic particle properties of H11 reference and eroded particles for DED-LB/M

Property	H11 reference	Eroded particles
$x_{10,3}$ in µm	19.4	22.8
$x_{50,3}$ in µm	30.1	39.5
$x_{90,3}$ in µm	61.7	60.6
Circularity	0.93	0.92
Hausner ratio	1.05	1.06

The chemical composition of EDM particles equals the H11 alloy composition except the high carbon content of approx. 4.9 wt.%. Due to high temperature gradients, when the molten material solidifies in the dielectric, a high temperature carbon uptake takes place and C is entrapped in the Fe lattice caused by a pyrolysis of the dielectric [3]. Additional information about these EDM particles regarding morphology, XRD and phase analysis as well as their microstructure can be found in [4].

3.2. Appearence of Deposited Structures

Beads and single layers were successfully deposited with nearly no thermal or residual stress cracks despite the high carbon content. During the DED-LB/M process, a high evaporation rate was observed. Deposited structures appear smoothly shaped, and the melt pool and heat affected zone depth rule out effects of keyholing or lack of fusion. Just a few gas entrapments and barely any non-metallic inclusions are seen. Fig. 1 shows calculated dilution ratios against linear heat input with an exemplary bead in the top containing two smaller pores. Common dilution ratios are in the range of 10 % to 30 % [5], which is fulfilled by nearly all samples. Pre-heating the substrate (L2) leads to better and even crack-free results.
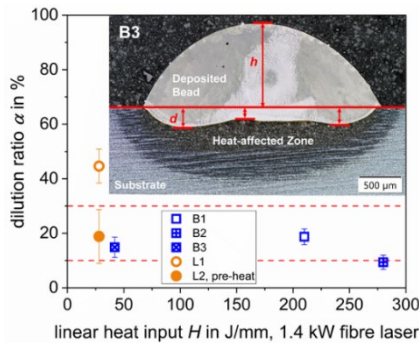
Figure 1: Dilution ratio against linear heat input of 3 deposited beads and 2 layers with micrograph of whole bead

3.3. Microstructure of Structures

Fig. 2 shows different microstructural areas of substrate and beads. Former one exhibits a fine-grained high-ferritic and low-pearlitic microstructure with a low carbon content. B1 features a fine-lamellar pearlitic microstructure with whiteish austenite dendrites corresponding with local hardness values. The composition of this region is clearly shifting to the eutectoid steel region, as no cementite is present, resulting from a mixture of high-C particles and low C-substrate as well as carbon evaporation. In B2 acicular primary cementite and pearlite are observed, as cementite can develop in the top region of the bead due to non-mixing of components as in the boundary region. Latter one is shown in B3 containing cementite in upper regions and known fine-lamellar pearlitic and dendritic austenite. In the heat-affected zone a martensitic structure is present as result of a mixture of substrate and eroded particle, which is solidifying austenic with high cooling gradients leading to a tetragonal distortion.
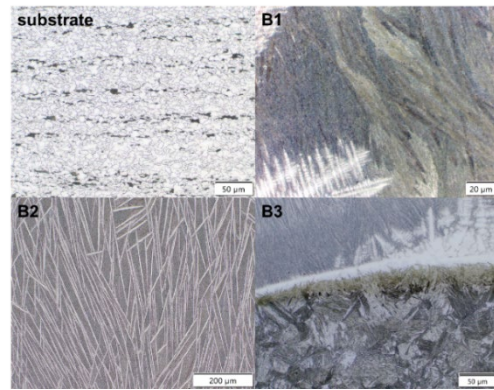
Figure 2: Micrographs of the substrate material and deposited beads B1-B3 at different phase regions

Fig. 3 shows the micrographs of deposited layers. In L1, one of several elongated residual stress cracks, related to high C, is observable surrounded by primary cementite needles. Moreover, some smaller areas are appearing as non-metallic inclusions. In general, the fine-lamellar pearlitic and dendritic austenitic microstructure is present again. For L2, a nucleation origin at the right edge with directed crystallization to the centre, possibly caused by a particle, can be assumed.
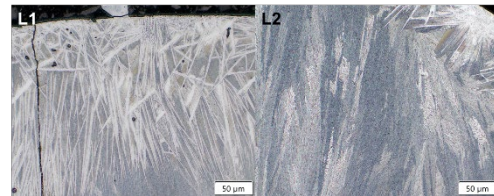
Figure 3: Microstructural image of deposited layer L1+L2

3.4. Hardness of Deposited Structures

As it can be assumed by carbon content and developed microstructures, quite high hardness ranging from 700 HV10 to 960 HV10 (see Tab. 2) is observable. Due to cracks and defects, the value for L1 is significantly lower. B2 shows the highest value due to the presence of hard and wear-resistant cementite.

Table 2: HV10 hardness values 3 deposited beads and 2 layers

Sample	HV10
B1	**704** ± 102
B2	**961** ± 21
B3	**834** ± 171
L1	**516** ± 36
L2	**920** ± 54

4. Outlook

DED-LB/M process was successfully used to deposite beads and layers using recycled EDM particles. Microstructure as well as hardness were analyzed. Deposited structures exhibit microstructures containing pearlite, austenite, martensite and cementite and show overall high hardness values. Future works will focus on powder mixtures with pristine particles to further decrease the C-content and supress the occurrence of cracks as well as enhance the final properties.

References

[1] Voigt, O. and Peuker, U.A., *Metals*, 2022. **12**(9).
[2] Ahn, D.-G., *International Journal of Precision Engineering and Manufacturing-Green Technology*, 2021. **8**(2): p. 703-742.
[3] Berkowitz, A.E. and J.L. Walter, *Journal of Materials Reasearch*, 1987. **2**(2): p. 277-288.
[4] Voigt, O., Wendler, M., Siddique, A., Stöcker, H., Quitzke, C. and Peuker, U.A., *Metals and Materials International*, 2023.
[5] Dass, A. and A. Moridi, *Coatings*, 2019. **9**(7).

On the design of an asymmetric temperature control platform towards the influencing of the heat balance of the DED-LB process

Fabian Bieg[1], Clemens Maucher[1], Hans-Christian Möhring[1]

[1]Universtiy of Stuttgart, Institute for machine tools (IfW), Holzgartenstr. 17, 70174 Stuttgart, Germany

fabian.bieg@ifw.uni-stuttgart.de

Abstract

During the laser based directed energy deposition (DED-LB) process, a large quantity of heat is introduced into the substrate or work piece geometry resulting from the melting process. The relatively high build-rate leads to various complex thermal mechanisms. In particular, the rapid cooling of the deposited structures has a significant impact on the process.

Since DED-LB is an additive process, geometry can vary, ranging from the buildup of complex structure to repair applications. Therefore, the thermal conditions also change depending on the geometry. As a result, controlling the heat balance during the process is important, and it is necessary to locally cool or heat areas in one substrate work piece to prevent possible defects, geometric deviations or to influence the mechanical properties.

In this paper, the design towards an asymmetric cooling and heating platform is demonstrated. This was done by DED process simulation to determine a range of values of the required heating and cooling energy depending on different deposition geometries. Based on these results, single combined heating and cooling units were designed in a modular way to achieve a scalable solution. In simulations, this approach already shows promising results in terms of reduced geometric deviation. Finally, the platform is mechanically designed to incorporate subsequent process steps on the same system and proof of concept is delivered.

Additive Manufacturing, Directed Energy Deposition, substrate tempering, cooling behavior, geometric deviation

1. Introduction

With the help of the laser-based Directed Energy Deposition (DED-LB) process, complex components or additive manufactured (AM) structures can be created on existing components. The DED-LB process combines the fundamental principles of welding and coating. In the powder-based DED-LB process, a laser beam is focused onto the substrate surface to create a melt pool. Within the melt pool, a portion of the substrate surface and supplied powder material are melted and structures are created. [1]

The thermal history of the DED-LB process involves a series of thermal phenomena, including rapid heating, melting and cooling of the melted powder material and the substrate with cooling rates ranging from 10^3 to 10^4 K/s [2]. This results in a structure with a characteristic microstructure, arising from numerous phase transformation within a single geometry. The thermal properties, such as the maximum temperature, the position of the maximum temperature, as well as the cooling rate can vary significantly within the deposited structure. These local changes in the cooling rate can occur due to heat accumulation, for example in thin-walled structures [1]. A characteristic of thermo-mechanical manufacturing process like the AM-processes is the generation of residual stresses within the microstructure. In case of the DED-LB process, rapid heating and cooling of the structure lead to the initiation of thermal stresses. These thermal stresses occur along the grain boundaries due to the higher contractions between the upper, hotter layer and the underlying colder layer or the substrate material [3].

The cooling behavior is determined by process parameters such as laser power, scanning speed and the deposition rate. Additionally, the cooling behavior is influenced by the geometry and size of the deposited structure and of the substrate work piece [2]. By adjusting the process parameters, the thermal balance can be influenced. However, the process parameters cannot be arbitrarily adjusted, as the process would otherwise become unstable. The cooling behavior of the deposited structure can be influenced by heating or cooling the substrate. This enables an influencing of the microstructure and properties. Additionally, the substrate tempering can prevent the formation of defects. Heating the substrate leads to a reduction of the cooling speed, while cooling results in a higher cooling speed. Due to the extended cooling time during the preheating, fewer residual stresses are initiated in the microstructure. This serves to mitigate the occurrence of cracks within the microstructure and in the interlayer bonding zone. Furthermore, preheating can improve the dimensional accuracy of the work pieces [4].

Substrate cooling helps to avoid geometric defects, such as warping of the topmost layer of a deposited structure. This effect is often observed in thin-walled structures. [5]. The use of substrate cooling allows for more precise contours with reduced geometric deviations, especially in thin-walled geometries. Overheating can occur in this kind of structures due to impaired heat dissipation into the substrate [1].

Various concepts for the temperature control of the substrate work piece are found in the literature. In addition to the use of resistance [6] and induction heaters [3] the laser of the DED machine can also be used for preheating [7]. Substrate cooing is commonly achieved with the help of water cooling systems [8]. The effect of substrate heating and cooling on the entire deposited structure has been discussed in the literature. Within the scope of this work, an asymmetric temperature control platform is designed for the investigation of the local tempering of the substrate work piece. The design of this device is based on a concept of a multi sensor platform, developed for monitoring the

laser-based powder bed fusion process (PBF-LB) [9]. The objective of this work is the design of a platform that enables localized control of the cooling rate within a deposited structure. This device is intended to enable further investigations in which asymmetrical and local substrate tempering is achieved by combining heating and cooling processes.

2. Effect of the asymmetric substrate tempering

For the investigation of the effect of the local and asymmetric substrate tempering, a simulation model based on Ansys Mechanical was created. The DED-LB process was modelled using the Ansys Additive DED extension. Within this extension, individual elements are generated and activated at a process temperature of 1750°C, which corresponds to the melt pool temperature of the available DED machine. The material used for these investigations was 316L for the powder material and structural steel for the substrate material. Table 1 shows the parameters used for the simulation. The deposition of a simple single thin wall structure was considered with a length of 175 mm and height of 30 mm. The track width corresponds to the diameter of the powder nozzle available for future experiments.

Table 1 Simulation parameters of the DED-LB process

process temperature	1750°C
deposition rate	24 mm³/s
element size	3 mm
layer height	3 mm
scanning speed	1000 mm/min
track width	3 mm
thin wall dimensions	175 x 30 mm

The model is based on a thermomechanical simulation, where first the thermal behavior of the deposition was determined, and afterward the mechanical behavior in form of the deformation was examined. For the investigation of the asymmetric tempering, two different temperatures were used: 150°C and 300°C. These temperatures were applied during the deposition at the center and end of the thin walls. During the deposition, the heat transfer between the deposition process and the tempering process is calculated. Furthermore, an idealized temperature control is assumed, ensuring that the specific temperatures at the respective locations remain constant throughout the deposition process. Figure 1 shows an exemplary simulation result of the deformation with the geometric model used in the simulation.
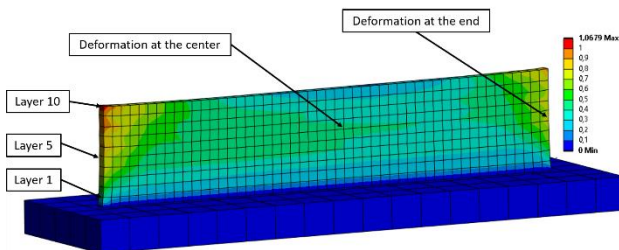
Figure 1. Geometric model of the deformation simulation

In Figure 2, the deformations at the center of the thin walls in each layer are illustrated for different tempering strategies documented in Table 3. The impact of local substrate tempering is clearly evident in this deception of the deformation. In the parameter set without local substrate tempering during deposition, a variation in deformation across different layers is observed. The deformation in parameter set two is lower, but an increase in deformation can be observed in the top layer. For

parameter sets three and four with substrate temperatures of 300 °C, a broader distribution is noticeable. In some layers, the deformation is significantly below and above the initial state in parameter set one. Parameter set three, where the substrate work piece temperature was set to 150°C at the center of the wall, shows a narrower distribution with the lowest deformation values, compared to the non-preheated substrate.
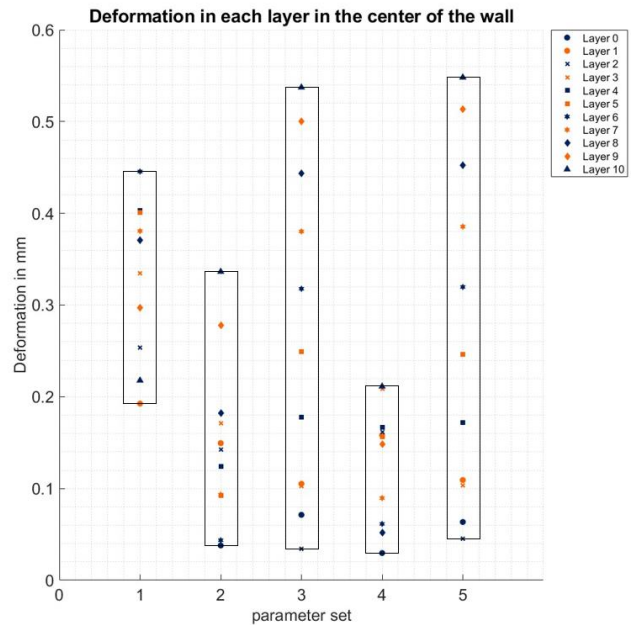
Figure 2. Deformation on each layer at the center of the wall

A similar influence was also found when examining the deformation at the ends of the walls, whereby the width of the distribution and the values of the change in deformation are significantly higher.

Table 2 Tempering strategies for the different samples

Parameter set	Center of the wall	End of the wall
1	-	-
2	-	150°C
3	-	300°C
4	150°C	-
5	300°C	-

3. Design of an asymmetric cooling

To investigate the impact of asymmetric substrate tempering on the DED-LB process, a specialized device has to be engineered to enable the implementation of asymmetric tempering within the DED-LB machine. The platform should consist of individual, modular elements whose temperature can be controlled as required to locally control the cooling rate of the deposited structures. These elements are implemented in the form of cuboids. Due to the large number of individual elements, the substrate temperature can be influenced in different local areas of the deposited structure. As part of the design of the asymmetric heating and cooling platform, the size and arrangement of these cuboid elements must be determined.

3.1 Determination of the element size and arrangement

The size and arrangement of the cuboid elements determines not only the resolution of the asymmetric tempering but also the size and geometry of the deposited structures, which are considered in the context of further investigations.
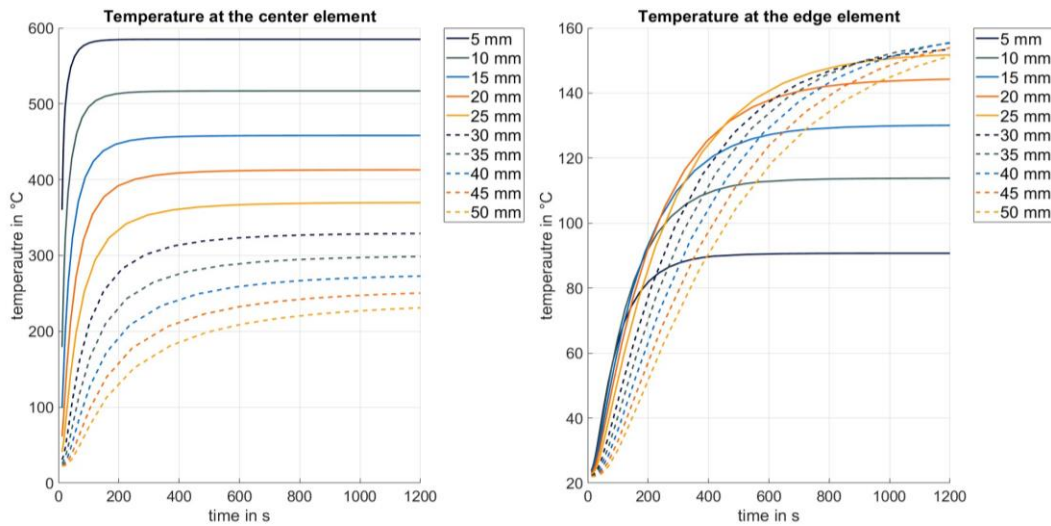
Figure 3. Temperature at the center and edge cuboid element

A thermal simulation of the design was carried out to determine the size and arrangement. The design consisted of a 180x180 mm baseplate on which cuboid elements with a height of 20 mm, different edge lengths and distances to each other were positioned. The edge length of the baseplate results from the requirement to achieve a system that is as compact as possible. This size limitation allows the investigation of smaller deposited structures in subsequent investigations, and thus reduces process times and powder consumption for economic reasons. Three different edge length were examined for the elements in a thermal model, 20 mm, 30 mm and 50 mm. By placing the cubes on the baseplate, the different. When placing the cubes on the given base area, the number of cubes resulted from the distance between the cubes. As part of the simulation, a square heat input was considered on a substrate plate placed on the cube. The temperature of the stationary heat input was 650 °C and the duration was 1200 seconds. The temperature results from previous simulations of the DED-process, where the temperature of the substrate surface immediately after the heat input of the laser was determined. During the simulation period, the temperature and heat flow of the individual elements were recorded. In the simulation, the cuboid elements with an edge length of 30 mm showed the best result regarding the resolution of the temperature distribution and thus the local substrate temperature control. Furthermore, this edge length provides sufficient resolution for temperature control and the accommodation of the heating and cooling technology. In terms of arrangement, three different grids of elements were compared, documented in table 3.

Table 3 Element arrangement

grid	distance between elements
5x5	5 mm
4x4	12 mm
3x3	22.5 mm

Thermal simulations with identical parameters as those used for determining the element size were conducted. The temperature and heat flux of the individual elements were recorded. In figure 4, the temperature distribution for different numbers of grid elements is shown. In the arrangement with fewer and a larger spacing between the elements, the temperature of the individual elements is higher, within the range of direct heat input. Therefore, the thermal power for the cooling and heating for each element is lower than for the grids with fewer elements.

Additionally, a higher resolution for influencing the substrate temperature is achievable with a smaller distance between the individual elements of the grid. A higher number of temperature-controllable elements not only allows for influencing the heat balance in multiple distinct areas but also enables more flexible experimental geometries. Therefore, a grid with 5x5 elements was determined for the design.
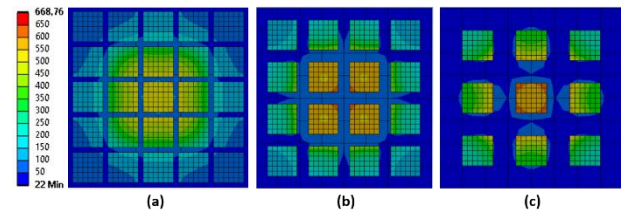
Figure 4. Temperature distribution (a) 5x5 grid, (b) 4x4 grid, (c) 3x3 grid

As part of additional thermal simulations, the impact of the thickness of the substrate plates on the measurable temperatures of all individual cuboid elements within the 5x5 grid was investigated. For this investigation, equal parameters were applied as in the simulations before. Figure 3 shows the temperature profiles of two of these elements, the cuboid element in the center and the edge. In the central element, the temperature rises quickly to a maximum value and remains at a constant value. The temperature can be clearly differential depending on the thickness of the substrate plate. This also applies to the edge element, although the temperature increase is lower, and no constant temperature is achieved for the thicker substrate plates during the considered simulation period. With these simulations, the heat flux of the deposition process could be documented as a function of the position of the element, regardless of the substrate thickness. This enables the localized influence of the heat flux at these individual points.

3.2 Determination of heating and cooling power

The thermal power required for cooling and heating the elements is determined by several factors. The thermal power needed for heating a single cuboid element from room temperature (22 °C) to 500 °C, the set limit temperature of the experiments, can be calculated by using the following assumptions. The thermal power required to heat an object to a certain temperature can be calculated by the following formula 1, where c_p represents the heat capacity of the used steel material, and m represents the mass of the element.

$$P_{heat} = c_p \cdot m \cdot \frac{\partial T}{\partial t} \qquad (1)$$

$$P_{heat} = 434\,\frac{J}{Kg \cdot K} \cdot 0.1413\,kg \cdot \frac{(500\,°C\text{-}22\,°C)}{60\,s} = 488.55\,W$$

The heat loss due to thermal radiation of the surface of the element can be calculated as follows, with formula 2 with the emissivity of the surface ε_{rad} = 0.7 and the Stefan Boltzmann constant $\sigma = 5.67 \cdot 10^{-8}\,W/(m^2 K^4)$.

$$P_{Rad} = \varepsilon_{Rad} \cdot \sigma \cdot A \cdot \left(T_2{}^4\text{-}T_1{}^4\right) \qquad (2)$$

$$P_{Rad} = 0.7 \cdot 5.67 \cdot 10^{-8}\,\frac{W}{\left(m^2 K^4\right)} \cdot 0.0045\,m^2 \cdot \left(500\,°C\,{}^4\text{-}22°C^4\right)$$

$$P_{Rad} = 86.04\,W$$

Heat losses due to convection are calculated using formula 3, where h represents the heat transfer coefficient with stagnant ambient air, and A defines the surface of the cuboid element.

$$P_{conv} = h \cdot A \cdot (T_2\text{-}T_1) \qquad (3)$$

$$P_{conv} = 4\,\frac{W}{m^2} \cdot 0.0045\,m^2 \cdot (500\,°C\text{-}22\,°C) = 11.162\,W$$

By adding the thermal power and the power that must be applied to compensate for the losses, a power of P_{Heat} = 585.75 W is required. To compensate for thermal losses due to heat conduction, which were not considered in this calculation, the heating power is provided with commercially available resistance heating cartridges with an output of 750 W are integrated for the heating process.

To determine the thermal power for the cooling operation, the heat flux at the center element of the platform was analyzed. The thinnest substrate plate shows a maximum heat flux in the first 200 seconds of 1.4 W/mm². To neutralize this heat flux, the central element needs a cooling power of 1440 W to bring the element down to room temperature.

3.3 Design of the asymmetric temperature control platform

Figure 5 shows the resulting design of the asymmetric temperature control platform. The platform consists of the predetermined 25 cuboid elements with an edge length of 30 mm and a height of 20 mm. The sectional view shows a hole for the heating cartridge and channels for water cooling. The individual elements are positioned on a baseplate, in which connection options for the energy and water supply are also to be integrated. Furthermore, thermocouples are integrated into the individual elements to record the thermal behavior of the process.
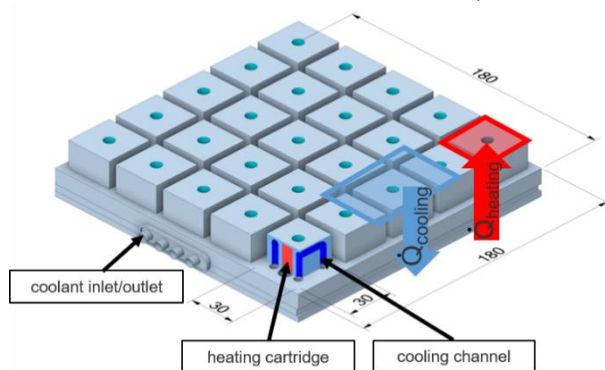
Figure 5. Final design of the asymmetric heating platform

4. Conclusion

In this work, the design process of an asymmetric temperature control platform for the DED-LB process was considered. In the course of the development process, the basic design of the platform was defined in the form of a system of modular elements, and the size and arrangement of the elements were determined. Furthermore, the required thermal performances were estimated. A grid of cuboid elements with an edge length of 30 mm was determined for the monitoring and influencing of the local heat fluxes. In further steps, the construction and manufacturing of the developed design will take place. This work serves as the foundation for further investigations into asymmetric substrate tempering. In subsequent research, the platform will be utilized to investigate the effect of locally influencing the cooling rate for simple thin walled structures. Additionally, heating and cooling strategies and a temperature control system need to be developed to influence the properties of these deposited structures.

References

[1] Gibson, Ian; Rosen, David; Stucker, Brent; Khorasani, Mahyar: Additive Manufacturing Technologies. *Cham: Springer International Publishing*, 2021

[2] Saboori, Abdollah; Aversa, Alberta; Marchese, Giulio; Biamino, Sara; Lombardi, Mariangela; Fino, Paolo: Microstructure and Mechanical Properties of AISI 316L Produced by Directed Energy Deposition-Based Additive Manufacturing: A Review. In: *Applied Sciences 10 (2020)*, Nr. **9**, S. 3310

[3] Zhou, Lin; Chen, Suiyuan; Wei, Mingwei; Liang, Jing; Liu, Changsheng; Wang, Mei: Microstructure and properties of 24CrNiMoY alloy steel prepared by direct laser deposited under different preheating temperatures. In: *Materials Characterization* **158** (2019), S. 109931

[4] Zhao, Yuhui; Wang, Zhiguo; Zhao, Jibing; He, Zhen Feng; Zhang, Hogweed: Comparison of Substrate Preheating on Mechanical and Microstructural Properties of Hybrid Specimens Fabricated by Laser Metal Deposition 316 L with Different Wrought Steel Substrate. In: *Crystals 10* (2020), Nr. **10**, S. 891

[5] Ishiyama, Keiya; Koike, Ryo; Kakinuma, Yasuhiro; Suzuki, Tetsuya; Mori, Takanori: Cooling Process for Directional Solidification in Directed Energy Deposition. In: Volume **1**: *Additive Manufacturing; Bio and Sustainable Manufacturing: American Society of Mechanical Engineers*, 2018

[6] Dill, Jessica; Soshi, Masakazu; Yamazaki, Kazuo: A study on the effect of directed energy deposition substrate energy on clad geometry. In: *The International Journal of Advanced Manufacturing Technology* **109** (2020), 1-2, S. 315–333

[7] Bieg, Fabian; Scheider, David; Kledwig, Christian; Maucher, Clemens; Möhring, Hans-Christian; Reisacher, Martin: Development of a laser preheating concept for directed energy deposition. In: *Journal of Laser Applications* **35**, Nr.4 (2023)

[8] Nie, Jianwen; Chen, Chaoyue; Liu, Longtao; Wang, Xiaodong; Zhao, Ruixin; Shuai, Sansan; Wang, Jiang; Ren, Zhongming: Effect of substrate cooling on the epitaxial growth of Ni-based single-crystal superalloy fabricated by direct energy deposition. In: *Journal of Materials Science & Technology* **62** (2021), S. 148–161

[9] Maucher, Clemens; Werkle, Kim Torben; Möhring, Hans-Christian: In-Situ defect detection and monitoring for laser powder bed fusion using a multi sensor build platform. In: *Procedia CIRP* **104** (2021), S. 146-151

Machining characteristics of Ti6Al4V in electrochemical machining (ECM) and hybrid laser-ECM

Muhammad Hazak Arshad[1,2], Krishna Kumar Saxena[1,2], Dominiek Reynaerts[1,2,*]

[1]*Micro- & Precision Engineering Group (MPE), Manufacturing Processes and Systems (MaPS), Dept. of Mech. Eng., KU Leuven, Leuven, Belgium*
[2]*Member Flanders Make (https://www.flandersmake.be/nl), Leuven, Belgium*

[*] dominiek.reynaerts@kuleuven.be

Abstract

The titanium alloy (Ti6Al4V) exhibits lightweight, high strength, biocompatibility, thermal stability at extreme temperatures and corrosion resistance which makes it attractive for a wide range of industries. However, these properties contribute to its low machinability which is further complicated for microscale features. Additive manufacturing (AM) offers good flexibility and accuracy but the high thermal load generates internal pores and alters the material properties making it unsuitable for high-end applications. Electrochemical machining (ECM) can anodically dissolve materials independent of their hardness and preserve their properties, but the multiphase and passivating nature of Ti6Al4V limits its performance. Aggressive reagents or glycol-based electrolytes are needed for improved EC-dissolution but are harmful or have low current efficiency, respectively. Hybrid laser-ECM (LECM) was recently developed to circumvent these issues and improve the material processing window of ECM in aqueous neutral salt electrolytes by coaxially applying laser assistance simultaneously in the machining zone.

Therefore, in this work the machining characteristics of Ti6Al4V in ECM and LECM are presented to evaluate the processing improvement with laser assistance in terms of removal localisation, material removal rate (M.R.R.) and surface quality (Sa). With the growing interest in flexible manufacturing, samples manufactured with selective laser melting (SLM) were machined along with rolled samples to also investigate the influence of porosity and microstructure generated by SLM on EC/Laser-EC dissolution.

Keywords: Electrochemical machining (ECM), Hybrid laser-ECM (LECM), hybrid manufacturing, micromachining.

1. Introduction

Titanium alloys like Ti6Al4V are key industry materials with applications in automotive, aerospace, biomedical, etc. due to their lightweight, corrosion resistance, high strength, high hardness, biocompatibility and thermal stability at extreme temperatures. However, its high strength and low thermal conductivity create machining challenges [1], which are further magnified for microscale features. Additive manufacturing (AM) is gaining interest for net shaping Ti6Al4V parts due to its good flexibility and accuracy [2]. However, the high thermal loads in AM generate pores and change the material properties, which limit high-end aerospace and biomedical applications.

Electrochemical machining (ECM) can anodically dissolve materials independent of their hardness in the presence of an electrolyte and voltage source [3]. The athermal nature of ECM ensures good surface integrity and preservation of material properties which makes it suitablefor high-end applications. Unfortunately, the multiphase and highly passivating nature of Ti6Al4V also complicates EC-dissolution in aqueous neutral salt electrolytes, resulting in inhomogenous dissolution [4], [5]. Aggressive acid and base additives are needed to overcome the passivation barrier which are harmful for both the users and machine tool. A safer approach is to use ethylene glycol-based electrolytes to homogenously process Ti6Al4V, since the absence of water mitigates passive layer formation [6]. However, these electrolytes suffer from low current efficiency which limits their industrial scalability and the research is still on-going. Recently, a hybrid machining approach i.e. hybrid laser-electrochemical machining (LECM) was developed to circumvent the passivation and multiphase EC-dissolution challenges [7].

LECM can simultaneously apply the laser and ECM process energies at the machining zone, and the process parameters are controlled to avoid electrolyte boiling. Hence, the laser improves ECM material processing windows and capabilities by increasing the local current density, weakening the passive layer and enhancing reaction kinetics, making it promising for processing Ti6Al4V. Since LECM is being development for difficult-to-cut materials, it is necessary to evaluate its machining performance and process-material interactions using advanced materials currently facing machining challenges.

Therefore, the processing of Ti6Al4V is investigated for the first time with LECM using design of experiments (DOE) alongside ECM towards assessing and optimising the LECM machining performance. Furthermore, with the growing interest of AM for net shaping Ti6Al4V and subsequently, postprocessing it to improve surface integrity [8], as-built samples prepared through selective laser melting (SLM) [9] were used alongside monolythic rolled samples. The machining characteristics of the material and ECM/LECM were evaluated in terms of material removal rate (M.R.R.), surface roughness (*Sa*) and removal localisation, to correlate the LECM processing improvement as well as influence of material microstructure and process parameters. The results indicated that material processing improved with LECM whereas, the SLMed samples performed poorly owing to internal porosities and a less reactive martensitic microstructure.

2. Experimental

The experiments were conducted on the in-house built hybrid-LECM setup. The details of the process and experiments are provided in the following subsections.

2.1. Process principle

In the LECM process shown in Fig. 1, the laser and electrolyte flow coaxially through the tubular electrode for simultaneous application of the process energies in the machining zone. The tubular tool (1.2 mm O.D. and 0.65 mm I.D.) which has an inner quartz capillary serves as both the multimodal waveguide and ECM tool. The nanosecond (ns) pulsed green laser (532 nm) has the least absorption in water (α = 0.0045 /m) so, it mainly heats the workpiece surface. This focuses the least resistance current path towards the laser exit area and changes the ring shaped tool dependent current density distribution towards the center. These synergised effects lead to an increase in local current density which enhances transpassive dissolution, passivation weakening and removal localisation. The passive layer weakening is achieved via dissolution of material underneath the porous layer, which leads to layer flake-off with the electrolyte flow. Furthermore, the higher local current density with LECM provides sufficient energy to dissolve less reactive phases making it a promising technique for passivating multiphase materials like Ti6Al4V.
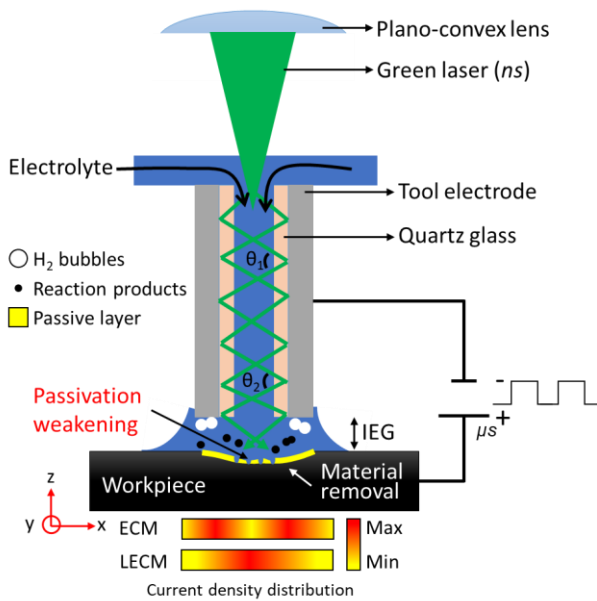
Figure 1. The process scheme of LECM process.

2.2. Experiments

The experiments were performed in 20% aq. sodium nitrate electrolyte (112 mS/cm at 20 °C) using a multi-level factorial design using parameters based on preliminary experiments (Table 1). The other fixed parameters were: 80 µm interelectrode gap (IEG), 0.35 mL/s electrolyte flow rate, 10 µs voltage pulse width at 50% duty cycle. The parameters for the LECM process mode were: 25 µJ laser pulse energy, 35 ns pulse width, 150 kHz pulse frequency. Two channels of 4 mm length were machined for each parameters combination on the 20x20x5 mm SLMed and rolled Ti6Al4V samples leading to a total of 48 experimental runs.

Table 1. Design of experiments (DOE) with factors and levels.

Parameter	Levels	Level values		
Material	2	Rolled	SLMed	-
Process Mode	2	ECM	LECM	-
Voltage	3	25 V	35 V	45 V
Feed rate	2	0.03 mm/s	0.06 mm/s	-

The scanning electron microscopy (SEM) images of the microstructure of etched samples are shown in Fig. 2. The rolled sample exhibited equiaxed α phase with β phase at grain boundaries whereas, the SLMed sample had an acicular α' martensitic microstructure due to rapid cooling during SLM. The SLMed sample had a density of 4.388 g/cm^3 (99.63% of rolled sample) due to the process generated porosity, which was also verified by the 0.16% defect volume measured by a CT scan.

After ultrasonic cleaning in deionized water for 20 mins, the samples were weighed on a Mettler Toledo® XS105 microbalance to calculate the M.R.R. and the channel dimensions were measured using the Keyence® VHS6000 digital microscope. The *Sa* was measured using Sensofar S neox with a 300x300 µm section area in the highest current density region (10x objective, L-filter 25µm, S-filter 2.5µm, ISO 16610-61). The DOE analysis was performed using Minitab®. Six measurements were performed for each experimental run.
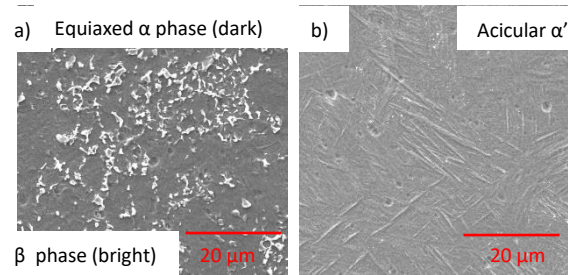
Figure 2. Microstructure of a) rolled and b) SLMed Ti6Al4V samples.

3. Results and discussion

The machining characteristics on the basis of M.R.R., *Sa* and channel dimensions measurements were used to investigate the influence of material, process parameters and processing improvement with LECM. These machining characteristics are discussed in the following subsections using the DOE analysis with main effects plots (error bars are standard errors of fitted means) and Pareto charts of the standardized effects with significance level at 95% of confidence level.

3.1. Material removal rate (M.R.R.)
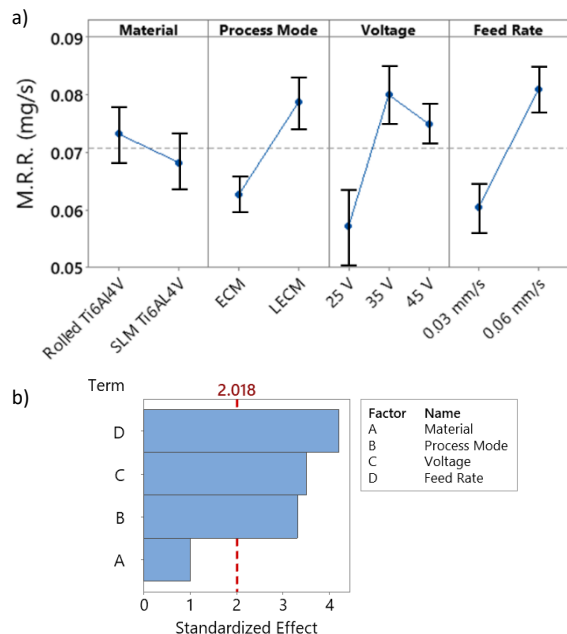
Figure 3. a) Main effects plots and b) Pareto chart for M.R.R.

The main effects plot (Fig. 3a) indicates that the material processing was 6.7% slower with the SLMed sample. This can be attributed to the less reactive martensitic phase. However, it seems that it did not have a significant influence on M.R.R.

(Fig. 3b) since the material composition was the same. The M.R.R. increased by 25% with LECM as the laser helped in increasing transpassive dissolution and passivation weakening, which was also a significant parameter. The influence of increasing voltage was peculiar since M.R.R. first increased (40%) and then decreased (6%). The increase in M.R.R. was expected since a higher voltage provides more current for material dissolution. The M.R.R. decrease at 45 V was probably due to increased joule heating which led to increase in re-passivation at the used electrolyte flow rate [10]. This heating was further increased during LECM at 45 V with possible boiling of small electrolyte packets. Feed rate was the most significant parameter and the M.R.R. increased by 34% with the higher feed rate of 0.06 mm/s. Faster scanning means that the gap is more clear due to less accumulation of by-products in the IEG, leading to improved material processing.

3.2. Surface roughness (*Sa*)
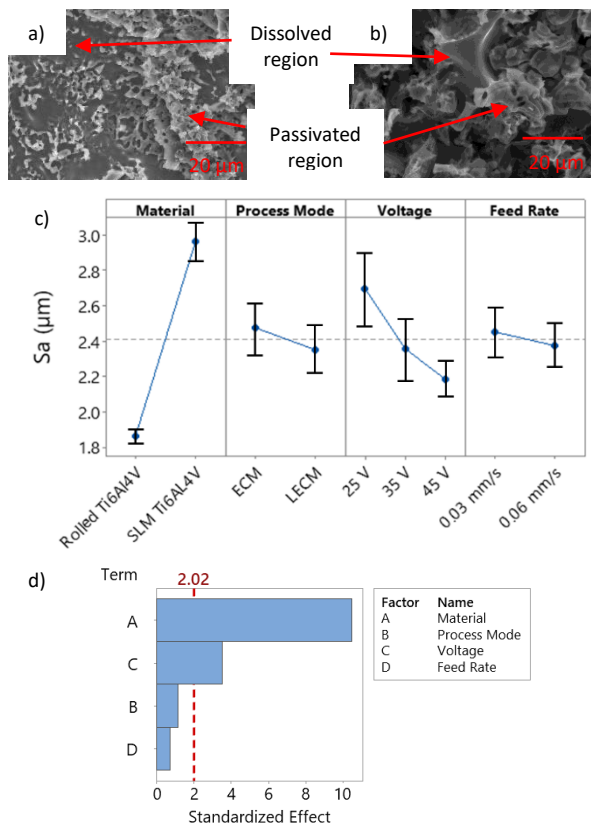
Figure 4. Machined surface (35 V and 0.06 mm/s) of a) rolled and b) SLMed samples. c) Main effects plots and d) Pareto chart for *Sa*.

The machined surfaces had distinct randomly distributed passivated and dissolved regions (Fig. 4a,b). *Sa* was selected to estimate the influence of LECM and process parameters in weakening the passivation to smoothen the surface. For the case of surface roughness, material was the most significant parameter (Fig. 4d) as the SLMed sample had a 59% higher *Sa* (Fig. 4c). This was due to the inherent rough surface (6.9±0.4 μm) of the as-built SLMed sample which was ~8 times higher than the rolled sample (0.86±0.03 μm). The porosity and less reactive microstructure possibly also played a role. The surface quality improved with both LECM and increasing voltage, which was expected since the surface asperities level out at higher current densities due to improved formation of the polishing salt film. The *Sa* was less sensitive (66%) to LECM than voltage because the primary dissolution mechanism is still anodic dissolution in LECM. Laser helps improve surface quality through increase in local current density which weakens passivation and enhances

uniform multiphase dissolution at a particular voltage level [7]. Whereas, increasing the voltage level has a larger influence as it significantly increases the current density which accelerates the polishing salt film formation. The *Sa* was least sensitive to feed rate since the relatively cleaner gap conditions at 0.06 mm/s may have slightly improved the uniformity of the current density distribution across the workpiece surface.

3.3. Channel dimensions
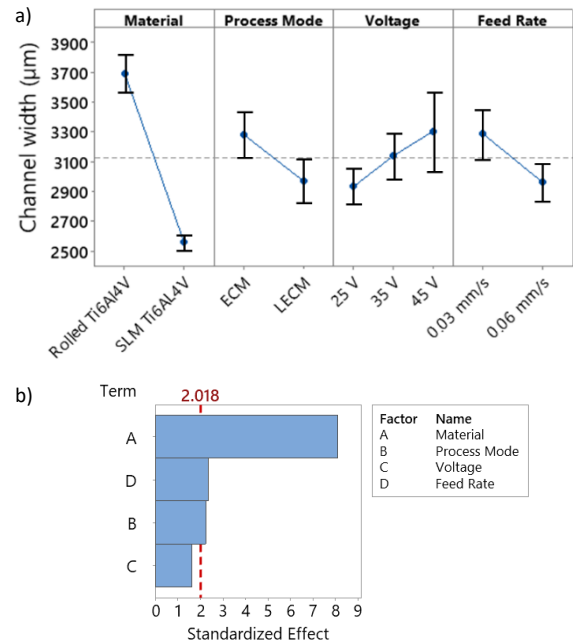
Figure 5. a) Main effects plots and b) Pareto chart for channel width.

The channel width and depth measurements represent removal localisation with LECM, process parameters and sample material.

The channels on rolled samples were 44% wider than SLMed samples at the same parameters (Fig. 5a), making material the most influential parameter (Fig. 5b). The passivation on the channel walls of the less reactive martensitic phase SLMed samples possibly created an overall higher resistance barrier which reduced lateral dissolution. The internal porosity also had an influence which is discussed with channel depth analysis. The tool feed rate and process mode had a similar degree of influence. At the higher feed rate the relatively uniform current density distribution reduces stray lateral dissolution and the less residence time reduces overall material removal, contributing to 11% width decrease. With LECM, the stray lateral dissolution reduces (9.5%) due to the change in current density distribution from ring shape to the laser exit area which reduces stray current around the tool [7]. Additionally, since the laser is directed towards the depth direction, the increase in local current density primarily weakens the passive layer on the channel basal surface and wall passivation is largely unaffected, which helps in removal localisation. This makes LECM especially suitable for processing passivating materials. Interestingly, the channel width was least sensitive to voltage and increased (~7%) with voltage, since a higher voltage leads to increased stray current around the tool.

Similar to channel width, the depth was most sensitive to material with 45% deeper channels on SLMed samples than rolled samples (Fig. 6). The higher channel depth and lower width of SLMed samples are largely influenced by the manufacturing process induced internal keyhole porosity. As the material dissolution front progresses in the depth direction, the surface passivation layer on the rolled sample always exists

which hinders material removal. Whereas, in the SLMed sample as the dissolution front proceeds, the internal pores possibly get exposed which reveal fresh unpassivated surfaces thatbecome preferential dissolution sites. These fresh surfaces on the basal surface promote dissolution in the depth direction due to incomplete surface passivation as shown in Fig. 7. LECM further accelerates this mechanism due to improved passivation weakening on the basal surface. This finding may provide the manufacturing community a new approach for engineering the part to posses high porosity at locations that require postprocessing after AM to facilitate easier material removal and precision. Apart from this, feed rate also had a significant influence as the depth decreased by 39% with higher feed rate owing to the decreased residence time. With voltage increase to 35 V the depth increased by 44% due to higher current density but decreased by 6% upon further increase to 45 V due to increased heating and re-passivation which are amplified by LECM [10]. This decrease at 45 V was also reflected in the decrease in M.R.R. since dissolution retardation and depth decrease by increased re-passivation had a larger influence than increase in channel width. Furthermore, LECM increased channel depth due to passivation weakening (Fig. 7) and removal localisation however, compared to other parameters its influence was less significant as the laser improves EC-processing at a particular voltage level.
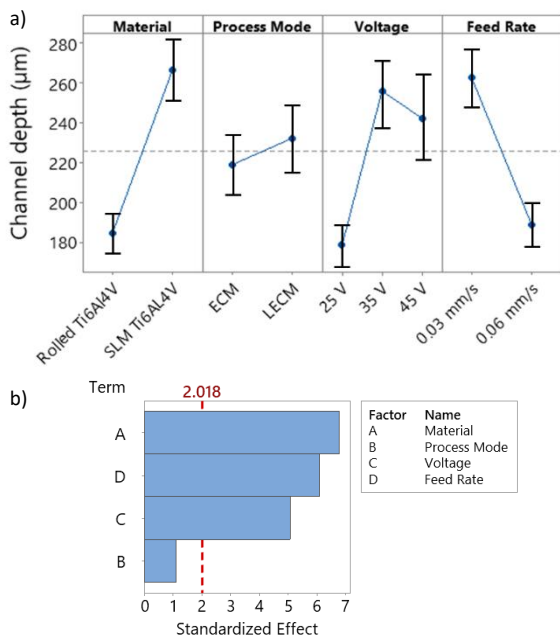
Figure 6. a) Main effects plots and b) Pareto chart for channel depth.
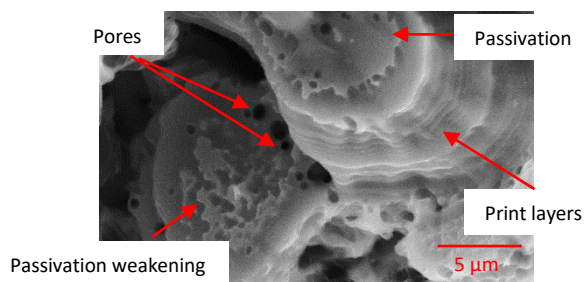
Figure 7. Processed surface of SLMed sample with LECM at 35 V and 0.06 mm/s with exposed pores.

4. Conclusion

The machining characteristics of Ti6Al4V samples in ECM and LECM produced by rolling and SLM were investigated in this study. The different manufacturing process dependent microstructure has a lower influence on the removal behaviour governed by first principles (M.R.R.) due to the same material composition. However, the combined effect of microstructure and internal porositiy considerably affects the surface topography and shape morphology. The less reactive martensitic phase of SLMed samples decreases material removal and stray dissolution whereas, the internal porosities expose unpassivated sites on the basal surface that preferentially dissolve to increase channel depth. This is interesting for manufacturing engineers to optimise the AM part design for postprocessing. The synegistics effects of LECM improved material processing for both samples and it performed better on all the criteria studied as long as the adverse heating effects are avoided by controlling the process parameters. These aspects make LECM promising for machining passivating multiphase materials and will be explored in the future on more 'difficult-to-cut' and 'difficult-to-dissolve' materials as means to improve surface integrity and machining localisation.

References

[1] F. Klocke, M. Zeis, A. Klink, and D. Veselovac, "Experimental research on the Electrochemical Machining of modern titanium- and nickel-based alloys for aero engine components," *Procedia CIRP*, vol. 6, pp. 368–372, 2013.

[2] B. Vrancken, L. Thijs, J. P. Kruth, and J. Van Humbeeck, "Heat treatment of Ti6Al4V produced by Selective Laser Melting: Microstructure and mechanical properties," *J. Alloys Compd.*, vol. 541, pp. 177–185, 2012.

[3] K. K. Saxena, J. Qian, and D. Reynaerts, "A review on process capabilities of electrochemical micromachining and its hybrid variants," *Int. J. Mach. Tools Manuf.*, vol. 127, no. July 2017, pp. 28–56, 2018, doi: 10.1016/j.ijmachtools.2018.01.004.

[4] A. Speidel, J. Mitchell-Smith, I. Bisterov, and A. T. Clare, "Oscillatory behaviour in the electrochemical jet processing of titanium," *J. Mater. Process. Technol.*, vol. 273, no. May, p. 116264, 2019, doi: 10.1016/j.jmatprotec.2019.116264.

[5] S. Hizume and W. Natsu, "Problems and solutions in scanning electrochemical machining of titanium alloys," *Procedia CIRP*, vol. 95, pp. 712–716, 2020, doi: 10.1016/j.procir.2020.02.285.

[6] W. Liu, Z. Luo, and M. Kunieda, "Electrolyte jet machining of Ti1023 titanium alloy using NaCl ethylene glycol-based electrolyte," *J. Mater. Process. Technol.*, vol. 283, no. April, p. 116731, 2020, doi: 10.1016/j.jmatprotec.2020.116731.

[7] K. K. Saxena, J. Qian, and D. Reynaerts, "A tool-based hybrid laser-electrochemical micromachining process: Experimental investigations and synergistic effects," *Int. J. Mach. Tools Manuf.*, vol. 155, no. May, p. 103569, 2020.

[8] H. Zeidler and F. Böttger-Hiller, "Plasma-Electrolytic Polishing as a Post-Processing Technology for Additively Manufactured Parts," *Chemie-Ingenieur-Technik*, vol. 94, no. 7, pp. 1024–1029, 2022, doi: 10.1002/cite.202200043.

[9] J. Metelkova, C. De Formanoir, H. Haitjema, A. Witvrouw, W. Pfleging, and B. Van Hooreweder, "Elevated edges of metal parts produced by laser powder bed fusion : characterization and post-process correction," *Proc. Spec. Interes. Gr. Meet. Adv. Precis. Addit. Manuf.*, no. September, pp. 1–4, 2019.

[10] M. H. Arshad, M. Wu, K. K. Saxena, and D. Reynaerts, "Analysis of passivation during ECM and hybrid laser-ECM through automated current pulse analysis," in *18th International Symposium on Electrochemical Machining Technology*, 2022, pp. 123–130.

Additive Manufacturing of hard magnetic materials via Cold Spray Additive Manufacturing

E. Uhlmann[1, 2], J. Polte[1, 2], T. Neuwald[1], J. Fasselt[1], T. Hocke[2]

[1]*Fraunhofer Institute for Production Systems and Design Technology IPK, Germany*
[2]*Institute for Machine Tools and Factory Management IWF, Technische Universität Berlin, Germany*

tobias.neuwald@ipk.fraunhofer.de

Abstract

The Additive Manufacturing of hard magnetic materials, used in applications such as electrical drives, is achieved by exploiting the special characteristics of the Cold Spray Additive Manufacturing (CSAM) technology. This work aims to develop processing parameters for the Additive Manufacturing of magnets made of a neodymium-iron-boron-alloy (NdFeB). In order to enable the manufacturability using CSAM, a pure aluminium binder with a mass fraction of $w_{Al;a}$ = 25 wt. % and $w_{Al;b}$ = 10 wt. % was added to two different NdFeB powders with the particle size distributions of $D_{50;NdFeB;a}$ = 5 μm and $D_{50;NdFeB;b}$ = 22 μm. For this study, the gas pressure p_g was varied between 4 MPa ≤ p_g ≤ 6 MPa and the resulting remanence B_r and coercivity H_{cj} were analysed. A material combination and parameter set for the Additive Manufacturing of magnetic material via CSAM with a magnetic remanence of B_r = 414 mT and an intrinsic coercivity of H_{cj} = 854 kA/m was derived.

Additive Manufacturing, Cold Spray, Electrical Drives, Magnets

1. Introduction

Electrical drives play a pivotal role in steering various industries and the transportation sector away from combustion engines and fossil fuels in order to meet stricter environmental regulations. As a key part for rotors of electrical drives, magnets are responsible for 53 % of the total costs [1]. This is in part caused by the current manufacturing technologies, such as sintering, with a low shape complexity, expensive tooling and the need for assembly processes [2]. Additive Manufacturing technologies, such as CSAM enable the direct manufacturing of complex shapes onto rotors without tooling, thus increasing flexibility [3, 4]. LAMARRE AND BERNIER [5] showed, that CSAM can be used to produce magnets with good comparable magnetic properties at various fixed processing parameters. As a key process parameter for achieving layer binding, the influence of gas pressure p_g on the magnetic properties of remanence B_r and coercivity H_{cj} has yet to be investigated.

2. Experimental procedures

In order to investigate the effects of the gas pressure p_g on remanence B_r and coercivity H_{cj}, cubic samples measuring 5 mm x 5 mm x 5 mm were manufactured using an Impact Spray System 6/10 EvoCSII from IMPACT INOVATIONS GMBH, Rattenkirchen, Germany. Magnetic charging and measurement were carried out with a pulsed current generator in an axial coil by M-PULSE, Berlin, Germany.

3. Powder material

Four powder mixtures were prepared and tested. The particle size distribution D_{50} of the individual powders was examined with a Camsizer X2 from MICROTRAC RETSCH GMBH, Haan, Germany. Figure 1 shows the fractions p_3 and the cumulative distribution Q_3 of the processed powder.
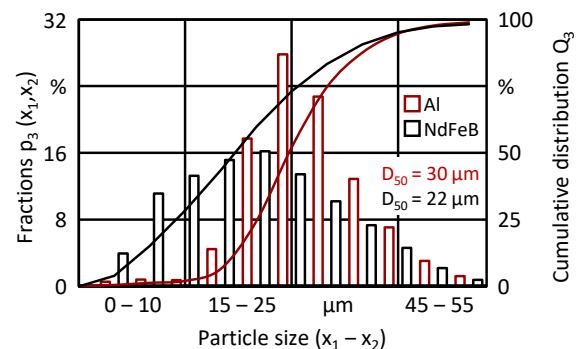
Figure 1: Particle size distribution of Al and NdFeB powder

Magnequench MQP 14-12 Isotoropic NdFeB Powders from MAGNEQUENCH INTERNATIONAL INC., Singapur with a particle size distribution of $D_{50;NdFeB;a}$ = 5 μm and $D_{50;NdFeB;b}$ = 22 μm were mixed with 99.7 % pure aluminium powder from TOYAL-EUROPE, Guyancourt, France with a particle size distribution of $D_{50;Al}$ = 30 μm in a mass fraction $w_{Al;a}$ = 25 wt. % and $w_{Al;b}$ = 10 wt. %.

3.1 Processing parameters

For this investigation, the gas pressure p_g was varied while the gas temperature $θ_g$, nozzle distance l_{gun}, spray angle α and travel speed v_{gun} were kept constant. Table 1 shows an overview of the processing parameters.

Table 1. Processing parameters

Parameter		Value
Gas pressure	p_g	40 MPa – 60 MPa
Gas temperature	$θ_g$	500 °C
Nozzle distance	l_{gun}	30 mm
Spray angle	α	90 °
Travel speed	v_{gun}	500 mm/s

4. Experimental results

The properties remanence B_r and coercivity H_{cJ} are key indicators to evaluate the performance of magnets. Figure 2 shows the remanence B_r and coercivity H_{cJ} of the manufactured cubic samples for different material combinations and varying gas pressures p_g. Firstly, it was established that a test specimen can be produced for each combination of material and gas pressure p_g. Due to material constraints, only one sample per parameter combination was produced. Therefore, the determined values could not be checked statistically and variation of parameters was limited. Looking at the influences of material and gas pressure p_g, it

can be determined, that choosing the right magnetic material and mass fraction w_{Al} is more important than choosing the right gas pressure p_g when optimizing magnetic properties. Specifically focusing on particle size distribution $D_{50;NdFeB}$, for an identical mass fraction w_{Al}, the measured data shows that a particle size distribution $D_{50;NdFeB;b} = 22$ µm yields a better remanence B_r compared to $D_{50;NdFeB;a} = 5$ µm. On the other hand, coercivity H_{cJ} is improved when choosing larger particle size distribution $D_{50;NdFeB}$. The highest combined values of remanence $B_r = 414$ mT with a high coercivity of $H_{cJ} = 741$ kA/m was achieved with a mass fraction $w_{Al,b} = 10$ % and a particle size distribution $D_{50,NdFeB;b} = 22$ µm at a gas pressure $p_g = 5$ MPa.

▲ $D_{50;NdFeB;b} = 22$ µm; $w_{Al;a} = 25$ wt. %
☐ $D_{50;NdFeB;a} = 5$ µm; $w_{Al;a} = 25$ wt. %
⬤ $D_{50;NdFeB;b} = 22$ µm; $w_{Al;b} = 10$ wt. %
◆ $D_{50;NdFeB;a} = 5$ µm; $w_{Al;b} = 10$ wt. %

Process:
Cold Spray Additive Manufacturing
with Impact Spray System 6/10 EvoCSII

Parameters:

Θ_g	=	550 °C
a_d	=	30 mm
v_{gun}	=	500 mm/s
Process gas	=	Nitrogen
Binder	=	Aluminium

Figure 2: Remanence B_r and coercivity H_{cJ} in dependency of the gas pressure p_g with respect to particle size distribution D_{50} and mass fraction w_{Al}

5. Conclusion and outlook

This paper shows, that it is possible to manufacture magnets using CSAM. It can be concluded, that a bigger particle size distribution $D_{50;NdFeB}$ and a lower mass fraction of aluminium w_{Al} lead to a better remanence B_r. It was also shown, that a higher coercivity H_{cJ} is achieved when using a smaller mass fraction of aluminium w_{Al}. The influence of the gas pressure p_g was negligible when compared to the influence of the magnetic material. The best achieved remanence $B_r = 414$ mT and coercivity $H_{cJ} = 854$ kA/m translate to a relative remanence $B_{r;rel} = 50$ % and a relative coercivity $H_{cJ;rel} = 91$ % when compared to a conventionally sintered magnet, made from the same powder material. Especially an improvement of the relative remanence up to $B_R > 90$ % would enable the wide adaption of the process for manufacturing electrical drives. However, due to the freedom of design and tool-free manufacturing of complex shapes, Cold Spray offers a promising solution for manufacturing permanent magnets.

References

[1] Rogers, S.; Boyd S.: Overview of the DOE Advanced Power Electronics and Electric Motor R&D Program, *U.S. Department of Energy Report* (2014).

[2] Sugimoto, S.: Current status and recent topics of rare-earth permanent magnets. *Journal of Physics D: Applied Physics, Volume 44, Number 6* (2011).

[3] Vladimir Popov, V.; Koptyugb, A.; Radulovc, I.; Maccaric, F.; Muller, G.: Prospects of additive manufacturing of rare-earth and non-rare-earth permanent magnets. *Procedia Manufacturing, Volume 21* **100 – 108** (2018).

[4] Boulos, M. I.; Fauchais, P. L.; Heberlein J. V.: Thermal Spray Fundamentals: From Powder to Part. *Springer Nature Switzerland AG* **173 – 233** (2021).

[5] Lamarre J.; Bernier, F.:Permanent Magnets Produced by Cold Spray Additive Manufacturing for Electric Engines. *J Therm Spray Tech 28* **1709 – 1717** (2019).

In-situ transient current detection in local anodic oxidation nanolithography using conductive diamond-coated probes

Jian Gao[1], Wenkun Xie*[1], Xichun Luo[1]

[1]Centre for Precision Manufacturing, DMEM, University of Strathclyde, Glasgow, UK

w.xie@strath.ac.uk

Abstract

Achieving precise control over oxidation growth has become a key bottleneck in quality control in local anodic oxidation (LAO) nanolithography due to the lack of effective process monitoring and feedback control approaches. In this context, this paper proposed and presented an *in-situ* current detection approach to monitor the status of oxidation growth in real-time in the LAO processes using highly durable conductive diamond-coated probes. Research findings indicate that the use of diamond-coated probes can induce controllable LAO with transient current at the microampere level and create nanostructures with heights exceeding 18 nm, which are notably superior to those obtained using doped silicon probes. It was also demonstrated that, within a certain range of voltage, the detected current could reflect the oxidation growth during the fabrication of nanolines, with the detected current correlating to the conductivity of the oxidised surface, indicating the extent of oxidation. It is expected that the combination with flexible pulse modulation will promise a flexible and simple approach to tuning oxidation growth, paving the way for the production of high-quality oxide lines.

Atomic force microscopy, Monitoring, Nano manufacturing, Oxidation

1. Introduction

Local anodic oxidation (LAO) nanolithography is emerging as a flexible and versatile nanofabrication technique [1,2] to advance the development of next-generation nano and quantum devices, such as nanopore-based single molecule detection devices [3], nanowire transistors [4], nanooptics [5], etc. Through applying a positive voltage to the substrate with respect to the probe in ambient or environment-controlled condition, LAO can create nanostructures on various materials with a variety of shapes [1,6,7]. Moreover, it has shown various advantages, including atomic-level resolution, direct surface patterning, high reproducibility and compatibility, and low environmental requirements and instrument costs [1]. However, as LAO is a complex electric field-assisted nano-oxidation process [8], the final quality of the processed structures is controlled by various parameters, such as voltage amplitude and duration, substrate materials, environmental humidity, tip scan parameters, etc. Due to its open-loop nature, the lack of effective process monitoring and feedback control approaches has become a key challenge in achieving precise quality control in the LAO process.

Fundamentally, LAO is an electrochemical reaction process, with the oxidation growth governed by Faradaic current. Thus, in-situ detection of Faradaic current is a dominant factor that reflects the reaction status and promises to become an ideal indirect measurement target to create an effective process monitoring and feedback-controlled process [9]. In previous studies, current detection has been performed in combination with various analyses for LAO on silicon surfaces. Avouris et al. [10,11] measured current evolution during LAO and found it aligned with Faraday current calculated from the measured volume growth according to the electrochemical reaction:

$$Si + 4h^+ + 2OH^- \rightarrow SiO_2 + 2H^+ \qquad (1)$$
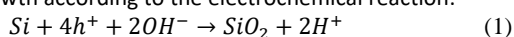
noting a charge efficiency of 50%. Similarly, Ruskell et al. [12] associated the current observed during LAO with the reduction of H^+ ions on the AFM probe. Dagata et al. [13,14] determined that the majority of current in high voltage LAO does not contribute to surface oxide growth. They also investigated the roles of ionic and electrical contributions during LAO, finding that contact currents were much larger than noncontact despite similar volumes. Martin et al. [15] simultaneously measured force and current versus tip-surface distance, successfully gauging the electrical conductivity of the water meniscus. Murano et al. [16] focused on the initial moments of LAO through measuring current during tip separation from the surface, which provided insights into oxide growth kinetics, the influence of meniscus geometry on electrical conduction, and the role of space charge at small tip-sample distances. Kuramochi et al. [17–20] achieved precise current detection at sub-picoampere levels by enclosing electronic components in a sealed unit, eliminating the effects of humidity. They monitored the LAO process using Faradaic current detection, noting that current flow starts promptly once the tip-substrate bias exceeds a certain threshold and decreases over time as oxidation progresses. Kuramochi et al. [21] also used current detection in carbon nanotube probe-induced LAO, demonstrating sensitivity for detecting thin oxides and small features, and evaluated the meniscus dimension during nano-oxidation through *in-situ* Faradaic current detection and edge broadening. Current detection was also performed for LAO on other substrates. Kim et al. [22] explored the reaction kinetics of LAO on Ti substrates using transient current data, revealing insights into space charge buildup and oxide morphology, and determined the optimal exposure time. Kuang et al. [23] studied LAO in Ti thin films, finding a linear relationship between protrusive oxide line heights, applied voltages, and tunneling currents. Perez-Okada et al. [24] measured the current during the LAO of GaAs and found that the electron transport follows the Fowler-Nordeim

tunnelling mechanism over a range of bias. They also studied the current flow, which revealed the relationships between Faradaic current and leakage current in LAO processs [25]. Fernandez-Cuesta et al. [26,27] disclosed two distinct AFM-induced oxidation mechanisms on thin Si_3N_4 layers on silicon by studying the kinetics via electrical current detection during LAO: the transformation of Si_3N_4 to silicon oxide, and the integration of silicon into the base of the Si_3N_4 layer. Shimada et al. [28] and their group [29] investigated the Faradaic current during the LAO of NiFe thin films and Si substrates. They discovered that LAO on silicon consistently shows a 50% current efficiency, unaffected by tip scan speed, and that larger nano-oxide structures result from increased bias voltage. In addition, they found that NiFe exhibited lower current efficiency than silicon, with excess non-oxidative current that could be minimised by insulating oxide layers, which also stabilised oxidation due to their hydrophilicity, benefiting nanostructure and nanodevice fabrication. Schneegans et al. [30] noted Faradaic currents were minimal compared to total current in the AFM probe contact-junction during the LAO of $(TMTSF)_2PF_6$. Faucett and Mativetsky [31] conducted in-situ current measurements during oxide reduction on graphene, revealing that the process is rate-limited, governed by the generation and transport of hydrogen ions. Martin et al. [32] monitored the current during the LAO of PMMA films, uncovering a local electrochemical reaction involving the transport of OH^- ions through the PMMA.

In addition to mechanism study, *in-situ* current detection promises the feedback current control of the LAO process, with potentials to achieving improvement of accuracy and controllability of LAO for rapid prototyping of nanoproducts or devices. However, this has rarely been reported in comparison with using current detection to reveal reaction mechanisms. Johannes et al. [33] developed a velocity-controlled approach for LAO nanolithography through adjusting translational speed in reaction to in-situ detected current fluctuations. This method successfully maintains a steady current flow at the tip-sample interface, proving to be effective for real-time quality control. Pellegrino et al. [34] used current as a feedback to perform voltage controlled LAO nanolithography on $SrTiO_{3-\delta}$ thin films. They demonstated that constant current control can realise lines with uniform widths down to 150 nm over a total length of hundreds of micrometers. However, these methods were focusing on structures with simple shapes, limiting their applications in developing next-generation nanoscale products and devices. Constant current power supply was also used for LAO, in order to achieve consistent oxidation. Through this method, the single-electron transistor [35] and self-aligned gate structures [36] were fabricated. However, there have been relatively few studies of LAO on silicon using diamond-coated probes. It is not clear what effect the conductive diamond coating will have on oxidation growth and current characteristics while bringing improved wear resistance and conductivity.

In this work, we studied the LAO experiments using conductive diamond probes and silicon substrates in combination with *in-situ* current monitoring, aiming to reveal more insights on the oxidation growth and current features. We expect this study can provide necessary guidance to develop feedback-controlled, reliable, and durable LAO nanofabrication process.

2. Methods

LAO experiments and monitoring were performed using a Bruker D3100 atomic force microscope (AFM) combined with a pulse generator power supply (Aim-TTi TGF4042) and D22 picoammeter. During the LAO, AFM is operated under contact mode with the vertical position of the cantilever kept constant by maintaining the same referenced setpoint. The schematic of

LAO reaction is illustrated in **Figure 1**. To induce oxidation, a voltage signal was introduced onto the AFM, with the conductive probe at a negative bias to the sample substrate. The bias could induce the formation of highly nonuniform electric field between the tip and sample, further inducing a series of physical and chemical reactions, enabling the nanopatterning on the sample surface. In an atmosphere of a certain humidity, tip-sample interface is filled with water. The applied voltage induces current passing through from the substrate to the probe, which is measured using a picoammeter. As concluded in previous research [25], the transient current during contact-mode LAO includes two different types, Faradaic current and electrical current (ohmic and tunnelling), while the Faradaic current is responsible for the electrochemical reaction within the water bridge and forms the oxides in the reaction region.

The wafer used in this work has been double-side polished, resulting in a surface roughness (Ra) of less than 0.3 nm. Before performing the LAO experiment, the wafers were cleaved into small pieces using a diamond cutter. Then, these small-piece samples were cleaned by sonication in an $NH_4OH/H_2O_2/H_2O$ (1:1:5) solution for 10 mins to remove surface contaminations. Finally, they were rinsed with deionised water and blown with a dry N_2 gas jet. Conductive AFM probes (model CDT-CONTR) with a nominal tip radius between 100 and 200 nm and nanoroughness of 10 nm were used for the nanofabrication and imaging. These probes were made by silicon cantilevers with highly doped diamond coatings to increase the conductivity and wear resistance. Given the significant impact of humidity on the LAO process, the nanofabrication conducted in this work was always carried out under atmospheric conditions (20 °C) with relative humidity at 25–30%. To ensure precise humidity control, a hygrometer with an accuracy of ±1% was employed to monitor and maintain the desired humidity levels throughout the experiments. The oxide patterns were imaged right after their creation, and the AFM images were analysed using the Bruker NanoScope Analysis 1.7 software.
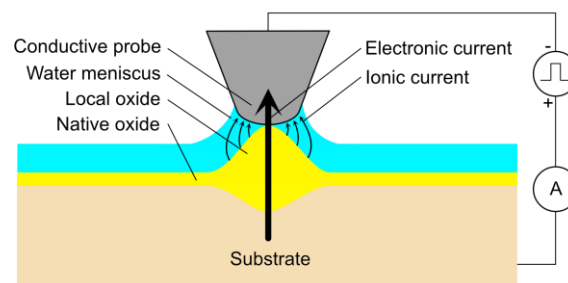
Figure 1. Schematic of local anodic oxidation with current feedback.

3. Results and discussions

This experiment encompasses the fabrication of nanodots and nanolines, with the evaluation involving current measurement and topographical mapping of the resulting nanostructures.

3.1 Dots

Nanodots were generated by applying two pulses separately with the voltages of 8 and 9 V and the same duration of 5 s to a static probe in contact with the surface. This process produced two distinct nanodots by maintaining the probe's position over targeted areas on a silicon surface. The morphology of the nanodots and their cross-sectional profiles are depicted in **Figure 2** (a) and (b). The results indicate that the oxide dots have heights of 11.8 and 13.6 nm, respectively, significantly surpassing the heights of oxide dots fabricated in prior studies using contact conductive probes [18]. The progression of the transient current during LAO is illustrated in **Figure 2** (c). It is evident that an increased pulse amplitude can promote

oxidation growth and augment current flow. In addition to the enhanced oxidation resulting from this increased current, the low stiffness of the cantilever may also contribute to the process by imposing fewer constraints on oxidation development.

Contrary to the patterns observed by Dagata et al. [13] and other researchers, where current typically first reached a peak and then decreased over the pulse duration, the current in our study fluctuated between 3 and 8 µA. This current is significantly higher than the anticipated Faraday current, calculated based on experimentally measured volume growth and incorporating charge transfers for a standard silicon anodic reaction, as per Equation (1). Our measured current exceeds the calculated value by more than six orders of magnitude. The findings indicate that the majority of the measured current is electrical, with the Faradaic current responsible for oxidation growth, representing only a small portion. This could be due to the probe's low resistance and the substrate's thinness, allowing for a greater flow of electrical current during the LAO process. As shown in **Figure 1**, additional leakage pathways will also be generated, which contributes to the recorded current and extend beyond the Faraday current and direct tunnel current through the oxide layer. These observations are consistent with previous research [25].
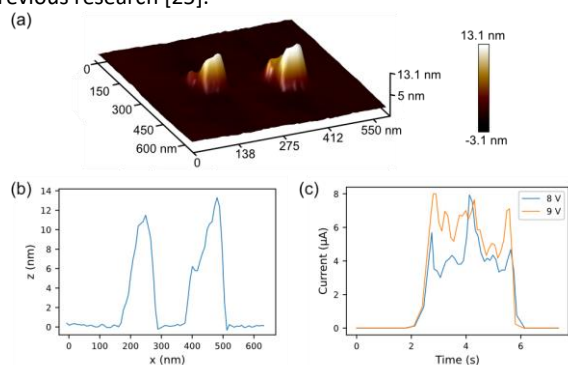
Figure 2. (a) Schematic of oxide dots created by LAO. (b) Cross-sectional profile for two nanodots. (c) Current evolution during LAO.

3.2 Nanolines

Nanolines are commonly fabricated to demonstrate their practical use in the device development of transisters and sensors [4]. In our study, we applied a sequence of pulses to conductive diamond probes at the same scanning speed of 200 nm/s to assess the production of oxide nanolines. These pulses were of uniform duration, each lasting 4 seconds.

Implementing four pulses with amplitudes ranging from 5 to 9 V resulted in the formation of four distinct line nanostructures, as depicted in **Figure 3** (a). **Figure 3** (b) and (c) demonstrate that both the height of the oxide lines and the transient current surge correlated with an increase in pulse amplitude from 5 to 9 V. Oxide lines with relatively consistent shapes were observed with pulse amplitudes between 5 to 7 V. Above 7 V, the oxidation process appeared discontinuous, exhibiting multiple peaks with heights fluctuating between 8 to 18 nm, as observed in **Figure 3** (d). The maximum oxide height appears to be around 18 nm, which is much higher than the results obtained from LAO using doped silicon probes. We posit that the intermittent formation of oxide lines stems from an unstable water meniscus, likely due to ununiform water film thickness at low humidity conditions. According to previous conclusions from experimental and simulation results [7,37], LAO at higher voltages can incur intense oxidation, leading to rapid oxide growth and simultaneous depletion of the water meniscus. This process can occur so rapidly that water diffusion fails to replenish the water meniscus sufficiently to maintain consistent oxidation. Therefore, while the tip scans, the LAO leads to intermittent

oxide lines. In contrast, at lower voltages, severe oxidation is less likely to happen, allowing for a continuous oxidation process with an adequate consumption of water. As a result, this leads to the formation of oxide lines with fairly continuous shapes. However, the nanolines created do not seem to be straight but present a curved shape compared with the nanolines created by tapping-mode LAO [6]. The underlying reason could be the randomness during the lateral diffusion of oxynians during contact-mode LAO. The large-radius probe in contact with the sample increases the linewidth and at the same time, facilitates the oxidation growth at lateral direction, making the centre of oxide lines not directly underneath the tip.

The current detected during our experiments is significantly higher than the Faradaic current calculated from the oxidation growth volume by approximately a million times. Consequently, we are unable to observe the expected changes in Faradaic current, such as peak heights corresponding to maximum current. Interestingly, at certain points, an inverse relationship was observed, where insufficient oxide growth led to higher current levels, as shown in **Figure 3** (b). It is hypothesised that the current flowing through the tip depends on the height of oxide protrusions at the tip-sample contact region. Since LAO reaction can happen in a very short time scale of picoseconds, the detected current mainly reflects the electrical current passing through the reaction cell, which is mainly affected by the conductivity of a closed circuit. These results agree well with a previous study on LAO using Rh-coated probes [33], demonstrating that the current detection can serve as a process monitoring approach that reflects the difference in the oxidation status due to the variation in the oxidation conditions.
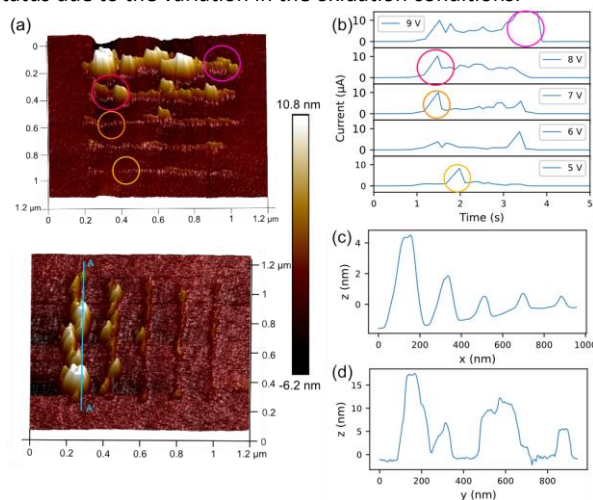
Figure 3. (a) Schematic of oxide lines created by LAO. (b) Current evolution during LAO. (c) Average height profile from 'Step' analysis. (d) Cross-sectional profile along A-A'.

4. Conclusions

This paper details the nanofabrication outcomes and current monitoring used for LAO nanolithography with conductive diamond probes. By fabricating nanoscale dots and lines and monitoring transient currents, we have deepened our understanding of the LAO process using these probes. Notably, these probes can induce LAO to create oxide dots exceeding 18 nm in height, surpassing the results achieved with doped silicon probes. Current measurements indicate that the transient current is significantly higher than expected and previously reported, reaching microampere levels. This suggests that the Faradaic current constitutes only a small fraction of the total current. However, the measured transient current can indicate the degree of oxidation, as higher currents typically occur in areas where oxidation is insufficient.

This study establishes current detection as a valuable tool for real-time monitoring in LAO nanolithography, offering insights into the reaction process as it occurs. Looking ahead, integrating this approach with a feedback-controlled system, complemented by pulse modulation, holds great potential for augmenting LAO's nanofabrication capabilities, particularly in enhancing durability, reliability, and controllability. These aspects will form the cornerstone of our future research endeavors.

Acknowledgements

References

[1] Ryu Y K and Garcia R 2017 Advanced oxidation scanning probe lithography *Nanotechnology* **28** 142003

[2] Fan P, Gao J, Mao H, Geng Y, Yan Y, Wang Y, Goel S and Luo X 2022 Scanning Probe Lithography: State-of-the-Art and Future Perspectives *Micromachine* **13** 228

[3] Ovenden C, Farrer I, Skolnick M S and Heffernan J 2022 Nanoscale wafer patterning using SPM induced local anodic oxidation in InP substrates *Semicond. Sci. Technol.* **37** 025001

[4] Chiesa M, Cardenas P P, Otón F, Martinez J, Mas-Torrent M, Garcia F, Alonso J C, Rovira C and Garcia R 2012 Detection of the Early Stage of Recombinational DNA Repair by Silicon Nanowire Transistors *Nano Lett.* **12** 1275–81

[5] Chen C-F, Tzeng S-D, Chen H-Y and Gwo S 2005 Silicon microlens structures fabricated by scanning-probe gray-scale oxidation *Opt. Lett.* **30** 652

[6] Luo X C, Gao J, Xie W K, Hasan R Md M and Qin Y 2023 Flexible single-step fabrication of programmable 3D nanostructures by pulse-modulated local anodic oxidation *CIRP Annals* **72** 177–80

[7] Gao J, Luo X C, Xie W K, Qin Y, Hasan R Md M and Fan P F 2023 Atomistic insights into bias-induced oxidation on passivated silicon surface through ReaxFF MD simulation *Applied Surface Science* **626** 157253

[8] Dagata J A, Schneir J, Harary H H, Evans C J, Postek M T and Bennett J 1990 Modification of hydrogen-passivated silicon by a scanning tunneling microscope operating in air *Appl. Phys. Lett.* **56** 2001–3

[9] Fan Z, Xiaochen Hu, and Robert X. Gao 2022 Indirect Measurement Methods for Quality and Process Control in Nanomanufacturing *Nanomanuf Metrol* **5** 209–29

[10] Avouris P, Martel R, Hertel T and Sandstrom R 1998 AFM-tip-induced and current-induced local oxidation of silicon and metals *Applied Physics A: Materials Science & Processing* **66** S659–67

[11] Avouris P, Hertel T and Martel R 1997 Atomic force microscope tip-induced local oxidation of silicon: kinetics, mechanism, and nanofabrication *Appl. Phys. Lett.* **71** 285–7

[12] Ruskell T G, Pyle J L, Workman R K, Yao X and Sarid D 1996 Current-dependent silicon oxide growth during scanned probe lithography *Electronics Letters* **32** 1411–2

[13] Dagata J A, Perez-Murano F, Martin C, Kuramochi H and Yokoyama H 2004 Current, charge, and capacitance during scanning probe oxidation of silicon. I. Maximum charge density and lateral diffusion *J. Appl. Phys.* **96** 2386–92

[14] Dagata J A, Perez-Murano F, Martin C, Kuramochi H and Yokoyama H 2004 Current, charge, and capacitance during scanning probe oxidation of silicon. II. Electrostatic and meniscus forces acting on cantilever bending *Journal of Applied Physics* **96** 2393–9

[15] Martin C, Murano F P and Dagata J A 2003 Measurements of electrical conductivity of a nanometer-scale water meniscus by atomic force microscopy 2003 Third IEEE Conference on Nanotechnology, 2003. IEEE-NANO 2003. vol 2 pp 781–4 vol. 2

[16] Pérez-Murano F, Martín C, Barniol N, Kuramochi H, Yokoyama H and Dagata J A 2003 Measuring electrical current during scanning probe oxidation *Applied Physics Letters* **82** 3086–8

[17] Kuramochi H, Tokizaki T, Yokoyama H and Dagata J A 2007 Why nano-oxidation with carbon nanotube probes is so stable: I. Linkage between hydrophobicity and stability *Nanotechnology* **18** 135703

[18] Kuramochi H, Pérez-Murano F, Dagata J A and Yokoyama H 2004 Faradaic current detection during anodic oxidation of the H-passivated p-Si(001) surface with controlled relative humidity *Nanotechnology* **15** 297–302

[19] Kuramochi H, Ando K, Tokizaki T and Yokoyama H 2004 In situ detection of faradaic current in probe oxidation using a dynamic force microscope *Applied Physics Letters* **84** 4005–7

[20] Kuramochi H, Ando K and Yokoyama H 2003 Minute Current Detection during Anodic Oxidation by Atomic Force Microscope At High Humidity *Jpn. J. Appl. Phys.* **42** 5892–5

[21] Kuramochi H, Ando K, Shikakura Y, Yasutake M, Tokizaki T and Yokoyama H 2004 Nano-oxidation and in situ faradaic current detection using dynamic carbon nanotube probes *Nanotechnology* **15** 1126

[22] Kim T Y, Ricci D, Zitti E D and Cincotti S 2007 A study of the transient current during the formation of titanium oxide nanodots by AFM anodic oxidation *Surface Science* **601** 4910–4

[23] Kuang D, Liu Q, Guo W, Zhang S and Hu X 2005 Current detection during tip-induced anodic oxidation of titanium by atomic force microscope *Nanophotonics, Nanostructure, and Nanometrology* Nanophotonics, Nanostructure, and Nanometrology vol 5635 (SPIE) pp 305–12

[24] Okada Y, Iuchi Y, Kawabe M and Harris J S Jr 2000 Basic properties of GaAs oxide generated by scanning probe microscope tip-induced nano-oxidation process *Journal of Applied Physics* **88** 1136–40

[25] Okada Y, Iuchi Y and Kawabe M 2000 Scanning probe microscope tip-induced oxidation of GaAs using modulated tip bias *Journal of Applied Physics* **87** 8754–8

[26] Fernandez-Cuesta I, Borrisé X and Pérez-Murano F 2005 Atomic force microscopy local oxidation of silicon nitride thin films for mask fabrication *Nanotechnology* **16** 2731–7

[27] Fernandez-Cuesta I, Borrisé X and Pérez-Murano F 2006 Atomic force microscopy local anodic oxidation of thin Si3N4 layers for robust prototyping of nanostructures *Journal of Vacuum Science & Technology B: Microelectronics and Nanometer Structures Processing, Measurement, and Phenomena* **24** 2988–92

[28] Shimada Y, Yamada T, Shirakashi J and Takemura Y 2008 Measurement of Reaction Current during Atomic Force Microscope Local Oxidation of Conductive Surfaces Capped with Insulating Layers *Jpn. J. Appl. Phys.* **47** 768

[29] Takemura Y, Shimada Y, Watanabe G, Yamada T and Shirakashi J 2007 Measurement of faradaic current during AFM local oxidation of magnetic metal thin films *J. Phys.: Conf. Ser.* **61** 1147

[30] Schneegans O, Moradpour A, Boyer L and Ballutaud D 2004 Nanosized Electrochemical Cells Operated by AFM Conducting Probes *J. Phys. Chem. B* **108** 9882–7

[31] Faucett A C and Mativetsky J M 2015 Nanoscale reduction of graphene oxide under ambient conditions *Carbon* **95** 1069–75

[32] Martín C, Rius G, Borrisé X and Pérez-Murano F 2005 Nanolithography on thin layers of PMMA using atomic force microscopy *Nanotechnology* **16** 1016–22

[33] Johannes M S, Cole D G and Clark R L 2007 Velocity controlled anodization nanolithography with an atomic force microscope using Faradaic current feedback *Appl. Phys. Lett.* **90** 103106

[34] Pellegrino L, Bellingeri E, Siri A S and Marré D 2005 Current-controlled lithography on conducting SrTiO3−δ thin films by atomic force microscopy *Appl. Phys. Lett.* **87** 064102

[35] Keyser U F, Schumacher H W, Zeitler U, Haug R J and Eberl K 2000 Fabrication of a single-electron transistor by current-controlled local oxidation of a two-dimensional electron system *Applied Physics Letters* **76** 457–9

[36] Held R, Heinzel T, Studerus P, Ensslin K and Holland M 1997 Semiconductor quantum point contact fabricated by lithography with an atomic force microscope *Applied Physics Letters* **71** 2689–91

[37] Snow E S, Jernigan G G and Campbell P M 2000 The kinetics and mechanism of scanned probe oxidation of Si *Appl. Phys. Lett.* **76** 1782–4

Modelling nanomechanical behaviour of additively manufactured Ti6Al4V alloy

Jelena Srnec Novak[1, 2], David Liović[1], Ervin Kamenar[1, 2], Marina Franulović[1]

[1]University of Rijeka, Faculty of Engineering, Vukovarska 58, 51000 Rijeka, Croatia
[2]University of Rijeka, Centre for Micro- and Nanosciences and Technologies, Radmile Matejčić 2, 51000 Rijeka, Croatia

jsrnecnovak@riteh.hr

Abstract

This study investigates the elastoplastic behaviour of additively manufactured Ti6Al4V alloy at micro and nano scale using nanoindentation device, imposing different indentation loads. Additionally, finite element analysis (FEA) is employed to obtain numerically load – displacement (*P-h*) curve for varying input parameters. To obtain meaningful results, comparison between experimental and numerical results has been performed to explore the influence of Berkovich tip radius on the load – displacement curve. Finally, it has been observed that FEA enables a reliable estimation of hardness and maximum indentation load at higher loads, exhibiting alignment with experimental curves. When lower indentation loads were used, the differences between numerically and experimentally determined maximum indentation loads were higher. These findings contribute to advancing the understanding of elastoplastic behaviour of additively manufactured Ti6Al4V alloy, when subjected to both high and low indentation loads.

Nanoindentation, elastoplastic material behaviour, numerical analysis, additive manufacturing

1. Introduction

In recent years, additive manufacturing (AM) has become increasingly popular as it offers many benefits over conventional manufacturing methods. As such, understanding the elastoplastic behaviour at the nano and micro scale is crucial, particularly for small and topologically complex components produced with AM techniques. In these components, the reliable determination of the intrinsic mechanical properties is challenging by performing traditional tensile tests. Nevertheless, nanoindentation tests allow determination of material properties (i.e. nano-hardness and Young's modulus) at small-scale and on low-volume specimens that may have complex structures.

It is observed that increasing the strain rate for indentation loads of 10 mN results in a significant reduction in the maximum indentation depth, thereby affecting the elastoplastic behaviour of the Ti6Al4V alloy produced using electron beam powder bed fusion process [1]. However, applying such low loads leads to indentation depths below 300 nm, where higher scatter in Young's modulus and nano-hardness for LB-PBF Ti6Al4V alloy is reported [2]. The elevated data scatter at such low indentation depths is attributed to the highly textured microstructure characteristic of additively manufactured Ti6Al4V alloy [3].

Therefore, in this study, both low and high indentation depths are considered to increase the relevance of the results. In addition, the effectiveness of the employed numerical procedure in estimating elastoplastic response is evaluated by comparison with experimental results on both high and low indentation depths. This paper investigates the possibility of modelling elastoplastic behaviour under indentation load at micro and nanoscale of widely used additively manufactured Ti6Al4V alloy by applying different indentation loads.

2. Materials and methods

Within this research, a total of nine cubic specimens (10×10×10 mm³) are produced using the laser beam powder bed fusion (LB-PBF) method with Concept Laser M2 machine. After manufacturing, all specimens are annealed under argon inert atmosphere by maintaining temperature of 840°C for 2h. Only one specimen is selected to evaluate finite element method (FEM) applicability in modelling of elastoplastic behaviour of Ti6Al4V alloy subjected to different indentation loads. Selected specimen for experimental and numerical investigation is manufactured using laser power of 250 W and scanning speed of 1000 mm/s. Detailed description of LB-PBF process and annealing heat treatment can be found in [2].

To determine nano-hardness, it is necessary to calculate contact stiffness (*S*), which is defined as slope at the maximum displacement of unload part of *P – h* curve [4].

$$S = \frac{dP_{\text{unload}}}{dh}\bigg|_{h=h_{\text{max}}} \tag{1}$$

Furthermore, the projected area of Berkovich tip (A_{p}) is defined as follows [4]:

$$A_{\text{p}} = 24.56 \cdot h_{\text{c}}^2 + C_1 \cdot h_{\text{c}} \tag{2}$$

where h_{c} is contact depth, and C_1 is the area coefficient of the Berkovich tip, determined through calibration procedure. Contact depth can be calculated as [4]:

$$h_{\text{c}} = h_{\text{max}} - \varepsilon^* \cdot \frac{P_{\text{max}}}{S} \tag{3}$$

where h_{max} represents maximum displacement, P_{max} maximum load and $\varepsilon^* = 0.75$ is a constant for the Berkovich tip. Nano-hardness (*H*) is defined as [4]:

$$H = \frac{P_{\text{max}}}{A_{\text{p}}} \tag{4}$$

Equation (5) is used both in experimental and numerical analysis to determine nano-hardness values according to procedure described as follows.

2.1. Nanoindentation experimental procedure

Nanoindentation experiments are performed at room temperature utilizing a three-sided Berkovich diamond indenter mounted on the Nanoindenter Keysight G200. Load controlled mode is used and three different indentation loads (10 mN, 100 mN and 200 mN) are considered to investigate elastoplastic

behaviour both at low and high indentation depths. Prior to nanoindentation experiments, all specimens are grinded, polished and etched using Kroll's reagent.

2.2. Numerical analysis

Numerical simulations are conducted using Abaqus/Standard 2020, with the specimen modelled in 3D, incorporating cyclic symmetry. A 3D model has been chosen to accurately depict the Berkovich tip (three-sided pyramid) and investigate the influence of tip and edges blunting on the results, whereas a 2D model only permits incorporating blunting of the tip without affecting the edges. Utilizing cyclic symmetry enables a reduction in computational time by modelling only one-third of the entire model. This approach resulted in a one-third model, enhancing computational efficiency. The Berkovich tip is treated as a discrete rigid entity with hard and frictionless contact with the specimen. The specimen model (Fig. 1), with a height of 25 μm, and diameter of 20 μm, underwent mesh refinement near the indentation site and gradual coarsening in distant regions to balance computational efficiency and accurate representation of stress and strain gradients. Numerical model of the specimen is defined with a mesh of total 88200 eight-node linear brick elements (C3D8) and 93738 nodes. Young's modulus (E) is determined to be 141 GPa, representing the mean value from Tab. 1 and the Poisson's ratio is set to 0.33 which corresponds to Ti6Al4V alloy [5]. The Johnson-Cook plasticity model is used to model plastic hardening during indentation, with parameters adopted from [6], where A=997 MPa, B=746 MPa and n=0.325. In AM Ti6Al4V alloys, microstructural anisotropy predominantly influences ductility, whereas Young's modulus, yield strength, and tensile strength exhibit negligible directional dependence [7]. Additional analysis assessed the blunting effect of the Berkovich tip radius on the loading section of the P-h curve.

3. Results and discussion

In nanoindentation, indenter blunting is unavoidable. To mitigate this, the standard procedure involves calibration of the Berkovich tip using additional coefficients for the A_p calculation as defined by Equation (3). While this reduces errors in determining E and H, the impact of blunting persists in the elastoplastic response, particularly evident with increased indentation loads, as illustrated in Fig. 1.
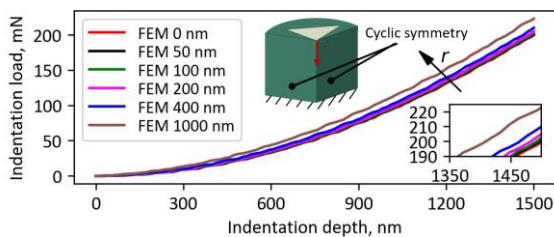
Figure 1. Tip radius influence on loading parts of P-h curves

Increasing the tip radius from 0 to 1000 nm causes an upward shift in the loading regime of the P-h curve, indicating a higher indentation force requirement for the same displacement. The radius of a new and unused Berkovich tip typically ranges from 20 to 100 nm, depending on the manufacturer. Since elastoplastic response for ideally sharp Berkovich tip and Berkovich tip with radius <100 nm is almost identical, the ideally sharp Berkovich tip is used in further analysis. Fig. 2 depicts experimentally and numerically determined P-h curves for three distinct indentation loads. As can be seen, there is a certain discrepancy between experimental and numerical results due to difference in Berkovich tip radius and exact Young's modulus. The Berkovich tip radius in this study may fall outside the usual range of 20 to 100 nm, as trial measurements are performed before the reported measurements in this paper. This preliminary experimental phase might have led to the blunting

of the Berkovich tip, thereby contributing to the observed disparities in the reported results. Furthermore, Young's modulus value of 141 GPa is used for all three simulations, inducing differences particularly in the unloading part of the P-h curve which has elastic nature. Experimentally determined values in Tab. 1 are reported in form of mean value ± STD. The highest difference between experimentally and numerically determined P_{max} is found when the lowest indentation loads were utilized, while the lowest difference was found when the highest indentation loads are used. Furthermore, hardness values determined both experimentally and numerically are reported in Tab. 1.
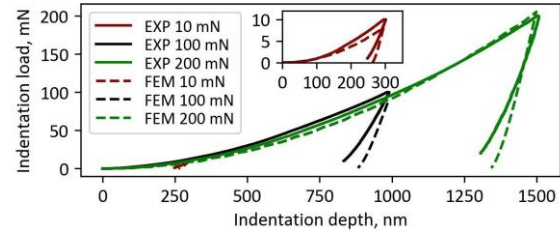
Figure 2. Comparison between experimental and FEM P-h curves

Table 1. Experimentally and numerically determined P_{max} values.

Test ID	E, GPa	$P_{max-exp}$, mN	$P_{max-sim}$, mN	Dif., %
10 mN	130 ± 11	10	8.18	18.2
100 mN	147 ± 13	100	90.22	9.8
200 mN	146 ± 19	200	205.39	2.7
Test ID	H_{exp}, GPa	COV,%	H_{sim}, GPa	Dif., %
10 mN	4.417 ± 0.72	16.3	4.33	2
100 mN	4.654 ± 0.65	14	4.27	8.3
200 mN	4.038 ± 0.37	9.2	4.20	4

As can be seen, the differences between H_{exp} and H_{sim} are within the range of variability considering the coefficient of variation (COV). In general, the microstructure of the PBF-LB Ti6Al4V alloy consists of α+β laths which have different mechanical properties. Therefore, employing higher indentation loads leads to increased indentation depths, incorporating a greater number of α+β laths and thereby reducing their individual effects, resulting in more robust and averaged results.

4. Conclusions and outlook

The application of the FEA methodology in this study enables reliable estimation of nano-hardness and maximum indentation load especially when high indentation depths were used. In that case maximum indentation load and hardness errors were 2.7% and 4%, respectively. However, at lower indentation loads, the presence of higher error in maximum indentation load is notable. Furthermore, the numerically derived P-h curve for the LB-PBF Ti6Al4V alloy under indentation load showed reasonable alignment with the experimentally determined curve further supporting application of proposed FEA approach.

In future work, possibility to obtain stress-strain curves from the experimentally and numerically determined P-h curves for different indentation loads, will be investigated.

References

[1] Peng H et al. 2021 *Materials* **14** 3004
[2] Liović D et al. 2023 *Materials* **16** 4341
[3] Cepeda-Jiménez C et al. M 2020 *Mater. Charact.* **163** 110238
[4] Oliver W C et al. 1992 *J. Mater. Res.* **7** 1564-83
[5] Xu Y et al. 2019 *J. Mech. Behav. Biomed. Mater.* **99** 225-39
[6] Wang Z and Li P 2018 *Mater. Sci. Eng. A* **725** 350-58
[7] Carroll B E et al. 2015 *Acta Mater.* **87** 309-20

Fabrication and evaluation of freeform surfaces in Directed Energy Deposition

Adriano Nicola Pilagatti, Federica Valenza, Giuseppe Vecchi, Eleonora Atzeni, Alessandro Salmi, Luca Iuliano

Politecnico di Torino, Department of Management and Production Engineering

adriano.pilagatti@polito.it

Abstract

Additive Manufacturing (AM) represents a paradigm shift in fabrication methodologies, enabling the creation of intricate geometries through sequential deposition. Among AM processes, Directed Energy Deposition (DED) is a metal-based technique that is particularly relevant for repair and remanufacturing applications, especially for high-value components. When coupled with 5-axis CNC, DED offers the unique ability to construct freeform surfaces, such as those typically found in the aerospace, marine and automotive industries. The focus of this research is to elucidate the interdependencies between the capabilities of a DED system and the achievable dimensional accuracy in freeform structures. To this end, on the basis of a parametrization approach, a comprehensive methodology has been formulated to tailor the design of a sinusoidal freeform to the capabilities and constraints of the specific DED system, taking into account, for example, the deposition head configuration and the number of controlled axes. The dimensional accuracy of the fabricated freeform was evaluated using 3D scanning technologies. The results showed that thermal distortion could significantly affect the geometry and may require thermal compensation. Additionally, acceleration transients may require appropriate path control strategies. The findings of this study offer valuable insights for future research on the influence of critical process parameters and production strategies on the dimensional accuracy of freeform components by DED.

3D printing, Accuracy, Manufacturing, Surface

1. Introduction

Additive manufacturing (AM) has developed significantly in the past decade and is increasingly being used in various industrial sectors due to its ability to fabricate complex geometries, reducing material waste and having a positive impact on the environment [1]. Directed Energy Deposition of metallic powders using a laser beam as energy source (DED-LB/Powder) is a promising metal-based AM technology. In this process, the laser beam is focused on a substrate, generating a local heating area and a melt pool, while powder material is conveyed to the deposition area in an inert gas stream through a nozzle. The component is produced by the mutual motion of the laser beam and the substrate along a deposition path generated by computer-aided manufacturing (CAM). DED-LB is suitable for producing large and complex metal structures with high deposition rates, and for repairing and remanufacturing high-value components, finding broad application in the automotive, biomedical, and aerospace industries [2].

DED solutions are usually 5-axis CNC systems or complex arrangements where the head is integrated into a robotic arm. The enhanced flexibility provided by multiple degrees of freedom allows for the adaptation of the slicing direction to the surface normals, overcoming the traditional 2.5-axis approach of powder bed systems. Multi-axis deposition represents a significant shift in the AM paradigm. Depositing material in different planes based on the variable slicing direction, and preventing collision between the deposition head and the deposited layers becomes significantly more complex. Therefore, advanced pre-process software support is required for manage the process effectively. Numerous articles in the literature have explored these aspects. As a starting point for multi-axis AM, Murtezaoglu *et al.* [3] emphasised the importance of decomposing the part geometry into discrete volumes, that will be deposited in sequence. Regarding the build

order, Ramos *et al.* [4] proposed a strategy to determine the optimal slicing approach and building sequence for each decomposed volume. This involves solving a global optimisation sub-problem, which minimises the staircase effect and building time for each volume. The deposition of successive volumes may require several re-orientations of the substrate during the building process, and the previously deposited volumes could interfere with the deposition trajectories. Moreover, curved three-dimensional paths may result in build-up peaks where transition areas are present due to an increased curvature or reoriented axes. Another concern arises from the need to prevent the molten pool from spilling over the sides of the components [1]. To achieve this, the deposition head should be normal to the substrate or the previous deposited material. According to Xiao *et al.* [5], there is a shortage of automated process planning software that fully supports the use of 5-axis machine tools.

The flexibility of DED-LB systems enables the deposition of support-free freeform surfaces, even those with small thickness. Freeform surfaces, defined as surfaces containing one or more non-planar non-quadratic surfaces, are generally represented by parametric or tessellated models. Freeform surfaces have been widely used in various engineering applications, such as aerospace, automotive and mould industry [6]. Although DED has been shown to be effective in fabricating complex freeform geometries, current research primarily focuses on process planning and evaluating manufacturability of specific case studies, making generalization difficult [7, 8].

Exploring the boundaries of freeform manufacturing by DED, this investigation proposes a parametric design approach for freeform surfaces, wherein the surface parameters are adjustable based on the geometric characteristics inherent to the DED system. More specifically, a shaping algorithm is developed to design a sinusoidal freeform surface taking into account specific DED system constraints such as the deposition

head configuration, the laser beam diameter, the number and type of controlled axes, to identify the limit conditions to avoid collision. Concurrently, the accuracy of the deposited geometry is assessed by comparison with the nominal geometry. The deposited geometry is evaluated by using a structured-light 3D-scanner. The observed deviations allow to evaluate the combined effect of geometry and deposition path management on the accuracy.

2. Methodology

This research presents a methodology for evaluating the capabilities of a generic DED system when fabricating a freeform surface. The freeform geometry is designed parametrically to conform to the geometric constraints of a generic DED system being investigated.

2.1 Freeform design

A surface generated by the 90° rotation around the z'-axis of the sinusoidal generatrix function was selected:

$$z'(x') = A \cdot sin[B \cdot (x' + C)] + D$$

where A is the amplitude, B the frequency, C the phase shift, and D the vertical offset. A characteristic length (L) is used to define the cubic box containing the surface. This length is chosen based on the configuration of the DED system, such as the working volume, kinematics, or deposition head geometry, to prevent interference. The kinematic configuration of the system includes consideration of the number and type of controlled axes, joints, and capabilities of the computer numerically controlled (CNC) interpolator. These elements collectively determine the ability of the system to reach designated points in space (path) by following a specific temporal law (trajectory) [9]. The coefficients A, B, C and D of the sinusoidal function are computed numerically as the solution of a system of four non-linear equations. These equations constrain the starting point of the curve, S, at the coordinates $z'_S = 0$, $x'_S = L/4$, and the end point, E, at the coordinate $x'_E = L$. The tangency angles at these two points are equal to the minimum leading angle, α, and the maximum trailing angle, β, respectively, as depicted in Figure 2.

The three-dimensional surface has a biparametric (u-v) shape. The radii of curvature vary continuously along both the u- and v-directions. This approach ensures a smooth transition from the minimum leading angle, α, to the maximum trailing angle, β, accommodating the full motion capabilities of the DED system and ensuring the integrity of the deposition process. The freeform geometry can be classified as open inclined wall
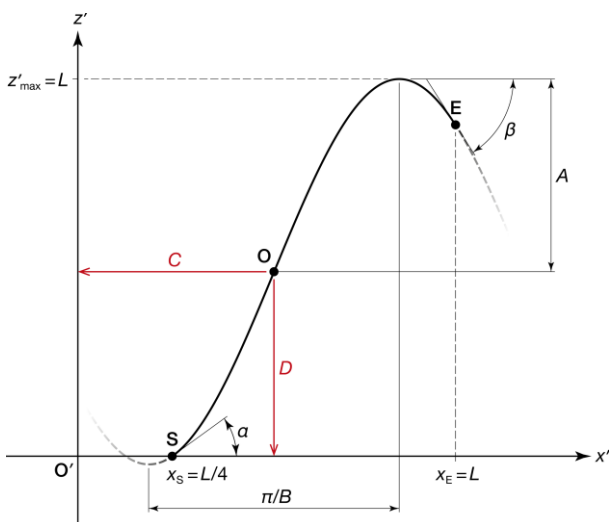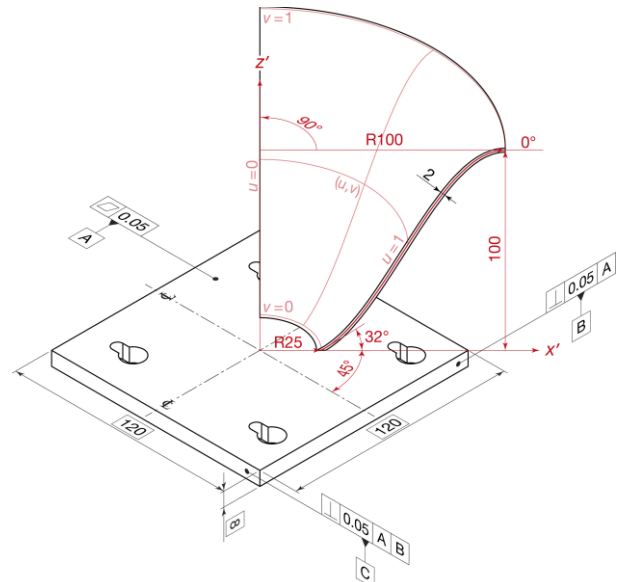
Figure 1. Freeform geometry and datum reference system.

according to the standard ASTM F3413-19e1 [10]. The three-dimensional model is realized in Rhinocheros by Robert McNeel & Associates (Seattle, USA) and is shown in Figure 1.

2.2 Programming

A variable direction slicing strategy is adopted, which means that the slicing follows the surface curvature in the u- and v-directions. Specifically, several parallel u-curves are defined by setting $v = v_0$, where v_0 values correspond to equally distant points on the v-direction based on the chosen value of slicing thickness. The slicing thickness is chosen based on the process parameters and the desired tolerance. The u-curves describe the path of the deposition head. At each point of the u-curves, the surface tangent in the v-direction determines the orientation of the deposition head.

A unidirectional deposition x'_E strategy is adopted to realize a single-track wall, with the mid-surface being the designed freeform surface. Furthermore, to ensure that the head axis is normal to the previous deposit, a key pathing constraint is implemented. This constraint orients the axis of the deposition head to the tangent to the freeform surface at all points.

The Grasshopper module in Rhinocheros is selected to slice the freeform surface. The deposition program is defined in the Mastercam software by CNC Software, LLC (Tolland, CT, USA). A linear interpolation is opted due to its more general applicability to any geometrical shape, adopting a tolerance of 0.02 mm. This value is lower than the typical accuracy of a DED system and is

Table 1. Constitutive parameters of the sinusoidal function used to model the generatrix curve of the freeform surface.

Sinusoid Parameter	Value
A	51.39 mm
B	3.75×10^{-2} rad·mm^{-1}
C	−58.09 mm
D	48.61 mm

Table 2. Process parameters used for freeform surface deposition.

Parameter	Value
Laser power, P	750 W
Travel speed, v	15.63 mm·s^{-1}
Layer height, ΔZ	0.5 mm
Powder mass flow rate, Q_p	9.2 g·min^{-1}
Carrier gas flow rate, V_{Ar}	5 L·min^{-1}

Figure 2. Parametric sinusoidal curve (O is the inflection point).

small enough to ensure a smooth surface, without implying the definition of an excessive number of points per each layer. In fact, an excessive number of points used to define the path of the deposition could result in difficulties from the control system to elaborate the motion of the axes with the right timing [11].

2.3 Fabrication

The freeform is tailored to the DED system under investigation and fabricated. In this study, the Laserdyne 430 by Prima Additive (Collegno, Italy) is used for production. It is a 5-axis DED system equipped with the TWA-160 roto-tilting table, by Tsudakoma (Kanazawa, Japan). The feedstock is a pre-alloyed stainless steel powder. To prevent the deposition head from colliding with the flat substrate, a minimum leading angle of 32° is required, which is achieved by tilting the table 58°. The kinematic configuration of the machine allows for a trailing angle of 0°, which is achieved by tilting the table 90°. A characteristic length L equal to 100 mm is selected for the fabrication. These assumptions lead to the coefficients in Table 1. Process parameters are set according to Pilagatti *et al.* [12] and are listed in Table 2.

2.4 Evaluation

The accuracy of the deposited geometry is evaluated by means of a structured-light 3D-scanner. 3D scanning is often employed in the assessment of freeform geometries, facilitating the acquisition of the actual deposited surface [13]. Specifically, the ATOS compact system by Carl-Zeiss GOM Metrology GmbH (Braunschweig, Germany) is used, with a resolution of 0.02 mm. Later, GOM Inspect 2021 is used to evaluate the deviations [14].

3. Results and Discussion

The deposition of the freeform was successfully completed (Figure 3). The surfaces were then 3D scanned by means of the ATOS compact system. The scanned geometry was then compared to the nominal one, which was constructed by offsetting the freeform surface by 1 mm on each side, taking into account that 2 mm is the track width at the given process parameters, as measured in preliminary experiments. Actual and nominal geometries were aligned by defining the datum reference system visible in Figure 1. The datum features were reconstructed from the scanned data using a best-fit algorithm. The analysis of the deviations led to the colour maps shown in Figure 4. Measured deviations were in the range ± 1 mm, with most of the occurrences being inside an even tighter interval, ± 0.6 mm. The resulting deviations were one order of magnitude larger than the chordal deviation of the deposition path generated by the linear interpolation. This proves that the segmentation did not significantly affect the final deposition accuracy of the freeform surface.

Figure 3. Deposited freeform geometry.

Overall, the deviations from the nominal geometry became more significant as the deposition progressed. The scanned geometry was found to be below the nominal one near the edges of the freeform surface from half height, while the opposite trend was observed at the centre of the freeform surface along its symmetry plane, where the scanned geometry was above the nominal one. The observed behaviour is consistent with the thermal evolution that occurs during the heating and cooling phases of the DED deposition. Especially, tangential compressive stresses arise from the thermal contraction of the material during the cooling phase. Along the v-direction, the deviations are localized in a middle area because the surface is constrained at the base to the substrate and is rigid at the top due to the increased curvature. Effects due to the acceleration/deceleration of the axes were observed near the edges. A peak was clearly visible at the left edge in Figure 4a, where deposition starts at each layer.

Profiles of the freeform geometry were extracted at three different values along the u-direction to provide information about the profile deviation from the nominal. The values were taken near the edge ($u = 0.1$), excluding the side effect caused by the transient, in the middle ($u = 0.5$), and in an intermediate zone ($u = 0.3$). Results are shown in Figure 5. Once again, it can be seen that the deviation from the nominal profile is very limited in the lower half of the profile and comparable for the three sections, whereas the largest deviations are observed in the upper region near the edge, with the actual upper surface being approximately 1 mm below the nominal one.

Finally, in assessing the quality of the achieved geometry, particular attention was paid to the leading and trailing edges of the surface. Leading and trailing angles were measured on the three sections. To avoid the effect of the first deposited tracks,
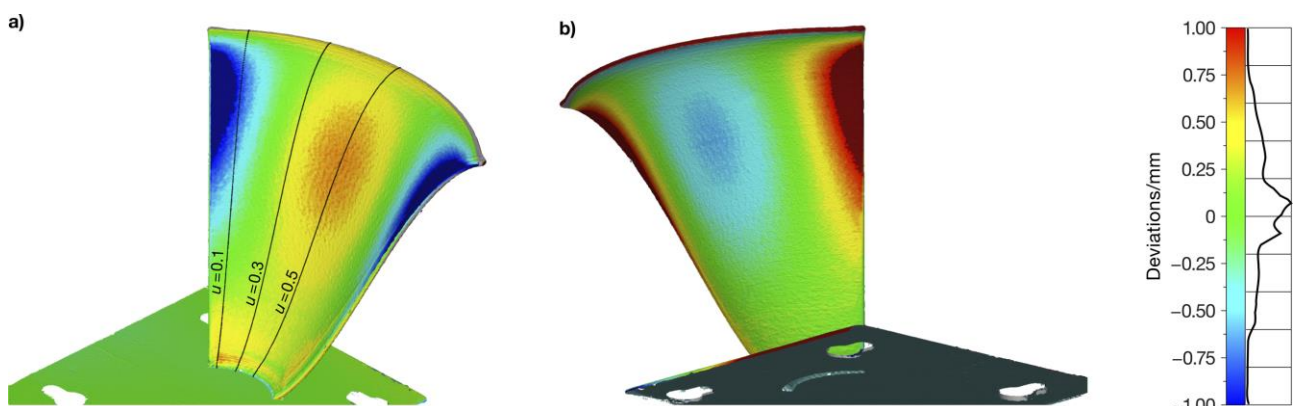
Figure 4. Comparison between deposited freeform surface and nominal freeform surface of the a) upper surface and b) lower surface.
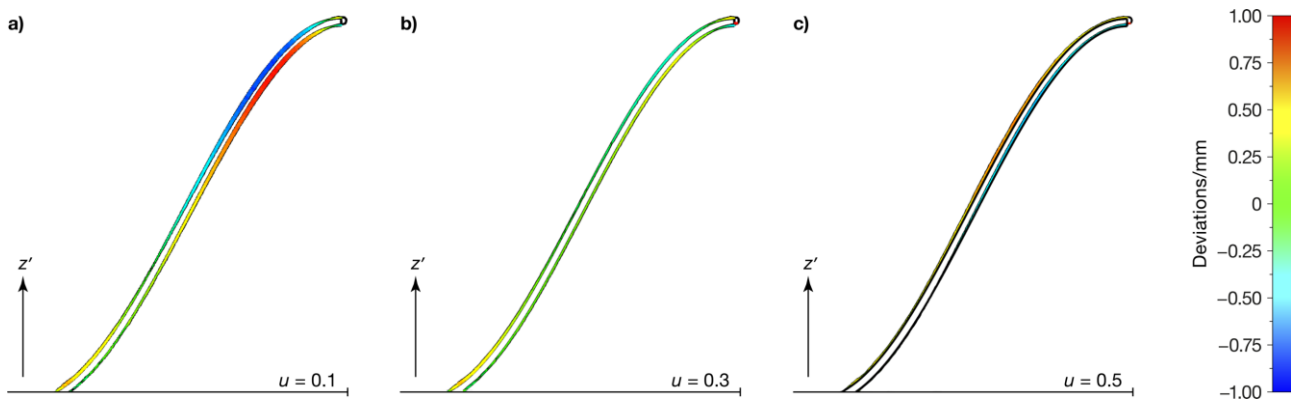
Figure 5. Section comparisons between deposited freeform surface and nominal geometry for a) $u = 0.1$, b) $u = 0.3$ and c) $u = 0.5$.

the leading angle was measured at a distance of 3 mm along the v-direction from the S point. At this measurement point, the tangency angle is 38.2°. The combined uncertainty assessment also incorporated the resolution error of the measuring instrument [15]. The mean value of the leading angle was determined to be (37.9 ± 1.8)°. In this context, a bilateral t-test with a 5% Type I error was conducted to compare this mean value with the nominal value. The p-value obtained for the leading angle was 90%, indicating that the null hypothesis cannot be rejected. Similarly, the trailing angle was measured at (86.1 ± 1.0)° with a p-value of 6%, also above the significance threshold. These values are promising, suggesting that the measurement accuracy is within acceptable limits.

4. Conclusions

This work proposes a novel method for assessing the capabilities of a generic DED system in the production of a freeform geometry, combined with the evaluation of the freeform accuracy. The manufacturability of the freeform geometry was ensured by the methodology adopted, which took into account the physical constraints of the system under study in the design phase. The 5-axis programming of the deposition path was developed by three-dimensional slicing, to follow the tangent to the generatrix curve, and linear interpolation technique. The geometric accuracy of the deposited freeform surface, captured by an optical scanner, was within the typical capabilities of the DED-LB system.

The availability of an evaluation method for the manufacturing potential of DED for freeform surfaces is particularly useful for industries where such geometry may be used for advanced applications. The proposed methodology allows for comparative analysis of DED systems. While the approach is promising, its current application is limited to controlled experimental conditions. Future research should be extended to real-world manufacturing environments to investigate the robustness of the process under varying conditions.

References

[1] Maffia S, Chiappini F, Maggiani G, Furlan V, Guerrini M and Previtali B 2023. Comparison between Eight-Axis Articulated Robot and Five-Axis CNC Gantry Laser Metal Deposition Machines for Fabricating Large Components. *Appl. Sci.* **13** 5259

[2] Ding Y, Dwivedi R and Kovacevic R 2017. Process planning for 8-axis robotized laser-based direct metal deposition system: A case on building revolved part. *Rob. Comput. Integr. Manuf.* **44** 67-76

[3] Murtezaoglu Y, Plakhotnik D, Stautner M, Vaneker T and van Houten F J A M 2018 Geometry-Based Process Planning for Multi-Axis Support-Free Additive Manufacturing *Procedia CIRP (Web Conference)* 78 p 73 - 8

[4] Ramos B, Pinho D, Martins D, Vaz A I F and Vicente L N 2022. Optimal 3D printing of complex objects in a 5–axis printer. *Optim. Eng.* **23** 1085-116

[5] Xiao X and Joshi S 2020. Process planning for five-axis support free additive manufacturing. *Addit. Manuf.* **36** 101569

[6] Lasemi A, Xue D and Gu P 2010. Recent development in CNC machining of freeform surfaces: A state-of-the-art review. *Comput.-Aided Des.* **42** 641-54

[7] Gibson B T, Mhatre P, Borish M C, Atkins C E, Potter J T, Vaughan J E, et al. 2022. Controls and process planning strategies for 5-axis laser directed energy deposition of Ti-6Al-4V using an 8-axis industrial robot and rotary motion. *Addit. Manuf.* **58** 103048

[8] Kaji F, Jinoop A N, Zardoshtian A, Hallen P, Frikel G, Tang T, et al. 2023. Robotic laser directed energy deposition-based additive manufacturing of tubular components with variable overhang angles: Adaptive trajectory planning and characterization. *Addit. Manuf.* **61** 103366

[9] Stavropoulos P, Athanasopoulou L, Souflas T and Tzimanis K 2023 Adaptive Toolpath Planning for Hybrid Manufacturing Based on Raw 3D Scanning Data *32nd Int. Conf. on Flexible Autom. Intell. Manuf., FAIM 2023 (Porto, PT)* p 273-82

[10] ASTM F3413-19e1, Guide for Additive Manufacturing - Design - Directed Energy Deposition, American Society for Testing and Materials (ASTM) International, 2022

[11] Plakhotnik D, Glasmacher L, Vaneker T, Smetanin Y, Stautner M, Murtezaoglu Y, et al. 2019. CAM planning for multi-axis laser additive manufacturing considering collisions. *CIRP Ann.* **68** 447-50

[12] Pilagatti A N, Atzeni E, Iuliano L and Salmi A 2023 The role of the carrier gas flow in the directed enegy deposition process *10th ECCOMAS Thematic Conf. on Smart Struct. Mater., SMART 2023 (Patras, GRE)* p 1258-69

[13] Savio E, De Chiffre L and Schmitt R 2007. Metrology of freeform shaped parts. *CIRP Ann. - Manuf. Technol.* **56** 810-35

[14] ISO 1101:2004, Geometrical Product Specifications (GPS) — Geometrical tolerancing — Tolerances of form, orientation, location and run-out, Genève, 2005

[15] JCGM 100:2008, Evaluation of measurement data - Guide to the expression of uncertainty in measurement (GUM), Bureau International des Poids et Mesures (BIPM), Sèvres (FRA), 2008

Micro-hole fabrication on polymer by electrochemical discharge machining

Julfekar Arab[1,2] Shih-Chi Chen[1,2]

[1]*Department of Mechanical and Automation Engineering, The Chinese University of Hong Kong, Shatin, N.T., Hong Kong*
[2]*Centre for Perceptual and Interactive Intelligence, Hong Kong Science Park, Shatin, N.T., Hong Kong*

arabjulfekar@gmail.com

Abstract

Micromachining of Polymer materials is vital for different micro/nano-systems such as micro-fluidics and micro-electronics. In recent times, the PMMA is demonstrated to be an upright candidate for the point-of-care microfluidic devices owing to its properties such as higher mechanical strength with relatively lower glass transition temperature, lower cost, and biocompatibility. Microfeatures such as holes and channels are important parts of a microfluidic device. Machining based on the electrochemical discharges (ECDM) has emerged as the cost-effective and simple method with relatively lower thermal damages with smooth sidewalls. In ECDM, the EC discharges generated at the micro-tool tip in the aqueous alkaline-KOH electrolyte and the following high heat energy due to the discharges eradicates the material from PMMA by heating, evaporation followed by thermal etching. In the current work, an attempt has been made to explore the micro-hole formation in PMMA polymer using ECDM for the first time. Identification of the electric power specifications (machining current-Im, machining voltage-Vm) and process parameters (KOH electrolyte-5M level-EL, machining time-Tm) has been done via experimentation and succeeding micro-hole geometric characteristics (size, depth heat affected zones) were analysed. The erosion of micro-tool after the ECDM have also been detected. The optimal range of parameters to get appropriate hole quality (optimal hole size: ~0.2±0.05 mm, and machining depth: ~0.103±0.03 mm) were found to be:-V:30 ± 0.5 V, Im:0.42±0.02 A, EL: 1.5 mm.

Keywords: PMMA, electro-chemical discharges, Polymers, micro-fluidics

1. Introduction

The need for micro structuring of electrically non-conductive materials utilising cost effective as well as efficient techniques rises from the increasing demand for micro/nano-scale structures and related devices in numerous fields, namely, microelectronics, healthcare, micro-fluidics etc. Electrically non-conductive materials, such as glass, ceramics, and polymers, are widely used in various fields, such as microelectronics, microfluidics, biomedical engineering, and optics [1,2]. These devices frequently need multifaceted, complicated and accurate features on electrically non-conductive materials such as glass and polymers with high accuracy. Micro fabrication of electrically non-conductive materials, such as glass, ceramics, and polymers, is a challenging task due to their high brittleness and low thermal conductivity.

Traditional methods, such as mechanical force-based milling or cutting, which includes high-speed rotating machining tool to eliminate material from the workpiece, are frequently futile as well as random and can consequence in less accurate as well as poor surface quality and micro-features dimensional accurateness [3]. Laser ablation and plasma-based etching are two well recognized methods. Laser ablation comprises using a high-energy laser beam to eradicate material. This technique gives high accuracy with ability to produce intricate geometries. Nevertheless, laser ablation has limits, such as inadequate material removal rates, exposure to thermal impairment, and high apparatus and maintenance related costs [4]. Plasma based etching can give very fine and miniaturized micro holes in electrically non-conductive materials. Yet, they need expensive equipment and complex tooling, cleanroom, lesser production rate and less cost-effective for minor productions [5,6].

In recent decade, electrochemical discharge machining (ECDM) has arose as a capable substitute for micro machining of polymer and related non-conductive materials [7]. Considering the competence of method, there is a rising interest in developing low-cost methods for ECDM-based micro machining. ECDM method proposes a cost-effective solution for micro machining of non-conductive materials, with potential applications in various fields [8]. Most of the works in the ECDM deals with glass-based micromachining using various types of the electrolytes, different shape/size tool electrodes, as well as machining approaches [9,10]. Very few researchers have discovered the capability of ECDM for other than glass material. Recently few researchers tried the fabrication of microchannels in PDMS and PMMA material [11,12]. Though, the experimental analysis is constrained preliminary inspections to microchannels only. Thus, there is a research gap for micro-fabricating this PMMA polymer material for micro-holes fabrications. This present article focuses on study of lower cost technique i.e. ECDM micro machining of PMMA polymer material. The range of values for process parameters (machining voltage and current) associated with the ECDM process are recognized and suitable values were confirmed for PMMA material for fabrication of blind micro holes.

2. Mechanism of ECDM process

Electro-chemical discharge machining is often understood as the mixture method of micro- machining that incorporates the EDM based process as well as the ECM based process [13]. Material eradicating mechanism includes thermal based melting at

advanced localized temperature followed by the material evaporation. Furthermore, the chemical etching-based removal also takes place as the etching nature of the KOH electrolyte. The basic electrochemical cell and the setup of ECDM consists of the three main parts, i.e. tool, KOH electrolyte, and counter electrode.

The aqueous alkaline KOH solution is used as an electrolyte the conducts electric charge between the tool and counter electrode plate when a potential difference (V) is applied across them. The tool electrode is provided with negative polarity from power supply i.e. cathode and auxiliary electrode i.e. anode, as positive polarity is provided here from power supply. Due to application of the potential difference, the hydrogen gas bubbles creation starts which subsequently get collected around the tool surface making a gas film eventually. This gas film turns as an insulation barricade between the tool and the surrounding electrolyte. After the providing potential difference past a critical voltage, the gas film collapse resulting into the EC discharge generation. The discharge delivers the adequate heat energy to melt as well as evaporate as well as chemically etch the PMMA material reserved in the close neighbourhood of the tool [14].

3. Materials and methods

The experiments for the ECDM process carried out on an inhouse developed experimental set up as shown in the Fig.1. The main components electrochemical cell, tool fixture, and power supply unit. The electrochemical cell consists of the workpiece holder, counter electrode plate and electrolyte. The power supply with DC output used for all the experiments. The tool fixture is micro drill chuck attached vertical moving fixture. The details of parameters are shown in the following table 1.

Table 1 Processing parameters

Parameter	Value/remark
Workpiece and thickness	PMMA, 1-1.5 mm
Counter electrode	Stainless steel ring with thickness (dia.17 cm)
Tool immersion depth	1.5 mm
Tool workpiece gap	In contact position (~0 mm)
Power supply voltage	0-30 V DC
Power supply current	0-3 A
Electrolyte type	Potassium Hydroxide (KOH)
Electrolyte concentration	5 M aqueous
Tool electrode and tip diameter	Needle tool (0.09±0.02 mm)
Tool electrode material	Stainless steel

The tool -workpiece gap was kept as zero i.e. in contact position using a slip gauge of known thickness. The micro features obtained after the experimentations were characterized using the optical microscope (leica Inc.) to obtain the micro dimple size as well as the heat affected zone. The developed experimental set up as well as the tool electrodes optical image are illustrated in the following figure 1.
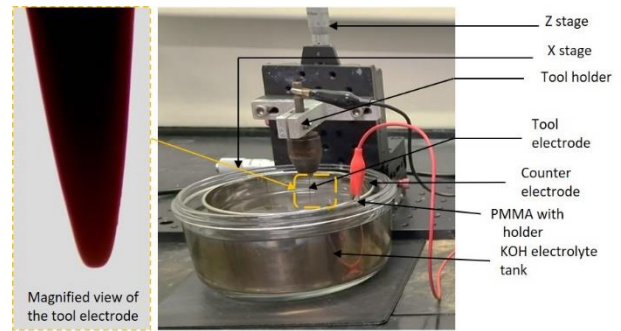
Figure 1. Experimental set up with all accessories and tool electrode

The circularity is measured as the ratio of the minimum to maximum micro-hole diameters whereas the HAZ was quantified by measuring the linear dimension of the thermally influenced areas at the peripheries of eopening end of the micro holes. The selected material for the analysis i.e. soda lime glass and PMMA have following important material properties as mentioned in the Table 2.

Table 2 Properties of the material and tool electrode

Properties/composition	PMMA	Stainless steel
Melting point (° C)	160	~1500
Electrical resistivity (Ω.m)	2×10^{15}	6.9×10^{-7}

4. Results and Discussions

In ECDM, the application of the sufficient voltage (>2-3 V) is allowed between the smaller tool electrode which is a cathode terminal and the larger counter ring electrode which anode terminal in an electrochemical cell, the electrolysis action of aqueous potassium hydroxide-KOH electrolyte happens. This results in generation of the gas bubbles of hydrogen (H_2) at cathode terminal and of oxygen(O_2) at anode terminal, respectively. At cathode H_2 gas bubble generation rate is very high as the current density is larger. Further increment in the voltage results into merger of gas bubble forming envelope of gas film around the tool electrode separating it from nearby electrolyte. This gas film layer is broken when voltage is elevated (> 24 V) and electrochemical discharges are produced. EC discharges generate heat energy which helps in material removal from the PMMA workpiece. The Critical point (~24 V) shown in the I-V curve is a point of highest value of the current is seen during the process and past which EC discharges are generated.

The identification of suitable machining voltage (Va) and corresponding mean discharge current (Id) in the EC discharge zone is important in order to get the precise micro-hole. Initially the machining voltage of 26 V i.e. VC+2 was used for formation of the micro-holes. Further, the machining voltage was varied with increase of 2 V. The Current-time (I-t) graphs are analysed first and are shown in the Fig. 2.
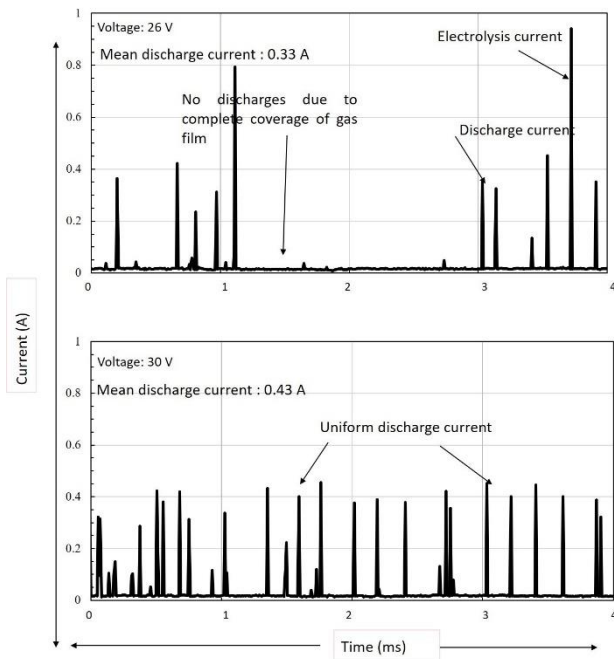
Figure 2. EC discharge behaviour different machining voltage
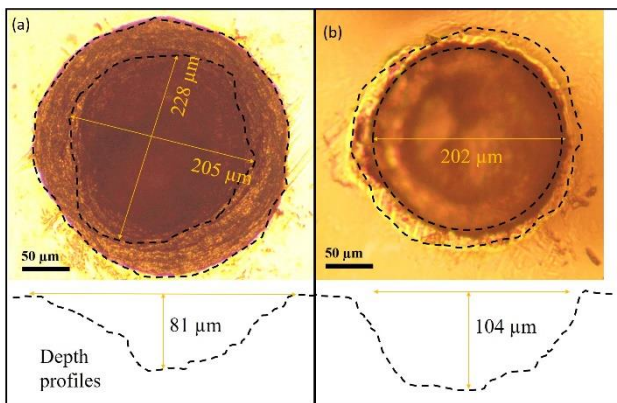
Figure 3. Machined micro-hole in the PMMA at different voltages (a) 26 V, (b) 30 V

Here, current values over the time step of 1 ms are recorded and it indicates the behaviour and trend of EC discharges as these parameters can influence as well as impact the micro-holes quality. EC discharges with higher uniformity and stability are essential to get circular, less thermally damaged micro holes with higher depths. I-t graphs were recorded and plotted by measuring the current values using multi-meter during the process. In case of 26 V machining voltage, the current spikes higher than Id of 0.33±0.02 A were measured as electrolysis current where sporadic gas film or incomplete merger of gas bubbles may be happening. When the Va was augmented to 30 V i.e. Vc+6 and the Id was recorded to be 0.42 ±0.02. Here, the current peaks are also steady and unvarying with no sporadic electrolysis current value. This clearly indicates appropriate collapse of H_2 gas film and generation of even uniform discharges.
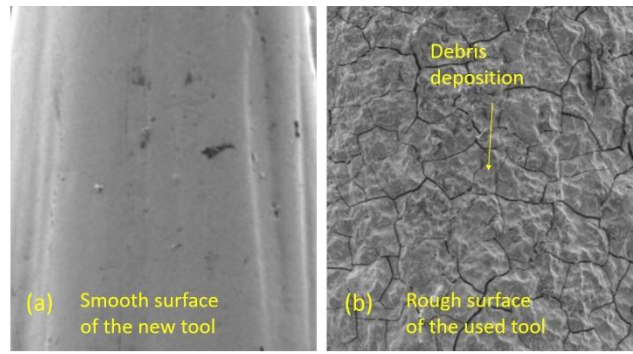
Figure 4. Tool electrode condition before and after machining

As can be seen from the Fig. 3(a), the micro hole at the voltage of 26 V which is Vc+2, has lesser circularity (0.83±0.05) and hole diameter with higher standard deviation (225 ±8 μm). The HAZ can be seen as non- uniform in nature having the higher value of 45 ±10 μm. The measured depth was 82 ±10 μm which is less due to the lesser depth of penetration due to non-uniform EC discharges. The micro hole with application of 30 V found to be having lesser HAZ (23 ±3 μm) and good circularity (0.96±0.01) as shown in the Fig. 3(b)

In case of 30 V highly consistent and uniform EC discharges occurred due to proper and complete collapse of gas film enveloped around tool electrode which resulted into appropriate circular holes with lesser standard deviation (size: 201±2 μm). Here, the measured depth is higher (102±1 μm) than the previous case due to higher penetration depth due to concentrated heat energy as a result of the uniform EC discharges with higher stability.

Next, to analyse effect of tool condition on the EC discharge behaviour and micro-hole features, new and used tools were recorded for the same applied voltage of 30 V. Fig. 4(a, b) shows the surface profiles for the fresh and used In case of used tool, where the tool was subjected to machining for a total time duration of 5 minutes, the EC discharges are observed to be unstable with intermittent electrolysis current peaks indicating intermittent gas films formation and its due to the fact that the used tool electrode surface was observed to be eroded and machining debris deposition which led to non-uniformity and irregularity in the machined depth. The possible remedies for reduction in tool wear will be the use of sidewall coating of non-conductive nature which may result in the reduction of stray EC discharges from the sidewall. Moreover, providing the tool vibration mat possibly reduces the tool erosion.

4. Conclusions

The ECDM process capability to machine the micro-holes in PMMA is demonstrated successfully. The major parameter i.e. machining voltage and its effect on EC discharges and subsequent micro hole quality has been studied The machining voltage desirable for the suitable machining quality with unvarying EC discharges should be 4-6 V higher than the critical voltage. The optimal hole quality with higher circularity, higher depth as well as lower HAZ obtained when suitably high voltage of 30 V is applied. The lesser values of voltage (26 V) which indicates the region of instability leads to uneven as well as non-uniform EC discharges, which resulted into high deviations into hole size, HAZ and lesser depths. The EC discharge quality also degrades in case of the used tool with poor surface quality.

References

[1] X. Zhou, D.P. Poenar, K.Y. Liu, W. Li, M.S. Tse, H. Chen, C.K. Heng, S.N. Tan, Glass-based BioMEMS devices for optically excited cell impedance measurement, Sens Actuators A Phys. 133 (2007) 301–310.

[2] V. Cornean, Development of Through Glass Vias (TGVs) for Interposer Applications, (2014) 4–11.

[3] A.H. Elsheikh, T. Muthuramalingam, S. Shanmugan, A.M. Mahmoud Ibrahim, B. Ramesh, A.B. Khoshaim, E.B. Moustafa, B. Bedairi, H. Panchal, R. Sathyamurthy, Fine-tuned artificial intelligence model using pigeon optimizer for prediction of residual stresses during turning of Inconel 718, Journal of Materials Research and Technology. 15 (2021) 3622–3634.

[4] L.A. Hof, J.A. Ziki, Micro-hole drilling on glass substrates-A review, Micromachines (Basel). 8 (2017) 1–23.

[5] R. Li, Y. Zhang, Y. Zhang, W. Liu, Y. Li, H. Deng, Plasma-based isotropic etching polishing of synthetic quartz, J Manuf Process. 60 (2020) 447–456.

[6] K.Kolari, Deep plasma etching of glass with a silicon shadow mask, Sensor and Actuators A. 141 (2008) 677–684.

[7] A. Dvivedi, Developments in tandem micro-machining processes to mitigate the machining issues at micron level: a systematic review, challenges and future opportunities, Machining Science and Technology. 26 (2022) 515–570.

[8] R. Wüthrich, V. Fascio, Machining of non-conducting materials using electrochemical discharge phenomenon - An overview, Int J Mach Tools Manuf. 45 (2005) 1095–1108.

[9] T. Singh, A. Dvivedi, On pressurized feeding approach for effective control on working gap in ECDM, Materials and Manufacturing Processes. 33 (2018) 462–473. https://doi.org/10.1080/10426914.2017.1339319.

[10] T. Singh, A. Dvivedi, Developments in electrochemical discharge machining: A review on electrochemical discharge machining, process variants and their hybrid methods, Int J Mach Tools Manuf. 105 (2016) 1–13.

[11] J. Arab, D.K. Mishra, H.K. Kannojia, P. Adhale, P. Dixit, Fabrication of multiple through-holes in non-conductive materials by Electrochemical Discharge Machining for RF MEMS Packaging, J Mater Process Technol. 271 (2019) 542–553.

[12] T. Muthuramalingam, R. Akash, S. Krishnan, N.H. Phan, V.N. Pi, A.H. Elsheikh, Surface quality measures analysis and optimization on machining titanium alloy using CO2 based laser beam drilling process, J Manuf Process. 62 (2021) 1–6.

[13] J. Arab, P. Dixit, Formation of macro-sized through-holes in glass using notch-shaped tubular electrodes in electrochemical discharge machining, J Manuf Process. 78 (2022) 92–106.

[14] A. Torabi, M.R. Razfar, The capability of ECDM in creating effective microchannel on the PDMS, Precis Eng. 68 (2021) 10–19.

Fiber-reinforced Fused Filament Fabrication for diamond cutting tools

J. Polte[1, 2], E. Uhlmann[1, 2], F. Heusler[1], S. Bode[1], G. Al-Sanhani[1]

[1]*Institute for Machine Tools and Factory Management IWF, Technische Universität Berlin, Germany*
[2]*Fraunhofer Institute for Production Systems and Design Technology IPK, Germany*

f.heusler@tu-berlin.de

Abstract

Additive manufacturing technologies open up new possibilities for the production of highly complex and geometrically flexible components. The reduction of material accumulations and single parts as well as the integration of lattice and numerically simulated structures enable a type of lightweight construction that is unattainable with conventional manufacturing processes. Furthermore, the integration of inserts during the process enables local reinforcement. Therefore, additive manufacturing processes are already being used in aerospace technology, the automotive sector and in mold and die making industry. In addition, Fused Filament Fabrication (FFF) enables the integration of continuous fiber-reinforcement into components made of carbon short fiber-reinforced polyamide. This technology provides mechanical strength properties that allow the substitution of aluminum. In this study, the possibilities resulting from these process properties were investigated for the manufacturing of diamond cutting tools. For this purpose, different flycutter geometries were developed to be manufactured by dual fiber-reinforced FFF. The geometries were evaluated regarding their suitability for the application in ultra-precision machining. A finite element analysis was carried out to analyze the deformation of a suited fly cutter geometry during use in dependence of the integrated content of continuous fiber. A reduced displacement for continuous fiber-reinforcement parts could be demonstrated which implies a higher stiffness due to the reinforcement superposition. Furthermore, eigenfrequency calculations showed that a higher content of fiber-reinforcement results in an improved deflection of the vibrations during use. These findings provide a basis for future research in the field of FFF-based manufacturing of diamond cutting tools. This offers the opportunity to adapt them more easily to individual requirements and enables a more cost-effective tool production with shorter iteration cycles.

Keywords: fiber-reinforcement Fused Filament Fabrication, FEM simulation, ultra-precision machining tools

1. Introduction

Additive manufacturing (AM) enables the implementation of complex structures, short lead times and the economical production of small batch sizes. Due to these properties AM technologies have become established in an increasing number of areas like aerospace technology, the automotive sector as well as production technology including tool and mold making [1]. In this sector, AM has been used primarily for the production of casting molds [2]. Novel advances in AM open up new potentials to build lightweight and stiff tools for ultra-precision machining by implementing numerically simulated geometries and integrating superimposed fiber-reinforcement during the manufacturing process. The AM-technology Fused Filament Fabrication (FFF) enables the integration of continuous fiber-reinforcement during the manufacturing process. During the build job a continuous fiber coated in fusible resin is placed between the layers of the component by a second nozzle. A carbon short fiber-reinforced polyamide serves as matrix material which leads to a superposition of continuous and short fiber-reinforcement. This process facilitates the production of extremely lightweight components with high rigidity and strength through the integration of complex structural elements and undercuts [3]. This potential can be increased by using numerical simulations to develop complex geometries that allow a reduction in material while maintaining a high rigidity of the component [4, 5].

2. Experimental setup

2.1. Development of the tool geometry

To investigate the potentials dual fiber-reinforced FFF opens up for ultra-precision machining, four different tool geometries of a flycutter were developed considering the manufacturing guidelines for FFF. Reinforcement and cross brace structures resulting from topology optimization analysis were implemented into the tool geometries in order to reduce material while keeping the stiffness at a maximum to fulfill the requirements for ultra-precision machining tools. To analyze the response of the geometries to mechanical loads, Finite Element Method (FEM) simulations were carried out. All numerical simulations were carried out using the software INSPIRE by ALTAIR, Troy, United States.

The developed tools were to be mounted on an ultra-precision spindle, the tool dimensions were set accordingly. Two different shaft-hub connection concepts were examined for the assembly. All developed geometries were designed in the CAD software NX by SIEMENS DIGITAL INDUSTRIES SOFTWARE, Plano, USA. To analyze the printability of the tool geometries they were manufactured on an ONYX PRO FFF-printer by MARKFORGED INC., Waltham, United States, using carbon short fiber-reinforced polyamide (PA 66) with an embedded continuous glass fiber, both by MARKFORGED INC., Waltham, United States. All components were printed with an infill density of d_i = 100 % and a layer thickness of d_l = 0.1 mm. The most suitable geometry was identified on the basis of the results of the numerical simulations and the feasibility for FFF manufacturing, taking into account the impact on the

ultra-precision machining process. Therefore, the factors of balancing, weight, manufacturing effort, ease of mounting, material and machining volume were considered within the scope of a utility value analysis.

2.2. Numerical analysis

To investigate the mechanical behavior, the tool geometry was subjected to a mechanical analysis using finite element analysis (FEM). This includes the calculation of the of the expected displacement under load as well as the determination of the eigenfrequencies. To consider the influence of continuous fiber-reinforcement simulations with and without glass fiber-reinforcement were carried out. For each simulation a cutting force of $F_c = 10$ N was applied, a minimum element size of $A_{e,min} = 0.1$ mm and an average element size of $A_e = 0.5$ mm was used for the calculation. The resulting displacement and eigenfrequencies of the simulations are shown in figure 1.
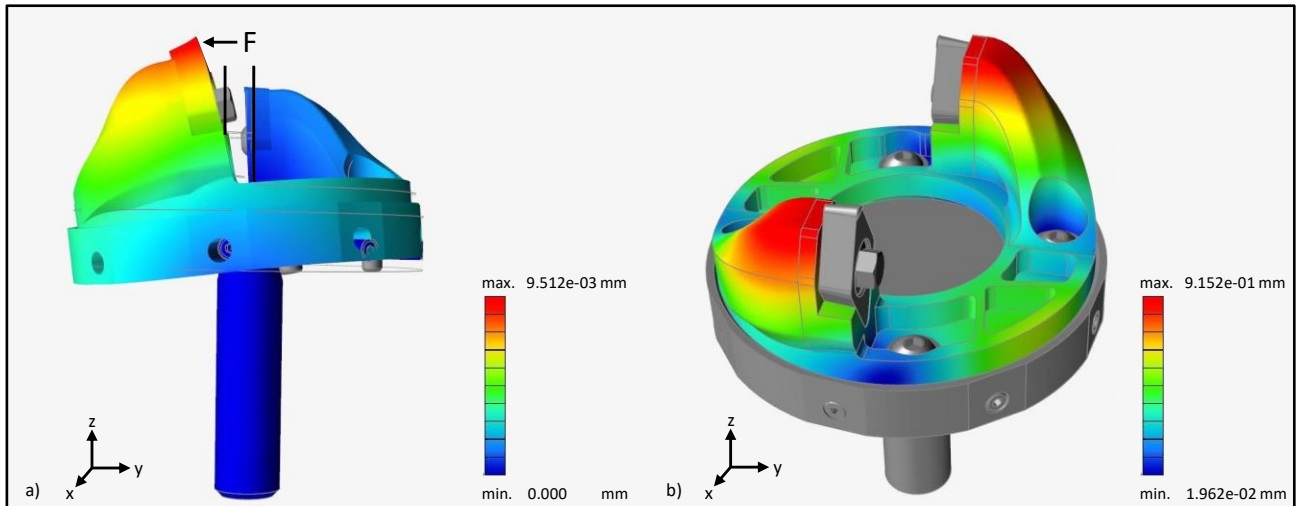
Figure 1. Results of the numerical analysis of the flycutter with integrated continuous fiber-reinforcement; a) displacement; b) eigenfrequencies

At applied load, the simulation showed a significantly greater maximum displacement of $\Delta L_{max} = 9.5$ µm for the tool without continuous glass fiber-reinforcement. Under the same conditions, a maximum displacement of $\Delta L_{max} = 2.6$ µm resulted for the continuous fiber-reinforced components. For these components eigenfrequency simulations also resulted in improved deflection of the vibrations during use compared to simulations not considering continuous glass fiber-reinforcement. Figure 2 shows the additively manufactured flycutter in a process environment.
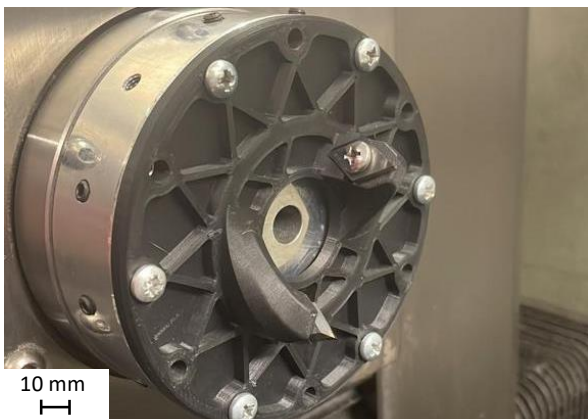
Figure 2. Additively manufactured flycutter
mounted to the spindle of the ultra-precision machine tool

3. Conclusion

The findings of this ongoing research show the potential additive manufacturing holds for a more cost-effective tools production in ultra-precision machining. With the development of a tool geometry optimized for fiber-reinforced FFF a basis for a lightweight and rigid flycutter geometry could be introduced. The simulations demonstrated the potential of superimposed fiber-reinforcement in additively manufactured components and provided new approaches for the further development of tool geometries. Compared to conventionally manufactured flycutters, significant material savings and the possibility of implementing complex geometries with local reinforcement were demonstrated. This results in the possibility of adapting tools for ultra-precision machining to individual requirements faster and more easily. The choice of materials and the optimized geometry make it possible to manufacture these tools more cost-effectively and with shorter iteration cycles. Due to the vibrations and deflections that occur during machining, a reduction in surface quality and changes in the effective rake angle γ_0 are to be expected. These challenges need to be addressed in future research.

References

[1] Mohanavel, V.; Ali, K.; Ranganathan, K.; Jeffrey, J.; Ravikumar, M.; Rajkumar, S.: The roles and applications of additive manufacturing in the aerospace and automobile sector. *Materials Today: Proceedings* **47**, 405 – 409, 2021.

[2] Tan, C.; Wang, D.; Ma, W.; Chen, Y.; Chen, S.; Yang, Y.; Zhou, K.: Design and additive manufacturing of novel conformal cooling molds. *Materials & Design* **196**, 2020.

[3] Goh, G.; Dikshit, V.; Nagalingam, A.; Goh, G.; Agarwala, S.; Sing, S.; Yeong, W.: Characterization of mechanical properties and fracture mode of additively manufactured carbon fiber and glass fiber reinforced thermoplastics. *Materials & Design* **137**, 79 – 89, 2018.

[4] Almeida Jr., J.; Christoff, B.; Tita, V.; St-Pierre, L.: A concurrent fibre orientation and topology optimisation framework for 3D-printed fibre-reinforced composites. *Composites Science and Technology* **232**, 2023.

[5] Rakotondrainibe, L.; Allaire, G.; Orval, P.: Topology optimization of connections in mechanical systems. *Structural and Multidisciplinary Optimization* **61**, 2.253 – 2.269.

euspen's 24th International Conference &
Exhibition, Dublin, IE, June 2024
www.euspen.eu

Advanced camera calibration for lens distortion correction in hybrid manufacturing processes: An exemplary application in laser powder bed fusion (PBF-LB/M)

B. Merz[1,2], K. Poka[1], G. Mohr[1], K. Hilgenberg[1], J. Polte[2,3]

[1]Additive Manufacturing of Metallic Components, Bundesanstalt für Materialforschung und –prüfung (BAM), Berlin, Germany
[2]Institute for Machine Tools and Factory Management IWF, Technische Universität Berlin, Berlin, Germany
[3]Fraunhofer Institute for Production Systems and Design Technology IPK, Pascalstraße 8-9, 10587 Berlin, Germany

Benjamin.Merz@bam.de

Abstract

Hybrid additive manufacturing is becoming increasingly important in the field of additive manufacturing. Hybrid approaches combine at least two different manufacturing processes. The focus of this work is the build-up of geometries onto conventionally manufactured parts using Powder Bed Fusion with Laser Beam of Metals (PBF-LB/M). The hybrid build-up requires a precise position detection system inside the PBF-LB/M machines to determine the exact position of the existing component. For this purpose, high-resolution camera systems can be utilized. However, the use of a camera system is associated with several challenges. The captured images are subject to various distortions of the optical path. Due to these distortions, it is not possible to use the images for measurements and, therefore, it is not possible to calculate the positions of objects. In this study a homography matrix is calculated to correct keystone distortion in the images. Different calibration patterns have been tested for the calculation of the homography matrix. The influence of the number of calibration points on the precision of position detection of objects is determined. Furthermore, the influence of an additional camera calibration by using ChArUco boards is evaluated. The result is a camera calibration workflow with associated calibration pattern for a precise position detection of parts inside PBF-LB/M machines allowing a hybrid build-up with minimum physical offset between base component and build-up.

Keywords: Additive manufacturing, hybrid build-up, position detection, camera calibration

1. Introduction

One possible application of hybrid additive manufacturing (AM) is the build-up of geometries onto existing components [1,2]. Powder bed usion of metals utilizing a laser beam (PBF-LB/M) can be used to achieve a precise build-up with minimal offset between the component and the AM structure to avoid subsequent machining. Standard PBF-LB/M machines are not designed to build-up onto existing components. For this reason, the position of the mounted component has to be determined with high accuracy and precision. A high resolution camera system can be used to achieve this [3].

Images acquired by camera systems are subject to different levels of distortion. Lens distortion is primarily caused by the inherent imperfections in the design and manufacturing of camera lenses. This type of distortion manifests as either barrel distortion, where straight lines appear curved outward, or pincushion distortion, where straight lines seem to curve inward [4]. It can be corrected utilizing a camera matrix, which can be calculated by using ChArUco boards [5]. CharUco boards combine the traditional chessboard pattern with binary matrix markers, similar to QR codes, called ArUco markers, thereby improving calibration accuracy and robustness for calculation of the camera matrix. The position of the camera is off-axis to the component whose position has to be detected, resulting in a keystone distortion in the image. This type of distortion manifests that straight parrallel lines in real world converge or diverge on the projection displayed in the image. A homography matrix can be utilized to correct this distortion and transform the component position into the machine coordinate system [3,6]. In this paper, the influence of the number of calibration points

for the calculation of the homography matrix is determined. Subsequently, the influence of a simultaneous correction of the lens distortion correction by using ChArUco boards is analyzed.

2. Experimental Setup

The setup for position detection is integrated in the commercial PBF-LB/M machine SLM 280 HL, SLM SOLUTIONS GROUP AG, GERMANY. The high resolution camera is a monochrome VLXT-650M.I, BAUMER HOLDING AG, SWITZERLAND with a resolution of 65.4 MPixel in combination with the modular lens system APO-COMPONON 4.5/90, JOS. SCHNEIDER OPTISCHE WERKE GMBH, GERMANY with a focal length of 90 mm. The camera is mounted outside the build chamber by using a tilt-shift-adapter to avoid vignetting effect. This setup results in a field of view (FOV) of approx. 160 x 120 mm² and an idealised spatial resolution of 17.2 μm/pixel [7]. The experimental setup is shown in Figure 1.
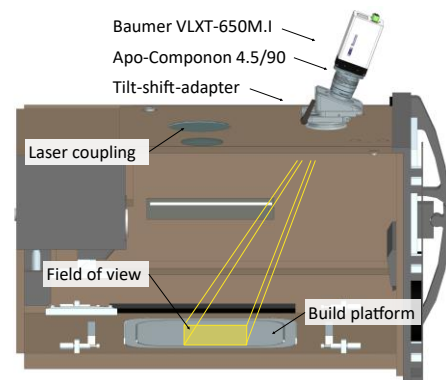
Figure 1. Experimental setup in SLM 280HL [7]

3. Accuracy and precision of calibration method

3.1. Influence of homography matrix

The calculation of a homography matrix is required to compensate keystone distortion in perspective distorted images. It is calculated by superimposing real source and ideal target points. The calibration points are generated by engraving reference markers on a black calibration plate with the laser of the PBF-LB/M machine. For calculation of the homography matrix, four different patterns with 5, 25, 169 and 529 reference markers are engraved by the laser. The calibration points are arranged symmetrically around a center point. This results in a grid of reference points with constant pitch between the points. The calibration pattern with 25 reference points is shown as an example in Figure 2. With respect to the 160 x 120 mm² FOV, the marker size is reduced with increasing number of reference points.
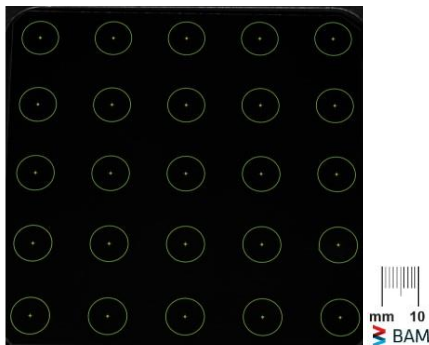
Figure 2. Exemplary image of 25 reference markers calibration pattern with detected marker positions

The coordinates of these ideal points, representing the target points, are known from the CAM system. After engraving the calibration patterns, an image of each pattern is captured by the camera. The real positions of the reference markers on the calibration plate can vary due to systematic errors of the PBF-LB/M process [8]. By directly detecting the reference markers positions in the images, these errors are considered for calculation of the homography matrix. To detect the position of the reference markers, the images are first binarised using a global threshold. After detecting the marker contours using the border following algorithm, the centroid of the markers are determined by the first order image moments [3,9]. These identified positions serve as the pivotal source points essential for the calculation of the homography matrices. In the proposed method, the determination of the target points is based on the positional data of the source points. First, the distances between all the source points are determined seperately along the x- and y-direction. It is known from the CAM system that the distances between points are equal. Consequently, the minimum distance value from these calculations is used to calculate new corresponding points, starting from the center point of the calibration pattern. A schematic representation of the calculated target points using the example of 25 source points is shown in Figure 3. These new corresponding points are the target points essential for the calculation of the homography matrix. By superimposing the determined source points with the calculated target points, the homography matrices for all calibration patterns are calculated.

The influence of the different perspective corrections on the precision and accuracy of the position detection is then determined. For this, a distinct test pattern is engraved onto calibration plates utilizing the laser. Different geometries are engraved to ensure variation in the appearance of the shape in the camera image. A total of seven geometric shapes were engraved three times each at different positions on the calibration plate. The design and layout of the test pattern is shown in Figure 4.
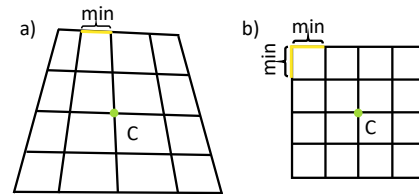
Figure 3. Schematic of target point calculation with highlighted center point a) determined source points from camera images; b) calculated target points based on minimum reference marker distance

Figure 4. Contrast enhanced image of test pattern

In total the test pattern is engraved 12 times and images are captured. With the 21 geometrical shapes on each plate this results in 252 reference positions for validation of the influence of the number of calibration points to the accuracy and precision of position detection. The keystone distortion in the acquired images is successively corrected using the different homography matrices H_5, H_{25}, H_{169} and H_{529}, where the indeces correspond to the number of calibration points. From each perspective corrected image, the positions of the objects are determined using the workflow described above. The deviations between the ideal positions derived from the CAD system and the determined positions are calculated. The deviation is calculated separately for the x- and y-direction. The results are shown in Figure 5.

It is observed that the dispersion of values along the y-axis is more pronounced compared to the x-axis. Furthermore, an increase in the number of calibration points is associated with a larger deviation from the ideal values. Notably, more calibration points also results in a shift of the deviations towards the negative x-direction. This is evidenced from the accuracy of the mean values, which otherwise indicate a systematic offset. The reason for this can be found in small installation inaccuracies of the camera, which cause a stronger perspective in the negative x-direction, which is amplified by additional calibration points.

The descriptive statistics, shown in Figure 5, confirm the observations made. The standard deviations for all perspective corrections are within a similar range. This indicates a similar level of precision across the various rectifications of keystone distortion. Notably, the standard deviation in the y-direction is at least twice as large as that in the x-direction. As Figure 1 illustrates the machine setup, it can be seen that the camera is aligned centrally in the x-direction. To capture relevant areas of the build platform, the camera is tilted around the x-axis. This leads to a more pronounced perspective distortion in the y-direction, resulting in a larger residual deviation after keystone correction. This is reflected in the higher standard deviation observed in the y-direction.
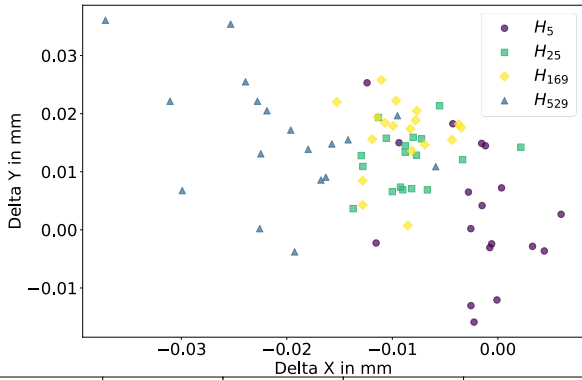
	$mean_X$	σ_X	$mean_Y$	σ_Y
H_5	-0,0051	0,0184	-0,0038	0,0469
H_{25}	-0,0113	0,0174	0,0068	0,0456
H_{169}	-0,0123	0,0176	0,0105	0,0461
H_{529}	-0,0233	0,0182	0,0093	0,0471

Figure 5. Deviation and scatter of values for keystone correction using different homography matrices (outlier corrected)

The smallest deviations from the mean values to the ideal values can be observed by correction of the keystone distortion using the homography matrix H_5. The deviation is - 0.0052 mm in the x-direction and - 0.0038 mm in the y-direction. The result indicates, that a higher number of calibration points is associated with a less accurate compensation of keystone distortion. To support this hypothesis, statistical significance was assessed via p-values, and effect sizes were quantified using Cohen's d. As depicted in Table 1, both the x-direction and y-direction exhibit low p-values with a significane level below 0.05, stating a statistically significant difference in perspective correction accuracy between H_5 and the other corrections, with a moderate effect size denoted by Cohen's d. This validates the hypothesis that a greater number of calibration points results in reduced precision in correcting keystone distortion.

Table 1 Statistical significance of the observed deviations (p-value) and effect size (Cohen's d).

	Cohen's d_X	p-value$_X$	Cohen's d_Y	p-value$_Y$
H_5 to H_{25}	0,3327	2.09e-04	-0,22275	1.27e-02
H_5 to H_{169}	0,3845	1.91e-05	-0,29935	8.38e-04
H_5 to H_{529}	0,9545	2.92e-24	-0,27232	2.36e-03

One possible reason for this is that increasing the number of calibration points leads to overfitting the perspective distortion in one plane. In addition, the size of the reference markers becomes smaller as their number increases, making them more susceptible to errors during image processing. These errors compromise the accuracy of position detection via image moments, leading to incorrect estimations of the minimum distance between source points. Therefore, the target point grid is inaccurately determined (see Figure 3), which eventually affects the calculation of the homography matrix.

The results indicate that utilizing 5 reference points for perspective correction significantly enhances accuracy. Therefore, it can be concluded that rectification utilizing a homography matrix calculated from 5 calibration points is sufficient.

3.2. Influence of camera matrix

Additional lens distortion correction can improve the accuracy, precision and robustness of the camera calibration process [10, 11]. Lens distortion can be corrected by calculating the camera intrinsic parameters, summarised in the camera matrix **C**. To calculate the camera matrix, it is necessary to have reference images of a known object. ChArUco boards can be used for this purpose [5]. For accurate computation of the

camera matrix, a dataset of 30 images featuring a ChArUco board is captured, with a focus on ensuring a high variability in the orientations of the ChArUco board within these images. This data set is used to calculate the camera matrix C_0.

The influence of simultaneously correcting lens distortion and perspective distortion is validated using the same set of 12 images featuring the test pattern with 21 geometric shapes. Lens distortion and keystone distortion are corrected in the images. The positions of the test objects are then determined using the workflow described above. The deviations between the ideal positions derived from the CAD system and the determined positions are calculated. The deviations are calculated separately for the x-and y-directions. For reference, the results of correcting only keystone distortion by H_5 are shown. The result is shown in Figure 6.
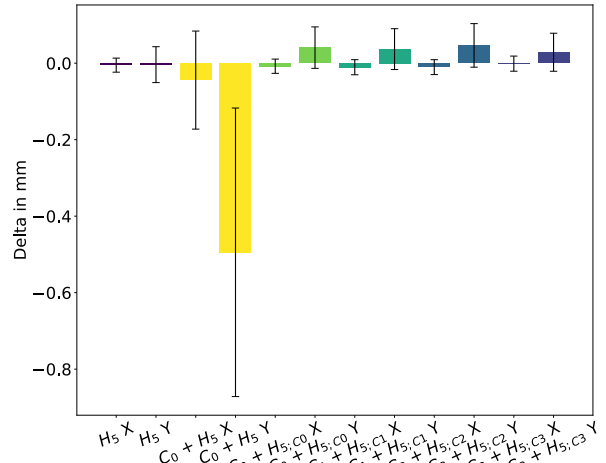
	$mean_X$	σ_X	$mean_Y$	σ_Y
H_5	-0,0051	0,0184	-0,0038	0,0469
$C_0 + H_5$	-0,0442	0,1282	-0,4945	0,3772
$C_0 + H_{5; C0}$	-0,0079	0,0186	0,0407	0,0542
$C_1 + H_{5; C1}$	-0,0106	0,0197	0,0368	0,0534
$C_2 + H_{5; C2}$	-0,0103	0,0195	0,0465	0,057
$C_3 + H_{5; C3}$	-0,0012	0,0198	0,0286	0,0497

Figure 6. Deviation between ideal and determined positions after different distortion corrections

In the initial test, lens distortion is corrected by C_0, followed by keystone distortion using H_5. Compared to the reference, a significant increase in both mean values and standard deviations is observed. This may be due to the fact that the homography matrix H_5 is calculated from an image subject to lens distortion. Consequently, the projective transformation between the source points and target points does not align correctly, resulting in an inaccurate calculation of the homography matrix. Such miscalculation leads to larger deviations and increased scatter from the nominal values. For this reason, the lens distortion is corrected in the input image before calculating the homography matrix, resulting in the new matrix $H_{5; C0}$. The lens distortion in the 12 test images is then corrected by C_0, followed by compensation of the keystone distortion using $H_{5; C0}$. This approach improves accuracy and precision, but it does not reach the accuracy level of corrections using H_5 alone. A potential reason for this is that the corner points of the ChAruCo boards in set of 30 images are not recognized with sufficient accuracy, leading to inaccuracies when calculating the camera matrix.

To minimize inaccuracies in detecting ChArUco boards, various methods for refining the detection of corner locations within the ArUco marker are examined. The different methods subpix, contour and AprilTag from the OpenCV library are applied for corner refinement [12, 13]. The subpix method is refining the corner locations with subpixel accuracy. The contour method is fitting lines to the detected contour points. The AprilTag method is using the improved AprilTag 2 deception algorithm [12,13].

Based on the refined detection of the ChArUco boards, the three new camera matrices C_1 for subpix refinement, C_2 for corner refinement and C_3 for AprilTag refinement are calculated. These matrices are then utilized to correct the lens distortion in the input images for calculation of the new homography matrices subpix ($H_{5;c1}$), corner ($H_{5;c2}$) and AprilTag ($H_{5;c3}$). For evaluation, the lens distortion in the 12 test images is corrected using the new camera matrices, followed by the correction of keystone distortion using the new homography matrices.

With the subpix refinement, the standard deviation of the values can be reduced compared to the results of no correction. The accuracy in the x-direction decreases, while the accuracy in the y-direction increases. The results can not be further improved by the method contour refinement. An improvement in accuracy can be achieved using the AprilTag refinement. Compared to the other refinements, the deviations are reduced in both the x- and y-direction. The standard deviation in the y-direction can be improved, while the standard deviation in the x-direction increases slightly. The reason for the improvement of the AprilTag method is that 12 more ArUco markers are detected in the images due to the corner refinement. As a result, the accuracy of lens distortion correction can be increased.

Compared to the H_5 reference method, which only corrects keystone distortion, the precision in the x-direction improves from -0.0051 mm to -0.0012 mm. In the y-direction, the AprilTag method, with an mean value of 0.0286, is about 7 times lagerer than the H_5 reference. There is also a slight increase in the standard deviation. In all cases, the deviation of the mean values can only be improved in one direction. Simultaneous enhancement of both the x- and y-directions, in terms of mean values and standard deviations, cannot be attained through additional correction of lens distortion. One potential reason for this is the accuracy of the ChArUco board, which was printed at a resolution of 1200 dpi using a laser printer, equivalent to a dot resolution of approx. 0.0212 mm. Consequently, the inherent error margin in the ChArUco board exceeds the spatial resolution of the camera system. These inherent errors lead to an inaccurate calculation of the camera matrix. Given the wide variability in the 30 images used for the camera matrix calculation, these inaccuracies impact all directions. Hence, no consistent improvement trend is observed in both the x-direction and y-direction simultaneously.

4. Conclusion

In this paper, the influence of different distortion corrections in images on the accuracy and precision of position detection for the hybrid build-up using PBF-LB/M is investigated. An imprecise calibration of the camera can lead to errors in detecting objects within the process chamber of the PBF-LB/M machine. It is important to keep this error as small as possible to ensure the smallest possible offset between the component and the AM structure. Large offsets can be particularly disadvantageous when building fine structures, for which the PBF-LB/M process is particularly advantageous. Depending on the size of the structures built, even small offsets can lead to waste or compromise process stability. Additionally, reworking internal surfaces or cavities of hybrid parts may be difficult or not possible. For components with internal cooling channels, an offset may reduce the flow quality of the coolant, which could compromise its intended purpose.

The influence of correction of keystone distortion is analyzed using calibration patterns with 5, 25, 169 and 529 reference markers. These markers were engraved on calibration plates using the laser of the PBF-LB/M machine. The positions of the reference markers were detected through image processing to calculate the homography matrices. The accuracy and precision

of perspective correction on the position detection of objects is evaluated by validating them using 12 test images. The best results are found with the calibration of 5 reference points. One possible reason for this could be that the reference markers become smaller as their number increases, making them more susceptible to errors during image processing. This leads to an incorrect calculation of the homography matrix.

The effect of additional calibration for lens distortion is also examined. The camera matrix is derived from 30 images of a ChArUco board. The accuracy and precision of position detection are evaluated using the same set of 12 test images, where lens distortion is corrected first, followed by keystone distortion correction. The calibration of lens distortion did not result in significant improvement compared to correcting keystone distortion alone. This might be attributed to the inherent errors in the ChArUco board used for calibration, leading to a flawed camera matrix calculation for lens distortion correction.

The high-performance APO-COMPONON 4.5/90 lens used exhibits very low lens distortion, particularly in the center of the image, which is the region of interest. Additional correction of lens distortion does not significantly improve the already minimal distortion in this area. Although a slight improvement in accuracy in the x-direction can be achieved by the additional correction of lens distortion using the AprilTag method, the correction from the perspective with 5 reference points is considered to be sufficient.

The transfer of camera calibration to the hybrid build-up of real components has been demonstrated on single demonstrator geometries [3,7] and will be the subject of future investigations on a larger scale.

References

[1] Popov, V. V.; Fleisher, A.: Hybrid additive manufacturing of steels and alloys. Manufacturing Review **7** (2020).

[2] Andersson, O.; Graichen, A.; Brodin, H.; Navrotsky, V.: Developing Additive Manufacturing Technology for Burner Repair. Journal of Engineering for Gas Turbines and Power **139** (2017).

[3] Merz, B.; Nilsson, R.; Garske, C.; Hilgenberg, K.: Camera-based high precision position detection for hybrid additive manufacturing with laser powder bed fusion. Int J Adv Manuf Technol **125** (2023).

[4] Neale, W. T.; Hessel, D.; Terpstra, T.: Photogrammetric Measurement Error Associated with Lens Distortion. SAE 2011 World Congress & Exhibition (2011).

[5] An, G. H.; Lee, S.; Seo, M.-W.; Yun, K.; Cheong, W.-S.; Kang, S.-J.: Charuco Board-Based Omnidirectional Camera Calibration Method. Electronics **7** (2018)

[6] Lee, J.-Y.: Robust Camera Calibration with a Single Image by Planar Homography. Proceedings of the 18th IEEE Int. Conference on Advanced Video and Signal Based Surveillance, Madrid (2022).

[7] Merz, B.; Poka, K.; Mohr, G.; Hilgenberg, K.: Precise Position Detection for Repair of Gas Turbine Blades using PBF-LB/M. Proceedings of the 5th International Symposium Additive Manufacturing ISAM (2023).

[8] Gradl, P. R.; Tinker, D. C.; Ivester, J.; Skinner, S. W.; Teasley, T.; Bili, J. L.: Geometric feature reproducibility for laser powder bed fusion (L-PBF) additive manufacturing with Inconel 718. Additive Manufacturing **47** (2021).

[9] Suzuki, S.; Abe, K.: Topological structural analysis of digitized binary images by border following. Computer Vision, Graphics, and Image Processing **30** (1985).

[10] Gao, D.; Yin, F.: Computing a complete camera lens distortion model by planar homography. Optics & Laser Technology **49** (2013).

[11] Rudakova, V.; Monasse, P.: Camera Matrix Calibration Using Circular Control Points and Separate Correction of the Geometric Distortion Field. Proceedings of the Canadian Conference on Computer and Robot Vision (2014).

[12] Bradski, G.: The OpenCV Library. Dr. Dobb's Journal of Software Tools (2000).

[13] Wang, J.; Olson, E.: AprilTag 2: Efficient and robust fiducial detection. Proceedings of the IEEE/RSJ International Conference on Intelligent Robots and Systems (IROS) (2016).

Analysis of the dimensional accuracy of a fiber composite material manufactured by fused filament fabrication

J. Polte[1, 2], E. Uhlmann[1, 2], S. Bode[1], F. Heusler[1], G. Al-Sanhani[1]

[1]*Institute for Machine Tools and Factory Management IWF, Technische Universität Berlin, Germany*
[2]*Fraunhofer Institute for Production Systems and Design Technology IPK, Germany*

stefanie.bode@tu-berlin.de

Abstract

Additive manufacturing is used in many areas of production, due to the increasing technological development of manufacturing processes. The technology provides a high degree of freedom concerning the design and manufacturing of complex and detailed structures. The level of dimensional accuracy is essential to ensure that inserts can be embedded with the correct tolerances and joints maintain their degree of freedom. This dimensional accuracy is related to the system and material. Therefore, it has to be assessed individually in advance. To demonstrate this, a test geometry was designed and manufactured from a fiber composite material, Onyx, using Fused Filament Fabrication. The sample geometry is based on the guideline for testing AM systems "Geometric capability assessment of additive manufacturing systems" ISO/ASTM 52902:2019 and includes several geometric aspects, including linear tolerance, roundness, wall thicknesses and diameters. For a precise assessment of the geometry in all sectional layers, the samples were measured with a CT scanner and compared with the CAD model. The results show, that there are deviations of $\Delta d = \pm 72$ µm in the X / Y direction and the warping effect that often occurs with polyamide-based materials. Precisely fitting components can be manufactured on the basis of the measured deviations by adapting the CAD model in advance.

Keywords: Fused filament fabrication, additive manufacturing (AM), 3D printing, dimensional accuracy, Design, Onyx

1. Introduction

Additive manufacturing (AM) is used in various areas, including aerospace, medical and the automotive industry. AM offers many advantages, such as the production of lighter objects with optimized use of materials and a decreased the number of assembly steps. This leads to shorter lead times and reduces costs. Due to the layer-by-layer build-up process, components can also be realized with a high degree of design freedom along with complex and filigree structures. The resolution of the component therefore depends on the selected manufacturing process and material. There are already several publications that describe the influence of printing parameters on surface quality and dimensional accuracy [1, 2]. In order to apply the components with high precision and maintain tolerances, it is necessary to record any influence on the dimensions in a standardised procedure.

2. Limitations of the Fused Filament Fabrication process

Due to its low costs, simple and safe handling and the wide range of materials that can be used Fused Filament Fabrication (FFF) is widely used technology. In the process, a line of melted material is deposited layer by layer. The nozzle movement is realized by a plotter with separate linear axis control in the X, Y and Z directions. The resolution and physical properties of the components can be modified by process parameters such as printing speed v_x, layer height s, infill density ρ_i, extrusion temperature T_x, screen width w and infill structure [2]. The nozzle diameter determines the smallest possible geometry or the representation of corners. A smaller nozzle diameter d_n can therefore increase the

resolution in the X / Y direction. Due to its influence on the resolution in z direction surface quality is affected by layer thickness s. Depending on the material, warping, a slight shrinking during cooling can occur. This causes a deformation of the part which leads to detachment from the build platform. Another major influence is the extrusion temperature T_x and extrusion flow F_x, which can affect the surface quality as well as the appearance of voids.

3. Experimental setup

For dimensionally accurate components, it is important to know the geometric resolution of the AM system. For this purpose, a resolution test body was designed based on the standard "Geometric capability assessment of additive manufacturing systems" ISO/ASTM 52902:2019 [3]. These test geometries cover the geometric performance in linear axis Δd_{lin}, roundness ΔD_C, wall thicknesses Δd_w, gap dimensions Δd_g and planarity Δw, as shown in figure 1.
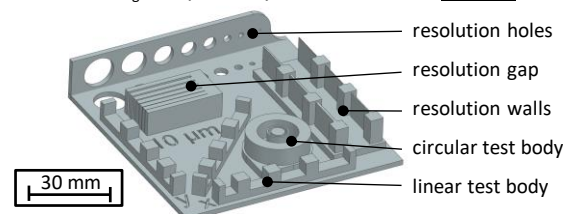
Figure 1. Test geometry for geometric capability of AM systems

On the linear test body, dimensional accuracy Δd_{lin} is measured between the peaks. These show distances between $2.5\ \text{mm} \leq d_{lin} \leq 12.5\ \text{mm}$ and are arranged with different orientations. The circular test body is used to measure the

roundness ΔD_C of the cylindrical surfaces and consists of three concentric rings with diameters in the range of 5.0 mm ≤ D_C ≤ 23.5 mm. The resolution test walls provide information on the finest detail to be produced and the walls measurements are between 0.1 ≤ d_w ≤ 1.0 mm. The resolution gaps from 0.1 mm ≤ d_g ≤ 1.0 mm are in contrast to this. The resolution holes show the smallest possible cylindrical features and include diameters between 0.5 mm ≤ D_H ≤ 12.0 mm. For an analysis of the layered structure, the resolution holes are positioned flat and upright on the base plate. The test geometry was designed in the CAD software NX from SIEMENS DIGITAL INDUSTRIES SOFTWARE, Plano, USA an. An Onyx Pro FFF-printer and carbon short-fiber-reinforced polyamide (PA 6), both by MARKFORGED INC., Waltham, United States, is used for the evaluation of the geometric performance. The Metrontom 800 computer-tomograph by CARL ZEISS IMT GMBH, Oberkochen, Germany, was used for the following measurement of the samples [4]. The evaluation is then carried out using Zeiss Calypso software by CARL ZEISS IQS DEUTSCHLAND GMBH, Oberkochen, Germany. The Zeiss Calypso software can be used to measure geometries and program inspection plans to compare the sample with the original CAD file [5].

4. Geometric measurements

The printed samples shows warping of Δw = 587 µm (± 175 µm). Specific structures, such as resolution gaps with a range of 0.1 mm ≤ d_g ≤ 0.2 mm, resolution holes with a range of 0.05 mm ≤ D_H ≤ 0.10 mm, and resolution wall with a range of 0.1 mm ≤ d_w ≤ 0.2 mm, are neither visible nor measurable. This can be clearly seen in the CT image shown in underline figure 2. The edges of the sample are curved upwards, which is why the blue plane is only visible in the center. Such warping could be prevented by a brim or a heated build platform and build chamber.
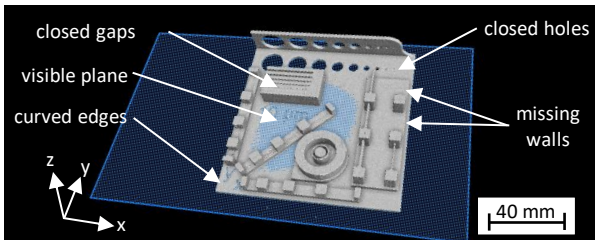
Figure 2. CT Image of the sample showing warping

Figure 3 shows the measurements of the deviations, which are shown as absolute values for better comparability. The measurements show average deviations of Δd_{lin} = 65 µm (± 40 µm) on the linear test body. It can also be seen in figure 3 that different results are achieved in the X and Y directions. This is also represented by the deviations in the roundness ΔD_C of the circular test body of ΔD_C = 121 µm (± 105 µm). These deviations occur due to slightly oval cylindrical surfaces. It can therefore be seen that the axes of the AM system have a different resolution. In addition, the resolution holes also show these deviations from $\Delta D_{Hx/y}$ = 63 µm (± 127 µm) in the dimensional accuracy. The deviations of the resolution holes placed upright in the Z-direction show a higher deviation of ΔD_{Hz} = 123 µm (± 93 µm) due to the layer structure and bridging. The ability to outline the resolution walls depends on the nozzle diameter D_n = 0.4 mm and therefore only the resolution walls bigger than d_w ≥ 0.4 mm are visible. The resolution gaps show the smallest deviations from Δd_g = 19 µm (± 40 µm).
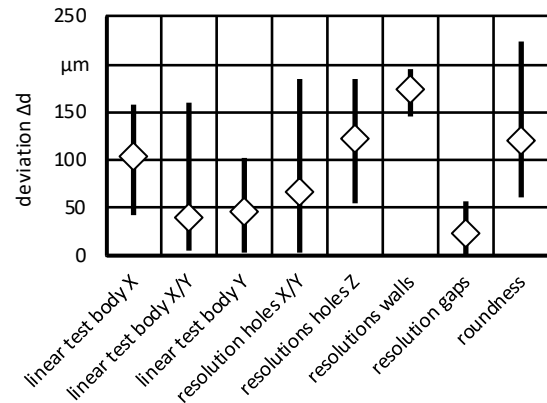
Figure 3. Measured Deviation in the geometry

A closer look at the individual results reveals that inner contours have a general deviation of Δd_{In} = -65 µm and outer contours a deviation of Δd_{out} = 49 µm. The higher deviation for inner contours results from the fact that contours such as a circle are traced several times by the nozzle, while an outer contour such as an outer corner is only traced once. Internal structures as holes must therefore be designed larger and external structures smaller. This results from the material line deposited in the FFF-process, which must be wider than intended and is over-extruded.

5. Conclusion and outlook

An overall deviation of Δd = 72 µm (± 54 µm) in the X/Y direction can be seen from the test bodies. This complies with the accuracy of Δa = 160 µm in the plane given by the manufacturer [6]. Nevertheless, there is a clear trend towards over-extrusion, which is why this must be taken into account when creating designs and the required tolerances. These deviations are different for each material and AM system and must be tested individually in order to obtain precise components. As an alternative, the existing slicer systems could also be optimized to prevent these accuracy issues through extrusion adjustments.

References

[1] Kechagias, J.; Chaidas, D.; Vidakis, N.; Salonitis, K.; Vaxevanidis, N.M., (2022) Key parameters controlling surface quality and dimensional accuracy: a critical review of FFF process. *Materials and Manufacturing processes* **37,** p. 963 – 984.

[2] Pulipaka A., Gide K. M., Beheshti A., Bagheri Z. S., (2023) Effect of 3D printing process parameters on surface and mechanical properties of FFF-printed PEEK. *Journal of Manufacuturing Processes* **85,** p. 368 – 386.

[3] DIN EN ISO/ASTM 52902 (05.2020) Additive Fertigung – Testkörper – Allgemeine Leitlinie für die Bewertung der geometrischen Leistung additiver Fertigungssysteme (AM-Systeme). Berlin: Beuth.

[4] Carl Zeiss IQS Deutschland GmbH: 3D Röntgenmessung in der Qualitätssicherung. URL: https://www.zeiss.de/ messtechnik/ produkte/systeme/computertomographie/metrotom.html (available on-line 23.08.2023).

[5] Carl Zeiss IQS Deutschland GmbH: Der direkte Weg zu aussagefähigen Ergebnissen: Zeiss Calypso. URL: https:// www.zeiss.de/messtechnik/produkte/software/calypso-uebersicht/calypso.html (available on-line 05.01.2024).

[6] Markforged Inc.: Onyx Pro (Gen 2) REV 3.6. Datasheet. 2022.

Investigation of acoustic emission behaviors and their synchronization with discharge pulse signals in micro electrical discharge machining

Long Ye[1,2], Jun Qian[1,2], and Dominiek Reynaerts[1,2,*]

[1]Manufacturing Processes and Systems (MaPS), Department of Mechanical Engineering, KU Leuven, Leuven, Belgium.
[2]Members Flanders Make, Leuven, Belgium

*Corresponding author: dominiek.reynaerts@kuleuven.be

Abstract

Process monitoring is a key-enabling technology to offer an indirect insight into the intricate spatio-temproal discharge phenomena and, consequently, the removal mechanism in micro electrical discharge machining. Recent research has explored the monitoring of acoustic emission (AE), showcasing its potential to complement the breadth of process knowledge. This paper delves into an investigation of AE behaviors synchronized with electrical pulse signals, grounded in empirical understanding. The synchronization, examined in both single discharge and consecutive discharges, facilitates a fundamental interpretation of the AE mechanism and its correlation with the removal mechanism.

Electrical discharge machining, acoustic emission, process monitoring

1. Introduction

Micro electrical discharge machining (µEDM) is an established non-contact machining technique for processing difficult-to-cut materials such as superalloy, metal matrix composites and technical ceramics. Despite its established status, the intricacies of the removal mechanism in µEDM remain elusive primarily due to its complex spatial-tempral phenonmena. This knowledge gap poses constraints on further advancements and applications in precision engineering. To address this challenge, process monitoring emerges as a viable approach to providing an indirect insight into the real-time process dynamics and therefore receives industrial applications for process diagnosis, process control and quality control.

Traditional µEDM process monitoring mainly focuses on electrical signals because of their interpretable association with the removal mechanism and widespread accessibility through electrical sensors. However, these signals are susceptible process noise and can be insensitive to the discharge positions. Acoustic emission (AE) signals present a compelling alternative for high-quality monitoring, being immune to low-frequency electrical noise. Craig and Smith [1] applied two AE sensors for locating the discharge spots in the context of successive discharges. Goodlet and Koshy [2] validated the feasibility of applying AE for monitoring in real time the gap flushing and found its efficacy for indicating material removal at each individual discharge. A fundamental study of AE phenomena was conducted by Klink et al. [3] through synchronization of discharge forces and gas bubbles. They attributed the main variation of AE bursts to the dynamic pressures caused by bubble collapse and provided an alternate explanation to the effects of electrical parameters on material removal.

Despite these valuable insights, a significant gap persists in understanding the association between AE and discharge phenomena. This research aims to bridge this gap by conducting an in-depth investigation into AE fundamentals, employing a synchronization study with discharge pulse signals.

2. Experimental setup

The monitoring experiments were conducted on a desktop µEDM machine (SARIX® SX-100-HPM). The workpiece material was Titanium alloy (Ti-6Al-4V) and the electrode with diameter of 0.5 mm was made of tungsten carbide (WC). HEDMA® hydrocarbon oil was used as dielectric fluid. Electrical discharge and AE signals were acquired in real time by external sensors, as illustrated in Figure 1. Particularly, the structure-borne piezoelectric AE sensor (Kistler® 8152C, sensitive frequency band 100 ~ 900 kHz) was located around 15 mm away from the discharge spots. Silicon grease was applied as a coupling medium between the sensor and the workpiece surface, whose connection was secured by screwing. All signals were recorded simultanously by different channels of an oscilloscope.
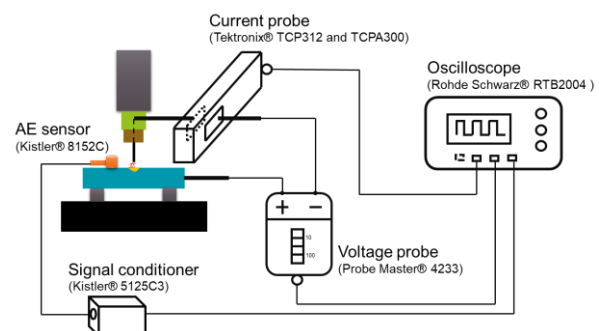
Figure 1. Expriemental setup for monitoring both electrical and acoustic emission signals. The sampling rate is 100 MHz and 20 MHz for single discharge test and consecutive discharges test, respectively.

3. Results and discussion

3.1. Single discharge test

A single discharge experiment was performed to investigate the AE phenomena and material removal mechanism. As shown

in Fig. 2 (a) and (b), an AE burst consisting of consecutive imbricate transient hits with time-varying strengths is generated, lagging a certain time behind the ignition of the electrical discharge. The time lag, caused by the AE signal transmission, depends on the distance between the AE sensor location and actual discharge spot. Different from the momentary discharge phenomena, the AE phenomena can maintain for a much longer period of time. This is attributed to the AE mechanism where the gas bubble continually exerts a dynamical pressure on the workpiece surface. Klink et al. [3] have confirmed the cycle of the bubble dynamics up to around 200 times as long. In particular, several peaks, which are registered by the recurring cycles of bubble collapse and rebound, can be noticed on the AE burst. This aligns with the observations in [3]. In addition, the AE burst energy can provide complemtary information to the removal mechanism, as indicated by Fig. 2(c). As shown in Fig. 2(d), it is not uncommon that higher electrical discharge energy can contribute to more removal of materials. However, this removal process can approach to a limitation after a high current index. This limitation can be implicated by the increasing AE energy that can affect the portion of energy partitioned to the electrodes.
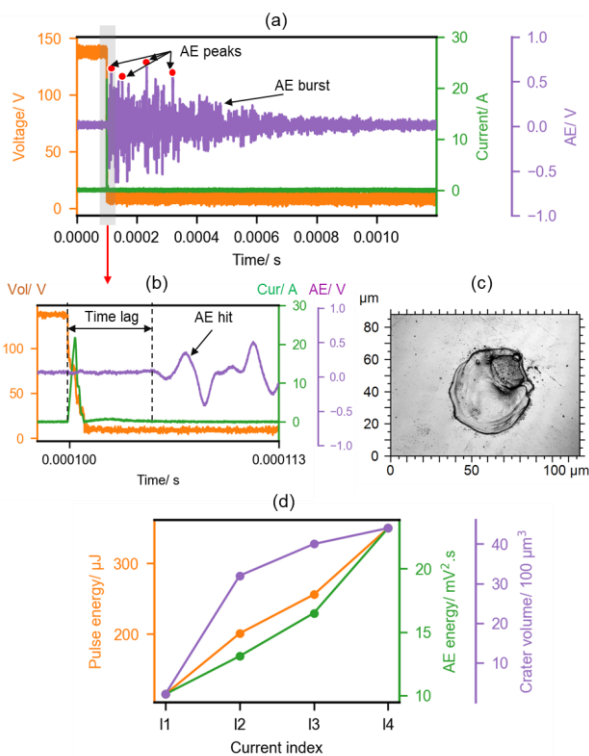
Figure 2. Single discharge and AE monitoring: (a) synchronization of AE with electrical signals; (b) zoom-in details of discharge moment; (c) single crater resulted from the single discharge and (d) correlation of AE energy, discharge energy and crater volume.

3.2. Consecutive discharges test

The synchronization of AE signals with electrical discharge signals are presented in Fig. 3 where consecutive discharges were produced for a constant time of 12 ms. In general, the AE bursts are temproally correlated with discharge clusters that consist of a train of effective discharges. This finding suggests the generation of consecutive discharges within the same bubble cycle. It is empirically acknowledged that the collapse of bubbles can facilitate the removal of molten materials. Therefore, this facilitation can only be provided for very limited discharges according to this finding. Comparing to the single discharge test, the average AE energies are much lower in the consecutive discharges because of cumulative effects caused by

the generated debris and bubbles. This can be further evidenced by a comparison between Fig. 3 (a) and (b), where the former typically yields a more contaminated gap condition by the intensively produced discharges and correspondingly by-products. In this case, the AE decaying stage is hardly found and AE bursts can not be easily differentiated from each other because of overlapped bubble cycles. While for the sparsely distributed discharges, AE bursts are discernible with typical registration of peaks and intervals. The particular AE energy, however, indicates an inefficient removal process in this situation. It is worth noting that there is no AE activity when a train of short-circuits appear as illustrated in Fig. 3 (c). This can be useful for identifying the unique process condition.
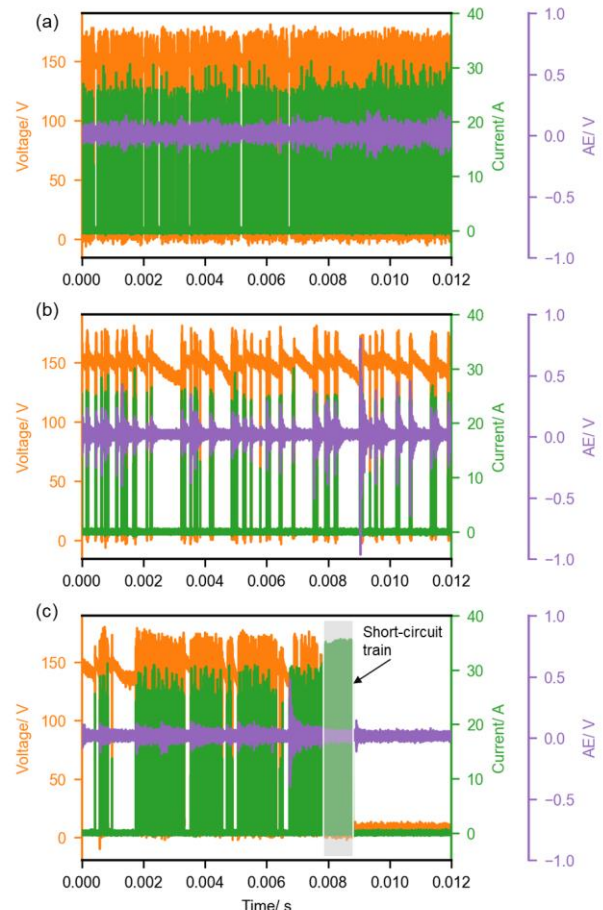
Figure 3. Correlation of AE signals with discharge signals under different discharge process conditions: (a) intensive discharge train; (b) sparse discharge train and (c) aggressive discharge train.

4. Conclusion

The paper investigates the synchronization between acoustic emission (AE) signals and electrical pulse signals in both single discharge and consecutive discharges tests. The AE energy is proven to provide complementary information for the material removal. Notably, the observed variations in AE signal characteristics with respect to discharge clusters underscore the efficacy of AE features in discerning unique discharge conditions.

References

[1] Smith C, Koshy P 2013 Jan. Applications of acoustic mapping in electrical discharge machining. *CIRP Annals*. 62(1):171-4.
[2] Goodlet A, Koshy P 2015 Jan. Real-time evaluation of gap flushing in electrical discharge machining. *CIRP Annals*. 64(1):241-4.
[3] Klink A, Holsten M, Schneider S, Koshy P 2016 J. Acoustic emission signatures of electrical discharge machining. *CIRP Annals*. 65(1):229-32.

Dimensional accuracy assessment in Rapid Investment Casting: Evaluating metal components with Additive Manufacturing wax patterns

Amogh V Krishna[1], Tim Malmgren[2], Vijeth V Reddy[1], Paulo Kiefe[2], Stellan Brimalm[2] and B-G Rosen[1]

[1]Halmstad University, Functional surfaces research group, Halmstad, Sweden
[2]3Dialog, Halmstad, Sweden

amogh_vedantha.krishna@hh.se

Abstract

Rapid Investment Casting (RIC) is an advanced manufacturing technique that combines the capabilities of Additive Manufacturing (AM) technologies to fabricate complex metal parts through the creation of wax models for investment casting. The success of this process relies heavily on the dimensional quality and precision of the initial wax patterns. The growing adoption of Material Jetting Technology (MJT), a type of AM process, for crafting these wax patterns necessitates a thorough investigation of dimensional properties imparted by this approach.

The analysis involves a direct comparison of the final 3D scanned metal parts with the corresponding CAD model, offering insights into the accuracy of the MJT-generated wax patterns. A structured light projection 3D optical scanner was utilized to capture the 3D models of casted parts, and Geomagic Control X was utilized to point out the dimensional discrepancies between the scanned and CAD models. Additionally, the research provides a comparative analysis between MJT and Vat-photopolymerization (VPP) methods in RIC processes, contributing to the understanding of the impact of Additive Manufacturing (AM) on dimensional precision. The findings aim to enhance the knowledge surrounding the efficacy of MJT in RIC, paving the way for advancements in precision casting.

Rapid Investment Casting, Additive Manufacturing, Material Jetting Technology, Vat-photopolymerization, Dimensional Accuracy, Precision Metrology.

1. Introduction

The pursuit of enhanced precision in metal component manufacturing has led to the integration of innovative processes such as Rapid Investment Casting (RIC) [1]. RIC is a casting process in which the lost-wax molds are produced using Additive Manufacturing (AM) technology, making it possible to produce complex geometrical designs. The RIC method offers shorter lead times, enhanced design flexibility, and reduced material waste, making it one of the most reliable methods for producing complex metal components. This process finds its applications in various fields such as aerospace, medical, and dental sectors and, most commonly, jewelry applications [2]. However, the success of this process mainly depends on the accuracy and precision of the AM-produced wax components.

Several research has been conducted to optimize the dimensional accuracy and surface roughness of AM wax patterns for the RIC process [3, 4, 5]. Most of the research has been based on the Stereolithography (SLA) technology, which is the Vat-photopolymerization (VPP) AM method. In this method, the wax patterns are fabricated layer-by-layer by selectively curing the liquid polymer wax resin by exposing it to UV radiation [6].

However, this present study focuses on using another type of AM process, namely, Material Jetting Technology (MJT), to produce these wax patterns required for the RIC process. This study aims to understand the dimensional accuracy of the produced wax pattern by evaluating metal components produced through the RIC process, emphasizing the role of AM technology in wax pattern production. MJT is central to this investigation, offering a unique approach to generating wax patterns. MJT is similar to an ink-jet printer, where several tiny nozzles selectively spray the material layer-by-layer to build the part [6]. Figure 1 displays a wax pattern produced by the MJT method using a 3Dialog CeraCaster® printer. Figure 2 presents some examples of cast metal components through this technology.
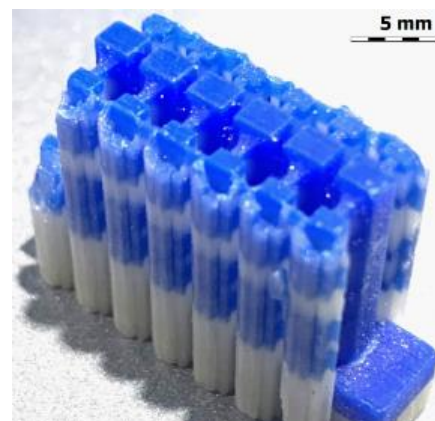
Figure 1. Example of the wax pattern produced by 3Dialog CeraCaster® MJT technology. The build material is represented by blue, and the support material by white paraffin wax.

The objective of the study is to conduct a direct comparison between the final metal parts and their CAD models, shedding light on the accuracy of MJT-produced wax patterns. Additionally, a comparative analysis with Vat-photopolymerization (VPP) [6] contributes valuable insights into the evolving landscape of AM techniques. Through this exploration, the research aims to advance precision casting methods, setting the stage for the integration of cutting-edge technologies into traditional manufacturing practices.
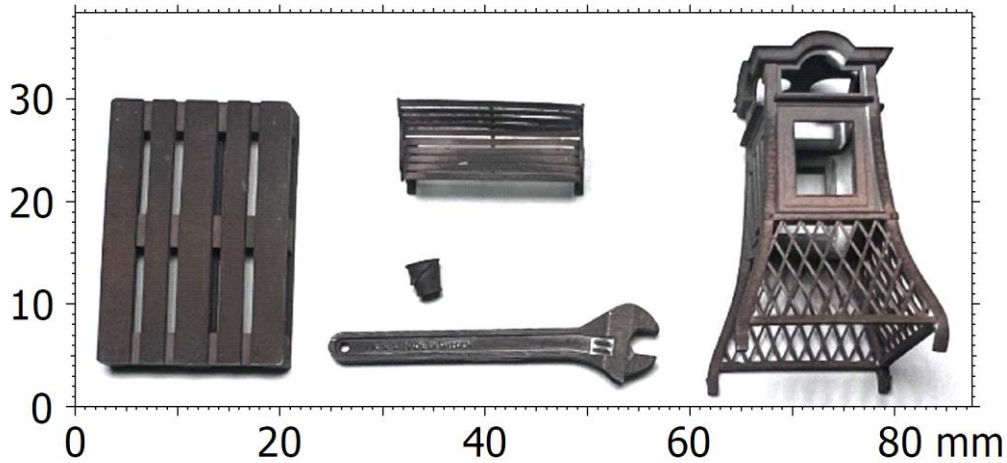
Figure 2. Examples of metal components produced by the RIC process using MJT wax patterns.

2. Material and Methods

The wax patterns required for the RIC process were produced using 3Dialog CeraCaster®, based on the Material Jetting Technology (MJT) 3D printing process. The metal sample examined in this paper was created using a wax pattern printed using draft settings, with a print resolution of 720 dpi, corresponding to a layer thickness of 35 μm. It is worth noting that the CeraCaster® in its latest version can print at 2540 dpi, resulting in a layer thickness of 10 μm, which can significantly improve the dimensional quality compared to the findings in this paper. The produced wax patterns were then utilized to create gypsum molds, during this phase, the wax melts and gets recycled. The molten metal was then poured into hollow gypsum molds in a vacuum environment and further pressurized with inert gas to ensure the fill in the cavities, consequently improving the casting quality and minimizing the porosity.

From the sustainability perspective, the wax patterns utilized for mold-making get recycled, while the recycling of gypsum molds comes with limitations related to purity, moisture, processing capabilities, cost, and quality.

The casted metal component was scanned using a Shining 3D AutoScan Inspec optical scanner (see Fig. 3). This scanner is based on the structured light 3D scanning principle with a resolution of less than 10 μm.

Figure 3. Shining 3D AutoScan Inspec 3D optical scanner.

Before actual measurements, the instrument was calibrated as per the specifications provided by the manufacturer. In order to establish a sense of fidelity of scanned measurements, it is crucial to note the accuracy and repeatability and thereby understand the uncertainty of the measurements. The ISO/IEC 98-3 Guide to the expression of uncertainty in measurement (GUM) [7] provides general rules for expressing measurement certainty. It states that the uncertainty of a measurement is usually a complex expression consisting of several variables, namely, environmental conditions (temperature variations), limited instrument resolution, human errors, and so on [7]. Generally, the easiest way to estimate uncertainty is to calculate the standard uncertainty of the measuring instrument, which is expressed as a standard deviation of several repeated measurements taken on standard gauge blocks. Hence, the repeatability test was performed by measuring a standard dimensional gauge block of 10 mm in width, which was scanned repeatedly five times, and the dimensional variation was noted.

For performing the dimensional analysis, the scanned STL model of the metal component was imported into the Geomagic® Control X™ metrology software, where it was superimposed on the reference CAD model for comparison. Figure 4 shows the 3D comparison between the reference CAD (grey) and the scanned model (blue). These models were aligned by using the "best-fit" method in the software, which is based on a Rigid Registration through point-to-point Iterative Closest Point (ICP) algorithm [8]. The alignment minimizes the mesh distance between each corresponding data point based on the least-squares principle. Rigid registration through the ICP algorithm does not explicitly designate any single point or surface as the datum or reference throughout its process. Instead, it continually updates the correspondence between points on the scanned model and the closest points on the CAD model, minimizing the overall distance between these pairs through iterative adjustments [9].

Figure 4. The scanned model in blue is superimposed on the reference CAD model in grey.

This paper is a form of a pre-study presenting an initial assessment of the dimensional accuracy of the parts produced by MJT for the RIC process. The methodology employed in this paper is mainly based on a direct comparison between the CAD model and the scanned metal object based on one example. This perhaps illustrates the capability and feasibility of CeraCaster® in producing wax patterns for the RIC process. As a next step, a comprehensive analysis involving dimensional test artifacts with detailed statistical analysis will follow to assess the quality of the casted metal components firmly.

3. Results and Discussion

As mentioned earlier, to reduce the measurement uncertainty, the 3D scanner was calibrated, and uncertainty was calculated by performing the repeatability tests using the standard gauge block, noting the standard deviation in measurements. The standard uncertainty of the 3D optical scanner was found to be less than 0.2% measured on a 10mm width gauge block. This establishes a sense of understanding regarding variation in actual measurements.

Figure 5 illustrates the discrepancies between the reference CAD model and the scanned 3D model of a wrench. The discrepancies are in the form of a color map demonstrating the dimensional accuracy of the manufactured sample. The tolerance of ±0.01mm was set, and the regions corresponding to the green color on the wrench marked the area where the differences between the two models are within tolerance. It must be noted that the tolerance set is an arbitrary value and highly depends on the application where the sample will be used. In this example, a tolerance of ±0.01mm is irrelevant, and it is mainly utilized for illustration purposes to bring out the discrepancies between the models.

It may be seen from Figure 5 and also from generated data shown in Tables 1 & 2 that a maximum of ±0.27mm was observed with an overall average deviation of 0.02mm was observed between the models. Table 1 also illustrates that nearly 23% of the total volume of the wrench is within the tolerance limits of ±0.01mm, and the volume increases considerably and achieves almost 90% for the tolerance limit of ±0.08mm. These results reveal that the MJT exhibited notable advantages in achieving superior dimensional accuracy.
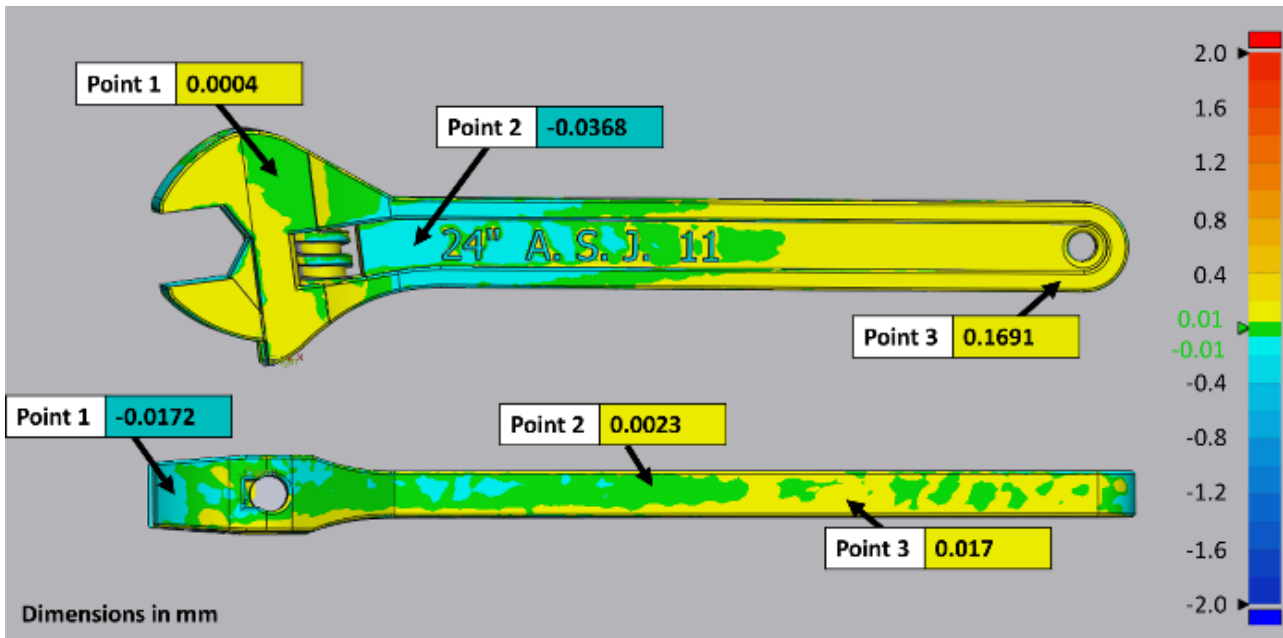
Figure 5. Dimensional deviations are represented as a color map

Table 1. The percentage volume of the wrench within the corresponding tolerance limits

Tolerance Limit in mm	Volume in %
± 0.01	23
± 0.02	42
± 0.04	67
± 0.08	90
± 0.16	99
± 0.27	100

Comprehensive research has been conducted using the Stereolithography (SLA) method for wax patterns for the RIC process, assessing dimensional accuracy [4, 5]. Results showed that a square artifact measuring the dimension of 6.5*4*2.5mm

(X*Y*Z), when measured using CMM, the deviations between the CAD model and cast part in Z direction was 0.1% and in X-Y directions average deviations were observed to be 2.1%. This gives a slight understanding of where the MJT technology stands in comparison to the SLA method for the RIC process. However, to compare the two methods, further research is needed.

Table 2. Statistics of the measured dimensional deviation between reference and scanned models

Description	Value
Ovr. Avg.	0,0206
RMS	0,0491
Std. Dev.	0,0445
+Avg.	0,042
-Avg.	-0,0222

Furthermore, the SLA method typically uses acrylate photopolymer formulated with liquid wax, which, during the burn-out cycle, leaves behind traces of polymer ash that reduce the purity of the cast metal components, especially while casting gold in the jewelry-making process. In contrast, MJT technology does not encounter this issue since it utilizes pure paraffin wax for pattern production. Paraffin wax, with its low melting point, chemically inert nature, and ease of removal, serves as an effective sacrificial support material in casting applications. Its low melting point allows for easy removal without compromising the properties of the casted material. Additionally, its chemical inertness prevents the formation of residues that could compromise the quality of the final casted part [10].

These unique advantages over the SLA process positions the 3Dialog CeraCaster® as a promising technology for not only achieving stringent dimensional requirements in investment casting but also potentially reducing production costs and enhancing overall efficiency.

4. Conclusion and Future work

In conclusion, this study has demonstrated the promising feasibility of employing Material Jetting Technology (MJT) in investment casting, with a specific focus on achieving enhanced dimensional accuracy in the printed patterns. A systematic comparison between MJT and SLA processes is necessary to assess the capabilities of respective AM technologies. Nonetheless, the present study highlights the superior performance of MJT, which is attributed to its high precision due to its fine layer resolution and ability to produce intricate details.

Building upon these findings, future work should further investigate optimizing the MJT process parameters to enhance dimensional accuracy. Additionally, extending the study to include the evaluation of mechanical properties and surface finish of the casted parts produced using MJT patterns would offer a comprehensive understanding of the overall quality and performance. Furthermore, exploring the scalability of MJT for mass production and assessing its environmental sustainability aspects would be critical for a holistic evaluation of its potential in industrial applications.

References

[1] Sarojrani P, Karunakar D B and Jha P K 2012 *J. Mater. Process Technol.* **212** 11 2332 – 2348.
[2] Ripetskiy A V, Khotina G K, Arkhipova O V 2023 *E3S Web Conf.* **413**
[3] Mukhangaliyeva A, Dairabayeva D, Perveen A, and Talamona D 2023 *J. Polymers* **15** 20 4038.
[4] Badanova N, Perveen A and Talamona D 2022 *J. Manuf. and Mater.ials Proc.* **6** 5.
[5] Mukhtarkhanov M, Perveen A, and Talamona D 2020 *J. Micromachines* **11** 10.
[6] ISO/ASTM 52900 2021 Additive manufacturing — General principles — Terminology.
[7] ISO/IEC GUM 98-3 2008 Guide to the expression of uncertainty in measurement.
[8] O'Toole S, Osnes C, Bartlett D and Keeling A 2019 *J. Dental Mater.* **35** 3 495–500.
[9] Mitra N J, Gelfand N, Pottmann H, and Guibas L 2004 *Proc. Eurographics* 22–31
[10] Bemblage O and Karunakar D B 2011 *Proc. WCE* **1** 721–727

Evaluation of the print geometry limitations of 3D printed continuous stainless steel fibre reinforced polymer composites

Alison Clarke[1], Vladimir Milosavljievic[2], Andrew Dickson[1] & Denis P. Dowling

[1]I-Form Centre, School of Mechanical and Materials Engineering, University College Dublin, Dublin, D04 V1W8, Belfield, Ireland
[2]Technological University Dublin, Park House, 191 N Circular Rd, Grangegorman, Dublin 7, D07 EWV, Ireland

alison.clarke1@ucdconnect.ie

Abstract

This study investigates the geometrical limitations of 3D printing continuous stainless steel fibre reinforced polymer composites. The printing study was carried out using a 316L stainless steel fibre (SSF) bundle with an approximate diameter of 0.15 mm. This bundle is composed of 90 fibres with a 14 μm diameter. This fibre bundle was firstly coated with polylactic acid (PLA), in order to produce the polymer coated continuous stainless steel filament, with diameters tailored in the range of 0.5 to 0.9 mm. These filaments were then used to print composite parts using the material extrusion (MEX) technique. To evaluate the geometry limitations of the printed polymer-SSF composites a series of prints were carried out through which print filament cornering and turning, a selection of angles and semi-circle radii were investigated. This investigation included printed part angles between 5 to 90°, along with semi-circles, with radii diameters between 2 and 20 mm, resulting in a series of 'teardrop' shaped geometries.

3D printing, stainless steel fibre, polylactic acid, curvature bending stiffness

1. Introduction

One of the most widely used 3D printing techniques is material extrusion (MEX) [1], [2]. Polymer composites are fabricated through the addition of fibres (short or continuous), alternatively powder particles, beads, and pellets [1], [3]–[6]. Reinforcing fibres available for MEX printed composite reinforcing fibres include glass, metal, carbon, and basalt [7]–[9]. The most commonly used thermoplastic feedstocks include Polylactic acid (PLA), Polycarbonate (PC), Polyamide (PA or nylon), and Acrylonitrile butadiene styrene (ABS) [1], [2], [4]–[6], [10].

The addition of particle and fibre reinforcing can substantially enhance the mechanical properties of 3D printed polymers. For example, PLA reinforced with continuous carbon fibre (PLA-CCF) was investigated by Li et al. [11]. The continuous carbon fibre bundle used contains up to a maximum of 1000 individual fibres. The resulting composite had a fibre volume fraction (Vf) of 34%, along with a tensile strength of up to 91 MPa. Nylon reinforced with continuous fibres of Kevlar, glass, and carbon, supplied by Markforged. The interlaminar shear strength was evaluated for Nylon-Kevlar, Nylon-glass, and Nylon-CF, with resultant strengths of 14.3, 21.0 and 31.9 MPa, respectively. Fibre content plays an important role in determining the properties of MEX composite filaments, with, for example, tensile strength generally increasing with increasing fibre content [1]. A difficulty, however, is that composite filaments, with high fibre content, can be very difficult to print, arising from issues with nozzle clogging, in addition to the excessive viscosity of the melted composite filament [10], [12]–[17].

In a previous study by the current authors filaments of continuous stainless steel fibre bundles within a polylactic acid (PLA) polymer were fabricated using a laboratory scale extrusion system [18]. By systematically controlling the 3D printing conditions, along with the use of a novel polymer pressure vent within the printer nozzle, 3D printed composites with fibre volume fractions between 4 and 30% were achieved. Good impregnation and adhesion of the PLA matrix into the stainless steel fibre were found based on an x-ray micro Computed Tomography (μCT) analysis, with the porosity of the resulting composites being in the range of 2 to 21%. The interlaminar shear strength ($\tau ILSS$) of the PLA-SSF with a volume fraction of 30% is found to be 28.5 MPa (±2.0), which is six times that of PLA only parts. Both the interlaminar shear strength and tensile strength properties of the composites were found to increase significantly as the stainless steel volume fraction (Vf) increased from 6 to 30%. The PLA-SSF composites exhibited tensile strengths of up to 249.8 MPa (±13.5), along with tensile modulus values of 14.3 GPa (±1.2). In the literature, the tensile strengths obtained with the highest stainless steel Vf in this study, are approximately four times higher than those reported for other printed metal fibre reinforced composites.

The objective of the current study is to evaluate the geometry limitations in the printing of continuous polymer-SSF parts. The study was carried out by varying the print geometries with part angles, between 5 to 90°, and semi-circles, with radii ranging from 2 to 20 mm.

2. Materials and methods

2.1. Materials and processing parameters

A continuous 316L stainless steel fibre (SSF) bundle was obtained from NV Bekaert SA (Belgium)[19]. The fabrication of a PLA - SSF filament was carried out from this steel fibre using a 3devo, laboratory-scale filament maker [20]. This was modified, to facilitate the introduction of the fibre into the molten polymer during filament extrusion as described previously [18]. The resulting PLA-SSF filaments were then used for the 3D printing of composite parts using a modified Anycubic i3 Mega polymer

extrusion printer as described previously [18]. To evaluate the continuous polymer-SSF materials' printability and geometrical limitations throughout cornering and turning, a selection of angles and semi-circle radii were investigated. The combination of angles, between 5 to 90°, and semi-circles, with radii ranging from 2 to 20mm, results in a series of 'teardrop' shaped geometries, as shown in Fig. 1.
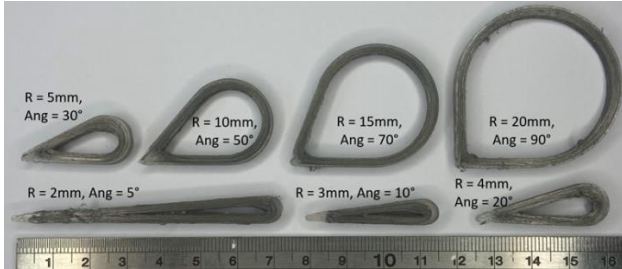
Figure 1. PLA-SSF 3D printed teardrop geometries

2.2. Composite characterisation

After printing the PLA-SSF teardrop composites (Figure 1), their dimensions, internal structure and morphology were examined. This evaluation was carried out by µCT scanning software VG studios, digital callipers and Dinolight microscope combined with a lighting box. The as-printed teardrop measurements are recorded and compared to the design dimensions. Measurements collection points are repeated on each sample by mapping and coding each geometry position.

Complementing the teardrop print study, an adaptation of the curve bend stiffness test standard ISO 14125, is used to determine the stiffness of the stainless steel reinforced composite as illustrated in Figure 2 [21]. The study investigated radii from 2 to 20 mm, with a minimum of five samples tested from each radius of 2, 3, 4, 5, 10, 15 and 20 mm. Along with testing the PLA-SSF semi-circles radii, neat PLA, Markforged Onex (Nylon – short carbon fibre) and Onex reinforced with continuous carbon fibre (Onex-cCF) were also printed with the same dimensions for comparison stiffness performance.
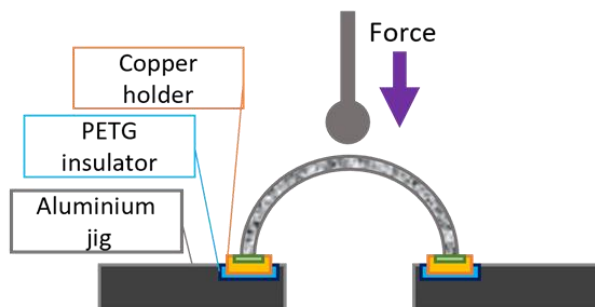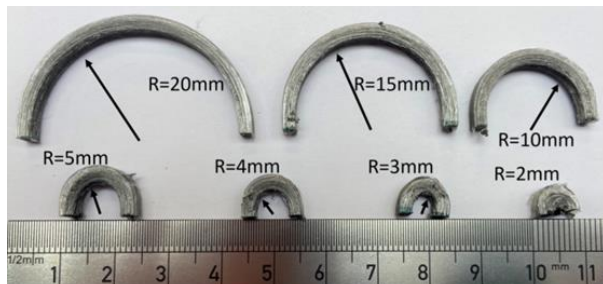
Figure 2: Curvature stiffness testing (CST), with a photograph of the PLA-SSF semi-circle test samples with radii as indicated (Top) and schematic of the test apparatus (Bottom)

The composite volume fraction and porosity are examined and evaluated using an X-ray µCT scanner, using ImageJ to cross-reference scanning electron microscope (SEM) and microscope cross-sections. The PLA-SSF tensile and ILSS samples resulted in a volume fraction of 30 V_f%. Where the teardrop and semi-circles in the range of 20-25 V_f%, this variation is due to the excess polymer surrounding the SSF and measurement position in the structure. All components result in a porosity of approximately 2%.

The PLA-SSF teardrop internal structure, morphology and dimensions are investigated by µCT scanning software VG studios, digital callipers and Dinolight microscope combined with a lighting box. The as-printed teardrop measurements are recorded and compared to the design dimensions. Measurements collection points are repeated on each sample by mapping and coding each position.

3. Results and discussion

The objective of this study is to evaluate the geometry limitations in the printing of continuous polymer-SSF parts. It was demonstrated that despite variations in the investigated angle and radii the printed teardrop samples with angles and radii greater than 30° and 5 mm respectively, exhibited print geometries which were close fit to those targeted. Overall the fit was in the range of 74-93% of the designed geometries, this was in contrast with the prints for the smallest angle and radii, for which the fit was reduced to 50%, as illustrated in Fig. 3.
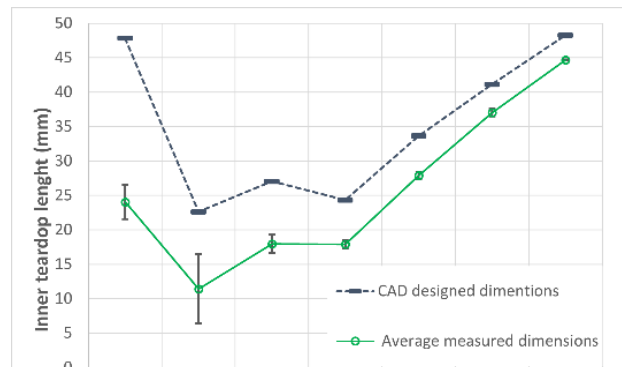
Figure 3: Teardrop geometry inner length dimensional comparison.

The width dimensions were found to increase at the end of a turn or radii, which was evaluated based on µCT scans which facilitated the measurement of the degree of distortion. The travel direction of the printer head moves in an anti-clockwise direction, as the printer head initiates the turning the SSF stays in the desired position however as it comes towards the end of the turn there it was observed to give rise to a higher level of distortion. In the case of the teardrop shapes printed at smaller angles (<5°) and radii (<4 mm); a significantly higher level of geometric distortion was observed. A further issue was the presence of fibre stringing in a number of the print geometries with lower radii semi-circles (Figure 4). This is likely to be associated with the slow solidification of the polymer as the print head changes direction, as a result, the SSF moves out of the targeted print track position. Controlling the speed at which the printer head travels around corners was found to be successful in successfully reducing the level of stringing for the smaller radii print structures.

4. Conclusion

This study investigates the geometrical limitations of 3D printing continuous 316L stainless steel fibre reinforced PLA polymer composites. Curve bend stiffness results in an increase in stiffness as the radii decrease in all materials tested.
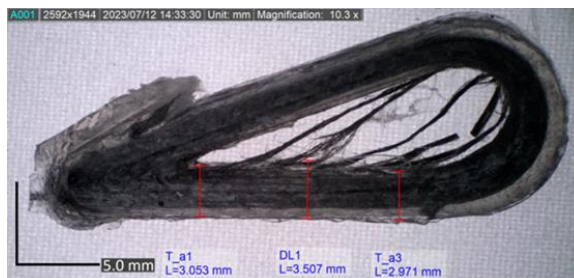
Figure 4: Teardrop with a radius of 4 mm and an angle of 20° illustrating the presence of significant levels of stringing.

The PLA-SSF showed the most significant stiffness increase at radii below 5 mm.

Teardrop-shaped components combine an angle and semi-circle dimensionally evaluated, showing repeatability in sample sets. As expected, the internal radii and acuteness of the angles degrade at smaller angles and radii. Across all samples, the effect of print height was found not to significantly influence the part geometry.

A statistical analysis has been conducted to evaluate the repeatability of the 3D printed composite samples with radii in the range from 2 to 20 mm, along with print angles between 5 to 90°. Geometric dimensions estimated based on marginal means analysis indicate a decrease in dimensional accuracy as both the print radii and angle are reduced in size. An approximately linear increase in curvature bending stiffness with a reduction in the print radii was observed.

References

[1] A. N. Dickson, H. M. Abourayana, and D. P. Dowling, "3D printing of fibre-reinforced thermoplastic composites using fused filament fabrication-A review," *Polymers (Basel).*, vol. 12, no. 10, pp. 1–20, 2020, doi: 10.3390/POLYM12102188.

[2] H. L. Tekinalp *et al.*, "Highly oriented carbon fiber-polymer composites via additive manufacturing," *Compos. Sci. Technol.*, vol. 105, pp. 144–150, 2014, doi: 10.1016/j.compscitech.2014.10.009.

[3] M. Á. Caminero, J. M. Chacón, E. García-Plaza, P. J. Núñez, J. M. Reverte, and J. P. Becar, "Additive manufacturing of PLA-based composites using fused filament fabrication: Effect of graphene nanoplatelet reinforcement on mechanical properties, dimensional accuracy and texture," *Polymers (Basel).*, vol. 11, no. 5, 2019, doi: 10.3390/polym11050799.

[4] Y. Ibrahim, "3D Printing of Continuous Wire Polymer Composite for Mechanical and Thermal Applications," YORK UNIVERSITY, 2019.

[5] M. A. Saleh, R. Kempers, and G. W. Melenka, "3D printed continuous wire polymer composites strain sensors for structural health monitoring," *Smart Mater. Struct.*, vol. 28, no. 10, 2019, doi: 10.1088/1361-665X/aafdef.

[6] A. Le Duigou, G. Chabaud, R. Matsuzaki, and M. Castro, "Tailoring the mechanical properties of 3D-printed continuous flax/PLA biocomposites by controlling the slicing parameters," *Compos. Part B Eng.*, vol. 203, no. July, p. 108474, 2020, doi: 10.1016/j.compositesb.2020.108474.

[7] ASTM, "ASTM D2344/D2344M: Standard Test Method for Short-Beam Strength of Polymer Matrix Composite Materials and Their Laminates," 2003.

[8] P. J. Hine, H. Rudolf Lusti, and A. A. Gusev, "Numerical simulation of the effects of volume fraction, aspect ratio and fibre length distribution on the elastic and thermoelastic properties of short fibre composites," *Compos. Sci. Technol.*, vol. 62, no. 10–11, pp. 1445–1453, 2002, doi: 10.1016/S0266-3538(02)00089-1.

[9] I. P. Beckman, C. Lozano, E. Freeman, and G. Riveros, "Fiber selection for reinforced additive manufacturing," *Polymers (Basel).*, vol. 13, no. 14, pp. 1–53, 2021, doi: 10.3390/polym13142231.

[10] R. Matsuzaki *et al.*, "Three-dimensional printing of continuous-fiber composites by in-nozzle impregnation," *Sci. Rep.*, vol. 6, no. December 2015, pp. 1–8, 2016, doi: 10.1038/srep23058.

[11] J. Li, Y. Durandet, X. Huang, G. Sun, and D. Ruan, "Additively manufactured fiber-reinforced composites: A review of mechanical behavior and opportunities," *J. Mater. Sci. Technol.*, vol. 119, pp. 219–244, 2022, doi: 10.1016/j.jmst.2021.11.063.

[12] L. Tack, "Bekinox® VN and Bekiflex®for Heatable Textiles," 2019.

[13] S. Oxygen *et al.*, *Inorgainc and Composite Fibers*, no. 105. Elsevier Ltd., 2018.

[14] A. Hamidi and Y. Tadesse, "Single step 3D printing of bioinspired structures via metal reinforced thermoplastic and highly stretchable elastomer," *Compos. Struct.*, vol. 210, no. March 2018, pp. 250–261, 2019, doi: 10.1016/j.compstruct.2018.11.019.

[15] D. Quan, S. Flynn, M. Artuso, N. Murphy, C. Rouge, and A. Ivanković, "Interlaminar fracture toughness of CFRPs interleaved with stainless steel fibres," *Compos. Struct.*, vol. 210, no. 1, pp. 49–56, 2019, doi: 10.1016/j.compstruct.2018.11.016.

[16] S. M. F. Kabir, K. Mathur, and A. F. M. Seyam, "A critical review on 3D printed continuous fiber-reinforced composites: History, mechanism, materials and properties," *Compos. Struct.*, vol. 232, no. June 2019, p. 111476, 2020, doi: 10.1016/j.compstruct.2019.111476.

[17] M. Gunes and I. Cayiroglu, "Mechanical Behaviour of 3D Printed Parts with Continuous Steel Wire Reinforcement," *El-Cezeri J. Sci. Eng.*, vol. 9, no. 1, pp. 276–289, 2022, doi: 10.31202/ecjse.969810.

[18] A. J. Clarke, A. Dickson, and D. P., "Fabrication and Performance of Continuous 316 Stainless Steel Fibre-Reinforced 3D-Printed PLA Composites," *Polymers (Basel).*, pp. 1–19, 2024, [Online]. Available: https://www.mdpi.com/2073-4360/16/1/63.

[19] Bekaert, "Metal fiber composite reinforcement," Zwevegem, 2018. [Online]. Available: https://www.bekaert.com/en/products/basic-materials/textile/composite-reinforcement.

[20]   3devo, "Composer 350," 2020. [Online]. Available:
         https://cdn2.hubspot.net/hubfs/4595257/Product Spec
         Sheets/Composer-350-Specs.pdf.

[21]   ISO, "ISO 14125 Fibre-reinforced plastic composites
          Determination of flexural properties," Genève, 1998.

Session 6: Mechatronics and Machine Tools

Exploring a compact piezo-driven inchworm motor for LISA space mission

Narendra Mahavar[1,2], Shashwat Kushwaha[1 2], Jonathan Menu[3], Michael Houben[4], Dominiek Reynaerts[1,2]

[1]Department of Mechanical Engineering, KU Leuven, Celestijnenlaan 300, Leuven 3001, Belgium
[2]Member Flanders Make, Belgium
[3]Department of Physics and Astronomy, KU Leuven, Celestijnenlaan 200D, Leuven 3001, Belgium
[4]Founder MACH 8, Belgium

narndra.mahavar@kuleuven.be

Abstract

LISA is an ongoing joint-European effort to develop a system capable of detecting low-frequency gravitational waves in space with high precision. This interferometry-based measurement system suffers from tilt-to-length coupling noise leading to misalignment of laser beam with the detector. An optical beam alignment mechanism actuated with a rotary mechanism will be developed and integrated with the optical bench of the measurement system. This paper talks about the design and development of compact piezo-driven inchworm rotary mechanism adhering to LISA requirements. The device can rotate a shaft by 47 mDeg in a single actuation cycle while maintaining the parasitic translational and angular displacements within ± 0.75 µm and 5.1 mDeg, respectively.

LISA, BAM, Piezo-driven inchworm motor.

1. Introduction

The Laser Interferometer Space Antenna (LISA) [1] is an on-going European effort for a mission to be launched in space in 2035. LISA aims to detect gravitational waves in space with high accuracy and precision. Three spacecraft will therefore be launched in space. These spacecrafts will be arranged in an equilateral triangle form where each arm length is about 2.5 million kilometers. Each spacecraft carries two optical benches which house optical components to detect and measure interference between different pairwise combinations of laser beams, both incoming beams (from the other two spacecraft) and local beams (from the spacecraft itself). Since the system works on the interferometric principle, it suffers from tilt-to-length (TTL) coupling noise. Any kind of parasitic movement of the beam shifts the beam on the detector, leading to TTL noise. One way to address the TTL noise is to laterally shift the incoming and/or local beam to realign with the detector. To achieve this functionality, Beam Alignment Mechanisms (BAM) will be developed and integrated on each optical bench.

A tilted optical flat can shift a beam laterally. Furthermore, the combination of two of these tilted flats enables an arbitrary lateral shift of the beam within a full circle if they are rotated about the axis of the impending beam. To achieve this functionality in space, a space-qualified precision motor with micro-radian rotation resolution is required. Some of the important functional and material requirements for LISA-BAM are shown in Table-1.

Table 1 LISA-BAM functional and material requirements for pre-development

Materials	Avoid ferromagnetic material and optical sources
Cleanliness	Avoid particle generation
Speed	$\geq 0.1\,°/s$
Parasitic transl. disp.	$< \pm 1\,µm$
Parasitic angular disp.	$< 10\,mDeg$

Non-magnetic piezo-driven precision motors can be divided into three categories based on their working principle namely ultrasonic or resonance motors, inertia driven motors, and inchworm motors. Ultrasonic and stick-slip principle-based motors beat inchworm motors in terms of speed but they generate particles [2]. On the other hand, inchworm principle-based motors produce minimal particles but are relatively slow. Since the desired speed for LISA-BAM mechanism is quite low, inchworm-based motors are preferred if they can provide rotation speed of $0.1\,°/s$. Apart from BAM, article [3] summarizes the development of other extremely stable piezo-driven mechanisms in the scope of LISA, namely, Point Angle Ahead Mechanism (PAAM), Fiber Switching Unit Actuator (FSUA), and In Field Pointing Mechanism (IFPM).

After an initial trade-off of available piezo-driven inchworm motors, a particular inchworm design [4] was chosen for further development due to its lower volume and fewer piezo actuators. As mentioned in Table-1, parasitic translational and angular displacements are some of the important requirements for the motor to maintain the beam stability. Since this data was not available in [4], a prototype was developed using aluminium for quick results. This article presents incremental development of the BAM and reports the findings.

2. Piezo-driven inchworm motor based on C-clamp: BAM-1

2.1. BAM-1 Design

The mechanism uses two identical clamping structures operating in two parallel planes, mounted on a common carrier, but as they are separated by a small gap (Fig. 1 (b)), it allows them to move independently. The rotor is held by the concentric annular clamps (referred to as C-clamps hereafter). Furthermore, the top section also includes a rotation mechanism.

For this inchworm design, a single cycle of rotation refers to the small incremental rotation (Δθ) achieved by the shaft after six steps (Fig. 1 (c)) of actuation, which are described below. By sequentially repeating these six steps, large rotation angles can
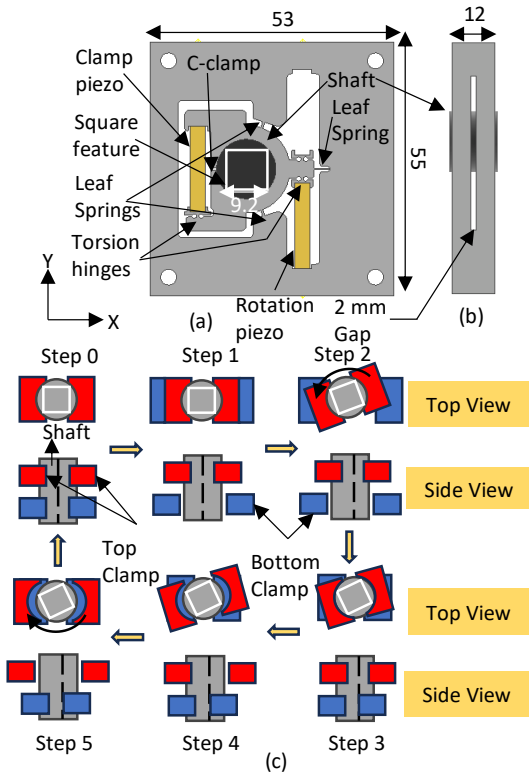
Figure 1. Schematic showing BAM-1 (a) Top view (b) side view, and (c) steps of actuation for single cycle of rotation (all dimensions are in mm).

be achieved. At rest, the shaft is held by both—top and bottom—clamping units.

Step-1: Bottom clamp releases the shaft.

Step-2: Rotation piezo is actuated to rotate the shaft by Δθ.

Step-3: Bottom clamp holds the shaft.

Step-4: Top clamp releases the shaft.

Step-5: Rotation piezo comes back.

Step-0: Top clamp holds the shaft.

Note that a 33 mDeg/cycle of rotation was set as a derived requirement assuming that the BAM can perform at least 3 cycles of rotation in a second if actuated at a higher frequency.

2.2. BAM-1 Simulation

Before manufacturing, finite-element static structural simulations were performed to predict the functional operation of design. The indicated holes in Fig. 2 (a) were fixed. The maximum stress developed at the fixed end of L3 leaf spring is 106 MPa at the end of rotation operation which is less than the yield strength of aluminum ($\sim$ 240 MPa). Fig. 2 (a) and (b) show the total displacements after clamp opening and rotation operation, respectively.

To open the clamp, opposing equal forces of magnitude 2.3 N were applied at the faces 'Q1' and 'Q2' along the Y-axis to increase the gap between the two by 10 μm . This results into release of the shaft as, 'U1' and 'U2' move away by 1.2 μm along the Y-axis.

For rotation, opposing equal forces of magnitude 57 N were applied at the faces 'Q3' and 'Q4' along the Y-axis to increase the gap between the two by 10 μm. This resulted in a rotation of 28.62 mDeg of the point 'C1' about the center 'C'. Furthermore, the center displaces by about 0.14 μm -0.29 μm about the X-axis and Y-axis, respectively.

2.3. BAM-1 Experimental setup and manufacturing

Tokin piezo elements (AE0505D16DF) were used for this prototype. The size of these piezo elements was 5x5x20 mm³. Power amplifiers (790A01, AVL) were used to actuate the piezo while actuation waveforms were generated using NI data
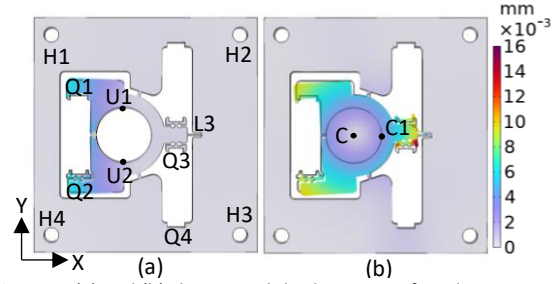
Figure 2. (a) and (b) shows total displacement after clamp opening and rotation, respectively.

acquisition system (PXI 7851R, National Instruments). An optical coordinate measurement machine (Werth VideoCheck HA CMM) was used to measure the position of the shaft from the top. To simplify the measurement process, a square (size of 9.2 mm) was machined at the top of the shaft (Fig. 1 (a)).

BAM-1 prototype was manufactured by wire-EDM. A stainless-steel shaft of 13 mm diameter was used as the rotor of the motor.

2.4. BAM-1 Experiments and results

Two major experiments were performed to characterize the performance of BAM-1. First, the parasitic motion of the shaft was measured during the handover (refer Fig. 3 (a)) of the shaft between the two clamping units. Second, multiple rotation cycles were performed to measure the repeatability of the rotation and the functionality for large angle rotations.

Shaft's center displacement

After each step of handover, the coordinates of the center of the shaft is shown in Fig. 3 (b) for five cycles. The random trajectory of displacements suggests low repeatability of the system. The center of the shaft was found to be displaced by ±15 μm.

Shaft's top plane tilt about the Z-axis

The change in the angle between the unit normal vector of shaft's top plane and the Z-axis (refer Fig. 1 (a)) w. r. t. initial angle at rest after each step of handover is plotted in Fig. 3 (c). The worst-case angle was measured to be 14 mDeg while the BAM requirements for the parasitic angular movement is 10 mDeg.

Multiple rotation cycles of BAM-2

The BAM-2 prototype was programmed to rotate the shaft in an incremental manner. The position of the four points of the square at the top surface of the shaft were measured after 100, 200, 300 and 500 cycles. Fig. 3 (d) shows the angles of rotation of these points calculated about the original center of the shaft's top plane at rest. The average speed of rotation was found to be 10 mDeg/cycle, while the derived LISA-BAM requirement is 33 mDeg/cycle.

Please note that for this inchworm motor design, the center of rotation does not coincide with the center of the C-clamp. This leads to unequal displacement (hence, rotation) of the four corners, as evident from significant drift in the plot. Furthermore, after each cycle of rotation, there are residual displacements in the center of the shaft. This problem can be fixed by constraining the shaft within a bearing.

2.5. BAM-1 Conclusions

From the above results, one can see that BAM-1 does not satisfy desired speed of rotation and parasitic displacements. Furthermore, the shortcomings of this design, as observed during the experiments, are:

- Unknown and multi-point contacts of C-clamp with the shaft ⇒ Large displacements of the rotation center.
- The pre-stressing of the clamping piezo also leads to opening of the C-clamp. This may lead to the unequal
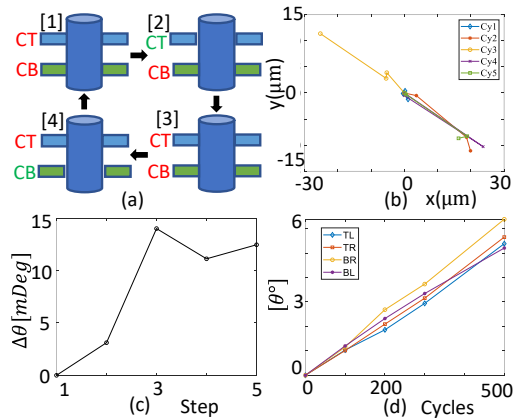
Figure 3. (a) Schematic showing steps during shaft's handover between the two clamps. (Text in red: clamped, green: unclamped), (b) Plot showing shaft's center displacement after each step of handover for five cycles, (c) Plot showing the tilt of the shaft: change in the angle between the unit normal vector of shaft's top plane and the Z-axis w. r. t. initial angle at rest, (d) Plot showing angle of rotation of the four points of the square at the top surface of the shaft, measured after 100, 200, 300 and 500 number of cycles. (TL: top left, TR: top right, BR: bottom right, BL: bottom left coordinates of the square at the top of the shaft).

diameter of the C-clamps of the two clamping sections, resulting in initial tilt of the shaft about the Z-axis.

3. Piezo-driven inchworm motor based on three-point contact: BAM-2

3.1. BAM-2 Design

To overcome the above-mentioned shortcomings, a new design called 'Cymbal design' or 'BAM-2' (Fig. 4 (a)) is proposed. This design has two main advantages over BAM-1.

- The clamping mechanism has deterministic three-point contact with the shaft. This will reduce the parasitic angular and translational displacements of the shaft.

- Secondly, additional elastic hinges have been added to decouple the pre-stress on the piezo from the clamp opening. The stiffness of these hinges (refer Fig. 4 (a)) is designed to be an order of magnitude less than the stiffness of the clamp. During piezo pre-stress, only the hinges undergo bending without deforming the cymbal clamping.

3.2. BAM-2 Simulation

For simulation, the indicated holes in Fig. 5 (a) were fixed. The maximum stresses developed at the fixed end of L3 leaf spring and at the center of the cymbal beam are 90 MPa and 120 MPa, respectively which are less than the yield strength of aluminum. Fig. 5 (a) and (b) shows the total displacements after clamp opening and rotation operation, respectively.

To open the clamp, equal forces of magnitude 49 N were applied at the faces 'Q1' and 'Q2' along the Y-axis to increase the gap between the two by 10 μm. This results into a total increment in the distance between point 'A' and 'B' by 3 μm.

For rotation, opposing forces of magnitude 18 N were applied at the faces 'Q3' and 'Q4' along the Y-axis to achieve a rotation of 45.13 mDeg of the point 'C1' about the center 'C'
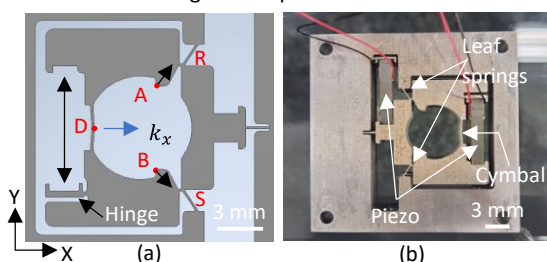
Figure 4. BAM-2 (a) CAD design (b) Image of the fabricated part.
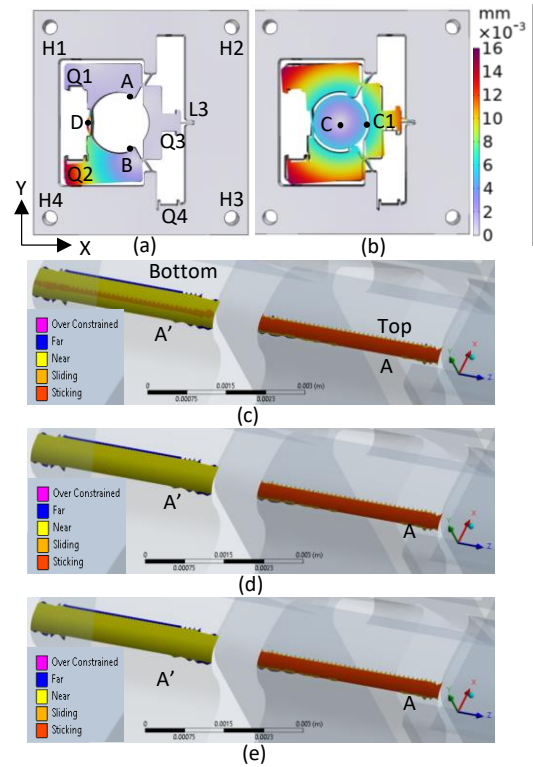
Figure 5. (a) and (b) shows total displacement after clamp opening and rotation, respectively. Contact status at point 'A' when (c) clamped from top and bottom and at the end of (d) bottom clamp open, and (e) subsequent rotation at the top.

which is assumed to remain fixed. Furthermore, the center displaces by about 0.16 μm and -0.05 μm. about the X-axis and Y-axis, respectively.

Additional simulations were performed to understand the contact status and the contact reaction forces. The contacts between the shaft and the contact points 'A', 'B' and 'D' were defined as frictionless and bonded (no relative motion at the contact location) for the bottom and top section respectively.

A three-step finite-element static structural simulations (Ansys, 2023) was performed. Step-1: to simulate the shaft clamping, equal and opposing forces of 62.2 N are applied at Q1 and Q2 faces (refer Fig. 5 (a)) to bring them closer. This results in a certain amount of force on the shaft which is balanced by the reaction forces at 'A' and 'B'. In step-2 bottom clamp is opened by 10 μm to release the shaft from the bottom while it is still held from the top clamp. In step-3 the top section is rotated by 45 mDeg about the center 'C'. Fig. 5 (d) and (e) show the plots of contact status at points 'A' (top section) and 'A''' (bottom section) at the end of the opening of the bottom clamp, and after subsequent rotation at the top, respectively.

For the bottom section, initially, the shaft is held by 5.94 N clamping reaction force from line contact at 'A'''. After the bottom clamp opening, the contact reaction force at point 'A''' reduces to 2.55 μN as it moves away from the shaft by 1.8 μm. The plots also confirm this behavior where the line contact (sliding contact shown in brown color) in Fig. 5 (c) vanishes completely (Fig. 5 (d)). It further reduces to 2.52 μN after the subsequent rotation from the top clamp. Fig 5 (e) shows that there is no sliding at the bottom while the top section undergo rotation, ensuring no particle generation.

For the top section, initially, the shaft is held by 7.52 N clamping reaction force from line contact at 'A'. After the bottom clamp opening, the contact reaction force at point 'A' reduces to 6.11 N, but later increases to 7.64 N due to additional force resulting from the subsequent rotation from the top clamp. These results show that when the top section undergoes
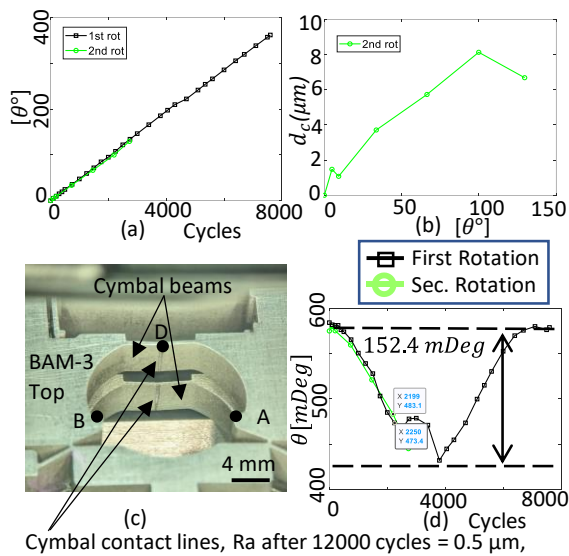
Figure 6. (a) The angle of rotation of the shaft in function of cycles, (b) Shaft's center displacement with respect to the angle of rotation, (c) Image of the actuator module cymbals showing contact lines after 12000 cycles of rotation, (d) The angle between unit normal vector of the shaft's top plane and the Z-axis with respect to the cycles.

rotation, there is minimal friction/contact between the shaft and the bottom contact points.

3.3 BAM-2 Experiments and results

As described earlier for BAM-1, the same manufacturing technique, material, power amplifier, data acquisition system, measurement system and shaft were used for BAM-2. An image of the fabricated BAM-2 is shown in Fig. 4 (b). The part was fabricated within 6 μm from the nominal dimension (diameter of the circle defined by points 'A', 'B', and 'D'). Space-qualified multi-stack piezo actuators from PI were used in this prototype. The size of the piezo (PICMA, P-883.51) was 3x3x18 mm³. The position of the shaft was measured for a first rotation of 362° by performing 7600 stepping cycles, and for a second rotation of 129° performing 3000 stepping cycles. The BAM-2 prototype had already done 1300 run-in cycles before these measurements. From the recorded data, the angle of rotation, shaft's center displacement and the tilt of the shaft about the Z-axis were extracted.

Angle of rotation

Fig. 6 (a) shows the angle of rotation of the shaft for a range of 362° with respect to the number of cycles. The average rate of rotation was found to be **(47.61 ± 0.25) mDeg/cycle** when the rotation piezo was actuated at 90 V generating 11 μm. displacement. The speed can be increased up to 80.5 mDeg/cycle by driving it at the maximum rated voltage of 120 V. As per the requirement, the desired speed of 0.1 °/s can be achieved successfully.

Shaft's center displacement

As per requirement, the parasitic displacements should be within a circle of radius 1 μm. After 129° of rotation, no further rotation was observed for the shaft. This is due to wear of the contact surface after roughly 12000 cycles. The contact lines have become smoother (refer Fig. 6 (c)) resulting in reduced friction. Fig. 18 shows the center displacement of the shaft during second rotation for 129° of rotation. The center displaces by ±**4 μm**.

Shaft's top plane tilt about the Z-axis

Fig. 6 (d) shows the plot of the angle between unit normal vector of the shaft's top plane and the Z-axis with respect to the number of cycles. At the beginning, the shaft's top plane is not

normal to the XY-plane, resulting in an initial tilt of about 0.58 Deg. During the rotation, a maximum deviation of this tilt was found to be around **152.4 mDeg**, which goes back to the initial tilt after full rotation. During the second rotation, a **10 mDeg** repeatability of this tilt angle was measured as compared to the first rotation. The behavior remains thus similar to the first full rotation.

3.4 BAM-2 Conclusion

The BAM-2 mechanism works as intended and is capable of full rotation at the desired speed. But this design is off by 4 and 15 times for the parasitic translational and angular BAM requirements, respectively. Further, material selection/surface treatment is important for a satisfactory performance of the BAM in long-run.

4. Discussion and conclusion

Table 2 Comparison of BAM-1 and BAM-2 performance till 6° of rotation.

BAM	Avg. Speed	Para. ang. disp.	Para. transl. disp.
BAM-1	10 mDeg/Cy	14 mDeg	±15 μm
BAM-2	47 mDeg/Cy	5.1 mDeg	±0.75 μm

Since BAM-1's measurements were only performed till 6° of rotation, Table-2 provides the performance comparison between the two designs till 6° of rotation. As shown BAM-1's parasitic displacements are worse than BAM-2's. This is due to the low positional repeatability of the C-clamp based BAM-1 compared to BAM-2. Furthermore, BAM-2 results are far better than BAM-1 in terms of speed, and repeatability. In a longer test, BAM-2 shows degradation in holding of shaft due to wear. The wear of contact points is a clear culprit.

Recommendation: It is clear that the designs explored here are incompatible with the parasitic displacement requirements for LISA-BAM. One of the ways to address these issues is to hard constrain the shaft translation and tilt, while allowing free rotation. For this reason, it is proposed to include a bearing in the design and develop a new prototype. The design of the 3-point contact of the BAM-2 can be adapted to be used with bearings.

Material selection and use of coatings to reduce the wear and improve the life of the mechanism is another open issue. The tribological study of the BAM is required.

References

[1] K. Danzmann, "LISA Mission Overview", *Advances in Space Research* Vol. **25**, Issue 6, 2000, 1129 – 1136.
[2] K. Spanner, and B. Koc, (2016, February). Piezoelectric motors, an overview. In *Actuators* (Vol. **5**, No. 1, p. 6). MDPI.
[3] J. Pijnenburg, N. Rijnveld, and H. Hogenhuis (2012, September). Extremely stable piezo mechanisms for the new gravitational wave observatory. In *Modern Technologies in Space-and Ground-based Telescopes and Instrumentation II* (Vol. **8450**, pp. 105-119). SPIE.
[4] S. Shao, S. Song, K. Liu, and M. Xu, (2019). A piezo-driven rotary inchworm actuator featured with simple structure and high output torque. *International Journal of Applied Electromagnetics and Mechanics*, **59(1)**, 317-325.

Mitigating friction induced limit cycles by an intermediate flexure stage

J.J. de Jong[1], J.A. Fix[1], and D.M. Brouwer[1]

[1]University of Twente, Enschede, The Netherlands, Precision Engineering lab

j.j.dejong@utwente.nl

Abstract

Friction-induced limit cycling, termed hunting, bounds the positioning performance of precision systems. A friction isolator mitigates this issue through an intentionally passive compliance between the friction-inducing bearing and the actuator. This compliance omits the sudden change in friction force felt by the controller close to standstill. Many design parameters influence the performance of such a friction isolator, including its compliance and damping, system mass, travelled path, and control parameters. Currently, a general design guideline for these friction isolators is missing. This research presents a simulation environment with a metric for identifying hunting cycles, from which a design guideline is distilled. The simulations demonstrated, and experiments confirmed, that a limited controller bandwidth and a significant gap between static and dynamic friction forces can lead to hunting limit cycles. With a friction isolator in place, these hunting cycles are avoided under specific conditions. A parameter study revealed that the friction isolator' drive stiffness should be kept as low as possible for optimal hunting cycle mitigation. On the other hand, the design of the friction isolator is constrained by parasitic frequencies of this mechanism and the stiffness in supporting directions. The experimental setup demonstrated that hunting cycles could be prevented with a friction isolator even with a control bandwidth of only 5 Hz, whereas the non-isolated system necessitated 3 times higher controller bandwidth. A 0.3 mm stroke of the friction isolator proved sufficient to prevent hunting. These experiments validate the suitability of the friction isolator as a solution for systems exhibiting hunting behavior.

Friction, Friction isolation, Hunting, Limit cycles, Flexure mechanism

1. Introduction

Contact-based bearings are widely used in positioning mechanisms for their relatively low cost and high support stiffness. However, nonlinear friction effects in rolling of sliding linear guides can limit the positioning performance, especially over time as wear deteriorates the system [1]. Typically, an integral action of a Proportional-Integral-Derivative (PID) controller will try to push the carriage of a linear guide through the friction towards a setpoint. However, the stick-slip effect introduces a discontinuity in the friction force, resulting in a sudden transition from standstill to movement. This stick-slip effect can lead to hunting limit cycles, which negatively affect the positioning performance of a servo system [2, 3]. This hunting behavior, also called friction-induced limit cycles, is a result of the combination of a controller with an integral action and a system containing a sudden transition between the static friction and smaller dynamic friction, the stick-slip effect [4, 5].

To prevent hunting from occurring in a positioning system, the integral action could be removed from the controller, but this could lead to tens of microns steady-state position error of the servo system. Reduction of friction is another option by using aerostatic bearings, but this type of bearing are not easily integrated into clean-room environments and significantly increases the cost. An alternative method to decrease the friction in mechanical bearings has been presented by Dong et al. [6], in which high frequency vibrations are exerted on the bearing rail to mitigate the undesirable nonlinear friction effects like stick-slip. This method called vibration assisted nano-positioning (VAN), shows a improvement in settling time up to 52% without a significant increase in heat and wear in the system. Introducing vibration into a high-precision positioning system, however, might be unwanted due to parasitic resonances which might jeopardize performance. Dong et al. later introduce the Friction Isolator (FI) concept [7–10], in which an intentional compliant joint - allowing limited movement in one direction - is inserted between the bearing and the actuator of the system. Figure 1 illustrates this principle.

This passive second stage atop the standard linear stage introduces a smooth force-position relationship close to the setpoint, at potentially low cost. Experimental results showed mitigation of hunting cycles and improved settling times.

Many parameters are of influence on the working of a friction isolator, such as the friction isolator's compliance and damping, system mass, travelled path, and control parameters. In recent studies [7-10] some of these have been investigated, however the influence of these parameters on the hunting behavior and the performance of a friction isolator is not always clear and a
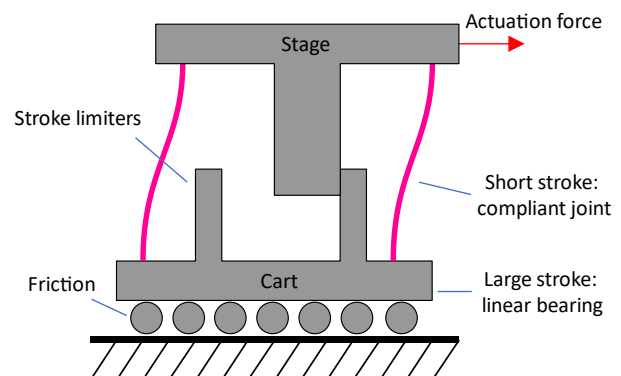
Figure 1. A schematic representation of a friction isolator. The actuation force positions the 'stage', which is connected through a compliant joint to the linear bearing cart. Stroke limiters are used to limit the maximum stroke of the friction isolator.
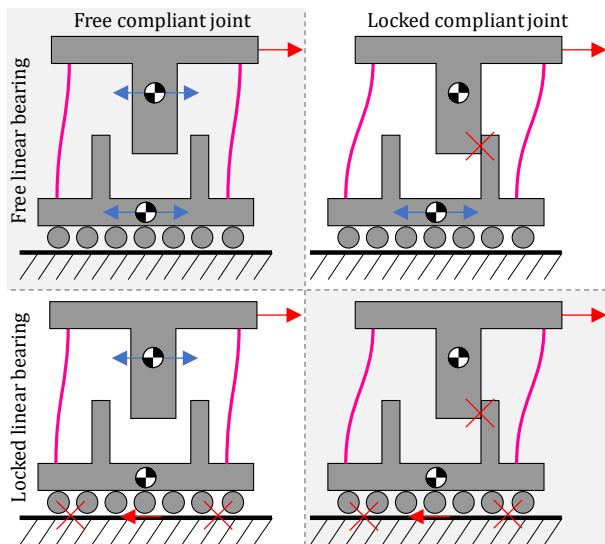
Figure 2. The controller experiences four limit cases, depending on whether the stroke limiter engages and locks the compliant joint (left vs right) or whether stiction at the linear bearing locks the cart (top vs bottom)

general guideline on designing a friction isolator is still missing and therefore the aim of this research [11].

Here, a general design strategy will be presented for a friction isolator system. This strategy is based on a parameter study in combination with simulations, from which it is identified which system parameters influence the hunting behavior. A setup is built to verify the model and showcase the improved settling behavior.

2. Methods

2.1. Simulations

The effects of friction in controlled systems have been extensively studied in literature, using various friction models. A sufficiently complex and computationally feasible model is the LuGre friction model [12,13], which is accurate in modelling presliding friction and the stick-slip effect. In the LuGre model, the contact between two bodies at asperities is modelled as elastic bristles. These bristles will deflect like springs when a tangential force is applied, leading to a friction force. If the tangential force is large enough, bristles will start to slip.

In our simulations, the friction isolator is modeled as two masses, which are connected through a spring damper (the compliant joint). On one of the masses LuGre friction forces are acting while on the other the actuation forces act, and the position is measured. The stroke limiters introduce reaction force between the two masses when engaged.

2.2. Controller design

The friction isolator is controlled by a PID controller. Here we use the cross-over frequency as main tuning parameter since it determines the bandwidth of the system and with that the response time of the controller. Using the moving mass of the system, the P, I, and D gains are computed [1].

The system to be controlled contains 4 limit cases (Figure 2) ; whether the cart is moving or stopped due to friction and whether the compliant mechanism is moving or stopped as it engages the stroke limiters. Between these cases, the moving mass and thus system dynamics differs significantly, it is either only the mass of the shuttle or the combined mass of the shuttle and the cart. Since a single controller is used to control all cases, the controller should be stable and have satisfying performance and stability in all cases. It was found that using the maximum
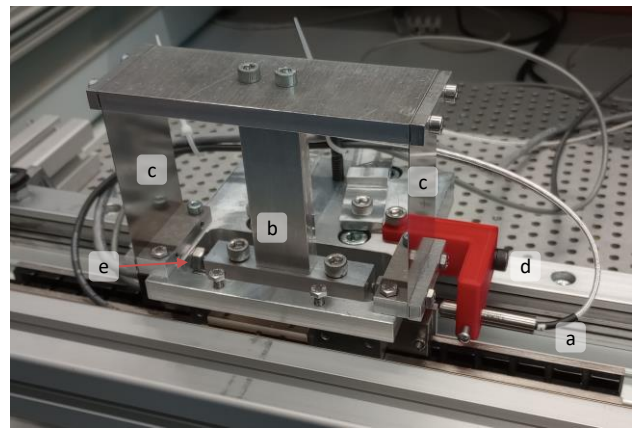
Figure 3. The experimental setup of a friction isolator. The linear actuator (a) positions the stage (b), which is connected through the compliant joint (c) to the linear bearing (d). Stroke limiters (e) are used to limit the maximum stroke of the compliant joint. A linear encoder and a capacitive sensor measure the displacement of the stage and the friction isolator, respectively.

mass for tuning the controller yields the best results, as is shown by Dong et al. [8].

2.3. Hunting metric

To quantify hunting, we propose here to count the number of oscillations in a fixed duration after expected settling time. Previous research [4] showed that hunting cycles have a duration in the order of seconds, with an amplitude in the order of millimeters. To find out whether a system shows stable hunting cycles the number of peaks in the position signal is counted after 10 seconds and over a period of 10 seconds (Figure 5). This provides sufficient time for the system to settle and if hunting cycles are observed, it can be stated that the system is affected by stable hunting cycles. The peaks are identified with a minimum time between the peaks of 0.5 seconds and a minimum peak height of 0.1 mm. Each hunting cycle will correspond to one peak.

2.4. Parameter study

A parameter study is conducted to find optimal parameters for the friction isolator and to study the effect of multiple parameters on the hunting behavior. Specially, two parameters are varied over a grid while the remaining parameters are kept constant. Firstly, the effect of static and coulomb friction parameters on a non-isolated system is investigated. Secondly, the influence of controller bandwidth and system mass parameters are varied for the non-isolated system. Thirdly, the stroke and stiffness of the friction isolator is changed. Lastly, the controller bandwidth and stroke of the friction isolator is changed to see if limit cycles will appear. Note that not all parameter variations are presented in this paper due to space limitations.

2.5. Experimental setup

A test setup is designed and built to experimentally verify the simulations and design method (Figure 3). On this set-up the friction isolator can be engaged or disengaged to see its effect on hunting. Furthermore, the controller bandwidth and friction isolator stroke are varied in a grid search to compare to the analytic results.

3. Results

3.1. Parameter study

Four pair-wise sets of parameters where varied to investigate their combined influence on hunting as illustrated by Figure 4..
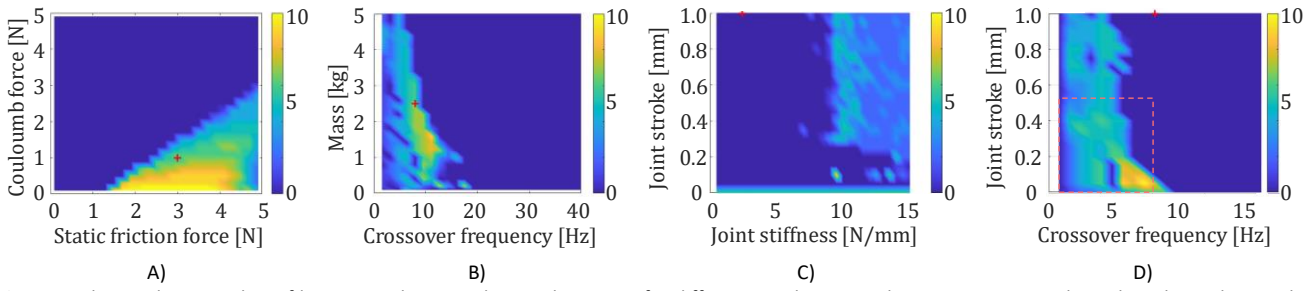
Figure 4. The resulting number of hunting cycles according to the metric for different combinations design parameters. The red marker indicates the evaluation point for the other studies. A) and B) are for the non-isolated case whereas C) and D) are for the isolated case. Be aware of the different horizontal scale when comparing B) to D). The box indicates the area of the experimental tests in D).

Here we selected a baseline parameter set, indicated with a cross and vary the parameter pair. The number of hunting cycles within the given time frame was selected as a hunting metric.

In Figure 4.A., it can be seen that the static friction force must be significantly larger than the Coulomb friction force for hunting to occur, approximately 1N in this case. This is logically explained by the stick-slip conditions, in which the static friction must be larger than the dynamic friction. A larger gap between the static and coulomb friction force leads to more hunting cycles. At the point of breakaway of the bearing, the control force is therefore also significantly larger than the dynamic friction force, resulting in a larger overshoot. Due to a larger error, the proportional part of the controller generates a larger force, and the build-up rate of the integral action is increased as well. This results in the breakaway force being reached sooner.

In Figure 4.B, it can be seen that with a higher cross-over frequency, larger than around 20 Hz in this case, no hunting occurs. With a higher cross-over frequency, the controller responds faster which can prevent hunting cycles from occurring. A higher required cross-over also places more stringent requirements on the system dynamics such as parasitic dynamics and time delays.

Figure 4.C shows that the stiffness of the compliant joint should be limited for the isolator to work. This is to be expected when taking the principle of the friction isolator into account. At a smaller stroke of the compliant joint, the stiffness of the joint can be higher, since the force applied to the bearing at the maximum stroke is then still smaller than the static friction force.

From this study it is found that the cross-over frequency also affects the hunting behavior of the friction isolator system (Figure 4.D). At smaller cross-over frequencies, hunting can still occur even in the isolated system. The boundary values of the cross-over frequency below which hunting occurs is affected by

the stiffness of the compliant joint. A lower drive stiffness lowers the cross-over frequency at which hunting occurs.

3.2. Experimental validation

The friction isolator is tested for its ability to mitigate the hunting effect. Figure 5 shows a typical result of moving the setup back and forth over 100 mm, with a prescribed acceleration of 100 m/s². Results of both the isolated and non-isolated system are plotted in this graph, from which it can be seen that hunting cycles are present in the non-isolated system, while the friction isolator settles to the reference position. The simulations are not exactly equal to reality but show hunting in the same order of magnitude.

The same motion has been prescribed to the non-isolated system for a range of cross-over frequencies of the controller. The results of these experiments can be seen in Figure 6. This experiment shows that increasing cross-over frequency increases the performance of the system, since the response time to errors becomes smaller and the overshoot in the hunting cycles decreases. As expected from the parameter study, with increasing cross-over frequency the hunting cycles eventually are mitigated. Though the required cross-over frequency to mitigate the hunting behavior is found to be 14.3 Hz in this experiment. While for the isolated system 5 Hz is sufficient. Also, observe that no hunting seems to occur at the cross-over frequency of 9.5 Hz. This indicates that hunting is a partly understood behavior, that depends on a multitude of stochastic factors, as in other runs hunting was introduced with the same controller settings.
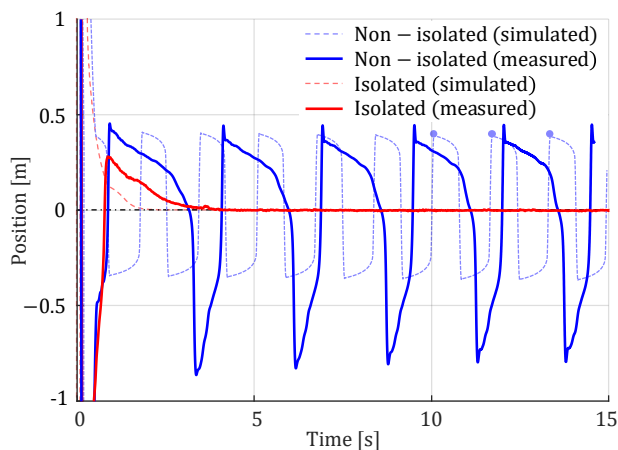
Figure 5. The simulated and measured position of the non-isolated and isolated system after settling from a step movement. The same cross-over frequency is used in all cases. The blue circles indicate the counting points as to compute the metric (section 2.3).
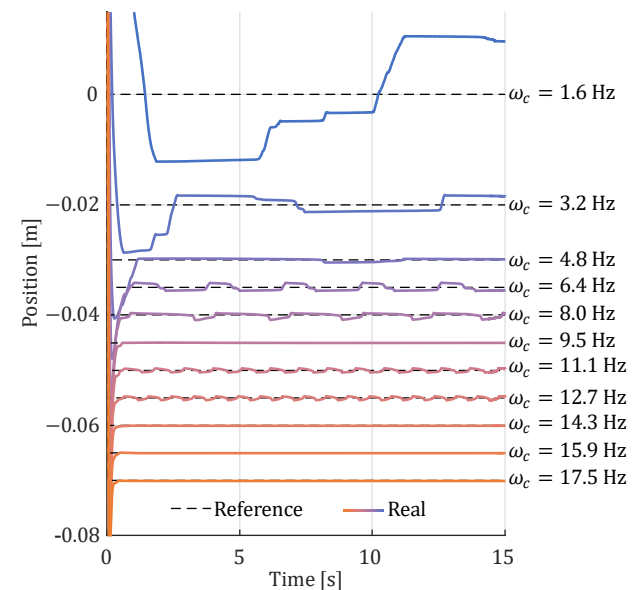
Figure 6. The settling behavior for a range of cross-over frequencies for the non-isolated system. To make a clear distinction between the different lines a small virtual offset is introduced while the actual set-point was the same for all experiments.

The stroke of the compliant joint and the cross-over frequency of the controller have been varied for experiments on the test setup. The results of this experiment can be found in Figure 7. At higher cross-over values, hunting is not present in the system at all. The trend is similar to the friction isolator cross-over parameter study of Figure 4.D, albeit grainier. This validates both the simulation setup and the finding that for a sufficiently high cross-over frequency no hunting cycles appear. It should be noted that the amount and frequency of hunting differs significantly between simulations and set-up due to the time and position varying nature of the friction parameters.

4. Design guidelines

To determine if a friction isolator is needed and what design parameter are to be chosen, we propose the following four step approach:

1. Determine the friction values of the bearing. If the difference between static and coulomb friction of the bearing is small, in this case < 1N, stick-slip might not occur and thus hunting cycles will not be an issue.
2. Determine the desired and reachable cross-over frequency of the system, if this frequency is limited, a friction isolator might be useful. A higher possible cross-over frequency can mean hunting cycles do not occur in the system and the benefit of a friction isolator is limited. This desired cross-over also gives minimal value for the parasitic frequency as used to design a compliant joint.
3. From the static friction value, combined with the maximum stroke of the compliant joint, a maximum drive stiffness can be determined. Based on this, a compliant joint is designed such that the parasitic frequencies do not interfere with the desired cross-over frequency.
4. Finally, the PID controller parameters can be determined when the mass of the system is known [1].

5. Conclusions

The conducted parameter study on the main parameters of a friction isolator system showed that a limited bandwidth of the applied PID controller and a significant gap between static and dynamic friction forces may result in hunting cycles to occur.

Introducing a compliant joint in a system can prevent these unwanted hunting cycles. It is found that the drive stiffness of this compliant joint should be as low as possible, for the best mitigation of hunting cycles. The design of the compliant joint is limited by the stiffness in supporting directions and the parasitic resonance frequencies that are introduced by this mechanism. The parameter study showed that the friction isolator is a robust method to mitigate hunting cycles against various friction values.

The experimental setup showed mitigation of hunting cycles using a friction isolator for a control bandwidth of only 5 Hz, while the non-isolated system requires a higher bandwidth of 15 Hz. A compliant joint stroke of 0.3 mm is sufficient to prevent hunting from occurring. These experiments verify that the friction isolator is a suitable solution for systems that show hunting behavior.

References

[1] Yoshihiro Maeda and Makoto Iwasaki. Rolling friction model-based analyses and compensation for slow settling response in precise positioning. IEEE Transactions on Industrial Electronics, 60(12), 2013.
[2] Farid Al-Bender and Jan Swevers. Characterization of Friction Force Dynamics. IEEE Control Systems Magazine, 28(6):64–81, 2008.
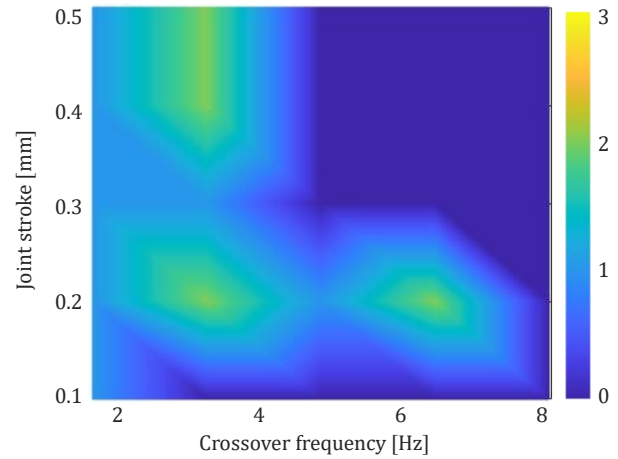
Figure 7. The measured number of hunting cycles for a range friction isolator joint strokes and cross-over frequency. These test results parallel measured results in the boxed area of Figure 4.D.

[3] Henrik Olsson. Control Systems with Friction. PhD thesis, Lund institute of technology, Lund, 1996.
[4] Ron H.A. Hensen and Marinus J.G. Van de Molengraft. Friction induced hunting limit cycles: An event mapping approach. Proceedings of the American Control Conference, 3:2267–2272, 2002.
[5] Ron H.A. Hensen, Marinus J.G. Van de Molengraft, and Maarten Steinbuch. Friction induced hunting limit cycles: A comparison between the LuGre and switch friction model. Automatica, 39(12):2131–2137, 12 2003.
[6] Xin Dong, Deokkyun Yoon, and Chinedum E. Okwudire. A novel approach for mitigating the effects of pre-rolling/pre-sliding friction on the settling time of rolling bearing nanopositioning stages using high frequency vibration. Precision Engineering, 47:375–388, 1 2017.
[7] Xin Dong, Xingjian Liu, Deokkyun Yoon, and Chinedum E. Okwudire. Simple and robust feedforward compensation of quadrant glitches using a compliant joint. CIRP Annals - Manufacturing Technology, 66(1), 2017.
[8] Xin Dong and Chinedum E. Okwudire. An experimental investigation of the effects of the compliant joint method on feedback compensation of pre-sliding/pre-rolling friction. Precision Engineering, 54:81–90, 10 2018.
[9] Xin Dong and Chinedum E. Okwudire. Influence of design parameters on the effectiveness of friction isolators in mitigating pre-motion friction in mechanical bearings. Mechatronics, 71:102444, 11 2020.
[10] Jiamin Wang, Xin Dong, Oumar R. Barry, and Chinedum Okwudire. Friction-induced instability and vibration in a precision motion stage with a friction isolator. JVC/Journal of Vibration and Control, 28(15-16):1879–1893, 8 2022.
[11] Jasper A. Fix. A Linearized Parameter Study Of A Friction Isolator System: Towards A Frequency Domain Design Guideline. MSc. Thesis of Mechanical Engineering, University of Twente, the Netherlands. Aug 2023.
[12] C. Canudas de Wit, P. Lischinsky, K. J. ˚Aström, and H. Olsson. A New Model for Control of Systems with Friction. IEEE Transactions on Automatic Control, 40(3), 1995.
[13] Karl Johan Astrom and Carlos Canudas-De-Wit. Revisiting the LuGre Friction Model. IEEE Control Systems, 28(6), 2008.

euspen's 24th International Conference &
Exhibition, Dublin, IE, June 2024
www.euspen.eu

Analysis of the vibration characteristics of an air bearing spindle to identify and control the magnitude of the radial run-out with an active magnetic bearing

Felix Zell[1], Andreas Lange[1], Benjamin Kirsch[1], Jan C. Aurich[1]

[1]RPTU Kaiserslautern, Institute for Manufacturing Technology and Production Systems

felix.zell@rptu.de

Abstract

One way to improve surface quality and tool life in micro machining is to constantly adapt the spindle speed to the current feed rate, i.e., maintaining a constant feed per tooth. Air bearing spindles, which are commonly used in micro machining, are not suitable for this cutting mode. Their passive control behaviour combined with a low damping leads to increased error motions during the required changes in spindle speed. The increased error motions then impair geometric accuracy during milling. An additional active magnetic bearing could provide active control capabilities to reduce radial error motions during speed changes. This could enable the application of constant feed per tooth without the ramifications (e.g., high complexity) of a fully magnetic bearing spindle.

This paper presents a concept to introduce active control capabilities to an air bearing spindle by adding a single active magnetic bearing acting directly on the micro end mill. Hence, a hybrid spindle system with closed-loop feed-forward (radial) run-out control is created without redesigning the air bearing spindle itself.

A detailed explanation of the hybrid spindle concept and the construction of a fully functional prototype will be provided, highlighting the necessary steps for development. Additionally, initial results of the analysis of the vibration characteristics of the air bearing spindle will be presented and discussed. The magnitude of the radial error motions of the analysed air bearing spindle is found to be 1.5 µm at a spindle speed of 95 000 min^{-1} with dominant frequency components up to 6 400 Hz.

Micromachining, Actuator, Magnetic bearing, Control

1. Introduction

As the trend towards the miniaturisation of components continues, the demand for more efficient manufacturing processes to produce micro structured components is also increasing [1]. Micro machining is a promising alternative to other commonly used micro manufacturing processes, like lithography-based manufacturing, with high geometrical freedom, a wide range of machinable materials and short production times [2]. To enable production of those small geometrical features, the milling tool diameter must be small (D < 100 µm) as well. In turn, spindle speed and concentricity requirements for the tool spindle are high to achieve sufficient cutting speeds and geometric accuracy. [3]

The required speeds are generally achieved using either air bearing spindles or spindles with active bearings [1, 4]. Air bearing spindles impress with their simple and robust design, but their passive system behaviour limits their possible applications. Any concentricity deviations that occur only subside slow and lead to geometric deviations in the workpiece. As changing spindle speeds result in additional radial error motions, milling with constant feed per tooth, generally a viable option to improve surface quality in micro machining, is not possible when using air bearing spindles [5].

Spindles with active bearings, such as magnetic bearing spindles, generally allow the rotor position to be controlled and dynamic damping behaviour to be achieved. However, they are rarely used in micro machining due to their complex and expensive design. [6]

Another approach are hybrid spindles in which active bearings enhance the capabilities of air bearing spindles. For example, [7] added a magnetic bearing to an air bearing spindle and was thus able to dampen natural vibrations and increase the maximum spindle speed. However, the focus was on specific resonance frequencies rather than a wide range of spindle speeds. The approach pursued here for controlling the rotor position with the specific application goal of micro-machining has already been described by [8], but with the focus set on theoretical feasibility.

A detailed explanation of the hybrid spindle concept and the construction of a fully functional prototype will be provided, highlighting the necessary steps for development. Additionally, initial results of the analysis of the vibration characteristics of the air bearing spindle will be presented and discussed.

2. Hybrid spindle concept

The hybrid spindle concept aims to enhance the geometric precision of micro milling operations by adding a single magnetic actuator to an air-bearing spindle. Its purpose is to control the rotor position during operation, particularly during speed changes, to allow for constant feed per tooth milling operations with improved geometric accuracy.

The combination of the two components and the division of tasks between the air-bearing spindle, which ensures the necessary load capacity, rigidity and emergency running properties, and the magnetic actuator, which only has to compensate for the radial error motions, minimises the complexity of the system.

The procedure for developing the hybrid spindle is as follows.

First, the spindle has to be characterised to determine the design requirements for the control loop dynamics and the magnetic actuator, as well as the forces of the magnetic

actuator. The main objective is to identify the maximum radial error motions and the highest relevant vibration frequency. While the amplitude of the radial error motions will set design requirements for the magnetic actuator, the maximum disturbance frequency will also affect the control loop design. This is done by integrating a displacement measurement system (section 3.1) and measuring the radial run-out over the full speed range of the air bearing spindle. The model-based design of the control loop and the magnetic actuator is based on these results. Due to the high complexity, the non-linear relationships in the calculation of the magnetic bearing forces and the mutual interactions between the controller and the magnetic force development, a model-based approach is chosen here. To account for non-linear relationships in the magnetic bearing forces calculation (e.g., eddy current losses, non-linear material behaviour, fringing effects) a numerical magnetostatic simulation will be utilised [6]. The results of the numerical simulation are implemented in the control loop model in form of 4D look-up tables to reduce the computation time needed for each time step and hence the overall simulation time. Figure 1 illustrates the difference between the open-loop control of an air bearing spindle and the closed-loop control of the proposed hybrid spindle. The displacement measurement system creates the feedback path to close the control-loop in conjunction with the PID-controller and the magnetic actuator. For the optimisation of the control parameters model-based automatic tuning methods within the control system environment (MATLAB Simulink[1]) will be used. To improve response time and control accuracy of the control loop, a feed-forward approach will be investigated (see figure 1 c)). The rotor speed is used to predict the spindle error motion response. For the prediction model, information about recurring periodic error motions (also known as synchronous error motions) is essential. The spindle characterisation therefore focuses on these synchronous error motions. After the successful design and optimisation of the magnetic actuator and control parameters over several iteration loops, a functional model of the magnetic actuator is produced and integrated into the air-bearing spindle. Finally, the hybrid spindle system is validated via milling tests. Comparing cutting forces, tool wear and processing results of milling operations with and without activated closed-loop control will allow for an assessment of the influence of the hybrid spindle system.
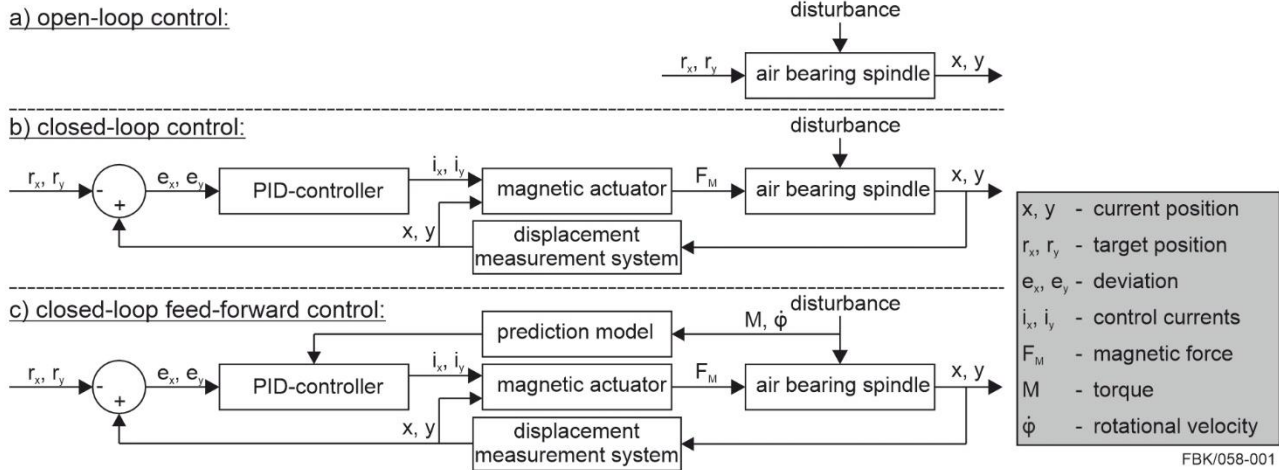
Figure 1. Schematic control loop configurations: a) open-loop air bearing spindle, b) closed-loop hybrid-spindle, c) closed-loop feed-forward control hybrid spindle

3. Methods

As outlined, the first step in developing the hybrid spindle is to characterize the radial error motion behaviour of the air bearing spindle (ABL[1] 160 MM). Therefore, a series of test runs at differing spindle speeds is performed. The displacement of the spindle rotor, i.e., a 3 mm diameter artefact with high concentricity, is measured during each test run individually. Starting at the minimum spindle speed (25 000 min⁻¹), the spindle speed is increased by increments of 5 000 min⁻¹ until 120 000 min⁻¹ is reached. See section 3.1 for details on the measurement system.

The artefact is assumed to be perfectly round and centred along the axis of rotation. Thus, the measured radial run-out of the artefact surface is equated to the radial error motion of the spindle axis of rotation. To analyse the measurements in detail, the spindle error motion is broken down into its individual components using a frequency classification method. This enables the identification and characterisation of regularly occurring vibration components. Detailed information on the frequency classification method is given in section 3.2.

3.1. Measurement system for radial error motions

A capacitive displacement measurement system was used to measure the radial error motions for its high resolution and bandwidth, small measurement spots and it being not affected by adjacent magnetic fields. Two sensors measured the rotor

displacement along the x and y axis respectively (see figure 2). An additional third sensor was used to provide accurate instantaneous spindle speeds and angular position information, as there is no encoder built into the air bearing spindle itself. By measuring against a triangular section at the end of the artefact and evaluating the peaks in the sensor signal, it was possible to reliably assign the x and y displacements to their individual revolutions. The three analogue sensor signals were simultaneously digitised by a DAQ at a sampling rate of 50 000 samples/s and recorded via a MATLAB[1] script. Refer to table 1 for additional data on the sensor system and the DAQ.

Table 1. Specifications of the measurement system

Micro-Epsilon[1] capaNCDT 6222/DL 6222	
Measuring range	0.2 mm
Resolution @20 kHz	0.05 % FSO
Bandwidth	20 kHz (-3dB)
Analogue output	-5 V – +5 V
Axial position x-sensor / y sensor	13.5 mm / 8 mm
National Instruments[1] NI-USB DAQ 6210	
Nominal range - Full scale	-1 V – +1 V
ADC resolution	16 bit
Absolute accuracy at full scale	310 µV
Sensitivity	10.4 µV
Sample rate	50 000 samples/s
Sample time	3 s
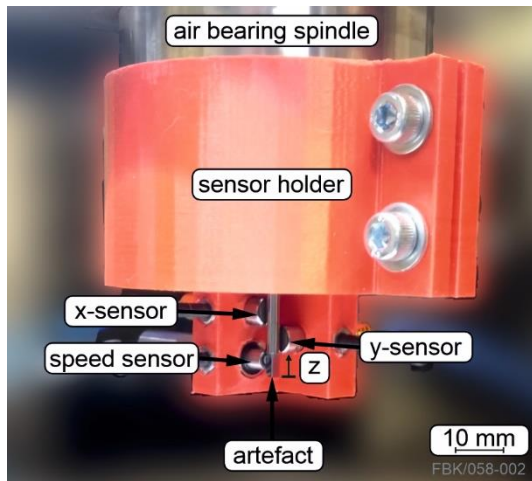
Figure 2. Placement of the capacitive sensors for x-, y-run-out and speed measurements

3.2. Spindle metrology

The total spindle error motion can be decomposed based on its frequency components i.e., synchronous and asynchronous [9]. It is useful to normalise the frequency contents using the rotational frequency, also known as fundamental frequency. As a result, the frequency spectrum is given in units of undulations per revolution. Multiples of the fundamental frequency are referred to as order.

There are two ways of calculating the different frequency components, either in the time or frequency domain. In the time-based domain, the synchronous error motion is calculated by averaging the total spindle error motion over all sampled revolutions at each individual angular rotor position. The asynchronous error motion is calculated as difference between total and synchronous error motion. In the frequency domain synchronous and asynchronous error motions are separated by first transforming the raw data with a fast Fourier transformation (FFT), then separating integer and non-integer Fourier components, respectively, and finally retransforming the frequency information with the inverse FFT. The Fundamental error motion can be easily identified as the once per revolution component.

The synchronous and asynchronous error motions describe periodic error motions that occur at integer and non-integer multiples of the fundamental frequency respectively.

Apart from the frequency classification the spindle error motions can also be separated with respect to the sensitive direction, which describes the direction perpendicular to the workpiece/artefact surface at the point of machining/measurement [9]. Based on whether the point of machining/measurement is fixed and the workpiece is rotating or vice versa, fixed sensitive and rotating sensitive directions can be distinguished respectively. The spindle error motion is measured in the fixed sensitive direction, but in milling operations with a single point tool, as is the case in micro milling, the errors affect the workpiece according to the rotating sensitive direction. Therefore, the spindle error motion measured in the fixed sensitive direction (X and Y) has to be converted to the rotating sensitive direction error motion R according to equation 1 as a function of the spindle rotation angle θ .[9]

$$R = X \cdot \cos(\theta) + Y \cdot \sin(\theta) \tag{1}$$

Finally, the spindle error motion can also be classified based on directional information. In case of the hybrid spindle control, only the radial error motion at the tool tip is relevant. The radial error motion (R_{new}) at any location (a_{new}) along the rotation axis can be computed according to equation 2 once the pure radial error motion (R) at a given axial location (a) and the tilt error motion (α) are known [9].

$$R_{new} = R + \alpha \cdot (a_{new} - a) \tag{2}$$

To compute the tilt error motion with the chosen measurement setup, two measurements of the radial error (R_1 and R_2) at a known axial spacing l are required [9].

$$\alpha = (R_2 - R_1)/l \tag{3}$$

4. Results

The fundamental and residual synchronous error motion values are shown in figure 3 a) and b) respectively.

Generally, the fundamental error motion values rise moderately with increasing spindle speed up to 80 000 min^{-1}. Beyond this point, the fundamental error motion values in the fixed x (fixed y) sensitive direction drop significantly from 1.7 µm (2.0 µm) to 0.4 µm (0.75 µm). This may be due to a shift in the axis of rotation of the spindle, caused by the rising imbalance forces, which are proportional to the square of the rotational speed.

The residual synchronous error motions are almost constant over a wide span of spindle speeds with one exception. At a spindle speed of 95 000 min^{-1} the maximum error occurs with values as high as 1.5 µm, probably due to resonance with a natural oscillation frequency of the spindle. Increasing spindle speeds further led to a rise in the fixed sensitive direction synchronous error in the y-direction, but not in the x-direction. This implies that either some components of the spindle may exhibit structural asymmetry or there is additional tilt error motion at play.

To identify the shape and highest relevant orders of the radial error motion at this spindle speed, the polar plot and the frequency spectra of the residual synchronous error motion are plotted in figure 4. Although the polar plots of the fixed x- and y-sensitive direction reveal a three lobed shape of the error motion, the rotating sensitive direction, which correlates to the resulting form errors of a milling operation with this spindle, display a predominantly two and four lobed shape. Hence, the control loop and the magnetic actuator must be designed to compensate spindle error motions of 1.5 µm occurring at frequencies of up to 6 400 Hz, because of dominant error motion components at four times the fundamental frequency of approximately 1 600 Hz.
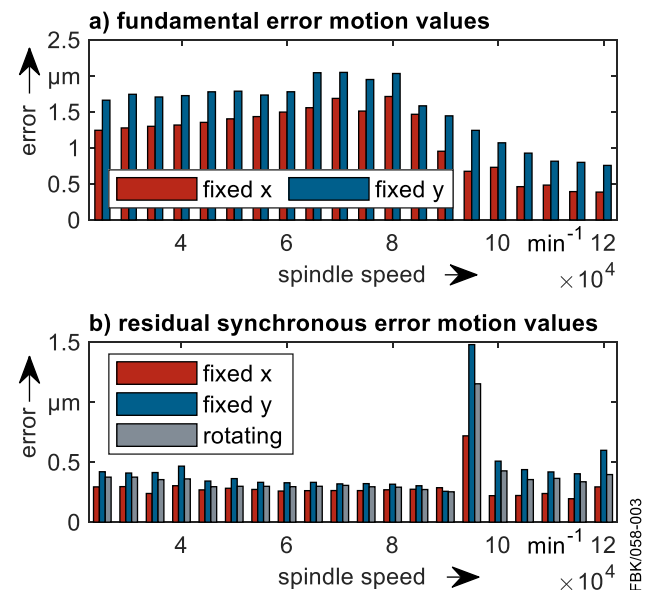
Figure 3. a) fundamental and b) residual synchronous error motion values for the entire spindle speed range
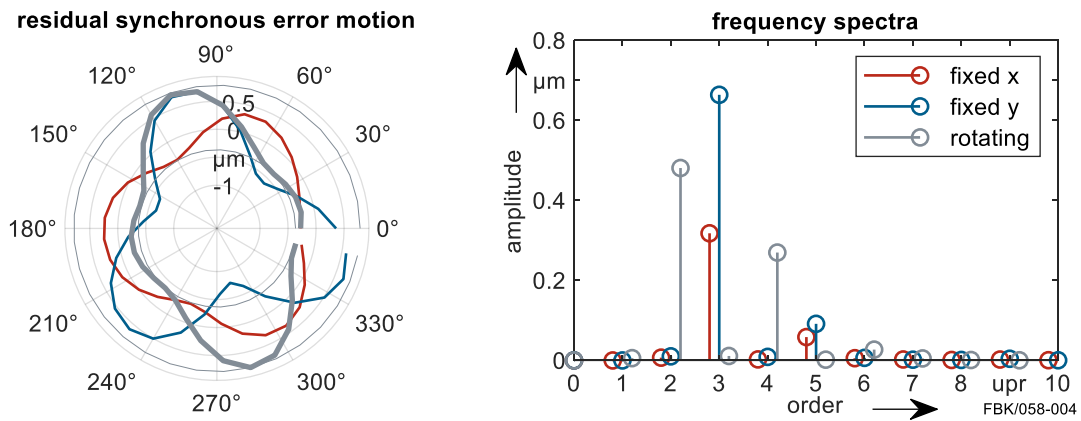
Figure 4. Polar plots and frequency spectra of the residual synchronous error motions at a spindle speed of 95 000 min⁻¹

5. Conclusion and outlook

In this paper, we introduced a concept for controlling the radial error motions of air bearing spindles in micro machining with an additional active magnetic bearing. Enabling speed changes required for micro milling with constant feed per tooth without compromising manufacturing accuracy due to additional radial error motions is the main objective of this hybrid spindle concept under development.

Essentially, there are four major steps involved in the development of the hybrid spindle according to the proposed concept. 1. Characterisation of the air bearing spindle i.e., measuring and analysing the spindle error motion. 2. Model-based design of the magnetic actuator and the control loop. 3. Design and integration of the magnetic actuator. 4. Validation of the hybrid spindle performance through milling tests.

The first step was described in detail. A capacitive displacement sensor system alongside a precision ground artefact was utilised to measure the radial error motions near the tool tip in x- and y-direction simultaneously. Error motion data was gathered for the entire spindle speed range in 5 000 min⁻¹ increments. For the in-depth analysis of this raw displacement data a frequency classification method was used.

The fundamental error motion values slowly rose with increasing spindle speed to a maximum of 2.0 μm for the y-direction at 80 000 min⁻¹. Increasing spindle speed further led to a significant drop in the fundamental error motion values. The residual synchronous error motion values showed a sharp exception at a spindle speed of 95 000 min⁻¹ with a three to fourfold amplification of the fixed sensitive direction value to approximately 1.15 μm. A detailed investigation of the polar plot and the frequency spectrum of the residual synchronous error motion in the rotating sensitive direction at 95 000 min⁻¹ revealed the predominant influence of the second and fourth harmonic order elements.

The following conclusions can be drawn from these results:
- Radial error motions of the air bearing spindle can be measured with the implemented capacitive displacement measurement system. By attaching the probes to the spindle body, the system is also suitable to measure the radial error motions and provide the feedback path for the closed control-loop during milling operations.
- Differences between the measurements in x- and y-direction suggest either the presence of structural asymmetries or an influence of tilt error motion. This needs further investigations in future works.
- As the exception in the residual synchronous error motion values may be due to resonance with a natural oscillation frequency of the spindle, smaller speed increments are required in this range. In order to find the exact resonance frequency, a more detailed characterisation of the spindle

will be carried out in the range of 90 000 min⁻¹ to 100 000 min⁻¹.
- The magnetic actuator and the control loop are required to at least compensate for a radial rotor error motions of up to 1.5 μm at a frequency of approximately 6 400 Hz (i.e., four times the rotational frequency of 1 600 Hz).

With these initial results for the vibration characteristics of the air bearing spindle and the derived requirements for the control loop and the magnetic actuator, the second step of the hybrid spindle concept will be conducted next. Any findings of the additional investigations into structural asymmetry of the spindle, rotor tilt error motion and the exact resonance frequency will also be considered in the model-based design of the magnetic actuator and the control loop.

References

[1] Uhlmann E, Mullany B, Biermann D, Rajurkar K P, Hausotte T and Brinksmeier E 2016 Process chains for high-precision components with micro-scale features *CIRP Annals* **65** 549–572

[2] Sorgato M, Bertolini R and Bruschi S 2020 On the correlation between surface quality and tool wear in micro–milling of pure copper *Journal of Manufacturing Processes* **50** 547–560

[3] Aurich J C, Bohley M, Reichenbach I G and Kirsch B 2017 Surface quality in micro milling: Influences of spindle and cutting parameters *CIRP Annals* **66** 101–104

[4] Kimman M H, Langen H H and Munnig Schmidt R H 2010 A miniature milling spindle with Active Magnetic Bearings *Mechatronics* **20** 224–235

[5] Shi J, Jin X and Cao H 2022 Chatter stability analysis in Micro-milling with aerostatic spindle considering speed effect *Mechanical Systems and Signal Processing* **169** 108620

[6] Schweitzer G and Maslen E H 2009 *Magnetic Bearings* Springer Science & Business Media

[7] Jang H-D, Kim J, Han D-C, Jang D-Y and Ahn H-J 2014 Improvement of high-speed stability of an aerostatic bearing-rotor system using an active magnetic bearing *Int. J. Precis. Eng. Manuf.* **15** 2565–2572

[8] Lange A, Müller D, Kirsch B and Aurich J C 2020 Magneto-structural modelling of mirco machining spindles supported by active magnetic bearings *Proc. euspen's 20th International Conference & Exhibition* (Bedford, UK: euspen) **20** 221-224

[9] Marsh E R 2010 *Precision spindle metrology* sec ed (Lancaster, PA: DEStech Publications)

Integrated capacitive measurement of air gap height in aerostatic bearings

Petteri Haverinen[1], Mikael Miettinen[1], Luke Harding[1], Valtteri Vainio[1], Onni Leutonen[1], René Theska[2], Raine Viitala[1]

[1]Aalto University
[2]TU Ilmenau

petteri.haverinen@aalto.fi

Abstract

Measurement of air gap height in aerostatic bearings is often necessary, for example, in closed-loop position control of precision stages. The air gap height can be measured directly with distance sensors, or indirectly from pressure in the bearing gap when the performance is well known.

The present study investigated an air gap height measurement method for aerostatic bearings using an integrated capacitive sensor. The method was investigated experimentally with a thrust bearing. The structure of the bearing was made from conductive material which was used for one of the electrodes for the capacitive sensor. The second electrode, in this case, was the steel guide surface of the bearing. Thus, a plate capacitor was formed between the steel guide surface and the graphite restrictor, where the air gap is the dielectric medium. The distance between the two plates in a plate capacitor is inversely proportional to its capacitance. Therefore, measurement of the air gap between the bearing and the guide surface is possible.

The integrated capacitive sensor consisted of a modified aerostatic bearing and a measuring circuit. The circuit consisted of a Wien bridge oscillator and an LC-tank in which the aerostatic bearing acted as the capacitor. Current through the LC-tank was measured using a resistor and an amplifier. The measurement results of the proposed method were compared to measurements obtained using an external gap-height sensor in a static test bench. The results show corroborative evidence on the feasibility of the proposed method.

Capacitive displacement sensor, porous aerostatic bearings, integrated sensors

1. Introduction

Capacitive sensing is a widely researched topic with over 2,000 publications in 2018 alone [1]. Capacitive sensing is a noncontact, low cost, and low-power sensing technique which uses the change in capacitance across two electrodes to measure the distance between them. The resolution of this technique is limited primarily by achievable signal to noise ratio [2].

Measurement of the height of the air gap in aerostatic bearings is interesting, for example, in academical research and in precision applications. Because the performance of these types of bearings heavily relies on the thickness of the air gap between the restrictor and the guide surface, the accurate measurement can be useful in a multitude of applications. Typically, the air gap height is measured with external capacitive sensors [3, 4, 5]. These sensors are often mounted on the outside of the bearing or in the air gap region. The air gap height of aerostatic bearings is typically between 2 to 20 μm, which is well within the measurement range and resolution of even simple capacitive sensing methods.

Using an integrated approach to air gap measurement, instead, could reduce measurement uncertainty by reducing effects of external factors on the measurement loop and permit in-situ measurement in applications of the bearings.

Furthermore, the integrated gap sensing could be used in actively controlled aerostatic bearings or in condition monitoring of aerostatic seals. Because it is critical that aerostatic bearings do not collide with or draw too near to their guide surfaces during operation, the live monitoring of a bearing's air gap may be a useful tool in certain applications.

The present study investigated a proof-of-concept method for the direct measurement of air gap height of a porous-restrictor- type aerostatic bearing using capacitive sensing methods. The proposed gap-sensing concept was investigated experimentally and compared to the current state-of-the-art externally mounted capacitive sensors.

2. Measurement principle

A plate capacitor is formed between the graphite restrictor of the aerostatic bearing and the steel guide surface (Figure 1) since both surfaces are conductors separated by insulator. The air gap between the restrictor and steel surface of the bearing is a variable-thickness insulator with a relative permittivity of approximately 1. The capacitance of a plate capacitor is given by the well-known equation:

$$C = \varepsilon_0 \varepsilon_r \left(\frac{A}{d} \right) \tag{1}$$

where ε_o is the permittivity of free space, ε_r is the relative permittivity (dielectric constant), A is the surface area of the electrode, i.e., the bearing, and d is the height of the air gap. From the equation, it is evident that the capacitance is directly proportional to the distance between the electrodes, i.e., the air gap height: $C \propto d$.
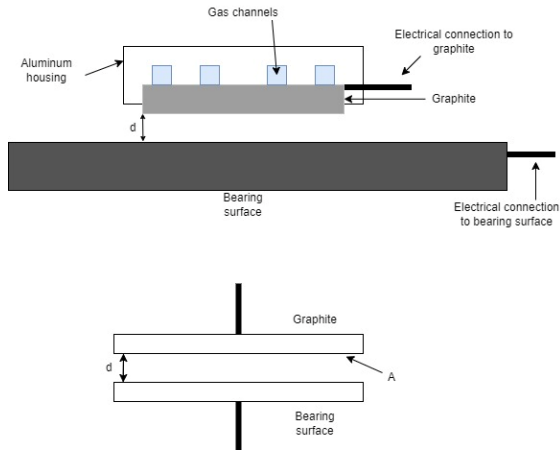
Figure 1. An axis-symmetric porous aerostatic bearing as a capacitor with conducting bearing surface.

The capacitance, and, thus, the air gap height, can be measured using multiple methods such as frequency counting or by measuring the current running through the capacitor and its adjacent circuit [2, 6]. In the present study, an RLC-circuit was used to allow for the tuning of the resonant frequency of the circuit to match a specific gap height range to be measured. The basic circuit, presented in Figure 2, possesses a resonant frequency, f_0. At this frequency, the reactance of the inductor and capacitor are at a minimum therefore allowing the greatest amount of current to flow through the circuit. The resonant frequency can be calculated using the formula:

$$f_0 = \frac{1}{2\pi\sqrt{LC}}$$

where L is the inductance and C is capacitance of the capacitor. The reactance of the inductor and capacitor are defined as:

$$X_L = 2\pi f L \text{ and } X_C = \frac{1}{2\pi f C}$$

where L is the inductance of the inductor, C is the capacitance between the aerostatic bearing and its counter surface, and f is the frequency of the supply voltage which is set to be f_0. The current through the RLC-circuit can be found using:

$$I = \frac{U_{supply}}{\sqrt{R^2 + (X_L - X_C)^2}} \tag{2}$$

where U_{supply} is the oscillator output voltage, R is the current sense resistor, X_L is the inductors reactance and X_C is reactance of the capacitor formed between the aerostatic bearing and the bearing surface. The denominator of the equation 2 is the impedance Z_{RLC} of the RLC circuit.
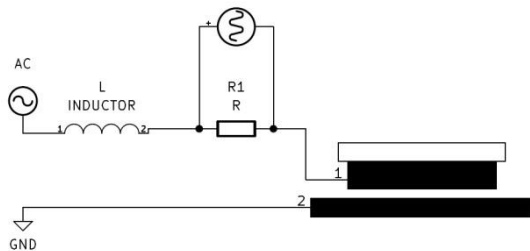
Figure 2. Simplified circuit diagram used in the experiments.

2.1. Measurement circuit

The capacitive sensing circuit consisted of an oscillator, an embedded sensor (capacitor formed between the bearing surface and aerostatic bearing), a rectifier and an output amplifier. The circuit design is presented in Figure 3. A Wien-bridge oscillator consisting of a TL031 amplifier and adjacent RC-tanks was used for the AC voltage source. The frequency of the oscillator was set at 27 kHz and the circuit was tuned for corresponding measurement range of 5 to 20 μm. The voltage-drop over the current-sensing resistor (Fig. 3, R5) was rectified with a 1n4148 diode, and amplified with TL031 as the output amplifier. A virtual ground regulator TLE2426 was used for the amplifiers power supply.
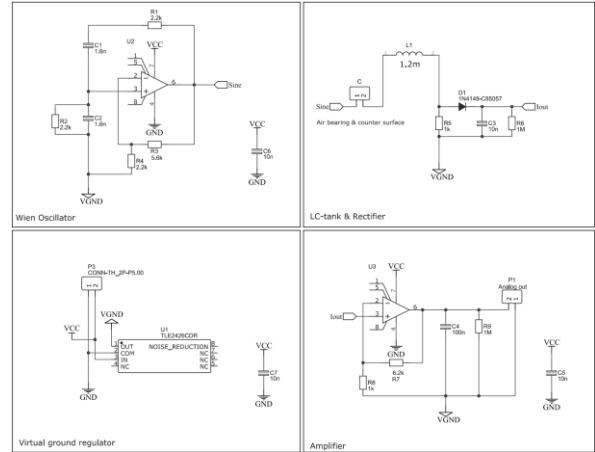
Figure 3. Capacitive sensing circuit. The circuit consisted of a Wien bridge oscillator and an LC Tank.

2.2. Capacitance-Distance relationship

The sensor output was not linear due to the nature of the RLC circuit. Thus, the voltage output signal was converted to displacement using equation 5. The voltage-drop over the current sensing resistor $R5$ (Figure 3.) is proportional to the change in the capacitance of the circuit. The current through the resistor is given by Equation 2.

The sensor output is the voltage drop over the resistor multiplied by the gain of the amplifier. This relates the current through the sensing resistor and output voltage as:

$$I_R = \frac{U_{out}}{GR} \tag{3}$$

where U_{out} is the sensor output and G is the gain of the output amplifier (Figure 3. U3).

Setting Equation 2 equal to Equation 3 yields:

$$\frac{U_S}{Z_{RLC}} = \frac{U_{out}R}{G} \tag{4}$$

which allows the displacement to be calculated as a function of the output voltage:

$$d(U_{out}) = 2A\,\varepsilon_0\,\varepsilon_r\,f_0\,\pi\,\frac{\left(R\,\sqrt{-(U_{out} + G\,U_s)(U_{out} - G\,U_s)} + 2\,\pi\,L\,U_{out}\,f_0\right)}{U_{out}} \tag{5}$$

2.3. Parasitic capacitance

The aluminum body of the bearing was anodized with a layer of epoxy between the anodization and the graphite. This effectively insulated the graphite from the aluminum body. The wires used to connect the bearing surface and the graphite to the sensing circuit introduced some parasitic capacitance and inductance. The floating bearing body has some parasitic capacitance between itself and the bearing surface. However, this parasitic capacitance is minimal since the aluminum was recessed 2 mm from the graphite surface. The parasitic capacitance due to the bearing body was analyzed with equivalent circuit presented in Figure 4.
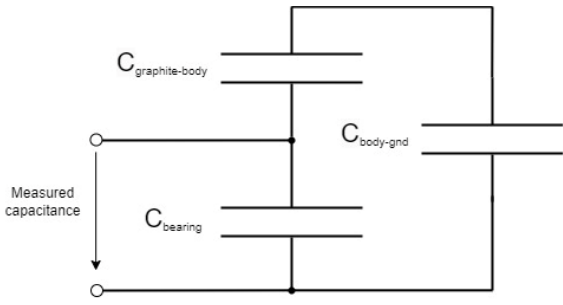
Figure 4. Equivalent circuit of parasitic capacitance due to the bearing body. $C_{bearing}$ is the capacitance formed between the bearing surface and the graphite, $C_{graphite-body}$ is the capacitance between the graphite and the bearing body and $C_{body-gnd}$ is the capacitance between the body and the bearing surface.

The total parallel parasitic capacitance over the measured $C_{bearing}$ is formed from series connected $C_{graphite-body}$ and $C_{body-gnd}$. The total parasitic capacitance can be calculated with:

$$C_{parasitic} = \frac{C_{graphite-body}C_{body-gnd}}{C_{graphite-body} + C_{body-gnd}} \quad (6)$$

The total parasitic capacitance due to the bearing body was below 1 pF, which was insignificant compared to the capacitance of the $C_{bearing}$.

3. Experiment

A test setup, presented in Figure 5, was used for investigating the feasibility of the proposed capacitive sensing concept. A flat, 40mm diameter aerostatic thrust bearing sourced from New Way Air Bearings was selected for use in the study. The investigated bearing was loaded against the guide surface with loads ranging from 50 N to 600 N, corresponding to gap heights of approximately 20 μm to 1 μm. The supply pressure of the bearing was kept constant at 0.6 MPa during the experiments. The bearing was loaded incrementally to maximum load force and unloaded to minimum load force. This cycle was repeated twice. In each measurement trial, 24 points were measured and averaged from the force and displacement sensors.

The measurements were conducted in two parts. The investigated integrated sensor and the external reference sensors could not be used simultaneously due to the interference from the electric field applied to the bearing surface. First, a reference measurement was made using external reference sensors. The reference sensors were Micro-Epsilon CSH-05 capacitive displacement sensors with range of 0-500 μm and accuracy of ±0.3% FS. In the second measurement, the integrated capacitive sensor was used instead of the external capacitive sensors. Both parts were conducted in succession using the same investigated bearing together with the same experiment parameters.
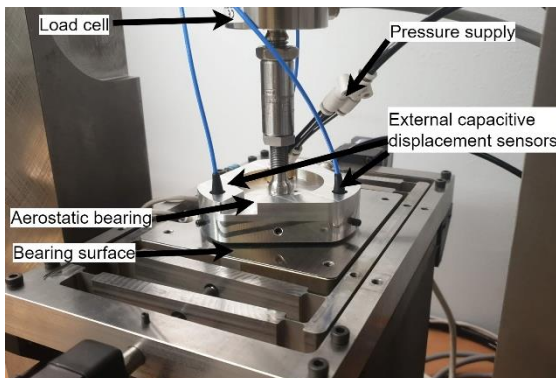
Figure 5. Experiment setup.

4. Results

The sensor output voltage as a function of the air gap height is presented in Figure 6. The useable range of the investigated integrated sensor, limited by the nonlinearity of the RLC circuit and saturation of the output amplifier, was 4 to 12 μm. A comparison between the reference sensors and the integrated sensor is presented in Figure 7.
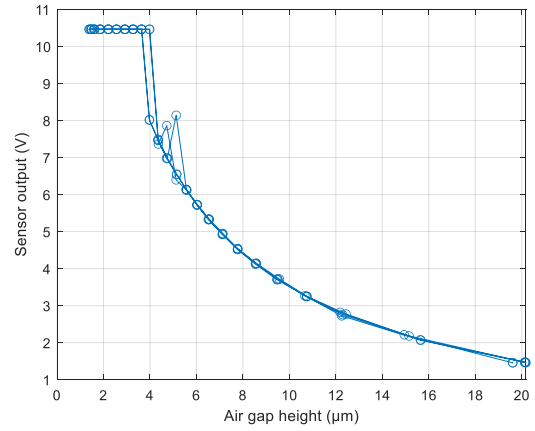
Figure 6. Raw sensor output voltage vs air gap height measured with external sensors. The output saturates at approximately 4 μm gap height.
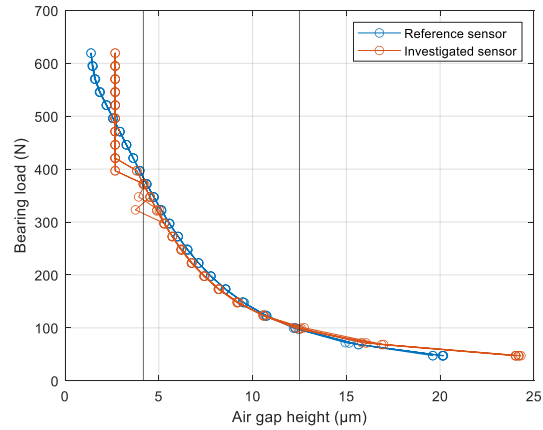
Figure 7. Air gap height measured with the investigated integrated capacitive sensor (orange) and the external reference sensor (blue). Usable range of the investigated sensor, limited by the circuit, is shown with grey vertical lines.

5. Discussion

The results of the present study show that the proposed gap height measurement method is feasible. Figure 7 shows acceptable correlation between the investigated method and the reference method in the usable range of the measurement circuit (4 μm to 12 μm) of the investigated proof-of-concept sensor. The limitation in the measurement range is due to the tuning of the signal conditioning circuit.

The output frequency of the signal conditioning circuit is proportional to $1/\sqrt{LC}$ [2], as an LC oscillator was used. Thus, the output signal increases exponentially as the air gap decreases. Further studies include hysteresis analysis on the loading and unloading test cycles and improvements in circuit design, such as implementation of a synchronous demodulator circuit instead of an LC oscillator to aid in the linearization of the output voltage [2].

One goal of further studies using an integrated sensor is to attain successful, accurate gap height measurements through the full gap height range of the bearing. The performance of the integrated sensor should be able to match the performance of

the external sensors to become a viable replacement for external capacitive sensing methods.

Another possibility for future work includes the air gap measurement of radial aerostatic bushings using integrated capacitive sensing methods. Live measurement of air gap height for radial aerostatic bearings could be useful in high-load, high-speed, and varying-load applications.

6. Conclusions

The present research investigated a proof-of-concept method for the measurement of air gap height of aerostatic bearings using capacitive sensing. The performance of the developed sensor was investigated experimentally with a comparison to external sensors. The results show that the integrated sensor performs effectively and can accurately measure the air gap in the specified usable range of 4 to 12 µm. Outside the range, the performance of the investigated sensor decreases rapidly before becoming unusable below 4 µm. The usable measurement range could be improved significantly by improving the design of the circuit.

Overall, the results demonstrated the feasibility of the concept of integrated capacitive sensing in aerostatic bearings. The developed sensor is a low-cost solution, which could be implemented in applications where other methods are not suitable due to space or cost limitations. However, the method is limited for use only when conductive guide surfaces are present due to its reliance on forming a plate capacitor between the bearing and the guide surface. In further work, possible improvements in the measurement range, accuracy and hysteresis of the sensor will be further investigated.

References

[1] Y. Ye, C. Y. Zhang, C. L. He, X. Wang, J. J. Huang, and J. H. Deng, "A Review on Applications of Capacitive Displacement Sensing for Capacitive Proximity Sensor," (in English), Ieee Access, vol. 8, pp. 45325-45342, 2020, doi:10.1109/Access.2020.2977716.

[2] L. K. Baxter, R. J. Herrick, and I. I. E. Society, Capacitive sensors: design and applications (IEEE Press series on electronics technology). New York Piscataqay, New Jersey: IEEE Press IEEE Xplore (in English), 1997.

[3] F. Colombo, L. Lentini, T. Raparelli, and V. Viktorov, "Experimental Identification of an Aerostatic Thrust Bearing," (in English), Mech Mach Sci, vol. 47, pp. 441-448, 2017, doi: 10.1007/978-3-319-48375-7_47.

[4] V. Vainio, J. Majuri, M. Miettinen, R. Viitala, "Air gap pressure distribution measurement device," Proceedings of the 23rd international conference of the European society for precision engineering and nanotechnology, pp. 249-250, 2023, ISBN 978-1-19989991-3-2.

[5] M. Miettinen, V. Vainio, P. Haverinen, O. Leutonen, R. Viitala, and R. Theska, "Validation of experimental setup for aerostatic bearing simulation," in Engineering for a Changing World: Proceedings; 60th ISC, Ilmenau Scientific Colloquium, Technische Universität Ilmenau, September 04-08, 2023, Ilmenau, 2023. doi: 10.22032/dbt.58841.

[6] D. S. Nyce and ProQuest, Linear position sensors: theory and application. Hoboken, NJ: Wiley-Interscience (in English), 2004.

Measuring the traction properties of water at high pressures between rolling contacts

Trevor Murphy[1], Alex Slocum[1], Minna Wyttenbach[2] and Jesse Granados[2]

[1]Department of Mechanical Engineering Precision Engineering Research Group Massachusetts Institute of Technology
[2]Department of Mechanical Engineering Massachusetts Institute of Technology

trmurphy@mit.edu

Abstract

In this work, rolling contacts are designed for evaluating water as a traction drive fluid. In traction drives, lubrication is secondary to providing traction for power transfer between rollers. Roller contacts offer an accessible high-pressure environment for testing. As lubricants often reach a solid-like transition in the contact area, water is hypothesized to undergo a similar transition with the potential to form Ice VI.

In order to study the performance of water as a traction fluid in elements of rolling contact, a system is designed, built, and tested to measure properties as a function of contact stress and relative velocities between rollers. The experimental apparatus takes advantage of commercially available bearing systems. The system was used in static tests and can be further updated for dynamic tests.

Bearing, Design, Evaluation, Experimentation

1. Background and Introduction

In traction drives, lubrication is secondary to providing traction for power transfer between smooth rollers. Traction drive transmissions are like gear drives where the teeth are replaced by smooth rollers that transmit the power through the shearing of a highly pressurized, viscous layer of traction fluid; the high pressure causes traction fluids to become more viscous and approach something similar to a solid like phase transition. With the replacement of teeth by a traction fluid, traction drives offer no backlash, no direct contact in operation, and lower noise [1]. Additionally, the lubricant film protects against wear and damps torsional oscillations [2]. Because power transmission is done by the tractive fluid, having good measurements of friction data is key to the design and modeling of traction drives.

Previous research indicates that, if sufficient pressure is applied, water has the potential to perform comparably to oils as a traction fluid. Water can freeze into ice VI by increasing the pressure to around 1 GPa at room temperature and 0.6 GPa at 0°C [3]. The coefficient of friction of steel on ice I is around 0.24 [4] compared to the about 0.1 of oiled steel systems [2]. Additionally, the limiting shear stress of Ice I is comparable to the limiting shear stress of traction oils ice [5]. Since Ice I has a slightly different structure than Ice VI, the tractive properties of Ice VI with bearing steels is to be studied.

To study tractive properties, there are general guidelines to consider. Traction is considered a system phenomena and consequently testing should be focused on matching the test system with actual application [6] since deviations can lead to tests not matching application observations. [7] says a list of things that can affect the measurement include "material, surface finish, environment, load, velocity of relative motion, nature of relative motion, nature of contact, temperature, sliding history, characteristics of surrounding machine and

fixtures" which are influenced by the application and system of interest.

Thus, in this work, a rolling contacts system is designed for evaluating water as a traction fluid. Water is hypothesized to undergo a transition to ice VI within the rolling contacts to then have its tractive properties evaluated. This work focuses on the development of a rotary benchtop test rig to explore the performance of water as traction fluid.

2. Design Process

2.1. Functional Requirements

The main functional requirements for the developed test system involve the measurement of the coefficient of friction (COF) of ice VI in a bearing steel system and flexibility for future developments. The system must create contact pressures large enough to create ice VI (around 1 GPa), measure the COF between the pressurized water and roller, and entrain water in between roller contacts with film thickness larger than the surface roughness of the rollers for full lubrication. The latter is required because if the layer is smaller than the surface roughness, the plates are considered essentially in contact, as lubrication cannot effectively occur at that condition.

The system must also withstand water's corrosive effects for longer than the duration of the experiments. For the initial rendition of the test, the test rig should be benchtop scale for easy build and test, and simple to assemble with few components. Lastly, for future work, the setup should have the capability to facilitate both static and dynamic tests.

2.2. What was built and why

A rotary static friction test apparatus is selected to best match the geometry of roller elements in a traction drive. This setup can initially confirm whether speed is required to entrain water and form a lubrication layer between the roller contacts. Static tests require much fewer components and a simpler design to

start while providing the structural foundation for future dynamic tests.
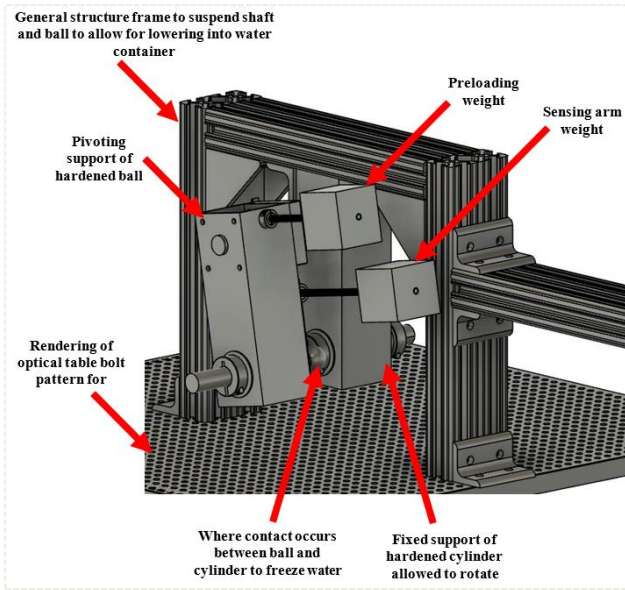
Figure 1. Model of Test Apparatus
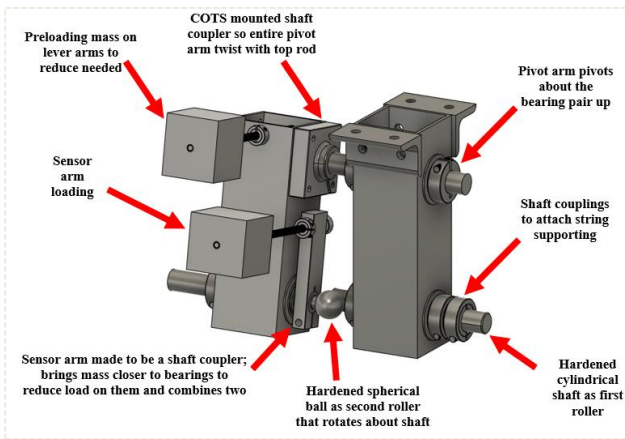
Figure 2. Zoom-in of Test Apparatus Rollers

Figure 1 shows the general concept of the rolling contact system built and tested in this work where **Figure 2** is a zoom-in on the portions that hold the rollers. The rollers consist of a commercial-off-the-shelf (COTS) hardened steel shaft and a tooling ball press fit to be collinear with a second shaft. The nonconformal hertz contact between the sphere and the cylinder allows for smaller, benchtop-sized weights to still reach desired 1 GPa pressures in the contact patch to freeze water due to the very small contact patch area. The sphere is attached to a shaft so that the axis of rotation can be controlled to be the axis of the shaft. Misalignments of the shaft change the radius that the sphere touches at to apply the friction for torque transfer. A 1" sphere and ¾" shaft are selected based on force requirements and Hertz theory scaling:

$$p_m = \frac{2}{3}\left(\frac{6F_{norm}Y_e^2}{\pi^3 R_e^2}\right)^{\frac{1}{3}} \tag{1}$$

In equation (1), p_m is the mean contact pressure set by the pressure needed to freeze the ice, F_{norm} is the normal force on the contact patch, Y_e is the effective Young's modulus of the rollers, and R_e is the effective radius of the rollers.

The supports holding the hardened steel shaft and sphere are oriented vertically in order to submerge as little of the apparatus in water as possible. Additionally, threaded rods are used for

precise control over the location of the weights on lever arms providing preload and sensing force. Having the preload and sensing force provided by lever arms about pivots allows for using mechanical advantage to provide desired forces in a configuration that matched the size of the surrounding general structure.

Corrosion-resistant materials such as acetal plastic bearings, hardened stainless steel, and aluminum are selected to address corrosion concerns. COTS ball bearings are used to decrease bearing friction that might confound with the traction properties to be measured.
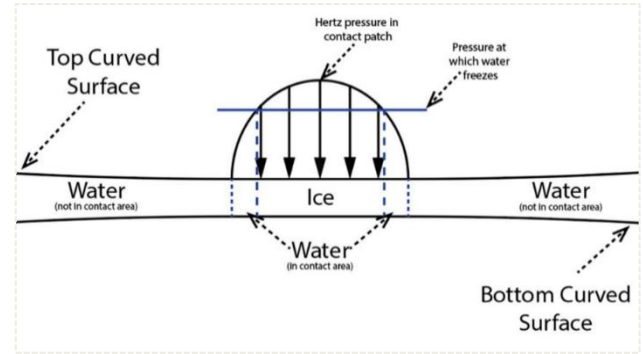
Figure 3. Schematic of Water Freezing in Hertz Contact Patch
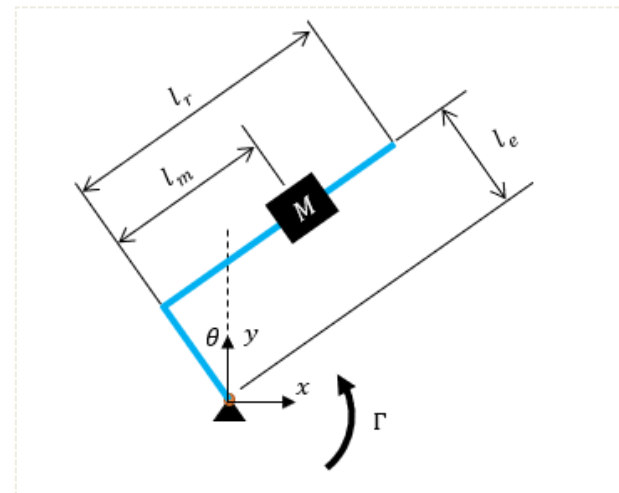
Figure 4. Diagram of Sensing Arm Torque Balance

2.3. How it works

As shown in **Figure 3**, if water is entrained between the rollers, the hypothesis is that ice will form in the center of the contact patch where the hertz pressure reaches and exceeds the freezing pressure, and water will stay liquid elsewhere.

Once ice is presumably formed, the setup is designed to measure the point of slip of the sensing arm, indicating the moment the loading torque overcomes the friction in the system. This angle can be related to a COF of the system from a torque balance applied to the shaft holding the sensor arm with

$$\mu = \frac{\left(-m_e\frac{l_e}{2}\sin\theta + m_r\left(-l_e\sin\theta + \frac{l_r}{2}\cos\theta\right) + M(-l_e\sin\theta + l_m\cos\theta)\right)g}{F_{norm}r_{ball}} \tag{2}$$

where the geometry of the balance is shown **in Figure 4**, m_b, m_e, m_r are the masses of the lengths l_b, l_e, and l_r respectively, F_{norm} is as previously described, r_{ball} is the radius of the ball, M is the mass of the sensing arm weight placed whose center of mass is at l_m, g is the acceleration of gravity, and θ is the angle at which the sensor arm slips completely.

2.4. Testing Conditions

The general test procedure involves resetting the rollers to a position that the sensor arm would not immediately slip, pushing the sensor arm slowly to the point of complete slip and recording the angle at which it happened. This procedure is repeated in different environment conditions (dry, wet, cold) and shaft constraints (fixed, unfixed). The environment conditions of dry, wet, and cold correspond to tests run where the system was dry, placed in room-temperature water, and placed in ice water respectively. The typical temperature of the room was around 20°C and the ice water reached bulk temperature of 5°C during testing. The shaft constraints correspond to whether or not the shaft without the sensor arm was prevented from rolling. Fixed constraint corresponds to the shaft being constrained and unable to rotate with the other shaft during the test. Unfixed corresponds to the shaft being free to rotate with the other shaft during the test.

Throughout the tests the preloading on the rollers is set such that high enough pressures occur for water to freeze at 0°C. One final test condition involves increasing the preload such the freezing would be expected to occur at water temperatures above 9°C and is labelled as "Higher Preload".

3. Data

Figure 5 shows the data collected during the static tests with the ranges set by two standard deviations above and below the mean of ten repeated tests, exceptfor the test condition Cold Fixed. Outliers are ignored. The data is presented in the order that it was taken going left to right. The data includes initially a wet fixed and unfixed condition that was done on a separate day.

Beyond the uncertainty from repeatability shown, there is expected extra uncertainty in the accuracy caused by uncertainty in the angle, mass, and length measurements used to calculate the COF with equation (2). The angle sensor had an uncertainty of 1° corresponding to about 0.01 variation in COF. The mass and length measurement uncertainties could contribute 0.02 and 0.001 variation in the values reported.
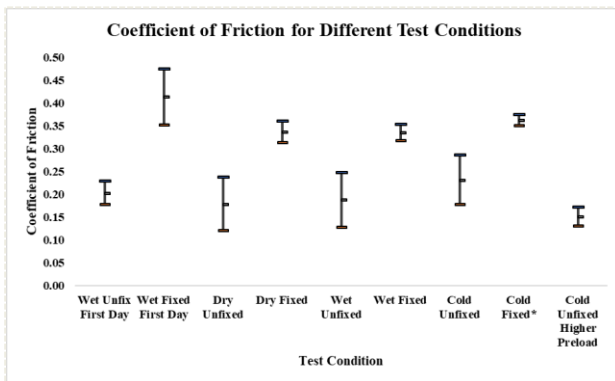
Figure 5. COF Data from 10 Tests in each Condition except Cold Fixed which had only 3 Tests.

4. Discussion

In comparing friction coefficient data, [6][8] recommend using statistical analysis where one of the simplest tests is comparing the ranges of values between data sets where the range is made up of two standard deviations in both directions about the mean. If two ranges overlap, the two sets of data are not statistically different. Following this method of assessment, the majority of unfixed tests are not statistically different despite variation in testing conditions; the majority of fixed tests are not statistically different despite variation in testing conditions; and

for the majority of testing conditions, fixed data and unfixed data are statistically different.

Within the fixed condition, the similarity of results despite changing environment suggests that water did not play a role in affecting the COF measurements in the static test. The similarity within unfixed conditions despite changing environment suggests the same.

Water not playing a role in the static tests seems reasonable since water can squeeze out of the contact area faster than it would experience the pressure to freeze, leading to surface contact instead of lubricated contact. As a first order calculation, the liquid evacuation time, defined as the time it takes for the water thickness to decrease from full film lubrication to thinner than the surface roughness of the plates, can be calculated using lubrication equations [9]. These lubrication equations treat the water-filled contact patch area as two flat plates pressed together with some normal force and result in an evacuation time of

$$t_f = \frac{9\mu\pi^2 p_0 R_s R_c}{4Y_e^2 h_0^2} \qquad (3)$$

where R_s is the radius of the sphere, R_c is the radius of the cylinder, h_0 is the initial film thickness, and μ is the viscosity of the fluid. The value that this equation predicts is on the order of tens of nanoseconds to tens of microseconds meaning that it takes very little time for water to evacuate from the contact area, resulting in surface contact.

One way to counteract the liquid evacuation is to entrain the water into the contact by having the contacts move in a dynamic test as opposed to a static test. The speed at which to move the roller surfaces can be estimated by applying Poiseuille-Couette flow between two moving plates and finding the speed of the plates that leads to a net inflow of fluid which gives

$$v > \frac{\Delta P h^2}{12a\mu} \qquad (4)$$

where v is the speed of the moving plates, ΔP is the pressure change between the edge and center of the contact patch, a is the contact patch size, and h is the film thickness. Alternatively, one could use the elastohydrodynamic film layer thickness fits provided by [9].

The difference between fixed and unfixed configurations is interesting. In the fixed configuration, the shaft roller is prevented from rotating while the ball roller can rotate under the driving force of the sensing arm. Thus, the motion is always pure sliding between the roller surfaces. The unfixed configuration involves the surfaces rolling on each other. It is unclear what the difference between these two conditions implies at the moment.

One thought is that the rolling surfaces produce less friction between them. The question then is why the friction is so large still since rolling frictions are often much smaller than sliding friction values, often around 0.001. Another possibility is that the rolling allows for movement of the elements below what friction could counteract at its maximum. Friction force can be any value below the max limit it can achieve to initiate motion and the friction force measured in the unfixed condition may be this less-than-max value.

Another possibility is slippage between the surfaces during rolling might affect the measured COF. To test this, a separate test was applied to the setup after the friction tests to see if the shafts slipped relative to each other in the unfixed condition. This test was performed by preloading the setup in the dry unfixed condition and manually rotating the shafts various amounts and comparing the output rotation to the rotation expected if there was no slip. The results of that test suggest that there was no relative slippage within the angle sensor's measurement error for the unfixed conditions, ruling out this possibility.

5. Conclusions and Next Steps

A rotary benchtop test rig was designed and built to test the traction properties of ice VI. The static tests suggest that water did not participate in the system friction, possibly since there was no entrainment motion of the rollers to prevent the water evacuating the contact patch before freezing. To get ice VI traction properties, surface motion is needed to entrain the fluid for measurement. The test rig is a good foundation for development of these dynamic tests in the future for assessment of the traction properties of ice VI.

References

[1]   "Speed Reducers with Traction Drive Technology," *Designatronics Inc*. [Online]. Available: https://www.sdp-si.com/products/Gearheads-Speed-Reducers/traction-drive.php. [Accessed: 16-Feb-2023].

[2]   S. H. Loewenthal and E. V. Zaretsky, "Design of traction drives.," Cleveland, Ohio, 1985.

[3]   P. W. Bridgman, "Water, in the Liquid and Five Solid Forms, under Pressure," *Proc. Am. Acad. Arts Sci.*, vol. 47, no. 13, pp. 441–558, Jun. 1912.

[4]   N. Nakazawa, T. Terashima, and H. Saeki, "Factors Influencing the Coeffecient of Friction Between Sea Ice and Various Materials," *Proc. Civ. Eng. Ocean*, vol. 8, pp. 141–145, 1992.

[5]   H. Saeki, T. Ono, N. E. Zong, and N. Nakazawa, "Experimental Study on Direct Shear Strength of Sea Ice," *Ann. Glaciol.*, vol. 6, pp. 218–221, 1985.

[6]   G. E. Totten, *ASM Handbook, Volume 18 - Friction, Lubrication, and Wear Technology (2017 Revision)*. ASM International, 2017.

[7]   P. J. Blau, "Appendix: Static and Kinetic Friction Coefficients for Selected Materials," *ASM Handbook, Volume 18 - Friction, Lubrication, and Wear Technology*. ASM International, pp. 70–75, 1992.

[8]   K. G. Budinski, "Laboratory Testing Methods for Solid Friction," *ASM Handbook, Volume 18 - Friction, Lubrication, and Wear Technology (2017 Revision)*. ASM International, pp. 44–55, 2017.

[9]   B. J. Hamrock, S. R. Schmid, and B. O. Jacobson, "Fundamentals of Fluid Film Lubrication," *Fundam. Fluid Film Lubr.*, 2004.

Dynamic estimation of the point of interest based on sensor positions using an observer

Anna-Carina Kurth[1], Viviane Bauch[1], Martin Glück[1], Jakob Köhler-Baumann[1]

[1]*Carl Zeiss SMT GmbH, Oberkochen, Baden-Württemberg, Germany*

{anna-carina.kurth, viviane.bauch, martin.glueck, jakob.koehler-baumann}@zeiss.com

Abstract

For the precise positioning of a flexible object using control, a specific point of interest is usually used as a reference point. If the position of this point cannot be detected directly by sensors, it is reconstructed from the positions of the sensors using a rigid body assumption. However, as soon as the object deforms, this assumption is no longer correct, so that the control system calculates the input of the actuators based on an incorrect position. This can lead to unstable system behaviour and performance losses. In this contribution, an observer-based approach is proposed that dynamically estimates the point of interest based on the signals from the sensors and the control signal from the actuators. This allows the control system to obtain correct position information even at higher frequencies and hence leads to an increase in performance and robustness.

Position Estimation, Luenberger Observer, Flexible bodies

1. Introduction

In high-precision applications a very common task is the precise positioning of an object with a feedback controller. Due to the elasticity of the object the position of a special point of interest (POI) is controlled.

The POI position is measured by sensors at locations distributed over the object because of the use of highly sensitive unidirectional sensors. Hence, the system is not collocated, since the sensors and actuators are not at the same position [1,2]. The POI is reconstructed from the sensor positions by using a rigid body transformation, which leads to a collocated layout if the assumption of a rigid body holds true. As soon as first flexible resonances occur, the calculated POI does not match the actual POI. Therefore, the control cannot position the right POI and servo errors or even instability can occur [1,2].

The commonly used approach is to use a lowpass-filter or notch filters that turn off the control as soon as flexible resonances occur [2]. Hence, the bandwidth of the controller is limited by the flexible resonance frequencies. This contribution focuses on an alternative approach to dynamically estimate the POI even in frequency regions, where the object has flexible resonances. Thus, a controller with a higher bandwidth can be used and the positioning of the object as well as disturbance rejection is improved.

The dynamic estimation is based on a Luenberger observer, which is a basic observer suitable for systems without noise, but typically not used for virtual collocation. The POI is estimated by the observer using the sensor and actuator signals and a mechanical model. A model order reduction is needed to achieve real-time applicability.

The observer output is used as an input for the controller, which can be either a full state feedback or output feedback, which uses only part of the estimated positions namely the POI. The advantage of using the whole state for feedback instead of just the output is that the object can be positioned with respect to the POI by a reduced occurrence of flexible mode shapes.
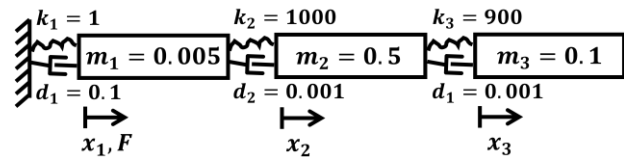
Figure 1. Considered system with three masses connected via springs and dampers and their respective values.

2. Problem statement

This section describes the basics needed to do model order reduction and design a Luenberger observer for the original as well as the reduced system to estimate the POI of a flexible object.

2.1. Modelling & analysis of the plant

An elastic object can be interpreted as an interconnection of several spring-mass-damper systems, as is also done in modelling using FEM. For proof of concept, a system with three masses is chosen in this contribution. The masses m_1, m_2, m_3 with their respective positions x_1, x_2, x_3 are coupled by springs with stiffness k_1, k_2, k_3 and dampers with damping d_1, d_2, d_3. The lowest mass m_1 is the POI, which is actuated and coupled to the fixed world. The third mass m_3 is measured by sensors, see Fig. 1. Therefore, the system is not collocated. The equations of motion result in the system dynamics Σ_y with the measured output $y \in \mathbb{R}^1$, which is the position of mass m_3 resp. Σ_z with the POI output $z \in \mathbb{R}^1$, which is the position of mass m_1

$$\begin{aligned}\dot{x}(t) &= Ax(t) + Bu(t) \\ y(t) &= C_1 x(t) \\ z(t) &= C_2 x(t)\end{aligned} \qquad (1)$$

Hereby, the states $x \in \mathbb{R}^6$ represent the positions and velocities of the masses and the input $u \in \mathbb{R}^1$ displays the force acting on mass m_1. The dimensions of the dynamic matrix A, the input matrix B and the output matrices C_1 and C_2 are accordingly.

If looking at system Σ_z, alternating resonances and antiresonances arise in the Bode plot. Hence, the phase of the input-output behaviour will always be between 0 degree and -180 degree. From a control point of view, this is particularly advantageous, since in the Nyquist diagram no further encirclement of the critical point can occur with any amount of amplification by a controller [1]. Therefore, the gain margin (GM) is infinity. However, this holds only true for academic examples without sensor or actuator dynamics or delay for example. If these parasitic effects are considered bounded phase shifts can occur, but not phase jumps like for the case with two resonances directly after each other.

If looking at the input-output behaviour of system Σ_y, three resonances appear directly after each other. Therefore, phase jumps occur, and control design is more challenging regarding robust stability. With the observer, designed in the next section, the system is virtually collocated by estimating the position of the POI, which can then be used for control. However, normally FEM are high dimensional and cannot be used in the observer. Hence, system Σ_y is reduced by balanced truncation resulting in system Σ_r. Hereby, states that contribute only slightly to the transmission behaviour are neglected. The dimension of the reduced system is then four, such that one resonance is missing in the reduced system. Differences between the reduced and the original model occur only high-frequent.

2.2. Luenberger Observer

A Luenberger observer estimates not measurable states of a system based on a mechanical model. The observer structure is simple and suitable for systems without or little noise. Two approaches are considered in this contribution: In the first approach system Σ_y is used in the observer as model resulting in overall system Σ_{full}, in the second approach the reduced model Σ_r is used as basis for the observer design resulting in combined system Σ_{red}.

If the observer uses system Σ_y as model, the separation theorem can be used to design observer and control. Therefore, the controller is designed based on system Σ_z or with the whole state x as feedback.

If the reduced model is used, the separation theorem is not valid anymore. However, the differences due to the reduction only occur at high frequencies. Therefore, either a low-pass filter can be used, or the observer can be designed especially robust to take the differences between plant and observer model into account. Hereby, the reduction method via balanced truncation is beneficial, since it delivers also an error bound. In this contribution the assumption is made that the separation theorem is also valid for the case with the reduced model.

The observer gain is designed with an LQR approach to get an optimal gain. The input to the observer is the input u as well as the output y. The output of the observer is either the estimated position of the POI z or the estimated state x, whose dimension is dependent on the choice of the model in the observer.

2.3. Control design

The goal of the control is the positioning of mass m_1 by actuating it but using the measurement of mass m_3.

For proof of concept a simple proportional controller with gain k_P is used for output-feedback, which is aggressively tuned. For the state feedback a LQR control approach is used to show the potential of the presented approach [2]. In case without observer output y is fed back. In case with observer the estimated position of the POI z is used for the output feedback and the estimated states x for state feedback. The interesting output is in all cases the position of the POI z.

3. Simulations

The open loop of system Σ_y from the control error to the measured output has a GM of 58.3 dB and a phase margin of 10.4°, while the open loop of the observer with the full system as model from the estimated control error of the POI to the estimated position of the POI has an infinitely high GM and a phase margin of 12.8° and with the reduced system from the same input to output has a GM of 60.2dB and phase margin of 12.8°. Increasing the proportional gain k_P leads to a linearly increasing bandwidth while linearly decreasing the gain margin. Therefore, with the same robustness criterions a higher bandwidth can be achieved by using an observer. However, it must be considered that the observer shall be faster than the controller, which limits performance.

For comparison an impulse output disturbance is applied. As performance criterion, the peak amplitude (PA), which is the maximum position of the POI z, and the transient time (T), which is when the position of the POI z is converged, are chosen, see Table 1. As proportional gains 90% of the values are chosen for which one of the systems is close to instability. If a bar appears in the table, the respective system is unstable. For the LQR approach no special tuning was done. The Q- and R-matrix are chosen as simple unity matrices.

The higher the gain, the less high is the PA for the observer with the full model. However, from a certain gain decreasing PA comes with an increasing T. The observer Σ_{red} performs better for lower gains, which is due to the mismatch of the plant Σ_r used in the observer and system Σ_y. The best performance can be achieved by a state-feedback. The PA as well as the T are low compared to the output feedback.

Table 1 PA | T (s) of the position of the POI.

System	$k_P = 740$		$k_P = 920$		$k_P = 2000$		LQR	
	PA	T	PA	T	PA	T	PA	T
Σ_y	18	221	-		-			
Σ_{red}	15	163	15	910	-		1	3
Σ_{full}	16	313	15	192	12	427	1	3

4. Conclusion

In this contribution an approach to estimate the POI of an elastic object based on sensor positions and the applied control force was presented. Firstly, the problem was stated, and the resulting system was analysed with a special focus on collocation. Afterwards, the model was reduced with respect to its dimension and the basics for an observer design were presented. With the introduced control design, simulations were carried out. By using an observer concept, the control performance is increased. Using a reduced model in the observer leads to slightly decreasing performance. However, if a state-feedback is chosen, which is enabled due to the estimation of the full state, a huge performance increase is achieved even though the controller was not tuned especially. This translates directly into a more precise positioning of the object and therefore into increased system performance. In future work, the results will be transferred to more realistic models and finally validated in experiments.

References

[1] Gosiewski, Zdzislaw, and Zbigniew Kulesza. Virtual collocation of sensors and actuators for a flexible rotor supported by active magnetic bearings. Proceedings of the 14th International Carpathian Control Conference (ICCC). IEEE, 2013.
[2] Preumont, Andre. Vibration control of active structures. Vol. **2**. *Dordrecht: Kluwer academic publishers*, 1997.

Modelling and control of turbine-driven spindles for micro machining with constant feed per tooth

Andreas Lange[1], Nicolas Altherr [1], Felix Zell[1], Benjamin Kirsch[1], Jan C. Aurich[1]

[1]RPTU Kaiserslautern; Institute for Manufacturing Technology and Production Systems

felix.zell@rptu.de

Abstract

Micro machining requires high spindle speeds but only needs low cutting power, making turbines a potential alternative to electric motors. As an increased surface quality and tool life can be achieved through a constant feed per tooth when using micro end mills, it is necessary to adapt the spindle speed to the feed rate alteration. Hence, the drive's dynamics and torque must be sufficient to ensure fast adaptions of the spindle speed to the feed rate alteration, which is more difficult with turbines.

This paper aims to model a speed control system for turbine-driven spindles, examining the suitability of a turbine's dynamics and torque to adapt the spindle speed to feed rate alterations. The modelling approach consists of three stages: 1. Setup of a fluid dynamics simulation to determine torque across various inlet mass flow rates and generating lookup tables for later control system implementation. 2. Designing a controller featuring a feedback loop with feedforward control for fast adaptation and accurate control of model uncertainties and disturbances. 3. Integrating the turbine's flow dynamics and rotor's dynamics into the feedback loop.

The evaluation of the control behaviour shows that effective control can be achieved. Hence, the devised control concept theoretically enables fast speed adjustments. However, the turbine's torque is not high enough to enable the required fast changes of the rotational speed to maintain a constant feed per tooth. A higher mass flow rate could generate sufficient torque, as shown by artificially increasing the mass flow rate, but it was not possible to increase the mass flow rate further with the chosen geometry and fluid dynamics boundary conditions. Turbine optimization could increase torque but might necessitate trade-offs between added rotor inertia and improved torque. Additionally, the employed turbines exhibit lower efficiency compared to electric motors.

Micromachining, Simulation, Turbine blade, Control

1. Introduction

Micro machining is crucial for manufacturing high-precision and complex microstructures [1, 2]. In micro machining processes such as micro milling, it is desirable to employ a constant optimal feed per tooth, as this can significantly influence the process result and reduce tool wear [2, 3]. As such, the spindle speed must be adapted to the feed rate to maintain a constant feed per tooth, which requires sufficient spindle torque and dynamics to enable fast speed control.

High-frequency spindles used for micro machining are usually driven by electric motors [4], but this generates electromagnetic fields that can affect the run-out [5]. An alternative drive method is a turbine, which has no electromagnetic fields. Further, high-frequency spindles are often equipped with air bearings [6], which enables the use of compressed air for both the bearings and the turbine. In addition, turbines generate less heat than electric motors, which improves the thermal stability of the spindle-system [7]. Disadvantage of turbines in high-frequency spindles are their low efficiency, power output, and dynamics, as previous works have shown [8].

In this study, a speed control of a spindle's turbine drive is developed. For this purpose, the control loop is modelled, including the flow dynamics of the turbine. Further, the cutting torque is considered. The turbine is modelled via a numerical fluid dynamics model, which is implemented in the control loop in the form of lookup tables to enable efficient access to the required mass-flow-rate-speed-torque characteristics of the turbine. A compensation controller is designed using root locus analysis.

2. Methods

First, the fluid dynamics simulation is conducted to determine the mass-flow-rate-speed-torque characteristics of the turbine. Next, the kinematics for micro milling a groove with constant feed per tooth are described, as needed for defining the requirements for the speed control to keep a constant feed per tooth. Subsequently, the feedback loop and controller are modelled.

2.1. Fluid dynamics simulation

To determine the mass-flow-rate-speed-torque characteristics of the turbine, a fluid dynamics simulation was conducted, describing the behaviour of the fluid volume (air) between the turbine and the casing. In Figure 1a), the CAD model of the rotor is depicted, consisting of a single axial and two radial bearing surfaces and two turbine geometries with eight semi-circular blades each. Two turbines with blades facing opposite directions are required for fast acceleration and deceleration. At the front end of the rotor, the micro milling tool can be mounted. Figure 1b) shows the CAD model of the fluid volume. The CAD model of the fluid volume was imported into ANSYS[1] Fluent[1] for computation of the resulting torque.

The simulation requires boundary conditions defining external influences on the flow. In this case, the boundary conditions include mass flow rate at the inlet, rotor speed, and ambient pressure at the outlet. The simulation was performed for four different combinations of mass flow rate and rotor speed. For each combination, the resulting turbine torque was computed. Only four combinations were simulated because the torque is linearly

dependent on both the rotor speed and mass flow rate. Thus, four combinations/result points are sufficient to describe the characteristics.

The mass-flow-rate-speed-torque characteristics of the turbine were derived from the fluid dynamics simulation results by fitting a plane through the four result points using linear regression. The resulting values were stored in lookup-tables for the implementation in the feedback loop. The Curve Fitter App[1] in MATLAB[1] was employed for linear regression.
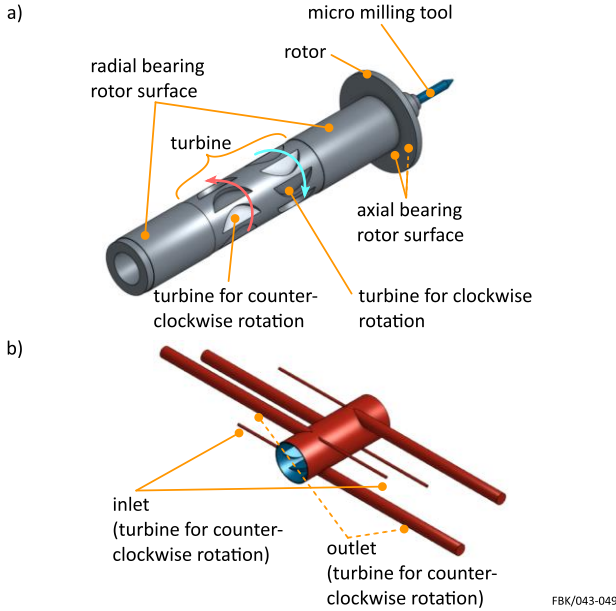
Figure 1. a) schematic view of the spindle rotor with incorporated turbines, b) modelled fluid region and boundary conditions

2.2. Requirements to enable constant feed per tooth

To keep the feed per tooth constant, the rotational speed n of the tool spindle must be adapted to the feed rate to maintain a constant feed per tooth. Hence, to fully define the requirements for speed control, the kinematics for micro milling a groove with a rounded corner are described in dependence of the feed rate. The feed per tooth f_z is defined as the ratio between the feed rate v_f and the product of the spindle rotational speed n and the number of cutting edges z:

$$f_z = \frac{v_f}{n \cdot z} \qquad (1)$$

The milling path is divided into five regions, as shown in Figure 2a). The corresponding feed rate of the feed axis to maintain a constant feed per tooth (equation (1)) is shown in Figure 2b).
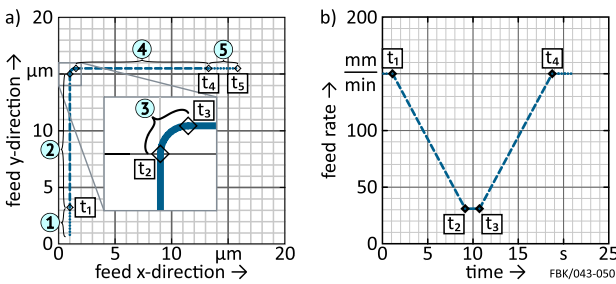
Figure 2. a) trajectory of a groove with rounded corner and b) corresponding change of feed rate

Regions 1 and 5 have a constant feed rate $v_{f,0}$ (up to t_1 and t_5 respectively), derived from the optimal feed per tooth and initial spindle speed n_0. Regions 2 and 4 reduce the feed rate (up to t_2 and t_4 respectively) to a reduced value $v_{f,red}$ before the transition

area to lessen the demands on response time of the speed control. The feed rate decreases linearly in these regions when assuming maximum acceleration. Region 3 describes the transition area, where the feed rate is the lowest (up to t_3).

2.3. Feedback loop

For the control system, the overall dynamics of the plant must be modelled in the feedback loop. This includes the rotor's angular dynamics, start-up dynamics of the inlet valve, the cutting torque, and the mass-flow-rate-speed-torque characteristics of the turbine. Herein, instead of the full fluid dynamics model of the turbine, the lookup tables featuring the turbine's characteristics were implemented in the feedback loop to avoid a time-consuming recomputation during every simulation step. The mass-flow-rate-speed-torque characteristics of the turbine were limited to a maximum value corresponding to a maximum pressure of 8 bar at the valve/inlet of the turbine. A dynamic torque equilibrium was established for the rotor, considering the resultant angular acceleration due to the applied turbine torque. Additionally, frictional torque of the rotor's bearings is calculated based on fluid shear forces as presented in [9]. The resulting differential equation from the dynamic torque equilibrium can be converted into a state-space representation. Here, the rotor's angular velocity is the state vector $\mathbf{x}(t)$, turbine torque is the input vector $u(t)$, and angular velocity is the output vector $y(t)$. The state-space representation simplifies the differential equation by reducing its order through substitution to a first-order linear differential equation, eliminating the need for linearization. The state-space representation (the rotor's inertia included in **A** and the input matrix **B** and the frictional torque of the bearings included in the the state matrix **A**) is given in equation (2), the required input parameters are given in Table 1.

$$\dot{x}(t) = \mathbf{A}x(t) + \mathbf{b}u(t), \ \ y(t) = \mathbf{c}^T x(t) + du(t)$$
$$x(0) = x_0, \ \ x(t) = \omega_R, \ \ u(t) = M_T, \ \ y(t) = \omega_R$$
$$\mathbf{A} = -\frac{\mu_A \cdot 2\pi \cdot R_i^3 \cdot l_{ra}}{J_z \cdot h_{ra}} - \frac{\mu_L \cdot \pi \cdot (R_o^4 - R_i^4)}{2 \cdot J_z \cdot h_{ax}} \qquad (2)$$
$$\mathbf{b} = 1/J_Z; \ \mathbf{c}^T = 1; \ d = 0; \ x_0 = n_{max} \cdot \pi/30$$

Table 1. Input parameters required for modelling and simulation

parameter	value
dynamic viscosity of air μ_A	18 µPa·s
inner radius of rotor R_i	10.5 mm
outer radius of rotor R_o	19 mm
length of radial bearing l_{ra}	67 mm
mass moment of inertia in z-direction J_z	185,4 g·cm^2
air gap height of radial bearing h_{ra}	21.5 µm
air gap height of axial bearing h_{ax}	25 µm
intended maximum rotational speed n_{max}	125,000 min^{-1}

The start-up dynamics of the inlet valve can be modelled as part of the feedback loop or be considered during the controller design. However, the valve's fast rise times make it unsuitable for controller design, as its impact is brief and would increase controller complexity. Hence, the start-up dynamics of the inlet valve are considered as a disturbance input in the feedback loop.

The cutting torque was also modelled as a disturbance input in the closed-loop model. The cutting force was simplified as a sinusoidally oscillating force with zero crossings instead of negative values. An amplitude of 0.2 N and a tool radius of 25 µm was assumed, adopted from previous works [10]. The sinusoidal frequency was based on spindle speed.

2.4. Controller design

The desired control behaviour for the process variable (actual value of speed) was specified to follow the setpoint value (setpoint speed). A second-order (PT2) response was sought for stability, characterized by simple and stable control with a short

settling time and minimal overshoot. For this, a PIT1 compensation controller was designed using the root locus method. The PIT1 controller inherently has an integrator pole at zero, a system pole defined by the plant, and another adjustable pole and root. Parameters were chosen to ensure a PT2 response for the closed-loop system, offering a short settling time with minimal overshoot: Initially, the gain factor was set for the desired settling time, and then the rightmost pole was shifted along the real axis. Using the Controller System Designer App[1] in MATLAB[1] to determine parameters for the adjustable pole and root through linear regression results in the equation for the controller:

$$G_R(s) = 0{,}045 \cdot \frac{1 + \frac{0{,}02}{s}}{s + 100} \tag{3}$$

To enable fast speed adjustments, a feedforward control was added. This anticipates the setpoint value, reducing control error. The feedforward control consists of the inverse model of the plant, multiplied by a PT1 element. The feedforward time of the PT1 element is an adjustable parameter and was iteratively set to 20 s, offering good control behaviour without introducing additional oscillatory behaviour. The derived equation for the feedforward control is:

$$G_{VS}^{real}(s) = \left(\frac{53940}{s + 0{,}03713}\right)^{-1} \cdot \frac{1}{1 + 20 \cdot s} \tag{4}$$

The complete closed-loop model was set up in Simulink[1], as shown in Figure 3. It includes feedforward control (green, solid lines), the controller (red, dashed lines), and the plant (yellow, dotted lines), consisting of the turbine's mass-flow-rate-speed-torque characteristics, the rotor's angular dynamics, start-up dynamics of the inlet valve, and the cutting torque (see section 2.3). The setpoint speed was calculated corresponding to the change of the feed rate during the manufacture of a groove with constant feed per tooth (see Section 2.2 and Figure 2).
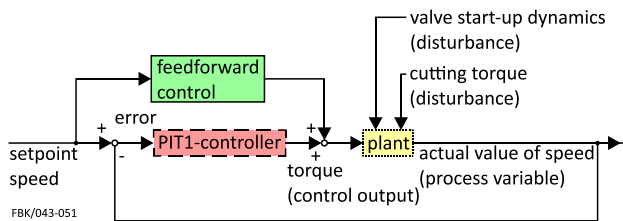
Figure 3. Schematic view of the modelled feedback loop with feedforward control

3. Results

This section examines how well the control requirements (see section 2.1) are met and how the maximum mass flow rate and torque affect the speed control. The results (Figure 4 to 6) include a numbering of regions (1 to 5), as outlined in the modelling of the milling path and feed rate in Section 2.2 and Figure 2.

3.1. Test with unlimited mass flow rate and torque

To evaluate the performance of the developed controller (equation (3)) and the feedforward control (equation (4)), the controller's transient response under ideal conditions is examined with a time-varying setpoint, without limits of the mass flow rate and torque imposed by the turbine drive. Figure 4 shows the behaviour of the setpoint value (setpoint speed) and the process variable (actual value of speed) during adjustments of the rotational speed as required to machine the described

grooves with constant feed per tooth (see section 2.2 and Figure 2). The results show that the combination of controller and feedforward control provides fast and accurate speed adjustment. Further, there is no oscillatory characteristic of the process variable, the rise and settling times are very low, and the process variable converges without steady-state error. By deliberately omitting a derivative term (D-term) in the controller, the high-frequency signal of the cutting force is not amplified further and has a negligible influence on the process variable.
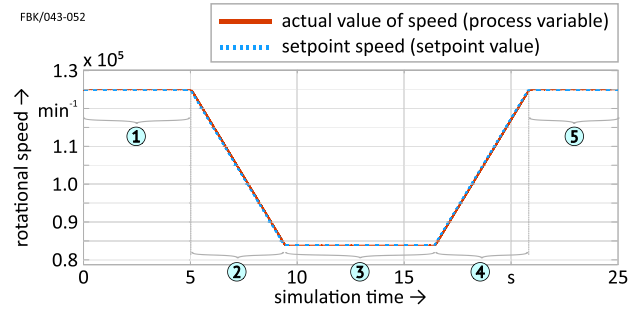
Figure 4. Behaviour of the setpoint value (setpoint speed) and the process variable (actual value of speed) during adjustments of the rotational speed with unlimited mass flow rate and torque

3.2. Test with maximum mass flow rate and torque

The control input (mass flow rate) of the control loop is limited by the maximum possible mass flow rate, which is determined by the mass throughput through the inlet valve, inlet nozzle and the geometry of the turbine. This subsequently limits the control output (torque). Figure 5 shows the additional influence on the control output and the process variable (actual value of speed) due to the maximum achievable turbine torque.
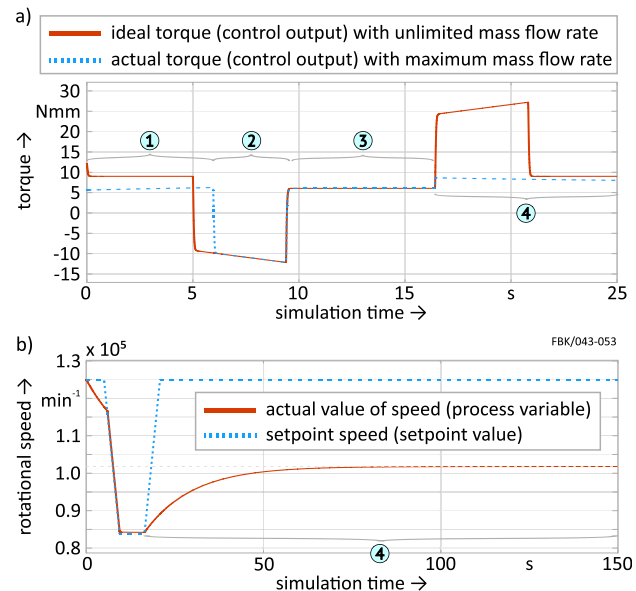
Figure 5. a) control output (torque) during adjustments of the rotational speed with maximum mass flow rate and torque and b) setpoint value (setpoint speed) and process variable (actual value of speed)

Figure 5a) shows that the achieved torque is lower than the required ideal torque, which also leads to torque having to be applied for a longer time (as seen by the longer required simulation time (150 s) to achieve a steady-state behaviour in Figure 5b)). This leads to the process variable no longer being able to match the setpoint value, as the available torque is not suffi-

cient to control the speed sufficiently quickly and reach the target speed, as Figure 5b) shows. This is reflected in an increased rise and settling time, an overshoot, and a steady-state error.

3.3. Test with artificially increased mass flow rate and torque

For further assessment of the controller, in this section an artificially increased maximum mass flow rate of 0.005 kg/s is assumed, which is higher than the actual possible mass flow rate (approx. 0.002 kg/s). The new transient response resulting from the higher maximum mass flow rate is shown in Figure 6a). This new transient response only exhibits a slight overshoot that converges slowly (as seen by the longer required simulation time (150 s) to achieve a steady-state behaviour in Figure 6a)). This is again a consequence of the maximum mass flow rate. The overshoot characteristics can be improved with further increase of mass flow rate and thus torque.

The feed per tooth can be calculated (using equation (1)) and compared for the two cases without and with speed control, as seen in Figure 6b). Due to the limited mass flow rate and thus low torque, constant feed per tooth is not achieved, even when speed control is used. Due to the controller and feedback loop, the speed adjustment leads to an increase in the feed per tooth. This increase is smaller than the reduction of the feed per tooth when no speed control is used (blue dotted lines in Figure 6b)). The small increase in feed per tooth may be better suited for machining applications, because lowering the feed per tooth can cause the minimum chip thickness to be undercut. This is not the case for a small increased feed per tooth. In that case, the optimal value for the feed per tooth is not reached for a short time and the wear of the micro milling tool is increased for the period.
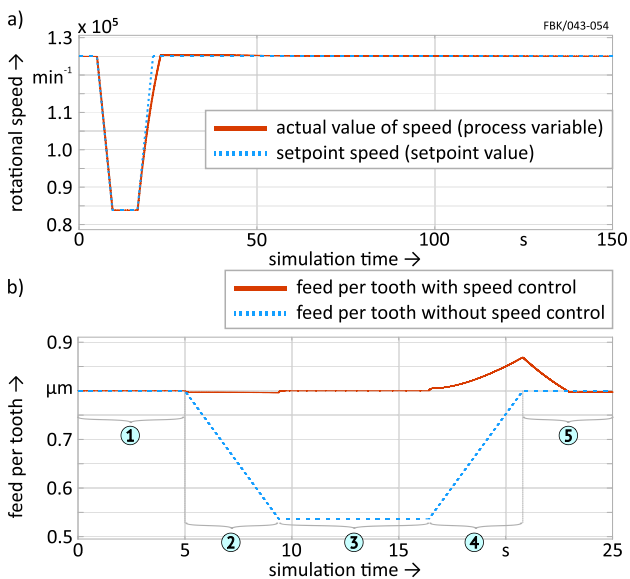
Figure 6. a) setpoint value (setpoint speed) and process variable (actual value of speed) and b) feed per tooth during adjustments of the rotational speed with artificially increased mass flow rate and torque

4. Conclusion

In this study, a control system for the speed control of a spindle's turbine drive was developed. For this purpose, a fluid dynamics model of the turbine was set up to determine the dependence between mass flow rate, rotational speed, and torque. The resulting characteristics were then stored in the form of lookup tables. The speed control was modelled as a controller in a feedback loop with feedforward control for fast adaptation and accurate control of model uncertainties and disturbances such as cutting torque. The following conclusions can be drawn:

- Tests with unlimited mass flow rate and torque show that effective speed control is possible with the devised controller and feedback loop.
- Tests with the actual possible mass flow rate and torque show that the turbine's power output is too low to adapt the spindle speed sufficiently quickly and to reach the target speed. Thus, while the presented control system is suitable, the modelled turbine is not feasible for the required speed control to enable constant feed per tooth.
- Tests with artificially increased mass flow rate show how much torque of the turbine is necessary to enable efficient speed control. Based on this, the turbine can be optimised towards a defined torque and thus required target mass flow rate and pressure at the inlet.

In future works, necessary turbine optimisations to increase the torque will be investigated to evaluate if the required inlet mass flow rate and pressure is feasible. Additionally, the turbine diameter can be increased. However, the increased moment of inertia of the rotor and the low efficiency of turbine drives in high-frequency spindles compared to electric motors must be considered.

[1]Naming of specific manufacturers is done solely for the sake of completeness and does not necessarily imply an endorsement of the named companies nor that the products are necessarily the best for the purpose.

References

[1] Chae J, Park S S, Freiheit T 2006 Investigation of micro-cutting operations. *International Journal of Machine Tools and Manufacture*

[2] Balázs B Z, Geier N, Takács M, Davim J 2020 A review on micro-milling: recent advances and future trends. *The International Journal of Advanced Manufacturing Technology*

[3] Vavruska P, Bartos F, Pesice M 2023 Effective feed rate control to maintain constant feed per tooth along toolpaths for milling complex–shaped parts. *International Journal of Advanced Manufacturing Technology* **128** 3215–3232

[4] Abele E, Altintas Y, Brecher C 2010 Machine tool spindle units. *CIRP Annals* 59 **2** 781-801

[5] Kim T, Kim K T, Hwang S, Lee S, Park N G 2001 Analysis of radial runout for symmetric and asymmetric HDD spindle motors with rotor eccentricity. *Journal of Magnetism and Magnetic Materials* 226 1232-1234.

[6] Gao Q, Chen W, Lu L, Huo D, Cheng K 2019 Aerostatic bearings design and analysis with the application to precision engineering: State-of-the-art and future perspectives. *Tribology International*

[7] Li W, Zhou Z X, Huang X M, He Z J, Du Y 2014 Development of a High-Speed and Precision Micro-Spindle for Micro-Cutting. *International Journal of Precision Engineering and Manufacturing* **15** 2375-2383

[8] Müller C, Kirsch B, Aurich J C 2017 Compact Air Bearing Spindles for Desktop Sized Machine Tools. In: Wulfsberg J, Sanders A. (eds) Small Machine Tools for Small Workpieces. *Lecture Notes in Production Engineering* 21-34

[9] Powell J W 1970 The design of aerostatic bearings. The Machinery Publishing Co. Ltd

[10] Kieren-Ehses S, Bohley M, Mayer T, Kirsch B, Aurich J C 2020 Effect of high spindle speeds on micro end milling of commercially pure titanium. *Proceedings of the 20th euspen International Conference* 63-66

Optimal active damping of a wafer gripper in presence of multiple disturbances

Castor Verhoog[1], Marcin B. Kaczmarek[1], Maurits van den Hurk [2], S. Hassan Hossein-Nia[1]

[1]Department of Precision and Microsystems Engineering; Delft University of Technology, Mekelweg 2, 2628 CD Delft, The Netherlands
[2]VDL Enabling Technologies Group B.V., De Schakel 22, 5651 GH Eindhoven, The Netherlands

m.b.kaczmarek@tudelft.nl

Abstract

The vibrations of an end effector of a wafer handling system, moving wafers between the atmospheric and vacuum environments, can be excited during systems operation. Conventionally, to cope with this, the operations of a system are slowed down and dwell intervals are introduced so any undesired vibrations can settle. This requires significant time, since the damping levels in the system are low, because of the materials used. Vibration attenuation in thin structures, like the considered wafer gripper, can be improved with active means. Collocated piezoelectric patch sensors and actuators are attached to the gripper and the damping is increased using appropriate controllers. In the literature, such controllers are tuned with the aim of minimizing the transfer of vibrations from a selected disturbance source to a single measurement point or a modal response. This approach is not effective if multiple disturbance sources are present in the system. Especially, the influence of electronic noise is amplified as the gains of a controller are increased. In this paper, the effect of multiple disturbances on beam-like active vibration control systems is investigated using the dynamic error budgeting approach. The system dynamics are studied with a focus on disturbance propagation paths in open and closed loops. The performance of the system is represented by the cumulative power spectrum (CPS) of acceleration at the point of interest. The well-established Positive Position Feedback (PPF) is used as the controller, and a tuning method, based on the optimisation of the predicted CPS, is presented. The overall performance of the proposed and conventional tuning methods is compared, which highlights the trade-off between resonance peak reduction and noise amplification. The improvement over the conventional method is clear, with almost 75% smaller noise amplification and 13% decrease in the total CPS in the considered case.

Keywords: Active Vibration Control, Dynamic Error Budgeting, Positive Position Feedback, Piezoelectric Patch Transducers

1. Introduction

The demand for smaller and more potent chips is ever-growing, leading to higher requirements for all the systems involved in the semiconductor manufacturing process, which must be met while maintaining high productivity. The same applies to the wafer handling systems, moving the wafers in and out of the machines where the production steps happen. The main component of the wafer handling system is a robot arm with a gripper for manipulating the wafers, illustrated in Figure 1. It is a thin structure with beam-like prongs with wafer attachment points at the tips.

During the operation of the wafer handler, the vibration modes of the gripper may be excited. The vibrations of the base of the gripper are amplified at the resonance frequencies, leading to large accelerations at the tips of the prongs, which may result in mispositioning or damaging wafers. Stiffening the end-effector by using a ceramic material was not sufficient to alleviate the problem. To cope with the vibrations, the operations of a system are slowed down, and dwell intervals are introduced so any undesired vibrations can settle. However, this requires significant time, since the damping levels in the system are low, because of the materials used. In the previous investigation it has been shown that the damping of the gripper cannot be sufficiently increased by passive means like viscoelastic materials[1], tuned mass dampers[2] or shunted piezoelectric transducers[3].

Vibration attenuation in thin structures, like the considered wafer gripper, can be improved actively using piezoelectric patch transducers. When attached to a structure, the patch sensor output is related to the average beam curvature at its location, and the actuator produces a pair of moments with amplitudes proportional to the applied voltage[4]. While ample configurations are available in the literature, collocating sensors and actuators assures predictable dynamics[4] and facilitates robust stability of the system[5]. When the loop is closed, vibration attenuation can be improved with an appropriate controller. Low-order fixed-structure controllers are preferred rather than elaborate optimization-based schemes, which are sensitive to model inaccuracies. Especially well-established is Positive Position Feedback (PPF) control, in which signal
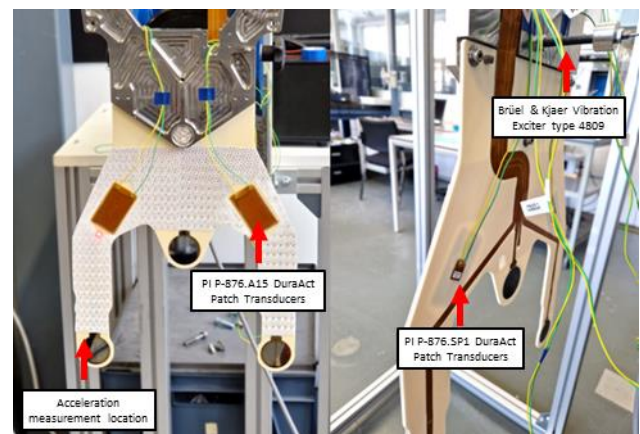
Figure 1. Experimental setup. The wafer gripper with piezoelectric transducers attached is suspended on elastic cords. The base of the gripper is connected to a shaker by a thin strut. Accelerations at the tips of grippers prongs are measured for performance validation.

measured by the patches, related to the generalized position, is fed back to the actuators via a second-order low-pass filter[6]. This provides a stronger vibration attenuation at the target frequency thanks to the presence of the resonance and smaller amplification of high-frequency noise thanks to the roll-off.

In the literature, PPF controllers are tuned with the aim of minimizing the transfer of vibrations from a selected disturbance source to a single measurement point or a modal response[7], [8]. This approach is not effective if multiple disturbance sources are present in the system. The use of more aggressive controllers, for example with a higher gain, leads not only to stronger attenuation of resonance peaks but also to amplification of noise entering the system via electronic components used for implementation. Consequently, the system does not work as intended.

In this paper, the effect of multiple disturbances on beam-like active vibration control systems is investigated using the dynamic error budgeting approach[9]. The performance of the system is represented by the cumulative power spectrum (CPS) of acceleration at the point of interest. The disturbances acting on the system, as well as the transfer functions relating them to the performance measurement, are studied. This information is used to design an optimal PPF controller in the frequency domain, using experimental data. The obtained performance is then compared with the conventionally tuned controllers.

The details of the studied problem are presented in section 2, section 3 presents the obtained results, and the paper is concluded in section 4.

2. System analysis

In this section, we clarify the studied problem. In 2.1 we introduce the plant, with the focus on all the considered input and output signals. In 2.2 we define the performance of the system using the dynamic error budgeting approach. Sections 2.3 and 2.4 introduce the disturbances and their propagation within the system. The controller design is studied in section 2.5.

2.1. Plant description

Figure 1 presents the experimental setup and the signals acting on it are shown in figure 2. The wafer gripper is suspended on flexible cords and attached to a shaker, applying the disturbances z_{in}, that represent the excitation of the system during operation. Two pairs of collocated piezoelectric patch sensors and actuators are attached to the gripper, so the low-frequency vibration modes can be influenced. The location selection for the piezo transducers was a subject of a previous study[10]. With appropriate amplifiers included, the measured and applied signals are denoted $V_{in,i}$, $V_{out,i}$ respectively. To check the performance, the accelerations $z_{out,i}$, are measured at the two tips of the fingers, where the wafer is attached. The complete system is represented by a transfer matrix with three input and four output signals

$$\begin{bmatrix} z_{out,1} \\ z_{out,2} \\ V_{out,1} \\ V_{out,2} \end{bmatrix} = \begin{bmatrix} P_{11} & P_{12} & P_{13} \\ P_{21} & P_{22} & P_{23} \\ P_{31} & P_{32} & P_{33} \\ P_{41} & P_{42} & P_{43} \end{bmatrix} \begin{bmatrix} z_{in} \\ V_{in,1} \\ V_{in,2} \end{bmatrix}.$$

2.2. Performance definition

The goal of the AVC system is to minimize the movement of tips of the prongs, in the presence of disturbances. Formally, this can be expressed using the Dynamic Error Budgeting (DEB)[9] approach. Due to systems symmetry, a single acceleration measurement $z_{out,1}$ is used for the controller design and the objective is then to minimize the variance of this signal. For all the calculations the signals are assumed to be stochastic and zero-mean. In such a case, the variance of a signal $x(t)$ is equal to its power

$$\sigma_x^2 = \bar{x}^2 = \int_{-\infty}^{\infty} x(t)^2 dt.$$

The power disruption of a signal over frequencies can be modelled using one-sided Power Spectral Density (PSD), denoted $S_x(f)$. The Cumulative Power Spectrum (CPS) shows how different frequencies contribute to the total power of the signal and is defined by

$$C_x(f_0) = \int_0^{f_0} S_x(f)df,$$

with $\lim_{f_0 \to \infty} C_x(f_0) = \sigma_x^2$. The CPS is useful for visualising the biggest contributions to the error, that should get the designers attention. The influence of different disturbance sources on the total PSD can be calculated as

$$S_{z_{out}}(f) = \sum_{j=1}^{n} S_j(f) T_j(f)^2,$$

where S_j represents the PSD of the jth disturbance signal and T_j denotes the transfer function form that source to the performance signal z_{out}, presented in equation (TFS). If the disturbances due to sensors and amplifiers are negligible, the simplification $S_{z_{out}}(f) \approx S_{z_{in}}(f) T_{z_{in}}(f)^2$ can be used. Then, for a given $S_{z_{in}}(f)$ it is sufficient to minimize $T_{z_{in}}(f)$. While this assumption supports the use of H_2 or H_∞ tuning methods for AVC controllers, it is often not satisfied in practice.

2.3. Disturbance signals

The disturbance z_{in} acting on the base of the gripper is created by the shaker. In this paper, a signal consisting of ten 20ms impulses with 3s pauses between them is considered. The disturbances due to the piezo actuator amplifier $n_{u,1/2}$ were neglected, since their contribution was expected to be small. The noise sources acting on the measurements of the piezoelectric patch sensors $n_{v,1/2}$ were assumed to be equal. This is explained by the fact that both measurements were filtered by charge amplifiers implemented using the same integrated circuit and the same power supply. Assuming uncorrelated noise sources in this case would lead to significant overestimation of the total CPS. PSD of z_{in} and n_v are presented in Figure 3.
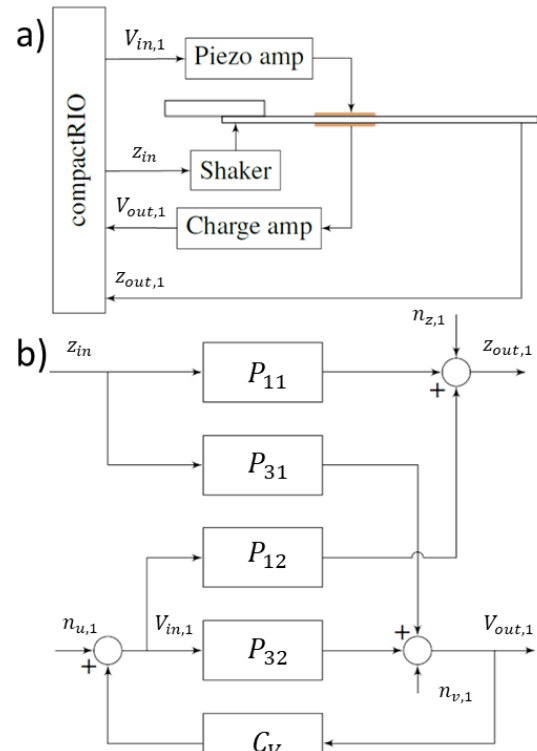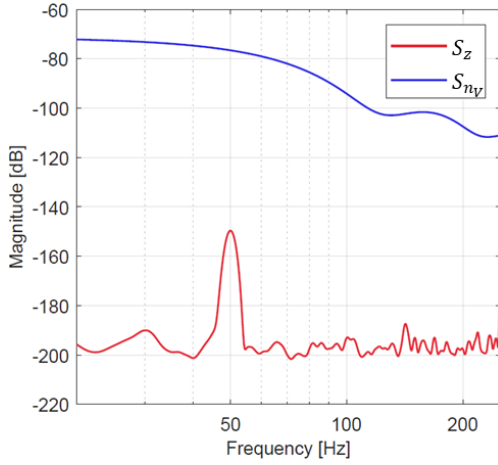

Figure 2. a) Schematic representation of the experimental setup, b) Overview of signals in a single prong of the gripper in closed loop.

Figure 3. Power spectral densities of the base excitation z_{in} (blue) and the actuator noise n_V (red).

2.4. Disturbance propagation

First, for clarity, the propagation of signals in the wafer gripper will be presented only for a single prong, which is justified by systems symmetry. Figure 2.b presents the closed-loop active vibration control system for a single prong, with the disturbance signals included, where n_u is the noise introduced by the piezo amplifier and n_z, n_v denote the measurement noise of the accelerometer and the piezoelectric transducer respectively. The propagation of the signals through the simplified system is described by transfer functions

$$T_{z,1} = \frac{z_{out,1}}{z_{in}} = P_{11} + P_{31}\frac{C_V}{1 - C_V P_{32}}P_{12},$$

$$T_{n_u,1} = \frac{z_{out,1}}{n_{u,1}} = P_{12}\frac{1}{1 - C_V P_{32}},$$

$$T_{n_V,1} = \frac{z_{out,1}}{n_{V,1}} = P_{12}\frac{C_V}{1 - C_V P_{32}},$$

$$T_{n_Z,1} = \frac{z_{out,1}}{n_{Z,1}} = 1.$$

In reality, there is a strong coupling between the halves of the gripper which cannot be ignored in final systems analysis. To represent it, the closed loop transfer function is calculated as

$$P_{cl} = C(I + PC)^{-1},$$

with $C_{2,3} = C_{3,4} = C_V$ and all other components of C equal to 0. Note, that the same controller is applied for both piezoelectric sensor-actuator pairs, which is justified by systems symmetry. Considering all the transducers, the transfer function from the base disturbance to acceleration at the tip of the first prong is

$$T_{z,1} = \frac{N_z}{D_z},$$

$$\begin{aligned}N_z = \ &P_{11} + C_V(P_{11}P_{32} - P_{12}P_{32} + P_{11}P_{43} - P_{13}P_{41}) \\ &+ C_V^2(P_{11}P_{32}P_{43} - P_{11}P_{33}P_{42} - P_{12}P_{31}P_{43} \\ &+ P_{12}P_{33}P_{41} + P_{13}P_{31}P_{42} - P_{13}P_{32}P_{41}),\end{aligned}$$

$$D_z = C_V^2(P_{32}P_{43} - P_{33}P_{42}) + C_V(P_{32} + P_{43}) + 1.$$

Using the assumption that sensor noise acting on both piezo patch sensors is equal, the noise contribution to the acceleration on the tip of the first prong depends on the transfer function

$$T_{nV,1} = T_{n_V,1} + T_{n_V,2} = C_V P_{cl,12} + C_V P_{cl,13} = \frac{N_{n_V}}{D_{n_V}},$$

$$N_{n_V} = C_V^2(P_{13}P_{42} - P_{12}P_{33} - P_{13}P_{32} - P_{12}P_{43}) + C_V(P_{12} + P_{13}),$$

$$D_{n_V} = C_V^2(P_{32}P_{43} - P_{33}P_{42}) + C_V(P_{32} + P_{43}) + 1.$$

The transfer function from $n_{u,1/2}$ is not shown for the full system as these contributions are neglected. As a result, we have for the total PSD of the AVC system

$$S_z(f) \approx S_z T_{z,1}^2 + S_{n_V} T_{n_V,1}^2 + S_{n,z}.$$

Since $S_{n,z}$ is not influenced by control, the optimal controller can be found by minimizing

$$S_C(f) = S_z T_{z,1}^2 + S_{n_V} T_{n_V,1}^2 \propto S_z(f).$$

2.5. Controllers

In this section, the controller designs used in the study are presented. Positive position feedback (PPF) controllers

$$C_V = \frac{g}{s^2/\omega_c^2 + 2\zeta_c s/\omega_c + 1},$$

are considered, with ω_c denoting the resonance frequency, ζ_c the damping ration and g the gain of the controller. As explained earlier, due to systems symmetry, the same values of ω_c and ζ_c are applied for both transducer pairs in each considered case. The stability of a system with a PPF controller is determined from a condition on the steady-state loop gain

$$C_{V,1}(0)P_{32}(0) < 1, \quad C_{V,1}(0)P_{43}(0) < 1.$$

To satisfy this condition with a sufficient margin, the gains $g_1 = kP_{32}^{-1}(0), g_2 = kP_{43}^{-1}(0)$ with $P_{32}(0) \approx P_{43}(0)$ and $k = 0.7$ are selected for each of the considered cases. The remaining parameters of the controllers are selected using three methods:

1. Analytical solution minimizing the H_2 norm of the transfer function $T_{z,1}$ [7]
2. Analytical solution minimizing the H_∞ norm of the transfer function $T_{z,1}$ [7]
3. Minimizing the $S_C(f)$, which corresponds to minimal $S_z(f)$.

3. Results

The transfer functions of controllers designed in the three considered cases are show in figure 4.a. The controller designed for minimizing the $S_z(f)$ is characterized by significantly higher damping and lower resonance peak than the two others. This corresponds to less aggressive attenuation of the resonance peaks of $T_{z,1}$, visible in figure 4.b, where the closed loop transfer functions are shown.

Figure 5 compares the cumulative power spectra obtained in absence of control and in all the considered closed-loop scenarios. In all the cases, the predicted values of the CPS underestimate the measured value but are sufficiently close for designing the controllers. From the open-loop plot it is clear that the second resonance mode at 78 Hz has the strongest influence on the systems performance and is therefore the target for the active damping controllers. A strong reduction of the CPS was achieved in all the considered closed-loop cases. For the analytically derived H_2 and H_∞ controllers' aggressive reduction of the resonance peak corresponds to a large decrease of the contribution from the base vibration. However, the overall performance is deteriorated by the influence of amplified noise, highest at the frequency of 50 Hz. When the controller is designed for $S_z(f)$, improved reduction of total CPS is possible, despite less radical attenuation of the resonance peaks. While the contribution due to the base excitation remains stronger than for H_2/H_∞ optimized controllers, the noise in the system is amplified to a lesser extent. For the proposed controller, the contribution due to the noise is nearly 75% smaller than in the H_2 case, which leads to 13% decrease in the total CPS.

While the obtained results are promising, the issue of optimal active damping of the wafer gripper requires further studies. The measured transfer functions, crucial for the tuning of the controllers, depend strongly on the boundary conditions of the gripper. Additionally, the final optimization results depend on the disturbance present in the systems. For these reasons, experiments in operational conditions of the device are necessary to fully validate the usability of the proposed design. Additionally, the large differences in the noise amplification between the analytical H_2/H_∞ controllers and the optimization-based one cannot be intuitively explained by the differences in the final controllers presented in Figure 4.a, which requires further investigation. To further reduce the noise contribution at 50 Hz additional passive and active filters can be used. The
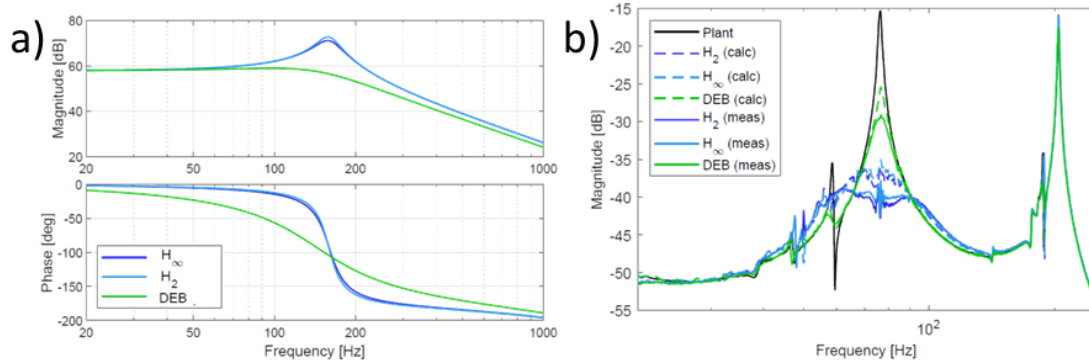
Figure 4. a) Bode plots of controllers designed using the analytical H_2 and H_∞ design approaches and with the DEB method. b) Calculated and measured closed-loop transfer functions from the base excitation z_{in} to tip acceleration $z_{out,1}$.
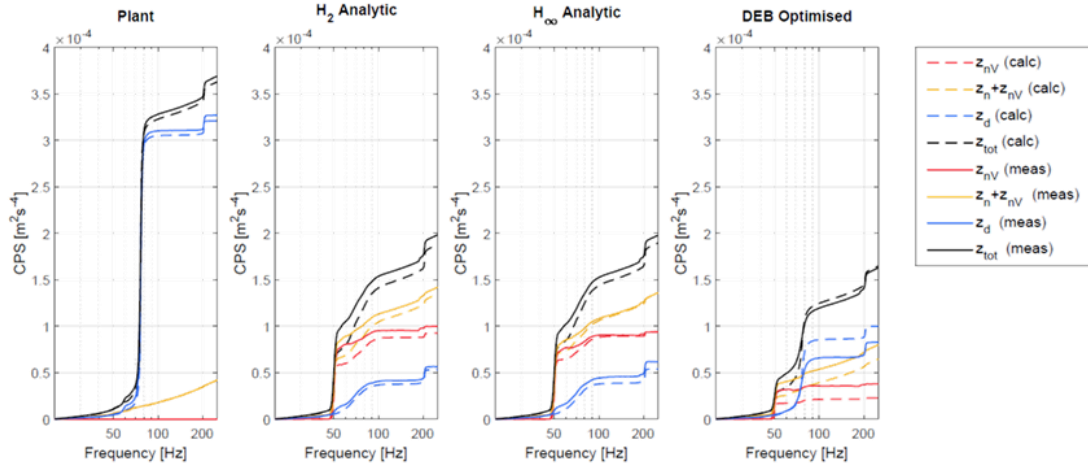
Figure 5. Cumulative power spectra of the tip acceleration $z_{out,1}$ in open and closed loop with different considered controllers.

obtained results suggest that even simple measures like use of notch filters could be sufficient for to achieve strong performance improvements.

4. Conclusion

In this paper, the effect of multiple disturbances on an active vibration control system for a wafer gripper was investigated using the dynamic error budgeting approach. The system dynamics were studied with a focus on disturbance propagation paths. The performance of the system was represented by the cumulative power spectrum (CPS) of acceleration at the point of interest. A tuning method for a PPF controller, based on the optimisation of the predicted CPS, was applied. A clear improvement over conventional tuning method was achieved, with almost 75% smaller noise amplification and 13% decrease in the total CPS in the considered case.

This paper demonstrates how both the structure excitations and electronic noise determine the performance of an AVC system. This means one must not only look at a transfer function from the excitation to performance measurement, but also the propagation paths and frequency domain characteristics of all the expected excitation and disturbances to design an effective AVC system. The best overall performance of the system can be achieved by balancing the resonance peak attenuation and noise amplification. As a continuation of this research, further studies on the disturbance sources and propagation in distributed AVC systems should be conducted. To facilitate the practical use, more intuitive design methods sufficient for an initial design of a well performing controller will be developed. Moreover, the applicability of the proposed method will be validated in the operational conditions of the device.

References

[1] D. I. G. Jones, *Handbook of viscoelastic vibration damping*. Wiley, 2001.

[2] H. C. Tsai and G. C. Lin, "Explicit formulae for optimum absorber parameters for force-excited and viscously damped systems," *J. Sound Vib.*, vol. 176, no. 5, pp. 585–596, Oct. 1994, doi: 10.1006/jsvi.1994.1400.

[3] J. A. B. Gripp and D. A. Rade, "Vibration and noise control using shunted piezoelectric transducers: A review," *Mechanical Systems and Signal Processing*, vol. 112. Academic Press, pp. 359–383, Nov. 01, 2018, doi: https://doi.org/10.1016/j.ymssp.2018.04.041.

[4] A. Preumont, *Vibration Control of Active Structures*, 4th ed., vol. 246. Cham: Springer International Publishing, 2018.

[5] I. R. Petersen, "Negative imaginary systems theory and applications," *Annu. Rev. Control*, vol. 42, pp. 309–318, Jan. 2016, doi: 10.1016/j.arcontrol.2016.09.006.

[6] J. L. Fanson and T. K. Caughey, "Positive position feedback control for large space structures," *AIAA J.*, vol. 28, no. 4, pp. 717–724, May 1990, doi: 10.2514/3.10451.

[7] B. Seinhorst, M. Nijenhuis, and W. B. J. Hakvoort, "Gain margin Constrained H2 and H∞ Optimal Positive Position Feedback Control for piezoelectric vibration suppression," in preparation.

[8] S. M. Kim, S. Wang, and M. J. Brennan, "Comparison of negative and positive position feedback control of a flexible structure," *Smart Mater. Struct.*, vol. 20, no. 1, Jan. 2011, doi: 10.1088/0964-1726/20/1/015011.

[9] W. Monkhorst, "Dynamic Error Budgeting: A design approach." 2004, Accessed: Jun. 29, 2023.

[10] M. El Ajjaj, M. B. Kaczmarek, M. A. C. . van den Hurk, and S. H. HosseinNia, "Vibration suppression of a state-of-the-art wafer gripper," 2022, [Online].

Robust system performance analysis for viscoelastic damper materials

Martin Glück[1], Ulrich Schönhoff [1]

[1]Carl Zeiss SMT GmbH, Oberkochen, Baden-Württemberg, Germany

martin.glueck@zeiss.com

Abstract

High precision positioning of mechatronic components in industrial applications requires a robust system design. Resonances within mechanical structures affect the stability of position control loops. To achieve high positioning bandwidth, passive damping strategies such as relative or tuned-mass dampers are used. Passive dampers are often made of viscoelastic materials such as elastomers, which are sensitive to temperature and vary in manufacturing tolerances. Due to the large uncertainties of viscoelastic materials system performance needs to be guaranteed for all possible configurations. In this contribution we present the use of the μ-analysis for viscoelastic materials to evaluate robust system performance for geometrical, material and temperature tolerances.

The system performance can be evaluated by analyzing the sensitivity function of the closed loop system within the μ-analysis. The used dynamic model is based on a finite element model, where viscoelastic damper models are added by a feedback loop. Tolerances such as variations in Young's modulus are also represented by a feedback loop, typical structure for the μ-analysis. The frequency dependent Young's modulus of viscoelastic materials is approximated by a linear transfer function based on a dynamic mechanical analysis. For elastomers the Young's modulus mainly varies in amplitude and shifts in frequency due to temperature. There is a direct relation between temperature change and frequency shift of the Young's modulus. Considering the temperature change instead of a stiffness change reduces conservatism in the performance analysis. For example, using several elastomers and considering only stiffness variations leads to the possibility that one elastomer sees an increase and the other a decrease in stiffness as a worst-case scenario, a non-physical behavior. μ-analysis with reduced conservatism improves design costs of mechatronic components and gives a robustness guarantee instead of a time-consuming Monte-Carlo simulation.

Robust control, Viscoelastic material, μ-Analysis

1. Introduction

Neglected component tolerances in system design of high precision mechatronic systems can lead to system performance losses during qualification of series production. Consequently, significant costs occur for solving the out of specification situation. Therefore, a robust design of mechatronic systems is necessary, where the tolerance effects on system performance are investigated. For example in high precision positioning systems passive dampers are used to prevent instabilities of the control loop due to undamped structural dynamics. These dampers are often made of viscoelastic materials, which are strongly sensitive to temperature and the manufacturing process such as geometry and the material properties. Occasionally, a Monte-Carlo simulation is used for investigating the system performance with tolerances. However, in high precision mechatronic systems there are several tolerances, where you cannot guarantee a robust performance within a Monte-Carlo simulation in finite time due to the large number of combinations. For that reason, we use the μ-analysis [1], an optimization-based approach to investigate robust performance of a controlled system. This approach can guarantee robustness for a large number of tolerances. For that reason, we present in this paper the use of the μ-analysis for large mechanical structures with viscoelastic damper materials. The temperature, geometrical and material tolerances are considered within the μ-analysis.

The paper is organized as follows: First, we show a structural dynamic model generation out of a finite element solver. Then, we describe how to add viscoelastic damping to that model. A dynamic model for the Young's modulus is derived in the time domain, where a description of the temperature, geometrical and material tolerances is included. Based on the parametric model an overall state-space model is presented for the use in the μ-analysis. Then, conditions for robust performance based on the μ-analysis are defined. Finally, the approach is applied to a three mass-spring example.

2. Viscoelastic damper modeling

Due to the small movements in high precision position control the mechanics can be described by the linear elasticity theory. The corresponding analytical partial differential equations are approximated by the finite element method (FEM). In order to analyze the dynamic behavior of the viscoelastic dampers, we extract a state space description from the FE solvers such as *MSC Nastran* or *Ansys*. Because of the large number of degree of freedoms (DOF) only the information of the modal analysis is used. To also consider viscous dampers, the normalization of the eigenvectors needs to be considered. In a FE-solver the modal analysis is performed by the created model based on the mass M, stiffness K and viscous damping D matricesThe equations of motion can be represented by [2]

$$\underbrace{\begin{bmatrix} D & M \\ M & 0 \end{bmatrix}}_{\tilde{M}} \begin{bmatrix} \dot{x}_{\text{FE}} \\ \ddot{x}_{\text{FE}} \end{bmatrix} + \underbrace{\begin{bmatrix} K & 0 \\ 0 & -M \end{bmatrix}}_{\tilde{K}} \underbrace{\begin{bmatrix} x_{\text{FE}} \\ \dot{x}_{\text{FE}} \end{bmatrix}}_{z_{\text{FE}}} = \underbrace{\begin{bmatrix} f_{\text{FE}} \\ 0 \end{bmatrix}}_{f}, \qquad (1)$$

where x_{FE} is the displacement and f the force at each node in all considered DOFs. The ordinary differential equations can be transformed into modal space by $z_{FE} = Qq_{FE}$, where Q contains the eigenvectors of eq. (1). Due to symmetry eigenvectors are normalized to $Q^T \tilde{M} Q = I$, where I corresponds to the unity matrix. Considering this normalization in the modal analysis of the FE-solver a state space in modal representation can be generated based on calculated eigenvectors within the FE-solver

$$\Sigma_{FE}: \dot{q}_{FE} = -\underbrace{Q^T \tilde{K} Q}_{\Lambda} q_{FE} + Q^T f$$
$$z_{FE} = Qq_{FE}, \tag{2}$$

where q_{FE} denotes the state in modal coordinates. Due to the frequency-dependent Young's modulus of viscoelastic materials the damping behavior cannot be considered in the modal analysis. However, the damping can be added by a dynamical model in a feedback loop afterwards, which is mechanically comparable to a parallel frequency-dependent spring. For that reason, the in- and outputs (IOs) of the Σ_{FE} state space are modified by only selecting the IOs with respect to the viscoelastic dampers and to the position control

$$\begin{bmatrix} x_M \\ x_{VE} \end{bmatrix} = \begin{bmatrix} C_M \\ C_{VE} \end{bmatrix} z_{FE}$$
$$f = \begin{bmatrix} B_A & B_{VE} \end{bmatrix} \begin{bmatrix} f_A \\ f_{VE} \end{bmatrix}, \tag{3}$$

where C_M, C_{VE} selects the displacements and F_A, F_{viscIO} the forces for the position control and the viscoelastic damper element nodes, respectively. The FE model already contains the stiffness of the viscoelastic damper. Therefore, only the stiffness change over frequency is described by an additional force to the FE model

$$\mathbf{f}_{VE}(s) = \left(\frac{\mathbf{e}(s)}{\mathbf{e}(0)} - 1 \right) K_{VE} \mathbf{x}_{VE}(s), \tag{4}$$

where s represents the variable of the Laplace transformation, bold letters correspond to the laplace transformed variable and K_{VE} is the stiffness matrix of the viscoelastic damper. The viscoelastic material behavior is described by a frequency-dependent Young's modulus e. Based on the introduced equations an overall state space Σ_{VE} can be derived

$$\Sigma_{VE}: \dot{q}_{FE} = -(\Lambda + Q^T B_{VE} K_{VE} C_{VE} Q) q_{FE}$$
$$+ Q^T B_A f_A + \frac{1}{\mathbf{e}(0)} Q^T B_{VE} f_e$$
$$x_M = C_M Q q_{FE}$$
$$x_e = K_{VE} C_{VE} Q \, q_{FE}. \tag{5}$$

in Figure 1 the feedback loop with respect to the Young's modulus is represented.
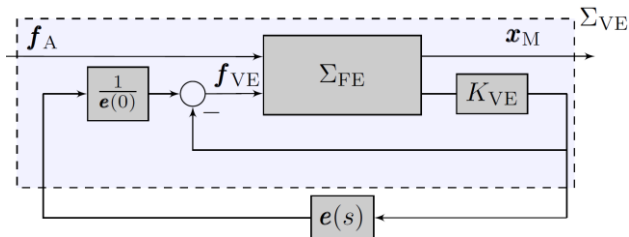
Figure 1. Considering viscoelastic materials in dynamic models by a feedback of a frequency-dependent Young's modulus.

The dynamic behavior of the Young's modulus of the viscoelastic material is often determined by a FRF measurement, also known as the dynamic mechanical analysis (DMA). In order to analyze the impact on the position control, a dynamic model is fitted into the measurement data. The number of poles and zeros of the

transfer functions are chosen to be equal, to obtain a proper transfer function. Here, the fitting can also be interpreted as a parameter estimation of the generalized Maxwell model [3], a physical model. Then, the frequency-dependent Young's modulus is described by

$$\mathbf{e}(s) = g \prod_{i=0}^{n-1} \frac{(s+z_i)}{(s+p_i)}, \tag{6}$$

where p_i and z_i describe the poles and zeros, and g a scaling factor. Moreover, the Young's modulus of viscoelastic materials significantly depends on temperature T, which can be modeled by frequency scaling of the dynamic Young's modulus. For viscoelastic material the Williams-Landel Ferry model is a state of the art approach for shifting frequencies of the Young's modulus [4]

$$\mathbf{e}_T(j\omega, T) = \mathbf{e}(ja(T)\omega)$$
$$\log_{10}(a) = -\frac{c_1(T-T_0)}{c_2+(T-T_0)}, \tag{7}$$

where a_T is the frequency scaling factor, c_1, c_2 are viscoelastic material parameters, T_0 is the reference temperature of the measured Young's modulus FRF and j is the complex number. In order to study the temperature-dependent control performance, we need a dynamic model, that represents the frequency shift as in eq. (7). A frequency shift can be realized by scaling the poles and zeros of the Young's modulus in eq. (6). For the μ-analysis the Young's modulus is described in a modal state space representation

$$\dot{q}_e = \underbrace{\begin{bmatrix} -p_1 & 0 & \dots & \dots & 0 \\ 0 & -p_2 & 0 & \dots & 0 \\ \vdots & \ddots & \ddots & \ddots & \vdots \\ \vdots & & \ddots & \ddots & 0 \\ 0 & \dots & \dots & 0 & -p_{n-1} \end{bmatrix}}_{A_e} q_e + \underbrace{\begin{bmatrix} 1 \\ \vdots \\ \vdots \\ \vdots \\ 1 \end{bmatrix}}_{b_e} x_e$$
$$f_e = -g \underbrace{\begin{bmatrix} r_0 & \dots & r_{n-1} \end{bmatrix}}_{r_e^T} q_e + g x_e, \tag{8}$$

where r_e describes the residual based on the zeros and poles of the transfer function. Now, the system matrix and the residuals are scaled to

$$\dot{q}_e = a(T) A_e q_e + b_e x_e$$
$$f_e = -a(T) g r_e^T q_e + g x_e. \tag{9}$$

2.1. Uncertainty modeling

In this paper the robust system performance of a position controlled system is analyzed by the μ-analysis. In order to use the corresponding framework, uncertainties are represented in a feedback structure as depicted in Figure 2. The mechanical system from actuator forces to position measurements, also called plant, are combined with two feedback loops for the position controller and the uncertainties. The Δ block represents the tolerances of the viscoelastic material, where we consider structured uncertainties, diagonal blocks for each tolerance scaled to $-1 \dots 1$. Plant and Controller combined to the nominal system Σ_N.
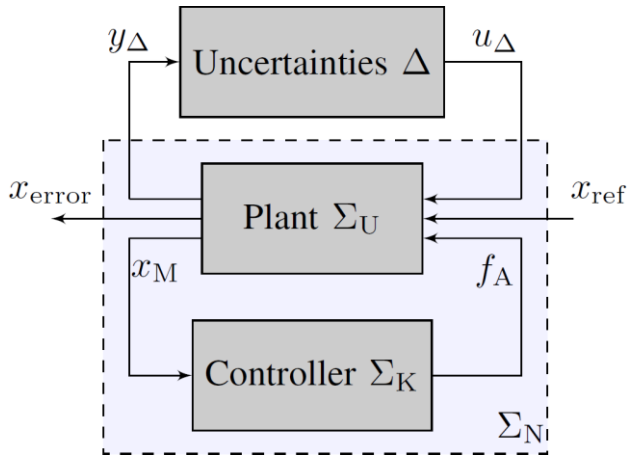
Figure 2. Generalized plant representation of the mechatronic system for the µ-analysis framework.

The uncertain parameters of the viscoelastic Young's modulus need to be described in a relative representation to receive a uncertainty between -1 and 1. For the temperature we can derive the interval of the shift factor by

$$
\begin{aligned}
a_\Delta &= a_0(1 + \Delta_T a_r), \; \Delta_T = -1\ldots1 \\
a_0 &= \frac{a(T_{max}) + a(T_{min})}{2} \\
a_r &= \frac{a(T_{max}) - a(T_{min})}{a(T_{max}) + a(T_{min})},
\end{aligned}
\tag{10}
$$

where a_0 corresponds to the mean value of the interval, a_r scales uncertainty feedback to -1...1 and T_{min}, T_{max} are the minimum and maximum temperature of the tolerances. The geometrical and material uncertainties are considered in the gain factor of the Young's modulus

$$
g_\Delta = g_0\big(1 + \Delta_g g_r\big),
\tag{11}
$$

where g_0 corresponds to the center of the interval and g_r the relative change of the scaling factor. Based on the relative representation the state space of the Young's modulus can be formulated in a structure, where the introduced uncertainties are described within a feedback loop

$$
\begin{aligned}
\dot{q}_e &= a_0 A_e q_e + b_e x_e + [I \quad 0]u_T \\
f_e &= -a_0 g_0 r_e^T q_e + g_0 x_e + [0 \quad g_0 I]u_T + g_r u_g \\
y_T &= \begin{bmatrix} a_r a_0 A_e \\ -a_0 r_e^T \end{bmatrix} q_e \\
u_T &= \Delta_T y_T \\
y_g &= -a_0 g_0 r_e^T q_e + g_0 x_e + [0 \quad g_0 I]u_T \\
u_g &= \Delta_g y_g.
\end{aligned}
\tag{12}
$$

Combining eq. (3) and eq. (6) results in an overall state space of the mechatronic system with uncertainties Σ_U, which can be used for the µ-analysis. The nominal model is based on the closed-loop system without uncertainties. A typical position controller in mechantronic system is based on a proportional-integral-derivative (PID) controller $c(s)$. The feedback law is defined by

$$
f_A(s) = c(s)x_{error}(s) = c(s) \underbrace{\big(x_M(s) - x_{ref}(s)\big)}_{x_{error}(s)},
\tag{13}
$$

x_{ref} defines the position reference. A parallel PID structure is used and for the derivative part a pole is added to not amplify high frequency flexible modes, which can lead to instabilities. Then, we obaint the following controller transfer function

$$
c(s) = \frac{f_A(s)}{x_{error}(s)} = k_P + k_I \frac{1}{s} + k_D s \frac{1}{1 + \tau_d s},
\tag{14}
$$

where k_P, k_I and k_D are the controller gains and τ_d the roll-off time constant for the derivative part. In order to combine the controller in a state space model, the transfer function is reformulated in the time domain by

$$
\Sigma_K: \begin{bmatrix} \dot{z}_1 \\ \dot{z}_2 \end{bmatrix} = \begin{bmatrix} 0 & 0 \\ -\frac{k_P}{\tau_d^2} & -\frac{1}{\tau_d} \end{bmatrix} \begin{bmatrix} z_1 \\ z_2 \end{bmatrix} + \begin{bmatrix} 1 \\ -\left(\frac{k_P}{\tau_d} + \frac{k_D}{\tau_d^2}\right) \end{bmatrix} x_{error}
$$
$$
f_A = \begin{bmatrix} \left(k_I + \frac{k_P}{\tau_d}\right) & 1 \end{bmatrix} \begin{bmatrix} z_1 \\ z_2 \end{bmatrix} + \left(k_P + \frac{k_D}{\tau_d}\right) x_{error}.
\tag{15}
$$

From eq. (12), eq. (13) and eq. (15) we obtain an overall state space for our nominal model Σ_N with in- and outputs for the uncertainties.

2.2. Robustness analysis

For analyzing the robust performance, we use the µ-analysis, a frequency domain approach. Therefore, from the Σ_N state space a transfer function $N(s) = C_N(sI - A)^{-1}B_N + D_N$ is determined. The transfer matrix can be divided into the following representation

$$
\begin{bmatrix} y_\Delta \\ x_{error} \end{bmatrix} = \begin{bmatrix} N_{11}(s) & N_{11}(s) \\ N_{21}(s) & N_{22}(s) \end{bmatrix} \begin{bmatrix} u_\Delta \\ x_{ref} \end{bmatrix},
\tag{16}
$$

where y_Δ, u_Δ are the in- and outputs for the uncertainties. For studying the robust performance, the output sensitivity is used, the transfer from reference to servo error signal, a quantity for the distance from open-loop function to the critical point of the Nyquist stability criterion. The structured singular value, also known as μ is defined by

$$
\mu(M) = \frac{1}{\inf\{\sigma_{max}(\Delta) \mid \det(I - M\Delta) = 0\}},
\tag{17}
$$

where σ_{max} denotes the maximum singular value of the block matrix Δ. If the nominal system is stable and $\mu(N_{11}) < 1$, the system is robust stable. Performance criteria can be considered by uncertainties as well. To fulfill feedback values < 1, the corresponding sensitivity outputs need to be scaled. As a performance criterion we claim a maximum output sensitivity S_{max} Therefore, we get a scaling factor $W_o = \frac{1}{S_{max}}$. For the µ-analysis a new transfer matrix is defined by

$$
O(s) = \begin{bmatrix} N_{11}(s) & N_{11}(s) \\ N_{21}(s) & W_o N_{22}(s) \end{bmatrix}
\tag{18}
$$

Robust performance is achieved, if $\mu(O) < 1$.

3. Example

The robustness analysis of viscoelastic materials for temperature, geometrical and material tolerances is applied for a three mass-spring system to illustrate the method. In Figure 3 the spring-mass system is depicted. A mass m is controlled by a actuator with a clearly smaller mass m_A and stiffness k_A. Then, the corresponding resonance frequency can be approximated by $\omega_A^2 = \frac{k_A}{m_A}$. The resonance frequency is significantly higher than the cross-over frequency of the control loop, but it causes instabilities without damping.
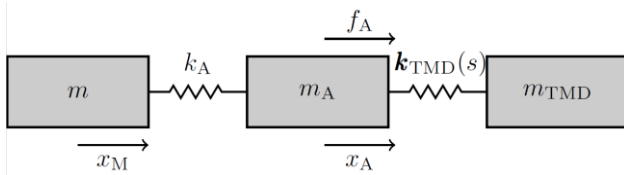
Figure 3. Depiction of a three mass-spring system example to analyze robust performance with viscoelastic materials.

For that reason, the actuator is damped by a tuned-mass-damper (TMD), which is modeled by a mass m_{TMD} and a frequency dependent stiffness $\mathbf{k}_{TMD}(s)$. The TMD mass is also by a factor ten smaller and the stiffness is designed in a way that the actuator resonance is sufficient damped. The viscoelastic damping effect is modeled by the frequency dependent Young's modulus. The corresponding stiffness and mass matrix of the example is described in the representation from eq. (1), where the frequency-dependent stiffness $\mathbf{k}_{TMD}$ is chosen at 0 Hz. Moreover, the used normalized Young's modulus for the frequency dependency is depicted in Figure 4. A transfer function with three poles and zero is fitted into a data set of an elastomer by the least square approach.
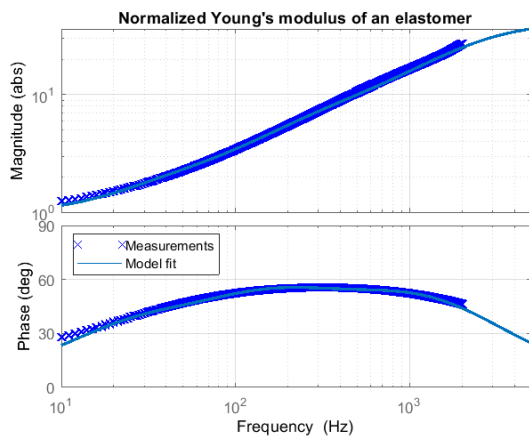
Figure 4. Comparison of the measured Young's modulus of an elastomer and the fitted transfer function. There is a significant deviation between 1 Hz and 10 Hz due to the limited number of poles and zeros to three. In our example the interesting damping frequency is larger 100 Hz.

The position controller is tuned for a cross-over frequency of 160 Hz. For the geometrical and material tolerances we assume 20 % deviation at the maximum. Moreover, two temperature intervals for a robust (22 °C … 27 °C) and non-robust case (22 °C ... 37 °C) are considered. The calculated μ-values over frequency are depicted in Figure 5. For the robust case the μ-value is clearly smaller than one. Worst case parameters are at 20 % for geometrical and material deviations and at 27 °C. For an interval 22 °C … 37 °C the robust performance is violated around the resonance frequency of the actuator, μ-values clearly larger 1. The worst-case parameters are at -20% geometrical and material deviations, and at 37 °C. As a result, the stiffness for the TMD is as weak as possible for the non-robust case. In Figure 6 impact on output sensitivities are depicted of the nominal, non-robust and robust case.

4. Summary

In this paper a method is shown to analyze robust performance of mechatronic systems with viscoelastic damper materials. A
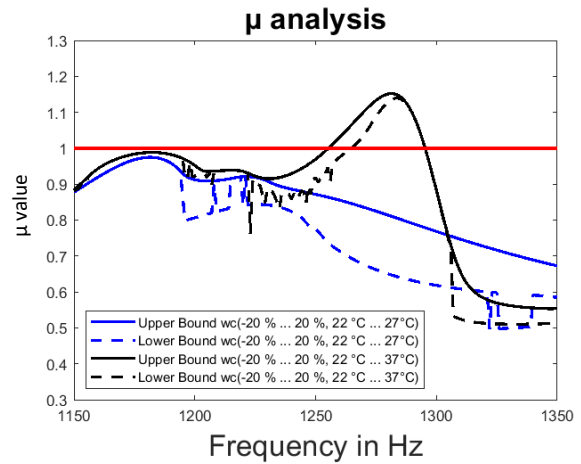
Figure 5. Example results of the μ-analysis for a non-robust and robust performance. An interval of the μ value based on lower and upper bound are given due to complex calculation of μ. Increasing the temperature tolerances leads to a performance violation.
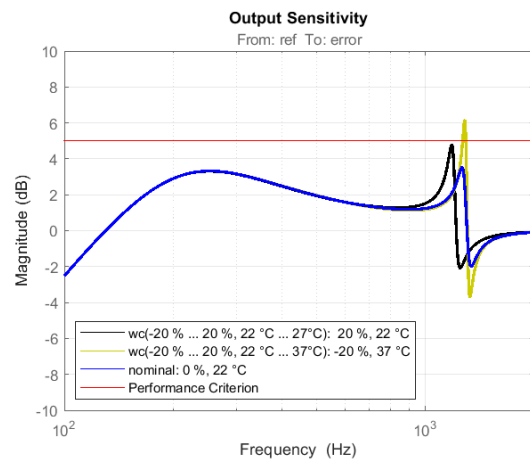
Figure 6. Representation of the 5 dB robust performance criterion, the output sensitivity with worst case parameters, for the nominal, robust and non robust case.

dynamic model is fitted into measured frequency response functions of the Young's modulus. The dynamics model can be adapted to different temperatures and geometrical and material tolerances. In order to study the impact on position control of mechatronic system, the robustness can be investigated by the μ-analysis. The presented method allows an analysis of large FE models with viscoelastic damping materials. This cannot be considered in the FE-solvers by default. Moreover, temperature effects can be covered within the robustness analysis by taking in account of the frequency-dependent effect of the Young's modulus. Based on that conservatism can be taken out from the μ-analysis by using temperature tolerances instead of pure stiffness variation.

References

[1] John Doyle, "Analysis of feedback systems with structured uncertainties," IEE Proceedings, Part D, vol. 129, no. 6, pp. 242-250,1982

[2] Craig Jr, Roy R., and Andrew J. Kurdila. Fundamentals of structural dynamics. John Wiley & Sons, 2006

[3] I.R.C. Koeller, "Applications of fractional calculus to the theory of viscoelasticity," Journal of Applied Mechanics 51 299–307, 1984

[4] John D. Ferry and Henry S. Myers,"Viscoelastic Properties of Polymers ,"J. Electrochem. Soc. 108 142C, 1961

[5] Skogestad, Sigurd, and Ian Postlethwaite. Multivariable feedback control: analysis and design. john Wiley & sons, 2005.

Response of a numerically controlled machine-tool to the modification of its position feedback using real-time solution

Flore Guevel [1], Charly Euzenat [1], Fabien Viprey [1], Guillaume Fromentin [1]

[1]*Arts et Métiers Institute of Technology, LaBoMaP, Université Bourgogne Franche-Comté, HESAM Université, Rue Porte de Paris, Cluny 71250, France*

flore.guevel@ensam.eu

Abstract

The dimensional accuracy of machined parts can be influenced by numerous factors, among which inaccuracies in the machine's structural loop and thermal expansion of components have the biggest impact. Hence, highly accurate machining requires effective error compensation. This motivates the development of a real-time compensation system implemented on a five-axis machine tool. In this study, a physical monitoring device is installed in the feedback loops of the machine's axial position control circuit, to intercept and modify linear encoder signals. It communicates with a custom software application that processes the data and generates corrected signals according to geometric model based on the rigid body assumption. The numerical controller (NC) is then induced to perform volumetric error correction based on its default programming. The key advantage of this software-based compensation strategy over the use of look-up tables or NC program modification is the total independence from the NC. The same real-time program is also used for the characterization of linear axis controls. This article outlines the behaviour of an NC machine when an axis displacement is generated via the modification of measuring systems feedback. The rate of change of the virtually added movement appears to be more of a limiting factor to the controller than the magnitude. Moreover, virtual displacements can be injected with discontinuous velocity profiles, resulting in unbounded acceleration and jerk.

Machining – Compensation– Positioning – Monitoring

1. Introduction

In machine-tools, many sources of errors, including geometric, thermal, loading, and servo errors may contribute to the inaccuracies during manufacturing processes. Quasi-static errors, such as link and motion errors, are highly responsible for the contouring error [1]. If they cannot be avoided during machine design, or mechanically corrected, the so-called volumetric error can be modelled by applying the rigid-body assumption for the elements in the machine structure [2]. The tool positioning is then modified accordingly, through a software compensation strategy. The main approaches are the use of compensation tables that can be filled with axis motion or link errors, the discretization and modification of NC program [3], and the interception and modification of feedback signal in the position control loop [4]. When a CNC is customizable enough, the addition and multiplication of look-up tables are available and compensation algorithms can run in real-time. This is, for instance, a Siemens 840D numerical controler feature [[5] – [6]].

Implementing the re-computation of tool path before machining is the easiest compensation method because it does not require extra hardware. However, it is not the best industrial strategy. Indeed, different programs are required for machining one type of part on different machines and each compensated program is referenced to a specific origin point within each workspace. Other compensation methods mostly rely on the CNC controller, whereas the modification of feedback signals strategy can be developed on any machine tool. It has the advantage of being independent of numerical controller algorithms, which are often proprietary and not exposed to the end-user. Nevertheless, the response of the controller to the modification of its position feedback signals needs to be investigated, so as to determine kinematic limitations for the simulated displacement. Indeed, the feedback signal change induces a shift between the axis position deduced by the rotational velocity sensor and the linear position sent to the controller. This can be interpreted as the application of a virtual force on the axis, inducing a virtual displacement, to which the controller reacts. However, such multi-axis machines tend to have built-in restrictions on the response to such displacements, and if this is not properly considered, the machine's internal emergency stop may be triggered. This type of study has been done in the past with the use of a compensation register of a specific incremental encoder interface board [7]. The present article introduces a real-time system running on a dSPACE Scalexio *LabBox*, that is installed in the axis position control feedback loops. It intercepts and regenerates analog position signals and can be used for system identification. This report will first introduce the software's functionalities and architecture, before the measured magnitude, velocity, acceleration and jerk's limitations of the virtual displacement injected into the controller are presented. Finally, the proposed solution is used for the position control loops identification and its applicability in error compensation problems is discussed.

2. Materials and methods

The experimental setup is installed in a GFMS HSM600U 5-axis machine-tool with a [wC'B'XbYZ(C1)t] architecture. The associated CNC is a Heidenhain iTNC530 (cf. Figure 1). The linear position is estimated by the motor's rotary encoder but the value used in the position control loop is measured by a linear encoder closest of the linear guideway. To date, the proposed solution is developed for linear axes X, Y and Z.
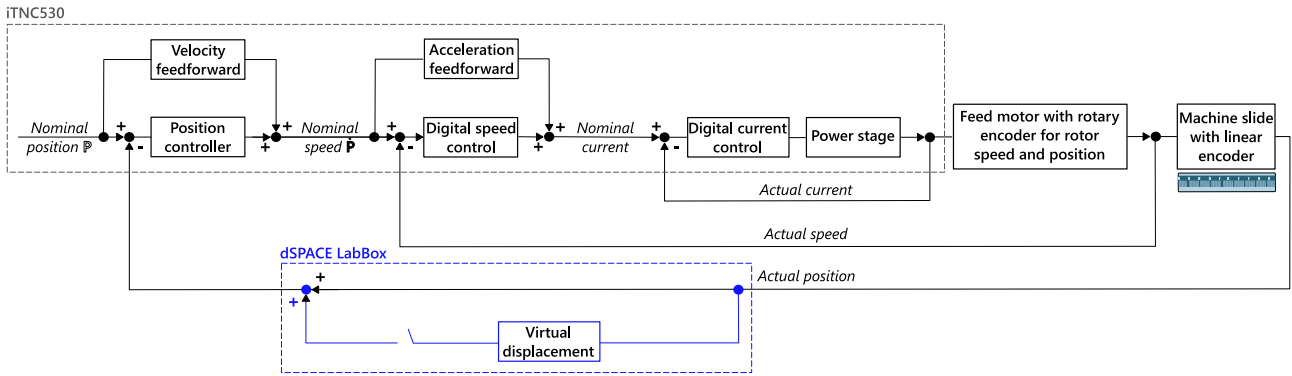
Figure 1. Cascade control loops of the iTNC530, for linear axes, with the addition of a feedback signal modification block. The usual configuration is shown in black (inspired by iTNC530 Technical Manual [8]).

2.1. Virtual encoder principle

The linear encoders mounted in the machine-tool used for experiments are Heidenhain DIADUR LS486C. The position information is obtained through the counting of individual increments from any set point of origin. Moreover, an additional track bears distance-coded reference marks. The distance between two marks is unique and provides the absolute reference. This distance is read by the NC during the homing procedure, but also each time the axis is moved.

The response of an NC machine-tool to the modification of its position feedback is studied by comparing the virtually added displacement (ΔX in Figure 2) to the actual compensation movement of the axis. The basic principle is to regenerate the sine analog signals of the linear encoders, simulating an axis movement whereas it is not caused by motor rotation. The NC then compensates for a linear positioning error by moving its axes. The virtual encoder principle is depicted in Figure 2 and can be summarised as follows:
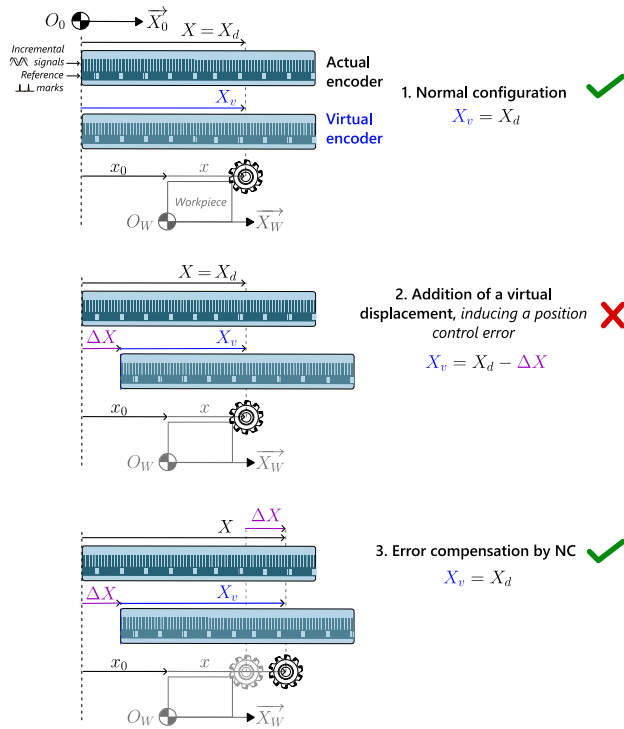
Figure 2. Virtual linear encoder principle: a virtual displacement of the linear encoder induces a real shift of the tool in the workspace (W frame).

1. In the normal configuration, the virtual encoder is read by NC and its value matches the desired joint coordinate X_d, set by the NC as the nominal position.

2. A gradual displacement is induced on the virtual encoder whereas the actual position X remains the same. The NC compares the command position X_d to the virtual encoder value X_v and measures a positioning error ΔX.

3. The NC signals for a linear displacement to compensate the previously estimated positioning error. Therefore, the tool is shifted by ΔX in workspace compared to the nominal configuration. The NC assumes that the actual axis position is $X = X_d$ while it is $X = X_d + \Delta X$.

2.2. Real-time software and hardware architecture

The signal interception and modification block, shown in blue in Figure 1, is a real-time software running on a dSPACE real-time platform (i.e. Scalexio LabBox), equipped with a DS6001 processor board. To achieve the signal manipulation, a block diagram is constructed within MATLAB Simulink© and signal conditioning is performed with ConfigurationDesk© software. Afterwards, the C code is generated with Matlab and uploaded to the LabBox. The signal acquisition is enabled by DS6121 Multi I/O and DS6221 A/D boards while the signal generation is performed by a DS6241 D/A board.
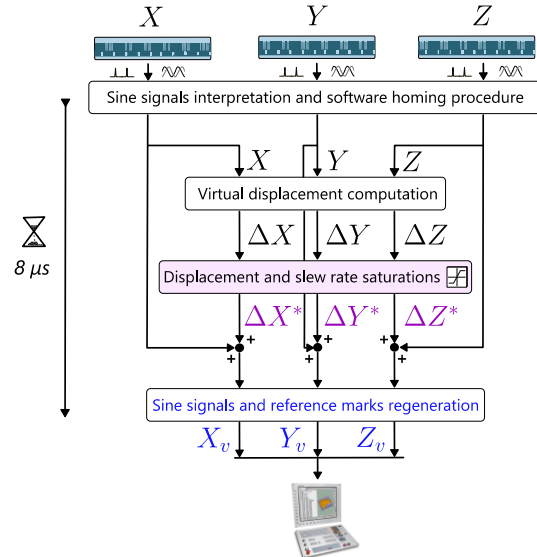
Figure 3. Real-time developed software architecture.

The software reads the sine analog signals of each linear encoder. It interpolates the actual axes positions, and regenerates the analog signals with a possible additional shift. This virtual displacement is also called "virtual perturbation". It can be controlled by the operator thanks to a computer connected to the LabBox on which runs the software interface (i.e. ControlDesk©). Any other signal or program's variables can be monitored with this real-time interface. The global

architecture of the Simulink block diagram is depicted in Figure *3*.

Multiple tasks are running simultaneously when the real-time system is on. For instance, the virtual displacement computation can take more time, and therefore has a lower priority, than the basic task which has to copy the positions from the actual encoders towards the NC. This task has a 125 kHz running frequency, meaning that the signal delay induced by the LabBox is about 8 μs and could represent a following error of 1 μm if the axis moves at 10 m/min. This delay is mostly negligible for the presented purpose.

3. Solution performance: results and discussion

The proposed solution is characterised by firstly investigating the kinematic and temporal response of the NC to virtual displacements. The performance of the solution for error compensation is then analysed.

3.1. Kinematic properties of the simulated displacement

As emphasized in Figure 3, virtual perturbations must be inserted carefully into the feedback loop to avoid triggering an emergency stop. Their computation can depend on axis position, to perform volumetric error compensation for instance. It can also be configured in the real-time interface as, for example, a sine wave or a step command. The following precautions must be taken when generating virtual displacements:

- *Magnitude*: When a virtual displacement is simulated, the NC measures a gap between the axis position estimated by the motor's rotary encoder and its feedback position, sent by the virtual encoder. This difference can reach 10 mm, as set by the CNC provider, which is a substantial compensation range. Nevertheless, a range limit of ± 2 mm is imposed on the displacement computation, in case of the compensation algorithm diverging.
- *Velocity*: Virtual incremental travel speeds were tested until the emergency stop was triggered. The maximum velocity was found to be 35 mm/s. For safety purpose, a rate of change limiter is installed after the magnitude limiter. Its limit is chosen to be set to 10 mm/s for linear axes.
- *Acceleration and jerk*: Virtual displacement can be injected with discontinuous velocity profiles, resulting in unbounded acceleration and jerk. As shown in Figure 4, the jerk measured by the NC integrated oscilloscope exceed the limits (i.e. 100 m/s³) used for the tool-path generation, without causing any internal errors, because actual acceleration is filtered by the axis control-loop.

As shown in Figure 5, the compensation reaction of the NC is particularly slow. Indeed, a delay is induced by the position controller's cycle time which is equal to 2 ms. Moreover, the acceleration at which the axis reacts does not reach the maximum value set for trajectory generation (i.e. 10 m/s²).

3.2. Position control closed-loop behaviour and identification

In order to improve the response time of the NC to a virtual displacement with a corrector, a transfer function of the position control closed loop needs to be identified. Models were fitted for each linear axis, with the virtual displacement as input and the actual position as output, meaning that the function includes every filter, NC algorithms, feed drives and physical behaviour of the axis (according to the parameters of Figure 1). A series of time- and frequency- domain experiments were conducted so as to identify a transfer function.
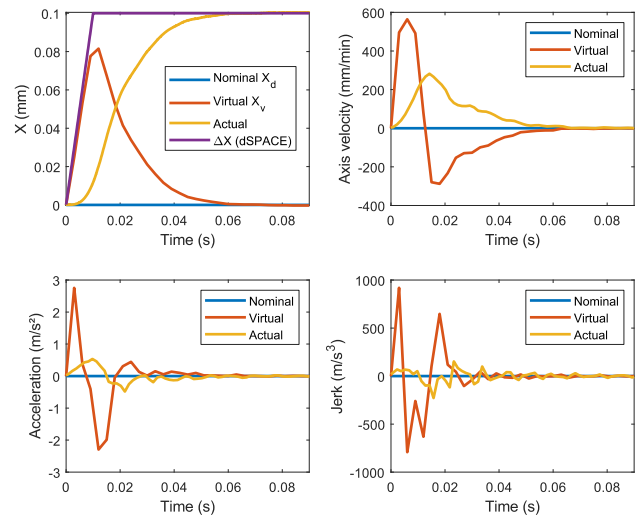
Figure 4. Kinematic measurements of a 100 μm virtual displacement (NC integrated oscilloscope measurements for the nominal and virtual curves, dSPACE measurements for the actual ones).

On the one hand, gain and phase of the position control closed-loop system were measured using sine displacements injection. On the other hand, a transfer function was estimated with time-domain measurements like those displayed in Figure 5.
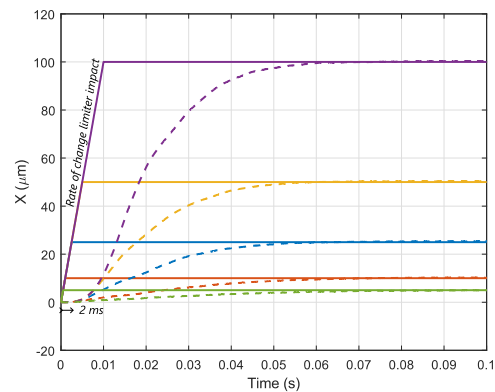
Figure 5. Virtual displacements (continuous lines) and machine response (dashed lines) for various step magnitudes.

The transfer function estimation algorithm is the Simplified Refined Instrumental Variable method for Continuous-time systems (SRIVC) with the implementation in the System Identification Toolbox in MATLAB [9]. Results of the two types of identification experiments are superposed on Figure 6. The differences between the two identification methods, particularly in terms of gain, are due to the numerous non-linearities of the system modelled (e.g. NC algorithm, axes mechanical behavior).
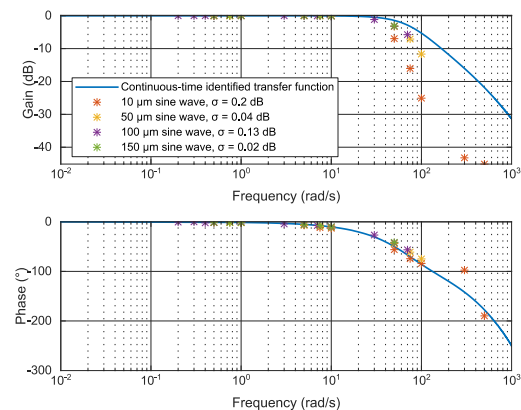
Figure 6. Bode diagrams of X-axis position control-loop.

3.3. Error compensation application

The main objective of studying the response of the NC to the modification of its position feedback is the development of a new software geometric error compensation method. However, dynamics of the studied response is slow and could induce volumetric error. This is why modelling of linear axes position control loops helps predicting the residual tracking error. This error depends on the compensation geometric rate $\frac{dC}{dX}$ and on the axis feed rate $\frac{dX}{dt}$, with C the necessary virtual displacement for a given volumetric error compensation. Kinematic properties specified in the previous section bound the rate of change of the virtual displacement to be:

$$\frac{dC}{dt} = \frac{dC}{dX}\frac{dX}{dt} < 10 \text{ mm/s} \tag{1}$$

A surface predicting the tracking error on a linear axis is plotted in Figure 7, and compared to experimental points. For example, for a finishing operation in an aluminium alloy, the linear axes can move at up to 6000 mm/min. For a compensation slope of 10 µm/mm, the expected maximum tracking error reaches 22 µm.
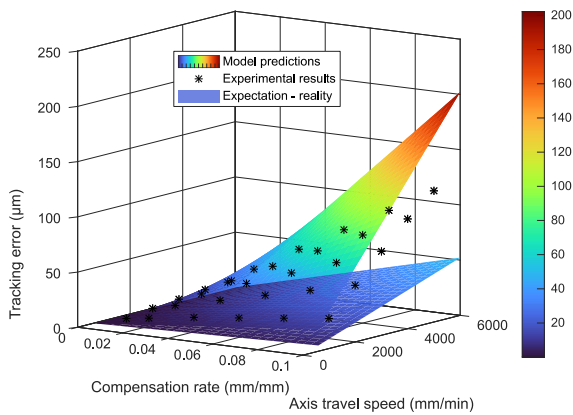
Figure 7. Estimation of the tracking error along a linear axis (X), superimposed with experimental results.

Despite a low-performance modelling (the difference between experiments and expectations can reach 50 µm in the tested - speed and compensation rate – area, especially in unrealistic compensation conditions), the tracking error can be reduced with the addition of a feed-forward controller H_{FC} [10] just after the virtual displacement computation block (Figure 3). Its coefficients are estimated via the axis model H_X and the desired NC response H_{ideal} as:

$$H_{FC}. \ H_X = H_{ideal} \tag{2}$$

Because of the 2 ms delay and the fact that the trajectory of command is not known by the LabBox in advance, H_{ideal} cannot be equal to 1. Nevertheless, this feed-forward controller gives promising performances as shown in Figure 8, where the maximum measured tracking error was reduced from 31.6% to 4.7 % of the set point.

4. Conclusion and outlook

A device for modifying the axis position signal in real-time has been introduced and tested in a CNC machine-tool. The linear position control closed-loops were modelled via the virtual encoder principle. Feed-forward controllers were then added to the software solution so as to ensure better virtual displacement tracking performances. Moreover, no noticeable slowdown was measured due to any coupling between the axes. For the future work, geometric errors of the machine must be identified.

Afterwards, the real-time compensation solution can be applied to the machining of a part, using three-axis milling first, before extending to 5-axis machines via including both swivel and rotational degrees of freedom in the software and develop multi-axis compensation strategy.

(a)

(b)
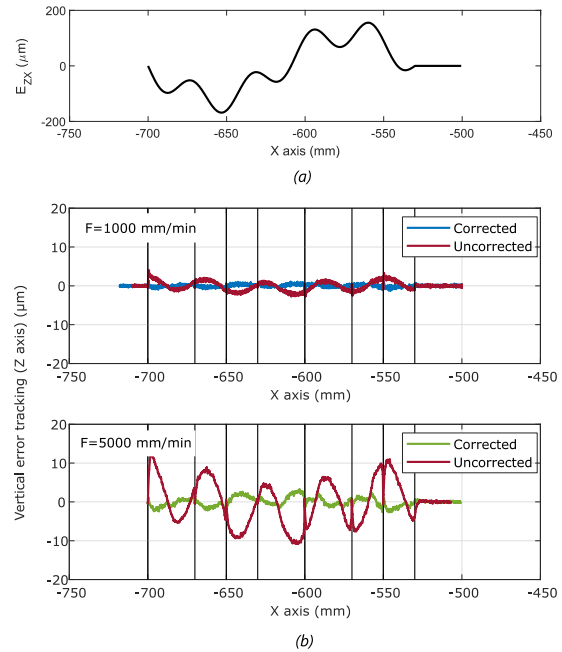
Figure 8. (a) Vertical straightness error supposed along X-axis − (b) Tracking error before and after inserting a feed-forward controller, for two different feedrates F. Vertical black lines correspond to X-axis stops.

References

[1] Andolfatto L, Lavernhe S and Mayer J R R 2011 Evaluation of Servo Geometric and Dynamic Error Sources on Five-Axis High-Speed machine Tool *International Journal of Machine Tools and Manufacture* 51, **10-11** : 787-96

[2] Lei W T and Hsu Y Y 2003 Accuracy enhancement of five-axis CNC machines through real-time error compensation *Internal Journal of Machine Tools and Manufacture* **43** : 871–77

[3] Liang R, Wang Z, Chen W, and Ye W 2021 Accuracy Improvement for RLLLR Five-Axis Machine Tools: A Posture and Position Compensation Method for Geometric Errors *Journal of Manufacturing Processes* **71** : 724–33

[4] Postlethwaite S R and Ford D G 1999 A practical system for 5-axis volumetric compensation *Laser Metrology and Machine Performance* **5**

[5] Esmaeili S M and Mayer J R R 2021 CNC Table Based Compensation of Inter-Axis and Linear Axis Scale Gain Errors for a Five-Axis Machine Tool from Symbolic Variational Kinematics. *CIRP Annals* **70**, no. 1 : 439–42

[6] Longstaff A P, Fletcher S and Myers A 2005 Volumetric compensation for precision manufacture through a standard CNC controller *Conference: 20th Annual Meeting of the American Society for Precision Engineering*

[7] Freeman J M and Ford D G 2005 The Digital Injection of Signals into Machine Feedback Loops via Incremental Encoder Interfaces *Proceedings of the Institution of Mechanical Engineers, Part C: Journal of Mechanical Engineering Science* **219**, no. 3 : 325–29

[8] Heidenhain 2006 Technical Manual iTNC530

[9] Ljung L 2022 System identification Toolbo User's guide

[10] Tomizuka M 1987 Zero Phase Error Tracking Algorithm for Digital Control *Journal of Dynamic Systems, Measurement, and Control* **109 :** 65 – 68

Embedded algorithm for the diagnosis of machine tool spindles

Jooho Hwang[1,2], Nguyen Minh Dung[2], Jongyoup Shim[1]

[1]Dept. of Ultra-Precision Machines & Systems, Korea Institute of Machinery and Materials, 156, Gajeongbuk-Ro, Yuseong-Gu, Daejeon 34103, Republic of Korea

[2]Dept. of Mechanical Engineering, KIMM School, University of science & Technology, 156, Gajeongbuk-Ro, Yuseong-Gu, Daejeon 34103, Republic of Korea

Abstract

Spindle maintenance is a crucial process in the metal-cutting industry. If the spindle's operation is not adequately observed, it could lead to significant damage that increases exponentially with each use. Therefore, a spindle maintenance system is a top priority for any metal-cutting factory looking to enhance spindle performance while reducing overall operating costs. The most vulnerable part of the spindle is the bearing, which can fail due to factors such as a lack of lubrication, over-lubrication, contamination, overloading, excessive temperature, or misalignment. These issues can result in inner race fault (BPFI), outer race fault (BPFO), ball defect (BSF), or cage failure (FTF). Edge computing devices have emerged as a promising solution for reducing traffic load to the cloud and can be employed to monitor machine operation and diagnose spindle failures. In this article, we present an algorithm for diagnosing BPFI, BPFO, BSF, and FTF based on Kurtosis, Hilbert transform, and Wavelet Transform methods. The results demonstrate that the developed algorithms are accurate and computationally efficient, meeting the demands of edge devices.

Embedded algorithm, Edge device, Spindle, Bearing fault diagnosis

1. Introduction

Spindles play critical role in machining processes, offering rotational motion to cutting tools for precision and efficiency in manufacturing. Being crucial components of machine tools, their performance directly impacts machining quality. Ensuring spindle reliability requires focused maintenance, particularly in bearing fault detection and chatter detection.

Early fault identification is critical to prevent costly failures, minimize downtime, and ensure safety. By implementing effective bearing fault detection techniques, particularly vibration monitoring, potential issues can be identified in their early stages. The types of bearing faults include inner race fault (BPFI), outer race fault (BPFO), ball defect (BSF), or cage failure (FTF) and grease failure [1][2]. In comparison to ISO 17243 [3], our method has incorporated the signal enhance technique for better bearing fault detection.

Chatter refers to the unwanted vibration and oscillation that can occur during metal-cutting processes, leading to poor surface finish quality, accelerated tool wear, and, in extreme cases, catastrophic tool failure. Chatter detection is essential to prevent these detrimental effects and optimize the machining process. By employing advanced sensing technologies and real-time monitoring systems, manufacturers can promptly identify the presence of chatter and take corrective actions, such as adjusting cutting parameters or implementing damping techniques.

2. Bearing fault detection algorithm

To detect the ball bearing parameters, the Hilbert transform is employed. The Hilbert transform of the signal $x_H(t)$, is obtained through the convolution of the original signal $x(t)$ with $1/\pi t$. The crucial step in utilizing the Hilbert transform for bearing fault diagnosis involves acquiring the envelope of the analytic signal

$s(t)$. The envelope reflects variations in the amplitude of the signal over time, aiding in the identification of fault-related frequency components. The analytic signal is formed using the following formula, and the power spectral density of this analytic signal is capable of detecting bearing fault frequencies.

$$s(t) = x(t) + j\, x_H(t) \qquad (1)$$

There are alternative ways to address the noise problem in the signal, such as Kurtosis and wavelet transform, which are compared with experimental results. We gathered spindle vibration data and implemented the system for the bearing with the following configuration:

Table 1 Bearing configuration and its calculated fault frequencies (f_s, N_b, D_b, d_c, and α are spindle speed(Hz), # of ball, ball diameter, pitch diameter, and contact angle respectively):

	Theoretical Bearing fault frequency	Bearing fault frequency
BPFI	$f_s \dfrac{N_b}{2}\left(1 + \dfrac{D_b}{d_c}cos(\alpha)\right)$	$11.7076 \times f_s$
BPFO	$f_s \dfrac{N_b}{2}\left(1 - \dfrac{D_b}{d_c}cos(\alpha)\right)$	$9.2924 \times f_s$
FTF	$\dfrac{f_s}{2}\left(1 - \dfrac{D_b}{d_c}cos(\alpha)\right)$	$0.4425 \times f_s$
BSF	$f_s \dfrac{N_b}{2}\left(1 - \left(\dfrac{D_b}{d_c}cos(\alpha)\right)^2\right)$	$4.1438 \times f_s$

In Table 1, theoretical bearing fault frequencies such as BPFI, BPFO, BSF, and FTF coexist with the calculated bearing fault frequencies derived from the current spindle system. In Figure 1, raw data is captured from a spindle with an inner race fault, and the calculated BPFI is depicted using the three aforementioned algorithms. As investigation from experiment data, the BPFI and its harmonic 1x, 2x, 3x appear as 585.8 Hz,

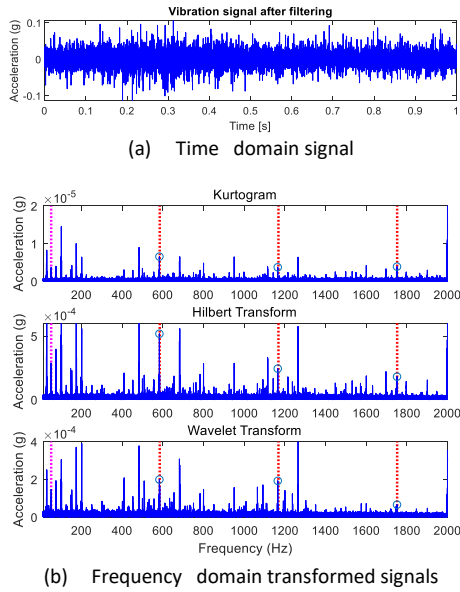1070.7 Hz, 1756.14 Hz in the frequency domain implying fault in the inner raceway (red lines in Fig. 1 (b)).

(a)   Time   domain signal

(b)   Frequency   domain transformed signals

Figure 1. BPFI fault signal in time and frequency domain

3. Chatter detection algorithm

Chatter refers to undesirable vibrations or oscillations that occur during machining, resulting in poor surface quality, tool wear, reduced machining efficiency, and potential damage to the workpiece, cutting tool, or the machine itself. Two methods for chatter detection include analyzing the power spectrum density (PSD) of the signal and employing the wavelet packet decomposition transform or stationary wavelet transform (SWT).

Each cutting condition is associated with the tool passing frequency, f_c. This frequency represents the integer multiplication of the spindle speed, i.e., the number of flutes on the tool. The vibration signal we collected consists of the periodic component $s_p(t)$, aperiodic component $s_a(t)$, and noise $s_n(t)$ as indicated with its indies a and p. In the scope of this noise is considered to be negligible. The PSD of the signal is calculated by:

$$PSD_{total} = PSD_a + PSD_p \qquad (2)$$

The energy of aperiodic signal is

$$E_a = \sum_0^{N-1} PSD_a$$
$$E_p = \sum_0^{N-1} PSD_p$$
$$E = \sum_0^{N-1} PSD_{total} \qquad (3)$$

The chatter index (CI) is calculated by the formula:

$$CI = E_a/E \qquad (4)$$

The E_a is representative of the aperiodic signal, signifying that when the CI is large, i.e., close to the normalization value , there is the presence of unwanted signal. The PSD of the periodic signal is associated with vibrations generated from collisions between the tool flute and the workpiece. This periodic data occurs consistently, regardless of the presence of chatter. Therefore, this part is excluded from the PSD_{total} obtain the PSD of the aperiodic signal.[4]

The Chatter Index can also be determined using the wavelet transform, specifically the SWT, similar to the PSD method. This approach leverages the wavelet transform's ability to detect transient features in vibration signals, which are often signs of bearing faults. Unlike the PSD, the wavelet transform uniquely identifies various data frequencies over time, making it a good

method for chatter detection. The calculation is based on the randomness of the wavelet coefficients, with higher randomness indicating a higher chance of chatter. This principle underlies our method for calculating the Chatter Index using the wavelet transform.

(a)CI from PSD   (b) CI from SWT
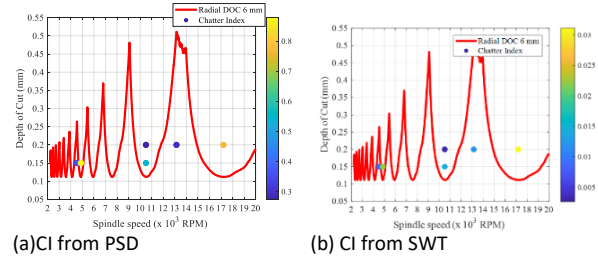
Figure 2. Chatter index based on PSD and SWT (red line is SLD, dots indicate cutting condition, and are colored according to CI level)

Table 2 shows the cutting conditions and their Chatter Index (CI) using the SWT and PSD methods. Despite a cutting speed of 10500 rpm showing no clear chatter indicator, both methods effectively predict chatter, as shown in Figure 2's red line of stable lobe diagram (SLD). The dots are the cutting condition from experiment with spindle speed and depth of cut. Conditions below this line are stable, while those above are unstable.

Table 2 Cutting condition and the corresponding chatter index

ADOC (mm)	Speed (RPM)	CI (SWT)	CI (PSD)
0.15	4500	0.007	0.35
0.15	4785	0.015	0.39
0.15	4870	0.022	0.87
0.15	10500	0.0144	0.54
0.2	10500	0.0026	0.27
0.2	13140	0.0119	0.29
0.2	17200	0.0311	0.77

4. Conclusions

In this paper, we present an embedded algorithm for bearing fault detection and chatter detection, designed for application in embedded systems. A robust and easily calculable algorithm is essential for embedded systems. Therefore, the Hilbert transform and PSD approach are recommended for bearing fault and chatter detection due to their robustness and fast calculation. The choice of method depends on the operator's requirements. If there is no constraint on the edge calculation system, more complex methods like fast kurtosis for bearing fault detection and wavelet transform, along with SWT for chatter detection, are viable options. These methods offer a deeper analysis, but it is crucial to consider the trade-off between calculation time and performance.

References

[1] Jerome A 2007 Fast computation of the kurtogram for the detection of transient faults *Mechanical Systems and Signal Processing* **21** 108-124

[2] Yanxue W, Zhengjia H, Yanyang Z, 2010 Enhancement of signal denoising and multiple fault signatures selecting in rotating machinery using dual-tree complex wavelet transform *Mechanical Systems and Signal Processing* **24** 119-137

[3] ISO 17243 (Part 1 to 3) – Machine tool spindles

[4] Michele P, Francesco C, Francesco G, Domenico M 2022 In-Process Chatter Detection Using Signal Analysis in Frequency and Time-Frequency Domain *Machine* **10**

Dynamic machining and motion performance in state-of-the-art linear motor and ball screw-based CNC machine tools

Jeong Hoon Ko[1], Chee Wang Lim[2], Yuting Chai[2]

[1]*Taizhou Institute of Zhejiang University, 618, West Section of Shifu Avenue, Taizhou City, Zhejiang Province*
[2]*Akribis Systems Pte Ltd, Department of Aplos Machines, 5012 Ang Mo Kio Ave 5, Singapore 569876, Singapore*

Email: jhkolioneagle@gmail.com

Abstract

Linear motor-based CNC machine tools have been competitively advanced for higher machining and motion performance. While linear motor and ball screw-based feed drives have been reviewed in academics and industries, performance differences between the two drive systems have yet to be rigorously examined with machining and motion analysis. This article details the performance comparisons between the direct drive and ball-screw-based feed systems with dynamic tool paths and external impulse responses. The tracking errors from dynamic motion were measured using a linear-scale encoder and analyzed for both feed drive systems. From experimental comparisons for the given adaptive machining paths, it is found that the linear motor-based direct drive system generates errors of 0.023 mm less in one direction and 0.012 mm less in the other direction than the ball screw-based one. While the linear motor-based feed drive was known to have less servo stiffness than a ball screw-based system, the difference in servo displacements at external impulse forces of 4000 N is found to be only within a few micrometers. Based on the test result, the configured linear motor-based machine is capable of performing heavy machining like face milling as well as adaptive dynamic machining, and it can maintain a precision motion without backlash over disturbance. In addition, a comprehensive evaluation is tabularized to contrast the strengths and weaknesses of two different drive-based machine tools.

Computer Numerical Control (CNC), Drive, Machining, Motion

1. Introduction

Linear motor-based feed drive systems in CNC machine tools have recently made significant strides in terms of machining and motion performance. The benefit of linear motor-based direct drive is that it achieves higher acceleration and speeds with less wear and tear than a ball screw-based machine [1-2]. Moreover, it is widely acknowledged that the linear motor-based feed drive maintains better tracking accuracy in complex tool paths and high-speed motion than the conventional feed drive system. Despite the extensive academic and industrial reviews of linear motor and ball screw-based feed drives, the performance between the two drive systems has yet to be experimentally examined and compared under actual CNC tool paths and external disturbances.

CNC tool paths are composed of constant speed vectors and transient varying speed ones, which may generate errors during acceleration and deceleration [3-4]. The feed rates for the tool paths critically affect machining quality and productivity [5-7]. Since the feed drive performance has been dramatically improved in the last decades, various dynamic tool paths, such as rapid trochoidal ones, have been enabled and exploited [8-10]. The adaptive toolpaths aim to maintain constant tool engagement or constant material removal at each point along the path. The tool paths have the advantages of reducing cutting forces, reducing tool wear, minimizing vibration, etc. However, it is not to overlook control tracking accuracy, which may worsen at such rapid speed vector changes during the trochoidal motion. Tracking errors need to be examined at high accelerations and decelerations of adaptive transient speed. In order to benefit from trochoidal motion, dynamic tracking errors

should be minimized when speed vectors change frequently. This article compares tracking accuracy from linear motor-based and ball screw-based feed drives during the adaptive motion.

The drawback of the linear motor drive system was known as less damping due to less contact stiffness from mechanical components, and researchers worked on the compensation method against disturbance [11-12]. As impulse responses exhibit how the system acts against disturbance forces, two feed drive responses are benchmarked under the same magnitude of impulse forces. In this article, the precise feed drive motion is measured with a resolution of less than 0.05 micrometer and 3-millisecond sampling using the linear scale encoder attached between the moving table and the fixed bed as the impulse force is applied to the table connected to the feed drive.

Overall, two modern commercial CNC systems, linear motor-based feed drives (LMFD) and ball screw-based feed drives (BSFD), installed with linear scale encoders, are selected to compare the servo responses at the adaptive motion and the impulse disturbance. The experimental results are analyzed to explain the characteristics of the feed drives in terms of the tracking errors and disturbance responses from both systems. Finally, further comparisons and discussions are summarized, and future direction is suggested based on these experimental comparisons.

## 2. Feed drive performance under dynamic tool path

In order to utilize dynamic feed motion, the feed drive should be able to provide a rapid dynamic response that encompasses acceleration and jerk. While the controller could be tuned with high acceleration and jerk values, it should still be noted that the tracking errors may be accordingly increased by fast-moving

mass, which is a bottleneck for high-speed dynamic motion. The feed drivers' responses can be benchmarked under the moving velocity profiles by comparing the tracking errors under the same dynamic tool path.

Figure 1 illustrates the machined geometry and tested adaptive tool path at the feed drive systems. The dynamic tool path has 0.25 mm lifts in the tool axis when the tool returns to the machining position, which induces more cooling and less tool wear, as depicted in Figure 2. The return feed rate is 8000 mm/min, the cutting feed rate is 4500 mm, and the cutting depths are Ae = 1.5 and Ap = 5 mm for the dynamic motion. The solid carbide flat-end mill tool has four flutes and a diameter of 12 mm. Limited information from commercial controllers is listed for control parameters in Table 1; it is not permissible to change or disclose the detailed controller parameter sets of the commercial system. As the tested LMFD system has a higher maximum acceleration and jerk setting than the BSFD system, the LMFD system may have a disadvantage regarding tracking error, which tends to increase at high acceleration and jerk for the comparisons.

Table 1 Commercial machine controller setting

	The tested commercial LMFD	The tested commercial BSFD
Maximum acceleration setting	X 10000, Y 10000, Z 10000 mm/s^2	G0 X 5263, Y 4412, Z 3750 G1 X 2222, Y 2222, Z 2222 mm/s^2
Maximum feed rate	60000 mm/min	X 48000 Y 36000 Z 36000 mm/min
Controller version	Heidenhain TNC 620	Fanuc professional P
Look ahead function	HSC mode on	AICC2 mode on
Position control	Closed loop control with linear scale encoder	Closed loop control with linear scale encoder
Interpolator cycle time	3 msec	3 msec
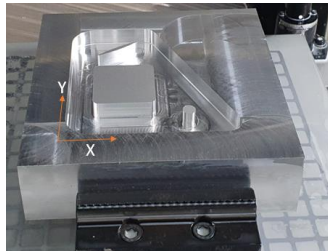
(a) The machined geometry with the material Al6061-T6
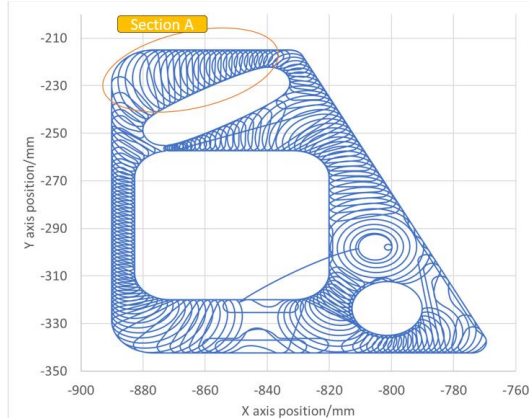
(b) The adaptive tool paths in XY plane

Figure 1. The machined geometry with the material Al6061-T6 and the adaptive tool path
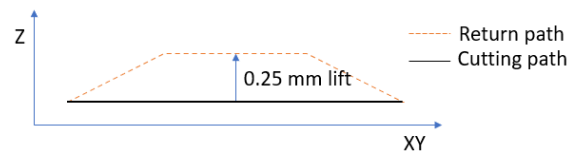
Figure 2. Return and cutting feed rates

According to the total adaptive tool paths shown in Figure 1(b), Figures 3(a) and 3(b) display the resultant feed rates in the XY plane from the LMFD and BSFD systems, respectively. Due to the different controller settings, the actual feed rates cannot be the same for the given adaptive tool path. Figure 3(c) illustrates the comparisons of the resultant feed rates for the path section A. As expected from the maximum acceleration setting shown in Table 1, LMFD may lead to a shorter operation time than the BSFD.

In order to perform a fair comparison over the different controller settings, the analysis is performed to benchmark the ratio of tracking error over acceleration in both systems since changing the controller parameters in the commercial system is not allowed. Tracking errors are generated by the acceleration or deceleration of the fast-moving masses in each axis, as those may excite the structure from the acceleration or deceleration force. For example, if acceleration increases, the tracking error is expected to increase accordingly.
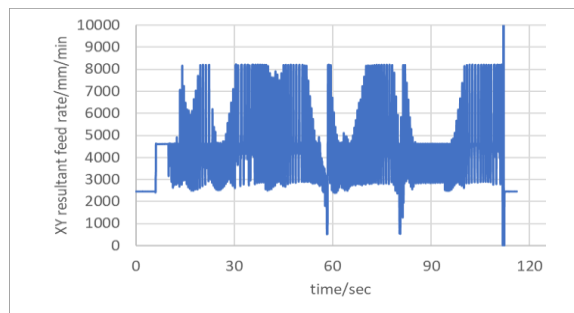
(a) X and Y axis resultant feed rates profile from the LMFD system
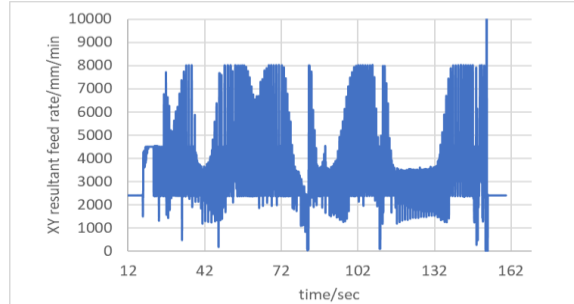
(b) X and Y axis resultant feed rates profile from the BSFD system
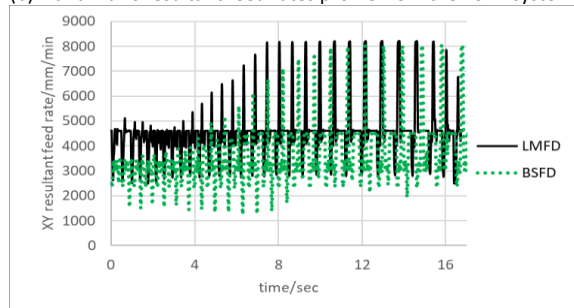
(c) XY resultant feed rates for section A

Figure 3. Resultant feed rates for LMFD and BSFD system for the adaptive tool path

The actual feed rate and acceleration profiles are measured from the linear encoder of LMFD for the tool path section A, as displayed in Figures 4(a) and 4(b), respectively. The tracking errors in the x and y directions are visualized in Figures 4(c) and

4(d). The x-axis tracking errors are from -0.005 mm to 0.00438 mm, while the x-axis acceleration ranges from -2.420 g to 1.870 g. The y-axis tracking errors are from -0.0194 mm to 0.0189 mm, while the y-axis acceleration ranges from -2.370 g to 2.370 g. The ratio (mm/g) of displacement over acceleration in terms of the range magnitude is 0.0022 and 0.0081 in the x-axis and y-axis, respectively.

(a) X and Y axis feed rate profiles measured from linear encoder

(b) X and Y axis acceleration profiles measured from linear encoder

(c) X axis tracking errors

(d) Y axis tracking errors

Figure 4. Corresponding tracking errors for feed rate and acceleration profiles from the tested LMFD system for the tool path section A

The experimental velocity and acceleration profiles and the corresponding tracking errors from BSFD are displayed in Figure 5. The BSFD system has a lower range of acceleration profiles during the adaptive motion, as shown in Figure 5(b), than the LMFD system, as displayed in Figure 4(b). The x-axis tracking errors range from -0.0168 mm to 0.0145 mm, while the x-axis acceleration ranges from -1.512 g to 1. 198g. The y-axis tracking errors are from -0.0366 mm to 0.0221 mm, while the y-axis acceleration ranges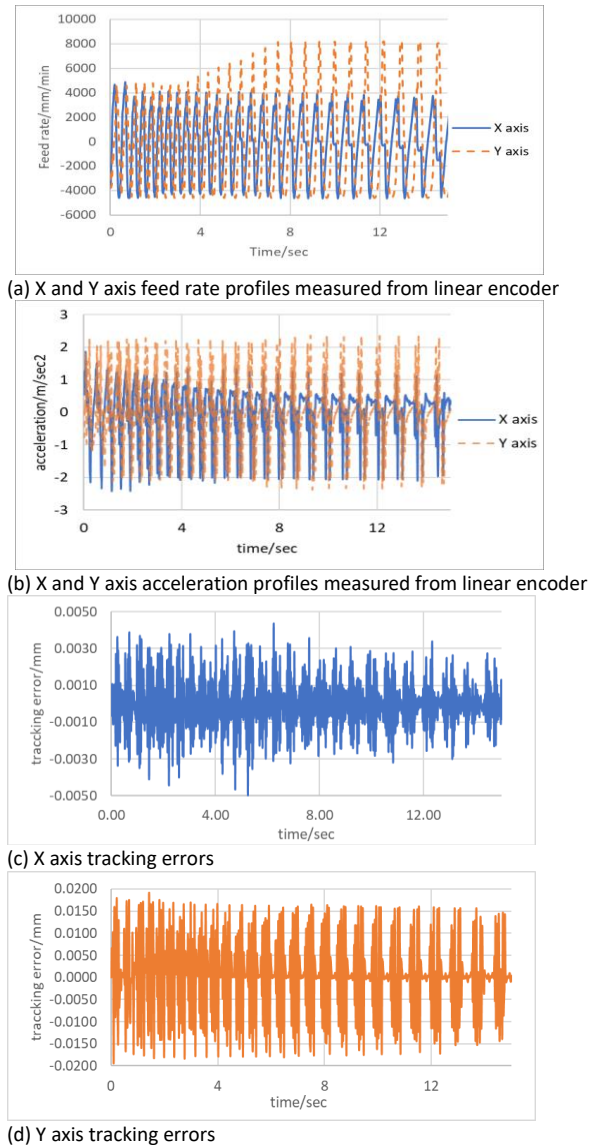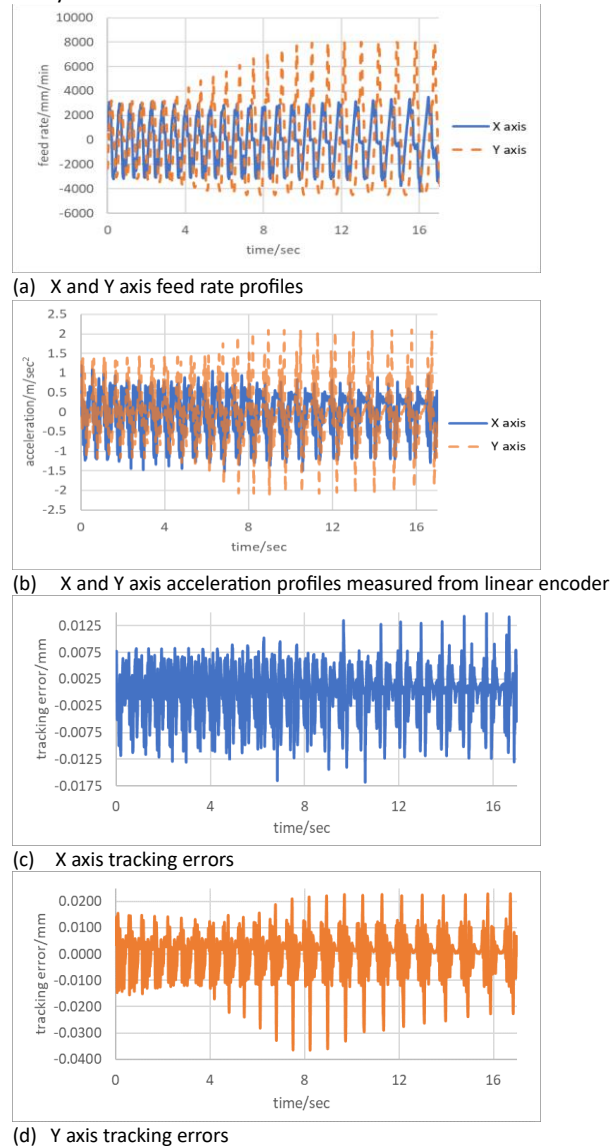 from -2.078 g to 2.098 g. The ratio (mm/g) of displacement over acceleration in terms of the range is 0.0116 and 0.0140 in the x-axis and y-axis, respectively.

The x-axis motion driven by the BSFD has larger tracking errors in the adaptive motion than the LMFD. From the tested results, the LMFD generates lower ranges of tracking errors over acceleration than the BSFD. Even though higher acceleration is executed in the LMFD system, the tracking error over acceleration is smaller than in the BMFD system, which is found

to be the benefit of the LMFD system from the experimental study.

(a) X and Y axis feed rate profiles

(b) X and Y axis acceleration profiles measured from linear encoder

(c) X axis tracking errors

(d) Y axis tracking errors

Figure 5. Corresponding tracking errors for feed rate and acceleration profiles from the tested BSFD system for the tool path section A

3. Feed drive response under external impulse forces

Impulse responses of two feed drive systems have been compared to analyze the dynamic responses against disturbance. The impulse magnitude of 4000 N with a bandwidth of less than 1KHz was applied to the table feed axis center using the Kistler impact force hammer (9728A20000). Both feed drive responses are measured using the linear scales installed beside the linear guide of the feed drive system. Linear scale encoder measurements display the relative motion of the machine bed and the moving table, which is a precise indicator of feed drive motion.

Figure 6(a) displays the test configuration example in the BSFD. As the impulse force shown in Figure 6(b) is applied, the linear scale measurements from the LMFD and the BSFD are displayed in Figure 6(c). With an impulse force of 4000 N, the LMFD system has a peak-to-valley response of 0.0164 mm, which is larger than the BSFD system's response of 0.0144 mm. This is because the linear motor-based feed drive has less damping than the ball screw-based feed drive due to fewer mechanical components. Both systems' dynamic displacements are reduced within 1 micrometer in less than 50 msec. However, it takes longer for the displacement to reduce to less than 0.5 micrometer in the

case of BSFD (129 msec) compared to LMFD (50 msec). This phenomenon may be attributed to the pitch error of the ball screw tested, which can be minimized by using a fine-pitch ball screw with backlash compensation.
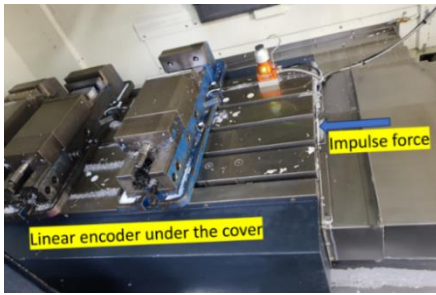
(a) Impulse response test in BSFD
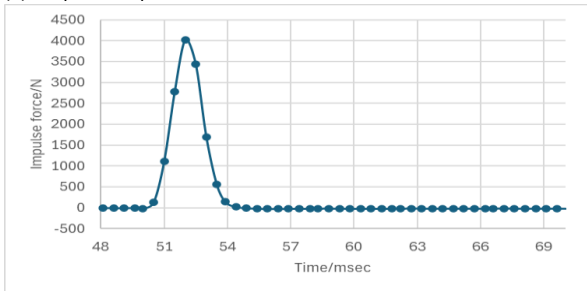
(b) Impulse force applied to table center in X direction
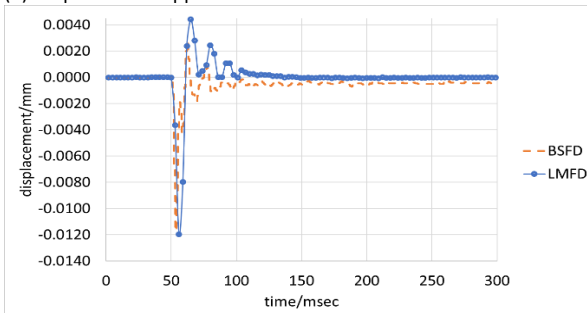
(c) Impulse responses from LMFD and BSFD

Figure 6. Feed drive responses with external impulse forces

It is commonly understood that the linear motor, which has fewer mechanical components, generally has less damping than the ball screw-based feed drive system. However, the difference between the two system responses is found to be insignificant. For a 4000 N impulse disturbance, the difference is only 0.002 mm.

For additional insights regarding the analysis, it is important to note that the response to disturbances can vary depending on factors such as motor performance, control algorithm, and structural design, regardless of whether a linear or rotary motor is used. By implementing advanced control algorithms and optimizing the structural design of the system, the dynamic stiffness of each system can be further enhanced, thus improving the system's ability to resist disturbances.

4. Summary and discussions

As linear motor-based feed drive (LMFD) has been increasingly adopted, it is necessary to compare it with a ball screw-based feed drive (BSFD) in terms of control accuracy under dynamic motion and disturbances. This article compares two different systems' dynamic responses under the adaptive motion requiring moving mass control with continuous acceleration and deceleration. For the machining tool paths, the tested LMFD generates less tracking error (0.023 mm difference in the X-axis and 0.012 mm in the Y-axis) than the BSFD. This relative comparison indicates that the tested LMFD has better control

accuracy in dynamic motion than the BSFD and can generate better control accuracy for complex motion profiles requiring frequent acceleration and deceleration.

Another aspect is whether the systems have high dynamic stiffness and damping against external disturbance. In order to see the relative dynamic response between the table and the base, linear encoder data was recorded and analyzed with the application of impulse forces around 4000 N. As BSFD is known to have more damping than the other, it exhibits less peak-to-valley displacement, but the difference between the two systems' responses is within a few micrometers at 4000 N. Even though BSFD also has a shorter time to settle within 0.001 mm, it has a 79 msec longer time to settle within 0.0005 mm than LMFD, which may be due to ball screw specifications like screw pitch. Based on the test result, the configured LMFD is capable of performing heavy machining like face milling as well as dynamic machining, and it can maintain a precision motion without backlash over disturbance.

Two kinds of test results provide some insights into the different commercial feed drive systems, and with other well-known facts, the relative comparisons are presented in Table 2. As cycle time mainly depends on control setting and motor power, it is not meaningful to mention which system is faster in cycle time. In addition, LMFD has an advantage in terms of life span and backlash compared to BSFD. As LMFD has relatively better control accuracy than BSFD under acceleration or deceleration, precision engineering industries are also increasingly adopting LMFD to achieve fine surface finish and tight dimensional requirements.

The insights gained from the experimental results will be used to further study the feed drive design and control and to overcome the drawbacks of each drive. Furthermore, by optimizing the physical properties and structures of the entire machine tool based on the studied feed drive characteristics, better performance can be achieved for high precision and high-performance cutting.

Table 2 Relative comparisons between LMFD and BSFD

	LMFD	BSFD
Disturbance dynamic stiffness or damping	++	+++
Backlash	+++	++
Tracking error under dynamic motion	+++	++
Cycle time	++	++
Life span considering wear/tear	+++	++

(+ means positive point. More + means better only in relative manner.)

References

[1] Altintas Y, Verl A, Brecher C, Uriarte L, and Pritschow G 2011 *CIRP annals* **60** 779-96
[2] Pritschow G 1998 *CIRP annals* **47** 541-8
[3] Tsai MS, Huang YC 2016 Int. *J. Adv. Manuf. Technol*. **87** 279-92.
[4] Ko JH, Yun WS, and Cho DW 2003 *Comput. Aided Des.* **35** 383-93
[5] Krajnik P, J. Kopač J, 2004, *J. Mater. Process. Technol*. **157-158** 543-552
[6] Vavruska P, Pesice M, Zeman P, Kozlok T, 2022 *Results in Engineering* **16** 1-11
[7] Ko JH, Cho DW, 2004 *Int. J. Mach. Tools Manuf.* **44** 1047-1059
[8] Rauch M, Duc E, and Hascoet JY 2009 *Int. J. Mach. Tools Manuf.* 2009 **49** 375-83
[9] Chang CH, Huang M, and Yau HT 2023 *Int. J. Adv. Manuf. Technol.* **125** 1757-76
[10] Shixiong W, Wei M, Bin L, and Chengyong W 2016 *J. Mater. Process. Technol.* **233** 29-43
[11] Jamaludin Z, Van Brussel H, Pipeleers G, and Swevers J 2008 *CIRP annals* **57** 403-6
[12] Altintas Y, Okwudire CE. 2009 *CIRP annals*. **58** 335-8

Frequency domain optimization of the tracking performance of a piezo actuator using reset control

Marvin Hakvoort[1,2], Christopher Mock[2], S. Hassan HosseinNia[1]

[1]*Department of Precision and Microsystems Engineering; Delft University of Technology, Mekelweg 2, 2628 CD Delft, The Netherlands*
[2]*Physik Instrumente (PI) GmbH &. Co. KG., Auf der Römerstraße 1, 76228 Karlsruhe, Germany*

m.hakvoort@student.utwente.nl; *s.h.hosseinniakani@tudelft.nl*;

Abstract

Customer demands for piezo positioning systems focus on higher closed-loop bandwidths and increased precision. However, poorly damped resonance frequencies often limit achievable bandwidths. Linear control limitations, such as Bode's gain-phase relation and the waterbed effect, constrain controller performance. Recent research suggests that nonlinear control methods, like reset control, can overcome these limitations. The "Constant in Gain – Lead in Phase (CgLp)" structure offers a lead in phase without sacrificing gain, unlike its linear counterpart. This work aims to leverage this property to improve closed-loop bandwidth, steady-state tracking, and disturbance rejection while maintaining the transient properties of the systems.

The controllers have been implemented and tested on a one-degree-of-freedom precision positioning stage with multiple dominant resonance frequencies. The CgLp element is used as an extension to the linear control structure in series with a proportional-integral (PI) tracking controller. To dampen the first dominant resonance frequency, a Positive Position Feedback (PPF) controller has been used in the inner loop. The controllers have been optimized solely based on the describing function (DF) analysis of the system using a Particle Swarm Optimization (PSO) algorithm. It has been shown that when properly setting the CgLp parameters, the effect of higher-order harmonics introduced by the resets is negligible, and the first-order DF approximation delivers an accurate frequency domain analysis. The results have shown that by using the additional CgLp element-based structure, the closed-loop bandwidth could be improved by 60%, and the overshoot could be kept below 5%. Additionally, steady-state tracking performance and disturbance rejection capabilities could be significantly improved.

1. Introduction

The current customer demands for nanopositioning systems such as piezo actuators go towards even higher closed loop bandwidths, increased precision and disturbance rejection capabilities. However, the maximum achievable bandwidths of these systems are often limited by one or multiple poorly damped resonance frequencies. The maximum achievable closed loop bandwidth of these systems is typically below the value of the first resonance frequency [1]. Additionally, fundamental limitations of linear control such as Bode's gain phase relation and the waterbed effect limit the achievable performance of these controllers.

Recent work has shown that nonlinear control strategies such as reset control can be used to overcome these limitations and improve the tracking performance of these systems [2]. Two of the most promising reset elements are called "Constant in gain – Lead in phase (CgLp)" and "Continuous Reset – Constant in gain – Lead in phase (CRCgLp)" and are typically used as an addition to a linear tracking controller [3]. In contrast to linear controllers, these elements are able to provide a lead in phase while having an almost constant gain. With linear controllers, Bode's phase gain relation for minimum phase systems states that a lead in phase always coincides with an increase in gain. Hence, if the robustness of the system has to be improved by for instance adding phase in the crossover region using a lead element, that also comes along with a decreased slope of the loop gain at the crossover frequency. This is not desired since a high gain at low frequencies and low gain at high frequencies with a steep crossover is desired for a proper tracking

performance, according to the loop shaping constraints. With the previously mentioned CgLp and CRCgLp elements, this increase in gain can be avoided. Therefore, this additional phase can be used to either increase the phase margin of the system while maintaining a similar tracking performance or to increase the loop gain of the system compared to the linear case without affecting the stability margins according to the describing function (DF) analysis.

There are various methods for analyzing reset control systems or in general nonlinear controllers in the frequency domain. However, to make them an appropiate choice for industrial applications, the tuning and optimization process should be intuitive and take as little time as possible. One of the most well known methods is DF analysis of the reset control system which is based on the first order Fourier series expansion of the elements output [4]. Even though higher order harmonics of the signal are neglected with this approach, it can deliver an accurate estimation of the performance of the system, when it is ensured that these higher order harmonics are low enough in magnitude. This paper validates this approach using a single degree of freedom nanopositioning system. The CgLp and CRCgLp element based control structures are adjusted manually to ensure that the mentioned higher order harmonics are low enough in magnitude and the remaining parts of the linear control structure is optimized using the closed loop frequency response of the system. For a fair comparison, the reset controller based structures are also compared to the optimized linear controllers in terms of closed loop bandwidth, steady-state tracking performance and disturbance rejection capabilities.

Section 2 of this paper introduces the reset control fundamentals including an overview of the CgLp and CRCgLp elements. In section 3, the linear control structure is introduced. The tuning and optimization procedure as well as the results are shown and compared in section 4. Finally, section 5 concludes the paper and gives recommendations for future work.

2. Reset Control

This section introduces the relevant reset control essentials ranging from the basic state-space description of the reset controllers to the relevant frequency domain analysis tools. The general state-space description of the most basic reset element is given by [4]:

$$\begin{cases} \dot{\vec{x_r}}(t) = A_r \vec{x_r}(t) + B_r e(t) & \text{if } e(t) \neq 0 \\ \vec{x_r}(t^+) = A_\rho \vec{x_r}(t) & \text{if } e(t) = 0 \\ u(t) = C_r \vec{x_r}(t) + D_r e(t), \end{cases}$$

where A_r, B_r, C_r and D_r are the base-linear state-space matrices of the reset control system and A_ρ is the so called reset matrix which determines the portion of reset and is given by:

$$A_\rho = \begin{bmatrix} A_{\rho_r} & 0 \\ 0 & I \end{bmatrix},$$

with $A_{\rho_r} = diag(\gamma_1, \gamma_2, \dots, \gamma_{n_r})$ and $\gamma_i \in [-1, 1]$ being the resetting part of the reset matrix. The identity matrix can hence be used for states that should not reset. When looking at the state-space description above, it can be seen that a γ-value of zero represents a full reset of the state and that negative values even negate the states.

In figure 1, the output of this general reset element is shown as well as the first order Describing Function. Here, the clear advantage of the reset control element can be seen by taking a look at the phase difference between the input and output signal, which in this case is in fact only -38° instead of the -90° of the standard linear integrator.
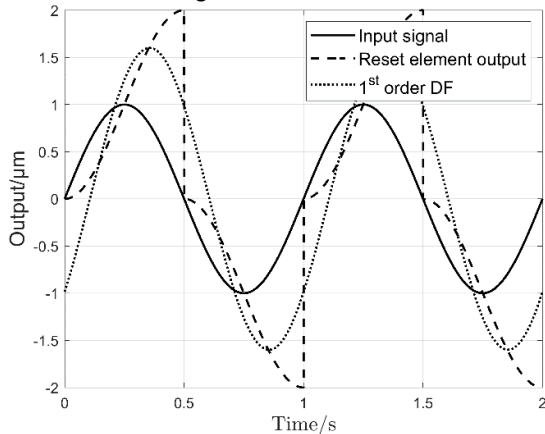

Figure 1. Output of a general reset element and the 1st order Describing Function of the output

The set of equations to analytically calculate the first order describing function and the higher order harmonics of the output is given in [4]. As already mentioned, these higher order harmonics are generally not desired, especially in the low frequency region. There are also other methods for analyzing reset control systems in the frequency domain such as the so called pseudo-sensitivity method [2]. Whereas these methods are considered to be more accurate than the DF-based analysis, the calcution requires significantly more time and hence limits their industrial applicability. In addition to that, the reset control system can be designed such that the DF-based analysis delivers an accurate estimation of the frequency response.

To make use of the phase advantages of the reset controller only in the approppriate frequency range, which is typically the open loop crossover region, the CgLp and CRCgLp elements have been introduced.

An overview of the CgLp and CRCgLp elements can be seen in figure 2.
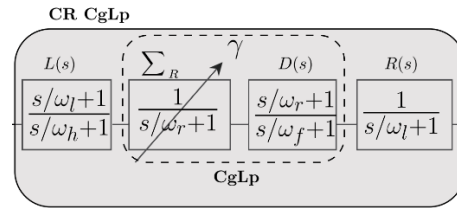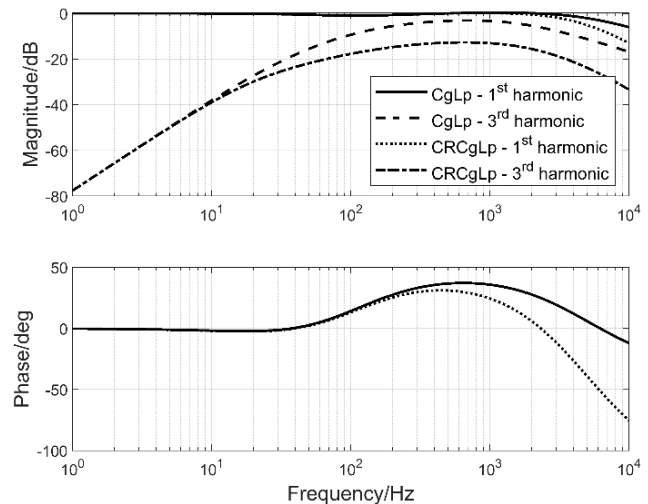

Figure 2. Structure of the CgLp and CRCgLp elements [3] (The arrow indicates the output of the filter reset to γ)

The CgLp element consists of a so called "First order reset element (FORE)" [5] which is essentially the nonlinear equivalent of a linear first order lowpass filter [4]. Similar to the previously introduced reset integrator, this element shows a reduced phase lag. In addition to that, a lead filter is located behind this FORE element. The advantage of this combination is that the gains of these elements almost exactly cancel but due to the reduced phase lag, a total lead in phase is obtained, which can not be achieved with linear controllers. The CRCgLp element contains an additional lead filter in front of the CgLp element and a lag filter behind it. Due to the lag filter behind the reset element, the influence of the higher order harmonics can be reduced compared the CgLp element. In addition to that, the lead filter changes the reset condition to [4]:

$$\frac{\dot{e}(t)}{\omega_l} + e(t) = 0$$

The lead and lag filters do not influence the DF of the open loop if $\omega_h \gg \omega_r$ and $\omega_h \gg \omega_c$. Another interesting property of this lead element is that a reduction of the ratio ω_l/ω_c decreases the overshoot of the system, which can be used to optimize the transient response of the system. However, a reduction of this ratio also leads to a longer settling time.

Figure 3. High Order Sinusoidal Inout Describing function (HOSIDF) comparison between a CgLp and CRCgLp element.

Figure 3 shows the frequency response of the 1st and 3rd order harmonics of an example CgLp and CRCgLp element. The constant gain of the two elements can clearly be seen up until a frequency which is far above the desired control bandwidth. Similarly, the additional phase lead of the elements is visible which starts approximately at the frequency ω_r. When taking a look at the magnitude of the 3rd order harmonics, it can be seen

that the magnitude is significantly lower for the CRCgLp element due to the additional lag filter after the CgLp element.

3. Linear control structure

As already mentioned before, the CgLp and CRCgLp structures are typically used as an addition to the linear control structure. For the tracking controller, a proportional-integral (PI) controller has been used with an integrator cut-off well before the crossover frequency. This prevents the phase lag of the integrator from influencing the phase in the crossover region.

To effectively attenuate the resonance frequency of the system, an active damping control scheme has been implemented. Therefore, a Positive Position Feedback (PPF) controller has been used, which is given by [6]:

$$C_{\mathrm{ppf}}(s) = \frac{\Gamma}{s^2 + 2\zeta_{\mathrm{d}}\omega_{\mathrm{d}}s + \omega_{\mathrm{d}}^2}$$

where Γ is the gain of the PPF controller, ζ_{d} the damping ratio and ω_{d} is cut-off frequency. An overview of the complete control scheme can be seen in figure 4.
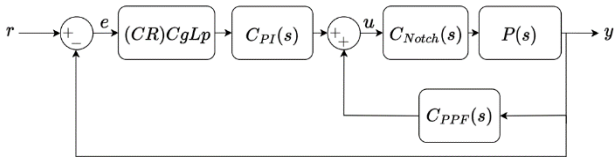

Figure 4. Overview of the control structure.

During initial optimizations it has been observed that the PPF damping controller was not sufficient to effectively dampen higher frequency resonance modes. Hence, a notch filter has been used in the inner loop as well.

4. Results

The results obtained with a single degree of freedom piezo actuator will be shown in this section. This includes an introduction to the system as well as the optimization algorithm that has been used to tune the controllers.

4.1. Plant model

The piezo actuator that has been used in this work has multiple weakly damped resonance frequencies ranging from 125 Hz to 350 Hz. The frequency response measurement (solid line) as well as the frequency response of an identified model of the system (dashed line) can be seen in figure 5.
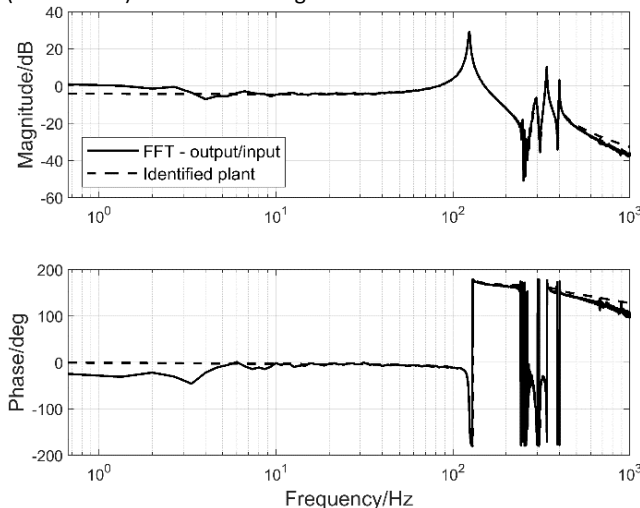

Figure 5. Frequency response of the measured and identified system

4.2. Optimization algorithm

To optimize the control structure in the frequency domain, a Particle Swarm Optimization (PSO) algorithm has been used [7]. The cost function that has been used is based on the closed loop frequency response of the system and is given by:

$$J_{\mathrm{T}} = \int_{\omega_{\mathrm{min}}}^{\omega_{\mathrm{max}}} W(\omega)\big||T(j\omega)| - |T_{\mathrm{ideal}}(j\omega)|\big|d\omega$$

where $T(j\omega)$ is the complementary sensitivity function obtained with the parameter set and $T_{\mathrm{ideal}}(j\omega)$ is a targeted closed loop frequency response that is set beforehand. The frequency dependent weighting function $W(\omega)$ has been set to:

$$W(\omega) = \frac{1}{\sqrt[4]{\omega}}$$

to ensure that low frequency deviations of the complementary sensitivity function are penalized more than high frequency ones.

Furthermore, a constraint for the sensitivity function has been implemented which is essentially just an upper limit for the sensitivities. Since the peak sensitivity is a measure for the robustness of the system, this parameter could be adjusted according to the desired robustness properties of the system. In this work a peak sensitivity of 3.5 dB has been used.

To evaluate the stability of the systems during the optimizations, the so-called Nyquist Stability Vector [8] has been used. To reduce the required time for the optimization, the stability has been checked first, such that the cost function has only been evaluated for stable systems.

4.3. Measurement results

For a fair comparison, the control structure which is solely based on the linear PI and PPF controllers is optimized as well using the PSO algorithm. To evaluate the performance of the optimized controllers in terms of closed loop bandwidth, steady-state tracking performance and disturbance rejection capabilities, the system has been excited by sinusoidal inputs for frequencies between 1 Hz and 1 kHz and the steady-state inputs and outputs have been recorded. To ensure that the higher order harmonics introduced by the reset controller are significantly lower in magnitude than the first harmonic, such that the DF analysis delivers an accurate analysis of the frequency response, the reset control parameters have been fixed and tuned prior to the optimization. Since it could be expected that higher open loop crossover frequencies can be achieved with the CgLp and CRCgLp elements, ω_r has been set to 100 Hz, which is slightly larger than the achievable crossover for the linear control structure only. This frequency determines the start of the phase lead which is desirable in the crossover region of the system. The reset parameter has been set to $\gamma = 0.4$ for the CgLp element and $\gamma = 0.15$ for the CRCgLp. The lower value for the CRCgLp element is possible since higher order harmonics are further reduced to the additional lag filter behind the CgLp element. The two taming pole frequencies have been set to $\omega_f = \omega_h = 2\pi/(10T_s)$ such that they do not interfere with the relevant dynamics. The cut-off frequency of the lead and lag filter ω_l when using the CRCgLp element has been set to 60 Hz. Hence, the only parameters left to optimize using the PSO algorithm were the PI control and PPF controller parameters: Γ, ζ_{d}, ω_{d}, k_{p} and ω_{i}.

Figure 6 shows the closed loop response comparison of the steady-state outputs of the systems for the linear controllers only (PI-PPF) and the CgLp and CRCgLp controller-based structures. The CgLp and CRCgLp controllers significantly outperform the linear control structure in terms of the achieved closed loop bandwidths of the systems.

In figure 7 the steady-state peak to peak error values for the chosen frequency range is shown for the three control structures which is essentially the sensitivity response of the systems. The lower sensitivity in the low frequency region indicates a superior steady-state tracking performance of the CgLp and CRCgLp based control structures compared to the linear structure. This is due to the higher loop gains that could be achieved because of the additional phase the reset elements can provide. The higher loop gains also indicate an improved disturbance rejection capability of the reset controller-based systems.
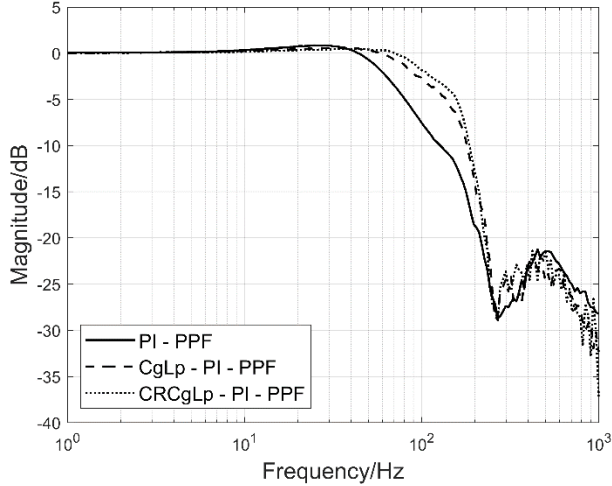

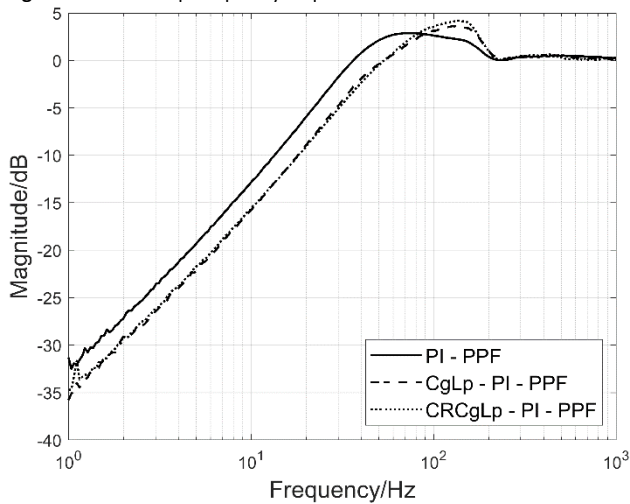**Figure 6.** Closed loop frequency response of the three controllers.

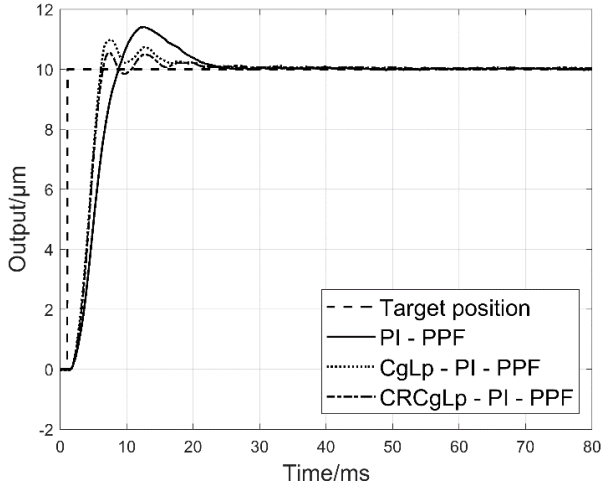**Figure 7.** Sensitivity comparison of the three controllers.

Figure 8. Step response comparison of the three controllers.

A step response comparison for the three control structures can be seen in figure 8. The higher loop gains and crossover frequencies of the two reset controller optimization results can clearly be seen in the reduced rise time of the response. In addition to that the overshoot of the CgLp and CRCgLp structures is reduced compared to the linear control structure only and could be reduced to 5 % for the CRCgLp based controller.

5. Conclusion

In this paper, a DF analysis based frequency domain optimization method has been investigated for the usage with a single degree of freedom nanopositioning stage. The reset control parameters have been tuned prior to the optimization process to ensure the exclusive use of the DF analysis of the system delivers an accurate estimation of the system's frequency response and to reduce the required time for time for the optimization algorithm to converge. The results have shown a significant improvement of the closed loop bandwidth, the steady-state tracking performance and disturbance rejection capabilities of the systems based on the CgLp and CRCgLp elements. The closed loop bandwidth of the system with the CRCgLp element has improved by 60 % and the overshoot in the step response was kept below 5 %.

Given the current customer demands of higher closed loop bandwidths and an improved steady-state tracking performance and disturbance rejection capabilities, linear control reaches its limits at some point. This paper has shown that reset control can help to overcome these limitations using a DF-based analysis of the system. Due to the optimization in the frequency domain, not much time is required for the algorithm to converge, which makes it a promising procedure for industrial usage. Further research could investigate an improvement of the linear control structure which does not require the usage of the additional notch filter. In addition to that, more intuitive design methods for the initial design of the linear controller could be developed.

References

[1]   D. Russel, A. San-Millan, V.Feliu and S. S. Aphale, "Butterworth pattern-based simultanuous damping and tracking controller design for nanopositioning systems," 2015 European Control Conference (ECC), vol.2, 2016.

[2]   A. A. Dastjerdi, K. Heinen, and S. H. HosseinNia, "A frequency-domain tuning method for a class of reset control systems," IEEE Access, vol.9, pp. 40950-40962, 2021.

[3]   N. Karbasizadeh and S. H. HosseinNia, "Continuous reset element: Transient and steady-state analysis for precision motion systems," Control Engineering Practice, vol. 126, p. 105232, 2023.

[4]   N. Saikumar, K. Heinen, and S. H. HosseinNia, „Loop-shaping for reset control systems," Control Engineering Practice, vol. 111, p. 104808, 2021.

[5]   L Zaccarian, D Nesic, AR Teel, First order reset elements and the Clegg integrator revisited, Proceedings of the 2005, American Control Conference, 2005., 563-568

[6]   R. Moon, A. San-Millan, M. Aleyaasin, V. Feliu, and S. Aphale, "Selection of positive position feedback controllers for damping and precision positioning applications," Communications in Computer and Information Science, pp. 289-301, 2017.

[7]   J. M. Shashank, Nature-inspired optimization algorithms with Java: A look at optimization techniques. Apress, 2022.

[8]   A. A. Dastjerdi, A. Astolfi, and S. H. HosseinNia, "Frequency-domain stability methods for reset control systems," Automatica, vol. 148, p. 110737, 2023.

Development of flexure-based moving reflector with voice coil motor for the optical gas imaging

Ho Sang Kim[1#], Jin Woo Kim[1], Dong Chan Lee[1], Yong Kwon Moon[2], Hyo Wook Bae[2], Do Hyun Park[2]

[1]*Institute for Advanced Engineering, 175-28, Goan-ri 51 beon-gil, Yongin-si, Gyeonggi-do, 17180, South Korea*
[2]*MOORI Technologies, 909, 42 Changeop-ro, Sujeong-gu, Seongnam-si, Gyeonggi-do, 13449, South Korea*

[#] *Submitting Author / Email: hoskim@iae.re.kr, TEL: +82-31-330-7332*

Abstract

The moving reflector is a key component of the multi-species gas detection in the optical gas imaging device which can serve a repetitive high-speed moving function in the spectroscopic sensor. In particular, it is very important to stably acquire a spectral signal by generating a linear motion of the moving reflector assembly as precise as possible. In addition, by miniaturizing a bulky element in an interferometer, it can have many advantages in portability. In this study, a moving reflector for an optical gas imaging device capable of detecting various harmful gases at a distance was manufactured and performance tests were performed. A moving reflector that satisfies the requirements of the spectroscopic sensor in the optical gas imaging device was manufactured using a voice coil motor and a flexure mechanism. The fabricated flexure mechanism is installed on both sides of the drive unit to realize the requirement of the stroke in the direction of the optical axis and to constrain the movement in the radial direction. A prototype was fabricated through precision machining technique and its performance was tested. The experimental test result shows that the flexure-based moving reflector is capable of motion with its stroke of 0.974 mm and 0.5 Hz. Therefore, optical testing result shows that the proposed flexure-based moving reflector can be applied to the actual spectroscopic interferometer in the future.

Keywords: Moving reflector, Flexure, Voice coil motor, optical gas imaging

1. Introduction

The spectroscopic sensor has been widely used for gas monitoring at a distance and Michelson interferometer unit among the components that make up this spectroscopic sensor plays most important role for the multi-species gas detection. Especially, inside the Michelson interferometer unit, the light path difference between two divided beams which are reflected by a fixed and a moving mirror respectively, is very important for precise detection of various several gases [1,2]. In most cases, the optical path difference is generated by precision electromagnetic actuators which can produce a linear repeated motion of several millimetres and nearly flat motion profile [3]. However, the optical path generated by these actuators can be distorted due to the product assembly and other environmental errors which can occur in the mechanical actuation unit guided by bearing components. Also, because of the portability of the spectroscopic sensors, smaller electromagnetic actuators are increasingly being demanded in industrial settings.

In this study, a flexure-based moving reflector with voice coil motor for the gas imaging was designed and fabricated, and a performance test was conducted. A flexure-based moving reflector that can satisfy the required specifications of the spectroscopic sensor was manufactured using voice coil motor and flexure spring with pantograph pattern. By finite element method, these specifications were reviewed in advance whether the proposed flexure-based moving reflector can meet the required specifications or not, for example, the moving distance and yield condition, etc. Also, after fabrication, the performance of the proposed flexure-based moving reflector has been

verified in the optical test bench. Especially, for the portability of the spectroscopic sensors, the mechanical structure with small-sized voice coil motor and flexure spring, were proposed. Also, in order to verify the possibility to an actual spectroscopic sensor, its moving distance and tilting error were measured in the optical test bench by measuring the amount of deviation using an autocollimator.

2. Design and testing of flexure-based moving reflector

2.1. Design and manufacture

Our moving reflector assembly is applied to the Michelson type interferometer unit in the spectroscopic sensor as shown in figure 1. Example of the interferometer unit is shown in this photograph. In this interferometer unit, there are several components including moving reflector assembly, fixed mirror assembly, interferometer housing, beam splitter, etc. Among these components, moving reflector assembly performs the function of receiving the incident light from the external environment and reflecting the light to the beam splitter. Meanwhile, fixed mirror can perform the function of reflecting the light in the same way along the other optical path. These optical path difference between these two lights are essential for the precise detection of several gases. Here, moving reflector assembly should make very linear motion along the optical axis and as precise as possible. But this device can have a motion error and this is due to product assembly and other environmental errors. In order to overcome these difficulties, by introducing flexure-based moving reflector, it is possible to prevent the performance degradation and secure the alignment

of actual spectral sensor. Also, the user wants to handle the spectroscopic sensor easily, smaller moving reflector assembly should be designed.
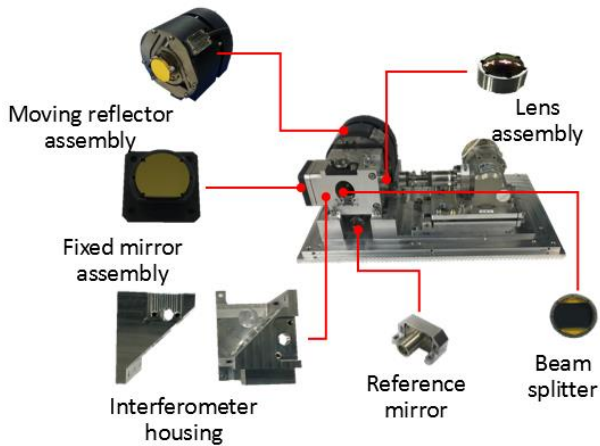

Figure 1. Optical components of Michelson interferometer unit

The moving reflector assembly has several design specifications including moving distance, dimensions and tilting error, etc. It should be able to move at least ±0.5 mm and its tilting error should be below dozens of arcseconds. Also, size of the total assembly should be as small as possible for the portability of the spectroscopic sensor [4]. For these purposes, the moving reflector assembly in this study is equipped with flexure springs at both ends of the voice coil motor to supplement the linear motion. These flexure springs are installed on both sides of the shaft so that the voice coil motor can move in a straight line. Also, the moving distance of the reflector is determined by the thrust of the voice coil motor and the stiffness of the flexure spring. This pantograph flexure spring part with a diameter of 20.9 mm can secure a longer arm length compared to those of other shapes, so the axial stiffness can be designed to be very small. Also, it can bring about an advantage in manufacturing costs using mass production facilities [5,6].

Table 1. Design specifications of flexure-based moving reflector

Name	Items	Design specification
Moving reflector	Moving distance	±0.5 mm
	Dimensions	Ø20 mm X 2.5 mm (mirror)
	Tilting error	10 arcsecond
	Speed	0.5 Hz

Figure 2 shows the flexure-based moving reflector assembly that has been designed for the application of spectroscopic sensor considered in this investigation. The moving reflector holds a flat fused silica mirror with diameter of 20 mm and it is bonded on a mirror adapter guided with two flexure springs. We determined the dimensions of the flexure spring so that the moving reflector assembly can satisfy the design specification by reducing the axial stiffness. Also, we designed the flexure spring with higher lateral stiffness so that its motion should be as straight as possible in the optical axis by reducing the parasitic motion in the lateral direction. Before manufacture, the finite element analysis was performed to predict whether the proposed moving reflector assembly can meet the design specification. Figure 4(a) shows the deformation contour when the force of 1 N is applied in axial(y) direction. As in the analysis result, the axial stiffness is estimated to be 1.30 N/mm which is sufficiently enough to satisfy the design specification of ±0.5

mm. Similarly, figure 4(b) shows the deformation contour when the force of 1 N is applied in lateral(z) direction resulting in the lateral stiffness of 12.9 N/mm. Also, its maximum stress level of 269 MPa at 1 N can be estimated as shown in figure 4(c). Therefore, the stress level when the moving reflector assembly moves at ±0.5 mm is below the yield strength of the material. Also, for the portability as a spectroscopic sensor, the dimensions of flexure springs and other components of the moving reflector were designed as small as possible.
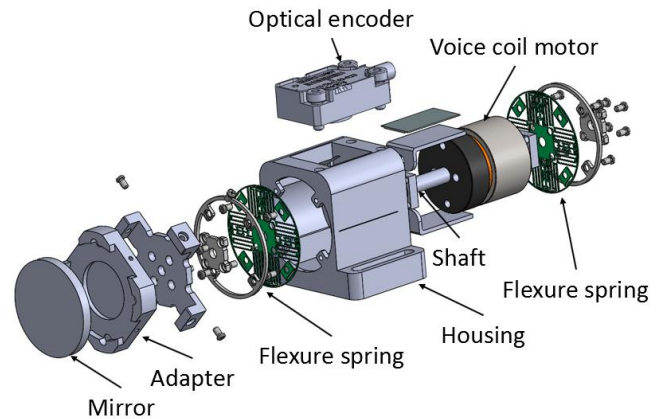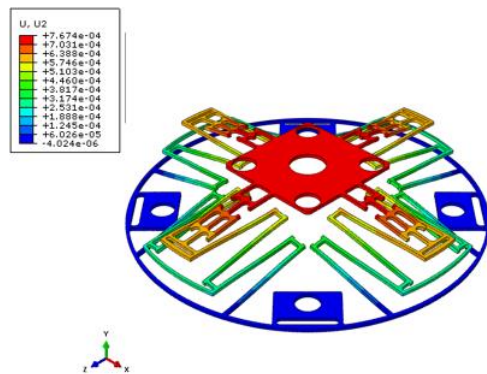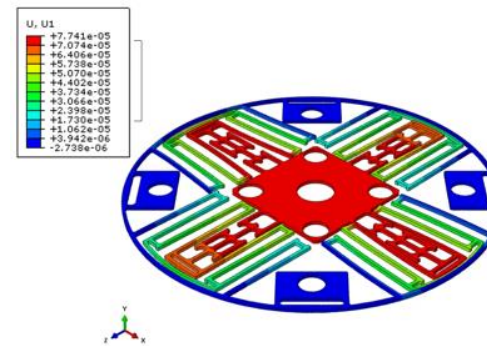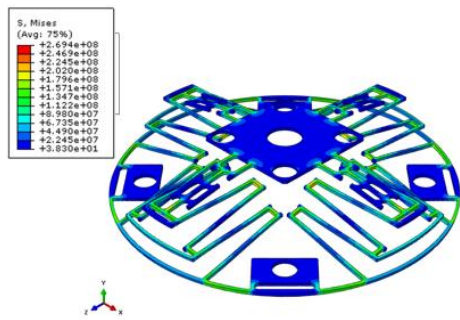

Figure 2. Solid drawings of flexure-based moving reflector assembly

(a) Deformation contour when the axial force of 0.24 N is applied at the center of the flexure

(b) Deformation contour when the lateral force of 1 N is applied at the center of the flexure

(c) Maximum stress contour when the axial force of 1 N is applied at the center of the flexure
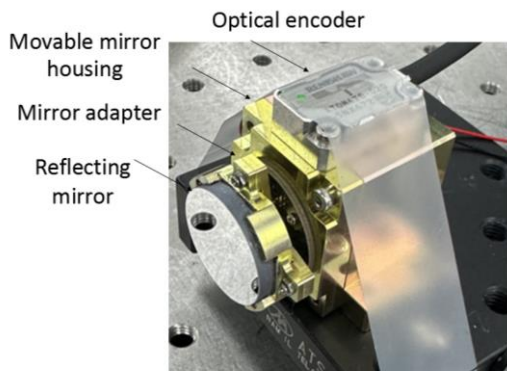
Figure 3. Proposed design of flexure-based moving reflector and deformation contour of the flexure when the mirror was moved

2.2. Testing

As shown in figure 4(a), the reflecting mirror is moved by voice coil motor with small circular cross-section, whose dimensions are 16x16mm. An optical encoder assembly with high resolution is installed within the moving reflector to measure the linear motion of the voice coil motor, which is subsequently closed loop controlled to compensate for the displacement error. As shown in figure 4(b), a prototype of flexure-based moving reflector was manufactured with a size of 30.9x31.7x30.1 mm, horizontal × vertical × length. It was built with titanium alloy (Grade 5) and the flexure spring was manufactured by wire electrical discharge machining technique. Figure 4(c) shows the photograph of the moving reflector assembly with prism element installed in the interferometer unit for spectroscopic sensor.
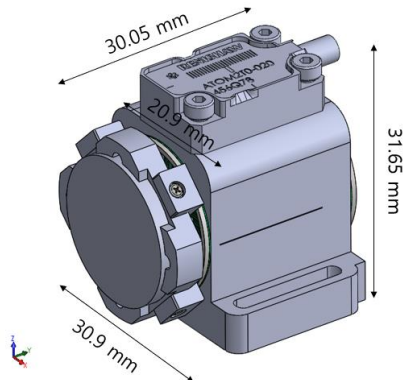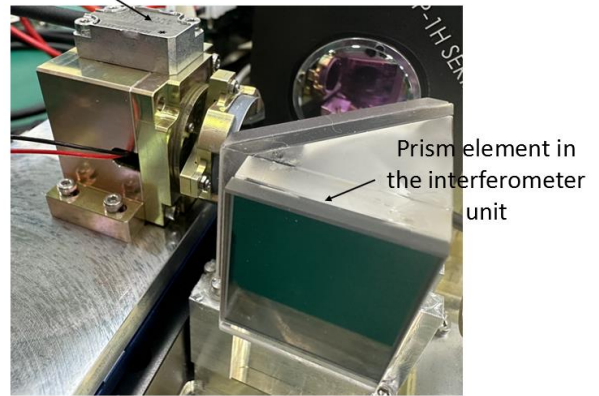

(a) Proposed design of flexure-based moving reflector

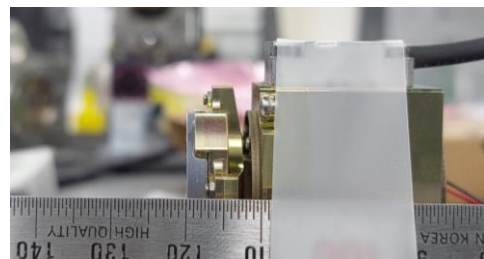(b) Flexure-based moving reflector manufactured for spectroscopic sensor

(c) Photograph of the moving reflector assembly installed in the interferometer unit

Figure 4. Proposed design and manufactured flexure-based moving reflector with prism element in the interferometer unit

To measure the moving distance of the proposed moving reflector assembly, driving test was performed as shown in figure 5(a). For a sinewave with amplitude of ±0.5 mm and frequency of 0.5 Hz, the moving reflector assembly can move back and forth and its moving distance can be measured by optical encoder mounted inside the assembly housing. As a result of driving test of the moving reflector, figure 5(b) shows that the moving distance was measured to be 0.974 mm at the frequency of 0.5 Hz. The measurement results that do not meet the design specifications are because the actual displacement did not reach the commanded value (±0.5 mm) during the closed-loop control process resulting in an error. In actual operation, these errors can be overcome by resetting the commanded values during actual operation.

Also, the tilting error of the moving reflector can be measured by applying the autocollimator as shown in the figure 5(c). When the moving reflector moves repeatedly with movement distance of 0.974 mm and frequency of 0.5 Hz, the tilting error was measured by aligning the moving reflector assembly and autocollimator. As a result of the measurement, tilting error of 30 arcsecond was obtained and shows that the proposed moving reflector can be applied to an actual spectroscopic sensor successfully by performing the additional alignment when installing the interferometer unit.

(a) Photograph of the driving test setup of flexure-based moving reflector
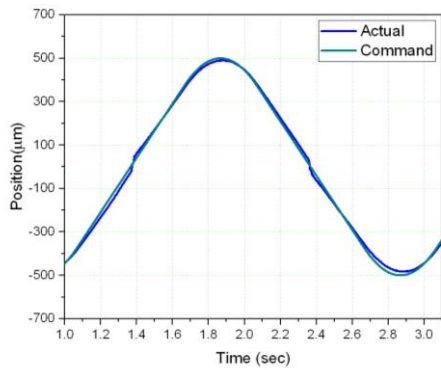
(b)　Repsonse of proposed moving reflector for a sinewave with amplitude of ±0.5 mm and frequency of 0.5 Hz
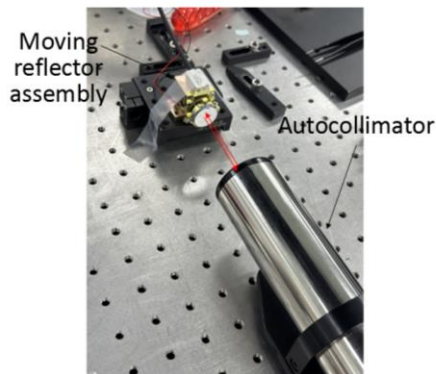
(c) Photograph of experimental setup for measurement of straightness by autocollimator

Figure 5. Driving test of proposed moving reflector for a sinewave with amplitude of ±0.5 mm and frequency of 0.5 Hz and photograph of experimental setup for measurement of straightness by autocollimator

3. Conclusions

We designed and manufactured a flexure-based moving reflector in a spectroscopic sensor for optical gas imaging. It is composed of a voice coil motor and flexure springs that generate the axial displacement which is required for the optical path length in the interferometer unit. Also, to minimize the tilting errors, two mechanical flexure springs which can reduce the lateral displacement were installed at both ends. Also, the several dimensions of flexure springs were examined advance by finite element analysis in advance. As a result of the performance test, axial displacement of 0.974 mm was measured at the driving frequency of 0.5 Hz. Also, the moving reflector assembly can move with tilting error of 30 arcsecond by autocollimator. This measurement shows that proposed moving reflector assembly can be applied to an actual spectroscopic sensor successfully.

Acknowledgement

References

[1]　Nelsson C, Lundberg, F, Nilsson, P and Mattias M *Proc. SPIE*, **4029** 324-336
[2]　Beil A, Daum R, Harig R and Matz G *Proc. SPIE*, **3493** 32-43
[3]　Thilo S, Thomas G, Eric G, Harald S and Andreas K, J. of Microlithography, Microfabrication and Microsystems. 13. 011115
[4]　Kim J, Lee D, Kim H, *Heliyon*, **9**, e22560
[5]　Bae H, Jang H, Park D, and Kim H, *J. Korean Soc. Precis. Eng.*, **38**, 581-587
[6]　Lee J, Kim H, Kim J, Nam H, Kang Y, et al., *Optical Engineering*, **57**, 084105

Measurement of workpiece deformation based on a sensory chuck

Berend Denkena[1], Heinrich Klemme[1], Eike Wnendt[1]

[1]Leibniz University Hannover, Institute of Production Engineering and Machine Tools

wnendt@ifw.uni-hannover.de

Abstract

Achieving tight tolerances is a challenging problem encountered during turning of thin-walled workpieces. Due to the low stiffness of thin-walled workpieces, inadequate workpiece deformation can occur even when clamping forces are low. Therefore, the workpiece deformation needs to be precisely controlled. Conventional approaches use additional measuring devices (e.g. a touch probe) to measure the workpiece deformation. Afterwards, the clamping force is adjusted accordingly in an iterative, manual process step resulting in non-productive time. To ensure low workpiece deformation and reduce non-productive time, a chuck is required which combines workpiece deformation measurement and automatic clamping force adjustment. Thus, this paper presents a novel method to measure workpiece deformation using a chuck with four integrated electric drives. The electric drives are used to precisely adjust the clamping force. Based on the measured clamping force, the workpiece deformation is calculated considering previously identified correlations between the clamping force and the workpiece deformation. To identify these correlations, workpieces with different ratios between inner to outer diameter are clamped and the resulting workpiece deformation is measured using a coordinate measuring machine. The new method allows to measure workpiece deformations within a tight tolerance grad of up to ISO 286 IT5.

Keywords: Sensory chuck, thin-walled workpieces, deformation, precision clamping

1. Introduction

Precision turning of thin-walled workpieces such as bearings, tubes or hollow shafts is of key importance in aerospace, automotive and medical applications [1, 2]. The system to clamp the workpiece has a significant influence on the achievable machining accuracy [3]. To ensure high machining accuracy, clamping systems with special designs, e.g. floating jaws, collet or diaphragm chucks were developed [4, 5]. However, these clamping systems are only suitable for certain workpiece diameters or manufacturing processes. In contrast, the most commonly used clamping device in turning are chucks with three or four jaws [3]. Jaw-chucks allow an adaptable clamping of different workpiece diameters. Therefore, jaw-chucks are universally used for turning. However, the clamping forces of the jaws applied to a thin-walled and thus elastic workpiece lead to shape deformation (Fig. 1) even when clamping forces are low [7].
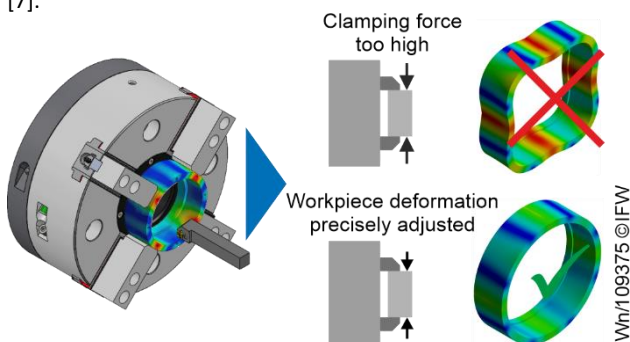
Figure 1. Workpiece deformation caused by clamping force

For jaw-chucks, the workpiece deformation needs to be determined in order to adjust the clamping force if necessary. Conventional approaches measure the workpiece deformation directly by a contact measurement device (e.g. a touch probe or dial test indicator) [8]. In addition, systems for contactless measurement of workpiece deformation have been developed [9-11]. Furthermore, methods to indirectly measure workpiece deformation based on FE-simulations or analytical calculations have been proposed [12]. In this context, Sergeev et al. proposed an algorithm to adjust the appropriate clamping force by an external clamping cylinder [13]. However, due to losses in the force transmission between cylinder and chuck, high clamping force errors and thus shape deviations of 12-15% occur.

In summary, the deformation determination and clamping force adjustment is typically performed manually in an iterative and thus time-consuming process step. For this reason, a novel chuck is presented in this paper, which combines workpiece deformation measurement and automatic clamping force adjustment. The design of the chuck and the concept to measure workpiece deformation are explained in section 2. In section 3, the achievable workpiece deformation measurement accuracy is analysed.

2. Sensory chuck for thin-walled workpieces

In this section, the design of the sensory chuck is described in section 2.1. Afterwards, the concept to measure and control workpiece deformation is explained in section 2.2.

2.1. Sensory chuck design

The design of the sensory chuck is shown in Fig. 2. It is composed of two different modules: A standard four-jaw-chuck VT-S031 from HWR Spanntechnik GmbH and a module with four electrical actuator units. A four-jaw chuck is capable of clamping cylindrical, prismatic as well as irregularly shaped workpieces. This is achieved by a balancing clamping mechanism. The

clamping mechanism ensures that the clamping force F_{cl} is only applied on the workpiece once there is contact on all four clamping jaws. To apply the clamping force, the actuation force F_{act} is required. Therefore, four electrical actuator units are integrated into the chuck. Each of the four actuator units consists of a leadscrew and a FHA-14C gear motor from Harmonic Drive SE. The leadscrew allows the transmission of rotational movement of the motor into a linear positioning movement required to actuate the four-jaw-chuck. The leadscrews are mechanically connected in parallel via a coupling element to transmit the actuating force F_{act}.
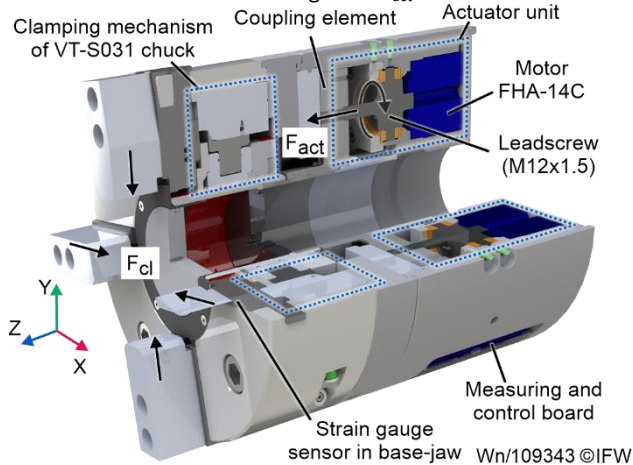

Figure 2. Sensory chuck design

A total of four EJ7411 measuring and control boards from Beckhoff Automation GmbH & Co. KG are integrated into the chuck. Each EJ7411-module can measure and control the drive signals (motor current I_m, angular position p) in a closed feedback loop. Furthermore, a strain gauge sensor of type N2A-06-S1783 from ME-Meßsysteme GmbH is integrated into the base-jaw to measure the clamping force. The EJ7411-modules as well as the strain gauge sensor are part of the measurement and control scheme for workpiece deformation as explained in the following section.

2.2. Concept to measure and control workpiece deformation

The concept to measure workpiece deformation is shown in Fig. 3. The concept is designed for thin-walled, ring-shaped workpieces.
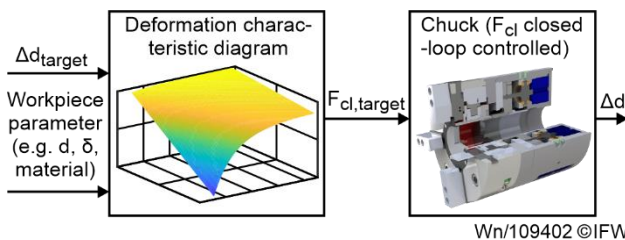

Figure 3. Concept to measure and control workpiece deformation

A linear-elastic workpiece deformation is assumed for the control system. The resulting workpiece deformation Δd correlate therefore linearly proportional to the applied clamping force F_{cl} and the stiffness of the workpiece. The workpiece stiffness is determined by material properties and the geometry of the workpiece. Such workpiece parameters (e.g. workpiece diameter d, diameter ratio δ or material) are provided by the chuck operator and serve as input variables for the deformation characteristic diagram. Based on a provided workpiece deformation tolerance Δd_{target}, the appropriate clamping force is calculated by the deformation characteristic diagram. The calculated clamping force $F_{cl,target}$ is then applied by the chuck in a closed-loop control. The system to measure and control the clamping force does already exist. As described in [14], a low

clamping force error of $\Delta F_{cl} = 1.4\%$ was achieved. In section 3, the deformation characteristic diagram is characterised.

3. Experimental setup and results

In this section, the experimental setup to obtain the deformation characteristic diagram is described in section 3.1. Afterwards, the results are discussed in section 3.2. In this paper, only the influence of geometry parameters on the characteristic diagram is investigated. The experiments were carried out for a total of nine workpiece samples made from the constant material 16MnCr5. Each workpiece sample represents a hollow cylinder with a cylinder height $h_Z = 60$ mm. The outer diameter d_o is varied between 80 mm and 120 mm, which is a typical workpiece diameter range for the chuck. The other geometry parameters are listed in Table 1. With the selected geometry parameters, the influence of varying geometry parameters (outer diameter d_o, inner diameter d_i, wall thickness s and diameter ratio δ) on the workpiece deformation measurement is analysed in the following chapters.

Table 1 Geometry parameters of the nine workpiece samples

No.	d_o	d_i	$s = (d_o-d_i)/2$	$\delta = d_o/d_i$
1	80 mm	52 mm	14 mm	1,53
2	80 mm	60 mm	10 mm	1,33
3	80 mm	64 mm	8 mm	1,25
4	100 mm	72 mm	14 mm	1,38
5	100 mm	80 mm	10 mm	1,25
6	100 mm	84 mm	8 mm	1,19
7	120 mm	92 mm	14 mm	1,30
8	120 mm	100 mm	10 mm	1,20
9	120 mm	104 mm	8 mm	1,15

3.1. Experimental setup to measure workpiece deformation

The experimental setup is shown in Fig. 4. A coordinate measuring machine was used to determine the contour of the inner surface along the Z-axis on the four clamping jaws.
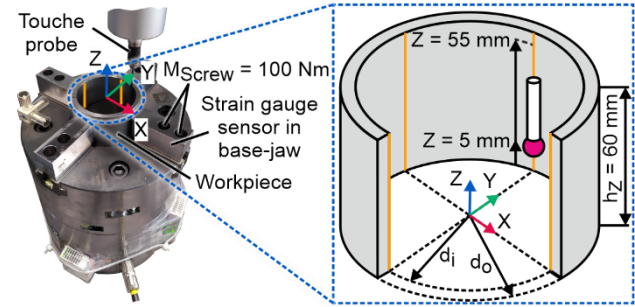
Parameter
Workpiece material 16MnCr5   Inner diameter $d_i = 54 ... 104$ mm
Touche probe Leitz X5HD-S   Outer diameter $d_o = 80 ... 120$ mm
Coordinate measuring machine Leitz Reference XI

Figure 4. Experimental setup to determine the deformation characteristic diagram

The workpiece contour along the four clamping jaws was measured with five repetitions. This process was repeated for ten clamping force steps (between minimum and maximum clamping force). In the first step, each workpiece sample was clamped with a minimal clamping force $F_{cl,min} \approx 250$ N. Up to the minimum clamping force, a rigid body displacement of the workpiece can occur due to movements of the clamping mechanism. The position of the workpiece can be assumed to be constant above the minimum clamping force. In addition, all nine workpieces are deformed by $\Delta d < 1$ μm at the minimum clamping force and therefore below the measuring accuracy of the coordinate measuring machine. The workpiece shape at the minimum clamping force is therefore used as an almost

undeformed reference state. The workpiece deformation is the difference between the inner surface area in the reference state and the inner surface area for the respective clamping force step.

3.2. Deformation characteristic diagram

The workpiece deformation measured along the four clamping jaws is shown as an example for workpiece sample 3 in Fig. 5. For each jaw, the workpiece deformation Δd is shown as the mean value from five measurements for a clamping force F_{cl} = 74 kN.

Parameter

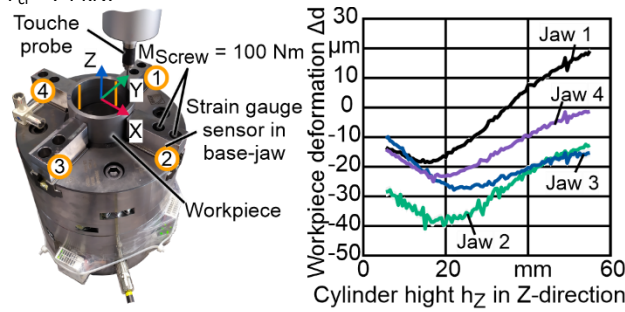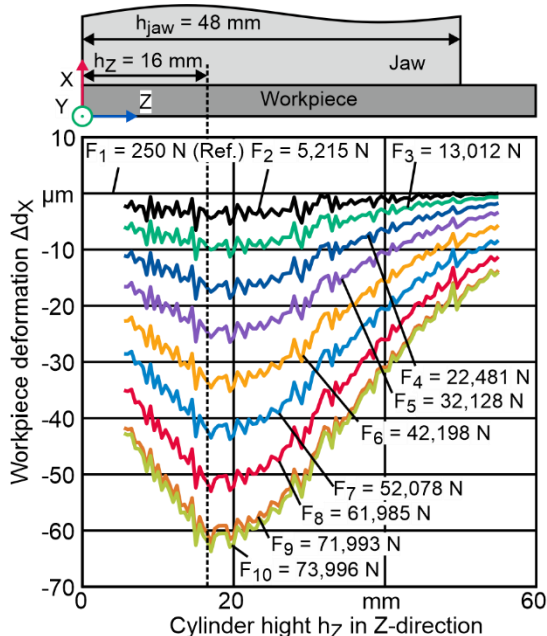|	
Workpiece material 16MnCr5	Inner diameter d_i = 64 mm
Touche probe Leitz X5HD-S	Outer diameter d_O = 80 mm
Coordinate measuring machine Leitz Reference XI	Wn/109404©IFW

Figure 5. Workpiece deformation of sample 3

The workpiece deformation varies depending on the clamping jaw. This is due to an uneven force distribution on the for four clamping jaws. In contrast, uniform deformation curves are achieved for the sum of the deformation on the opposing clamping jaws. The deformation sum for jaw 1 and jaw 3 is the workpiece deformation Δd_Y and the workpiece deformation Δd_X is the sum of jaw 2 and jaw 4. In Fig 6., the workpiece deformation in X-direction is shown. The curves for both the Y-direction and the other workpiece samples show a similar behaviour.


Parameter

Workpiece material 16MnCr5	Inner diameter d_i = 64 mm
Touche probe Leitz X5HD-S	Outer diameter d_O = 80 mm
Coordinate measuring machine Leitz Reference XI	Wn/109405©IFW

Figure 6. Workpiece deformation for sample 3 in X-direction

Due to the workpiece roughness, deformation peaks occur for every clamping force step at stochastically distributed cylinder heights. In addition, the deformation along the cylinder height occurs unevenly. This is due to the application point of the

clamping force, which is located at 1/3 of the total clamping jaw height h_{jaw} = 48 mm [15]. This corresponds to a cylinder height h_Z = 16 mm, at which the maximum deformation nearly occurs in both X and Y direction. The deformation maximum is key for the achievable manufacturing accuracy. The deformation maxima are therefore used for the deformation characteristic diagram. In addition, a single deformation characteristic diagram is needed for the proposed deformation control concept. Therefore, the deformation is combined as the mean value of the X and Y directions. The combined deformation maxima for all nine workpiece samples are shown for the clamping force $F_{cl,max}$ = 80 kN in Fig. 7. At a constant clamping force, there is a reciprocal correlation between the diameter ratio of the workpiece samples and the workpiece deformation. For the asymptote δ = 1 (infinite compliance of the workpiece), an infinitely high deformation occurs. For the asymptote δ = ∞ (infinite stiffness of the workpiece), only the chuck is deflected by Δd = 17 μm.
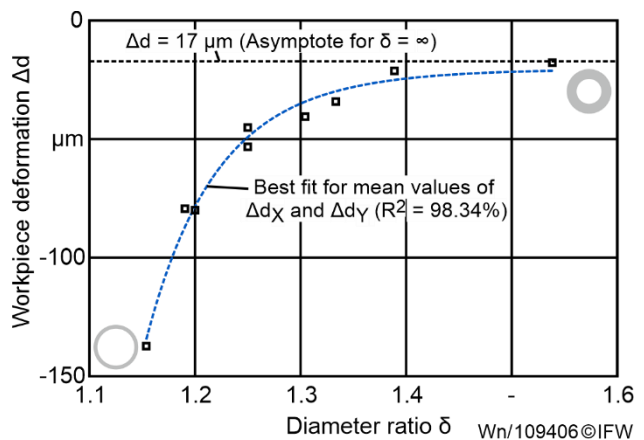
Figure 7. Correlation between diameter ratio and workpiece deformation for $F_{cl,max}$ = 80 kN

If the clamping force is varied (Fig. 8), a linear proportional correlation between the clamping force and the workpiece deformation can be observed.
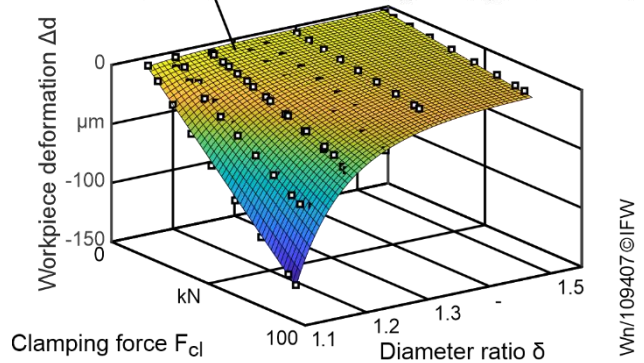
Figure 8. Deformation characteristic diagram

A low standard deviation occurs for each data point with a mean value of σ = 0.65 μm. The chuck can therefore achieve a very high repeatability. In addition, both the linear and the reciprocal correlation between the clamping force F_{cl}, the diameter ratio δ and the resulting workpiece deformation Δd can be approximated by equation (1).

$$\Delta d = (a + b \cdot F_{cl}) \cdot (c \cdot \delta^n + \delta)^2 \qquad (1)$$

a = -0.1858; b = -0.07932; c = 12.91; n = -9.109

Equation (1) approximates the deformation characteristic diagram with a high coefficient of determination of R^2 = 99.54%. To evaluate the accuracy of the deformation characteristic diagram, the difference between the characteristic diagram and the measured workpiece deformation was calculated (Fig. 9).
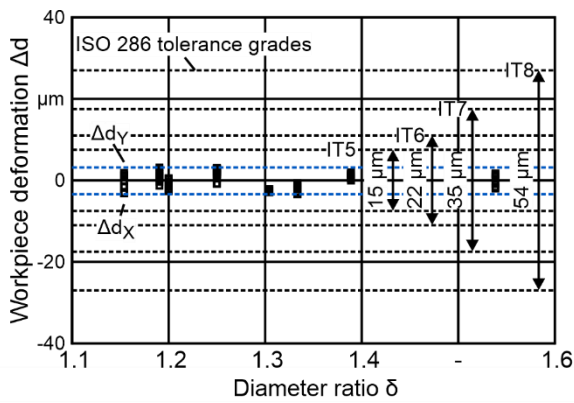
Figure 9. Accuracy of the deformation characteristic diagram

Overall, the characteristic diagram shows a deviation in the range of -3.4 µm to +3.16 µm to the measured deformations. In addition, typical target tolerances for turning according to ISO 286 are shown. The deviations are within a tolerance grade of IT5, which is a commonly used tolerance for precise turning. Consequently, the method for workpiece deformation measurement allows a precise measurement of workpiece deformation. However, the following possible influencing factors on the deformation characteristic diagram must be mentioned:

- The measurements were carried out while the chuck was at a standstill. According to [15], the clamping force varies significantly due to centrifugal forces during turning. Such influence has not yet been quantified.
- In Fig. 5, the deformations on the individual clamping jaws are uneven. This indicates a workpiece tilting due to an alignment error caused by the clamping mechanism. Alignment errors are minimized by jaw boring [16]. However, jaw boring was not performed to maintain identical jaws and thus a constant chuck stiffness.
- Concentricity errors of the workpiece samples occur of up to 194 µm. The influence of shape errors on the deformation characteristic diagram has not yet been quantified.
- An error of up to 2.5 kN occurs when measuring the clamping force with the integrated strain gauge sensor.

4. Conclusion

This paper presents a novel sensing chuck for determining workpiece deformation. The workpiece deformation is calculated considering previously identified correlations between the clamping force and the workpiece deformation. This correlation is approximated by a deformation characteristic diagram with a high coefficient of determination of $R^2 = 99.54\%$. The measurement deviations are within a tolerance grade of ISO 286 IT5, which is a commonly used tolerance for precise turning. Thus, future work aims to evaluate the machining tolerance achieved in cutting processes. In addition, further possible influences on the chuck accuracy (e.g. workpiece misalignment, centrifugal forces during turning) will be investigated.

Acknowledgements

References

[1] Brinksmeier E, Sölter J, Grote C 2007 Distortion engineering – identification of causes for dimensional and form deviations of bearing rings *CIRP Ann.* **56**(1) 109-112

[2] Viitala R 2020 Minimizing the bearing inner ring roundness error with installation shaft 3D grinding to reduce rotor subcritical response *CIRP J. of Manuf. Sci a. Tech.* **30** 140-148

[3] Fleischer J, Denkena B, Winfough B, Mori M 2006 Workpiece and tool handling in metal cutting machines *CIRP Ann.* **55**(2) 817-839

[4] Denkena B, Hülsemeyer L 2015 Investigation of a fine positioning method in lathes using an active clamping chuck *Euspen's 15th Int. Conf. & Exh.* 245-246

[5] Khaghani A, Cheng K 2020 Investigation on an innovative approach for clamping contact lens mould inserts in ultraprecision machining using an adaptive precision chuck and its application perspectives *Int. J. Adv. Manuf. Tech.* **111** 839-850

[6] Karpuschweski B, Byrne G, Denkena B, Oliveira J, Vereschaka A 2021 Machining Processes *Springer Handb. of Mech. Eng.* 409-460

[7] Estrems M, Carrero-Blanco J, Cumbicus W E, de Francisco O, Sánchez H T 2017 Contact mechanics applied to the machining of thin rings *Proc. Manuf.* **13** 655-662

[8] Valiño G., Suárez C M, Rico J C, Alvarez B J, Blanco B 2012 Comparison between a laser micrometer and a touch trigger probe for workpiece measurement on a CNC lathe *Adv. Mater. Res.* **498** 49-54

[9] Che J K, Ratnam M M 2020 Real-time monitoring of workpiece diameter during turning by vision method *Measurement* **126** 369-377

[10] Fan K C, Chao Y H 1991 In-process dimensional control of the workpiece during turning *Prec. Eng*. **13** (1) 27-32

[11] Kuschmierz R, Davids A, Metschke S, Löffler F, Bosse H, Czarske J, Fischer A 2016 Optical, in situ, three-dimensional, absolute shape measurements in CNC metal working lathes *Int. J. of Adv. Manuf. Tech.* **84** 2739-2749

[12] Manikandan H, Chandra Bera T 2021 Modelling of dimensional and geometric error prediction in turning of thin-walled components. *Prec. Eng*. **72** 382-396

[13] Sergeev A S, Tikhonova Z S, Krainev D V 2017 Automated thrust force calculation of machine tool actuators in fastening and turning steels *Proc. Eng.* **206** 1148-1154

[14] Denkena B, Klemme H, Wnendt E, Meier M 2022 Sensing chuck for thin-walled workpieces *19th Int. Conf. on Prec. Eng.*

[15] Association of German Engineers (VDI) 2004 VDI 3106 – Determination of permissible speed (rpm) of lathe chucks (jaw chucks) *VDI Standards*

[16] Byun J, Liu C 2012 Methods for improving chucking accuracy *J. of Manuf. Sci. and. Eng.* 134 (5)

Control waveform and frequency of an inchworm-type actuator using piezoelectric element

Hayata Takashima[1], Akihiro Torii[1], Suguru Mototani[1], Kae Doki[1]

[1]Aichi Institute of Technology, Japan

torii@aitech.ac.jp

Abstract

A control waveform and frequency of an inchworm-type actuator utilizing piezoelectric elements (piezos) are described. Linear and rotational displacements are generated by the rapid deformation of three piezos connected in an equilateral triangle on a horizontal plane. The inchworm-type actuator takes advantage of friction and inertial forces. The rapid deformation of two piezos produces a minute displacement based on the law of inertia. The piezos are driven by rectangular waveforms, with either two piezos extending and contracting simultaneously or one piezo extending while the other contracting. The repeated minute displacements achieve both linear and rotational displacement. The deformation of the piezo and the frequency of deformation vary the velocity of the inchworm. The velocity is proportional to the drive frequency, and a small voltage applied to the piezo reduces the displacement. These results contribute to the improvement of the inchworm-type actuator.

Inchworm, piezoelectric actuator, friction, inertia drive

1. Introduction

The goal of this project is to realize a long-travel stage without guide mechanisms. Conventional positioning components usually require guide mechanisms and typically have one degree-of-freedom (DOF). We have developed multi-DOF inchworm-type actuators (inchworms) using piezoelectric actuators (piezos) and electromagnets [1]. The inchworms are implemented in a compact manufacturing system that saves energy and materials. In contrast, rapid deformations of piezos are used in precise positioning [2]. The rapid deformation of the piezos can achieve step movements of several nanometers. In this paper, the inchworm's piezos are controlled by rectangle waveforms. Although nanopositioning stages are realized by sinusoidal waveform inputs and control circuit [3], the rectangular waveform is easily prepared by a microprocessor.

2. Inchworm

Figure 1(a) shows a photograph of an inchworm. An equilateral triangle is formed by three multi-layered piezos (AE0505D18F, TOKIN) inserted into holders. Three weights are attached to the apexes of the triangle, with each weight having a mass of 0.12 kg. Figure 1(b) illustrates the fundamental displacements of Weight A. When two piezos rapidly extend, Weight A moves perpendicular to Piezo a. When one piezo extends and the other contracts, Weight A moves parallel to Piezo a.

The motion principle of linear displacement is shown in Figure 2(a). Weight A moves according to the rapid extension of Piezo b and Piezo c, while the equivalent mass of Weight b and Weight c inside the broken rectangle is approximately twice of that of Weight A. The moving direction of Weight A is perpendicular to Piezo a. Subsequently, in sequence A(ii), Piezo c contracts and Piezo a extends simultaneously, causing Weight B to move in parallel with Piezo b. Next, Piezo b and Piezo a contract, resulting in Weight C moving perpendicular to Piezo c. This sequence tilts the angle of the inchworm. To counteract this, sequence B, where the contraction of the piezo is reversed, is introduced. Piezo b contracts first while Piezo a extends, and then Piezo c contracts wile Piezo a contracts. By repeating the two sequences of three intervals, the inchworm moves in Y-direction.

Figure 2(b) shows the motion principle of rotational displacement in counterclockwise (CCW) direction. One piezo extends and the other piezo contracts simultaneously. During the contraction of Piezo c and extension of Piezo a, Weight B moves parallel to Piezo b. As Piezo a contracts and Piezo b extends, Weight C moves parallel to Piezo c. Finally, when Piezo b contracts and Piezo c extends, Weight A moves in parallel with Piezo a. By repeating these three intervals, the inchworm moves in the CCW direction.
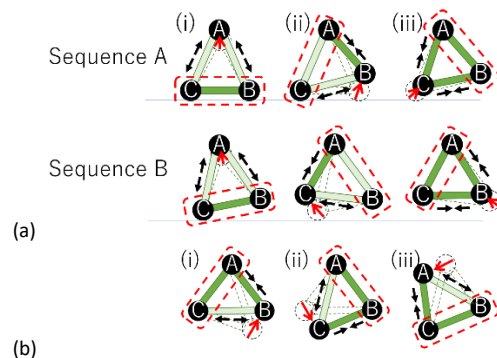

Figure 1. (a) Photograph and (b) illustration of inchworm-type actuator.

Figure 2. Motion principle of inchworm for (a) linear displacement in Y-direction, and (b) rotational displacement in CCW direction.

Figure 3(a) shows the waveforms for linear motion. In Squence A(ii), Piezo c contracts and Pieozo a extends. Then in A(iii), Piezo a and Piezo b contract. In Sequence B(ii), Piezo b contracts first, and then Piezo c contracts in B(iii). Repeating these two sequences makes the inchworm actuator move in the linear displacement. Figure 3(b) shows the waveforms for rotational displacement. One piezo contracts and other pipezo extends, simultaneously. The control waveforms of the rotational displacement consist of three intervals.
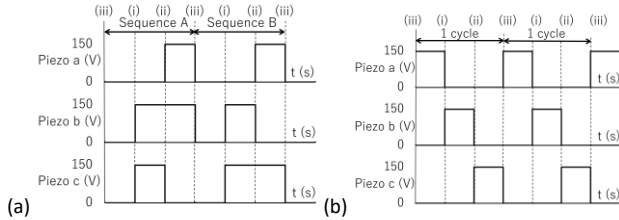

Figure 3. Control waveforms for (a) linear displacement in Y-direction, and (b) rotational displacemt in CCW direction.

3. Experiment

Control signals are generated by a microprocessor, and applied to the piezos through an amplifier. The control waveform is on/off signal with 150 V. The control frequency is from 1 Hz to 100 Hz. Voltages of 100 V and 50 V are used to realize small displacements. The position of the inchworm in Y-direction is defined by the position of Weight A. The rotational displacement of the inchworm is defined by X-displacement of weight A divied by the radius of the inchworm, 88 mm. Displacement is measured with a laser displacement meter (Keyence, LK-G5000 series). The inchworm repeats a constant displacement, and therefore an open-loop control is used.

4. Results and discussion

Figure 4(a) shows the linear displacements at 1 Hz. One step displacement is approximately 15 μm which agrees with the rapid deformation of the piezos. However, a drawback of approximately 11 μm is observed, resulting in a total displacement is 4 μm. Figure 4(b) shows the displacement at 90 Hz. The displacement for two cycles is 14 μm. These results indicate the drawback caused by the inertia of the inchworm changes the displacement per cycle. Since the inset of Figure 4(b) does not display any rectangular waveforms, the maximum frequency based on this principle would be a few hundred Hz.
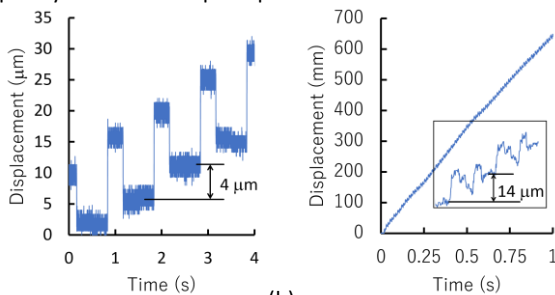
(a)   (b)
Figure 4. Linear displacement at (a) 1 Hz and (b) 90 Hz.

The displacement per cycle and the velocity are summarized in Figure 5. In principle, the displacement per cycle is constant. However, it slightly changes as the frequency varies. Under our experimental conditions, the vibration amplitude of the inchworm fluctuates, and this variation in vibration causes fluctuations in the one-cycle displacement. The velocity of the inchworm is mostly proportional to the drive frequency.
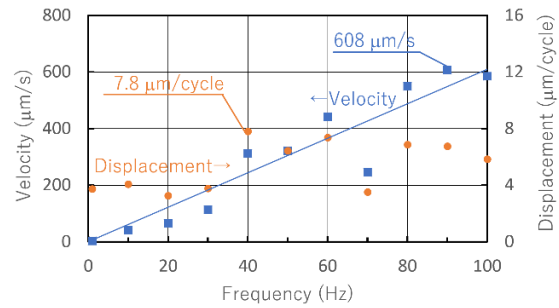
Figure 5. Displacement and velocity of inchworm.

The voltage of the rectangle waveform influences the step displacement. Figure 6 shows the results obtained by three different voltages; 150 V, 100 V, and 50 V. A lower voltage results in a reduced displacement.
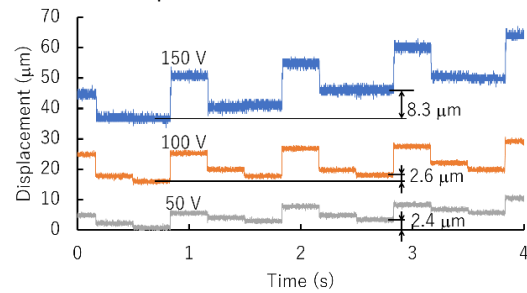
Figure 6. Displacement with 150 V, 100 V, and 50 V.

Figure 7 shows the rotational displacements at 1 Hz and 90 Hz. The rectangle waveforms applied to the piezos can achieve the rotational displacement of the inchworm actuator. Due to the law of inertia, a drawback occurs; however, the drawback is smaller than the displacement in the designed direction.
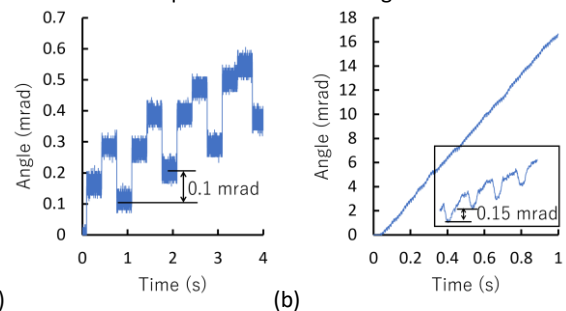
(a)   (b)
Figure 7. Rotational displacement at (a) 1 Hz and (b) 90 Hz.

5. Conclusion

This paper described the control waveforms of the inchworm. The rectangle waveforms were used to move the inchworm in the linear and rotational directions. The step displacement was mostly constant, and the velocity was proportional to the drive frequency. The use of a small voltage realized small displacements. The results are effective for driving the inchworm, as on/off control makes it easy to apply voltage to piezos. In future, weights which generate electromagnetic or electrostatic forces synchronizing with the piezo deformation are used to reduce the drawback motion

References

[1] Kato H, Hayakawa K, Torii A, Ueda A 2000 *Electrical Engineering in Japan* **131(4)** 44-51, 2000
[2] Higuchi T, et al., IEEE Proceedings on Microelectromechanical Systems, 1990, pp. 222-226, doi: 10.1109/MEMSYS.1990.110280.
[3] Merry R.J.E, et al., IEEE/ASME Trans. Mechatronics **14(1)** 21-31,2008, doi: 10.1109/TMECH.2008.2006756.

Relationship between thermally induced shaft displacement and temperature measured on an outer surface of motorized spindle for developing thermal displacement feedback control system

Yohichi Nakao[1], Ryota Ishida[1], Shumon Wakiyta[1], and Jumpei Kusuyama[1]

[1]Kanagawa University

nakao@kanagawa-u.ac.jp

Abstract

A main objective of this study is to minimize machining error due to thermal deformation of motorized spindle. In the spindle considered in this study, water cooling structures are designed. In our previous study [1], a feedback temperature control system was developed and tested for temperature control of the spindle. A main feature of the feedback temperature control system is to mix water flows that are different temperatures from different water supply sources. The supplied water temperature can be arbitrary controlled by controlling the mixing flow rates in real time using flow control valves. Based on the control system, the temperature control of spindle body was made by designing appropriate feedback control system. An effectiveness of the control system was verified experimentally. In the previous study, the temperature of the spindle outer surface was successfully maintained even internal thermal generation of the spindle was changed. In this present study, the relation between resultant thermally induced displacement of the spindle shaft and outer surface body temperature is compared. A final goal of this study is to develop a feedback control system of thermal shaft displacement in order to achieve zero thermal displacement of spindle shaft without direct thermal displacement as well as temperature measurements of spindle shaft during cutting operations.

Spindle, Temperature control, Thermally induced displacement, and Cooling

1. Introduction

Minimization and control of thermal deformation of machine tools is a very important issue to improve machining accuracy. In particular, the machine tool spindle directly affects the relative displacement error between workpiece and cutting tool. Therefore, it is significantly important to suppress thermally induced displacement of the machine tool spindle. In particular, the thermally induced axial displacement of the spindle system has to be minimized. There are research reports and developments on the thermal deformation suppression, such as efforts through sophisticated structural design of machine tool. The use of materials with a low expansion coefficient is one of the examples. As alternative approaches, compensation technique of thermal deformation using machine tool control system can be implemented.

Another countermeasure is also being taken to suppress temperature changes through effective cooling system. In many cases of commercialized machine tool, constant temperature of cooling fluid at a constant flowrate is supplied into the heat-generating parts of the machine tool. In this case, temperature changes due to heat generation changes in the heat sources such as machine tool spindle are inevitable. Therefore, a temperature control method that can effectively minimize the temperature changes in response to heat generation changes is desired.

The authors have developed a temperature feedback control system for machine tool components and structures including spindles. In our previous study [1], it was however shown that the spindle end-shaft displacement cannot be sufficiently suppressed when the casing temperature of a

spindle was kept constant using the developed temperature control system.

Therefore, alternative temperature measurement way is considered in order to control thermally induced shaft end displacement in this study. Then, we focused on the cooling water temperature supplied to the spindle as an alternative parameter for feedback. The relationship between the cooling water temperatures and shaft end displacement are presented to show strong correlation between them.
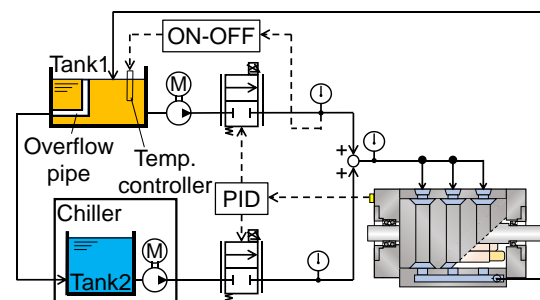
Figure 1. Developed temperature control system

2. Developed feedback control system

The temperature control principle of the developed feedback control system is based on the flowrate controls of cooling waters from two supply sources [1]. Temperature of the cooling waters with different temperatures are supplied from the sources. In Fig. 1, a basic structure of the developed control system is presented. In the control system, the tank 1 provides higher temperature fluid. Normally the water temperature in the tank 1 is the room temperature. Contrary, the tank 2 provides lower temperature fluid cooled by a commercialized

chiller. Flowrate control valves that are independently controlled are used to control the flowrates from the tank 1 and tank 2. The flow ratio of the higher and lower temperature fluids is controlled in real time such that temperature control objective is achieved. In the previous our study, temperature of a surface of the spindle near spindle shaft was measured and fedback.

3. Experiments

3.1. Tested spindle

A spindle depicted in Fig. 2 was used to the experiments. Figure 2 shows a structure of the spindle. Rated power of the built-in motor is 1.1 kW. Rated rotational speed is 30050 min^{-1}. In the experiments, temperatures of cooling water at the inlet and outlet ports of the spindle were measured. Thermally induced axial displacement of the spindle shaft was measured a laser displacement sensor that was fixed at a jig made by the super invar so that thermally induced displacement of the jig can be avoided. The jig was fixed on an end surface of the spindle [2].

Figure 2. Structure of motorized spindle

3.2. Results and considerations

The performance of temperature control of spindle by the control system developed in previous studies was verified through experiments. In the experiments, a temperature sensor was attached to an outer surface of the spindle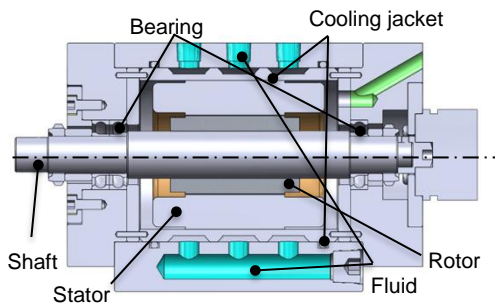 casing near spindle end shaft and the temperature was controlled to keep the surface temperature constant, regardless of the inner heat generation. The control results are shown in Fig. 3. In the experiment, the spindle temperature was varied by varying the spindle rotational speeds from 10000 min^{-1} to 5000 min^{-1}. In this case, if cooling water is controlled to be constant by a conventional cooling system, the spindle temperature is changed by about -1.7°C according to the change in heat generated by the spindle. In contrast, it can be confirmed that the developed temperature control system sufficiently suppresses the spindle surface temperature change though small transient change in temperature is observed.

Thermally induced axial displacement of an end surface of spindle shaft during temperature feedback control presented in Fig. 3 was evaluated as well. The experimental results indicate that if comparing the result of the conventional commercialized chiller, the shaft end displacement is slightly suppressed by the developed feedback control system, though, the effect to reduce thermal induced displacement is not sufficient.

A reason why the control effect is not sufficient is considered that temperature of the outer suface of casing and one of the shaft end is different. In fact, in our preliminary experiment, the temperature of the end surface of the shaft is higher about 5°C than that of the casing surface.

Based on the results, it is indicated that control of the spindle casing surface is not sufficient to suppress thermally induced axial displacement. In order to control the thermally induced

displacement of the spindle shaft, measurement of the displacement or temperature of the shaft is desirable. However, a measurement and feedback of the displacement and/or temperature of the rotating spindle shaft itself is not adequate from a viewpoint under actual machining environments.
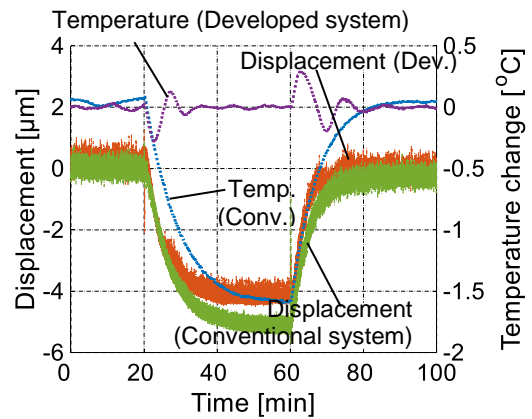
Figure 3. Thermally induced displacements

From above consideration, we focused on the cooling water temperatures measured at a supply port and a drain port of spindle, respectively. Specifically, the relationship between the temperature difference between drain water and supply water and shaft end displacement was investigated. Figure 4 indicates the experimental result.

From Figure 4, it is considered that the shaft end displacement can be predicted from the temperature difference between the cooling water supplied to and discharged from the spindle. This is because the temperature of the cooling water rises due to the amount of heat generated inside the spindle, which affects the shaft end thermally induced displacement.
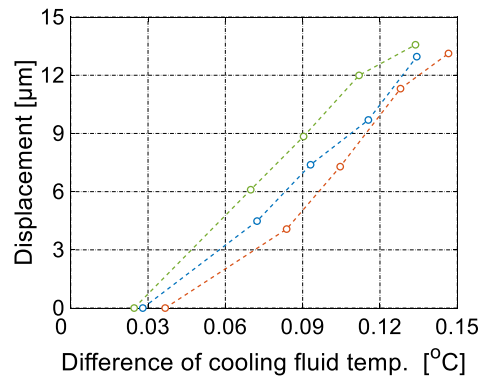
Figure 4. Relationship between difference of cooling water temperature and thermally induced displacement of end shaft

4. Conclusion

In this study, an appropriate feedback signal for the feedback temperature control system developed in our previous study was considered. From the experimental investigations in this study, it was clarified that the cooling water temperatures can be used as the feedback signal. This research was supported in part by a Grant-in-Aid for Scientific Research from the Japan Society for the Promotion of Science and The Die and Mould Technology Promotion Foundation.

References

[1] Wakiya S, Ishida R, Kusuyama J, and Nakao Y, Temperature control performance of a built-in motor spindle by developed temperature feedback control system, IJAT, Vol. 17, No. 5, pp512-pp520, (2023.9)

[2] Ishida R, Wakiya S, Kusuyama J, and Nakao Y, Temperature control of built-in motor spindle and resultant thermal displacement, The 38th Annual Meeting of ASPE, (2023.11)

Levitation estimation using electrical characteristics of the levitation actuator with stacked piezoelectric element

Hidetoshi Miyata[1], Takeshi Inoue[1], Akihiro Torii[1], Suguru Mototani[1], Kae Doki[1]

[1]Aichi Institute of Technology, Japan

V23724vv@aitech.ac.jp

Abstract

This paper describes levitation estimation for a levitation actuator that can be used in non-contact mechatronic systems. The levitation height is estimated using electrical characteristics. The levitating actuator consists of a vertically vibrating stacked piezoelectric actuator (piezo), a weight and a disc plate. The piezo is sandwiched between the weight and the disc plate. The levitating actuator is levitated by applying the appropriate voltage and frequency to the piezo. A squeeze air film is generated below the disc plate. The positive pressure of the squeeze air film under the disc plate supports the levitation actuator. At the beginning of levitation, the piezo vibration causes the weight to start vibrating and the actuator begins to levitate. Afterwards the piezo continues to vibrate and the levitation actuator continues to levitate. As the integration of levitation height sensors into the non-contact mechatronic systems is difficult in practice, levitation estimation technology plays an important role. The instantaneous levitation height and electrical signals are measured simultaneously. The power, phase difference and admittance are determined based on the voltage and current supplied to the levitation actuator, and the levitation height is estimated. The results of the experiments reveal the following. (i) The higher the applied voltage is, the higher the levitation height and the wider the levitation frequency band is. (ii) The levitation height of the levitation actuator can be estimated by power and admittance. (iii) The maximum levitation height is revealed to be correlated with the phase difference of the levitation actuator.

Levitation actuator, estimation levitation height, piezoelectric actuator, electrical characteristics

1. Introduction

The demand for miniaturization of industrial robots is increasing. This is because products are becoming miniaturized at manufacturing sites with space constraints and small lot production of many products. The use of piezoelectric elements (piezos) in precision mobile robots enables miniaturization and micro displacement. We are developing inchworm robots using piezo and electromagnets to enable precise movement [1]. However, the inchworm robot is affected by friction while moving. Therefore, we propose a moving actuator with levitation in order to reduce the effects of friction [2]. The levitation actuator levitates by generating a film of air. A non-contact platform using near-field acoustic levitation has been proposed[3]. However, there has been no estimation of the levitation height for levitation systems using vibration.

The purpose of this paper is to clarify the relationship between the levitation height and electrical characteristics of the levitation actuator. We propose a sensorless method for estimating the levitation height.

2. Levitation actuator

Figure 1 shows the levitation actuator. It consists of a weight, piezo, and plate. Each component is fixed by cyanoacrylate adhesive. The mass of the weight is 36.9 g. The thickness of plate is 3 mm, and its weight is 5.6 g. The diameter of plate is 30 mm. The total length of the levitation actuator is 38 mm and the weight is 47.6 g.

The piezo used in the levitation actuator is AE0505D16DF (TOKIN), which exhibits a deformation of 11.6 μm when 100 V_{DC}

is applied. When a sinusoidal voltage is applied to the piezo, it generates the amplitude in vertical vibration. In conjunction with the vibration of the piezo, the plate also vibrates. As the plate vibrates, positive pressure is generated between the plate and the floor surface. The squeeze film effect which generates a film of air causes the plate to levitate. The levitation actuator continues to levitate by continuously applying the appropriate voltage and frequency. The levitation height is measured at the top of the plate by a displacement sensor (Keyence LK-H053). The levitation height is the vertical displacement of the plate, and is defined from the average value for one second (1 s). This is because the plate vibrates at the frequency applied to the piezo and the instantaneous value of the levitation height oscillates. Vibration amplitude is defined as shown in Figure 1 (b). Time domain signals are collected using an oscilloscope and recorder.
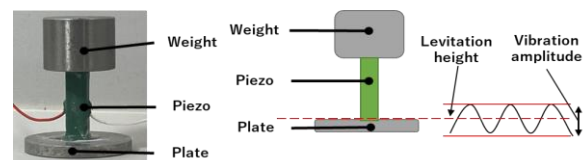
Figure 1. (a) Levitation actuator.   (b) Definition of levitation height

3. Experiment and results

A sinusoidal voltage is applied to the levitation mechanism from a bipolar power supply. The amplitude of the input voltage is varied from 4 V to 10 V with a 2 V interval, and the frequency is scanned from 10 kHz to 16 kHz with a 0.1 kHz interval. Electric properties, such as voltage, current, power, admittance, and phase difference between the voltage and current, are measured by a power meter (Hioki, PW3335).

3.1. Levitation height

Figure 2 shows the levitation height. The maximum levitation height is 33.8 μm at 12.7 kHz when 10 Vpp was applied. As the voltage applied to the levitation actuator increases, the levitation height also increases. This phenomenon indicates that the frequency band in which the levitation is obtained is widening.
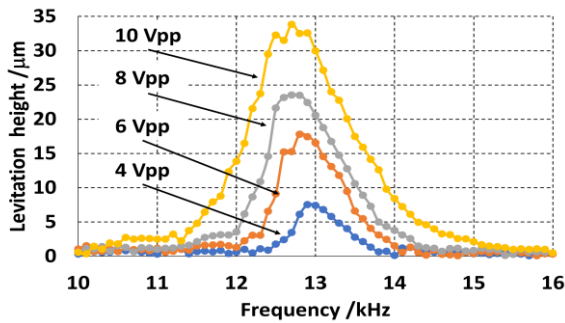
Figure 2. Levitation height

3.2. Power

Figure 3 shows the electric power. The maximum power is 2.6 W at 12.5 kHz when 10 Vpp is applied. It shows that the change in power generally corresponds to the change in the levitation height in Fig. 2. As the applied voltage increases, the frequency showing the maximum value of both the levitation height and power decreases.

Figure 3. Power

3.3. Admittance and Phase difference

Figure 4(a) shows the admittance, which is calculated by dividing by the instantaneous current by the instantaneous voltage. The frequencies of the maximum power and the maximum admittance almost agree.

Figure 4(b) shows the phase difference. The frequency where the phase difference equals zero and the frequency where the maximum levitation heig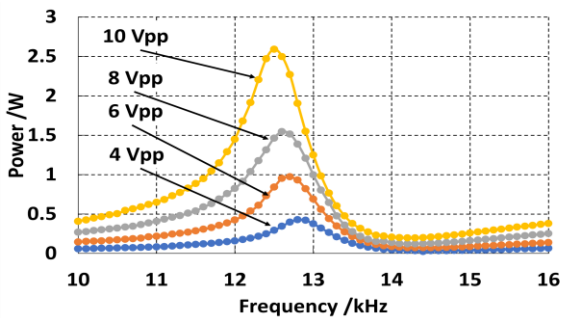ht agree. As the same with the power in Fig.3 and the admittance in Fig.4(a) and the phase difference in Fig.4(b), the curves also shift to lower frequency side as the applied voltage increases. This phenomenon shows that the levitation height at the resonant frequency is higher than that at the anti-resonant frequency.
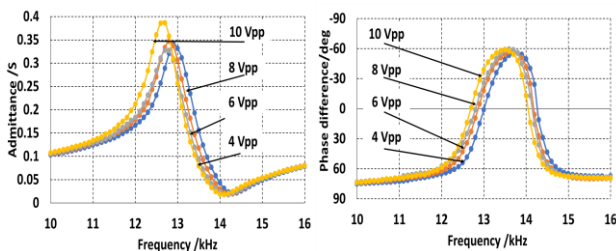
Figure 4. (a)Admittance   (b)Phase difference

4. Levitation estimation

Figure 5 and Figure 6 show the levitaiton height estimation equations. In Fig. 5, the levitation height (y) is estimated by power consumed (x) and the voltage applied. In Fig. 6, the levitation height (y) is estimated by the admittance (x) and the voltage. The estimating equations are obtained from the data shown in Fig. 2 where the levitation height from 3 μm to the maximum and the corresponding data in Fig. 3 and Fig. 4. The difference between the estimation line and measured plots indicates estimation error.
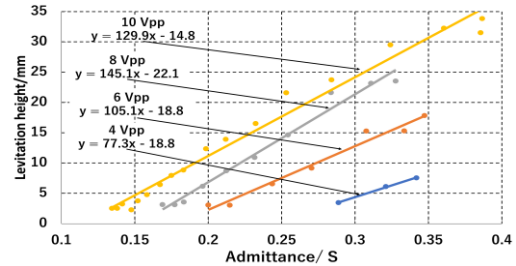
Figure 5. Power versus levitation height
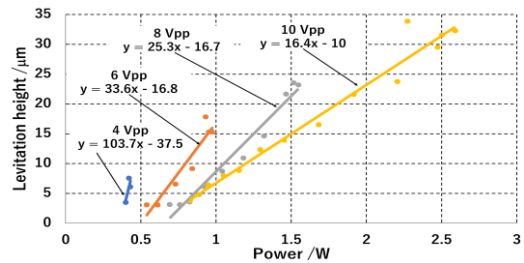
Figure 6. Admittance versus levitation height

Figure 7 shows the relationship between phase difference and levitation height. The data shown in Fig. 2 and Fig. 4(b) are summarized. As the phase difference approachs zero, the levitation height increases. Since the phase difference and power are related through a trigonometric function, the relationship between the phase and the levitation will be studied in detail in future.

Figure 7. Phase difference versus levitation height
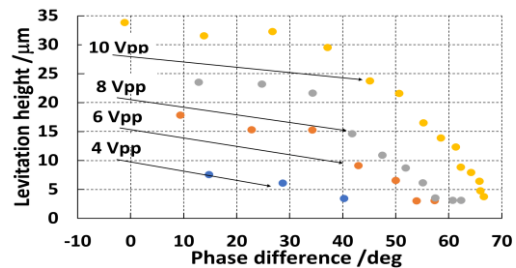
5. Conclusions

In this paper, we described a levitation height estimation using the characteristics of the levitation actuator to achieve sensorless operation. By measuring the levitation height, power, admittance of the actuator, and phase difference, we showed the possibility of the sensorless levitation height estimation and levitation height control. This work was supported by JSPS KAKENHI Grant 21K03972.

Reference

[1] Kato H, Hayakawa K, Torii A, Ueda A 2000 Electrical Engineering in Japan vol 131 pp 44-51

[2] Torii A, Itatsu Y, Nishio M, Ueda A, Doki K 2015 Electrical Engineering in Japan vol 190 pp 19-25

[3] Li W, Zhang P, Yang S, Cai S, Feng K 2024 International Journal of Mechanical Sciences vol 265, 108865

euspen's 24th International Conference &
Exhibition, Dublin, IE, June 2024
www.euspen.eu

Iterative learning control for nano-positioning stage of defect imaging equipment

Hyunchang Kim[1], Kyung-Rok Kim[1], Dongwoo Kang[1], Jaeyoung Kim[1]

[1]Department of Flexible and Printed Electronics, Korea Institute of Machinery and Materials(KIMM), Daejeon, 34103, Republic of Korea

hckim0128@kimm.re.kr

Abstract

In recent years, the semiconductor industry has witnessed a significant transformation in the semiconductor exposure process, with the adoption of EUV (Extreme Ultraviolet) light sources. This paradigm shift necessitates the use of EUV light sources in mask inspection equipment for exposure, demanding impeccable performance in defect imaging. To achieve these requirements, the stage components within such equipment must exhibit the capability to align the optical system and mask in parallel while precisely operating within nanometer-level tracking errors. Furthermore, these stages must function effectively in a vacuum environment. Among the various technologies available, ultra-precision stages employing piezoelectric elements is most suitable.

This research is focused on enhancing the dynamic tracking performance of the developed XY scanning stage for defect imaging. To achieve this objective, we designed a parallel compliant mechanism that effectively decouples motion along the x- and y-axes and minimizes the coupling crosstalk between these two axes. This design incorporates mechanical symmetry, resulting in nearly identical dynamics for both axes. Piezoelectric stack actuators are strategically integrated into both axes, facilitating a maximum displacement of 14.9 μm.

To realize superior tracking performance, we implemented Proportional-Integral (PI) control and iterative learning control techniques. By adapting these control strategies, we achieved an impressive tracking performance of ±5 nm (3σ) at a scan speed of 400 μm/s

Nano-positioning stage, Iterative learning control, Ultra precision, Tracking performance

1. Introduction

A nano-positioning stage represents a pivotal technological advancement widely employed across diverse fields including inspection equipment, optical systems, and atomic force microscopy (AFM) [1-3]. In a previous study [4], we proposed an ultra-precision XY stage for use in defect review imaging system. Utilizing a decoupled parallel compliant mechanism, the stage achieves similar dynamics in both x- and y-axes while minimizing coupling crosstalk. The implementation of a proportional double integral (PII) feedback control algorithm enables a tracking error performance of ±3 nm in the 20 μm/s constant velocity region, though significant error peaks persist during acceleration and deceleration. However, in order to fulfill the requirements for integration with the equipment, ±5 nm tracking performance at 400 μm/s was necessary. To address this issue, iterative learning control (ILC) is applied in this study to enhance dynamic tracking performance across the entire motion profile.

2. Design and fabrication of stage

Figure 1 illustrates the ultra-precision XY nano-positioning system utilized in this study [4]. A parallel compliant mechanism is designed to decouple motion along the x- and y-axes and minimize coupling crosstalk. The system employs piezoelectric stack actuators in both axes, providing a maximum displacement of 14.9 μm, with resulting displacements measured using capacitive sensors. Constructed from AL6065, the XY stage supports a 1.8kg payload, exhibiting a first resonant frequency of 297 Hz in the yaw direction and a translational mode frequency of 1012 Hz. The frequency response of the X-axis is experimentally measured and illustrated in Figure 2 (a). The XY stage measures 200×200×20 mm and is mounted atop a ZTilt

stage, although the details of the latter are not elaborated upon as it remains fixed during XY plane scan motions.
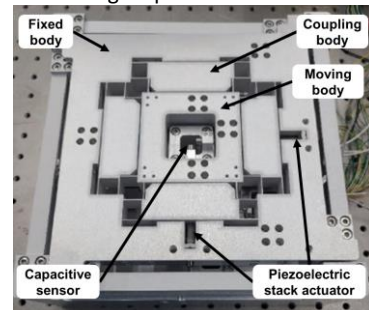
Figure 1. Fabricated nano positioning stage

3. Feedback controller design
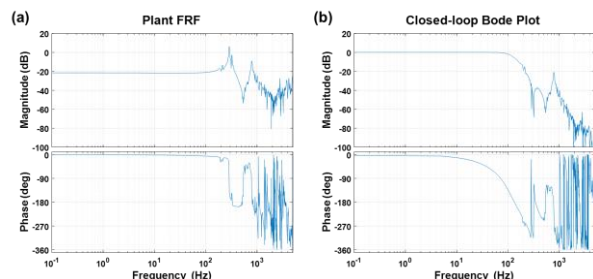
Figure 2. Frequency response measurement in X-axis(a) and Closed-loop bode plot with PI controller(b)

As shown in Figure 2(a) utilizing experimentally obtained Frequency Response Function (FRF) data, a Proportional-Integral (PI) controller is formulated through loop-shaping techniques. Preceding the PID controller design, a notch filter at 297 Hz is implemented to counteract yaw-direction resonance, followed

by the application of a 200 Hz low-pass filter to diminish sensor noise interference. The PI controller is meticulously tailored to meet specific design criteria, ensuring a phase margin of ≥ 60°, gain margin of ≥ 5 dB, and bandwidth of ≥ 50 Hz. Through loop-shaping, the PI controller gains are determined as Kp=6.242 and Ki=3804. The attained performance metrics encompass a phase margin of 60° at 50 Hz, a gain margin of 5.89 dB at 135 Hz, and noise attenuation of -42.5 dB at 1 kHz. The closed-loop bode plot of the implemented PI controller is depicted in Figure 2(b).

4. Stage motion profile

The proposed XY stage outlined in this study is intended for integration into a defect review imaging system, facilitating defect detection across a comprehensive area by traversing a maximum 10x10 μm square region through raster scanning. Given the symmetrical design of the X and Y axes, scanning along either axis is viable. In this investigation, scanning primarily occurs along the X-axis, with step-wise movement along the Y-axis. Figure 3(a) illustrates the plane motion, while Figure 3(b) depicts the motion profiles for both axes over one scanning cycle. The motion profile along the X-axis is characterized by an acceleration-limited S-curve. During constant velocity motion of the X-axis, the Y-axis remains stationary. Subsequently, during acceleration or deceleration phases of the X-axis, Y-axis step motion is initiated, synchronized with the acceleration phase of the acceleration-limited S-curve. The duration of the acceleration and deceleration phases for X-axis scan motion are set at 5ms.
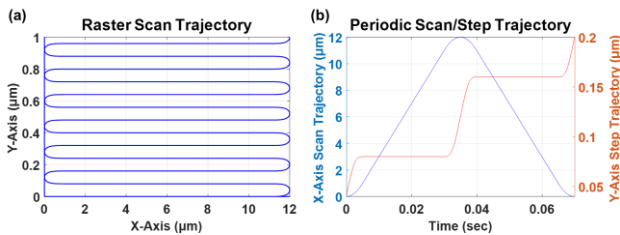

Figure 3. X, Y raster scan and motion profile for single scan period

5. Iterative learning controller design

In this paper, we introduce iterative learning control (ILC) as a method to enhance dynamic tracking performance across the entire motion profile, aiming to achieve tracking precision of ±5 nm or less throughout the scanning process and consequently reduce tac time. Derived from the concept that performance in subsequent tasks can be improved by leveraging outcomes from previous tasks, ILC focuses on attaining better transient tracking performance. The ILC control utilizes the preceding round-trip scan as the foundation for a single cycle, retaining the tracking errors encountered in both the X and Y axes from the previous scan in memory. These errors are then iteratively updated to construct a control diagram, as illustrated in Figure 4 [5,6]. The ILC input for each iteration is computed based on the error from the previous iteration stored in memory and is adjusted by modifying the loop gain L and Q filter. This resulting ILC input is then added before the PI controller, following an 'input injection method'[6]. Additionally, alongside the designed PI controller, ILC logic is implemented in parallel.
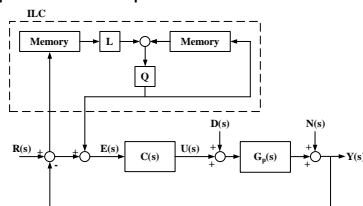

Figure 4. Control block diagram (PI + ILC)

6. Experimental Verification

An experiment is conducted to evaluate the tracking performance of the designed PI controller. A motion profile is generated with an 400 μm/s constant maximum speed and a 10 μm constant velocity region in the X-axis, along with an 80 nm grid for the Y-axis. The tracking error for this scenario is depicted in Figure 5. With an acceleration time set to 5 ms, the experimental results reveal notable findings. Along the step axis (Y), the controller demonstrates some degree of tracking during the constant speed segment but exhibits an offset error, alongside significant tracking errors in the acceleration and deceleration phases. Conversely, on the scan axis (X), the controller showcases substantial tracking errors throughout, including during the constant speed segment, rendering the attainment of a target tracking error unfeasible solely with the PI controller.
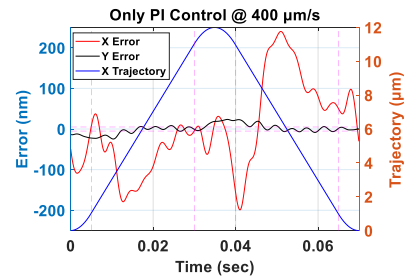
Figure 5. Tracking error with only PI controller

Subsequent tracking experiments are conducted using the same motion profile as in the case of the PI controller alone, with results shown in Figure 6. Through the application of ILC, tracking errors of ±5 nm or less are achieved across the entire scanning area, significantly reducing 3-sigma errors to 4 nm for the X-axis and 3 nm for the Y-axis.
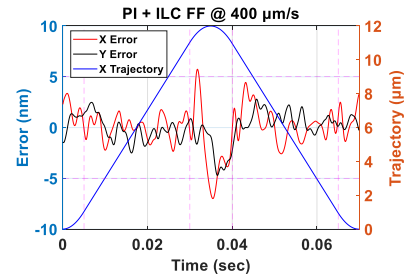
Figure 6. Tracking error with ILC + PI controller

7. Conclusion

It was confirmed that as the iterations progress through iterative learning control (ILC) when the same motion is repeated, the motion tracking performance can be improved.

It was observed that solely applying PI control resulted in a tracking error of ±250 nm during the constant speed section. However, when PI control was combined with ILC, the tracking error reduced significantly to ±5 nm under identical conditions. In the future, it is intended to theoretically and experimentally validate the performance based on various applied ILC methods.

References

[1] Gu L, Li X, Bao H, Liu B, Wang Y, Liu M, Yang Z, Cheng B 2006 *J. Micromech. Microeng* **16** 1349

[2] Schitter G, Astrom KJ, DeMartini BE, Thurner PJ, Turner KL, Hansma PK 2007 *IEEE Trans. Control Syst. Technol.* **15** 906-915

[3] Ru C, Liu X, Sun Y 2016 2016 *J. J. Springer Cham* 295-324

[4] Kim J, Kang D, Kim KR, Kim H 2021 *IEEE Access* **9** 88931-88941

[5] Bristow DA, Tharayil M, Alleyne AG 2006 *IEEE Control Systems Magazine* **26** 96-114

[6] Fine BT, Mishra S, Tomizuka M, 2009 *American Control Conference* 931-936

Measurement of rotation angle of a small mobile robot by measuring surface potential of insulators

Takeshi Inoue[1], Hidetoshi Miyata[1], Akihiro Torii[1], Suguru Mototani[1], Kae Doki[1]

[1]*Aichi Institute of Technology, Japan*

v23701vv@aitech.ac.jp

Abstract

The authors are developing a compact equilateral triangle-shaped mobile robot using piezoelectric elements and electromagnets. The robot consists of an equilateral triangle with electromagnets at the apexes and piezoelectric elements at the sides. The robot operates by controlling the timing of the attraction and release of the electromagnets and extension and contraction of the piezoelectric elements. The robot moves in three directions (x, y, and θ). We used a desktop measurement system to measure the robot's rotation angle and provided feedback to the robot to follow a reference route. Previously, the rotation angle was measured by means of displacement measurements of electromagnets with three laser displacement sensors. In this paper, we propose a method to measure the rotation angle by measuring the surface potential of an insulator plate with a DC power supply connected to its sides. By measuring the potential difference at the vertices of an equilateral triangular robot, the rotation angle is determined by geometrical analysis. This method, which is unlike the laser encoder method, does not require communication with external devices since the sensor is mounted on the robot. Therefore, this method can contribute to an autonomous movement of the robot. By measuring the potential difference at the vertices of an equilateral triangular robot, it becomes possible to measure the rotation angle. Therefore, it can contribute to autonomous movement of the robot. In addition, by applying a high electric field to the insulator plate, high sensitive rotation angle measurement can be achieved, and therefore the measurement resolution can be improved.

Piezo-electric, inchworm, surface potential, measurement systems

1. Introduction

We have been developing inchworm actuators that can be applied to positioning and motion devices [1]. Many research groups have developed various types of inchworms [2]. The unique feature of the inchworm we have developed is that it does not have a guiding mechanism. The inchworm incorporates an electromagnet for clamping and a piezoelectric actuator (piezo) for movement. The disadvantage of the inchworm, however, is that it tends to follow a path that deviates from the target path. Reference [1] used a laser displacement meter to correct the angle. However, the method using a laser displacement meter requires communication with an external device, which hinders the autonomous operation of the actuator. Therefore, this paper proposes a method to measure the rotation angle of an inchworm-type moving mechanism by detecting the potential difference between the surface potential of an insulating plate with a DC power supply connected to its side and a needle-shaped electrode placed at each vertex of the inchworm. We also propose a method to perform angle compensation from the detection results.

2. Inchworm

Figure 1 shows the inchworm actuator we are developing. This actuator has a delta-shaped structure with three electromagnets at the apex of a triangle and three piezos on both sides of the triangle. Electromagnets are positioned perpendicular to the direction of piezoelectric expansion and contraction. The position of the actuator is defined from the position of the electromagnets as measured by a laser displacement sensor.
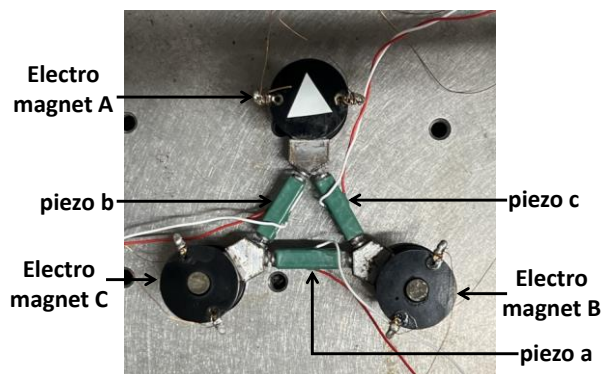
Figure 1. Inchworm

2.1. Linear motion of Inchworm

Figure 2 shows the principle of linear motion of the actuator. In Fig. 2(1), electromagnets B and C are excited. In Fig. 2(2), the applied voltage causes piezos B and C to elongate and attract the magnetic floor. This excitation causes the unexcited electromagnet A to move in the Y direction. At Fig. 2(3), electromagnets A and C are excited and attracted to the magnetic floor, while electromagnet B remains unexcited and piezo c contracts, causing electromagnet B to move. In Fig. 2(4), electromagnets A and B are excited and attracted to the magnetic floor, electromagnet C remains unexcited and piezo b contracts. This causes electromagnet C to move. The sequence Fig. 2(1)~Fig. 2(4) is repeated to propel the inchworm actuator.

Figure 2. Control signals and principle of operation for straight-line motion
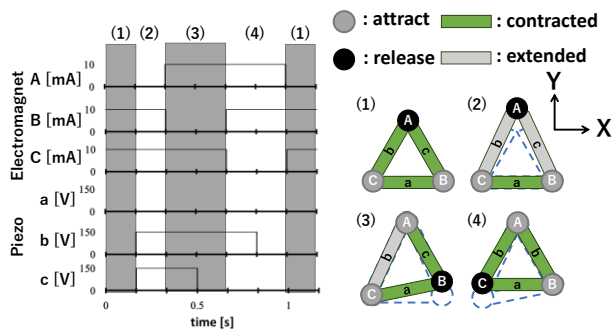
2.2. Angular motion of inchworm

Figure 3 shows the control signal and principle of operation for angular motion. In Fig. 3(1), electromagnets A and B are excited and electromagnet C is de-energized. At this time, voltage is applied to piezo b, and piezo b is extended. In Fig. 3(2), electromagnets A and B are kept excited and electromagnet C is kept de-energized. Piezo a is extended. At this time, electromagnet C moves in the direction of the combined force of the contraction direction of piezo b and the extension direction of piezo a. In Fig. 3(3), electromagnets A and C are excited and electromagnet B is de-energized. At this time, voltage is applied to piezo a to keep it extended. In step Fig. 3(4), electromagnets A and C are excited and electromagnet B is de-energized. The application of voltage to piezo a is stopped, and voltage is applied to piezo c. At this time, electromagnets A and C is in a state of extension, and electromagnet B is de-energized. At this time, electromagnet B moves in the direction of the combined force of the contraction direction of piezo a and the extension direction of piezo c. In Fig. 3(5), electromagnets B and C are excited and electromagnet A is de-energized. At this time, voltage is applied to piezo c to keep it extended. In Fig. 3(6), electromagnets B and C are excited and electromagnet A is de-energized. The voltage application to piezo c is stopped, and voltage is applied to piezo b. At this time, electromagnet B is in a state of excitation, and piezo b is in a state of extension. At this time, electromagnet A moves in the direction of the combined force of the contraction direction of piezo c and the extension direction of piezo b. By repeating the operation Fig. 3(1)~Fig. 3(6), the inchworm rotates around its center of gravity in the direction of the +C axis. The voltage amplified to three piezos are determined by V_{BC}, which is amplified and is applied to the three piezos.

3. Angle sensing by surface electric potential

The angle sensing of the moving mechanism proposed in this paper uses the electric potential generated on the surface of an insulator with electrodes on its sides. When the electrodes are parallel plates, the potential is uniformly distributed because the electrolysis between the plates is uniform. Figure 4 shows the angle detection system proposed in this paper. From the potential distribution generated on the surface of the insulator, the potential difference between the electrodes is detected by a differential potential measurement sensor using needle-shaped electrodes placed at each vertex of the Inchworm. The potential difference V at each vertex is determined by the electric field E applied to the insulator, the length l of one side of the inchworm, and the angle θpiezo between one side and the equipotential line. This method does not require communication with an external device because the angle is detected by a sensor mounted on the inchworm.

$$V = El \sin \theta_{piezo} \quad (1)$$

Figure 5 shows the potential difference between each vertex when l is 6 mm and E is 0.1 V/mm. In this study, the angle θ between the direction of the electric field and the direction of the inchworm was set to 0°, 30°, 45°, and 60°, and the voltage applied to the piezo was varied to operate the inchworm.
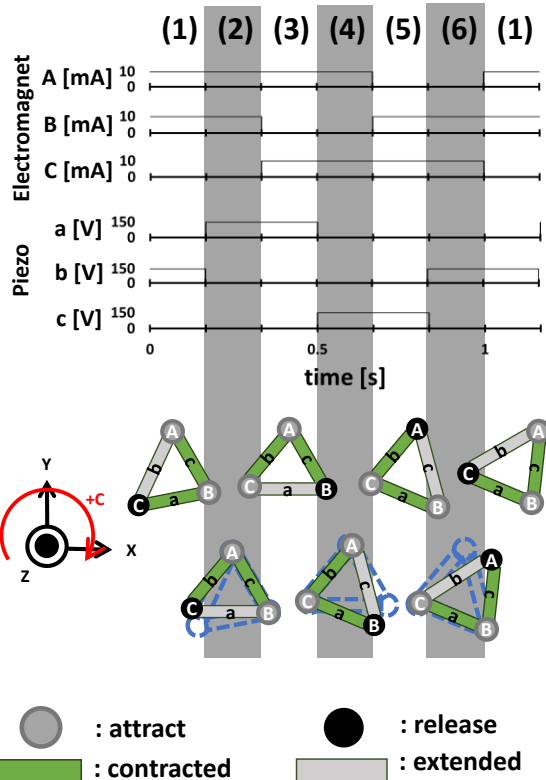
Figure 3. Control signals and principle of operation for rotational motion
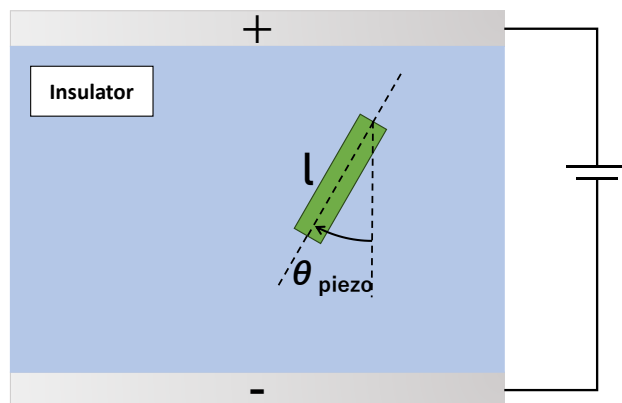
Figure 4. Potential difference between vertices at each angle

Table 1 shows the voltage between the vertices at each angle. The orientation of the inchworm varies the electric potential difference of the verteices of the triangle. The sum of the three potential differences equals zero in all four cases. The potential difference is determined by the electric field. In this case, the electric field is defined as 0.1 V/mm. The analytical error is not easily estimated. However, the measurement error of the potential difference is approximately 10 mV which corresponds to the measurement error.

is applied to piezo b, and the voltage amplified by V_{AB} is applied to piezo c. The voltage applied to each piezo in rotational motion is the amplified voltage of V_{BC}.

The behavior of the inchworms with compensation is shown in Fig. 6. The inchworm is placed in four orientations, such as 0°, 30°, 45°, and 60°. Figure 6 shows the case of 60°. The original position of the inchworm is bottom right, and the voltage applied to piezo c, which is in proportional to V_{AB}, and piezo b, which is in proportional to V_{CA}, is bottom left in Fig. 6. The target orientation of the inchworm is 0° shown at the top in Fig. 5. In case of Fig. 6, the inchworm moves in the linear direction drawn with a dot-dash line, and its orientation changes according to different voltage applied to piezo c and piezo b. In case of Fig. 6, the voltage applied to piezo b is larger than that to piezo c and the inchworm rotates in the clockwise direction.

Table 1 Potential difference between vertices at each angle

	Electric potential difference [V]		
	V_{AB}	V_{BC}	V_{CA}
0 °	5.20	0.00	-5.20
30 °	3.00	3.00	-6.00
45 °	1.55	4.24	-5.80
60 °	0.00	5.20	-5.20

High potential
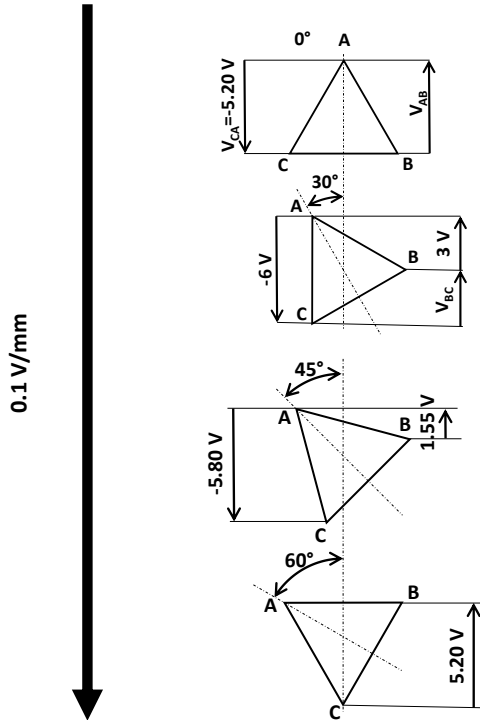
Low potential

Figure 5. Potential difference between vertices at each angle

4. Angle compensation for inchworms

The potential difference between each vertex of the inchworm is amplified by an amplifier, and the voltage is given to the piezoelectric element of the inchworm to control piezoelectric elongation and correct the angle. Angle correction is performed by controlling the magnitude of the applied voltage to the piezos in the linear motion in Chapter 2. Voltage amplified by V_{AB} is applied to piezos c and voltage amplified by V_{CA} is applied to piezos b. If $|V_{AB}| < |V_{CA}|$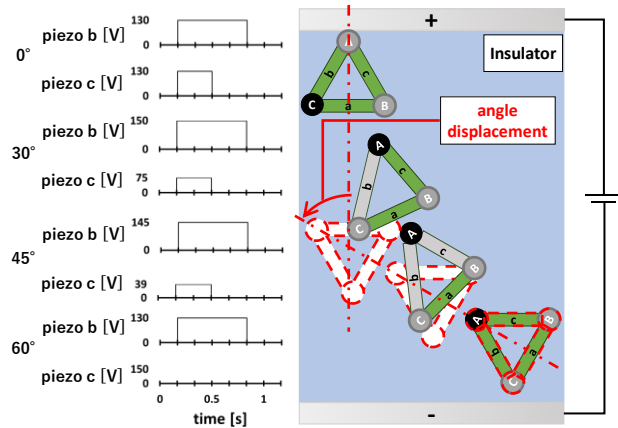, the elongation of the piezo is piezo c < piezo b. This causes the inchworm to deviate to the right toward the direction of travel. If $|V_{CA}| < |V_{AB}|$, piezoelectric elongation is piezoelectric b < piezoelectric c. This causes the inchworm to move leftward in the direction of travel.

5. Experimental Methods and Results

This time, the angle θ between the electric field and the perpendicular bisector between B and C in Fig. 2 is assumed, and the angle correction operation is performed by applying a potential difference with reference to Equation (1). The potential difference in Table 1 is given to the differential amplifier circuit, amplified by the amplifier as a signal, and applied to the piezo. In linear motion, the voltage amplified by V_{CA} is applied to piezo b, and the voltage amplified by V_{AB} is applied to piezo c. In linear motion, the voltage amplified by V_{CA}

Figure 6. Angle compensation operation in straight-line operation

The angular displacement of the inchworm is measured by measuring the displacement of the Y-axis of electromagnets B and C. The inchworm is driven at 1 Hz. Figure 7 shows the angular displacement per cycle for the linear motion. Figure 8 shows the angular displacement per cycle for the rotational motion. The parameters are the original rotational angle of the inchworm.

Figure 7 shows the angle displacement of the inchworm from the original angle position. The angle displacement per one cycle at 60° and 45° is larger than that at 0° and 30°, due to the greater difference in voltage applied to piezo b and piezo c, as shown in Fig. 6.
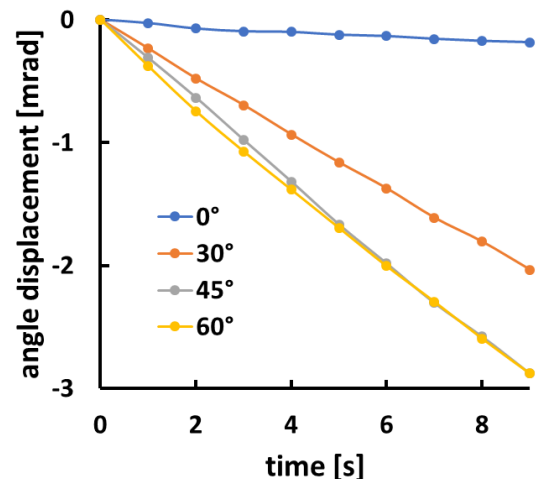
Figure 7. Angular displacement in straight-line motion

Figure 8 shows the angle displacement of the inchworm from the original angle position. The target orientation is 0°, as shown at the top in Fig. 5. The voltage applied to three piezos of the inchworm is determined by the potential difference V_{BC}, which is amplified by the drive circuit. The larger the original rotational position is, the greater the angle displacement per cycle is. This corresponds to the rotational speed being relative to the rotational position.

Table 2 shows the average angular displacements for the straight-line and rotational movements. The inchworm moves in the direction of θ closer to 0°. The displacement speed in the rotational motion of the inchworms was increased by increasing the voltage applied to the piezo in the rotational motion.
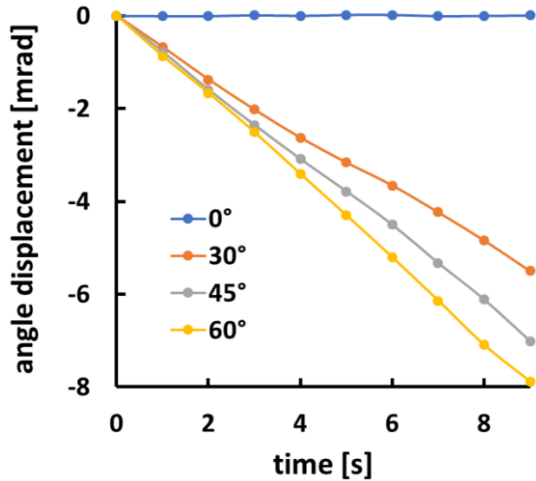
Figure 8. Displacement angle in rotational motion

Table 2 Displacement angle for each cycle

	angle displacement [mrad]	
	straight-line	rotation
0 °	-0.02	0.00
30 °	-0.22	-0.61
45 °	-0.32	-0.78
60 °	-0.32	-0.88

7. Conclusions

In this paper, we proposed a method to detect the angle of inchworms from the surface potential of an insulating plate with electrodes attached to its sides, and to perform angle compensation by analogously controlling the voltage applied to the piezo. The larger the phase between the target angle and the inchworm, the larger the displacement angle during operation, and the smaller the displacement angle became as the direction of the inchworm approached the target angle.

Acknowledgement

References

[1] Torii A, Mitsuyoshi Y, Mototani S, and Doki K, 2018 *Int. J. of Automation Technology,* **Vol. 12**, No. 5, pp.784-790

[2] Li j, Huang H, Morita T, *Sensors and Actuators A: Physical,* **Vol. 292**, pp. 39-51, 2019

Online-correction of the thermally induced Tool-Center-Point-deviation based on integrated deformation sensors

Nico Bertaggia[1], Daniel Zontar[1], Christian Brecher[1, 2]

[1]*Fraunhofer Institute of Production Technology (IPT), Steinbachstr. 17, 52074 Aachen, Germany*
[2]*Laboratory for Machine Tools and Production Engineering (WZL) of the RWTH Aachen University, Campus-Boulevard 30, 52074 Aachen, Germany*

nico.bertaggia@ipt.fraunhofer.de

Abstract

It is known, that up to 75 % of geometrical errors are caused by thermally induced TCP (Tool-Center-Point)-deviations. To be able to correct these thermally induced errors a method to measure the thermal deflection of the machines structural parts was developed by Fraunhofer IPT. This method uses Integrated Deformation Sensors (IDS) attached to the machine structure and calculates the TCP-deviation based on a structural machine model. The IDS utilize a rod made out of CFRP (Carbon-Fiber-Reinforced Polymers) as a reference as this material has a significantly lower TEC (Thermal Expansion Coefficient) than commonly used materials in machine tools structural components. The developed model converts the measured structural deformations into the TCP-deviation is based on theories like the Euler-Bernoulli beam theory for one dimensional beams, if the structural part meets the assumptions of a rigid beam, or the Timoshenko beam theory if shear needs to be considered. A similar classification is made for two-dimensional theories. In difference to former publications where the calculated deviation is compared to the measured TCP-deviation in this paper the correction is sent to the machine to reach the goal of an online-correction. To reach this the calculated deflection of the total working area is entered in correction tables which are then transferred to the machine's control to correct the calculated thermally induced error.

The functionality of this method shall be demonstrated in this paper using a demonstrator machine equipped with the sensor-system. For the experiments shown in this paper thermal loads are applied to the machine by moving the machine axes individually while measuring the TCP-deviation using a tactile sensor intermittently. To be able to make statements about the effectiveness of the method said experiment is performed in two variants: one where the correction is disabled to see the uncorrected machine behavior and one where the correction is enabled to see the corrected behavior. The results show that the TCP-deviation is reduced whilst the correction is active.

Keywords: thermal deformation; thermo-elastic behavior; machine tools; Tool Center Point; correction

1. Motivation

Thermal issues in machine tools, may their origin be internal or external heat sources or radiaton, lead to a thermally induced deformation of the machines structure which leads to deviations of the TCP (Tool-Center-Point) [1, 2]. The current industry standard is using countermeasures like air-conditioned production halls, warm-up processes or control measurements, all of which are expensive for the producing companies and not sustainable [3]. As an alternative to these measures the IDS (Integrated Deformation Sensors) were developed [4]. While there are multiple methods that have the goal of lowering the TCP-deviation like e.g. [5, 6] most compare their prediction to a TCP-measurement but do not correct this error on the actual demonstrator.

2. Integrated Deformation Sensors

The idea of the IDS is measuring the thermally induced deformation of the machines structure. The sensors can be retrofitted to an existing machine or initially be mounted while the machine is built. A model is used to calculate the TCP-deviation resulting from thermal changes in the machine structure and correct said TCP-error by sending the calculated information to the machine. The methology used shall be explained closer in the following chapters.

2.1. Principle of measurement

The Integrated Deformation Sensor consists of the components schematically shown in **Figure 1**. To measure the elongation respectively the shortening of the machines structure a rod made of CFRP (Carbon-Fiber-Reinforced Polymers) is used. This rod has, provided that the carbon fibers are arranged in a certain way and the ratio between carbon fiber and the matrix surrounding them are fitting, the characteristic that its TEC (Thermal Expansion Coefficient) is significantly lower than the TEC of materials commonly used in the structure of the structural parts of machine tools, like steel, aluminum or casting materials [4]. While the TEC for CFRP is close to zero or can even be slightly negative the TEC for steel is around $11 \cdot 10^{-6} \ K^{-1}$ depending on which steel is chosen, the TEC for aluminum being even higher at $23 \cdot 10^{-6} \ K^{-1}$. [3]

displacement sensor

loose bearing of CFRP rod

thermally stable CFRP rod

fixed bearing of CFRP rod

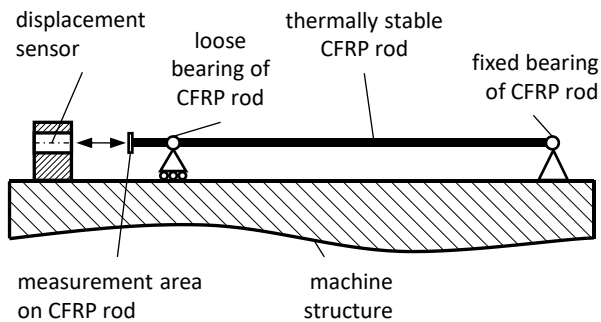measurement area on CFRP rod

machine structure

Figure 1. Schematic principle of the IDS

Said CFRP-rod can therefore be used as a reference for the measurement of the structures length-change. The CFRP-rod is, in the example of *Figure 1*, helt by a fixed bearing on the right hand side and a loose bearing on the left end of the rod. The displacement sensor itself is also connected directly to the machines structure as can be seen on the left hand side of *Figure 1*. As the displacement that is measured, shown by the arrow in *Figure 1*, is a superposition of the thermally induced length change and the mechanically induced length change of the structure the measured values need to be filtered. This is in the first place done by a low-pass filter to eliminate elastic length changes that can for example be induced by fast movements of axes or the jerk that can occur e.g. in the moment when a tool is exchanged for another.

2.2 Demonstrator and modeling of the machines deformation

To show the potential of the sensors a demonstrator machine, shown in *Figure 2*, was equipped with twelve sensors visualized by the dashed lines.
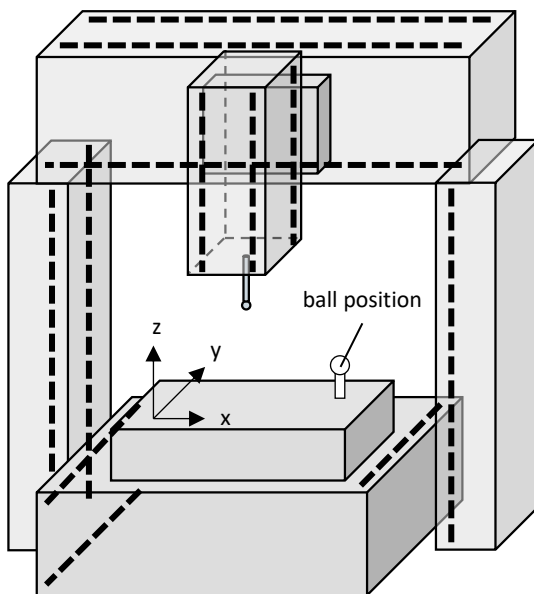

ball position

z

y

x

Figure 2. Demonstrator with position of sensors and ball

Five structural parts of the demonstator, a 3-axis machine tool, are fitted with IDS. These include the machine bed, the left and the right column, the portal beam as well as the headstock. The placement of the IDS can be determined either by expert knowledge or with the help of simulations. In these the expected thermal deformations can be estimated by simulating the machines structure together with the sources of thermal energy generated by friction, motors or for example chips that sum up in the process of milling.

To calculate the TCP-deviation from the measured thermal deformation values a model of the machine based on mechanical theories is built. This theory can e.g. be for one-dimensional elements the Euler-Bernoulli beam theory

which is used to model beam shaped structural parts where a neglectable amount of shear is expected or the Timoshenko beam theory if the second of these assumptions is not met. In the case of for example the machines bed these dimensional assumptions can not be met, therefore two-dimensional theories are introduced. Similarly to the beam theories the Love-Kirchhoff plate theory is used when there is not a significant amount of shear expected and one dimension of the structure is significantly smaller than the other two. If otherwise there is shear expected the Reissner-Mindlin plate theory is used. These separations are made depending on the shape of all the relevant structural parts of the machine. Whether there is shear to be expected or not is also a part of the simulations done prior. In case of this demonstrator for example the headstock is modelled as an beam because the length in z-direction, according to *Figure 2*, is significantly larger than the other two spatial directions. The reason this is modelled as an Euler-Bernoulli beam, not a Timoshenko beam, is that from prior simulations where expected heat sources and therefore deformations are simulated there is not a significant amount of shear expected.

This model brings the advantage that no time-intensive data training is needed like in e.g. [7, 8] or also shown in [9, 10]. Instead the model discussed in this paper is based on physical theories used in common mechanics. The deviation of the TCP in the whole working area is then calculated in the form of compensation tables which are iteratively sent to the machine's control which then corrects the TCP by the values in said table. However the point of time for the update of the table is critical as explained in the following section.

2.3 Point of time for the correction

To explain the importance of the point of time in which the correction is updated a simplified example is shown in *Figure 3*.

direction of tool-movement

tool

desired height of the surface

period of thermal change

$t_{correction}$

z

x
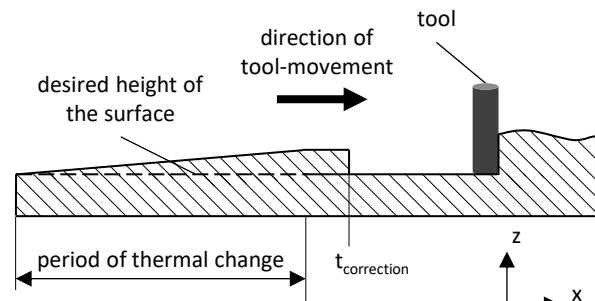
Figure 3. Problem description for the point of time of the correction

In this figure the machining goal would be to machine a planar surface like indicated with the dotted line. However due to thermal influences during the period of thermal change the TCP is deflected in positive z-direction while the tool is progressing in positive x-direction. Therefore the machined surface is deviating from the desired form. If the correction table is updated and the NC (Numerical Control) instantly implements the correction values at the marked place the tool will move in negative z-direction back to the height of the dotted line, creating an undesired edge in the surface of the machined part. It is therefore not only important to model the deviation of the TCP as closely to reality as possible but also to find the right point in time for the update of the correction values.

3. Options for the timing of updating the correction

In this section the possible methods to update the correction table shall be discussed in increasing order of implementation effort and complexity.

The easiest way to implement the iterative update of the correction would be updating it after having passed a certain period of time. Although this brings the risk of manufacturing edges into the workpiece as the the simplification in *Figure 3* shows. One way to avoid that would be to interpolate between the old correction values and the updated ones to reach a smoother transition.

Another possibility is to update the table when the tool is not engaged. However, this does not solve the problem shown in *Figure 3* for every case. If for example the tool finished one line of the surface and goes on to the next one there would still be a height difference in this simple example. However, this method, as well as the following ones, would need more information than only the IDS measurement either from the machines NC or from an additional sensor system.

Once this communication is established it is also thinkable to update the correction when the machine is changing the tool. This would also solve the problem described above. A similar approach would be to schedule the updating according to work stages like between roughing and finishing. Beneficial for this method is that the roughing usually brings more heat into motors and workpiece as the forces for this step are higher, which would lead to a higher thermal change of the machine.

The technologically most advanced procedure would be implementing lines into the NC-code so that the update of the correction would happen only at advantageous points in time. However this would mean, that while creating said code knowledge of the expected deformation and the correction method would be needed, in contrary to the first method which would be easily automatable completly. This could be feased by an expert who has accumulated knowledge of machine and similar workpieces or for example by implementing an automated method like training an AI-system which aims to predict the optimal moment of time respectively line of NC-code for the update of the table.

Regardless of the point in time when the correction is updated another objective needs to be considered. Usually machine tools already utilize compensation tables, e.g. for slack correction. In this case the machine is calibrated geometrically and based on that measurement a compensation table is calculated which is either constant or updated over long time periods. As there are now multiple compensation tables, it needs to be considered if switching all of these on together, meaning effectively adding them up to the single vector by which the TCP is corrected is the most beneficial possibility or if there are other compensation methods that need to be disabled when using the IDS-based compensation method.

4. Results

To show the functionality of the model experiments under comparable conditions were executed. The demonstrator was switched on but left in idle for the night before the experiments began. Then a warm-up cycle of roughly four hours was performed by continuously moving the x-axis back and forth at top speed to change the thermal state of the machine. The length of the warm-up cycle was set by the number of repetitions of the motions which is why it does not equal four hours exactly but slightly shorter. This warm-up phase was followed by a cool-down phase of 5 hours. As the x-axis was moved it can be expected that especially in y-direction a high change rate of the TCP-deviation will be measured as there is considerable friction from the linear guides and heat coming from the motors going into the portal beam carrying the x-sledge and headstock, leading to a bending motion around the z-axis of the machine. Iteratively every 15 minutes the TCP-deviation was

measured tactily over the whole duration of the experiment at four balls mounted to the table, while for reasons of clarity only one ball is shown in this paper, as depicted in *Figure 2*. The sensor used for this measurement is the Heidenhain TS 649. Due to this procedure the point of time of the update of the correction as discussed in *Section 2.3* is not as timecritical as when manufacturing a workpiece. Still for the industrialization of the method the point in time for the update is critical. Therefore the update was done every two minutes which corresponds to the simplest method of updating as described in *Section 2.3*. In this experiment only one defined position in the working area and only the TCP-displacement of this specific point is considered, relative to the beginning of the experiment. Therfore it is not relevant which compensation tables are in use or deactivated.

To determine the quality of the correction the experiment was performed with the correction deactivated during one execution of the experiment, as a reference measurement, and with the correction activated in three repititions. There were comparable temperature conditions in the shopfloor on all versions of the experiment considered. The following figures show the TCP-displacement in x-, y- and z-direction for the uncorrected case, which corresponds to the reference measurement, and the TCP-displacement for the version of each experiment where the correction was activated over the duration of each measurement.

	uncorrected		corrected
x	——	x	··········
y	- - - - -	y	— –
z	– ·– ·–	z	· ·
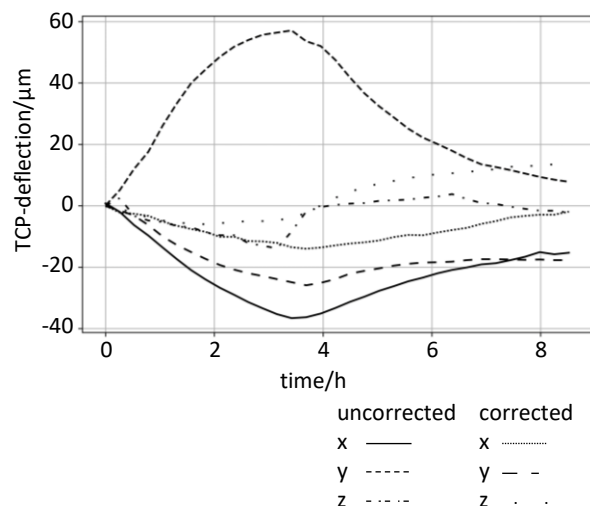
Figure 4. Result of the first experiment conducted

Figure 4 as well as the following show the measured TCP-displacement over the time of the experiments executed while the reference experiment is compared to each one of the three experiments where the correction method was acticated.

The maximum values of the uncorrected case to the x-direction are -37 µm, in y-direction 58 µm and in z-direction 24 µm. With the correction method described in this paper these values are lowered to a maximum of -16 µm in x-direction, 12 µm in y-direction and 7 µm in z-direction.
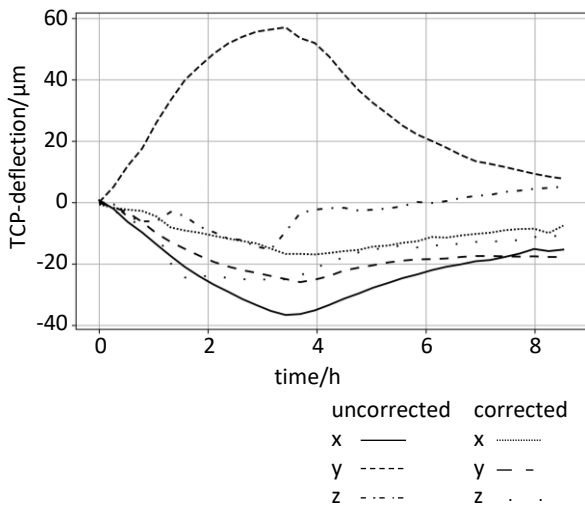
Figure 5. Result of the second experiment conducted

In *Figure 5* the results of the second experiment are shown, again compared to the same reference measurement. It is also visible that also while the course of the graph differs compared to the first corrected experiment the maximum value of the corrected TCP-displacement is close to the values mentioned before. It is also visible that while the residual TCP-deviation in z-direction for all three corrected experiments is lower than for the uncorrected case it is not as low as the other two spatial directions, which offers room for improvement of the model.
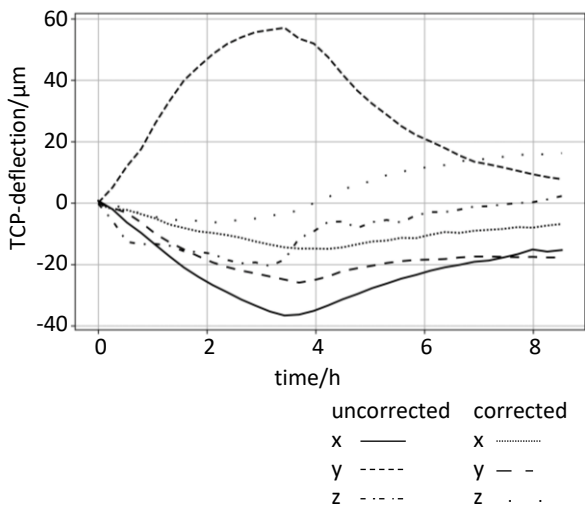

Figure 6. Result of the third experiment conducted

While the corrected and uncorrected values at the end of the experiment have similar values for the TCP-deviation in the z-direction, neglecting positive or negative direction, *Figure 6* shows that during all periods of the experiment TCP-deviation is lowered by the correction method.

Figure 4, *Figure 5* and *Figure 6* show that the corrected and therefore residual TCP-deviation is significantly lowered in every point of time in comparison to the uncorrected case. This is especially the case for the y-direction, as there was the highest displacement of the three spatial directions before the correction due to the bending of the portal beam as described before.

5. Conclusion and outlook

The IDS use a thermally stable CFRP-rod to measure the thermally induced TCP-deviation by measuring the structurual length change of the machine. These measurements are calculated into correction tables using mechanical theories for each of the structural parts equipped with the IDS. The correction tables are then sent to the machines numerical control to lower the said TCP-deviation. As shown in *Section 4* the IDS-based correction method can lower the thermally induced deviation of the TCP by around 60 % over the course of the shown experiments and therefore improve the thermal stability of machine tools.

In future works the point in time of the update of the correction should be investigated to bypass the potential problems described in *Section 2.3*. One solution to this would be to implement the point in time for the update of the correction into the NC-code of every part, however this would have the downside that expert knowledge is needed for every new part that is to be manufactured. An alternative to expert knowledge would be the implementation of an automated process that can be based on the known NC-code to find out the ideal point of time respectively line of code to update the table. Additionally it is to be shown if there are already existing correction methods used in machine tools that should not be combined with the method described in this paper, e.g. slack correction. These further experiments could also be conducted using different equipment for the TCP measurement to cover a bigger volume of the working area than in this case four ball positions. Also the influence of machining a workpiece can be considered in further studies, as the heat from this process will also change the machines structural temperature.

Acknowledgements

References

[1] Mayr J, Jedrzejewski J, Uhlmann E, Donmez MA, Knapp W, et al. Thermal issues in machine tools. CIRP Annals - Manufacturing Technology; 2012. p. 771-791.
[2] M. Putz, C. Richter, J. Regel, M. Bräunig, Industrial relevance and causes of thermal issues in machine tools, in: S. Ihlenfeldt, C. Brecher, M. Putz, D. Billington (Eds.), Conference on Thermal Issues in Machine Tools, Dresden, 2018, pp. 1–12.
[3] Weck M. Werkzeugmaschinen 2. Springer Vieweg. Edition 8.
[4] Brecher C. Zontar D, Tzanetos F, Bertaggia N, Investigation of thermally induced TCP-displacement under load of the machine axes in different areas, 55th CIRP Conference on Manufacturing Systems, 2022
[5] Li J et al. Thermal-error modeling for complex physical systems: the-state-of-arts review. Int. J. Adv. Manuf. Technol. 42; 2009. p. 168–179.
[6] Li Y, Yu M, Bai Y, Hou Z, Wu W. A Review of Thermal Error Modeling Methods for Machine Tools. Applied Sciences Journal. Volume 11. Issue 11; 2021
[7] P.-L. Liu, Z.-C. Du, H.-M. Li, M. Deng, X.-B. Feng, J.-G. Yang, Thermal error modeling based on bilstm deep learning for cnc machine tool, Advances in Manufacturing 9 (2) (2021) 235–249.
[8] Abdulshahed A, Longstaff A, Fletcher S, Potdar A. Thermal error modelling of a gantry-type 5-axis machine tool using a Grey Neural Network Model. Journal of Manufacturing Systems. Volume 41. Elsevier BV; 2016. p. 130-142
[9] Turek P, Jedrzejewski J, Modrzycki W. Methods of machine tool error compensation. Journal of Machine Engineering. Volume 10. Issue 4; 2010
[10] Li J et al. Thermal-error modeling for complex physical systems: the-state-of-arts review. Int. J. Adv. Manuf. Technol. 42; 2009. p. 168–179.

Face diagonal positioning and straightness error motions of machining centres according to ISO standards

Morteza Dashtizadeh, Andrew Longstaff, Simon Fletcher[1]

[1]*Centre for precision technologies, University of Huddersfield, UK*

Morteza.dashtizadeh@hud.ac.uk

Abstract

According to ISO 230-6:2002, diagonal tests can be applied to evaluate the volumetric performance of a machine tool. In the mentioned standard, "positioning errors" of four body diagonals are measured separately and compared with each other. The same can be done for every pair of face diagonals in XY, YZ and ZX planes. The latest revision of ISO 230-1 in 2012 introduced the concept of "diagonal straightness tests" of the linear trajectories made by interpolation of two or three linear axes of a machine tool on its face and body diagonals respectively. In this research work, some positioning and straightness tests are conducted along linear trajectories at different angles (partial face diagonals) in the horizontal XY plane of a vertical machining centre with kinematic chain of [w X' Y' b Z (C) t]. To present the results, we introduce two components of face diagonal straightness, not yet covered in current ISO standards. These additions offer a more comprehensive analysis of the results and performance of the machine tool under test. The results of experiments are compared with the predicted results obtained by simulation computed based on the homogeneous transformation matrices (HTM) method in XY plane via error motions of the linear axes and their squareness error.

Keywords: Machine tools performance, ISO standards, diagonal tests, face diagonal straightness, face diagonal positioning, volumetric accuracy of machine tools, planar accuracy of machine tool

1. Introduction

ISO 230-6:2002 [1] specifies positioning tests to be carried out along face and body diagonals of machine tools as a metric to evaluate their planar and volumetric performance. ISO 230-1:2012 [2] not only explains positioning errors of linear trajectories obtained from interpolation of multiple linear axes, but also mentions the straightness of these linear trajectories. This standard states "The (simultaneously coordinated) two or more linear axes are moved nominally on a straight line, on a face or a body diagonal of the prismatic work volume. During such movement, the positioning or straightness error motions are measured, and deviations are recorded and evaluated." while in the current ISO 230-6, only positioning of the linear trajectories (diagonal tests) is checked which is probably not a complete indicator of the volumetric behaviour of the machine under test. However, ISO 230-1 does not define straightness components for face/body diagonals and only expresses the main concept. From a practical point of view and for the reproducibility of test results, it is evident that these two straightness components must be defined thoroughly. In some machine-specific standards such as ISO 10791-6:2014 [3] and ISO 13041-6:2015 [4] for evaluating the interpolation performance of machining centres and turning centres respectively, there is a test in which straightness of a linear trajectory is checked over a length of 100 mm. This test determines behaviour of the machine while interpolating with two linear axes to generate a linear trajectory. Since this trajectory is very short, it cannot show the planar/volumetric performance of the machine.

There have been some controversial research on using body diagonal tests to identify errors of machine tools, as well as for compensation purposes. Wang and Liotto [5] proposed step diagonal tests and expanded the use of side information from this test for identifying different error motions of linear axes of the machine along with its squareness errors. They also attempted to compensate machine tool errors with mathematical computations derived from diagonal tests. Chapman [6] explained limitations of body diagonal measurements and provided a simple example of a machine tool with two linear axes equal in their axis stroke, one with negative scaling error and another with identical positive scaling error. Considering the ideal third axis, he argued that in this situation, the body diagonal positioning test according to ISO 230-6 does not provide a useful metric for volumetric performance of the machine. By this ideal example, he conveyed the message that the diagonal positioning tests individually cannot be used reliably as volumetric index without the results of regular tests. However, he did not provide any reasons how a liear axis might show straightness and angular error of zero. It is obvious that all these errors are synthetised together and their cumulative effects are observed as diagonal positioning test results. Even if in some special cases the diagonal positioning component might become zero, but the other two straightness components are very unlikely to show zero deviations simultaneously. Svoboda [7] carried out some diagonal experiments and rejected Wang's approach by demonstrating some contradictions in practical results. Ibaraki and Hata [8, 9] highlighted the necessary conditions such as the alignment of the laser, flat mirror, and test direction under which Wang's formulations are valid for taking advantage of the results of step diagonal tests for error compensation.

This research work defines straightness components of face/body diagonal trajectories. Then, based on this definition, it shows some experimental test results conducted with a laser system on a 3-axis VMC, along with the simulation outputs employing Homogeneous Transformation Matrices (HTM)

method. Discussing the main applications of diagonal tests is another major message of this article

2. Defining diagonal straightness components

For any body diagonal trajectory, a vertical plane can be crossed in a way that it contains the nominal body diagonal trajectory. The direction of the positioning deviation at any target, e_{DD}, is the same as the direction of the nominal body diagonal. Since two straightness components must be mutually perpendicular to the positioning deviation, the first straightness deviation, e_{S1D}, lies in the passing vertical plane. The positive sign of e_{S1D} is defined like the positive direction of the Z-axis. By having positive sign and direction of e_{DD} and e_{S1D}, the positive direction of e_{S2D} is determined by the cross product of e_{DD} to e_{S1D} as shown in equation (1).

$$u_{eS2D} = u_{eDD} \times u_{eS1D} \qquad (1)$$

where u_{eDD}, u_{eS1D}, and u_{eS2D} are unit vectors of the positioning deviation, straightness 1, and straightness 2 deviations respectively.
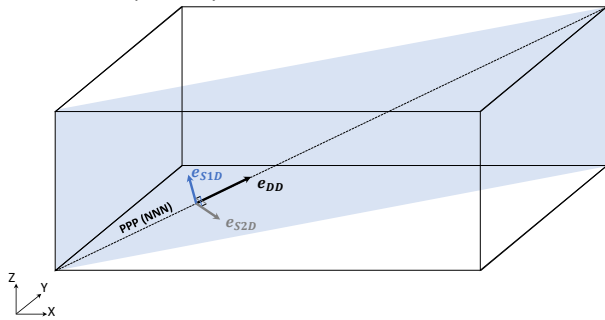

Figure 1. Direction and sign of straightness components of body diagonal trajectories

Figure 1 shows a PPP(NNN) body diagonal with its positioning and two straightness deviations at an arbitrary target position in the working volume of a machine tool. In this research work, face diagonal trajectories in XY plane are studied. Therefore, a simplified form of **Figure 1** is used to determine directions of straightness components. *Figure 2* shows e_{S1D} and e_{S2D} for a face diagonal trajectory located in XY plane with Positive-Positive directions of X and Y-axes. In this case, e_{S1D} is parallel to Z-axis and e_{S2D} is derived from the cross product of e_{DD} to e_{S1D}.
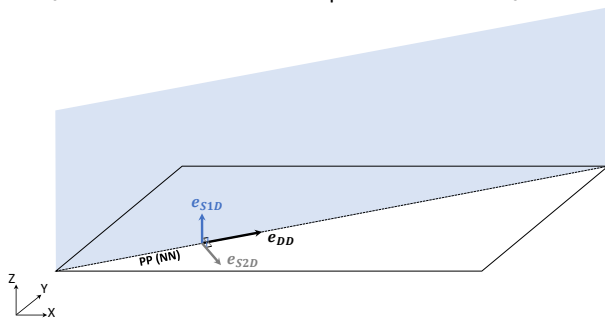

Figure 2. Direction and sign of straightness components of face diagonal trajectories

A plane whose normal vector is the body diagonal trajectory is depicted in **Figure 3**. From analytical geometry point of view, e_{S1D} and e_{S2D} vectors lie in this plane. As shown in this schematic figure, the resultant vector of these two straightness deviations is a dashed orange segment. This resultant vector can be decomposed into infinite numbers of straightness pairs. In other words, two straightness deviation components can be defined in many ways. Therefore, by passing a vertical plane from the body diagonal, the location of e_{S1D} is fixed. As illustrated in **Figure 1** and **Figure 2**, e_{S1D} direction is unique for any individual body and face diagonals.
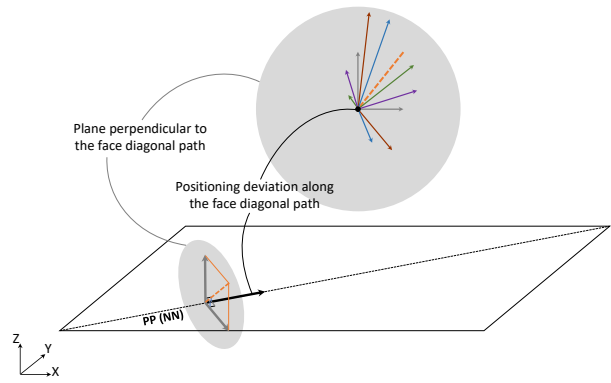

Figure 3. Possible directions of straightness components

3. Volumetric error modelling

To derive volumetric errors of machine tools, Homogeneous Transformation Matrices (HTM) method was applied to 2-axis and 3-axis machines by Donmez et al [10] , and Okafor and Ertekin [11], respectively. Dashtizadeh et al [12] demonstrated probable volumetric errors of machining centres made with conformance to tolerances of ISO 10791 series for machines with 500 mm stroke of all linear axes using the HTM method.

HTM method can compute error vectors at all target positions at which experimental data is available. To derive volumetric error vectors at the other coordinates, mathematical interpolation of captured data is employed. If the machine axis under test behaves differently in areas where there is no captured data, the error model shows some deviations from the experimental data gathered from different linear and other free-shape trajectories.

To derive the aforementioned e_{DD}, e_{S1D}, and e_{S2D} for any diagonal trajectory, some geometrical computations need to be executed. Firstly, all volumetric error vectors along the diagonal trajectory is to be calculated. These vectors result in the positioning deviation at any target position. The same operation is implemented to derive e_{S1D} and e_{S2D}. For this study, a MATLAB code was developed to predict the positioning and two straightness components. As input, error motions of the linear axes of the machine along with their squareness values were entered into the MATLAB code. Then, any linear trajectory with its E_{DD}, E_{S1D}, and E_{S2D} as the peak-to-peak value of all deviations were extracted for any input coordinates of start and end positions.

For this study, a 3-axis vertical machining centre with the kinematic chain of [w X' Y' b Z (C) t] was modelled. **Figure 4** shows this configuration with the coordinate frames attached to its components used for generating HT matrices.
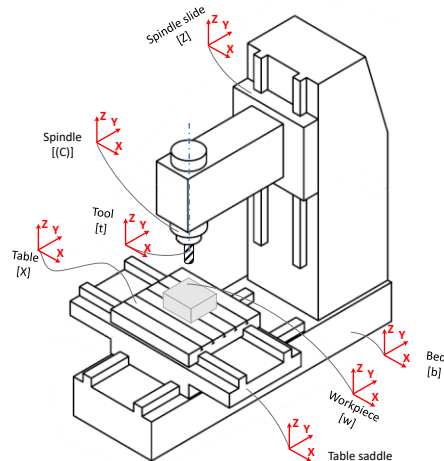

Figure 4. VMC with kinematic chain of [w X' Y' b Z (C) t] and its c oordinate frames (modified from ISO 10791-2 [13])
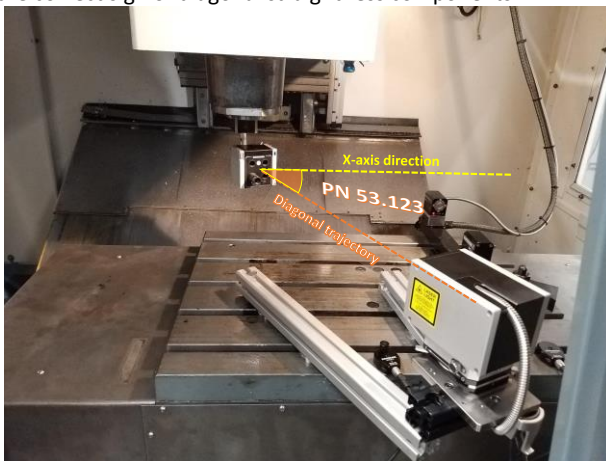
4. Experimental tests

Some experiments were conducted on Cincinnati Arrow 500 3-axis VMC with the same kinematic chain shown in **Figure 4**, at different angles between X and Y-axes along face diagonals. These tests were carried out with Renishaw XM-60 laser system. **Figure 5** and **Figure 6** show the setup of the experiments for face diagonal trajectories of PP 46.397 and PN 53.123, respectively. PP 46.397 denotes that both X and Y-axes move along their positive directions while the diagonal trajectory makes an angle of approximately 46.397 degree with the X-axis direction.
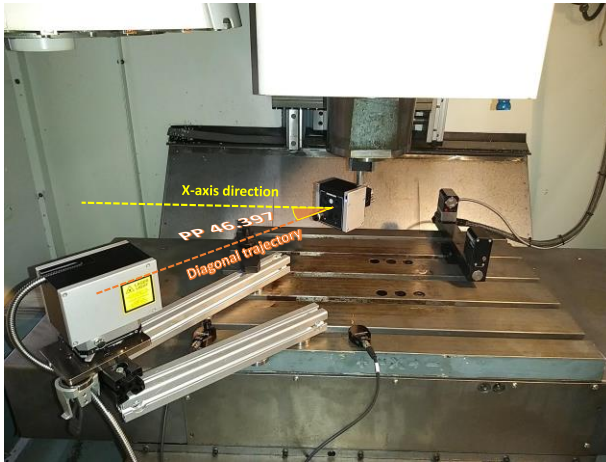
Figure 5. Experimental setup with Renishaw XM-60 laser system for f ace diagonal tests in XY plane of a VMC at PP 46.397 deg.

With the setup shown in **Figure 5** and **Figure 6**, the Renishaw XM-60 directly measures E_{DD}, E_{S1D}, and E_{S2D} errors. However, its current commercial software does not provide appropriate notations for diagonal tests. As a practical approach, the diagonal trajectory (D), can be set as one of the usual linear axis (e.g. X-axis). In this case, E_{ZX} and E_{YX} will represent E_{S1D} and E_{S2D}, respectively, for the face diagonal under test. One challenge in the execution of this test is the proper setting of the correct sign of diagonal straightness components.

Figure 6. Experimental setup with Renishaw XM-60 laser system for f ace diagonal tests in XY plane of a VMC at PP 46.397 deg.

5. Results of the tests and simulations

As an example, **Figure 7** shows positioning deviations, e_{DD}, derived by HTM and those measured by the laser system at 10.388 degrees when X and Y-axes move along their positive directions.
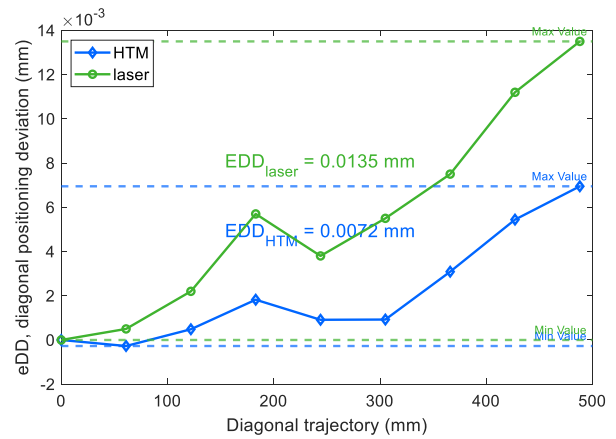
Figure 7. Face diagonal positioning deviations, measured by laser and derived by HTM at PP10.388

Figure 8 and **Figure 9** illustrate e_{S1D} and e_{S2D} for the same direction/angle, respectively. As demonstrated, pattern of the experimental data and HTM simulations follows the same shape with some deviations from each other.
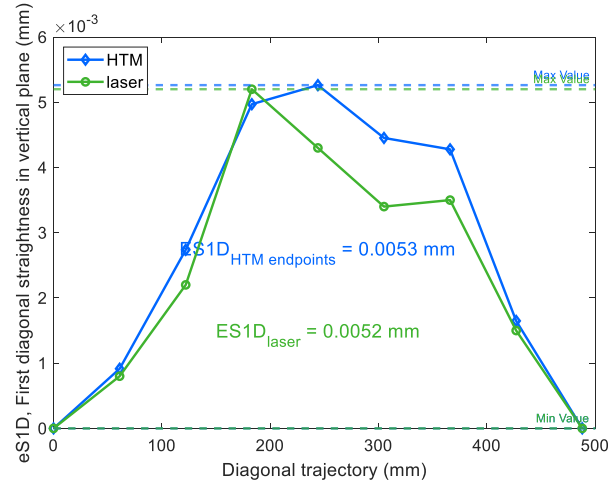
Figure 8. Face diagonal straightness 1 deviations, measured by laser and derived by HTM
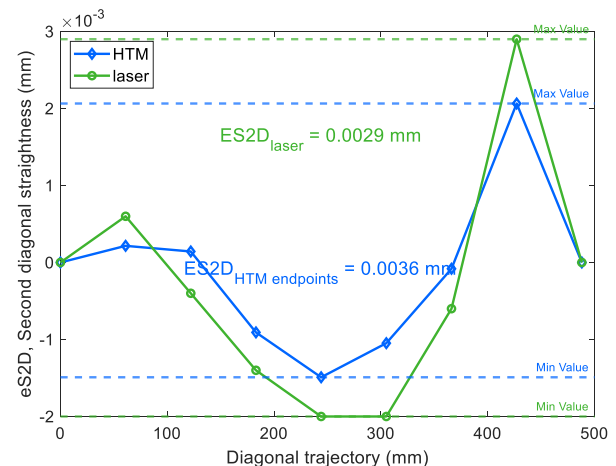
Figure 9. Face diagonal straightness 2 deviations, measured by laser and derived by HTM

Face diagonal tests were conducted at 18 different direction/angles. Comparative results of experiments versus HTM simulations are depicted in **Figure 10**, **Figure 11**, and **Figure 12** for positioning (E_{DD}), straightness 1 (E_{S1D}) and straightness 2 (E_{S2D}) errors respectively.

As explained in ISO 230-1 and ISO 230-6, squareness between linear axes can be extracted from a pair of face diagonal

positioning tests (PP and PN at the same angle). This technique is quite useful to measure squareness of large machines with small uncertainty. The range and uncertainty of current measuring instruments commonly used for squareness measurements pose challenging issues for large machine tools with tight tolerances.
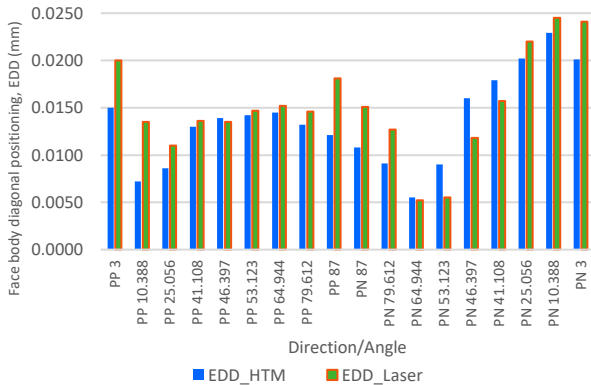
Figure 10. Comparison between laser readings and HTM output for positioning error at different direction/angle

Figure 11. Comparison between laser readings and HTM output for straightness 1 error at different direction/angle

Figure 12. Comparison between laser readings and HTM output for straightness 2 error at different direction/angle

By combination all these three errors, one diagonal positioning and two diagonal straightness errors, a better understanding of volumetric behaviour of any machine tool is achievable. Furthermore, it can be used as a suitable index to check whether the compensation of the linear axes of the machine was implemented properly.
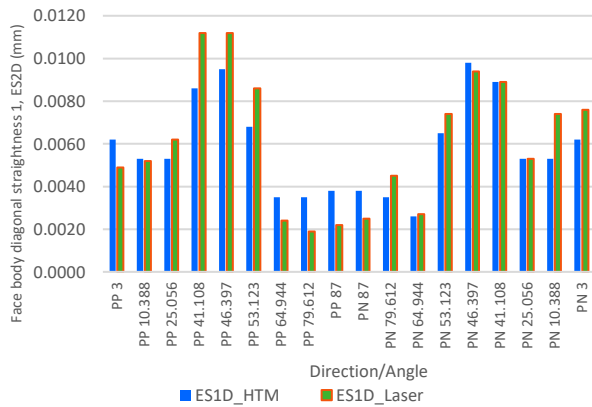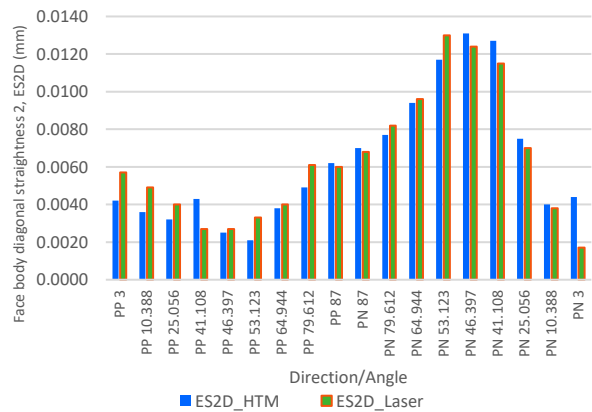
Body and face diagonal test results could also be used to check non-rigid body behaviour of machine tools within a short time, which is a useful tool for research studies as well as for specific industrial applications.

6. Summary and conclusion

This paper defined straightness components of body/face diagonal trajectories and demonstrated the practicality of face diagonal straightness measurements. It also presented some experimental tests conducted at different direction/angles in the XY plane of the machine. The experimental results were compared with the output of computer simulations. These new definitions of diagonal straightness could potentially be introduced to ISO 230-6 to provide a clearer view of planar/volumetric performance of machine tools. The diagonal tests can efficiently be used for verification of machine tools compensation. Additionally, these tests can be applied for fast regular checks on large-size machines.

In near future, body diagonal positioning and straightness components of machines with various kinematic chains will be investigated.

References

[1] ISO 230-6:2002, Test code for machine tools — Part 6: Determination of positioning accuracy on body and face diagonals (Diagonal displacement tests).

[2] ISO 230-1:2012, Test code for machine tools — Part 1: Geometric accuracy of machines operating under no-load or quasi-static conditions

[3] ISO 10791-6:2014, Test conditions for machining centres — Part 6: Accuracy of speeds and interpolations

[4] ISO 13041-5:2015, Test conditions for numerically controlled turning machines and turning centres — Part 5: Accuracy of speeds and interpolations

[5] C. Wang and G. Liotto, "A Theoretical Analysis Of 4 Body Diagonal Displacement Measurement And Sequential Step Diagonal Measurement," WIT Transactions on Engineering Sciences, vol. 44, 2003, doi: 10.2495/LAMDAMAP030401.

[6] M. A. V. Chapman, "Limitations of laser diagonal measurements," (in English), Precision engineering, vol. 27, no. 4, pp. 401-406, 2003, doi: 10.1016/S0141-6359(03)00041-2.

[7] O. Svoboda, "Testing the diagonal measuring technique," Precision Engineering, vol. 30, no. 2, pp. 132-144, 2006, doi: 10.1016/j.precisioneng.2005.06.002.

[8] S. Ibaraki, T. Hata, and A. Matsubara, "A new formulation of laser step-diagonal measurement—two-dimensional case," (in English), Precision engineering, vol. 33, no. 1, pp. 56-64, 2009, doi: 10.1016/j.precisioneng.2008.03.007.

[9] S. Ibaraki and T. Hata, "A new formulation of laser step diagonal measurement—Three-dimensional case," (in English), Precision engineering, vol. 34, no. 3, pp. 516-525, 2010, doi: 10.1016/j.precisioneng.2010.02.004.

[10] M. A. Donmez, D. S. Blomquist, R. J. Hocken, C. R. Liu, and M. M. Barash, "A general methodology for machine tool accuracy enhancement by error compensation," Precision Engineering, vol. 8, no. 4, pp. 187-196, 1986/10/01/ 1986, doi: https://doi.org/10.1016/0141-6359(86)90059-0.

[11] A. C. Okafor and Y. M. Ertekin, "Derivation of machine tool error models and error compensation procedure for three axes vertical machining center using rigid body kinematics," International journal of machine tools & manufacture, vol. 40, no. 8, pp. 1199-1213, 2000, doi: 10.1016/S0890-6955(99)00105-4.

[12] M. Dashtizadeh, A. Longstaff, and S. Fletcher, "Estimation of volumetric errors of a machining centre fabricated with conformance to geometric tolerances of ISO 10791 series," presented at the Laser Metrology and Machine Performance, Edinburgh, Uk, 2023.

[13] ISO 10791-2:2023, Test conditions for machining centres — Part 2: Geometric tests for machines with vertical spindle (vertical Z-axis)

Simulation design of vibration blade for silicon wafer dicing system

Rendi Kurniawan[1], Shuo Chen[1], Hanwei Teng[1], Pil Wan Han[2], Tae Jo Ko[1,*]

[1]Precision Machining Laboratory room 214, Department of Mechanical Engineering, Yeungnam University, South Korea
[2]Electric Machines and Drives Research Center, Korea Electrotechnology Research Institute, South Korea

rendi@ynu.ac.kr, 22250068@yu.ac.kr, 1950806860@ynu.ac.kr, pwhan@keri.re.kr, tjko@yu.ac.kr

Abstract

This article presents a recent work regarding the design of an ultrasonic vibration blade for use in ultrasonic wafer dicing applications. The design of the vibration blade comprises the main hub plate, support hub plate, piezo-ring, and diamond blade. Finite element analysis (FEA) was used in the simulation design of the vibration blade to identify the optimal parameters for generating radial vibrations. The analysis revealed that the radial vibration mode can be generated at a frequency of approximately 40 kHz. A thin piezo-ring was selected to induce radial vibrations into the body structure. The main hub was designed with specific slots to facilitate the radial propagation of vibrations. The slot count, slot angles, and pitch angles were adjusted to find the optimal frequency. Additionally, this analysis investigated variables such as inner diameter, outer diameter, and piezo thickness to determine the ideal frequency value. According to the simulations, a slot angle of 20 degrees, a pitch angle of 60 degrees, and six slots provided the best frequency result which is close to 40 kHz. This study conducted experimental impedance frequency tests to validate the simulation's findings. The results demonstrated a close similarity between the experimental frequency and the frequency predicted in the simulation.

Piezo-electric, Simulation, Ultrasonic, Vibration

1. Introduction

The dicing method is a traditional cutting technique used to slice the silicon wafer as the final step in the microchip manufacturing process. In this process, it is crucial to maintain the standard quality of the kerf/groove without any chipping, fractures, or damage. The conventional approach in silicon wafer processing typically involves using grinding grains or abrasive cutters on the tool. However, a significant drawback exists in this conventional method due to the brittle nature of silicon, leading to numerous edge chippings when the abrasive particles impact the workpiece.

There are various dicing methods used to slice silicon wafers besides the conventional approach, including scribing [1], laser dicing [2], plasma dicing [3], ultrasonic dicing [4], and more. Scribing is a straightforward method for cutting silicon material. However, a significant challenge arises when the depth of the cut exceeds the critical depth of brittle-ductile transition, leading to cracks or breakage [1]. Laser dicing shows promise as a future dicing method, despite significant drawbacks such as the thermal effect, formation of a porous layer, and high-stress concentration on the material [5]. Additionally, plasma dicing is considered one of the best candidates; however, its real industrial implementation poses challenges.

One of the methods is ultrasonic dicing [4], which involves imparting simultaneous vibration to the saw blade. Consequently, the abrasive grains can cut a minimal depth of the material. Ultrasonic dicing offers several advantages over other methods, including reduced damage and fracture of the kerf, ease of implementation, lower cost, and comparable processing time to conventional dicing methods. To implement the ultrasonic dicing technique, the design of an ultrasonic vibration dicing blade has been developed.

The primary objective of this brief paper is to introduce the simulation and prediction of vibration amplitude. The slot count, slot angles, and hinge angles were adjusted to determine the optimal desired frequency. Subsequently, the impedance frequency was identified at approximately 40.604 kHz.

2. Design, Simulation and Experimental Setup

2.1. Design and FE simulation setup

Figure 1(a) illustrates the design of the ultrasonic dicing blade, comprising a piezo, main hub, saw-blade, and support hub. The material composition of each component is depicted in Table 1. The main hub was intricately designed with specific slots to facilitate radial propagation of vibrations, utilizing a triangular double slot configuration. Throughout the design process, adjustments were made to the slot count, slot angles, pitch angles, and the dimensions of the piezo were roughly examined to understand its impact. The piezo vibrates along radial direction. As shown by the red arrow in Figure 1(b).

Table 1 Material composition of each component

No	Component	Material
1	Piezo	Ceramic
2	Main-Hub	Aluminum
3	Saw-Blade	Diamond
4	Support-Hub	Aluminum

(a)

(b)
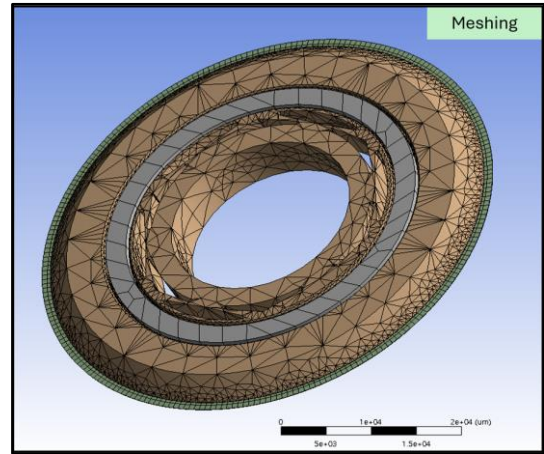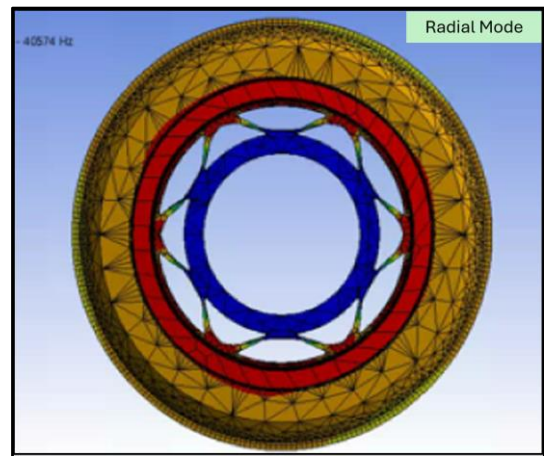
Figure 1. Ultrasonic dicing blade design

Finite Element (FE) simulation was conducted using ANSYS v19.2, with modal analysis performed to assess the radial vibration mode. Figure 2 depicts the setup for the FE simulation in ANSYS v19.2, showcasing the boundary conditions, meshing, and frequency results.

(a)

(b)

(c)
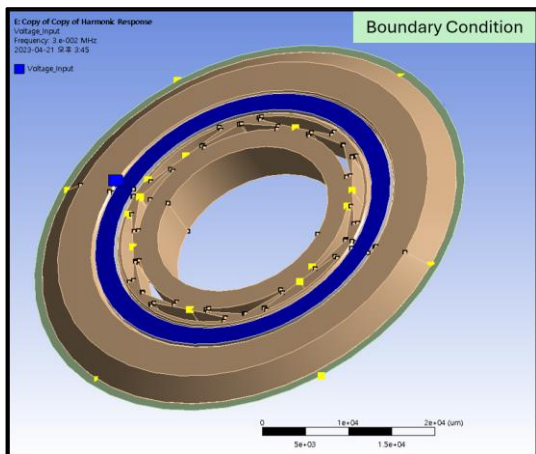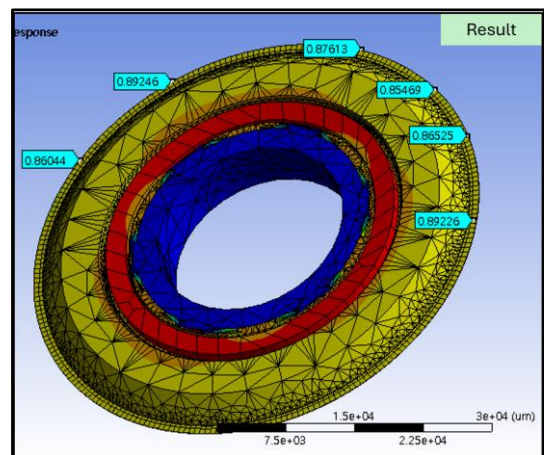
(d)

Figure 2. FE simulation setup in the ANSYS software

2.2. Experimental setup

Figure 3 illustrates the experimental setup for impedance frequency testing. In Figure 3(a), the impedance analyzer was employed to validate the ultimate design of the ultrasonic dicing blade. The blade was connected with the impedance analyzer by cable, the positive electrode is connected to the piezo and the negative electrode is connected to the body. A frequency range of 30 to 50 kHz was chosen with an input voltage of approximately 10 V. Figure 3(b) shows schematic diagram of the measurement. The displacement optical sensor was used to obtain the amplitude of the blade.
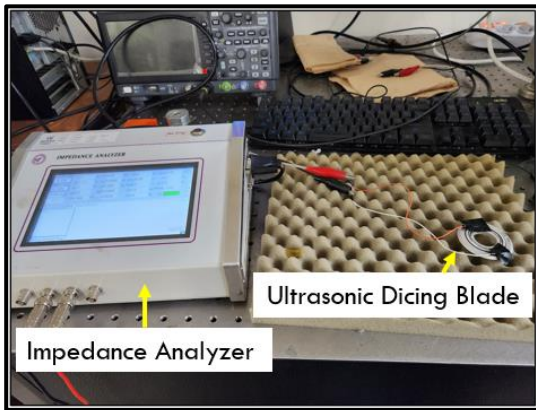
(a)
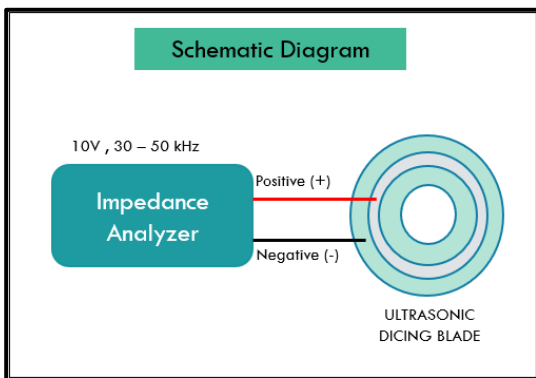
(b)

Figure 3. Impedance frequency experimental setup

3. Simulation Result

Table 2 presents the results of FE simulation for modal analysis. The radial mode is approximately 41.334 kHz for a slot angle of 20°, pitch angle of 60°, and slot count of 6. The radial frequency experiences a slight increase with a slot count of 8. However, the radial mode is nonexistent with a slot count of 12. The torsional frequency values range between 13 and 18 kHz, making them potentially beneficial for vibration-assisted cutting applications requiring low frequencies (< 20 kHz). A frequency of 41.334 kHz is considered sufficient for vibration-assisted applications.

Table 2 Frequency and slot dimension

Slot Angle /°	Pitch angle /°	Slot count	Torsional /kHz	Radial /kHz
10	30	12	18.992	NA
15	45	8	16.181	42.638
20	60	6	13.539	41.334

Table 3 Frequency and piezo thickness variation

Inner DIA /mm	Outer DIA /mm	Thickness /mm	Torsional /kHz	Radial /kHz
32.3	37	0.5	13.539	41.334
32.3	37	1	13.253	40.201
32.3	37	1.5	12.943	39.056
32.3	37	2	12.591	37.792
32.3	37	2.5	12.183	36.078
32.3	37	3	11.684	32.448

Table 4 Frequency and piezo outer diameter variation

Inner DIA /mm	Outer DIA /mm	Thickness /mm	Torsional /kHz	Radial /kHz
32.3	37	0.5	13.539	41.334
32.3	38.5	0.5	13.461	40.999
32.3	40	0.5	13.366	40.674
32.3	41.5	0.5	13.253	40.357
32.3	43	0.5	13.139	40.054

Table 5 Frequency and piezo inner diameter variation

Inner DIA /mm	Outer DIA /mm	Thickness /mm	Torsional /kHz	Radial /kHz
32.3	43	0.5	13.139	40.054
33.5	43	0.5	13.207	40.304
35	43	0.5	13.284	40.623
36.5	43	0.5	13.367	40.951
38	43	0.5	13.454	41.293

Tables 3, 4, and 5 display the frequency results with variations in the piezo dimensions, including inner diameter, outer diameter, and thickness, respectively. The frequency decreases as the thickness increases, because in piezo, the thickness determines the resonance mode. Thinner piezo exhibits higher resonance frequencies because they support higher-order resonance modes, where the waves travel shorter distances, and there is a slight decrease in frequency when the outer diameter increases. This indicates that the piezo thickness has a significant impact on the frequency. In the case of inner diameter variation, the frequency does not exceed 41.334 kHz.

4. Impedance Frequency Result

The ultrasonic dicing blade has been manufactured with the final dimensions set at a slot angle of 20, pitch angle of 60, and slot count of 6. In Figure 4, the impedance frequency of the ultrasonic dicing blade is depicted with a piezo thickness of 0.5 mm. The resonance frequency (f_s) is measured at approximately 40.604 kHz, and the anti-resonance (f_p) frequency is measured at about 40.790 kHz. The mechanical quality factor (Q_m) is approximately 275.32. The resonance frequency prediction closely aligns with the experimental value, with an error of approximately 1.79%.
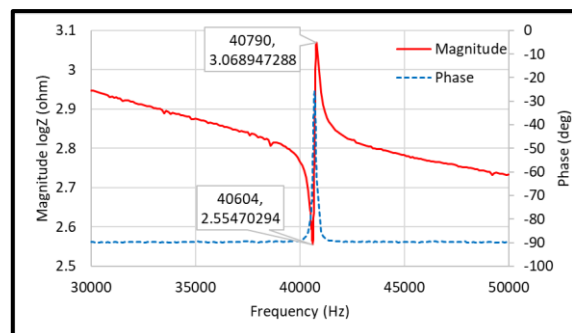
Figure 4. Impedance frequency of ultrasonic dicing blade

5. Conclusion

According to the FE simulation results, the frequency closely aligns with 40 kHz when the design incorporates a slot angle of 20, a pitch angle of 60, and a slot count of 6. The piezo dimension, particularly the thickness, has a significant impact on the frequency. Additionally, the resonance frequency prediction is nearly identical to the experimental value, with an error of approximately 1.79%. The established resonance frequency of the ultrasonic dicing blade is approximately 40.604 kHz.

Acknowledgment

References

[1] Peizhi W, Bing W and Shreyes N M 2020 Modeling and simulation of phase transformation and crack formation during scribing of mono-crystalline silicon *Int. J. Mech. Sci.* **175** 105527.

[2] Tang Y, et al. 2008 Laser dicing of silicon wafer *Surface Review and Letters* **15** 153-159.

[3] Matsubara N, et al. 2012 Plasma dicing technology *Proceedings 2014 4th Electronic System Integration Technology Conference*.

[4] Jianyun S, Xu Z, Jianbin C, Ping T and Xian W 2019 Investigation on the edge chipping in ultrasonic assisted sawing of monocrystalline silicon *Micromachines* **10** 616.

[5] Michael R J, Kuan Y C and Zainuriah H Femtosecond laser dicing of ultrathin Si wafers with Cu backside layer – A fracture strength and microstructural study *J. Manuf. Proc.* **62** 859-872.

Method for optimizing cam workspeed utilizing Artificial Intelligence technique

Michael Skinner[1], Daniel Turner[1]

[1]Fives Landis Ltd, UK

Michael.skinner@fivesgroup.com

Abstract

Optimisation of a cylindrical grinding process is usually considered to be an art which relies on experts who have many years of grinding experience. This problem is made worse when grinding out-of-round components as this adds machine dynamics and non-uniform thermal limitations to an already complex situation.

As always in manufacturing, the desire to increase productivity and 'speed up' conflicts with product quality. Historically product quality is maintained at the expense of productivity, and for cams the approach has been to use a variable work-speed to slow down over complex sections to try to mitigate geometric error, or to slow where there are thermal issues to lower the metal removal rate.

This has proved difficult to solve mathematically. There are competing objectives, and the problem space is circular and continuously dynamic with no 'at rest' starting point. Consequently, the calculated work-speeds end up rather subjective and it's left to the skill and experience of the process engineers to get the most out of the grind.

We present how the problem was sub-divided such that the machine dynamics and part quality is separated out and each given a single numerical optimisation target which is ideal for an Artificial Intelligence (AI) based optimisation [1]. With the former 'solved' by AI, the later while complex, can use that as its starting point and be solved with conventional spreadsheet-like mathematics.

Patent granted 2019 [2]

AI, grinding, asymmetric profiles, optimised grinding feed rates

1. Background
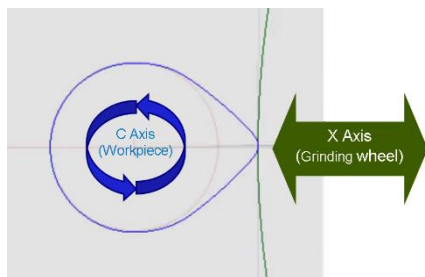
Figure 1. Cam grinding principle

In grinding operations, the workpiece typically rotates about the C-axis while the grinding wheel traverses along the X-axis. For achieving circular geometries, a steady X-axis advance leads to the desired diameter. However, complex shapes necessitate the X-axis to follow intricate contours during its movement. This requires rapid and precise control of the X-axis position.

2. The Challenge

The arbitrary nature of workpiece shapes translates to irregular, non-sinusoidal oscillation profiles for the X-axis. While moderate C-axis rotation speeds allow the X-axis to track the desired path accurately, increasing production demands necessitate higher operating speeds.

This presents a major challenge:

- **Reduced Axis Position Accuracy**: At high C-axis speeds, the X-axis struggles to follow the rapidly changing path, leading to deviations and compromised grinding quality.
- **Risk of Damage**: Sharp changes in the workpiece profile encountered at higher speeds, translate to high material removal rates, increasing the risk of burn and workpiece defects.

The key bottleneck lies in identifying the areas within the grinding profile that are most detrimental to high-speed operation. These critical sections limit the allowable C-axis speed for the entire workpiece revolution.

Fortunately, slowing down the C-axis only during these sections, instead of throughout the entire cycle, presents a potential solution, and represents the traditional strategy of creating an angular velocity profile known as a 'Workspeed'.

3. Traditional Workspeeds

The traditional workspeed strategy, involves tailoring the C-axis speed throughout the grinding cycle based on strategically slowing down only during critical sections with steep profiles. This can make a huge difference to cycle time and quality as the majority of the profile is run at 'full' speed.
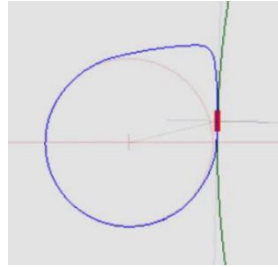

Figure 2. Cam grinding critical section – large contact region
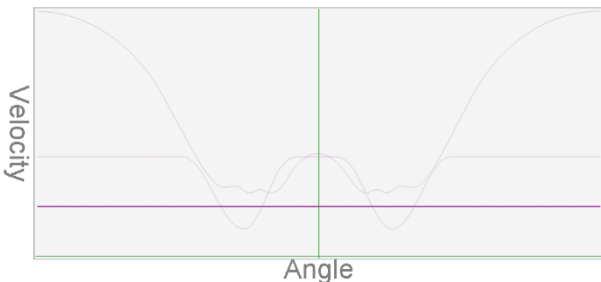
Comparing to a constant workspeed:

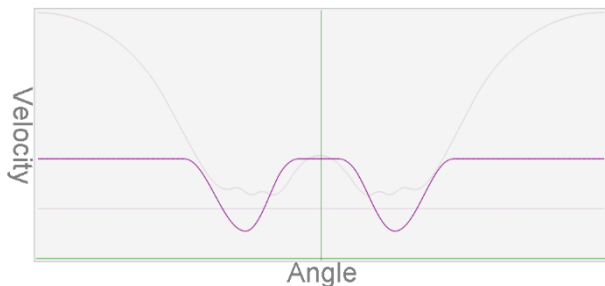**Figure 3.** Constant Velocity – slowed over whole revolution

Figure 4. Slowed only over steep sections

- **Axis Position Accuracy**: Lowering the C-axis speed during peak X axis movements allows the X-axis to accurately follow the intended path, minimizing tracking errors and enhancing grinding quality.
- **Minimize Damage Risk**: Lowering the C-axis speed during peak material removal sections mitigates the risk of burn and workpiece defects.

By implementing Workspeed variation, we can leverage the benefits of high-speed grinding while addressing the limitations imposed by complex workpiece geometries. This approach has the potential to significantly enhance grinding efficiency and quality, while maintaining machine competitiveness in a demanding production environment.

3.1. Calculation

The traditional "Workspeed" approach prioritizes equalizing Metal Removal Rate (MMR) or cutting surface speed while adhering to constraints imposed by the machine and process. Avoiding burn and surface finish are the final objective, and because burn is seen as a result of MMR and therefore grinding energy, the calculations are framed such that achieving a constant MMR is the primary goal. Other factors like jerk and other high-order derivatives while important and always factored in, are often side-lined.

Within this framework, the MMR is maximized around a "base circle" (a circular section at the back of the cam). Subsequently, sections of the Workspeed profile are slowed down to maintain a constant MMR throughout the machining process. This slowdown may be further adjusted if axis constraints dictate.

3.2. Limitations

Despite offering an improvement over constant feed rate machining, the traditional Workspeed approach suffers from several limitations:

- **Oversimplification of Burn Mitigation**: Using MMR as the sole factor for burn control is overly simplistic. Numerous variables influence burn, such as material properties, tool geometry, spindle power, coolant effectiveness, and cutting speed. Relying solely on MMR for burn mitigation is inadequate.
- **Counterintuitive Effects on Burn**: Paradoxically, maintaining constant MMR to control burn can actually worsen the situation. Slowing down the tool creates a hot spot and allows more time for heat transfer, concentrating the thermal energy in a specific region and potentially exacerbating burn.
- **Mathematical Complexity**: Back-calculating the required feed rate based on axis dynamics is mathematically challenging. Jerk calculation involves solving a third-order integration, and all constraints must be simultaneously considered, further complicating the process.

Ultimately, while the traditional variable workspeed approach represents a significant advancement compared to constant workspeed machining, its results often resemble an informed guess due to its limitations. Successful application still requires significant skill and experience from a human to get right.

4. Reframing The Optimization

Traditional approaches to grinding optimization have heavily focused on optimising the workspeed as a singular solution to address cycle time and quality issues. Cutchall [3] and Krajnik et al. [4] exemplify this approach, proposing simultaneous optimization of axis dynamics, MMR, power, wheel wear, and surface temperature as constraints for a given cut depth which can then be varied to discover some kind of optimum.

Many papers have noted that increasing workpiece speed has the effect of reducing the temperatures generated and consequently lower the possibility of thermal damage on the component.[5,6] This is because by allowing the work to rotate as fast as possible the grinding hot-spot spends the least possible time in any given area and so the energy has less time to transfer to the work before the hotspot moves on.

Ultimately, for customers there are only two key quality constraints; Form error and thermal damage, with cycle time as an optimisation that can be mitigated by cost (by adding more machines in parallel).

We propose switching away from calculating a workspeed based on maximising cut depth within multiple hard limits, to a two phase approach each focused on one customer quality constraint.

4.1. Phase one: Maximize part velocity while maintaining form.

No consideration is given at this stage to thermals, wheel wear etc. The focus is solely on axis dynamics constraints: axis speed, acceleration, jerk, and snap. While existing research tends to focus on acceleration and jerk [7], anecdotally these correlate closely with motor mechanics, drive electronics, form error and surface finish respectfully. More research to confirm this is needed.

Back calculating the speed based on the axis dynamics directly is mathematically hard – Jerk requires solving 3rd order integration, and all the limits must be solved as a simultaneous system. Forward calculations however are significantly easier as we are only concerned with movement derivatives. This gives us the opportunity to generate 'proposition' workspeeds and to run the forward calculations and give them a score – the lower the time per revolution the better.

This is an ideal candidate for an AI based solution. Instead of attempting to back-calculate via an extremely complex mathematical problem "absolutely", we apply an Evolutionary Artificial Intelligence technique (EA) to provide a very close estimation and use the forward calculation to 'score' each proposition.

The EA can very rapidly make repeated proposition groups, each better than the last as the AI learns from the score of previous results. The technique is evolutionary as it takes inspiration from the way natural selection promotes successful individuals, and uses them as the basis for future generations.

Eventually, the propositions converge to a solution – this may not be the mathematically perfect optimum and doesn't have to be, just very close and good enough.
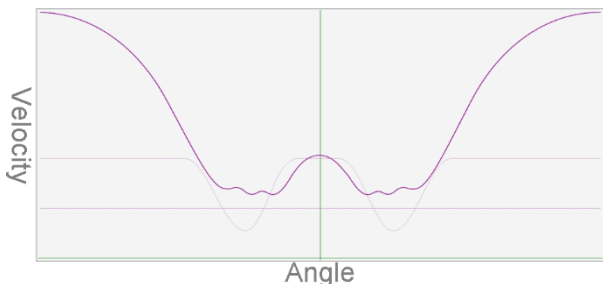

Figure 5. Fully optimised

The result of this phase is a finished workspeed profile which can then be used as the basis for phase 2.

4.2 Phase two: Maximise feed rate while staying within thermal envelope

Now there is a given workspeed profile, the feed rate (cut depth) can be optimized by focusing on only the surface temperature. Other factors will come into play as part of the calculation (MMR, power etc) but we are only concerned about maximising cut depth while not exceeding the thermal limit. While not trivial, this is a straightforward calculation which can be fed a number of cut depths until an optimum is found.

5. Conclusions

This paper has presented a novel two-phase approach to workspeed optimization in high-speed grinding operations for complex workpieces. By reframing the problem around customer quality constraints (form error and thermal damage) and utilizing the power of Evolutionary Artificial Intelligence (EA), the proposed method overcomes the limitations of traditional approaches.

The resulting work-speed and feed parameters can be quite surprising, but also result in a dramatic reduction of feed time. Not only is Jerk significantly reduced but thermal impact too. In a customer case study involving multiple cams on a single shaft, the whole process was improved such that a floor-to-floor time saving of 18% was achieved.

5.1 Key findings:
- Traditional Workspeed limitations: Oversimplification of burn mitigation, counterintuitive effects on burn, and mathematical complexity limit the effectiveness of traditional methods.
- Two-phase optimization: Phase 1 maximizes part velocity while maintaining form through AI-driven workspeed generation, while Phase 2 maximizes feed rate within the thermal envelope.
- Benefits: This approach offers improved:
  - Axis position accuracy for better grinding quality.
  - Minimized damage risk by reducing peak material removal rates.
  - Grinding efficiency and quality through faster operation for certain sections.
  - Machine competitiveness in demanding production environments.

5.2 Future work:
- Validate the proposed approach through experimental testing and comparison with existing methods.
- Investigate the potential of applying the two-phase framework to other advanced machining processes.
- Further explore the application of AI techniques for optimizing machining parameters.

Overall, this paper presents a promising new direction for workspeed optimization in high-speed grinding. By leveraging AI and focusing on customer-centric quality constraints, the proposed method offers significant potential to improve productivity and quality in demanding manufacturing environments. There is also the possibility of artificially suppressing some of the derivative limits to create a sliding scale between targeting productivity or quality.

References

[1] Ashlock, D. (2006). Evolutionary Computation for Modeling and Optimization. Springer, New York.

[2] UK Patent No. 2569307, 2019

[3] Cutchall, D. (1990) Optimization of the cam grinding process 4th INTERNATIONAL GRINDING CONFERENCE

[4] Krajnik, P., Jerina, M., & Kolar, M. (2000). Computer-aided design of a grinding process with limitations related to thermal damage of the workpiece. Transactions of the ASME, 122(3), 306-310.

[5] Howes, T., & Gupta, H. (1990). AVOIDING THERMAL DAMAGE IN GRINDING, 1990 Joint Industry Conference of the Abrasive Engineering Society, 1990 (https://www.abrasiveengineering.com/therm.htm)

[6] Hahn, R. S. (1956). The relation between grinding conditions and thermal damage in the work-piece. Transactions of the ASME, 807-812.

[7] Xu Liming, Wang Kunzi, Xie Chaolong, Shi Lun (2023) Improved spatial acceleration and jerk distributions for grinding force smoothness and energy-saving in reciprocating machining. Journal of Manufacturing Processes Volume 98, 28 Pages 186-195

The compensation of large grinding machine, rotary bearing synchronous errors using a vertical axis, optimised by a non-influencing counterbalance system

Mark Stocker[1], Colin Knowles-Spittle[1]

[1]*Cranfield Precision, Division of Fives Landis Ltd*

Mark.stocker@fivesgroup.com

Abstract

Cranfield Precision supplies a large grinding machine, the OGM1600, that is used in the production of ultra precision freeform surfaces of up to 1.6 m diameter. This paper describes the discovery of errors that appeared in ground components after Covid lockdown restrictions began to be lifted, the interim solution to enable the machine to continue in production and the corrective action taken once Covid travel restrictions were lifted.

Keywords: Grinding, error compensation, vertical axis counterbalance, hydrostatic oil varnish.

1. Introduction

The OGM grinding tool path is an interpolated spiral using the worktable (C-Axis), synchronised with the machine's horizontal and vertical linear axes. During the Covid pandemic, the machine spent a lengthy spell with all of the machine's hydrostatic bearing axes grounded.

After lockdown was partially lifted, component measurements showed evidence of nine, equally spaced 'spokes' of around 300 nm amplitude superimposed upon the surface. The surfaces were still within specification, but as these features were new, it was essential that the source of the problem be understood and corrected. This paper describes the scale of the problem that was encountered, the interim compensation method deployed and the correction of the issue one the machine was able to be serviced.
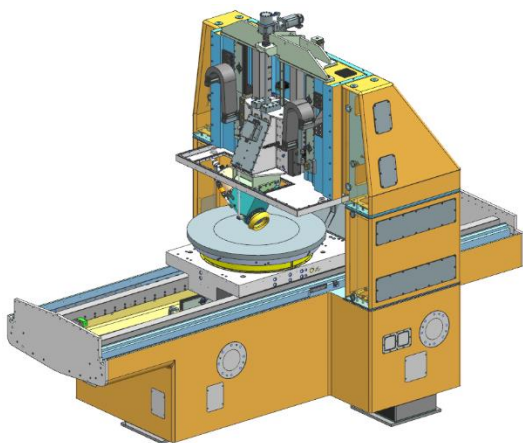
Figure 1. OGM1600 machine configuration

2. The problem encountered

By the time production re-started after the Covid lockdowns started to be lifted, the OGM machine had been powered off, with hydrostatic bearings grounded, for an extended period.

Initial components ground after lockdown, began to show evidence or regular spoke patterns superimposed upon the desired, ground surface. The regular spokes had peak to valley errors of up to 300 nm. The components were still inside specification, but this new patterning had to be understood and eliminated.
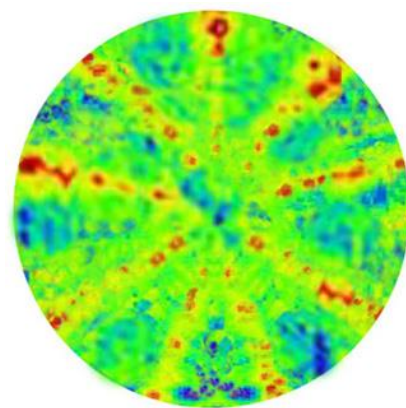
P-V error ~300 nm

Figure 2. Measured error pattern, superimposed upon the required form ground after Covid shutdown.

Once it had been confirmed that the nine spoke pattern was evident in all ground components, the next step was to identify the source of the issues.

The workhead C-Axis is an in-house manufactured hydrostatic bearing. The axial error motion of the bearing during machine pass off was measured at <100 nm asynchronous and <1 μm synchronous error motion. The synchronous axial error motion plot had a consistent two lobes per revolution over the full range of operating speeds.

To further investigate the source of the nine spoke error pattern, a spindle error analysis (SEA) was performed with Lion Precision's SEA. Measurements were taken over several revolutions and at a range of rotational speeds. The resulting measurement data was analysed and it became clear that there were now nine lobes.
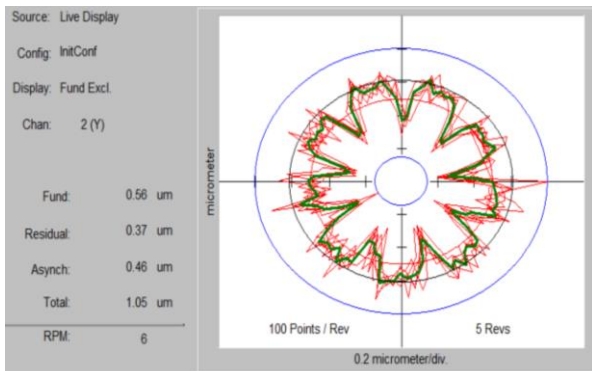

Figure 3. Axis error motion of worktable (C Axis) over five revolutions.

It is clear that there is an axial error motion, nine times per revolution of the C-Axis rotor. The spindle rotor moves downwards, which results in a local increase in the ground surface height.
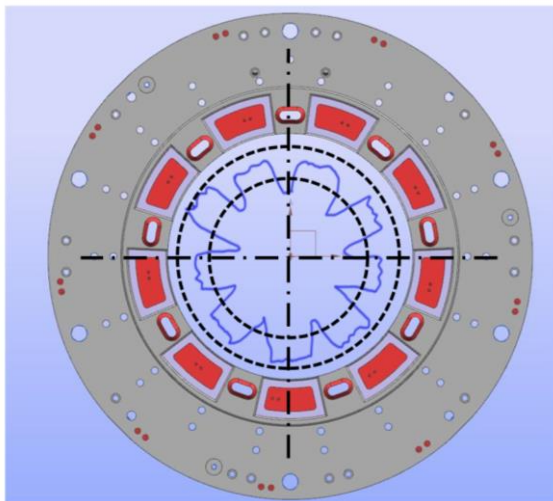

Figure 4. Alignment of vertical error motions relative to hydrostatic bearing pad positions.

The vertical error motion plot was compared to the hydrostatic bearing pad positions. Figure 4 shows the stationary housing bearing pad positions, The rotary spindle is mounted above these pads. The vertical error motions were aligned perfectly to the bearing pad positions. Thus, a mechanism whereby the spindle could be caused to drop, nine times per revolution had been identified.

There was clearly a problem with the C-Axis spindle that needed to be corrected. However, Covid travel restrictions precluded travel to the customer's site to investigate and carry out a repair.

2.1. Potential cause of the problem

It appeared that the spindle rotor was lifting up at the bearing pad positions, and lowering in between the pads. It seemed as though there was something positively imprinted onto the spindle rotor spindle that was aligned to the bearing pad, causing the bearing to lift (and drop) nine times per revolution.

A possible cause was proposed based on experience from around 10 years ago when a machine using hydrostatic linear rails was supplied to a customer in a humid location. The machine had been delivered and it was noticed that the container had been opened (probably by customs) and not re-sealed properly. When the commissioning team was sent to install the machine, it was found that where the machine's linear axis linear bearings had been sitting on the bearing rail during shipment, there were pad shaped rust patterns on the bearing rail. Machines cannot be exported with oil in situ, so must be delivered dry, making them vulnerable to rusting if exposed to humid conditions. The rust was light and superficial and easy to remove, enabling the machine to be commissioned.

The OGM machine, although unused and depressurised for an extended period, had not been exposed to humid conditions and the oil had not been drained from the machine. A theory proposed was that as the C-Axis spindle had been in contact with the bearing pads, it was possible that contamination in the oil had settled between and rotor and pads and dried/hardened, leaving imprints on the spindle rotor.

A potential mechanism for this was 'varnish' that had build up in the oil. Although the OGM oil is continuously filtered and recirculated, it is possible that over time small amounts of varnish could be produced in the oil.

2.2. Varnish in OGM oil

Varnish is commonly found in machine oils [1]. In extreme cases, varnish can be found as dark yellow/brown stains on surfaces within the oil circulation system.

Hydrostatic oil systems are highly filtered and extreme varnish stains are very rarely encountered. The OGM machine is replaced every few months, but tests indicated that very small levels of varnish are present in the oil after just a few months of use.

Figure 5. Oil from OGM before and after reconditioning by off-line filtration.

Figure 5 shows a sample of OGM oil, a few months old and not yet scheduled for replacement. After off-line reconditioning (and analysis) very low levels of varnish were found to be present in the oil. Potentially, the root cause of the OGM bearing issue.

However, because Covid travel restrictions had not yet been lifted, it was not possible for Cranfield Precision staff to visit the machine, so an alternative, interim solution was required.

3. Tool path generation (and compensation)

The OGM machine uses custom designed MöbiusCAM software to generate the desired machine tool path.
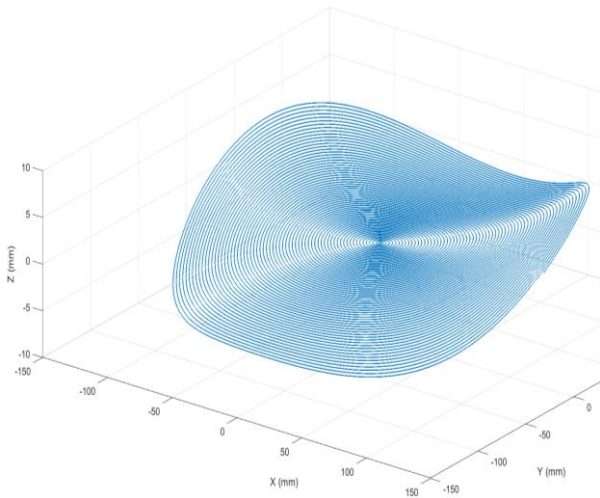Figure 6 shows a typical spiral ground OGM tool path to create a freeform surface.

Figure 6. Desired component profile

It has been found to be possible, on machines, with low inertia linear axes and at low component rotational speeds, to compensate for ground surface ripples induced by workhead motor torque ripples. These component ripples are caused by the elastic time constant of the machine stiffness loop. As the rotational speed reduces, the grinding wheel effectively has slightly longer to cut the surface, with the infeed force being maintained by the stiffness loop spring force.
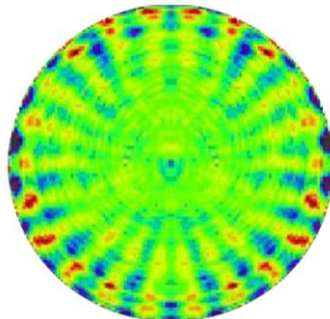

Figure 7. Component surface errors resulting from workhead torque ripple

Using MöbiusCAM, it is possible to modify the tool path in order to compensate for synchronous errors. The example shown here is a modified tool path deployed to minimise the effects of workhead motor torque ripple.
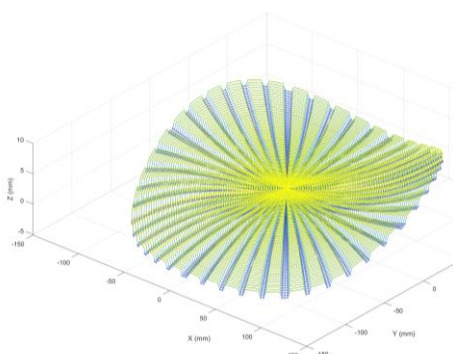
Figure 8. Modified tool path to compensate for synchronous errors

4. OGM C-Axis error compensation

The challenge was to determine whether it was possible compensate errors using the vertical axis which has a mass of around 800 kg, nine times per revolution of the C-Axis, operating at up to 60 rev per minute.

4.1. OGM Z-Axis vertical counterbalance
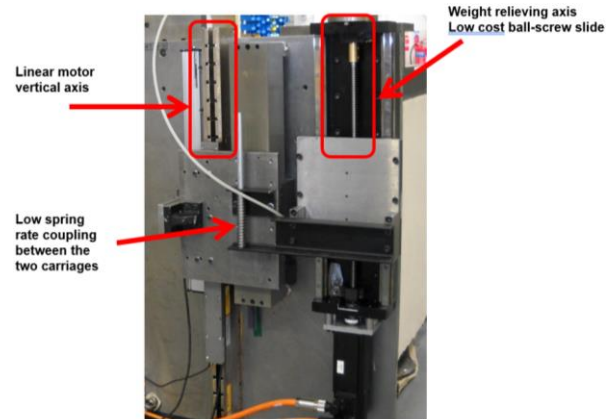
Figure 9. Basis principle of the OGM Z-Axis vertical axis counterbalance

This is the basic principle of the patented OGM vertical counterbalance [2, 3]. The primary linear axis (in the test system shown here, an air bearing) is driven by linear motor. A secondary, ball screw driven axis, takes the weight of the primary axis via a connecting spring. The secondary axis is commanded to follow the primary axis. The result is that the primary axis linear motors, are required only to respond to inertia and process forces. The mass of the primary carriage is at all times countered by the secondary axis.
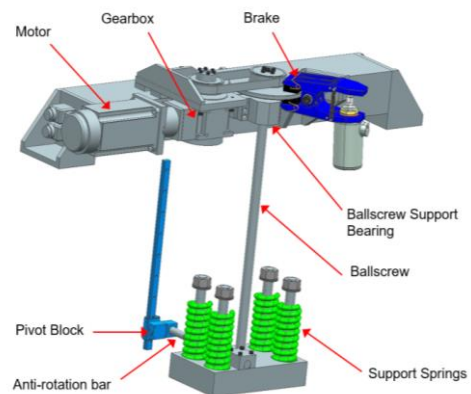
Figure 10. Counterbalance as configured on OGM

The configuration of the counterbalance in the OGM, follows the same principles as the test system. It is compact and effectively enables the vertical axis to perform as though it were a horizontal axis.
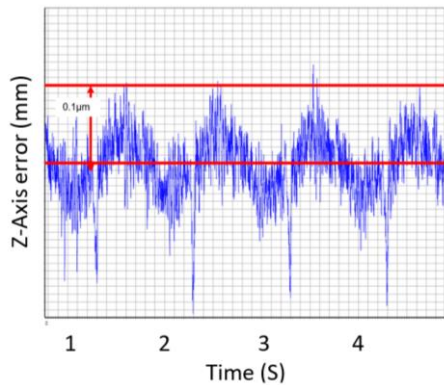
Figure 11. Vertical axis error: +/- 1 mm, 1 Hz

Tests using the OGM counterbalance had demonstrated that it is possible for the primary vertical axis to reciprocate at +/- 1mm, 1 Hz with a following error of 100 nm.

To compensate for the measured C-Axis errors of, compensations of around 300 nm at up 9 Hz (at C axis speed of 60 rev/min)

In order to determine the shape and amplitude of the compensation values to be superimposed upon the tool path, a sensor was mounted upon the grinding spindle housing and a reference flat mounted upon the C-Axis.

The errors were measures over a number of rotations of the C-Axis.

Figure 12. C-Axis axial position error (Z direction), with thermal drift removed

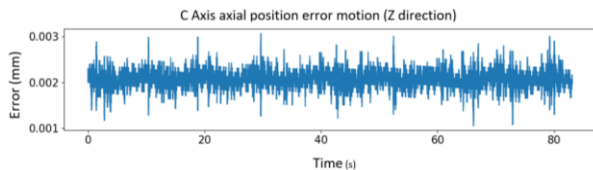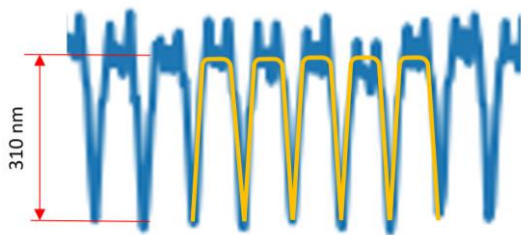**Figure 13.** C-Axis axial position error motion signature, per revolution with simplified error plot superimposed.

From the raw axil position error, the signature of the nine cycles per revolution C-Axis axial position motion was established.
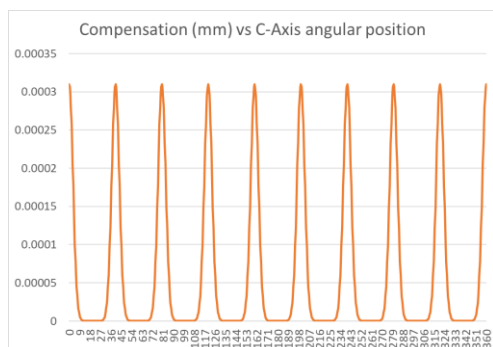

Figure 14. C-Axis error compensation applied to Z-Axis

The compensation profile in figure 14 was applied to the Z-Axis and synchronised to C-Axis angular position. Effectively, the inverse of the simplified error plot in figure **13**.

5. Results

After the Z-Axis compensation was deployed, the measured axis error motions reduced by over 80%. But the real test was the effect on grinding results. Fig 15 shows a typical post-compensation component error plot.

P-V error ~20 nm
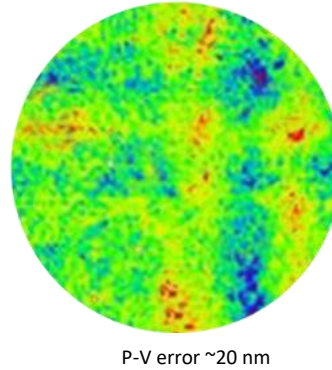
Figure 15. C-Axis error compensation applied to Z-Axis

6. OGM machine corrective action

Once Covid travel restrictions were lifted, it was possible to visit the OGM machine and test the theory that the source of the problem was indeed, bearing pad imprints of oil varnish on the spindle rotor.

The procedure was simple and low risk. The bearing pressure was reduced until it only just floated. The pressure was reduced a little more and the spindle turned over around 90 degree by hand.

The C-Axis was re-calibrated and the vertical compensation values were now present in the error plot. The compensation values were then removed and the C-Axis error plots returned to the levels measured before the Covid shut down.

Although the levels of varnish in the OGM hydrostatic oil remains very low between each change cycle, it is now proposed to retrofit machines (not only OGMs) with stand-alone oil reconditioning systems to virtually eliminate the build-up of varnish in oil systems.

7. Conclusions

The vertical axis counterbalance system deployed in OGM machine, was originally designed to enable Z-Axis following errors of <1 μm. However, it has been demonstrated to enable error compensations to down to around 20 nm.

References

[1] Discovering the Root Cause of Varnish Formation. Atherton, B, United Air Specialists, Inc./Kleentek https://www.machinerylubrication.com/Read/998/varnish-formation

[2] A New Improved Counterforce Mechanism for Vertical Machine Tool Axes as Applies to a Large Optics Grinding Machine Pierse, M. G.; Wenham, R. (Cranfield Precision, Division of Fives Landis Ltd.) Proceedings 31st ASPE Annual Meeting 2016, p 67.

[3] A counterforce mechanism and methods of operation thereof, Pierse, M. EP2862670B1

High precision thermal control of fluidic mediums

Matthew Tucker[1], Jenny Ingrey[1]

[1]Cranfield Precision

matthew.tucker@fivesgroup.com

Abstract

Thermal issues remain amongst the primary sources of error in modern mechanical machinery, especially in the high and ultra precision regimes. Managing the thermal changes on a machine to maintain stability over long periods of time can prove to be very challenging. It is also much more difficult to control the temperature of oils compared with water, as oils are relatively insulating, and heat will transfer less efficiently through the oil. This research project studied the effects of a system designed to take any given fluid, primarily focused on oils and water-based coolant, and control said fluid to a given temperature ± 0.01°C, where the given temperature suits the application. The Thermal Control Units (TCUs) designed as part of the project had a few other constraints to make them more suitable for general applications, such as being able to handle up to 100 bar of pressure, and being able to handle the largest flow rates possible for given fluids. The TCUs primary usage is as a trimming device, where the fluid is controlled by a chiller, usually in the ± 0.3°C range, which is often done with heat exchangers.
The TCUs have held water-based process coolant to ± 0.01°C, over a period of 18 hours, at flow rates exceeding 20 l/min, with future versions scaling this to double in a single unit, and the capability to utilise multiple units in parallel to achieve greater total flow rates. The TCUs have been used on ultra precision machines, holding temperatures to ± 0.01°C, at flow rates over 10 l/min for days at a time, with further testing required to determine how much more flow rate would be attainable for a single unit, with typical thermal disturbances.

Thermal control, thermal issues, oils, coolant

1. Introduction

It has been reported [1] that up to 75% of geometric workpiece errors can be attributed to thermal issues and that up to 60% of a machine's power consumption can be attributed to thermal control. With advances and innovations in technology, the drive to manufacture smaller and more precisely is becoming even more critical. With the requirements being tighter tolerances, surface finishes, forms etc., thermal issues become magnified and become a much more critical issue to remove.

Complex (and variable) machine thermal loops present significant machine stability issues, but even considering a simple example of a typical spindle shaft with a distance of 100 mm between the thrust bearing and the tool will grow 120 nm with a change in shaft temperature of +0.1 °C [see *Figure 2*], consuming a significant percentage of the error budget when for example, machining optical components with sub-micron form error tolerances. Controlling the shaft temperature to +0.01 °C would reduce spindle growth to 12 nm [see *Figure 2*]. Thus, more reliable methods are required for controlling temperature, either over specific circuits, or an entire machine.

Existing temperature control systems typically consist of vapor-compression systems that remove heat from a liquid via an intermediate refrigerant. Typically, these struggle to get below ±0.1 °C without drastically increasing both the cost and the size of the unit.

A unit was schemed and designed for initial testing, with the design evolving over the years to account for the results and outcomes obtained through testing. Multiple units can be used in parallel, as long as the in-built temperature probes for each unit are all calibrated relative to each other.

The units are usually utilised as a trimming device with a bulk chiller acting in front of them, usually in the form of a heat exchanger, typically in the range of ±0.1 °C, which remove any and all of the aggressive coolant temperatures in the system, such as those generated through machining operations.

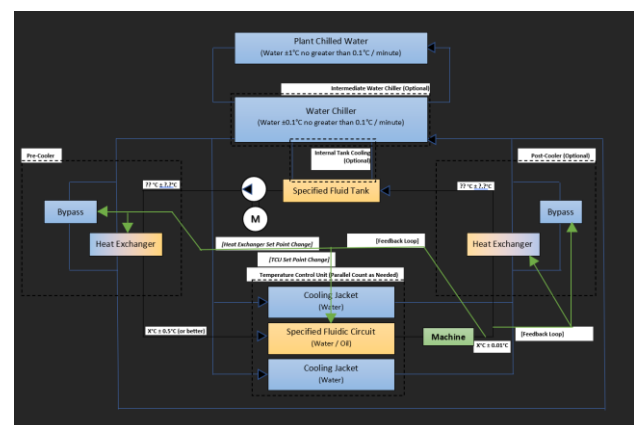**Figure 1.** Example circuit diagram.

$$0.1m \text{ x } 12\frac{\mu m}{m.°C} \text{ x } 0.100°C = 120nm$$
$$0.1m \text{ x } 12\frac{\mu m}{m.°C} \text{ x } 0.010°C = 12nm$$

Figure 2. Thermal growth calculations.

2. Methodology

One medium that is commonly used across the manufacturing world is oil, which has a much lower heat transfer coefficient (VG10 ≈ 0.130 W/(m.K)) than water (0.6 W/(m.K)). After CFD simulations, it was shown that for any reasonable flow of oil past a highly conductive wall at a different temperature to the medium, the temperature would penetrate efficiently to a maximum depth of 1 mm from the wall.

This lead to the thinking that if a balance could be obtained between holes small enough to maximise the thermal transfer, but large enough to minimise pressure drop, then a pattern of holes in a highly thermally conductive block could lead to an optimal heat transfer into a medium. Combined with Thermo-Electric Devices (TEDs), which are a solid state, rapid response device that can provide both heating *and* cooling, a device was designed to this effect.

2.1. The Temperature Control Unit (TCU)

The design was originally based around a block with as many 3mm diameter holes as it was feasible to package into a given area, as 3mm gave a good balance between the thermal penetration [see **Figure 3**] and pressure drop. The higher the total count of holes, for a given total flow rate, the lower the individual hole flow rate (and therefore time spent in each hole), and the more surface area for the medium to be in contact with the walls. Longer drilled holes lead to an increase in the surface area and time spent in the holes, but increase the pressure drop.

The holes are always drilled in a way that they end in a cross-directional large bore [see **Figure 3**] so that any wandering drills from the starting surfaces do not cause any issues other than fractional reductions in the utilisable metal cross sectional area.
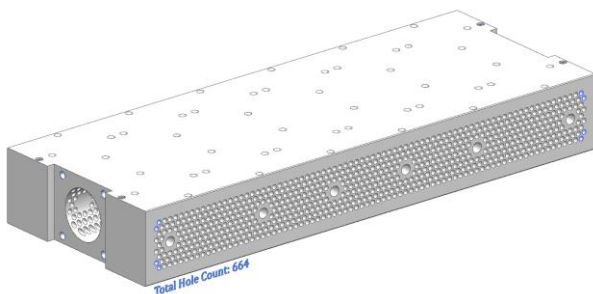

Figure 3. TCU primary block.

On the upper and lower surfaces of the block, are the TEDs, which give the rapid response heating and cooling as required by the system [see *Figure 4*]. The polarity of the current supplied to the TEDs will cause the unit to change between heating and cooling, and the unit can therefore react much more quickly, where required, that a conventional temperature control system that is focused on only heating or cooling.
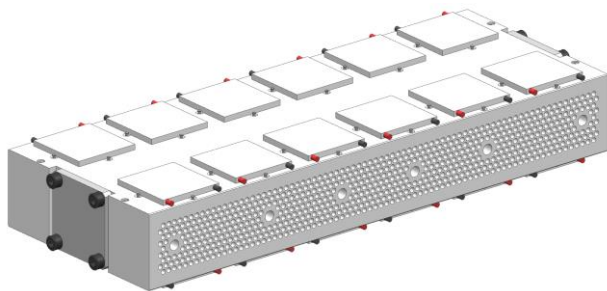
Figure 4. TCU primary block with TEDs, top and bottom.

On the outer surfaces of the TEDs are the control blocks, one of which has an integrated electrical box in the latest designs to improve the overall form of the design [see *Figure 5*]. These take a cooling medium, typically temperature-controlled water, and use it to remove any changes in temperature caused by the TEDs.
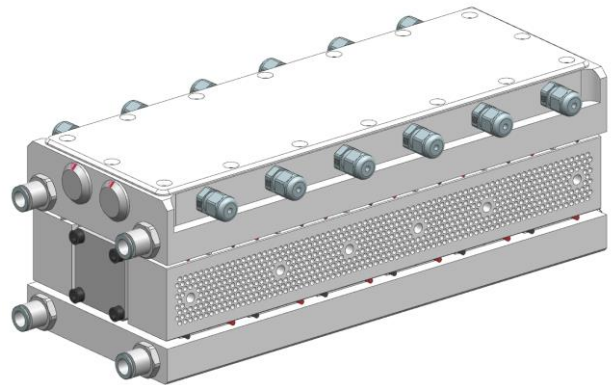
Figure 5. TCU primary block with TEDs and control blocks.

The remainder of the design is primarily around the inlet and outlet of the medium, as well as the internal mixing that occurs before the temperature probe that controls the unit as close to the TEDs as possible [see **Figure 6**]. A variety of inlet and outlet combinations can be used depending on what suits the target application best.
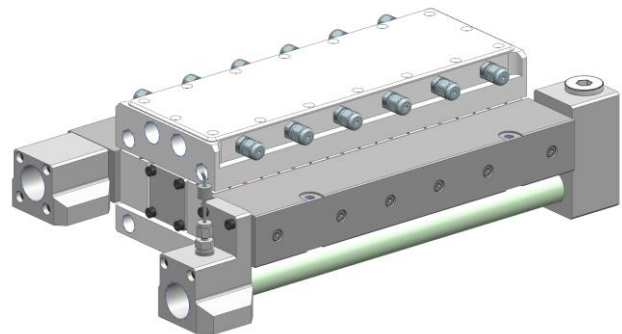
Figure 6. Example of fully built setup of TCU.

2.2. Scaling the TCU capabilities

The latest iterations of the TCUs have pushed the manufacturability, ease of assembly and size / weight of an individual unit to a point where larger is going to be too difficult to manufacture.

However, providing that the output of each unit is the target temperature within a certain range (usually ±0.01 °C or better), and all of the temperature probes are calibrated so that they are all outputting the same value as accurately as possible, then multiple units in parallel [see *Figure 7*] will combine in a way that the combined output will *still* be within the permitted range [see *Figure 8*]. In principle, this should equate to an averaging effect, but assuming worst case scenario, where no oil streams mix, any probe measurement will measure within specification.
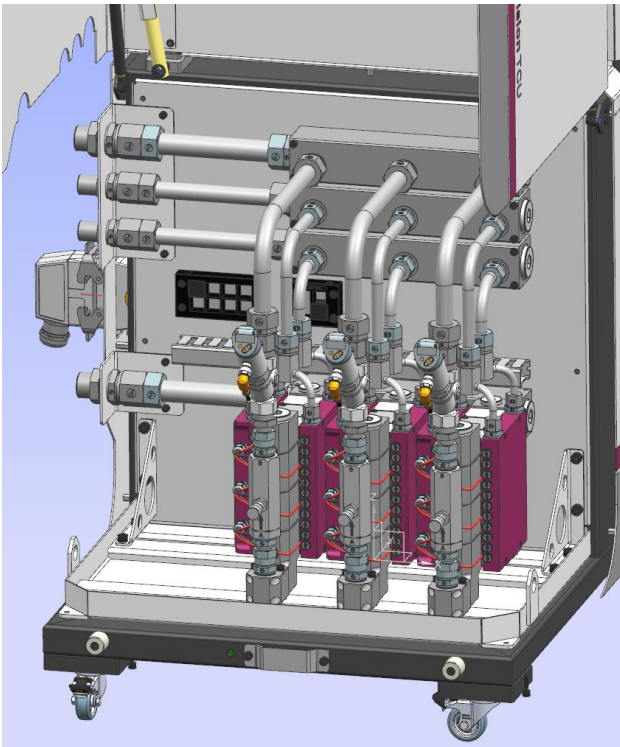
Figure 7. Example of multi-TCU parallel setup capable of 60 l/min
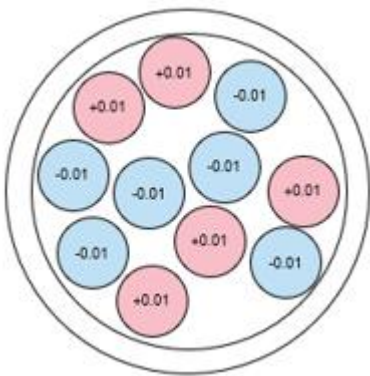
Figure 8. Example of worst-case multi-TCU combined output

3. Results and real machine examples

For most of the testing, a combination of the probe on the unit itself, and additional probes in other locations in the flow, as well as thermocouples at specific points around the circuit are used to measure and verify the test results. In most cases, the measurement devices are not calibrated to each other, because proving the *change* in temperature is much more important than the *absolute* temperature. As the investigations move to units truly in parallel, getting the probes calibrated to a master becomes much more critical.

The units have been in use on the Twin Turret Generator (TTG) family of machines for a number of years, controlling both oil and water circuits, continuously running.

The oil circuits for these machines are typically running VG5 to VG64 oils, and the graph [see *Figure 9*] shows two of them holding temperature to ±0.005 °C over a 30 minute period with a flow rate of 10 l/min through each unit.
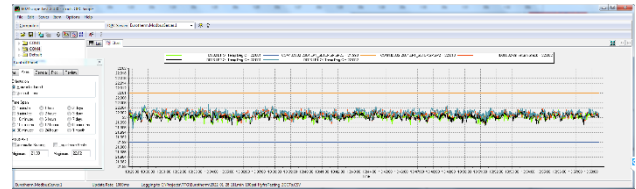
Figure 9. Two TCU outputs over 30 minutes, VG5 and VG 64 oils

The units have also been run with process coolant (oil emulsion) at flow rates of 22 l/min, and the graph [see *Figure 10*] shows that the unit was holding ±0.0065 °C for an hour.
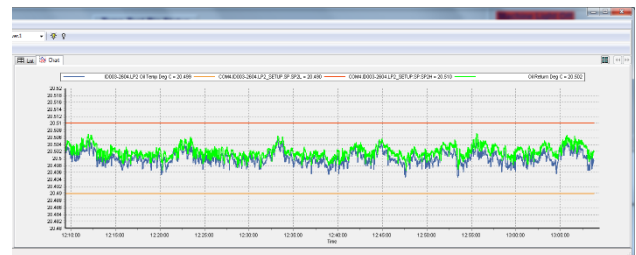
Figure 10. Single TCU output over 1 hour, with two probes, 22 l/min

The latest tests were done on an in-house grinding operation, on one of our most stable machines. The facility itself has a conditioned environment where the air is always held to ±0.1 °C. The chillers in the facility are all water-condensing, to minimise the thermal load.

When the customer optic [see **Figure 11**] was generated [see *Figure 12*], ripples could be seen on the optic [see **Figure 13**] which, although still well within specification, would have a large reduction in post-process polishing time if they could be removed.

After installing a TCU in the coolant line, controlling 20 l/min to a temperature of ±0.01 °C, the measured surface became sub-micron PV form error.
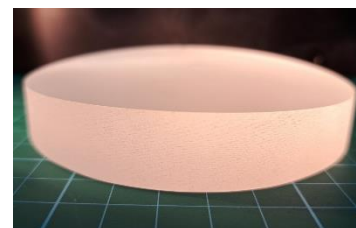
Figure 11. Customer optic.
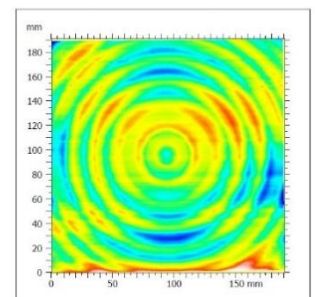
Figure 12. Measured surface with ≈ 3 µm PV form error
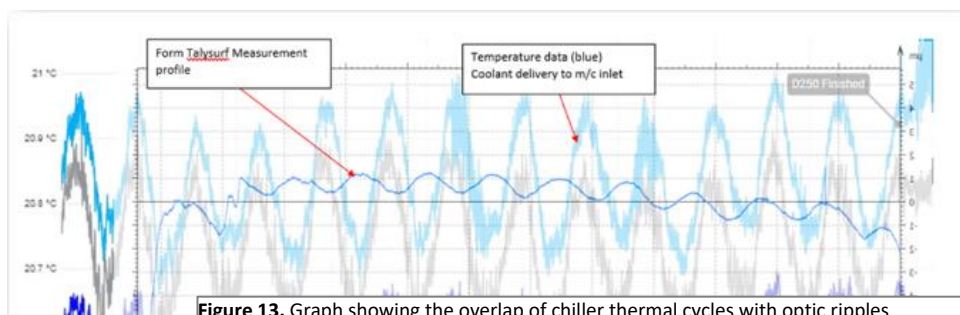
Figure 13. Graph showing the overlap of chiller thermal cycles with optic ripples

The units have also been tested at pressures of 100 bar, and left pressurised for several hours, with no loss of pressure or leakage. Primarily, this was due to an actual target of 70 bar, with a factor of safety of 1.3.

In a test done for a customer, the surface profile of a 250 mm plano optic showed ripples of ±0.5 µm, which could be overlayed almost perfectly with the cycling of the chiller connected to the system. Upon installation of TCUs in the process coolant feed, the ripples decreased to ±0.1 µm, which directly reduces the polishing requirements of following operations.

4. Summary

The units, with demanded flow rates of 5 to 10 l/min have been in operation on multiple TTG machines over numerous years and have had a clear benefit to the output quality of numerous components, frequently reducing post-grinding polishing operations on optical components by half or better.

As the requirements for utilising the units has tended to higher volumetric requirements of medium, larger and more optimised units have been designed, as well as the concept and proofing out of the parallel units.

Calculations around each unit can be done to determine approximate values for parameters such as time take for the medium to travel the hole length and the pressure drop across the holes [see **Figure *16Error! Reference source not found.* and Figure *14***].

Pressure drops are difficult to measure across the units due to the calculated, and measured, drop being almost negligible until the flow rates reach the highest flow rate limits of the units. Most of the measured drops tend to be in the fittings that get connected to the units to create the inlets and outlets.

5. Conclusion and future work

The TCUs are a customisable solution to many thermal issues, that can be applied to a broad range of fluidic mediums to achieve temperature controls exceeding ±0.05 °C, improving with the initial control of the supplied medium.

Utilised within spindles, they have helped minimise any change of position of tools. Utilised as part of a coolant delivery system that have prevented growth of both the tools and the components during long cycles that could otherwise remove the ability to control the manufacturing to the tight required tolerances.

The primary goal of evolving the TCUs is to maximise the flow rate capability within a single unit with minimal compromises to other variables, such as pressure drop and thermal inertia.

As the unit approaches a semi-optimum point, a much more in-depth study is required to quantify the capabilities of the unit for a variety of mediums, flow rates and other variables. This will allow graphs to be generated that would give end users a starting point to look up their specific mediums and determine what would be required to make a functioning system.

Another thing that has been important is stability of the incoming water, that controls the temperature of the outside plates [see **Figure 3**]. Although the stability is not absolutely critical, it can be seen that variations in these temperatures cause an imprinting effect onto the medium itself. One of the future tests will be to determine how beneficial it will be to have an additional TCU in the flow of the water, to stabilize that channel, where the output feeds all additional units, as well as its own cooling plate.

More work is also being done to investigate the effect of putting

multiple units in series, with both the same, and different power levels of TCUs to investigate the effects of using the TCUs as their own version of the bulk thermal management.

Another important phase of the unit will be utilising 3D printing. Calculations and computations fluid dynamics (CFD) have both shown that narrow slot perpendicular to the faces that the TEDs sit on give lower pressure drops, higher surface area and minimised thermal inertia of the block, while making the manufacturing stages much simpler. There are other manufacturing methods, such as electrical discharge machining (EDM) and electrical chemical machining (ECM) which could both create the deep slots, but current investigation have shown that the costs would be prohibitive over deep hole drilling.

References

[1]   Thermal issues in machine tools. Knapp, W et al, CIRP annals, Manufacturing Technology 61.pp771-791.2012

[2]   Temperature Control in Machine Tools UK Patent GB 2591168 B, M Pierce, M Tucker, B Pike, 2019

Fluidic System Information

Supply Pressure	Ps	20	Bar	2000000	Pa
Fluid Chosen		ISO VG46			
Working Temperature	T	20	°C	20	°C
Fluid Kinematic Viscosity @ T	ν	178.000	cSt	0.000178	m²/s
Fluid Density	ρ	875	kg/m³	875	kg/m³
Fluid Dynamic Viscosity @ T	η	155.75	cP	0.15575	N.s/m²
Calculate Fluid Specific Heat Capacity	cSHC	2230.901	J/kg/°K	2230.900585	J/kg/°K
Confirm / Modify Specific Heat Capacity	mSHC	2231	J/kg/°K	2231	J/kg/°K
Finalised Fluid Specific Heat Capacity	SHC	2231.000	J/kg/°K	2231	J/kg/°K
Total Supply Flow Rate	Q	100	l/min	0.001666667	m³/s

Figure 16. Example fluidics system information

Hole(s) Pressure Drop Calculator

Number of Holes	Nh	664		664	
Hole Length	Lh	100	mm	0.1	m
Hole Diameter	Øh	3	mm	0.003	m
Flow Through Singular Hole	Qh	0.151	l/min	2.51004E-06	m³/s
Pressure Drop	ΔPh	0.197	Bar	19664.54054	Pa
Hole Cross Sectional Area	Ah	7.069	mm²	7.06858E-06	m²
Velocity in Hole	Vh	0.355	m/s	0.355098043	m/s
Suggested Min. Hole Diameter	Øhs	N/A	mm	N/A	m
Total Time in Hole	Th	0.282	s	0.281612365	s

Figure 14. Example hole drop calculations

Oil Penetration Depth(s)

Diameter of Hole (mm)	Diameter of Core (mm)	Area of Hole (mm²)	Area of Core (mm²)	Area of Non-Core (mm²)	Ratio of Controlled to Uncontrolled	Percentage of Controlled to Uncontrolled
2	0	3.142	0.000	3.142	1.000	100.0%
2.5	0.5	4.909	0.196	4.712	0.960	96.0%
3	1	7.069	0.785	6.283	0.889	88.9%
3.5	1.5	9.621	1.767	7.854	0.816	81.6%
4	2	12.566	3.142	9.425	0.750	75.0%

Figure 15. Table showing thermal penetration percentages for various hole sizes

Design of a contactless handling system using compliant surface elements

Sifeng He[1], Ron A.J. van Ostayen[1], S. Hassan HosseinNia[1]

[1]Department of Precision and Microsystems Engineering; Delft University of Technology, Mekelweg 2, 2628 CD Delft, The Netherlands

S.He-3@tudelft.nl

Abstract

Handling thin, fragile substrates is a challenging and critical task in semicon industry, where any physical contact between substrate and system is a risk. Thus, handling systems without any physical contact are needed. Based on the active air-bearing working principle, contactless handling systems have previously been developed requiring high supply pressure and deep vacuum air, in which the handling performance is proportional to the pressure difference. In other words, a high pressure difference is desired for better dynamic response resulting in higher acceleration for rapid substrate transport and positioning. In the previous research, a deep vacuum pressure p_v was required to obtain a high pressure difference and thus a high traction force. However, a deep vacuum supply is expensive and it is hard to maintain. Therefore, in order to make the best use of the vacuum source, a new air-bearing surface design with compliant surface elements has been developed in which a high pressure difference is realised without requiring a deep vacuum supply. According to the simulation results using COMSOL, the new surface design has pushed the boundary of the actuation performance further with the same vacuum air pressure. The optimized contactless handling and positioning system is capable of driving a 100-mm silicon wafer with over 0.3 g acceleration.

Contactless, Handling, Air-bearing, Vacuum.

1. Introduction

As high-end electronics industries advance, the optimization and continual reduction of integrated chip feature sizes are pursued to attain lighter and more compact configurations. In semiconductor manufacturing, microchips are crafted on thin silicon substrates, with efforts directed towards decreasing substrate thickness to lower production costs. Nevertheless, when substrate thickness falls below 200 µm, the substrates become highly fragile, posing a risk of easy damage during manufacturing processes [1].

Thus, how to handle this kind of substrate for achieving miniaturization and higher productivity simultaneously has become a fundamental issue. Using the active air-bearing working principle, contactless handling systems have previously been developed requiring high supply pressure and deep vacuum air [2]. In the previous research, a deep vacuum pressure p_v was required to obtain a high pressure difference and thus a high traction force due to the pressure equilibrium condition.

Nonetheless, a deep vacuum supply proves to be costly and challenging to sustain. To optimize the utilization of the vacuum source, an innovative approach has been introduced. This involves the development of a new air-bearing surface design featuring compliant surface elements, which achieves a high pressure difference without the need for a deep vacuum supply.

2. Compliant Design

A contactless handling system has been proposed with a deformable air-bearing surface by Vuong [2]. As implied by the name, this design has the capability of deforming or tilting the air-bearing surface by actuating the bottom plate to generate viscous force for driving substrates. However, the developed system has an issue concerning manufacturability. In detail, each actuator cell contains more than five individual parts, posing a big challenge for assemblage. In addition, the corresponding high pressure difference relies on the deep vacuum supply due to the surface configuration.
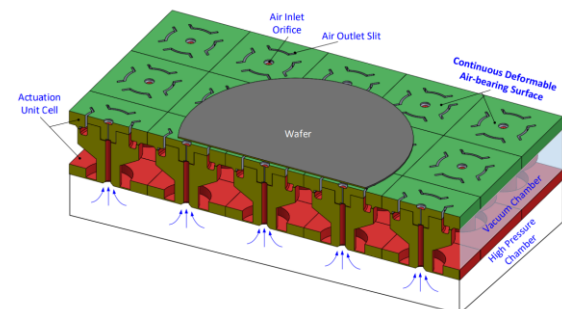
Figure 1. Cross-section view of the designed contactless actuator for handling system with compliant elements implemented.
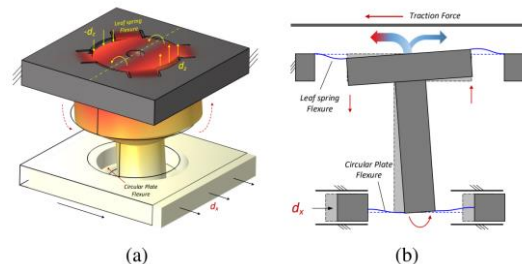
Figure 2. Working principle of single unit cell with the deformable air-bearing.

Given this challenge, a novel compliant deformable air-bearing surface is designed, which consists of many compliant-based actuation unit cells. This whole mechanical structure contains two monolithic parts, the top part with a

deformable surface and the middle part with air supply channels. It can be seen that the mechanical structure is compact and easy to assemble. Compared with the original deformable surface concept, in the new system all the deformable air-bearing surfaces of the actuation unit cells are integrated into one monolithic component. This monolithic mechanical feature enables the whole system to be built with much less effort and cost.

In addition to the good manufacturability, the new design features a different pressure configuration of the air bearing surface, which enables the system to have higher pressure difference without deep vacuum supply. Specifically, it has two independent regions including the deformable one and the outer vacuum one for each unit cell (see Figure 3), where the outer vacuum region makes a huge pressure bias for the pressure equilibrium condition.

For the design without the vacuum area:

$$\int p_a dA \approx \int \frac{p_{in} + p_m}{2} dA.$$

where A is the total area, p_a is the pressure of ambient air, p_{in} is the inlet high pressure, p_m is the outlet vacuum pressure.

Then we can get the pressure difference:

$$\Delta p_1 = p_{in} - p_m \approx 2(p_a - p_m).$$

For the new design with the vacuum area:

$$\int p_a dA \approx \int p_m dA_v + \int \frac{p_{in} + p_m}{2} dA_d.$$

where A_v is the vacuum area and A_d is the working deformable area.

As shown in Figure 3, the equation can be re-written as follows:

$$p_a l^2 \approx p_m(l^2 - \pi r^2) + \frac{p_{in} + p_m}{2} \pi r^2.$$

where l is the length of the whole square, r is the radius of the deformable circle.

Then we can get the pressure difference:

$$\Delta p_2 = p_{in} - p_m \approx 2(p_a - p_m)\frac{l^2}{\pi r^2} = \frac{l^2}{\pi r^2}\Delta p_1.$$

It can be seen that Δp_2 is bigger than Δp_1 with a same vacuum supply p_m, which means the new configuration have more potential for driving performance.
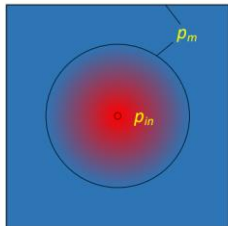
Figure 3. Pressure distribution of the top surface with simplified boundary condition.

3. Simulation and Evaluation

In order to validate the pressure distribution and the traction force performance, COMSOL Multiphysics has been used. Firstly, the vacuum pressure is set to 80 kPa (absolute) based on the results from the pretests, and the high pressure for the air inlet is calculated as 270 kPa according to the floating pressure equilibrium condition. With these specific settings, the pressure distribution profiles are simulated and obtained. As shown in Figure 4, it shows the pressure distribution difference between the condition without displacement input. It is worthwhile mentioning that a modular design has been adopted for 100-mm wafer with seven unit cells in hexagon shape.
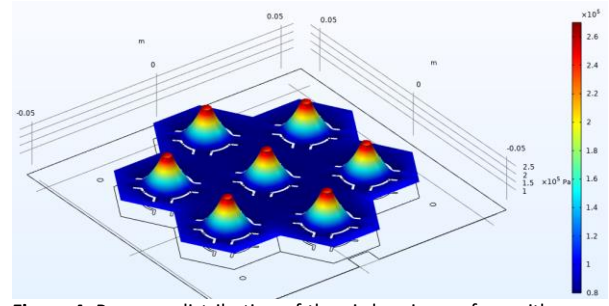
Figure 4. Pressure distribution of the air-bearing surface with seven unit cells.

Given the pressure distribution profiles, the traction force can be generated by having some displacement inputs (the displacement d_x in Figure 2b). As shown in Figure 5, the traction forces with different displacement inputs are collected, which shows that 34 mN actuation force is achieved with 20-μm input. For 100-mm wafer, it can provide more than 0.3g acceleration.
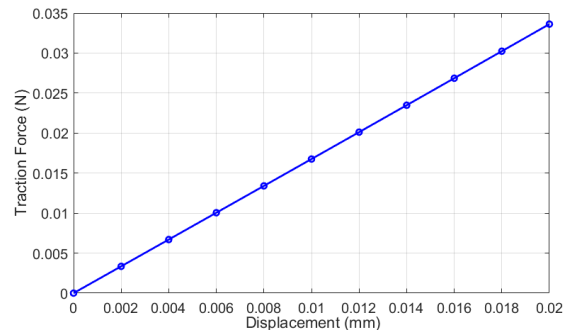
Figure 5. Simulation results of traction force performance with different displacement inputs.

4. Conclusion

Contactless handling systems have great potential for handling fragile substrates carefully. Substrates can be transferred, actuated, and positioned in a mechanical contact-free manner to prevent breakages and contamination. In this work, a contactless handling system integrated with a novel compliant active air-bearing surface has been proposed, where the compliant elements ensure a good manufacturability and high pressure difference for high actuation force without deep vacuum needed. Finally, the simulation result shows that a maximum actuation force of 34 mN is validated for 100-mm wafers.

References

[1] Z. Dong and Y. Lin, "Ultra-thin wafer technology and applications: A review," Materials Science in Semiconductor Processing, vol. 105, p. 104681, 2020.

[2] P. H. Vuong, "Air-based contactless actuation system for thin substrates: The concept of using a controlled deformable surface," Ph.D. dissertation, Delft University of Technology, 2016.

On vibration transmissibility in a machine tool-support-foundation-subsoil system

Paweł Dunaj[1] and Andreas Archenti[2]

[1]West Pomeranian University of Technology, Szczecin, Poland
[2]KTH Royal Institute of Technology, Stockholm, Sweden

pdunaj@zut.edu.pl

Abstract

The optimal combination of machine tool support and foundation type is vital for high precision manufacturing. However, there is limited knowledge and few models available for predicting the behavior of a machine tool, including its operational environment. The study presents the estimation of the machine tool-support-foundation-subsoil system parameters change onto transmissibility change. The analysis was carried out using a finite element model of a vertical lathe with a steel-polymer concrete main frame placed on a block type foundation. The purpose of this work is to identify the model parameters that have the significant impact on the vibration's transmissibility. Based on the analysis conducted it was found that the machine tool as well as foundation properties have the greatest impact on the transmissibility.

Keywords: machine tool; foundations; transmissibility; vibration isolation

1. Introduction

Within the construction of the machine tool, many different mechanical interfaces can be distinguished. They determine the static and dynamic properties of the machine, thus affecting the machining efficiency [1]. One such interface is between the machine tool and the surroundings it operates in, it consists of the following components: (i) machine tool, (ii) support, (iii) foundation, and (iv) subsoil [2]. The proper modelling and design of mentioned elements is crucial from the point of view of vibration isolation and thus the machining performance [3].

Kono *et al.* [4] pointed out that the support stiffness greatly influences the machine tool rocking vibrations, that deteriorate the surface finish of workpieces. In general, greater stiffness of machine tool supports can reduce rocking vibrations caused by drives of the machine. Conversely, vibrations caused by ground disturbances increase. Therefore, the stiffness of machine tool supports should be meticulously designed for both levels of disturbance. Consequently, the study developed models of machine tool supports and contact stiffness proposed by Shimizu *et al.* [5]. In addition, to obtain the necessary parameters values, the unit contact stiffness with several materials was measured in the normal and tangential directions to the interface. This issue has been developed in more detail in [6].

The later study by Kono *et al.* [7] provides the methodology for tuning the stiffness of machine tool supports. Using the previously described contact stiffness approach the mathematical relationship between the load of the support and its stiffness was established. On this basis, a method of arranging supports was proposed to increase their rigidity without the use of anchor bolts. The proposed method was applied to increase the lowest natural frequency of a horizontal milling machine. In the result it was increased by 15–55 % compared to popular placements schemes of three supports. The method was then further developed in [8]. The similar problem was also analyzed by Lin and Li [9] and Havlik *et al.* [10].

Mori *et al.* [11] addressed the issue of minimizing rocking vibrations using the viscoelastic damper support developed in [12]. Authors developed a model that enables quantitatively to estimate the behavior of the damper in the machine tool. Based on the model, the damper support system was applied to reduce the rocking vibration of three axis vertical machining center. As a result, it was found that the damper can attenuate residual vibrations approximately 0.5 s shorter than the original condition to the steady-state condition. Further studies by Mori *et al.* [13], [14] concerns a model-based level adjustment method, thus supplementing previous work.

Next to the support, a crucial element of the machine tool-foundation interface is the foundation itself. It plays a key role in damping vibrations transmitted from other machines, it also provides the stiffness needed for machines with low structural stiffness and is the main element in leveling and aligning the machine [15].

Tian *et al.* [16] analyzed the influence of different types of concrete foundations and subsoil properties on the dynamic characteristic of a heavy-duty machine tools. The analysis was performed using a scaled model based on multibody transfer matrix method. The established model consisted of elastic elements (i.a. bed, transverse beam, foundation) and rigid elements (i.a. spindle, slides) interconnected by experimentally identified joint interface elements. Based on the model, an analysis of the impact of the size of the foundation and the stiffness of concrete and subsoil on the vibration of the tool tip was carried out. It was found that increase of foundation size significantly increases decaying tool tip vibrations, the concrete stiffness has rather insignificant influence, and in the case of subsoil, as it becomes stiffer, the maximum displacement of the dynamic response at the tool tip decreases, but the number of oscillations increases. The work was developed in [20].

Cai *et al.* [17] analyzed the efficacy of different types of isolation trenches used in machine tool foundations. The conducted analysis was based on a finite element model of a heavy-duty machine tool and its foundation-subsoil interaction. Based on fractal theory the equations for calculating the stiffness and damping of these interactions were determined. Next, using a cloud computing the effectiveness of the varied materials used to fill the isolation trench to different depths, widths, lengths, and locations were examined. It was

found that the open trench and concrete-filled trench exhibited the best isolation compared to the other materials, moreover the increasing depth of the trench showed promising effects in comparison to changing the width and length of the trench.

Although the previously cited works on modeling foundations consider both subsoil properties and foundation-subsoil interactions, the subsoil seems to be only briefly analyzed.

Summing up the review of the literature, it can be stated that, despite the considerable achievements in the field, there is currently no coherent modeling method that considers the interactions occurring at the machine tool-support-foundation-subsoil system. Hence, the purpose of this work can be formulated as follows: identification of the model parameters that have the most significant impact on the transmissibility of vibrations. The identification of these parameters should contribute to the development of an effective methodology for modeling machine tool-support-foundation-subsoil systems and, as a result, its further optimization.

The paper is structured as follows. Section 2 presents the fundamentals of transmissibility analysis and finite element model of a machine tool used in the study. In Section 3, contains the results of the analysis of the machine tool-support-foundation-subsoil system parameters change onto transmissibility change. In Section 4, discussion of the results obtained was carried out. Section 5 contains the final conclusions that summarize the most important observations presented in the paper.

2. Methodology

2.1. Fundamentals of vibration transmissibility

The fundamental understanding of vibration transmissibility, begins with the relationships between responses and forces in terms of receptance: if one has a vector f_A of magnitudes of the applied forces at coordinates A, a vector x_U of unknown response amplitudes at coordinates U and a vector x_K of known response amplitudes at coordinates K [18]. The relation between a set of responses x and the applied forces f is given by the frequency response matrix H, which can be written as:

$$x = Hf \tag{2}$$

Next, if the only non-zero generalized forces are f_A one can write:

$$x_U = H_{UA}f_A \tag{3}$$

$$x_K = H_{KA}f_A \tag{4}$$

where H_{UA} and H_{KA} are the receptance frequency response matrices relating coordinates U and A, and K and A, respectively. Eliminating f_A between Eq. (3) and Eq. (4), it follows that:

$$x_U = H_{UA}H_{KA}^+x_K \tag{5}$$

where H_{KA}^+ is the pseudo-inverse of H_{KA}. Hence, the transmissibility matrix is defined as:

$$T_{UK}^{(A)} = H_{UA}H_{KA}^+ \tag{6}$$

The set of coordinates where the forces are applied need not coincide with the set of known responses. The only restriction is that – for the pseudo-inverse to exist – the number of K coordinates must be greater or equal than the number of A coordinates.

2.2. Finite element model of machine tool

The analyzed machine tool is a lightweight vertical lathe with steel-polymer concrete frame. The frame of the lathe is a welded structure composed of steel hollow profiles which are filled with polymer concrete, this increases the structure dynamic stiffness.

The finite element model of a lathe in question was built using the Midas NFX preprocessor [19]. The model consisted of

347,655 degrees of freedom and 92,703 finite elements. The detailed description of the model can be found in [20] and [21]. The structural loop and finite element model of the lathe in question was depicted in Figure 1.
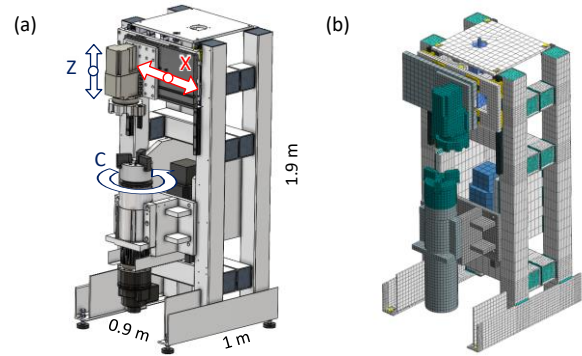
Figure 1. Vertical lathe with steel-polymer concrete frame: structural loop (a) and finite element model (b).

For the purposes of the presented analysis, the remaining elements of the machine tool-environment interface had to be considered in the machine tool model, i.e. (i) support, (ii) block type foundation, and (iii) subsoil. The model of the machine tool-support-foundation-subsoil system is depicted in Figure 2.
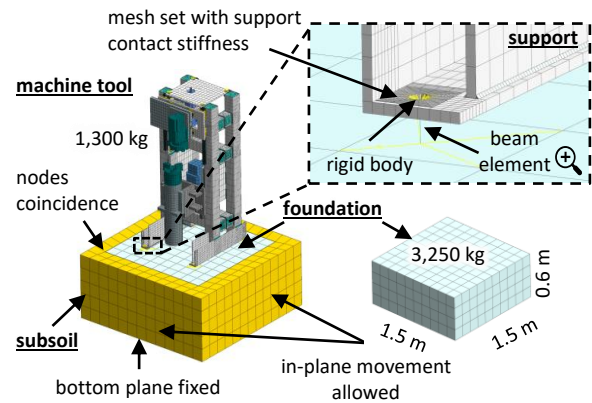
Figure 2. Simplified model of the machine tool-support-foundation-subsoil system.

To describe the damping of the subsoil model a complex stiffness damping was used, thus damping matrix C can be expressed as [22]:

$$C = j\eta K \tag{7}$$

where: K – model stiffness matrix; j – imaginary unit, η – loss factor.

Next, using Nastran Solver (SOL108) direct frequency response analysis was conducted, the excitation force placement and response measurement points were depicted in Figure 3.
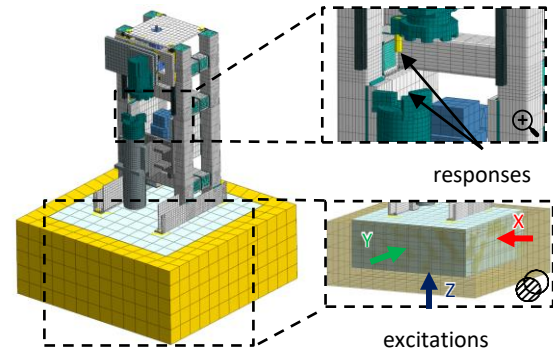
Figure 3. Direct frequency response analysis setup.

3. Results

Based on the finite element model developed, the analysis of how the change of machine tool-support-foundation-subsoil system parameter values influences the vibration transmissibility, was conducted. The mass-spring-damping properties (i.e., Young's moduli, densities, and loss factors) of each of the system components were changed (increased by a 10 %) and then the resulting transmissibilities were compared to the original system case. The analysis was carried out in three perpendicular directions (consistent with the axes adopted in Figure 1 and Figure 3). The exemplary results: (i) transmissibility from foundation to tool T_{FT} and (ii) transmissibility from foundation to workpiece T_{FW} in X direction, are depicted in Figure 4.
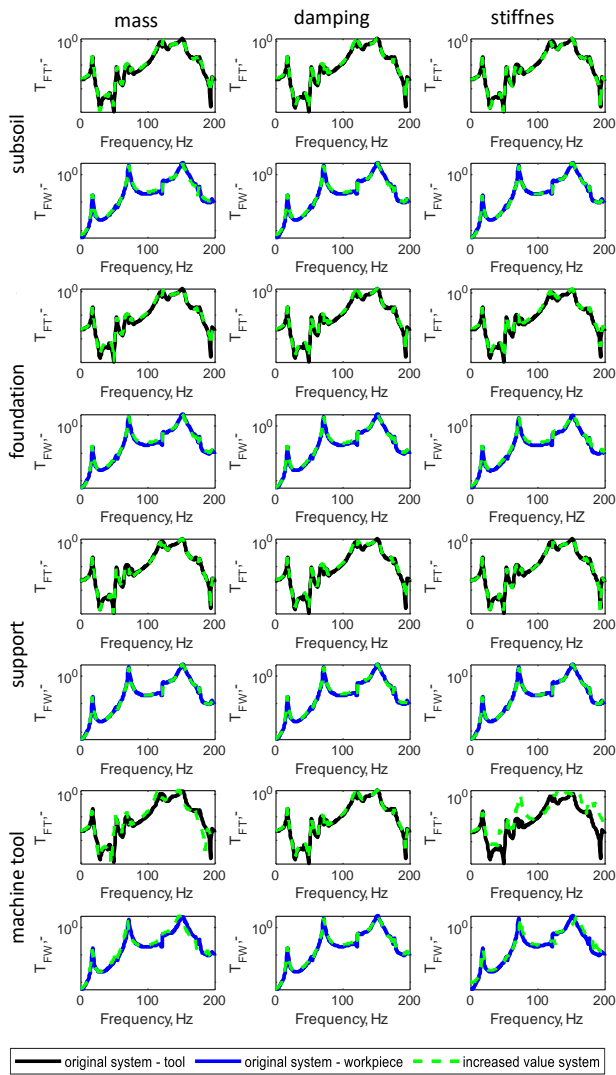
Figure 4. Comparison of transmissibilities in X axis – logarithmic scale.

Analyzing the obtained results, the differences are barely visible (slightly better on a linear scale, but still). This is due to the sensitivity analysis method adopted, where a 10 % change in the parameter was assumed. This allowed to avoid distorting the actual relationship between the parameters describing individual elements of the machine tool-support-foundation-subsoil system, although the obtained differences are not vivid (this does not mean that the system parameters have negligible impact). To present the impact of individual parameters more clearly on the change in transmissibility, it was decided to

introduce the indicator Δ that describes the difference between compared transmissibilities:

$$\Delta_{FT,FW} = \sum_{\omega_{start}}^{\omega_{end}} \left| T_{FT,FW}^{orig}(\omega_i) - T_{FT,FW}^{inc}(\omega_i) \right| \cdot 100 \% \qquad (8)$$

where: $T_{FT,FW}^{orig}(\omega_i)$ – vector of original system transmissibility between foundation and tool (FT) or foundation and workpiece (FW); $T_{FT,FW}^{inc}(\omega_i)$ – analogously determined vector for a system with increased parameter values.

The Δ indicators for tool Δ_{FT} and workpiece Δ_{FW}, were calculated for each parameter and then normalized within subsequent directions to maximum value. The results were depicted on a bar plot in Figure 5.
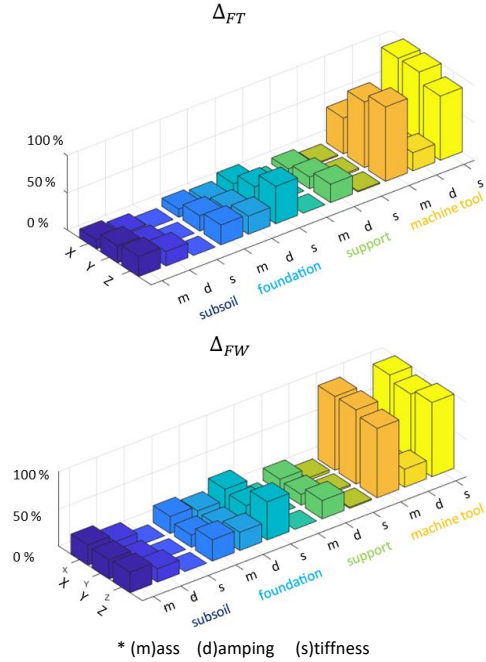
Figure 5. Sensitivity analysis results, the Δ indicators values.

4. Discussion

Analyzing the obtained results, the properties of the machine tool itself have the greatest impact on the vibration transmissibility. And here, of course, the variability of the properties characterizing the structural loop of the machine may be significant, although the user often does not have the opportunity to shape them. However, the user may influence the properties of a subsoil-foundation-support system on which the machine will rest. Analyzing these, it can be noticed that the most significant are properties of foundation as well as mass and damping of a subsoil.

The subsoil seems to be particularly interesting due to the significant possibility of shaping or selecting its properties – the selection of various materials often significantly differing in the values of individual properties [23]. However, in order to fully exploit this potential, the selection of subsoil should be preceded by a model analysis of the solution. Thus, particular care must be taken in case of subsoil modeling. However, the literature states that it is extremely difficult to map the subsoil properties [24].

Moreover, the relationships between subsoil properties and machine tool dynamics may be not so obvious in real life application (it should be stressed that the presented research only covers sensitivity analysis of independent parameters of mass-spring-damping properties of the system in question), since with increased subsoil stiffness comes the increased subsoil mass (increased compaction of subsoil), with increased mass of foundation comes the increased subsoil compaction, *etc.*

When it comes to analyzing the support, it can be seen that in all three directions its stiffness seem to have only a limited impact, which in fact coincides with the studies presented by Kono *et al.* [7], [8] and Mori *et al.* [13], [14]. This does not mean, however, that support properties do not determine the nature of rocking modes that characterize the machine tool. This is still a significant part of the system, although of less importance compared to the others analyzed components. However, when it comes to support damping, it is clear that it has a significant impact on vibration transmissibility. Hence, the search for methods to increase support damping seems particularly justified and appropriate [11], [12].

The presented research should be treated as a preliminary study. Its main limitation is the lack of incorporating the damping at the foundation-subsoil interface in the model. Moreover, the analysis of only one machine tool and one type of foundation makes it difficult to generalize the observations at this stage.

5. Conclusions

Despite significant progress in modeling the static and dynamic properties of machine tools, there is still a lack of a consistent methodology that considers subsoil, foundations and supports.

The paper presents an analysis of machine tool-support-foundation-subsoil system parameters change onto vibration transmissibility change. Based on a finite element model established it was found that foundation properties as well as the properties of a machine tool itself have the greatest impact on vibration transmissibilities. The other factors that have a significant impact on the vibration transmissibility are damping of the subsoil and the support. Therefore, in case of modelling a particular care must be taken in modeling them. Additionally, an important aspect to consider is the incorporation of foundation-subsoil interaction into the analysis, as this aspect can contribute to additional system damping [25], [26] .

Further work should include the analysis of diverse types of foundations as well as the different structural loops and sizes of machine tools.

References

[1] E. Budak, A. Matsubara, A. Donmez, and J. Munoa, "Mechanical interfaces in machine tools," *CIRP Ann.*, vol. 71, no. 2, pp. 647–670, 2022, doi: https://doi.org/10.1016/j.cirp.2022.05.005.

[2] B. W. Peukert and A. Archenti, "Dynamic Interaction Between Precision Machine Tools and Their Foundations," *Int. J. Autom. Technol.*, vol. 14, no. 3, pp. 386–398, 2020, doi: 10.20965/ijat.2020.p0386.

[3] C.-J. Kim, J.-S. Oh, and C.-H. Park, "Modelling vibration transmission in the mechanical and control system of a precision machine," *CIRP Ann.*, vol. 63, no. 1, pp. 349–352, 2014, doi: https://doi.org/10.1016/j.cirp.2014.03.133.

[4] D. Kono, T. Inagaki, A. Matsubara, and I. Yamaji, "Measurement of Contact Stiffness for Stiffness Estimation of Machine Tool Supports," in *Emerging Technology in Precision Engineering XIV*, in Key Engineering Materials, vol. 523. Trans Tech Publications Ltd, Nov. 2012, pp. 457–462. doi: 10.4028/www.scientific.net/KEM.523-524.457.

[5] S. SHIMIZU, K. NAKAMURA, and H. SAKAMOTO, "Quantitative Measurement Method of Contact Stiffness of the Joint with Different Material Combination," *J. Adv. Mech. Des. Syst. Manuf.*, vol. 4, no. 5, pp. 1044–1053, 2010, doi: 10.1299/jamdsm.4.1044.

[6] D. Kono, T. Inagaki, A. Matsubara, and I. Yamaji, "Stiffness model of machine tool supports using contact stiffness," *Precis. Eng.*, vol. 37, no. 3, pp. 650–657, 2013, doi: https://doi.org/10.1016/j.precisioneng.2013.01.010.

[7] D. Kono, S. Nishio, I. Yamaji, and A. Matsubara, "A method for stiffness tuning of machine tool supports considering contact stiffness," *Int. J. Mach. Tools Manuf.*, vol. 90, pp. 50–59, 2015, doi: https://doi.org/10.1016/j.ijmachtools.2015.01.001.

[8] K. Mori, D. Kono, I. Yamaji, and A. Matsubara, "Support Placement for Machine Tools Using Stiffness Model," *Int. J. Autom. Technol.*, vol. 9, no. 6, pp. 680–688, 2015, doi: 10.20965/ijat.2015.p0680.

[9] S.-Y. Lin and G.-C. Li, "Estimation and Adjustment of Interface Stiffnesses for Machine-Tool," *Appl. Sci.*, vol. 12, no. 23, 2022, doi: 10.3390/app122312384.

[10] L. Havlik, L. Novotný, and P. Souček, "Method for Precise and Repeatable Machine Tool Adjustment on Foundation," *MM Sci. J.*, 2022, doi: 10.17973/MMSJ.2022_10_2022095.

[11] K. Mori, D. Kono, I. Yamaji, and A. Matsubara, "Modelling of viscoelastic damper support for reduction in low frequency residual vibration in machine tools," *Precis. Eng.*, vol. 50, pp. 313–319, 2017, doi: https://doi.org/10.1016/j.precisioneng.2017.06.004.

[12] K. Mori, D. Kono, I. Yamaji, and A. Matsubara, "Vibration Reduction of Machine Tool Using Viscoelastic Damper Support," *Procedia CIRP*, vol. 46, pp. 448–451, 2016, doi: https://doi.org/10.1016/j.procir.2016.03.129.

[13] K. Mori, D. Kono, A. Matsubara, and H. Saraie, "Implementation of jack bolts with built-in preload sensors for level condition monitoring of machine tool," *Procedia CIRP*, vol. 77, pp. 509–512, 2018, doi: https://doi.org/10.1016/j.procir.2018.08.250.

[14] K. Mori, D. Kono, and A. Matsubara, "A robust level error estimation method for machine tool installation," *Precis. Eng.*, vol. 58, pp. 70–76, 2019, doi: https://doi.org/10.1016/j.precisioneng.2019.04.014.

[15] L. Uriarte *et al.*, "Machine tools for large parts," *CIRP Ann.*, vol. 62, no. 2, pp. 731–750, 2013, doi: https://doi.org/10.1016/j.cirp.2013.05.009.

[16] Y. Tian, Q. Shu, Z. Liu, and Y. Ji, "Vibration Characteristics of Heavy-Duty CNC Machine Tool-Foundation Systems," *Shock Vib.*, vol. 2018, p. 4693934, Sep. 2018, doi: 10.1155/2018/4693934.

[17] L. Cai, Y. Tian, Z. Liu, Q. Cheng, J. Xu, and Y. Ning, "Application of cloud computing to simulation of a heavy-duty machine tool," *Int. J. Adv. Manuf. Technol.*, vol. 84, no. 1, pp. 291–303, Apr. 2016, doi: 10.1007/s00170-015-7916-2.

[18] A. M. R. RIBEIRO, J. M. M. SILVA, and N. M. M. MAIA, "ON THE GENERALISATION OF THE TRANSMISSIBILITY CONCEPT," *Mech. Syst. Signal Process.*, vol. 14, no. 1, pp. 29–35, Jan. 2000, doi: 10.1006/mssp.1999.1268.

[19] I. T. Midas, "User's Manual of midas NFX," *MIDAS IT*, 2011.

[20] P. Dunaj, B. Powałka, S. Berczyński, M. Chodźko, and T. Okulik, "Increasing lathe machining stability by using a composite steel–polymer concrete frame," *CIRP J. Manuf. Sci. Technol.*, vol. 31, pp. 1–13, Nov. 2020, doi: 10.1016/j.cirpj.2020.09.009.

[21] P. Dunaj, M. Dolata, J. Tomaszewski, and P. Majda, "Static stiffness design of vertical lathe with steel-polymer concrete frame," *Int. J. Adv. Manuf. Technol.*, vol. 121, no. 1, pp. 1149–1160, Jul. 2022, doi: 10.1007/s00170-022-09391-x.

[22] S. Neumark, *Concept of complex stiffness applied to problems of oscillations with viscous and hysteretic damping*. HM Stationery Office, 1962.

[23] Hicher Pierre-Yves, "Elastic Properties of Soils," *J. Geotech. Eng.*, vol. 122, no. 8, pp. 641–648, Aug. 1996, doi: 10.1061/(ASCE)0733-9410(1996)122:8(641).

[24] C. Brecher and M. Weck, "Installation and Foundation of Machine Tools," in *Machine Tools Production Systems 2: Design, Calculation and Metrological Assessment*, C. Brecher and M. Weck, Eds., Berlin, Heidelberg: Springer Berlin Heidelberg, 2021, pp. 135–155. doi: 10.1007/978-3-662-60863-0_4.

[25] F. M. Wani, J. Vemuri, C. Rajaram, and D. V. Babu R, "Effect of soil structure interaction on the dynamic response of reinforced concrete structures," *Nat. Hazards Res.*, vol. 2, no. 4, pp. 304–315, Dec. 2022, doi: 10.1016/j.nhres.2022.11.002.

[26] R. D. Ambrosini, "Material damping vs. radiation damping in soil–structure interaction analysis," *Comput. Geotech.*, vol. 33, no. 2, pp. 86–92, Mar. 2006, doi: 10.1016/j.compgeo.2006.03.001.

Autonomous chatter detection using displacement sensors in turning

Bartosz Powałka[1], Krzysztof Jaroszewski[2], Jan Tomaszewski[3]

[1]*West Pomeranian University of Technology in Szczecin, Faculty of Mechanical Engineering and Mechatronics*
[2]*West Pomeranian University of Technology in Szczecin, Faculty of Electrical Engineering*
[3]*Research and Development Department, Andrychowska Fabryka Maszyn DEFUM S.A., Andrychów, Poland*

bartosz.powalka@zut.edu.pl

Abstract

Chatter vibrations lead to poor surface finish and tool wear. A reliable chatter detection is prerequisite for its avoidance. The paper presents the lathe spindle equipped with displacement sensors used to detect chatter vibrations. The sensors are integrated with the machine tool through communication with the CNC control system and protected against cutting fluids and chips. The data collected during machining is used to calculate the chatter indicator which is based on the multiple sampling per revolution procedure. The use of displacement sensors made it possible to define an additional indicator that allows distinguishing between the appearance of chatter vibrations and the entry or exit from the workpiece. This, in turn, allowed the use of an artificial neural network as a machining state classifier, characterised by a simple structure which positively contributes to computational efficiency. The network was trained and the optimal number of input parameters was elaborated. The neural network is an integral part of the chatter detection algorithm which operates on data updated every revolution of the spindle. The use of the neural network eliminated the need to determine the threshold value, which was an obstacle to the autonomy of the detection process. Numerous experimental tests have confirmed the reliability of the proposed algorithm.

intelligent spindle, chatter, detection of chatter

1. Introduction

Regenerative chatter leads to a poor surface finish, premature tool wear and in extreme cases machine tool damage. Therefore, it is very important to monitor the occurrence of chatter vibrations. Researchers use various signals such as accelerometers, microphones, AE sensors, force sensors for monitoring the cutting process [1]. Frequently accelerometers used for chatter detection in turning are attached to the tool [2]. This limits applicability to the machining process without coolant. Force sensors can be used for effective chatter detection [3] but the main limitation is a frequency bandwidth and price of dynamometers. Sound signals are used by many researchers to detect chatter [4,5]. The main disadvantage of microphones is their susceptibility to interference from the environment. Hence, their use in industry may not be as effective as in laboratory applications.

Acquired signals are processed to extract features sensitive to the chatter occurrence. Frequently chatter detection methods are based on threshold criterion *i.e.* chatter is identified when a chatter indicator exceeds a preset threshold value. Establishing a threshold value usually requires processing a large, even huge, number of signals and classifying them into chatter/stable cases. A necessity to perform tests required for establishing a threshold value is an obstacle in the autonomation of the monitoring process. Several researchers proposed methods for automated threshold calculation. Albertelli et. al. [6] used signal collected before entering in the workpiece and applied 3σ principle to autonomously compute threshold value. Li *et. al.* [7] compared the difference of power spectra entropy determined for the unfiltered signal and signal with removed harmonics of spindle rotational speed. Unfortunately, despite universal

threshold value, this method cannot be fully automated because it requires the identification of natural frequencies prior to the cutting process.

Recently more and more intelligent algorithms are used for chatter detection. Intelligent algorithms used for chatter detection include support vector machine [8], neural network [9], k-means clustering algorithms [10], self-organizing map algorithms [11]. These methods provide better robustness and adaptability to changing cutting conditions than threshold methods but require a lot of data for training procedure. Rahimi *et. al.* [12] presented chatter detection with a hybrid machine learning and physics based model. Diagnostic decision is based on the output from machine learning algorithm combined with energy ratio [13]. Machine learning algorithm distinguishes between chatter and transient states whereas physical-based approach improved chatter detection accuracy. Although the reduction of the network architecture to achieve better computational efficiency was performed, the time needed to build the spectrogram and perform calculations is still significant.

This paper proposes an application of displacement sensors for chatter detection in turning. The sensors are integrated with the machine tool through communication with the CNC control system and protected against cutting fluids and chips. Because the sensors enable measurement of the DC component, entry and exit from the material can be distinguished from chatter occurrence. Consequently, a very simple neural network could be used to determine stable and unstable states. Input parameters to a neural network include chatter indicator and its standard deviation. Chatter indicator proposed in the paper is calculated using once-per-revolution sampling [14,15]. In this paper, chatter indicator is constructed which is adapted to

handle signals coming from sensors not located in close proximity of the cutting process.

2. Experimental setup

Cutting tests were performed on AFM TAE 35 horizontal lathe equipped with the EddyLAB T05-G-KA-112 displacement
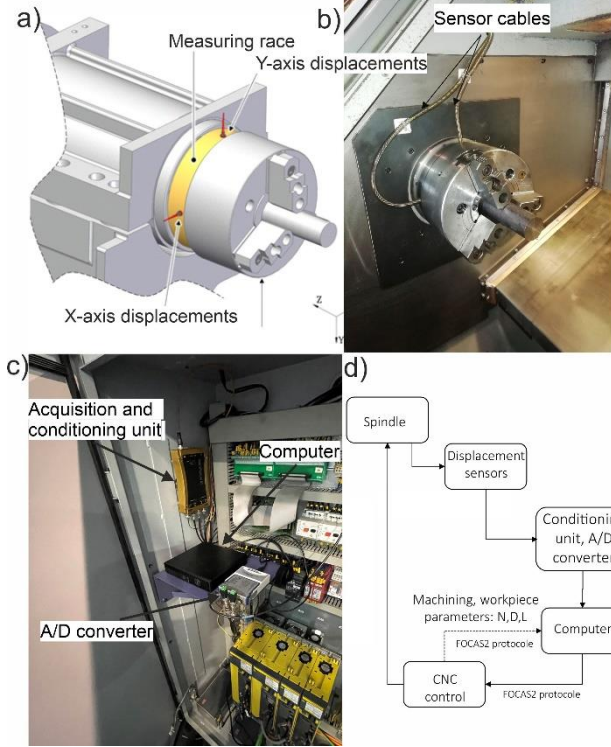
Figure 1. Experimental setup a) location of the sensors, b) spindle with built-in sensors, c) electrical cabinet equipped with signals conditioning unit, A/D converter and computer, d)scheme of the monitoring system

sensors integrated with the lathe spindle. The sensors measure relative displacements between the headstock and the spindle (Figure 1a). The sensors are protected from metal chips and cutting liquids enabling industrial application of the system (Figure 1b). Signals from the sensors are transferred to the TX2-24-16-420A signal acquisition and conditioning module. This module is connected to the National Instruments A/D converter NI9234 and the NI9162 USB module with a sampling frequency of 51.2 kHz. This system is connected to a DELL OptiPlex 3090 i5 computer. The above elements are placed in the machine's electrical cabinet, as shown in Figure 1c. The general scheme of the chatter detection system is shown in Figure 1d. Figure 2 presents an illustration of cutting tests carried out to confirm
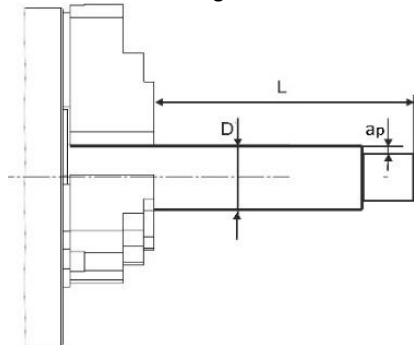
Figure 2. Basic parameters of the cutting tests

the effectiveness of chatter detection. The cutting tests were carried out for 3 workpieces with 3 sets of cutting parameters. The parameters of the cutting tests are given in Table 1.

Table 1 Cutting parameters used in experimental tests

D [mm]	L [mm]	ap	ap	ap	f [mm/rev]
30	190	0.5	1.5	2.0	0.15
35	205	0.5	1.5	2.0	0.15
40	220	0.5	1.5	2.0	0.15
N [rpm]		1400	1700	1700	

3. Computation of chatter and machining indicators

Signals from displacement sensors are denoted to as *X(t)* and *Y(t).* Then amplitude calculated as:

$$R(t) = \sqrt{X(t)^2 + Y(t)^2} \tag{1}$$

is used to build the R_k matrix. Each row of the matrix corresponds to one revolution. The matrix is updated every revolution. Assuming that n_τ samples are recorded during one revolution and considering 3 subsequent revolutions, this matrix takes form:

$$R_k = \begin{bmatrix} R_{(k-3)n\tau+1} & R_{(k-3)n\tau+2} & \cdots & R_{(k-2)n\tau} \\ R_{(k-2)n\tau+1} & R_{(k-2)n\tau+2} & \cdots & R_{(k-1)n\tau} \\ R_{(k-1)n\tau+1} & R_{(k-1)n\tau+2} & \cdots & R_{kn\tau} \end{bmatrix}. \tag{2}$$

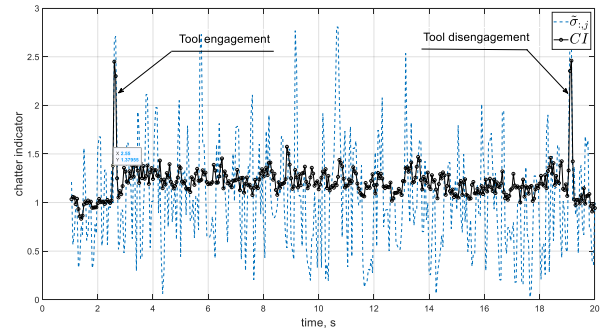Standard deviation estimator is calculated for each column of the matrix:

$$\hat{\sigma}_{:,j} = \frac{T_{:,j}}{\alpha_3}, \tag{3}$$

where $T_{:,j}$ is range of the *j-th* column, α_3 is statistical constant. Finally, these values are averaged to calculate chatter indicator at *k-th* spindle revolution:

$$CI(k) = \frac{1}{n_\tau}\sum_{j=1}^{n_\tau} \hat{\sigma}_{:,j}. \tag{4}$$

Figure 3. Comparison of the chatter indicator (CI) and standard deviation calculated once per revolution during stable cut

Neural network model applied in the monitoring algorithm uses standard deviation of the chatter indicator calculated as:

$$\hat{\sigma}\big(CI(k)\big) = \sqrt{\frac{1}{n_\tau-1}\sum_{j=1}^{n_\tau}\left(\hat{\sigma}_{:,j} - CI(k)\right)^2}. \tag{5}$$

Figure 2 shows chatter indicator (black line) and standard deviation calculated for a single column during stable cut. Large variability of non-averaged standard deviation standard makes it unsuitable for a reliable chatter detection.

Transient states *i.e.* entry into the workpiece and exit from the workpiece result in an increase of chatter indicator. So, to avoid false alarms an additional machining indicator (*MI*) is introduced. Application of displacement sensors enabled measurement of the DC component of spindle deflection. This component changes during transient states. Hence, when the tool enters (or leaves) the workpiece DC component of *R(t)* signal changes at each rotation. This is reflected by the range of average values of *R(t)* calculated over present *(k)* and two preceding revolutions:

$$MI(k) = \max(\bar{R}_k, \bar{R}_{k-1}, \bar{R}_{k-2}) - \min(\bar{R}_k, \bar{R}_{k-1}, \bar{R}_{k-2}), \tag{6}$$

where: $\bar{R}_k, \bar{R}_{k-1}, \bar{R}_{k-2}$ are averages of the rows of R_k matrix. Transient states are identified when *MI* exceeds threshold values determined during air-cutting as:

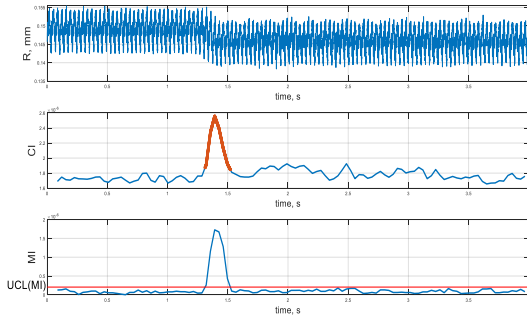$$UCL(MI) = D_4(3)\overline{MI}_{ac} = 2.575\overline{MI}_{ac}. \tag{7}$$

Figure 4. Displacement amplitude, chatter indicator (CI) and machining indicator (MI) - identification of tool entry

Figure 3 presents signal *R(t),* chatter indicator *CI* and machining indicator *MI* during stable cut. As tool enters the workpiece machining indicator exceeds threshold value (red line). Hence, a transient state is identified and corresponding chatter indicator is neglected. The decrease of the machining indicator below the threshold means full entry into the material. Further classification of the state *i.e.* labelling states as stable or chatter is performed by the neural network.

4. Artificial neural network

The assumption when selecting the structure of the neural network was its simplicity. Low number of operations performed by a neural network enables real-time operation of the monitoring system. Moreover, it requires small amount of data for teaching purposes which is beneficial when implementing the monitoring system in industrial plants producing small production batches. Limitation of detectable states to two (stable and chatter) is a major contributor to network simplification. Hence, the neural model consists of only one perceptron – general schema of the perceptron and transfer function used are shown in Figure 5,
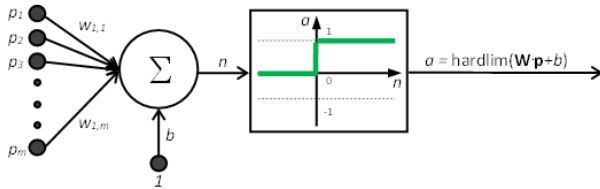

Figure 5. Neural network model

4.1. Selection of features

Time domain features were selected as the inputs to the neural network. Selected features include mean value, standard deviation, variance of chatter indicator and Y axis displacements. These features were calculated from signals corresponding to air cut and steady-state cut (Table 2). The cutting tests used for training and validation of the network were carried out with parameters given in Table 1. Hence, 9 different cutting configurations were used. Each configuration was repeated 3 times which gives 27 cutting tests. Cutting tests with depth of cut equal 0.5 mm were stable (9 cuts), whereas remaining 18 cuts (ap=1.5; 2.0 mm) were unstable. Training of the neural network was performed using 18 cutting tests (12 unstable and 6 stable). The rest of the data (6 unstable and 3 stable cuts) were used for the neural network validation. Initially, the net with 12 input was designed and trained. Then the number of inputs was gradually reduced to two inputs. Finally, 10 models with different combinations of inputs were subjected to training procedure.

Table 2 Tested neural network models

set of features desribing sample	Model no.									
	1	2	3	4	5	6	7	8	9	10
mean of chatter coefficient (air cutting)	1	1	1	1	0	1	1	1	0	0
standard deviation of chatter coefficient (air cutting)	1	1	1	1	1	0	1	0	1	0
variance of chatter coefficient (air cutting)	1	1	1	1	1	1	0	0	0	1
mean of signal in axis Y (air cutting)	1	0	0	0	0	0	0	0	0	0
standard deviation of signal in axis Y (air cutting)	1	1	0	0	0	0	0	0	0	0
variance of signal in axis Y (air cutting)	1	1	1	0	0	0	0	0	0	0
mean of chatter coefficient (machining)	1	1	1	1	0	1	1	1	0	0
standard deviation of chatter coefficient (machining)	1	1	1	1	0	0	1	0	1	0
variance of chatter coefficient (machining)	1	1	1	1	1	1	0	0	0	1
mean of signal in axis Y (machining)	1	0	0	0	0	0	0	0	0	0
standard deviation of signal in axis Y (machining)	1	1	0	0	0	0	0	0	0	0
variance of signal in axis Y (machining)	1	1	1	0	0	0	0	0	0	0
number of features used in model	12	10	8	6	4	4	4	2	2	2
performace goal (error = 0) meet?	YES	YES	YES	YES	NO	YES	YES	NO	NO	NO

It turned out that nets with only two inputs (Model no. 9 and 10) could not be successfully trained. Therefore, in order to minimize number of inputs, the neural network with 4 inputs (Model no. 7) was chosen for further investigation. Figure 6 shows mean values of chatter indicator during air cutting and
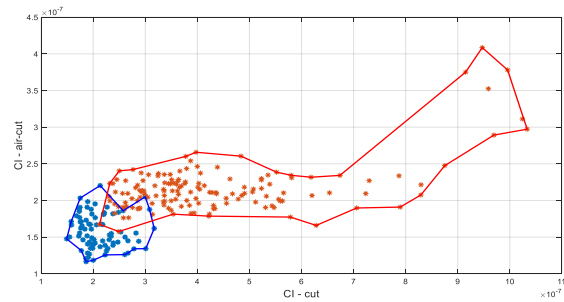

Figure 6. Values of chatter indicator during air cutting (Y-axis) and cutting (X-axis) during stable (blue) and unstable (red) cuts

actual cutting. Blue and red markers correspond to stable and unstable cuts respectively. These two sets intersect which means that such a combination of input parameters is not capable of distinguishing between stable and unstable cuts. Obviously, determination of the universal threshold values is impossible due to observed overlap in chatter indicator values for stable and unstable cuts.

## 5. Application of the method for on-line chatter monitoring

Monitoring of the cutting process can be described by the following steps:
1. Start of the cutting. The machine executes instructions from the G-code. One of the preliminary instructions executed after is initialization of the monitoring process (M500). Sensors begin to record signals. Matrix R_k is built.
2. Check whether $MI(k)$ exceeds threshold value. Exceeding threshold value means entry into the workpiece. Data recorded before tool entrance is used to calculate mean value and standard deviation *of* $CI_{air\_cutting}(\overline{CI}_{air\_cutting}, \hat{\sigma}(CI_{air\_cutting}))$.
3. After $MI(k)$ decrease below threshold value, chatter indicator $CI(k)$ and standard deviation $\hat{\sigma}(CI(k))$ are calculated at each workpiece rotation. These values along with the $\overline{CI}_{air\_cutting}$ and $\hat{\sigma}(CI_{air\_cutting}))$ are fed to the neural network. The neural network returns one from two possible states: "stable" and "chatter".
4. If chatter is detected the monitoring algorithm changes the spindle speed to match rotational frequency harmonic with natural frequency by taking into account permissible cutting speed as $N_{opt} = 60 f_c/k$ with $k = 1,2,\dots, f_c$ – chatter frequency.

Otherwise, the spindle speed is kept constant. In both cases four input parameters are continuously fed to the neural network (Step 3 is repeated).

5. Check whether $MI(k)$ exceeds threshold value. Exceeding threshold value means exit from the workpiece.

Effectiveness of the chatter monitoring was verified using all data employed for training and validation. Also additional 9 cutting tests were used. It must be noted that according to the algorithm presented above, the parameters fed into the neural network are updated every rotation contrary to the training process when a single value of each parameter was used.
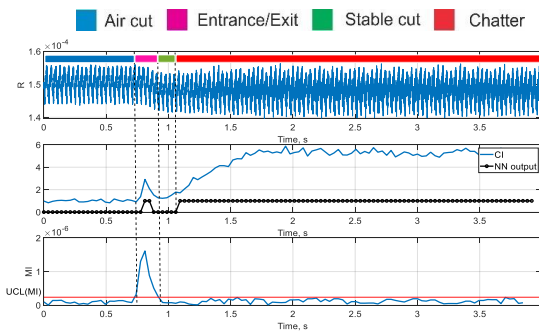
Figure 7. Detected machining states during unstable cut. Cutting conditions: ap=1.5 mm, N=1700 rev/min, D=35 mm, L=205 mm
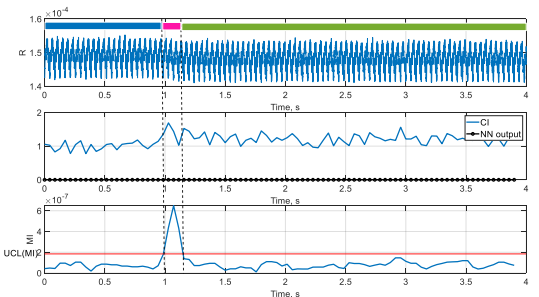
Figure 8. Detected machining states during stable cut. Cutting conditions: ap=0.5 mm, N=1400 rev/min, D=35 mm, L=205 mm
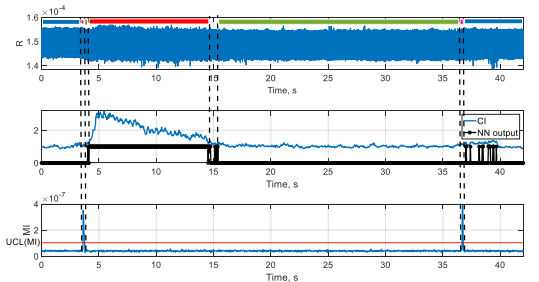
Figure 9. Detected machining states during unstable/stable cut. Cutting conditions: ap= 0.5mm, N=1800 rev/min, D=40 mm, L=205 mm

Figures 7-9 present performance of the method. The machining indicator detects entrance and exit from the workpiece. Then the neural network is activated to qualify state as stable or unstable. It is observed in Figure 9 that NN returns value "1" (chatter) after the tool leaves the workpiece. This is associated with rapid motion with high acceleration and deceleration causing vibration but having no effect on DC component of the displacement signals. Hence the machining indicator remains below threshold value and the state is qualified as "air cut".

5. Conclusion

The requirements for the proposed chatter monitoring system were integration with the machine tool, reliability of inference, computational efficiency and autonomy. Integration with the machine tool means communication with the machine tool's CNC system and a sensors location that does not limit the machine tool's machining capabilities including use of cutting fluids. The proposed system meets these conditions, which made it impossible to locate the sensors close to the cutting point. However, the proposed *CI*, thanks to averaging, allows reliable evaluation of the process state. Autonomy of the system was achieved by using the neural network. An additional advantage of the proposed neural network is simplicity, which translates into computational efficiency.

References

[1] Wang, W.-K., Wan, M., Zhang, W.-H., and Yang, Y., 2022, Chatter Detection Methods in the Machining Processes: A Review, *J. Manuf. Process.*, **77**, pp. 240–259.

[2] Sun, Y., and Xiong, Z., 2016, An Optimal Weighted Wavelet Packet Entropy Method With Application to Real-Time Chatter Detection, *IEEEASME Trans. Mechatron.*, **21**(4), pp. 2004–2014.

[3] Grabec, I., Gradišek, J., and Govekar, E., 1999, A New Method for Chatter Detection in Turning, CIRP Ann., **48**(1), pp. 29–32.

[4] Delio, T., Tlusty, J., and Smith, S., 1992, Use of Audio Signals for Chatter Detection and Control, *J. Eng. Ind.*, **114**(2), pp. 146–157.

[5] Hynynen, K. M., Ratava, J., Lindh, T., Rikkonen, M., Ryynänen, V., Lohtander, M., and Varis, J., 2014, Chatter Detection in Turning Processes Using Coherence of Acceleration and Audio Signals, *J. Manuf. Sci. Eng.*, **136**(4), p. 044503.

[6] Albertelli, P., Braghieri, L., Torta, M., and Monno, M., 2019, Development of a Generalized Chatter Detection Methodology for Variable Speed Machining, *Mech. Syst. Signal Process.*, **123**, pp. 26–42.

[7] Li, X., Wan, S., Huang, X., and Hong, J., 2020, Milling Chatter Detection Based on VMD and Difference of Power Spectral Entropy, *Int. J. Adv. Manuf. Technol.*, **111**(7–8), pp. 2051–2063.

[8] Chen, G. S., and Zheng, Q. Z., 2018, Online Chatter Detection of the End Milling Based on Wavelet Packet Transform and Support Vector Machine Recursive Feature Elimination, *Int. J. Adv. Manuf. Technol.*, **95**(1–4), pp. 775–784.

[9] Lamraoui, M., Barakat, M., Thomas, M., and Badaoui, M. E., 2015, Chatter Detection in Milling Machines by Neural Network Classification and Feature Selection, *J. Vib. Control*, **21**(7), pp. 1251–1266.

[10] Dun, Y., Zhu, L., Yan, B., and Wang, S., 2021, A Chatter Detection Method in Milling of Thin-Walled TC4 Alloy Workpiece Based on Auto-Encoding and Hybrid Clustering, *Mech. Syst. Signal Process.*, **158**, p. 107755.

[11] Cao, H., Zhou, K., Chen, X., and Zhang, X., 2017, Early Chatter Detection in End Milling Based on Multi-Feature Fusion and 3σ Criterion, *Int. J. Adv. Manuf. Technol.*, **92**(9–12), pp. 4387–4397.

[12] Rahimi, M. H., Huynh, H. N., and Altintas, Y., 2021, On-Line Chatter Detection in Milling with Hybrid Machine Learning and Physics-Based Model, *CIRP J. Manuf. Sci. Technol.*, **35**, pp. 25–40.

[13] Caliskan, H., Kilic, Z. M., and Altintas, Y., 2018, On-Line Energy-Based Milling Chatter Detection, *J. Manuf. Sci. Eng.*, **140**(11), p. 111012.

[14] Schmitz, T. L., Medicus, K., and Dutterer, B., 2002, exploring once-per-revolution audio signal variance as a chatter indicator, *Mach. Sci. Technol.*, **6**(2), pp. 215–233.

[15] Zhao, Y., Adjallah, K. H., Sava, A., and Wang, Z., 2021, MaxEnt Feature-Based Reliability Model Method for Real-Time Detection of Early Chatter in High-Speed Milling, *ISA Trans.*, **113**, pp. 39–51.

Modelling and control of tunable magnet actuators

Endre Ronaes[1], S. Hassan Hossein-Nia[1], Ron van Ostayen[1], Andres Hunt[1]

[1]Department of Precision and Microsystems Engineering; Delft University of Technology, Mekelweg 2, 2628 CD Delft, The Netherlands

Email: E.P.Ronaes@tudelft.nl

Abstract

High-precision disturbance rejection systems that exploit the low stiffness of electromagnetic actuators are susceptible to positioning errors stemming from excessive heat dissipation and thermal expansion under sustained actuation loads. Conventional vibration isolators and gravity compensators utilise permanent magnets to compensate for static forces, generating a position-dependent magnetic flux bias between the stator and the mover. This static compensation force can be varied by displacing either the mover or the magnets. Displacement of the mover is often not admissible and moving the magnets can substantially restrict bandwidth and complicate the mechanical design. As an alternative, recent research has sought to control the bias flux by altering the magnetisation level of the low coercivity magnets *in-situ*. Due to the nonlinear variation in magnetic flux during magnetisation pulses, a secondary actuator is required to maintain control over force; however, introducing two actuators is often infeasible due to space restrictions. Combining a traditional reluctance actuator and the Tunable Magnet Actuator in a single stator-core design allows to share the biasing flux, resulting in a much more compact design. This paper presents a magnetic equivalent circuit-based modelling approach to describe such a combined actuator, with which the ability to generate a smooth increase in force is demonstrated. Lastly, a tuning algorithm using the least possible energy for magnetising the Tunable magnet is experimentally validated.

Actuator, design method, mechatronic, modelling

1. Introduction

Magnetic actuators have an extensive history of use in high-precision machines. They offer an ability to track precise and fast motions with no direct contact, and thus with no friction and particle generation. However, as the limits in throughput of high-precision machines are pushed, thermal dissipation from actuated stages with higher actuation forces becomes a source of positioning errors due to thermal expansion [1]. This is a particular cause for concern in gravity-compensating stages with quasi-statically varying normal and torsional loading conditions.

A new form of reluctance actuator incorporating a Low Coercive Force (LCF) magnet within the stator core that can be tuned between remnant magnetisation states may provide an energy-efficient solution for sustained actuation forces. In [2] such an actuator is combined with a Lorentz coil actuator for gravity compensation of quasi-statically varying loads. Another concept of a Tunable Magnet (TM) actuator is further explored in a design where High Coercive Force (HCF) NdFeB magnets are integrated to give bi-directional and linear control of the actuation force through control of the magnetisations states [3].

Here we show that the topology described in [3] can be furthered to include an additional reluctance force to compensate for unwanted dynamics during magnetisation pulses, resulting in a compact design that removes the need for separate parallel actuators as in [2].

2. Lumped model

The duration and energy of magnetisation pulses depend on the voltage across the magnetising coil and the initial magnetisation state of the magnet. In a lumped parameter approximation of the TM actuator, the voltage V and current i in the electric circuit is given by (1), and the magnetomotive force (MMF) $\mathcal{F}$ across and magnetic flux ϕ through equivalent magnet circuit components by (2).

$$V = iR + d\lambda/dt, \qquad \lambda = N\phi, \qquad (1)$$

$$\mathcal{F} = \phi\mathcal{R} + \gamma, \qquad \gamma = Ni, \qquad (2)$$

where λ and γ are respectively the flux- and current coupling coefficients, R is the electrical resistance, $\mathcal{R}$ is the reluctance of magnetic bodies, and N is the number of turns of the coil. The inductive field H, flux density B and $\mathcal{R}$ are dependent on the length l and cross-sectional area A of the lumped bodies,

Magnetomotive force (MMF): $\qquad \mathcal{F} = Hl \qquad (3)$

Flux: $\qquad \phi = BA \qquad (4)$
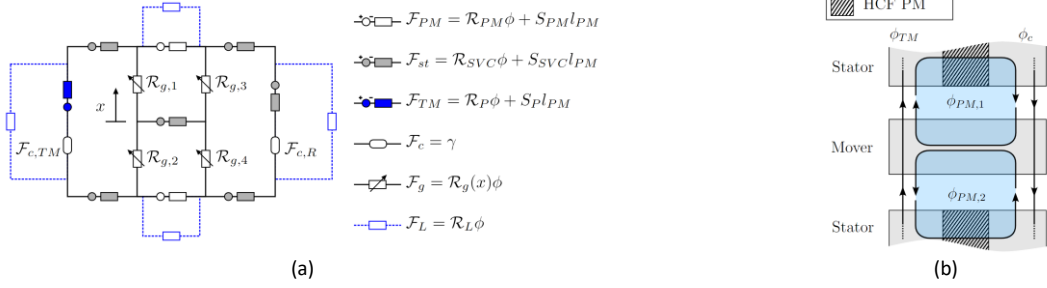
Reluctance: $\qquad \mathcal{R} = l/\mu A \qquad (5)$

The permeability μ is equal to the derivative dB/dH. From (1) it is apparent that the inductance L of the coil depends on μ (6).

$$\frac{d\lambda}{dt} = NA\frac{dB}{dt} = \frac{N^2 A}{l}\frac{dB}{dH}\frac{di}{dt} = L(\mu)\frac{di}{dt} \qquad (6)$$

Due to magnetic hysteresis, the value of μ in the TM can change by two orders of magnitude during magnetisation, causing proportional variations in the inductance of the magnetising coil. This nonlinearity is considered through the implementation of a Preisach model, while the comparatively anhysteretic B-H relation of laminated steel segments is determined from a single-value curve (SVC). As in [4], Eddy current effects in the steel are added to the output of the SVC. The resulting nonlinear field problem is solved through a method of fixed-point iterations described in [5] wherein the B-H relation is linearly approximated as a series combination of a reluctance and an MMF-source (7) as shown in Figure 1a. In the HCF magnets these terms are assumed to be constant. The subscripts: PM, SVC and P, in Figure 1, denote the method of estimation for the HCF magnets, the laminated steel and the TM, respectively.

$$\mathcal{F}_m = H_m l_m = \phi_m \mathcal{R}_m + S_m l_m \qquad (7)$$

Figure 1. (a) An equivalent magnetic circuit of the actuator, where ferromagnetic elements are a series equivalent of a reluctance and an MMF-source. $\mathcal{R}_{g,1-4}$ are the air-gap reluctances, and $\mathcal{F}_{c,TM}$ and $\mathcal{F}_{c,R}$ are MMFs of the magnetising and non-magnetising coils, respectively. (a) Illustration of the flux paths of the TM ϕ_{TM}, the non-magnetising coil ϕ_c, and the bias-flux of the NdFeB magnets $\phi_{PM,1}$ and $\phi_{PM,2}$.

2. Tunable magnetisation and dynamic reluctance forces

A problem with the magnetisation process is that it requires some overshoot of the reference signal. This is shown in Figure 2a of the results of the lumped parameter model when the remnant magnetisation state of the TM is tuned from 0 T to 0.7 T, requiring a transient magnetisation pulse to 1.2 T. This results in a spike in the actuation force at 13 ms in Figure 2b (*solid line*).

To compensate for this spike, an additional coil shown in Figure 1a is added to induce a field $\mathcal{F}_{c,R}$ that generates a reluctance force without magnetising the TM. To achieve this, HCF magnets are placed between the two coils, producing flux biases to the magnetic flux through the magnetising coil ϕ_{TM} and non-magnetising coils ϕ_c, while roughly isolating the two circuits, as illustrated by the schematic in Figure 1b.
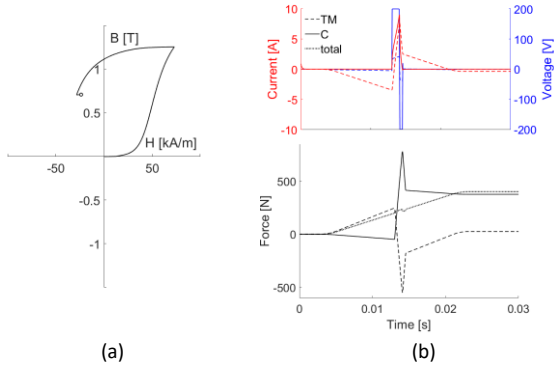
Figure 2. Transient change in electric currents, magnetic flux and forces during a step change in the actuation force

The dashed lines in **Figure 1**Figure 2b show how the additional inductor contributes to an actuation force that increases relatively smoothly over a 20 ms duration (*dotted line*). The current in both coils subsides to roughly zero when the force is constant again at 23 ms, thus mitigating continued joule heating.

Due to the superposition of the flux from the HCF PMs ϕ_{PM} with the controlled flux paths ϕ_{TM} and ϕ_c, the actuation force on the mover, when centred, is linearly dependent on these control inputs based on Maxwell's stress tensor:

$$F_{a,x=0} = \frac{4}{\mu_0}\phi_{PM}\left(\frac{\phi_{TM}}{A_{TM}} + \frac{\phi_c}{A_c}\right),\qquad(8)$$

where μ_0 is the permeability of air.

3. Magnetisation state tuning

A control algorithm was devised for a demonstrator that includes an Alnico 5 (LNG44) magnet (Figure 3a). The algorithm uses the modelled method in Figure 2b, whereby a magnet is tuned with two consecutive maximum voltage pulses, thus expending the least possible amount of energy.

The algorithm estimates the timing of magnetising pulses using look-up tables of linearised hysteretic reversal curves. The magnetisation state is manipulated in a range of -1 T to +1 T within a Root Mean Squared Error (RMSE) of 7.2 mT [7]. As shown in Figure 3c the steady-state flux density error reduces for consecutive states with a larger difference in flux density $|\Delta B_{rem}|$. Reversal curves become steeper when the magnetisation states are further apart, causing the inductance to increase and the rate of magnetisation to reduce. Thus reducing the error resulting from sampling delay. The lab setup and control algorithm is further detailed in [7].
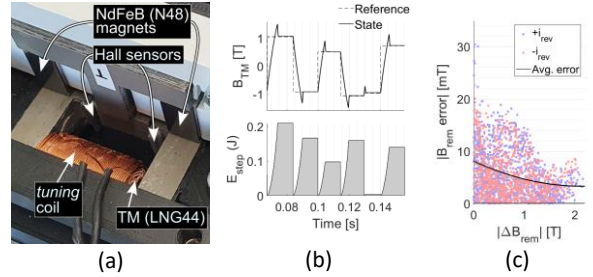
Figure 3. (a) Test setup for remnant magnetisation state tuning (b) Measurements of flux density (B_{TM}) and calculated accumulation of joule heating (E_{step}) during 6 random tuning steps. (c) Error across 2000 remnant magnetisation states initiated by either positive or negative current pulses (+i_{rev} and +i_{rev}, respectively)

4. Conclusion

A model is proposed as a basis for studying the energy efficiency of Tunable Magnet Actuators. This model is used to demonstrate the feasibility of compactly designing such actuators with the ability to exert a smoothly varying force. Furthermore, a tuning method is experimentally validated for changing the magnetisation state of the Tunable magnet with two magnetising pulses, within an RMSE of 7.2 mT.

References

[1] Schmidt R.M., Schitter G., van Eijk J. *"The Design of High Performance Mechatronics,"* Delft University Press, 2020.

[2] Pechhacker A., Wertjanz D., Csencsic, E., Schitter, G. *"Integrated Electromagnetic Actuator With Adaptable Zero Power Gravity Compensation,"* in IEEE Trans. Ind. Electron., 71(5). 5055-5062, 2024

[3] Hoekwater W.B., Ronaes E.P, HosseinNia S.H, (2023) "Hybrid Tunable Magnet Actuator," in IEEE Trans. Ind. Electron., 71(5), 5073-5082

[4] Ceylan D., Zeinali R., Daniels B., Boynov K.O., Lomonova E.A *"A novel modeling technique via coupled magnetic equivalent circuit with vector hysteresis characteristics of laminated steels,"* IEEE Trans. Ind. Appl., 59(2), 1481-1491, 2023

[5] E. A. Dlala, "Magnetodynamic Vector Hysteresis Models for Steel Laminations of Rotating Electrical Machine," PhD, Helsinki University of Technology, 2008.

[6] Ronaes E., Hunt A., HosseinNia H., *"Remnant Magnetisation State Control for Positioning of a Hybrid Tunable Magnet Actuator,"* Energies, 16(12):4548, 2023

A study of Holms and Greenwood contact resistance models for Hertzian electrical contacts in sustained high-current applications

Aditya Mehrotra[1], Emma Rutherford[1], Ian Lindberg[1], Alexander Slocum[1]

[1]Department of Mechanical Engineering, Massachusetts Institute of Technology (MIT)

adim@mit.edu

Abstract

With the push towards decarbonizing heavy industries such as construction, mining, and long-distance transportation, swappable batteries have the potential to enable widespread electrification of these industries using currently available battery technology. Kinematic couplings provide an economical and deterministic interface to repeatedly mechanically constrain a body at six contact points which we have found to also function as electrical contacts. We propose that a kinematic coupling with electrically conducting contact surfaces could improve the simplicity and tractability of a high-power battery swap interface.

This paper explores linking known analytical models of Holm's and Greenwood contact theory to Hertzian electrical contacts by comparing experimentally measured contact resistance and metrology data. Contact resistance is predicted analytically, and then measured to a precision of 1μΩ up to preloads of 15kN on a 300mm radius contact during both loading and unloading cycles. Contacts are machined using a diamond turning operation that enables precise control of both roughness (Ra) and skew properties of the finished surface.

Additional considerations for contact reliability and lifetime are also explored. Ohmic losses at high currents due to the contact resistance could induce an electrical potential across the contact, which in the case of Hertzian surfaces could cause arcing between surfaces that are not in contact, and we explore mitigation methods. Thermal performance of the contact is predicted and evaluated. Contact welding of smooth surfaces under high currents and pressures are also explored via experimentation, and the results are very promising.

Hertz theory suggests that larger radii surfaces enable both higher load capacity and increased contact area, which is beneficial for structural and electrical loads, but due to manufacturing issues, may decrease the tolerance for misalignment. Therefore, analysis is conducted to determine allowable tolerances for the ball-groove geometry to avoid edge loading in the contact.

Measurement, Mechatronic, Resistance, Validation

1. Introduction

Electrical connections to batteries are typically made with a bolted joint connection or high voltage connector with High-Voltage Interlock (HVIL) if the battery is to remaind fixed. For removable or swappable batteries, a flexible blade or multi-blade "tulip," connector is generally employed. Swappable batteries have been broadly considered in the push towards decarbonization in the context of making electric vehicles more practical for years, yet have not obtained wide-spread adoption [1].

A tulip connector or HVIL system still requires mechanical alignment and connection. Kinematic couplings, on the other hand, have the potential to provide for mechanical and electrical connection in a deterministic manner [2]; and thus we explore them here as a possible constraining mechanism for swappable batteries. Such a contact could widthstand inertial loads, and even transfer electrical power with the proper contact design and appropriate insulation. This could greatly simplify the process for swapping as mechanical and electrical connections are created simultaneously, while also providing the potential for creating a standard interface to simplify infrastructure requirements. For the design of such a system to be valid, the electro-mechanical stresses of a kinematic coupling ball-groove pair must be characterized and understood especially in the high force, and current regimes.

Previous work in the area of electro-mechanical Hertzian contacts is extensive, and generally assumes a weakly-coupled model in the form of independent electrical and mechanical models for problem simplification [3]. Generally speaking, Hertz contact theory is used to predict the stresses on the contact, as well as the mechanical contact area which is considered a good upper-bound on the area used to calculate electrical contact resistance [4]. Several models for contact resistance have been proposed including the Holms and Greenwood formulations for contact resistance, these models and others (and the importance of understanding the concept of contact resistance) will be presented in later sections [5][6][7][8]. Many combined electro-mechanical models have been previously verified using experimental data and Finite Element Analysis (FEA) in the low-force (<100N), and low-current (<10A) regimes [9][10][11]. However, it's important to understand how these models scale when contacts are subject to the high forces and currents of electric vehicle contacts for swappable batteries.

In addition, the effects of surface roughness on contact resistance has been an extensive subject of study in electrical
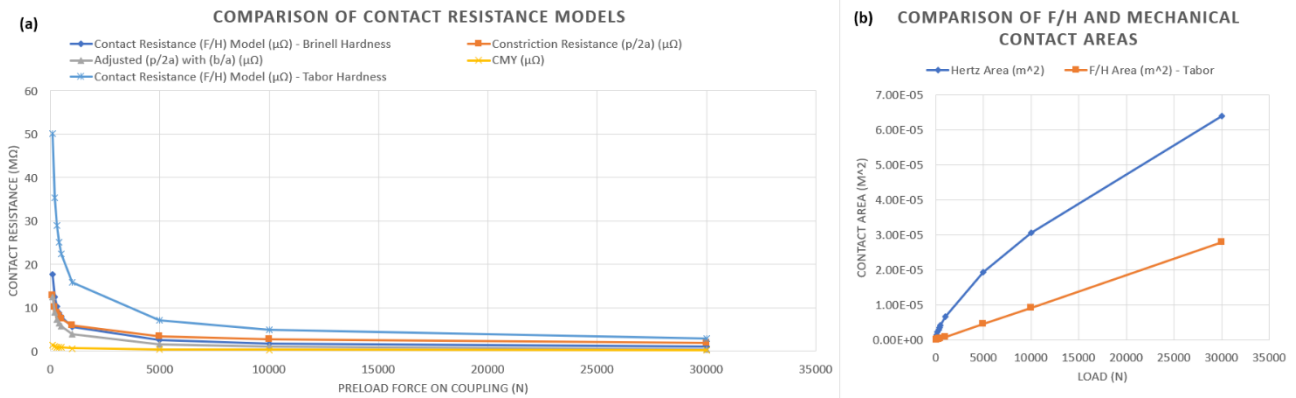
Figure 1. (a) Predicted contact resistance across common models in literature. (b) Predicted Hertz area of contact compared to Holms area.

contact literature [12]. Generally, electrical contacts undergo polishing or finishing operations to achieve low surface-roughnesses to minimize contact resistance [13]. However, alternative manufacturing methods such as diamond-turning have the potential to reduce steps, and therefor cost in the manufacturing process [14]. These manufacturing techniques are considered here as well.

This paper starts by presenting and comparing the results of various electrical contact resistance models used in literature on a high-radius, diamond-turned Copper 182 alloy ball-flat pair. It then presents measured contact resistance data averaged across multiple trials. Results from experiments are compared to the original mathematical model presented in the first section. Finally, the possibilities for contact welding, and arcing are explored through a scaled testing setup. High-current loading tests are conducted on a pair of small copper balls up to current densities of 2.74×10^7 A/mm^2 at low preloads.

2. Electro-mechanical Model of Hertzian Contacts

2.1. Mechanical Model

Hertz contact is an established method of modelling the mechanical loading of a ball pressing on a flat plane [15]. The theory is not presented here in detail for brevity. Hertz theory for a 300mm Copper 182 ball against a Copper 182 flat predicts shear failure at a load of 30kN. Figure 1 (b) presents the predicted Hertzian area up to the failure load.

2.2. Electrical Models

Electrical models for contacts generally center around predicting the contact resistance. Contact resistance is a method to model the energy generated as heat when a certain current is passed through two contacting bodies. Typically, this is split into a constriction and a film resistance. The constriction resistance comes from the convergence of the electrical field lines from the bulk material into the location of the contact spot according to the solution to Laplace's equation, and the film resistance comes from resistance due to coatings including oxides, dust, oil, and other surface iterations. These two resistances can be modelled as a series pair that is also in series with the bulk resistance of the contact. Surface roughness generally increases the constriction resistance according to Holm's a-spot theory. Constriction resistance is far more predictable than film resistance, and film resistance is generally experimentally determined [15].

The simplest method of predicting constriction resistance is the Holm's model presented in [5] which uses the resistivity of the material and a circular contact area. Greenwood's formulas presented in [6] and [7] are generalizations of this model that include multiple contact areas, as well as surface roughness. Both [11] and [16] indicate the use of the Cooper-Miklavic Yanovic Conductance (CMY) presented in [17]. However, both

[8] and [13] agree that the most common and most accurate prediction for contact resistance comes from the F/H relation which is, interestingly, independent of geometry. In this case, the Holmic contact area is predicted by Equation 1 [13]. Where H is the Tabor hardness of the material, and F is the preload [18].

$$A_c = F \cdot H \qquad (1)$$

The relation between A_c and the predicted mechanical area of contact is plotted in Figure 1 (b). Figure 1 (a) compares the contact resistance predicted by all the models for a 300mm Copper 182 ball-flat pair assuming a perfect surface finish with the properties listed in Table 1. Note the Vicker's hardness was used for the CMY conductance prediction in place of 'micro-hardness,' and the shear limit was assumed to be half of the Ultimate-Tensile Strenght (UTS) for Copper 182.

Table 1. Properties of Copper 182 Alloy.

Property	Value
Young's Modulus	130 GPa
Yield Strenght	379 MPa
Ultimate Tensile Strenght	450 MPa
Poisson's Ratio	0.34
Tabor Hardness	1076.36 MPa
Vicker's Hardness	2451.66 MPa
Resistivity	1.274×10^{-8} (ohm·m)

Properties were obtained from Matweb [19] with the exception of Tabor Hardness which was calculated based on [10].

3. Measuring Contact Resistance

Experimental verification of contact resistance was performed on pairs of hertzian electrical contacts manufactured using diamond turning. The test setup is shown in Figure 2 below. An Instron machine was used to preload the contacts from 0-15kN, and a low-resistance kelvin test setup with a resolution of 1μΩ was used to measure the contact resistance. Future setups should use a resistance meter with at least two more decimals of precision, but these initial tests are still indicative and useful.
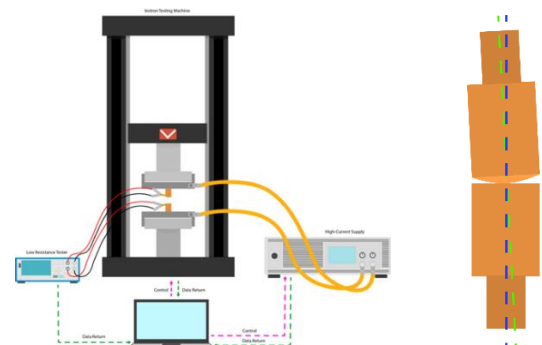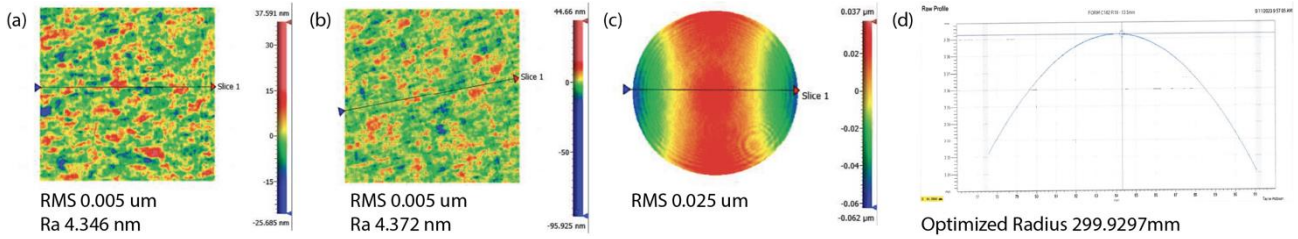

Figure 2. (a) Method for electrical contact resistance, and high-current testing measurement setup. (b) Misalignment of copper contacts.

Figure 3. (a) surface roughness of round, (b) surface roughness of flat, (c) surface profile of flat, (d) surface profile of round C182 test samples.

Contacts were manufactured out of Copper 182 Alloy to a radius of 300mm for the ball, and a flatness of <0.1μm for the flat. These measurements were verified on a profilometer and white-light interferometer, the results of which are shown in Figure 3.
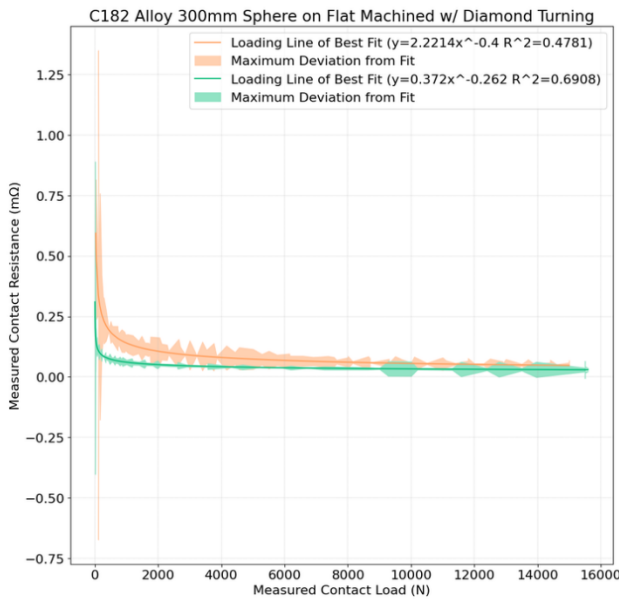

Figure 4. Measured contact resistance of high-radius ball-falt pair subject to large loads.

Figure 4 shows the contact resistance as a function of load during both the loading and unloading phase averaged across three sample pairs of diamond-turned contacts. A standard power regression was performed to estimate a line of best fit from the data, and error bars are plotted as the shaded area. At 15kN, the contact resistance of the pair can be estimated to be between 30μΩ and 47μΩ. Similar to [3], the data shows a distinct difference in contact resistance during the loading phase as compared to the unloading phase. This indicates even in diamond-turned surfaces, the distribution and height of asperities are a significant source of contact resistance, and undergo compression during first-step loading. The error in the data is significantly higher in the low-force regime due to misalignment in the test setup. High radius contacts are difficult to align, therefor multiple tries were required to avoid edge loading the contacts. A geometric tolerance analysis indicated a maximum of 1.49° of angular misalignment of the central axis of the contacts before edge loading would occur, as seen in Figure 2 (b). Figure 5 shows the machining of the contacts.
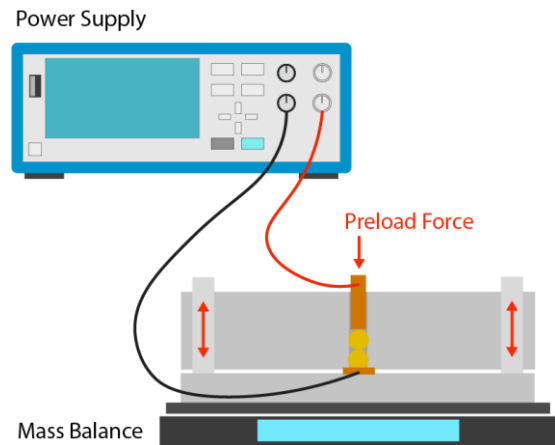
4. High-Current Electrical Testing

As a preliminary study of high current density contact testing, a scaled testing setup with polished copper balls (McMaster PN 64715K18) was created. The surface was then cleaned with HCl to strip any potential oxidation layer that may have formed during storage or transport. A hole was drilled in a plastic fixture and a brass pin was used to load the setup to a Hertz stress of 25% of shear yield. A current of 0.5A was applied to the testing setup which achieves a current density based on the Hertzian area of contact of 2.74×10^7 A/mm^2, which is equivalent to passing 5200A of current through an electrical contact with a contact spot of 15mm in diameter. The balls were then examined under a microscope for signs of physical deformation, contact welding, and arcing, and none were observed. Figure 6 shows the test setup.
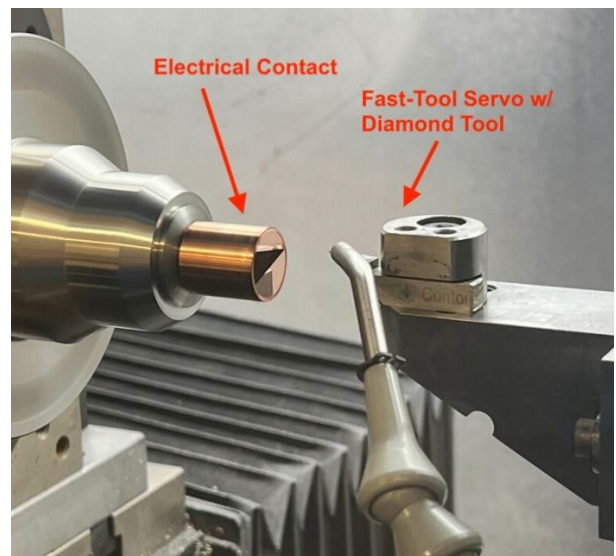
Figure 5. Diamond machining setup for high-current electrical contacts.

Figure 6. Copper balls, high-current testing setup.

The next step in testing the full scale contacts will thus be high-current electrical contact testing. High-current tests will check for welding, arcing, and other forms of breakdown for the full scale contacts at currents >500A, and take measurements of thermal performance of the contacts under significant electrical loads. Experimental data will be compared to theoretical values predicted based on contact resistance, solutions to Laplace's equations, and finite-element models.

5. Results

Based on the above experiments, the measured contact resistance of high-radius, smooth Hertzian electrical contacts under high mechanical loads is off by abount an order of magnitude as compared to the F/H model, the Holm's a-spot model, and the Cooper-Miklavic Yanovic Conductance. However, we strongly believe that more testing is required to rigorously make this claim, so we leave this open for future work. But the results may indicate that a change in modelling will be required for high-radius, high-load, high-current Hertzian electrical contacts.

While being able to predict contact resistance is important, and minimization of contact resistance is desired, defining what an adequate contact resistance for electric vehicle applications is equally crucial. Therefor, perhaps equally interesting, is the comparison of the achieved contact resistance from diamond turning to that of typical electric vehicle high voltage contactors in industry. Table 2 shows typical contact resistance of common electric vehicle contactors, as well as their current ratings.

Table 2. Contact resistances of common electric vehicle contactors.

Contactor Model	Contact Resistance (mΩ)	Continuous Current Rating (A)
EVC500[1]	0.5[*]	500
EVC250-800[1]	0.2[*]	250-800
EVC250[1]	0.8[†]	80
GV200[2]	0.15-0.3[†]	500
GV21[2]	0.5 (max)[†]	150
GV22[2]	0.3-0.4[†]	200
GV24[2]	0.3-0.4[†]	400
GV35[2]	0.15-0.2[†]	500
GVB35[2]	0.15-0.2[†]	500
MX56[2]	0.25[*]	600
MX110[2]	0.15[*]	1000

[1]**Manufactured by TE Connectivity**, [2]**Manufactured by Sensata Technologies**, [*]**Calculated from Datasheet Values**, [†]**Reported by Datasheet**

According to Table 2, even the MX110 contactor by Sensata Technologies, which is designed to carry 1000A continuously, has a contact resistance of 0.15mΩ which is 3-5X higher than the measured contact resistance of our high-radius diamond-turned electrical contacts. This may suggest that diamond-turned Hertzian electrical contacts have the potential to be used in high voltage connections in electric vehicles.

6. Summary, Conclusions, and Future Work

Our study suggests that while the applicability of Holms contact theory increases with contact pressure, further work may be required to accurately model high-radii Hertzian electrical contacts under high mechanical and electrical loads. However, we found that diamond-turned Hertzian electrical contacts may be able to compete with industry standard electric vehicle connections when considering the applications of swappable battery interfaces. We additionally observed that at high current densities of up to 2.74×10^7 A/mm^2, and up to ¼ of the yield stress, polished Hertzian electrical contacts show little sign of degradation, welding, or arcing. These results indicate that the design of a Kinematic coupling for a swappable battery for both mechanical constraint, and the transfer of electrical power is a promising application to be studied further.

References

[1] IEA (2023), Global EV Outlook 2023, IEA, Paris https://www.iea.org/reports/global-ev-outlook-2023, License: CC BY 4.0

[2] A. Slocum, "Kinematic couplings: A review of design principals and applications." *International Journal of Machine Tools and Manufacture* **50.4** (2010): 310-327.

[3] V. A. Yastrebov et al., "Three-level multi-scale modeling of electrical contacts sensitivity study and experimental validation," 2015 IEEE 61st Holm Conference on Electrical Contacts (Holm), San Diego, CA, USA, 2015, pp. 414-422, doi: 10.1109/HOLM.2015.7355130.

[4] R.S. Timsit, "Electrical contact resistance: Fundemental principles," in Electrical Contacts: Principals and Applications, P.G. Slade, Ed. CRC Press, pp3-111, 2013.

[5] R. Holm, *Electric Contacts.* 1976. doi: https://doi.org/10.1007/978-3-662-06688-1

[6] J A Greenwood 1966 *Br. J. Appl. Phys.* **17** 1621

[7] L. Boyer, "Contact resistance calculations: generalizations of Greenwood's formula including interface films." *IEEE Transactions on Components and Packaging Technologies* **24**, no. 1, pp. 50-58, March 2001, doi: 10.1109/6144.910802.

[8] R. L. Jackson, R. D. Malucci, S. Angadi and J. R. Polchow, "A Simplified Model of Multiscale Electrical Contact Resistance and Comparison to Existing Closed Form Models," 2009 Proceedings of the 55th IEEE Holm Conference on Electrical Contacts, Vancouver, BC, Canada, 2009, pp. 28-35, doi: 10.1109/HOLM.2009.5284427.

[9] V. A. Yastrebov et al., "Three-level multi-scale modeling of electrical contacts sensitivity study and experimental validation," 2015 IEEE 61st Holm Conference on Electrical Contacts (Holm), San Diego, CA, USA, 2015, pp. 414-422, doi: 10.1109/HOLM.2015.7355130.

[10] M. Leidner, H. Schmidt and M. Myers, "Simulation of the Current Density Distribution within Electrical Contacts," 2010 Proceedings of the 56th IEEE Holm Conference on Electrical Contacts, Charleston, SC, USA, 2010, pp. 1-9, doi: 10.1109/HOLM.2010.5619467.

[11] Y. Slavchev, R. Tzeneva and V. Mateev, "Coupled Mechanical-Electric Analysis of Hemi-Spherical Bodies in Hertzian Contact," 2020 21st International Symposium on Electrical Apparatus & Technologies (SIELA), Bourgas, Bulgaria, 2020, pp. 1-4, doi: 10.1109/SIELA49118.2020.9167130.

[12] P. Zhang, "Effects of Surface Roughness on Electrical Contact, RF Heating and Field Enhancement," Nuclear Engineering and Radiological Sciences, The University of Michigan, 2012.

[13] P.G. Slade, *Electrical Contacts: Principals and Applications*, Ed. CRC Press, 1999

[14] Abdulkadir, L.N., Abou-El-Hossein, K., Jumare, A.I. et al. "Ultra-precision diamond turning of optical silicon—a review." *Int J Adv Manuf Technol* **96**, 173-208 (2018). https://doi.org/10.1007/s00170-017-1529-x

[15] K. L. Johnson, *Contact mechanics.* Cambridge: Cambridge University Press, 2004.

[16] "Theory for Thermal Contact," *doc.comsol.com.* (accessed Jan. 13, 2024).

[17] M.G. Cooper, B.B. Mikic, M.M. Yovanovich, Thermal contact conductance, *International Journal of Heat and Mass Transfer* **12** Issue 3, 1969, Pages 279-300, ISSN 0017-9310, https://doi.org/10.1016/0017-9310(69)90011-8.

[18] D. Tabor, The Hardness of Materials. Oxford: Clarendon Press, 1951.

[19] Matweb: Online Materials Information Resource. https://matweb.com

Metrological evaluation of Integrated Electronics Piezo-Electric Accelerometer measurement chains in industrial applications: Modelling and characterisation of noise

Ali Iqbal[1]*, Naeem. S. Mian[2], Andrew. P. Longstaff[2], Simon Fletcher[2]

[1]College of Aeronautical Engineering, National University of Sciences and Technology (NUST), H-12, Islamabad, Pakistan
[2]Centre for Precision Technologies, School of Computing and Engineering, University of Huddersfield, Queensgate, Huddersfield HD1 3DH, UK

ali.iqbal@cae.nust.edu.pk (A. Iqbal).

Abstract

Integrated Electronics Piezo-Electric (IEPE) accelerometers are widely used for vibration monitoring in industrial manufacturing applications due to their linearity, dynamic range, and robustness. However, the accuracy of the vibration data using such sensors can be limited by noise sources within the measurement chain. This paper experimentally characterizes the noise parameters of IEPE accelerometers to improve measurement uncertainty. The metrological traceability of the IEPE sensor to a laser interferometer standard is established according to the ISO 16063-11. Sources of electronic, mechanical, and environmental noise, both internal and external to the accelerometer, are quantified through a series of static and dynamic tests. Noise modelling techniques are presented to optimize sensor configuration, cabling, and data acquisition parameters based on the target frequency range and environment. This work provides a rigorous metrology approach for industrial users for effective application of IEPE accelerometers considering a more robust approach towards their calibration, incorporating factors of noise. It is anticipated that the outcomes from this approach will further support traceable, and low-uncertainty vibration monitoring to enhance process control and machining accuracy.

Industrial Metrology, Measuring Instruments, Noise Estimation, Accelerometers, Calibration

1. Introduction

Mechanical error sources in precision engineering can have an impact on the machined part, the machine itself, or the manufacturing process [1]. Such errors in machine tools must be prevented or mitigated in order to ensure machine tool accuracy. Unwanted vibration is one of the major sources of dynamic errors in machine tools. Therefore, in order to ensure the accuracy of the machine tool, the vibrations must be measured, classified, and minimised in order to prevent their undesirable effect on the manufactured part [1].

Transformation driven by Industry 4.0 in the area of machine tool metrology, emphasizes the need for the optimization of manufacturing processes while focusing on high-end manufacturing [2]. To accomplish this, it is necessary to monitor vibration parameters, tool cutting speeds, high spindle rotation frequencies, and feed rates. As a result, vibration sensors are widely used in industry to monitor vibrations, such as to monitor and protect CNC machines throughout the manufacturing process. This is made possible through correlation of observed vibration and common wear-out mechanisms such bearings, gears, chains, belts, brushes, shafts, coils, and machine tools [3-5]. Such sensing mechanisms also permit recognition of chatter or self-excited vibrations in machine tools, which can be detrimental to the manufacturing process as it can lead to undesirable outcomes such as dimensional errors, poor surface finish, tool wear, and, if not immediately identified, potential machine damage [6].

Accelerometers are one of the most commonly used vibration sensors to make quantifiable measurements of vibration and shock [7]. Other sensors employed for vibration include velocity transducers, non-contact displacement transducers (NCDT), and laser doppler vibrometers (LDV). Incorporation of such vibration sensors, especially in the case of precision manufacturing, requires a high level of engineering confidence in the ability of the sensor to reliably detect and process excitation characteristics.

Integrated Electronics Piezo-Electric (IEPE) are the most popular class of accelerometers that have been traditionally employed for high-precision industrial manufacturing applications. Their response is characterised by a wide dynamic bandwidth and sharp frequency response, which provides an accurate time domain and spectral analysis. However, they have IEPE, has inherent technical limitations [8] such as source impedance and noise issues [9] which requires placement of sensors close to source of vibration, in addition to their high cost and setup requirements (data acquisition systems and cabling). They also suffer from frequency dependent noise performance and response saturation when subjected to shock or impact vibrations.

Therefore, in order to accurately sense vibrations on machine tools, an objective evaluation of errors and noise in vibration sensors should enable the development of a control model for reducing residual uncertainty. According to ISO 2954:2012 [10] which stipulates the requirements measuring vibration on machinery , sensors require evaluation of sensor parameters including sensitivity, frequency range , bandwidth, resolution of complete vibration measurement system (transducer, acquisition system and cabling) along with compliance with specified uncertainty limits.

Previous work has been performed for the characterization of baseline errors [11] and uncertainties in vibration sensors [12]. It was demonstrated that all sensor measurements have an

associated level of uncertainty and noise [13], which can be attributed to systematic and random errors.

This paper experimentally characterizes the noise parameters of IEPE accelerometer measurement chains. The metrological traceability of the IEPE sensor to a laser interferometer standard is established according to the ISO 16063-11 [14]. Sources of electronic, mechanical, and environmental noise, both internal and external to the accelerometer, are quantified through a series of tests. Noise modelling techniques are presented to optimize sensor configuration, cabling, and data acquisition parameters based on the target frequency range and environment. This work provides a rigorous metrology approach for industrial users for effective application of IEPE accelerometers considering a more robust approach towards their calibration, incorporating factors of noise.

2. Noise in IEPE Accelerometer Measurement Chains

IEPE accelerometers are often considered the state of the art for usage in most industrial and engineering applications due to their ease of use, tri-axial capabilities, high precision, excellent linearity over their dynamic range, and wide frequency range (<10 Hz to 10000 Hz) [15]. The internal signal conditioning unit of the IEPE accelerometer enables for the use of regular co-axial cable over extended distances with negligible deterioration for any acquisition equipment. Few drawbacks which may limit their application includes maximum operating temperature due to internal circuitry, poor DC response due to low frequency roll-off, amplification at resonance, and saturation of the internal charge amplifier [16].

In instrumentation and sensors, noise, comprising intrinsic and extrinsic elements, remains a challenging and expanding area requiring ongoing research. In measurements, it is defined as any undesired signal in the sensor output (Figure 1).
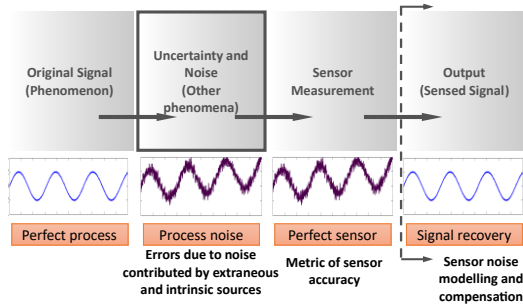

Figure 1. Vibration signal measurements subject to noise

While sensor calibration minimizes systematic errors, intrinsic noise persists post-calibration due to the complex nature of measurement systems. Comprising components such a sensing elements, pre-amplifiers, cabling, and a data acquisition systems, in the sensor measurement chain also exhibit an inherent noise. Mathematically it can also be shown that for the accelerometer output ($x_{meas}(t)$) is actually sum of actual signal of vibration ($a_{true}(t)$) and noise ($n(t)$), as shown in equation below

$$x_{meas}(t) = a_{true}(t) + n(t) \qquad (1)$$

This emphasizes the necessity for probing into the noise within IEPE measurement chains utilized in precision manufacturing setups, as it plays a crucial role in maintaining stringent tolerances of machine product. The study identifies and models noise in industrial vibration sensors, specifically focusing on fundamental noise sources intrinsic to IEPE measurement chains, which are pivotal for expected instrument performance in metrological applications.

2.1. Characterisation of Noise in Accelerometer Measurements

Noise in accelerometer measurements $x_{meas}(t)$ or simply $x(t)$ can be characterised by modelling it as a stochastic process and analysing it using techniques like Power Spectral Density (PSD), Auto-Correlation Function (ACF) and so on. Within the scope of this work, noise is assumed to be additive (Equation 1). In such cases, noise in vibration sensors is often modelled as white noise to aid analysis, representing additive noise in sensor readings. The resultant sum of all noise sources represented by the noise (stochastic) model is denoted by $n(t)$.

The auto-correlation function of vibration signal $x(t)$ commonly used to assess self-similarity, serves as a valuable tool for noise analysis, representing the correlation of the signal with a time-delayed or noise-corrupted version of itself, $x(t - \tau)$. Assuming stationary ergodic noise affects the vibration sensor readings, the autocorrelation of $x(t)$ mathematically is expressed as Equation 2, where T is the time duration of sensor measurements for $x(t)$ and $\tau = t_1 - t_2$, the time delay between measurements taken at time instance t_1 and t_2.

$$\phi_{xx}(\tau) = \lim_{T \to \infty} \frac{1}{2T} \int_{-T}^{T} x(t + \tau)x(t)dt \qquad (2)$$

The Power Spectral Density (PSD) $S_x(f)$ of a vibration signal $x(t)$ can be defined as Fourier transform of its Auto-correlation Function (ACF) $\phi_{xx}(\tau)$. Mathematically the PSD [17, 18] can be shown be as. Where f is the frequency in Hz and $i = \sqrt{-1}$.

$$S_x(f) = \int_{-\infty}^{+\infty} \phi_{xx}(\tau)e^{-2\pi i f \tau}d\tau, -\infty < f < \infty \qquad (3)$$

In vibration measurements PSD has units of $g/\sqrt{Hz}$. For noise estimation it signifies the spread of noise over the frequency bandwidth f_{BW} of the signal. Thereby by definition mathematically Equation 3, can be manipulated to estimate the total and average noise power (Equation 3) in sensor measurements recorded over time T.

$$S_x(f) = \frac{1}{2T}|X(f)|^2 \qquad (4)$$

Where $X(f)$ is the Fourier transform of accelerometer measurements represented by $x(t)$. The RMS noise in sensors with bandwidth $f_{BW} = f_2 - f_1$ is more practical to compute using Equation 5 and has units of μg.

$$RMS\ noise\ f_1 to\ f_2 = \sqrt{\int_{f_1}^{f_2} PSD(f)df}\ \ \mu g \qquad (5)$$

2.2. Sources of Noise in IEPE Measurement Chains

During the design of an accelerometer, trade-offs must be considered between small size and weight in comparison to low-noise and output sensitivity [19]. For IEPE accelerometers, multiple noise sources exist within the acceleration chain. However, this discussion would be limited to noise generated by the sensor's electrical and mechanical components, the amplifier, and cables, excluding sources such as ground loops, etc. [20]. This section provides a concise overview of noise sources and contributions in IEPE accelerometer measurement chains [21] to educate the reader.

The sources of noise in an IEPE accelerometer measurement chains can be broken down in terms of mechanical-thermal noise (a_{nm}) and electrical-thermal noise (a_{ne}). Noise estimates are typically presented in terms of the Power Spectral Density (PSD) of a sensor whose units are ($g/\sqrt{Hz}$). The noise spectral density P_{SD} for IEPE can be represented by Equation 6 [19].

$$P_{sD} = \sqrt{a_{nm}^2 + a_{ne}^2} \qquad (6)$$

Previous experimental findings reveal that mechanical-thermal noise (a_{nm}) is significantly less than the electrical-

thermal noise (a_{ne}) contribution across the entire frequency range [19]. However, it is crucial to note that mechanical-thermal noise dominates electrical-thermal noise above 10 kHz [9, 21]. To mitigate mechanical-thermal noise in a sensor due to mass-spring constant and mechanical resistance, steps include increasing mass and quality factor or decreasing resonant frequency during sensor fabrication. Effect of contributions from 1/f or pink noise and gate circuit shot noise are considered insignificant in IEPE sensors.

Electrical-thermal noise is an additional noise component from internal or external electronics in the measurement chain [21]. The accelerometer's noise source is influenced by the sensor material, where selecting materials with fewer defects and impurities can mitigate noise. Introducing capacitance to the system can lead to increased losses and subsequent electrical noise, predominantly noticeable at frequencies below 10 kHz [9, 19]. Modern accelerometers, designed with integrated electronics, strategically reduce the distance between the sensor and the charge amplifier, minimizing capacitance in the chain—a significant noise source—thus enhancing the Signal-to-Noise Ratio (SNR) [20].

3. Methodology

In this study, a mathematical analysis of sensor readings from the IEPE measurement chain is conducted to determine the contributions of various types of noise and random effects to sensor measurements. The noise parameters are modeled during measurements at a location with low vibration levels and minimal background noise influence. Prior to data collection, measures are taken to minimize temperature variations during tests, as these can impact the stochastic characteristics of noise parameters in vibration sensors.

To estimate and characterize noise in accelerometers, tests are conducted in accordance with the ISO 16063-11:1999 standard [14], ensuring traceability by comparing results to a reference laser interferometer in static conditions. A continuous long-term static test lasting approximately 60 hours is performed in a vibration-isolated and temperature-controlled environment to characterize and quantify different noise error terms in the sensor. The subsequent section details the experimental setup for metrological noise estimation.

3.1. Experimental Setup

An industrial grade tri-axial IEPE accelerometer (PCB 356A02) [22] was chosen to model noise parameters in industrial measurement chains. A Renishaw XL-80 laser interferometer [23] served as a traceable reference in acceleration measurement for setup benchmarking. The sensors were mounted on a 110 mm x 80 mm x 5 mm aluminum plate using bolts, and adhesive clamps secured the sensor cables to minimize unwanted vibrations. Digital temperature sensors (Maxim DS18B20) on the sensor plate and at a 25 cm distance recorded temperature variations throughout the test duration.
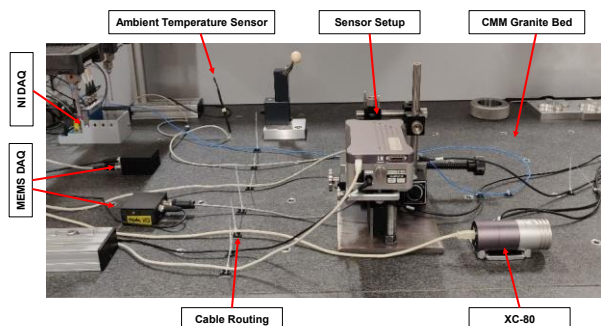

Figure 2. Experimental Setup for IEPE Noise Estimation on CMM Bed

The experimental setup, depicted in Figure 2, prioritized characterizing and modeling the noise parameters of vibration sensors within a vibration-isolated and thermally stable environment. Therefore, the test was conducted in a temperature-controlled environment of $\pm 1\ °C$ on a vibration-isolated, stable granite bed of the Zeiss Prismo Coordinate Measuring Machine (CMM). Furthermore, to minimize background noise contribution to the sensor from external sources such as opening and closing doors, movement of people, and so on, the tests were conducted over the weekend.

For accurate noise floor modelling, the IEPE sensor operated within its nominal operating range of $50\ g$. with a sampling rate set at $2000\ Hz$. The setup's vibrational stability, benchmarked at $0.316\ \mu g$ using the laser interferometer, was maintained in a temperature-controlled room to prevent environmental-induced bias in process noise characterization. Recorded temperatures indicated a stable sensor setup temperature of $18.83\ °C \pm 0.36\ °C$, with the ambient room temperature at $18.46\ °C \pm 0.85\ °C$.

4. Result and discussion

In the current research project, the noise contribution from various sources within the equipment and measurement chain of IEPE accelerometers was estimated. The measurement chain consists of a tri-axial PCB356A02 IEPE accelerometer [22] with a nominal sensitivity of $S = 10\ mV/g$, a 10 feet long low-noise coaxial cable, National Instruments NI-9234 Sound and Vibration module [24] and NI cDAQ-9174 four slot chassis [25]. While operating the equipment with a sampling rate of 2000 Hz the NI-9234 acquisition module contributes noise of $25\ \mu V_{rms}$ or a noise density of $780 nV/\sqrt{Hz}$ to sensor outputs. This converts to a contribution of $2.5\ mg$ noise contribution to sensor readings over the bandwidth due to acquisition module.

Similarly, the vendor for IEPE has specified the noise density values for the sensor in its datasheet. A comparison of theoretical versus experimental values for IEPE sensor was conducted. The noise density values were computed using Power Spectral Density (PSD) as visualized in Figure 3. The results are tabulated in Table 1. Using values in Table 1, the noise contribution to sensor measurements can be computed based on the bandwidth of sensor. For example, for a bandwidth $P_f = 100\ Hz$, the noise contribution in Z-axis can be computed as $30\ \mu g/\sqrt{Hz} \times \sqrt{100\ Hz} = 0.3\ mg$. Where $P_f = f_2 - f_1$ and f_2 and f_1 are upper and lower frequency limits for vibration measurement. Similarly, the values can be computed for any specified bandwidths from the PSD plots (Figure 3) of sensor as well.
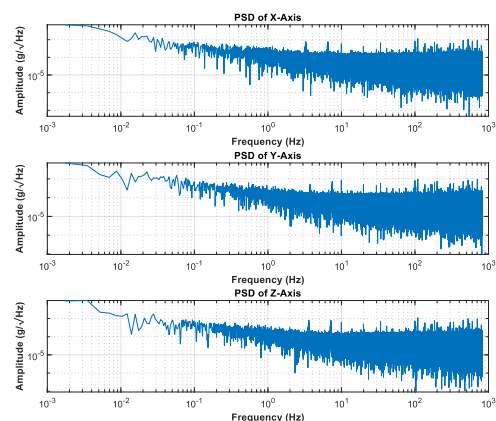

Figure 3. IEPE Measurement Chain Noise Density Estimation via PSD

3.1. Reducing Noise in IEPE Measurement Chains

The discussion on noise in IEPE measurements has predominantly focused on manufacturing and design aspects within controlled testing setups. However, users of the equipment play a crucial role in ensuring a noise-free sensor output, particularly in industrial setups.

Table 1 IEPE Measurement Chain Noise Density Estimation Results

S No	Frequency Bandwidth (Hz)	Experimentally Estimated Noise ($\mu g/\sqrt{Hz}$)			Theoretical [22]
		X-Axis	Y-Axis	Z-Axis	
1	1	211	112	167	150
2	10	112	62	45	25
3	100	16	76	30	10
4	825.80	39	62	72	4.12
5	1000	32	57	52	$5\ \mu g$

Reducing the noise floor involves key considerations such as minimizing sensor cable length to mitigate noise addition, as cables act like capacitors and longer lengths contribute to increased noise for example an AWG 24 will typically have a nominal capacitance of 35 pF/ft. While IEPE accelerometers typically use low-impedance co-axial cables to minimize noise pick-up, longer co-axial cables can inadvertently function as antennas, introducing higher noise levels. The choice of cabling fixtures is vital to prevent cable motion-induced self-generated noise (Triboelectric effect), and shielded, clean, and dry cable connectors are essential for precision measurements.

Another critical aspect is the selection of amplifiers, data acquisition, and power sources for lower noise acceleration signals. Experimental evaluations highlight the potential contribution of noise from these components to the vibration measurement chain. Users must be mindful of the equipment characteristics, as any noise generated can impact the accelerometer's output signal [21].

5. Conclusion

This paper presented a metrological approach for characterizing and modeling the noise parameters of IEPE accelerometers used in industrial vibration monitoring applications. Through experimental testing, the noise floor of a representative tri-axial IEPE accelerometer was quantified and sources of electronic, mechanical, and environmental noise were identified.

The metrological traceability of the IEPE sensor to a laser interferometer standard was established per ISO 16063-11 to benchmark the test setup. The result signify that noise density values computed from the power spectral density of the sensor outputs aligned closely with theoretical values from the sensor datasheet. For example the 100 Hz bandwidth, noise contribution was estimated to be 0.3 mg in the Z-axis. From the presented results specific values for designated bandwidths can also be computed as demonstrated.

In addition to quantifying the intrinsic sensor noise, techniques were presented to optimize the sensor configuration, cabling, and data acquisition parameters based on target frequency range and ambient conditions. This enables industrial users to make informed sensor deployment choices to minimize extrinsic noise pickup.

The rigorous noise characterization and modelling methodology provides improved understanding of uncertainty contributors in IEPE accelerometer measurements. By considering both intrinsic and extrinsic noise factors, the metroducal reliability of vibration monitoring systems can be enhanced. This will in turn support precision manufacturing through traceable, low-uncertainty measurements for predictive maintenance and process control.

As Industry 4.0 brings tighter manufacturing tolerances and increased reliance on sensor feedback, the measurement uncertainty insights from this work will be key to unlocking the value of vibrational signatures. Further research can expand the noise model to additional sensor types leveraged in smart factory initiatives. Wider adoption of this metrological approach will aid in leveraging IEPE accelerometers and other integrated vibration sensors for preventive maintenance and optimized machining accuracy. Overall, the quantitative noise insights obtained will aid industrial adoption of next-generation sensing for quality and productivity gains.

References

[1] Dornfeld D A and Lee D-E 2008 *Precision manufacturing* (no. Book, Whole).(Springer).

[2] Gilchrist A 2016 *Industry 4.0: The Industrial Internet of Things*, 1 ed. (no. Book, Whole).(Apress).

[3] Pascual D G, Daponte P, and Kumar U 2019 *HANDBOOK OF INDUSTRY 4.0 AND SMART SYSTEMS*.(CRC Press).

[4] Dorst T, Ludwig B, Eichstädt S, Schneider T, and Schütze A 2019 *2019 IEEE International Instrumentation and Measurement Technology Conference (I2MTC)*. 1-5 IEEE

[5] Wszołek G, Czop P, Słoniewski J, and Dogrusoz H 2020 *Journal of Vibroengineering* **22** 735-750

[6] Buckwar E. K R, L'Esperance B, Soo T. 2006

[7] Bruel and Kjaer 1982 *Measuring Vibration : All about accelerometers*

[8] Petkov P and Slavov T 2010 *Cybernetics and information technologies* **10** 31-40

[9] Levinzon F "Fundamental Noise Limit of an IEPE Accelerometer," in *Piezoelectric Accelerometers with Integral Electronics*Springer, 2015, pp. 107-116.

[10] BS ISO 2954:2012 : Mechanical vibration of rotating and reciprocating machinery. Requirements for instruments for measuring vibration severity 2012

[11] Iqbal A, Mian N, Longstaff A, and Fletcher S 2022 *International Journal of Automation Technology*

[12] Iqbal A, Mian N, Longstaff A, and Fletcher S 2021 *21st International Conference of the European Society for Precision Engineering and Nanotechnology*. 513-516 euspen

[13] Iqbal A, Mian N, Longstaff A, and Fletcher S 2021 *14th International Conference and Exhibition on Laser Metrology, Coordinate Measuring Machine and Machine Tool Performance*. 78-87 euspen

[14] BS ISO 16063-11:1999: Methods for the calibration of vibration and shock transducers. Primary vibration calibration by laser interferometry 2001

[15] Levinzon F 2014 *Piezoelectric Accelerometers with Integral Electronics*.(Springer International Publishing AG).

[16] Hanly. S. (2021). *Accelerometers: Taking the Guesswork out of Accelerometer Selection*.

[17] IEEE STD 1293-2018 (Revision of IEEE STD 1293-1998): IEEE Standard Specification Format Guide and Test Procedure for Linear Single-Axis, Nongyroscopic Accelerometers 2019

[18] BORRIE J 1992 *Englewood Cliffs, NJ, Prentice Hall, 1992, 296*

[19] Levinzon F "Noise of an IEPE Accelerometer," in *Piezoelectric Accelerometers with Integral Electronics*Springer International Publishing, 2015, pp. 117-133.

[20] Levinzon F 2007 *Endevco Sensing Technical Paper* **324**

[21] Wang Y, Yang Z, Cheng P, and Li H 2015 *Journal of Applied Science and Engineering* **18** 295-302

[22] Piezotronics 2019 PCB 356A02 Tri-axial Accelerometer

[23] Renishaw 2019 XL-80 Laser Measurement system

[24] Instruments N. (2019). *NI-9234 C Series Sound and Vibration Input Module Datasheet*.

[25] Instruments N. (2021). *NI cDAQ-9174*.

High speed air bearing spindle for ultra precision machining

Byron Knapp, Dan Oss, and Dave Arneson

Professional Instruments Company, Hopkins, Minnesota, USA

bknapp@airbearings.com

Abstract

Increasing demands for deterministic direct machining of infrared optics and molds require a precision air bearing spindle with high stiffness capable of higher cutting speeds. This paper describes design and testing of a new porous graphite air bearing spindle for diamond machining capable of 18 000 RPM. The design uses porous graphite journal sleeves and compound compensated captured thrusts. The spindle is water-cooled to maintain thermal stability and vacuum is supplied to the chuck for workpiece fixturing via a non-contact rotary union. Proper testing techniques and apparatus required for critical aspects of an ultra-precision spindle are described. Static stiffness testing demonstrates radial stiffness at the nose better than 50 N/μm and axial stiffness of 280 N/μm. Dynamic response shows the first natural frequency is highly damped and above 1 400 Hz. Spindle error motions less than 5 nm are demonstrated enabling optics with sub-micrometer form and sub-nanometer finish.

Keywords: porous graphite air bearing spindle, infrared optics, micro optics

1. Background

The ultra-precision air bearing work spindle shown in Figure 1 has been newly developed to address the increasing number of applications requiring infrared and micro optics [1]. Brittle single crystal semiconductors and micro optic molds and can be machined at higher spindle speeds to reduce brittle fracture [2] and improve productivity [3]. However, rotational speed is often limited to 10 000 RPM in an effort to mitigate dynamic spindle errors [4, 5]. To address this need, a new porous graphite air bearing spindle has been developed capable of 18 000 RPM with high stiffness and nanometer-level errors beyond the current state-of-the-art.

With higher speeds, reduction and control of heat generated due to shearing is a primary design consideration. Petrov's equations for the journal and thrust bearings are [6]:

$$P_J = \frac{\pi^3}{450} \frac{\mu\ell}{\hbar} r^3 N^2$$

where P_J is the power to shear the journal air film, μ is the absolute viscosity, r is the shaft radius, $\hbar$ is the film thickness, ℓ is the journal length, and N is the rotational speed in units of revolutions per minute.

$$P_T = \frac{\pi^3 \mu N^2}{1800\hbar}(r_o{}^4 - r_i{}^4)$$

where P_T is the power to shear the thrust air film, r_i is the inner radius of the thrust, and r_o is the outer radius of the thrust. With 8 μm air films to provide high stiffness, 200 W due to shearing is expected at 18 000 RPM which can be managed using water cooling. The spindle housing (aluminium) has a larger coefficient of thermal expansion than the shaft (stainless steel) to prevent thermal runaway. Due to the difference in thermal coefficients, as the spindle warms up from shearing, the air film thickness increases resulting in less heat and a stable thermal system.

The cross section in Figure 2 shows porous graphite journals and compound compensated captured thrusts (grooved thrust face fed by journal flow). A brushless permanent magnet motor and a 1 650 line-count encoder are mounted directly to the spindle shaft. Vacuum is supplied to the chuck for workholding via a non-contact rotary union.

Figure 1. Porous graphite air bearing spindle for diamond turning.

2. Static stiffness

Static stiffness is a crucial indicator for spindles to be used in precision machining applications—particularly central stiffness under light cutting loads. Specially-built hardware to measure radial load capacity and radial static stiffness is shown in Figure 3. An air bearing piston pulls the rotor at the nose of the spindle in the radial direction. In a separate metrology loop, a twisted band Abramson movement indicator (CEJ Mikrokator) with 250 nm resolution measures radial displacement of the rotor. Ultimate radial load capacity at the spindle nose is 700 N with 0.7 MPa inlet pressure. Resulting radial stiffness at the nose is 54 N/μm with 0.7 MPa inlet pressure. The stiffness is linear through the load range which is critical especially in the low-load region typical of precision machining.
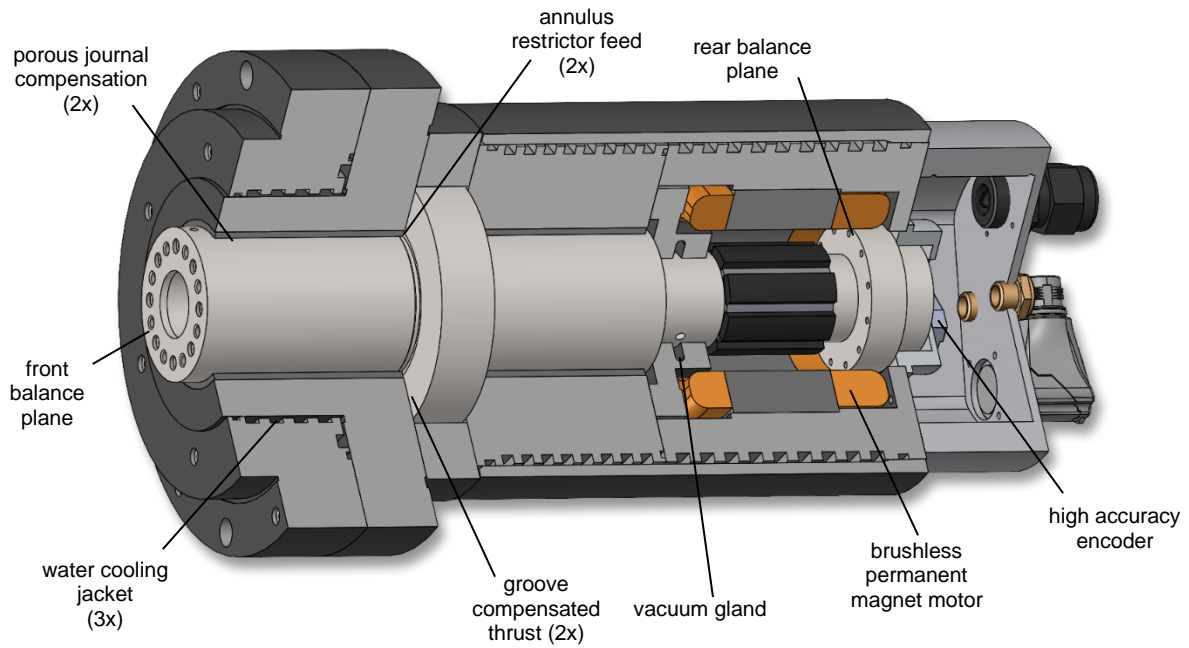
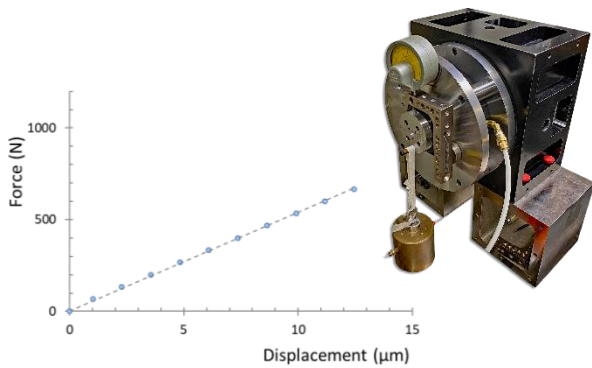Figure 2. Cross section of porous graphite work spindle for diamond machining.

Figure 3. Radial stiffness and load capacity at the spindle nose is 54 N/μm and 700 N with 0.7 MPa inlet pressure.

Hardware to measure axial load capacity and axial static stiffness is shown in Figure 4. In this test, an air bearing piston pushes the rotor at the top of the spindle in the axial direction. At the bottom of the setup, in a separate metrology loop, axial displacement of the rotor is recorded. Ultimate axial load capacity is 1 450 N and axial stiffness is 280 N/μm with 0.7 MPa inlet pressure.
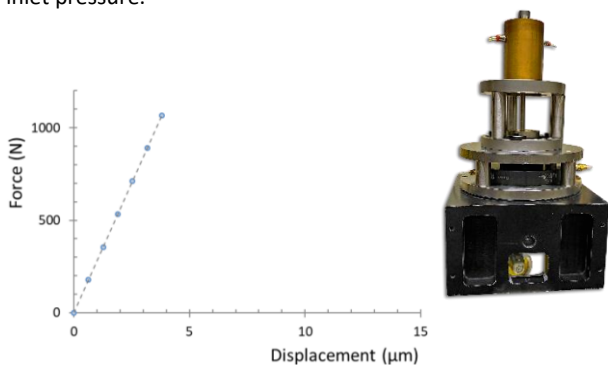
Figure 4. Axial stiffness and load capacity is 280 N/μm and 1 450 N with 0.7 MPa inlet pressure.

3. Dynamic stiffness

Modal analysis is used to determine dynamic response with natural frequencies and mode shapes in the radial and axial directions. The spindle is supported on compliant foam to minimize boundary condition influences. An impact hammer (Kistler 500 N) excites the housing in the radial direction whilst an accelerometer (Kister K-Shear 25g), attached to the rotor, measures the radial direction response. A 24-bit dynamic signal analyzer (Data Physics SignalCalc Ace) records excitation and response to calculate frequency response functions. The radial response is dominated by a heavily damped mode at 1 400 Hz.
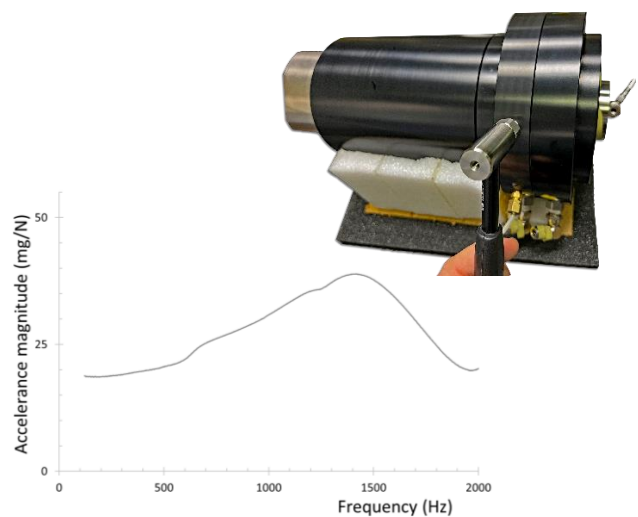

Figure 5. Radial direction frequency response function shows a highly damped mode at 1 400 Hz.

A modal impact test in the axial direction and resulting frequency response is shown in Figure 6. For this test, an impact hammer excites the rotor in the axial direction while an accelerometer mounted to the structure measures the axial response. With an inlet pressure of 0.7 MPa, the first mode is highly damped and again at 1 400 Hz. Heavily damped modes in the axial direction help prevent axial spoking (star pattern) in an optical surface machined with this spindle [7].
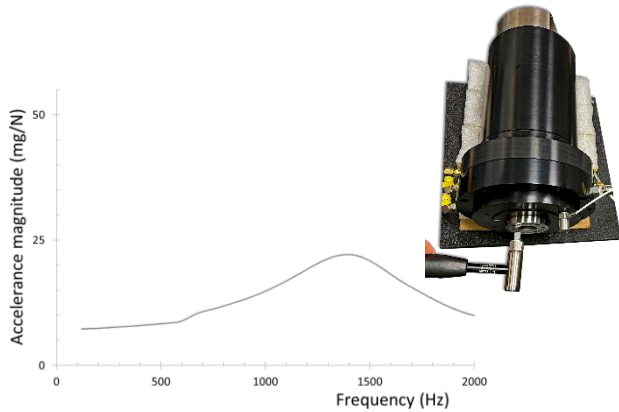

Figure 6. Axial direction frequency response function shows a highly damped mode at 1 400 Hz.

4. Error motion

Precision spindle metrology is typically accomplished by measuring the surface of an artifact mounted to a spindle [8]. This is complicated by the fact that artifact out-of-roundness often exceeds error of a precision spindle and separation techniques must be used to extract the desired measurement. Donaldson's reversal technique provides an elegant mathematical solution for separating spindle radial error motion from artifact form error [9]. However, in practice, measurement accuracy of this reversal technique suffers due to a variety of potential error sources. To address this issue, Whitehouse developed a multiprobe technique which avoids some of the problems with reversal [10].

Bespoke tooling to implement a modified version of Whitehouse's multiprobe radial error separation is shown in Figure 7. Harmonic suppression is minimized by using angular indexing of a single capacitive sensor at asymmetrically spaced angles of 0°, 99.844° and 202.5° [11]. Axial error motion is also measured with this tooling at a single angular orientation because separation is not required for axial measurements.
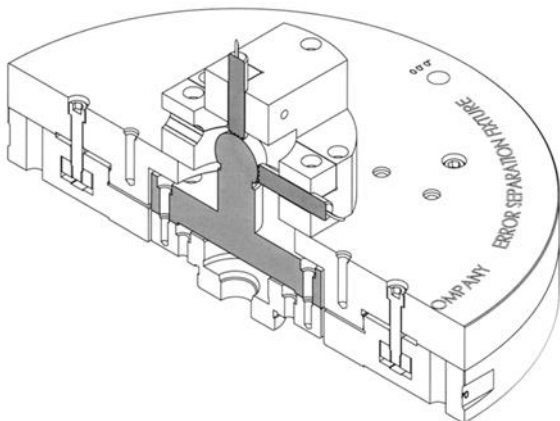

Figure 7. Bespoke multiprobe error separation tooling with 25 mm diameter spherical artifact.

In Figure 8, a capacitive sensor (Lion Precision C23-C, 0.4 µm/V) targets a 25 mm diameter lapped sphere. The sensor amplifier (Lion Precision CPL190) incorporates a 15 kHz first-order, low-pass analog filter with linear phase response. The data acquisition system (Lion Precision SEA) is triggered by the 1 650 line-count encoder, providing immunity to synchronization errors caused by speed variation. A low-pass digital filter with a 150 UPR cut-off is applied to the axial and radial error motion plots. Total radial and axial error motions less than 5 nm are shown in Figure 9 and Figure 10.
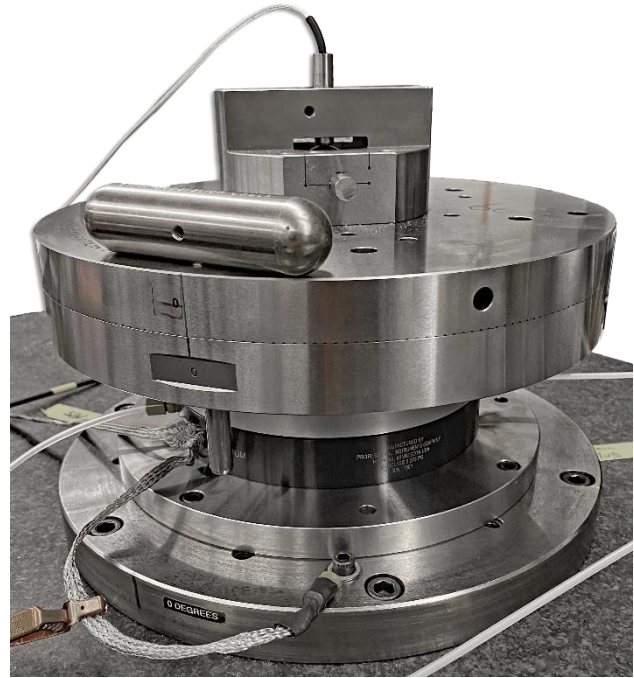

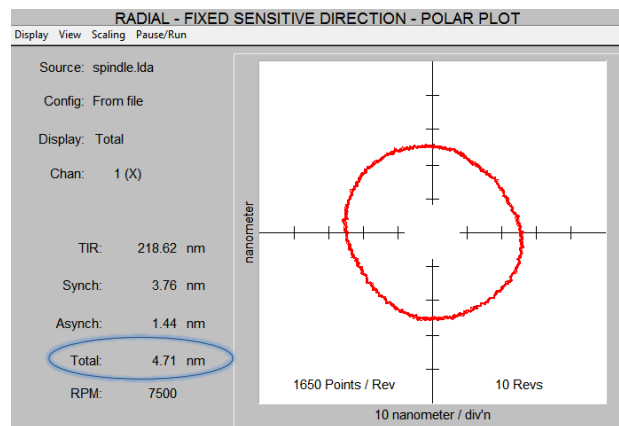**Figure 8.** Setup for radial and axial spindle error measurement.

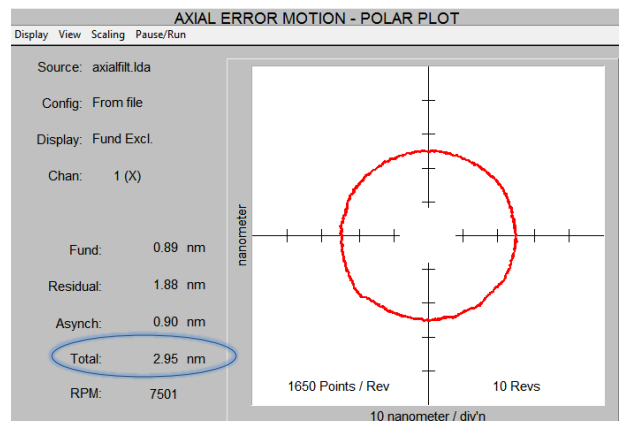**Figure 9.** Radial spindle error motion after separation.

Figure 10. Axial spindle error motion.

555

5. Summary

Proper testing techniques of three critical aspects of a new porous graphite air bearing spindle for diamond machining are revealed. Static stiffness and load capacity is demonstrated by using air pistons to apply a load while recording displacement in a separate metrology loop. With modal analysis, dynamic response is shown to have a high first natural frequency that is well-damped. Finally, bespoke tooling is used to perform multiprobe error separation with results better than 5 nm.

6. Conclusion

An increasing number of small optics must be machined at higher spindle speeds for increased productivity. A new porous graphite air bearing workholding spindle which extends the current state-of-the-art has been developed to address this need. Static stiffness testing demonstrates radial stiffness at the nose and axial stiffness better than 50 N/μm and 280 N/μm respectively. The dynamic response shows the first natural frequency is highly damped and above 1 400 Hz. Equipment and techniques to measure radial and axial spindle error motion less than 5 nm are demonstrated.

References

[1] MA Davies et al. Application of precision diamond machining to the manufacture of microphotonics components. *Proc. SPIE 5183*, 2003.

[2] M Tunesi et al. Effect of cutting speed in single point diamond turning of (100)Ge. *Manufacturing Letters*. **38**: 15-18, 2023.

[3] E Brinksmeier and L Schönemann (Eds.) Ultra-precision High Performance Cutting. Report of DFG Research Unit FOR 1845. Springer Nature Switzerland AG Cham: 2020.

[4] P Huang et al. Investigation of the effects of spindle unbalance induced error motion on machining accuracy in ultra-precision diamond turning. *Int J of Machine Tools & Manufacture*. **94**: 48–56, 2015.

[5] D Huo and K Cheng. Micro-Cutting: Fundamentals and Applications - Diamond turning and micro turning, 153-183, 2013.

[6] NP Petrov. Friction in Machines and The Effect of The Lubricant *Inzhenernii Zhurnal*, Volume **1-4**, 1883.

[7] M Tauhiduzzaman et al. Form error in diamond turning. *Precision Engineering*, **42**: 22-36, 2015.

[8] E Marsh. Precision Spindle Metrology, Second Edition. Destech Publications, Inc. Lancaster, PA: 2010.

[9] R Donaldson. A simple method for separating spindle error from test ball roundness error. *Annals of CIRP*, **21**(1):125-126, 1972.

[10] D Whitehouse. Some Theoretical Aspects of Error Separation Techniques in Surface Metrology. *J. of Phys. E: Sci. Inst.* **9**:531-536, 1976.

[11] E Marsh et al. A Comparison of Reversal and Multiprobe Error Separation. *Precision Engineering*. **34**:85-91, 2010.

Development of test panel for measurement of temperature in chamber

Jaehyun Park[1], Kihyun Kim[2], Hyo-Young Kim[2], Seungtaek Kim[1#]

[1]Smart Manufacturing System R&D Department, Korea Institute of Industrial Technology, Republic of Korea
[2]Department of Mechatronics Engineering, Tech University of Korea, Republic of Korea

#Corresponding Author / E-mail : stkim@kitech.re.kr

Abstract

Recently, semiconductor processes utilize a lithography process to form fine patterns and copper pillars. The lithography process is a process that requires PR (Photoresist) coating. PR is made up of PR ink and solvent and maintains a certain viscosity. After coating, the PR solvent is evaporated through the bake process. The bake process is a process in which PR-coated wafers and panels are heated using a high-temperature heater within a chamber. In the bake process, it is important to keep the wafer and panel at a uniformly high temperature to evaporate the solvent. Multiple temperature sensors are placed within the chamber to maintain a high temperature environment. However, it is difficult to confirm whether uniform temperature is maintained in the actual wafer and panel. For this reason, this study developed a test panel to measure the temperature of the target in the chamber. A panel substrate that is robust to high temperatures was selected and a calibrated temperature sensor was placed at several positions. Through electrical connection, we confirmed that the temperature was measured with high repeatability from the temperature sensor.

Test, Panel, Temperature, Chamber

1. Introduction

As semiconductors become smaller, complex and diverse devices must be connected within the same space, and next-generation package technology that can integrate devices at high density at low cost is required. As the number of devices in one package increases, there are limits to integrating devices on a 1D plane. Therefore, chiplet packages that integrate devices in 2.5D and 3D within a limited space are required.

Tall Cu pillars are required for high-density vertical interfaces in 2.5D and 3D integrated packaging. To manufacture a tall Cu pillar, a pillar mold is required. Pillar molds are manufactured through the photolithography process. The photolithography process is a process that forms a pattern by coating PR (Photoresist) and then applying light. A PR mold can be produced through etching process. The photolithography process requires a PR coating process. Generally, wafers are coated with PR through spin coating. Recently, PLP (Panel level Package) is being required to improve yield. To perform spin coating on a panel, the spinner size becomes larger and PR consumption increases. To solve this problem, Inkjet based PR coating was proposed by using PR ink. To make PR ink, solvent is combined with PR. Since PR ink is a mixture of PR and solvent, a baking process to evaporate the solvent after inkjet coating is required to form the final PR layer. In response to PLP, a heater and chamber for the panel were manufactured to evaporate the PR solvent coated on the panel. In this panel baking process, in order to form a PR mold with a constant thickness, a uniform temperature must be maintained in the panel. To achieve this, it is necessary to check whether the temperature of the glass panel rises uniformly during the baking process.

In this study, we designed a test panel that can perform temperature tests at high temperatures instead of actual process panels. Considering the baking chamber, we designed a PCB board suitable for high temperatures and designed a circuit to process and monitor temperature data signals.

2. Heat Chamber

The target size of the glass panel in this study is 650x650 mm². In the bake chamber, the heater must be large enough compared to the glass panel to allow the glass panel to rise in temperature uniformly. The size of the heater is 800x800mm². Proximity pins were placed on the hot plate to prevent direct contact between the heater and the glass panel and to maintain a certain distance so that uniform heat can be applied to the glass panel. Since the glass panel on top of the proximity pin may sag and affect the uniformity of the PR after the baking process, multiple proximity pins were placed. Figure 1 shows the heater and glass panel.

Figure 1. Heater and glass panel for bake chamber

The bake chamber has a heater inside, as shown in Figure 2. A glass panel is on top of the heater. When the chamber is sealed and the heater temperature rises, it is difficult to measure the temperature of the glass panel by the heater. Therefore, we plan to develop a test panel of the same size as the glass and measure the temperature of the glass panel heated by a heater.
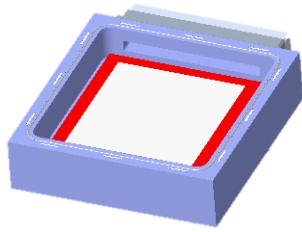
Figure 2. Bake chamber for baking process

3. Concept Design of Test Panel

The test panel can measure temperature at high temperatures, and it is necessary to select a sensor applicable to the PCB board to be manufactured in panel form. In this study, we will consider and apply two sensors.

The SMD Type PCB mount type temperature sensor was selected as PTS 1206 sensor, a Platinum Thin Film Chip Resistor . This sensor is a small temperature sensor measuring 3.2mm wide and 1.6mm tall. The temperature range is from -55 ℃ to +150 ℃. It is an ultra-small sensor that can be attached to a PCB and can be used to measure temperature distribution.
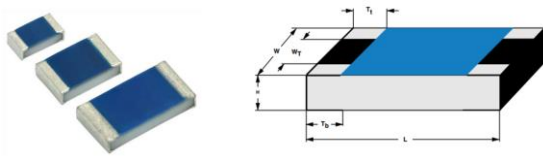
Figure 3. Platinum thin film chip resistor sensor

The TMP126 IC-based digital temperature sensor was selected as a temperature sensor for heater testing to ensure temperature accuracy through digital temperature measurement. The temperature range of this sensor is from -55 ℃ to +175 ℃ , and it is a sensor that measures digital temperature through the SPI protocol.
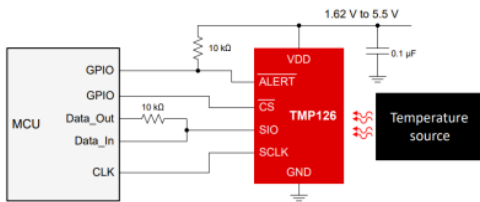

Figure 4. TMP126 IC temperature sensor interface

Based on the TMP126 IC, we designed a PCB for measuring temperature distribution through a 3x3 temperature sensor arrangement with a size of 650x650mm^2. Each temperature sensor requires 3 strands of wire for the SPI protocol, and 2 strands of power positive and negative power wires are required in common, so a total of 29 strands of wire are required. It was designed with a microprocessor that can operate at 150 ℃ installed inside the high-temperature PCB.
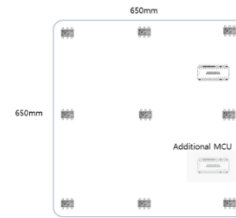

Figure 5. PCB design for 3x3 array temperature distribution measurement

4. Electric Circuit

The sensor to be applied in this study requires sensor data processing through signal processing, and the signal processing method is different for each sensor. Platinum Thin Film Chip Resistor sensor converts the change in resistance value according to the temperature of the sensor into voltage through a Wheatstone bridge circuit. Design a circuit that amplifies the signal to a range where the ADC module can read the voltage value and delivers the signal to the anode and cathode of the ADC module.
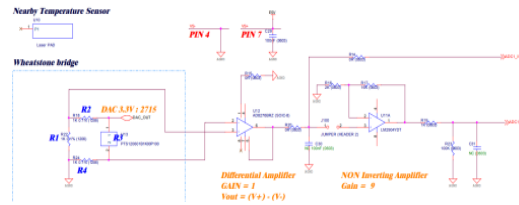

Figure 6. Designed amplifier circuit

We designed a processing module to transmit data to a PC based on a microprocessor (STM32F103). A 16-bit 4-channel ADC module with an input range of ±10V was selected and designed to connect the MSFK3.2 sensor and Platinum Thin Film Chip Resistor sensor so that the digital signal can be used as a resource for the visualization program.

5. Conclusion

In this study, we designed a test panel that can perform temperature tests at high temperatures instead of panels for actual processes during the panel bake process. We designed the PCB board considering the size and maximum temperature of the baking chamber and designed the circuit to process and monitor temperature data signals.

In the future, we plan to apply the test panel to an actual chamber to test the temperature distribution of the panel and improve it so that it can be applied to the actual process.

References

[1] Hamid Eslampour et al, "Low Cost Cu Pillar fcPOP Technology", Electronic Components and Technology Conference, 2012. ECTC 2012. 62nd, San Diego, CA, pp.871-876, May 29th-June 1st, 2012.

[2] C. Melvin, et. al., "Fan-out packaging: a key enabler for optimal performance in mobile devices," Chip Scale Review, Vol 21, No. 1, 40-44, 2017.

Characterization and compensation of volumetric error variations over time in medium size machine tools

Beñat Iñigo[1,2], Natalia Colinas-Harmijo[1], Luis Norberto López de Lacalle[2], Harkaitz Urreta[1], Gorka Aguirre[1]

[1]IDEKO, BRTA Member, Design and Precision Engineering Department, Elgoibar
[2]UPV/EHU, Mechanical Engineering Department, Bilbo

binigo@ideko.es

Abstract

An artifact-based fast and automated volumetric error mapping solution for medium size 3-axis machine tools that enables the calibration of a 1m3 workspace in less than one hour is proposed for characterizing how temperature variations affect the volumetric accuracy of the machine without a priori knowledge of the temperature variations. A continuous measurement during seven days is performed on a medium sized milling machine affected by different heat sources and a volumetric error variation model is identified. Residual errors remaining from the identification process are used to estimate the uncertainties of individual parameters and motion errors, and Monte Carlo simulations are used to propagate them to the TCP. This model is used to understand how the volumetric positioning error of the machine changes over time and how it is generated within the kinematic chain of the machine.
Finally, a second experimental test is carried-out, this time equipping the machine with several temperature sensors. A compensation model based in multiple linear regression is implemented to predict the different component errors affecting the volumetric accuracy of the machine tool.

Machine tool, volumetric error, thermal error, uncertainty

1. Introduction

In modern manufacturing industries, precision in machine tools is crucial for ensuring the dimensional accuracy of manufactured parts. Geometric and thermal errors represent significant sources of deviation in the volumetric accuracy of machine tools and have been studied independently for decades [1]. Traditional approaches, exemplified by [2] and [3], have treated geometric and thermal errors separately, employing distinct methodologies for their characterization [4].

Geometric error characterization and compensation have been extensively explored, particularly in medium and large-sized machine tools, using advanced technologies such as Laser Trackers (LT) and multilateration-based solutions [5]. An alternative, cost-effective method involves artefact-based solutions, despite limitations in range and measurable positions [6]. These solutions primarily focus on the characterization of the geometric errors due to manufacturing and assembly imperfections [7]. However, thermal errors can influence the characterization of geometric errors, leading to two main approaches: assuming stable thermal conditions for geometric error characterization [8] or incorporating thermal effects as uncertainties in calibration [9]. The latter approach, while more reliable, often relies on oversimplified models that may lead to inaccurate assessments of thermal effects.

On the other hand, approaches to characterize thermal effects usually focus on very localized effects, ignoring the variation of the error along the whole working volume. Digital Twin-based approaches, utilizing Finite Element models, offer a potential solution to volumetric limitations. However, challenges arise in accurately modelling complex thermomechanical systems, making these approaches difficult to implement in industrial environments with diverse machines and strict production deadlines. While experimental training for phenomenological models appears promising, comprehensive error characterization across the entire volume requires addressing constraints.

Preceding works have explored artifact-based volumetric calibration methods [10], with an optimized implementation for an automatic and repeatable procedure [11]. This work introduces a compensation model for thermal errors within the machine tool's volume, treating geometric and thermal errors as a unified source of error. The study focuses on a moving column milling machine, conducting two distinct thermal tests to establish and validate the compensation model. A network of up to 52 temperature sensors was employed to comprehensively capture the machine's thermal state over time.

The structure of this paper is as follows: Section 2 provides a comprehensive account of the methodology employed, showing both the experimental setup and the theoretical basis of the volumetric calibration and thermal compensation model. Section 3 presents a summary of the experimental results, with some in-depth analysis. Section 4 closes with conclusions and outlook.

2. Methodology

2.1. Experimental setup

Following the methodology developed in previous works, an artifact-based calibration procedure is carried out in a medium-sized milling machine. It is a moving column type milling machine, with fixed table in the workpiece side. The actual setup is shown in Figure 1.
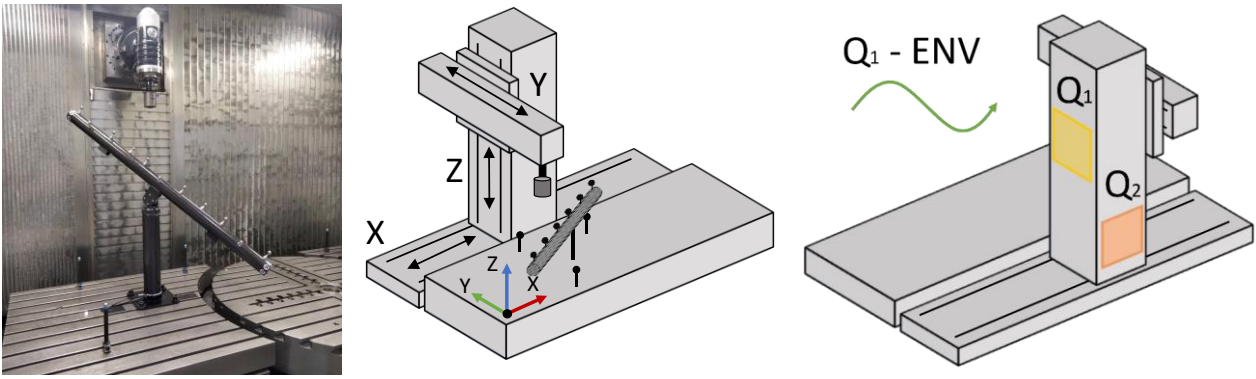
Figure 1. (left) Calibration setup with the ball array and 3 individual spheres on the machine table and the measuring probe mounted in the machine head. (middle) Schematic depiction of the machine kinematics. (right) Schematic depiction of the heat sources
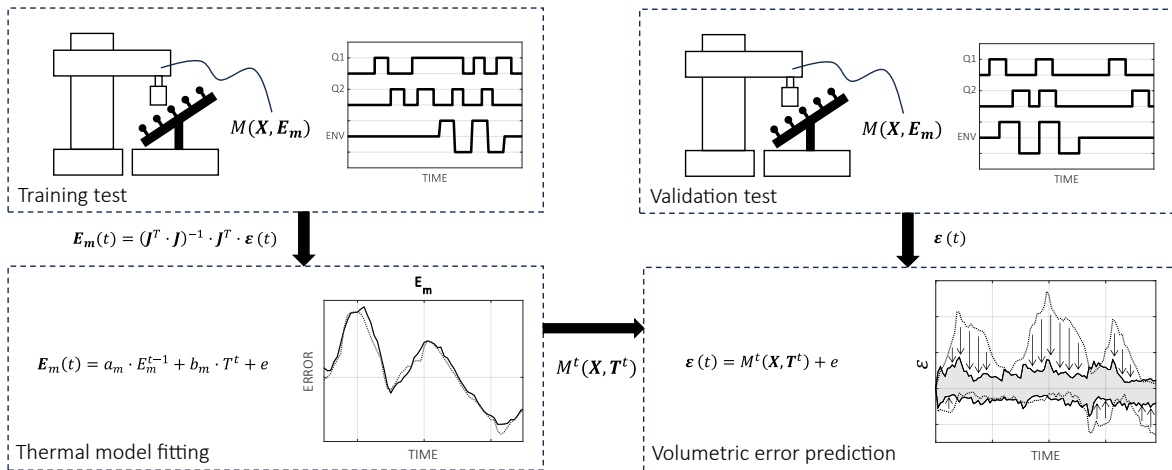
Figure 2. Summary of process for the obtention of a thermal volumetric error prediction model. (Top-left) Training test with the consequent obtention of the volumetric errors changing over time; (Bottom-left) ARX regression with temperatures as inputs obtaining a compensation model; (Top-right) Validation test measuring distance errors; (Bottom right) Volumetric error prediction and compensation using model M over errors measured in validation test.

The calibration process consists of measuring a ball array with high precision spheres over several orientations inside the machine working volume. These measurements are repeated over several days in order to capture the thermal variation of the machine errors. To make this process automatic, the artefact is mounted in a cylindrical base with an embedded rotary motor. The inclination around horizontal (elevation) angle is set manually and locked through all the test as the rotation around the vertical (azimuth) angle is provided by the rotary motor. To map the thermal state of the machine, up to 50 temperature sensors have been installed in different parts of the structure: 10 in the workpiece side table, 10 in the X axis bed, 16 in the column, 12 in the ram and 4 ambient sensors. Three controlled heat sources (two local hot air ventilators and room climate) can be activated or deactivated during the thermal test.

2.2. Volumetric thermal error model

In order to calculate TCP errors at any axis position a kinematic model of the machine is developed using Homogeneous Transformation Matrices (HTM), which is a widespread technique for machine tool modelling [12]. The result is a model capable of predicting the volumetric error at any point in the calibrated space, which will be referred generically as M(X,E_X), denoting its dependence on axes positions (X) and component errors motions (E_X). The position dependent error motions for each axis are modelled by linear combinations of Legendre polynomials of order n.

In [10] the shape of the artefact and the measurement positions were optimized, resulting in a pseudo-1D ball array

with a primary longitudinal direction and small transversal offsets between 11 spheres. It is necessary to measure the ball array at 8 different orientations in order to get a proper compensation model. The geometric errors contained in E_X are estimated by minimizing the error between the calibrated and measured distances between the spheres in the ball array using least square regression.

The procedure is repeated periodically every hour, and a volumetric error model is obtained for each measurement cycle while thermal conditions are varied. Thus, the parameters obtained for the volumetric error model will experience a variation over time that is then fitted to a multiple linear regression model relating temperatures and parameter variations. A training test and a validation test are carried out separately varying the three thermal sources with different intensities and frequencies. Figure 2 summarizes the procedure.

3. Experimental results

As mentioned in the previous section, training and validation tests are carried out in a medium sized milling machine. The thermal model obtained from the training test is applied in the validation test and the improvement in distance errors is observed. Figure 3 shows distance errors between spheres before and after applying the compensation model for both tests.

Alternatively, error prediction capabilities can be evaluated by observing individual parameter predictions made by the thermal
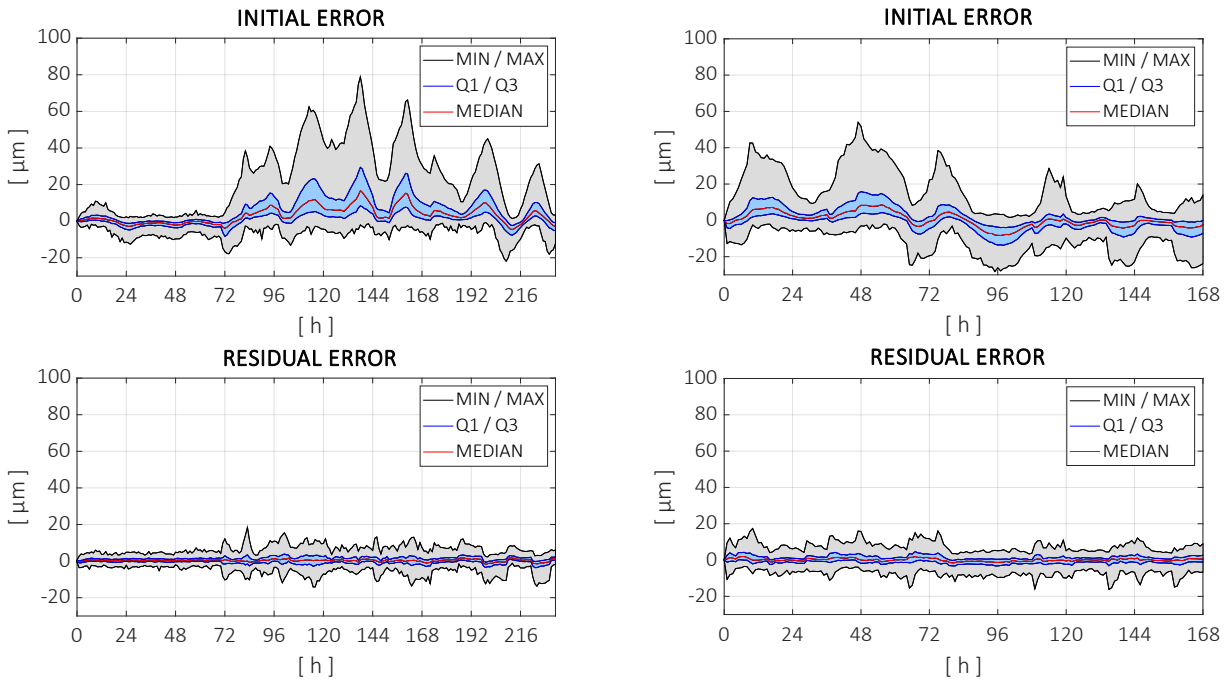
Figure 3. Distance error between spheres relative to the first measurement for the training test (left) and validations test (right). Errors are shown before (top) and after (bottom) the compensation model has been applied.
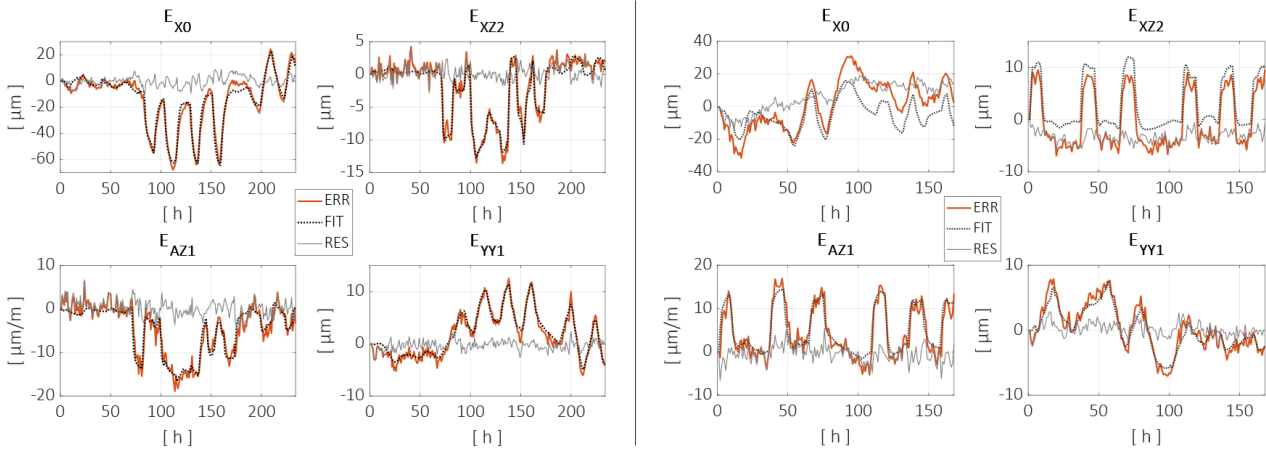
Figure 4. Evolution of specific error parameters during the training (left) and validation (right) tests. Model fit and prediction are shown respectively with a black dotted line. Residual error is shown in grey.

model for the validation test. Figure 4 shows the evolution of some parameters for the training test and the validation test along with the model prediction made based on temperature inputs.

To fully evaluate the error improvement in the working volume X, Y and Z straight trajectories are simulated using the kinematic model of the machine before and after compensation. These straight lines are evaluated for each time step so that the evolution of the error and the improvement can be observed. Figure 5 shows the evolution of the error along a straight line in X direction, centred in the working volume in Y and Z positions. Error reduction of 50% (RMS) is achieved in X direction error and improvements up to 65% in Y and Z directions.
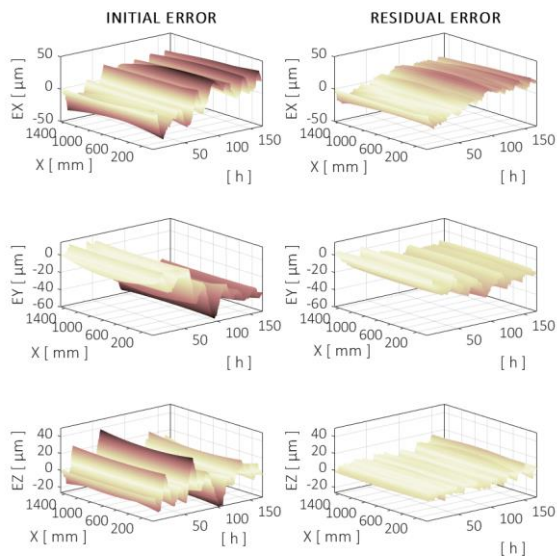
Figure 5. Evolution of the directional errors at TCP over a centered trajectory along the X axis during the validation test. Initial (left) and compensated (right) errors are shown.

4. Conclusions

This work introduces a novel methodology for measuring and compensating thermal variations of volumetric errors in machine tools. Unlike traditional approaches that separate geometric and thermal errors, this work acknowledges that all geometric errors in a machine tool can change over time due to temperature influence. The proposed unified methodology combines spatial and temporal dimensions, utilizing a fully automated measuring process to calibrate geometric errors, repeated over time. The compensation model relies on the assumptions that geometric errors can be approximated by lower-order polynomials and that the parameters of these polynomials experience temporal variations predictable by temperature changes. While the first assumption is widely accepted, the second assumption, though less common, is validated through the paper's results, demonstrating a correlation between temperatures and most parameters.

The key enabler for understanding and validating measurements is a kinematic model of the machine that incorporates position-dependent behavior of geometric errors and temperature-dependent effects. The model predicts errors at the tool center point (TCP) based on machine position and temperatures, serving as a powerful tool for validation using various trajectories and workpiece machining tests. Despite the promising results, compensation outcomes are not perfect, revealing uncertainties related to the measurement system, calibration procedure, and the extent to which the assumptions hold. Long-term drifts and dissimilar results in compensating errors of different time intervals are attributed to uncertainties, incomplete temperature field information, and the inherent approximations in the methodology.

References

[1] Bryan J 1967 *CIRP Annals* **16** 203
[2] Mayr J, Jedrzejewski J, Uhlmann E, Alkan Donmez M, Knapp W, Härtig F, Wendt K, Moriwaki T, Shore P, Schmitt R, Brecher C, Würz T and Wegener K 2012 *CIRP Annals* **61** 771–791
[3] Schwenke H, Knapp W, Haitjema H, Weckenmann A, Schmitt R and Delbressine F 2008 *CIRP Annals* **57** 660–675
[4] Weck M, McKeown P, Bonse R and Herbst U 1995 *CIRP Annals* **44** 589–598
[5] Schwenke H, Franke M, Hannaford J and Kunzmann H 2005 *CIRP Annals* **54** 475–478
[6] Belforte G, Bona B, Canuto E, Donati F, Ferraris F, Gorini I, Morei S, Peisino M, Sartori S and Levi R 1987 *CIRP Annals* **36** 359–364
[7] Szipka K, Laspas T and Archenti A 2018 *Precision Engineering* **51** 59–67
[8] Maeng S and Min S 2020 *Precision Engineering* **63** 94–104
[9] Liebrich T, Bringmann B and Knapp W 2009 *Precision Engineering* **33** 1–6
[10] Iñigo B, Colinas-Armijo N, López de Lacalle LN and Aguirre G 2021 *Precision Engineering* **72** 823–836
[11] Iñigo B, Ibabe A, López de Lacalle LN and Aguirre G 2021 *Precision Engineering* **81** 167–182
[12] Srivastava A K, Veldhuis S C and Elbestawit M A 1995 *International Journal of Machine Tools and Manufacture* **35** 1321–1337

Laser triangulation-based thermal characterization of machine tool spindles according to ISO 230-3

Matthias Geiselhart[1], Andoni Iribarren Indaburu[1,2], Pedro José Arrazola Arriola[2], Giuliano Bissacco[1]

[1]*Technical University of Denmark, Department of Civil and Mechanical Engineering, Nils Koppels Allé B425, 2800 Kongens Lyngby, Denmark*
[2]*Mondragon University, Faculty of Engineering, Loramendi Kalea, 4, 20500 Arrasate/Mondragon, Spain*

mgeis@dtu.dk

Abstract

To characterize the spindle displacement of a machine tool over time due to the heat generated by the spindle motor during operation, a measurement setup was developed consisting of five laser triangulation sensors arranged according to ISO 230-3. It is based on a modular, lightweight frame with features for quick disassembly for easier transportation and re-assembly with high repositioning accuracy enabling to run the test at different locations on different machines. To localize the laser spot on a rotating tungsten carbide bar, an on-machine laser beam origin and direction detection strategy for laser triangulation sensors was developed. The position of the bar was mapped in the three-dimensional space by a best-fit algorithm. The characterization of the thermal deformation of a machine tool at 15000 rpm over 1.7 hours showed robustness to the underlying laser origin and direction measurements and was demonstrated as suitable tool to analyze machine tool's thermal compensation strategies. The most influential error contributors were identified and discussed.

Machine, Measuring instrument, Precision, Thermal error

1. Introduction

To ensure the performance of machine tools and thus the quality of machined parts, the ISO 230 series of standards covers methods and tests for evaluating machine characteristics. ISO 230-3 [1] describes displacement sensor-based tests for characterization of thermal distortions and drifts from rotating spindles. Commercial spindle error analysis systems typically consist of either three or five capacitive displacement sensors, placed in a fixture and measuring on a rotating artifact mounted on the spindle [2,3]. The displacement of the spindle with respect to the machine table in X-, Y-, and Z-direction can be characterized with three sensors, the tilt error movements in the XZ-, and YZ-plane can be characterized with one additional sensor each in the X- and Y-direction at known distances.

A versatile test setup to characterize machine tools according to ISO 230-3 consisting of five laser triangulation sensors (LTS) on a compact modular frame allowing for easy handling and assembly with high repositioning accuracy was developed. LTSs have been selected because they are insensitive to the shape and material of the target and are suitable for high-resolution non-contact measurements at high rotational speeds of the measured object at sampling rates up to 50 kHz and are less expensive compared to other high performance measurement technologies.

2. Methodology

2.1. Laser triangulation sensor

LTS are typically used for displacement, position, thickness, or dimensional measurements as they offer high resolution down to 30 nm, high linearity of 600 nm, a small beam spot size, long measuring ranges, high reference distance between sensor and target reducing the risk of damage during setup, and independence on the target material [4]. However, the relatively large sensor compared to confocal, capacitive or eddy current

sensors makes the setup bulkier and a relatively clean optical path is required for reliable operation.

The distance measuring technique is based angle calculation and illustrated in Figure 1. A laser beam is projected onto the object to be measured. The distance to the object is determined using the known distance from the transmitter to the receiving element and the angle of reflection of the laser beam on the receiving element. Its components are assembled in an aluminum casing, among which the laser diode and processing unit are potential heat sources. The thermal behavior of the LTSs used was investigated. The results are presented in Section 3.

Five LTSs type optoNCDT ILD-2300-2 from Micro-Epsilon with 670 nm wavelength, mid of measuring range (MMR) at 25 mm, 2 mm measurement rage, 30 nm resolution and a maximum sampling rate of 49 kHz were used [4], operated in diffuse mode without any filter nor averaging.
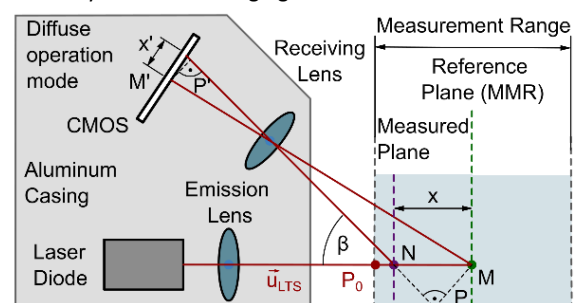

Figure 1. Laser triangulation principle in diffuse mode.

2.2. Modular frame

A modular, lightweight frame concept shown in Figure 2 was developed and additively manufactured from tool steel. Each sensor is permanently fixed in its own bracket with machined reference surfaces allowing for further use of the sensors in other measurement setups without losing their positions within the brackets. Three ceramic spheres per measurement direction are fixed on the frame. The brackets are attached to the frame with magnets that align with the ceramic spheres allowing the

sensors to be quickly assembled and repositioned with high accuracy to perform the test in different locations.

Three parallel groves perpendicular to the measuring direction with 5 mm spacing on the brackets enable measurements on bars with diameters of 10, 20, and 30 mm in diffuse mode, as shown in Figure 2. A second set of groves rotated by 10.25° on the bracket and six additional spheres on the frame allow to operate the LTS pairs in X- and Y-direction alternatively in direct reflection mode. The position of the LTS in the Z-direction is fixed and therefore only suitable for diffuse measurement mode.

Figure 2. LTS setup for measurement on a 10 mm bar in diffuse mode.

2.3. On-machine alignment procedure

To characterize the thermal behavior of a machine tool, a calibrated bar is mounted on the spindle and placed in front of the five LTSs as shown in Fig. 2, and its displacement is measured over time. However, the measured distance to the bar does not contain any information about the measurement location and therefore coplanarity of spindle axis and laser beam cannot be assumed. To describe the linear displacement signal as measurement position in the machine space, the laser beam direction vector u and the sensor's zero position P_0 at start of measuring range (SMR) must be known for each sensor. Calibration methods in the context of laser triangulation on-machine measurement technology (LTOMM) have been presented, where a calibrated sphere on the machine table is scanned with a LTS mounted on the spindle [6,7].

In this work, an incremental laser origin and direction scanning method without synchronous reading of the machine positions was developed to enable a quick installation on various machines independent on their control type. The method uses a probe-like artifact with spherical tip mounted on the machine spindle and consists of three steps: i) arc profiles of the sphere are probed on multiple positions along the laser beam; ii) a line and thus the laser beam vector u is fitted to the intersecting circles; iii) the measured distances are used to determine the origin P_0. A profile of the artifact's spherical tip, consisting of a steel sphere with a diameter of 10 mm, is probed with the laser beam by moving it along one of the two machine axes, which are quasi perpendicular to the direction of the laser beam, while recording the distance values. The measured distance profile along the sphere is a circular arc with unknown diameter due to the misalignment between the laser beam and the machine axis along which the LTS is oriented, indicated in red in Figure 3a. The measured arc profile lies in the plane spanned by the scanning direction v and the laser beam direction u. However, point I on the scanned profile, at which the smallest distance value is measured, lies in the plane that passes through the center of the sphere C perpendicular to the scanning direction v (green in Figure 3a). Thus point I is part of a circle with radius r, normal vector v and center point C, whose position is known in machine coordinates. The measurement is repeated along the second

Figure 3. Sphere profile probing principle illustrated for the laser direction in X: a) Scanning along the Y-axis; b) Scanning along the Z-axis; c) Circle set in space intersected by laser beam and probed distances to origin P_0; d) Incremental moving strategy and data analysis.

quasi perpendicular machine axis to the laser beam u, as shown in Figure 3b. With measurements at various positions i along the measuring range of the LTS, a set of circles is obtained in space which are all intersected by the laser beam, as shown in Figure 3c. This line and thus the location of the intersection points I is determined by using a best-fit where the distance of the line to the circles is minimized. The origin P_0 is determined as the mean of the intersection points I, which are shifted along the laser direction u by the measured minimum distance d_{min}.

To determine the position of the sphere centre C during the measurement without synchronous reading of the machine axis positions, the sphere is moved in incremental steps in front of the LTS. First the minimum distance position is manually determined at mid of measuring range P_{MMR} and stored for each LTS as reference point in the machine control. Subsequently, six profile measurements are taken per LTS at three different distances from P_0 along the measuring range at 0.2 mm, 1 mm and 1.8 mm using a NC-routine. For each measurement, the sphere is: *i)* placed at its starting position P_i; *ii)* moved by -1 mm in the scanning direction; *iii)* incrementally moved to +1 mm in +20 µm steps with 1 second waiting time in between; and *iv)* returned to P_i. This results in 101 measurement points per run including the starting point of the 2 mm travel, illustrated in Figure 3d. The measured distance profile is recorded. The signal is stepped while the arc is sampled over the 2 mm stretch, segmented for each sampling position, and averaged over 0.3 sec, starting at the center of the signal segment to avoid unstable areas due to the spindle movement between each sampling step using MATLAB R2022b. As the starting point P_i for each incremental profile scanning run is known in relation to P_{MMR}, the 101 distance points are assigned to the sphere position in scanning direction. By fitting a circle with unknown diameter to the points, the shortest distance d_{min} and the offset of the circle centre point to the reference point P_{MMR} in scanning direction are determined.

2.4. Continuous measurement on rotating spindle

A calibrated tungsten carbide bar is mounted on the spindle and placed at mid measurement range (MMR) in front of all five

LTSs. Spindle speed is selected to the operator's choice. The distance signals, sampled at 20 kHz, contain the oscillation resulting from the radial runout of the bar and noise due to optical effects on the bar surface. Such oscillations are canceled out by averaging the signal every 0.5 seconds, thus a data point contains multiple rotations. A resolution of 2 Hz is sufficient to characterize the thermal behavior of a machine tool.

As five points on the bar are known in space, the rotational axis of the spindle at any time instance is calculated by fitting a cylinder with 10 mm diameter to the four points measured in X- and Y-direction. The displacements in X- and Y- direction are calculated at two constant Z-heights, called L2 between Z_{Y2}, Z_{X2} and L1 for Z_{Y1} and Z_{X1}. The angular drift to the initial spindle position is calculated through the differential displacements at L1 and L2. The displacement in Z is calculated by the intersection of the rotation axis with its normal plane through the point measured in Z. This method enables continuous measurement of the spindle rotation axis instead of assuming its position.

3. Results

3.1 Thermal stability of LTS

One LTS was clamped on a granite table measuring the distance towards a granite block over 16,5 hours in a temperature-controlled environment, as shown in Figure 4a. The ambient temperature was measured by the Extech RHT20 temperature datalogger with a resolution of 0.1 K and the temperature on the sensor housing with a thermocouple logged with a NI-9213 module with a resolution of 0.3 mK. The results are shown in Figure 4b. The LTS stabilizes after a heat up phase of 2 hours and a distance offset of 10.5 μm. The decrease in the ambient temperature of 0.8°C over the remaining measurement period led to a concurrent temperature decrease on the sensor casing by 1.0°C and an increase in the measured distance to the granite block by 1.5 μm. It is considerably greater than the temperature stability of ±0.01 % FSO/K specified by the manufacturer [4], which corresponds to 0.2 μm, as it also includes the shrinkage of the measurement setup.

3.2 Direction and origin detection

The measurement setup was placed on the table of a 3-axis machine tool. The laser direction and origin were determined twice for all five LTSs according to the method described in section 2.3, labeled as run 1 (r1) and run 2 (r2). The variation in X, Y and Z of the laser origins P_0 and laser direction unit vectors u and the resulting distance d and angle α between the laser beam pairs are listed in Table 1. The maximum deviation between the two measurements is 4.7 μm and 168 arc seconds.

a)

b)
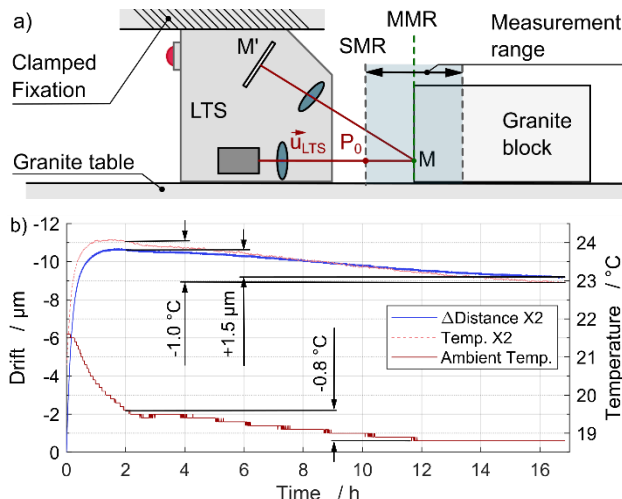
Figure 4. Thermal drift measurement of LTS X2: a) setup; b) results.

Table 1 Difference between two consecutive LTS calibration runs.

	$\Delta P_{0,x}$	$\Delta P_{0,y}$	$\Delta P_{0,z}$	d	Δu_x	Δu_y	Δu_z	α
	μm	μm	μm	μm	·10⁻⁴	·10⁻⁴	·10⁻⁴	arc sec
X1	-0.7	0.2	0.4	0.9	0.0	-0.6	3.8	78
X2	-0.6	0.6	1.5	1.7	-0.0	1.9	-1.9	55
Y1	0.4	-1.7	0.4	1.8	0.0	0.0	4.4	90
Y2	0.1	4.7	0.4	4.7	-1.3	0.0	1.3	36
Z	2.1	-1.1	-3.7	4.4	-8.1	0.6	-0.0	168

3.3 Spindle drift over time

The setup was used to characterize the spindle displacement and inclination and the efficiency of the thermal compensation strategy of a 3-axis machine tool with a C frame construction at 15000 rpm. The measurement was performed on a calibrated 10 mm carbide bar over 104 minutes with a cold spindle at the start. After 101 minutes, the compensation in Z-direction, and after 102 minutes the compensation in Y-direction were deactivated. The results are evaluated for three laser position sets, r1 and r2 and the theoretical LTS positions according to the CAD model (CAD), on which the bar position in space cannot be corrected.

The spindle displacements in X-, Y-, and Z-direction are shown in Figure 5a, the spindle inclination in XZ- and YZ-plane in Figure 5b and the difference in displacements over time compared to laser position set r2 in Figure 5c. The zero point was set to 0.75 sec, where full rotational speed was reached. However, the zero point depends on the residuals of the fit, which is highest in the first few points, which can lead to a jump in the curves at the beginning. The results for the two probed LTS position sets in space r1 and r2 agree well and their difference ($\Delta X_{1,r1}$, $\Delta X_{2,r1}$, $\Delta Y_{1,r1}$, $\Delta Y2_{,r1}$) is of the same magnitude of the residuals of the cylinder fit on the four points is space.

The correction due to the probed laser positions in space (r2) can be seen in the difference to the CAD results compensating for the errors due to off-center measurements positions on the bar to the extent of 2 μm at Y1 and 1 μm at X1 over the first 101 minutes. In this period, the results display the residuals of the machine thermal compensation strategy at 15000 rpm and after 102 minutes the uncompensated spindle position. The spindle displacement by 9 μm due to the deactivation of the compensation in Y is 1 μm less than displayed in the machine control but is only attributed to Y_{L1} and Y_{L2} when correcting for the LTS positions in space, compared to 1.8 μm in $X_{1,CAD}$ and $X_{2,CAD}$. The largest spindle displacement occurs in the Z-direction, which amounts to 19.3 μm after 101 minutes and increases to 48.6 μm after deactivating the compensation. The drop by 29.3 μm agrees well with the 29 μm displayed in the machine control. The correction in Z due to the inclination of the front surface of the bar and of centered measurement position is negligibly small. The inclination curves for the two probed LTS position sets in space r1 and r2 in Figure 5c agree well. The gradual rise of inclination in the YZ-plane α_{YZ} by 25 arc seconds is twice as large as the inclination in XZ-plane by -12 arc seconds.

4. Discussion and Conclusion

The presented setup, the measurement method and the data analysis are subject to uncertainties. The establishment of the uncertainty budget is ongoing work. The goal is to perform a spindle thermal characterization with full uncertainty budget. The most influential error contributors, specifically the ambient temperature, machine tool repositioning accuracy, sensor specific errors such as speckle noise and inclination error have been identified and are briefly discussed in the following.

The measurement setup used is subject to thermal effects. To avoid the drift during the start phase of the sensors, shown in
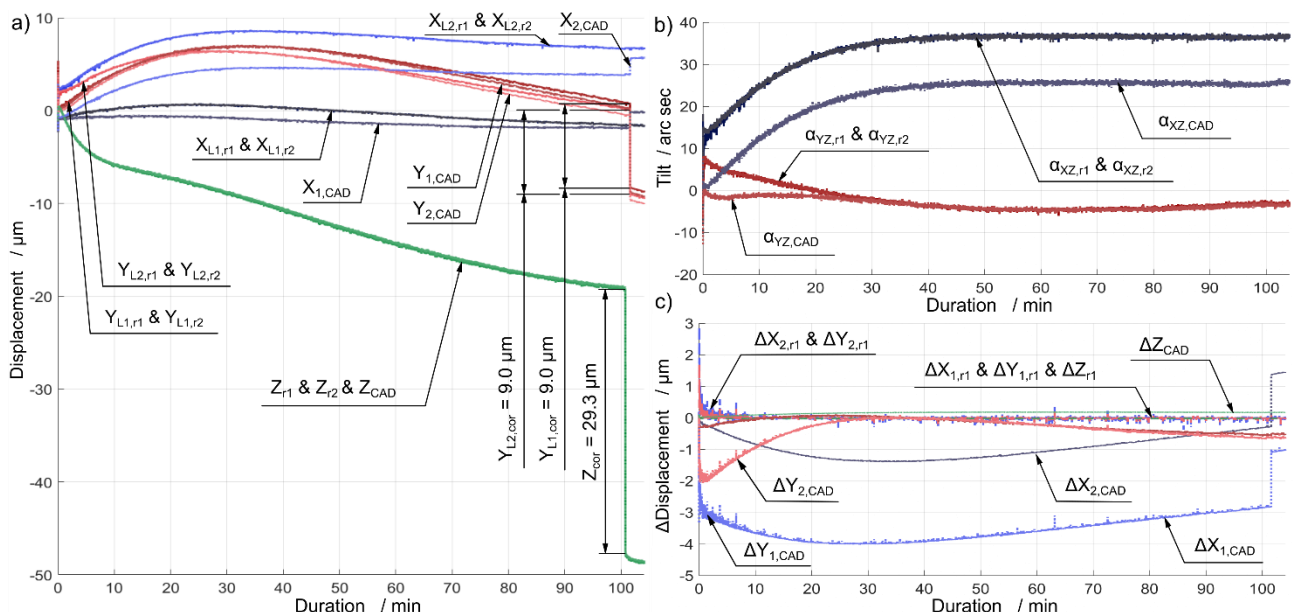
Figure 5. Thermal drift measurements of spindle displacement at 15000 rpm in relation to laser positions probed on-machine in run 1 (r1), reference run 2 (r2), and positions in the CAD-model (CAD): a) Displacements; b) Angular tilt; c) Difference of displacement values to reference run 2 (r2).

Figure 4b, the sensors must be switched on 2 hours prior to the measurements. In addition, the frame and the tool steel brackets expand when the temperature changes during the measurements. For reference, the expansion of the frame made of tool steel with a coefficient of thermal expansion (CTE) of 10 µm/(m K) [7] in X, Y, and Z for 1 K uniform temperature change is 2,1 µm, 2,4 µm, and 1,3 µm. This will be addressed in a future step where the frame will be equipped with thermocouples to continuously record the temperature during the measurement. By simulating the thermal expansion of the setup using the finite element method (FEM), from the results of which a metamodel can be derived, the deformation of the frame structure and thus the displacement of the sensors as a function of temperature can be calculated and compensated for in real time. Nevertheless, at present, great attention should be paid to temperature stability in the measuring room.

There are sensor-specific limitations to the data acquisition accuracy of LTSs. Inclination errors due to a non-perpendicular alignment of the laser beam to the inspected surface can be quantitatively calculated based on a mathematical model derived from the optical triangulation principle, the object equation of the optical path relationship and the deviation of the laser point center allowing to compensate for the error [8]. The speckle effect is a granular noise on the analyzed light spot texture degrading the signal quality of coherent imaging systems as a consequence of interference among wavefronts on surfaces [9]. This error is superimposed as noise on the signal with amplitudes depending on the object's surface topography [10], and is repeatable due to the optical interference as a result of the surface characteristics. On rotating objects, such as the calibrated bar during the presented thermal drift measurement, the repeating pattern of the speckle noise per rotation is canceled out. The influence of speckle noise on the data analysis can be further reduced by low-pass filtering of the measurement signal [7], and calibrated measurement objects with surface roughness values between 0.4 µm to 3 µm Sa [10].

A crucial part of the presented method is the assessment of the LTS alignment quality and repeatability to determine its influence on the measured quantities which despite the speckle effect is also influenced by the machine positioning accuracy. While machine tool positioning accuracy affects the estimation of the laser beam directions and thus of the spindle thermal deformation, spindle thermal compensation with an accuracy

better than the machine positioning accuracy is not required as finer displacements cannot be controlled by the machine.

The runout and speckle noise contributions are removed in the presented data analysis by averaging the sensor signal over a period of 0.5 sec containing 125 spindle rotations.

The presented frame setup has proven its viability as a robust and cost-effective solution to characterize spindle elongation in machine tools and characterization of compensation strategies according to ISO 230-3. Tests have been performed at different industrial partners in the context of the Erasmus+ project PREFAM [11], proving suitability for machine spindle thermal characterization as well as educational on-site activities.

Acknowledgement

References

[1] ISO 230-3:2007, Test code for machine tools - Part 3: Determination of thermal effects, 2007.

[2] Lion Precision Inc., Machine Tool Inspection, 2024.

[3] IBS Precision Engineering GmbH, Spindle measurement tools analyzer systems, 2024.

[6] MICRO-EPSILON MESSTECHNIK GmbH & Co. KG, Instruction Manual optoNCDT 2300, 2023.

[4] Ding, D et al., Research progress of laser triangulation on-machine measurement technology for complex surface: A review, Measurement: J of Int Meas Conf, 2023.

[5] Ibaraki S et al., Formulation of influence of machine geometric errors on five-axis on-machine scanning measurement by using a laser displacement sensor, J of Man Sci & Eng, ASME, 2015.

[7] Cverna F and Materials Properties Database Committee, ASM Ready Reference: Thermal Properties of Metals, 2002.

[8] Dong Z, Measurement of free-form curved surfaces using laser triangulation, Sensors 2018.

[9] Dorsch R G et al., Laser triangulation: fundamental uncertainty in distance measurement, 1994.

[10] Ding D et al., Error Modeling and Path Planning for Freeform Surfaces by Laser Triangulation On-Machine Measurement, IEEE Trans Instrum Meas, 2021.

[11] Phillips D. et al., The PREFAM project: towards the European framework for continuous professional development in precision engineering for advanced manufacturing, euspen ICE2021, 2021.

List of authors